Schlüsseltechnologien / Key Technologies
Band / Volume 52
ISBN 978-3-89336-833-4

JÜLICH
FORSCHUNGSZENTRUM

52

Member of the Helmholtz Association

44th IFF Spring School 2013

Quantum Information Processing

Lecture Notes

JÜLICH
FORSCHUNGSZENTRUM

Schlüsseltechnologien
Key Technologies

44th IFF Spring School 2013
Quantum Information
Processing

Lecture Notes

JÜLICH

Schriften des Forschungszentrums Jülich
Reihe Schlüsseltechnologien / Key Technologies Band / Volume 52

Forschungszentrum Jülich GmbH
Jülich Centre for Neutron Science
Peter Grünberg Institute
Institute of Complex Systems
Institute for Advanced Simulation

Lecture Notes of the
44th IFF Spring School 2013

David DiVincenzo (Ed.)

Quantum Information Processing

This Spring School was organized
by the Peter Grünberg Institute,
the Institute for Advanced Simulation,
the Jülich Centre for Neutron Science and
the Institute of Complex Systems
of the Forschungszentrum Jülich
on February 25 – March 8, 2013.

In collaboration with
universities, research institutes and industry.

Schriften des Forschungszentrums Jülich
Reihe Schlüsseltechnologien / Key Technologies Band / Volume 52

ISSN 1866-1807 ISBN 978-3-89336-833-4

Bibliographic information published by the Deutsche Nationalbibliothek.
The Deutsche Nationalbibliothek lists this publication in the Deutsche Nationalbibliografie; detailed bibliographic data are available in the Internet at http://dnb.d-nb.de.

Publisher: Forschungszentrum Jülich GmbH
JCNS, PGI, ICS, IAS
52425 Jülich
Phone +49 (0)2461 61-1739 · Fax +49 (0)2461 61-2410

Cover Design: Grafische Medien, Forschungszentrum Jülich GmbH

Printer: Schloemer + Partner GmbH, Düren

Copyright: Forschungszentrum Jülich 2013

Distributor: Forschungszentrum Jülich GmbH
Zentralbibliothek, Verlag
52425 Jülich
Phone +49 (0)2461 61-5368 · Fax +49 (0)2461 61-6103
e-mail: zb-publikation@fz-juelich.de
Internet: http://www.fz-juelich.de

Schriften des Forschungszentrums Jülich
Reihe Schlüsseltechnologien / Key Technologies Band / Volume 52

ISSN 1866-1807
ISBN 978-3-89336-833-4

Neither this book nor any part of it may be reproduced or transmitted in any form or by any means, electronic or mechanical, including photocopying, microfilming, and recording, or by any information storage and retrieval system, without permission in writing from the publisher.

Contents

Preface

A Basics of Quantum Information

A1 Origins of Quantum Information Science
D. P. DiVincenzo
A2 Introduction to Quantum Information
D. Bruß
A3 Introduction to Physical Implementations of Quantum Information Processing
S. Dürr
A4 Superconducting Qubits
W. Oliver
A5 Topics in Quantum Information
B. Kraus
A6 Spin Qubits – Introduction and GaAs quantum dots
H. Bluhm

B Solid State Qubits

B1 Quantum computing based on donor spins in silicon
L. C. L. Hollenberg
B2 Majorana Qubits
F. Hassler
B3 New Developments in Spin Qubits
L. R. Schreiber
B4 Control of Superconducting Qubits
J. M. Gambetta

C Informatics and Qubits

C1 Quantum Error Correction for Quantum Memories
B. M. Terhal
C2 Ion Traps and Quantum Simulations
E. Solano
C3 Entanglement and Exchange in Correlated Electron Systems
E. Koch
C4 Condensed Matter Applications of Entanglement Theory
N. Schuch

D Contemporary Qubits

D1 Fluxonium qubit
V.E. Manucharyan
D2 Coherent control of single spins in diamond
F. Jelezko
D3 Qubits and the New Semiconductors
G. Burkard
D4 Optical Quantum Dot Qubits
T. D. Ladd
D5 Spintronics and Emergent Qubits
T. Schäpers

Index

Preface

Quantum Information Science is a cross-disciplinary subject that has arisen in the last twenty years. It concerns itself with the consequences of our most complete description of the physical world (that is, quantum mechanics) for the reliable, secure, private, and rapid processing of information, both in communication and computation. While its invention is often ascribed to the famous theoretical physicist Richard Feynman in the 1980s, his contributions were only one of many that initiated the field around that time.

While he perceived that new types of physical devices, in which the quantum laws of superposition and entanglement function at the logical level, could give new power in the simulation of quantum physics, it was others (Bennett, Brassard) who showed that the uncertainty principle led to fundamentally more secure ways of communicating secret messages. It was yet others (Deutsch, Vazirani) who understood that quantum theory defined a new kind of Turing machine, and that not only quantum physics simulations, but potentially many other computational problems, are sped up in this machine. And it was yet another (Shor) who found a simple, very fast algorithm for prime factorization.

The word "qubit" was coined only in 1995. Its introduction is indicative of a new mindset that has developed in recent years for studying and using quantum systems. "Qubit" now stands for a durable paradigm that spans a very wide variety of fields. It thus has many sub-meanings: first, it is the basic abstract unit of information for workers ranging from optical communication engineers to NMR spectroscopists to black-hole theorists. Second, it is the name we now routinely give to physical two level systems, as they are realized by photons, atomic and ionic eigenlevels, electronic and nuclear spin, structural defects in solids, and circulating-current states of superconducting devices. Physics has long dealt with some of these two-level systems, but calling them qubits implies a whole suite of interrelated ideas and capabilities that we ascribe to these systems: the ability to precisely set, and to precisely measure, the quantum state of one unique specimen, to avoid its coupling with the environment while at the same time strongly and controllably coupling the qubits together, to exploit the resulting quantum entanglement as a resource for metrological, cryptographic, and computational tasks.

Quantum Information is a very diverse subject pursued today in many different directions, by many hundreds of researchers internationally: In theoretical physics, it has enlivened and sharpened the understanding of efficient representations of entangled many-particle wavefunctions, and has provided the prospect of applications for new concepts such as anyons and majorana fermions. Information theorists has benefitted from having a rigorous extension of the basis of their field, in which classical information theory is subsumed into a greatly broader subject. Theoretical computer scientists continue the search for new quantum algorithms, and have used quantum concepts to prove new results about the classification of computational complexity. Coding theorists have had the new and subtle problem of quantum error correction to analyse and conquer.

Most strikingly, the program of experimental physics has been influenced in many directions by Quantum Information Science. State-of-the-art optics experiments transmit quantum states over long distances and perform precision manipulations in single quanta (atomic ions, impurity spins, quantum dots) in the quest to have working quantum cyptography and quantum computing. Quantum Hall systems, and topological insulators, are being assiduously examined for new elementary excitations for use as qubits. In the course of ten years, superconducting devices have improved by over four orders of magnitude in their quantum coherence, a metric made precise by the ideas of quantum computing.

In the current stage, engineering arts such as amplifier design and analog signal processing are looking to take the stage.

Much of this points to the question that has been asked repeatedly in the last fifteen years, "when will the quantum computer be built". While the answer remains "we don't know", it is possible that the scientific developments of the last couple of years will, in retrospect, have brought us to the point that a realistic path to the development of this technology is now clear.

The 2013 IFF Spring School provides a comprehensive introduction to the important developments in Quantum Information Science. The first lectures will look at the roots of the field, which lie in the foundations of quantum theory, and require us to take a careful look at the nature and meaning of the quantum wave function. A great conceptual success in the field has been to take the philosophical concept of quantum entanglement and give it a precise, mathematical meaning. Lectures cover the calculations of distillable entanglement and their relationship to quantum channel capacity, and the use of quantum entanglement as a resource in quantum teleportation, superdense coding, and in quantum cryptography. Early on in the programme, a survey will be made of the great influence that quantum information theory has had on the course of quantum experimental science, and the outlook and criteria for making progress towards the construction of a quantum computer will be discussed. Further lectures will follow from experts active in the specialist fields of quantum bits and quantum circuits: in single-spin quantum dots, in graphene, in photonic devices, in topological insulators and other structures which incorporate Majorana fermions, and in superconducting devices. Other lectures will focus on the latest developments in entanglement theory and their application in the efficient representation and simulation of many-particle quantum systems.

Topics of the lectures include:

- The emergence of quantum information theory from quantum mechanics
- Quantum entanglement and teleportation
- Quantum Communication, error correction
- Physical implementation of Quantum Computers
- Many-body quantum simulation
- Qubits: semiconductor quantum dots
- Qubits: Josephson-junction devices
- Qubits: Trapped ions and quantum simulations
- Qubits: Majorana fermions

This school could not take place without the help and dedication of many colleagues. I acknowledge the time and effort the following colleagues spent to prepare the manuscripts and the lectures:

- ***Hendrik Bluhm**, RWTH Aachen*
- ***Dagmar Bruss**, Uni Düsseldorf*
- ***Guido Burkard**, Uni Konstanz*
- ***Stephan Dürr**, MPQ Garching*
- ***Jay Gambetta**, IBM Yorktown Heights*
- ***Fabian Hassler**, RWTH Aachen*
- ***Lloyd Hollenberg**, Uni Melbourne*
- ***Fedor Jelezko**, Uni Ulm*
- ***Erik Koch**, GRS Jülich*
- ***Barbara Kraus**, Uni Innsbruck*
- ***Thaddeus Ladd**, HRL Co. Malibu*
- ***Vladimir Manucharyan**, Harvard U.*
- ***Will Oliver**, MIT Lincoln Labs*
- ***Lars Schreiber**, RWTH Aachen*
- ***Thomas Schaepers**, FZ Jülich*
- ***Norbert Schuch**, RWTH Aachen*
- ***Enrique Solano**, UPV-EHU Bilbao*
- ***Barbara Terhal**, RWTH Aachen*

Without the participation of all these colleagues, the program would not be nearly as interesting, versatile, and attractive. I would like to express our thanks to all of them for the effort and enthusiasm that they have put into the preparation and presentation of their lectures and manuscripts. I am very grateful to the board of directors of the Forschungszentrum Jülich for its continuous organizational and financial support of this school and of this book of lecture notes. Finally, our special thanks go to Mr. M. Beißel and Ms. L. Snyders for the general management and the help in compiling this book.

David DiVincenzo February 2013

HOW'S YOUR QUANTUM COMPUTER PROTOTYPE COMING ALONG?
GREAT!
Dilbert.com DilbertCartoonist@gmail.com
THE PROJECT EXISTS IN A SIMULTANEOUS STATE OF BEING BOTH TOTALLY SUCCESSFUL AND NOT EVEN STARTED.
4-17-12 ©2012 Scott Adams, Inc./Dist. by Universal Uclick
CAN I OBSERVE IT?
THAT'S A TRICKY QUESTION.

A 1 Origins of Quantum Information Science[1]

David P. DiVincenzo
Peter Grünberg Institut
Forschungszentrum Jülich GmbH

Contents

1 What is Quantum Information Science? 2

2 Pioneers of Quantum Information Science 3

3 Postscript: the 2012 Nobel Prize in Physics 11

[1]Lecture Notes of the 44^{th} IFF Spring School "Quantum Information Processing" (Forschungszentrum Jülich, 2013). All rights reserved.

1 What is Quantum Information Science?

In this volume you will learn a great deal about current developments in Quantum Information Science. I would like first to define the term, since it didn't exist, with its current meaning, fifteen years ago. The term tries to convey the idea that an entirely new field has been created (or, more accurately, is in the making) that, while it has strong affinities to Physics, Informatics, Computer Engineering (and, less obviously, to pure Mathematics, to Electrical Engineering, Materials Science, and Chemistry), it can stand as its own subject. As the title of this school we use the related phrase *Quantum Information Processing* (QIP), because there is a strong emphasis here on the devices that will manipulate quantum information. Beware: QIP is also the title of one of the longest-running series of international conferences in this field, but the QIP conferences have evolved to mainly cover the specialty of theoretical quantum computer science.

I have already used a few additional phrases worth noting. *Quantum information* is, one might say, the descriptor of the raw material of the subject, the stuff that is actually processed or communicated. *Theoretical quantum computer science* concerns itself with rigorous formal properties of quantum information; but, the acronym QCS is in use in the USA as the name of a major national research program that is oriented towards rather more practical computer science issues. *Quantum Computing* is sometimes used as a generic phrase for the whole field, but is more properly reserved for the part of the field concerned with the implementation of *Quantum Algorithms*, a central but in fact quite difficult specialty in the field. *Quantum Communications* and *Quantum Cryptography* are two more terms that are more-or-less self defining.

Returning to Quantum Information Science itself, it is worth quoting in full a carefully thought out definition that was created in a workshop with this name sponsored by the National Science Foundation of the United States in 1999[1]:

Quantum information science (QIS) is a new field of science and technology, combining and drawing on the disciplines of physical science, mathematics, computer science, and engineering. Its aim is to understand how certain fundamental laws of physics discovered earlier in this century [20th] can be harnessed to dramatically improve the acquisition, transmission, and processing of information.

You will hear in this school our progress in achieving these dramatic improvements. Indeed, it must be admitted that we still have not built the quantum computer, or anything other than the most rudimentary quantum communications system. The things we have achieved in this new science are less tangible, but arguably more profound. Here is my personal list of present-day successes of QIS:

New ways have arisen of teaching and learning the quantum theory. Many computer science curricula include lectures in quantum theory today, something that was almost unheard of and unthinkable fifteen years ago. This shows that quantum mechanics is more than what its originators thought it was: it is a theory of knowledge, a theory of the transformations of information, in addition to its being a theory of matter and energy. Lectures in theoretical physics are also gradually adopting both these points of view. On the research side, it has enlivened discussions of what the quantum world is (does quantum mechanics require many worlds) and what it could be (there is a theory called quantum boxes, which is like quantum theory but is even more nonlocal in the correlations are possible between separated systems).

A mathematically sophisticated and rigorous information theory has been developed around quantum mechanics. This refers to specific technical developments that have been decisively influenced by QIS concepts. I have two rather different things in mind here: first, the highly

developed entropic characterizations of quantum properties and protocols that have arisen in a large literature. They are natural outgrowths of the reasoning introduced by Shannon in communication theory; a great variety of "Shannon entropies" are used to quantify a large number of things, for example, the carrying capacity of a noisy qubit channel. Second, there is a surge of interest in QIS in the areas of quantum gravity and astrophysics. I am not competent to comment in any detail about these developments, but evidently quantum entanglement has been a very useful concept in making more sense of Hawking radiation, and about the question of whether information is truly lost in a black hole. This seems to be still going strong, as you could read in a current semi-popular account of "firewalls" in black holes[2].

We have a new mindset for discussing quantum experiments. QIS has defined a set of metrics that we apply confidently and profitably to experiments from many different fields of experimental quantum physics and chemistry. We can talk about process fidelities, leakage rates, and decoherence times for experiments from a vast range of fields – nuclear magnetic resonance, quantum dots, ion traps, or optical lattices. We have both a good grasp of the fundamentals of this work, and we have a reasonably accurate assessment of how there different systems progress towards achieving real quantum information processing. In some fields, QIS has completely turned around the idea of what is interesting. In the 1980s, it was fashionable in quantum dot research to design experiments to see how *fast* the relaxation times could be made. Since the advent of QIS, we have recognized that it is also scientifically interesting for these experiments to investigate how *slow* relaxation can be. Slow is good, if what is slow is decoherence.

Quantum experiments have gone in entirely new directions. Building a quantum computer is really hard, in the 1990s we realized that, despite a century of remarkable advances, we had only taken the first baby steps towards such a machine. This has motivated experiments to tackle quantum phenomena in a remarkably ambitious new way. We had to think about ion traps, not just for studying single ions, but for large arrays of ions that could be shuttled around, recooled, and coupled at will. This exciting science would not have happened without QIS. In quantum dot research, we have achieved not only one-by-one control of trapped electrons, not only precise temporal control of exchange couplings, not only exquisite control of the nuclear spins in the crystal lattice, not only intricate coherence-recovery protocols, not only precise and accurate in-place quantum measurements, but all of these things together in a single complex device. In superconducting devices, we have gone in ten years from the barest hint of quantum coherence to fidelities that rival those in atomic systems, with designed-to-order qubits with tailored coupling networks on the way. Experiments in this area are now driven explicitly by architectural ideas for a fault-tolerant quantum computer.

In the remainder of this introductory chapter, I will tell the story, as I have seen it and reconstructed it, of how we got to where we are. Of course, a tale of personalities, as I will tell it, is intrinsically limited. It does not by itself convey the detailed implications of the discoveries, and it is certainly very unfair to the large number of other persons that took part in these developments and played many different roles, major and minor, in moving them along.

2 Pioneers of Quantum Information Science

How did QIS happen?

The inventors of modern quantum theory in the 1920s certainly did not think of a quantum computer. It would have been anachronistic for them to have done so: it should be recalled that the whole notion of an automatic computing device barely existed at the time. Also, the

(a) Erwin Schrödinger. (b) Rolf Landauer.

Fig. 1: *Schrodinger clarified the ideas of correlations as introduced, by Einstein, Podolsky, and Rosen, introducing the notion of quantum entanglement. Landauer articulated ideas of the information-carrying capacity of physical systems.*

concept of the ”bit” was hardly in use – such mechanical calculators as existed in those times implemented base-10 arithmetic in their gearworks, rather absurdly imitating human calculating hardware. But there was a further reason why the first generation of quantum theorists did not think about quantum computers: being just barely understood for the first time, quantum theory was only comprehended as a special theory of the very small – nuclei, electrons, molecules, the smallest quanta of light. The idea that one could manufacture something that intentionally followed chosen features of the quantum theory was utterly foreign to them. Thus, even when there arose a next wave of scientists like von Neumann and Turing, both at the forefront of new developments in computing machines and quite aware of current developments in quantum mechanics, the connection of information processing and quantum theory was barely made.

I say “barely” because there was a significant intellectual stir triggered in 1935 by the publication of the paper of Einstein, Podolsky, and Rosen[3] (EPR), which put into print the misgivings that Einstein had had for many years about quantum theory. This paper featured the strangeness of correlations between two observers sharing parts of a quantum state, which convinced Einstein that quantum theory was incorrect or incomplete. Others were not convinced. Of all the popular and scholarly reaction in 1935 to the EPR paper, in my opinion the most relevant and interesting from our current perspective is that of Schrödinger (Fig. 1(a)), in a set of immortal papers in 1935-6[4]. Schrödinger gave us the name for correlations in quantum states that we still use in English and in German (entanglement/Verschränkung). Schrödinger accepted quantum theory, and accepted that it was very weird – he famously gave us his Cat in these papers. Famous as they are, I think that these papers deserve to be more famous. In the technical side, he develops the relation of mixed quantum states and the pure states from which they must arise – the work presages by many decades the Uhlmann theorem that you will learn in quantum

(a) Alexander Holevo.

(b) Yuri Manin.

Fig. 2: *Earliest contributors in the U.S.S.R. to quantum information.*

information theory. He rather poetically expresses himself about quantum measurement, thus: *Es ist ein Unterschied zwischen einer verwackelten oder unscharf eingestellten Photographie und einer Aufnahme von Wolken und Nebelschaden./ There is a difference between a shaky or out-of-focus photograph and a snapshot of clouds and fog banks.* A modern, technical translation would run: there is a difference between a weak quantum measurement on a pure quantum state and a strong quantum measurement on a mixed state. This insight is very central to what you will learn in quantum information theory about measurement.

Schrödinger, in his discussion of entanglement and how it is created by interaction and then separation of two subsystems, in fact gives us the rudiments of a theory of communication with quantum systems. There was perhaps only one other instance of an information-theoretic argument in physics before this, in the discussion of the paradox of the Maxwell demon, for example, in the Habiltationschrift of Szilard[5]. In fact, both Schrödinger's entanglement and Szilard's engine played some role in the next few steps in the development of quantum information theory, as we will now see.

These developments were, however, a long time in coming. From the 1930s to the 1960s, practitioners of quantum science were solving momentous practical problems at a furious pace, and there was not very much room for "philosophy". Computer science underwent tremendous development in those times, the classification of the hardness of mathematical problems from an algorithmic perspective was well underway; and, of course, we became comfortable with the concept of the "bit". Two contributors in quantum physics in those times are worth mentioning: David Bohm, in the midst of many practical contributions to quantum mechanics, pointed out the canonical example of entanglement of two qubits that we use today, states like $(|00\rangle + |11\rangle)/\sqrt{2}$, loosely called "EPR pairs". The role of the other worker, John Wheeler, is a little harder to pin down. It is clear that in this period, Wheeler became convinced that quantum theory was some sort of information science. We have from this period his catchphrase, "it from bit"[6]. His influence on QIS becomes much clearer in a later period, in the group of other scientists with whom he surrounded himself.

In 1961 Rolf Landauer (Fig. 1(b)) ushered in the contemporary period of the physics of information with his article[7] on heat generation in computing. His $k_B T \ln 2$ formula for dissipated

(a) Steven Wiesner. (b) Charles H. Bennett.

Fig. 3: *Seminal American contributors to quantum information.*

energy per logical operation, an important milestone today in digital computing, was understood to come from the *discarding* of logical information during the performance of boolean logic operations. The refinement of this understanding in the following decade[8] was crucial in the acceptance of quantum mechanics as a valid platform for a computing theory.

The discovery by John Bell of his inequalities in 1964 [9] gave an entirely new motivation for doing quantum experiments. He showed that classes of non-quantum physical theories could be straightforwardly ruled out by the measurement of correlations of entangled, separated quantum particles. The experiments that resulted (e.g., [10], and especially later [11]) were clear forerunners of experiments done today in quantum communication; they evolved towards much more reliable and copious sources of EPR quantum states, in the form of photon pairs created by spontaneous downconversion [12]. A very readable, semi-technical account of these developments may be found in [13]. In fact, even more powerful physical resources for the implementation of quantum computation were gestating in these times: see my Postscript to this chapter.

While much had happened up to the year 1970, no one at that time recognized any trend in the making. The developments of the next decade were still isolated; but we see in them the seeds from which the current trends clearly sprang up.

A singular individual in the Soviet Union invented the modern, rigorous information-theoretic treatment of quantum channels. This was Alexander Holevo (Fig. 2(a)), whose "Bounds for the Quantity of Information Transmitted by a Quantum Communication Channel [14] in 1973 ushered in the application of Shannon entropies the quantum questions. First Holevo, and very gradually others, added to this corpus of ideas, which is a large and flourishing area of analysis today.

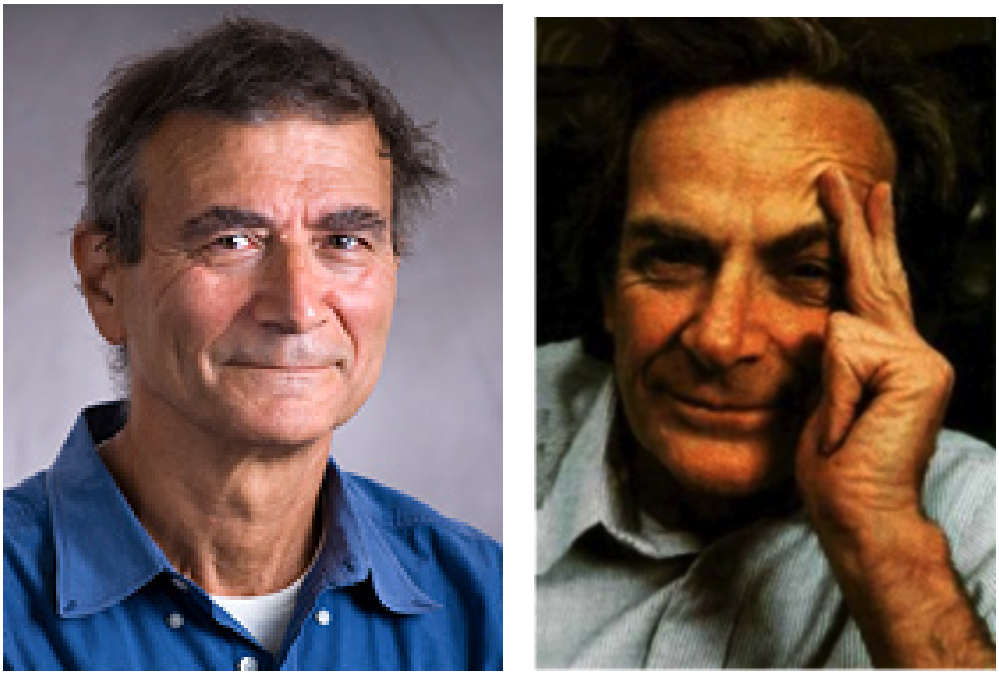

(a) Tomasso Toffoli. (b) Richard Feynman.

Fig. 4: *These two contributed essential ideas to quantum computing in the early 1980s.*

Even more isolated was the advent of Steven Wiesner's observations (Fig. 3(a)) on "conjugate coding" – the potential applications of preparing and measuring a two-state quantum system in one of two bases defined by non-commuting operators. Wiesner was quite serious and explicit in using this feature of quantum mechanics for cryptographic purposes, he immediately conceived of the possibility of money that could not be counterfeited. It would perhaps not be useful to date his contribution to around 1970, as it was known to hardly any other person at that time, appearing in publication only in 1983 [15]. But, crucially, Wiesner's ideas were well known and appreciated by his University classmate Charles Bennett (Fig. 3(b)), who will figure prominently in the remainder of this history. In the following 25 years Bennett worked very effectively to make Wiesner's concepts known, and to greatly extend them to produce some of the best-known discoveries in QIS.

Independent of Wiesner's ideas, Bennett in 1973 contributed his revolutionary correction [16] to Landauer's arguments about the energy consumption in computing, by showing that there is *no* lower limit on how little heat needs to be dissipated during the computational process; Landauer's $k_B T \ln 2$ is avoided by efficiently eliminating the need to erase workspaces. This discovery of *reversible computation* initially had no impact on quantum research – but by the time of Bennett's review of the subject in 1982 [17] it had begun to. In the meantime, Bennett's result, which had been formulated for the Turing machine model of computation, was extended to the logic-gate model of computation in a series of papers by Toffoli (see Fig. 4(a)) and Fredkin [18]. Toffoli's gate was his concept for an all-purpose Boolean logic gate that could perform the logical OR or the logical AND as desired, and would be reversible – the inputs could be reconstructed from the outputs. In its minimal form, as everybody today knows, it involves three bits. But it is only known to us as the "Toffoli gate" on account of Richard Feynman (Fig. 4(b)).

Feynman had been speculating about the physics of the very small for a long time; his 1959

Fig. 5: *The group of John A. Wheeler attending the NATO Advanced Study Institute on Quantum Optics and Experimental General Relativity, held August 16-29, 1981, in Bad Windsheim, Bavaria, Federal Republic of Germany. Left to right are William Wootters (see Fig. 7), Kip Thorne, Wheeler, Wojciech Zurek, and William Unruh.*

speech "There's Plenty of Room at the Bottom" [19] is considering a founding manifesto of the field of nanoscience. He connected his own thoughts about quantum physics with his recent awareness of the work of Landauer, Bennett and Toffoli to put in print in 1982[20], for (almost) the first time, the phrase *quantum computer*, and some (but not all) of the thoughts that we associate today with this phrase. I say "almost" because our Russian friends tell us that the well known mathematician Yuri Manin (Fig. 2(b)) made some reasonable speculations about the idea of a quantum computer in 1980 [21]. I have never seen this reference, and I don't believe it has been read outside the Russian community. Feynman's vision of a quantum computer arose from his understanding that determining the properties of many-particle quantum systems is computationally intractable; thus he introduced the quantum computer as a computer simulator. In his only follow-up to his 1982 work[22], Feynman groped towards a more definite model for the quantum computer, which he built as an extension of the idea of reversible computing, quantum evolution being a more general version of reversible dynamics. It was in this work that he gave the world Toffoli's name for the three-bit logic gate. But Feynman's final work was also notable for the crucial element that he (and others like Benioff) missed: he failed to recognize that *entangled* quantum states, and entangling logic gates, would be crucial for the real quantum aspects of this new computer. This lack was made up in the next seminal work towards quantum computation.

Before getting to this, I might mention that the set of papers I have been citing from 1982, in the International Journal of Theoretical Physics, were all written for a conference, on "The Physics of Computation" held at MIT in May, 1981. There were about 60 participants, including Bennett, Feynman, Fredkin, Landauer, and Toffoli, as well as others like Dyson, Büttiker, Greenberger (of the Greenberger, Horne, Zeilinger (GHZ) state), and prominent computer ar-

(a) David Deutsch. (b) Peter Shor.

Fig. 6: *The workers who began and completed the revolution in quantum algorithms.*

chitects Hillison and Cocke. One should not get the impression that quantum computing then became a large-scale enterprise; the conference was not repeated until about a dozen years later. Important developments began to occur with some regularity, but I can think of no quantum information papers in 1983 or in 1987. But these were perhaps the last years for which this could ever be said.

Not present at the 1981 conference, but soon to contribute decisively to further developments, was the active group around Wheeler at that time; Fig. 5 shows part of his group then. Two of those pictured, Wootters and Zurek, gave the essential formal underpinning for the Wiesner ideas, which were just beginning to be known to a wider circle. They proved (as Dieks did independently at the same time) that a single, unknown quantum state cannot be copied, or "cloned" [23]. This work provided a simple physical insight into why quantum systems could be interesting for cryptography, where privacy is of paramount importance. Bennett had been continuing to follow up on Wiesner's concepts, culminating in the announcement in 1984, with cryptographer Gilles Brassard (see Fig. 7), of a full protocol for distributing keys for secret message transmissions, as well as secure, remote coin tossing[24]. Even at this juncture, it was still some years before "BB84" was a widely known concept.

The next, and perhaps *the*, decisive step in the further articulation of the quantum computer came also indirectly out of the Wheeler group. Another member of the group in Texas shortly after the time of Fig. 5 was David Deutsch (Fig. 6(a)), who came on a postdoctoral fellowship from Oxford. Deutsch's 1985 paper [25] took the crucial step of generalizing Bennett's reversible computing to the quantum case, taking the step which had eluded Feynman. Working with Bennett's original reversible Turing machine approach, Deutsch makes a small change to its definition; this change permits the bits of the machine to evolve into entangled states. He exhibits a Turing machine program for the "EPR experiment". Further, he points out that the equivalence concept that had developed in computer science at that time, that all reasonable physical implementations of a computing device had the same scaling of efficiency up to "small" polynomial factors, would in all likelihood not apply to his simple quantum generalization. The quantum computer would be in a different complexity class. In this paper Deutsch is silent on the connection that his discovery had to ideas in the Texas group, but one tiny detail

Fig. 7: *The discoverers of quantum teleportation; photo taken c. 2004, 11 years after the discovery. Left to right: Gilles Brassard, Richard Jozsa, William Wootters (see Fig. 5), Claude Crepeau, Charles Bennett (see Fig. 3), and Asher Peres.*

gives it away: he acknowledges grant PHY8205717, which a short investigation reveals to be Wheeler's National Science Foundation grant in the early 1980s.

Deutsch's follow up in 1989 [26] took several more giant steps, and put the field irrevocably on that track that it has gone on ever since. This paper introduced the circuit model of quantum computing that we are most familiar with today, provided us with the notion of a universal set of quantum gates (he gave a simple generalization of the three-bit Toffoli gate – simpler universal sets came later), discussed the controlled NOT gate and its roles in producing entanglement and performing noninvasive quantum measurements. Finally, it reinforced the notion of his 1985 paper of quantum computing being in a different class from ordinary computation, by introducing a problem for which a quantum algorithm provably took fewer steps than on any classical machine! This algorithm was "useless" in itself, but was revolutionary in what it made possible.

Indeed, the timeline from Deutsch's toy algorithm to Peter Shor's (Fig. 6(b)) renowned factoring algorithm was, by the standards of the rest of this history, very fast and sure. (I will not give a reference, since the student can find this in any textbook.) Also, a much wider circle of workers soon came into the picture. The Deutsch-Jozsa algorithm (1992) [27] was followed by the Bernstein-Vazirani algorithm from Berkeley workers (1993) [28], followed within months by the Simon algorithm (Montreal, 1994) [29]. Shor's work at Bell labs came a few months afterwards. I will not take my story into this era; the prehistory of QIS, at this point, was complete. To say that the discovery of the factoring algorithm was inevitable once Deutsch's algorithm came to light perhaps has some truth to it, but it unfairly minimizes the great innovations of these five years, and Shor's remarkable synthesis of the ideas of others with sophisticated knowledge of the structure of integer factoring.

It should also not be understood that the only activity of the time was the advancement of quantum algorithms. In fact, the founding ideas of QIS were being developed on many fronts by the early 1990s. I will not tell the story of the considerable insights of quantum cryptography, of the further innovations in quantum communication theory, in the developing concepts in quantum measurement and in quantum decoherence, and the fortuitous dramatic improvements in the manipulation of single quanta in the lab (but see Postscript), that occurred in these few years. Wootters and Schumacher coined the term *qubit* in this time period. I must say a word, however, about quantum teleportation [30] (Fig. 7), which was a synthesis of many ideas that I have been mentioning: EPR states as a kind of communication channel, the conjugate bases of Wiesner, quantum logic circuits, and entangling quantum measurements. Within a few years quantum teleportation entered quantum computer theory in a big way, as a predecessor of quantum error correcting codes and fault tolerant quantum computing; of course, in many ways, this 1993 paper has become an iconic representative of our entire field.

After 1994 the field took on a different character, with the involvement, in succession, of many additional communities in theoretical and experimental physics. Much of our school will concentrate on a rather later wave, the advent of solid state devices as high-quality qubits. With scarcely an hour going by without a new paper appearing on some aspect of QIS, it is clear that the telling of the post-1994 history is a very much harder job than the one I have done in my story of the pioneers of the field.

3 Postscript: the 2012 Nobel Prize in Physics

After the construction of the above history, the 2012 Nobel Prizes for Physics were announced. While the laureates Serge Haroche and David Wineland (Fig. 8) did not figure in my discussion, they are in fact the outstanding representatives of one of the important specialties that got pulled into the QIS orbit almost immediately after the advent of Shor's factoring algorithm. While Bell's work in the 1960 had already caught the attention of the quantum optics community, and downconverted photon pairs became a readily available resource for simple experiments on entanglement, workers like Haroche and Wineland progressed to qualitatively more powerful control of single quantum systems. As we will hear in this school, they worked on controlled entanglement and measurement, Haroche using Rydberg states (highly excited states) of atoms passing through microwave cavities, Wineland using vibrational and other states of individual ions in Paul-style traps.

I am delighted and proud that the Nobel Committee had honored their outstanding work, and that it has seen fit to present their work to the public in the language of its contributions to the further development of Quantum Information Science.

Haroche and Wineland did not work on qubits or quantum gates – the terms had not been invented in the 1980s when they began their work. But by the mid-90s, their systems became prime testing ground for the new ideas from QIS. Haroche, especially, was not an unabashed supporter of quantum information concepts at that time; he wrote a commentary entitled "Quantum Computing: Dream or Nightmare" [31]. But he engaged in serious and fair debates on the future of our subject at that time, being an especially spirited participant in the discussions at the end of our Program on Quantum Computing at the Institute for Theoretical Physics (now Kavli) at Santa Barbara in 1996. I would like to end by quoting Preskill's final remarks during that debate, as set down in his written lecture notes of the time[32]:

Serge Haroche, while a leader at the frontier of experimental quantum computing, continues

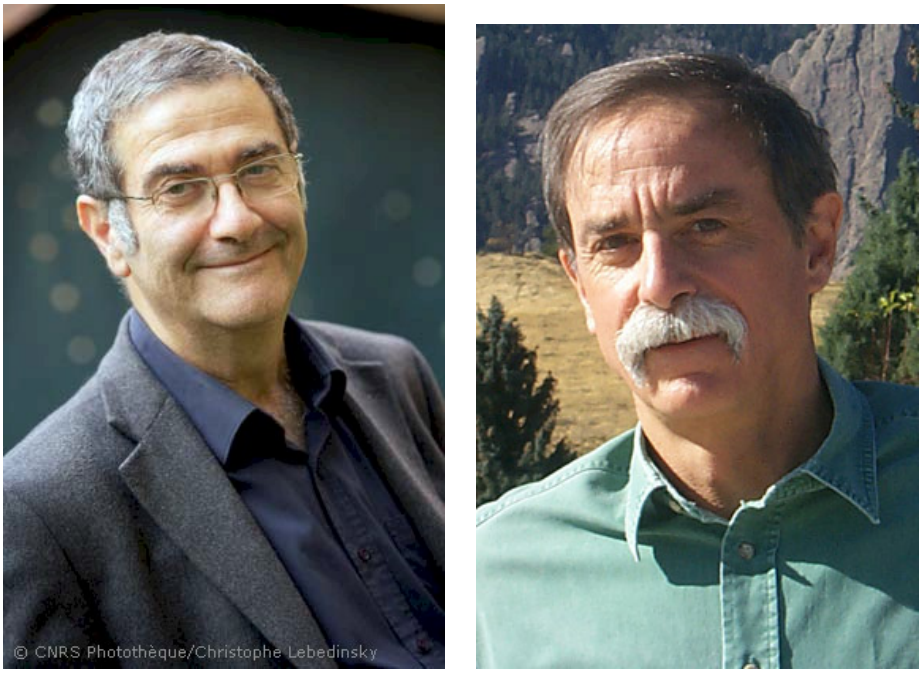

(a) Serge Haroche. (b) David Wineland.

Fig. 8: *Nobel laureates in physics for 2012: they are experimentaists who brought single quanta under control in atomic physics in the 1980s.*

to deride the vision of practical quantum computers as an impossible dream that can come to fruition only in the wake of some as yet unglimpsed revolution in physics. As everyone at this meeting knows well, building a quantum computer will be an enormous technical challenge, and perhaps the naysayers will be vindicated in the end. Surely, their skepticism is reasonable. But to me, quantum computing is not an impossible dream; it is a possible dream. It is a dream that can be held without flouting the laws of physics as currently understood. It is a dream that can stimulate an enormously productive collaboration of experimenters and theorists seeking deep insights into the nature of decoherence. It is a dream that can be pursued by responsible scientists determined to explore, without prejudice, the potential of a fascinating and powerful new idea. It is a dream that could change the world. So let us dream.

References

[1] "Quantum Information Science: An Emerging Field of Interdisciplinary Research and Education in Science and Engineering," Report of the NSF Workshop, October 28-29, 1999, Arlington, Virginia, http://www.nsf.gov/pubs/2000/nsf00101/nsf00101.htm; An update of this can be found in "Quantum Information Science," Report of the United States National Science and Technology Council Workshop, 23-25 April 2009, Tysons Corner, Virginia, http://calyptus.caltech.edu/qis2009/QIS-Workshop-Report-1-July-2009.pdf.

[2] J. Polchinski, "Black Holes, Complementarity, and Firewalls," http://blogs.discovermagazine.com/cosmicvariance/2012/09/27/.

[3] A. Einstein, B. Podolsky, N. Rosen, "Can quantum-mechanical description of physical reality be considered complete?," Phys. Rev. **47** (1935), 777 - 780.

[4] Erwin Schrödinger, "Die gegenwärtige Situation in der Quantenmechanik," Naturwissenschaften **48**, pp. 807-812; **49**, pp. 823-828; **50**, 844-849 (1935); "Discussion of probability relations between separated systems," Proceedings of the Cambridge Philosophical Society, **31**, (1935), 555-563; "Probability relations between separated systems," *ibid.* **32**, (1936), 446-452.

[5] Leo Szilárd: "Über die Entropieverminderung in einem thermodynamischen System bei Eingriffen intelligenter Wesen." Zeitschrift für Physik **53** (1929), pp. 840 - 856.

[6] This may be seen in much later writing, e.g., John A. Wheeler, "Hermann Weyl and the Unity of Knowledge," American Scientist, Vol. 74, July-August 1986, pp. 366-375.

[7] Rolf Landauer, "Irreversibility and heat generation in the computing process," IBM Journal of Research and Development, **5**, pp. 183-191 (1961).

[8] see Rolf Landauer, "Information is Physical", Physics Today, **44**, no. 5, p. 23 (May 1991).

[9] J. S. Bell, On the Einstein-Podolsky-Rosen paradox, Physics (Long Is. City, N. Y.) **1**, 195-200 (1964).

[10] Stuart J. Freedman and John F. Clauser, "Experimental Test of Local Hidden-Variable Theories", Phys. Rev. Lett. **28**, 938-941 (1972).

[11] Alain Aspect, Phillipe Grangier, and Gérard Roger, "Experimental Tests of Realistic Local Theories via Bell's Theorem," Phys. Rev. Lett. **47**, 460 (1981).

[12] Paul G. Kwiat, Klaus Mattle, Harald Weinfurter, Anton Zeilinger, Alexander V. Sergienko and Yanhua Shih, "New High-Intensity Source of Polarization-Entangled Photon Pairs," Phys. Rev. Lett. **75**, 43374341 (1995).

[13] Louisa Gilder, *The Age of Entanglement: When Quantum Physics Was Reborn* (A. A. Knopf, New York, 2008).

[14] A. S. Holevo, "Bounds for the Quantity of Information Transmitted by a Quantum Communication Channel, Probl. Peredachi Inf., **9**:3 (1973), 311; "On the capacity of quantum communication channel," Probl. Inform. Transm. **15**, 3-11 (1979).

[15] S.J. Wiesner, "Conjugate Coding", SIGACT News **15**:1, pp. 7888, 1983.

[16] C. H. Bennett, "Logical reversibility of computation," IBM Journal of Research and Development, **17**, no. 6, pp. 525-532 (1973).

[17] Bennett, C. H. (1982). "The thermodynamics of computation – a review". International Journal of Theoretical Physics **21** (12): 905940.

[18] T. Toffoli, "Computation and Construction Universality of Reversible Cellular Automata," J. Computer and System Sciences, **15**:2 213-231 (1977); T. Toffoli, "Reversible Computing," Laboratory of Computer Science Report MIT/LCS/TM-151 (MIT, February 1980);

T. Toffoli: "Bicontinuous Extensions of Invertible Combinatorial Functions." Mathematical Systems Theory, **14**, 13-23 (1981); E. Fredkin and T. Toffoli, "Conservative Logic", International Journal of Theoretical Physics **21**, Numbers 3-4 (1982), 219-253.

[19] R. P. Feynman, "There's plenty of room at the bottom," Caltech Engineering and Science, **23**:5, February 1960, pp 22-36.

[20] Feynman, Richard (1982). "Simulating Physics with Computers". International Journal of Theoretical Physics **21** (67): 467488.

[21] Yu. Manin, "Computable and Uncomputable" (in Russian), Sovetskoye Radio, Moscow (1980).

[22] Richard P. Feynman, "Quantum Mechanical Computers," Optics News **11**(2), 11-20 (1985).

[23] W.K. Wootters and W.H. Zurek, "A Single Quantum Cannot be Cloned," Nature **299** (1982), pp. 802803; D. Dieks, "Communication by EPR devices," Physics Letters A **92** (1982) 271272.

[24] C. H. Bennett and G. Brassard, Quantum Cryptography: Public key distribution and coin tossing, in Proceedings of the IEEE International Conference on Computers, Systems, and Signal Processing, Bangalore, p. 175 (1984).

[25] Deutsch, David (July 1985). "Quantum theory, the Church-Turing principle and the universal quantum computer". Proceedings of the Royal Society of London A **400**: pp. 97117.

[26] Deutsch, D.: "Quantum computational networks." Proceedings of the Royal Society of London A **425**, 7390 (1989).

[27] David Deutsch and Richard Jozsa (1992). "Rapid solutions of problems by quantum computation." Proceedings of the Royal Society of London A **439**: 553.

[28] E. Bernstein and U. Vazirani, "Quantum complexity theory," in Proc. 25th Annual ACM Symposium on Theory of Computing, ACM, New York, 1993, pp. 11-20.

[29] D. Simon, "On the power of quantum computation," in Proc. 35th Annual IEEE Symposium on Foundations of Computer Science, IEEE Press, Piscataway, NJ, 1994, pp. 116-123.

[30] Bennett C H, Brassard G, Crepeau C, Jozsa R, Peres A and W K Wootters 1993 "Teleporting an unknown quantum state via dual classical and EPR channels," Phys. Rev. Lett. **70** 1895-1899.

[31] Serge Haroche and Jean-Michel Raymond, "Quantum Computing: Dream or Nightmare?" Physics Today **49**(8), p. 51 (1996).

[32] John Preskill, "Quantum Computing: Pro and Con," Proc. Roy. Soc. Lond. **A454** (1998) 469-486 (quant-ph/9705032).

A 2 Introduction to Quantum Information [1]

Dagmar Bruß
Institut für Theoretische Physik III
Heinrich-Heine-Universität Düsseldorf, Germany

Contents

1 Fundamental concepts in quantum mechanics and in information processing 2
1.1 Schrödinger equation and unitary time evolution 2
1.2 Pure versus mixed quantum states 2
1.3 Measurements 4
1.4 Some basic information theoretic quantities 6

2 Basic notions in quantum information 8
2.1 Qubits 8
2.2 Composite quantum systems and entanglement 10
2.3 The no-cloning theorem 15
2.4 Entanglement as a resource 16

3 Models of quantum computation 17
3.1 Quantum gates and the circuit model 17
3.2 One-way quantum computing 21

4 Quantum channels and quantum noise 24

[1] Lecture Notes of the 44^{th} IFF Spring School "Quantum Information Processing" (Forschungszentrum Jülich, 2013). All rights reserved.

Quantum information processing, science of:
The theoretical, experimental and technological areas covering the use of quantum mechanics for communication and computation.

Encyclopedia of Mathematics, Springer

1 Fundamental concepts in quantum mechanics and in information processing

1.1 Schrödinger equation and unitary time evolution

In the Schrödinger picture, the quantum state of a system, fully described by the vector $|\psi\rangle$, which is an element of a Hilbert space $\mathcal{H}$, evolves with time. The equation describing the time evolution of a quantum state is the Schrödinger equation:

$$\hat{H}\,|\psi(t)\rangle = i\hbar\frac{\partial\,|\psi(t)\rangle}{\partial t}, \tag{1}$$

where $\hat{H}$ is the Hamilton operator. The formal solution of eq. (1) is

$$|\psi(t)\rangle = \hat{U}(t)\,|\psi(0)\rangle\,, \tag{2}$$

where $\hat{U}(t)$ is the time evolution operator, which for the case of a time-independent Hamiltonian is given by

$$\hat{U}(t) = e^{-i\frac{\hat{H}t}{\hbar}}. \tag{3}$$

The time evolution operator in eq. (3) is *unitary*, i.e.

$$\hat{U}(t)\hat{U}(t)^\dagger = \hat{U}(t)^\dagger\hat{U}(t) = \mathbb{1}. \tag{4}$$

This property follows directly from the fact that $\hat{H}$ is Hermitian, i.e. $\hat{H}^\dagger = \hat{H}$. The unitarity of the time evolution of quantum states is a fundamental property that is widely used in quantum information processing: as we will see, quantum gates consist of the action of a suitable Hamiltonian for an appropriate time and can be represented as unitary matrices. Thus, quantum gates are *reversible*, in contrast to classical gates. Note also that unitary operations preserve the scalar product of two quantum states $|\psi\rangle$ and $|\phi\rangle$, as $\langle\psi(t)|\,\phi(t)\rangle = \langle\psi(0)|\,\hat{U}(t)^\dagger\hat{U}(t)\,|\phi(0)\rangle = \langle\psi(0)|\,\phi(0)\rangle$.

1.2 Pure versus mixed quantum states

A *pure quantum state* $|\psi\rangle$ can be represented by a vector in a Hilbert space $\mathcal{H}$. Let us denote a complete orthonormal set of basis vectors as $\{|n\rangle\}$ (which may e.g. correspond physically to the eigenstates of a Hamiltonian $\hat{H}$). Completeness means that it is possible to expand the identity into a sum of projectors onto the eigenstates $P_n = |n\rangle\langle n|$, i.e. $\mathbb{1} = \sum_n |n\rangle\langle n|$. Remember here the defining property of a projector P, namely $P^2 = P$. Any quantum state $|\psi\rangle$ can be expanded in the basis $\{|n\rangle\}$ as

$$|\psi\rangle = \sum_n c_n\,|n\rangle\,, \tag{5}$$

with complex coefficients c_n. The value $|c_n|^2$ is the probability to find the state $|n\rangle$, when measuring in the basis $\{|n\rangle\}$. We will always assume quantum states to be normalised, i.e. $\sum_n |c_n|^2 = 1$.
An alternative method to describe a pure state $|\psi\rangle$ is to use its density matrix, which is defined as

$$\rho_{\text{pure}} = |\psi\rangle \langle\psi| . \tag{6}$$

The properties of density matrices of *pure* quantum states are[2]:

1. Normalisation: $\text{tr}\rho = 1$
   (Proof: $\text{tr}\rho = \text{tr}\left(|\psi\rangle \langle\psi|\right) = \sum_n \langle n|\ \psi\rangle \langle\psi|\ n\rangle = \sum_n \langle\psi|\ n\rangle \langle n|\ \psi\rangle = \langle\psi|\ \psi\rangle = 1$)
2. Projector: $\rho^2 = \rho$ (Proof: $\rho^2 = |\psi\rangle \langle\psi|\ \psi\rangle \langle\psi| = |\psi\rangle \langle\psi| = \rho$)
3. Hermiticity: $\rho^\dagger = \rho$ (Proof: $\rho^\dagger = (|\psi\rangle \langle\psi|)^\dagger = |\psi\rangle \langle\psi| = \rho$)
4. Positivity: $\rho \geq 0$ (Proof: $\langle\chi|\, \rho\, |\chi\rangle = \langle\chi\,|\psi\rangle \langle\psi\,|\chi\rangle = |\,\langle\chi\,|\psi\rangle\,|^2 \geq 0 \quad \forall\, |\chi\rangle$)

The expectation value of the operator $\hat{A}$ in the state $|\psi\rangle$ is:

$$\langle\hat{A}\rangle_\psi := \langle\psi|\, \hat{A}\, |\psi\rangle = \sum_n \langle\psi|\, \hat{A}\, |n\rangle \langle n|\ \psi\rangle = \sum_n \langle n|\ \psi\rangle \langle\psi|\, \hat{A}\, |n\rangle = \text{tr}(|\psi\rangle \langle\psi|\, \hat{A}) = \text{tr}(\rho\hat{A}). \tag{7}$$

In a *mixed quantum state* the pure state $|\psi_i\rangle$ occurs with probability p_i, where $\sum_i p_i = 1$. The expectation value of an operator $\hat{A}$ is then the weighted average over the pure states, i.e.

$$\langle\hat{A}\rangle = \sum_i p_i \langle\psi_i|\, \hat{A}\, |\psi_i\rangle = \sum_i p_i \text{tr}(|\psi_i\rangle \langle\psi_i|\, \hat{A}) = \text{tr}(\sum_i p_i\, |\psi_i\rangle \langle\psi_i|\, \hat{A}) = \text{tr}(\rho_{\text{mixed}}\hat{A}), \tag{8}$$

where we defined the mixed state

$$\rho_{\text{mixed}} := \sum_i p_i\, |\psi_i\rangle \langle\psi_i| . \tag{9}$$

The properties of density matrices of *mixed* quantum states are:

1. Normalisation: $\text{tr}\rho_{\text{mixed}} = 1$
   (Proof: $\text{tr}\left(\rho_{\text{mixed}}\right) = \text{tr}(\sum_i p_i\, |\psi_i\rangle \langle\psi_i|) = \sum_n \sum_i p_i \langle n|\ \psi_i\rangle \langle\psi_i|\ n\rangle$
   $= \sum_i p_i \sum_n \langle\psi_i|\ n\rangle \langle n|\ \psi_i\rangle = \sum_i p_i \underbrace{\langle\psi_i|\ \psi_i\rangle}_{=1} = \sum_i p_i = 1$.)
2. No projector: $\rho^2_{\text{mixed}} \neq \rho_{\text{mixed}}$
   (Proof: $\rho^2_{\text{mixed}} = \sum_i \sum_j p_i p_j\, |\psi_i\rangle \langle\psi_i|\ \psi_j\rangle \langle\psi_j| \neq \sum_i p_i\, |\psi_i\rangle \langle\psi_i|$, unless only one $p_i > 0$, i.e. pure state. The trace is $\text{tr}(\rho^2_{\text{mixed}}) = \sum_{ij} p_i p_j |\,\langle\psi_i|\ \psi_j\rangle\,|^2 < 1$ if more than one $p_i > 0$.)
3. Hermiticity: $\rho^\dagger_{\text{mixed}} = \rho_{\text{mixed}}$
   (Proof: $\rho^\dagger_{\text{mixed}} = \sum_i p_i \left(|\psi_i\rangle \langle\psi_i|\right)^\dagger = \sum_i p_i\, |\psi_i\rangle \langle\psi_i| = \rho_{\text{mixed}}$.)

[2]Remember that the trace of $\hat{B}$ is defined as $\text{tr}\hat{B} := \sum_n \langle n|\, \hat{B}\, |n\rangle$ and is basis independent.

4. Positivity: $\rho \geq 0$

   (Proof: $\langle\chi|\,\rho\,|\chi\rangle = \sum_i p_i \langle\chi\,|\psi_i\rangle\langle\psi_i\,|\chi\rangle = \sum_i p_i |\langle\chi\,|\psi_i\rangle|^2 \geq 0 \quad \forall\,|\chi\rangle$.)

Thus, a pure density matrix has always rank one (remember that the rank of a Hermitian matrix is the number of non-vanishing eigenvalues), while a mixed density matrix has rank larger than one.
Regarding the property of positivity (to be precise, of positive semidefiniteness), note that $\langle\chi|\,\rho\,|\chi\rangle \geq 0 \Leftrightarrow \lambda_i \geq 0$, where λ_i are the eigenvalues of ρ, i.e. a Hermitian matrix is positive semidefinite iff all eigenvalues are positive or zero. (This fact follows from the spectral decomposition $\rho = \sum_i \lambda_i\,|i\rangle\langle i|$.)
In the context of pure versus mixed quantum states it is important to understand the difference between a superposition and a mixture: a *superposition* is the (normalised) sum of the vectors of two pure states, e.g. $|\psi\rangle = \alpha\,|0\rangle + \beta\,|1\rangle$, with $\alpha, \beta \in \mathbb{C}$ and $|\alpha|^2 + |\beta|^2 = 1$. A *mixture* is the weighted (normalised) sum of two density operators, e.g. $\rho = |\alpha|^2\,|0\rangle\langle 0| + |\beta|^2\,|1\rangle\langle 1|$, with $|\alpha|^2 + |\beta|^2 = 1$. The difference in the density matrix for these two examples consists in the presence of off-diagonal elements of the type $|0\rangle\langle 1|$ and $|1\rangle\langle 0|$ in the first example (sometimes called "coherences"), which are absent in the incoherent mixture of the second example.

1.3 Measurements

An *orthogonal projection measurement* (or *von Neumann measurement*) is a set of orthogonal projectors $\{\hat{P}_\mu\}$, i.e. $\hat{P}_\mu\hat{P}_\nu = \delta_{\mu\nu}\hat{P}_\mu$ [3], which fulfil $\sum_\mu \hat{P}_\mu = \mathbb{1}$. Here $\hat{P}_\mu$ projects on the eigenspace of the μ-th measurement outcome. The probability to get the outcome μ in a mixed state ρ is given by

$$p_\mu = \mathrm{tr}(\hat{P}_\mu\rho). \tag{10}$$

After the measurement the system is found in the state

$$\rho' = \frac{\hat{P}_\mu\rho\hat{P}_\mu}{\mathrm{tr}(\rho\hat{P}_\mu)}. \tag{11}$$

As an example consider the well-known Stern-Gerlach experiment, which performs a von Neumann measurement on a spin-1/2 system, with the projectors $\hat{P}_\uparrow = |\uparrow\rangle\langle\uparrow|, \quad \hat{P}_\downarrow = |\downarrow\rangle\langle\downarrow|$. Given a general spin-1/2 state $|\psi\rangle = \alpha\,|\uparrow\rangle + \beta\,|\downarrow\rangle$ with $|\alpha|^2 + |\beta|^2 = 1$, the probability to measure "spin up" is then given by

$$p_\uparrow = \mathrm{tr}[\hat{P}_\uparrow\,|\psi\rangle\langle\psi|] = |\langle\uparrow\,|\psi\rangle|^2 = |\alpha|^2 = 1 - p_\downarrow. \tag{12}$$

Von Neumann measurements are a special case of the most general measurements, the so-called *positive operator valued measurements (POVM)* [1].

Definition 1.1 (POVM) *A set of positive operators $\{\hat{F}_\mu\}$, i.e. $\hat{F}_\mu \geq 0$, which is a resolution of the identity, i.e. $\sum_\mu \hat{F}_\mu = \mathbb{1}$, is called positive operator valued measurement (POVM).*

The probability to find the μ-th outcome when performing the above measurement on ρ is given by

$$p_\mu = \mathrm{tr}(\hat{F}_\mu\rho). \tag{13}$$

[3] The Kronecker delta is defined as $\delta_{ii} = 1$ and $\delta_{ij} = 0$ for $i \neq j$.

Note that a POVM can be seen as a von Neumann measurement on a higher-dimensional Hilbert space: let ρ^{aux} be an auxiliary quantum system (*ancilla*) in a known state, i.e. the total state of system and ancilla is given by

$$\rho^{\mathrm{tot}} = \rho \otimes \rho^{\mathrm{aux}}. \tag{14}$$

Here, the symbol $\otimes$ denotes the tensor product - its properties will be discussed in section 2.2. Let $\{\hat{P}_\mu\}$ be a set of orthogonal projectors, which act on the total Hilbert space. Then the probability to find outcome μ is given by

$$p_\mu = \mathrm{tr}\left(\hat{P}_\mu[\rho \otimes \rho^{\mathrm{aux}}]\right) = \sum_{i,j,r,s} (\hat{P}_\mu)_{ir,js}\rho_{ji}\rho^{\mathrm{aux}}_{sr} = \mathrm{tr}(\hat{F}_\mu\rho), \tag{15}$$

if the POVM element $\hat{F}_\mu$ is defined as

$$(\hat{F}_\mu)_{ij} := \sum_{r,s}(\hat{P}_\mu)_{ir,js}\rho^{\mathrm{aux}}_{sr}. \tag{16}$$

Examples for POVMs:

1. Define the following four operators:

$$\hat{F}_1 = \frac{1}{2}\left|0_x\right\rangle\left\langle 0_x\right|, \quad \hat{F}_2 = \frac{1}{2}\left|1_x\right\rangle\left\langle 1_x\right|, \quad \hat{F}_3 = \frac{1}{2}\left|0_z\right\rangle\left\langle 0_z\right|, \quad \hat{F}_4 = \frac{1}{2}\left|1_z\right\rangle\left\langle 1_z\right|, \tag{17}$$

   where $|0_x\rangle = \frac{1}{\sqrt{2}}[|0_z\rangle + |1_z\rangle]$, $|1_x\rangle = \frac{1}{\sqrt{2}}[|0_z\rangle - |1_z\rangle]$. Obviously the operators $\hat{F}_\mu$ are not orthogonal to each other, and they are no projectors, thus (17) does not describe a von Neumann measurement. However, $\sum_{\mu=1}^{4}\hat{F}_\mu = \mathbb{1}$ holds, and thus the operators in eq. (17) constitute a POVM.

2. Consider the two nonorthogonal states

$$\begin{aligned} \left|u\right\rangle &= \cos\alpha\left|0\right\rangle + \sin\alpha\left|1\right\rangle, \\ \left|v\right\rangle &= \sin\alpha\left|0\right\rangle + \cos\alpha\left|1\right\rangle, \end{aligned} \tag{18}$$

   which have the scalar product $\langle u\,|\,v\rangle = \sin 2\alpha$. The following POVM can be used to distinguish unambiguously between these states (i.e. not to mistake one state for the other):

$$\hat{F}_1 = \hat{F}_{|u\rangle} = \frac{F_{\mathrm{not}|v\rangle}}{1+2\sin\alpha}, \tag{19}$$

$$\hat{F}_2 = \hat{F}_{|v\rangle} = \frac{F_{\mathrm{not}|u\rangle}}{1+2\sin\alpha}, \tag{20}$$

$$\hat{F}_3 = \hat{F}_? = \mathbb{1} - \hat{F}_1 - \hat{F}_2, \tag{21}$$

   where $\hat{F}_{\mathrm{not}|u\rangle} := \mathbb{1} - |u\rangle\langle u|$ and $\hat{F}_{\mathrm{not}|v\rangle} := \mathbb{1} - |v\rangle\langle v|$ project onto the subspace orthogonal to $|u\rangle$ and $|v\rangle$, respectively. There are three possible outcomes: For the outcome $\mu = 1$ the state $|u\rangle$ was found with certainty, for the outcome $\mu = 2$ the state $|v\rangle$ was found with certainty, and the outcome $\mu = 3$ is inconclusive.

1.4 Some basic information theoretic quantities

How can the information content of a message be quantified? Here, a *message* is a string of *letters* x_i. Letters are elements of an *alphabet*, i.e. a set $\{x_1, x_2, \ldots, x_k\}$. A *random variable* X can take the value x_i with the probability $p_i := P(X = x_i) \leq 1$, where $\sum_i p_i = 1$.
The number N of possibilities to arrange n outcomes of X (compatible with the probabilities p_i of the occurrence of x_i) is given by

$$N = \frac{n!}{(np_1)!(np_2)! \cdots (np_k)!} \,. \tag{22}$$

For large n we can use Stirling's approximation $\log n! = n \log n - n + O(\log n)$. Using $n_i := np_i$ and omitting terms of order $O(\log n)$ we arrive at

$$\log N \approx n \log n - n - \left(\sum_{i=1}^{k} n_i \log n_i - n_i \right) = -n \sum_{i=1}^{k} p_i \log p_i. \tag{23}$$

Definition 1.2 (Shannon entropy) *The Shannon entropy of a probability distribution* $\{p_1, p_2, ..., p_k\}$ *is defined as*

$$H(\{p_i\}) := -\sum_{i=1}^{k} p_i \log p_i. \tag{24}$$

It can be easily verified that H is maximal for an equiprobable distribution, i.e. for $p_i = \frac{1}{k}$: We can express H as $H = -\sum_{i=1}^{k-1} p_i \log p_i - p_k \log p_k$ and eliminate $p_k = 1 - \sum_{i=1}^{k-1} p_i$. Then we find:

$$\frac{\partial H}{\partial p_x} = -\log p_x - \frac{p_x}{p_x} + \log p_k + \frac{p_k}{p_k} \stackrel{!}{=} 0 \Leftrightarrow p_x = p_k \tag{25}$$

Since x can be chosen arbitrarily and $\sum_i p_i = 1$, it must be $p_i = 1/k$ for all i.
So far we did not define the basis of the logarithm in Def. 1.2. Note that two logarithms with different bases differ only by a constant factor. In the following we will use the base 2, if not specified otherwise. - We point out that the realisation of a message is physical, in the sense that the variable X is represented by a switch that can be on or off, by some acoustical signal - or, in the case of quantum information, by a quantum state.
We now ask the question whether a given message consisting of n letters can be compressed without losing information. In the following we consider binary alphabets. The probability of the numbers 0 and 1 can then be written as: $p_0 = p,\ p_1 = 1 - p$. The binary Shannon entropy is

$$H(p) = -p \log_2 p - (1 - p) \log_2 (1 - p). \tag{26}$$

Fig. 1 shows this function - notice its concavity, which is typical for entropic quantities.
The number of possible arrangements of the n letters is given by $N \approx 2^{nH(p)}$. Thus, it is possible to encode the message with less than n bits, if $H(p) < 1$. In Shannon's noiseless coding theorem it is shown that the minimal number of needed letters is given by $n' = nH(p) \leq n$. Thus, there exists a code which encodes each letter asymptotically, i.e. for $n \to \infty$, to $H(p)$ bits. No encoding which needs less then $H(p)$ bits is possible. In this sense the Shannon entropy quantifies how much information is contained in a letter.

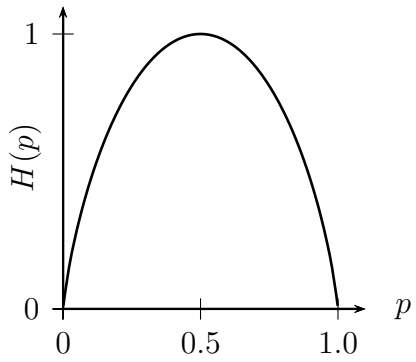

Fig. 1: *The binary Shannon entropy.*

- Example: Consider an alphabet {1,2,3,4} with 2-bit block encoding {00,01,10,11} with the probability distribution $p_1 = \frac{1}{2}$, $p_2 = \frac{1}{4}$, $p_3 = p_4 = \frac{1}{8}$. We use the following compression scheme (which is constructed such that the measage can be decoded in an unambiguous way):

$$\left.\begin{array}{rcl} 1 & \hat{=} & 0 \\ 2 & \hat{=} & 10 \\ 3 & \hat{=} & 110 \\ 4 & \hat{=} & 111 \end{array}\right\} \text{average length: } \frac{1}{2}1 + \frac{1}{4}2 + 2\frac{1}{8}3 = \frac{7}{4} \text{ bits.}$$

Compare this to the Shannon entropy:

$$H(\{p_i\}) = -\frac{1}{2}\log\frac{1}{2} - \frac{1}{4}\log\frac{1}{4} - 2\frac{1}{8}\log\frac{1}{8} = \frac{1}{2} + \frac{2}{4} + 3\frac{2}{8} = \frac{7}{4}.$$

This means that no better compression is possible.
Generally, information theoretic quantities are entropies: An entropy can be interpreted as a measure of the "lack of knowledge" about the variable X, or equivalently as the "information gain" after learning X.
In the following, we introduce some entropies for two variables X and Y.

Definition 1.3 (Joint entropy) *Given two variables $X \in \{a_1, \ldots, a_k\}$ and $Y \in \{b_1, \ldots, b_l\}$ with joint probabilities $p(a_i, b_j) = P(X = a_i, Y = b_j)$ for X taking the value a_i and Y taking the value b_j, the joint entropy is defined as*

$$H(X,Y) = -\sum_{i=1}^{k}\sum_{j=1}^{l} p(a_i, b_j)\log p(a_i, b_j).$$

Definition 1.4 (Conditional entropy) *Let $p(a_i|b_j) = p(a_i, b_j)/p(b_j)$ be the conditional probability for X taking the value a_i, if Y has the value b_j. The conditional entropy is defined as*

$$H(X|Y) = -\sum_{i,j} p(a_i, b_j)\log p(a_i|b_j).$$

Thus we have

$$\begin{aligned} H(X|Y) &= -\sum_{i,j} p(a_i, b_j)\log\frac{p(a_i, b_j)}{p(b_j)} \\ &= H(X,Y) - H(Y), \qquad (27) \\ H(Y|X) &= H(X,Y) - H(X), \qquad (28) \end{aligned}$$

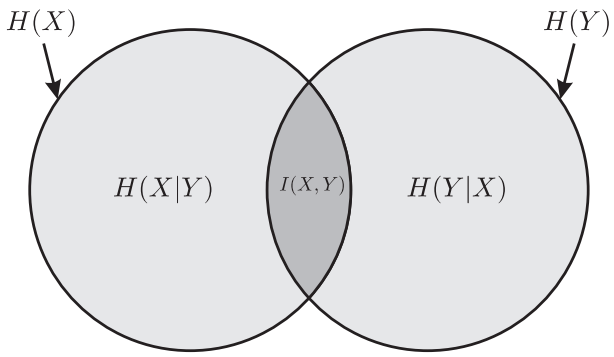

Fig. 2: *Venn diagram of information theoretic quantities for two variables.*

with the Shannon entropies $H(X), H(Y)$. Note that the conditional entropy is not symmetric in its arguments.

Definition 1.5 (Mutual information) *The mutual information is defined as*

$$\begin{aligned} I(X;Y) &= H(X) - H(X|Y) \\ &= H(X) + H(Y) - H(X,Y) \end{aligned}$$

The mutual information of X and Y is the amount of information that can be gained about X, if one learns Y, or vice versa. It is zero if and only if X and Y are uncorrelated. The Venn diagram in Fig. 2 illustrates the relation between mutual information, conditional entropy and Shannon entropy.

2 Basic notions in quantum information

In this section we provide some fundamental concepts of quantum information processing. Much more material can be found in textbooks such as [2], [3], etc.

2.1 Qubits

In classical information processing usually a binary alphabet is used, i.e. a variable can take two possible values, 0 or 1, and is referred to as *bit*. In quantum information processing the information carriers are quantum states - due to the superposition principle they can not only be in the basis states $|0\rangle$ or $|1\rangle$, but also in any superposition of these. A quantum bit or *qubit* can be realised by any two-level quantum system, with the basis vectors $\{|0\rangle, |1\rangle\}$ being elements of the two-dimensional Hilbert space $\mathcal{H}_2$. Some physical examples for such systems are a two-level atom with $|0\rangle = |n_0, l_0, m_0\rangle$ and $|1\rangle = |n_1, l_1, m_1\rangle$; linearly polarized photons with $|0\rangle = |\updownarrow\rangle$ and $|1\rangle = |\leftrightarrow\rangle$; a spin-1/2 particle with $|0\rangle = |\uparrow\rangle$ and $|1\rangle = |\downarrow\rangle$, etc.
A general pure state of a qubit can be described by two parameters as

$$|\psi\rangle = \cos\frac{\vartheta}{2}|0\rangle + \mathrm{e}^{i\varphi}\sin\frac{\vartheta}{2}|1\rangle, \tag{29}$$

with $0 \leq \vartheta \leq \pi$ and $0 \leq \varphi \leq 2\pi$. Here, the normalization condition $\langle\psi|\psi\rangle = 1$ is obeyed, and a possible overall phase has been eliminated.

Writing the basis states in vector notation as

$$|0\rangle = \begin{pmatrix} 1 \\ 0 \end{pmatrix}, \quad |1\rangle = \begin{pmatrix} 0 \\ 1 \end{pmatrix}, \tag{30}$$

the density matrix of a qubit in a *pure* state is given by

$$\rho = |\psi\rangle\langle\psi| = \begin{pmatrix} \cos^2\left(\frac{\vartheta}{2}\right) & \cos\left(\frac{\vartheta}{2}\right) \mathrm{e}^{-i\varphi} \sin\left(\frac{\vartheta}{2}\right) \\ \cos\left(\frac{\vartheta}{2}\right) \mathrm{e}^{i\varphi} \sin\left(\frac{\vartheta}{2}\right) & \sin^2\left(\frac{\vartheta}{2}\right) \end{pmatrix}. \tag{31}$$

It is easy to convince oneself that this density matrix has the properties of having trace 1, being a projector, being Hermitian, and being positive, see subsection 1.2.
The density matrix of a qubit in a general *mixed* state can be written as

$$\rho = \sum_i p_i |\psi_i\rangle\langle\psi_i| = \begin{pmatrix} \rho_{00} & \rho_{01} \\ \rho_{10} & \rho_{11} \end{pmatrix}, \tag{32}$$

where the following properties have to be fulfilled: normalisation, i.e. $\mathrm{tr}\rho = 1$, leading to $\rho_{00} = 1 - \rho_{11}$; Hermiticity, i.e. $\rho^\dagger = \rho$, requiring ρ_{00} and ρ_{11} to be real, and $\rho_{01} = \rho_{10}^*$; and positivity, i.e. $\rho \geq 0$. From the properties of normalisation and Hermiticity it follows that ρ can be described by three real parameters.
A quantum state of a qubit can be conveniently described with the *Bloch sphere:* Any Hermitian 2×2 matrix can be decomposed into the three Pauli matrices σ_i and the identiy $\mathbb{1}$, i.e.

$$\rho = a\mathbb{1} + \sum_{i\in\{x,y,z\}} b_i \sigma_i, \tag{33}$$

with the Pauli matrices (the generators of SU(2)):

$$\sigma_x = \begin{pmatrix} 0 & 1 \\ 1 & 0 \end{pmatrix}, \quad \sigma_y = \begin{pmatrix} 0 & -i \\ i & 0 \end{pmatrix}, \quad \sigma_z = \begin{pmatrix} 1 & 0 \\ 0 & -1 \end{pmatrix}. \tag{34}$$

Since $\mathrm{tr}\rho = 1$, it follows that $a = 1/2$, and thus we can write

$$\rho = \frac{1}{2}(\mathbb{1} + \vec{s}\cdot\vec{\sigma}), \tag{35}$$

where $\vec{s}$ is called the *Bloch vector*. The Bloch vector can be read off the density matrix ρ easily:

$$s_x = 2\,\mathrm{Re}\,\rho_{01}, \quad s_y = -2\,\mathrm{Im}\,\rho_{01}, \quad s_z = \rho_{00} - \rho_{11}. \tag{36}$$

E.g. for a pure state, one finds from eq. (31) that $\vec{s} = (\sin\vartheta\cos\varphi, \sin\vartheta\sin\varphi, \cos\vartheta)^T$. For pure states, i.e. $\rho^2 = \rho$, the Bloch vector thus fulfils $|\vec{s}| = 1$ and lies on the surface of a sphere, the so-called *Bloch sphere*. Since for a mixed state $\mathrm{tr}\rho^2 < 1$ holds, the Bloch vector of a mixed state lies in the interior of the Bloch ball. The three real parameters that determine any quantum state ρ uniquely are the two angles and the length of the Bloch vector $\vec{s}$.
For qubits, any possible Bloch vector corresponds to a physical state. Fig. 3 illustrates the Bloch sphere. Note that the Bloch vectors of two orthogonal pure states point in opposite directions.
- This picture can in principle be extended to d-dimensional quantum states (sometimes called *qudits*), where the density matrix can be expanded in the $(d^2 - 1)$ generators of SU(d), and a (d^2-1)-dimensional Bloch vector can be defined in an analogous way as above. Note, however, that due to the positivity condition not every higher-dimensional Bloch vector corresponds to a physical state [4].

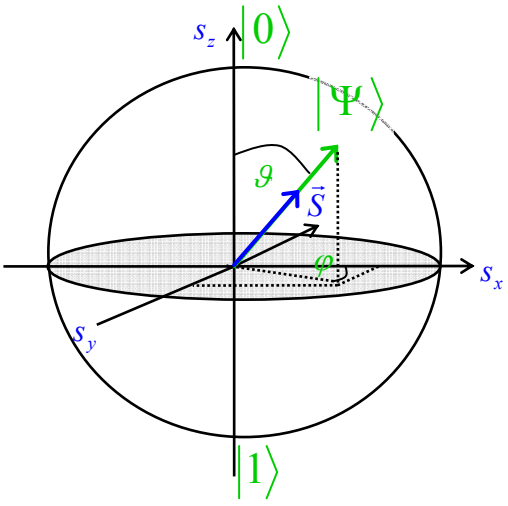

Fig. 3: *Illustration of a qubit in a pure (green) and a mixed (blue) state in the Bloch picture. The Bloch vector is represented by its three components s_x, s_y and s_z, or by its length and the angles ϑ and φ. The Bloch vector for a pure state can take any point on the surface of the sphere, while it can take any point inside the Bloch ball for mixed states.*

2.2 Composite quantum systems and entanglement

Let us consider two quantum systems with Hilbert spaces $\mathcal{H}_\mathrm{A}$ and $\mathcal{H}_\mathrm{B}$, i.e. the total Hilbert space is $\mathcal{H}_\mathrm{AB} = \mathcal{H}_\mathrm{A} \otimes \mathcal{H}_\mathrm{B}$, where the symbol $\otimes$ denotes the tensor product. If party A (in the following referred to as Alice) has state $|\Psi_\mathrm{A}\rangle \in \mathcal{H}_\mathrm{A}$ and party B (in the following referred to as Bob) has state $|\Psi_\mathrm{B}\rangle \in \mathcal{H}_\mathrm{B}$, the state of the composite system is $|\Psi_\mathrm{AB}\rangle = |\Psi_\mathrm{A}\rangle \otimes |\Psi_\mathrm{B}\rangle \in \mathcal{H}_\mathrm{AB}$. A possible choice for the basis vectors of the total Hilbert space is a *product basis*, i.e. the tensor products of the basis vectors of the subsystems. E.g. for two two-level systems (qubits) a product basis is given by $\{|0\rangle_\mathrm{A} \otimes |0\rangle_\mathrm{B}, |0\rangle_\mathrm{A} \otimes |1\rangle_\mathrm{B}, |1\rangle_\mathrm{A} \otimes |0\rangle_\mathrm{B}, |1\rangle_\mathrm{A} \otimes |1\rangle_\mathrm{B}, \}$, where the vector notation reads

$$|0\rangle_\mathrm{A} \otimes |0\rangle_\mathrm{B} \equiv \begin{pmatrix} 1 \\ 0 \end{pmatrix}_\mathrm{A} \otimes \begin{pmatrix} 1 \\ 0 \end{pmatrix}_\mathrm{B} = \begin{pmatrix} 1 \\ 0 \\ 0 \\ 0 \end{pmatrix}_\mathrm{AB} , \tag{37}$$

and analogously for the other basis states. The tensor product is bilinear, i.e. it has the following properties $\forall\, |\Psi_\mathrm{A}\rangle, |\Phi_\mathrm{A}\rangle \in \mathcal{H}_\mathrm{A}$ and $\forall\, |\Psi_\mathrm{B}\rangle, |\Phi_\mathrm{B}\rangle \in \mathcal{H}_\mathrm{B}$ and $c \in \mathbb{C}$:

$$c(|\Psi_\mathrm{A}\rangle \otimes |\Psi_\mathrm{B}\rangle) = (c\,|\Psi_\mathrm{A}\rangle) \otimes |\Psi_\mathrm{B}\rangle = |\Psi_\mathrm{A}\rangle \otimes (c\,|\Psi_\mathrm{B}\rangle) , \tag{38}$$

$$(|\Psi_\mathrm{A}\rangle + |\Phi_\mathrm{A}\rangle) \otimes |\Psi_\mathrm{B}\rangle = |\Psi_\mathrm{A}\rangle \otimes |\Psi_\mathrm{B}\rangle + |\Phi_\mathrm{A}\rangle \otimes |\Psi_\mathrm{B}\rangle , \tag{39}$$

$$|\Psi_\mathrm{A}\rangle \otimes (|\Psi_\mathrm{B}\rangle + |\Phi_\mathrm{B}\rangle) = |\Psi_\mathrm{A}\rangle \otimes |\Psi_\mathrm{B}\rangle + |\Psi_\mathrm{A}\rangle \otimes |\Phi_\mathrm{B}\rangle . \tag{40}$$

The tensor product of two general two-dimensional vectors is calculated as follows:

$$\begin{pmatrix} \alpha \\ \beta \end{pmatrix}_\mathrm{A} \otimes \begin{pmatrix} \gamma \\ \delta \end{pmatrix}_\mathrm{B} = \begin{pmatrix} \alpha\gamma \\ \alpha\delta \\ \beta\gamma \\ \beta\delta \end{pmatrix}_\mathrm{AB} . \tag{41}$$

In the following we will use as equivalent notations:

$$|0\rangle_{\rm A} \otimes |0\rangle_{\rm B} \equiv |0\rangle_{\rm A} |0\rangle_{\rm B} \equiv |00\rangle_{\rm AB} \equiv |00\rangle \ . \tag{42}$$

The most general state of a composite system of two qubits is a superposition of the basis states, i.e.

$$|\psi\rangle = A_{00} |00\rangle + A_{01} |01\rangle + A_{10} |10\rangle + A_{11} |11\rangle \,, \text{ with } \sum_{i,j=0}^{1} |A_{ij}|^2 = 1. \tag{43}$$

Composite systems can be entangled or separable. For pure states, a *separable* state is a product state, i.e.

$$|\psi\rangle_{sep} = |\psi\rangle_{\rm A} \otimes |\psi\rangle_{\rm B} \ , \tag{44}$$

e.g.

$$|\psi_1\rangle = \frac{1}{\sqrt{2}} |00\rangle + \frac{1}{\sqrt{2}} |01\rangle = |0\rangle_{\rm A} \otimes \frac{1}{\sqrt{2}}[|0\rangle + |1\rangle]_{\rm B}. \tag{45}$$

An *entangled* state *(in German: "verschränkter Zustand" [5])* is not separable, i.e. for pure states it cannot be written as a product state:

$$|\psi\rangle_{ent} \neq |\psi\rangle_{\rm A} \otimes |\psi\rangle_{\rm B} \ . \tag{46}$$

Important examples for entangled states of two qubits are the four *Bell states*:

$$\begin{aligned} \left|\phi^{\pm}\right\rangle &:= \frac{1}{\sqrt{2}}[|00\rangle \pm |11\rangle], \\ \left|\psi^{\pm}\right\rangle &:= \frac{1}{\sqrt{2}}[|01\rangle \pm |10\rangle]. \end{aligned} \tag{47}$$

The four Bell states form an orthogonal entangled basis of the Hilbert space of two qubits.
The question whether a given state $|\psi\rangle$ is separable or entangled can be answered easily for pure *bipartite states* (i.e. states composed of two subsystems), due to the following bi-orthogonal decomposition:

Lemma 2.1 (Schmidt decomposition) *Let $\mathcal{H}_{\rm A}$ and $\mathcal{H}_{\rm B}$ be two Hilbert spaces with dimension $d_{\rm A} := \dim \mathcal{H}_{\rm A}$ and $d_{\rm B} := \dim \mathcal{H}_{\rm B}$, respectively, and $\mathcal{H}_{\rm AB} = \mathcal{H}_{\rm A} \otimes \mathcal{H}_{\rm B}$. Any state $|\psi\rangle \in \mathcal{H}_{\rm AB}$ can be written as*

$$|\psi\rangle = \sum_{k=1}^{r} a_k \, |e_k\rangle_{\rm A} \otimes |f_k\rangle_{\rm B} \ , \tag{48}$$

with a_k being real and positive, $\sum_k a_k^2 = 1$ and $\langle e_i \, | e_j \rangle_{\rm A} = \delta_{ij} = \langle f_i \, | f_j \rangle_{\rm B}$. The number r is called the Schmidt rank *and fulfils $1 \leq r \leq min(d_A, d_B)$. The state $|\psi\rangle$ is separable iff $r = 1$.*

Proof: The state $|\psi\rangle$ can be written as

$$|\psi\rangle = \sum_{i,j} A_{ij} \, |ij\rangle \tag{49}$$

with a $d_{\rm A} \times d_{\rm B}$-matrix A. Using the singular value decomposition we can decompose any matrix A as

$$A = U A_d V^{\dagger}, \tag{50}$$

where U and V are unitary and A_d is a real diagonal matrix with diagonal elements $a_1, a_2, \ldots, a_d$. Thus we have:

$$\sum_{i,j} A_{ij} |ij\rangle = \sum_{i,j,k} U_{ik} a_k V^*_{jk} |ij\rangle \,. \tag{51}$$

Defining

$$|e_k\rangle := \sum_i U_{ik} |i\rangle \ , \qquad\qquad |f_k\rangle := \sum_j V^*_{jk} |j\rangle \,, \tag{52}$$

we found the Schmidt decomposition, eq. (48). Orthogonality of $\{|e_k\rangle\}$ and $\{|f_k\rangle\}$ follows from unitarity of U and V, as

$$\langle e_l |\, e_k\rangle = \sum_{i,j} \langle j|\, U^*_{jl} U_{ik} \,|i\rangle = \sum_{i,j} U^*_{jl} U_{ik} \delta_{ij} = \sum_i U^*_{il} U_{ik} = \delta_{lk} \ , \tag{53}$$

and analogously for $\{|f_k\rangle\}$. □

The Schmidt rank of a given state can be determined via the *partial trace*, which is the trace over one of the subsystems, defined as

$$\rho_{\rm A} = {\rm tr}_{\rm B}(\rho_{\rm AB}) = \sum_i \langle i|_{\rm B} \, \rho_{\rm AB} \, |i\rangle_{\rm B} \ , \tag{54}$$

where $\{|i\rangle_{\rm B}\}$ is any basis of B. Choosing the basis $\{|f_i\rangle\}$ for B leads to the partial trace of a bipartite state written in the Schmidt decomposition:

$$\begin{aligned} \rho_A &= {\rm tr}_B(\rho_{\rm AB}) = \sum_k \langle f_k| \left(\sum_{i=1}^r a_i \, |e_i\rangle \, |f_i\rangle \right) \left(\sum_{j=1}^r a_j^* \, \langle e_j| \, \langle f_j| \right) |f_k\rangle \\ &= \sum_k |a_k|^2 \, |e_k\rangle\langle e_k| \,, \end{aligned} \tag{55}$$

i.e. $|a_k|^2$ are the eigenvalues of $\rho_{\rm A}$, and also of $\rho_{\rm B}$ (analogous calculation). Thus, the Schmidt rank corresponds to the number of the eigenvalues of $\rho_{\rm A}$ or $\rho_{\rm B}$ which are larger than zero - in other words, ${\rm rank}(\rho_{\rm A}) = {\rm rank}(\rho_{\rm B}) =$ Schmidt rank$(\rho_{\rm AB})$.

Given an entangled bipartite state, how can one quantify its entanglement? A suitable *entanglement measure* for a pure bipartite state $|\psi_{AB}\rangle$ is the *von Neumann entropy* of its reduced density matrix ρ_A or ρ_B.

Definition 2.1 (Von Neumann entropy) *The von Neumann entropy of a quantum system with density matrix ρ is defined as*

$$S(\rho) := -{\rm tr}(\rho \log \rho), \tag{56}$$

where here and in the following the log *is taken to base 2, if not specified otherwise.*

The logarithm (or any function) of the operator ρ is given via the spectral decomposition, i.e.

$$f(\rho) = \sum_i f(\lambda_i) \, |i\rangle \, \langle i| \,, \tag{57}$$

where λ_i is the eigenvalue of ρ corresponding to the eigenstate $|i\rangle$.

The von Neumann entropy of ρ can be computed as

$$S(\rho) = -\sum_k \langle k| \left(\sum_i \lambda_i \log \lambda_i |i\rangle\langle i| \right) |k\rangle = -\sum_k \lambda_k \log \lambda_k. \tag{58}$$

Thus, the von Neumann entropy is the quantum analogon of the classical Shannon entropy, see section 1.4, and $0 \leq S(\rho) \leq 1$ holds. The entanglement $E(|\psi\rangle)$ of a pure state $|\psi\rangle$ is given by the von Neumann entropy of its reduced density matrix:

$$E(|\psi\rangle) = S(\rho_{\rm A}) = S(\rho_{\rm B}). \tag{59}$$

For a bipartite pure state $|\psi\rangle$ of the form in eq. (48), its entanglement is therefore $E(|\psi\rangle) = -\sum_k |a_k|^2 \log |a_k|^2$. Thus, the Bell states in eq. (47) are maximally entangled.
- Examples:

$$|\psi\rangle = |00\rangle \;\; \Rightarrow \;\; \rho_{\rm A} = \begin{pmatrix} 1 & 0 \\ 0 & 0 \end{pmatrix} \;\; \Rightarrow S(\rho_{\rm A}) = 0, \tag{60}$$

$$|\psi\rangle = \frac{1}{\sqrt{2}}[|00\rangle + |11\rangle] \;\; \Rightarrow \;\; \rho_{\rm A} = \frac{1}{2}\mathbb{1} \;\; \Rightarrow S(\rho_{\rm A}) = 1. \tag{61}$$

For *mixed* quantum states it is not as easy as for pure states to decide whether a given state is separable or entangled.

Definition 2.2 (Separability versus entanglement) *A quantum state* $\rho = \sum_i p_i |\psi_i\rangle \langle\psi_i|$ *is* separable *if and only if there exists a decomposition*

$$\rho = \sum_i p_i |a_i\rangle \langle a_i|_{\rm A} \otimes |b_i\rangle \langle b_i|_{\rm B} \tag{62}$$

with $p_i \geq 0$ *and* $\sum_i p_i = 1$. *An* entangled *state is a state for which no decomposition as in eq. (62) exists*.

The mixture of projectors onto product states in eq. (62) is not necessarily a spectral decomposition, i.e. in general $\langle a_i | a_j \rangle \neq \delta_{ij}$ and $\langle b_i | b_j \rangle \neq \delta_{ij}$. Note that a separable state can be prepared locally with classical communication, and thus may exhibit correlations, without being entangled. Recently, much interest has been devoted to studying quantum correlations beyond entanglement (e.g. a mixture of non-orthogonal product states in eq. (62)), see [6]. - We point out that the von Neumann entropy of the reduced density matrix is not a suitable measure of entanglement for mixed states, as e.g. $S(\rho_A) = 1$ for $\rho_{\rm sep}$ in eq. (63) below, although the state is separable. For an overview over entanglement measures for mixed states, see [7].
Two examples for bipartite mixtures:

$$\rho_{\rm sep} \;\; = \;\; \frac{1}{2} |00\rangle \langle 00| + \frac{1}{2} |11\rangle \langle 11| \;\; , \tag{63}$$

$$\rho_{\rm ent} \;\; = \;\; (1-p)\frac{1}{4}\mathbb{1} + p \left|\phi^+\right\rangle \left\langle\phi^+\right| \;\; . \tag{64}$$

The first state is separable, while the second one is entangled for $1/3 < p \leq 1$ and separable for $0 \leq p \leq 1/3$. As we will see, this fact follows from properties of the *partial transpose* of ρ. The *Peres-Horodecki criterion* or criterion of a *positive partial transpose (PPT)* is necessary for separability of a bipartite quantum state.

Definition 2.3 (Partial transpose) *The partial transpose w.r.t. Alice of a density matrix*

$$\rho = \sum_{i,j,\mu,\nu} a_{i\mu,j\nu} \left|i\right\rangle \left\langle j\right| \otimes \left|\mu\right\rangle \left\langle \nu\right| \tag{65}$$

in the basis $\{\left|i\right\rangle \left\langle j\right|\}$ *for Alice and* $\{\left|\mu\right\rangle \left\langle \nu\right|\}$ *for Bob is given by*

$$\rho^{\mathrm{T_A}} = \sum_{i,j,\mu,\nu} a_{j\mu,i\nu} \left|i\right\rangle \left\langle j\right| \otimes \left|\mu\right\rangle \left\langle \nu\right| . \tag{66}$$

Theorem 2.1 (Peres criterion) *Let* $\rho \in \mathcal{B}(\mathcal{H}_{\mathrm{A}} \otimes \mathcal{H}_{\mathrm{B}})$. *Then it holds [8]:*

$$\rho \textit{ is separable} \Rightarrow \left\{ \begin{array}{lcl} \rho^{\mathrm{T_A}} & \geq & 0 \quad \textit{and} \\ \rho^{\mathrm{T_B}} & \geq & 0. \end{array} \right.$$

Proof: Writing a separable ρ in the form of eq. (62), it immediately follows that

$$\rho^{\mathrm{T_A}} = \sum_i p_i (\left|a_i\right\rangle \left\langle a_i\right|)^{\mathrm{T}} \otimes \left|b_i\right\rangle \left\langle b_i\right| = \sum_i p_i \left|a_i^*\right\rangle \left\langle a_i^*\right| \otimes \left|b_i\right\rangle \left\langle b_i\right| \tag{67}$$

is a valid density matrix and thus positive. The same holds for $\rho^{\mathrm{T_B}}$. Note that ρ is then called "PPT", since it has positive partial transpose. □

It was shown that for low dimensions the Peres criterion is not only necessary, but also sufficient for separability:

Theorem 2.2 (Horodecki) *Let* $\mathcal{H} = \mathcal{H}_{\mathrm{A}} \otimes \mathcal{H}_{\mathrm{B}}$ *with* $\dim \mathcal{H}_{\mathrm{A}} = 2$ *and* $\dim \mathcal{H}_{\mathrm{B}} = 2$ *or* 3. *Then for* $\rho \in \mathcal{B}(\mathcal{H})$ *it holds [9]:*

$$\rho \textit{ is separable} \Leftrightarrow \rho^{\mathrm{T_A}} \geq 0 . \tag{68}$$

The proof follows from the theory of positive maps. Note that physically the partial transpose corresponds to time reversal in the corresponding subsystem. - For higher dimensions, there exist states which are PPT but nevertheless entangled; they are called *bound entangled*.

Explicitly, one determines the partial transpose of a composite density matrix as follows: let ρ be written with the block matrices M, N and L as

$$\rho = \left(\begin{array}{cc} M & L \\ L^\dagger & N \end{array} \right) . \tag{69}$$

Then the partial transposes w.r.t. Alice and w.r.t. Bob are given by

$$\rho^{\mathrm{T_A}} = \left(\begin{array}{cc} M & L^\dagger \\ L & N \end{array} \right) ; \qquad \rho^{\mathrm{T_B}} = \left(\begin{array}{cc} M^{\mathrm{T}} & L^{\mathrm{T}} \\ L^* & N^{\mathrm{T}} \end{array} \right) . \tag{70}$$

As an example we consider the Werner state [10]

$$\rho_{\mathrm{w}} = (1-p)\frac{1}{4}\mathbb{1} + p \left|\phi^+\right\rangle \left\langle \phi^+\right| , \quad 0 \leq p \leq 1 , \tag{71}$$

with $|\phi^+\rangle = 1/\sqrt{2}[|00\rangle + |11\rangle]$. The matrix representation of the Werner state is

$$\rho_{\rm w} = \begin{pmatrix} \frac{1}{4}(1-p)+\frac{p}{2} & 0 & 0 & \frac{p}{2} \\ 0 & \frac{1}{4}(1-p) & 0 & 0 \\ 0 & 0 & \frac{1}{4}(1-p) & 0 \\ \frac{p}{2} & 0 & 0 & \frac{1}{4}(1-p)+\frac{p}{2} \end{pmatrix} . \tag{72}$$

The transpose is taken with respect to Bob by transposing all 2×2-submatrices. The eigenvalues of $\rho_{\rm w}^{\rm T_B}$ are then found to be

$$\lambda_{1,2,3} = \frac{1}{4}(1+p) \; ; \qquad \lambda_4 = \frac{1}{4}(1-3p). \tag{73}$$

Since $\lambda_{1,2,3} \geq 0$ always holds and $\lambda_4 \geq 0$ for $p \leq 1/3$, but $\lambda_4 < 0$ for $p > 1/3$, the state ρ is entangled for $p > 1/3$, and separable otherwise.
Several further entanglement criteria have been developed, see e.g. [11, 7]. Among them are the reduction criterion, the majorisation criterion, the realignment criterion, positive maps, and entanglement witnesses. - In this section, we have only considered bipartite entanglement. The generalisation to multipartite entanglement will be shown in a later lecture.

2.3 The no-cloning theorem

A fundamental difference between classical and quantum information processing is that classical information can be copied perfectly, while this is not possible for quantum states. This is the content of the famous no-cloning theorem.

Theorem 2.3 (No-Cloning Theorem) *It is impossible to clone an unknown quantum state perfectly [12].*

Proof: A linear unitary transformation U that copies (clones) the orthogonal basis states $|0\rangle$ and $|1\rangle$ perfectly is given by:

$$\begin{aligned} U\,|0\rangle\,|i\rangle &= |0\rangle\,|0\rangle\,, \\ U\,|1\rangle\,|i\rangle &= |1\rangle\,|1\rangle\,, \end{aligned} \tag{74}$$

where $|i\rangle$ is an arbitrary initial state. If we want to clone an unknown state $|\psi\rangle = \alpha\,|0\rangle + \beta\,|1\rangle$, we get

$$U\,|\psi\rangle\,|i\rangle = \alpha U\,|0\rangle\,|i\rangle + \beta U\,|1\rangle\,|i\rangle = \alpha\,|0\rangle\,|0\rangle + \beta\,|1\rangle\,|1\rangle\,, \tag{75}$$

where the first equality follows from linearity. The obtained state is not equal to $|\psi\rangle\,|\psi\rangle = [\alpha\,|0\rangle + \beta\,|1\rangle][\alpha\,|0\rangle + \beta\,|1\rangle]$. Thus, it is not possible to clone an unknown state perfectly. □
The above proof is somewhat simplified, as it does not take into account a possible ancilla, and it does not cover the case where a finite ensemble of initial states should be cloned. However, the claim remains valid also in these situations: only an ensemble of orthogonal states can be copied perfectly, with or without ancilla.
The question about the best possible approximate cloning process has been studied in the literature, for example see [13], [14]. There, the optimal quality of a cloning process has been described in terms of the *fidelity*, which is a widely used figure of merit in quantum information. The fidelity between an initial pure state $|\psi\rangle$ and an output state ρ is defined as

$$F = \langle\psi|\,\rho\,|\psi\rangle \; . \tag{76}$$

2.4 Entanglement as a resource

The new vision of quantum information processing is to consider entanglement as a resource, rather than as a mystery. One of the most famous quantum information processing protocols is *quantum teleportation*.

Teleportation (Oxford dictionary): *"Teleportation is the apparently instantaneous transportation of persons etc. across space by advanced technological means."*

If one deletes "apparently instantaneous" and replaces "persons etc" by "information", then this definition holds for quantum teleportation.

The quantum teleportation protocol which will be presented here was published in [15]. The first successful experiments were performed in Innsbruck [16] and Rome [17]. We consider the following scenario: Alice and Bob share an entangled two-qubit state $|\psi^-\rangle_{\rm AB}$ (a singlet). Alice has an additional qubit in an unknown state

$$|\varphi\rangle_{\rm Z} = \alpha\,|0\rangle_{\rm Z} + \beta\,|1\rangle_{\rm Z} \tag{77}$$

and wants to transfer it to Bob.

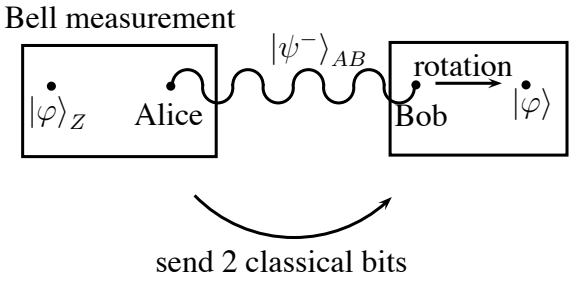

Fig. 4: *Quantum teleportation.*

We write the total state $|\varphi\rangle_{\rm Z} \otimes |\psi^-\rangle_{\rm AB}$ in the Bell basis, i.e. using eqs. (47) the following holds:

$$\begin{aligned}
\left|\psi^{\rm total}\right\rangle &= [\alpha\,|0\rangle + \beta\,|1\rangle]_{\rm Z} \otimes \frac{1}{\sqrt{2}}[|0\rangle_{\rm A}\,|1\rangle_{\rm B} - |1\rangle_{\rm A}\,|0\rangle_{\rm B}] \\
&= \frac{1}{2}\left(\alpha[\left|\phi^+\right\rangle + \left|\phi^-\right\rangle]_{\rm ZA}\,|1\rangle_{\rm B} - \alpha([\left|\psi^+\right\rangle + \left|\psi^-\right\rangle]_{\rm ZA}\,|0\rangle_{\rm B}\right. \\
&\quad \left. +\beta[\left|\psi^+\right\rangle - \left|\psi^-\right\rangle]_{\rm ZA}\,|1\rangle_{\rm B} - \beta[\left|\phi^+\right\rangle - \left|\phi^-\right\rangle]_{\rm ZA}\,|0\rangle_{\rm B}\right) \\
&= \frac{1}{2}\left(\left|\phi^+\right\rangle_{\rm ZA}[\alpha\,|1\rangle - \beta\,|0\rangle]_{\rm B} + \left|\phi^-\right\rangle_{\rm ZA}[\alpha\,|1\rangle + \beta\,|0\rangle]_{\rm B}\right. \\
&\quad \left. + \left|\psi^+\right\rangle_{\rm ZA}[-\alpha\,|0\rangle + \beta\,|1\rangle]_{\rm B} + \left|\psi^-\right\rangle_{\rm ZA}[-\alpha\,|0\rangle - \beta\,|1\rangle]_{\rm B}\right).
\end{aligned} \tag{78}$$

The teleportation protocol consists of the following steps:

1. Alice performs a Bell measurement on her two qubits A and Z, i.e. she does a von Neumann measurement with the set of projectors

$$\{P_\mu\} = \left\{\left|\phi^+\right\rangle\left\langle\phi^+\right|, \left|\phi^-\right\rangle\left\langle\phi^-\right|, \left|\psi^+\right\rangle\left\langle\psi^+\right|, \left|\psi^-\right\rangle\left\langle\psi^-\right|\right\}. \tag{79}$$

   She finds each of the four Bell states with equal probability. The state after the measurement is given by

$$\left|\psi_\mu^{\rm total}\right\rangle = \frac{P_\mu\left|\psi^{\rm total}\right\rangle}{\sqrt{\left\langle\psi^{\rm total}\right| P_\mu \left|\psi^{\rm total}\right\rangle}}. \tag{80}$$

2. Alice communicates classically (e.g. via the phone) with Bob and tells him which of the four possible outcomes of her Bell measurement she found. Thus she has to transmit two classical bits of information.

3. Bob rotates his quantum state with a unitary operation, namely one of the four Pauli matrices, see eq. (34). From Eq. (78) we see that Bob's operation has to be performed according to the following recipe (where the overall phases do not matter):

Alice's outcome	$\|\phi^+\rangle$	$\|\phi^-\rangle$	$\|\psi^+\rangle$	$\|\psi^-\rangle$
Bob's rotation	$i\sigma_y$	σ_x	$-\sigma_z$	$-\mathbb{1}$

Remarks: With this quantum teleportation protocol no matter is transported, but only information. The process is not instantaneous, since classical information has to be transmitted from Alice to Bob, before Bob can reconstruct Alice's state. Entanglement, namely the state $|\psi^-\rangle_{\mathrm{AB}}$, is used as a resource, which is destroyed after the teleportation. At no time two copies of the state $|\varphi\rangle$ exist, such that no contradiction to the No-Cloning-Theorem is found, see section 2.3.

3 Models of quantum computation

As we have seen above, information processing with qubits is fundamentally different from classical information processing. It has been shown that certain computational tasks can be performed faster with quantum tools than with any known classical algorithm (see later lecture and [2, 3]). In this chapter we will discuss two models of quantum computation: the *gate model* (or *circuit model*) was developed in analogy to classical computing, while the model of *one-way quantum computing* has no classical analogon.

3.1 Quantum gates and the circuit model

A *classical logic gate* computes the *Boolean function* $f : \{0,1\}^n \longrightarrow \{0,1\}^l$ with n input and l output bits. In Fig. 5 we show some important examples. Note that every Boolean function can be computed with a network consisting of AND- and NOT-gates only, i.e. the set {AND, NOT} is *universal*. (Other universal sets of classical gates exist as well.)
A *quantum logic gate* (or circuit of quantum gates) computes a function $f : \{|0\rangle, |1\rangle\}^n \longrightarrow \{|0\rangle, |1\rangle\}^l$ from n input qubits to l output qubits by performing a linear, unitary operation. Thus, all quantum gates are reversible, see section 1.1. More information on this topic can be found in Ekert *et al*. [18]. We show some important 1-qubit gates in Fig. 6 and some important 2-qubit gates in Fig. 7.

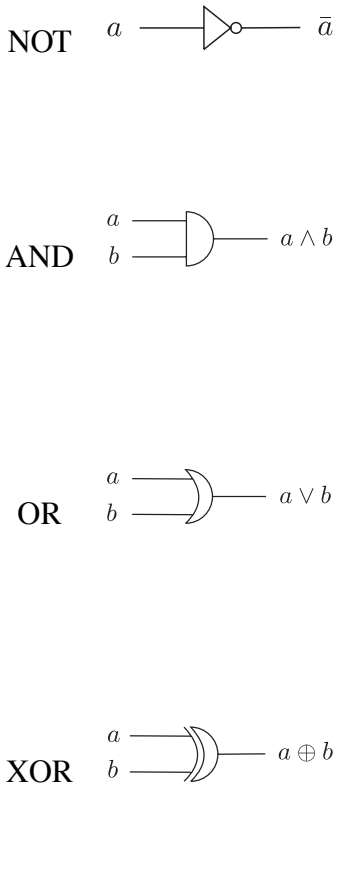

a	$\bar{a}$
0	1
1	0

a	b	$a \wedge b$
0	0	0
0	1	0
1	0	0
1	1	1

a	b	$a \vee b$
0	0	0
0	1	1
1	0	1
1	1	1

a	b	$a \oplus b$
0	0	0
0	1	1
1	0	1
1	1	0

Fig. 5: *Classical logic gates, with the symbolic notation on the left and the corresponding truth table on the right. The inputs* a *and* b *take binary values. Note that the 2-bit gates given above are not reversible.*

Hadamard:

$$H = \frac{1}{\sqrt{2}} \begin{pmatrix} 1 & 1 \\ 1 & -1 \end{pmatrix}$$

$\|x\rangle$	$H\|x\rangle$
$\|0\rangle$	$1/\sqrt{2}[\|0\rangle + \|1\rangle]$
$\|1\rangle$	$1/\sqrt{2}[\|0\rangle - \|1\rangle]$

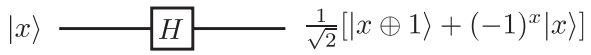

Phase shift gate:

$$\Phi = \begin{pmatrix} 1 & 0 \\ 0 & e^{i\phi} \end{pmatrix}$$

$\|x\rangle$	$\Phi\|x\rangle$
$\|0\rangle$	$\|0\rangle$
$\|1\rangle$	$e^{i\phi}\|1\rangle$

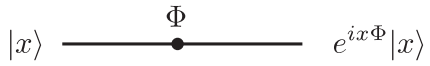

Fig. 6: *Two important 1-qubit gates: the Hadamard gate and the phase gate, with their symbolic notation, matrix representation and truth table. The symbol $\oplus$ means addition modulo 2.*

CNOT (controlled NOT):

$$C = \begin{pmatrix} 1 & 0 & 0 & 0 \\ 0 & 1 & 0 & 0 \\ 0 & 0 & 0 & 1 \\ 0 & 0 & 1 & 0 \end{pmatrix}$$

$\|x\rangle$	$\|y\rangle$	$C\,\|x\rangle\,\|y\rangle$
$\|0\rangle$	$\|0\rangle$	$\|0\rangle\,\|0\rangle$
$\|0\rangle$	$\|1\rangle$	$\|0\rangle\,\|1\rangle$
$\|1\rangle$	$\|0\rangle$	$\|1\rangle\,\|1\rangle$
$\|1\rangle$	$\|1\rangle$	$\|1\rangle\,\|0\rangle$

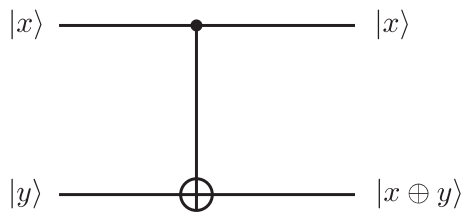

Controlled phase shift:

$$B(\phi) = \begin{pmatrix} 1 & 0 & 0 & 0 \\ 0 & 1 & 0 & 0 \\ 0 & 0 & 1 & 0 \\ 0 & 0 & 0 & e^{i\phi} \end{pmatrix}$$

$\|x\rangle$	$\|y\rangle$	$B(\phi)\,\|x\rangle\,\|y\rangle$
$\|0\rangle$	$\|0\rangle$	$\|0\rangle\,\|0\rangle$
$\|0\rangle$	$\|1\rangle$	$\|0\rangle\,\|1\rangle$
$\|1\rangle$	$\|0\rangle$	$\|1\rangle\,\|0\rangle$
$\|1\rangle$	$\|1\rangle$	$e^{i\phi}\,\|1\rangle\,\|1\rangle$

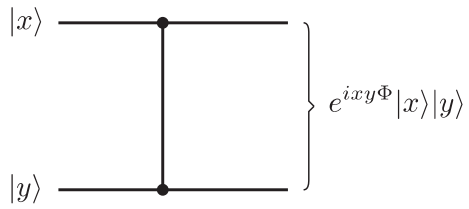

Controlled U:

$$CU = \begin{pmatrix} 1 & & \\ & 1 & \\ & & \boxed{\text{U}} \end{pmatrix}$$

$\|x\rangle$	$\|y\rangle$	$CU\,\|x\rangle\,\|y\rangle$
$\|0\rangle$	$\|y\rangle$	$\|0\rangle\,\|y\rangle$
$\|1\rangle$	$\|y\rangle$	$\|1\rangle\,(U\,|y\rangle)$

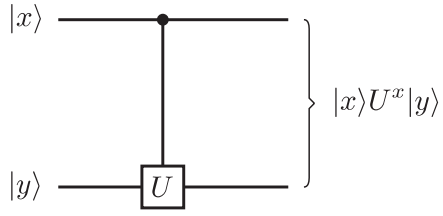

Fig. 7: *Some important 2-qubit gates: the CNOT gate, controlled phase shift and controlled unitary gate, with their symbolic notation, matrix representation and truth table.*

Looking at the truth table for the CNOT gate, it "copies" the basis states onto the target qubit. However, it does not clone an unknown state, as $|x\rangle\,|0\rangle \overset{\text{CNOT}}{\longrightarrow} |x\rangle\,|x\rangle$ only holds for $x = 0, 1$. The CNOT gate creates entanglement, as one can see from its action $(\alpha\,|0\rangle + \beta\,|1\rangle)\,|0\rangle \overset{\text{CNOT}}{\longrightarrow} (\alpha\,|0\rangle\,|0\rangle + \beta\,|1\rangle\,|1\rangle)$. In a rotated basis the roles of control and target qubits are interchanged, see Fig. 8, where we encounter a first network of quantum gates. Its action is obvious from multiplying the corresponding unitary matrices.

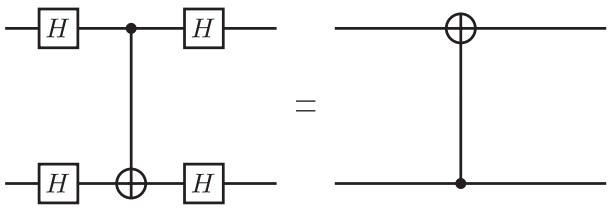

Fig. 8: *CNOT gate in a rotated basis*.

An important 3-qubit gate, the Toffoli gate, is shown in Fig. 9.

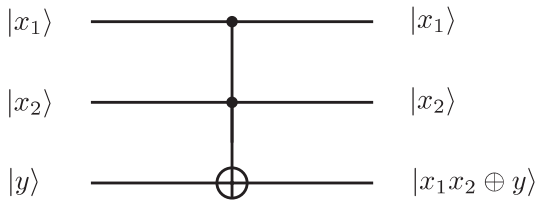

Fig. 9: *The Toffoli gate (controlled-controlled-NOT gate)*.

How many types of gates does one need to construct a general quantum network? An important result for quantum computing is the *universality of quantum gates*, see [19], where it was shown that the set $\{H, \Phi, \text{CNOT}\}$ is universal, i.e. all unitary transformations $U(2^n)$ in 2^n dimensions can be performed with them. Thus, one only needs to build certain simple 1- and 2-qubit quantum gates, into which any quantum network can be decomposed.

3.2 One-way quantum computing

The concept of *one-way quantum computing* (or *measurement-based quantum computing*) was introduced in [20]. The idea is to implement a computation by performing a sequence of measurements of specific qubits in specific bases (later measurement bases depend on earlier measurement outcomes) on a certain type of entangled state of many qubits (a so-called *cluster state*). The entanglement is consumed during this process. The final result is given by the classical data of all measurement outcomes. It can be shown [20, 21] that the one-way quantum computer is computationally equivalent to quantum circuit model (see section 3.1).

Let us first introduce the states which are the basic ingredient of measurement-based quantum computation. We start with a reminder about graphs: An (undirected, finite) *graph* $G = (V, E)$ consists of a finite set of *vertices* V and a finite set of *edges* E. The *neighbourhood* $N_a \subset V$ of a vertex $a \in V$ is the set of vertices $\{b\}$ which are neighbours of a, i.e. $\{a, b\} \in E$.

Definition 3.1 (Graph states and cluster states) *A* graph state $|G\rangle$*, assigned to a graph* $G = (V, E)$*, is defined via*

$$K_G^{(a)} |G\rangle = |G\rangle \qquad \forall\, a \in V\ , \tag{81}$$

where $K_G^{(a)}$ *is the following correlation operator:*

$$K_G^{(a)} = \sigma_x^{(a)} \bigotimes_{b \in N_a} \sigma_z^{(b)}\ . \tag{82}$$

A cluster state $|C\rangle$ *is a graph state associated with a particular type of graph, namely a connected subset (a cluster C) of a rectangular lattice in* $d \geq 1$ *dimensions.*

The set of eigen equations in eq. (81) uniquely (up to a global phase) defines $|G\rangle$. Note that the operators $K_G^{(a)}$ are the generators of a finite Abelian group S_G which is called *stabiliser* of the graph state $|G\rangle$.
Let us give an example for the most simple graph of two connected vertices, named 1 and 2: Here, the stabiliser operators are $K^{(1)} = \sigma_x^{(1)} \otimes \sigma_z^{(2)}$ and $K^{(2)} = \sigma_z^{(1)} \otimes \sigma_x^{(2)}$. Thus,

$$\left.\begin{aligned} \sigma_x^{(1)} \otimes \sigma_z^{(2)} |G_2\rangle &= |G_2\rangle \\ \sigma_z^{(1)} \otimes \sigma_x^{(2)} |G_2\rangle &= |G_2\rangle \end{aligned}\right\} \qquad \Rightarrow |G_2\rangle = \frac{1}{\sqrt{2}}(|0\rangle_z |0\rangle_x + |1\rangle_z |1\rangle_x)\ , \tag{83}$$

where $|0\rangle_x = \frac{1}{\sqrt{2}}(|0\rangle_z + |1\rangle_z)$ and $|1\rangle_x = \frac{1}{\sqrt{2}}(|0\rangle_z - |1\rangle_z)$. Here we have used the action of the Pauli operators: $\sigma_z |0\rangle_x = |1\rangle_x$, $\sigma_z |1\rangle_x = |0\rangle_x$, and $\sigma_x |0\rangle_z = |1\rangle_z$, $\sigma_x |1\rangle_z = |0\rangle_z$. The state in eq. (83) is also the most simple example for a cluster state in $d = 1$. For $n = 3$ and $d = 1$ the corresponding cluster state is

$$|C_3\rangle = \frac{1}{\sqrt{2}}(|0\rangle_x |0\rangle_z |0\rangle_x + |1\rangle_x |1\rangle_z |1\rangle_x)\ . \tag{84}$$

The state in eq. (84) is often also referred to as Greenberger-Horne-Zeilinger- or *GHZ-state*, i.e. a superposition of all subsystems being in the ground state and all being in the excited state. For $n = 4$ and $d = 1$ the corresponding cluster state is *not* a 4-party GHZ state, but

$$|C_4\rangle = \frac{1}{2}(|{+}0{+}0\rangle + |{+}0{-}1\rangle + |{-}1{-}0\rangle + |{-}1{+}1\rangle)\ , \tag{85}$$

where we have used the notation $|+\rangle = |0\rangle_x = \frac{1}{\sqrt{2}}(|0\rangle_z + |1\rangle_z)$, and $|-\rangle = |1\rangle_x = \frac{1}{\sqrt{2}}(|0\rangle_z - |1\rangle_z)$.
One can *prepare* a cluster state $|C\rangle$ by performing pairwise Hadamard operations and then turning on an Ising interaction between all neighbours:

- Prepare a product state, $|+\rangle_C = \bigotimes_{a \in C} |+\rangle_a$.

- Apply a control-σ_z gate S^{ab} between neighbouring qubits:

$$S^{(C)} = \prod_{a,b \text{ neighbours} \in C} S^{ab}\ , \tag{86}$$

where the action of the control-σ_z gate is given by

$$\begin{aligned} S^{ab} : |00\rangle_{ab} &\to |00\rangle_{ab} \ , \\ |01\rangle_{ab} &\to |01\rangle_{ab} \ , \\ |10\rangle_{ab} &\to |10\rangle_{ab} \ , \\ |11\rangle_{ab} &\to -|11\rangle_{ab} \ . \end{aligned} \tag{87}$$

It is straightforward to show that $|C\rangle = S^{(C)} |+\rangle_C$ is a cluster state, i.e. it fulfils the eigenvalue equations for a cluster state, see eq. (81).

Thus, the gate S^{ab} creates an edge between vertices a and b in the graph. Note that the interaction term of the Hamiltonian that corresponds to this operation is an *Ising* Hamiltonian:

$$H_{\text{int}} = \hbar g \sum_{a,b \text{ neighbours}} \sigma_z^{(a)} \otimes \sigma_z^{(b)} \ , \tag{88}$$

where g is the coupling constant.
The essential building blocks to implement an algorithm on the one-way quantum computer are *local* measurements:
Let $G = (V, E)$ be a graph, with associated graph state $|G\rangle$ (remember that cluster states are particular graph states). A measurement of $\sigma_x^{(a)}$, $\sigma_y^{(a)}$ or $\sigma_z^{(a)}$ of the qubit at the vertex $a \in V$ leads to the following state (which depends on the measurement result ± 1):

$$P_{\tau,\pm}^{(a)} |G\rangle = |\tau, \pm\rangle^{(a)} \otimes U_{\tau,\pm}^{(a)} |G'\rangle \, ; \qquad \tau = \ \text{x, y, z} \, , \tag{89}$$

where $P_{\tau,\pm}^{(a)} = \frac{1 \pm \sigma_\tau^{(a)}}{2}$ is the projector onto $|\tau, \pm\rangle$, e.g. $|z, +\rangle = |0\rangle$, $|x, -\rangle = \frac{1}{\sqrt{2}}(|0\rangle - |1\rangle)$ etc. Here, for the case $\tau = z$ we have

$$U_{z,+}^{(a)} = \mathbb{1}; \quad U_{z,-}^{(a)} = \prod_{b \in N_a} \sigma_z^{(b)} \, , \tag{90}$$

and the remaining graph G' is $G' = G - \{a\}$ (i.e. all edges that contain a are removed). The cases $\tau = x, y$ are more involved, i.e. the unitary operations $U_{\tau,\pm}$ and the remaining graph G' are much more complicated. We therefore refer for more details and the proof to the original literature [20].
In [20, 22] the computational model underlying the one-way quantum computer was discussed, and it was shown that any quantum network can be implemented on a suitable cluster state. The essential steps are qualitatively described as follows: 1. Remove the superfluous qubits by a measurement in σ_z-basis (see above). 2. Realisation of a general rotation $U_R \in SU(2)$ local measurements related to the Euler angles. 3. Realisation of a CNOT-gate via a suitable cluster and according local measurements. 4. Realisation of other simple gates, e.g. Hadamard, phase gate. 5. Concatenation of gates (sequential or non-sequential). - Thus, a universal set of quantum gates can be implemented on a cluster state via local measurements, and the gates can be connected. For details we refer to [20, 22].

4 Quantum channels and quantum noise

As discussed in section 1.1, the time evolution of an *isolated* (closed) quantum system is unitary, due to the structure of the Schrödinger equation. *Open systems* are systems which interact with an environment. For quantum information processing on one side one needs interaction with the environment (e.g. to read out a result), but on the other side it may destroy the fragile quantum effects by introducing noise. Two main effects play an important role here:

1. Dissipation (loss of energy), where the diagonal elements of the density matrix are modified.

2. Decoherence (loss of coherence), where the off-diagonal elements of the density matrix are modified.

In order to study the influence of the environment let us first consider the system plus the environment as a new total (closed) system, which is isolated and evolves unitarily. As a model for decoherence of a two-level system A in an environment E we consider the *phase-damping channel*, which is defined via the following unitary evolution of the total system in the Hilbert space $\mathcal{H} = \mathcal{H}_{\rm A} \otimes \mathcal{H}_{\rm E}$:

$$|0\rangle_{\rm A}\,|0\rangle_{\rm E} \;\longrightarrow\; \sqrt{1-p}\,|0\rangle_{\rm A}\,|0\rangle_{\rm E} + \sqrt{p}\,|0\rangle_{\rm A}\,|1\rangle_{\rm E}\ , \tag{91}$$

$$|1\rangle_{\rm A}\,|0\rangle_{\rm E} \;\longrightarrow\; \sqrt{1-p}\,|1\rangle_{\rm A}\,|0\rangle_{\rm E} + \sqrt{p}\,|1\rangle_{\rm A}\,|2\rangle_{\rm E}\ , \tag{92}$$

where $0 \leq p \leq 1$. A general initial state of the system $|\psi\rangle_{\rm A}^{\rm in} = \alpha\,|0\rangle_{\rm A} + \beta\,|1\rangle_{\rm A}$ then evolves as follows:

$$|\psi\rangle_{\rm A}^{\rm in}\,|0\rangle_{\rm E} \longrightarrow [\alpha\sqrt{1-p}\,|0\rangle_{\rm A} + \beta\sqrt{1-p}\,|1\rangle_{\rm A}]\,|0\rangle_{\rm E} + \alpha\sqrt{p}\,|0\rangle_{\rm A}\,|1\rangle_{\rm E} + \beta\sqrt{p}\,|1\rangle_{\rm A}\,|2\rangle_{\rm E}\,. \tag{93}$$

The reduced density matrix of the system is thus given by:

$$\rho_{\rm red,A}^{\rm f} = \begin{pmatrix} |\alpha|^2 & (1-p)\alpha\beta^* \\ (1-p)\alpha^*\beta & |\beta|^2 \end{pmatrix}\ . \tag{94}$$

We observe that the off-diagonal elements (the "coherences") of the system's density matrix decrease with the factor $(1-p)$, i.e. the state undergoes *decoherence*. Note that, if decoherence acts on a composite system, the decay of the off-diagonal elements of the density matrix will reduce or destroy its entanglement. - Dissipation can be similarly described by the so-called *amplitude damping channel*.
If one is not interested in the evolution of the environment, but only in the evolution of the system, like above, one traces out the environment from the unitary evolution of the total system. An equivalent description consists in the application of a *completely positive (CP) map*.

Definition 4.1 (Completely positive maps) *A map Λ is called positive, if it takes positive operators to positive operators, i.e. if $\rho \geq 0$ then $\Lambda(\rho) \geq 0$. A positive map Λ is called completely positive, if any extension $\mathbb{1}_d \otimes \Lambda$ is positive for arbitrary d.*

Any physical quantum operation (e.g. a noisy channel) can be described with a CP map. (Remark: maps which are positive, but not completely positive, like the transposition, can detect entanglement, as they may lead to a non-positive operator when applied to only a subsystem.)

Any CP map can be written as [23]

$$\Lambda_{CP}(\rho) = \sum_k \hat{A}_k \rho \hat{A}_k^\dagger \,, \tag{95}$$

where $\hat{A}_k$ are the so-called *Kraus operators*. The map Λ is trace preserving, iff $\sum_k \hat{A}_k^\dagger \hat{A}_k = \mathbb{1}$ is fulfilled.
The Kraus operators for the phase-damping channel are given by

$$\hat{A}_1^{\rm pd} = \begin{pmatrix} 1 & 0 \\ 0 & \sqrt{1-p} \end{pmatrix} ; \qquad \hat{A}_2^{\rm pd} = \begin{pmatrix} 0 & 0 \\ 0 & \sqrt{p} \end{pmatrix} . \tag{96}$$

The Kraus operators for the amplitude-damping channel are given by

$$\hat{A}_1^{\rm ad} = \begin{pmatrix} 1 & 0 \\ 0 & \sqrt{1-p} \end{pmatrix} ; \qquad \hat{A}_2^{\rm ad} = \begin{pmatrix} 0 & \sqrt{p} \\ 0 & 0 \end{pmatrix} . \tag{97}$$

Let us also mention another type of channel which often occurs, the *depolarising channel*. Its action consists in mixing a given state ρ with the identity, with probability p, i.e. for a qubit its action is given by

$$\Lambda^{\rm dep}(\rho) = (1-p)\rho + p\frac{1}{2}\mathbb{1} \,. \tag{98}$$

The Kraus operators for the depolarising channel are given by

$$\hat{A}_1^{\rm dep} = \sqrt{1-\frac{3p}{4}}\,\mathbb{1} \,; \qquad \hat{A}_2^{\rm dep} = \sqrt{\frac{p}{4}}\,\sigma_x \,; \qquad \hat{A}_3^{\rm dep} = \sqrt{\frac{p}{4}}\,\sigma_y \,; \qquad \hat{A}_4^{\rm dep} = \sqrt{\frac{p}{4}}\,\sigma_z \,, \tag{99}$$

where σ_i are the Pauli operators, see eq. (34). - Note that the Kraus operators can also be seen as error operators: in the example of the depolarising channel an error corresponding to the application of a Pauli operator $\sigma_x, \sigma_y, \sigma_z$ happens with equal probability. - How to correct a quantum state after the action of a noisy quantum channel will be discussed in the lecture on quantum error correction.

References

[1] A. Peres, *Quantum Theory: Concepts and Methods*, Kluwer Academic Publishers, Dordrecht (1998)

[2] M. Nielsen and I. Chuang, *Quantum Computation and Quantum Information*, Cambridge University Press (2000)

[3] D. Bruß and G. Leuchs, *Lectures on Quantum Information*, Wiley-VCH (2007)

[4] R. Bertlmann and P. Krammer, J. Phys. A: Math.Theor. **41**, 235303 (2008)

[5] E. Schrödinger, Naturwissenschaften **23**, 807 (1935)

[6] K. Modi, A. Brodutch, H. Cable, T. Paterek, and V. Vedral, Rev. Mod. Phys. **84**, 1655 (2012)

[7] R. Horodecki, P. Horodecki, M. Horodecki, and K. Horodecki, Rev. Mod. Phys. **81**, 865 (2009)

[8] A. Peres, Phys. Rev. Lett. **77**, 1413 (1996)

[9] P. Horodecki, M. Horodecki, and R. Horodecki, Phys. Lett. **A 233**, 1 (1996)

[10] R.F. Werner, Phys. Rev. A, **40**, 4277 (1989)

[11] D. Bruß, J. Math. Phys. **43**, 4237 (2002)

[12] W. Wootters and W. Zurek, Nature **299**, 802 (1982)

[13] D. Bruß, D. P. DiVincenzo, A. Ekert, C. A. Fuchs, C. Macchiavello, and J. A. Smolin, Phys. Rev. A **57**, 2368 (1998)

[14] V. Scarani, S. Iblisdir, N. Gisin, and A. Acin, Rev. Mod. Phys. **77**, 1225 (2005)

[15] C.H. Bennett, G. Brassard, C. Crepeau, R. Jozsa, A. Peres, and W.K. Wootters, Phys. Rev. Lett. **70**, 1895 (1993)

[16] D. Bouwmeester, J.-W. Pan, K. Mattle, M. Eibl, H. Weinfurter, and A. Zeilinger, Nature **390**, 575 (1997)

[17] D. Boschi, S. Branca, F. De Martini, L. Hardy, and S. Popescu, Phys. Rev. Lett. **80**, 1121 (1998)

[18] A. Ekert, P. Hayden, and H. Inamori, arXiv:quant-ph/0011013

[19] A. Barenco, C. H. Bennett, R. Cleve, D. P. DiVincenzo, N. Margolus, P. Shor, T. Sleator, J. Smolin, and H. Weinfurter, Phys. Rev. **A 52**, 3457 (1995)

[20] R. Raussendorf and H.J. Briegel, Phys. Rev. Lett. **86**, 5188 (2001)

[21] R. Raussendorf, D. Browne, and H.J. Briegel, Phys. Rev. A **68**, 022312 (2003)

[22] R. Raussendorf and H.J. Briegel, Quantum Inf. Comp. **6**, 433 (2002)

[23] K. Kraus, *States, Effects and Operations*, Springer, Berlin (1983)

A 3 Introduction to Physical Implementations of Quantum Information Processing[1]

Stephan Dürr

Max-Planck-Institut für Quantenoptik, Garching

Contents

1 Quantum Information Processing with Atoms and Ions **2**

2 Qubits in Ions **2**

3 The Cirac-Zoller Quantum Computer for Ions **4**

4 Qubits in Atoms **7**

5 Atoms as Single-Photon Sources **9**

6 Atoms as Quantum Memories for Photonic Qubits **13**

7 Creation of Remote Entanglement **15**

A Lambda Systems: STIRAP and Dark-State Polaritons **16**

[1]Lecture Notes of the 44^{th} IFF Spring School "Quantum Information Processing" (Forschungszentrum Jülich, 2013). All rights reserved.

1 Quantum Information Processing with Atoms and Ions

When comparing atomic systems (including ions) with solid-state systems regarding their suitability for applications in quantum information processing (QIP), one finds that atomic systems have the advantage of long coherence times for the quantum bits (qubits) because it is easy to isolate the qubits from the environment. Solid-state systems offer the advantage that only moderate effort is needed to adapt existing fabrication technologies to produce a really large number of replicas of building blocks for QIP.

The strength of each system reveals the weakness of the other. People trying to scale up atomic systems to a really large number of qubits quickly enter uncharted territory. On the other hand, many solid-state qubits suffer from short qubit coherence times which are caused by poor isolation of the qubits from their environment. The latter is due to the fact that a qubit in a solid is always surrounded by other nearby particles; and short distances tend to cause poor isolation. A recent experiment [1] achieved a qubit coherence time exceeding 1 s in a room-temperature solid. But the isolation techniques used there are not necessarily applicable to all kinds of solid-state experiments. As of now, nobody knows which systems will turn out to be most suitable for QIP in the long run.

Obviously, short coherence times can easily prevent experimentalists from performing first proof of principle experiments, whereas potential issues with future scalability will not. This is why early experiments on QIP were typically performed with photons, atom, and ions several years prior to corresponding solid-state experiments. The demonstration of quantum key distribution using photons in 1992 [2] can arguably be regarded as the first experiment on QIP. In 1995, an experiment using an atom in a cavity measured a conditional phase shift [3] and was published back-to-back with the first quantum logic gate demonstrated with ions [4]. The first solid-state quantum logic gate followed in 2003 [5]. Many of the insights gained from the experiments with photons, atoms, and ions are directly relevant for solid-state QIP.

Hybrid systems are an attempt to get the best of both worlds. They couple different kinds of systems; e.g. an early proposal suggested coupling trapped molecules with a nearby solid-state qubit [6]. The experimental implementation of such systems has started only recently. The strength of hybrid systems lies in the fact that they offer a perspective to take advantage of the long coherence times of atomic systems and of the scalability of solid-state systems.

The present chapter A3 concentrates on QIP in atoms and ions. The objective is to give a brief introduction which can clearly not be a comprehensive review. Excluded here are topics which are – at least traditionally – purely photonic, such as quantum cryptography [2], dense coding [7], quantum teleportation [8, 9], and entanglement swapping [10], because they are discussed by Barbara Kraus in chapter A5. Another field not covered here uses continuous variables (i.e. squeezed light and spin squeezing) instead of qubits, see e.g. the review article [11]. We begin with ions and then turn to atoms.

2 Qubits in Ions

This section briefly introduces some experimental techniques for QIP in ions. Further details on these techniques and further references can be found e.g. in the textbook [12] or in the review articles [13, 14]. There is also some coverage on ions by Enrique Solano in chapter C2 where the focus is more on quantum simulations.

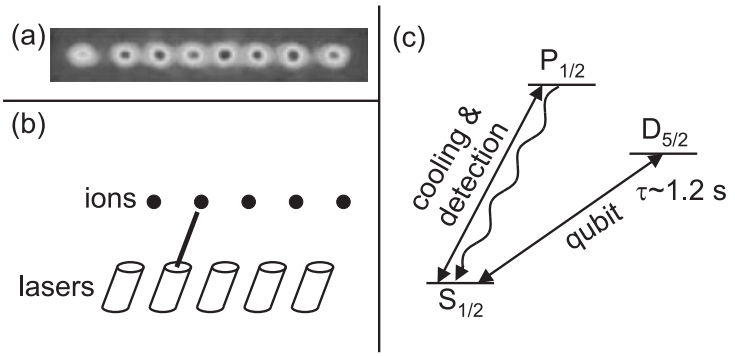

Fig. 1: *(a) Experimental image of a chain of 8 trapped ions. For imaging, the ions are illuminated with laser light. The florescence is recorded with a digital camera. The ions are essentially at rest. The distance between ions is ∼5 μm. Reproduced from Ref. [15]. (b) Each ion can be addressed with an individual laser beam. (c) A simplified level scheme of $^{40}Ca^{+}$. A qubit is encoded in the two-dimensional space spanned by the $S_{1/2}$ ground state and the metastable $D_{5/2}$ state with a lifetime of ∼1.2 s. The closed-cycling transition $S_{1/2} \leftrightarrow P_{1/2}$ is used for Doppler cooling and for state detection.*

Cooling and Trapping. Ions are electrically charged and respond correspondingly strongly to electric fields. A clever design of an electrode geometry and a suitable choice of applied ac- and dc-voltages suffices to trap an ion. Once trapped, an ion can be stored for several months. The two standard geometries are called Paul trap and Penning trap. For several years now, some groups have fabricated the electrodes by micro-structuring of wires on solid-state substrates. These systems are called chip traps and offer a better perspective for scalability to a large number of qubits.

Laser light is used to cool the trapped ions. The two regimes of laser cooling employed here are called Doppler cooling and sideband cooling. The latter makes it possible to cool essentially all the population into the vibrational ground state of the trap.

It is possible to trap many ions simultaneously in an ion trap. If the ions are cold enough, then the Coulomb repulsion between the ions will cause the formation of an ion crystal. For an appropriate trap geometry, the ions form a linear chain in which the distance between adjacent ions is approximately 5 μm. This makes it possible to address each ion individually with a tightly focused laser beam, as illustrated in Fig. 1(b).

Qubits. An obvious way to encode a qubit in a single ion is to pick a suitable pair of internal states. When implementing a qubit, one typically wants long coherence time combined with experimental techniques for the following general procedures: single-qubit rotations, state preparation, and state detection. For single ions one typically reaches these goals in the following way.

Coherence Time. Typical experiments encode the qubit values $|0\rangle$ and $|1\rangle$ in a pair of internal states. One strategy uses one ground state and one metastable state (optical qubit), another strategy uses two ground states with different hyperfine or Zeeman quantum numbers (hyperfine qubit or Zeeman qubit). The lifetimes of these states against spontaneous emission of a photon are extremely long. In addition to this long lifetime against population decay from the qubit states $|0\rangle$ and $|1\rangle$ (T_1 time), one also needs a long lifetime of the phase in a coherent

superposition of the qubit states (T_2 time). Here, fluctuating magnetic fields often impose limitations because they introduce fluctuations in the energy difference between the qubit states.[2] The longest T_2 limes will be achieved if one picks a pair of states that have the same linear Zeeman effect. A transition between such a pair of states is called clock transition because its insensitivity to magnetic-field fluctuations will also be advantageous if used for an ion clock. Another option is the use of a decoherence-free subspace, see e.g. Ref. [16].

Single-Qubit Rotations. In order to obtain a straightforward implementation of arbitrary single-qubit rotations, one typically chooses a pair of states that is connected by an optical transition (for an optical qubit) or by a radio-frequency transition or optical Raman transition (for a hyperfine or Zeeman qubit). To achieve high fidelity of these rotations, one needs to control the intensity, detuning, and duration of the applied pulses very accurately. In some cases, techniques based on adiabatic following, photon echoes, or geometric phases can be used to relax the control requirements on the experimental parameters somewhat.

State Preparation. Optical pumping is a standard technique for preparing the internal state of the ion. This is possible with high fidelity. If for a specific internal state no efficient optical pumping scheme is available, then one will typically use, first, optical pumping into a different state and, second, radio-frequency pulses for a coherent population transfer into the desired state.

State Detection. Many ions offer what is called a closed-cycling transition. This refers to an optical transition where an excited internal state has only one ground state into which it can decay spontaneously. If a single ion is initially in this ground state and it is excited by a laser, then this can be used to scatter a large number of photons. If the ion is in another long-lived state, however, no photon scattering occurs. Even if only a small fraction of the photons are collected and counted, one will obtain a high-fidelity internal state detection. An example is shown in Fig. 1(c).

3 The Cirac-Zoller Quantum Computer for Ions

The above-listed techniques for preparation, detection, and single-qubit rotations are relatively straightforward because they involve only single-ion physics. Implementing a universal two-qubit gate, however, requires an interaction between two ions. The Coulomb repulsion between ions is an obvious candidate for this interaction. This insight lies at the heart of the seminal 1995 paper by Cirac and Zoller [17] which is one of the first proposals for a physical realization of a quantum computer.

Motional Sidebands. For a linear chain of ions in a trap, the Coulomb interaction gives rise to normal modes of the collective motion of the cold ions. The Cirac-Zoller scheme uses the center-of-mass (CM) mode with angular frequency ω_{CM}. We consider the optical transition between an internal ground state $|g\rangle$ and an excited state $|e\rangle$. This transition can change the

[2] If this energy difference is $\hbar\omega_{01}$, then the free evolution of the off-diagonal element of the density matrix will be given by $\rho_{01}(t) = \rho_{01}(0)e^{i\omega_{01}t}$. Hence, fluctuations of ω_{01} cause a decay of ρ_{01}.

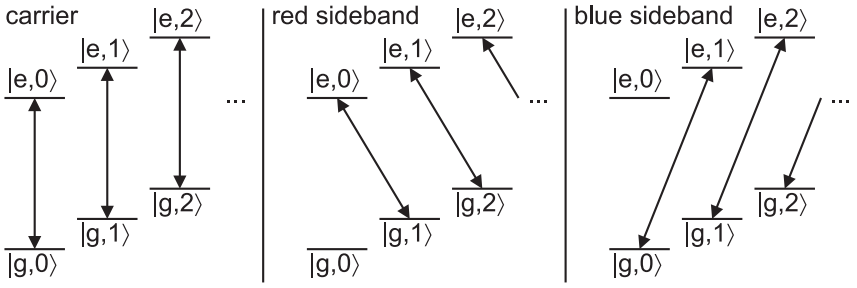

Fig. 2: *Level scheme including motional sidebands. The levels are labeled* $|g, n_{CM}\rangle$ *and* $|e, n_{CM}\rangle$*, respectively, where* n_{CM} *is the phonon number. The red sideband, carrier, and blue sideband drive the transitions* $|g, n_{CM}\rangle \leftrightarrow |e, n_{CM} + \Delta n_{CM}\rangle$ *with* $\Delta n_{CM} = -1,\ 0,$ *and* $1,$ *respectively. Note that the red sideband does not affect the state* $|g, 0\rangle$*.*

number of phonons in the CM mode n_{CM} by $\Delta n_{CM} = 0$ or $\Delta n_{CM} = \pm 1$. The angular frequency of the light resonant with this transition is

$$\omega_{eg} + \omega_{CM}\Delta n_{CM}. \tag{1}$$

In typical experiments, the width of these resonances is much less than ω_{CM}, so that the motional sidebands are well resolved. A light pulse applied with this frequency will drive coherent Rabi flopping on the transitions

$$|g, n_{CM}\rangle \leftrightarrow |e, n_{CM} + \Delta n_{CM}\rangle \tag{2}$$

for all n_{CM} simultaneously. The transitions with $\Delta n_{CM} = +1$ and -1 create a blue and red sideband, respectively, relative to the carrier frequency at ω_{eg}. A level scheme for the $|g\rangle \leftrightarrow |e\rangle$ transition including n_{CM} is shown in Fig. 2.
ω_{CM} is typically on the order of several MHz. If a light pulse is to resolve the sideband from the carrier, then the light pulse must be longer than $1/\omega_{CM}$ to make interaction-time broadening negligible. This sets the speed limit for the Cirac-Zoller gate. In addition, other normal modes of the vibration of the ions must also be separated. This will become a serious issue if the number of ions is large, because then the sidebands of different vibrational modes lie close to each other. In passing we note that the sideband cooling mentioned earlier is based on these very sidebands.

The Cirac-Zoller Two-Qubit Gate. Using the motional sidebands, one can implement a two-qubit quantum-logic gate in a chain of N ions. The n-th ion carries a qubit encoded in a ground state $|g_n\rangle$ and one long-lived excited state $|e_n\rangle$. There is an auxiliary excited state $|a_n\rangle$, which does not carry a qubit but will be useful during the gate operation. The gate is accomplished by consecutively applying three light pulses as follows:

(i) a red-sideband π-pulse for the $|g\rangle \leftrightarrow |e\rangle$ transition on the m-th ion,
(ii) a red-sideband 2π-pulse for the $|g\rangle \leftrightarrow |a\rangle$ transition on the n-th ion, and
(iii) the same as (i).

We consider the action of pulse (i). With the initial qubit values $|e_m\rangle$ or $|g_m\rangle$ combined with $n_{CM} = 0$, one drives the transition

$$|e_m, 0\rangle \leftrightarrow |g_m, 1\rangle. \tag{3}$$

The state $|g_m, 0\rangle$ is unaffected by the red sideband, because the number of phonons n_{CM} cannot become negative; see also Fig. 2. However, amplitude in state $|e_m, 0\rangle$ is fully transferred into state $|g_m, 1\rangle$, thus creating one phonon. In this process, a phase factor of $-i$ is picked up.
We turn to pulse (ii). With the initial qubit values $|e_n\rangle$ or $|g_n\rangle$ combined with $n_{CM} = 0$ or 1, one drives the transition

$$|g_n, 1\rangle \leftrightarrow |a_n, 0\rangle. \tag{4}$$

The state $|g_n, 0\rangle$ is unaffected, as above. The states $|e_n, n_{CM}\rangle$ are generally not coupled at all by this light. The state $|g_n, 1\rangle$, however, will undergo a 2π cycle to state $|a_n, 0\rangle$ and back. The amplitude will pick up a factor of -1 in the process. This phase factor is crucial because it will be picked up, if and only if the initial state before pulse (i) is $|e_m, g_n, 0\rangle$.
We now come to pulse (iii). As the population of all states was unchanged after pulse (ii), pulse (iii) essentially reverses the action pulse (i). It adds another phase factor of $-i$ in the transition from $|g_m, 1\rangle$ to $|e_m, 0\rangle$. In the absence of pulse (ii), one would simply obtain a total phase factor of -1 for state $|e_m, 0\rangle$ from pulses (i) and (iii).
Overall, we obtain

$$\begin{array}{cccccc} |g_m, g_n, 0\rangle & & |g_m, g_n, 0\rangle & & |g_m, g_n, 0\rangle & & |g_m, g_n, 0\rangle \\ |g_m, e_n, 0\rangle & \xrightarrow{\text{(i)}} & |g_m, e_n, 0\rangle & \xrightarrow{\text{(ii)}} & |g_m, e_n, 0\rangle & \xrightarrow{\text{(iii)}} & |g_m, e_n, 0\rangle \\ |e_m, g_n, 0\rangle & & -i|g_m, g_n, 1\rangle & & i|g_m, g_n, 1\rangle & & |e_m, g_n, 0\rangle \\ |e_m, e_n, 0\rangle & & -i|g_m, e_n, 1\rangle & & -i|g_m, e_n, 1\rangle & & -|e_m, e_n, 0\rangle \end{array} . \tag{5}$$

This is a unitary transformation with matrix representation

$$U_{\text{phase}} = \begin{pmatrix} 1 & 0 & 0 & 0 \\ 0 & 1 & 0 & 0 \\ 0 & 0 & 1 & 0 \\ 0 & 0 & 0 & -1 \end{pmatrix}. \tag{6}$$

This is called a conditional phase gate. This two-qubit gate is universal, i.e. an arbitrary computation on a quantum computer can be decomposed into two-qubit conditional phase gates and single-qubit rotations. For example, single-qubit rotations can convert this gate into a controlled NOT (CNOT) gate with matrix representation

$$U_{\text{CNOT}} = \begin{pmatrix} 1 & 0 & 0 & 0 \\ 0 & 1 & 0 & 0 \\ 0 & 0 & 0 & 1 \\ 0 & 0 & 1 & 0 \end{pmatrix} \tag{7}$$

which is also universal.
Shortly after publication of the proposal, a first experiment [4] demonstrated a version of the Cirac-Zoller gate that uses two degrees of freedom of a single ion as the qubits. The full Cirac-Zoller gate for two ions was experimentally demonstrated in 2003 [18]. Data from this experiment are shown in Fig. 3. Part (a) shows the measured modulus squared of all matrix elements of U_{CNOT} from Eq. (7). This is called truth table. In principle, the phases of all 16 matrix elements remain to be measured. In practice, however, one often performs a test of phase coherence in an appropriate basis, such as the one shown in Fig. 3(b), and considers this as sufficient to show that the gate operates properly.

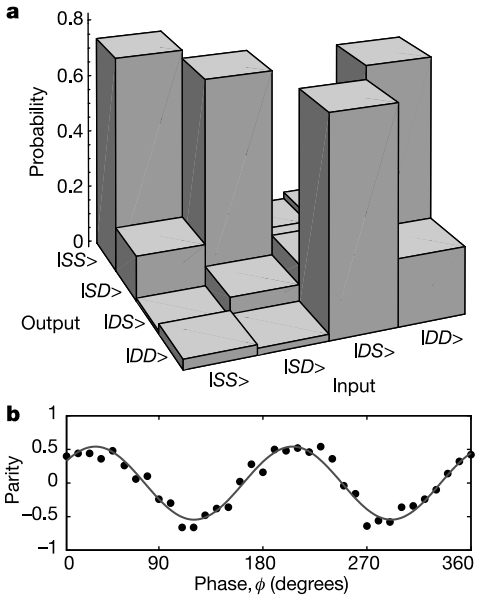

Fig. 3: *Experimental data on the Cirac-Zoller gate. (a) Truth table for the gate, showing the measured modulus squared of the matrix elements of U_{CNOT} from Eq.* (7)*. (b) Demonstration of phase coherence. Reproduced from Ref. [18].*

Generalizations. The generalization of this scheme to an n-qubit conditional phase gate for arbitrary n is straightforward [17]. Having such gates is desirable, because if a complicated algorithm is decomposed into n-qubit gates, then the number of required operations will decrease with increasing n.

The Cirac-Zoller gate heavily relies on the assumption that $n_{CM} = 0$ initially. In an experiment, the probability for $n_{CM} = 1$ can be made small, but never exactly zero. This corresponds to a nonzero temperature in the population of this mode. This limits the achievable gate fidelity. A solution lies in the Mølmer-Sørensen gate, proposed in Refs. [19, 20, 21], which can tolerate nonzero temperatures much better. An addition advantage is that this gate does not require individual addressing of the ions during the gate operation.

Any universal two-qubit gate must be able to generate a maximally entangled state from an appropriately chosen, separable input state. This is called entangling gate operation. It is frequently used when experimentally demonstrating that a logic gate works as advertised. For example, the first experimental demonstration of the Mølmer-Sørensen gate entangled up to 4 ions [22]. More recent experiments entangled up to 14 ions [15, 23]. For entangled states of so many particles, it is a serious challenge to conceive and carry out a measurement procedure that proves the entanglement.

Another two-ion gate is the geometric phase gate, proposed in Ref. [24]. It shares the advantages of the Mølmer-Sørensen gate, but is less sensitive to various experimental imperfections. Its first experimental demonstration in 2003 [25] already achieved a fidelity of 97%.

4 Qubits in Atoms

A related line of research pursues QIP in neutral atoms. Coherence time, state preparation, state detection, and single-qubit rotations are largely similar to ions. Again, light forces created with

lasers are the standard tool for cooling the particles. But now, they also serve for trapping the particles, see the textbook [26] for details and for further references.

Cooling and Trapping. The magneto-optical trap (MOT) is an extension of the Doppler cooling scheme. It is used for capturing up to 10^{10} atoms from an atomic beam or from a vapor and for cooling the atoms to temperatures of $\sim$100 μK. After collection and cooling in a MOT, many experiments use what physicist call an optical dipole trap and biologists call optical tweezers. This trap is made of a focused laser beam that is far red detuned from all atomic transitions. The light induces an oscillating electric dipole moment in the atom, which experiences a potential energy in the light field. The atoms are attracted to regions of high light intensity. Optical dipole traps can be several mK deep, but many are much shallower.

Van-der-Waals Interaction. As discussed above, an interparticle interaction is needed to build a quantum logic gate. In this respect it is problematic, that the interaction between neutral ground-state atoms is much weaker than between ions. Instead of a charge, the interaction relies on the electric polarizability of the atoms. At large interatomic distance r, this creates a van-der-Waals tail of the atom-atom interaction potential, described by $V(r) = C_6/r^6$. The C_6 coefficient is typically on the order of 10^3 atomic units (1 a.u. $= 9.57 \times 10^{-80}$ Jm^6). The weakness of this interaction makes it difficult to achieve gate-operation times that are short enough to be interesting. For example, to achieve a gate operation time of 1 ms, one would need at least $V = 2\pi\hbar \times 1$ kHz. This requires an interparticle separation of $r \sim 20$ nm, which makes individual addressing with laser light impractical. For comparison, the Coulomb interaction between two ions at a distance of 5 μm amounts to $\sim 2\pi\hbar \times 70$ GHz.

Rydberg States. There are various options how to solve the problem of the weakness of the interaction. One option is the use of Rydberg states. They have a much larger polarizability and have recently been used to realize a universal quantum logic gate for neutral atoms [27, 28] and to build a single-photon source [29].

Atoms and Photons. Another option to influence one atom with another is by emitting a single photon from the one atom and absorbing it in the other. The polarization of the photon can carry a qubit. The tricky part is to emit only one photon and to make the emission directed and the absorption efficient. A brief look at the absorption process already illustrates the problem and hints at possible solutions. An atom has an absorption cross section of $\sigma = 3\lambda^2/2\pi$ for light at wavelength λ, resonant with a closed-cycling transition. It is very difficult to focus a laser beam down to small enough a spot size to obtain deterministic absorption in a single atom. However, there are two strategies to effectively enhance the atom-photon interaction.

Atomic Ensembles. One strategy is to use an ensemble, consisting of a large number of atoms. The single photon can be absorbed by any atom in the ensemble. It remains unknown, which atom absorbed the photon. Hence, the absorption creates a collective excitation involving all atoms. The collective excitation can carry a qubit. The absorption cross section is effectively multiplied by the number of atoms. The absorption probability can reach 100%, at least in principle, and atomic ensembles can thus be used to realize QIP protocols.

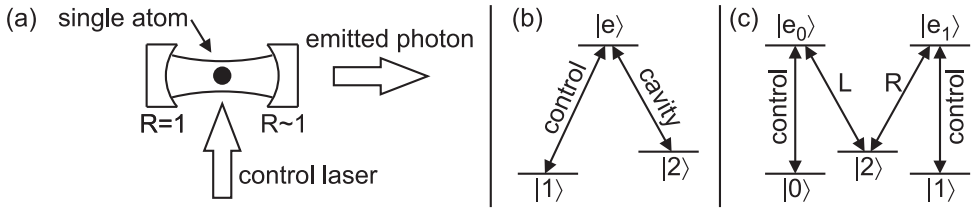

Fig. 4: *Deterministic single-photon source using a single atom. (a) A single atom is excited by a control laser. The scattered photon is preferentially emitted into the cavity mode, from which it is emitted due to the nonzero transmission of one mirror. (b) Simplified atomic level scheme. (c) Extended level scheme. An atomic qubit, encoded in states* $|0\rangle$ *and* $|1\rangle$*, can be mapped onto the polarization qubit of the single photon.*

Atoms-Cavity Systems. The other strategy is to place a single atom inside an optical resonator with highly reflective mirrors. If a photon is coupled into a resonant cavity mode, then it will bounce back and forth between the mirrors many times. To lowest approximation, one can think of this as the photon traveling through the atom many times, thus enhancing the absorption probability by the number of bounces from the mirrors.

QIP experiments based on either strategy, ensembles or cavities, are described in the following sections. We start our description with the emission in Sec. 5. Combining it with the absorption makes it possible to build quantum memories, as described in Sec. 6. Based on these basics, more complex tasks can be mastered. As an example, we consider an experiment that generates remote entanglement in Sec. 7. The techniques presented here offer perspectives for building quantum gates [30, 31, 32, 33] and quantum networks [34, 35, 36].

5 Atoms as Single-Photon Sources

We consider the process of photon emission. One needs a source for the triggered generation of a single photon with a collimated transverse mode. This can be realized either using a single atom in a cavity or an atomic ensemble.

Atom-Cavity Systems. A single atom in a Fabry-Perot resonator is well suited for generating a single photon, as illustrated in Fig. 4. The internal states of the atom form a Λ scheme, with two ground states, labeled $|1\rangle$ and $|2\rangle$, each coupled to the joint excited state $|e\rangle$. One mode of the resonator is tuned into resonance with the transition $|2\rangle \leftrightarrow |e\rangle$. To drive the process, a control laser beam containing many photons is sent onto the atom from the side. This light resonantly couples the atom in the initially prepared state $|1\rangle$ to the excited state $|e\rangle$. From here, the atom will decay back into a ground state. This can either be an undesired, spontaneous process with photon emission essentially into the full solid angle or it can be an emission into the resonator mode that is resonant with the $|2\rangle \leftrightarrow |e\rangle$ transition. Using high-reflectivity mirrors, small mode volume, and adiabatic techniques [37] (see also appendix A) one can make the emission into the resonator mode the dominant process [36]. One deliberately makes one mirror less reflective than the other. Hence, the photon almost always leaves the resonator through this mirror.
All properties of the emitted photon are well controlled: a useful, collimated transverse mode, the polarization, the center frequency, the emission time, and the spatiotemporal wave packet.

The temporal shape of the control laser pulse can be used to tailor the spatiotemporal wave packet of the single photon. As only one atom is inside the resonator and as the final atomic state is not coupled to the control laser, only one photon can be emitted. The efficiency for emitting the photon into the cavity mode is $\sim$60% in present experiments [36] and it can theoretically reach 100%. One can easily extend the atomic level scheme to map an atomic qubit encoded in states $|0\rangle$ and $|1\rangle$ onto the polarization qubit of the single photon; see Fig. 4(c). L and R denote the two circular photon polarizations.

The mathematical description of the flying single photon generated here is based on its spatiotemporal mode function $u(z,t) = u(0, t - z/c)$ with time t, longitudinal coordinate z, and light speed c. A Fourier decomposition of this mode function into plane waves $e^{-i\omega(t-z/c)}$ with angular frequencies ω combined with the standard quantization of these plane waves yields creation and annihilation operators $\hat{a}^\dagger$ and $\hat{a}$ for this mode. The single-photon state for this mode is obtained by applying this creation operator to the vacuum.

A Fock state with exactly one photon is non-classical. The non-classicality can be quantified using the pair correlation function [38]

$$g^{(2)} = \frac{\langle \hat{a}^\dagger \hat{a}^\dagger \hat{a} \hat{a} \rangle}{\langle \hat{a}^\dagger \hat{a} \rangle^2} = \frac{\sum_n n(n-1)p_n}{(\sum_n n p_n)^2} \tag{8}$$

where p_n denotes the probability for detecting n photons. A light pulse emitted by a laser has a Poisson distribution of the p_n, yielding $g^{(2)} = 1$. States with $g^{(2)} < 1$ are non-classical. They are called anti-bunched. Single-photon sources typically operate in the regime $p_{n+1} \ll p_n$ for $n \neq 0$ so that

$$g^{(2)} \sim \frac{2p_2}{p_1^2} \tag{9}$$

characterizes the probability p_2 for the undesired production of two photons normalized to the classical limit. A recent atom-cavity experiment reported a value as low as $g^{(2)} = 0.01$ [39].

Atomic Ensembles and Heralding: The DLCZ Single-Photon Source. An atomic ensemble can also serve as a single-photon source using a heralding scheme which is a downsized version of the Duan-Lukin-Cirac-Zoller (DLCZ) proposal [40, 41] for a quantum repeater [42, 43]. The DLCZ single-photon source was experimentally demonstrated in Ref. [44].

The basic idea is the following. If one had a detector that measured the photon number n nondestructively, then this device could herald (i.e. announce) n and one could discard all events with $n \neq 1$ to obtain a perfect single-photon source.

However, typical photon-counting detectors (avalanche photodiodes, photomultiplier tubes etc.) have two properties that make an immediate application of this idea unfeasible. First, they have a dead time after each detection event during which they cannot register any further photons and, second, they destroy the photons. We will discuss now how one can nevertheless construct a useful heralding scheme using such detectors.

First, we take the dead time into account but assume that the detector would not destroy the photons. The dead time implies that a detection event indicates that a nonzero number of photons arrived. Such a detector will still be useful if one starts from a Poissonian photon source with mean photon number per pulse much below 1. Such a source already has the desired property $p_{n+1} \ll p_n$ for $n \neq 0$. The strategy is to let the detector herald the pulses with $n \neq 0$ and to discard the other pulses. One can easily estimate $g^{(2)}$ for such a source. We denote the (conditional) probabilities for the heralded events as $\widetilde{p}_n$ and the corresponding pair-correlation

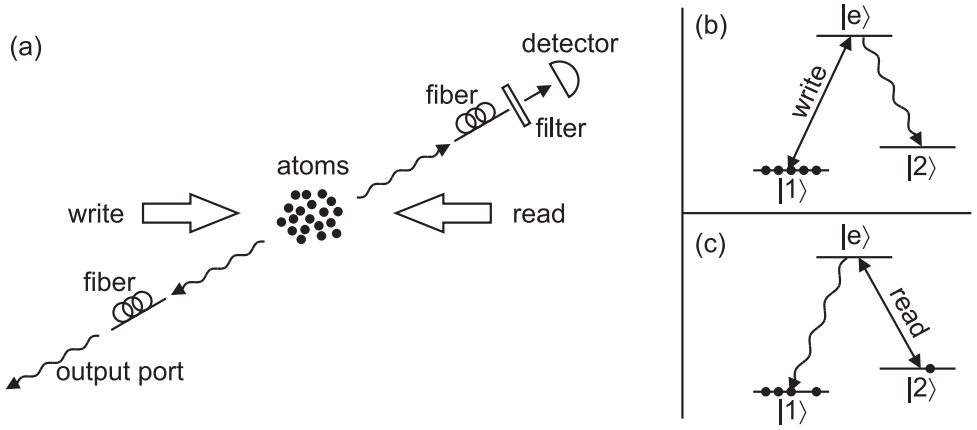

Fig. 5: *DLCZ source for single photons. (a) An atomic ensemble is illuminated by a weak light pulse for writing. If the detector registers a scattered photon, then this will project the ensemble into a state with one collective excitation. A subsequent light pulse for reading converts this into a single photon propagating towards the output port. (b) and (c) simplified atomic level schemes for the write and read process, respectively. The circles symbolize the atom number in each state before application of the pulse.*

function as $\widetilde{g}^{(2)}$. Ideally, we obtain $\widetilde{p}_0 = 0$ and $\widetilde{p}_n = p_n/(1-p_0) \sim p_n/p_1$ for $n \neq 0$. Eq. (9) yields

$$\widetilde{g}^{(2)} \sim \frac{2\widetilde{p}_2}{\widetilde{p}_1^2} \sim \frac{2p_2}{p_1} \sim p_1 g^{(2)} = p_1 \ll 1 \tag{10}$$

where we used $g^{(2)} = 1$ for the unheralded Poisson distribution. The smaller p_1, the better the suppression of $\widetilde{g}^{(2)}$. This scheme would yield an anti-bunched single-photon source if only we had such a detector.

We now turn to the second issue: the destruction of the photons in the detector. This is where atomic ensembles can help. Again, one uses internal atomic states that form a Λ scheme, as shown in Fig. 5. Using optical pumping, all atoms are initially prepared in the ground state $|1\rangle$. A pulse of laser light, called write pulse, illuminates the ensemble. The write pulse is resonant with the $|1\rangle \leftrightarrow |e\rangle$ transition and it must be weak (in a sense to be discussed below). The detector in Fig. 5 can detect scattered photons. In front of the detector, there is an optical fiber for transverse mode selection and a frequency filter (e.g. a filter cavity) that transmits only light resonant with the $|2\rangle \leftrightarrow |e\rangle$ transition. If the detector clicks, i.e. registers a photon, then this measurement result will be used as a herald. This event projects the ensemble into a state where an atom has been transferred to state $|2\rangle$. A subsequent read pulse with many photons, resonant with the $|2\rangle \leftrightarrow |e\rangle$ transition, optically pumps this atom back into the original state $|1\rangle$ under emission of a photon resonant with the $|1\rangle \leftrightarrow |e\rangle$ transition.

We now consider $g^{(2)}$. Each photon scattered from the write beam into the detector will ideally leave behind exactly one atom in state $|2\rangle$ so that the subsequent read process will ideally emit exactly one photon. This part is deterministic. However, a Poisson distribution does appear in this scheme; namely for the number of photons scattered from the write beam into the detector. Experimental parameters must be chosen such that the mean number of these photons is much below 1. In other words, one needs a heralding probability $1 - p_0 \ll 1$. Hence, Eq. (10) is applicable and the readout yields an anti-bunched single-photon source.

We now study the emission direction of the final photon. When the detector clicks, it is known

that exactly one atom was transferred into state $|2\rangle$. The probability that two photons reached the detector is negligible because $1 - p_0 \ll 1$. However, it remains unknown which atom was transferred. Hence, after the click the ensemble is in a coherent superposition of all these possibilities[3]

$$\frac{1}{\sqrt{N}} \sum_{n=1}^{N} e^{i(\boldsymbol{k}_w - \boldsymbol{k}_d)\cdot \boldsymbol{x}_n} \psi_n(x_n)|2\rangle_n \prod_{\substack{k=1 \\ k\neq n}}^{N} \psi_k(x_k)|1\rangle_k. \tag{11}$$

Here, $|1\rangle_n$ and $|2\rangle_n$ denote the internal states of the n-th atom. $\psi_n(x_n)$ denotes the initial spatial wave function of the n-th atom. We assumed that all N atoms were initially in internal state $|1\rangle$ and in a spatial product state. If the n-th atom is transferred into state $|2\rangle$, then its spatial wave function will pick up a phase factor $e^{i(\boldsymbol{k}_w - \boldsymbol{k}_d)\cdot \boldsymbol{x}_n}$ due to the differential photon recoil, where $\boldsymbol{k}_w$ and $\boldsymbol{k}_d$ are the wave vectors of the write photon and the detected photon. Typically, states $|1\rangle$ and $|2\rangle$ are two ground states with different hyperfine quantum numbers. Hence, the state in Eq. (11) describes a spin-wave excitation. Moreover, the fact that the number of transferred atoms is exactly one means that this state represents a single magnon, the quasi-particle of the spin wave.

When the read pulse is applied, the n-th atom is transferred back into state $|1\rangle$ and its spatial wave function picks up a phase factor $e^{i(\boldsymbol{k}_r - \boldsymbol{k}_f)\cdot \boldsymbol{x}_n}$, where $\boldsymbol{k}_r$ and $\boldsymbol{k}_f$ are the wave vectors of the read photon and the final photon. The final state of the ensemble is

$$\frac{1}{\sqrt{N}} \left(\sum_{n=1}^{N} e^{i(\boldsymbol{k}_w - \boldsymbol{k}_d + \boldsymbol{k}_r - \boldsymbol{k}_f)\cdot \boldsymbol{x}_n} \right) \prod_{k=1}^{N} \psi_k(x_k)|1\rangle_k. \tag{12}$$

In principle, $\boldsymbol{k}_f$ can have any direction. However, if the condition

$$\boldsymbol{k}_w - \boldsymbol{k}_d + \boldsymbol{k}_r - \boldsymbol{k}_f = 0 \tag{13}$$

is met, then all phase factors in Eq. (12) will be unity and all terms in the sum will interfere constructively. This gives the probability for this emission direction a collective enhancement factor of N, the number of atoms [41]. For large N, the emission into other directions becomes negligible. In Fig. 5, collective, directed emission towards the output port is obtained. The generated photon has a well-defined, collimated transverse mode.[4] Here we assumed that the radius of the ensemble is much larger than the optical wavelength. Otherwise, the phase factors do not change noticeably within the radius of the ensemble and the generated single photon will look as if it had been diffracted from an aperture with the size of the ensemble.

All properties of the emitted photon are well controlled: a useful, collimated transverse mode, the polarization, the center frequency, the emission time, and the spatiotemporal wave packet. The temporal shape of the read pulse can be used to tailor the spatiotemporal wave packet of the single photon. Moreover, it is possible to extend the atomic level scheme to map an atomic qubit onto the polarization qubit of the photon [45, 46].

Ref. [47] reports $\widetilde{g}^{(2)} = 0.007$ for a heralding probability of $p_1 \sim 4 \times 10^{-5}$ and a photon-emission efficiency of ∼45% conditioned on heralding. Here, $\widetilde{g}^{(2)}$ is a factor of ∼200 worse

[3] The state vector for each atom lies in the tensor product space of spatial part and spin part. Eqs. (11) and (12) use the position representation for the spatial part but no representation for the spin part. The total state vector $|\psi\rangle$ for all atoms is obtained by applying $\int d^3x_1 |x_1\rangle \cdots \int d^3x_N |x_N\rangle$ from the left to Eqs. (11) or (12).

[4] The directed character of the emission also implies that scattering of photons from the write beam into directions other than towards the detector is not a concern, because upon readout this will generate photons not sent towards the output port. Hence, the value of $g^{(2)}$ measured in the direction of the output port does not deteriorate.

than expected from the simple estimate Eq. (10). Several technical imperfections contribute to this deviation, such as non-unit detector efficiencies, detector dark counts, imperfect transverse mode matching etc. Note that in this experiment, the number of photons per write pulse was $\sim 10^4$. This number does not need to be small compared to one.
The disadvantage of a DLCZ source is that the probability p_1 that a herald is obtained must be made tiny if one wants a good suppression of $\widetilde{g}^{(2)}$. This makes count rates low and experiments may become tiresome. Unlike an atom-cavity system, the DLCZ source is inherently probabilistic. On the other hand, atom-cavity systems have the drawback that they are much harder to build.

6 Atoms as Quantum Memories for Photonic Qubits

In addition to the controlled emission of a single photon, one also needs a mechanism for the controlled absorption of a single photon. If one wanted to characterize only the absorption process, then one would need a direct measurement of the atomic state after the absorption. This is often difficult. Instead, one often maps the atomic state back to another photon in a subsequent emission process. If the photon carries a qubit, this combination of absorption and emission will represent a quantum memory [48].
In addition to the ability to store the qubit values $|0\rangle$ and $|1\rangle$, a quantum memory must also be able to store any coherent superposition thereof. This task cannot be performed by a classical apparatus, which performs a measurement, stores the result in a classical memory, and finally rebuilds the state from scratch upon readout. If this were possible, then the information in the classical memory could be copied many times and the apparatus could emit an arbitrary number of replicas of the single-photon qubit, thus violating the no-cloning theorem.[5] Hence, the qubit must be encoded in the state of a quantum system during the whole storage time.
The performance of a quantum memory is characterized by several figures of merit:

- The write-read efficiency η is the ratio of the retrieved photon number over the incoming photon number.
- The fidelity $F = \mathrm{Tr}(\rho_{\mathrm{in}}\rho_{\mathrm{out}})$ describes how well the density matrix of the incoming qubit state ρ_{in} is reproduced in the output state ρ_{out}. While some input states might be well preserved, others might not. To express this in one figure of merit, one averages F over the full Poincaré sphere of pure photon states, obtaining the average fidelity $\langle F\rangle$. The classical limit is $\langle F\rangle \leq 2/3$. An ideal quantum memory yields $\langle F\rangle = 1$.
- The lifetime of the efficiency characterizes how quickly η decays over time.
- The coherence time characterizes how quickly $\langle F\rangle$ decays over time.

Atom-Cavity Systems. The single-photon generation process for a single atom in a cavity, discussed in Sec. 5, can be reversed in time, resulting in controlled absorption, as proposed in Ref. [34]. The atom is initially prepared in state $|2\rangle$ of Fig. 4(b). For an almost arbitrary spatiotemporal wave packet of the incoming photon, one can tailor the temporal shape of the control pulse such that the photon is absorbed in the single atom with high probability, with a theoretical limit of 100% [49].

[5] If a von-Neumann measurement is performed, one will be forced to choose one basis and will obtain only one measurement result because there is only one incoming photon. It is obvious that this cannot yield all the information about the qubit state. However, if a series of weak measurements is performed, the situation will get more complex, but the argument with the no-cloning theorem remains valid.

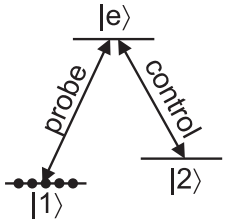

Fig. 6: *Level scheme for EIT. The circles symbolize the atom number in each state before application of the probe pulse.*

A recent experiment [36] used an atom-cavity system as a quantum memory and reported a write-read efficiency of $\eta = 10\%$ and an average fidelity of $\langle F \rangle = 92\%$. The coherence time in a similar experiment [50] was $\sim$0.2 ms.

Atomic Ensembles: Slow Light and EIT. Light storage is also possible in an atomic ensemble. It is essentially the time-reversed version of the readout part of the DLCZ single-photon source. More specifically, one uses the techniques of slow and stopped light in the context of electromagnetically induced transparency (EIT) [51].
Consider the Λ system of Fig. 6 with population initially in state $|1\rangle$ and with applied control light resonant with the $|2\rangle \leftrightarrow |e\rangle$ transition. Let probe light (the incoming single photon) resonant with the $|1\rangle \leftrightarrow |e\rangle$ transition impinge on the atomic ensemble. The control light drastically modifies the refractive index $n = \sqrt{1+\chi} \sim 1 + \frac{1}{2}\chi$ for the probe light. Here, χ is the electric susceptibility. Its real and imaginary parts are related to dispersion and absorption, respectively.
They are shown in Fig. 7. The Lorentzian absorption profile in $\mathrm{Im}\,\chi$ adopts a narrow transparency window due to the control light. This transmission phenomenon is called EIT; see appendix A for understanding its origin. In line with the Kramers-Kronig relations, a feature of similar width is obtained in the dispersive profile in $\mathrm{Re}\,\chi$. It has a steep, linear slope. The group velocity of a probe light pulse is inversely proportional to the steepness of this slope. The lower the control intensity, the narrower the EIT window and the smaller the group velocity, for reasons discussed in appendix A. A slowdown of the group velocity of light by 7 orders of

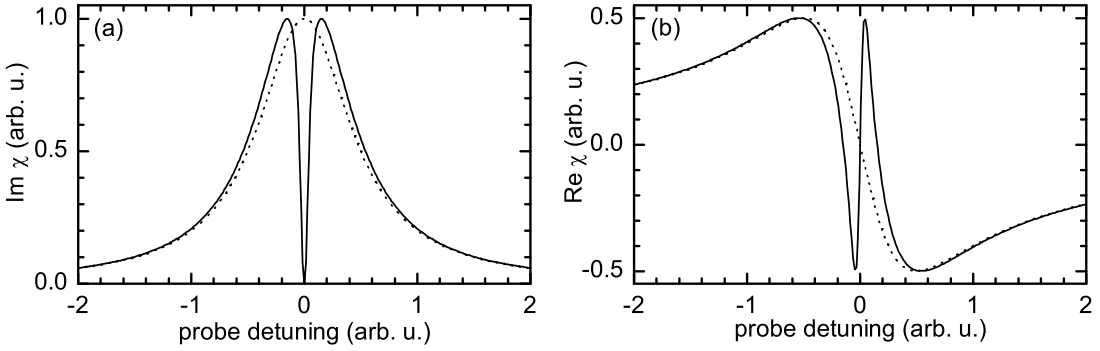

Fig. 7: *EIT and slow light. (a) Imaginary and (b) real parts of the electric susceptibility χ are shown. The dotted lines (without control light) show a Lorentzian absorption profile for $\mathrm{Im}\,\chi$ and a dispersive profile for $\mathrm{Re}\,\chi$. The solid lines (with control light) show a narrow transparency window for $\mathrm{Im}\,\chi$ and a corresponding slow-light region for $\mathrm{Re}\,\chi$.*

magnitude was demonstrated in Ref. [52].
The slowdown of the group velocity causes a drastic spatial compression of the pulse. If a probe pulse is 300 ns long, it will have a longitudinal extension of $\sim$100 m in vacuum. 7 orders of magnitude slowdown will compressed it to $\sim$10 μm which is small enough to fit into the atomic ensemble. Once the pulse is completely inside the ensemble, one ramps the control intensity to zero. This reduces the group velocity to zero. This is called stopped light. The incoming probe light was absorbed in a controlled fashion. This absorption process is the time reversed version of the readout part of the DLCZ source. Each probe photon is converted into a single excitation in the initially empty state $|2\rangle$. For a single probe photon, the state after storage looks much like Eq. (11). Again, the relative phases in the coherent superposition store the information about the propagation direction of the probe light. At a later time, the control light is ramped back on. This corresponds to the readout part of the DLCZ source (without time reversal). It reestablishes the probe pulse. Unlike the DLCZ source, the EIT memory is not inherently probabilistic.
Note that the slow-light effects will only be obtained if states $|2\rangle$ and $|e\rangle$ carry only a small fraction of the total atomic population at all times. Moreover, to obtain high write-read efficiency, it must be possible to longitudinally compress the complete pulse into the ensemble and at the same time have an EIT transparency window that is wide enough in frequency space to avoid irreversible absorption. This condition can only be met if the optical depth $\sigma\varrho L$ is much larger than unity, where L is the length of the ensemble, ϱ the number of atoms per volume, and σ the absorption cross section that one atom represents for resonant probe light.
EIT-based storage and retrieval was demonstrated in 2001 for classical probe light pulses [53, 54, 55] and in 2005 for anti-bunched single photons [56, 57]. A lifetime of the efficiency of half a second was reported in Ref. [58]. A recent experiment [59] realized a quantum memory for a photonic qubit in a Bose-condensed atomic ensemble and achieved $\eta = 0.53$, $\langle F\rangle = 1.000 \pm 0.004$, a lifetime of the efficiency of 0.5 ms, and a coherence time of 1.1 ms.

7 Creation of Remote Entanglement

As an example for the variety of possibilities offered by the techniques described above, we note that entanglement between two atomic systems at remote locations has been created in several experiments [36, 45, 60, 61, 62, 63, 64]. Specifically, we consider a recent experiment [39] that created remote entanglement between a single atom in a cavity and an atomic Bose-Einstein condensate (BEC).
The single atom serves not only as a single-photon source, but also as a source of two-particle entanglement [65]. This is achieved with the level scheme shown in Fig. 8(a). A light pulse from the trigger laser causes the emission of a single photon as described in Sec. 5. However, the photon can be L or R polarized. The final atomic state depends on the photon polarization. It is unknown which of the two paths was taken, so that the system is in a coherent superposition of the two possibilities. Hence after the emission, the Zeeman state of the single atom is entangled with the polarization of the single photon

$$|\psi_{\mathrm{atom}\otimes\mathrm{photon}}\rangle = \frac{1}{\sqrt{2}}\left(|1,1\rangle \otimes |L\rangle - |1,-1\rangle \otimes |R\rangle\right). \tag{14}$$

Here, $|f, m_f\rangle$ denotes the hyperfine and Zeeman quantum state of the atom. This single photon is transported through an optical fiber to a BEC in another laboratory. Here, the photon is absorbed using EIT, as described in Sec. 6. The BEC serves as a quantum memory. The single

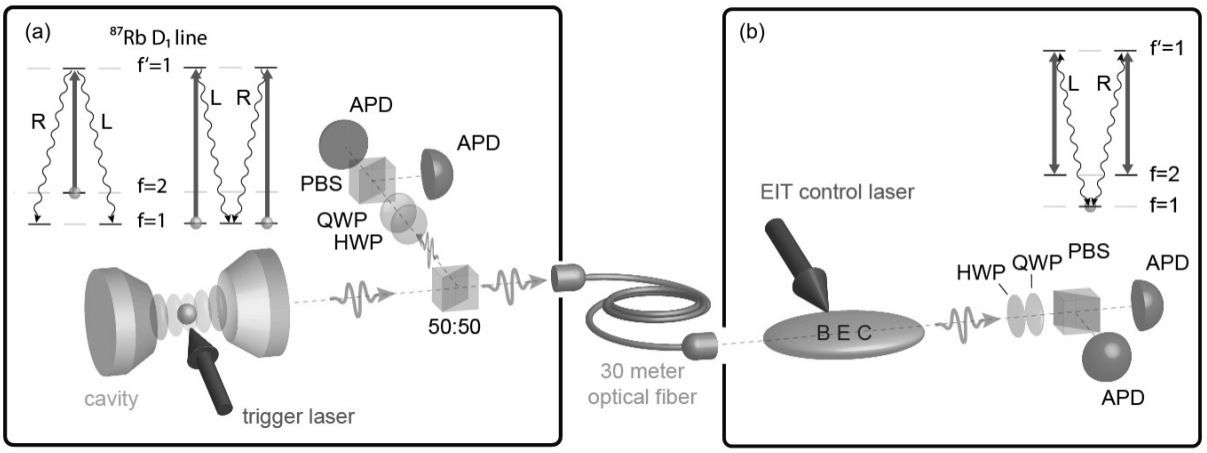

Fig. 8: *Scheme of an experiment for creating remote entanglement. (a) An atom-cavity system serves as a single-photon source and creates atom-photon entanglement upon photon emission. (b) A BEC serves as a quantum memory for the photon. Storage in the BEC maps the photonic qubit onto the BEC, thus creating atom-BEC entanglement. At a later time, both qubits are converted into photons, which are measured. Reproduced from Ref. [39].*

photon is stored as a single magnon. The polarization qubit is stored in a Zeeman qubit using the extended internal level scheme of Fig. 8(b). $|f, m_f\rangle$ denote the hyperfine and Zeeman quantum state of the single magnon. The storage establishes entanglement between the single atom and the BEC

$$|\psi_{\mathrm{atom}\otimes\mathrm{BEC}}\rangle = \frac{1}{\sqrt{2}}\left(|1,1\rangle \otimes |2,-1\rangle - |1,-1\rangle \otimes |2,1\rangle\right). \tag{15}$$

At a later time, the memory is read out, mapping the magnon qubit back to the polarization of the emitted photon. In addition, a second trigger pulse sent onto the single atom maps the Zeeman qubit of the single atom onto a second photon. After both emission processes, the two photons are entangled

$$|\psi_{\mathrm{photon}\otimes\mathrm{photon}}\rangle = \frac{1}{\sqrt{2}}\left(|R\rangle \otimes |L\rangle - |L\rangle \otimes |R\rangle\right). \tag{16}$$

The polarization of each photon is measured with avalanche photodiodes (APD) placed behind a polarizing beam splitter (PBS). A combination of a quarter wave plate (QWP) and a half wave plate (HWP) in front of each PBS makes it possible to select an arbitrary measurement basis on the two Poincaré spheres.

The fidelity of the measured final state with the desired, maximally-entangled state of Eq. (16) is $F = 0.95$. This characterizes the concatenation of all four processes: photon generation, storage, retrieval, and second photon generation. The coherence time for the decay of F is 0.1 ms.

Appendix

A Lambda Systems: STIRAP and Dark-State Polaritons

This appendix offers additional insights into Λ systems. This is relevant for the suppression of spontaneous emission in the atom-cavity single-photon source in Sec. 5 and for the emergence

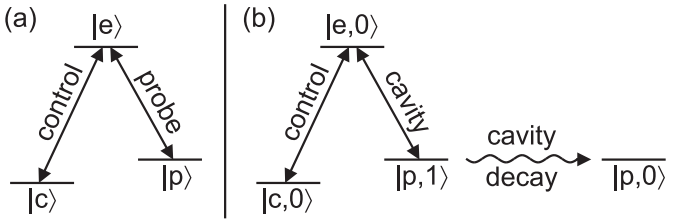

Fig. 9: *(a) Generic Λ system. (b) Vacuum STIRAP. The atomic level scheme of Fig. 4(b) is extended by including the photon number, n, in the cavity mode. The states are labeled $|c, n\rangle$, $|e, n\rangle$, and $|p, n\rangle$. Transmission of a photon through a cavity mirror is labeled cavity decay.*

of EIT and slow light in Sec. 6. A generic Λ system is shown in Fig. 9(a).

Two-Level Atom. Consider a single atom. Control light couples the atomic states $|c\rangle$ and $|e\rangle$ in Fig. 9(a). Let the electric field of the control light be $\boldsymbol{E}_c(t) = \mathrm{Re}(\boldsymbol{E}_{c,0}e^{-i\omega_c t})$ with amplitude $\boldsymbol{E}_{c,0}$ and angular frequency ω_c. Let $\hbar\omega_{ce}$ denote the energy difference of states $|c\rangle$ and $|e\rangle$. Assuming that the atom is much smaller than the optical wavelength, one can describe the atom-light interaction in the electric-dipole approximation $V(t) = -\boldsymbol{\mu}\cdot\boldsymbol{E}_c(t)$, where $\boldsymbol{\mu}$ is the operator of the electric-dipole moment. The control transition has a matrix element $\boldsymbol{\mu}_{ec} = \langle e|\boldsymbol{\mu}|c\rangle$. The operator $\boldsymbol{\mu}$ has negative parity and the states $|c\rangle$ and $|e\rangle$ have well-defined parity. Hence, the diagonal matrix elements $\langle c|\boldsymbol{\mu}|c\rangle$ and $\langle e|\boldsymbol{\mu}|e\rangle$ vanish. The Hamiltonian for the two-level system with basis $(|c\rangle, |e\rangle)$ reads $H = \hbar\omega_{ce}|e\rangle\langle e| - (\boldsymbol{\mu}_{ec}\cdot\boldsymbol{E}_c(t)|e\rangle\langle c| + \mathrm{H.c.})$. We move to an interaction picture with $|\widetilde{c}\rangle = |c\rangle$ and $|\widetilde{e}\rangle = e^{-i\omega_c t}|e\rangle$. We obtain

$$\widetilde{H} = \hbar\Delta_c|\widetilde{e}\rangle\langle\widetilde{e}| - \frac{1}{2}\left(\boldsymbol{\mu}_{ec}\cdot(\boldsymbol{E}_{c,0} + \boldsymbol{E}^*_{c,0}e^{2i\omega_c t})|\widetilde{e}\rangle\langle\widetilde{c}| + \mathrm{H.c.}\right) \tag{17}$$

with the detuning $\Delta_c = \omega_{ce} - \omega_c$. Now, we neglect the rapidly rotating term $\boldsymbol{E}^*_{c,0}e^{2i\omega_c t}$. This is called rotating wave approximation. Obviously, the strength of the remaining atom-light coupling is described by the parameter $\Omega_c = \boldsymbol{\mu}_{ec}\cdot\boldsymbol{E}_{c,0}/\hbar$ which is called Rabi frequency. In the following we always work in this interaction picture but drop the tilde to simplify the notation. We obtain

$$H = \hbar\Delta_c|e\rangle\langle e| - \frac{\hbar}{2}\left(\Omega_c|e\rangle\langle c| + \mathrm{H.c.}\right). \tag{18}$$

Three-Level Atom. The probe light couples the atomic states $|p\rangle$ and $|e\rangle$ in Fig. 9(a). A treatment similar to the control transition is applicable here. The corresponding detuning and Rabi frequency are Δ_p and Ω_p. We use a matrix representation with respect to the basis $(|p\rangle, |c\rangle, |e\rangle)$ and obtain [51]

$$H = -\frac{\hbar}{2}\begin{pmatrix} 0 & 0 & \Omega_p^* \\ 0 & -2(\Delta_p - \Delta_c) & \Omega_c^* \\ \Omega_p & \Omega_c & -2\Delta_p \end{pmatrix}. \tag{19}$$

Dark State. We assume that the two-photon Raman process connecting states $|c\rangle$ and $|p\rangle$ is resonant, i.e. $\Delta_p - \Delta_c = 0$. As a result, the state

$$|D\rangle \propto \Omega_c|p\rangle - \Omega_p|c\rangle \tag{20}$$

is an eigenstate of H with eigenvalue 0. It has no admixture of the excited state $|e\rangle$. So if spontaneous emission from the excited state is included in the model, an atom in this state will not show any spontaneous emission. This is why $|D\rangle$ is called a dark state. $|D\rangle$ has no admixture of $|e\rangle$ because the two amplitudes for exciting atoms to $|e\rangle$ from either $|c\rangle$ or $|p\rangle$ interfere completely destructively.

STIRAP. This dark state makes it possible to transfer all population adiabatically from one ground state to the other without causing spontaneous emission. To this end, start e.g. with all population initially in state $|c\rangle$. Turn on Ω_p. Next, slowly increase Ω_c from zero to a nonzero value and (subsequently or simultaneously) slowly decrease Ω_p to zero. This will slowly rotate the dark state $|D\rangle$ from $|c\rangle$ to $|p\rangle$. If the rotation is slow enough, then – by virtue of the adiabatic theorem of quantum mechanics – all population will remain in the dark state $|D\rangle$ at all times, causing a passage of the population from $|c\rangle$ to $|p\rangle$. This is called stimulated Raman adiabatic passage (STIRAP). Finally, Ω_c can be turned off.

Vacuum STIRAP. The atom-cavity single-photon source that we discussed in Sec. 5 relies on STIRAP to suppress spontaneous emission. To explain this, we include the number of cavity photons in the notation, see Fig. 9(b). The population is initially prepared in state $|c,0\rangle$. The control transition is $|c,0\rangle \leftrightarrow |e,0\rangle$. The cavity field couples the transition $|p,1\rangle \leftrightarrow |e,0\rangle$ with Rabi frequency Ω_p.
It is customary to use $g = \Omega_p/2$ instead of Ω_p. g is obviously nonzero for the absorption process $|p,1\rangle \rightarrow |e,0\rangle$ because the atomic state $|p\rangle$ is exposed to the field of one photon. The fact that the Hamiltonian is Hermitian implies that the time-reversed process has the same Rabi frequency (assuming that g is real). A rigorous treatment of the quantized light field confirms this result. Intuitively, it means that the vacuum field inside the cavity drives the emission $|e,0\rangle \rightarrow |p,1\rangle$. g is sometime called single-photon Rabi frequency and sometimes vacuum Rabi frequency.
g acts permanently, as long as the atom is inside the cavity. The single-photon generation process is the STIRAP sequence: Starting from zero, Ω_c is slowly increased to a value $\Omega_c \gg g$. This transfers almost all population into state $|p,1\rangle$ without spontaneous emission from state $|e,0\rangle$. The photon now present in the cavity mode will sooner or later be transmitted through the mirror, transferring the population into the final state $|p,0\rangle$. This is called vacuum STIRAP, because the emission into the cavity is driven by the vacuum field of the cavity.
If everything works adiabatically, the efficiency for emitting the photon by cavity transmission will reach 100%. Among other things, this requires $g \gg \Gamma_e$, where Γ_e is the spontaneous emission rate of state $|e\rangle$ into all directions other than the cavity mode. In present experiments the condition $g \gg \Gamma_e$ is not met well enough if one mirror is much more transparent than the other. This is the main reason why the efficiency in present experiments does not reach 100%.
If the STIRAP process transfers the population to $|p,1\rangle$ much slower than a cavity decay time, then the population of state $|p,1\rangle$ will remain small at all times. Still, a large fraction of the population can be emitted by cavity decay. In this case, the subsystem $|c,0\rangle, |e,0\rangle, |p,1\rangle$ experiences loss from state $|p,1\rangle$ but the general adiabatic nature of the population transfer without population reaching state $|e,0\rangle$ remains intact. This is used for shaping the single-photon pulse.

Dark-State Polaritons in EIT and Slow Light. EIT and slow light are other effects that can be understood as adiabatic following in the dark state $|D\rangle$. Initially all atomic population is in state $|p\rangle$, corresponding to state $|1\rangle$ in Fig. 6. Control light is turned on. Subsequently, a pulse

of probe light propagates through the atomic ensemble. The temporal variation of the envelope of the probe pulse is slow enough that the population adiabatically follows the dark state $|D\rangle$. When the probe pulse has left the medium, all atomic population is back in the initial state. At this time, the control light can be turned off. As the population is always in the dark state, no spontaneous emission occurs, yielding $\mathrm{Im}\,\chi = 0$ at the two-photon resonance. Away from the two-photon resonance, however, no dark state exists, yielding $\mathrm{Im}\,\chi \neq 0$, see Fig. 7(a).

As mentioned earlier, slow-light experiments must operate in the regime where the states $|c\rangle$ and $|e\rangle$ carry only a small fraction of the total atomic population at all times. The above discussion of STIRAP shows that the emergence of EIT at the two-photon resonance does not rely on this assumption. However, if the assumption is violated, no slow light will be obtained.

Generally, if light enters a medium, then the electric field will adopt a copropagating component of the induced dielectric polarization density $P = \epsilon_0 \chi E$. The corresponding quasi particle of the two co-moving components P and E in the medium is called polariton, rather than photon. In the context of EIT, this polariton follows a dark state and is therefore called dark-state polariton [66, 67].

To understand slow and stopped light, we consider a probe pulse initially containing a single photon. With all atoms initially in atomic state $|p\rangle$, the dark-state polariton has the form

$$|D\rangle \propto \Omega_c |1_{\mathrm{photon}}\rangle \otimes |\psi_{\mathrm{initial}}\rangle - \Omega_p |0_{\mathrm{photon}}\rangle \otimes |\psi_{\mathrm{magnon}}\rangle \tag{21}$$

in analogy to Eq. (20). Here, $|n_{\mathrm{photon}}\rangle$ is a state with n photons. $|\psi_{\mathrm{initial}}\rangle$ is the initial atomic state with all atoms in $|p\rangle$. $|\psi_{\mathrm{magnon}}\rangle$ is a single-magnon state in analogy to Eq. (11). $|D\rangle$ becomes a pure photon in the limit $\Omega_c \gg \Omega_p$, whereas it becomes a pure magnon in the limit $\Omega_c \ll \Omega_p$.

The control light is on before the pulse enters the medium. Hence, initially $\Omega_c \neq 0$ and $\Omega_p = 0$. $|D\rangle$ is a pure photon. The pulse enters the medium and for small Ω_c, it is adiabatically converted into an almost pure magnon. This suggests that the propagation speed of the polariton should be close to the propagation speed of the pure magnon. That speed is given by the differential photon recoil velocity, which is many orders of magnitude slower than the vacuum speed of light. This explains why the dark-state polariton is slow. It also explains why the group velocity is reduced when reducing Ω_c. To create stopped light, one ramps Ω_c slowly all the way to zero with the probe pulse inside the ensemble and converts $|D\rangle$ into a pure magnon, which is almost at rest. At this point, one has completed a STIRAP process with full transfer with respect to the dark state polariton Eq. (21) (but not with respect to the total atomic population). The readout process is the time-reversed version hereof.

References

[1] P. C. Maurer, G. Kucsko, C. Latta, L. Jiang, N. Y. Yao, S. D. Bennett, F. Pastawski, D. Hunger, N. Chisholm, M. Markham, D. J. Twitchen, J. I. Cirac, and M. D. Lukin, Room-temperature quantum bit memory exceeding one second, *Science* **336**, 1283–1286 (2012).

[2] C. H. Bennett, F. Bessette, G. Brassard, L. Salvail, and J. Smolin, Experimental quantum cryptography, *J. Cryptology* **5**, 3–28 (1992).

[3] Q. A. Turchette, C. J. Hood, W. Lange, H. Mabuchi, and H. J. Kimble, Measurement of conditional phase shifts for quantum logic, *Phys. Rev. Lett.* **75**, 4710–4713 (1995).

[4] C. Monroe, D. M. Meekhof, B. E. King, W. M. Itano, and D. J. Wineland, Demonstration of a fundamental quantum logic gate, *Phys. Rev. Lett.* **75**, 4714–4717 (1995).

[5] X. Li, Y. Wu, D. Steel, D. Gammon, T. H. Stievater, D. S. Katzer, D. Park, C. Piermarocchi, and L. J. Sham, An all-optical quantum gate in a semiconductor quantum dot, *Science* **301**, 809–811 (2003).

[6] P. Rabl, D. DeMille, J. M. Doyle, M. D. Lukin, R. J. Schoelkopf, and P. Zoller, Hybrid quantum processors: Molecular ensembles as quantum memory for solid state circuits, *Phys. Rev. Lett.* **97**, 033003 (2006).

[7] K. Mattle, H. Weinfurter, P. G. Kwiat, and A. Zeilinger, Dense coding in experimental quantum communication, *Phys. Rev. Lett.* **76**, 4656–4659 (1996).

[8] D. Boschi, S. Branca, F. De Martini, L. Hardy, and S. Popescu, Experimental realization of teleporting an unknown pure quantum state via dual classical and Einstein-Podolsky-Rosen channels, *Phys. Rev. Lett.* **80**, 1121–1125 (1998).

[9] D. Bouwmeester, J.-W. Pan, M. Mattle, K.and Eibl, H. Weinfurter, and A. Zeilinger, Experimental quantum teleportation, *Nature* **390**, 575–579 (1997).

[10] J.-W. Pan, D. Bouwmeester, H. Weinfurter, and A. Zeilinger, Experimental entanglement swapping: entangling photons that never interacted, *Phys. Rev. Lett.* **80**, 3891–3894 (1998).

[11] K. Hammerer, A. S. Sørensen, and E. S. Polzik, Quantum interface between light and atomic ensembles, *Rev. Mod. Phys.* **82**, 1041–1093 (2010).

[12] P. K. Ghosh, *Ion Traps* (Clarendon Press, Oxford, 1995).

[13] D. Leibfried, R. Blatt, C. Monroe, and D. Wineland, Quantum dynamics of single trapped ions, *Rev. Mod. Phys.* **75**, 281–324 (2003).

[14] H. Häffner, C. Roos, and R. Blatt, Quantum computing with trapped ions, *Phys. Rep.* **469**, 155–203 (2008).

[15] H. Häffner, W. Hänsel, C. F. Roos, J. Benhelm, D. Chek-al kar, M. Chwalla, T. Körber, U. D. Rapol, M. Riebe, P. O. Schmidt, C. Becher, O. Gühne, W. Dür, and R. Blatt, Scalable multiparticle entanglement of trapped ions, *Nature* **438**, 643–646 (2005).

[16] D. Kielpinski, V. Meyer, M. A. Rowe, C. A. Sackett, W. M. Itano, C. Monroe, and D. J. Wineland, A decoherence-free quantum memory using trapped ions, *Science* **291**, 1013–1015 (2001).

[17] J. I. Cirac and P. Zoller, Quantum computations with cold trapped ions, *Phys. Rev. Lett.* **74**, 4091–4094 (1995).

[18] F. Schmidt-Kaler, H. Häffner, M. Riebe, S. Gulde, G. P. T. Lancaster, T. Deuschle, C. Becher, C. F. Roos, J. Eschner, and R. Blatt, Realization of the Cirac-Zoller controlled-NOT quantum gate, *Nature* **422**, 408–411 (2003).

[19] K. Mølmer and A. Sørensen, Multiparticle entanglement of hot trapped ions, *Phys. Rev. Lett.* **82**, 1835–1838 (1999).

[20] A. Sørensen and K. Mølmer, Quantum computation with ions in thermal motion, *Phys. Rev. Lett.* **82**, 1971–1974 (1999).

[21] A. Sørensen and K. Mølmer, Entanglement and quantum computation with ions in thermal motion, *Phys. Rev. A* **62**, 022311 (2000).

[22] C. A. Sackett, D. Kielpinski, B. E. King, C. Langer, V. Meyer, C. J. Myatt, M. Rowe, Q. A. Turchette, W. M. Itano, D. J. Wineland, and C. Monroe, Experimental entanglement of four particles, *Nature* **404**, 256–259 (2000).

[23] T. Monz, P. Schindler, J. T. Barreiro, M. Chwalla, D. Nigg, W. A. Coish, M. Harlander, W. Hänsel, M. Hennrich, and R. Blatt, 14-qubit entanglement: creation and coherence, *Phys. Rev. Lett.* **106**, 130506 (2011).

[24] G. J. Milburn, S. Schneider, and D. F. James, Ion trap quantum computing with warm ions, *Fortschr. Physik* **48**, 801–810 (2000).

[25] D. Leibfried, B. DeMarco, V. Meyer, D. Lucas, M. Barrett, J. Britton, W. M. Itano, B. Jelenkovic, C. Langer, T. Rosenband, and D. J. Wineland, Experimental demonstration of a robust, high-fidelity geometric two ion-qubit phase gate, *Nature* **422**, 412–415 (2003).

[26] H. Metcalf and P. van der Straten, *Laser Cooling and Trapping* (Springer, Berlin, 1999).

[27] T. Wilk, A. Gaëtan, C. Evellin, J. Wolters, Y. Miroshnychenko, P. Grangier, and A. Browaeys, Entanglement of two individual neutral atoms using Rydberg blockade, *Phys. Rev. Lett.* **104**, 010502 (2010).

[28] L. Isenhower, E. Urban, X. L. Zhang, A. T. Gill, T. Henage, T. A. Johnson, T. G. Walker, and M. Saffman, Demonstration of a neutral atom controlled-NOT quantum gate, *Phys. Rev. Lett.* **104**, 010503 (2010).

[29] Y. O. Dudin and A. Kuzmich, Strongly interacting Rydberg excitations of a cold atomic gas, *Science* **336**, 887–889 (2012).

[30] T. Pellizzari, S. A. Gardiner, J. I. Cirac, and P. Zoller, Decoherence, continuous observation, and quantum computing: A cavity QED model, *Phys. Rev. Lett.* **75**, 3788–3791 (1995).

[31] L.-M. Duan and H. J. Kimble, Scalable photonic quantum computation through cavity-assisted interactions, *Phys. Rev. Lett.* **92**, 127902 (2004).

[32] A. Rispe, B. He, and C. Simon, Photon-photon gates in Bose-Einstein condensates, *Phys. Rev. Lett.* **107**, 043601 (2011).

[33] C. Vo, S. Riedl, S. Baur, G. Rempe, and S. Dürr. Coherent logic gate for light pulses based on storage in a Bose-Einstein condensate. http://arxiv.org/abs/1211.7240.

[34] J. I. Cirac, P. Zoller, H. J. Kimble, and H. Mabuchi, Quantum state transfer and entanglement distribution among distant nodes in a quantum network, *Phys. Rev. Lett.* **78**, 3221–3224 (1997).

[35] H. J. Kimble, The quantum internet, *Nature* **453**, 1023–1030 (2008).

[36] S. Ritter, C. Nölleke, C. Hahn, A. Reiserer, A. Neuzner, M. Uphoff, M. Mücke, E. Figueroa, J. Bochmann, and G. Rempe, An elementary quantum network of single atoms in optical cavities, *Nature* **484**, 195–200 (2012).

[37] A. Kuhn, M. Hennrich, and G. Rempe, Deterministic single-photon source for distributed quantum networking, *Phys. Rev. Lett.* **89**, 067901 (2002).

[38] R. J. Glauber, The quantum theory of optical coherence, *Phys. Rev.* **130**, 2529–2539 (1963).

[39] M. Lettner, M. Mücke, S. Riedl, C. Vo, C. Hahn, S. Baur, J. Bochmann, S. Ritter, S. Dürr, and G. Rempe, Remote entanglement between a single atom and a Bose-Einstein condensate, *Phys. Rev. Lett.* **106**, 210503 (2011).

[40] L.-M. Duan, M. D. Lukin, J. I. Cirac, and P. Zoller, Long-distance quantum communication with atomic ensembles and linear optics, *Nature* **414**, 413–418 (2001).

[41] L. M. Duan, J. I. Cirac, and P. Zoller, Three-dimensional theory for interaction between atomic ensembles and free-space light, *Phys. Rev. A* **66**, 023818 (2002).

[42] H.-J. Briegel, W. Dür, J. I. Cirac, and P. Zoller, Quantum repeaters: The role of imperfect local operations in quantum communication, *Phys. Rev. Lett.* **81**, 5932–5935 (1998).

[43] N. Sangouard, C. Simon, H. de Riedmatten, and N. Gisin, Quantum repeaters based on atomic ensembles and linear optics, *Rev. Mod. Phys.* **83**, 33–80 (2011).

[44] A. Kuzmich, W. P. Bowen, A. D. Boozer, A. Boca, C. W. Chou, L.-M. Duan, and H. J. Kimble, Generation of nonclassical photon pairs for scalable quantum communication with atomic ensembles, *Nature* **423**, 731–734 (2003).

[45] D. N. Matsukevich, T. Chanelière, S. D. Jenkins, S.-Y. Lan, T. A. B. Kennedy, and A. Kuzmich, Entanglement of remote atomic qubits, *Phys. Rev. Lett.* **96**, 030405 (2006).

[46] H. Tanji, S. Ghosh, J. Simon, B. Bloom, and V. Vuletić, Heralded single-magnon quantum memory for photon polarization states, *Phys. Rev. Lett.* **103**, 043601 (2009).

[47] J. Laurat, H. de Riedmatten, D. Felinto, C.-W. Chou, E. W. Schomburg, and H. J. Kimble, Efficient retrieval of a single excitation stored in an atomic ensemble, *Opt. Express* **14**, 6912–6918 (2006).

[48] A. I. Lvovsky, B. C. Sanders, and W. Tittel, Optical quantum memory, *Nat. Photon.* **3**, 706–714 (2009).

[49] J. Dilley, P. Nisbet-Jones, B. W. Shore, and A. Kuhn, Single-photon absorption in coupled atom-cavity systems, *Phys. Rev. A* **85**, 023834 (2012).

[50] H. P. Specht, C. Nölleke, A. Reiserer, M. Uphoff, E. Figueroa, S. Ritter, and G. Rempe, A single-atom quantum memory, *Nature* **473**, 190–193 (2011).

[51] M. Fleischhauer, A. Imamoglu, and J. P. Marangos, Electromagnetically induced transparency: Optics in coherent media, *Rev. Mod. Phys.* **77**, 633–673 (2005).

[52] L. V. Hau, S. E. Harris, Z. Dutton, and C. H. Behroozi, Light speed reduction to 17 metres per second in an ultracold atomic gas, *Nature* **397**, 594–598 (1999).

[53] C. Liu, Z. Dutton, C. H. Behroozi, and L. V. Hau, Observation of coherent optical information storage in an atomic medium using halted light pulses, *Nature* **409**, 490–493 (2001).

[54] D. F. Phillips, A. Fleischhauer, A. Mair, R. L. Walsworth, and M. D. Lukin, Storage of light in atomic vapor, *Phys. Rev. Lett.* **86**, 783–786 (2001).

[55] A. V. Turukhin, V. S. Sudarshanam, M. S. Shahriar, J. A. Musser, B. S. Ham, and P. R. Hemmer, Observation of ultraslow and stored light pulses in a solid, *Phys. Rev. Lett.* **88**, 023602 (2001).

[56] T. Chanelière, D. N. Matsukevich, S. D. Jenkins, S.-Y. Lan, T. A. B. Kennedy, and A. Kuzmich, Storage and retrieval of single photons transmitted between remote quantum memories, *Nature* **438**, 833–836 (2005).

[57] M. D. Eisaman, A. André, F. Massou, M. Fleischhauer, A. S. Zibrov, and M. D. Lukin, Electromagnetically induced transparency with tunable single-photon pulses, *Nature* **438**, 837–841 (2005).

[58] R. Zhang, S. R. Garner, and L. V. Hau, Creation of long-term coherent optical memory via controlled nonlinear interactions in Bose-Einstein condensates, *Phys. Rev. Lett.* **103**, 233602 (2009).

[59] S. Riedl, M. Lettner, C. Vo, S. Baur, G. Rempe, and S. Dürr, Bose-Einstein condensate as a quantum memory for a photonic polarization qubit, *Phys. Rev. A* **85**, 022318 (2012).

[60] B. Julsgaard, A. Kozhekin, and E. S. Polzik, Experimental long-lived entanglement of two macroscopic objects, *Nature* **413**, 400–403 (2001).

[61] C. W. Chou, H. de Riedmatten, D. Felinto, S. V. Polyakov, S. J. van Enk, and H. J. Kimble, Measurement-induced entanglement for excitation stored in remote atomic ensembles, *Nature* **438**, 828–832 (2005).

[62] C.-W. Chou, J. Laurat, H. Deng, K. S. Choi, H. de Riedmatten, D. Felinto, and H. J. Kimble, Functional quantum nodes for entanglement distribution over scalable quantum networks, *Science* **316**, 1316–1320 (2007).

[63] D. L. Moehring, P. Maunz, S. Olmschenk, K. C. Younge, D. N. Matsukevich, L.-M. Duan, and C. Monroe, Entanglement of single-atom quantum bits at a distance, *Nature* **449**, 68–71 (2007).

[64] Z.-S. Yuan, Y.-A. Chen, B. Zhao, S. Chen, J. Schmiedmayer, and J.-W. Pan, Experimental demonstration of a BDCZ quantum repeater node, *Nature* **454**, 1098–1101 (2008).

[65] T. Wilk, S. C. Webster, A. Kuhn, and G. Rempe, Single-atom single-photon quantum interface, *Science* **317**, 488–490 (2007).

[66] M. Fleischhauer and M. D. Lukin, Dark-state polaritons in electromagnetically induced transparency, *Phys. Rev. Lett.* **84**, 5094–5097 (2000).

[67] M. Fleischhauer and M. D. Lukin, Quantum memory for photons: Dark-state polaritons, *Phys. Rev. A* **65**, 022314 (2002).

A 4 Superconducting Qubits[1]

William D. Oliver
MIT Lincoln Laboratory
Lexington, MA, U.S.A.

Contents

1 Introduction **3**

2 Survey of Josephson junctions and superconducting qubit modalities **4**
2.1 Josephson junctions . . . 4
2.1.1 Josephson equations . . . 4
2.1.2 RCSJ model . . . 5
2.1.3 Thermal activation . . . 7
2.1.4 Macroscopic quantum tunneling . . . 8
2.2 DC SQUID: a tunable junction . . . 9
2.2.1 DC SQUID equations . . . 9
2.2.2 Zero-inductance case, $I_{c1} = I_{c2}$ . . . 10
2.2.3 Zero-inductance case, $I_{c1} \neq I_{c2}$ . . . 11
2.2.4 Non-zero inductance case . . . 11
2.2.5 Equivalence to a Josephson junction . . . 11
2.3 Superconducting qubits . . . 13
2.3.1 Charge qubit . . . 13
2.3.2 Quantronium . . . 16
2.3.3 Transmon . . . 18
2.3.4 Persistent-current flux qubit . . . 19
2.3.5 Phase qubit . . . 25
2.3.6 RF SQUID qubit . . . 27
2.3.7 Fluxonium and metastable RF-SQUID: inductively shunted qubits . . . 28

3 Free- and driven evolution of two-level systems 28
3.1 Representations of the qubit Hamiltonian . . . 29
3.1.1 Laboratory frame . . . 29
3.1.2 Qubit frame (qubit eigenbasis) . . . 29
3.1.3 Rotating frame . . . 31
3.2 General perturbation expansion of Hamiltonian . . . 32
3.3 Longitudinal and transverse relaxation . . . 34
3.3.1 Bloch-Redfield approach . . . 34
3.3.2 Modification due to $1/f$-type noise . . . 36
3.4 Power spectral density (PSD) . . . 36
3.5 Connecting T_1 to $S_\lambda(\omega)$ . . . 37
3.6 Connecting T_φ to $S_\lambda(\omega)$ . . . 38
3.7 Noise spectroscopy of a persistent-current flux qubit . . . 42
3.7.1 Inversion recovery: T_1 . . . 43
3.7.2 Free-induction decay (Ramsey): T_2^* . . . 43
3.7.3 Hahn echo (spin echo): $T_{2\mathrm{E}}$ . . . 44
3.7.4 CPMG (multi-pulse refocussing): $T_2^{(N)}$ . . . 45
3.7.5 Rabi oscillations: $T_{2\rho} \equiv T_{\mathrm{R}}$ . . . 45
3.7.6 Rotary echo: $T_{2\rho\mathrm{E}}$ . . . 45
3.7.7 Spin locking: $T_{1\rho}$ . . . 45

4 Control of superconducting qubits in the strong-driving limit 47
4.1 Flux qubit parameters . . . 47
4.2 Landau-Zener transitions . . . 50
4.3 Mach-Zehnder-type interferometry . . . 52
4.4 Microwave cooling . . . 54
4.5 Amplitude spectroscopy . . . 57
4.6 Summary and applications . . . 60

5 Acknowledgements 61

A Quantum conjugate operators $\hat{n}$ and $\hat{\phi}$ 62

B Two-level system Hamiltonian in the strong driving limit 63

C Summary of noise spectroscopy during free- and driven-evolution 65

[1]Lecture Notes of the 44^{th} IFF Spring School "Quantum Information Processing" (Forschungszentrum Jülich, 2013). All rights reserved.

1 Introduction

Superconducting qubits are solid-state artificial atoms, comprising lithographically defined Josephson tunnel junctions and superconducting interconnects [1]. When cooled to milli-Kelvin temperatures, these superconducting circuits exhibit quantized states of flux, charge, or junction phase depending on design parameters. Such superconducting artificial atoms have already proven a useful vehicle for advancing the scientific community's general understanding of coherence, quantum mechanics, and atomic physics, particularly in regimes not easily accessible with natural atoms and molecules. Their potential for lithographic scalability, compatibility with microwave control, and operability at nanosecond time scales make superconducting qubits a promising candidate for quantum information science and technology applications.

Spectacular improvement in the capabilities of superconducting qubits over the past decade has brought these qubits from a scientific curiosity to the threshold of technological reality [2]. Many individual efforts contributed to this improvement, starting with the demonstration of nanosecond-scale coherence in a Cooper pair box by Nakamura and co-workers [3] in 1999. In 2002, Vion *et al.* [4] developed a qubit with T_2 coherence time of hundreds of nanoseconds based on the concept of design and operation at first-order noise-insensitive bias points. Burkard *et al.* [5] elucidated the importance of symmetry in qubit designs, which in conjunction with Bertet *et al.* brought persistent-current flux qubit coherence times into the few microsecond range [6]. In 2005-2006, Ithier *et al.* [7] and Yoshihara *et al.* [8] measured extensively the noise properties of superconducting qubits to better understand the sources of decoherence. The "transmon" qubit developed by Schoelkopf and co-workers significantly reduced the charge sensitivity of the Cooper pair box, which would later bring microsecond times to the cavity-QED architecture [9, 10]. The MIT/NEC group increased T_2 above 20 μs with a persistent-current flux qubit in a 2D geometry using dynamical decoupling sequences [11], and the 3D-cavity approach developed at Yale [12] and now used by several groups has further increased this time above 100 μs [13] with as-yet unpublished reports above 150 μs. This *five-orders-of-magnitude* improvement in the primary single-qubit metric can be justly termed a "Moore's Law for quantum coherence" [14], approaching levels required for a certain class of quantum error correction codes (surface codes) [15, 16, 17]. In addition, the control of single- [18, 19, 20, 21] and coupled [22, 23] qubits has also advanced, with reports of gate fidelities as high as 99.85% [21].

In conjunction with these improvements, there have been numerous, increasingly sophisticated demonstrations involving quantum coherence in these systems. A few examples (in an admittedly incomplete list) include: coherent superpositions of macroscopic states [24, 25, 26], coherent and Rabi oscillations [3, 4, 27, 28, 29, 30, 31, 32, 33, 34, 35] in multiple qubit modalities, including a very long-lived (0.2 ms) CPB [36], Landau-Zener transitions [37], Stueckelberg oscillations [38, 39, 40, 41, 42, 43], microwave cooling [44, 45, 46, 47, 48, 49], amplitude spectroscopy [50, 51], electromagnetically induced transparency [52, 53] and coherent population trapping [54], geometrical phase [55], and cavity quantum electrodynamics [56, 57, 58, 59, 60, 61, 62, 63]. Significant progress has also been made toward their application to quantum information science [64, 65, 66], including state initialization [44, 49], tunable [67, 68, 69, 70, 71, 72] and long-distance [73, 74] coupling, quantum control [75, 76, 77, 78, 79, 80], quantum state [81, 133] and process [83, 84] tomography, randomized benchmarking [18, 19, 20, 21], measurement [85, 86, 87, 88, 89, 90, 91, 92, 93, 94, 95, 96, 97], architectures [16, 98, 99], preliminary demonstrations of error correction (without feedback) [100], and algorithm demonstrations [101, 102].

Based on these advances, there is a growing motivation to make further improvements and, indeed, there remains much work to do. The intrinsic and spin-echo T_2 times are generally not T_1-limited (i.e., $T_2 < 2T_1$) in the longest-lived samples (although exceptions do exist, e.g., Ref. [11]). Inhomogeneous dephasing arises from low-frequency (e.g., $1/f$-type) noise, although its microscopic origin is not yet well understood. The limiting source(s) of energy relaxation also remain unclear. Ideally, coherence times should be made as high as possible, as exceeding quantum error correction (QEC) thresholds reduces considerably their resource requirements. There is a general consensus within the community that understanding and mitigating sources of decoherence in superconducting qubits is one key that will enable more-advanced circuits and systems engineering [1].

In this light, these lecture notes serve to provide an admittedly brief overview of superconducting qubits with a focus on:

- survey of junctions and qubits
- noise spectroscopy and decoherence mitigation
- single qubit control.

We have made an effort to include relevant references so that interested readers can follow up on specific topics in more detail. Of course, in doing so, we have most certainly missed topics and references that deserve to be included. We also err on the side of presenting our own work a bit too much. While this can be somewhat annoying to readers, particularly to those who work in this field and are familiar with the broad range of excellent works available, our intent is to present experiments with an authority that comes from first-hand experience and not necessarily to ascribe to them a special status. In this spirit, we hope the reader finds this review useful.

2 Survey of Josephson junctions and superconducting qubit modalities

2.1 Josephson junctions

2.1.1 Josephson equations

We begin this section with a review of the Josephson junction, the elemental building block of superconducting qubits. The Josephson junction is formed by two superconducting electrodes separated by an insulating tunnel barrier [103, 104, 105, 106]. It is described by two constituent Josephson equations.

A supercurrent flows through the device, even in the absence of a voltage, due to Josephson tunneling. The value of the supercurrent is determined by the phase difference between the superconducting order parameters of the two electrodes according to the first Josephson equation,

$$I = I_{\rm c} \sin \phi \tag{1}$$

where $I_{\rm c}$ is the critical current of the junction and ϕ is the phase difference across it. The critical current is related to the superconducting gap of the electrode materials as well as the type and thickness of the insulating barrier. It is often characterized by a critical current density $J_{\rm c}$ and

the area A of the junction such that $I_c = J_c \times A$. The second Josephson equation relates the time evolution of the phase to the voltage drop across the junction;

$$V = \frac{\Phi_0}{2\pi}\frac{d\phi}{dt} \tag{2}$$

where $\Phi_0 \equiv h/2e$ is the superconducting flux quantum with value,

$$\Phi_0 = 2.07 \times 10^{-15}\ \text{Wb} = 2.07\ \text{mA} \cdot \text{pH} = 2.07\ \text{mV} \cdot \text{ps}. \tag{3}$$

Importantly for superconducting qubits, the Josephson junction exhibits a dynamic inductance inductance L_J that is nonlinear in the junction phase. Using the relation $V = L_J dI/dt$ with Eqs. 1 and 2, the standard definition for the Josephson inductance is:

$$L_J = \frac{\Phi_0}{2\pi I_c \cos\phi} = \frac{\Phi_0}{2\pi(I_c^2 - I^2)^{1/2}} = \frac{\Phi_0}{2\pi I_c(1-\gamma^2)^{1/2}} \equiv \frac{L_{J0}}{(1-\gamma^2)^{1/2}}, \tag{4}$$

where $\gamma \equiv I/I_c$ is the reduced current, L_{J0} is the inductance at $I = 0$, and $I < I_c$ is assumed. The inductance increases with current I and diverges as $I \to I_c$. An alternative definition that includes the time dependence of the inductance, $V = d\left[L_J I\right]/dt$, and does not diverge is given in Ref. [91]. In the $I \to 0$ limit, these two definitions both give L_{J0}.

For completeness, if the junction is biased with a constant voltage then the current will oscillate according to the relation (using Eqs. 1 and 2),

$$I = I_c \sin\left(\phi_0 + \frac{2\pi}{\Phi_0}\, V\, t\right) \tag{5}$$

with a frequency-to-voltage factor $483.6\ \text{MHz}/\mu V$. In turn, a transient fluctuation of the current through the junction will transiently change the phase creating a transient voltage fluctuation across the junction.

2.1.2 RCSJ model

A "short" Josephson junction may be modeled using the "resistively- and capacitively shunted junction" (RCSJ) model (the Stewart-McCumber model [107, 108]). It is sometimes just called the RSJ model. Here, "short" means that the junction is smaller than the typical length scale of variations in the Josephson phase (the size of a Josephson vortex), around $10 - 30\ \mu\text{m}$ for typical qubit materials [109]; qubit junctions tend to be much smaller than this. Within this model, the junction itself is an element that obeys Eqs. 1 and 2, in parallel with a capacitor (essentially a parallel plate capacitor due to the electrodes and tunneling barrier) and a resistor which models the intrinsic loss of the junction. When the junction is in its normal state ($I > I_c$), the Josphson element is omitted and the junction resistance is the normal tunneling resistance R_n. This resistance can be related to I_c through the Ambegaokar-Baratoff relation [110],

$$\frac{\pi}{4}V_{\text{gap}}(\Theta) = \frac{\pi}{4}\frac{2\Delta(\Theta)}{e} = I_c R_n \tag{6}$$

where $V_{\text{gap}} = 2\Delta/e$ is the total gap voltage for a Cooper pair, Δ is the temperature-dependent superconducting gap and Θ is temperature. For currents less than I_c, the resistance is the "subgap resistance" R_{sg}, which is explicitly manifest in the hysteretic $I - V$ trace of a junction.

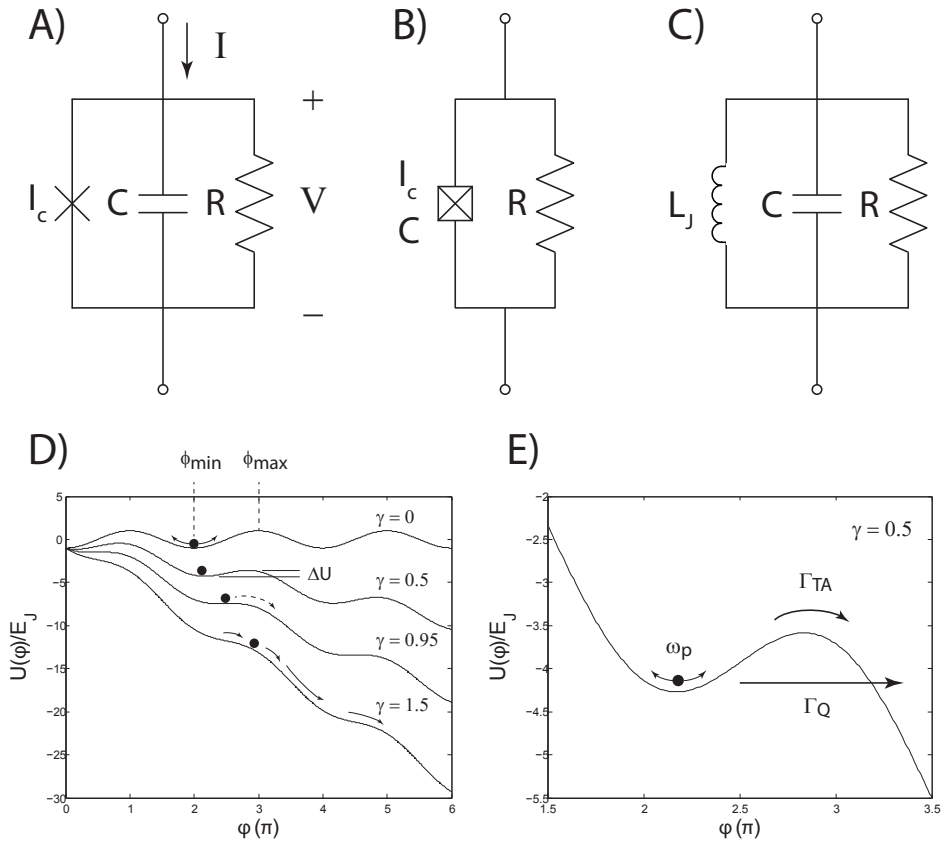

Fig. 1: A) *RCSJ model for a Josephson junction. The X indicates the junction with critical current $I_{\rm c}$, in parallel with a capacitor C and resistor R which damps the junction.* **B)** *Equivalent circuit using the "boxed-X" to represent the junction and its capacitance.* **C)** *Equivalent circuit that replaces the junction with an inductor that has the value of the Josephson inductance. The parallel combination is a resonant circuit oscillating at the plasma frequency.* **D)** *Washboard potential U for several values of reduced current γ. This potential represents the dynamics of the RCSJ model. For $\gamma = 0$, the "phase particle" representing the junction state is trapped in a well and oscillates at the plasma frequency. As γ is increased, the potential tilts. As $\gamma \rightarrow 1$, the phase particle may diffuse around the washboard, being occasionally retrapped by the damping. While ϕ is changing with time, a voltage exists across the junction. For $\gamma > 1$, the particle runs down the washboard, and the junction is manifestly in the normal state.* **E)** *Phase particle in a single well at $\gamma = 0.5$. The particle may escape the well due to thermal activation over the barrier with a rate $\Gamma_{\rm TA}$, or due to quantum tunneling through the well with a rate $\Gamma_{\rm Q}$.*

Ideally, a major component of the subgap resistance is due to equilibrium quasiparticles with resistance $R_{\rm qp} = R_{\rm n} \exp[\Delta/k_{\rm B}\Theta]$. In practice, at the $10 - 100$ mK temperatures used for superconducting qubits, the apparent losses are higher (*e.g.,* excess non-equilibrium quasiparticles) and the RCSJ model resistance may be used to parameterize the observed loss.

The circuit equation for the RCSJ model is obtained by summing the current along the three parallel paths (element, capacitor, and resistor),

$$I = I_{\rm c} \sin\phi + \frac{V}{R} + C\frac{dV}{dt} \tag{7}$$

$$= I_{\rm c} \sin\phi + \frac{1}{R}\frac{\Phi_0}{2\pi}\dot{\phi} + C\frac{\Phi_0}{2\pi}\ddot{\phi} \tag{8}$$

where the "dot" indicates time derivative. Bringing the current I over to the right side casts the equation in the form of a particle with "mass" $m \equiv C(\Phi_0/2\pi)^2$ in a tilted washboard potential $U(\phi)$,

$$0 = \frac{\partial U(\phi)}{\partial \phi} + m\frac{1}{RC}\dot{\phi} + m\ddot{\phi} \tag{9}$$

where the potiential $U(\phi)$ is

$$U(\phi) = E_{\rm J}\left(-\gamma\phi - \cos\phi\right), \tag{10}$$

and we have defined the Josephson energy $E_{\rm J} \equiv I_{\rm c}\Phi_0/2\pi$.

These equations describe a particle with mass m in a washboard potential that can be tilted by applying a current γ. If the well is not tipped too much, the particle remains in a single well. For small oscillations, the particle oscillates with a finite-bias plasma frequency $\omega_{\rm p}$ related to the curvature of the potential,

$$\omega_{\rm p} = \sqrt{\frac{1}{m}\frac{d^2U(\phi)}{d\phi^2}} = \frac{1}{\sqrt{L_{\rm J}C}} = \omega_{\rm p0}(1-\gamma^2)^{1/4} \tag{11}$$

$$\omega_{\rm p0} = \frac{1}{\sqrt{L_{\rm J0}C}} \tag{12}$$

where $\omega_{\rm p0}$ is the zero-bias, Josephson plasma frequency, defined in terms of the $I = 0$ Josephson inductance $L_{\rm J0}$ and the capacitance C. If the well is tilted too much, the particle will escape and start "running" down the washboard. A voltage develops across the junction, related to the temporal change in ϕ associated with the moving particle. There is also a damping term in Eq. 9 proportional to the phase velocity with a "viscous damping" coefficient m/RC. The dampling acts to localize the particle in a well such that, for moderate tilting, the particle may diffuse around the washboard, occasionally being retrapped by the damping.

2.1.3 Thermal activation

In the thermal regime ($k_{\rm B}\Theta \gg \hbar\omega_{\rm p}$), the rate at which a particle escapes from a well is related to thermal activation over the potential barrier ΔU,

$$\begin{aligned}\Delta U &= U(\phi_{\rm max}) - U(\phi_{\rm min}) \\ &= 2E_{\rm J}\left[\sqrt{1-\gamma^2} - \gamma\arccos(\gamma)\right] \\ &\approx E_{\rm J}\frac{4\sqrt{(2)}}{3}\left(1-\gamma\right)^{3/2}\end{aligned} \tag{13}$$

where $\phi_{\max} = \pi - \arcsin(\gamma)$ is the phase at the local maximum of the potential, $\phi_{\min} = \arcsin(\gamma)$ is the phase at a local minimum of a well, and the approximation holds for currents approaching the critical current, $\gamma \to 1$ [109, 113].

In the presence of Ohmic damping [111], the escape rate is

$$\Gamma_{\rm TA} = a_{\rm t} \frac{\omega_0}{2\pi} e^{-\frac{\Delta U}{k_{\rm B}\Theta}} \tag{14}$$

which contains the usual Arrhenius factor $\exp(-\Delta U/k_{\rm B}\Theta)$, an "attempt rate" to escape $\omega_0/2\pi$, and a prefactor $a_{\rm t}$ that incorporates the effect of damping [112],

$$a_{\rm t} = \frac{4a}{\left[(1 + Qk_{\rm B}\Theta/1.8\Delta U)^{1/2}\right]^{1/4}} \tag{15}$$

and contains the junction quality factor $Q = \omega_{\rm p} RC$ [113, 114, 115, 116]. Higher Q values correspond to lower damping.

2.1.4 Macroscopic quantum tunneling

The presence of a potential well raises the question, "Does a Josephson junction degree of freedom (the phase) exhibit quantum mechanical behavior?" In a series of papers foundational to the field of superconducting qubits, Clarke, Devoret, Esteve, and Martinis demonstrated that a junction indeed exhibits quantum mechanical tunneling through the junction's washboard potential barrier in addition to thermal activation over the barrier [113, 114, 115, 116].

The escape rate $\Gamma_{\rm TA}$ due to thermal activation has the property that it should go to zero as temperature is decreased to zero due to the Arrhenius factor $\exp(-\Delta U/k_{\rm B}\Theta)$. However, quantum tunneling provides another means of escape which becomes dominant and saturates the total escape rate at low temperatures. In the quantum regime ($k_{\rm B}\Theta \ll \hbar\omega_{\rm p}$), to lowest order in $1/Q$, the quantum tunneling rate at zero temperature is

$$\Gamma_{\rm Q} = \frac{a_{\rm q}\omega_{\rm p}}{2\pi} e^{\left[-\frac{7.2\Delta U}{\hbar\omega_{\rm p}}\left(1+\frac{0.87}{Q}\right)\right]} \tag{16}$$

where $a_{\rm q} \approx \left[120\pi(7.2\Delta U/\hbar\omega_{\rm p})\right]^{1/2}$ [115]. Dissipation suppresses quantum tunneling through the factor $1/Q$, and so a signature of quantum tunneling is one indication that Josephson junctions can have low dissipation.

Conceptually, the escape rate is measured at a particular current $I < I_{\rm c}$ while the junction is in the zero-voltage state, and then this current is stepped to find the escape rate for different barrier heights. In practice, the escape-rate measurements can be implemented by a different means: ramping the current through the junction at a rate slow compared with the other rates in the problem. One then records the current (or, equivalently, the time from the start of a linear current ramp) at which the junction switches to the normal state. Note that this current is properly called the "switching current" and not the "critical current," because thermal or quantum escape mechanisms will generally act before the critical current is reached. This experiment is repeated many times (typically thousands) to build up the switching-current distribution, from which the escape rate can be calculated [117]. The escape rate measurement is repeated as a function of the junction's ambient temperature, and the rate was shown to saturate at a particular "escape temperature" as the ambient temperature was reduced, an observation consistent with a quantum tunneling picture [115, 116]. For details related to these experiments, the reader is directed to the cited references and the references therein.

2.2 DC SQUID: a tunable junction

The DC SQUID (superconducting quantum interference device) is a superconducting loop interrupted by two junctions [118]. The net critical current of the SQUID can be tuned by threading a magnetic flux through the loop. In this sense, the SQUID is a tunable Josephson junction, and this feature is used to make "tunable" superconducting qubits, *i.e.,* qubits with a parameter related to the junction $I_{\rm c}$ that is tunable by the magnetic field that threads the SQUID loop.

2.2.1 DC SQUID equations

A SQUID is a superconducting loop interrupted by two junctions, as illustrated in Fig. 2A. A current I flows into the SQUID, and subsequently separates into two currents I_j in the branches ("arms") $j = 1, 2$. In each arm of the SQUID, there is a Josephson junction with critical current I_{cj}, phase ϕ_j, and Josephson inductance $L_{{\rm J}j}$ (not illustrated). There is also in general a geometric inductance L_j in each arm. The total inductance around the loop is L. The current passing through branch j is given by the Josephson current equation (Eq. 1), such that the total current is

$$I = I_{\rm c1} \sin\phi_1 + I_{\rm c2} \sin\phi_2. \tag{17}$$

Alternatively, one may transform into a basis of symmetric ($I_{\rm p}$) and antisymmetric (circulating current, $I_{\rm m}$) currents:

$$I_{\rm p} = \frac{I_1 + I_2}{2} \tag{18}$$

$$I_{\rm m} = \frac{I_1 - I_2}{2} \tag{19}$$

$$I = 2I_{\rm p}. \tag{20}$$

Note that only $I_{\rm m}$ is illustrated in Fig. 2A.

An external magnetic field $B_{\rm ext}$ is applied to the SQUID, and it contributes a flux $\Phi_{\rm ext}$ to the loop, illustrated in Fig. 2B. The superconducting order parameter must be single valued, and this requirement imposes a quantization condition: the total phase difference around the loop must quantized in units of the flux quantum Φ_0. This comprises a normalized superposition of the externally applied flux, a screening flux due to the SQUID current and geometric inductances, and the Josephson junctions. This condition may be expressed as,

$$\begin{aligned} 2\pi n &= \frac{2\pi}{\Phi_0} \oint_C (\vec{A} + \Lambda \vec{J_s}) \cdot d\vec{l} = \oint_C \nabla\phi \cdot d\vec{l} \\ 2\pi n &= \phi_2 + \beta_{\rm L2} \sin\phi_2 - \phi_1 - \beta_{\rm L1} \sin\phi_1 - \phi_{\rm ext} \end{aligned} \tag{21}$$

where n is the number of flux quanta Φ_0, $\beta_{\rm L1,\,L2} \equiv L_{1,2}/L_{\rm J1,\,J2}$ are the ratios of the geometric inductance to the Josephson inductance for arms 1 and 2, $\beta_{\rm L1,\,L2} \sin\phi_{1,\,2}$ are the flux contributions due to current passing through the geometric inductances $L_{1,\,2}$ normalized by $\Phi_0/2\pi$, and $\phi_{\rm ext} = 2\pi\Phi_{\rm ext}/\Phi_0$ is the external flux normalized by $\Phi_0/2\pi$. Note that we have chosen a path in the center of the superconductor where the current $\vec{J_s}$ is negligible. This means that we have assumed the kinetic inductance contribution, related to $\Lambda\vec{J_s}$, is negligible (see Ref. [104]).

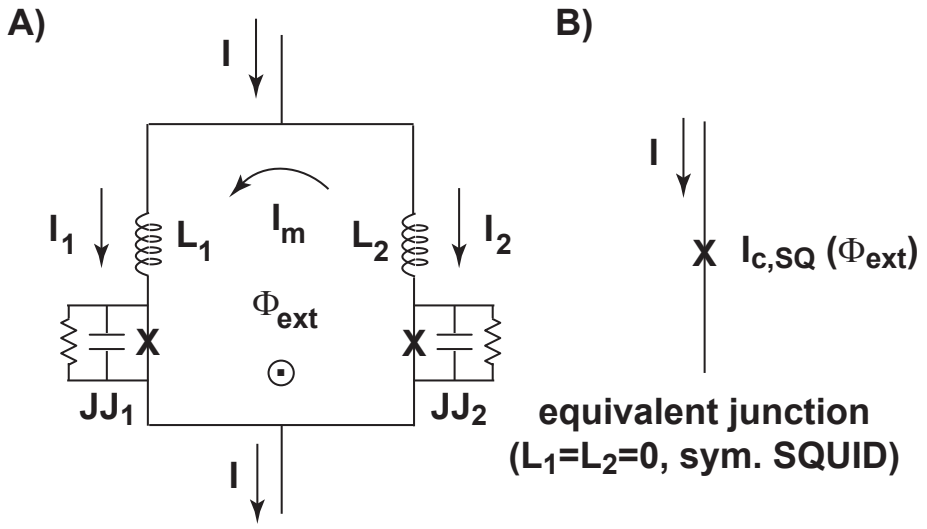

Fig. 2: **A)** *Circuit diagram of a SQUID. Current I enters and leaves the SQUID. The current I_j flows through branch $j = 1, 2$ with arm inductance L_j and a Josephson junction with phase critical current I_{cj}, phase ϕ_j, capacitance C_j, and damping resistor R_j. An external magnetic field B_{ext} threads a flux Φ_{ext} through the loop. A circulating current $I_{\rm m}$ develops in response to the applied flux.* **B)** *Equivalent Josephson junction with a critical current tuned by the external flux $\Phi_{\rm ext}$. The inductances are taken to be zero, and the equivalence is precise for symmetric SQUID junctions.*

2.2.2 Zero-inductance case, $I_{\rm c1} = I_{\rm c2}$

If the SQUID arm inductances are small compared with the Josephson inductancs, then the ratios $\beta_{\rm L1,\,L2}$ are negligible and can be dropped from Eq. 21. The equations for the SQUID current are:

$$I = I_{\rm c1}\sin\phi_1 + I_{\rm c2}\sin\phi_2 \tag{22}$$

$$2\pi n = \phi_2 - \phi_1 - \phi_{\rm ext}. \tag{23}$$

Furthermore, if one assumes the critical currents are equal, $I_{\rm c1} = I_{\rm c2} \equiv I_{\rm c}$, then these equations can be combine to yeild

$$I = 2I_{\rm c}\cos\left(\frac{\phi_{\rm ext}}{2}\right)\sin\left(\phi_1 + \frac{\phi_{\rm ext}}{2}\right). \tag{24}$$

The extrema occur for $dI/d\phi_1 = 0$, which leads to the relation (in terms of $\Phi_{\rm ext}$)

$$I_{\rm c,SQ}(\Phi_{\rm ext}) = 2I_{\rm c}\left|\cos\left(\frac{\pi\Phi_{\rm ext}}{\Phi_0}\right)\right|. \tag{25}$$

The critical current of the SQUID $I_{\rm c,SQ}$ is a function of the externally applied flux. As we show in Section 2.2.5, one may view the SQUID in Fig. 2A as a single junction with critical current given by Eq. 25, and a corresponding Josephson inductance that is now a function of both the current I and the SQUID flux $\Phi_{\rm ext}$ (Fig. 2B). The critical current can be tuned between 0 and $2I_{\rm c}$.

2.2.3 Zero-inductance case, $I_{c1} \neq I_{c2}$

In the case that the junctions have different areas and/or different critical current densities, their critical currents will not be identical. In this case, the critical currents can be tuned with the flux by the following expression (see Ref. [103] for a clever derivation),

$$I_{c,SQ}(\Phi_{ext}) = \left[I_{c1}^2 + I_{c2}^2 + 2I_{c1}I_{c2}\cos\left(\frac{2\pi\Phi_{ext}}{\Phi_0}\right)\right]^{1/2} \tag{26}$$

The form of Eq. 26 is indicative of an interference effect, and it will oscillate as a function of Φ_{ext} between a maximum $|I_{c1} + I_{c2}|$ and a minimum $|I_{c1} - I_{c2}|$. It reduces to Eq. 25 in the limit $I_{c1} = I_{c2}$.

2.2.4 Non-zero inductance case

The non-zero inductance case can be solved numerically (see Ref. [103] for an example using Lagrange multipliers to incorporate the quantization constraint). For a symmetric SQUID ($I_{c1} = I_{c2}$ and $L_1 = L_2$), the SQUID critical current $I_{c,SQ}(\Phi_{ext})$ modulates between its full value $2I_c$ and a non-zero minimum value $I_{c,min}$ that increases as the total inductance increases. For differing inductances ($L_1 \neq L_2$), the SQUID critical current $I_{c,SQ}(\Phi_{ext})$ becomes distorted with flux and is no longer symmetric about $\Phi_{ext} = 2\pi n$. One consequence is that the SQUID critical current will not be at its maximum value for $\Phi_{ext} = 0$. A similar asymmetry is used for convenience in the phase-qubit SQUID readout to obtain $dI_{c,SQ}/d\Phi_{ext} \neq 0$ sensitivity to an external magnetic field in the absence of a static bias, $\Phi_{ext} = 0$.

2.2.5 Equivalence to a Josephson junction

The formal equivalence between the SQUID (Fig. 2A) and a Josephson junction (Fig. 2B) can be clarified by writing the equation of motion for the SQUID while allowing for variations in component values. We adopt the following parameterization:

$$\mathcal{V} \equiv \frac{\mathcal{V}_1 + \mathcal{V}_2}{2} \tag{27}$$

$$\Delta\mathcal{V} \equiv \frac{\mathcal{V}_1 - \mathcal{V}_2}{2}, \tag{28}$$

in which $\mathcal{V}_{1,2}$ represents any pair of components, *e.g.*, the RCSJ critical currents, resistances, and capacitances. Using these definitions, one may write,

$$I_{c1} = I_c + \Delta I_c \qquad I_{c2} = I_c - \Delta I_c \tag{29}$$

$$R_1 = R + \Delta R \qquad R_2 = R - \Delta R \tag{30}$$

$$C_1 = C + \Delta C \qquad C_2 = C - \Delta C. \tag{31}$$

We take the inductances in Fig. 2A to be zero to show the equivalence.

Following the approach of Section 2.1.2, current conservation yields the following equations for the SQUID current:

$$I = I_1 + I_2 = I_{c1}\sin\phi_1 + \frac{1}{R_1}\frac{\Phi_0}{2\pi}\dot{\phi}_1 + C_1\frac{\Phi_0}{2\pi}\ddot{\phi}_1 + I_{c2}\sin\phi_2 + \frac{1}{R_2}\frac{\Phi_0}{2\pi}\dot{\phi}_2 + C_2\frac{\Phi_0}{2\pi}\ddot{\phi}_2. \tag{32}$$

Using the relations,

$$\lim_{\frac{\Delta R}{R}\ll 1} \frac{1}{1 \pm \Delta R/R} \approx 1 \mp \frac{\Delta R}{R}, \tag{33}$$

one may write,

$$\begin{aligned} I &= I_0 + \Delta I \qquad (34)\\ &= I_{\rm c}\left(\sin\phi_1 + \sin\phi_2\right) + \frac{1}{R}\frac{\Phi_0}{2\pi}\left(\dot{\phi}_1 + \dot{\phi}_2\right) + C\frac{\Phi_0}{2\pi}\left(\ddot{\phi}_1 + \ddot{\phi}_2\right)\\ &+ \Delta I_{\rm c}\left(\sin\phi_1 - \sin\phi_2\right) - \frac{\Delta R}{R^2}\frac{\Phi_0}{2\pi}\left(\dot{\phi}_1 - \dot{\phi}_2\right) + \Delta C\frac{\Phi_0}{2\pi}\left(\ddot{\phi}_1 - \ddot{\phi}_2\right), \qquad (35)\end{aligned}$$

in which I_0 is the expression assuming all parameters are symmetric between the left and right arms, and ΔI is the expression that accounts for asymmetries in the SQUID parameters. The only approximation made was to assume $\Delta R \ll R$; otherwise, the expression is exact within the RCSJ model. Using the trigonometric identities,

$$\sin\phi_1 + \sin\phi_2 = 2\cos\left(\frac{\phi_1 - \phi_2}{2}\right)\sin\left(\frac{\phi_1 + \phi_2}{2}\right) \equiv 2\cos\phi_{\rm m}\sin\phi_{\rm p} \tag{36}$$

$$\sin\phi_1 - \sin\phi_2 = 2\cos\left(\frac{\phi_1 + \phi_2}{2}\right)\sin\left(\frac{\phi_1 - \phi_2}{2}\right) \equiv 2\cos\phi_{\rm p}\sin\phi_{\rm m}, \tag{37}$$

where $\phi_{\rm p,m} \equiv (\phi_1 \pm \phi_2)/2$ are symmetric and antisymmetric phases of the SQUID, the expression for the SQUID current becomes

$$I_0 = 2I_{\rm c}\cos\phi_{\rm m}\sin\phi_{\rm p} + \frac{1}{R/2}\frac{\Phi_0}{2\pi}\dot{\phi}_p + 2C\frac{\Phi_0}{2\pi}\ddot{\phi}_p \tag{38}$$

$$\Delta I = 2\Delta I_{\rm c}\cos\phi_{\rm p}\sin\phi_{\rm m} - \frac{1}{R/2}\frac{\Delta R}{R}\frac{\Phi_0}{2\pi}\dot{\phi}_m + 2\Delta C\frac{\Phi_0}{2\pi}\ddot{\phi}_m. \tag{39}$$

The equation of motion for a symmetric SQUID (Eq. 38) is equivalent to Eq. 8 with the substitutions in Table 1. The last substitution in Table 1 follows from the assumption of zero-inductance

Josephson junction	**DC SQUID**
R	$R/2$
C	$2C$
ϕ	$\phi_{\rm p}$
$I_{\rm c}$	$2I_{\rm c}\cos\phi_{\rm m} = 2I_{\rm c}\cos\left(\frac{\pi\Phi_{\rm ext}}{\Phi_0}\right)$

Table 1: *Corresponding paramters between a Josephson junction and its DC SQUID equivalent.*

and fluxoid quantization (Eq. 23) with $n = 0$. By construction we have restricted the range $\pi\Phi_{\rm ext}/\Phi_0 \in (-\pi/2, \pi/2)$, although this may be generalized by taking $|\cos(\pi\Phi_{\rm ext}/\Phi_0)|$. The resistance and capacitance substitutions follow from their parallel combination in the SQUID,

again, in the absence of SQUID inductances. Defining $I_{\mathrm{c,SQ}} = 2I_{\mathrm{c}}|\cos(\pi\Phi_{\mathrm{ext}}/\Phi_0)|$, the current through the SQUID is

$$I = I_{\mathrm{c,SQ}} \sin\phi_{\mathrm{p}} \tag{40}$$

which is the first Josephson equation. The circulating current of the SQUID can similarly be related to $\sin\phi_{\mathrm{m}}$. It is interesting to note that the corrections to this ideal equivalence swaps the roles of ϕ_{p} and ϕ_{m}. The correction dynamics are governed by the circulating current.

2.3 Superconducting qubits

In this section, we review the basic construction and operation of superconducting qubits. We will focus on "first-generation" qubits, including the charge, quantronium, persistent-current flux qubit, and phase qubits. We will also discuss briefly the "next-generation" qubits, including their evolution from the first-generation, their similarities, and their differences. Our goal here is to provide a high-level overview, including the Hamiltonian and the fundamentals of their operation. We refer the readers to the original proposals and experimental papers for more details.

In the following, we will define the charging energy in terms of the single-electron charging energy $E_{\mathrm{C}} \equiv e^2/2C$ [121]. This means that a superconducting Cooper pair has charging energy $4E_{\mathrm{C}}$. On the other hand, we will define the Josephson energy $E_{\mathrm{J}} \equiv I\mathrm{c}\Phi_0/2\pi$ in terms of the superconducting flux quantum $\Phi_0 = h/2e$. This follows a somewhat general convention, although it is certainly not a universal one.

2.3.1 Charge qubit

The charge qubit was among the first superconducting devices to demonstrate properties of quantum coherence, including evidence for quantum superposition of charge states [122, 123, 124, 125]. It was also the first superconducting circuit used to demonstrate coherent control and temporal oscillations [3].

The charge qubit is a Cooper pair box (CPB) (Fig. 3A), comprising a small superconducting island isolated by a Josephson junction and a capacitor to ground. The key feature of this island is that it is sufficiently small that the charging energy required to add a single Cooper pair to the island is much larger than the thermal energy at the milliKelvin temperatures of a dilution refrigerator,

$$4E_{\mathrm{C}} = 4\frac{e^2}{2C_\Sigma} \gg k_{\mathrm{B}}\Theta \tag{41}$$

where the capacitance $C_\Sigma = C_{\mathrm{J}} + C_{\mathrm{g}}$ is the total capacitance and generally must be less than 1 fF. The amount of charge on the island that is induced by the gate, expressed in units of extra Cooper pairs,

$$n_{\mathrm{g}} = \frac{C_{\mathrm{g}}V_{\mathrm{g}}}{2e} \tag{42}$$

is controlled by the voltage source V_{g}. Although the Cooper pairs themselves are counted in discrete units, this reduced charge is continuous, because it is related to the polarization charge on the capacitor. Therefore, n_{g} is continuously tunable from n to $n+1$. The source of discrete

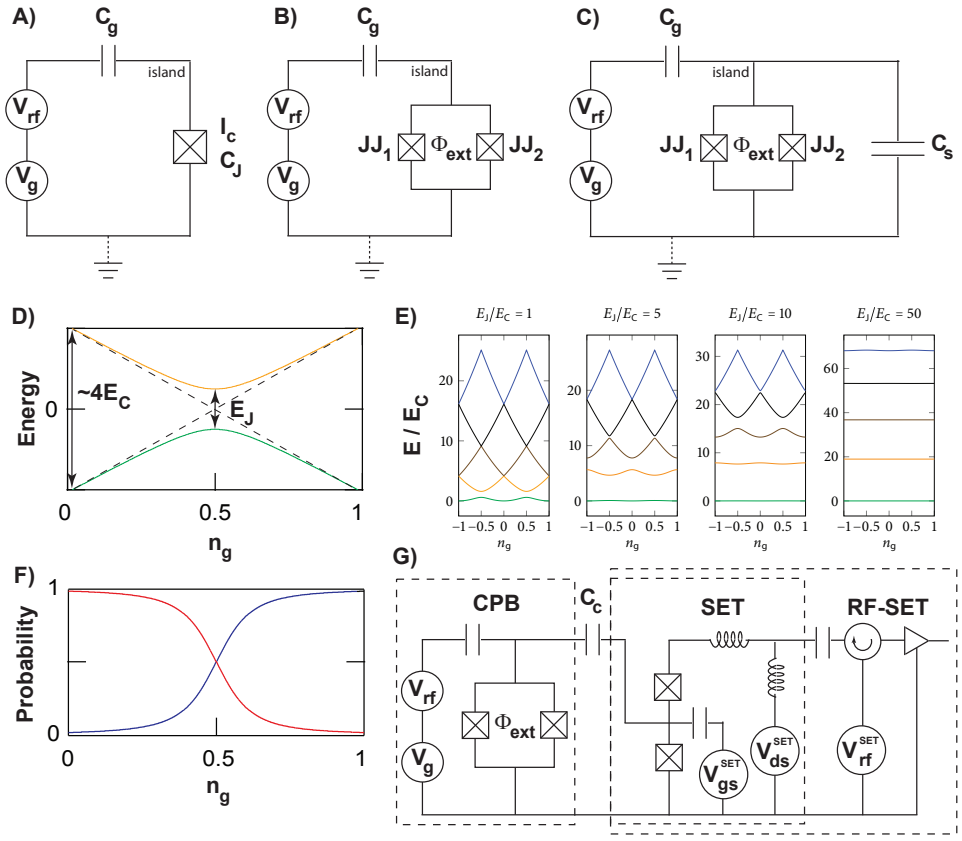

Fig. 3: Cooper Pair Box (CPB) and its derivatives. A) *Circuit diagram of a single-junction CPB. The number of extra Cooper pairs on the island, $n_{\rm g}$, is controlled by the gate voltage $V_{\rm g}$. The charge $n_{\rm g}$ is continuous, not discrete units of $2e$, because it is related to the polarization charge on the capacitor $C_{\rm g}$. Tuning $n_{\rm g}$ changes the electrostatic energy of the CPB by changing the amount of charge on the island subject to the charging energy $E_{\rm c}$.* **B)** *Split-junction CPB. A flux $\Phi_{\rm ext}$ tunes the critical current of the effective junction formed by the SQUID, thereby tuning the Josephson energy $E_{\rm J}$.* **C)** *Transmon: a capacitively shunted CPB. Adding a large parallel capacitor to the CPB flattens the energy levels and makes the CPB much less sensitive to charge fluctuations. The transmon may be realized as either a single junction (not shown) or a split-junction.* **D)** *Energy level diagram for the CPB within the two-level system approximation. The dashed lines are the classical charge states (diabatic energy levels). The solid lines are the eigenenergy levels that include Josephson coupling, which opens an avoided crossing of value $E_{\rm J}$. At the avoided crossing, the CPB is first-order insensitive to fluctuations in the charge.* **E)** *Multi-level energy diagram for the full CPB Hamiltonian assuming different values for the ratio $E_{\rm J}/E_{\rm C}$. As the ratio increases, the energy levels flatten and become less sensitive to charge. $E_{\rm J}/E_{\rm C} = 1$ is the CPB limit; $E_{\rm J}/E_{\rm C} = 50$ is the transmon limit.* **F)** *Probability of measuring 0 (red) or 1 (blue) Cooper pairs on the island using an SET readout. The probability is estimated by repeatedly measuring an identically prepared CPB. At the avoided crossing, the readout cannot distinguish the two classical states since $\langle n_{\rm g} \rangle = 0.5$.* **G)** *Simplified schematic for the readout of the CPB using a single-electron transistor (SET) operated in the DC transport regime, or as a resonant circuit (RF-SET). The CPB state modifies the SET island charge through the coupling capacitor $C_{\rm c}$, which modifies the DC current flowing through the island (drain-source current). Alternatively , it modifies the impedance seen by the RF source.*

island Cooper pairs is the junction itself via Josephson tunneling with Josephson energy $E_{\rm J}$. In the CPB, $E_{\rm C} \gg E_{\rm J}$ (or, at most, of order unity), and so the number of Cooper pairs on the island is a well-defined (localized) variable. The operator $\hat{n}$ will count the number of Cooper pairs that have tunneled on/off the island,

$$\hat{n}|n\rangle = n|n\rangle \tag{43}$$

and the classical (diabatic) states of the device are the charge states $|n\rangle$ and $|n+1\rangle$. The operator $\hat{n}$ is conjugate to the Josephson phase operator (the phase difference across a junction),

$$\hat{\phi}|\phi\rangle = \phi|\phi\rangle. \tag{44}$$

See Appendix A for a brief review of their properties.

The CPB Hamiltonian is a sum of two terms,

$$\hat{\mathcal{H}}_{\rm CPB} = 4E_{\rm C}(\hat{n} - n_{\rm g})^2 + E_{\rm J}(1 - \cos\hat{\phi}) \tag{45}$$

$$\rightarrow 4E_{\rm C}(\hat{n} - n_{\rm g})^2 - E_{\rm J}\cos\hat{\phi} \tag{46}$$

where the second line removes the static offset energy $E_{\rm J}$, but is otherwise equivalent to the first line. The first term is the electrostatic energy, which is related to the island charge. The electrostatic energy levels plotted versus $n_{\rm g}$ are parabolae, each associated with a discrete Cooper pair state $n = 0, 1, \ldots$ with minima that occurs at the respective value n (see Fig. 3E, $E_{\rm J}/E_{\rm C} = 1$). Tuning the gate voltage will increase the energy parabolically away from these minima. When the island charage reaches $n + 1/2$, the energy levels of the parabolae associated with charge states $|n\rangle$ and $|n + 1\rangle$ are degenerate. Josephson tunneling between n and $n + 1$ Cooper pairs on the island mixes these states and opens an avoided crossing with a strength dictated by the Josephson energy. This is the second term of the Hamiltonian, and it is the junction energy written in the phase basis. The mixing of charge states is elucidated by writing the Hamiltonian in the charge basis (see Appendix A),

$$\hat{\mathcal{H}}_{\rm CPB} = \sum_n \left[4E_{\rm C}(\hat{n} - n_{\rm g})^2 |n\rangle\langle n| - \frac{E_{\rm J}}{2}\left(|n\rangle\langle n+1| + |n+1\rangle\langle n|\right)\right]. \tag{47}$$

Alternatively, in the phase basis, the Hamiltonian is

$$\hat{\mathcal{H}}_{\rm CPB} = 4E_{\rm C}\left(\frac{1}{i}\frac{\partial}{\partial\hat{\phi}} - n_{\rm g}\right)^2 - E_{\rm J}\cos\hat{\phi} \tag{48}$$

The choice of representation is one of convenience, depending on what is being calculated. For example, the formal solutions to the Schrödinger equation in the phase basis are written in terms of Mathieu functions [197].

The CPB can have both a tunable gate charge $n_{\rm g}$ and a tunable splitting $E_{\rm J}$ at the avoided crossing by replacing the junction in Fig. 3A with a SQUID as shown in Fig. 3B. In this case, the Josephson energy is a function of the external magnetic field applied to the SQUID loop,

$$\hat{\mathcal{H}}_{\rm CPB,SQ} = 4E_{\rm C}(\hat{n} - n_{\rm g})^2 - E_{\rm J}(\Phi_{\rm ext})\cos\hat{\phi} \tag{49}$$

$$E_{\rm J}(\Phi_{\rm ext}) = E_{\rm J,max}\left|\cos\left(\frac{\pi\Phi_{\rm ext}}{\Phi_0}\right)\right| \tag{50}$$

where we have assumed a symmetric SQUID and $E_{\mathrm{J,max}} = E_{\mathrm{J1}} + E_{\mathrm{J2}}$.

The CPB can be written within a two-level system approximation by expanding the Hamiltonian about the charge degeneracy point at $n_{\mathrm{g}} = 1/2$, taking the charge states to be $|0\rangle$ and $|1\rangle$,

$$\hat{\mathcal{H}}_{\mathrm{CPB}}^{\mathrm{TLS}} = -\frac{1}{2}\left[4E_{\mathrm{C}}(1-2n_{\mathrm{g}})\hat{\sigma}_{\mathrm{x}} + E_{\mathrm{J}}(\Phi_{\mathrm{ext}})\hat{\sigma}_{\mathrm{z}}\right] \tag{51}$$

$$\equiv -\frac{\hbar}{2}\left[\varepsilon\hat{\sigma}_{\mathrm{x}} + \Delta\hat{\sigma}_{\mathrm{z}}\right] \tag{52}$$

where $\hat{\sigma}_{\mathrm{x,z}}$ are the Pauli spin matrices (see Fig. 3D), and we have made the association,

$$\hbar\varepsilon = 4E_{\mathrm{C}}(1-2n_{\mathrm{g}}) \tag{53}$$

$$\hbar\Delta = E_{\mathrm{J}}(\Phi_{\mathrm{ext}}) \tag{54}$$

Although this Hamiltonian is often written with $\hat{\sigma}_{\mathrm{x}}$ and $\hat{\sigma}_{\mathrm{z}}$ switched, we have chosen this representation so that this Hamiltonian is diagonalized (qubit along z) when biased at $n_{\mathrm{g}} = 1/2$. This conforms with our usage in Section 3. At $n_{\mathrm{g}} = 1/2$, the eigenstsates are σ_{z} and the energy levels are first-order insensitive to charge noise. Away from $n_{\mathrm{g}} = 1/2$, the eigenstates are σ_{x}-like, and the energy levels become sensitive to charge fluctuations due to there non-zero slope. The CPB is read out using a single-electron transistor (SET) operated as a sensitive charge electrometer (Fig. 3G). The SET is a superconducting island isolated by two junctions, similar to the CPB. The "drain" and "source" of the SET are the junction electrodes that connect to the island. When the SET is biased near a charge degeneracy point ($n_{\mathrm{g}} = n+1/2$), current can flow from drain to source with a value that depends strongly on the gate-source voltage V_{gs}. The CPB island is coupled capacitively to the island and modifies the SET gate charge depending on the state of the CPB. The voltage V_{gs} sets a bias point such that there is a maximal change in drain-source current between the CPB states $|0\rangle$ and $|1\rangle$. The probability of detecting states $|0\rangle$ and $|1\rangle$ as a function of the CPB n_{g} is illustrated in Fig. 3F. Note that at the CPB charge-degeneracy point ($n_{\mathrm{g}} = 1/2$), the SET cannot distinguish between $|0\rangle$ and $|1\rangle$, because their probabilities of detection are equally likely. This results from the fact that $|0\rangle$ and $|1\rangle$ are classical (diabatic) charges states that are mixed into an equal superposition state at the avoided crossing due to E_{J} coupling.

The DC-SET readout is generally dissipative, because the small junctions experience phase diffusion during the readout. Another approach is to use a resonant circuit that involves the SET biased solidly in its superconducting state. In this RF-SET approach [85], an RF pulse near resonance with this circuit is applied to the SET and is reflected back through a circulator to an amplifier (see Fig. 3G). The CPB state modifies the SET impedance which, in turn, modifies the reflected phase of the RF signal sent to the SET. The RF-SET is a much faster approach to readout, and it is less dissipative than its DC counterpart.

2.3.2 Quantronium

An early design modification to the CPB was the quantronium [4] qubit (Fig.4A). Quantronium was the first qubit to demonstrate the use of the charge degeneracy point operation to mitigate low-frequency fluctuation and thereby extend dephasing times. To measure the state of the qubit while remaining at the charge degeneracy point, a large junction was added in parallel to the CPB forming a loop. Flux through this loop controlled an additional degree of freedom and, thereby, a new noise channel. However, the energy along this flux dimension also had a

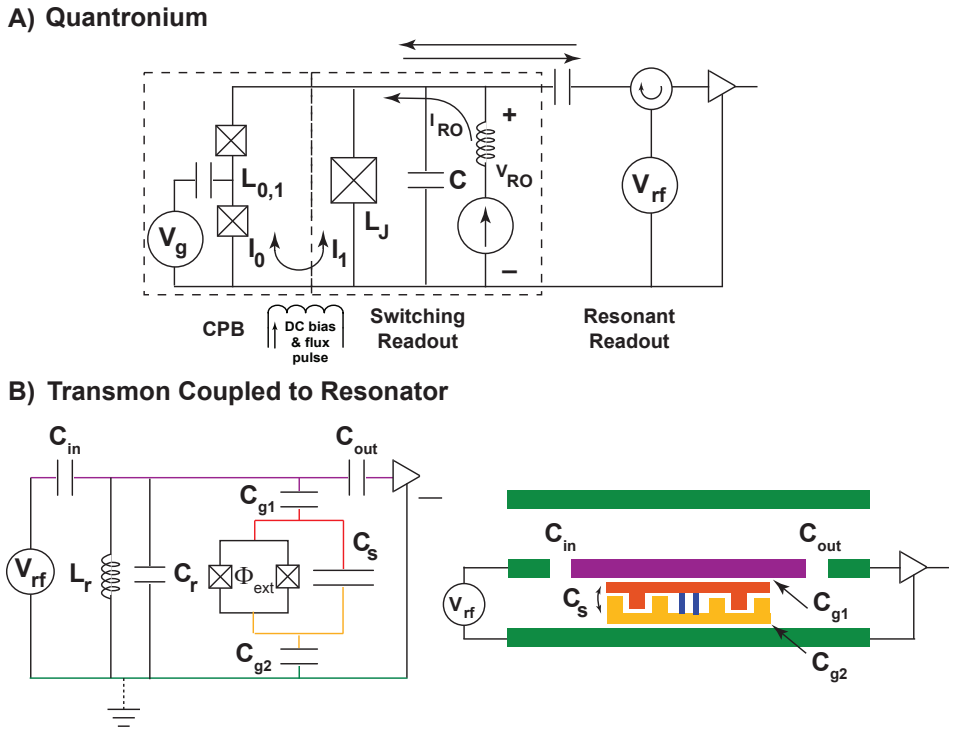

Fig. 4: Quantronium and transmon qubit readout A) *Quantonium circuit is a CPB with a large junction in parallel. The circuit has two degeneracy points: one charge and one flux due to the CPB-JJ loop. To read out quantronium, a flux pulse shifts the qubit away from the flux degeneracy point, and the qubit state corresponds to circulating currents clockwise or counter clockwise. The switching-current readout method sends a current pulse* $I_{\rm RO}$ *through the CPB-JJ circuit and monitors the voltage* $V_{\rm RO}$*from a state-dependent switching event. In the RF version of the readout, the large JJ and a parallel capacitor resonate at a frequency far detuned from the qubit (*e.g., *1.5 GHz in Ref. [181]), and the state-dependent CPB inductance shifts this resonant frequency. An RF pulse near resonance probes the circuit, and its reflection carries a state-dependent amplitude and phase. Figure adapted from Refs. [4, 181]* **B)** *Transmon coupled to a coplanar transmission line resonator, modeled in the circuit schematic as a lumped element resonator. In the dispersive limit,* $g \ll \Delta$*, an RF pulse probes the transmon-state-dependent resonance frequency and phase of the coplanar resonator. Adapted from Ref. [9].*

degeneracy point. The qubit was operated at this "double" charge-flux degeneracy point, and was thereby made insensitive to both charge and flux noise to first order. Dephasing times of around 500 ns were enabled by this approach, a 10x-100x improvement at the time [4].

Readout was performed by shifting the qubit away from the flux degeneracy point. In doing so, the qubit state was mapped onto circulating currents around the CPB-JJ loop. In the original work [4], a switching-current approach was used. A current pulse was applied to the loop close to the switching current of the large JJ. The exact value of the switching current was modified by state of the CPB; by choosing an appropriate current bias, the junction would switch for one state and not the other. By monitoring the presence or absence of a voltage pulse over several trials, one estimates the state occupation probability. The parallel capacitor in this approach acts as a "mass" to reduce phase fluctuations of the large junction and, thereby, narrow the switching-current distribution.

An alternative approach that does not rely on switching is to view the Josephson inductance $L_{\rm J}$ of the large JJ and its parallel capacitance C as a lumped-element resonant circuit with resonance frequency $\nu \approx 1.5$ GHz. The CPB itself has a state-dependent inductance which serves to modify the resonance frequency. By probing this resonator with an RF pulse and monitoring the frequency and/or phase of the reflected pulse, the qubit state is determined. The advantage here is three fold. First, the junctions need not switch and so there is much less dissipation using this approach. Second, the readout can be implemented much more quickly, because one does not need to wait for quasiparticle relaxation to repeat the experiment. And, third, the resonator itself is nonlinear and, at higher amplitudes, can be operated as a Josephson bifurcation amplifier (nonlinear readout) [86, 88, 89]. One potential disadvantage is that the qubit dephasing may occur due to photon number fluctuations in the resonator.

2.3.3 Transmon

The transmon and its readout will be covered in detail within another lecture in this series. Here, we provide a brief overview for completeness and to make the historical connection with the CPB.

The CPB is sensitive to $1/f$ charge noise fluctuations due to its energy dispersion. Even with the first-order insensitivity afforded at the degeneracy point, charge offsets due to nearby charge fluctuators severely impact the operation of the CPB. A solution to remedy this problem was offered in Ref. [9], which introduced the transmon. The transmon is essentially a CPB with a large capacitor in parallel (Fig. 3C). The capacitor acts to flatten the energy level dispersion by increasing the $E_{\rm J}/E_{\rm C}$ ratio (Fig. 3E). Typical values for transmons are $E_{\rm J}/E_{\rm C} = 50 \ldots 80$. As a consequence, as compared to the conventional CPB, the transmon is much less sensitive to low-frequency charge noise and therefore has dramatically improved dephasing times. Aside from the different regime of parameters, the transmon Hamiltonian and its solutions have the same form as the CPB.

Because the transmon has relatively small charge dispersion, there is a negligibly small charge signature of the transmon states and a different approach to readout is required. By strongly coupling the qubit transversally to a resonator (either lumped element resonator, 2D distributed waveguide resonator, or a 3D cavity), one realizes essentially a Jaynes-Cummings Hamiltonian (see Fig. 4B),

$$\hat{\mathcal{H}}_{\rm JC} = 4E_{\rm C}(\hat{n} - n_{\rm g})^2 - E_{\rm J}(\Phi_{\rm ext})\cos\hat{\phi} + \hbar\omega_{\rm r}\hat{a}^\dagger\hat{a} + \hbar g\hat{n}(\hat{a} + \hat{a}^\dagger) \tag{55}$$

where $\hat{a}^\dagger$ and $\hat{a}$ are creation and annihilation operators of the resonator field, the third term is

the energy of the resonator field, the fourth term is the coupling between the transmon and the resonator, and global energy offsets have been dropped. The prefactor g is the coupling strength between the transmon and the resonator, and $g = 2\beta e V^0_{\rm rms}$ for a coplanar waveguide, with $V^0_{\rm rms}$ the zero-point voltage of the cavity and β a voltage division ratio which is a function in terms of the capacitances in the circuit and acts to scale the coupling to the transmon. Within the two-level approximation for the transmon, the Hamiltonian is,

$$\hat{\mathcal{H}}^{\rm TLS}_{\rm JC} = \hbar\omega_{\rm r}\hat{a}^\dagger\hat{a} + \frac{\hbar\omega_{\rm q}}{2}\hat{\sigma}_{\rm z'} + \hbar g\hat{\sigma}_{\rm x'}(\hat{a} + \hat{a}^\dagger) \tag{56}$$

where the transmon portion of the Hamiltonian is written in its eigenbasis, as denoted by the prime notation on the $\hat{\sigma}_{\rm z',x'}$ operators. It has been demonstrated that superconducting circuits can operate within the strong-coupling regime $g \ll \gamma, \kappa$, where the coupling g is much larger than the decay rates of either the cavity, κ, or the transmon, γ.

In addition to enabling numerous beautiful cavity QED demonstrations with superconducting circuits, the Jaynes-Cummings-type Hamiltonian and its use of a strong, transverse coupling between the transmon and the resonator enables the readout of the transmon without the need for classical charge sensitivity. The readout is performed dispersively, by detuning the cavity frequency from the qubit frequency. This is a necessary operating condition in general, not just for readout, because the Purcell effect would otherwise enhance the decay rate of an atom (or qubit) resonantly coupled to a cavity field [10]. In the dispersive limit, the detuning $\Delta = \omega_{\rm q} - \omega_{\rm r}$ is larger than the coupling, $\sqrt{n}g \ll \Delta$. In this limit, the Hamiltonian can be expanded to second order in g/Δ [9] to yield the following dispersive, two-level system Hamiltonian,

$$\hat{\mathcal{H}}^{\rm TLS}_{\rm disp-JC} = \frac{\hbar(\omega_{\rm q} + \chi)}{2}\hat{\sigma}_{\rm z'} + \hbar(\omega_{\rm r} + \chi\hat{\sigma}_{\rm z'})\hat{a}^\dagger\hat{a}, \tag{57}$$

in which the original transverse coupling of the Jaynes-Cummings Hamiltonian is now manifest as a dispersive shift χ. The qubit frequency experiences a Lamb shift $\omega_{\rm q} + \chi$, and the resonator frequency experiences a transmon-state-dependent shift, $\omega_{\rm r} \pm \chi$, where $\chi = g^2/\Delta$ and we have ignored the shifts due to states outside the two-level manifold [9].

The primary trade-off made with the transmon is that the anharmonicity

$$\alpha = \frac{E_{12}}{E_{01}} - 1 \tag{58}$$

of the CPB has been dramatically reduced. In effect, by adding the capacitor, the CPB has come much closer to a harmonic oscillator ($\alpha = 0$). For the transmon, anharmonicities around $\alpha = -0.1$ are typical. This can be compared with the CPB anharmonicity typically around $\alpha = 5$. This is not catastrophic, obviously, given the success of the transmon, but it does carry implications for quantum control. To limit excitations to the two-level system manifold (and not simultaneously excite higher states), one must generally apply longer pulses. Longer temporal pulses correspond to narrower spectral width in the frequency domain; by lengthening the pulses, one can avoid off-resonantly driving nearby transitions. Another approach is to compensate the unwanted, off-resonance transitions with control methods [126].

2.3.4 Persistent-current flux qubit

The persistent-current flux qubit is a superconducting loop interrupted by three (Fig. 5A) or four (not shown) Josephson junctions. One the the junctions is smaller in area by a factor α, with

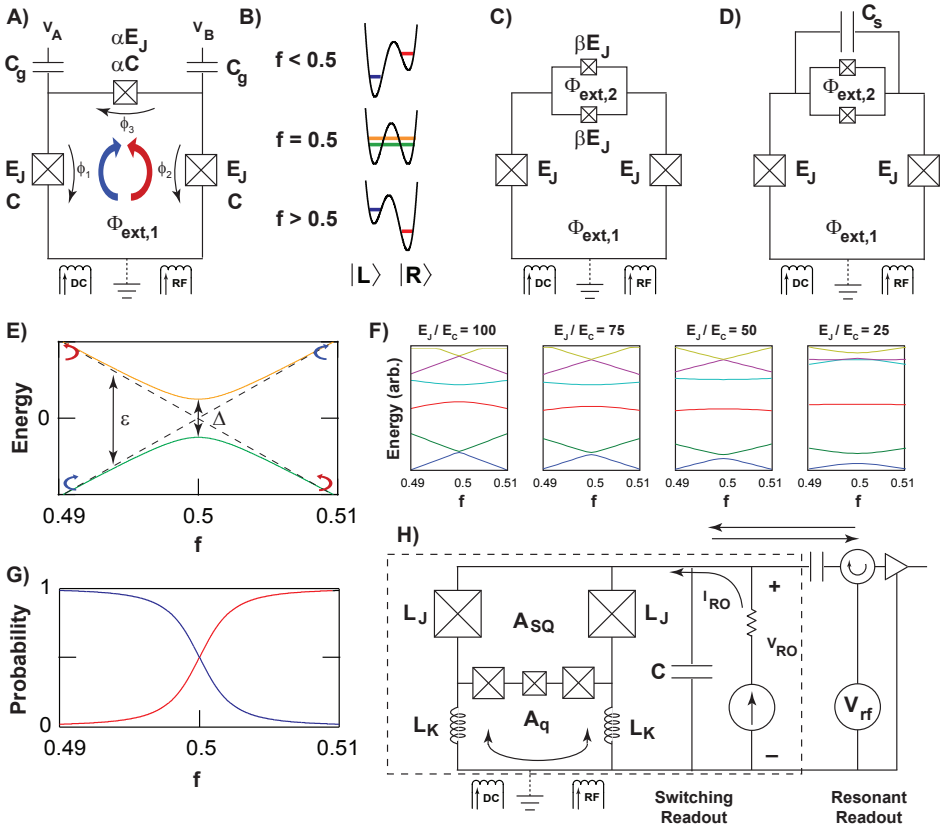

Fig. 5: Flux qubit and its derivatives A) *Three-junction flux qubit [128, 127]. One junction is smaller by a factor* α*. An external magnetic flux* $\Phi_{\mathrm{ext},1}$ *threads the loop, parameterized in reduced units,* $f = \Phi_{\mathrm{ext},1}/\Phi_0$*.* **B)** *Near* $f = 0.5$*, the qubit potential assumes a double well. For* $f < 0.5$*, the left well has a lower energy (clockwise current); for* $f > 0.5$*, the right well has a lower energy (counter-clockwise current). At* $f = 0.5$*, the diabatic state energies are degenerate. Tunnel coupling mixes the states, forming superpositions of the circulating currents and the qubit has no net magnetic polarization.* **C)** *Flux qubit with tunable* Δ *by splitting the small junction into a SQUID with its own flux bias* $\Phi_{\mathrm{ext},2}$*. The SQUID junctions are smaller by a factor* β*.* **D)** *Capacitively-shunted flux qubit. Decreasing the* $E_{\mathrm{J}}/E_{\mathrm{C}}$ *ratio flattens the energy bands but increases sensitivity to charge noise. A parallel capacitor across the small junction mitigates this noise [182, 129].* **E)** *Two-level system energy-level diagram. Flux tunes energy* ε *of the diabatic states (dashed lines). At* $f = 0.5$*, these states mix and open an avoided crossing* Δ*. At this point, the flux qubit is first-order insensitive to flux fluctuations.* **F)** *Multi-level energy level diagram for several values of the* $E_{\mathrm{J}}/E_{\mathrm{C}}$ *ratio. Larger capacitance (D) decreases this ratio, flattening the energy bands.* $E_{\mathrm{J}}/E_{\mathrm{C}} = 75$ *is a typical flux-qubit value.* $E_{\mathrm{J}}/E_{\mathrm{C}} < 50$ *is a capacitively shunted flux qubit.* **G)** *Probability of measuring clockwise (blue) or counterclockwise (red) circulating currents using a SQUID readout. At the avoided crossing, the readout cannot distinguish the two classical states since the net magnetic polarization is zero.* **H)** *Simplified schematic for the flux qubit readout using a DC SQUID magnetometer. The qubit is mutually coupled to the SQUID through either its geometric inductance (not shown) and/or the kinetic inductance* L_{K} *of a shared line. The qubit adds/subtracts a state-dependent flux to/from the SQUID, modifying its switching current. Ramping a current between these state-dependent values results in a switching event for one state, but not the other. Alternatively, the SQUID inductance in parallel with the capacitor* C *forms a resonant circuit. RF reflectometry techniques can be used to probe the state-dependent frequency and phase of this resonator.*

a typical value $\alpha = 0.75$ for the three-junction qubit and $\alpha = 0.5$ for the four-junction qubit. In this section, we will focus primarily on the three-junction version of this qubit. The four junction qubit has the certain advantages due to its symmetry when fabricated using double-angle shadow evaporation [5, 6], but otherwise it operates similarly to the three-junction qubit.

The small junction acts as a flux-shuttle value that lets a fluxoid in and out of the loop. The larger junctions serve to add loop inductance. The loop itself has negligible inductance. We will assume symmetric large junctions with $E_{\mathrm{J}2} = E_{\mathrm{J}3} \equiv E_{\mathrm{J}}$ and junction capacitances $C_2 = C_3 \equiv C$. The small junction has capacitance αC and Josephson energy αE_{J}. The gate capacitances are used to model the effect of offset charges in the environment. We will assume symmetric gate capacitances $C_{\mathrm{gA}} = C_{\mathrm{gB}} \equiv C_{\mathrm{g}}$, with a value $C_{\mathrm{g}} = \gamma C$.

The flux qubit has a potential energy U equivalent to the total Josephson energy of the three junctions,

$$U = \sum_i E_{\mathrm{J}i}(1 - \cos\phi_i). \tag{59}$$

The fluxoid quantization condition sets $\phi_1 - \phi_2 + \phi_3 = -2\pi f$, where $f \equiv \Phi_{\mathrm{ext}}/\Phi_0$ is the applied external magnetic flux Φ_{ext} normalized by the superconducting flux quantum Φ_0. Eliminating ϕ_3 yields,

$$\begin{aligned} U &= E_{\mathrm{J}}\left[2 + \alpha - \cos\phi_1 - \cos\phi_2 - \alpha\cos(2\pi f + \phi_1 - \phi_2)\right] && (60)\\ &= E_{\mathrm{J}}\left[2 + \alpha - 2\cos\phi_{\mathrm{p}}\cos\phi_{\mathrm{m}} - \alpha\cos(2\pi f + 2\phi_{\mathrm{m}})\right] && (61)\end{aligned}$$

where we have used the sum and difference phases $\phi_{\mathrm{p,m}} = (\phi_1 \pm \phi_2)/2$. The two-dimensional potential U forms an "egg carton" as a function of ϕ_{p} and ϕ_{m} with the unit cells periodic in 2π [128].

The electrostatic energy ($CV^2/2$) stored in the five capacitors in Fig. 5A is (see Ref. [128])

$$\begin{aligned} T &= \frac{1}{2}\left(\frac{\phi_0}{2\pi}\right)^2 \dot{\vec{\phi}}^{\mathrm{T}} \cdot \mathbf{C} \cdot \dot{\vec{\phi}} - \frac{1}{2}\vec{V}_{\mathrm{g}}^{\mathrm{T}} \cdot \mathbf{C}_{\mathrm{g}} \cdot \vec{V}_{\mathrm{g}} && (62)\\ &= \frac{1}{2}\vec{Q}_{\mathrm{tot}}^{\mathrm{T}} \cdot \mathbf{C}^{-1} \cdot \vec{Q}_{\mathrm{tot}} && (63)\end{aligned}$$

where $\dot{\vec{\phi}} = [\dot{\phi}_1, \dot{\phi}_1]^{\mathrm{T}}$, the gate voltage is $\vec{V}_{\mathrm{g}} = [V_{\mathrm{A}}, V_{\mathrm{B}}]^{\mathrm{T}}$, the total island charge is $\vec{Q}_{\mathrm{tot}} = \mathbf{C} \cdot (\Phi_0/2\pi)\dot{\vec{\phi}} \equiv \mathbf{C} \cdot \mathbf{V}$ in terms of the junction voltages $\mathbf{V}$, and the capacitance matrices are,

$$\mathbf{C} = C\begin{pmatrix} 1+\alpha+\gamma & -\alpha \\ -\alpha & 1+\alpha+\gamma \end{pmatrix} \qquad \mathbf{C}_{\mathrm{g}} = \gamma C\begin{pmatrix} 1 & 0 \\ 0 & 1 \end{pmatrix}. \tag{64}$$

The transition from classical Josephson and electrostatic energies to the quantum Hamiltonian follows the correspondance principle and is presented in detail in Ref. [128]. Here, we present the net results only.

In the phase basis, the three-junction flux-qubit Hamiltonian is

$$\begin{aligned} \hat{\mathcal{H}}_{\mathrm{FQB}} = 4E_{\mathrm{C}}\left[\frac{1}{2}\frac{1}{(1+\gamma)}\left(\frac{1}{i}\frac{\partial}{\partial\hat{\phi}_{\mathrm{p}}}\right)^2 + \frac{1}{2}\frac{1}{(1+2\alpha+\gamma)}\left(\frac{1}{i}\frac{\partial}{\partial\hat{\phi}_{\mathrm{m}}}\right)^2\right] + \ldots \\ - E_{\mathrm{J}}\left[2\cos\hat{\phi}_{\mathrm{p}}\cos\hat{\phi}_{\mathrm{m}} + \alpha\cos(2\pi f + 2\hat{\phi}_{\mathrm{m}})\right], \end{aligned} \tag{65}$$

where we have dropped the energy offset $(2+\alpha)E_{\rm J}$. Note that the kinetic energy term has the form $\hat{P}^2_{\rm p,m}/2M_{\rm p,m}$ for momenta $\hat{P}_{\rm p,m} = -i\partial/\partial\hat{\phi}_{\rm p,m}$ and masses $M_{\rm p,m}$. Writing the kinetic term in the charge basis, the Hamiltonian becomes:

$$\hat{\mathcal{H}}_{\rm FQB} = 4E_{\rm C}\left[\frac{1}{2}\frac{1}{(1+\gamma)}\hat{n}_{\rm p}^2 + \frac{1}{2}\frac{1}{(1+2\alpha+\gamma)}\hat{n}_{\rm m}^2\right] + \ldots \\ - E_{\rm J}\left[2\cos\hat{\phi}_{\rm p}\cos\hat{\phi}_{\rm m} + \alpha\cos(2\pi f + 2\hat{\phi}_{\rm m})\right], \quad (66)$$

where $\hat{n}_{\rm p,m} = \hat{n}_1 \pm \hat{n}_2$. Or, equivalently, in the mixed basis and in terms of the junction / island numbering,

$$\hat{\mathcal{H}}_{\rm FQB} = 4E_{\rm C}\left[\frac{1+\alpha+\gamma}{(1+\gamma)(1+2\alpha+\gamma)}(\hat{n}_1^2+\hat{n}_2^2) + \frac{2\alpha}{(1+\gamma)(1+2\alpha+\gamma)}\hat{n}_1\hat{n}_2\right] + \ldots \\ - E_{\rm J}\left[\cos\hat{\phi}_1 + \cos\hat{\phi}_2 + \alpha\cos(2\pi f + \hat{\phi}_1 - \hat{\phi}_2)\right]. \quad (67)$$

In either representation ($\hat{\phi}_{1,2}$ or $\hat{\phi}_{\rm p,m}$), the potential term can be converted to the charge representation using the relations in Appendix A.

When the applied flux is close to half a flux quantum, $f \approx 0.5$, the potential (within a unit cell) assumes a two-dimensional, double-well profile. A slice of this double well along the $\phi_{\rm m}$ direction is shown in Fig. 5B. The states in each well corresponds to a circulating persistent currents, clockwise or counterclockwise, around the loop with magnitude $I_{\rm p}$. As illustrated in Fig. 5, $f < 0.5$ tilts the left well (clockwise circulating current) to lower energy, whereas $f > 0.5$ tilts the right well (counterclockwise circulating current) to lower energy.

The two-level system model comprises the lowest-energy circultating current state in each well. These are the classical (diabatic) states (dashed lines, Fig. 5E), and they have energy,

$$\pm\frac{\hbar\varepsilon}{2} = \pm I_{\rm p}\Phi_0(f-1/2) \quad (68)$$

Note that $\delta f \equiv f - 1/2$ is sometimes used (*e.g.,* see Sections 3 and 4) to reference the flux to the degeneracy point at $f = 1/2$. At $f = 0.5$, the lowest-energy quantized states of the wells are degenerate. Quantum tunneling through the double-well barrier (Fig. 5B) hybridizes the classical (diabatic) states into superpositions of circulating currents, opening an avoided crossing of strength Δ (Fig. 5E). The value of Δ is generally found by diagonalizing the Hamiltonian, but it can be estimated using the WKB approximation to be

$$\hbar\Delta_{\rm WKB} \approx 1.3\sqrt{E_{\rm J}E_{\rm C}}e^{-0.64\sqrt{E_{\rm J}/E_{\rm C}}}. \quad (69)$$

Since $E_{\rm J} \propto A_{\rm J}$ and $E_{\rm C} \propto 1/A_{\rm J}$, where $A_{\rm J}$ is the junction area, Δ scales exponentially with the $A_{\rm J}$ and is thus highly sensitive to fabrication variations in the junction size.

The two-level system Hamiltonian for the flux qubit is,

$$\hat{\mathcal{H}}^{\rm TLS}_{\rm FQB} = -\frac{1}{2}\left[2I_{\rm p}\Phi_0(f-1/2)\hat{\sigma}_{\rm x} + \hbar\Delta\hat{\sigma}_{\rm z}\right] \quad (70)$$

$$\equiv -\frac{\hbar}{2}\left[\varepsilon\hat{\sigma}_{\rm x} + \Delta\hat{\sigma}_{\rm z}\right] \quad (71)$$

where $\hat{\sigma}_{\rm x,z}$ are the Pauli spin matrices (see Fig. 3D).

By splitting the small junction into a SQUID loop with two junctions having a Josephson energy $\beta E_{\rm J}$, one can tune Δ using a second external flux $\Phi_{\rm ext,2}$ (Fig. 5B). The Hamiltonians in Eqs. 65, 66, 67 are modified by making the following substitutions [128]

$$\alpha \rightarrow 2\beta \tag{72}$$

$$\alpha\cos(2\pi f + 2\hat{\phi}_{\rm m}) \rightarrow 2\beta\cos(\pi f_a)\cos(2\pi f_b + 2\hat{\phi}_{\rm m}) \tag{73}$$

where $f_a \equiv f_2$ is the reduced flux $\Phi_{\rm ext,2}$, and $f_b \equiv f_1 + f_2/2$ with $f_1 \equiv f$ in the single-loop qubit. Essentially, the flux f_2 tunes the value α via the factor $2\beta\cos(\pi f_a)$. However, because one of the junctions in loop 2 is shared with loop 1, the flux bias f_b which tilts the double wells picks up a factor $f_2/2$.

As with the CPB and transmon, there is a capacitively shunted version of the flux qubit [182, 129]. Decreasing α decreases the $E_{\rm J}/E_{\rm C}$ ratio in the flux qubit and tends to flatten the energy bands, thereby decreasing the qubit's sensitivity to low-frequency flux noise. However, decreasing the $E_{\rm J}/E_{\rm C}$ ratio also makes the qubit more sensitive to charge noise. This can be mitigated by shunting the small junction with a capacitor.

The flux qubit is read out using either a switching-current method, resonant readout technique, or cavity-QED approach (similar to Fig. 4B). In Fig. 3H, we show a simplified schematic of the SQUID-based switching-current and resonant-readout approach. The DC SQUID is a sensitive magnetometer which can detect the small fluxes generated by the circulating currents. The qubit is mutually coupled to the SQUID by a combination of geometric inductance and, for galvanically connected devices, kinetic inductance. In the conventional switching current readout, a pulse is applied to the SQUID close to its switching current. The precise value of the switching current depends on the state of the qubit, and the pulse amplitude is chosen such that the SQUID switches for one state of the qubit and not the other (see Fig. 15C for an example). By repeating the experiment many times, an estimate for the state probability is generated (Fig. 5G). Alternatively, the SQUID inductance forms a resonator with a parallel capacitor, and the resonance frequency becomes qubit-state dependent through the inductance. RF reflectometry can then be used to probe the SQUID resonator frequency or phase to estimate the qubit state. Since the SQUID inductance is non-linear with its current, the SQUID resonator can be operated in both the linear (low current) or non-linear (large current) regimes.

An example of resonant readout of the flux qubit is shown in Fig. 6. The circuit schematic shows the flux qubit geometrically coupled to a DC SQUID. RF impedance networks are used to match the SQUID to the 50-Ohm lines used to probe the resonator. This has the practical effect of increasing the resonator Q value near the resonance frequency.

A DC current is used to generate an external flux $\Phi_{\rm ext}$ through the SQUID and the qubit. By properly designing the relative areas of the SQUID and qubit, the qubit can be biased at $f = 0.5$ for a value of SQUID switching current that is approximately midway between its maximum and minimum values. In Fig. 6B, the SQUID resonance frequency is plotted as a function of the current that applies the external flux to the qubit and SQUID. The resonance frequency modulates due to the SQUID critical current $I_{\rm c}(\Phi_{\rm ext})$ which, in turn, modulates the SQUID inductance $L_{\rm J}$. Note that the SQUID inductance is only a portion of the total resonator inductance, and the observed modulation is about 300 KHz on top of a resonance frequency $\nu_0 \approx 420$ MHz. A "qubit step" is clearly observed as a "jump" in the resonance frequency; this step corresponds to the qubit ground state changing the polarity of its circulating current as the qubit is stepped through the avoided crossing at $f = 0.5$ (see Fig. 5E).

Because the SQUID Josephson inductance is nonlinear in the SQUID current (the SQUID is an effective Josephson junction, see Section 2.2.5), the SQUID resonator is fundamentally an-

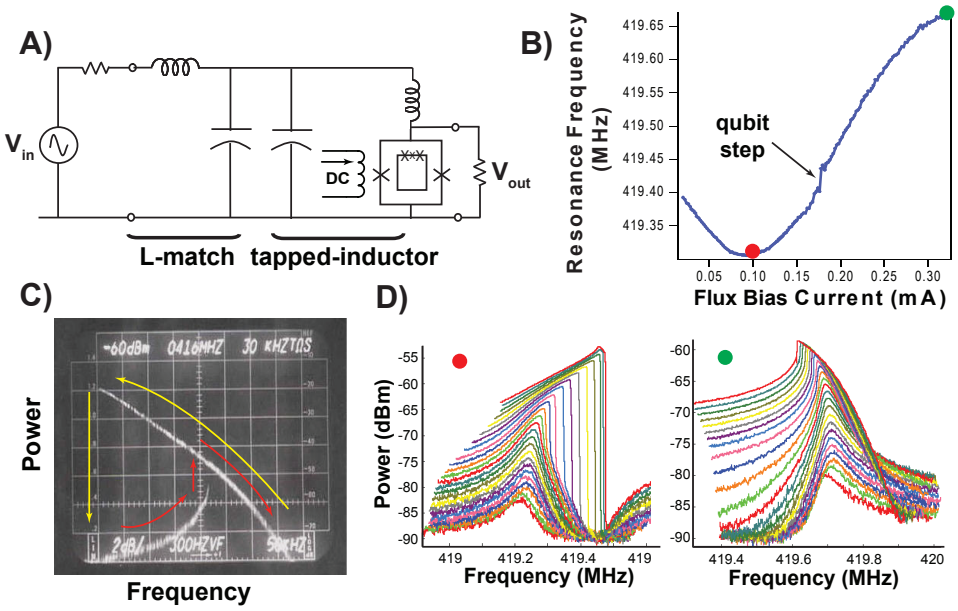

Fig. 6: Resonant readout of a flux qubit [87, 91] A) *Circuit schematic of the flux qubit and its SQUID. The SQUID is isolated from the 50-Ohm environment using an L-match and tapped-inductor impedance-matching network. The SQUID is shunted by a capacitor (not shown) and has a plasma frequency around 420 MHz. RF near the resonance frequency is applied from the left side, and measured at the load on the right side of the schematic in a through configuration.* **B)** *SQUID resonance frequency as a function of the flux applied to the qubit and SQUID. The SQUID critical current is modulated and, simultaneously, the qubit is biased. At a flux bias current around 0.18 mA, the resonance frequency makes an abrupt jump; this step corresponds to the qubit ground state changing the polarity of its circulating current.* **C)** *A strongly driven resonator will bifurcate. This picture is taken on an old oscilloscope that allows us to manually sweep from low- to high frequencies (path shown in red) and then from high- to low frequencies (path shown in yellow) while storing the trace on the screen. The strong asymmetry is indicative of a non-linear resonator.* **D)** *RF transmission as a function of frequency for several values of driving amplitude. As the amplitude increases, the resonance peak becomes asymmetric due to the SQUID nonlinearity. The resonance peak shifts to higher or lower frequency depending on the sign of the leading-order non-linear terms that govern the SQUID dynamics.*

harmonic and may exhibit non-linear behavior. At large amplitudes, the resonator bifurcates, having multiple solutions (two stable solutions and one unstable solution) over a range of frequencies. The stable solutions are accessed preferentially depending on the initial state of the resonator. For example, as shown in Fig. 6C, sweeping the RF probe signal from low to high frequency (red arrows) accesses the lower-amplitude branch of the resonance up to the bifurcation point, after which the resonator state jumps to the higher-amplitude branch. In turn, starting from the high-frequency side and sweeping to lower frequencies (yellow arrows), the resonator state remains along the high-amplitude branch until the resonance peak is reached, after which it jumps down to the single-valued low-amplitude state. Biasing a readout circuit near a bifurcation point therefore has the potential to increase signal-to-noise ratio (SNR) [88, 91, 92]. The resonance bends to lower or higher frequencies depending on whether the SQUID is at a high or low value of its switching current (Fig. 6D). This can be traced to the sign of the leading-order non-linear terms that govern the SQUID dynamics as discussed in [91]. Intuitively, bending to lower frequencies indicates an inductance that increases in value with increased current, whereas bending to higher frequencies indicates an inductance that decreases with current.

2.3.5 Phase qubit

The phase qubit is a current-biased Josephson junction (see Fig. 7A) [29]. When the junction is biased close to its critical current, the washboard potential (Fig. 7B) is sufficiently tilted that a potential well accommodates only a few quantized states. In this limit, the local potential well is sufficiently anharmonic that the ω_{01} transition can be distiguished from the ω_{12} transition. The leakage rates from the well to the running mode of the junction satisfy $\Gamma_0 \ll \Gamma_1 \ll \Gamma_2$, such that state $|0\rangle$ is metastable, state $|1\rangle$ is relatively long-lived, and state $|2\rangle$ tunnels rapidly. Qubit readout is performed by driving the transition ω_{12}. If the qubit were in state $|1\rangle$, it would quickly tunnel to the running mode upon being driven to state $|2\rangle$. In the running mode, there is a junction voltage; the presence of a voltage indicates the qubit was in state $|1\rangle$ whereas the absence of a voltage indicates state $|0\rangle$.

To better isolate the junction from its environment and readout circuitry, the phase qubit junction was placed in a loop of inductance L, forming essentially an RF SQUID (Fig. 7C and D) [130]. The qubit potential energy U is the sum of the junction energy and the inductive energy due to the circulating current, (inset, Fig. 7C),

$$\begin{aligned} U &= E_{\mathrm{J}}\left[1-\cos\phi+\frac{1}{2}LI_{\mathrm{circ}}^2\right] \\ &= E_{\mathrm{J}}\left[1-\cos\phi+\frac{(\phi-\phi_{\mathrm{ext}})^2}{2\beta_{\mathrm{L}}}\right] \\ &= E_{\mathrm{J}}(1-\cos\phi)+E_{\mathrm{L}}(\phi-\phi_{\mathrm{ext}})^2 \end{aligned} \tag{74}$$

where $\phi_{\mathrm{ext}} \equiv 2\pi\Phi_{\mathrm{ext}}/\Phi_0$, $\beta_{\mathrm{L}} = L/L_{\mathrm{J}} = 2\pi LI_{\mathrm{c}}/\Phi_0$, $E_{\mathrm{L}} = (\Phi_0/2\pi)^2/2L$ is the inductive energy, and the fluxoid quantization condition was used.

The qubit loop is biased with an external flux Φ_{ext}, effectively biasing the junction via the loop circulating current. Tuning the external flux effectively shifts the cosine potential wells along the parabola. At particular biases, one can achieve the potential profile illustrated in Fig. 7C, comprising a shallow well isolated by a potential barrier of height ΔU from a relatively deep well. The shallow and deep wells are separated by approximately Φ_0. Typical parameters that allow for a transition $\omega_{01}/2\pi \approx 6$ GHz are $I_{\mathrm{c}} = 2\ \mu$A, $C = 1$ pF, and $L = 700$ pH.

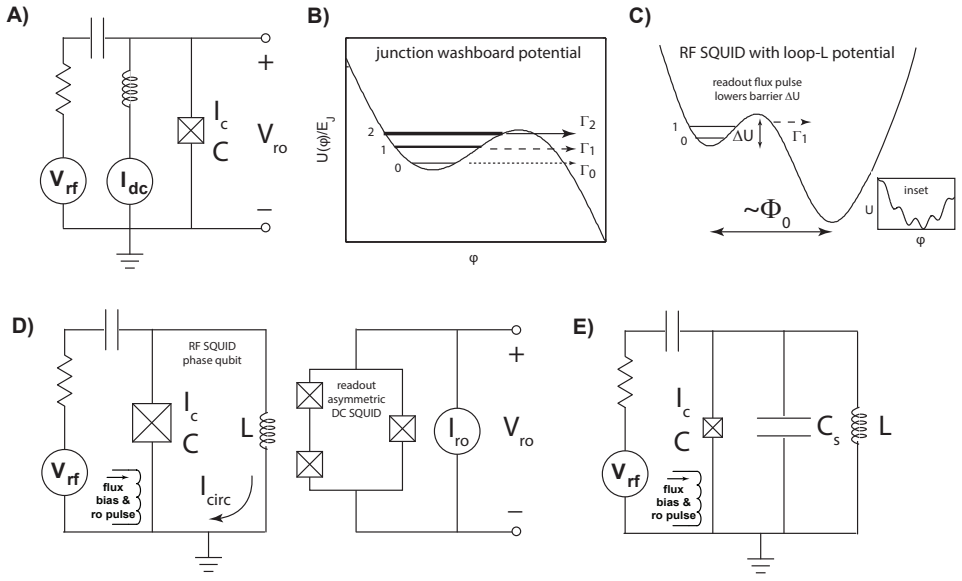

Fig. 7: Phase qubit and its derivatives A) *and* **B)***Single Josephson junction biased near its critical current is a phase qubit. The junction is biased such that the wells of the washboard potential have a few quantized states. Leakage rates to the running mode satisfy* $\Gamma_2 \gg \Gamma_1 \gg \Gamma_0$. *Driving the* ω_{12} *transition constitutes readout, which creates a voltage if the qubit were in state 1 due to tunneling from* $|2\rangle$ *to the running state.* **C** *and* **D)** *Flux-biased phase qubit realized in an RF SQUID geometry. The junction is placed in a loop with geometrical inductance* L*, resulting in a parabolic cosine potential (inset of C). The qubit is flux-biased with a pulsed current, and it is manipulated via RF pulses. Readout is achieved via a fast flux pulse which transiently reduces the potential barrier* ΔU*. If the qubit is in state 1, it will rapidly tunnel to the adjacent well associated with a flux change of about one* Φ_0*. An asymmetric DC SQUID senses the presence or absence of this flux to perform readout.* **E)** *Capacitively shunted phase qubit. Conventional AlOx junction dielectrics tend to be lossy and prone to defect states. Reducing the junction size (while maintaining its* I_c*) and adding a parallel shunt capacitor moves the capacitive energy outside the junction, improving qubit coherence times to the extent one can fabricate a high-Q capacitor.*

Qubit manipulation is through a combination of RF pulses capacitively coupled to the qubit and flux pulses that detune ω_{01} to realize Z rotations. The qubit state is readout is a two-step process. One first uses a fast flux pulse to transiently reduce the potential barrier ΔU (Fig. 7C). Doing so will exponentially increase the tunneling rate of state $|1\rangle$ to the right well, but leaves state $|0\rangle$ essentially metastable. A DC SQUID is then used in a switching-current type experiment (see sections 2.1.4 and 2.3.4) to look for a change in flux of approximately Φ_0 (a huge signal), indicating that a tunneling event occurred, and so the qubit was in state $|1\rangle$. An asymmetric DC SQUID (see section 2.2.4) is used, because it can have sensitivity $dI_{\rm c}/d\Phi_{\rm ext}$ to the external flux generated by the qubit without need for the SQUID having its own static flux bias. Finally, a flux pulse tilts the wells to reset the qubit state back into the left well.

The Hamiltonian for flux-biased phase qubit (an RF SQUID) is [183]

$$\hat{\mathcal{H}}_{\rm RFS} = 4E_{\rm C}(\hat{n} - n_0)^2 - E_{\rm J}\cos\hat{\phi} + E_{\rm L}(\hat{\phi} - \phi_{\rm ext})^2 \tag{75}$$

where n_0 represents fluctuating offset charges across the junction and shunt capacitances, and we have dropped the energy offset from the Josephson energy. Within the two-level system model, the phase qubit Hamiltonian is essentially a pseudospin with energy ω_{01} along $\sigma_{\rm z}$ with a transverse component related to changes in the circulating current $\delta I_{\rm circ}$. However, changing the circulating current will also change the frequency ω_{01}. As a result, the Hamiltonian is approximately [29, 131],

$$\hat{\mathcal{H}}^{\rm TLS}_{\rm RFS} = -\frac{1}{2}\left[\hbar\omega_{01}\hat{\sigma}_{\rm z} + \sqrt{\frac{\hbar}{2\omega_{01}C}}\delta I_{\rm circ}\,(\hat{\sigma}_{\rm x} + \chi\hat{\sigma}_{\rm z})\right] \tag{76}$$

where $\chi = \sqrt{\hbar\omega_{01}/3\Delta U} \approx 4$ for typical parameters.

In early experiments, the phase qubit suffered from loss and defects in the AlOx junction dielectric barrier [132]. An improvement was made by reducing the junction area (while maintaining $I_{\rm c}$) and adding a large external shunt capacitor to compensate for the reduced junction capacitance (Fig. 7E) [133]. This design change placed the focus on developing a high-Q capacitor dielectric for the external capacitor as opposed to improving the Q of the junction barrier. Of the various barriers attempted, amorphous silicon dioxide (a-SiOx) has a relatively high loss tangent (Q^{-1}) of $\sim 5\times10^{-3}$ compared with $\sim 1\times10^{-4}$ for amorphous silicon nitride (a-SiNx) and yet another factor 10 or so better for hydrogenated amorphous silicon (a-Si:H) [134]. Efforts continue to improve these dielectrics, their surfaces and interfaces, and the development of new materials and fabrication techniques consistent with high-Q qubits.

2.3.6 RF SQUID qubit

The RF SQUID qubit was among the first flux qubits to demonstrate quantized energy levels and an avoided level crossing [24] (the other was the persistent-current flux qubit [25]). Although its Hamiltonian (Eq. 75) is the same as the flux-biased phase qubit, its mode of operation is most similar to the persistent-current flux qubit. The RF SQUID is nominally operated near a symmetric double-well potential configuration. The classical (diabatic) states of the RF SQUID are the circulating current states, and resonant tunneling through the double-well barrier will open an avoided crossing. Coherence in the RF SQUID qubit has not improved as dramatically as other qubits over the past several years, in part due to its strong sensitivity to flux noise.

2.3.7 Fluxonium and metastable RF-SQUID: inductively shunted qubits

Most qubits surveyed thus far have a capacitively shunted version which provided a performance improvement. There are two complementary examples of inductively shunted qubits: the fluxonium qubit [135], and the metastable RF-SQUID qubit [183]. Both are single junction loops shunted by a large inductance, have large anharmonicity, and can be viewed as inductively shunted RF-SQUIDs described by the RF-SQUID Hamiltonian (Eq. 75). They operate in very different parameter regimes.

The fluxonium qubit demonstrated in Ref. [135] has parameters: $E_{\rm J} = 9.0$ GHz, $E_{\rm C} = 2.5$ GHz, and $E_{\rm L} = 0.52$ GHz. The shunt inductance is realized by a series array of junctions (43 junctions were used in Ref. [135]), each with an area about an order of magnitude larger than the small, single junction. The small, single junction acts as the flux-shuttle valve in and out of the loop. The series array of junctions both provides the shunt inductance and a DC short-circuit for offset charges on the islands connected to the small junction. The result is a qubit that is relatively immune to such charge noise. Each junction of the inductor array itself is designed to have parameters that suppress phase slips, that is, acting as a parallel flux-shuttle path to the small junction. These phase slips are in fact related to residual offset charges throughout the array. The coherent interaction of these phase slips across all junctions has led to a beautiful demonstration of Aharonov-Chasher physics with this superconducting qubit [136].

The metastable flux qubit, as designed in Ref. [183], has parameters: $E_{\rm J} = 120$ GHz, $E_{\rm C} = 6$ GHz, and $E_{\rm L} = 60$ GHz. The large shunt inductance is realized via the kinetic inductance of a 5-nm thick niobium nitride (NbN) nanowire of the type used in single-photon detectors. A key feature of the nanowire is that it is compact, exhibits extremely large kinetic inductance, and yet has an extremely low shunt capacitance. For example, a 10×10 $\mu{\rm m}^2$ meander of 100-nm wide wire has an inductance $L \sim 500$ nH and yet only 0.4 fF of capacitance (based on EM simulations) [183, 137]. The qubit is designed to have a very small tunnel coupling ($\Delta \sim 50$ kHz), which increases T_1 times by reducing the transverse coupling of the qubit states, making it metastable (*e.g.,* the qubit used in Ref. [38] had $\Delta \sim 10$ MHz and correspondingly $T_1 \rightarrow 1$ms away from the qubit degeneracy point). Although it remains to be tested, the quantum phase-slip rate through the nanowire, which acts to increase Δ and thereby decrease T_1, is expected to be much lower than for a series array of junctions. Since $\hbar\Delta \ll k_{\rm B}\Theta$ at degeneracy, the qubit must be operated far from the degeneracy point, $f \ll 0.5$ or $f \gg 0.5$. Although there is non-zero energy dispersion away from degeneracy, the large inductance serves to dramatically reduce the flux sensitivity $d\omega_{01}/df$, such that simulation suggests that $T_2 \sim 15$ μs (this "T_2" is actually a Gaussian decay time due to 1/f noise, see Section 3.3.2) is achievable with standard levels of 1/f flux noise. Qubit control is achieved by parametrically modulating Δ at frequency ω_{01} through a split-junction loop of the type discussed in Section 2.3.4. The large inductance suppresses the circulating current to a degree that a switching current readout is no longer feasible. Rather, both a dispersive-type readout or qubit-mediated coupling techniques [70] can be used to readout the metastable flux qubit.

3 Free- and driven evolution of two-level systems

Quantum gate operations in superconducting qubits (and most qubit modalities in general) are broadly realized by two categories of coherent evolution: free evolution and driven evolution. During these periods of evolution, unwanted environmental noise acts to decohere the qubit and increase the gate error rate. Characterizing the noise which couples to the qubit during these

two periods is therefore an important first step towards either mitigating or eliminating these sources of decoherence.

In this section, we will review the Bloch sphere representation of a two-level system, and consider how parameter fluctuations (*i.e.,* noise) impacts qubit dynamics in the laboratory, qubit (eigenstate), and rotating frames. We will then present a general perturbative approach to analyzing noise based on the approach used by Ithier *et al.* [7]. This will allow us to make a connection between the decay functions measured in experiments and the noise power spectral density $S_\lambda(\omega)$. The analogy between free- and driven evolution when viewed on a Bloch sphere allows us to define analogous energy-relaxation times (T_1 and $T_{1\rho}$) and coherence times (T_2 and $T_{2\rho}$) respectively for these two categories of evolution. The characteristic times need not correspond to exponential decay functions, and this is the case for decay functions corresponding to low-frequency noise. Table 3 summarizes the results discussed in this section.

3.1 Representations of the qubit Hamiltonian

3.1.1 Laboratory frame

In general, noise physically couples to a qubit in the laboratory frame. The Hamiltonian of the a two-level system in the laboratory frame (Fig. 8A) is

$$\begin{aligned}\hat{\mathcal{H}} &= \frac{\hbar}{2}\left\{\left[\Delta+\delta\Delta(t)\right]\hat{\sigma}_z + \left[\varepsilon+\delta\varepsilon(t)\right]\hat{\sigma}_x + A_{\rm rf}\cos(\omega_{\rm rf}t+\varphi)\hat{\sigma}_x\right\} \\ &= \frac{\hbar}{2}\left[\Delta\hat{\sigma}_z + \varepsilon\hat{\sigma}_x + A_{\rm rf}\cos(\omega_{\rm rf}t+\varphi)\hat{\sigma}_x\right] + \left[\delta\Delta(t)\hat{\sigma}_z + \delta\varepsilon(t)\hat{\sigma}_x\right] \\ &\equiv \hat{\mathcal{H}}_0 + \hat{\mathcal{H}}_F\end{aligned} \tag{77}$$

where $\hat{\sigma}_z$ and $\hat{\sigma}_x$ are Pauli operators. ε and Δ are parameters that depend on the particular physical qubit modality, for example, the energies corresponding to the circulating currents and tunnel coupling of a flux qubit. The oscillating term represents the harmonic drive with amplitude $A_{\rm rf}$, carrier frequency $\nu_{\rm rf} = \omega_{\rm rf}/2\pi$ and phase φ. Note that $A_{\rm rf}$ is generally shaped and of finite duration (*e.g.*, a Gaussian pulse) in order to implement a particular gate operation (*e.g.*, a $\pi/2$ pulse around X) or set to zero (free evolution). We consider $\delta\varepsilon(t)$ and $\delta\Delta(t)$ to be temporal fluctuations of the parameters ε and Δ. To avoid clutter, we will not continue to write explicitly the time dependence. To make the presentation clearer, we do not explicitly carry through fluctuations $\delta A_{\rm rf}$ of the driving field $A_{\rm rf}$, although they can be treated in a similar manner to $\delta\varepsilon$ and $\delta\Delta$. These fluctuations are considered to be the main physical sources of decoherence in many experiments. Although they have a clear physical manifestation in the lab frame, the decoherence they cause occurs in the frame spanned by the qubit eigenbasis. To facilitate presentation in what follows, we have gathered the terms in Eq. 77 into a static Hamiltonian $\hat{\mathcal{H}}_0$ and a fluctuating Hamiltonian $\hat{\mathcal{H}}_F$.

3.1.2 Qubit frame (qubit eigenbasis)

By making the transformation,

$$\begin{aligned}\hat{\sigma}_{x'} &= \cos\theta\,\hat{\sigma}_x - \sin\theta\,\hat{\sigma}_z\ , \\ \hat{\sigma}_{y'} &= \hat{\sigma}_y\ , \\ \hat{\sigma}_{z'} &= \cos\theta\,\hat{\sigma}_z + \sin\theta\,\hat{\sigma}_x\ ,\end{aligned} \tag{78}$$

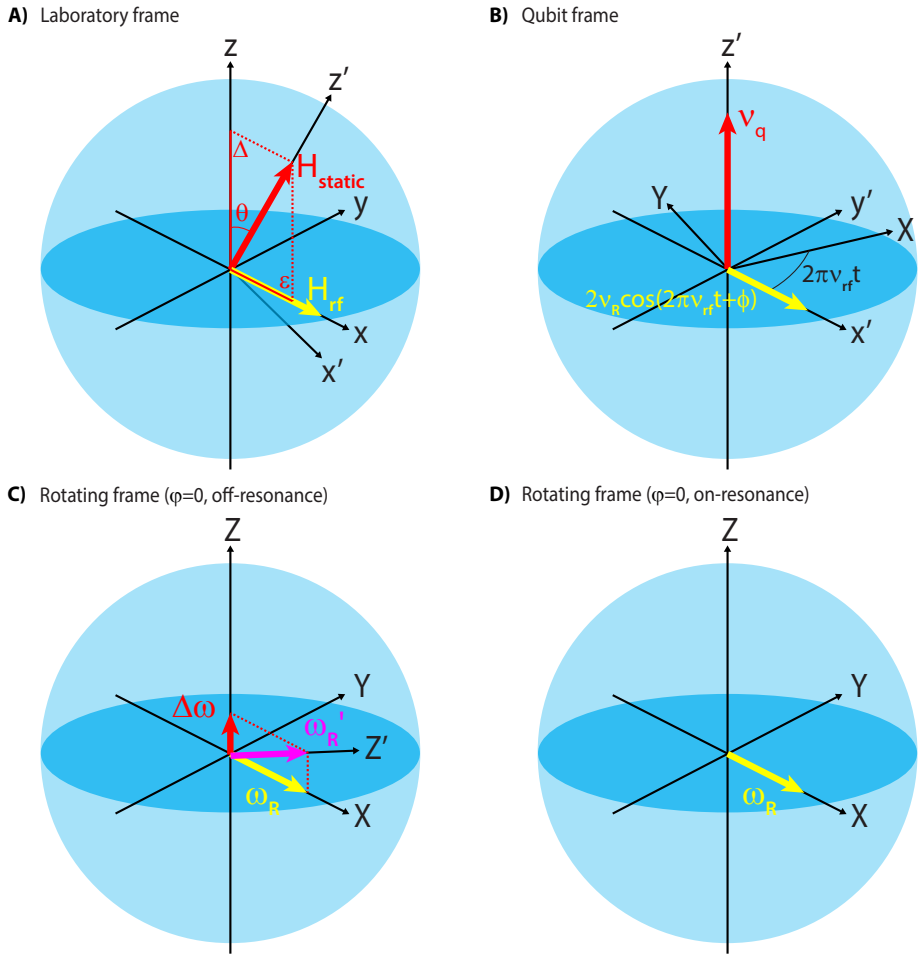

Fig. 8: The two-level system Hamiltonian represented in the Bloch picture for different reference frames. **A)** *Laboratory frame.* $\hat{\mathcal{H}}_{\rm static} = \Delta\hat{\sigma}_z + \varepsilon\hat{\sigma}_x$, $\hat{\mathcal{H}}_{\rm rf} = A_{\rm rf}\cos(\omega_{\rm rf}t + \varphi)\hat{\sigma}_x$. *$\theta$ indicates the rotation required transform into the qubit frame.* **B)** *Qubit frame. The qubit's eigenbasis. The red arrow ($\omega_{\rm q}$) is the free-evolution quantizing field. $\omega_{\rm rf}t$ indicates the time-dependent transformation required to transform into the rotating frame.* **C)** *Rotating frame ($\varphi = 0$). The pink arrow ($\omega'_{\rm R}$) indicates the effective driven-evolution quantizing (Rabi) field in the rotating frame in the presence of a finite drive-frequency detuning $\Delta\omega$.* **D)** *Rotating frame (same as (c) but with $\Delta\omega = 0$). The yellow arrow ($\omega_{\rm R}$) indicates the resonantly driven quantizing field, which corresponds to a pseudospin.*

where $\theta = \arctan(\varepsilon/\Delta)$ is the rotation angle of the quantization axis from the lab frame, we can write the Hamiltonian in Eq. 77 in the qubit (eigenbasis) frame (Fig. 8b):

$$\begin{aligned}\hat{\mathcal{H}}' &= \hat{\mathcal{H}}'_0 + \hat{\mathcal{H}}'_F \\ \hat{\mathcal{H}}'_0 &= \frac{\hbar}{2}\big[\omega_{\rm q}\hat{\sigma}_{z'} + A_{\rm rf}\cos\theta\cos(\omega_{\rm rf}t+\varphi)\hat{\sigma}_{x'} + A_{\rm rf}\sin\theta\cos(\omega_{\rm rf}t+\varphi)\hat{\sigma}_{z'}\big] \\ \hat{\mathcal{H}}'_F &= \frac{\hbar}{2}\left[(\delta\varepsilon\sin\theta + \delta\Delta\cos\theta)\,\hat{\sigma}_{z'} + (\delta\varepsilon\cos\theta - \delta\Delta\sin\theta)\,\hat{\sigma}_{x'}\right]\end{aligned} \tag{79}$$

where $\omega_{\rm q} = \sqrt{\varepsilon^2+\Delta^2}$ is the qubit's level-splitting. The coherence times T_1 and T_2 associated with free-evolution can be visualized in this reference frame (Fig. 9A and B).

3.1.3 Rotating frame

Driven-evolution dynamics are conveniently described in a reference frame which rotates around z' at the drive frequency $\nu_{\rm rf}$. This frame is accessed through a second transformation,

$$\begin{aligned}\hat{\sigma}_X &= \cos(\omega_{\rm rf}t)\hat{\sigma}_{x'} + \sin(\omega_{\rm rf}t)\hat{\sigma}_{y'}\ , \\ \hat{\sigma}_Y &= \cos(\omega_{\rm rf}t)\hat{\sigma}_{y'} - \sin(\omega_{\rm rf}t)\hat{\sigma}_{x'}\ , \\ \hat{\sigma}_Z &= \hat{\sigma}_{z'}\ ,\end{aligned} \tag{80}$$

which applied to the Hamiltonian in Eq. 79 yields (keeping only static terms for the moment):

$$\begin{aligned}\tilde{\hat{\mathcal{H}}}_0 = \frac{\hbar}{2}\big[&\Delta\omega\hat{\sigma}_Z + \frac{1}{2}A_{\rm rf}\cos\theta\big(\cos\varphi\,\hat{\sigma}_X + \sin\varphi\,\hat{\sigma}_Y\big) \\ &+ \frac{1}{2}A_{\rm rf}\cos\theta\big(\cos(-2\omega_{\rm rf}t-\varphi)\hat{\sigma}_X + \sin(-2\omega_{\rm rf}t-\varphi)\hat{\sigma}_Y\big) \\ &+ A_{\rm rf}\sin\theta\cos(\omega t+\varphi)\hat{\sigma}_Z\big]\ ,\end{aligned} \tag{81}$$

where $\Delta\omega = \omega_{\rm q} - \omega_{\rm rf}$ is the frequency detuning between the qubit and the driving field (Fig. 8C). In the weak driving limit ($\omega_{\rm R} \ll \omega_{\rm rf}$), the last two lines in Eq. 81 can be omitted, since these rapid oscillations average to zero on any appreciable time scale of the (weakly driven) qubit dynamics in this rotating frame; this is called the rotating wave approximation. The static Hamiltonian within the rotating wave approximation is:

$$\tilde{\hat{\mathcal{H}}}_0 = (\hbar/2)\big[\Delta\omega\hat{\sigma}_Z + \omega_{\rm R}(\cos\varphi\,\hat{\sigma}_X + \sin\varphi\,\hat{\sigma}_Y)\big]\ , \tag{82}$$

where $\omega_{\rm R} = \frac{1}{2}A_{\rm rf}\cos\theta$ is the Rabi frequency under resonant driving ($\omega_{\rm rf} = \omega_{\rm q} \rightarrow \Delta\omega = 0$) (Fig. 8D). More generally, in the presence of non-zero frequency detuning $\Delta\omega$ (Fig. 8C), Eq. 82 describes an effective driving field, whose effective Rabi frequency

$$\begin{aligned}\omega'_{\rm R} &= \omega_{\rm R}\sqrt{1+(\Delta\omega/\omega_{\rm R})^2} \\ &\approx \omega_{\rm R} + \Delta\omega^2/2\omega_{\rm R}\end{aligned} \tag{83}$$

is linearly sensitive to variations in $\omega_{\rm R}$ and quadratically sensitive in $\Delta\omega$.

Within the RWA, the full Hamiltonian (static and fluctuating terms) is

$$\tilde{\hat{\mathcal{H}}} = \tilde{\hat{\mathcal{H}}}_0 + \tilde{\hat{\mathcal{H}}}_F \tag{84}$$

$$\begin{aligned}\tilde{\hat{\mathcal{H}}}_0 &= (\hbar/2)\big[\Delta\omega\hat{\sigma}_Z + \omega_{\rm R}(\cos\varphi\,\hat{\sigma}_X + \sin\varphi\,\hat{\sigma}_Y)\big]\,,\\ \tilde{\hat{\mathcal{H}}}_F &= (\hbar/2)\big[\,(\delta\Delta\cos\theta + \delta\varepsilon\sin\theta)\,\hat{\sigma}_Z\ldots\\ &\qquad + (-\delta\Delta\sin\theta + \delta\varepsilon\cos\theta)\cos(\omega_{\rm rf}t)\hat{\sigma}_X\ldots\\ &\qquad - (-\delta\Delta\sin\theta + \delta\varepsilon\cos\theta)\sin(\omega_{\rm rf}t)\hat{\sigma}_Y\big]\,,\end{aligned} \tag{85}$$

where we have kept certain terms which contain sinusoids at frequency $\omega_{\rm rf}$, because these sinusoids will mix down any existing high-frequency components (*e.g.*, noise at frequencies $\omega\pm\omega_{\rm rf}$) of the fluctuation terms $\delta\varepsilon$ and $\delta\Delta$ to a lower frequency ω that *is* relevant for the time scales of the qubit dynamics and, therefore, cannot be omitted within the RWA. The coherence times $T_{1\rho}$ and $T_{2\rho}$ associated with driven-evolution can be visualized in this reference frame (Fig. 9C and D).

3.2 General perturbation expansion of Hamiltonian

Following Ithier *et al.* [7, 181] and using their notation, we consider a general expansion of the unperturbed Hamiltonian $\hat{\mathcal{H}}_0'$ so that we can make connections to the fluctuation terms in the laboratory, qubit, and rotating frame Hamiltonians.

The Hamiltonian in the absence of fluctuation (unperturbed Hamiltonian) is

$$\hat{\mathcal{H}} = -\frac{1}{2}\vec{H}_0(\lambda_0)\cdot\vec{\hat{\sigma}} \tag{86}$$

which is a function of parameter(s) λ_0, corresponding to the static values of flux, charge, critical current, *etc.* used to bias the qubits. Expanding to second order in the perturbation(s) $\delta\lambda$, that is, fluctuations in flux, charge, critical current, *etc.*, yields:

$$\hat{\mathcal{H}} = -\frac{1}{2}\left[\vec{H}_0(\lambda_0) + \frac{\partial\vec{H}_0}{\partial\lambda}\delta\lambda + \frac{\partial^2\vec{H}_0}{\partial\lambda^2}\frac{\delta\lambda^2}{2} + \cdots\right]\vec{\hat{\sigma}}. \tag{87}$$

Following Refs. [181, 7], we introduce the notation

$$\vec{D}_\lambda \equiv \frac{1}{\hbar}\frac{\partial\vec{H}_0}{\partial\lambda} \tag{88}$$

$$\vec{D}_{\lambda 2} \equiv \frac{1}{\hbar}\frac{\partial^2\vec{H}_0}{\partial\lambda^2} \tag{89}$$

In the eigenbasis of the qubit (section 3.1.2, Fig. 8B),

$$\hat{\mathcal{H}} = -\frac{1}{2}\hbar\left[\omega_{\rm q}\hat{\sigma}_{z'} + \delta\omega_{z'}\hat{\sigma}_{z'} + \delta\omega_\perp\hat{\sigma}_\perp\right] \tag{90}$$

$$= -\frac{1}{2}\hbar\left[\omega_{\rm q}\hat{\sigma}_{z'} + (D_{\lambda,z'}\delta\lambda + D_{\lambda 2,z'}\frac{\delta\lambda^2}{2} + \ldots)\hat{\sigma}_{z'} + (D_{\lambda,\perp}\delta\lambda + \ldots)\hat{\sigma}_\perp\right] \tag{91}$$

where $\hbar\omega_{\rm q} \equiv |\vec{H}_0(\lambda_0)| = h\nu_{\rm q}$ is the static unperturbed qubit level splitting. The longitudinal coefficients are

$$D_{\lambda,z} = \frac{\partial\omega_{\rm q}}{\partial\lambda} \tag{92}$$

$$D_{\lambda 2,z} = \frac{\partial^2\omega_{\rm q}}{\partial\lambda^2} - \frac{D_{\lambda,\perp}^2}{\omega_{\rm q}} \tag{93}$$

and the transverse coefficient is

$$D_{\lambda,\perp} = \frac{\partial\omega_{\perp}}{\partial\lambda} \tag{94}$$

Pure dephasing is related to the derivatives of $\omega_{\rm q}(\lambda)$, while the transverse decay (relaxation or depolarization) is related to $\omega_{\perp}(\lambda)$. The derivatives $\vec{D}_{\lambda}$ capture the Hamiltonian's sensitivity to a fluctuation $\delta\lambda$ and correspondingly to higher orders.

To calculate or simulate the effect of fluctuations in the qubit basis, Eq. 91, the first-order contribution of the fluctuations should be written using the chain rule:

$$\frac{\partial\omega_{\rm q}}{\partial\lambda} = \frac{\partial\omega_{\rm q}}{\partial\varepsilon}\frac{\partial\varepsilon}{\partial\lambda} + \frac{\partial\omega_{\rm q}}{\partial\Delta}\frac{\partial\Delta}{\partial\lambda}. \tag{95}$$

For second-order contributions, the chain rule becomes:

$$\frac{\partial^2\omega_{\rm q}}{\partial\lambda^2} = \left[\frac{\partial^2\omega_{\rm q}}{\partial\varepsilon^2}\left(\frac{\partial\varepsilon}{\partial\lambda}\right)^2 + \frac{\partial\omega_{\rm q}}{\partial\varepsilon}\frac{\partial^2\varepsilon}{\partial\lambda^2}\right] + \left[\frac{\partial^2\omega_{\rm q}}{\partial\Delta^2}\left(\frac{\partial\Delta}{\partial\lambda}\right)^2 + \frac{\partial\omega_{\rm q}}{\partial\Delta}\frac{\partial^2\Delta}{\partial\lambda^2}\right]. \tag{96}$$

The derivative of $\omega_{\rm q}$ with respect to ε and Δ from the definition $\omega_{\rm q} = \sqrt{\varepsilon^2+\Delta^2}$ accounts for the change in basis between the qubit and lab frames (i.e., the angle θ). These are written:

$$\frac{d\omega_{\rm q}}{d\varepsilon} = \frac{\varepsilon}{\left(\varepsilon^2+\Delta^2\right)^{1/2}} \tag{97}$$

$$\frac{d^2\omega_{\rm q}}{d\varepsilon^2} = \frac{\Delta^2}{\left(\varepsilon^2+\Delta^2\right)^{3/2}} \tag{98}$$

$$\frac{d\omega_{\rm q}}{d\Delta} = \frac{\Delta}{\left(\varepsilon^2+\Delta^2\right)^{1/2}} \tag{99}$$

$$\frac{d^2\omega_{\rm q}}{d\Delta^2} = \frac{\varepsilon^2}{\left(\varepsilon^2+\Delta^2\right)^{3/2}}. \tag{100}$$

We can make a connection between the first-order derivatives here and the longitudinal noise terms ($\sigma_{z'}$ terms) in Eq. 79. From a geometrical argument, since $\theta = \arctan(\varepsilon/\Delta)$,

$$\left(\frac{d\omega_{\rm q}}{d\varepsilon}\right)\delta\varepsilon = \frac{\varepsilon}{\left(\varepsilon^2+\Delta^2\right)^{1/2}}\,\delta\varepsilon = \sin\theta\;\delta\varepsilon \tag{101}$$

$$\left(\frac{d\omega_{\rm q}}{d\Delta}\right)\delta\Delta = \frac{\Delta}{\left(\varepsilon^2+\Delta^2\right)^{1/2}}\,\delta\Delta = \cos\theta\;\delta\Delta. \tag{102}$$

To make a connection to the physical noise source λ (flux, charge, critical current, *etc.*), we insert the noise sensitivities $\xi_{\varepsilon,\lambda} = d\varepsilon/d\lambda$ and $\xi_{\Delta,\lambda} = d\Delta/d\lambda$,

$$\left(\frac{d\omega_{\rm q}}{d\lambda}\right)\delta\lambda = \frac{d\omega_{\rm q}}{d\varepsilon}\frac{d\varepsilon}{d\lambda}\delta\lambda \rightarrow \sin\theta\ \xi_{\varepsilon,\lambda}\ d\lambda \tag{103}$$

$$\left(\frac{d\omega_{\rm q}}{d\lambda}\right)\delta\lambda = \frac{d\omega_{\rm q}}{d\Delta}\frac{d\Delta}{d\lambda}\delta\lambda \rightarrow \sin\theta\ \xi_{\Delta,\lambda}\ d\lambda. \tag{104}$$

For example, the flux (Φ) sensitivities in a typical persistent current qubit with tunable ε and static Δ are $\xi_{\varepsilon,\Phi} = 1$ GHz/mΦ_0 and $\xi_{\Delta,\Phi} = 0$. In general, these sensitivities are inferred either from experiment or from simulations.

3.3 Longitudinal and transverse relaxation

The dynamics of the qubit state within a two-level model can be visualized on the Bloch sphere (see Fig. 9A, B). We consider first the qubit reference frame in the absence of driving, $A_{\rm rf} = 0$. In this case, the Hamiltonian (Eq. 79) contains only the "qubit field" $\nu_{\rm q}$ (red arrow in Fig. 9) which defines the qubit quantization axis along z'.

3.3.1 Bloch-Redfield approach

Within the standard Bloch-Redfield [176, 177, 178] picture of two-level system dynamics, noise sources are weakly coupled to the qubits have short correlation times with respect to the system dynamics. In this case, the relaxation processes are characterized by two rates:

Bloch-Redfield longitudinal relaxation rate	$\Gamma_1 \equiv \dfrac{1}{T_1}$
Bloch-Redfield transverse relaxation rate	$\Gamma_2 \equiv \dfrac{1}{T_2} = \dfrac{\Gamma_1}{2} + \Gamma_\varphi$

which contains the pure dephasing rate Γ_φ. Note that the definition of Γ_2 as a sum of rates is only valid if the noise spectra are Lorentzian (centered at $\omega = 0$), that is, the decay functions are exponential. For an initial state ($t = 0$)

$$\alpha|0\rangle + \beta|1\rangle, \tag{105}$$

the density matrix for the qubit is written [181, 7],

$$\rho_{\rm BR} = \begin{pmatrix} 1 + (|\alpha|^2 - 1)e^{-\Gamma_1 t} & \alpha\beta^* e^{i\Delta\omega t} e^{-\Gamma_2 t} \\ \alpha^*\beta e^{-i\Delta\omega t} e^{-\Gamma_2 t} & |\beta|^2 e^{-\Gamma_1 t}. \end{pmatrix} \tag{106}$$

The longitudinal relaxation rate Γ_1 describes depolarization along the qubit quantization axis. It is caused by *transverse* noise, since off-diagonal elements of an interaction Hamiltonian will connect states $|0\rangle$ and $|1\rangle$. Depolarization in principle occurs due to both up (excitation from $|0\rangle$ to $|1\rangle$) and down (relaxation from $|1\rangle$ to $|0\rangle$) rates:

$$\Gamma_1 \equiv \frac{1}{T_1} = \Gamma_{1\downarrow} + \Gamma_{1\uparrow}. \tag{107}$$

In superconducting qubits, it is generally the case that $k_{\rm B}\Theta \ll h\nu_{\rm q}$ (although not always, e.g., see section 4.4), and the up rate is exponentially suppressed by the Boltzmann factor

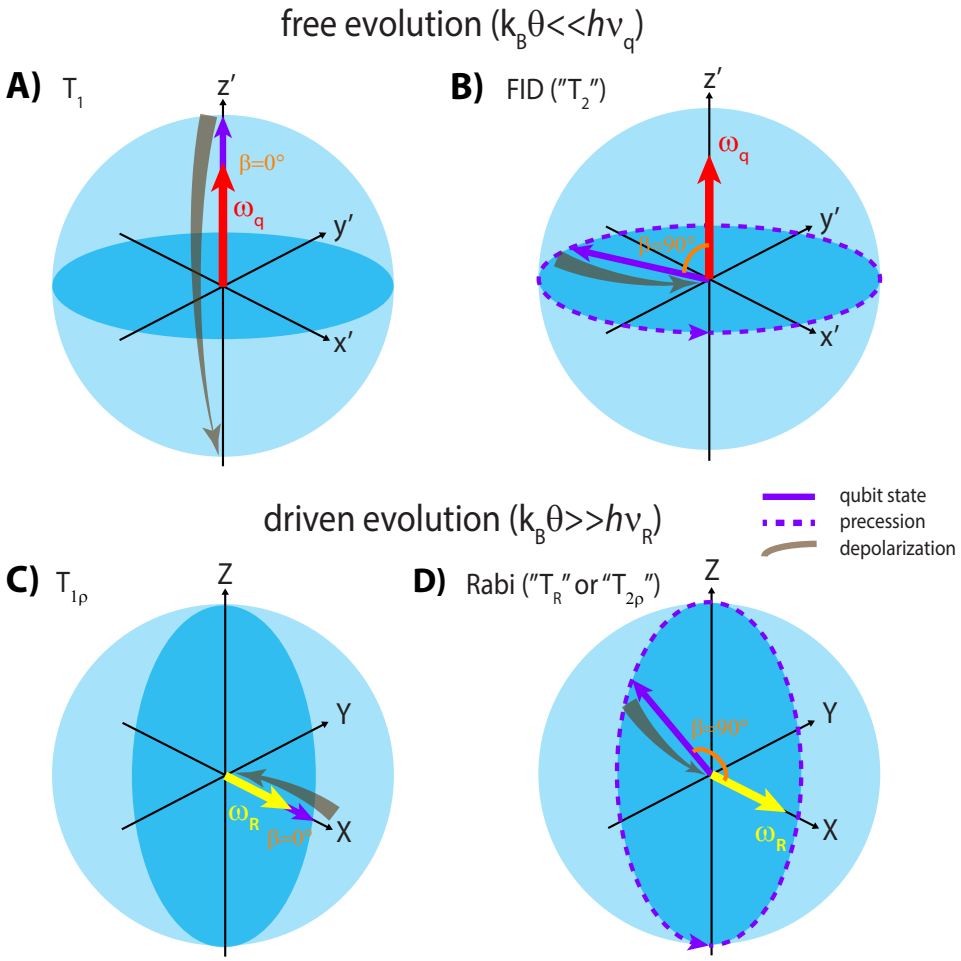

Fig. 9: Schematic diagram of system dynamics in analogous experiments between free evolution and driven evolution. **A)** *and* **B)** *illustrate depolarization during free-evolution in the qubit frame.* **A)** *longitudinal depolarization* T_1. **B)** *transverse free-induction decay (FID). The relaxation FID time is written "*T_2*", because the decay function need not be exponential, and the illustration ignores the effects due to longitudinal relaxation.* **C)** *and* **D)** *illustrate depolarization during driven-evolution in the rotating frame.* **C)** *longitudinal depolarization* $T_{1\rho}$ *in the qubit frame.* **D)** *transverse Rabi oscillations. The characteristic decay time is written "*$T_{\rm R}$*", because the decay function need not be exponential, and the illustration ignores the effects due to longitudinal relaxation. The illustrated longitudinal depolarization in* **A)** *and* **C)** *is based on the condition (typical for superconducting qubits),* $\hbar\omega_{\rm R} \ll k_{\rm B}T \ll \hbar\omega_{\rm q}$*, so that, in the steady state,* $\langle\hat{\sigma}_{z'}\rangle \approx -1$ *for the* T_1 *process, and* $\langle\hat{\sigma}_X\rangle \approx 0$ *for the* $T_{1\rho}$ *process. For the illustrated transverse depolarization in* **B)** *and* **D)***, dephasing (or dephasing-type) processes act to depolarize the Bloch vector to the origin.*

$\exp(-h\nu_{\rm q}/k_{\rm B}\Theta)$. Only noise at the qubit frequency mediates qubit transitions, whether absorption or emission, and this noise is generally "well behaved" (short correlation time, weakly coupled to qubit, no divergences) around the qubit frequency in superconducting qubits . Longitudinal depolarization measurements exhibit an exponential decay function, consistent with the Bloch-Redfield picture.

Longitudinal noise fluctuates the qubit field vector in Fig. 9B. This, in turn, varies the precession rate of the Bloch vector on the equator and causes dephasing Γ_φ. Since dephasing is not a resonant process, it is sensitive to broadband fluctuations. In superconducting qubits this noise (e.g., flux noise, charge noise, critical-current noise, ...) tends to exhibit a $1/f$-like behavior. This noise is singular near $\nu = 0$, has long correlation times, and generally does not fall within the Bloch-Redfield description. The decay function of the off-diagonal terms in Eq. 106 are generally non-exponential.

3.3.2 Modification due to $1/f$-type noise

If we assume that the qubit is coupled to many independent fluctuators, then, independent of their individual statistics, they will in concert generate noise with a Gaussian distribution due to the central limit theorem. We therefore say that the longitudinal fluctuations exhibit Gaussian-distributed $1/f$ noise. For $1/f$ noise spectra, the phase decay function is itself a Gaussian $\exp\left[-(\Gamma_\varphi t)^2\right]$, and it factors from the T_1 exponential decay because the noise remains regular at the qubit frequency. The density matrix in Eq. 106 becomes, following Refs. [181, 11],

$$\rho = \begin{pmatrix} 1+(|\alpha|^2-1)e^{-\Gamma_1 t} & \alpha\beta^* e^{i\Delta\omega t} e^{-\frac{\Gamma_1}{2}t} e^{-\chi_N(t)} \\ \alpha^*\beta e^{-i\Delta\omega t} e^{-\frac{\Gamma_1}{2}t} e^{-\chi_N(t)} & |\beta|^2 e^{-\Gamma_1 t} \end{pmatrix}. \tag{108}$$

where the decay function $\langle\exp(-\chi_N(t))\rangle$ contains the so-called coherence function χ_N and is used to describe dephasing. The subscript N labels the decay function, and it will refer to the number of π-pulses used to refocus the low-frequency noise, which impacts the form of the decay function.

3.4 Power spectral density (PSD)

The frequency distribution of the noise power for a stationary noise source λ is characterized by its PSD $S_\lambda(\omega)$

$$S_\lambda(\omega) = \int_{-\infty}^{\infty} d\tau\ \langle\lambda(\tau)\lambda(0)\rangle e^{-i\omega\tau}. \tag{109}$$

The PSD is the Fourier transform of the autocorrelation function $c_\lambda(\tau) = \langle\lambda(\tau)\lambda(0)\rangle$ of the noise source λ. Since the integration limits are $(-\infty, \infty)$, this is the bilateral PSD. Symmetrizing the PSD allows one to consider only positive frequencies, which is termed a unilateral PSD. Both unilateral and bilateral PSDs are used, often with the same notation, and so one needs to know how the PSD is defined, keep track of the factors of 2 and π, and also be aware of the implications for quantum systems.

For quantum systems, the autocorrelation function is in general complex due to non-commuting variables in the system (qubit-bath) Hamiltonian. This means that the PSD is not a symmetric function in frequency. Noise at a positive frequency $S(\nu_{\rm q})$ corresponds to energy transfer from the qubit to the environment, including both stimulated and spontaneous emission,

associated with the down-rate $\Gamma_{1\downarrow}$. Noise at a negative frequency $S(-\nu_{\rm q})$ corresponds to energy transfer to the qubit from the environment, associated with the up-rate $\Gamma_{1\uparrow}$. For a detailed discussion, see Refs. [184, 185].

In turn, the inverse Fourier transform of the PSD will yield the autocorrelation function. This implies that integrating the noise power spectral density with $\tau = 0$ yields the variance σ_λ^2 of the noise.

$$c_\lambda(\tau) = \frac{1}{2\pi}\int_{-\infty}^{\infty} d\omega S_\lambda(\omega) e^{i\omega\tau} \tag{110}$$

$$\sigma_\lambda^2 \equiv c_\lambda(0) = \frac{1}{2\pi}\int_{-\infty}^{\infty} d\omega S_\lambda(\omega) \tag{111}$$

Making a connection between $S_\lambda(\omega)$ and the measured qubit decay functions is the basis for noise spectroscopy.

3.5 Connecting T_1 to $S_\lambda(\omega)$

The connection between $S_\lambda(\omega)$ and the measured decay time T_1 can be made using Fermi's Golden Rule, within the assumption that the qubit is weakly coupled to its environment. Considering the transition rate from excited to ground state, $\Gamma_{1\downarrow,\lambda}$ due to a particular noise source λ, yields: (see Ref. [181, 182, 70, 185] for details):

$$\Gamma_{1\downarrow,\lambda} = \frac{2\pi}{\hbar}|m_\lambda|^2 \rho(\hbar\omega_{\rm q}) \tag{112}$$

$$= \frac{1}{\hbar^2}|d_\lambda|^2 \; S_\lambda(\omega_{\rm q}) \tag{113}$$

$$= \quad D_{\lambda,\perp}^2 \; S_\lambda(\omega_{\rm q}) \tag{114}$$

where $m_\lambda \equiv \langle 1|\hat{m_\lambda}|0\rangle = \langle 1|\hat{\mathcal{H}}_{\rm int}^{(\lambda)}|0\rangle$, and $\hat{m}_\lambda \equiv \hat{\mathcal{H}}_{\rm int}^{(\lambda)} = (d\hat{\mathcal{H}}_0/d\lambda)\delta\lambda$ is the first-order interaction Hamiltonian between the qubit and the environment due to a fluctuator λ and characterized by a density of states $\rho(\hbar\omega_{\rm q})$ at the qubit frequency. The second line writes the expression in terms of the qubit's (energy) susceptibility d_λ to external fluctuations,

$$d_\lambda \equiv \langle 1|\hat{d_\lambda}|0\rangle = \langle 1|\frac{d\hat{\mathcal{H}}_0}{d\lambda}|0\rangle = \hbar D_{\lambda,\perp}, \tag{115}$$

which is the energy-units version of $D_{\lambda,\perp}$ in Eq. 94, and it can be interpreted as the transition dipole for the fluctuator λ [70]. Adopting a PSD is useful, since noise is typically an aggregate effect over many fluctuators, each of which may have a different matrix element m_λ. The noise PSD is correspondingly defined

$$S_\lambda(\omega_{\rm q}) = 2\pi\hbar(\delta\lambda)^2\rho(\hbar\omega_{\rm q}) \tag{116}$$

and has units of λ^2/s^{-1}. The interaction Hamiltonian and the susceptibility (transition dipole) operators are simply related,

$$\hat{d}_\lambda = \frac{\hat{m}_\lambda}{\delta\lambda}. \tag{117}$$

Examples from the Hamiltonians written in section 2.3 are presented in Table 2.

With this definition, we can write a general result for the decay rate Γ_1,

$$\Gamma_{1\downarrow} = \sum_\lambda \Gamma_{1\downarrow,\lambda} = \sum_\lambda D^2_{\lambda,\perp}\, S_\lambda(\omega_{\rm q}) \tag{118}$$

$$\Gamma_{1\uparrow} = \sum_\lambda \Gamma_{1\uparrow,\lambda} = \sum_\lambda D^2_{\lambda,\perp}\, S_\lambda(-\omega_{\rm q}) \tag{119}$$

$$\Gamma_1 \equiv \frac{1}{T_1} = \Gamma_{1\downarrow} + \Gamma_{1\uparrow} \approx \Gamma_{1\downarrow} \tag{120}$$

where the approximation holds for $k_{\rm B}\Theta \ll \hbar\omega_{\rm q}$ when the qubit is in thermal equilibrium with its environment. This follows from the detailed balance of the transition rates $\Gamma_{1\uparrow} = \exp(-\hbar\omega/k_{\rm B}\Theta)\Gamma_{1\downarrow}$ required to obtain the correct state populations in thermal equilibrium.

3.6 Connecting T_φ to $S_\lambda(\omega)$

We consider a superposition state undergoing free evolution. For example, we could create an equal superposition state of the qubit (on the equator of the Bloch sphere) by driving the qubit from its ground state by a $\pi/2$ pulse (Fig. 9B, qubit frame). As the superposition state undergoes free evolution, noise in the qubit field will translate to noise in the precession rate, which acts to dephase the qubit.

The superposition state's accumulated phase (relative between the two states),

$$\varphi(t) = \int_0^t \omega_q dt' = \langle\omega_{\rm q}\rangle t + \delta\varphi(t) \tag{121}$$

diffuses due to adiabatic fluctuations of the transition frequency,

$$\delta\varphi(t) = (\partial\omega_{\rm q}/\partial\lambda)\int_0^t {\rm d}t'\delta\lambda(t') = D_{\lambda,z}\int_0^t {\rm d}t'\delta\lambda(t'), \tag{122}$$

where $\partial\omega_{\rm q}/\partial\lambda = D_{\lambda,z}$ (see Eq. 92) is the qubit's longitudinal sensitivity to λ-noise. For noise generated by a large number of fluctuators that are weakly coupled to the qubit, its statistics are Gaussian. Ensemble averaging over all realizations of the Gaussian-distributed stochastic process $\delta\lambda(t)$, the dephasing is

$$\langle e^{i\,\delta\varphi(t)}\rangle = e^{-\frac{1}{2}\langle\delta\varphi^2(t)\rangle} \equiv e^{-\chi_N(t)}, \tag{123}$$

$\hat{\mathcal{H}}_\lambda$	$\delta\lambda$	$\hat{\mathbf{m}}_\lambda$	$\hat{\mathbf{d}}_\lambda$
$4E_{\rm C}(\hat{n}-\hat{n}_{\rm g})^2$	δn	$8\delta n E_{\rm C}\hat{n}$	$8E_{\rm C}\hat{n}$
$-E_{\rm J}\cos(\hat{\phi}+2\pi f)$	δf	$2\pi\delta f E_{\rm J}\sin(\hat{\phi}+2\pi f)$	$2\pi E_{\rm J}\sin(\hat{\phi}+2\pi f)$
$-E_{\rm J}\cos(\hat{\phi}+2\pi f)$	δi	$-\delta i E_{\rm J}\cos(\hat{\phi}+2\pi f)$	$-E_{\rm J}\cos(\hat{\phi}+2\pi f)$

Table 2: *Examples of interaction Hamiltonians used to calculate interaction matrix elements $\hat{m}_\lambda \equiv \hat{\mathcal{H}}_{\rm int}$ and susceptibilities $\hat{d}_\lambda \equiv \hat{\mathcal{H}}_{\rm int}/\delta\lambda$. Note that $\delta i \equiv \delta I_{\rm c}/I_{\rm c}$ is the reduced critical current fluctuation.*

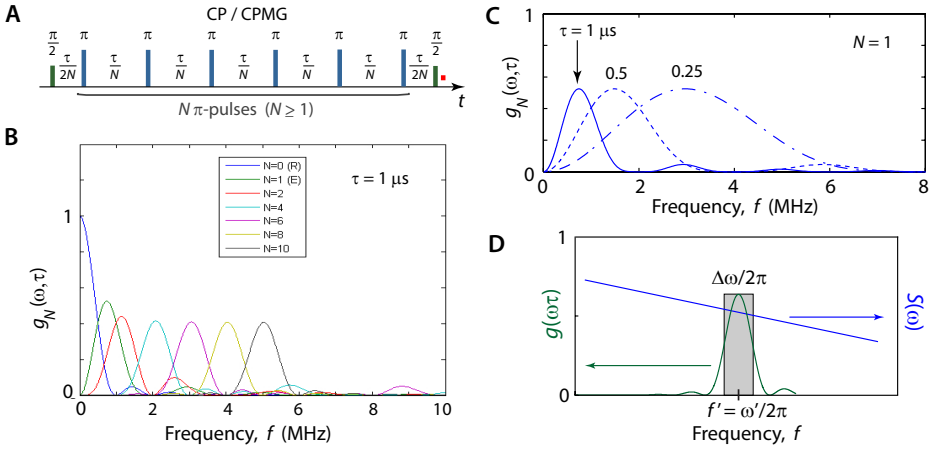

Fig. 10: Filter function $g_N(\omega,\tau)$. A) *Carr-Purcell-Meiboom-Gill sequence with N π-pulses (refocussing pulses). The total time duration between the two $\pi/2$-pulses is τ + $N\tau_\pi$, where τ is the free evolution time, and τ_π the time during during the π pulses.$N = 0$ is a Ramsey experiment, which has only free evolution and no refocusing pulses. $N = 1$ is a Hahn echo (spin echo) experiment.* **B)** *Filter function for $N = 0 \ldots 10$ with $\tau = 1$ μs. For $N = 0$, the Ramsey case, the filter function is peaked at zero frequency, making Ramsey highly susceptible to $1/f$-type noise. As the number N increases, the bandpass filter shifts to higher frequencies and thereby decreases the effective noise power dephasing the qubit. The area under all curves is the same.* **C)** *Filter function for $N = 1$ and $\tau = 0.25,\ 0.5,$ and 1 μs.* **D)** *The filter function shapes the noise PSD $S(\omega)$ and depends on the number of π-pulses N used to refocus the low-frequency noise. In turn, since it connects the PSD to the decay function, and for parameters that give a function narrow in frequency, it can be used to back out the PSD.*

with the coherence integral

$$\chi_N(\tau) = \frac{\tau^2}{2} \sum_\lambda \left(\frac{\partial \omega_\mathrm{q}}{\partial \lambda} \right)^2 \int_{-\infty}^{\infty} \mathrm{d}\omega \, S_\lambda(\omega) \, g_N(\omega,\tau), \tag{124}$$

where τ is the free evolution time, N will denote the number of π pulses (if any, $N = 0$ allowed) in pulse sequences applied to the qubit to reduce the noise (e.g., $N = 1$ is the Hahn echo, $N > 1$ are CPMG, *etc.*) [189, 190, 11], and g_N is a dimensionless weighting function defined in equation (125).

The function $g_N(\omega,\tau)$ can be viewed as a frequency-domain filter of the noise $S_\lambda(\omega)$. In general, its filter properties depend on the number N and distribution of π-pulses [191, 189, 192, 190, 193, 11],

$$g_N(\omega,\tau) = \frac{1}{(\omega\tau)^2} \left| 1 + (-1)^{1+N} \exp(i\omega\tau) + 2 \sum_{j=1}^{N} (-1)^j \exp(i\omega\delta_j\tau) \cos(\omega\tau_\pi/2) \right|^2, \tag{125}$$

where $\delta_j \in [0,1]$ is the normalized position of the centre of the jth π-pulse between the two $\pi/2$-pulses, τ is the total free-induction time, and τ_π is the length of each π-pulse [190, 193], yielding a total sequence length $\tau + N\tau_\pi$. As the number of pulses increases for fixed τ, the filter function's peak shifts to higher frequencies (Fig. 10B), leading to a reduction in the net integrated noise (Eq. 124) for $1/f^\alpha$-type noise spectra with $\alpha > 0$. Similarly, for a fixed N, the

filter function will shift in frequency with τ (Fig. 10C). Additionally, for a fixed time separation $\tau' = \tau/N$ (valid for $N \geq 1$), the filter sharpens and asymptotically peaks at $\omega'/2\pi = 1/2\tau'$ as more pulses are added (Fig. 10D). Note that we have have purposefully written $g_N(\omega, \tau)$ as a band-pass filter (Fig. 10), which we will effectively utilize to sample the environmental noise $S_\lambda(\omega)$ by varying the number of pulses N and the total sequence time τ. This interpretation can be contrasted with several previous works [189, 194, 192, 190, 193], in which the quantity $(\omega\tau)^2 g_N(\omega, \tau)$ was interpreted as a high-pass filter acting on a phase noise $S_\lambda(\omega)/\omega^2$.

In the $N = 0$ case, a Ramsey experiment, the decay function is

$$e^{-\chi_0(t)} = \langle e^{i\Delta\phi(t)} \rangle = e^{-\frac{1}{2}\langle \Delta\phi(t)^2 \rangle} \tag{126}$$

$$= \exp\left[\frac{t^2}{2} D_{\lambda,z}^2 \int_{-\infty}^{\infty} d\omega \; S_\lambda(\omega) \mathrm{sinc}^2 \frac{\omega t}{2}\right] \tag{127}$$

$$\equiv \exp\left[\frac{t^2}{2} D_{\lambda,z}^2 \int_{-\infty}^{\infty} d\omega \; S_\lambda(\omega) g_0(\omega, t)\right]. \tag{128}$$

which follows from Eqs. 109, 122, and 123. The Ramsey decay function is proportional to a sinc-function (Fig. 10B) which is centered at $\omega = 0$. For noise that decreases with frequency, *e.g.*, $1/f$-type noise in superconducting qubits, the Ramsey experiment windows $S(\omega)$ where it has the highest value. In this sense, it is a worst possible (noisiest) choice of filter function (see Fig. 11A).

In the $N = 1$ case, a Hahn echo (spin echo) experiment, there is a single π-pulse that is applied at time $\tau/2$ which acts to refocus the Bloch vector. The phase fluctuation $\delta\phi_E(t_1, t_2)$ during the two periods t_1 and t_2 of free evolution is

$$\Delta\phi_E(t_1, t_2) \equiv -\Delta\phi_{t1} + \Delta\phi_{t2} = -D_{\lambda,z} \int_0^{t1} dt' \; \delta\lambda(t') + D_{\lambda,z} \int_{t_1}^{t_1+t2} dt' \; \delta\lambda(t') \tag{129}$$

and using $t_1 = t_2 = \tau/2$, the echo decay function is

$$e^{-\chi_1(t)} = \langle e^{i\Delta\phi_E(t_1=t_2)} \rangle = e^{-\frac{1}{2}\langle \Delta\phi_E(t_1=t_2)^2 \rangle} \tag{130}$$

$$= \exp\left[\frac{t^2}{2} D_{\lambda,z}^2 \int_{-\infty}^{\infty} d\omega \; S_\lambda(\omega) \sin^2 \frac{\omega t}{4} \mathrm{sinc}^2 \frac{\omega t}{4}\right] \tag{131}$$

$$\equiv \exp\left[\frac{t^2}{2} D_{\lambda,z}^2 \int_{-\infty}^{\infty} d\omega \; S_\lambda(\omega) g_1(\omega, t)\right]. \tag{132}$$

In Fig. 10B, the $N = 1$ filter function peaks away from $\omega = 0$. For noise that decreases with frequency, as is the case with superconducting qubits, this is advantageous; the integrated noise and, thereby, the decay rate is lower with the echo than with the Ramsey experiment.

The general trend is confirmed as a function of flux detuning $\delta f \equiv f - 1/2$ in Fig. 11A. At the degeneracy point $\delta f = 0$, the qubit is first-order insensitive to flux fluctuations (Fig. 11B)), and so the decoherence rates are lowest at this bias. In fact, the echo rate is T_1-limited, $\Gamma_\mathrm{E} = \Gamma_1/2$. Away from $\delta f = 0$, the qubit becomes more sensitive to flux fluctuations, and so both the Ramsey and echo decoherence rates increase [8, 11]. However, since the echo filter function g_1 peaks at higher frequency than the Ramsey filter function g_0, and because the flux noise is $1/f$ type, the echo decay rate is better than the Ramsey decay rate, $\Gamma_\mathrm{E} < \Gamma_\mathrm{R}$, for any flux bias. The relaxation rate Γ_1 is observed to relatively constant over this range of flux.

This concept extends for N π-pulses in a CPMG experiment (Fig. 11C and Fig. 12). As the number of pulses, N, increases, the filter function g_N continues peak at higher and higher

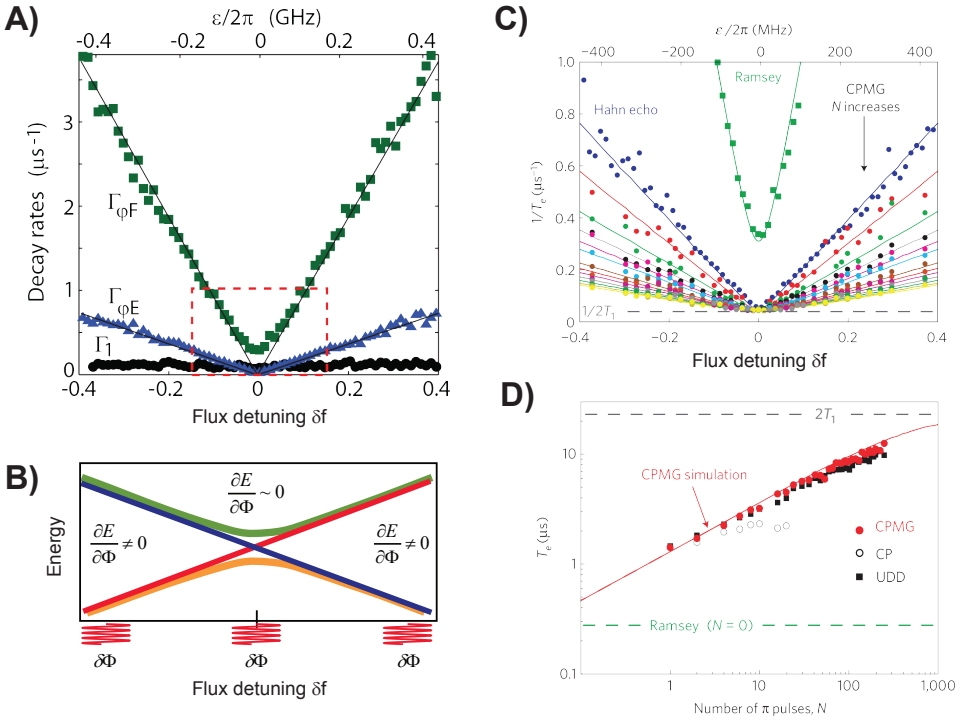

Fig. 11: Dephasing and its relation to Ramsey, spin echo, and CPMG dynamical decoupling *[11].* **A)** *The free-induction Ramsey decay rate* $\Gamma_{\phi \mathrm{F}}$*, spin-echo decay rate* $\Gamma_{\phi \mathrm{E}}$*, and energy relaxation rate* Γ_1 *as a function of flux detuning* $\delta f \equiv f - 1/2$ *for the qubit shown in Fig. 13.* $\Gamma_{\phi \mathrm{F}}$ *is generally larger than* $\Gamma_{\phi \mathrm{E}}$ *due to the filter function. At the degeneracy point* $\delta f = 0$*,* $\Gamma_{\phi \mathrm{F}}$ *and* $\Gamma_{\phi \mathrm{E}}$ *are smallest due to the qubit's first-order protection from flux noise. At this point,* $\Gamma_{\phi \mathrm{E}} = \Gamma_1/2$*,* i.e., $T_{2\mathrm{E}} = 2T_1$*.* **B)** *Energy level diagram illustrating the sensitivity* $\partial E/\partial \Phi$ *due to fluctuation in the flux* $d\Phi$*. At the degeneracy point* $\delta f = 0$*, the energy levels have zero slope, and the qubit is first-order insensitive to flux noise. At* $\delta f \neq 0$*, the energy levels shift with flux, and the qubit is therefore sensitive to flux noise.* **C)** *Decay rates for Ramsey (*$N = 0$*), Hahn (spin) echo (*$N = 1$*), and CPMG with* $N = 1,\ 2,\ 4,\ 6,\ 8,\ 10,\ 16,\ 20,\ 24,\ 30,\ 36,\ 42,\ 48$*. As* N *increases, the filter function* g_N *shifts to higher frequencies, and so the qubit becomes less sensitive to* $1/f$ *flux noise. At degeneracy, a single* π *pulse improves the decay rate to* $\Gamma_2 = \Gamma_1/2$*.* **D)** *Away from degeneracy,* $\delta f = -0.4\ \mathrm{m}\Phi_0$*, the qubit is highly sensitive to flux noise. Increasing* N *up to 200 pulses improves the decay time towards the* $T_2 = 2T_1$ *limit. CPMG (*π*-pulses in quadrature to* $\pi/2$*-pulses) is compared with CP (all pulses in phase) and UDD (sinusoidal pulse spacing) pulse sequences (see Fig. 12 and Ref. [11]).*

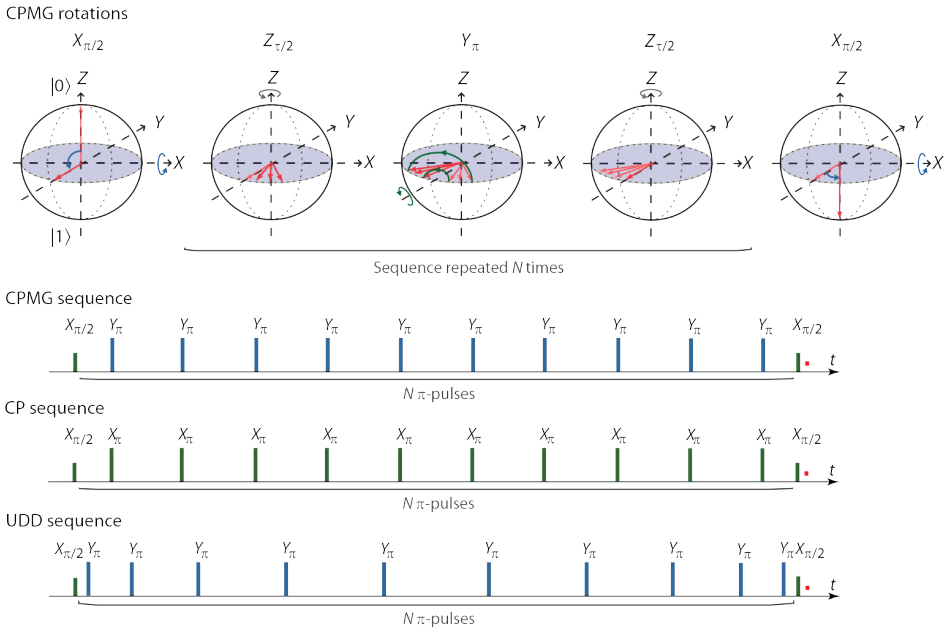

Fig. 12: CP, CPMG, and UDD dynamical decoupling *[11].* **A)** *Bloch sphere representation of refocussing sequences. The Carr-Purcell (CP) sequence has all pulses in phase and equally spaced. The Carr-Purcell-Meiboom-Gill (CPMG) sequence has the π-pulses in quadrature to the $\pi/2$-pulses and equally spaced. The UDD sequence has the π-pulses in quadrature to the $\pi/2$-pulses and the pulses are spaced sinusoidally in time. CPMG is less sensitive to pulse imperfections than CP. For $1/f$ type noise, CPMG and UDD give similar performance.*

frequencies, reducing the integrated noise seen by the qubit, and so the decay rates Γ_N continue to improve.

The filter functions in Eq. 125 and plotted in Fig. 10B all have the same integrated area. Therefore, if the noise PSD is white noise (uniform with frequency), then there will be no difference in the integrated noise for any number N. Similarly, if a system has a PSD that increases with frequency, than adding more pulses will increase the noise seen by the qubit and therefore decrease its coherence times.

3.7 Noise spectroscopy of a persistent-current flux qubit

In this section, we review several experiments which probe coherence metrics of a persistent-current flux qubit during both free evolution (T_1 and T_2) and driven evolution ($T_{1\rho}$ and $T_{2\rho} = T_{\rm R}$), where the subscript ρ refers to "rotating frame," and $T_{\rm R}$ is the Rabi decay time. By analyzing the form of the decay function (see Table 3), we can extract information about the noise spectra seen by the qubit in the laboratory frame. In turn, these pulse sequences can be used to mitigate dephasing. The CPMG pulse sequence mitigates dephasing T_ϕ during free evolution, and the rotary echo can mitigate dephasing $T_{\phi\rho}$ during driven evolution.

The device used in this section is a 4-junction persistent current flux qubit (see Fig. 13A) with the small junction a factor $\alpha = 0.54$ smaller in area than the remaining identically sized junctions. The qubit states are coupled with a strength $\Delta \approx 5.4$ GHz, $E_{\rm J} = 210$ GHz, and $E_{\rm C} = 4$ GHz. The qubit is read out using a DC SQUID, which is galvanically connected to the

qubit to leverage the kinetic inductance of the shared lines, approximately 30 pH, to increase the readout signal. The device was fabricated at NEC using an aluminum double-angle shadow evaporation process, and measurements were made at MIT. For more details regarding the qubit parameters and the measurement setup, see Ref. [11].

Note that in the following, the label T_2 is simply used to designate a process (transverse relaxation), even though the decay function need not be exponential. The actual decay functions are listed in Table 3.

3.7.1 Inversion recovery: T_1

Longitudinal relaxation in the qubit frame is measured via an inversion recovery experiment. The qubit is prepared in its excited state, and the readout is delayed with respect to this preparation pulse in order to monitor the time it takes for the qubit to decay back to the ground state (see pulse sequence in Fig. 13B). As the qubit is not begin driven during the decay period, inversion recovery is a measure of energy decay during free evolution (Fig. 9A).

A typical decay trace taken at the qubit degeneracy point, $f = 0.5$, is shown in Fig. 13B [11]. In this example, $T_1 = 12$ μs. For most superconducting qubits, the observed decay function is exponential. However, the decay function can become non-exponential due to experimental factors, *e.g.*, repeating an experiment too rapidly, which can lead to a non-equilibrium quasiparticle accumulation.

By measuring thd T_1 time versus qubit frequency, we were able to map the noise PSD at frequencies above 5.4 GHz (see Fig. 14A) [11].

3.7.2 Free-induction decay (Ramsey): T_2^*

Transverse relaxation in the qubit frame is measured via a free-induction decay measurement, or Ramsey measurement. The pulse sequence is shown in Fig. 13B, and it comprises a pair of $\pi/2$ pulses. The first pulse brings the Bloch vector to the equator. In the qubit frame, the spin will precess about the the qubit field $\omega_{\rm q}$ (see Fig. 9B). After a time τ, the second $\pi/2$ pulse followed by measurement will project the state against the quantization axis. This projection as a function of τ defines the decay function.

Fluctuations in the qubit frequency will cause the spin to precess at a faster or slower rate, leading to dephasing. Due to $1/f$-type flux noise, the dephasing decay function is typically Gaussian rather than exponential (see Table 3). Repeated trials of the experiment will likely have different precession rates due to low-frequency fluctuations, and it is not possible to "identically prepare" the qubit for each trial. This type of "temporal inhomogeneity" can be compared with the spatially inhomogeneous field distribution in an atomic lattice. The "*" is used to indicate inhomogeneous broadening. In Fig. 13B, the decay function is not purely exponential, but is a combination an exponential function related to T_1 and the Gaussian dephasing function for T_ϕ. The $1/e$ time (the time to reach a factor$1/e$ of the initial value, not an exponential decay time) is 2.5 μs for this device at $f = 0.5$. Despite the qubit being biased at $f = 0.5$, there was enough residual Δ noise in this qubit to dephase the qubit and keep $T_2^* < T_1$ (we were able to rule out second-order flux noise, see Ref. [11]).

It should be noted that the decay trace shown in Fig. 13B is usually interpreted within a frame rotating at the qubit frequency. Detuning the frequency of the $\pi/2$ pulses then results in oscillations at the detuning frequency as observed in Fig. 13B. We have instead chosen to

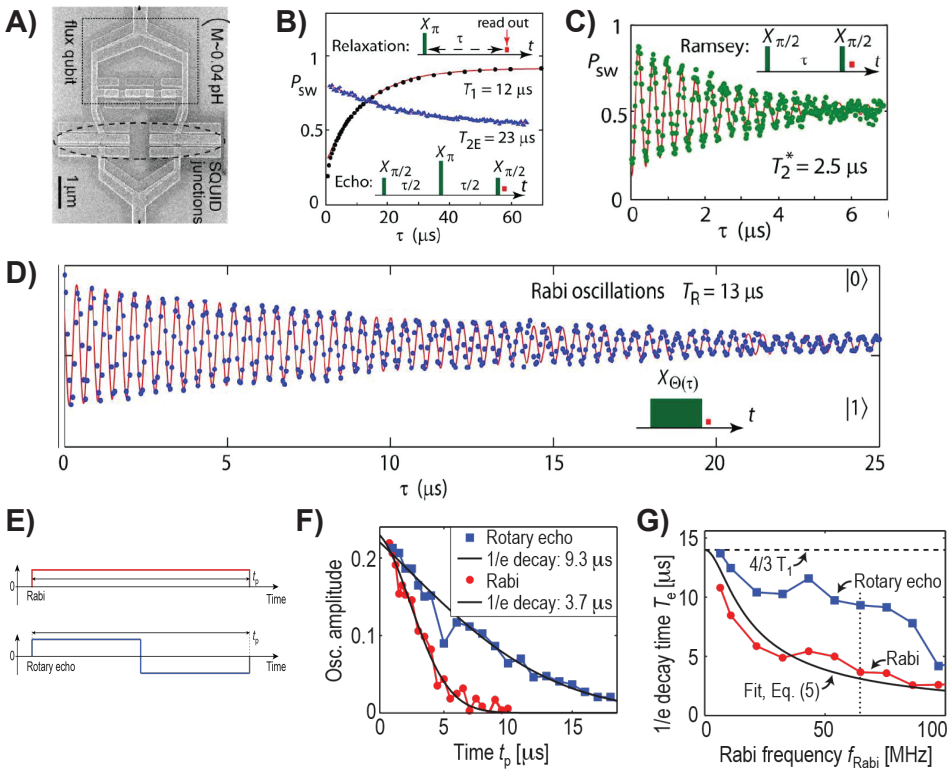

Fig. 13: Free- and driven evolution of a flux qubit. **A)** *SEM image of the flux qubit and SQUID [11].* **B)** *Inversion recovery experiment to extract the relaxation time T_1 (black line). Hahn (spin) echo experiment to extract the echo time T_{2E}. Both traces taken at the flux qubit degeneracy point.* **C)** *Ramsey interferometry with inhomogeneously broadened $T_2^* = 2.5$ μs, measured at the flux qubit degeneracy point.* **D)** *Rabi oscillations at the flux qubit degeneracy point. The Rabi time $T_R \equiv T_{2\rho}$ is approximately T_1 limited: $T_R = 4/3T_1$.* **E)** *Comparison of Rabi and rotary echo pulse sequences. The rotary echo is the driven-evolution analog of spin echo.* **F)** *$1/e$ decay times for a Rabi and rotary echo experiment for a particular driving amplitude (Rabi frequency), and* **G)** *as a function of driving amplitude (Rabi frequency).*

view the Ramsey experiment in the qubit frame to make a clear analogy between the T_2 of free-evolution (Fig. 9B) and the $T_{2\rho}$ of driven evolution (Fig. 9D).

Finally, by rapidly sampling repeated Ramsey measurements, we were able to measure the noise PSD in the 10^{-4} - 10^{2} Hz limit (see Fig. 14A) [11, 138].

3.7.3 Hahn echo (spin echo): T_{2E}

The Hahn (spin) echo (see Section 3.6) is a Ramsey experiment with a single π-pulse located midway between the two $\pi/2$-pulses. For low-frequency fluctuations, this π pulse serves to refocus the errant precession of the Bloch vector. This is achieved (in an ensemble sense) by "swapping" the leading and lagging spins on the equator such that they will all meet (refocus) at the same point and time coincident with the second $\pi/2$-pulse. How "low" a frequency is "low enough" is dictated by the filter function g_1 described in Section 3.6, but, intuitively, the noise cannot change significantly over the refocusing time.

The spin echo pulse sequence shown in Fig. 13B was implemented with the qubit biased at $f = 0.5$, the first-order flux insensitive point. In this qubit, and at this bias point, the echo was

efficient, that is, $T_{2E} = 23\ \mu\text{s} \approx 2T_1$. This means that the observed decay trace is exponential (it is limited by T_1), and the dephasing time after refocussing exceeds $100\ \mu\text{s}$.

3.7.4 CPMG (multi-pulse refocussing): $T_2^{(N)}$

Away from $f = 0.5$, where the qubit is more susceptible to flux noise, the echo was less efficient as described in Section 3.6. In this case, adding additional, equally spaced π-pulses (CPMG) improved the refocussing efficiency. This is because the filter function peak moves to higher frequencies with larger numbers of pulses. Characterizing the decay functions for N-pulse CPMG sequences in conjunction with the filter function enabled the reconstruction of the PSD (see Fig. 10, Fig. 14A) [11].

3.7.5 Rabi oscillations: $T_{2\rho} \equiv T_{\text{R}}$

Decay during driven evolution is typically measured via a Rabi experiment (Fig. 13D). The qubit is prepared in its ground state. A harmonic field then continuously drives the qubit state for a time τ, and then a measurement projects the qubit state on the measurement axis. This projection as a function of τ determines the Rabi decay function. The observed decay time at $f = 0.5$ is $T_{\text{R}} = 13\ \mu s$, nearly T_1 limited ($T_{\text{R}} \approx 4/3T_1$).

The Rabi experiment can be viewed in the rotating frame (Fig. 9D) as "precession" about the driving field ω_{R} in the plane perpendicular to the driving field vector. This is analogous to the Ramsey precession about the qubit field in the free-evolution case (Fig. 9D). Within this language, the decay time T_{R} is alternatively called $T_{2\rho}$.

Unless limited by T_1 (as it is here at the degeneracy point), the Rabi decay function is generally not exponential. The corresponding decay function is somewhat complicated due to low-frequency noise of the driving field and qubit parameters (see Table 3). Nonetheless, noise at the Rabi frequency can be extracted using the functions in Table 3 to infer points on the PSD (yellow dots, Fig. 14A)) [11, 186].

3.7.6 Rotary echo: $T_{2\rho\text{E}}$

The rotary echo pulse sequence (Fig. 13E) is the driven-evolution analog to the spin echo. To implement rotary echo, the Rabi driving field is split into two equally sized sections, with the driving field phase flipped 180 degrees for the second section. This results in the driving field going from $+X$ to $-X$ in Fig. 9D. As a result, the spin "precesses" about the driving field in the opposite direction, ideally returning to its starting point. If the driving field has low-frequency amplitude fluctuations, the "precession frequency" (Rabi frequency) will also change. By reversing the direction of the spin evolution, this low-frequency noise is mitigated. Fig. 13F shows a standard Rabi decay trace and the corresponding rotary echo decay trace for a given driving field amplitude (Rabi frequency), and Fig. 13G presents the extracted decay times as a function of the driving field amplitude (Rabi frequency). The rotary echo exhibits longer decay times $T_{2\rho\text{E}}$ than the Rabi oscillation decay time $T_{2\rho} = T_{\text{R}}$ [140].

3.7.7 Spin locking: $T_{1\rho}$

$T_{1\rho}$ is an inversion-recovery-type experiment during driven evolution, and spin locking is a means to measure it. The spin-locking sequence is shown in Fig. 14B inset. The spin vector is first brought to the equator with a $\pi/2$ pulse. Then, a driving field is applied colinear with the

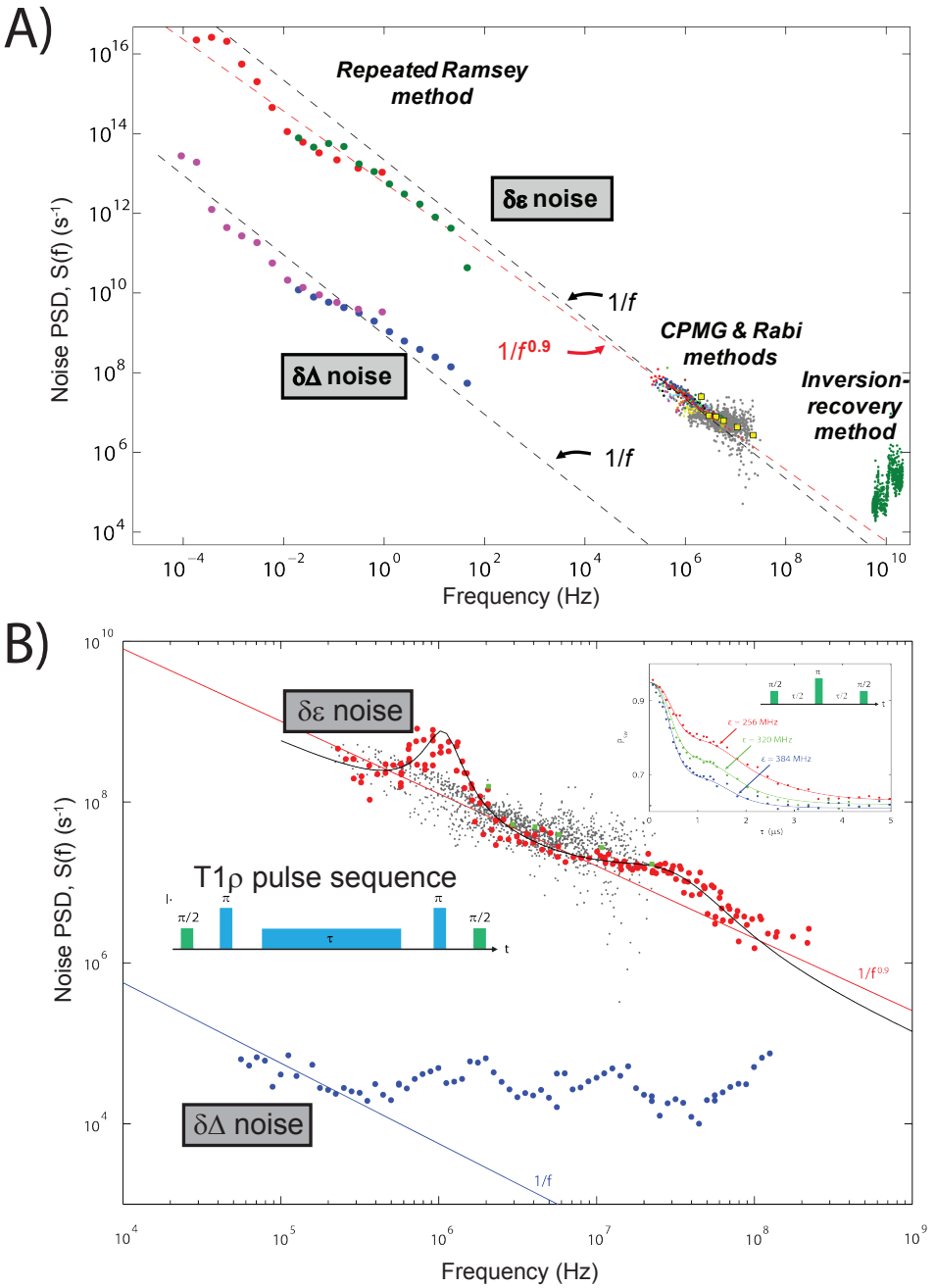

Fig. 14: Noise power spectral densities ($\delta\varepsilon$ noise and $\delta\Delta$ noise) for of a flux qubit during free- and driven evolution. **A)** *Noise spectroscopy during free evolution [11]. A low-frequency Ramsey method is used to obtain the PSD in the frequency range* 10^{-4} *to* 10^{2} *Hz range. CPMG is used to measure the noise in the* 50 *kHz - 20 MHz range. The yellow points are derived from Rabi measurements (driven evolution). The high frequency noise is measured through inversion recovery (green data).* **B)** *Noise spectroscopy of a flux qubit during driven evolution [186]. The* $T_{1\rho}$ *pulse sequence is used to extract relaxation and dephasing in the with respect to the driving field in the rotating frame. The* $\delta\varepsilon$ *noise exhibits Lorentzian features, corresponding to defects. The defect at 1 MHz is observed to be active in a free-evolution echo experiment (inset).*

spin vector (Fig. 9C). In the rotating frame and under resonant driving conditions, the driving field establishes a new quantization axis, and the spin is now pointing along this axis. This is analogous to the spin being collinear with the qubit quantization axis in the free-evolution case (Fig. 9A). The distinction for the driven evolution case is that the Rabi frequency is typically in the 10-100 MHz range, which is much smaller than the thermal energy at the operating temperature. As a result, both the up and down relaxation rates $\Gamma_{1\rho\uparrow}$ and $\Gamma_{1\rho\downarrow}$ contribute to depolarization. And, as with T_1, the decay function for $T_{1\rho}$ tends to be exponential provided the noise is "regular" about the Rabi frequency, which it generally is (see Table 3). The exponential decay function (with no oscillations) is straightforward to analyzer compared with the relatively complicated Rabi decay function. Using the $T_{1\rho}$ method, we extracted the noise PSD during driven evolution over a frequency range 50 kHz - 200 MHz for both $\delta\varepsilon$ and $\delta\Delta$. Interestingly, we observed two Lorentzian features in the $\delta\varepsilon$ noise during driven evolution. The 1-MHz feature was also manifest in the free-evolution spin-echo experiment (inset, Fig. 14B), causing a sharp drop in coherence around $1\ \mu\mathrm{s}$ when the echo filter function passes through $1\mathrm{MHz}$.

4 Control of superconducting qubits in the strong-driving limit

Due to their relatively large size, superconducting artificial atoms can be strongly coupled to their external control fields. It is this feature, along with their quantum coherence, that we utilize in the present section. A large-amplitude harmonic control field can drive an artificial atom throughout its energy-level spectrum. When driven through an avoided level crossing, a Landau-Zener-Stückelberg (LZS) transition occurs. This is a coherent process akin to a beamsplitter for photons, taking an input state of the atom and outputting a superposition of states. Repeated passages through an avoided crossing act as an atom interferometer, causing the atomic superposition state to interfere quantum mechanically with itself. Since the weighting of the superposition state depends sensitively on the size of the avoided crossing and the velocity with which it is traversed, the quantum interference reflects the energy spectrum of the artificial atom. In turn, the quantum interference can be leveraged to facilitate non-adiabatic quantum control.

We begin this sesction with an overview of Landau-Zener-Stückelberg (LZS) transitions. We then present three experimental works that utilize LZS transitions in a strongly-driven persistent-current qubit [127, 128]. The first is Mach-Zehnder-type interferometry between repeated LZS transitions [38], for which we observed quantum interference fringes in n-photon transition rates, with n=1 . . . 50 [39]. The second is microwave-induced cooling [44], by which we achieved effective qubit temperatures less than 3 mK, a factor 10-100 times lower than the environmental temperature. The third is amplitude spectroscopy [50, 51], a spectroscopy technique that monitors the system response to amplitude rather than frequency. Amplitude spectroscopy allowed us to probe the energy spectra of our artificial atom from 0.01 - 120 GHz, while driving it at a fixed frequency equal to 0.16 GHz. Finally, we consider the application of LZS transitions to quantum information science and technology.

4.1 Flux qubit parameters

In this section, we use a superconducting persistent-current qubit to implement an artificial atom [127, 128]. In this implementation, the persistent-current qubit is a superconducting loop interrupted by three Josephson junctions (Fig. 15A). When biased with a static magnetic flux

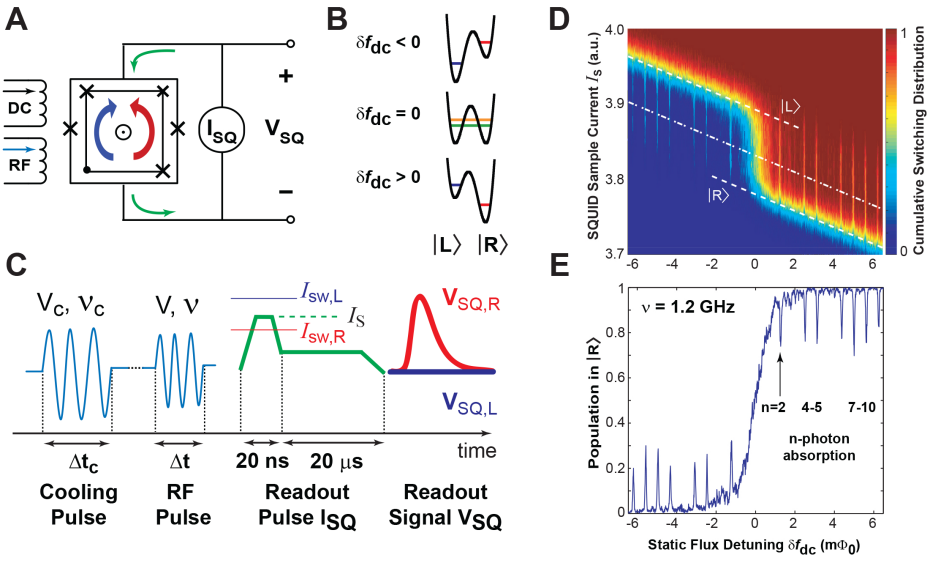

Fig. 15: Artificial atom (persistent current qubit) and measurement set-up. A) *Schematic of the qubit and surrounding DC SQUID readout.* **B)** *Double well qubit potential comprising energy levels for static magnetic flux bias δf_{dc} about $\Phi_0/2$, where Φ_0 is the superconducting flux quantum. Diabatic states of the left (right) well corresponds to a persistent current with clockwise (counterclockwise) circulation. At detuning $\delta f_{dc} = 0$, the double-well potential is symmetric and the diabatic-state energies are degenerate.* **C)** *Qubit excitation and read-out pulse sequence. The qubit is first prepared in its ground state with a harmonic cooling pulse with amplitude V_c and frequency ν_c. Quantum-state transitions are induced with a subsequent harmonic RF pulse with amplitude V and frequency ν. The qubit state is read-out using the DC SQUID switching response.* **D)** *Qubit step. Cumulative switching current distribution of the SQUID for each δf_{dc} value following a 3-μs RF driving pulse at 1.2 GHz applied to the qubit. Resonant multiphoton transitions (of order n) are observed between states $|L\rangle$ and $|R\rangle$.* **E)** *The switching distribution along the dashed-dotted line discriminates between states $|L\rangle$ and $|R\rangle$.*

$f_{\rm dc} \sim \Phi_0/2$, where Φ_0 is the superconducting flux quantum, the system assumes a double-well potential profile (Fig. 15B). The diabatic state of the left (right) well corresponds to a persistent current $I_{\rm p}$ with clockwise (counterclockwise) circulation. The lowest two diabatic energy levels have a separation $\varepsilon = 2I_{\rm p}\delta f_{\rm dc}$ linear in the flux detuning $\delta f_{\rm dc} \equiv f_{\rm dc} - \Phi_0/2$. Higher-excited states of the double-well potential (see Fig. 19C) will be considered in Subsections 4.4 and 4.5.

The two-level Hamiltonian for the lowest two diabatic states is shown in Eq. 133. At detuning $\delta f_{\rm dc} = 0$, the double-well potential is symmetric and the diabatic-state energies are degenerate. At this "degeneracy point," resonant tunneling between the diabatic states opens an avoided level crossing of energy Δ. Here, the qubit states are σ_x eigenstates, corresponding to symmetric and anti-symmetric combinations of diabatic circulating-current states. Detuning the double-well away from this point tilts the double well, allowing us to tune the eigenstates and eigenenergies of the artificial atom. Far from the degeneracy point, the qubit states are approximately σ_z eigenstates and have well-defined circulating current. The qubit is read out using a hysteretic DC SQUID (superconducting quantum interference device), a sensitive magnetometer that can distinguish the flux generated by circulating current states.

In addition to the static flux biases, the artificial atom is controlled and read out using the pulses illustrated in Fig. 15C. As we describe below, the qubit is first prepared in its ground state using a harmonic cooling pulse with amplitude $V_{\rm c}$ and frequency $\nu_{\rm c}$. Quantum-state transitions are then driven using a harmonic RF pulse with amplitude V and frequency ν. These fields are mutually coupled to the qubit through a small antenna. This is followed by a SQUID readout current pulse using the "sample and hold" technique [30, 38]. If the sample current exceeds the SQUID switching current, a voltage pulse will appear at the output during the hold phase. Threshold detection looks for the presence or absence of a SQUID voltage, and this constitutes a digital measurement of the qubit state. Alternatively, although not used in these experiments, we have incorporated the SQUID into a resonant circuit and realized qubit readout via the shift in resonance frequency and phase for both the linear and non-linear resonance regimes [87, 91].

The "qubit step" is shown in Fig. 15D as a function of the SQUID sample current and the flux detuning. The diabatic states $|L\rangle$ and $|R\rangle$ correspond to different levels of sample current (dashed lines) located symmetrically about the degeneracy point $\delta f_{\rm dc}$=0. This plot constitutes a cumulative switching current distribution of the SQUID for each $\delta f_{\rm dc}$ value. Additionally, a 3-μs RF pulse at 1.2 GHz is applied to the qubit, and resonant transitions can be observed as fingers extending down (up) from state $|L\rangle$ ($|R\rangle$) when n$\times$1.2 GHz becomes resonant with the energy-level separation. A best-estimator (dashed-dotted line) can be determined to provide the best statistical discrimination between states $|L\rangle$ and $|R\rangle$. The resulting qubit step with its saturated n-photon resonances along the best estimator line is shown in Fig. 15E.

The device used in this work was fabricated at Lincoln Laboratory using a fully-planarized niobium trilayer process and optical lithography. It has a critical current density $J_{\rm c} \approx 160\,{\rm A/cm^2}$, and the characteristic Josephson and charging energies are $E_{\rm J} \approx (2\pi\hbar)300\,{\rm GHz}$ and $E_{\rm C} \approx (2\pi\hbar)0.65\,{\rm GHz}$ respectively. The ratio of the qubit JJ areas is $\alpha \approx 0.84$, and $\Delta \equiv \Delta_{0,0} \approx (2\pi\hbar)10\,{\rm MHz}$. Although dependent on the flux detuning, the approximate values for coherence times are: interwell relaxation time $T_1 \sim 100\,\mu$s, intrawell relaxation time $T_1 \sim 0.1\,\mu$s, homogeneous transverse decay time $T_2 \sim 20\,$ns, inhomogeneous transverse decay time $T_2^* \sim 10\,$ns. The experiments were performed in a dilution refrigerator at a base temperature of 20 mK. The device was magnetically shielded, and all electrical lines were carefully filtered and attenuated to reduce noise (see Ref. [50] for details).

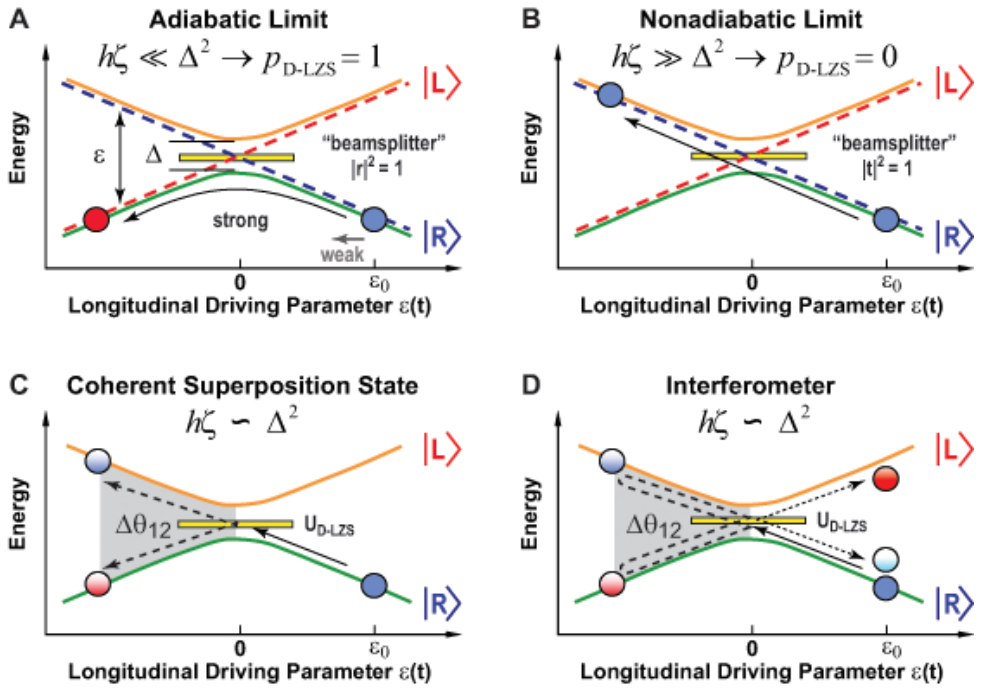

Fig. 16: Landau-Zener-Stückelberg transition. A) *Adiabatic limit: $h\zeta \ll \Delta^2$; the probability of a transition from state $|R\rangle$ to state $|L\rangle$ approaches unity.* **B)** *Nonadiabatic limit: $h\zeta \gg \Delta^2$; the probability of a transition from state $|R\rangle$ to state $|L\rangle$ approaches zero.* **C)** *Coherent superposition of states. At intermediate sweep velocities ($h\zeta \sim \Delta^2$) a superposition state $\alpha|L\rangle + \beta|R\rangle$ results from an excursion through the avoided crossing. A phase difference $\Delta\theta_{12}$ accrues due to the energy difference between the states $|L\rangle$ and $|R\rangle$.* **D)** *Quantum interference during a second excursion through the avoided crossing. Interference fringes appear at half-integer and integer values of $\Delta\theta_{12}/2\pi$, which is tunable via the drive amplitude.*

4.2 Landau-Zener transitions

Landau-Zener-Stückelberg (LZS) transitions occur when a quantum system is driven through an energy-level avoided crossing [141, 142, 143]. The resulting quantum dynamics of the LZS mechanism [144] in driven systems [145] have been developed [146, 147] within a two-level coherent scattering formalism [148, 149, 150, 151] with potential application to quantum information science and technology [150, 151, 152, 153, 154].

We model a LZS transition at a single crossing using the two-level Hamiltonian

$$\mathcal{H} = -\frac{1}{2}\begin{pmatrix} \varepsilon(t) & \Delta \\ \Delta & -\varepsilon(t) \end{pmatrix}, \tag{133}$$

in which ε is the energy difference between diabatic-state energy levels (dashed lines in Fig. 16A), and Δ is the size of the avoided crossing and corresponds to the coupling strength between diabatic states $|\mathrm{L}\rangle$ and $|\mathrm{R}\rangle$.

The system is prepared in state $|R\rangle$ at a static value $\varepsilon_0 \gg \Delta$ far from the avoided crossing (blue dot, Fig. 16A) and driven longitudinally from that point by making $\varepsilon(t)$ time dependent. We distinguish here between "weak driving," in which the system drive is not large enough to reach the avoided crossing, and "strong driving" for which the avoided crossing is traversed. Under strong-driving conditions, the asymptotic probability $P_{\text{D-LZS}}$ of a transition between dia-

batic states,

$$P_{\text{D-LZS}} \equiv 1 - P_{\text{E-LZS}} = 1 - \exp \frac{-\pi \Delta^2}{2\hbar \zeta_i}, \tag{134}$$

is governed by the relative-energy sweep rate ζ_i

$$\zeta_i = \frac{d\varepsilon(t)}{dt}|_{t=t_i} \tag{135}$$

evaluated at the time $t = t_i$ at which the system is swept through the avoided crossing. In the original LZS formulation, the system was driven with a fixed sweep rate, whereas we will later consider a harmonically driven system. We also note that we have elected to monitor the probability $P_{\text{D-LZS}}$ of a transition between the diabatic states $|L\rangle$ and $|R\rangle$, because our readout detector is sensitive to changes in diabatic state. This can be written with no loss of generality in terms of the probability $P_{\text{E-LZS}}$ of a transition between the system eigenstates.

There are two strong-driving limits characterized by the relative sizes of the sweep velocity ζ and the avoided crossing Δ. In the adiabatic limit (Fig. 16A), the sweep velocity is small ($h\zeta \ll \Delta^2$) and the probability of a transition from state $|R\rangle$ to state $|L\rangle$ approaches unity, $P_{\text{D-LZS}} \rightarrow 1$. In this case, the system dynamics are slow enough that the system adiabatically follows the ground eigenstate through the avoided crossing. In the nonadiabatic limit (Fig. 16B), the sweep velocity is large ($h\zeta \gg \Delta^2$) and the probability of a transition approaches zero $P_{\text{D-LZS}} \rightarrow 0$. In this case, the dynamics are too fast for the system to follow; the system remains in diabatic state $|R\rangle$ and, thereby, effectively jumps the energy gap at the avoided crossing.

More generally, a superposition state $\alpha|L\rangle + \beta|R\rangle$ results from an excursion through the avoided crossing, as illustrated in Fig. 16C. Following an idea discussed by Shytov *et al.* [150], the LZS transition acts as a beamsplitter for the atomic state. The amplitudes α and β are determined by a unitary transformation $U_{\text{D-LZS}}$, effectively a 2×2 "beamsplitter matrix" comprising complex reflection r and transmission t coefficients related to the adiabaticity parameter $\Delta^2/\hbar\zeta$ present in Eq. 134 [144] such that $|t|^2 = 1 - P_{\text{D-LZS}}$, $|r|^2 = P_{\text{D-LZS}}$, and $U^{\dagger}_{\text{D-LZS}} U_{\text{D-LZS}} = I$. Note that we have defined $|t|^2$ and $|r|^2$ from the perspective of a beamsplitter, which "transmits" ("reflects") an input state to the same (opposite) diabatic state, respectively. After the transition, a relative phase $\Delta\theta_{12}$ accrues due to the energy difference between the states $|L\rangle$ and $|R\rangle$. If the drive $\varepsilon(t)$ then returns the system through the avoided crossing a second time, the atomic state collides and quantum mechanically interferes with itself during the second LZS transition (Fig. 16D). The cumulative result is an atom-state interferometer whose output state depends on the LZS transition amplitudes and the interference phase.

An analogy can be made to a Mach-Zehnder interferometer: the atomic states play the role of the photon modes, the LZS transitions play the role of the photon beamsplitters, and the energy-level splitting, which determines the interference phase, plays the role of optical path length difference. The quantum interference is robust provided the evolution time of the state through the interferometer is short compared with the atom's coherence times. In addition to superconducting artificial atoms [38, 39, 27, 40, 41, 33], this concept is generally applicable to other solid-state artificial atoms [158, 159] and generalized spin systems [160] (e.g., molecular magnets [161, 162, 163], natural atoms [164, 165], and molecules [166, 167, 168]) that exhibit avoided level crossings, and it is extensible to multiple energy levels as we demonstrate in Section 19.

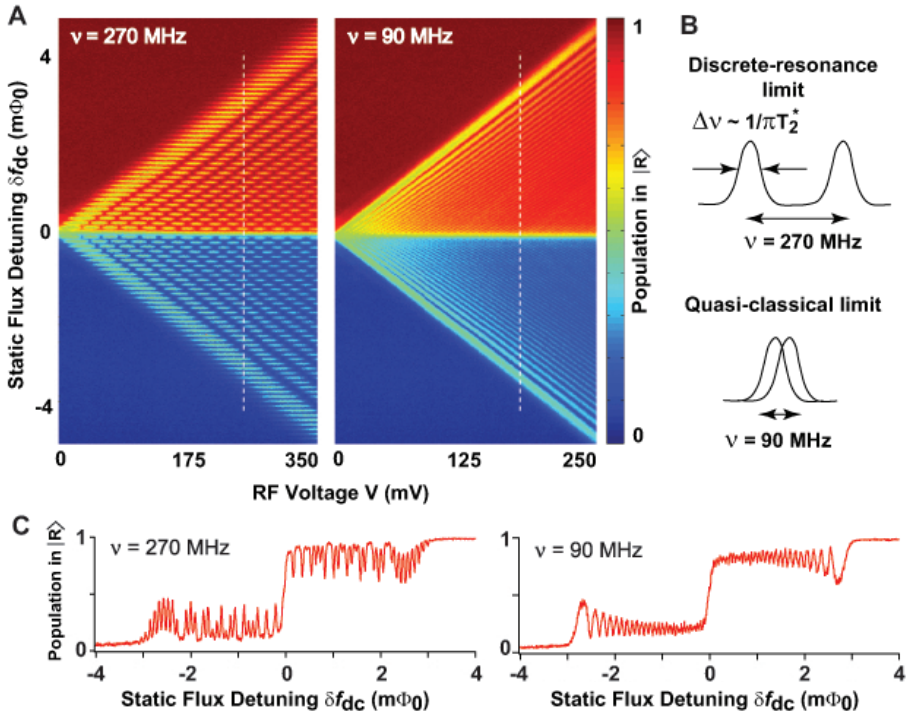

Fig. 17: Mach Zehnder interference. A) *Measured qubit population as a function of excitation amplitude and flux detuning in two excitation regimes. Left:* $\nu = 270$ *MHz. The resonance linewidth is smaller than the excitation frequency* **(B, top)***; individual n-photon resonances can be resolved and a Bessel staircase is observed. Right:* $\nu = 90$ *MHz. The resonance linewidth is larger than the excitation frequency* **(B, bottom)***; individual resonances are no longer resolved but coherent interference is still observed.* **C)** *Interference fringes in qubit population for* $\nu = 270$ *MHz (left)* $\nu = 90$ *MHz (right) along the vertical dashed lines in* **A**.

4.3 Mach-Zehnder-type interferometry

The structure of the n-photon spectroscopy peaks seen in Fig. 15E consists of regularly-spaced resonances positioned according to the condition n×1.2 GHz being resonant with the energy level separation. Notably, however, for this particular value of driving amplitude, the n=1, 3, and 6 photon peaks are missing. As we describe in this section, the presence and absence of these peaks arise from Mach-Zehnder-type quantum interference at a level crossing. The interference phase can be tuned through the driving amplitude, and leads to a "Bessel staircase" in the observed spectroscopy. The interference oscillations are known as Stückelberg oscillations [143], and they have been observed in both artificial [38, 39, 40, 41] and natural [164, 165, 166] atomic systems.

In a conventional Mach-Zehnder interferometer, an optical signal is passed through two beamsplitters. The first beamsplitter coherently divides the signal into two output paths, which may have different effective optical path lengths. These paths are then recombined at the second beamsplitter, where the signal waves interfere and exit the interferometer. The measured output exhibits interference fringes depending on the relative path length.

Here, we instead utilize LZS transitions at level crossings as beamsplitters for the atomic state [150]. We drive the persistent-current qubit with a harmonic driving field of the form

$$\varepsilon(t) = \varepsilon_0 + A\sin\omega t \tag{136}$$

with $\omega = 2\pi\nu$ the driving frequency and $A > \varepsilon_0$ the field amplitude (in units of energy), which is proportional to the RF voltage at the source. As illustrated in Fig. 16D, the qubit state undergoes two LZS transitions during one period of the driving field. The first LZS transition at time t_1 splits the qubit into a superposition of excited and ground states. A relative phase $\Delta\theta_{12}$ accumulates

$$\Delta\theta_{12} = \frac{1}{\hbar}\int_{t_1}^{t_2} \varepsilon(t)dt, \quad \varepsilon(t) = \varepsilon_{|R\rangle}(t) - \varepsilon_{|L\rangle}(t) \tag{137}$$

until the second LZS transition at time t_2, at which point the qubit state collides with itself and interferes. Interference fringes appear at half-integer and integer values of $\Delta\theta_{12}/2\pi$, which is tunable via the drive amplitude.

It is clear, however, that a second phase must also play a role in this problem, since the qubit state continues to evolve for the remainder of the driving period. It is physically meaningful to consider the total phase θ accumulated over a single period:

$$\theta = \frac{1}{\hbar}\oint \varepsilon(t)dt = 2\pi\varepsilon_0/\hbar\omega, \tag{138}$$

which is *independent* of the driving amplitude. Over many periods of the driving field, the cascaded pairs of LZS transitions (cascaded interferometers) will constructively interfere provided $\theta = 2\pi n$. One can view this as a "time-domain" formulation for the familiar n-photon resonance condition

$$\varepsilon_{0,n} = nh\nu \tag{139}$$

where n is the number of photons involved in the transition. It is only when the product $nh\nu$ equals the energy separation $\varepsilon_{0,n}$ that the cascaded LZS transitions lead to a net buildup of interference fringes. These oscillations are related to photoassisted transport [169, 170, 171] and Rabi oscillations [27, 33] in the multiphoton regime.

Mach-Zehnder-type interference in the discrete-resonance limit driven towards saturation is shown in Fig. 17A for driving frequency $\nu = 270$ MHz. This frequency is larger than the resonance linewidth (Fig. 17B), and so individual n-photon resonances can be resolved. There are two main features observable in this plot. The first is the presence of equally-spaced n-photon transitions as a function of flux detuning, symmetrically located about the qubit step at $\delta f_{\rm dc} = 0$. As one might expect, the onset of the higher-photon transitions requires larger driving amplitudes. Remarkably, we observe up to 50-photon transitions in this scan. The second main feature is that for each n-photon resonance, the spectroscopy appears and disappears as a function of amplitude, which sweeps the interference phase $\Delta\theta_{12}$. For example, 14 oscillation lobes are visible for the 1-photon transition. A vertical slice of the spectroscopy (dashed white line in Fig. 17A) is plotted in Fig. 17C; at this particular amplitude, one can see the enhancement and suppression of the spectroscopy peaks as was observed in Fig. 15E.

The Mach-Zehnder interference for an n-photon transition yields a modified amplitude-dependent matrix element [38, 27, 160]

$$\Delta_n = \Delta J_n(\lambda) \tag{140}$$

where $J_n(\lambda)$ is the nth-order Bessel-function, and its argument $\lambda = A/\hbar\omega$ is the dimensionless driving amplitude (see Appendix B). Intuitively, the Bessel-function dependence arises because the qubit is driven harmonically through energy levels that are linear in flux detuning and, as a result, the interference phase accumulates with a sinusoidal time dependence. The interference fringes for each n-photon resonance are related to the matrix element squared, Δ_n^2. At

specific amplitudes, there is a complete destructive interference of a transition due to the zeros of $J_n(\lambda)$; this is the coherent destruction of tunneling [155, 156, 157] condition for driven n-photon transitions [38, 39].

In the discrete resonance limit, n-photon resonances are distinguishable, because the coherence time of the qubit is sufficiently longer than the driving period. By reducing the frequency to $\nu = 90$ MHz (Fig. 17A, right panel), we effectively made the drive period comparable with the linewidth, $\nu T_2^* \sim 1$ (Fig. 17B). In this spectroscopy plot, the individual n-photon resonances are no longer resolvable. However, the Mach-Zehnder interference fringes (vertical slice, Fig. 17C) are clearly visible, because the qubit remains coherent during the critical fraction of the drive period during which the phase $\Delta\theta_{12}$ accumulates and the Mach-Zehnder interference occurs. Intuitively, provided $\nu T_1 \gg 1$, the output populations of each quantum interferometer are then preserved (frozen) until the subsequent interferometer is reached in the following period; therefore, although the resonance condition is lost, the Mach-Zehnder quantum interference remains. This behavior can be contrasted with driven Rabi oscillations, for which there would be no signature of coherence in the limit $\nu T_2^* \sim 1$.

4.4 Microwave cooling

The previous discussion involved driving transitions in the lowest two energy levels in the double-well potential of our artificial atom (Fig. 18A), which constitute the two-level qubit subsystem of a more complex energy level diagram (Fig. 19C). When higher-excited states are accessed, the driven system behavior can be markedly different from the population saturation observed when only two levels are involved. For example, at least three levels are required to achieve population inversion, and such a multi-level artificial atom coupled to a microwave cavity has been used to demonstrate masing (microwave lasing) [172]. In that work, Josephson quasi-particle states were driven to achieve inversion. Alternatively, population inversion can be established by accessing an ancilliary excited state via direct or LZS transitions. This will be briefly discussed in the next section.

Here, by reversing the cycle that leads to population inversion, we show that one can pump population from the qubit excited state $|0L\rangle$ to the qubit ground state $|0R\rangle$ (Fig. 18A) via an ancillary energy level $|1R\rangle$. In the case where the population in $|0L\rangle$ results from thermal excitation, the transfer of population to $|0R\rangle$ effectively cools the qubit by lowering its effective temperature. This kind of active cooling represents a means to initialize and reset qubits with high fidelity, key elements for quantum information science and technology. Alternatively, the pumping mechanism can be used to refrigerate environmental degrees of freedom [173], or to cool neighboring quantum systems [46, 47].

More explicitly, for a qubit in equilibrium with its environment, the population in $|0L\rangle$ that is thermally excited from $|0R\rangle$ follows the Boltzmann relation

$$p_{0L}/p_{0R} = \exp[-\varepsilon/k_{\rm B}T_{\rm bath}], \tag{141}$$

where $p_{0L,0R}$ are the qubit populations for energy levels $\varepsilon_{0L,0R}$, $\varepsilon = \varepsilon_{0L} - \varepsilon_{0R}$, $k_{\rm B}$ is the Boltzmann constant, and $T_{\rm bath}$ is the bath temperature. To cool the qubit subsystem below $T_{\rm bath}$, a microwave magnetic flux of amplitude A and frequency ν targets the $|0L\rangle \rightarrow |1R\rangle$ transition, driving the state-$|0L\rangle$ thermal population to state $|1R\rangle$, from which it quickly relaxes to the ground state $|0R\rangle$. Efficient cooling only occurs when the driving-induced population transfer to $|0R\rangle$ is faster than the thermal repopulation of $|0L\rangle$. The hierarchy of relaxation and absorption rates required, $\Gamma_{0R,1R} \gg \Gamma_{0L,1R}, \Gamma_{0L,0R}$, is achieved in our system owing to a relatively

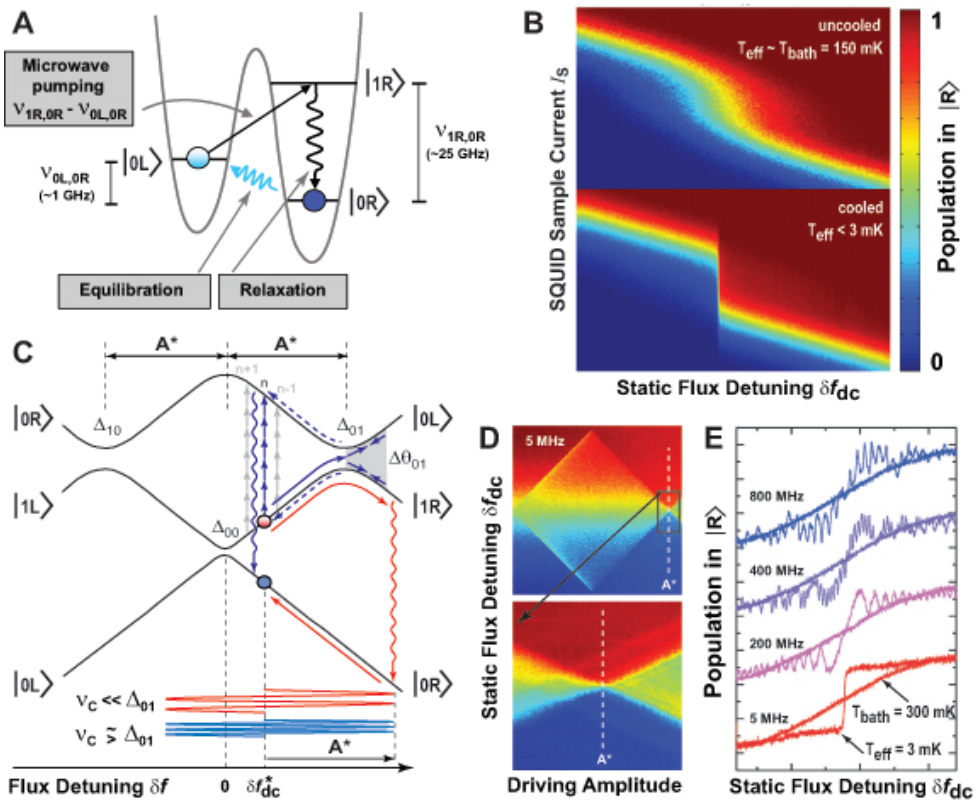

Fig. 18: Cooling of and artificial atom via an ancillary excited state. A) *External excitation transfers the thermal population from state* $|0L\rangle$ *to state* $|1R\rangle$ *(straight line) from which it decays into the ground state* $|0R\rangle$*. Wavy lines represent spontaneous relaxation and absorption leading to equilibration.* **B)** *Qubit step at* $T_{\rm bath}$ *= 150 mK in equilibrium with the bath (top) and after a 3-*μ*s cooling pulse at 5 MHz (bottom). The average level populations exhibit a qubit step about* $\delta f_{\rm dc} = 0$*, with a width proportional to* $T_{\rm bath}$ *(top) and* $T_{\rm eff} \ll T_{\rm bath}$ *(bottom).* **C)** *Schematic level diagram illustrating resonant and adiabatic cooling.* $|0L\rangle \rightarrow |1R\rangle$ *transitions are resonant at high driving frequency* ν *(blue lines) and occur via adiabatic passage at low* ν *(red lines).* Δ_{00} *and* Δ_{01} *are the tunnel splittings between* $|0R\rangle$ - $|0L\rangle$ *and* $|0L\rangle$ - $|1R\rangle$*.* **D)** *Optimal cooling parameters. State* $|0R\rangle$ *population vs. flux detuning* $\delta f_{\rm dc}$ *and driving amplitude* A *with* ν *= 5 MHz,* $\Delta t_c = 3\,\mu$s*, and* $T_{\rm bath}$*= 150 mK. Optimal conditions for cooling are realized at* $A = A^*$*, where* A^* *is defined in* **C**. **E)** *Cooling at driving frequencies* ν *= 800, 400, 200 and 5 MHz. State* $|0R\rangle$ *population vs.* $\delta f_{\rm dc}$ *for the cooled qubit and for the qubit in thermal equilibrium with the bath (black lines,* $T_{\rm bath} = 300\,$mK*). Measurements for* $\nu = 800$*, 200 and 5 MHz are displaced vertically for clarity. A cooling factor of 100, independent of detuning, is obtained in the adiabatic limit (5 MHz).*

weak tunneling between wells, which inhibits the interwell relaxation and absorption processes $|1R\rangle \rightarrow |0L\rangle$ and $|0R\rangle \rightarrow |0L\rangle$, compared with the relatively strong intrawell relaxation process $|1R\rangle \rightarrow |0R\rangle$.

Figure 18B shows the qubit step at $T_{\rm bath}$ = 150 mK in equilibrium with the bath (top) and after a 3-μs cooling pulse at 5 MHz (bottom). Under equilibrium conditions, the average level populations exhibit a thermally-broadened qubit step about $\delta f_{\rm dc} = 0$, with a width proportional to $T_{\rm bath}$. The presence of microwave excitation targeting the $|0L\rangle \rightarrow |1R\rangle$ transition acts to increase the ground-state population and, thereby, sharpens the qubit step. Cooling can thus be quantified in terms of an effective temperature $T_{\rm eff} < T_{\rm bath}$, a signature that is evident from the narrowing of the qubit steps in Fig. 18B after cooling. More precisely, using the notation from Fig. 16, the effective qubit temperature is obtained by fitting an effective temperature that would have been required in equilibrium to achieve the observed qubit population p_{0R},

$$p_{0R} = \frac{\varepsilon}{\sqrt{\varepsilon^2+\Delta^2}}\left[\tanh\left(\frac{\sqrt{\varepsilon^2+\Delta^2}}{2k_{\rm B}T_{\rm eff}}\right)+1\right]. \tag{142}$$

Universal cooling (cooling that is independent of flux detuning) occurs near an optimal driving amplitude A^* (Fig. 18C). This is demonstrated in Fig. 18D where we present the $|0R\rangle$ state population $P_{\rm sw}$ measured as a function of the microwave amplitude A and flux detuning $\delta f_{\rm dc}$ for $\nu = 5\,{\rm MHz}$. Cooling and the diamond feature can be understood in terms of the energy level diagram (Fig. 19C). As the amplitude of the microwave pulse is increased from $V = 0$, population transfer first occurs when the $\Delta_{0,0}$ avoided crossing is reached, *i.e.* $A > |\delta f_{\rm dc}|$; this defines the front side of the observed diamond symmetric about the qubit step (see also Fig. 17A). For amplitudes $A^*/2 \leq A \leq A^*$, the $\Delta_{0,1}$ ($\Delta_{1,0}$) side avoided crossing dominates the dynamics, resulting in a second pair of thresholds $A = A^* - |\delta f_{\rm dc}|$, which define the back side of the diamond. In the region outside of the diamond's backside, the qubit is cooled. As the diamond narrows to the point $A = A^*$, the narrowest qubit step is observed. This is the universal cooling condition: only one of the two side avoided crossings ($\Delta_{0,1}$ or $\Delta_{1,0}$) is reached and, thereby, strong transitions with relaxation to the ground state result for all $\delta f_{\rm dc}$. In contrast, for $A > A^*$, both side avoided crossings ($\Delta_{0,1}$ and $\Delta_{1,0}$) are reached simultaneously for $|\delta f_{\rm dc}| < A - A^*$, leading once again to a large population transfer between $|0R\rangle$ and $|0L\rangle$, and opening the second diamond feature (see Fig. 19).

The cooling exhibits a rich structure as a function of driving frequency and detuning, resulting from the manner in which state $|1R\rangle$ is accessed (Fig. 18C). Transitions occur via a (multiphoton) resonant or adiabatic passage process when the driving frequency is high or low enough, respectively [39, 44]. At high frequencies (800 and 400 MHz in Fig. 18E) well-resolved resonances of n-photon transitions are observed and cooling is thus maximized near resonances. At intermediate frequencies (400 and 200 MHz), Mach-Zehnder interference at the side avoided crossing Δ_{01} becomes more prominent and modulates the intensity of the n-photon resonances [38, 39]. Below $\nu = 200\,{\rm MHz}$, individual resonances are no longer discernible, but as in Fig. 17C, the modulation envelope persists [39]. At the lowest frequencies ($\nu < 10\,{\rm MHz}$), state $|1R\rangle$ is reached via adiabatic passage through the Δ_{01} crossing (Fig. 18C), and the population transfer and cooling become conveniently independent of detuning (see $\nu = 5$ MHz in Fig. 19E). As shown in Fig. 18E, we achieve an effective qubit temperature $T_{\rm eff}$ = 3 mK, even for $T_{\rm bath}$ = 300 mK. In our qubit, our determination of $T_{\rm eff}$ was limited primarily by decoherence (linewidth), which limited the resolution with which we could distinguish the states $|0R\rangle$ and $|0L\rangle$ near degeneracy. Nonetheless, we can estimate the ideally resolvable

cooling factor α_c for this type of cooling process using Eq. 141,

$$\alpha_c \sim \frac{T_{\rm bath}}{T_{\rm eff}} = \frac{\varepsilon_{1R\to 0R}}{\Delta}, \tag{143}$$

where $\varepsilon_{1R\to 0R} \approx h \times 25$ GHz is the energy separation where the relaxation $|1R\rangle \to |0R\rangle$ occurs and $\Delta \approx h \times 0.01$ GHz for our qubit, yielding a cooling factor $\alpha_c \sim 2500$. For a bath temperature $T_{\rm bath} = 50$ mK, this would correspond to an effective temperature $T_{\rm eff} = 20$ μK in our qubit. Using this approach, in principle, lower temperatures can be resolved in systems with smaller energy gaps.

Cooling a qubit in equilibrium with the bath requires a characteristic cooling time. In turn, a cooled qubit will thermalize to the environmental bath temperature over a characteristic equilibration time. The relationship between these two times determines if it is possible to drive the qubit while it is still cold. We found in this qubit that equilibration times are at least one order of magnitude larger than cooling times at $T_{\rm bath} < 250$ mK and up to three order of magnitude larger at $T_{\rm bath} < 100$ mK [44]. This allowed us ample time to drive the qubit after cooling it. The implementation of an active cooling pulse prior to a generic driving pulse is highly advantageous. On the one hand, it sensibly shortens measurement times, enabling us to acquire data at repetition rates that far exceed the intrinsic equilibration rate due to interwell relaxation after each measurement trial. By adopting active cooling, we gained a factor 50 in data acquisition speed, limited by the bandwidth of our readout circuit. On the other hand, by analogy to the cooling of trapped ions and atoms, active cooling greatly reduces thermal smearing, allowing us to analyze features in the data that would have been hidden otherwise. This type of active cooling protocol was required to obtain the detailed, clean data in Fig. 17. In fact, the necessity of active cooling becomes even more evident in the next section where, without the cooling pulse, the observed level of detail could not have been resolved over such a large parameter space in practical acquisition times.

4.5 Amplitude spectroscopy

Since Newton's dispersion of light into a continuous color "spectrum," spectroscopy has been viewed primarily as a frequency-based technique. Ångström, Bunsen, Foucault, Kirchhoff, and many others identified unique spectral lines for elements and compounds based on the emission and absorption of radiation at various frequencies. The series of spectral lines of hydrogen are named for Balmer and Rydberg, who observed them within and beyond the visible wavelengths. Such frequency-dependent absorption and emission spectroscopy played a fundamental role in the development of quantum mechanics and the "new" atomic theory by identifying discrete energy levels. With the invention of coherent microwave (maser) and optical (laser) sources, high-intensity radiation with tunable, narrow spectral linewidth allowed targeted absorption spectroscopy of atoms and molecules with high frequency resolution [174, 175].

However, the application of broadband frequency spectroscopy is not universally straightforward. This is particularly relevant for artificial atoms engineered from solid-state materials which, when cooled to cryogenic temperatures, assume quantized energy levels that extend into microwave and millimeter wave regimes (10-300 GHz). Although certainly not an impossible task, a broadband frequency-based spectroscopic study of these atoms in excess of around 50 GHz becomes extremely challenging and expensive to implement due to numerous frequency-dependent effects (*e.g.*, frequency dispersion and the requisite tolerances to control impedance).

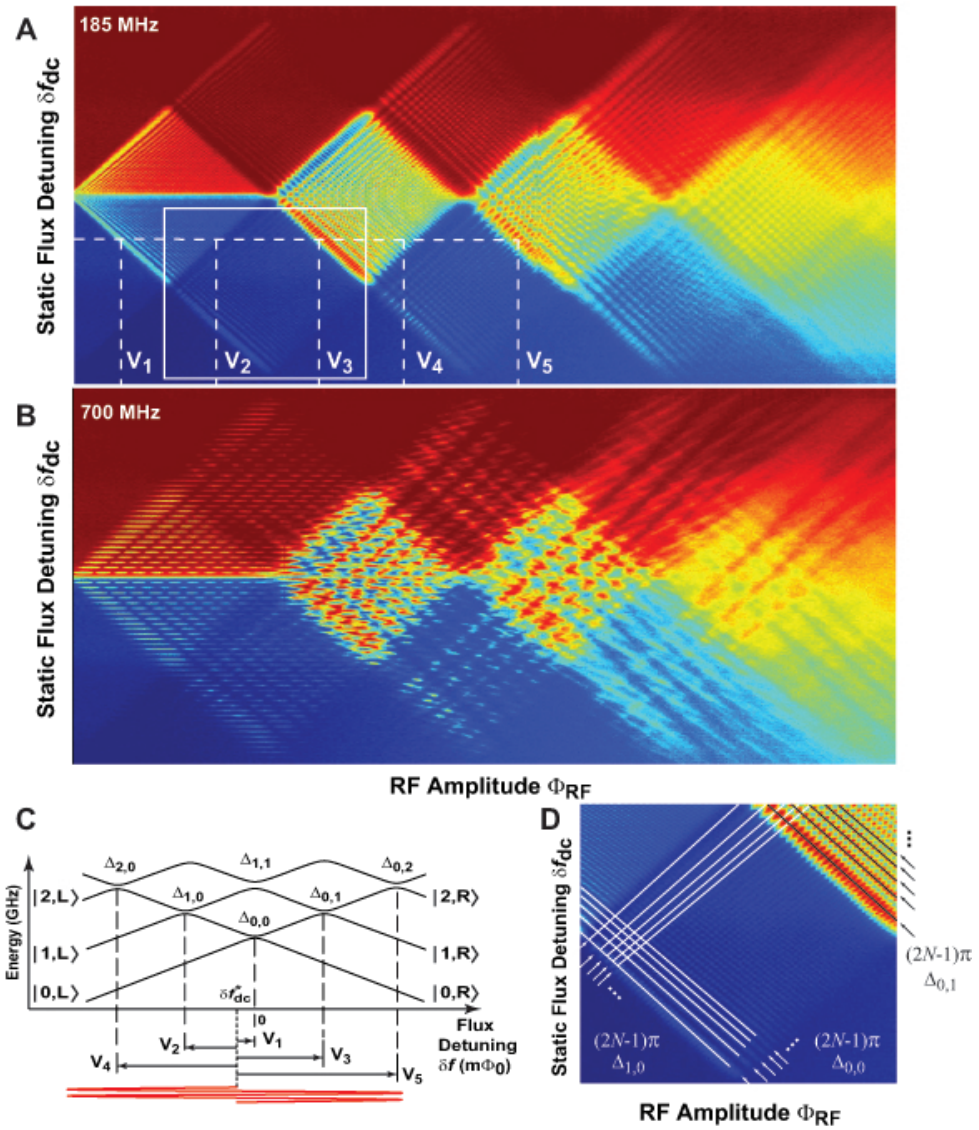

Fig. 19: *Amplitude spectroscopy with long-pulse driving towards saturation. Spectroscopy diamonds obtained at driving frequencies $\nu = 185$ MHz (A) and $\nu = 700$ MHz (B). The color scale represents the net qubit population in state $|q, R\rangle$, where R (L) labels diabatic states of the right (left) well of the qubit double-well potential, and $q = 0, 1, 2, ...$ labels the longitudinal modes. The excitation amplitude V is swept for each static flux detuning $\delta f_{\rm dc}$. The diamond edges mark the driving amplitude V for each value of $\delta f_{\rm dc}$ when an avoided level crossing is first reached (amplitudes $V_1 - V_5$ for $\delta f_{\rm dc} = \delta f^*_{\rm dc}$). C Schematic energy-level diagram illustrating the relation between V and the avoided crossing positions for $\delta f_{\rm dc} = \delta f^*_{\rm dc}$. The arrows represent the amplitudes $V_1 - V_5$ in A. (D) Zoom in of 185-MHz interference patterns (box region, Fig. 19A). The arrows point to lines of constant phase $(2N - 1)\pi$ along which LZS transitions are likely to occur for the avoided crossings $\Delta_{0,0}$, $\Delta_{0,1}$, and $\Delta_{1,0}$.*

Amplitude spectroscopy is an alternative approach to broadband spectroscopic characterization of a quantum system. With amplitude spectroscopy, spectroscopic information is obtained from the system response to driving-field amplitude at a *fixed* frequency. The resulting spectroscopic interference patterns, "spectroscopy diamonds," are mediated by multilevel LZS transitions and Mach-Zehnder-type interferometry, and they serve as a fingerprint of the artificial atom's multilevel energy spectrum. The energy spectrum is then determined by analyzing the atomic fingerprint. In this way, the amplitude spectroscopy technique complements frequency spectroscopy: although a less direct approach, it allows one to probe the energy level structure of a quantum system over extraordinarily large (even practically prohibitive) bandwidths by circumventing many of the challenges associated with a frequency-based approach.

In general, the spectroscopy diamonds arise due to an interplay between the static flux detuning $\delta f_{\rm dc}$ and driving amplitude V. As described in Sections 4.2 and 4.3, transitions occur when an avoided crossing is reached for a particular set of values ($\delta f_{\rm dc}$,V). For example, at a flux detuning $\delta f_{\rm dc}^{*}$, the diamond boundaries occur at $V = V_1, V_2, V_3....$ (Fig. 19 A and C). The Mach-Zehnder interference due to a phase accumulation $\Delta\theta_{q,q'}$ at a given avoided crossing $\Delta_{q,q'}$ can be modulated by varying both $\delta f_{\rm dc}$ and V.

There are two important contributions to the diamond spectroscopy patterns: LZS-mediated transitions and intrawell relaxation. In Fig. 19D, we show a subset of the diamond interference pattern in Fig. 19A. Arrows indicate lines of constant phase accumulation $\Delta\theta_{q,q'} = (2N-1)\pi$ in ($\delta f_{\rm dc}$,V)-space that leads to LZS transitions at each of the three listed avoided crossings, $\Delta_{0,0}$, $\Delta_{0,1}$, and $\Delta_{1,0}$. Where these lines cross, competition (coordination) between avoided crossings act to suppress (enhance) the net transition rate between pairs of energy levels. These crossing lines are the reason for the checkerboard patterns observed inside and outside the diamonds.

The second contribution, intrawell relaxation, provides another means to connect energy levels and results in both cooling and population inversion. In Section 4.4, Fig. 18C, $\Delta_{0,1}$ mediated the transition $|0L\rangle \rightarrow |1R\rangle$, and intrawell relaxation then mediated the transition $|1R\rangle \rightarrow |0R\rangle$; the net result was cooling, since the flux $\delta f_{\rm dc}$ was positive, making $|0R\rangle$ the ground state. However, in Fig. 19D $\delta f_{\rm dc}$ is negative. Furthermore, in the upper-right corner of Fig. 19D, both crossings $\Delta_{0,1}$ and $\Delta_{1,0}$ are accessed. In the bright red regions, $\Delta_{0,1}$ still tends to cause transitions $|0L\rangle \rightarrow |1R\rangle$, and relaxation puts that population in state $|0R\rangle$. However, the interference condition at $\Delta_{1,0}$ on the other side of the energy level diagram (Fig. 19C) tends to keep the population in $|0R\rangle$. Therefore, population builds in state $|0R\rangle$, the first excited state for negative flux detuning, resulting in strong population inversion. Varying the interference conditions at $\Delta_{0,1}$ and $\Delta_{1,0}$ by changing ($\delta f_{\rm dc}$,V) causes the observed modulation between population inversion and cooling.

We have developed several techniques for extracting information about the energy levels from the spectroscopy interference patterns [50, 51]. The key metrics are the positions of the avoided crossings in flux, the values of the splittings $\Delta_{q,q'}$, and the slopes of the energy levels. With this information, one can reconstruct a large portion of the energy level diagram.

The positions of the avoided crossings can be determined precisely from the diamond boundaries, because the onset of each diamond is associated with LZS transitions at a particular level crossing. The splitting of each avoided crossing can be obtained essentially by fitting the LZS formula in Eq. 134 to the Mach-Zehnder interference patterns. Alternatively, one can study the dynamical population transfer between states using the pulsed, short-time implementation of amplitude spectroscopy [50].

The energy level slopes can be determined by two means. The first is by relating the separation between interference nodes to the expected phase accumulation $\Delta\theta_{12}$, since the phase

accumulation depends sensitively on the energy-level slope. Alternatively, we show with Rudner *et al.* in Ref. [51] that the two-dimensional Fourier transform of the diamond patterns yields a family of *one-dimensional* sinusoids in Fourier space; the periods of these sinusoids are related to the energy-level slopes. The intuition is that the Fourier transform inverts the energy domain of the spectroscopy to the time domain (scaled by $\hbar$). This means that the sinusoids in Fourier space image the time-dependence of the quantum phase of the qubit, which, in turn, depends sensitively on the energy-level slopes.

Using amplitude spectroscopy, we were able to scan the energy level diagram continuously beyond the fourth energy-level avoided crossing ($\Delta_{0,0} \ldots \Delta_{0,4}$, $\Delta_{4,0}$) with splitting values ranging from $\Delta_{0,0} \approx 0.01$ GHz to $\Delta_{0,4}, \Delta_{4,0} \approx 2.2$ GHz [50]. The equivalent information obtained using frequency spectroscopy would have required scanning frequencies from 0.01 GHz out to beyond 100 GHz (each avoided crossing is separated by approximately 25 GHz). Remarkably, with amplitude spectroscopy, the entire scan performed in Fig. 19A was performed at a fixed frequency $\nu = 185$ MHz. The scan in Fig. 19B shows the amplitude spectroscopy of the same system for a fixed frequency $\nu = 700$ MHz, clearly in the discrete resonance limit. The resonance condition adds another constraint, making a more complex and interesting checkerboard pattern.

4.6 Summary and applications

Strongly driving a superconducting artificial atom through an avoided level crossing results in a Landau-Zener-Stückelberg transition, which, in general, creates a superposition of atomic states whose weighting depends on the size of the avoided crossing and the velocity with which it is traversed. In this sense, as we discussed in Section 4.2, the LZS mechanism acts as a beamsplitter for artificial atoms.

In Section 4.3, we described how harmonically driving the system cascades two LZS transitions per driving period, resulting in an atomic analog to a Mach-Zehnder interferometer. The relative phase acquired between LZS transitions is the interference phase of the interferometer, and it is tunable by the driving amplitude. The buildup of population over many driving periods exhibits Stückelberg oscillations as a function of the driving amplitude (interference phase) due to the cascaded Mach-Zehnder-type interference effect. To observe these oscillations, the coherence time must only be longer than the small portion of the drive period when the interference phase accrues, and the relaxation time must be long enough to maintain the population until readout.

The total phase accumulated over one period, in contrast, is amplitude independent. For coherence times longer than the drive period, cascaded interferometers yield a net population change when this round-trip phase accumulation is $2\pi n$ per driving period, a condition which can be viewed as the "time-domain" counterpart to the n-photon resonance condition $nh\nu = \varepsilon_{0,n}$. By making the drive period commensurate with the coherence time, we showed that we could still observe the Stückelberg oscillations, even though the discrete resonances were no longer discernable.

We utilized strong driving and the LZS mechanism with higher-energy levels to achieve both cooling and population inversion in our artificial atom. In Section 4.4, we described using a microwave pumping scheme to cool the atomic degrees of freedom a factor 10-100 times colder than the ambient dilution refrigerator temperature. The scheme involved pumping unwanted thermal population to an ancillary excited state, from which it relaxed to the ground state. In Section 4.5, we showed that by reversing the order, we could pump population through an

ancillary state to achieve inversion.

The energy level structure can be probed over extraordinarily large bandwidth using amplitude spectroscopy in Section 4.5. Since the LZS mechanism and Mach-Zehnder interference are sensitive to the defining features in the energy level diagram (energy band slopes, level splittings, and their locations), the interference patterns that result from sweeping the amplitude are a "fingerprint" of the artificial atom's energy spectrum. Using amplitude spectroscopy at a fixed driving frequency of only 185 MHz, we could access continuously multiple energy levels from about 10 MHz out to beyond 120 GHz.

Large-amplitude driving and the LZS mechanism have application to quantum information science and technology. Active cooling has utility as an "entropy pump" in state initialization and refreshing ancilla qubits in quantum error correction protocols. Amplitude spectroscopy provides an means to ascertain over large bandwidth the energy level structure of a qubit system beyond the lowest two levels. The Mach-Zehnder-type interference can facilitate nonadiabatic control schemes, in which the quantum interference at an avoided crossing is used to achieve state transitions that approach the intrinsic coupling rate Δ. In cold atoms and molecules, this kind of non-adiabatic control has been used to drive transitions that would otherwise be challenging to realize in a weak-driving limit. In addition, this type of non-adiabatic detuning is widely used for the implementation of single-qubit Z gates (phase gates) and coupled-qubit controlled-phase gates based on changing the energy-level separation of qubit states (although not generally involving Mach-Zehnder-type interference).

5 Acknowledgements

I wish to thank Simon Gustavsson, Jamie Kerman, and Terry Orlando for a careful reading of this manuscript. I also wish to acknowledge David Berns, Jonas Bylander, Janice Lee, Leonya Levitov, Yasunobu Nakamura, Mark Rudner, Sergio Valenzuela, Tsuyoshi Yamamoto, Fei Yan, Fumiki Yoshihara, and my other co-workers at MIT and Lincoln Laboratory for numerous discussions and collaborative works that have led to this manuscript.

Appendices

A Quantum conjugate operators $\hat{n}$ and $\hat{\phi}$

The correspondence between classical and quantum variables and their dynamics has been discussed in detail elsewhere Ref. [195, 196]. In this Appendix, we present several derivatives of those works that are relavent to the present discussion.

The general prescription is to start with a classical representation of the circuit using circuit network theory. This generally comprises a network of branches and nodes. One chooses either the branch or node variables, and proceeds to derive the classical Hamiltonian. For example, the sum of the branch energies in terms of the branch variables will yield the classical Hamiltonian. Alternatively, one can determine the Lagrangian of the classical circuit to obtain its classical equations of motion, and then proceed to derive the classical Hamiltonian. In either case, the classically conjugate variables satisfying a Poisson bracket equation are "transitioned" via the correspondence principle to quantum operators satisfying a quantum commutation relation.

For our purposes here, we take the number of Cooper pairs $\hat{n}$ and the Josephson phase $\hat{\phi}$ as the quantum operators [197]:

$$\hat{n}|n\rangle = n|n\rangle \tag{144}$$

$$\hat{\phi}|\phi\rangle = \phi|\phi\rangle \tag{145}$$

$$[\hat{\phi}, \hat{n}] = i. \tag{146}$$

As conjugate operators, their eigenstates are related through the Fourier transforms,

$$|\, n\rangle = \frac{1}{\sqrt{2\pi}} \int_0^{2\pi} d\phi\; e^{-i\hat{n}\phi}|\phi\rangle \tag{147}$$

$$|\, \phi\rangle = \frac{1}{\sqrt{2\pi}} \sum_n\; e^{in\hat{\phi}}|n\rangle. \tag{148}$$

The number operator $\hat{n}$ and the phase operator $\hat{\phi}$ are then expressed in their respective conjugate spaces via the relations

$$\hat{n}|\phi\rangle = |\phi\rangle \frac{1}{i}\frac{\partial}{\partial\phi}\langle\phi| \tag{149}$$

$$\hat{\phi}|n\rangle = |n\rangle i\frac{\partial}{\partial n}\langle n|. \tag{150}$$

Translation of the number and phase is represented by the following relations,

$$e^{in_0\hat{\phi}}|n\rangle = |n + n_0\rangle \tag{151}$$

$$e^{-i\hat{n}\phi_0}|\phi\rangle = |\phi - \phi_0\rangle \tag{152}$$

Based on these relations, we can make the following equivalence:

$$\cos\hat{\phi} = \frac{1}{2}\left(e^{i\hat{\phi}} + e^{-i\hat{\phi}}\right) \tag{153}$$

$$= \frac{1}{2}\sum_n |n+1\rangle\langle n| + |n-1\rangle\langle n| \tag{154}$$

$$= \frac{1}{2}\sum_n |n+1\rangle\langle n| + |n\rangle\langle n+1| \tag{155}$$

B Two-level system Hamiltonian in the strong driving limit

The two-level-system dynamics in the strong driving regime can be obtained by moving to a non-uniformly rotating frame with sinusoidal rotation frequency. One then rotates a second time to make a resonance approximation.

Applying a classical RF field of amplitude A, the Hamiltonian is

$$\mathcal{H} = -\frac{1}{2}\begin{pmatrix} \varepsilon + A\cos\omega t & \Delta \\ \Delta & -\varepsilon - A\cos\omega t \end{pmatrix}. \tag{156}$$

We use $\cos\omega t$ rather than $\sin\omega t$ for pedagogical reasons only. We are interested in the general case which includes the strongly driven regime, $|a| \geq \hbar\omega$ and $|a| \geq \varepsilon, \Delta$. Defining the transformation,

$$R_z(\Theta) = \exp\left[-i\frac{\sigma_z}{2}\Theta\right] \tag{157}$$

$$\tilde{\mathcal{H}} \equiv R_z(\Theta)\mathcal{H}R_z(-\Theta) + \frac{\sigma_z}{2}\hbar\Omega(t) \tag{158}$$

$$\Omega(t) = \frac{A}{\hbar}\cos(\omega t) \tag{159}$$

$$\Theta = \int_0^t dt'\Omega(t') = \frac{A}{\hbar\omega}\sin\omega t \equiv -\lambda\sin\omega t \tag{160}$$

where $\lambda = A/\hbar\omega$ is a dimensionless scaling of the RF amplitude to the drive frequency, we can obtain the form for the rotated Hamiltonian,

$$\tilde{\mathcal{H}} = -\frac{1}{2}\begin{pmatrix} \varepsilon & e^{-i\Theta}\Delta \\ e^{i\Theta}\Delta & -\varepsilon \end{pmatrix} = -\frac{1}{2}\begin{pmatrix} \varepsilon & e^{-i\lambda\sin\omega t}\Delta \\ e^{i\lambda\sin\omega t}\Delta & -\varepsilon \end{pmatrix}. \tag{161}$$

The generating function for the Bessel functions of the first kind of order n is:

$$e^{x(t-1/t)/2} = \sum_{n=-\infty}^{\infty} J_n(x)t^n \tag{162}$$

Identifying $t \equiv \exp(-i\omega t)$ and $x \equiv \lambda$, one obtains the off-diagonal factor:

$$\Delta e^{-i\lambda \sin \omega t} = \sum_{n=-\infty}^{\infty} \Delta J_n(\lambda) e^{i\omega n t} \tag{163}$$

$$\equiv \sum_{n=-\infty}^{\infty} \Delta_n e^{i\omega n t} \tag{164}$$

$$\Delta_n = \Delta J_n(\lambda) \tag{165}$$

$$\tilde{\mathcal{H}} = -\frac{1}{2} \begin{pmatrix} \varepsilon & \sum_{n=-\infty}^{\infty} \Delta_n e^{i\omega n t} \\ \sum_{n=-\infty}^{\infty} \Delta_n e^{-i\omega n t} & -\varepsilon \end{pmatrix}. \tag{166}$$

For flux biases $n\hbar\omega \approx \varepsilon$, only the n^{th} Fourier harmonic of the off-diagonal term dominates. This is effectively a resonance approximation. In its current form, all off-diagonal terms oscillate (rotate) at a large frequency compared with the present rotating frame. By rotating at one of the Fourier harmonic frequencies, $\Omega' = n\omega$, one reduces the Hamiltonian to

$$\tilde{\mathcal{H}}_n = -\frac{1}{2} \begin{pmatrix} \varepsilon - \hbar n\omega & \sum_{m=-\infty}^{\infty} \Delta_m e^{i\omega(m-n)t} \\ \sum_{m=-\infty}^{\infty} \Delta_m e^{-i\omega(m-n)t} & -(\varepsilon - \hbar n\omega) \end{pmatrix}, \tag{167}$$

in which only $m = n$ term will exist within the resonance approximation. It is in this limit that the diagonal energy terms are small compared with the coupling. Defining $\varepsilon_n \equiv \varepsilon - \hbar n\omega$, one obtains in the resonance approximation,

$$\tilde{\mathcal{H}}_n = -\frac{1}{2} \begin{pmatrix} \varepsilon_n & \Delta_n \\ \Delta_n & -\varepsilon_n \end{pmatrix}. \tag{168}$$

C Summary of noise spectroscopy during free- and driven-evolution

	Free-evolution decoherence	**Driven-evolution Decoherence**
Working frame	Qubit frame	Rotating frame
Quantization axis	z'-axis	X-axis
Nutation freq.	level splitting $\nu_{\rm q}$	Rabi frequency $\nu_{\rm R}$
	Longitudinal relaxation	
Method	Inversion recovery [30, 187]	Spin locking - $T_{1\rho}$ [7, 186]
Process	$T_1\,(=1/\Gamma_1)$	$T_{1\rho}\,(=1/\Gamma_{1\rho})$
Longitudinal decay	z'-axis	X-axis
Starting state	$\vert+z'\rangle$	$\vert\pm X\rangle$
Steady state	$\vert-z'\rangle$	$\vert\langle\hat{\sigma}_X\rangle=0\rangle$
Decay rate	Γ_1 (exponential)	$\Gamma_{1\rho}$ (exponential)
Decay law	$\exp\{-\Gamma_1\tau\}, \Gamma_1=\frac{1}{2}\,S_{x'}(\nu_{\rm q})$	$\exp\{-(\frac{1}{2}\,\Gamma_1+\Gamma_\nu)\tau\}, \Gamma_\nu=\frac{1}{2}\,S_{z'}(\nu_{\rm R})$
Noise susceptibility		
• in general	$S_{\perp z'}(\nu_{\rm q})$	$S_{\perp X}(\nu_{\rm R})$
• flux qubit	$S_{x'}(\nu_{\rm q})$	$S_{x'}(\nu_{\rm q}\pm\nu_{\rm R}\approx\nu_{\rm q}), S_{z'}(\nu_{\rm R})$
Noise of interest	$S_{x'}(\nu_{\rm q})$	$S_{z'}(\nu_{\rm R})$
	Transverse decoherence	
Method	FID [30, 8], CPMG [11]	Rabi [11, 188], Rotary echo [140]
Process	$T_2\,(=1/\Gamma_2)$	$T_{2\rho}\,(=1/\Gamma_{2\rho})$
Transverse decay	$x'-y'$ plane	$Y-Z$ plane
Starting state	e.g., $\vert\pm x', \pm y'\rangle$	$\vert-Z\rangle$ (= $\vert-z'\rangle$)
Steady state	$\vert\langle\hat{\sigma}_{x',y'}\rangle=0\rangle$	$\vert\langle\hat{\sigma}_{Y,Z}\rangle\approx0\rangle$
Decay rate		
• Bloch-Redfield	$\Gamma_2=\frac{1}{2}\,\Gamma_1+\Gamma_\varphi$ (exp.)	$\Gamma_{2\rho}=\frac{1}{2}\,\Gamma_{1\rho}+\Gamma_{\varphi\rho}$ (exp.)
• $1/f$-type noise	exp.$\times$Gaussian (linear)	exp.$\times$Gaussian$\times$algebraic (quadratic)
Decay law (FID/Rabi)	$\exp\{-\frac{1}{2}\,\Gamma_1\tau-\frac{1}{2}\,\langle\delta\nu^2\rangle\tau^2\}$ $\times\cos(2\pi\Delta\nu\tau)$	$\exp\{-(\frac{3}{4}\,\Gamma_1+\frac{1}{2}\,\Gamma_\nu)\tau-\frac{1}{2}\,\langle\delta\nu_{\rm R}^2\rangle\tau^2\}$ $\times[1+(\frac{\langle\delta\nu^2\rangle}{\nu_{\rm R}}\tau)^2]^{-1/4}\cos(2\pi\nu_{\rm R}\tau)$
Noise susceptibility		
• in general	Γ_1: $S_{\perp z'}(\nu_{\rm q})$; Γ_φ: $\Delta\nu$ inhom.	$\Gamma_{1\rho}$: $S_{\perp X}(\nu_{\rm R})$; $\Gamma_{\varphi\rho}$: $\nu'_{\rm R}$ inhom.
• flux qubit	Γ_1: $S_{x'}(\nu_{\rm q})$; Γ_φ: $\Delta\nu$ inhom.	$\Gamma_{1\rho}$: $S_{x'}(\nu_{\rm q}\pm\nu_{\rm R}\approx\nu_{\rm q}), S_{z'}(\nu_{\rm R})$; $\Gamma_{\varphi\rho}$: $S_{x'}(\nu_{\rm q})$, $\nu_{\rm R}$ and $\Delta\nu$ inhom.
Noise of interest	$\langle\delta\nu^2\rangle$	$\Gamma_\nu=\frac{1}{2}\,S_{z'}(\nu_{\rm R})$

Table 3: *Comparison of decohering properties of a superconducting flux qubit during free evolution and driven evolution (weak and resonant driving).*

References

[1] J. Clarke and F.K. Wilhelm, Superconducting quantum bits, Nature **453**, 1031-1042 (2008).

[2] D.P. DiVincenzo, "Quantum computation," Science **270**, 255-261 (1995).

[3] Y. Nakamura, Y.A. Pashkin, J.S. Tsai, Coherent control of macroscopic quantum states in a single-Cooper-pair box, Nature **398**, 786-788 (1999).

[4] D. Vion, A. Aassime, A. Cottet, P. Joyez, H. Pothier, C. Urbina, D. Esteve, and M. H. Devoret, Manipulating the quantum state of an electrical circuit, Science **296**, 886-889 (2002).

[5] G. Burkard, R.H. Koch, D.P. DiVincenzo, Multi-level quantum description of decoherence in superconducting flux qubits, Phys. Rev. B **69**, 064503 (2004).

[6] P. Bertet, I. Chiorescu, G. Burkard, K. Semba, C.J.P.M. Harmans, D.P. DiVincenzo, J.E. Mooij, Dephasing of a superconducting qubit induced by photon noise, Phys. Rev. Lett. **95**, 257002 (2005).

[7] G. Ithier, E. Collin, P. Joyez, P.J. Meeson, D. Vion, D. Esteve, F. Chiarello, A. Shnirman, Y. Makhlin, J. Schriefl, G. Schön, Decoherence in a superconducting quantum bit circuit, *Phys. Rev. B* **72**, 134519 (2005).

[8] F. Yoshihara, K. Harrabi, A.O. Niskanen, Y. Nakamura, and J.S. Tsai, Decoherence of flux qubits due to $1/f$ flux noise, *Phys. Rev. Lett.* **97**, 167001 (2006).

[9] J. Koch, T.M. Yu, J. Gambetta, A.A. Houck, D.I. Schuster, J. Majer, A. Blais, M.H. Devoret, S.M. Girvin, R.J. Schoelkopf "Charge insensitive qubit design derived from the Cooper pair box," Phys. Rev. A **76**, 042319 (2007).

[10] A.A. Houck, J.A. Schreier, B.R. Johnson, J.M. Chow, J. Koch, J.M. Gambetta, D.I. Schuster, L. Frunzio, M.H. Devoret, S.M. Girvin, R.J. Schoelkopf "Controlling the spontaneous emission of a superconducting transmon qubit," Phys. Rev. Lett. **101**, 080502 (2008).

[11] J. Bylander, S. Gustavsson, F. Yan, F. Yoshihara, K. Harrabi, G. Fitch, D.G. Cory, Y. Nakamura, J.S. Tsai, and W.D. Oliver, Noise spectroscopy through dynamical decoupling with a superconducting flux qubit, Nature Physics **7**, 565-570 (2011).

[12] H. Paik, D.I. Schuster, L.S. Bishop, G. Kirchmair, G. Catelani, A.P. Sears, B.R. Johnson, M.J. Reagor, L. Frunzio, L.I. Glazman, S.M. Girvin, M.H. Devoret, R.J. Schoelkopf, Observation of High Coherence in Josephson Junction Qubits Measured in a Three-Dimensional Circuit QED Architecture, Phys. Rev. Lett. **107**, 240501 (2011).

[13] C. Rigetti, J.M. Gambetta, S. Poletto, B.L.T. Plourde, J.M. Chow, A.D. Corcoles, J.A. Smolin, S.T. Merkel, J.R. Rozen, G.A. Keefe, M.B. Rothwell, M.B. Ketchen, M. Steffen, Phys. Rev. B **86**, 100506 (2012).

[14] M. Steffen, Viewpoint: superconducting qubits are getting serious, Physics **4**, 103 (2011).

[15] A.G. fowler, A.M. Stephens, and P. Groszkowski, High threshold universal quantum computation on the surface code, Phys. Ref. A **80**, 052312 (2009).

[16] D.P. DiVincenzo, Fault tolerant architectures for superconducting qubits, Phys. Scr. T **137**, 014020 (2009).

[17] A.G. Fowler, M. Mariantoni, J.M. Martinis, A.N. Cleland, Surface codes: towards practical large-scale quantum computation, Phys. Rev. A **86**, 032324 (2012).

[18] E. Lucero, M. Hofheinz, M. Ansmann, R.C. Bialczak, N. Katz, M. Neeley, A. D. OConnell, H. Wang, A. N. Cleland, and J.M. Martinis, High-Fidelity Gates in a Single Josephson Qubit, Phys. Rev. Lett. **100**, 224701 (2008).

[19] J.M. Chow, J.M. Gambetta, L. Tornberg, J. Koch, L.S. Bishop, A.A. Houck, B.R. Johnson, L. Funzio, S.M. Girvin, R.J. Schoelkopf, Randomized Benchmarking and Process Tomography for Gate Errors in a Solid-State Qubit, Phys. Rev. Lett. **102**, 119901 (2009).

[20] J.M. Chow, L. DiCarlo, J.M. Gambetta, F. Motzoi, L. Funzio, S.M. Girvin, R.J. Schoelkopf, Optimized driving of superconducting artificial atoms for improved single-qubit gates, Phys. Rev. A **82**, 040305 (2010).

[21] S. Gustavsson, O. Zwier, J. Bylander, F. Yan, F. Yoshihara, Y. Nakamura, T.P. Orlando, W.D. Oliver, Improving quantum gate fidelities by using a qubit to measure microwave pulse distortions, arXiv:1211.2175 (2011).

[22] T. Yamamoto, M. Neeley, E. Lucero, R.C. Bialczak, J. Kelly, M. Lenander, M. Mariantoni, A.D. OConnell, D. Sank, H. Wang, M. Weides, J. Wenner, Y. Yin, A.N. Cleland, J.M Martinis, Quantum process tomography of two-qubit controlled-Z and controlled-NOT gates using superconducting phase qubits, Phys. Rev. B **82**, 184515 (2010).

[23] J.M. Chow, J.M. Gambetta, A.D. Corcoles, S.T. Merkel, J.A. Smolin, C. Rigetti, S. Poletto, G.A. Keefe, M.B. Rothwell, J.R. Rozen, M.B. Ketchen, M. Steffen, Universal Quantum Gate Set Approaching Fault-Tolerant Thresholds with Superconducting Qubits, Phys. Rev. Lett. **109**, 060501 (2012).

[24] J.R. Friedman, V. Patel, W. Chen, S. K. Tolpygo, J. E. Lukens, Quantum superposition of distinct macroscopic states, Nature **406**, 43-46 (2000).

[25] C.H. van der Wal, A. C. J. ter Haar, F. K. Wilhelm, R. N. Schouten, C. J. P. M. Harmans, T. P. Orlando, S. Lloyd, J. E. Mooij, Quantum superposition of macroscopic persistent-current states, Science **290**, 773-777 (2000).

[26] A.J. Berkley, H. Xu, R. C. Ramos, M. A. Gubrud, F. W. Strauch, P. R. Johnson, J. R. Anderson, A. J. Dragt, C. J. Lobb, F. C. Wellstood, Entangled macroscopic quantum states in two superconducting qubits, Science **300**, 1548-1550 (2003).

[27] Y. Nakamura, Y.A. Pashkin, J.S. Tsai, Rabi oscillations in a large Josephson-junction charge two-level system, Phys. Rev. Lett. **87**, 246601 (2001).

[28] Y. Yu, S. Han, X. Chu, S.-I. Chu, Z. Wang, Coherent temporal oscillations of macroscopic quantum states in a Josephson junction, Science **296**, 889-892 (2002).

[29] J.M. Martinis, S. Nam, J. Aumentado, C. Urbina, Rabi oscillations in a large Josephson-junction qubit, Phys. Rev. Lett. **89**, 117901 (2002).

[30] I. Chiorescu, Y. Nakamura, C.J.P.M. Harmans, J.E. Mooij, Coherent quantum dynamics of a superconducting flux qubit, Science **299**, 1869-1871 (2003).

[31] J. Claudon, F. Balestro, F.W.J. Hekking, O. Buisson, Coherent oscillations in a superconducting multilevel quantum system, Phys. Rev. Lett. **93**, 187003 (2004).

[32] B.L.T. Plourde, T.L. Robertson, P.A. Reichardt, T. Hime, S. Linzen, C.-E. Wu, and John Clarke, Flux qubits and readout device with two independent flux lines, Phys. Rev. B **72**, 060506(R) (2005).

[33] S.Saito, T. Meno, M. Ueda, H. Tanaka, K. Semba, and H. Takayanagi, Parametric control of a superconducting flux qubit, Phys. Rev. Lett. **96**, 107001 (2006).

[34] J. Lisenfeld, A. Lukashenko, M. Ansmann, J.M. Martinis, and A.V. Ustinov, Temperature dependence of coherent oscillations in josephson phase qubits, Phys. Rev. Lett. **99**, 170504 (2007).

[35] H. Paik, S.K. Dutta, R.M. Lewis, T.A. Palomaki, B.K. Cooper, R.C. Ramos, H. Xu, A.J. Dragt, J.R. Anderson, C.J. Lobb, F.C. Wellstood, Decoherence in dc SQUID phase qubits, Phys. Rev. B **77**, 214510 (2008).

[36] Z. Kim, B. Suri, V. Zaretskey, S. Novikov, K.D. Osborn, A. Mizel, F.C. Wellstood, B.S. Palmer Decoupling a Cooper-pair box to enhance the lifetime to 0.2 ms, Phys. Rev. Lett. **106**, 120501 (2011).

[37] A. Izmalkov, M. Grajcar, E. Il'ichev, N. Oukhanski, Th. Wagner, H.-G. Meyer, W. Krech, M. H. S. Amin, A. Maassen van den Brink and A. M. Zagoskin, Observation of macroscopic Landau-Zener transitions in a superconducting device, Europhys. Lett. **65**, 844-849 (2004).

[38] W.D. Oliver, Y. Yu, J.C. Lee, K.K. Berggren, L.S. Levitov, and T.P. Orlando, Mach-Zehnder interferometry in a strongly driven superconducting qubit Science **310**, 1653 (2005).

[39] D. M. Berns, W. D. Oliver, S. O. Valenzuela, A. Shytov, K. K. Berggren, L. Levitov, and T. P. Orlando, Coherent quasiclassical dynamics of a persistent-current qubit, Phys. Rev. Lett. **97**, 150502 (2006).

[40] M. Sillanpaa, T. Lehtinen, A. Paila, Yu. Makhlin, P. Hakonen, Continuous-time monitoring of Landau-Zener interference in a Cooper-pair box, Phys. Rev. Lett. **96**, 187002 (2006).

[41] C.M. Wilson, T. Duty, F. Persson, M. Sandberg, G. Johansson, and P. Delsing, Coherent times of dressed states of a superconducting qubit under extreme driving, Phys. Rev. Lett. **98**, 257003 (2007).

[42] A. Izmalkov, S.J.W. van der Ploeg, S.N. Shevchenko, M. Grajcar, E. Il'ichev, U. Huebner, A.N. Omelyanchouk, and H.-G.Meyer, Consistency of ground state and spectroscopic measurements on flux qubits, Phys. Rev. Lett. **101**, 017003 (2008).

[43] S.N. Shevchenko, S. Ashhab, F. Nori, Landau-Zener-Stueckelberg interferometry, Phys. Rep. **492**, 1-30 (2010).

[44] S. O. Valenzuela, W. D. Oliver, D. M. Berns, K. K. Berggren, L. S. Levitov, T. P. Orlando, Microwave-induced cooling of a superconducting qubit, Science **314**, 1589-1592 (2006).

[45] A.O. Niskanen, Y. Nakamura, and J.P. Pekola, Information entropic superconducting microcooler, Phys. Rev. B **76**, 174523 (2007).

[46] J.Q. You, Yu-xi Liu, and Franco Nori, Simultaneous cooling of an artificial atom and its neighboring quantum system, Phys. Rev. Lett. **100**, 047001 (2008).

[47] M. Grajcar, S.H.W. van der Ploeg, A. Izmalkov, E. Il'ichev, H.-G. Meyer, A. Fedorov, A. Shnirman, and G. Schon, Sisyphus cooling and amplification by a superconducting qubit, Nature Phys. **4**, 612-616 (2008).

[48] J.E. Johnson, C. Macklin, D.H. Slichter, R. Vijay, E.B. Weingarten, J. Clarke, I. Siddiqi, Heralded state preparation in a superconducting qubit, Phys. Rev. Lett. **109**, 050506 (2012).

[49] D. Riste, J.G. van Leeuwen, H.S. Ku, K.W. Lehnert, L. DiCarlo, Initialization by measurement of a superconducting quantum bit circuit, Phys. Rev. Lett. **109**, 050507 (2012).

[50] D.M. Berns, M.S. Rudner, S.O. Valenzuela, K. K. Berggren, W. D. Oliver, L. S. Levitov, T. P. Orlando, Amplitude spectroscopy of a solid-state artificial atom, Nature **455**, 51-57 (2008).

[51] M.S. Rudner, A.V. Shytov, L. S. Levitov, D. M. Berns, W. D. Oliver, S. O. Valenzuela, T. P. Orlando, Quantum phase tomography of a strongly driven qubit, Phys. Rev. Lett. **101**, 190502 (2008).

[52] K.V.R.M. Murali, Z. Dutton, W.D. Oliver, D.S. Crankshaw, and T.P. Orlando, "Probing decoherence with electromagnetically induced transparency in superconductive quantum circuits," Phys. Rev. Lett. **93**, 087003 (2004).

[53] Z. Dutton, K.V.R.M. Murali, W.D. Oliver, and T.P. Orlando, Electromagnetically induced transparency in superconducting quantum circuits: effects of decoherence, tunneling, and multilevel crosstalk, Phys. Rev. B **73**, 104516 (2006).

[54] W.R. Kelly, Z. Dutton, J. Schlafer, B. Mookerji, T.A. Ohki, J.S. Kline, D.P. Pappas, Direct observation of coherent population trapping in a superconducting artificial atom, Phys. Rev. Lett. **104**, 163601 (2010).

[55] P.J. Leek, J.M. Fink, A. Blais, R. Bianchetti, M. Goppl, J.M. Gambetta, D.I. Schuster, L. Frunzio, R.J. Schoelkopf, and A. Wallraff, Observation of Berry's phase in a solid-state qubit, Science **318**, 1889-1892 (2007).

[56] I. Chiorescu, P. Bertet, K. Semba, Y. Nakamura, C.J.P.M. Harmans, and J.E. Mooij, Coherent dynamics of a flux qubit coupled to a harmonic oscillator, Nature **431**, 159-162 (2004).

[57] A. Wallraff, D. I. Schuster, A. Blais, L. Frunzio, R.-S. Huang, J. Majer, S. Kumar, S. M. Girvin and R. J. Schoelkopf, Strong coupling of a single photon to a superconducting qubit using circuit quantum electrodynamics, Nature **431**, 162-167 (2004).

[58] J. Johansson, S. Saito, T. Meno, H. Nakano, M. Ueda, H. Tanaka, K. Semba, and H. Takayanagi, Vacuum rabi oscillations in a macroscopic superconducting qubit LC oscillator system, Phys. Rev. Lett. **96**, 127006 (2006).

[59] F. Deppe, M. Mariantoni, E.P. Menzel, A. Marx, S. Saito, K. Kakuyanagi, H. Tanaka, T. Menon, K. Semba, H. Takayanagi, E. Solano, and R. Gross, Two-photon probe of the Jaynes-Cummings model and controlled symmetry breaking in circuit QED, Nature Phys. **4**, 686-691 (2008).

[60] J.M. Fink, M. Goppl, M. Baur, R. Bianchetti, P.J. Leek, A. Blais, and A. Wallraff, Climbing the Jaynes-Cummings ladder and observing its root n nonlinearity in a cavity QED system, Nature **454**, 315-318 (2008).

[61] A. Fragner, M. Goppl, J.M. Fink, M. Baur, R. Bianchetti, P.J. Leek, A. Blais, and A. Wallraff, Resolving vacuum fluctuations in an electrical circuit by measuring the Lamb shift, Science **322**, 1357-1360 (2008).

[62] M. Hofheinz, E.M. Weig, M. Ansmann, R.C. Bialczak, E. Lucero, M. Neeley, A.D. O'Connell, H. Wang, J.M. Martinis, and A.N. Cleland, Generation of Fock states in a superconducting quantum circuit, Nature **454**, 310-314 (2008).

[63] R.J. Schoelkopf and S.M. Girvin, Wiring up quantum systems, Nature **451**, 664-669 (2008).

[64] Y. Makhlin, G. Schon, A. Shnirman, Quantum-state engineering with Josephson-junction devices, Rev. Mod. Phys. **73**, 357-400 (2001).

[65] J. E. Mooij, The road to quantum computing, Science **307**, 1210-1211 (2005).

[66] T.D. Ladd, F. Jelezko, R. Laflamme, Y. Nakamura, C. Monroe, and J.L. OBrien, Quantum computers, Nature **451**, 664-669 (2008).

[67] T. Hime, P.A. Reichart, B.L.T. Plourde, T.L. Robertson, C.-E. Wu, A.V. Ustinov, and J. Clarke, Solid-state qubits with current-controlled coupling, Science **314**, 1427-1429 (2006).

[68] S.H.W. van der Ploeg, A. Izmalkov, A. Maassen van den Brink, U. Huebner, M. Grajcar, E. Il'ichev, H.-G. Meyer, and A.M. Zagoskin, Controllable coupling of superconducting flux qubits, Phys. Rev. Lett. **98**, 057004 (2007).

[69] A.O. Niskanen, K. Harrabi, F. Yoshihara, Y. Nakamura, S. Lloyd, and J.S. Tsai, Quantum coherent tunable coupling of superconducting qubits, Science **316**, 723-726 (2007).

[70] A.J. Kerman and W.D. Oliver, High-fidelity quantum operations on superconducting qubits in the presence of noise, Phys. Rev. Lett. **101**, 070501 (2008).

[71] J.M. Chow, A.D. Corcoles, J.M. Gambetta, C. Rigetti, B.R. Johnson, J.A. Smolin, J.R. Rozen, G.A. Keefe, M.B. Rothwell, M.B. Ketchen, M. Steffen, Simple All-Microwave Entangling Gate for Fixed-Frequency Superconducting Qubits, Phys. Rev. Lett. **107**, 080502 (2011).

[72] P.C. de Groot, J. Lesnfeld, R.N. Schouten, S. Ashhab, A. Lupascu, C.J.P.M. Harmans, J.E. Mooij, Selective darkening of degenerate transitions demonstrated with two superconducting quantum bits, Nature Phys. **10**, 763-766 (2010).

[73] M.A. Sillanpaa, J.I. Park, and R.W. Simmonds, "Coherent quantum state storage and transfer between two phase qubits via a resonant cavity," Nature **449**, 438-442 (2007).

[74] J. Majer, J.M. Chow, J.M. Gambetta, J. Koch, B.R. Johnson, J.A. Schreier, L. Frunzio, D.I. Schuster, A.A. Houck, A. Wallraff, A. Blais, M.H. Devoret, S.M. Girvin, and R.J. Schoelkopf, "Coupling superconducting qubits via a cavity bus," Nature **449**, 443-447 (2007).

[75] Y.A. Pashkin, T. Yamamoto, O. Astafiev, Y. Nakamura, D. V. Averin, and J. S. Tsai, "Quantum oscillations in two coupled charge qubits," Nature **421**, 823-826 (2003).

[76] T. Yamamoto, Yu. A. Pashkin, O. Astafiev, Y. Nakamura, J. S. Tsai, "Demonstration of conditional gate operation using superconducting charge qubits," Nature **425**, 941-944 (2003).

[77] R. McDermott, R. W. Simmonds, M. Steffen, K. B. Cooper, K. Cicak, K.D. Osborn, S. Oh, D. P. Pappas, J. M. Martinis, "Simultaneous state measurement of coupled Josephson phase qubits," Science **307**, 1299-1302 (2005).

[78] J.H. Plantenberg, P.C. de Groot, C.J.P.M. Harmans, and J.E. Mooij, "Demonstration of controlled-NOT quantum gates on a pair of superconducting quantum bits," Nature **447**, 836-839 (2007).

[79] M. Neeley, R.C. Bialczak, M. Lenander, E. Lucero, M. Mariantoni, A.D. OConnell, D. Sank, H. Wang, M. Weides, J. Wenner, Y. Yin, T. Yamamoto, A.N. Cleland, J.M. Martinis, Generation of three-qubit entangled states using superconducting phase qubits, Nature **467**, 570-573 (2010).

[80] L. DiCarlo, M.D. Reed, L. Sun, B.R. Johnson, J.M. Chow, J.M. Gambetta, L. Frunzio, S.M. girvin, M.H. Devoret, R.J. Schoelkopf, Preparation and measurement of three-qubit entanglement in a superconducting circuit, Nature **467**, 574-578 (2010).

[81] M. Steffen, M. Ansmann, R.C. Bialczak, N. Katz, E. Lucero, R. McDermott, M. Neeley, E.M. Weig, A.N. Cleland, and J. M. Martinis, Measurement of the entanglement of two superconducting qubits via state tomography, Science **313**, 1423-1425 (2006).

[82] M. Steffen, M. Ansmann, R. McDermott, N. Katz, R.C. Bialczak, E. Lucero, M. Neeley, E.M. Weig, A.N. Cleland, and J. M. Martinis, State tomography of capacitively shunted phase qubits with high fidelity, Phys. Rev. Lett. **97**, 050502 (2006).

[83] M. Neeley, M. Ansmann, R.C. Bialczak, M. Hofheinz, N. Katz, E. Lucero, A. O'Connell, H. Wang, A.N. Cleland, and J. M. Martinis, "Process tomography of quantum memory in a Josephson-phase qubit coupled to a two-level state," Nature Phys. **4**, 523-526 (2008).

[84] J.M. Chow, J.M. Gambetta, A.D. Corcoles, S.T. Merkel, J.A. Smolin, C.Rigetti, S. Poletto, G.A. Keefe, M.B. Rothwell, J.R. Rozen, M.B. Ketchen, M. Steffen, Universal quantum gate set approaching fault-tolerant thresholds with superconducting qubits, Phys. Rev. Lett. **109**, 060501 (2012).

[85] R.J. Schoelkopf, P. Wahlgren, A.A. Kozhevnikov, P. Delsing, D.E. Prober, "The radio-frequency single-electron transistor (RF-SET): a fast and ultrasensitive electrometer," Science **280**, 1238-1242 (1998).

[86] I. Siddiqi, R. Vijay, F. Pierre, C.M. Wilson, M. Metcalfe, C. Rigetti, L. Frunzio, and M.H. Devoret, "RF-driven Josephson bifurcation amplifier for quantum measurement," Phys. Rev. Lett. **93**, 297992 (2004).

[87] J.C. Lee, W.D. Oliver, T.P. Orlando, K.K. Berggren, "Resonant readout of a persistent current qubit," IEEE Trans. Appl. Supercond. **15**, 841-844 (2004).

[88] I. Siddiqi, R. Vijay, F. Pierre, C.M. Wilson, L. Frunzio, M. Metcalfe, C. Rigetti, R.J Schoelkopf, M.H. Devoret, D. Vion, D. Esteve, "Direct observation of dynamical bifurcation between two driven oscillation states of a Josephson junction," Phys. Rev. Lett. **94**, 027005 (2005).

[89] M.A. Sillanpää, T. Lehtinen, A. Paila, Yu. Makhlin, L. Roschier, P.J. Hakonen, "Direct observation of a Josephson capacitance," Phys. Rev. Lett. **95**, 206806 (2005).

[90] N. Katz, M. Ansmann, R.C. Bialczak, E. Lucero, R. McDermott, M. Neeley, M. Steffen, E.M. Weig, A.N. Cleland, J.M. Martinis, A.N. Korotkov, "Coherent state evolution in a superconducting qubit from partial-collapse measurement," Science 312, 1498-1500 (2006).

[91] J.C. Lee, W.D. Oliver, K.K. Berggren, T.P. Orlando, "Nonlinear resonant behavior of a dispersive readout circuit for a superconducting flux qubit," Phys. Rev. B **75**, 144505 (2007).

[92] A. Lupascu, S. Saito, T. Picot, P.C. de Groot, C.J.P.M. Harmans, J.E. Mooij, "Quantum non-demolition measurement of a superconducting two-level system," Nature Phys. **3**, 119-123 (2007).

[93] T. Yamamoto, K. Inomata, M. Watanabe, K. Matsuba, T. Miyazaki, W.D. Oliver, Y. Nakamura, and J.S. Tsai, "Flux-driven Josephson parametric amplifier," Appl. Phys. Lett. **93**, 042510 (2008).

[94] M.A. Castellanos-Beltran, K.D. Irwin, G.C. Hilton, L.R. Vale, and K.W. Lehnert, "Amplification and squeezing of quantum noise with a tunable Josephson metamaterial," Nature Phys. **4**, 929-931 (2008).

[95] O. Naaman, J. Aumentado, L. Friedland, J.S. Wurtele, I. Siddiqi, "Phase-locking transition in a chirped superconducting Josephson resonator," Phys. Rev. Lett. **101**, 117005 (2008).

[96] M.D. Reed, L. DiCarlo, B.R. Johnson, L. Sun, D.I. Schuster, L. Frunzio, R.J. Schoelkopf, High-fidelity readout in circuit quantum electrodynamics using the Jaynes-Cummings nonlinearity, Phys. Rev. Lett. **105**, 173601 (2010).

[97] N. Bergeal, F. Schackert, M. Metcalfe, R. Vijay, V.E. Manucharyan, L. Frunzio, D.E. Prober, R.J. Schoelkopf, S.M. Girvin, M.H. Devoret, Phase-preserving amplification near the quantum limit with a Josephson ring modulator, Nature **465**, 64-70 (2010).

[98] M. Mariantoni, H. Wang, T. Yamamoto, M. Neeley, R.C. Bialczak, Y. Chen, M. Lenander, E. Lucero, A.D. OConnell, D. Sank, M. Weides, J. Wenner, Y. Yin, J. Zhao, A.N Korotkov, A.N. Cleland, J.M. Martinis, Implementing the quantum von Neumann architecture with superconducting circuits, Science **333**, 61-65 (2011).

[99] A. Galiautdinov, A.N Korotkov, J.M. Martinis, Resonator-zero-qubit architecture for superconducting qubits, Phys. Rev. A **85**, 042321 (2012).

[100] M.D. Reed, L. DiCarlo, S.E. Nigg, L. Sun, L. Frunzio, S.M. Girvin, R.J. Schoelkopf, Realization of three-qubit quantum error correction with superconducting circuits, Nature **482**, 382-385 (2012).

[101] L. DiCarlo, J.M. chow, J.M. Gambeteta, L.S. Bishop, B.R. Johnson, D.I. Schuster, J. Majer, A. Blais, L. Frunzio, S.M. Girvin, R.J. Schoelkopf, Demonstration of two-qubit algorithms with a superconducting quantum processor, Nature **460**, 240-244 (2009).

[102] E. Lucero, R. Barends, Y. Chen, J. Kelly, M. Mariantoni, A. Megrant, P. OMalley, D. Sank, A. Vainsencher, J. Wenner, T. White, Y. Yin, A.N. Cleland, J.M. Martinis, Computing prime factors with a Josephson phase qubit quantum processor, Nature Phys. **8**, 719-723 (2012).

[103] A. Barone, G. Paterno, *Physics and applications of the Josephson effect* (John Wiley and Sons, New York, 1982).

[104] T.P. Orlando and K.A. Delin, *Foundations of applied superconductivity* (Prentice Hall, 1991)

[105] T. Van Duzer, C.W. Turner, *Principles of superconductive Devices and Circuits* (Elsevier, New York, 1998)

[106] M. Tinkham, *Introduction to Superconductivity* (Dover, 2004)

[107] W.C. Stewart, "Current-voltage characteristics of Josephson junctions," Appl. Phys. Lett. **12**, 277-280 (1968).

[108] D.E. McCumber, "Effect of ac impedance on dc voltage-current characteristics of superconductor weak-link junctions," J. Appl. Phys. **39**, 3113-3119 (1968).

[109] J. Lisenfeld, *Experiments on superconducting Josephson phase quantum bits* (Friedrich-Alexander-Universität Erlangen-Nürnberg, 2007).

[110] V. Ambegaokar, A. Baratoff, "Tunneling between superconductors," Phys. Rev. Lett. **10**, 486-489 (1963).

[111] H.A. Kramers, "Brownian motion in a field of force and the diffusion model of chemical reactions," Physica **7**, 284 (1940).

[112] M. Büttiker, E. Harris, R. Landauer, "Thermal activation in extremely underdamped Josephson-junction circuits," Phys. Rev. B **28**, 1268-1275 (1983).

[113] M.H. Devoret, J.M. Martinis, D. Esteve, J. Clarke, "Resonant activation from the zero-voltage state of a current-biased Josephson junction," Phys. Rev. Lett. **53**, 1260-1263 (1984).

[114] J.M. Martinis, M.H. Devoret, J. Clarke, "Energy-level quantization in the zero-voltage state of a current-biased Josephson junction," Phys. Rev. Lett. **55**, 1543-1546 (1985).

[115] M.H. Devoret, J.M. Martinis, J. Clarke, "Measurements of macroscopic quantum tunneling out of the zero-voltage state of a current-biased Josephson junction," Phys. Rev. Lett. **55**, 1908-1911 (1985).

[116] J.M. Martinis, M.H. Devoret, J. Clarke, "Experimental tests for the quantum behavior of a macroscopic degree of freedom: the phase difference across a Josephson junction," Phys. Rev. B **35**, 4682-4698 (1985).

[117] T.A. Fulton, L.N. Dunkleberger "Lifetime of the zero-voltage state in Josephson tunnel junctions," Phys. Rev. B **9**, 4760 (1974).

[118] J. Clarke, A.I. Braginski (ed.), *The SQUID Handbook, vol.1* (Wiley-VCH, New York, 1982).

[119] R.C. Dynes, r.A. Fulton "Supercurrent density distribution in Josephson junctions," Phys. Rev. B **3**, 3015 (1971).

[120] W.T. Tsang, T. van Duzer "D.C. analysis of parallel arrays of two and three Josephson junctions," J. Appl. Phys. **46**, 4573 (1975).

[121] H. Grabert, M.H. Devoret (ed.) *Single charge tunneling: Coulomb blockade phenomena in nanostructures* (Springer, 1992).

[122] P. Joyez, P. Lafarge, A. Filipe, D. Esteve, M.H. Devoret, "Observation of parity-induced suppression of Josephson tunneling in the superconducting single electron transistor," Phys. Rev. Lett. **72**, 2458-2461 (1994).

[123] D. Flees, S. Han, J. Lukens, "Interband transitions and band gap measurements in Bloch transistors," Phys. Rev. Lett. **78**, 4817-4820 (1997).

[124] Y. Nakamura, C.D. Chen, J.S. Tsai, "Spectroscopy of energy-level splitting between two macroscopic quantum states of charge coherently superposed by Josephson tunneling," Phys. Rev. Lett. **79**, 2328-2331 (1997).

[125] V. Bouchiat, D. Vion, P. Joyez, D. Esteve, M.H. Devoret, "Quantum coherence with a single Cooper pair," Physica Scripta T **76**, 165-170 (1998).

[126] F. Motzoi, J.M. Gambetta, P. Rebentrost, F.K. Wilhelm, Simple pulses for elimination of leakage in weakly nonlinear qubits, Phys. Rev. Lett. 103, 110501 (2009).

[127] J. E. Mooij, T. P. Orlando, L. S. Levitov, L. Tian, C. H. van der Wal, S. Lloyd, "Josephson persistent-current qubit," Science **285**, 1036-1039 (1999).

[128] T. P. Orlando, J. E. Mooij, L. Tian, C. H. van der Wal, L. S. Levitov, S. Lloyd, and J. J. Mazo, "Superconducting persistent-current qubit," Phys. Rev. B **60**, 15398-15413 (1999).

[129] M. Steffen, S. Kumar, D.P. DiVincenzo, J.R. Rozen, G.A. Keefe, M.B. Rothwell, M.B. Ketchen, High-coherence hybrid superconducting qubit, Phys. Rev. Lett. 105, 100502 (2010).

[130] K.B. Cooper, M. Steffen, R. McDermott, R.W. Simmonds, S. Oh, D.A. Hite, D.P. Pappas, J.M. Martinis, Observation of quantum oscillations between a Josephson phase qubit and a microscopic reonator using fast readout, Phys. Rev. Lett. 93, 180401 (2004).

[131] M.H. Devoret, J.M. Martinis, Implementing qubits with superconducting integrated circuits, Quantum Inf. Proc. 3, 163-203 (2004).

[132] J.M. Martinis, K.B. Cooper, R. McDermott, M. Steffen, M. Ansmann, K.D. Osborn, K. Cicak, S. Oh, D.P. Pappas, R.W. Simmonds, C.C. Yu, Decoherence in Josephson qubits from dielectric loss, Phys. Rev. Lett. 95, 210503 (2005).

[133] M. Steffen, M. Ansmann, R. McDermott, N. Katz, R.C. Bialczak, E. Lucero, M. Neeley, E.M. Weig, A.N. Cleland, J.M. Martinis, State tomography of capacitively shunted phase qubits with high fidelity, Phys. Rev. Lett. 97, 050502 (2006).

[134] J.M. Martinis, Superconducting phase qubits, Quant. Info. Proc. 8, 81-103 (2009).

[135] V.E. Manucharyan, J. Koch, L. Glazman, M.H. Devoret, Fluxonium: single Cooper-pair circuit free of charge offsets, Science 326, 113-116 (2009).

[136] V.E. Manucharyan, N.A. Masluk, A. Kamal, J. Koch, L. Glazman, M.H. Devoret, Evidence for coherent quantum phase slips across a Josephson junction array, Phys. Rev. B 85, 024521 (2012).

[137] A.J. Kerman, E.A. Dauler, W.E. Keicher, J.K.W. Yang, K.K. Berggren, G. Gol'tsman, B. Voronov Kinetic-inductance-limited reset time of a superconducting nanowire photon source, Appl. Phys. Lett. 88, 111116 (2006).

[138] F. Yan, J. Bylander, S. Gustavsson, F. Yoshihara, K. Harrabi, D.G. Cory, T.P. Orlando, Y. Nakamura, J.S. Tsai, W.D. Oliver Spectroscopy of low-frequency noise and its temperature dependence in a superconducting qubit, Phys. Rev. B 85, 174521 (2012).

[139] F. Yan, S. Gustavsson, J. Bylander, X. Jin, F. Yoshihara, D.G. Cory, Y. Nakamura, T.P. Orlando, W.D. Oliver $T_{1\rho}$ experiment as a noise spectrum analyzer of a superconducting qubit undrergoing driven evolution, under review (2013).

[140] S. Gustavsson, J. Bylander, F. Yan, P. Forn-Diaz, V. Bolkovsky, D. Braje, G. Fitch, K. Harrabi, D. Lennon, J. Miloshi, P. Murphy, R. Slattery, S. Spector, B. Turek, T. Weir, P.B. Welander, F. Yoshihara, D.G. Cory, Y. Nakamura, T.P. Orlando, W.D. Oliver Driven dynamics and rotary echo of a qubit tunably coupled to a harmonic oscillator, Phys. Rev. Lett. 108, 170503 (2012).

[141] L.D. Landau, "On the theory of transfer of energy at collisions II," Phys. Z. USSR **2**, 46-51 (1932).

[142] C. Zener, "Non-adiabatic crossing of energy levels," Proc. R. Soc. Lond. A **137**, 696-702 (1932).

[143] E. C. G. Stueckelberg, Helv. Phys. Acta **5**, 369-422 (1932).

[144] H. Nakamura, *Nonadiabatic Transition* (London, England: World Scientific, 2001).

[145] M. Grifoni and P. Hänggi, "Driven quantum tunneling," Phys. Rep. **304**, 229-354 (1998).

[146] Y. Kayanuma, "Phase coherence and nonadiabatic transition at a level crossing in a periodically driven two-level system," Phys. Rev. B **47**, 9940-9943 (1993).

[147] Y. Kayanuma, "Role of phase coherence in the transition dynamics of a periodically driven two-level system," Phys. Rev. B **50**, 843-845 (1994).

[148] Y. Kayanuma, "Stokes phase and geometrical phase in a driven two-level system," Phys. Rev. A **55**, R2495-R2498 (1997).

[149] Y. Kayanuma and Y. Mizumoto, "Landau-Zener transitions in a level-crossing system with periodic modulation of the diagonal energy," Phys. Rev. A **62**, 061401(R) (2000).

[150] A. V. Shytov, D. A. Ivanov, M. V. Feigel'man, "Landau-Zener interferometry for qubits," Eur. Phys. J. B **36**, 263-269 (2003)

[151] S. Ashhab, J.R. Johansson, A.M. Zagoskin, and Franco Nori, "Two-level systems driven by large-amplitude fields," Phys. Rev. A **75**, 063414 (2007).

[152] M. Wubs, K. Saito, S. Kohler, P. Hänggi, and Y. Kayanuma, "Gauging a quantum heat bath with dissipative Landau-Zener Transitions," Phys. Rev. Lett. **97**, 200404 (2006).

[153] K. Saito, M. Wubs, S. Kohler, P. Hänggi, and Y. Kayanuma, "Quantum state preparation in circuit QED via Landau-Zener tunneling," Europhys. Lett. **76**, 22-28 (2006).

[154] K. Saito, M. Wubs, S. Kohler, Y. Kayanuma, and P. Hänggi, "Dissipative Landau-Zener transitions of a qubit: bath-specific and universal behavior," Phys. Rev. B **75**, 214308 (2007).

[155] F. Grossmann, T. Dittrich, P. Jung, and P. Hänggi "Coherent destruction of tunneling," Phys. Rev. Lett. **67**, 516-519 (1991).

[156] J.M. Gomez Llorente and J. Plata, "Tunneling control in a two-level system," Phys. Rev. A **45**, R6958-R6961 (1992).

[157] Y. Kayanuma and K. Saito, "Coherent destruction of tunneling, dynamic localization, and the Landau-Zener formula," Phys. Rev. A **77**, 010101(R) (2008).

[158] W. G. van der Wiel, *et al.*, "Electron transport through double quantum dots," Rev. Mod. Phys. **75**, 1-22 (2003).

[159] R. Hanson, L.P. Kouwenhoven, J.R. Petta, S. Tarucha, and L.M.K. Vandersypen "Spins in few-electron quantum dots," Rev. Mod. Phys. **79**, 1217-1265 (2007).

[160] C. Cohen-Tannoudji, J. Dupont-Roc, and G. Grynberg, *Atom-Photon Interactions: Basic Processes and Applications* Ch. 6 (Wiley, 1992).

[161] F.R. Friedman, *et al.*, "Macroscopic measurement of resonant magnetization tunnelling in high-spin molecules," Phys. Rev. Lett. **76**, 3830-3833 (1996).

[162] L. Thomas, *et al.*, "Macroscopic quantum tunnelling of magnetization in a single crystal of nanomagnets," Nature **383**, 145-147 (1996).

[163] W. Wernsdorfer and R. Sessoli, "Quantum phase interference and parity effects in magnetic molecular clusters," Science **284**, 133-135 (1999).

[164] M. C. Baruch, T. F. Gallagher, "Ramsey interference fringes in single pulse microwave multiphoton transitions," Phys. Rev. Lett. **68**, 3515-3518 (1992).

[165] S. Yoakum, L. Sirko, P. M. Koch, "Stückelberg oscillations in the multiphoton excitation of helium Rydberg atoms: Observation with a pulse of coherent, field and suppression by additive noise," Phys. Rev. Lett. **69**, 1919-1922 (1992).

[166] M. Mark, T. Kraemer, P. Waldburger, J. Herbig, C.Chin, H.-C. Nägerl, and R. Grimm "Stückelberg interferometry" with ultracold molecules," Phys. Rev. Lett. **99**, 113201 (2007).

[167] M. Mark, F. Ferlaino, S. Knoop, J.G. Danzl, T. Kraemer, C.Chin, H.-C. Nägerl, and R. Grimm, "Spectroscopy of ultracold trapped cesium Feshbach molecules," Phys. Rev. A **76**, 042514 (2007).

[168] F. Lang, P.V.D. Straten, B. Brandstätter, G. Thalhammer, K. Winkler, P.S. Julienne, R. Grimm, and J. Hecker Denschlag, "Cruising through molecular bound-state manifolds with radiofrequency," Nature Physics **4**, 223-226 (2008).

[169] P. K. Tien and J. P. Gordon, "Multiphoton process observed in the interaction of microwave fields with the tunneling between superconductor films," Phys. Rev. **129**, 647 (1963).

[170] L. P. Kouwenhoven, S. Jauhar, J. Orenstein, P. L. McEuen, Y. Nagamune, J. Motohisa, and H. Sakaki, "Observation of Photon-Assisted Tunneling through a Quantum Dot," Phys. Rev. Lett. **73**, 3443 (1994).

[171] Y. Nakamura, J. S. Tsai, *J. Supercond.* **12**, 799 (1999).

[172] O. Astafiev, K. Inomata, A.O. Niskanen, T. Yamamoto, Yu. A. Pashkin, Y. Nakamura, and J.S. Tsai, "Single artificial-atom lasing," Nature **449**, 588-590 (2007).

[173] A.O. Niskanen, Y. Nakamura, and J.P. Pekola, "Information entropic superconducting microcooler," Phys. Rev. B **76**, 174523 (2007).

[174] A.L. Schawlow, "Spectroscopy in a new light," Rev. Mod. Phys. **54**, 697-707 (1982).

[175] R.C. Thompson, "High resolution laser spectroscopy of atomic systems," Rep. Prog. Phys. **48**, 531-578 (1985).

[176] R.K. Wangsness, F. Bloch, "The Dynamical Theory of Nuclear Induction," Phys. Rev. **89**, 728-739 (1953).

[177] F. Bloch, "The Dynamical Theory of Nuclear Induction," Phys. Rev. **105**, 1206-1222 (1957).

[178] A.G. Redfield, "On the theory of relaxation processes," IBM Journal of Research and Development **1**, 19 (1957).

[179] Y. Makhlin, "Dephasing of qubits by transverse low-frequency noise," JETP Letters **78**, 497 (2003).

[180] A. Shnirman, G. Schön, I. Martin, Y. Makhlin, "Low- and High-Frequency Noise from Coherent Two-Level Systems," Phys. Rev. Lett. **94**, 127002 (2005).

[181] G. Ithier, *Manipulation, lecture et analyse de la décohérence d'un bit quantique supraconducteur* (Ph.D. thesis, Université Paris VI, 2005).

[182] J.Q. You, X. Hu, S. Ashhab, F. Nori, "Low-decoherence flux qubit," Phys. Rev. B **75**, 140515 (2007).

[183] A.J. Kerman, "Metastable superconducting qubit," Phys. Rev. Lett. **104**, 027002 (2010).

[184] H.A. Haus, *Electromagnetic noise and quantum optical measurements* (Springer, New York 2000).

[185] A.A. Clerk, M.H. Devoret, S.M. Girvin, F. Marquardt, R.J. Schoelkopf, "Introduction to quantum noise, measurement and amplification," Rev. Mod. Phys. **82**, 1155-1208 (2010).

[186] F. Yan, S.Gustavsson, J. Bylander, X. Jin, F. Yoshihara, D.G. Cory, Y. Nakamura, T.P. Orlando, W.D. Oliver, "$T_{1\rho}$ experiment as a noise spectrum analyzer during driven evolution," in preparation (2013).

[187] "Quantum noise in the Joseephson charge qubit," Phys. Rev. Lett. **93**, 267007 (2004).

[188] F. Yoshihara, *et al.*, in preparation (2013).

[189] G.S. Uhrig, "Keeping a Quantum Bit Alive by Optimized π-Pulse Sequences," Phys. Rev. Lett. **98**, 100504 (2007).

[190] M.J. Biercuk, H. Uys, A.P. VanDevender, N. Shiga, W.M. Itano, J.J. Bollinger, "Optimized dynamical decoupling in a model quantum memory," Nature **458**, 996-1000 (2009).

[191] J.M. Martinis, S. Nam, J. Aumentado, K.M. Lang, C. Urbina, "Decoherence of a superconducting qubit due to bias noise," Phys. Rev. B **67**, 094510 (2003).

[192] L. Cywiński, R.M. Lutchyn, C.P. Nave, S. Das Sarma, "How to enhance dephasing time in superconducting qubits," Phys. Rev. B **77**, 174509 (2008).

[193] M.J. Biercuk, H. Uys, A.P. VanDevender, N. Shiga, W.M. Itano, J.J. Bollinger, "Experimental Uhrig dynamical decoupling using trapped ions," Phys. Rev. A **79**, 062324 (2009).

[194] G.S. Uhrig, "Exact results on dynamical decoupling by π pulses in quantum information processes," New J. Phys. **10**, 083024 (2008).

[195] B. Yurke, J.S. Denker, "Quantum network theory," Phys. Rev. A **29**, 1419-1437 (1984).

[196] M.H. Devoret, "Quantum fluctuations in electrical circuits" in *Quantum Fluctuations*, Les Houches Session LXIII (Elsevier, 1997).

[197] A. Cottet, *Implementation of a quantum bit in a superconducting circuit*, (Ph.D. thesis, Saclay, 2002).

A 5 Topics in Quantum Information [1]

B. Kraus
Institute for Theoretical Physics
University of Innsbruck, Austria

Contents

1 Introduction **2**

2 Quantum teleportation **2**

3 Dense coding **4**

4 Quantum cryptography **4**
4.1 Classical cryptography 4
4.2 Quantum cryptography: quantum key distribution 6

5 Quantum computation **12**
5.1 Classical computing 12
5.2 Quantum computing 13

6 Quantum simulation **19**

7 Quantum repeater **20**

8 Multipartite Entanglement **21**

[1] Lecture Notes of the 44^{th} IFF Spring School "Quantum Information Processing" (Forschungszentrum Jülich, 2013). All rights reserved.

1 Introduction

You have learned about several applications of quantum information, like for instance quantum error correction. Here, we will investigate some other applications, like quantum teleportation and quantum cryptography [1, 2].

2 Quantum teleportation

Teleportation is a process in which an unknown quantum state is transferred from one place to another. The sender, usually called Alice (A), knows neither the state to be teleported nor the location of the intended receiver, usually called Bob (B) [3].

- IDEA: Alice has a two–level system (qubit) in an unknown state $|\phi\rangle$, and she wants to teleport it to Bob. Prior to the teleportation process, Alice and Bob share an EPR pair, e.g. the state $|\,\Psi^-\,\rangle = \frac{1}{\sqrt{2}}(|\,01\,\rangle - |\,10\,\rangle)$. The idea is that Alice performs a joint measurement of the two–level system to be teleported and her EPR particle. Due to the nonlocal correlations, the effect of the measurement is that the unknown state appears instantaneously in Bob's hands, except for a unitary operation which depends on the outcome of the measurement. If Alice communicates to Bob the result of her measurement, then Bob can perform that operation and therefore recover the unknown state.

- INITIAL STATES: Let particle 1 be prepared in the unknown state $|\phi\rangle_1$, particle 2 be the member of the EPR that Alice possesses and particle 3 that of Bob. We write the state of particle 1 as
$$|\phi\rangle_1 = a|0\rangle_1 + b|1\rangle_1 \tag{1}$$
where a and b are (unknown) complex coefficients. The state of particles 2 and 3 is the singlet state
$$|\Psi^-\rangle_{23} = \frac{1}{\sqrt{2}}(|0\rangle_2|1\rangle_3 - |1\rangle_2|0\rangle_3). \tag{2}$$
The complete state of particles $1, 2$ and 3 is therefore
$$\begin{aligned} |\Psi\rangle_{123} &= \frac{a}{\sqrt{2}}(|0\rangle_1|0\rangle_2|1\rangle_3 - |0\rangle_1|1\rangle_2|0\rangle_3) \\ &\quad + \frac{b}{\sqrt{2}}(|1\rangle_1|0\rangle_2|1\rangle_3 - |1\rangle_1|1\rangle_2|0\rangle_3). \end{aligned} \tag{3}$$
Using the Bell basis for particles 1 and 2,
$$|\Psi^\pm\rangle_{12} = \frac{1}{\sqrt{2}}(|0\rangle_1|1\rangle_2 \pm |1\rangle_1|0\rangle_2) \tag{4}$$
$$|\Phi^\pm\rangle_{12} = \frac{1}{\sqrt{2}}(|0\rangle_1|0\rangle_2 \pm |1\rangle_1|1\rangle_2), \tag{5}$$
we find
$$\begin{aligned} |\Psi\rangle_{123} &= \frac{1}{2}[\,|\Psi^-\rangle_{12}(-a|0\rangle_3 - b|1\rangle_3) \\ &+ |\Psi^+\rangle_{12}(-a|0\rangle_3 + b|1\rangle_3) \\ &+ |\Phi^-\rangle_{12}(a|1\rangle_3 + b|0\rangle_3) \\ &+ |\Phi^+\rangle_{12}(a|1\rangle_3 - b|0\rangle_3)\,] \end{aligned} \tag{6}$$

- PROCEDURE:

  (1) *Alice' measurement*: Alice makes a joint measurement of her particles (1 and 2) in the Bell basis (see Eq. (4)).

  (2) *Alice' broadcasting*: Then she broadcasts (classically) the outcome of her measurement.

  (3) *Bob restoration*: Bob then applies a unitary operation to his particle to obtain $|\psi\rangle_3$. According to the state of the particles (Eq. 6) the possible outcomes are:

  - With probability $1/4$, Alice measured $|\Psi^-\rangle_{12}$. The state of the third particle is automatically projected onto
    $$a|0\rangle_3 + b|1\rangle. \tag{7}$$
    Thus, in this case Bob does not have to perform any operator.
  - With probability $1/4$, Alice measured $|\Psi^+\rangle_{12}$. The state of the third particle is automatically projected onto
    $$-a|0\rangle_3 + b|1\rangle. \tag{8}$$
    Teleportation occurs if Bob applies σ_z to his particle.
  - With probability $1/4$, Alice measured $|\Phi^-\rangle_{12}$. The state of the third particle is automatically projected onto
    $$a|1\rangle_3 + b|0\rangle. \tag{9}$$
    Teleportation occurs if Bob applies σ_x to his particle.
  - With probability $1/4$, Alice measured $|\Phi^+\rangle_{12}$. The state of the third particle is automatically projected onto
    $$a|1\rangle_3 - b|0\rangle. \tag{10}$$
    Teleportation occurs if Bob applies σ_y to his particle.

- REMARKS:

  - Alice ends up with no information about $|\,\phi\,\rangle$. In this sense, the state of particle 1 has been swapped to particle 3.
  - There is no instantaneous propagation of information. Bob has to wait until he receives the (classical) message from Alice about her outcome. Before he receives the message, his lack of knowledge prevents him from having the state. Note that no measurement can tell him whether Alice has performed her measurement or not.
  - One can also generalize teleportation to N–level systems.
  - Note that the idea of teleportation is also useful from the theoretical point of view. The idea can for instance be used for gate teleportation.
  - Since teleportation is a linear operation applied to a state, it will also work for statistical mixtures, or in the case in which particle 1 is entangled with other particles. As we will see, this can be used to establish a long distant entangled pair (see quantum repeater).

3 Dense coding

- IDEA: Given a maximally entangled state, one can prepare any other maximally entangled state using local operations. In particular, one can prepare all four elements of the Bell basis. Thus if Alice sends the member of an EPR pair to Bob, he can apply one of four unitary operations and obtain 4 orthogonal states of the particles. Then, sending the particle back to Alice, she can know the operation performed by Bob, since she can distinguish among orthogonal states. In this sense, Bob can send two bits of information by only acting on one particle [4].

- PROCEDURE: Alice has two particles prepared in a singlet state $|\Psi^-\rangle_{AB}$. She sends one of the particles to Bob, who applies a local unitary operation one the particle he received, say 2, in order to encode classical information. He applies one of the operations, $\{\sigma_i\}_{i=0,3} = \{\mathbb{1}, \sigma_x, \sigma_y, \sigma_z\}$ to particle 2 and sends it back to Alice. Using that all four states $\mathbb{1} \otimes \sigma_i |\, \Psi^- \,\rangle$, with $\{\sigma_i\}_{i=0,3} = \{\mathbb{1}, \sigma_x, \sigma_y, \sigma_z\}$ are orthogonal Alice can perfectly distinguish them by measuring in the Bell basis, $\{\mathbb{1} \otimes \sigma_i |\, \Psi^- \,\rangle\}_{i=0}^3$. Thus she can decode the two bits of information sent by Bob.

4 Quantum cryptography

The aim of cryptography is to enable two legitimate persons, the sender (Alice) and the receiver (Bob), to communicate in absolute privacy even in the presence of an eavesdropper (Eve).

4.1 Classical cryptography

- TRADITIONAL METHODS: Cryptographic methods are known since a long time. For example, the Spartans used simple transposition methods to send secret messages, whereas Romans used substitution methods. Let us briefly review these methods.

  - TRANSPOSITION: It consists of changing the place (transposing) the letter that compose the message. For example, one can exchange consecutive letters: TEST→ETTS.
  - SUBSTITUTION: It consists of changing the order of the letters that compose the alphabet. For example, A→D, B→E, C→F, etc. In this case, TEST→WHVW.
  - SECURITY: These methods are not secure. For example, it is well known that the frequency of appearance of a given letter in any intelligible text is more or less constant. This means that if Eve takes the message (which is supposed to be long) and compares the relative frequency appearance of the signs with the standard tables, she can decode the message.

- ONE–TIME PAD: In 1917 a cryptographic scheme was proposed, which is provably secure (i.e., unbreakable). The ideas is that Alice and Bob, prior to the transmission, have a *Key*, which nobody else knows. This key is a random sequence of numbers $K_1, K_2, \ldots$. The procedure is as follows: Alice takes her message and encrypts it using the key. To do that, she uses first a public table to translate the letters of the message to numbers, $P_1, P_2, \ldots$ The encrypted message is obtained by adding P and K modulo N, the number of letters in the alphabet, i.e.

$$C_i = (P_i + K_i) \text{mod}(N). \tag{11}$$

She sends the encrypted message C to Bob, who decrypts it using the key, as

$$P_i = (C_i - K_i) \text{mod } (N). \tag{12}$$

Since the key is random, for somebody who does not know the key, the bits C_i are completely random. It can be proven that if the length of key is the same as the length of the message, and a given key is only used once and then discarded, this procedure is secure.

- EXAMPLE: Let us take the public table

A	B	C	D	...	Y	Z		?	,	.
01	02	03	04	...	25	26	27	28	29	30

In this case, $N = 30$. The random secret key is

12	01	18	27	03	23	05	10	21	24	...

The word TEST will be encrypted as

T	E	S	T
20	05	19	20
12	01	18	27
02	06	07	17
B	F	G	H

- PROBLEM: The problem is that Alice and Bob have to know the key in advance, and therefore they have to communicate to establish this key. This process is called *key distribution*. There are two ways of achieving that:

  - PUBLIC–KEY CRYPTOSYSTEMS: Public key cryptography was introduced in 1976. It is based on the existence of mathematical operations that are easy to perform, but whose inverse are difficult. For example, it is simple to multiply two numbers ($127 \times 229 = ?$) but it is difficult to decompose a number into its prime factors ($29083 = ? \times ?$). The idea is that Alice knows how to perform two mutually inverse transformations (a scrambling transformation and an unscrambling transformation). Then she publishes the directions (recipe) for performing the scrambling transformation, so that anybody can use this recipe to encode a message, but she is the only one who can perform the inverse transformation. This method is based on unproved mathematical assumptions, such that factoring is a difficult operation (i.e., that the time required to find the prime factors of a given number of size n with a computer scales as an exponential function of n).
  - SECRET–KEY CRYPTOSYSTEMS: As we have seen before, a secret– key cryptosystem (one–time pad) can be proven to be secure, but the problem is that A and B need to share a secret key, which is of the same length as the message. In order to establish this key they either have to meet or they have to trust a currier.

4.2 Quantum cryptography: quantum key distribution

As we have seen before, the problem of cryptography is reduced to the problem of establishing a secret key between Alice and Bob. Classically a secret key can only be established by either a meeting between the legitimate users, or by trusting a third party. Otherwise, they have to rely on an unproven computational assumption. In contrast to that, the security of quantum key distribution is solely based on the laws of quantum mechanics. There, Alice and Bob use quantum systems to establish the key. Due to the fact that any intervention of Eve, trying to obtain information about the key, will perturb the state describing those quantum systems, Alice and Bob are able to notice the presence of Eve and can abort the protocol. Thus, the security of Quantum Key Distribution (QKD) is based on the quantum no-clonig Theorem, which states that it is impossible to copy an unknown quantum state and on the fact that information gain implies disturbance.
There exist several quantum key distribution protocols. We will review here some of them.

4.2.1 BB84 Protocol

- GOAL: The goal for Alice and Bob is to share a random key. The key is a long sequence of random bits.

- PROCEDURE [5]:

  (1) *Preparation and transmission*: Alice prepares a set of two–level systems in states chosen randomly among the set $S = \{|0\rangle_z, |1\rangle_z, |0\rangle_x, |1\rangle_x\}$, where $|0\rangle_z$ and $|1\rangle_z$ are the eigenstate of the σ_z operator, and $|0\rangle_x$ and $|1\rangle_x$ are the eigenstate of σ_x. That is,

  $$|1\rangle_x = \frac{1}{\sqrt{2}}(|0\rangle_z + |1\rangle_z), \qquad |0\rangle_x = \frac{1}{\sqrt{2}}(|0\rangle_z - |1\rangle_z). \tag{13}$$

  She sends these qubits to Bob.

  (2) *Measurement:* For each of the qubits received, Bob chooses randomly among z and x, and correspondingly he measures either σ_z or σ_x.

  (3) *Shifting:* Bob announces publicly the operator he has measured for each of the qubits, without saying the outcome of the measurement. Then, Alice announces publicly for each qubit if the operator that Bob has measured corresponds to the operator she has used in her preparation. If the operators used in the preparation and measurement match for a given qubit, they take it. Otherwise, they discard this bit.

  (4) *Authentication:* Alice and Bob announce publicly the result of part of the qubits that remain. If they are all the same, it means that no eavesdropper tried to intercept the communication, and therefore they can use the rest of the bits as a key.

- EXAMPLE:

a	b	c	d	e	f	g	h	i	j
1	0	σ_x	$\|0\rangle_x$	σ_z	0				
2	1	σ_x	$\|1\rangle_x$	σ_x	1	OK			1
3	1	σ_z	$\|1\rangle_z$	σ_x	1				
4	1	σ_z	$\|1\rangle_z$	σ_z	1	OK	1	OK	
5	0	σ_x	$\|0\rangle_x$	σ_x	0	OK			0
6	0	σ_z	$\|0\rangle_z$	σ_x	1				
7	1	σ_x	$\|1\rangle_x$	σ_x	1	OK	1	OK	
8	0	σ_z	$\|0\rangle_z$	σ_z	0	OK	0	OK	
9	1	σ_z	$\|1\rangle_z$	σ_x	1				
10	0	σ_z	$\|0\rangle_z$	σ_z	0	OK			0

Here: (a) qubit; (b) Random bit selected by Alice; (c) Random operator selected by Alice; (d) State sent by Alice; (e) Random operator selected by Bob; (f) Bob's result of the measurement (0 if measures -1 and 1 if he measures 1); (g) result of the public discussion; (h) Authentication; (i) result of the authentication; (j) Key.

- EAVESDROPPING: If Eve tries to obtain the key, she will have to make measurements. Since this will disturb the state, the authentication step will tell Alice and Bob that Eve is present. The important point here is that Eve does not know the operators selected by Alice and Bob until Bob performs the measurement and publicly announces it. For example, imagine that Alice prepares the qubit in the state $|1\rangle_x$ (7–th qubit in the table). Consider the following two cases: (a) If Eve happens to measure σ_x, then she will measure 1 and will send again the state $|1\rangle_x$ to Bob; in that case, Alice and Bob cannot tell anything about the presence of Eve; (b) on the contrary, if she happens to measure σ_z then she will obtain 1 or 0 with probability $1/2$. If she obtains 1, she will send the state $|1\rangle_z$ to Bob, which is not the one sent by Alice. Therefore, in the process of authentication there is a probability $1/2$ that Alice and Bob check that there is an error. Analogous conclusions apply if Eve measures 0. The probability for Eve to be detected if she measures every qubit using this procedure is $1-(3/4)^N$ if Alice and Bob use N qubits in the authentication.

4.2.2 B92 Protocol

In contrast to the BB84, Alice uses here two non-orthogonal states [6]

$$|\,\varphi^0\,\rangle = \alpha|\,0\,\rangle + \beta|\,1\,\rangle \text{ and } |\,\varphi^1\,\rangle = \alpha|\,0\,\rangle - \beta|\,1\,\rangle \tag{14}$$

to encode her bit-values 0 and 1, respectively. Here, α and β are (without loss of generality) real coefficients with $\alpha^2+\beta^2=1$.

- PROCEDURE:

  (1) *Preparation and transmission:* Alice randomly prepares a sequence of quantum systems, in the states $|\,\varphi^0\,\rangle$ and $|\,\varphi^1\,\rangle$ to represent the bits 0 and 1 respectively and sends them to Bob.

  (2) *Measurements:* Bob randomly applies a measurement with respect to the basis

$$\{|\,\varphi^0\,\rangle, |\,\varphi^0\,\rangle^\perp\} \text{ or } \{|\,\varphi^1\,\rangle, |\,\varphi^1\,\rangle^\perp\}, \tag{15}$$

where $|\,\varphi^x\,\rangle^\perp$ denotes the normalized vector orthogonal to $|\,\varphi^x\,\rangle$, for $x = 0, 1$. He assigns the bit values 0 and 1 to the measurement outcomes $|\,\varphi^1\,\rangle^\perp$ and $|\,\varphi^0\,\rangle^\perp$, respectively.

(3) *Sifting:* In the sifting step, Alice and Bob discard all bit pairs where Bob measured either $|\,\varphi_0\,\rangle$ or $|\,\varphi_1\,\rangle$. If there has been no eavesdropping, the remaining instances, that is, those where Alice sent $|\varphi_0\rangle$ ($|\varphi_1\rangle$) and Bob measure $|\,\varphi^1\,\rangle^\perp$ ($|\,\varphi^0\,\rangle^\perp$), are perfectly correlated.

(4) *Authentication*: Alice and Bob compare a subensemble of the remaining instances to check for complete correlation.

- EAVESDROPPING: If Eve tried to measure the states sent by Alice, she would modified the states, which will be revealed in the authentication step.

- PREPARE–AND–MEASURE SCHEME: All these examples are within the class of prepare–and–measure schemes, where Alice prepares the systems in a certain state, sends them to Bob, who is measuring them right after he received them. Note that these schemes can be implemented with nowadays technology [7]. However, one might also use entanglement to generate a secret key, as we will see in the following.

4.2.3 E91 Protocol

- IDEA: Alice and Bob share pairs of two–level systems prepared in the singlet state

$$|\Psi^-\rangle = \frac{1}{\sqrt{2}}(|01\rangle - |10\rangle). \tag{16}$$

The idea is that if they measure one of these pairs along the same direction (that is, measure the same $\sigma_{\vec{n}}$ they will obtain completely correlated results [2]. That is, if one measures -1 the other will measure 1 and viceversa. Thus, they can establish the key by simply taking $-1 \to 0$ and by Alice exchanging $0 \leftrightarrow 1$.

- PROCEDURE [8]:

(1) *Preparation and transmission:* A source emits pairs of two–level systems (qubits) in a singlet state. The particles fly apart towards the two legitimate users of the channel (Alice and Bob). An other way to generate the entangled states shared between A and B would be the following. Alice prepares the entangled states and sends half of the qubits to B.

(2) *Measurements:* Alice and Bob perform measurement of the spin components along three different directions given by unit vectors $\vec{a}_i$ for Alice and $\vec{b}_j$ for Bob ($i, j = 1, 2, 3$). The vectors $\vec{a}_i$ and $\vec{b}_j$ lie in the $x - y$ plane, with

$$a_1 = \begin{pmatrix}1\\0\\0\end{pmatrix}, a_2 = \frac{1}{\sqrt{2}}\begin{pmatrix}1\\1\\0\end{pmatrix}, a_3 = \begin{pmatrix}0\\1\\0\end{pmatrix}, b_1 = \frac{1}{\sqrt{2}}\begin{pmatrix}1\\1\\0\end{pmatrix}, b_2 = \begin{pmatrix}0\\1\\0\end{pmatrix}, b_3 = \frac{1}{\sqrt{2}}\begin{pmatrix}-1\\1\\0\end{pmatrix}. \tag{17}$$

They choose these orientations randomly and independently for each pair.

[2] This can be easily seen by using that $U \otimes U|\,\Psi^-\,\rangle \propto |\,\Psi^-\,\rangle$ for any U

(3) *Sifting:* Alice and Bob announce publicly the directions used in each measurement, and divide the measurements in two groups: a first group for which they used different orientations, and a second one for which they used the same.

(4) *Authentication:* Alice and Bob reveal publicly the results they obtained but within the first group only. With these measurements they check whether their measurements violate CHSH inequality (i.e. if the value of $S = 2\sqrt{2}$). In case they find $S = 2\sqrt{2}$ they use the results of the second group to establish the key.

- EAVESDROPPING: Any attempt of Eve to measure or modify the singlet states will disturb them, and therefore S will decrease (for the set of measurements described above $S = 2\sqrt{2}$ only for a singlet state; otherwise it is smaller).

- COMPARISON BB84 and E91 PROTOCOLS: In contrast to the BB84 (and the B92) protocol, one uses maximally entangled states in the E91 protocol for quantum public key distribution. However, one can view the E91 protocol as follows: if Alice measures along the z direction and obtains $|0\rangle_z$ ($|1\rangle_z$), then Bob's particle will be projected onto the state $|1\rangle_z$ ($|0\rangle_z$) resp.. If Alice measures along the x direction and obtains $|0\rangle_x$ ($|1\rangle_x$), then Bob's particle will be projected onto the state $|1\rangle_x$ ($|0\rangle_x$) resp.. Therefore, Alice can prepare the sequence of random states as in the BB84 by performing appropriate measurements on the singlet pairs. It should also be noted, however, that the way the random bit string is generated is very different in the two protocols. In the BB84 protocol, Alice chooses this bit string randomly, whereas in the E91 the bit string is generated via the measurement. Thus, it is really random there.

4.2.4 Security proofs of QKD Protocols

We assumed in the protocols above that the transmission of quantum systems from Alice to Bob can be perfect. However, the qubits sent by A will always interact with the environment during the transmission. Thus, the bits Alice and Bob share after the sifting will never be perfectly correlated. There will always occur errors. Consequently, even in the absence of an adversary Eve, the quantum bit error rate (QBER), Q, is non-zero. Thus, one has to prove the security of QKD in the presence of errors. Moreover, one has to assume that all the noise is due to Eve. The reason for that is that Eve might in principle replace the real (noisy) quantum channel with an ideal noise-free channel and could thus tap into the quantum communication that precisely introduces the original amount of noise. Thus, one of the most challenging theoretical problems in the context of QKD is to find a lower bound on the secret key rate as a function of the QBER (see Fig. (1)).
In order to prove security one considers a model where Alice and Bob, are connected by a quantum channel as well as an authenticated, but otherwise fully insecure, classical channel [3]. Moreover, one might assume that Alice's source as well as Bob's detector are perfect, whereas an adversary (Eve) might have full control over the quantum channel.
We will briefly outline now how a secret key can be established in such a model. After the distribution of quantum information and the measurements, A and B hold the bit–strings X; Y respectively. Then, they proceed with the classical part of the protocol, which can be divided into the following three steps:

[3] If Alice and Bob initially share a short key, they can use a classical authentication scheme in order to implement an authentic channel.

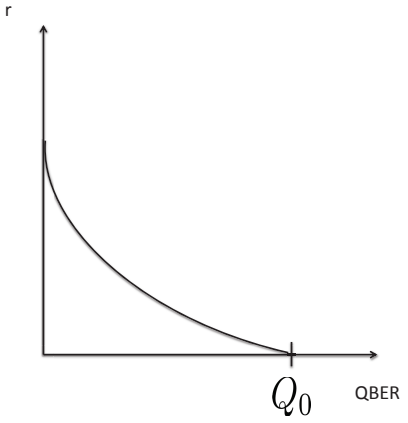

Fig. 1: *The secret key rate as a function of the QBER. For values smaller than the critical value, Q_0, of the QBER, one can find a classical postprocessing, which enables one to distill a secret key at the rate r.*

- PARAMETER ESTIMATION: Alice and Bob compare the bit-values for a randomly chosen sample of their strings, which gives an estimate for the quantum bit error rate (QBER), i.e., the fraction of positions where Alice and Bob's strings differ. Note that the QBER is a direct measure for the secrecy of Alice and Bob's strings, since any eavesdropping strategy would, according to the laws of quantum mechanics (no-cloning theorem) perturb the correlations between them. If the QBER is too high, Alice and Bob decide to abort the protocol. Otherwise, they apply a classical (post)-processing protocol to distill a secret key. This protocol, which could either be performed using one–way or two–way classical communication, consists of the following two subprotocols:

- INFORMATION RECONCILIATION: Alice sends certain error correction information W on X to Bob. Bob uses Y and W to reconstruct the bit string held by Alice, X.

- PRIVACY AMPLIFICATION: Once Alice and Bob have identical strings, X, privacy amplification is used to compute the final key on which the adversary has no information. In order to achieve that, the partially secure string X is transformed to a highly secret (much shorter) string using public discussion.

  It can be shown that if the QBER is sufficiently low such a classical postprocessing protocol can be used to establish a secret key between A and B. For instance, for the BB84 protocol it can been shown that if the QBER is smaller or equal to $12,4\%$, one can generate a secret key.

- FURTHER PROBLEMS:

  When realizing a QKD protocol, one has to make sure that the theoretical model, for which security has been proven, really describes the realization accurately. For instance, we assumed above that Alice sends single qubits to Bob, which are prepared in a certain state. However, this is a non–trivial task since it is still hard to prepare single photons in experiments. Thus, in several experiments weak coherent pulses are used for the transmission. Another important problem is that Eve might be able to "test" Alice' preparation,

or Bob's measurement device. In order to avoid investigating all possible attacks in a particular set–up, one is aiming for a so–called device independent security proof. The main idea is to show that if the bit strings of Alice and Bob are sufficiently correlated, more precisely, if they allow the legitimate persons to violate a Bell inequality, then they can be used to extract a secret key, independently of the devices used.

5 Quantum computation

Another interesting and very relevant application of quantum information is quantum computing. There, quantum systems are used in order to perform certain computations. Before we discuss how this can be achieved we discuss the basics of classical computation [9].

5.1 Classical computing

- COMPUTATION: A computation can be considered as a physical process that transforms an *input* into an *output*. In classical computation the physical process is based on classical laws.

- SLOW AND FAST ALGORITHMS:

  A fundamental measure of the difficulty of a computation is the amount of time (or space) it takes to carry out the computation [4]. Here, we will measure the complexity of a computation in terms of the number of fundamental operations, n_s, (addition, multiplication, bit comparisons, etc.) it takes to perform the computation as a function of the input size (recall that the number of bits required to store a number N is $\log_2(N)$):

  - *Fast:* The number of steps scale as a polynomial of the size of the input, that is $n_s \leq \mathrm{poly}[\log_2(N)]$ for all N.
  - *Slow:* The number of steps cannot be bounded by a polynomial of the size of the input, that is $n_s > \mathrm{poly}[\log_2(N)]$ for any polynomial and certain N.

- EXAMPLE: Multiplication of a number N by the number 123 requires $n_s < k \log_2(N)$ (for a given k), and therefore is fast. The factorization of a number N using an algorithm that checks if it is a divisor of $1, 2, \ldots, \sqrt{N}$ requires $\sqrt{N} = 2^{\log_2(N)/2}$, and therefore it is slow.

- UNIVERSAL COMPUTERS: One would like to have computers that are able to perform any algorithm; that is, changing from one algorithm to another should be done by the software. This leads to the concept of bits and gates.

  - BITS: Bits are (classical) systems with two different states 0 and 1. Any input and output number can be encoded in these systems using binary notation. For example, if we have 5 bits we can represent the number 23 as 10111.
  - GATES: The gates are the processes that transform bits. For example,

NOT	
Input	Output
0	1
1	0

AND		
Input		Output
0	0	0
0	1	0
1	0	0
1	1	1

[4] This is used to define different complexity classes.

– UNIVERSAL GATES: These are finite sets of gates such that any computation can be performed by a sequence of these gates. Examples of universal sets are: (NOT, AND, OR), Toffoli gate (see for instance [2]).

5.2 Quantum computing

- QUANTUM COMPUTATION: A *quantum* computation can be considered as a physical process that transforms an *input* state into an *output* state of a system. The physical process is based on the laws of quantum mechanics.

  – INPUT AND OUTPUT: Inputs and outputs are represented by states of the system. For example, enumerating the state of a given basis as $|1\rangle, |2\rangle, \ldots$, the number N would be represented by the N–th state of this basis.

  – RESTRICTIONS: The operation that transforms the input to output has to be unitary. For example, the operation that gives 1 if a number is odd and 2 if it is even could not be implemented:

$$\begin{aligned} |1\rangle &\rightarrow |1\rangle, \\ |2\rangle &\rightarrow |2\rangle, \\ |3\rangle &\rightarrow |1\rangle, \\ |4\rangle &\rightarrow |2\rangle. \end{aligned}$$

  This operation cannot be unitary since it is not reversible. One can however use an auxiliary system so that the output is written in that system:

$$\begin{aligned} |1\rangle|0\rangle &\rightarrow |1\rangle|1\rangle, \\ |2\rangle|0\rangle &\rightarrow |2\rangle|2\rangle, \\ |3\rangle|0\rangle &\rightarrow |3\rangle|1\rangle, \\ |4\rangle|0\rangle &\rightarrow |4\rangle|2\rangle. \end{aligned}$$

  – QUANTUM PARALLELISM: Using the laws of Quantum Mechanics, one can do more than with the laws of Classical Mechanics. To compute a function $f : N \rightarrow N$ for the numbers $1, 2, \ldots, n$, one has to run a classical computer n times. In a quantum computer one can do the same, by computing

$$\begin{aligned} |1\rangle|0\rangle &\rightarrow |1\rangle|f(1)\rangle, \\ |2\rangle|0\rangle &\rightarrow |2\rangle|f(2)\rangle, \\ &\ldots \\ |n\rangle|0\rangle &\rightarrow |n\rangle|f(n)\rangle. \end{aligned}$$

  Alternatively, one can prepare the following input state

$$|\psi\rangle = \frac{1}{\sqrt{n}} \sum_{k=1}^{n} |k\rangle|0\rangle \tag{18}$$

  and run the computer on this state only once, obtaining

$$\frac{1}{\sqrt{n}} \sum_{k=1}^{n} |k\rangle|f(k)\rangle. \tag{19}$$

All the values of f are in this superposition, but it is not possible to read them out in a measurement. However, as we will see, it will be possible to read out certain information.

- UNIVERSAL QUANTUM COMPUTERS: As in the classical case, one would like to have quantum computers that are able to perform any algorithm; that is, changing from one algorithm to another should be done by the software. This leads to the concept of qubits and quantum gates.

  - QUBITS: Quits are (quantum) systems with two different states $|0\rangle$ and $|1\rangle$. Any input and output number can be encoded in these systems using binary notation. For example, if we have 5 qubits we can represent the number $|23\rangle$ as $|10111\rangle$.
  - QUANTUM GATES: These are quantum processes and transform qubits. For example,

Single qubit gate: $\mathrm{I}(\alpha, \phi)$	
Input	Output
$\|0\rangle$	$\cos(\alpha)\|0\rangle - ie^{i\phi}\sin(\alpha)\|1\rangle$
$\|1\rangle$	$-ie^{-i\phi}\sin(\alpha)\|0\rangle + \cos(\alpha)\|1\rangle$

2–qubit gate: Control-NOT			
Input		Output	
$\|0\rangle$	$\|0\rangle$	$\|0\rangle$	$\|0\rangle$
$\|0\rangle$	$\|1\rangle$	$\|0\rangle$	$\|1\rangle$
$\|1\rangle$	$\|0\rangle$	$\|1\rangle$	$\|0\rangle$
$\|1\rangle$	$\|1\rangle$	$\|0\rangle$	$\|1\rangle$

  - UNIVERSAL GATES: It can be shown that any unitary operation acting on a set of qubits can be written as a sequence of Control–NOT and single qubit gates [2].

- SLOW AND FAST ALGORITHMS: Similarly to the classical case, the computational complexity measures how many basic operations (single and two-qubit gates) are required to implement an algorithm. Note that all operations that have fast algorithms in classical computation have fast algorithms in quantum computation. However, there are operations for which only classical slow algorithms are known, but there exist fast quantum algorithms. One of the most important example is factorization. Here, we will investigate some other examples.

- EXAMPLE: Consider the four functions, $f_1, f_2, g_1, g_2 : \{0,1\} \to \{0,1\}$, with

$$\begin{aligned} f_1 &= \mathbb{1} \\ f_2 &= \mathrm{NOT} \\ g_1 &= (1-x)\cdot \mathrm{I} + x \cdot \mathrm{NOT} \\ g_2 &= x \cdot \mathrm{I} + (1-x)\cdot \mathrm{NOT}, \end{aligned} \tag{20}$$

  where $\mathbb{1}$ denotes the identity function.

– Note that the first two functions, f_1 and f_2 give different results if acting on $\{0,1\}$, i.e. they are balanced, whereas the second two functions g_1 and g_2 give the same result, i.e. they are constant. That is $f_i(0) \neq f_i(1)$ and $g_i(0) = g_i(1)$, for $i = 1, 2$.
– PROBLEM: Given a function $h \in \{f_1, f_2, g_1, g_2\}$ the question is whether it is balanced or constant?
– CLASSICALLY: Classically, we have to apply the function twice in order to check whether the results are the same or different.
– QUANTUM MECHANICALLY: Quantum mechanically we can do better, as we will see now. Let U_f denote the unitary which is defined by $U_f|\, x, y\,\rangle = |\, x, f(x) \oplus y\,\rangle$, for some function f and consider the quantum algorithm

$$V_f \equiv U_f H \otimes H, \tag{21}$$

where

$$H = \frac{1}{\sqrt{2}} \begin{pmatrix} 1 & 1 \\ 1 & -1 \end{pmatrix} \tag{22}$$

denotes the Hadamard gate. We prepare the input state

$$|\psi_{\rm in}\rangle = |\, 0\,\rangle|\, 1\,\rangle. \tag{23}$$

Applying the Hadamard gates leads to

$$H \otimes H|\psi_{\rm in}\rangle = \frac{1}{2}(|\, 0\,\rangle|\, 0\,\rangle + |\, 1\,\rangle|\, 0\,\rangle - |\, 0\,\rangle|\, 1\,\rangle - |\, 1\,\rangle|\, 1\,\rangle). \tag{24}$$

Hence, the output state for a given function $h \in \{f_i, g_i\}_{i=1}^2$ is given by

$$U_h H \otimes H|\psi_{\rm in}\rangle = \frac{1}{2}(|\, 0\,\rangle(|\, h(0)\,\rangle - |\, 1 \oplus h(0)\,\rangle + |\, 1\,\rangle(|\, h(1)\,\rangle - |\, 1 \oplus h(1)\,\rangle). \tag{25}$$

Thus, the corresponding outputs for each possible functions are:

$$|\, \Psi_{f_1}\,\rangle = V_{f_1}|\psi_{\rm in}\rangle = \frac{1}{2}(|0\rangle - |1\rangle) \otimes (|0\rangle - |1\rangle) = |-\rangle|-\rangle, \tag{26}$$

$$|\, \Psi_{f_2}\,\rangle = V_{f_2}|\psi_{\rm in}\rangle = -\frac{1}{2}(|0\rangle - |1\rangle) \otimes (|0\rangle - |1\rangle) = -|-\rangle|-\rangle, \tag{27}$$

$$|\, \Psi_{g_1}\,\rangle = V_{g_1}|\psi_{\rm in}\rangle = \frac{1}{2}(|0\rangle + |1\rangle) \otimes (|0\rangle - |1\rangle) = |+\rangle|-\rangle, \tag{28}$$

$$|\, \Psi_{g_2}\,\rangle = V_{g_2}|\psi_{\rm in}\rangle = -\frac{1}{2}(|0\rangle + |1\rangle) \otimes (|0\rangle - |1\rangle) = -|+\rangle|-\rangle, \tag{29}$$

$$\tag{30}$$

where $|\pm\rangle = \frac{1}{\sqrt{2}}(|\, 0\,\rangle \pm |\, 1\,\rangle)$. Hence, in general we have (up to an irrelevant phase)

$$|\, \Psi_h\,\rangle = V_h|\psi_{\rm in}\rangle = |\, 0 + (-1)^{h(0)\oplus h(1)}\,\rangle|-\rangle, \tag{31}$$

for any function $h \in \{f_i, g_i\}_{i=1}^2$. Hence, the result given by f_1 and f_2 are orthogonal to those given by g_1 and g_2, and therefore we can distinguish whether we applied one of the f or g functions. For instance we can measure σ_x in the first system. If the result is 1 we know that h is balanced, otherwise it is constant. Note that we obtain the right result with probability 1.

  - ORACLE: Note that we assumed here that we can apply the unitary U_f, which is only possible if we would know f. These kind of algorithms are called oracle algorithms. The complexity of those algorithms is measured by the number of queries.
  - DEUTSCH ALGORITHM [10]: This algorithm, called Deutsch algorithm, was the first quantum algorithm which was invented by David Deutsch in 1985. As we have seen, the quantum algorithm outperforms the classical one since classically we would requirer 2 queries, however quantum mechanically we requirer only one query to determine whether the function is constant or balanced.

- DEUTSCH–JOZSA ALGORITHM [11]: The Deutsch algorithm has been generalized to functions

$$f : \{0,1\}^n \to \{0,1\}, \tag{32}$$

  which are promised to be either constant or balanced. It can be shown that classically one would requirer $2^{n-1}+1$ queries, however, quantum mechanically a single query is sufficient to determine whether the function is constant or not. Thus, this is an example of an exponential separation between classical and quantum computation. [5]

5.2.1 Further Quantum algorithms

Unfortunately, we do not have the time to investigate other, very important quantum algorithms, but we briefly mention some of them here [2].

- SIMON ALGORITHM [12]:
  - AIM: We are given a function, $f : \{0,1\}^n \to \{0,1\}^n$ which possesses a period. That is, there exists a n–bit string s such that for all n–bit strings x, y

$$f(x) = f(y) \tag{33}$$

    iff $x = y$ or $x = y \oplus s$, where the addition is modulo 2. The aim is to determine s with as few queries on the oracle as possible.
  - KIND OF ALGORITHM: Oracle Algorithm
  - NUMBER OF QUERIES: classically $\mathcal{O}(2^{n/2})$ queries are required, whereas quantum mechanically only $\mathcal{O}(n)$ queries are required. Thus, Simon algorithm is another example of an oracle algorithm which solves a problem exponentially faster than any classical algorithm.

- GROVER ALGORITHM [13]:
  - AIM: Search a unsorted data basis containing N items. For instance, given a telephone book with N names and numbers. The aim is to find the name corresponding to a certain number.
  - KIND OF ALGORITHM: Oracle Algorithm

[5] Note that this is only true for deterministic algorithms. A probabilistic classical algorithm would find the solution as fast as a quantum algorithm (in the asymptotic limit, i.e. for $n \to \infty$).

  - NUMBER OF QUERIES: classically it has been shown that $\mathcal{O}(N)$ queries are required. However, quantum mechanically $\mathcal{O}(\sqrt{N})$ queries suffice. Thus, there is a quadratic speed–up, which can be shown to be optimal.

- SHOR ALGORITHM [14]:
  - AIM: Given a n–bit number N, decompose N into its prime factors.
  - KIND OF ALGORITHM: Non–oracle algorithm
  - NUMBER OF COMPUTATIONAL STEPS: The best known classical algorithm to solve this problem requires a superpolynomial number of computational steps. Shor's algorithm is able to factorize the number in $\mathcal{O}(n^3)$ steps. Thus, there is an exponential separation between the classical and the quantum computation. Note that some classical cryptographic systems use the fact that factorization is a hard problem. However, as we see here, this is only true for classical computers.

5.2.2 Models for quantum computation

There exist several different models for quantum computation. We will very briefly summarize some here:

- QUANTUM CIRCUIT MODEL: Here the input state is usually considered to be a computational state, $|\, x_1, \ldots, x_n \,\rangle$, with $x_i \in \{0, 1\}$ and the computation is performed by applying a sequence of single and two–qubit gates. The measurement reveals the output. Note that due to the fact that any unitary can be decomposed into single and two–qubit operations, any unitary can be implemented in this way.

- ONE-WAY QUANTUM COMPUTATION [15]: The computation consists of the following steps. First, a highly entangled multipartite quantum state is prepared, the so–called 2D cluster state. Then, a sequence of adoptive one–qubit measurements (depending on the classical input) is performed. The unmeasured qubits are then, up to local unitary operations in the desired state, $|\, \Psi_{out} \,\rangle = U|+\rangle^{\otimes n}$.

- ADIABATIC QUANTUM COMPUTATION [16]: The aim is to find the global minimum of a given function $f : \{0, 1\}^n \to (0, \infty)$, where $min_x f(x) = f_0$ and $f(x) = f_0$ iff $x = x_0$, i.e. there is a unique minimum. The aim is to find x_0. In order to do so, one considers the Hamiltonian

$$H_1 = \sum_{x \in \{0,1\}^n} f(x)|\, x \,\rangle\langle\, x \,|, \tag{34}$$

  whose unique ground state is $|\, x_0 \,\rangle$. In order to find this ground state, one considers the Hamiltonian

$$H(\lambda) = (1 - \lambda)H_0 + \lambda H_1, \tag{35}$$

  with $\lambda \in [0, 1]$ and H_0 a Hamiltonian whose unique ground state can be easily constructed. The quantum adiabatic theorem states that if one would start in the ground state of $H(0) = H_0$ and one would slowly increase the parameter λ, then the system would evolve to the ground state of H_1, if $H(\lambda)$ is always gapped, i.e. there is no degeneracy for the ground state energy. Thus, if one would measure at the end of this process the system in the computational basis, one would obtain x_0.

All the above mentioned models of quantum computation are equivalent in the sense that one can simulate the other using just a polynomial overhead. There are several different physical systems which can be used to realize a quantum computer, for instance ions in ion–traps, neutral atoms in optical lattices, nuclear magnetic resonance (NMR), quantum dots, etc.. The requirements which have to be met are known as DiVincenzo criteria (see for instance lecture A3, B4, C2).

6 Quantum simulation

Another very useful and relevant application is quantum simulation. Suppose we are given a n–qubit system which is originally prepared in some state, $|\,\Psi(0)\,\rangle$ and where the qubits are interacting with each other according to some Hamiltonian, H. Our aim is to determine the state of the n–qubits after some time t. Since the Hamiltonian is a $2^n \times 2^n$ matrix, the evaluation of $|\,\Psi(t)\,\rangle = e^{-iHt}|\,\Psi(0)\,\rangle$ would be for most Hamiltonians unfeasible on a classical computer. Another problem along these lines is the determination of the ground state of some multipartite Hamiltonian H.
Thus, the exponential growth of the required resources, like space and time, as a function of the number of considered quantum systems, makes a simulation of certain quantum system on a classical computer an unfeasible task. As conjectured by Feynman and then proven by LLoyd, however, a quantum system can be used to simulate the behavior of another. The former one being such that the interactions between the systems are well–controllable and that the measurements can be performed sufficiently well.

- QUANTUM SIMULATION: For most of the physically relevant situations the Hamiltonian can be written as a sum of few–body Hamiltonians, H_k, where H_k is acting non–trivially only on a constant number of qubits. That is

$$H = \sum_{k=1}^{m} H_k, \tag{36}$$

  where m is at most a polynomial function of the number of qubits, n. Since H_k is acting only on a constant number of qubits, the unitary $e^{-iH_k t}$ can be decomposed into a constant number of single and two–qubit operators. The main idea to approximate e^{-iHt} efficiently on a quantum computer is to use the Lie–Trotter formula:

$$\lim_{N\to\infty} \left(e^{-iAt/N} e^{-iBt/N}\right)^N = e^{-i(A+B)t}, \tag{37}$$

  for any two hermitian matrices A and B and any real t. Using this formula, which can be easily verified by expanding the exponential function, one can show that

$$e^{-i(A+B)\Delta t} = e^{-iA\Delta t} e^{-iB\Delta t} + \mathcal{O}(\Delta t^2) \tag{38}$$

  and

$$e^{-i(A+B)\Delta t} = e^{-iA\Delta t/2} e^{-iB\Delta t} e^{-iA\Delta t/2} + \mathcal{O}(\Delta t^3). \tag{39}$$

  The important point now is, that the evolution operator e^{-iHt} can be approximated by polynomially many operators of the form $e^{-iH_k t}$, which can be implemented efficiently on a quantum computer.

- EXPERIMENTS: The suitability for the realization of such a quantum simulator has been shown for experimental schemes based on optical lattices or ion–traps. Recently, several experiments using for instance trapped ions, neutral atoms or NMR have realized quantum simulations.

- QUANTUM PHASE TRANSITION: An important application of the quantum simulator is also the study of the ground state properties of certain condensed matter systems. Quantum spin models are well suited for the investigations of quantum phase transitions [17], which occur at zero temperature due to the change of some parameter, like the strength of the magnetic field, or pressure. The 1D quantum Ising model, for instance, exhibits such a phase transition. It can be detected by measuring the magnetization as a function of the ratio between the interaction strength and the strength of the external magnetic field. One way to observe this phase transition is to use adiabatic evolution as explained in Sec. 5.2.2. Since the Ising interaction is relatively simple, this is a good model for the experimental demonstration of quantum simulation, even though it can be simulated classically efficiently.

7 Quantum repeater

We have seen now that entanglement plays an important role in quantum communication, for instance for quantum cryptography or quantum teleportation. We are going to address here the problem of how to establish a highly entangled state between two very distant parties. Due to the interaction with the environment, the entanglement contained in a state, which is for instance prepared by Alice, and where one of the qubits is sent to Bob, will always be diminished. In case the parties are very far away from each other, the state they share will no longer be entangled. Thus, quantum purification could not be used to distill maximally entangled states. One clever way to overcome this problem has been proposed in [18]. This method is known as quantum repeater. It provides a solution to this problem based on entanglement purification and entanglement swapping. The procedure is the following:

- DIVIDING DISTANCE: The distance L between the parties A and B is divided into N smaller segments. The distance between the different notes, L/N, is chosen in such a way that one can send parts of maximally entangled pairs through the channel such that the resulting state has a sufficiently high fidelity for entanglement purification.

- ENTANGLEMENT PURIFICATION: Once the pairs are distributed, they are purified via some entanglement purification protocol (see lecture A2). That is, via local operations and classical communication the parties transform several copies of a noisy state into one copy of a state, ρ, with a very high fidelity, $F = \langle \Phi^+ |\rho| \Phi^+ \rangle$.

- ENTANGLEMENT SWAPPING: Via entanglement swapping entangled pairs over larger distances are established.

  Entanglement swapping is the operation on two maximally entangled qubit pairs, where a Bell measurement is performed on one qubit of each pair with the result that the remaining two qubits are afterwards maximally entangled. For instance, consider two maximally entangled states, one shared between party A and B and the other one shared between B and C. Let us denote by B_1 and B_2 the two qubits at site B and let B perform a Bell measurement on his particles. That is, B measures P_i for $i \in \{0, \ldots, 3\}$, where P_i is the projector onto the maximally entangled state $|\Psi_i\rangle = \mathbb{1} \otimes \sigma_i |\Phi^+\rangle$ (see also Eq (4)). Here, σ_i denote the Pauli operators together with the identity operator. Then, the resulting state is

$$(P_i)_{B_1B_2} |\Phi^+\rangle_{AB_1} |\Phi^+\rangle_{B_2C} = |\Psi_i\rangle_{B_1B_2} \mathbb{1}_A \otimes (\sigma_i)_C |\Phi^+\rangle_{AC}, \tag{40}$$

where we ignored irrelevant global phases. Thus, after this measurement parties A and C share a maximally entangled state. Using classical communication they can easily transform it to the state $|\,\Phi^+\,\rangle$. Note that entanglement swapping can be viewed as a teleportation of the state of qubit B_1 to C and allowed us to generate a maximally entangled state between the more distant notes A and C.

- ENTANGLEMENT PURIFICATION: Observe that entanglement swapping decreases the fidelity of the resulting states, since the fidelity of the resulting long-distance pair will depend on the fidelity of the small-distance pairs (which is close to 1, but $F \neq 1$). In fact, the fidelity would decrease exponentially with the number of connected pairs, i.e. pairs where entanglement swapping has been performed. Thus, one may connect only a few segments before the entanglement can no longer be increased by purification. The key ingredient of the quantum repeater is to use the combination of purification and entanglement swapping in a nested scheme, i.e. on different repeater levels. After few connections are made, the resulting pair is again purified by several copies obtained in the same way, which leads to states with the same fidelity as originally, but now shared between two more distant parties.

- REPETITION: The sequence of entanglement swapping and purification is repeated until one has reached the desired distance between the parties.

- RESOURCES: It is important to note that one can show that the physical and temporal resources needed for the quantum repeater scale only polynomially with the distance between parties A and B. Thus, the quantum repeater can be implemented efficiently. Moreover, it has been shown, that the scheme outlined above can tolerate errors up to a percent for local operations and measurements.

8 Multipartite Entanglement

So far we have mainly seen applications of bi–partite entanglement. However, there are also several important applications of multipartite entangled states, like for instance quantum error correction, enhanced spectroscopy, quantum metrology, and quantum computation. Recently it has been shown that the tools and concepts developed in the context of multipartite systems can be utilized to shed new light into Condensed Matter Physics.
Many of the applications mentioned above are possible due to the subtle properties of quantum many–body systems. Thus, the investigation of these properties is at the heart of quantum information theory. We are going to highlight here some of the main differences between bi–partite and multipartite entanglement. We will mainly focus here on qubits, however, the definitions etc. can be easily generalized to higher–dimensional systems.

- ENTANGLEMENT: Like in the bi–partite case a n–qubit pure state, $|\,\Psi\,\rangle$ is called entangled if it cannot be written as a product state, i.e. as

$$|\,\phi_1\,\rangle \otimes |\,\phi_2\,\rangle \otimes \ldots \otimes |\,\phi_n\,\rangle, \tag{41}$$

with $|\,\phi_i\,\rangle \in \mathbb{C}^2$ for $i \in \{1, \ldots, n\}$.

– BISEPARABILITY: A n–qubit pure state, $|\Psi\rangle$, is called biseparable if it can be written as a product state between some part of the system and the remaining one, i.e. if it can be written as

$$|\Psi\rangle = |\phi_L\rangle|\phi_M\rangle, \tag{42}$$

where $L, M \subset \{1, \ldots, n\}$ and $L \cup M = \{1, \ldots, n\}$. For instance the three–partite state $|\Psi\rangle_{123} = |\Phi^+\rangle_{12}|0\rangle_3$ contains 2–body entanglement, but is not three–partite entangled, since the third party is not entangled to the other two. In case where all parties are entangled, i.e. if the state cannot be written as a product state in any bi–partite splitting, the state is called truely multipartite entangled.

– k–SEPARABILITY: More generally, one calls an n-partite state, $|\Psi\rangle$, k–separable if it can be written as a product of k states, i.e.

$$|\Psi\rangle = |\phi_1\rangle|\phi_2\rangle \ldots |\phi_k\rangle, \tag{43}$$

where each of the states $|\phi_i\rangle$ describe some qubits.

- GHZ-STATES: A very prominent example of a multipartite entangled state is the GHZ–state, invented by Greenberger, Horne and Zeilinger. It is of the form

$$|\Psi\rangle = \frac{1}{\sqrt{2}}(|0\rangle^{\otimes n} + |1\rangle^{\otimes n}). \tag{44}$$

It has been shown that this state can be used to violate some Bell inequalities.

- W-STATES: An other important n–qubit state is of the form

$$|W\rangle = \frac{1}{\sqrt{n}}(|0, \ldots, 0, 1\rangle + |0, \ldots, 0, 1, 0\rangle + |0, \ldots, 1, 0, 0\rangle + \ldots |1, \ldots, 0, 0\rangle). \tag{45}$$

- STABILIZER STATES: An other very relevant class of multipartite states are the so–called stabilizer states [19, 2]. Those states possess the special properties that they can be highly entangled and that their manipulation under a restricted set of operations is relatively simple. This enabled researchers to gain a lot of intuition about the usefulness and manipulation of stabilizer states. This knowledge in turn led to many of the fascinating applications of multipartite states.

- 3–QUBIT STATES: Already in the case of three qubits it has been shown that the GHZ–state and the W–state are fundamentally different. It has been shown that it is impossible to obtain even probabilistically one from the other by applying Local Operations and Classical Communication (LOCC). Mathematically this means that there exist no 2×2 matrices, A, B, C such that

$$A \otimes B \otimes C|GHZ\rangle \propto |W\rangle, \tag{46}$$

where $|GHZ\rangle$, ($|W\rangle$) denote the three–qubit GHZ (W)–state respectively.

- MIXED STATES: A mixed n–partite state, ρ is called fully separable if can be written as a convex combination of product states, i.e.

$$\rho = \sum_i p_i \rho_i^1 \otimes \rho_i^2 \otimes \ldots \otimes \rho_i^n, \tag{47}$$

where $p_i \geq 0$ and $\sum_i p_i = 1$ and $\rho_i \in \mathcal{B}(\mathbb{C}^2)$. ρ is called k-separable, if it can be written as a convex combination of k-separable pure states. That is,

$$\rho = \sum_i p_i |\, \Psi_i \,\rangle\langle\, \Psi_i \,|, \tag{48}$$

where $p_i \geq 0$ and $\sum_i p_i = 1$ and $|\, \Psi_i \,\rangle$ is k–separable. Note that the states $|\, \Psi_i \,\rangle$ are all k–separable, however, they might be k–separable under different partitions. Therefore, there does not need to a exist a partition, with respect to which the state ρ is separable to.

Already from these definitions we see that multipartite entanglement is much richer than bipartite entanglement. The exponential growth of the dimension of the Hilbert space as a function of the considered qubits makes it very difficult to qualify and quantify multipartite entanglement. Despite its relevance and an enormous effort of physicists, many of the problem related to multipartite entanglement are still open. Several entanglement measures for multipartite states, like the tangle, the Schmidt measure, the localizable entanglement, or geometric measure of entanglement have been introduced. Moreover, different classes of entangled states have been identified, and a normal form of multipartite states has been presented. However, even for few–qubit systems the entanglement properties are still not completely understood. One of the main reasons for the lack of knowledge is, arguably, that for many-body entangled states we do have only few applications. This results into the existence of few known operational entanglement measures [1].

References

[1] Most of the papers related to Quantum Information can be found under arxiv.org.

[2] M. Nielsen and I. Chuang, *Quantum Computation and Quantum Information*, Cambridge Univ. Press, Cambridge (2000).

[3] C. H. Bennett, G. Brassard, C. Crépeau, R. Jozsa, A. Peres, W. K. Wootters, Phys. Rev. Lett. **70**, 1895 (1993).

[4] C. H. Bennett and S.J. Wiesner, Phys. Rev. Lett. **69**, 2881 (1992).

[5] C. H. Bennett and G. Brassard, *Proceedings of International Conference on Computer Systems and Signal Processing*, p. 175 (1984).

[6] C. H. Bennett, Phys. Rev. Lett. **68**, 3121 (1992).

[7] see for instance http://www.idquantique.com; http://www.magiqtech.com.

[8] A. Ekert, Phys. Rev. Lett. **67**, 662 (1991).

[9] See for instance A.Yu Kitaev, A. Shen, M. N. Vyalyi, *Classical and Quantum Computation*, American Mathematical Society, 2002.

[10] D. Deutsch, Proc. R. Soc. Lond. A **400**, 97 (1985).

[11] D. Deutsch and R. Jozsa, Proc. R. Soc. Lond. A **439**, 553 (1992).

[12] D. R. Simon, "On the power of quantum computation", Foundations of Computer Science, 1994 Proceedings., 35th Annual Symposium on Foundations of Comp. Science, 116123 (1994).

[13] L. K. Grover, Phys. Rev. Lett. **79**, 325 (1997).

[14] P. W. Shor, *Algorithms for quantum computation: discrete logarithms and factoring*, *Proceedings of the 35th Annual Symposium on Foundations of Computer Science* (IEEE Press Los Alamitos CA, p. 124 (1994).

[15] R. Raussendorf and H. Briegel, Phys. Rev. Lett. **86**, 5188 (2001)

[16] E. Farhi, J. Goldstone, S. Gutmann und M. Sipser, arXiv:quant-ph/0001106 (2000).

[17] S. Sachdev, *Quantum Phase Transitions*, Cambridge University Pree, Cambridge, 1999.

[18] W. Dür, H.- J. Briegel, J. I. Cirac, P. Zoller, Phys.Rev.A **59**, 169 (1999)

[19] see for instance, D. Gottesman, *Stabilizer codes and quantum error correction*, Ph.D. Thesis, arXiv: quant-ph/9705052 (1997).

A 6 Spin Qubits - Introduction and GaAs quantum dots [1]

Hendrik Bluhm
Institute of Physics IIC
RWTH Aachen University

Contents

1 Introduction **3**

2 Survey of solid state qubits **3**

3 NMR based quantum information processing **5**

4 Quantum dots in a two-dimensional electron gas **6**

5 Single electron spin qubits **8**
5.1 Initialization and readout 9
5.2 Single spin control 11

6 Two-electron spin qubits **13**
6.1 Motivation and energy diagram 13
6.2 Control of the $S - T_0$ qubit 15

7 Hyperfine interaction with nuclear spins **16**
7.1 Hyperfine interaction 16
7.2 Probing nuclear spins 17
7.3 Nuclear spin dynamics 19

8 Dynamic nuclear polarization **21**
8.1 Nuclear spin pumping 21

8.2 Narrowing of nuclear field distribution using 'closed-loop' spin pumping 24

9 Two-qubit entangling gates **26**
9.1 Exchange based approaches 26
9.2 Charge coupled $S - T_0$ qubits 27

10 Quantum control techniques **31**
10.1 Rabi control and its limitations 31
10.2 Control beyond Rabi flopping 32
10.3 Composite pulses and dynamically corrected gates 32
10.4 Optimal control and related approaches 33

11 Outlook **34**

[1]Lecture Notes of the 44^{th} IFF Spring School "Quantum Information Processing" (Forschungszentrum Jülich, 2013). All rights reserved.

1 Introduction

Any implementation of a quantum information processor obviously needs a physical system to represent its qubits. A rather large variety of different types of qubits have been explored to various degrees. The challenge is to identify a truly scalable architecture that allows the controlled realization of thousands or even millions of interconnected qubits. Solid state qubits are attractive candidates for pursuing this goal because of their potentially small footprint and compatibility with well-established microfabrication techniques. This promise of scalability comes at the expense of a rather messy environment: solid state systems usually have a large number of degrees of freedom, such as nuclear spins, phonons, charge traps and bistable lattice defects. Any interaction of a qubit with such uncontrolled degrees of freedom leads to decoherence. Hence, care must be taken to pick physical qubits that couple weakly to their solid state environment, which is not an easy task.

Nevertheless, a range of solid state qubits have been proposed and experimentally realized. One of them are electron spin qubits in GaAs quantum dots, the main topic of this chapter. Before discussing them in detail, an overview of different types of solid state qubits is given in section 2. Section 3 summarizes early approaches to quantum computing using NMR. Section 4 describes how gate defined quantum dots can be formed in a 2DEG at a semiconductor heterostructure. Sections 5 and 6 deal with the two most developed kinds of quantum dot based spin qubits, which use one or two spins for encoding a single qubit. Section 6 also contains a detailed account of the theoretical framework for understanding two-electron spin qubits. The subject of sections 7 and 8 is the interaction of electron spins with nuclear spins, which is an important dephasing mechanism for GaAs based qubits, and dynamical nuclear polarization as a means to reduce it. Two-qubit gates for both types of qubits are presented in section 9. Section 10 and 11 conclude with a survey of advanced qubit control approaches and an outlook on open questions and challenges.

2 Survey of solid state qubits

The so far most advanced type of solid state qubits are superconducting qubits, of which a number of different types exist. The all rely on superconducting electronic circuits incorporating Josephson junctions. The superconductivity eliminates electrical resistance and thus slows down relaxation to the ground state, so that adequate coherence times are obtained. The nonlinearity of the Josephson junction leads to an anharmonic energy level spacing, which allows pairs of individual levels (usually the ground and first excited state) to be singled out and used to represent the qubit. These superconducting qubits are discussed in detail in chapter A4.

Another important kind of solid state qubits are spin qubits, which encode the quantum information in some spin degree of freedom. The spin is a natural choice for a qubit because it automatically provides a set of discrete levels (specifically two for a spin-1/2 particle). Spin qubits can broadly be categorized into electron and nuclear spin qubits. The latter employ the spin of the nucleus of some atom, which can be part of a molecule or embedded in a crystal. One way to study these is to use traditional nuclear magnetic resonance (NMR) techniques, which measure large ensembles of identical qubits or small groups of qubits. This method has been a proving ground for many concepts of quantum information and will be discussed briefly in section 3.

To utilize electron spins as qubits, the charge degree of freedom of the electrons is typically

frozen by tightly confining them. (Mobile, so called flying qubits, which could be based on traveling electrons, would also be of interest, but have received fairly little attention so far.) This confinement can either be created by engineering appropriate semiconductor structures, so called quantum dots, or by utilizing defects or impurities in a semiconductor host. The reason that semiconductors are preferred over metals is the absence of thermal excitations at temperatures well below the gap, so that decoherence from delocalized electrons can be avoided. (Insulators either contain no electrons at all or are effectively large-gap semiconductors.)

In this chapter, we will mostly focus on semiconductor spin qubits based on GaAs quantum dots. Relying on a relatively mature material technology, these are the most developed type of quantum dot qubit and have played a pioneering role in many seminal proof of principle experiments. However, a major drawback of GaAs (and all other III-V semiconductors) is that all the isotopes of their constituents carry nuclear spin. Through the hyperfine interaction, the nuclear spins interact with the qubit spins and are thus a major source of dephasing. While it appears that this decoherence channel can be mitigated quite effectively, doing so involves a significant overhead and complication. Hence, a number of alternative host materials are being pursued. Examples are Si/SiGe heterostructures, to be discussed in chapter B3, or carbon based systems such as graphene and carbon nanotubes (chapter D3). These rely on very similar principles as GaAs based quantum dots, but only a minority isotope carries nuclear spin. Hyperfine dephasing is thus much weaker and can be reduced further by isotopic purification. One particular variant of semiconductor quantum dots that recently have received significant attention are those based on nanowires, which are the subject of chapter D5 and might also allow the realization of Majorana qubits (chapter B2).

Another interesting type of quantum dots are so called self assembled dots, which are small islands of a semiconductor with a lower band gap than the surrounding host material. They are typically also based on III-V materials. In these structures, electrons and holes can be confined at the same time, which enables optical control and the creation of excitons. Results obtained in these structures will be the subject of chapter D4.

Two prominent examples of defect or impurity based spin qubits are P donors in Si, and Nitrogen vacancy (NV) centers in diamond. For P donors in Si, the electron is bound by the donor charge, and outstanding coherence times have been demonstrated. They will be discussed in chapter B1. NV centers in diamond consist of an N impurity next to a missing C atom (vacancy) and form an $s = 1$ spin. They feature optical readout and initialization and millisecond-scale coherence time at room temperature. Details will be presented in chapter D2. Another example, which is however much less developed, are magnetic molecules carrying a large magnetic moment [1].

The systems discussed above include most of the mainstream spin qubit types, but are not exhaustive. For example, several groups are searching for other types of impurities or defect centers in semiconductors with properties that are favorable for use as qubits. Besides bulk NMR measurements and single-electron-spin experiments, there are also efforts to utilize individual nuclear spins. Because of their good isolation from the environment, they are usually read out via a nearby electron spin (qubit). Examples are ^{31}P donor nuclei in Si [2] and ^{15}N or ^{13}C nuclei coupled to NV centers in diamond [3].

I conclude this section by discussing a couple of other types of solid state qubits. Given that quantum mechanics is typically first introduced to describe the motion of electrons, the perhaps most obvious type of qubit is the charge qubit, whose state is represented by two possible locations of an electron. Such devices have indeed been realized in GaAs quantum dots, [4, 5], but their coherence was found to be rather poor. Note that certain types of superconducting

qubits (Cooper pair boxes) are also charge qubits.
Making use of the band structure of semiconductors, one can conceive valley qubits encoded in the valley degree of freedom of an electron. The conditions for realizing those are particular favorable in materials with a degenerate band structure, such as graphene or Si. Some discussion of such qubits will be given in chapters B3 and D3.
In self assembled quantum dots and other structures with confinement for both holes and electrons, it is also possible to create exciton qubits (or at least coherent two level systems). Their basis states correspond to the absence or presence of an optically excitable confined electron-hole pair, called exciton. Due to the ns-scale exciton recombination time, their lifetime is rather short, but they can also be manipulated on the ps scale using short laser pulses.
Finally, it is worth mentioning that the study of the quantum dynamics of fairly macroscopic mechanical degrees of freedom has received significant attention for a number of years, however no fully functional qubits have emerged yet from these efforts. One difficulty lies in the fact that most mechanical systems have sub-GHz resonance frequencies, so that it is difficult to reach temperatures in which the ground state is predominantly occupied in thermal equilibrium. Several experiments used various active cooling methods to cool mechanical resonators much below the bath temperature, but cooling all the way to the ground state remains challenging. The first demonstration of quantum coherence of a phonon-like degree of freedom was achieved by engineering a resonance mode with an eigenfrequency of about 6 GHz and coupling it to a superconducting qubit [6]. This frequency is large enough to ensure a large equilibrium ground state occupation at a relatively easily achievable temperature of 25 mK. It was thus possible to transfer superposition states from the qubit to the resonator and back, showing that the resonator can be prepared and maintained (for some time) in a coherent superposition of harmonic oscillator eigenstates.

3 NMR based quantum information processing

This complete section was copied with minor adaptations from Ref. [7].
The first quantum computation experiments with spins were carried out using conventional liquid-state nuclear magnetic resonance [8]. Here, a large number of identical molecules is dissolved in liquid solution, where each molecule acts as a little quantum computer - the large number of copies of the molecules just serves to make the signal easily detectable. The molecules are chosen so that they have two or more spin-1/2 nuclei with well separated resonance frequencies. Thus, they can be individually addressed and read out by magnetic resonance. The spins within each molecule are coupled to each other through the electrons involved in the chemical bonds (the coupling between spins in different molecules is largely averaged out since they rapidly tumble around). The effect of this coupling is that one spin in the molecule will see its precession frequency about the magnetic field slightly enhanced or reduced, depending on whether another spin in the molecule points up or down. This coupling can be used for performing quantum logic gates. By combining a sequence of about 300 single-spin rotations interspersed with two-spin interactions, it was possible to demonstrate the operation of a quantum algorithm for factoring the number 15 in a molecule with seven nuclear spins [9]. Even though rapid progress was made using this approach, it also has well-understood scaling limitations. In particular, the experiments with liquid solutions were done at room temperature. Since the thermal energy at room temperature is much larger than achievable energy splittings between the two nuclear spin states, the spin-up and spin-down populations are roughly equal in thermal equilibrium.

Thermal equilibration is thus not a good way to initialize the spins to a specific state. Even though workarounds exist and were used for instance in the factoring experiment, these are not practical beyond about ten spins per molecule. It is also not clear how to synthesize molecules with hundreds or thousands of spins, which can all be selectively addressed and are part of a suitable coupling network.

4 Quantum dots in a two-dimensional electron gas

As mentioned in section 2, one way to capture electrons for use as spin qubits is to create so called quantum dots. In abstract terms, these are potential wells that confine the electrons in all three spatial directions. In order to completely eliminate the charge dynamics, the orbital level splitting needs to be much larger than the temperature and other relevant energy scales (e.g. the Zeeman splitting) so that only the orbital ground state is occupied.

We will now discuss a "classic" example of how to create such a confining potential, namely gate defined (also called lateral) quantum dots formed from a two-dimensional electron gas (2DEG) in a GaAs /AlGaAs heterostructure. Being based on semiconductors and standard lithography principles, one may hope to leverage the evidently very successful semiconductor technology for these devices. Hence, good prospects for scalability are foreseen for architectures of this sort. The kind of quantum dots discussed in this section was used for all the experiments discussed in the remainder of this chapter. A very similar approach is also being pursued with Si/SiGe heterostructures in order to reduce dephasing due to nuclear spins (see chapter B3).

The starting point of the fabrication of such devices is a commercially available wafer cut from a single GaAs crystal (Fig. 1 left). On top of this wafer, additional layers are grown using molecular beam epitaxy (MBE). This technique allows the deposition of one monolayer at a time, with impurity concentrations in the part-per-billion (10^{-9}) range and extremely low defect density. To achieve these extraordinary qualities, highly refined growth techniques are used and much effort is spent trying to trap impurities, for example using liquid nitrogen cooled UHV chambers.

After depositing enough GaAs for defects such as dislocations present in the lower quality substrate to heal, about 30% of the Ga is replaced with Al. The resulting semiconductor alloy has the same lattice constant, but a larger band gap. Near the surface, Si is added as a dopant before terminating the structure with a GaAs cap to prevent oxidation of the AlGaAs layer. The resulting layer structure, shown in Fig. 1(right), is called a heterostructure. For devices used as qubits, the depth of the GaAs$-$Al$_{0.3}$Ga$_{0.7}$As interface is typically about 100 nm below the surface.

To understand how such a heterostructure can be used to trap electrons, it is useful to review the basics of band structure theory. Bands describe the dependence of the energy of electrons on the k-vector. GaAs has a single conduction band and three valence bands. For our purpose, the Fermi energy will be near the conduction band edge and we can assume the valence band to be fully occupied (one could also work with holes instead of electrons in a very similar way). We will be interested in electrons near the Γ-point, where the conduction band can be approximated as quadratic. Hence, the electrons behave like free particles and their wave function envelope (which does not contain the microscopic structure resulting from the interaction with the lattice atoms) is governed by the Schrödinger equation. However, since the curvature of the band is different from that for free electrons, the effective mass, $m^* = 0.067m_\mathrm{e}$, is much smaller than

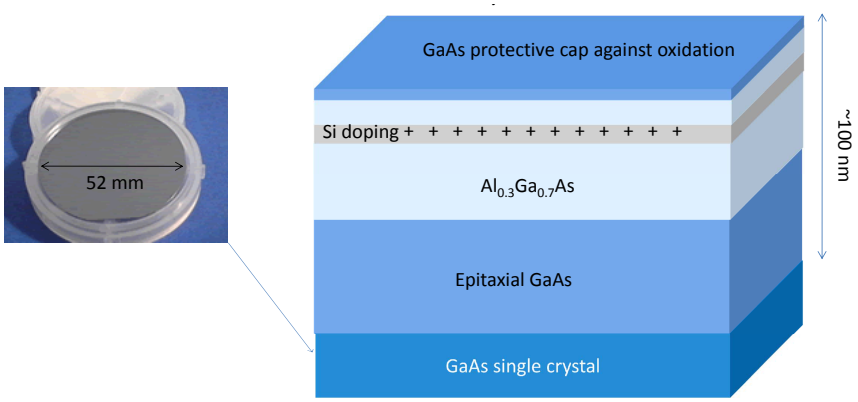

Fig. 1: ***GaAs/AlGaAs heterostructure. Left:*** *GaAs wafer.* ***Right:*** *layer-structure*

the free electron mass, m_e. This fact is quite useful since it leads to a much larger spread of the electronic wave function in a given potential. It is also useful to remember that the total energy of electrons is the sum of the band energy and the electrostatic potential.

We now consider the variation of the band edges along the z-direction (perpendicular to the surface). Without any dopants or other net charges, the bands would be flat. The band gap is larger in AlGaAs, as shown in Fig. 2(top left). The effect of the charge density, ρ, originating from the ionized dopants, is to introduce a positive curvature to the electrostatic potential, which satisfies the Poisson equation: $-\frac{\partial^2}{\partial z^2}\phi(z) = \rho(z)/\epsilon_0$. Hence, the bands are bent as shown in Fig. 2 (top right).

In practice, it is not (easily) possible to remove all electrons, as we have assumed so far, because they are strongly attracted by the remaining net positive charge. Instead the electrons will accumulate where their energy is lowest. With a proper choice of parameters, this point will be at the GaAs−AlGas interface, as shown in Fig. 2 (bottom). The negative electron charge leads to a downwards bending of the potential, resulting in nearly flat bands in the bulk ($z \to -\infty$). There will be additional charges in surface states at the top surface of the structure which will determine the details of the band structure near that surface.

Therefore each single electron sees a roughly triangular potential well along the z-direction at the interface. For densities that are not too large, it turns out that only one eigenstate of the z-component of the Schrödinger equation will be below the Fermi energy, so that all excited states are empty. As a result, all dynamics along the z-direction are completely frozen out, and the electrons behave like two dimensional objects – hence the name two-dimensional electron gas (2DEG).

2DEGs are not only of interest for realizing spin- and charge qubits, but have also been involved in a number of ground-breaking discoveries including at least three Nobel Prizes for the quantum Hall effect, the development of a resistance standard for metrology, high electron mobility transistors (HEMTs) for high frequency applications, and many fundamental studies on quantum transport. This success is largely due to the extraordinarily high electron mobility resulting from the spatial separation of the donors and the electrons, and the ability to locally or globally deplete these electrons using electrostatic gates (Fig. 2 bottom), to be discussed next.

In the structure described so far, electrons are only confined in the z-direction. To achieve lateral confinement, one defines metallic gates on the wafer surface using standard lithography. Furthermore, the 2DEG is contacted with so called Ohmic contacts, which are metal pads that

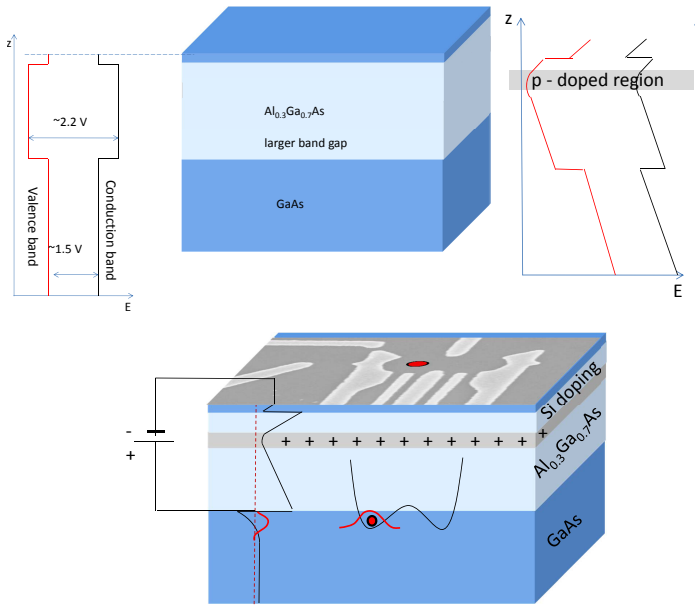

Fig. 2: ***Band bending and 2DEG in a heterostructure Top left:*** *Straddling gap of a GaAs/AlGaAs heterostructure without dopants.* ***Top right:*** *Valence and conduction band in the presence of silicon dopants.* ***Bottom:*** *Formation of a two-dimensional electron gas at the interface between GaAs and AlGaAs.*

partially diffuse into the 2DEG so that a metallic connection is formed.
Applying a negative voltage to a gate (with respect to the Fermi energy of the 2DEG) raises the electrostatic potential underneath it and hence reduces the local density of the 2DEG. The gate voltage essentially pushes electrons away. At sufficiently large voltages, the 2DEG disappears entirely. This effect allows the experimenter to define and fine-tune structures such as quantum point contacts (one dimensional tunnel barriers between areas of 2DEG) and quantum dots in various shapes and sizes.
For electron spin qubits, the dots have to be small enough to confine one or two single electrons. Furthermore, one often employs tunable tunnel barriers between adjacent dots and between the dots and the surrounding areas of 2DEG. The tuning of the tunnel coupling is effected by small adjustments of the gate voltages which change the tunnel barrier height. Two adjacent, tunnel coupled dots are called a double quantum dot, which is useful for realizing two qubits (section 9) or encoding a single qubit in two electron spins (section 6). Such a double quantum dot is shown in Fig. 3.

5 Single electron spin qubits

The conceptually simplest way to realize a spin qubit is to use a single electron spin (or other spin-1/2) to represent one qubit. Using an electron in a quantum dot (see section 4) was first proposed in 1998 by Loss and DiVincenzo [10], which is why this type of qubit is often referred to as Loss-DiVincenzo qubit. This section presents a few seminal experiment on the operation of such qubits.

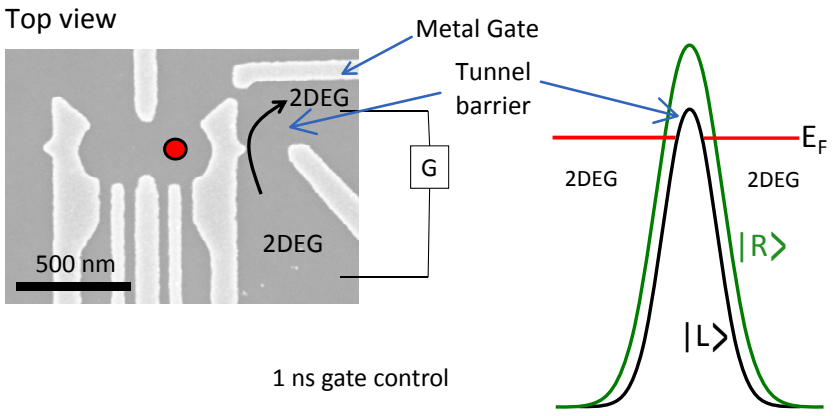

Fig. 3: ***Double quantum dot with charge sensor****. The two broad outer gates are also used to apply pulses for qubit manipulation. The state of the system is measured by a quantum point contact (QPC) on the right hand side of the double-dot. Depending on the charge state of the double dot, the potential barrier of the QPC and thus its conductance change.*

5.1 Initialization and readout

I will now discuss how a single spin can be initialized and read out, which was demonstrated in a rather neat experiment [11]. Directly determining the state of a spin is difficult because its magnetic moment is very small – the same weakness of coupling that ensures long spin coherence also impedes readout. Hence, one often first converts spin information to charge information (spin to charge conversion), as discussed in more detail below and in section 6. A convenient way to determine the resulting charge state is to use a charge detector capable of sensing whether an (additional) electron is present in the dot. The simplest charge detector is a quantum point contact, which is essentially a narrow tunnel barrier (with only one transverse channel contributing significantly) between two areas of 2DEG (Fig. 3). The height of the barrier changes the conductance of this contact and depends on whether a qubit electron resides on the nearby dot [12]. Hence, the sensor conductance G directly reflects the charge state. A better sensitivity was demonstrated by replacing the quantum point contact with another quantum dot, which is operated as a single electron transistor (SET). With modern amplification techniques [13], averaging times of less than 1 μs are sufficient to determine the charge state and hence to realize a projective measurement of the qubit [14, 15].

To read out a single spin, the authors of Ref. [11] placed a quantum dot (Fig. 4(a)) tuned to contain either zero or one electrons in a magnetic field of a few Tesla so that the Zeeman energy is much larger than $k_B T$. Using voltages pulses V_p on one of the gates, the energy levels in the dot can be moved above and below the Fermi energy (E_F) of the reservoir to which the dot is tunnel-coupled. The sequence discussed in the following is shown in Fig. 4(b). First, V_p is made negative enough that both the spin-up and the spin-down states are raised above E_F, causing the dot to be emptied regardless of the spin state of the electron inside. Subsequently pulling the two levels below E_F makes both of them energetically accessible, so that after some time either a spin-up or spin-down electron will tunnel into the dot with approximately equal probability.

To determine the spin state of the electron thus captured, V_p can be raised to bring only the spin-down state above E_F. If the electron is in the higher energy spin-down state, it can tunnel out of the dot. Another electron from the lead is now likely to tunnel into the dot because it is no longer repelled by the presence of an electron already inside the dot. This incoming electron will be

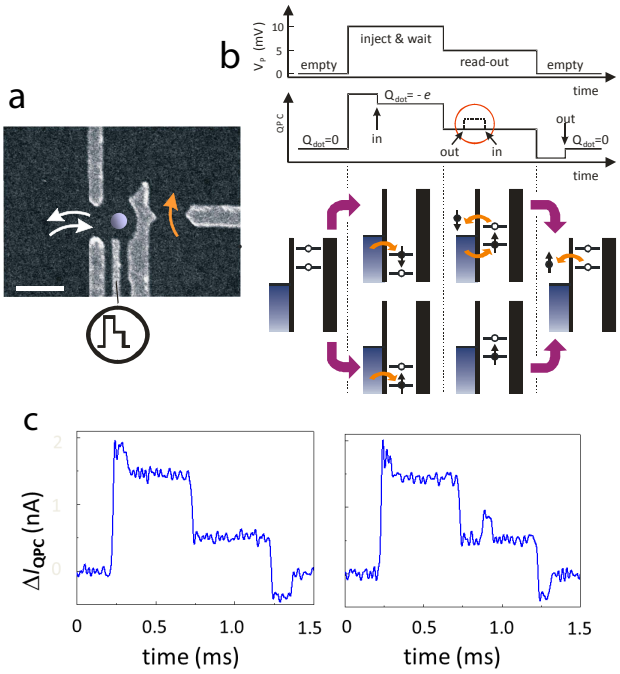

Fig. 4: ***Single-shot readout of a single spin*** ***(a)*** *Single electron quantum dot.* ***(b)*** *Readout mechanism for a single-dot qubit. Top: Gate voltage trace with injection and readout stage. Middle: Schematic of the corresponding readout signal. Bottom: Electron transitions between lead and dot for spin-down and spin-up states.* ***(c)*** *Corresponding data. In the left trace no signal appears at readout-time, indicating a spin-up occupation, while the right trace shows a bump in the QPC signal, indicating a spin-down electron tunneling from the dot to the leads and another electron tunneling back in.*

spin-up because only the spin-up state is below E_{F}. If, on the other hand, the dot was originally occupied by a spin-up electron, the electron cannot leave the dot so that nothing happens. The time scale of these tunneling events is determined by the tunnel coupling to the reservoir, which can be tuned by changing the gate voltages that determine the tunnel barrier.
During the whole process, the occupation of the dot can be monitored with a quantum point contact acting as a charge detector. The tunneling out (back in) associated with a spin down electron leads to an increase (decrease) in the detector current, because the absence (presence) of an electron in the dot makes it easier (harder) for other electrons to flow through the detector. This signature, step up then down, corresponds to a projective measurement of the spin state and is shown schematically in Fig. 4(b), while actual data is presented in Fig. 4(c). Note that at the end of the experimental cycle (before emptying the dot again), the electron is in a spin-up state independent of its initial state. Thus, the process can also serve to initialize the spin, and the DiVincenzo criteria for initialization and readout are (at least qualitatively) fulfilled.
By introducing a variable wait time between the preparation of the spin-up/spin-down mixture and the readout, it is also possible to measure the spin relaxation time: as the wait time is increased, the excited down-spin component of the initial mixture will relax to spin-up, so that the probability of detecting a spin-down, $p_{\downarrow}$, decreases. The decay of $p_{\downarrow}$ directly reflects the spin relaxation. Depending on the external magnetic field, relaxation times between a few milliseconds and up to a second have been demonstrated.

5.2 Single spin control

Having explained how a single spin can be initialized, we now turn to its manipulation. We consider a single spin-1/2 in a constant magnetic field B_0 along the z-direction driven by an ac field along x. The corresponding Hamiltonian is

$$H = \frac{g\mu_B B_0}{2}\sigma_z + \frac{g\mu_B}{2}B_1(t)\sigma_x$$

with $B_1(t) = B_{1,0}\sin\omega t$. By transforming into the reference frame rotating at the precession frequency $\omega_0 = g\mu_B B_0$ of the spin and neglecting rapidly oscillating terms (rotating wave approximation), one can show that for $\omega = \omega_0$ (resonant excitation), the spin rotates about a horizontal axis at an angular frequency given by $\omega_1 = g\mu_B B_1/2$ (see also section 10).
This control technique has been employed for decades in NMR and ESR on large ensembles of spins. It was shown experimentally in 2006 that it can indeed also be used to manipulate an individual spin in a quantum dot [16]. To this end, a short wire connected to an impedance-matched slot line was placed above the quantum dot and a ac electric current with frequency up to 700 MHz was driven through it in order to generate B_1 (Fig. 5(a)). To detect the resulting spin rotation, one could in principle have initialized a spin in the ground state, applied the microwave pulse, and determined the final state via spin to charge conversion. However, this technique requires rather large magnetic fields in order to achieve a Zeeman splitting that is larger then the thermal broadening of the Fermi level in the leads. Hence, very large frequencies would have been required for the excitation signal, which would be associated with excessive electric fields. Hence, the experiment was carried out at sub-GHz, and the lifting of the Pauli blockade of electron transport through a second dot in series with the first was used to detect spin rotations. For such Pauli blockade measurements, the dots are tuned such that for electrons to flow through them, the electron from one dot needs to tunnel to the second dot, which already contains an electron (Fig. 5(c)). Because of the Pauli exclusion principle discussed in more

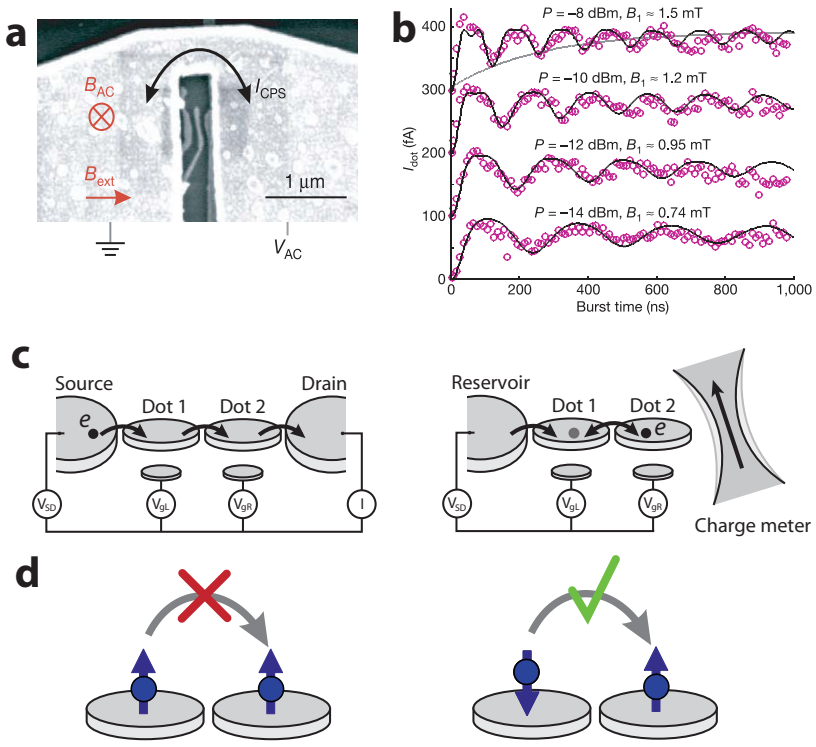

Fig. 5: ***Single spin rotation using ESR*** ***(a)*** *Shorted stripline over a double quantum dot used to generate an ac magnetic field.* ***(b)*** *Oscillation in the current through the double dot as a function of ac pulse duration, reflecting Rabi oscillations.* ***(c)*** *Transport measurement of the current through a double quantum dot as used for (b) (left) and corresponding measurement with a charge detector, which probes the occupation of each dot (right).* ***(d)*** *Principle of Pauli blockade, which is used for spin to charge conversion in double quantum dots. A spin triplet state (left) prevents the two electrons from occupying the same dot, whereas double occupancy is allowed for a spin singlet state (right). Data and schematics from [16] and [17].*

detail in section 6, this tunneling process is blocked for parallel spins (Fig. 5(d)). As a result, current flow stops once two parallel spins are in the dots. By rotating one (or both) of these two spins, the blockade is lifted and the average current increases. Hence, the average current reflects the final state of the spins at the end of the microwave pulse and reveals Rabi oscillations (Fig. 5(a)).

Similar experiments were carried out by replacing the magnetic driving field with an electric field, which can be converted into an effective magnetic field via spin orbit coupling [18] or magnetic field gradients created with micromagnets [19, 20]. In both cases, the ac electric field causes an oscillatory motion of the electron, which in turn results in an effective magnetic field. The advantage is that the bulky strip line dissipating a fair amount of heat can be eliminated. Furthermore, electric fields are easier to localize via electrostatic screening, which would facilitate the independent control of different nearby qubits. However, these techniques have the disadvantage that the coupling and thus the Rabi frequency is even lower than for magnetic drive, thus increasing gate errors due to decoherence.

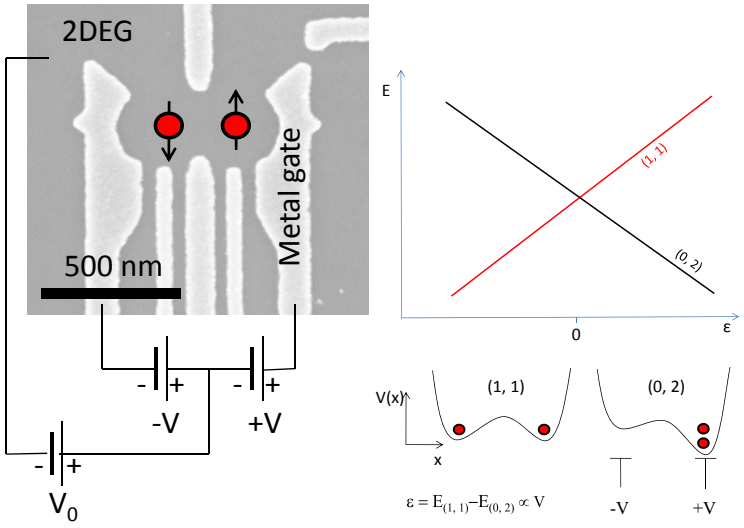

Fig. 6: ***Electrically controllable double quantum dot. Left:*** *double dot gate structure of a singlet-triplet spin-qubit.* ***Right:*** *Energy diagram for a singlet-triplet qubit in the absence of tunnel-coupling and singlet-triplet splitting, thus distinguishing only (1, 1) and (0, 2) states.*

6 Two-electron spin qubits

6.1 Motivation and energy diagram

One difficulty associated with single-electron spin qubits is the need to manipulate them via ac magnetic or electrically fields, which tends to be slow and thus sensitive to decoherence. One solution is to use two spins in a double quantum dot (Fig. 6 left) to encode a single qubit. Of the four possible spin states, only the $m = 0$ subspace spanned by $|\uparrow\downarrow\rangle$ and $|\downarrow\uparrow\rangle$ is used to store information. The main advantage of this encoding is that the exchange interaction between the two spins can be used to manipulate the qubit very rapidly using only electric fields, as we will see below and in section 6.2.

While the device is typically operated as a qubit with each of the electrons located in separate dots, it is possible to move both electrons into one single dot by changing the voltages on the large outer gates. How these gate voltages can be used to control the device is best understood by defining the detuning, ϵ, as the energy difference between the states with separated electrons (denoted as (1, 1)) and the (0, 2) state with both electrons in one dot (Fig. 6 right). The detuning is proportional to the difference between the voltages on the outer gates. A convenient tool to describe the effect of ϵ is the energy diagram, which plots the eigenenergies as a function of detuning ϵ. We will construct it in the following.

In the absence of tunnel coupling and disregarding spin for now, the energy diagram would contain two straight lines for the (1, 1) and (0, 2) states, as shown in Fig. 6(right). The corresponding Hamiltonian is $H = \frac{\epsilon}{2}\sigma_z$. An important effect to be considered next is the singlet-triplet splitting of the (0, 2) state. Due to the Fermi-statistics of the electrons, the total two-electron wave-function $\psi(x_1, x_2)$ must be antisymmetric under exchange of the two positions x_1 and x_2. For an antisymmetric spin-singlet state $|S\rangle = (|\uparrow\downarrow\rangle - |\downarrow\uparrow\rangle)/\sqrt{2}$, the orbital wave function has to be symmetric and, neglecting interactions, can be the product of two single particle ground states ψ_0: $\psi(x_1, x_2) = \psi_0(x_1)\psi_0(x_2)|S\rangle$. For a spin-triplet $|T\rangle$ on the other hand, the orbital component has to be anti-symmetric, which requires a second state

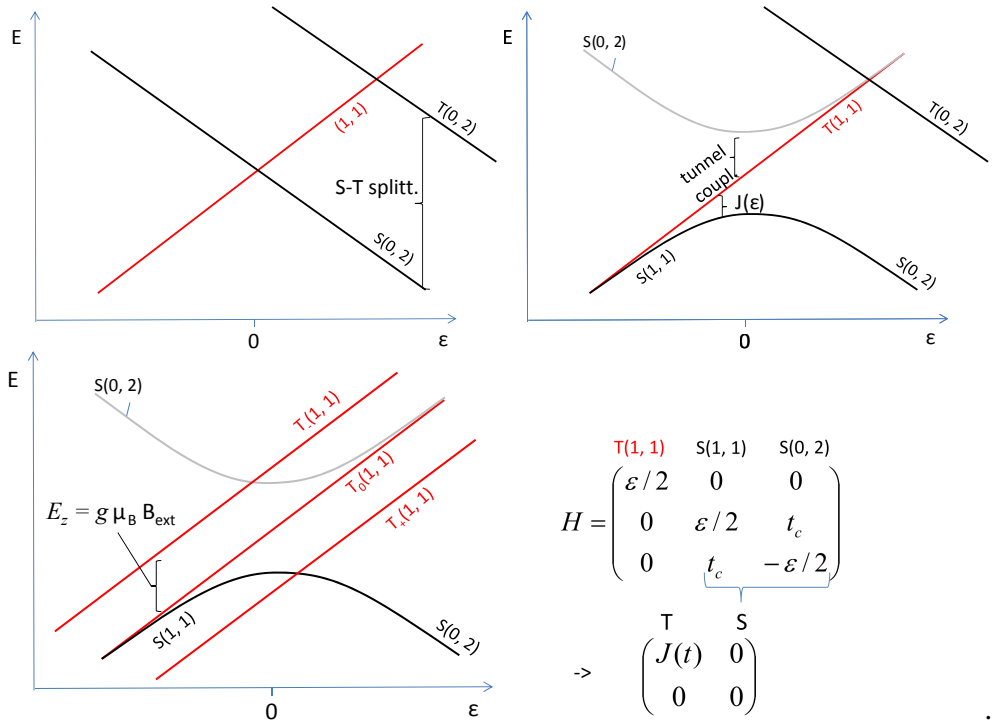

Fig. 7: ***Energy diagram of the spin states of a double quantum dot. Top left:*** *Energies of the (0, 2)-singlet and (0, 2)-triplet and the (1, 1) state as a function of detuning for zero tunnel coupling.* ***Top right:*** *Effect of introducing a finite tunnel coupling.* ***Bottom left:*** *Zeeman splitting of the three triplet states included.* ***Bottom right:*** *Qubit Hamiltonian for a tunnel coupled double dot.*

ψ_1: $\psi(x_1, x_2) = (\psi_0(x_1)\psi_1(x_2) - \psi_0(x_2)\psi_1(x_1))|T\rangle/\sqrt{2}$. Its energy is thus higher by the single-particle level splitting, i.e., the difference between the energies of ψ_1 and ψ_0. For a fully separated (1, 1) state, the single particle splitting and hence the singlet-triplet splitting vanishes. The resulting energy diagram is shown in Fig. 7(top left). While interactions between the two electrons reduce the singlet-triplet splitting effect, one can show that it can never be completely eliminated even at zero magnetic field.

We now consider the effect of tunnel coupling, which will induce transition between the (1, 1) and (0, 2) states and hence lead to avoided level crossings, shown in Fig. 7(top right). Due to the singlet-triplet splitting, the crossing occurs at different detunings for a singlet and triplet. For most practical purposes, it is sufficient to completely ignore the $T(0, 2)$ state and to assume that the triplet will always stay in (1, 1). We thus obtain an ϵ-dependent *exchange splitting* between the hybridized S-ground state and $T(1,1)$, which is usually denoted by $J(\epsilon)$. It can be formally derived by introducing the tunnel coupling t_c in the the three level Hamiltonian for $T(1, 1)$, $S(1, 1)$ and $S(0, 2)$ and by diagonalizing the S-block and keeping only $T(1, 1)$ and the lower of the two resulting S-states (Fig. 7(bottom right)). As we will see below, this electrically controllable exchange splitting plays an important role for realizing gate operations.

Finally, adding a magnetic field introduces a Zeeman splitting with Hamiltonian $H_Z = g\mu_B\hat{S}_z$ between the three triplets $|T_+\rangle = |\uparrow\uparrow\rangle$ $(m = 1)$, $|T_0\rangle = (|\uparrow\downarrow\rangle + |\downarrow\uparrow\rangle)/\sqrt{2}$ $(m = 0)$, and $|T_-\rangle = |\downarrow\downarrow\rangle$ $(m = -1)$, while the $|S\rangle$ with $m = 0$ remains unaffected. The complete energy diagram including the Zeeman splitting is shown in Fig. 7(bottom left). For qubit operation, the

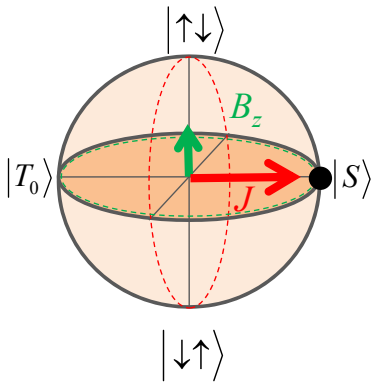

Fig. 8: *Bloch sphere representation for an $S - T_0$ qubit.*

$|T_+\rangle$ and $|T_-\rangle$ states can mostly be ignored as they are not part of the computational subspace. Note that $|S\rangle$ and $|T_0\rangle$ are an alternative basis of the computational space. Within this state, the qubit can be controlled by modulating ϵ and thus $J(\epsilon)$, provided that a magnetic field difference, ΔB, between the two dots splits the $|\uparrow\downarrow\rangle$ and $|\downarrow\uparrow\rangle$ states for $J \ll \Delta B$.

6.2 Control of the $S - T_0$ qubit

We now turn to the operation of two-electron spin qubits in double-quantum dots in the Bloch sphere picture. As discussed in section 6.1, the computational space of these qubits is spanned by the the states $\{|\uparrow\downarrow\rangle, |\downarrow\uparrow\rangle\}$ or equivalently by $|T_0\rangle = \frac{1}{\sqrt{2}}(|\uparrow\downarrow\rangle + |\downarrow\uparrow\rangle)$ and $|S\rangle = \frac{1}{\sqrt{2}}(|\uparrow\downarrow\rangle - |\downarrow\uparrow\rangle)$. Different conventions have been used to place these on the Bloch sphere. Here, we use the convention shown in Fig. 8, with $\{|\uparrow\downarrow\rangle, |\downarrow\uparrow\rangle\}$ on the north and south poles, respectively. $|S\rangle$ and $|T_0\rangle$ then lie on the x-axis. In section 6.1, we have seen that the exchange interaction described by $J(\epsilon)$ leads to an energy splitting between $|S\rangle$ and $|T_0\rangle$. Hence, the associated Hamiltonian is $H = \frac{J(\epsilon)}{2}\sigma_x$ and generates a rotation around the x-axis. If on the other hand the two separated electrons experience a difference in the local magnetic field, ΔB_z, which we assume to be applied in the z-direction common to both dots, the corresponding eigenstates at $J(\epsilon) = 0$ will be $\{|\uparrow\downarrow\rangle, |\downarrow\uparrow\rangle\}$, and their energy splitting is $g\mu_B \Delta B_z$. Hence, the total Hamiltonian is given by

$$H = \frac{g\mu_B \Delta B_z}{2}\sigma_z + \frac{J(\epsilon)}{2}\sigma_x.$$

Since it is difficult to realize sufficiently strong magnetic field gradients that can be varied on the nanosecond time-scale relevant for qubit operation, ΔB_z is practically fixed. $J(\epsilon)$ on the other hand can be varied very quickly via gate voltage pulses affecting ϵ, which is sufficient to gain universal control. For example, rotations around z are obtained at $J = 0$, while x-rotations are obtained approximately for $J(\epsilon) \gg \Delta B_z$. So far, qubit operation was mostly realized by switching between those two extremes. A y-rotation of $\pi/2$ could then be implemented by a $\pi/2$ z-rotation followed by $\pi/2$ rotation around x. Since this construction is subject to various systematic errors (e.g. limitations on $J(\epsilon)$ and finite pulse rise times), the identification of more accurate control gates is the subject of current research [21].

An interesting variant of encoded spin qubits are exchange-only qubits, which can be manipulated using only exchange without any magnetic field gradients [22]. This reduced requirement comes at the expense of using three spins to encode a single qubit, and significantly more elaborate control sequences for two qubit gates.

7 Hyperfine interaction with nuclear spins

The material from this section was adapted from a review article submitted to Nature Materials [17].

7.1 Hyperfine interaction

The spin of a confined electron in a gate-defined GaAs quantum dot is coupled to about $N = 10^6$ nuclear spins via the hyperfine interaction. This interaction is usually quantified in terms of an effective Overhauser magnetic field, B_{nuc}. Full polarization would correspond to an Overhauser field of about 4 T, while statistical fluctuations are a factor $\sqrt{N}$ smaller and thus amount to a few mT. The presence and dynamic properties of the Overhauser field thus have a significant impact on the coherence of the electron spin, and accordingly have received significant attention. Beyond the active research into a quiescent and controllable magnetic environment in solids, nuclear spins themselves have been suggested as a resource with extended coherence (potentially in the ms range) useful for QIP [23]. Besides its practical importance, understanding the dynamics of a single spin coupled to a bath of other spins, referred to as the central-spin-problem, is also of great fundamental interest as a quantum many body system.
The dominant contribution to the electron-nuclear hyperfine interaction originates from the contact Fermi interaction. In the first order perturbation theory, it can be described by the Hamiltonian [24]:

$$H_{hf} = \nu_0 \sum_j A_j |\psi(\mathbf{R}_j)|^2 \hat{\mathbf{S}} \cdot \hat{\mathbf{I}}_j \tag{1}$$

where ν_0 is the volume of the unit cell per atom, $\hat{\mathbf{S}}$ is the electron spin operator, $\psi(\mathbf{R}_j)$ is the electron envelope wave function at the j-th nucleus located at $\mathbf{R}_j$ and having spin $\hat{\mathbf{I}}_j$, and summation goes over all nuclei in the crystal. As an example, for all isotopes in GaAs, the A_j are of the order of 50 μeV.
Using the identity $\hat{\mathbf{S}} \cdot \hat{\mathbf{I}}_j = 1/2(I_+^j S_- + I_-^j S_+) + I_z^j S_z$ where $I_\pm^j$ and $S_\pm$ are the nuclear and electron spin raising and lowering operators, respectively, Eq.1 can be rewritten to emphasize the following two parts: a dynamical part $\propto 1/2(I_+^j S_- + I_-^j S_+)$ responsible for the transfer of the angular momentum between the two spin systems, and a static part $\propto I_z^j S_z$, contributing to the energies of the two spin systems. The effect of the static part can be described in terms of effective magnetic fields acting on the electron spin (the Overhauser field) and individual nuclear spins (the Knight field). The Overhauser field, a collective effect of a large number of nuclei, is described using the electron g-factor, g_e, as:

$$B_{nuc} = \frac{\nu_0}{g_e \mu_B} \sum_j A_j |\psi(\mathbf{R}_j)|^2 I_z^j \tag{2}$$

In terms of the mean spin of the nuclei of type η, $\langle I_\eta \rangle$, the Overhauser (or hyperfine) field is expressed as follows:

$$B_{nuc} = \frac{\sum_\eta A_\eta \langle I_\eta \rangle}{g_e \mu_B}. \tag{3}$$

The total electron Zeeman splitting, E_{eZ}, in the presence of both B_{nuc} and the external magnetic field B_{ext} is thus determined by the total magnetic field $B_{ext} \pm B_{nuc}$: (for simplicity, both fields are assumed to be directed along axis z.)

$$E_{eZ} = g_e \mu_B (B_{ext} \pm B_{nuc}) = g_e \mu_B B_{ext} + \Delta E_{eZ} \tag{4}$$

where $\Delta E_{eZ} = \pm g_e \mu_B B_{nuc}$ is the Overhauser shift.
The nuclear field B_{nuc} statistically fluctuates around its average as a result of the redistribution of nuclear spin polarization due to dipolar coupling or via virtual excitations of the electron spin. In the limit of large N, where N is the effective number of nuclei, this can be described by a Gaussian distribution with the standard deviation $\sigma_{B_{nuc}} \sim A/\sqrt{N}$ [25, 26]. For a typical number of 10^6 nuclei interacting with an electron confined in a gated GaAs quantum, dot this results in $\sigma_{B_{nuc}} \sim 3$ mT. (For self-assembled dots, N is about an order of magnitude smaller and $\sigma_{B_{nuc}}$ correspondingly larger.)
In an experiment with a large number of identical measurements, electron spins initialized in the same state (or superposition of states) will exhibit different dynamics as they will evolve in a slightly different effective magnetic field. When averaging over many measurements, this will effectively result in spin dephasing on the scale of a typical precession period of the electron in the field of the order of $\sigma_{B_{nuc}}$: the dephasing time T_2^* is of the order of 10 ns for $\sigma_{B_{nuc}} \approx 3$ mT [5, 27, 25, 26]. Much of this dephasing due to the random nuclear field can be unwound using spin-echo techniques, since the nuclear field evolves slowly on the timescale of the electron spin dynamics. The remaining decay of the electron spin coherence, with characteristic timescale $T_{2,echo}$, gives information on the timescale of the nuclear field fluctuations[5, 27, 28, 29, 30].

7.2 Probing nuclear spins

The nuclear polarization along the external magnetic field can be probed by measuring the shift the nuclear field B_{nuc} induces in the total electron (or hole) Zeeman splitting, E_{eZ} (see Eq. 4). Measuring E_{eZ} in a known B_{ext} thus tells us B_{nuc}. E_{eZ} can be measured for instance through electron spin resonance (ESR)[16, 31] or electric-dipole spin resonance (EDSR) [18, 32] of the electron spin. Typically, the resonance frequency, $f = E_{eZ}/h$, is in the microwave regime. The width of the resonance peak gives a bound on $\sigma_{B_{nuc}}$.
An alternative to spectroscopic measurements are time-resolved measurements in which one observes how the time evolution of the electron spin is affected by the nuclear field. For instance, a single spin precessing about a static magnetic field sees its Larmor precession frequency modified by $g_e \mu_B B_{nuc}/h$. Thus, a measurement of the precession rate reveals the value of B_{nuc}. If B_{nuc} fluctuates over time, a time-averaged measurement of the electron spin precession will contain a spread of precession rates, leading to decay of the envelope with time constant $T_2^* = \hbar\sqrt{2}/(g_e \mu_B \sigma_{B_{nuc}})$[27].
This principle has been applied in particular to two-electron spin qubits. Starting from the singlet ground state at large positive detuning, a fast pulse to large negative detuning initiates an oscillation between S and T_0 with frequency $f = |g_e \mu_B \Delta B_{nuc}|/h$ (Fig. 12(b) inset). Using single shot readout of the electrons via RF-reflectometry, such a measurement of ΔB_{nuc} involving thousands of samples can be completed within less than 10 ms [13, 33], thus allowing real time tracking of ΔB_{nuc} (Fig. 9b). The time resolution is sufficient to resolve the Overhauser field fluctuations, so that a detailed picture of the dynamics can be obtained. In particular, these rapid measurements are a powerful tool when controlling ΔB_{nuc} via dynamic nuclear polarization, as discussed in section 8. In both of the last two examples, a final triplet is distinguished from a singlet by pulsing to the $(0, 2)$ region and detecting the resulting charge state.
Measuring the precession frequency of an $S - T_0$ qubit only gives access to the Overhauser field gradient ΔB_{nuc}. The average Overhauser field in a double quantum dot can be measured from the inter-dot detuning ϵ^* for which T_+ (the $m = 1$ triplet) crosses S (the singlet branch, see Fig. 9a) [35]. At this degeneracy, the S and T_+ are subject to rapid mixing mediated by the nuclei,

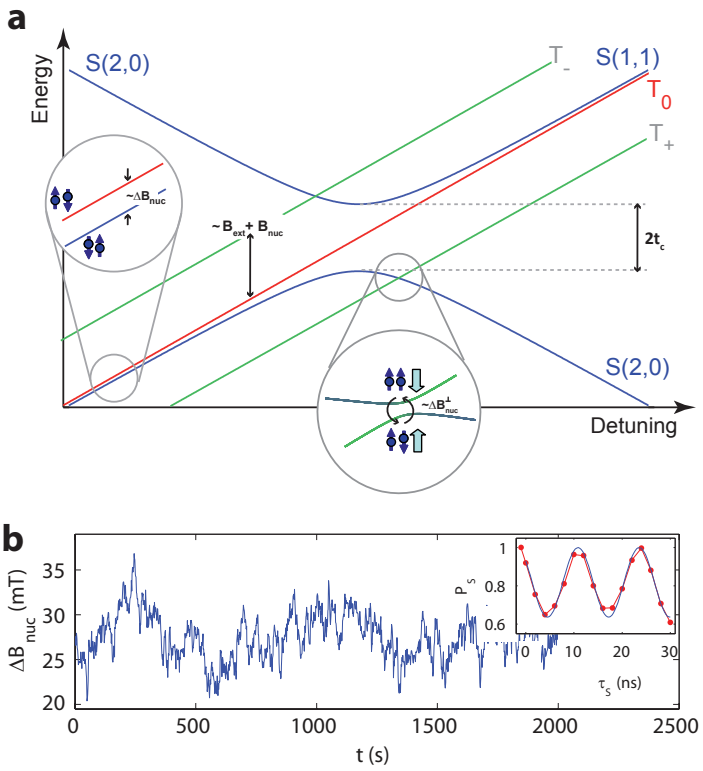

Fig. 9: Measurements of nuclear spin effects using electron transport in quantum dots. ***(a)*** *Effects of the hyperfine interaction illustrated on the energy diagram. At the far left where $J \approx 0$, the eigenstates in the presence of a difference in the local Overhauser fields, ΔB_{nuc}, have parallel and antiparallel spins. The degeneracy point of S and T_+ can be used for polarizing nuclear spins. Diagram adapted from Ref. [17]* ***(b)*** *Time trace of the difference between the z-components of the Overhauser field in the two dots, ΔB_{nuc}. Each data point reflects a measurement of the precession of the qubit in the Overhauser field (inset), with a frequency given by $g\mu_B \Delta B_{nuc}/h$. Data from Ref. [34].*

which can be detected via spin to charge conversion as in the case of $S - T_0$ mixing. Given the measured dependence of ϵ on $B_{ext} + B_{nuc}$, B_{nuc} can be extracted from ϵ^* obtained at a given B_{ext}. The underlying mechanism is that electron spins can be flipped whenever two states with different electron spins are (nearly) degenerate, so they can be mixed with each other through electron-nuclear flip-flops. For electron spin states that are well separated in energy, the energy mismatch between electron and nuclear Zeeman splitting suppresses such flip-flop processes.

7.3 Nuclear spin dynamics

In order to understand how nuclear spin fluctuations affect electron spin coherence, it is important to analyze their dynamics. Two different pictures are useful. At short times, the fluctuations of the Overhauser field are determined by the hyperfine interaction, the nuclear Larmor precession, and a few isolated flip-flop events between nuclear spins due to dipolar coupling. At longer times, series of nuclear flip-flops lead to a diffusion-like redistribution of the local nuclear polarization inside and outside the quantum dot. The cross-over between these regimes is roughly given by the coupling strength between nuclear spins ($\sim$ 10 kHz).

The diffusive long-time behavior of the nuclear polarization has been probed by directly measuring the fluctuations of the Overhauser field [36] using methods discussed in Sec. 7.2. Characterization up to 100 Hz shows a Lorentzian-like spectrum of the nuclear hyperfine field with roll-off frequencies in the range of 0.1 to 10 Hz (Fig. 10a). The relaxation dynamics of a dynamically induced nuclear polarization [37], which occurs on a time scale of tens of seconds to minutes, draws a similar picture. At low magnetic fields ($\lesssim$ 20 mT), one finds an about tenfold speedup of spin diffusion [36] that likely reflects the activation of additional diffusion channels by the reduced Zeeman energy mismatch, such as electron mediated spin transfer between nuclei. Such electron mediated diffusion also leads to a dependence of the decay rate of an induced polarization on the occupancy of the dot [37].

The short-time nuclear spin dynamics have been probed via electron spin dephasing under inversion of the electronic state halfway though an interval of free evolution [39], a procedure known as Hahn-echo. This technique is only sensitive to the changes of the Overhauser field during the evolution, whereas the effect of slower fluctuations is canceled out. Measuring the final electronic state gives detailed insight into the nuclear spin dynamics on the microsecond time scale [28]. Fig. 10(b) shows such measurements on double quantum dots from Ref. [28]. The monotonic decay of the Hahn-echo signal with total evolution time, τ, at high fields is a result of the diffusive dynamics of B^z_{nuc} due to dipolar coupling [40, 41]. The oscillations found at lower fields, which eventually turn into full collapses and revivals, were first predicted based on a fully quantum mechanical treatment [42, 43], but can also be understood with a semiclassical model [38] outlined below, which is in excellent agreement with the data.

For each electron spin, the Zeeman energy splitting is proportional to the total magnetic field $B_{tot} = \sqrt{(B_{ext} + B^z_{\rm nuc})^2 + {B^\perp_{\rm nuc}}^2} \approx B_{ext} + B^z_{\rm nuc} + {B^\perp_{\rm nuc}}^2/2B_{ext}$ (Fig. 10(c), top left). Dephasing is caused by fluctuations of this level splitting and thus related to the time-dependence of both the parallel and transverse nuclear components, $B^z_{\rm nuc}$ and ${B^\perp_{\rm nuc}}^2$. The time-dependence of $B^z_{\rm nuc}$ is mainly caused by nuclear spin diffusion as discussed above and is predicted to cause a $\exp(-(\tau/T_{SD})^4)$ decay of the echo [40, 41]. It appears that this decay law, which is generic for noise with low weight at high frequencies, physically originates in an upper cutoff in the fluctuation spectrum related to the time required for individual flip-flops to occur.

It is interesting to consider the origin of the collapses and revivals in the echo signal because it

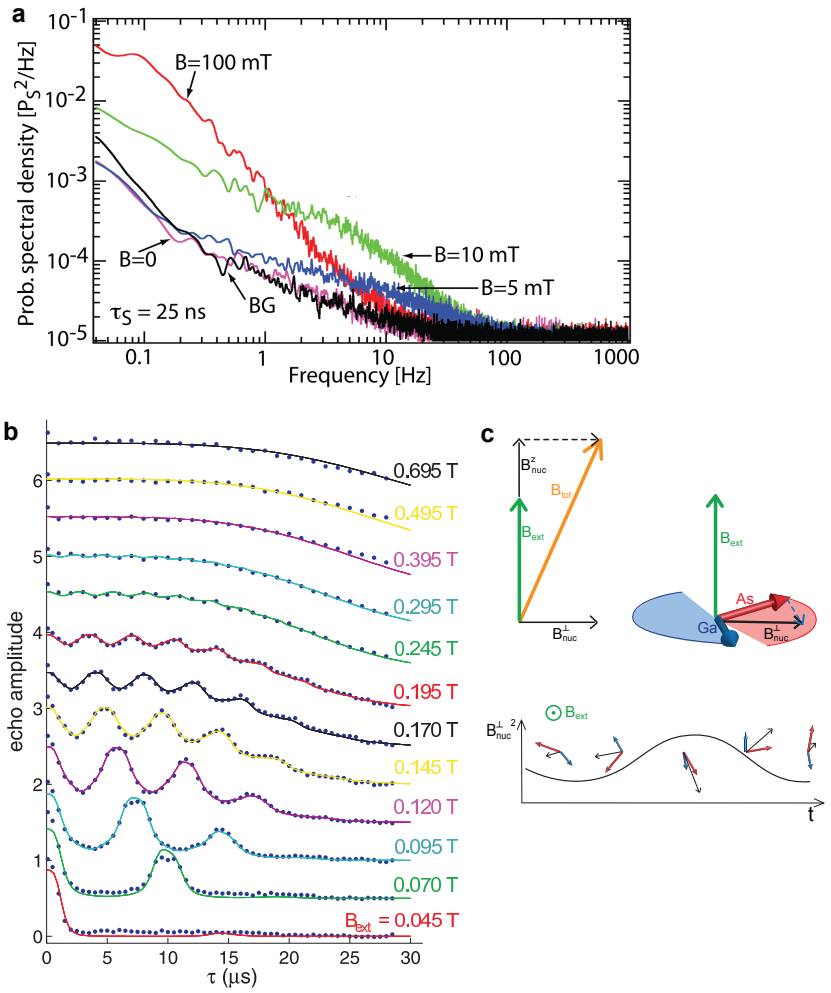

Fig. 10: Dynamics of nuclear spins in a double dot ***(a)*** *Spectra of the fluctuation of the nuclear hyperfine field, obtained from time traces of the singlet probability of the qubit after precession in the Overhauser field over a fixed evolution time τ_S. A significant speedup of the dynamics is observed at low magnetic fields. The shape of the spectrum can be explained in terms of nuclear spin diffusion.* ***(b)*** *Hahn echo signal from an $S - T_0$ qubit as a function of the total evolution time, τ, for different values of magnetic field. Exchanging the two electrons at time $\tau/2$ via a gate voltage pulse causes them to see the same static hyperfine field, so that only fluctuations during τ reduce the probability of the electrons to return to their initial state, which is reflected in the echo amplitude.* ***(c)*** *Illustration of the the semiclassical model [38] used for the fits (solid lines) in (b), as described in the text.. Adapted from Refs. [36] (a) and [28] (b, c).*

provides a rather intuitive picture of the nuclear dynamics causing this type of dephasing. These collapses arise from the phase associated with ${B_{\rm nuc}^{\perp}}^2$. The transverse nuclear field, $\vec{B}_{\rm nuc}^{\perp}$, is a vector sum of contributions from the three nuclear species ^{69}Ga, ^{71}Ga and ^{75}As (Fig. 10(c), top right). Due to the different precession rates of these species, ${B_{\rm nuc}^{\perp}}^2$ thus oscillates at the three relative Larmor frequencies (Fig. 10(c), bottom). While the Larmor precession frequencies are fixed, the amplitude and phase of the oscillating nuclear fields fluctuate over the course of many repetitions. Hence, the resulting phase is randomized and the echo signal is suppressed. However, if the precession interval is a multiple of all three relative Larmor periods, which is approximately possible due to a fortuitous equidistant spacing of these frequencies, the oscillations imprint no net phase on the electron spin and the echo amplitude revives. This intuitive picture can be turned into a quantitative model by treating the components of $\vec{B}_{\rm nuc}^{\perp}$ as classical variables and integrating over their initial values. The model also explains the faster decay of the echo envelope at low fields (Fig. 10(b)) in terms of dephasing of the nuclear spins themselves.

Substantially longer coherence times were obtained with a CPMG sequence [28], which consists of an n-fold repetition of the Hahn-echo, thus requiring n π-pulses, as shown in Fig. 11(a). Fig. 11(b) shows data for n = 6, 10 and 16. For n = 16, the echo signal clearly persists for more than 200 μs. It is likely that with improved pulses, a larger extension of the coherence time could be achieved with fewer pulses.

8 Dynamic nuclear polarization

Most of the material from this section was adapted from a review article submitted to Nature Materials [17].

8.1 Nuclear spin pumping

The hyperfine interaction not only causes dephasing and enables sensing of the nuclear magnetic field through measurement of the electron spins, but also enables manipulation of the nuclear spins via the electron spins: The transverse terms of the hyperfine interaction ($I_+^j S_- + I_-^j S_+$, see section 7.1) mediate electron-nuclear flip-flops [24] in which the electron changes its spin by ± 1 with a simultaneous change of the spin of one of the nuclei by ∓ 1. These flip-flop terms generate dynamic nuclear polarization (DNP) when the spin pump rates up versus down are asymmetric. A steady-state nuclear spin polarization is reached when nuclear spin pump rates are balanced by nuclear spin relaxation rates. Under most conditions, DNP is weak since nuclear spin pump rates are suppressed due to the mismatch between the nuclear and electron Zeeman splitting. However, there are a number of ways to overcome the energy mismatch and to induce a preferential pumping direction.

There have been a number attempts to find an efficient way of achieving DNP [44, 45, 35, 46], with the main motivation to achieve a nearly full polarization of nuclear spins, which would prevent nuclear-nuclear flip-flops, thus strongly suppressing the randomness in the nuclear field and concomitant electron spin decoherence [25]. Because of the difficulty of achieving such a large polarization and the rapidly diminishing improvement for polarizations below 99 %, this approach has not been very fruitful for extending coherence so far. Feedback methods that suppress fluctuations without requiring high polarization were shown to be quite effective though. Before discussing them in section 8.2, we discuss the underlying DNP methods.

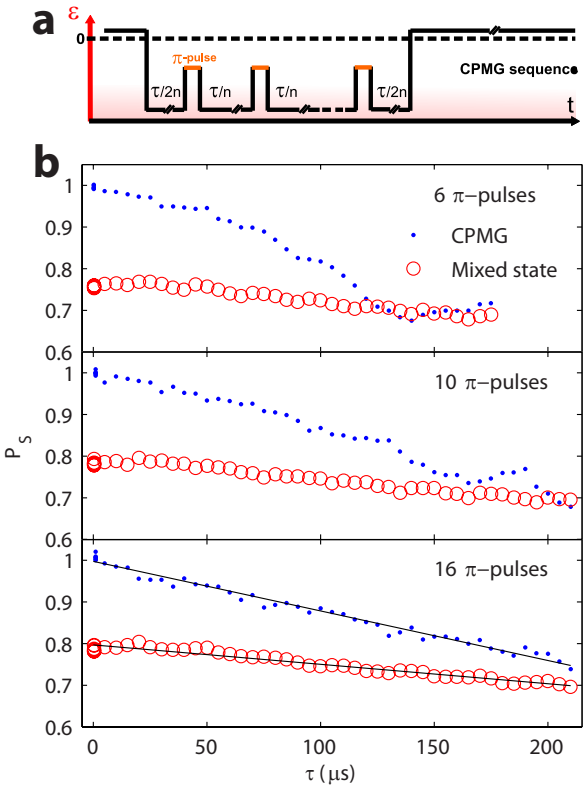

Fig. 11: Extension of the coherence time of an $S - T_0$ qubit via dynamical decoupling. ***(a)*** *CPMG pulse sequence consisting of a string of n Hahn echos.* ***(b)*** *Dephasing measurements under CPMG sequences. The blue dots show the readout signal of the CPMG pulses, the red circles represent reference measurements with the same evolution time without any π-pulses (equivalent to T_2^* measurements), which produce a completely dephased state. P_S is the sensor signal partially normalized so that a singlet corresponds to $P_S = 1$. The linear fits to the 16-pulse data (black lines) intersect at τ = 276 μs, which can be taken as a rough estimate or lower bound of the coherence time. Adapted from Ref. [28].*

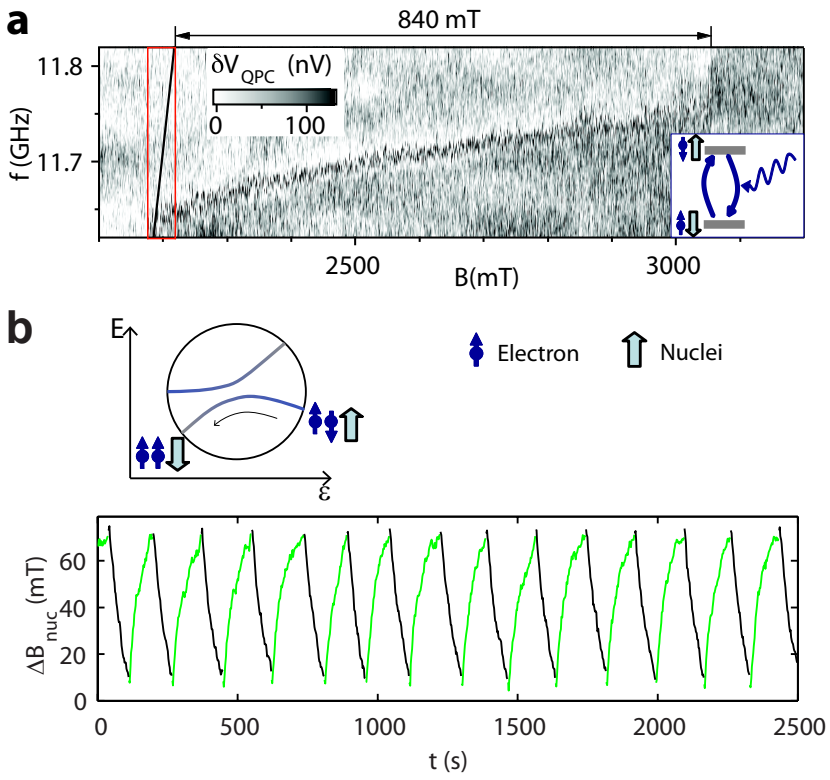

Fig. 12: Dynamic nuclear polarization in gate-defined quantum dots. ***(a)*** *Average charge occupation of a double quantum dot in the spin blockade regime under the influence of an ac electric field. When the excitation frequency f is resonant with the electron Zeeman splitting, it drives electron-nuclear flip flops (inset), thus lifting the spin blockade and changing the average occupation (darker regions). As the field B_{ext} (directed along z) is swept upwards, a nuclear polarization partly counteracts the change of B_{ext}, thus moving the resonance away from its equilibrium position (black diagonal line) by up to 840 mT. Data from [47].* ***(b)*** *Control of the hyperfine field gradient in a double quantum dot operated as an $S - T_0$ qubit. DNP is obtained by sweeping the detuning through the $S - T_+$ transition (top), causing spin transfer between electrons and nuclei. Each data point on the lower panel reflects a measurement of ΔB_{nuc} as shown in the inset. DNP pulses were applied between successive measurements. They increase or decrease ΔB_{nuc} depending on whether the DNP cycle starts from an S (green) or T_+ state (black). Diagram and data from Refs. [17, 34].*

The first observation of DNP in gated quantum dots was reported based on transport measurements in the Pauli blockade regime [48, 49, 45, 50, 45]. Here, we concentrate on experiments with specially designed gate voltage pulse cycles, which offer a more controlled way to realize a DNP pump scheme. In Ref. [35], the system is first initialized in the $S(0,2)$ state and subsequently, an adiabatic sweep across the $S-T_+$ degeneracy point (see Fig. 9 and 12(b)) transfers up to one unit of angular momentum into the nuclear spin bath. Finally, one electron is pushed out of the double dot and the next cycle begins. Spin transfer in the opposite direction and thus full bidirectional control (Fig. 12(c)) was demonstrated by Foletti et al. [51] by initialization of a $T_+(1,1)$ state followed by a similar slow passage through the $S-T_+$ degeneracy point. It is not clear a priori in which of the two dots a nuclear spin will flip, but using the techniques of Sec. 7.2, both the difference and the average of the nuclear fields in the two dots can be probed in detail. Foletti et al. found that the nuclei are polarized predominantly in one of the two dots [51], which likely is due to the different size of the two dots [52, 53]. In Sec. 8.2, we will show how these pump cycles can be extended to also reduce fluctuations of the hyperfine field.
Rather than exploiting level degeneracies, the energy for electron-nuclear flip-flops can alternatively be provided by a resonant ac electric field (inset to Fig. 12(b)). The electric field modulates the hyperfine coupling constant of each nucleus to the electron and therefore the transverse term of the hyperfine coupling. This directly drives electron-nuclear flip-flops. A preferential direction for the driven transitions resulting in a net increase in the nuclear polarization has been observed by Laird et al. [47] (see Fig. 12(b)) and Vink et al. [31]. The origin of the asymmetry is spin-orbit mediated electron spin relaxation, which creates an unbalance in the electron $\uparrow$ and $\downarrow$ probabilities without exchange of angular momentum with the nuclear spins. Since the driven flip-flops rely on a resonance condition, which in itself depends on the nuclear magnetic field, this pump cycle can lead to feedback between electron and nuclear spins, which has been explored in more detail by Vink et al. [31], see Sec. 8.2.

8.2 Narrowing of nuclear field distribution using 'closed-loop' spin pumping

The preceding sections discussed experiments where angular momentum is transferred from the local electron spin to the nuclear spin bath in an open-loop mode. As a result, the nuclear field was always subject to statistical fluctuations. Here we present a development of the last few years, realized by both optical and electrical means, which is closed-loop control of the nuclear field, suppressing its randomness to well below the statistical fluctuations. The suppression of the bath fluctuations immediately leads to extended dephasing times and better control of the time evolution of the electron spin(s).
Several approaches to achieve this goal have been demonstrated. The conceptually simplest possibility is to rapidly measure Overhauser field (or its gradient) and to use DNP to restore its desired value. For $S-T_0$ qubits, this approach [34] permitted a reduction of the rms-fluctuations of the hyperfine field gradient, $\sigma_{\Delta B_{nuc}}$, by about a factor of 2. A more powerful approach relies on directly conditioning the spin transfer from the electrons to the nuclei on the current value of the hyperfine field, thus letting the electron spin itself act as a complete feedback loop not requiring external intervention. This approach was used to control both the hyperfine field in the individual halves of a double quantum dot using an ESR-based spin transfer technique [31], and the field gradient ΔB_{nuc} between the two dots of an $S-T_0$ qubit via exchange mediated spin transfer [34]. For a discussion of the two polarization methods, see Sec. 8.1.
Such feedback schemes can be understood based on the so called pumping curve, which pro-

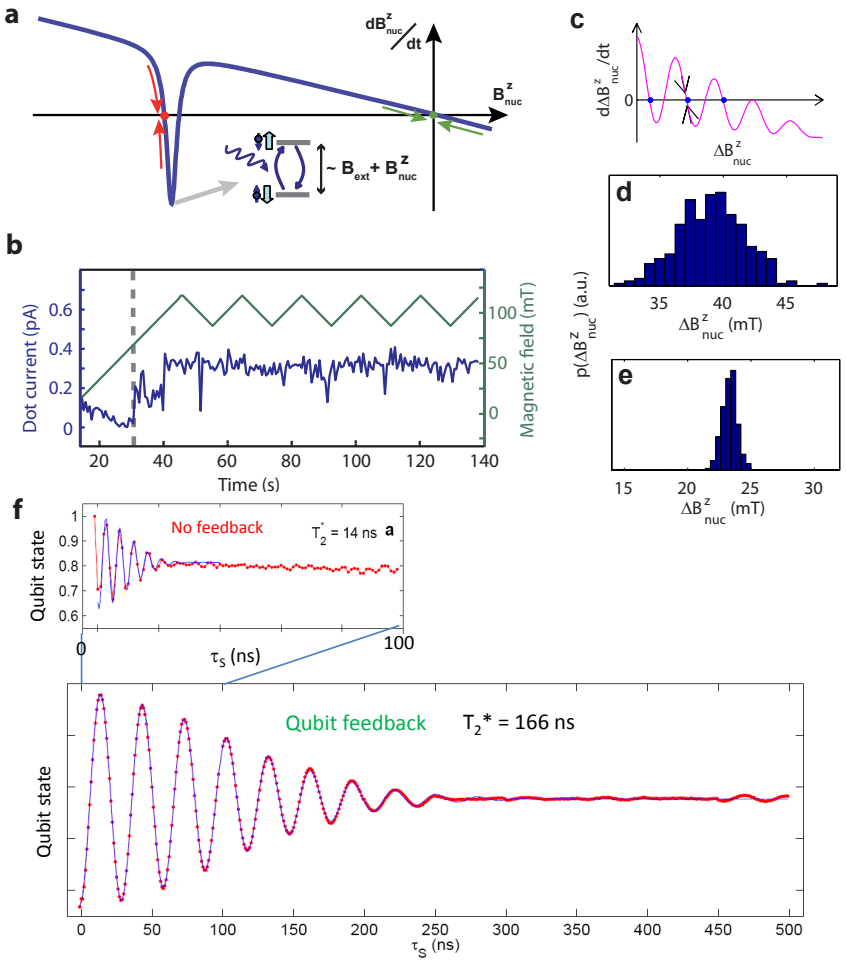

Fig. 13: Nuclear spin narrowing experiments *(a) Schematic illustration of the pumping curve for ESR based feedback [31] on a single electron spin. Fluctuations away from the fixed points are compensated by a restoring pump effect (arrows).* ***(b)*** *Polarization dragging experiment for single electron spins using ESR. As the field increases from near zero, the singlet-triplet mixing is suppressed while the CW-ESR signal is off resonant and has no effect. At $B_{ext} \approx 50$ mT, a resonance condition is met, thus breaking spin blockade. Subsequently, the resulting high current condition is maintained even while sweeping B_{ext} up and down, thus demonstrating the locking of the total field $B_{ext} + B_{nuc}$ to the resonance frequency: any change in B_{ext} is compensated by an opposite change in the nuclear polarization.* ***(c)*** *Pumping curve for voltage pulse based feedback on an $S - T_0$ qubit. The oscillatory structure arises from first letting the qubit precess in the hyperfine field and then executing a DNP step that is conditional on the state emerging from this evolution.* ***(d)*** *Distributions of ΔB_{nuc} for fixed pumping, obtained by histogramming instantaneous values of ΔB_{nuc}.* ***(e)*** *Same measurement, but with feedback pumping applied between measurements, which narrows the distribution.* ***(f)*** *Extension of the dephasing time T_2^* resulting from the narrowing (different dataset) Top: Oscillation of the qubit state in the presence of an unstabilized, DNP induced field gradient. Bottom: Same measurement with feedback (and smaller value of the gradient), leading to a tenfold enhancement of T_2^*. (a)-(e) adapted from [17]*

vides the polarization rate as a function of the current value of the hyperfine field. Figs. 13(a),(c) show pumping curves for both feedback methods. A stable fixed point is obtained whenever the pumping curve crosses zero with a negative slope so that fluctuations away from the fixed point are corrected by an opposing pump effect.
The ESR pumping curve (Fig.13(a)) emerges from the resonance condition of the microwave excitation with the Zeeman field $B_{ext} + B_{nuc}$ seen by the electron, with the overall negative background slope arising from relaxation of the spin polarization. The oscillatory behavior of the corresponding curve for the $S - T_0$ qubit (Fig.13(c)) was generated by initializing it in S and then letting it precess between S and T_0 for a time τ_{FB} under the influence of ΔB_{nuc}. Upon subsequently sweeping the gate voltages across the $S-T_+$ transition, a nuclear spin can only be flipped by the S-component of the qubit's state emerging from the evolution. Thus, the average pump rate is proportional to the ΔB_{nuc}-dependent singlet probability. An overall negative offset was added by pumping in the opposite direction without conditioning on the current value of ΔB_{nuc}.
For the gradient nuclear field, the stabilizing effect of the feedback scheme was demonstrated by interleaving it with measurements of the $S - T_0$ qubit precession. Narrowing of the distribution of ΔB_{nuc} around a fixed point (Figs.13(d),(e)) enhanced the qubit's T_2^* from 16 ns to more than 150 ns. For the ESR-based experiment, the narrowing effect was inferred from dragging and locking of the ESR resonance frequency in response to changes of the external applied field (Fig.13(b)), which were found to be compensated by nuclear polarization such that the total field remained constant.

9 Two-qubit entangling gates

9.1 Exchange based approaches

As discussed in chapter A2, an important requirement for quantum computing (within the circuit model) is the availability of two- (or multiple) qubit gates that can couple and entangle several qubits. In section 6.2, we have seen that the electrically controllable exchange splitting $J(\epsilon)$ can be used to manipulate a two-electron-spin qubit by driving transitions between $|\uparrow\downarrow\rangle$ and $|\downarrow\uparrow\rangle$ for $\Delta B_z = 0$. By considering each individual spin as one single-spin qubit, a π rotation corresponds to a so called $SWAP$ gate that interchanges the two qubit states. Executing only a $\pi/2$ rotation realizes a so called $\sqrt{SWAP}$ gate, which is universal in combination with single qubit gates. For example, starting in $|\uparrow\downarrow\rangle$ puts the two spins into $(|\uparrow\downarrow\rangle + i\ |\downarrow\uparrow\rangle)/\sqrt{2}$, which is a maximally entangled state. Thus, the exchange interaction can be used to realize universal multi-qubit operations for single spin qubits. Such a coherent exchange between two spins was first demonstrated in 2005 [5] (Fig. 14(a)). Here, the Pauli blockade was used for readout, so that only singlets and triplets could be distinguished. In this experiment, an initial $|\uparrow\downarrow\rangle$ (or $|\downarrow\uparrow\rangle$) state was created by preparing a singlet S and adiabatically reducing $J(\epsilon)$ to zero, thus mapping S onto the ground state for $J = 0$. More recently, very similar experiments were carried out using ESR pulses for single spin control instead [54], and independently with single-shot readout of each individual spin [55], as described in section 5.1 (Fig. 14(b)). The latter results show the expected oscillations in the probabilities for $\uparrow$ and $\downarrow$ and anti-correlations between the two qubits. Since the measurement was carried out only along one axis, these results are not a direct proof of entanglement, but entanglement can be inferred from the known system dynamics.

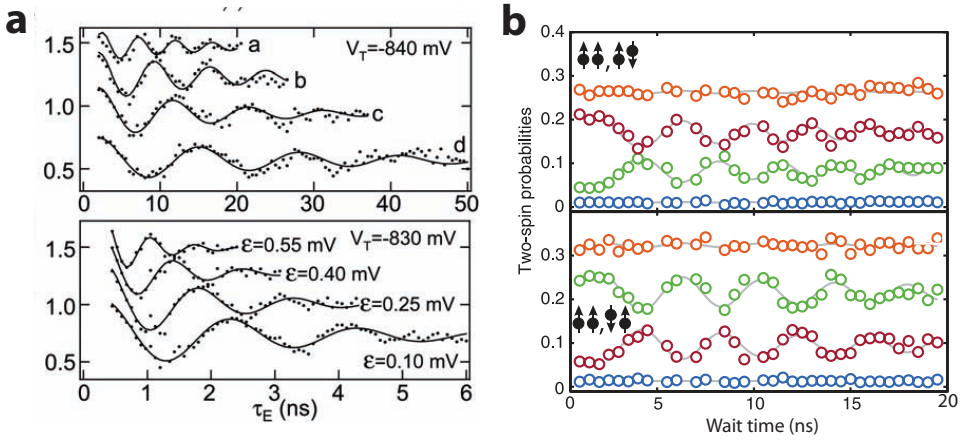

Fig. 14: ***Exchange operations on two electrons in double quantum dots.*** ***(a)*** *Exchange oscillations between $|\uparrow\downarrow\rangle$ and $|\downarrow\uparrow\rangle$ probed by adiabatic initialisation and readout via Pauli blockade. Data from [5].* ***(b)*** *Similar experiments probing the correlations of two-spin single shot readout after exchange operations. Data from [55].*

For two-electron spin (i.e, $S-T_0$) qubits, one can in principle also use the exchange interaction to realize a two qubit gate, however care must be taken to avoid leakage out of the logical subspace. For example, applying a $SWAP$ operations to the inner two spins of two qubits prepared in $|\uparrow\downarrow\rangle\otimes|\uparrow\downarrow\rangle$ yields a $|\uparrow\uparrow\rangle\otimes|\downarrow\downarrow\rangle$ state, which is outside the logical subspace of each quit. In other words, it is not a valid computational state for our encoded qubits. One way to solve this problem is to use a composite sequence as shown in Fig. 15, where the qubits may temporarily leave the logical subspace, but return to it at the end of the sequence [56]. The key idea is that a $\pi/2$ pulse around the ΔB_Z axis of each qubit is sandwiched between two $SWAP$ pulses of a pair of spins belonging to different qubits. The $\pi/2$ pulses can only induce a phase if both qubits are left in their logical space by the $SWAP$, which is the case if they started in opposite states. As a result, the dynamics of the two qubits becomes correlated and entanglement can be created. A different pulse combination was proposed in Ref. [57]. Yet another alternative is to use very large magnetic field gradients between the two dots. They suppress spin exchange and thus leakage so that switching on the exchange coupling J only leads to a phase accumulation of the logical states. None of these gates has been experimentally realized yet.

9.2 Charge coupled $S-T_0$ qubits

This subsection including the figures has been adapted from Ref. [58].
For $S-T_0$ qubits, a two qubit gate was recently demonstrated and characterized in detail using state tomography. The gate operation was based on the Coulomb interaction between two adjacent double quantum dots that were placed such that are capacitively coupled, but tunneling between them is suppressed (Fig. 16(a)). When J is nonzero, the S and T_0 states have different charge densities in the two quantum dots (Fig. 16(b)) because the Pauli exclusion principle allows only the singlet state S to hybridize with a (0,2) state while T_0 remains locked in (1, 1) (Figs. 5(d), 7). This charge density difference, which is a function of ϵ, causes the S and T_0 states in one qubit to impose different detuning ϵ on the other qubit. Since J varies with ϵ, the change imposed by the first qubit causes a shift in the precession frequency of the second qubit,

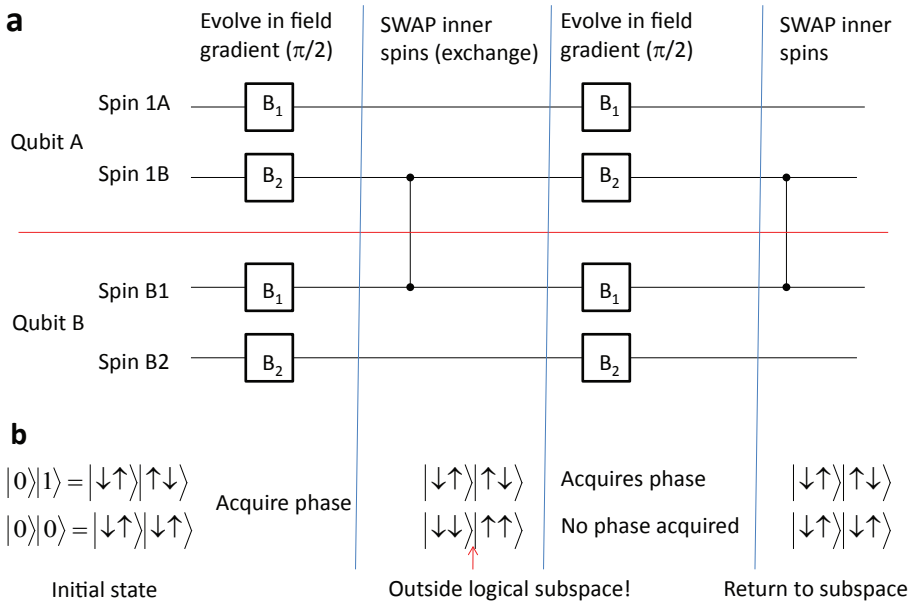

Fig. 15: ***Exchange-based two-qubit operations for*** $S-T_0$ ***(a)*** *Sequence to implement an nAND two-qubit gate using exchange coupling.* ***(b)*** *Comparison of the evolution of two initial states, indicating the underlying principle of the gate.*

whose state may thus be conditioned on that of the first.
The underlying two-qubit Hamiltonian is given by:

$$\mathcal{H}_{2-qubit} = \frac{\hbar}{2}\left\{J_1(\sigma_z \otimes I) + J_2(I \otimes \sigma_z) + J_{12}(\sigma_z \otimes \sigma_z) + \Delta B_{z,1}(\sigma_x \otimes I) + \Delta B_{z,2}(I \otimes \sigma_x)\right\} \tag{5}$$

where $\sigma_{x,y,z}$ are the Pauli matrices, I is the identity operator, $\Delta B_{z,i}$ and J_i are the magnetic field gradients and values of the exchange splitting ($i = 1, 2$ for the two qubits), and J_{12} is the two-qubit coupling, which is roughly proportional to the product of the dipole moments of each qubit.
In principle, evolving both qubits under exchange leads to a CPHASE gate, which can produce a maximally entangled state. However, the time to execute this operation exceeds the inhomogeneously broadened coherence times of each individual qubit, rendering this simple implementation of the two-qubit gate ineffective for current device parameters.
To solve this problem, a dynamically decoupled entangling sequence was used (Fig. 16(c)). In this sequence, each qubit is prepared in $|S\rangle$ and is then rotated by $\frac{\pi}{2}$ around the x-axis (J_i =0, $\delta B_{z,i}/2\pi \approx 30$ MHz) to prepare an initial state in the xy-plane. The two qubits are subsequently both evolved under a large exchange splitting ($J_i/2\pi \approx 300$ MHz $\gg \Delta B_Z$) for a time $\frac{\tau}{2}$, during which the qubits begin to entangle (and possibly disentangle). A π-pulse around the x-axis (ΔB_Z) is applied simultaneously to both qubits, after which the qubits are again allowed to exchange for a time $\frac{\tau}{2}$.
This Hahn echo-like sequence removes the dephasing effect of noise that is low frequency compared to $1/\tau$, while the π-pulses preserve the sign of the two-qubit interaction. For $\tau = \tau_{ent} = \frac{\pi}{2J_{12}}$ the resulting state is a maximally entangled generalized Bell state $|\Psi_{ent}\rangle = e^{i\pi(\mathbf{I}\otimes\sigma_y+\sigma_y\otimes\mathbf{I})/8}|\Psi_-\rangle$, which differs from the Bell state $|\Psi_-\rangle = \frac{1}{\sqrt{2}}(|SS\rangle - |T_0T_0\rangle)$ only by single qubit rotations.
The ΔB_z rotations for initialization, π-pulse and state tomography were realized by stabilizing a nuclear hyperfine field gradient of 30 MHz with reduced fluctuations as described in section

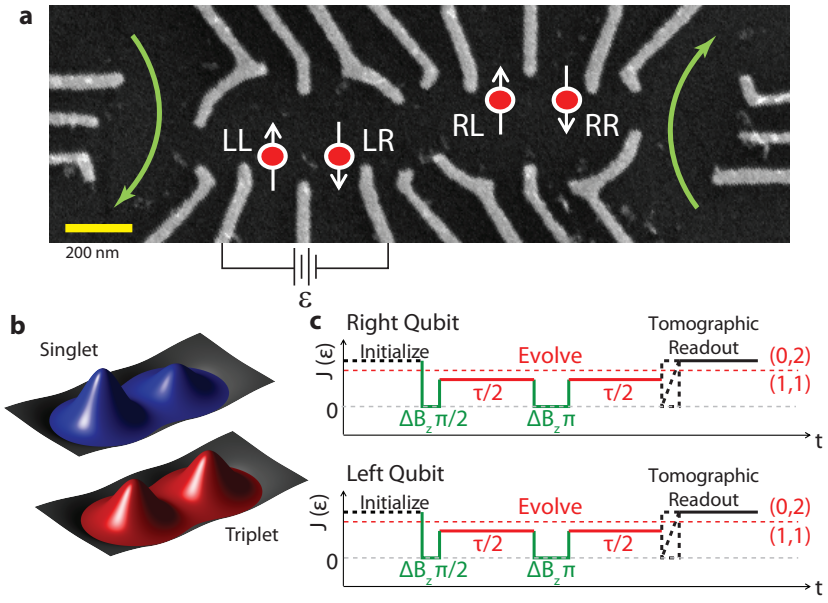

Fig. 16: ***Two-qubit device and its operation.*** ***(a)*** *SEM image of the device used with the approximate locations of the electrons in the two qubits (red), and current paths for the sensing dots (green arrows).* ***(b)*** *Schematic of the electronic charge configurations for the $|S\rangle$ (blue) and the $|T_0\rangle$ (red). This difference in charge configuration is the basis for the electrostatic coupling between the qubits.* ***(c)*** *The pulse sequence used to entangle the qubits: initialize each qubit in a $|S\rangle$, perform a $\pi/2$ rotation around the x-axis, allow the qubits to evolve under exchange for a time $\tau/2$, perform a π-rotation around the x-axis, thereby decoupling the qubits from the environment but not each-other, evolve under exchange for $\tau/2$, and perform state tomography to determine the resulting density matrix. Adapted from [58].*

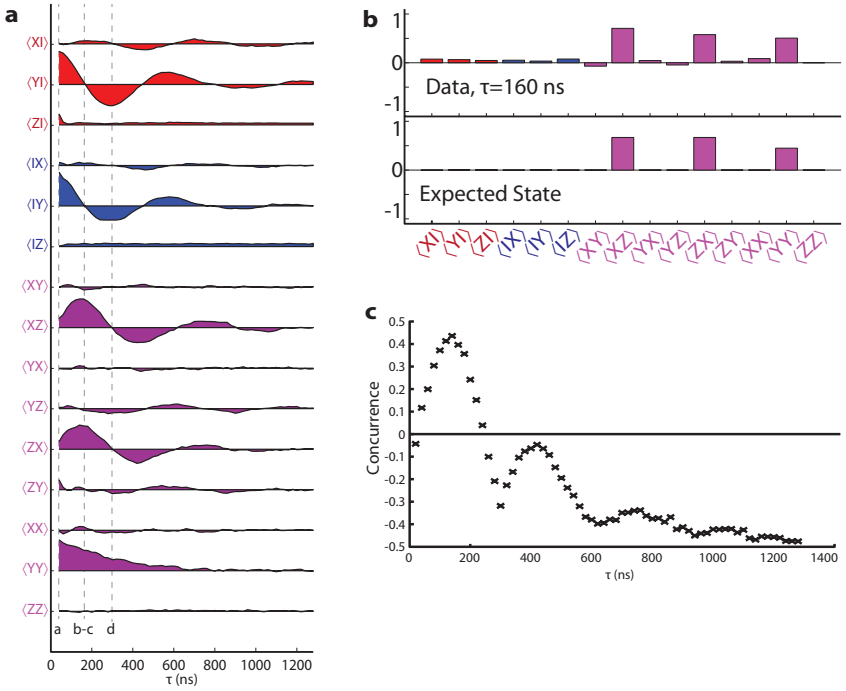

Fig. 17: ***Measurement results of the two-qubit entangling experiment.*** ***(a)*** *The full measured Pauli set as a function of τ, which shows the expected oscillations corresponding to entanglement and disentanglement.* ***(b)*** *The Pauli set of the measured and expected states for $\tau = 160$ ns, which realizes the CPHASE gate. Because of dephasing induced fidelity loss at larger time, the highest Bell state fidelity is obtained at 140 ns.* ***(c)*** *Concurrence (a common entanglement measure) as a function of interaction time τ. States with a concurrence greater than zero are necessarily entangled. The oscillations reflect entanglement and disentanglement under the influence of the two-qubit coupling, with entanglement being proven in the first lobe. Data from [58].*

8.2. A charge sensing quantum dot next to each qubit allowed for simultaneous and independent projective single shot measurement of each qubit [59, 14], thus giving access not only to single qubit probabilities, but also correlations.

In order to characterize their two-qubit gate and to verify that an entangled state is produced, the authors performed two-qubit state tomography and extracted the density matrix and appropriate entanglement measures. Fig. 17(a) shows the entire Pauli set as a function of time, which clearly shows oscillations in $\langle YI\rangle$,$\langle IY\rangle$ and $\langle XZ\rangle$, $\langle ZX\rangle$, with decays due to decoherence. At $\tau = 140$ ns or 160 ns (Fig. 17(b)), the weight in the $\langle XZ\rangle$, $\langle ZX\rangle$, $\langle YY\rangle$ components of the Pauli set corresponds to correlation along three measurement axis combinations, which are a hallmark of entanglement. This state has a fidelity with respect to the nearest Bell state of 0.72, which demonstrates the production of an entangled state because unentangled states can at most have a fidelity of 1/2. This state also exhibits a positive concurrence of 0.44, again demonstrating entanglement (Fig. 17(c)).

While this two-qubit gate is an important step toward quantum information processing with $S-T_0$ qubits, its fidelity is limited by dephasing from electrical noise and needs to be improved significantly by decreasing the ratio τ_{ent}/T_2^{echo}, where T_2^{echo} is the single-qubit coherence time with an echo pulse. It was shown based on electrostatic modelling that considerable improvements can be made by introducing an electrostatic coupler between the two qubits [60] in order

to increase the two-qubit coupling (J_{12}) and reduce τ_{ent}. Estimates indicate that in the absence of other losses but without improvements in electrical noise, if an electrostatic coupler were used, a Bell state with fidelity exceeding 90 % could be produced. Alternatively, it would permit a larger distance between qubits without reducing the coupling, which will likely be important for realizing quantum circuits with more qubits. In any case, a reduction of charge noise is extremely important.

10 Quantum control techniques

10.1 Rabi control and its limitations

A central requirement for quantum computing is the ability to control qubits with high fidelity. Mathematically, this means that any desired unitary operation must be realizable with high accuracy. The most direct and widespread approach for single-qubit gates is to use Rabi control, where transitions between qubit states are induced via a (typically resonant) ac drive. I briefly review this procedure before discussing possible problems and more advanced techniques to address them.
The standard Rabi Hamiltonian is given by

$$\begin{aligned} H(t) &= H_0 + H_1(t) \text{ with} \\ H_0 &= \frac{\hbar\omega_0}{2}\sigma_z \\ H_1(t) &= \hbar\Delta\sin(\omega t+\delta)\sigma_x. \end{aligned}$$

The sinusoidal time dependence of H_1 is reasonable because qubits are often operated with a large ($\sim$ 6 GHz) level splitting to prevent thermal occupation of the excited state and high-frequency signals are usually most easily available in sinusoidal form.
The dynamics can be simplified by transforming into a reference frame rotating at the frequency of the drive signal. For $\Delta \ll \omega, \omega_0$, on can neglect rapidly oscillating terms (rotating wave approximation, RWA) and obtains

$$\begin{aligned} \tilde{H} &= H_0 + U^\dagger(t)H_1(t)U(t) \\ &\approx \frac{\hbar(\omega_0-\omega)}{2}\sigma_z + \frac{\hbar\Delta}{2}\cos\delta\ \sigma_x + \frac{\hbar\Delta}{2}\sin\delta\ \sigma_y \end{aligned}$$

The Hamiltonian has become time independent and describes a rotation around the axis $\omega\vec{n} = (\Delta\cos\delta, \Delta\sin\delta, \omega_0-\omega)$ with angular velocity $\omega = \sqrt{\Delta^2+(\omega_0-\omega)^2}$. We see that by varying Δ, ω (or ω_0) and δ, all of which except ω_0 are properties of the ac signal in H_1, and the duration of the pulse, we can generate arbitrary single qubit rotations. Typically, one chooses resonant excitation ($\omega = \omega_0$), leading to a rotation around an axis in the xy-plane. The speed or rotation is then given by Δ. The direction of the rotation axis in the xy-plane can be tuned elegantly via the phase δ of the excitation. Examples include the ESR experiment discussed in section 5.2, but the same principle is used for the vast majority of qubits experiments.
Regardless of its widespread use, Rabi control is subject to a number of limitations:

- To minimize the effect of decoherence on gate fidelity, fast pulses are desirable, thus requiring large Δ. However, once Δ becomes comparable to ω, the rotating wave approximation breaks down, which leads to systematic errors unless they are corrected.

- Some qubits (e.g. the Josephson phase qubit and the transmon) have a low anharmonicity, so that the splitting between first and second excited states is similar to the qubit energy splitting between the ground state and first excited state. Once the drive amplitude Δ becomes comparable to the anharmonicity (i.e., the difference between the level splittings), driving the qubit transition also causes excitation into the second excited state and thus leakage out of the qubit space.

- Not all types of qubit lend themselves to Rabi control. For example, the $S - T_0$ qubit is typically controlled by rapid switching of the exchange coupling. (It should be possible to derive gate constructions from Rabi oscillations, but these are not commonly used.)

- While spin echo and other dynamical decoupling pulse sequences are often very successful for extending the lifetime of a qubit state, these techniques are not directly adaptable to improving the fidelity of Rabi oscillations.

To address the above shortcomings, a range of extensions and alternative approaches have been developed. These can broadly be designated as quantum control techniques.
Note that similar questions are also encountered elsewhere. In quantum chemistry, one might aim to speed up some reaction, for example by illumination with a suitably shaped laser pulse. In NMR, one may also want to use fast drive amplitudes and eliminate systematic errors, for example due to RF-field inhomogeneity. Some of the techniques and concepts developed in other fields are adaptable to quantum computing, but there is one important conceptual difference: qubit control requires that an operation is accurate independent of the initial state, which would not be known when a gate is part of an algorithm, for example. In other words, one needs to optimize gate fidelity rather than the final state fidelity for a single given input state. The situation is different, for example, when steering a chemical reaction, which usually starts from a single, well defined initial state.

10.2 Control beyond Rabi flopping

In the superconducting qubit community, it has become common to compensate errors associated with short pulse durations (typically a few ns at 6 GHz level splitting) and the low anharmonicity by using a technique called Derivative Removal by Adiabatic Gate (DRAG) and variants of it [61, 62, 63]. Simultaneously with a strong, short Rabi pulse, the qubit level splitting and a suitable out-of phase component are modulated such that the amplitude of leaking into the third level is minimized.
In some cases, one uses baseband control methods where some quit parameter is switched and left approximately constant over some period time. For example, the $S-T_0$ qubit is commonly operated by switching and modulating the exchange splitting J (see section 6.2). While the available choice of rotation axis is limited, composing several rotations at different J can be used to construct arbitrary single qubit gates (see, e.g., [64]). Similar methods are sometimes used for superconducting flux qubits [65]. In particular, it is common to implement z-rotations by pulsing the level splitting ω_0, for example using fast flux bias lines.

10.3 Composite pulses and dynamically corrected gates

Without special precaution, gate operations are sensitive to both high and low frequency fluctuations. In many qubit systems, the noise spectrum responsible for decoherence is much larger at

lower frequencies. Examples include nuclear- and electron spins for spin qubits, flux noise due to surface spins in superconducting qubits, and charge noise. The last two often have a $1/f$-like spectrum, and many other spin baths exhibit an even steeper high frequency decay. As a result, dynamical decoupling techniques that employ correlations in the noise bath associated with low frequency fluctuations are highly successful for extending the dephasing time T_2 much beyond T_2^*. The basic idea is to cancel the phase accumulated from the noise by (repeatedly) inverting the state of the qubit with π-pulses. The less the state of the bath changes over the course of a single experiment, the more successful are such procedures.

Standard dynamical decoupling sequences for extending the memory time are not directly suitable for improving the fidelity of a gate operation. However, it is possible to employ similar concepts to also protect nontrivial gate operations from slow fluctuations, obtaining so called dynamically corrected gates (DCGs). A prerequisite is that the correlation time of the relevant fluctuations is long compared to the duration of a single gate. In addition to environmental fluctuations, one can also compensate systematic (i.e., static) errors, although this ability is less important because they can also be reduced by calibration.

The basic idea for constructing such gates is to require that the derivative of the unitary gate operation with respect to the noise variable vanishes: if the gate U depends on some fluctuating quantity δ, we require that $dU/d\delta = 0$. For a given gate the derivatives can be evaluated (semi-) analytically via the Magnus expansion. In addition, the desired gate U_{target} must be realized: $U(\delta = 0) = U_{target}$. In the simplest case, only quasistatic fluctuations of the parameters are considered, but one can extend the concept to finite frequency fluctuations by computing filter functions analogous to those of dynamical decoupling sequences [66].

A general construction of DCGs that is portable between different qubit system, but relies on a number of somewhat restrictive prerequisites is given in Ref. [67]. Another, more specific approach to obtain DCGs is a concatenation of several Rabi-pulses around different axis. Such so called composite pulses have been known for some time in the NMR community. An example consisting of three segments known as BB1 is shown in Figs. 18(a),(b). It is able to compensate errors in both the resonance frequency and the RF field amplitude. Originally, these pulses were designed to be robust against systematic errors and inhomogeneities in NMR setups.

In situations where such known sequences are not applicable, it is possible to find DCGs by brute force numerical search. For example, it was shown that for exchange-controlled two-electron spin qubits, viable DCGs that are insensitive both to charge and nuclear spin fluctuations exist [21]. Estimates indicate that these can reduce errors due to slow noise components by more than an order of magnitude. However, it remains to be seen if more decoherence from fast noise resulting from the longer duration compared to non-decouple gates does not outweigh the gain with respect to low frequency noise.

10.4 Optimal control and related approaches

In addition to the above, largely experiment-driven approaches, a significant number of studies considered various types of control-theoretic approaches. Generally, the goal is to implement some desired action (e.g. a gate operation) subject to certain constraints (such as the maximum pulse amplitude or duration) while maximizing or minimizing another quantity (e.g. the energy of the pulse or the error induced by decoherence).

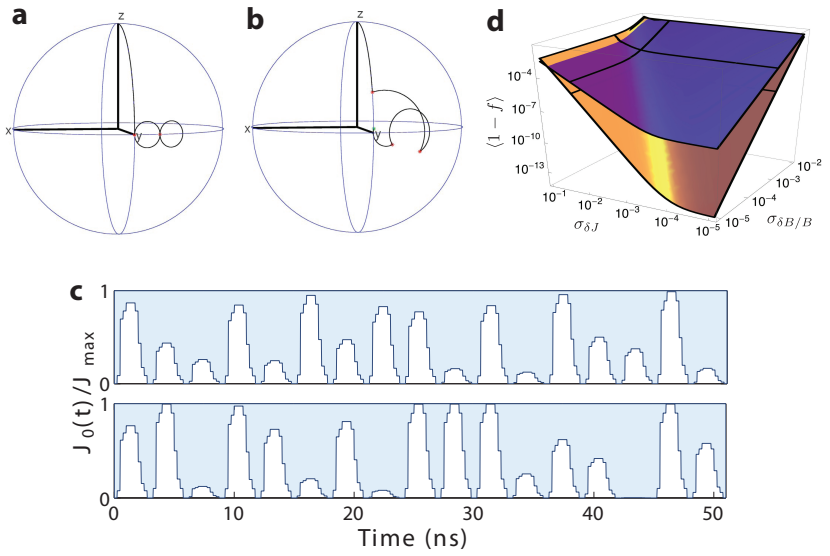

Fig. 18: ***Composite and dynamically corrected gates.*** ***(a)*** *Trajectory of the qubit state under a composite gate BB1 for optimal parameter.* ***(b)*** *Same pulse with 50 % overrotation. Even though there are large deviations at intermediate stages, the final state is nearly the same as in (a).* ***(c)*** *Pulse train $J(t)$ for an $S-T_0$ qubit that is to first order protected from slow fluctuations in both the magnetic field gradient ΔB_z and the detuning ϵ (see section 6.2).* ***(d)*** *Average error of the DCG from (c) (brown) and a similar but uncorrected gate (blue) as a function of the relative rms fluctuation amplitudes of the fluctuating parameters. (a),(b) from [8], (c),(d) from [21].*

11 Outlook

I conclude with a brief account of future directions for the development of quantum dot based spin qubits. A very important aspect that we have only mentioned in passing in section 9.2 is charge noise. It has become clear that it will be a limiting factor whenever the exchange interaction is used, in particular for two qubit gates relying on charge coupling. Given the significant progress in reducing dephasing due to nuclear spins (section 7), charge fluctuations are likely to be the most decisive parameter for qubit performance. Whether progress can be made here is mostly a question of material improvement, for example by eliminating dopants from the heterostructures. Regarding nuclear spins, it is conceivable that with further refinement of the techniques from section 7, another order of magnitude improvement of the performance metrics (coherence times, gate fidelities) is possible. At the same time, open questions related to DNP and hyperfine dephasing remain. These are of both practical and fundamental interest. Examples include quantum effects in the nuclear spin bath, fundamental limits to narrowing, and the interplay between spin-orbit coupling and the hyperfine interaction.
For further technological advances of spin qubits, the realization and operation of multi-qubit circuits will be a central topic of future research. The biggest fundamental challenge is to obtain a sufficiently strong coupling compared to the dephasing time for high fidelity two-qubit gates. At the same time, interacting qubits have to be placed far enough apart to route all required wires for gates and readout and possibly accommodate local control electronics. At the single quibt level, boosting and veryfying the gate fidelity is a high priority task.

References

[1] Bertaina, S., Gambarelli, S., Mitra, T., Tsukerblat, B., Müller, A., and Barbara, B. *Nature* **453**, 204–206 (2008).

[2] Morton, J. J. L., Tyryshkin, A. M., Brown, R. M., Shankar, S., Lovett, B. W., Ardavan, A., Schenkel, T., Haller, E. E., Ager, J. W., and Lyon, S. A. *Nature* **455**, 1085–1088 (2008).

[3] Robledo, L., Childress, L., Bernien, H., Hensen, B., Alkemade, P. F. A., and Hanson, R. *Nature* **477**, 574–578 (2011).

[4] Hayashi, T., Fujisawa, T., Cheong, H. D., Jeong, Y. H., and Hirayama, Y. *Phys. Rev. Lett.* **91**, 226804 (2003).

[5] Petta, J., Johnson, A., Taylor, J., Laird, E., Yacoby, A., Lukin, M., Marcus, C., Hanson, M., and Gossard, A. *Science* **309**, 2180 (2005).

[6] O'Connell, A. D., Hofheinz, M., Ansmann, M., Bialczak, R. C., Lenander, M., Lucero, E., Neeley, M., Sank, D., Wang, H., Weides, M., Wenner, J., Martinis, J. M., and Cleland, A. N. *Nature* **464**, 697–703 (2010).

[7] DiVincenzo, D., Lisenfeld, J., Ustinov, A. V., Schreiber, L. R., and Vandersypen, L. M. K. *Quantum Computing - Fundamentals and Solid-State Realizations*, chapter 25. Wiley-VCH, 3 edition (2012). in "Nanoelectronics and Information Technology", edited by R. Waser.

[8] Vandersypen, L. M. K. and Chuang, I. L. *Rev. Mod. Phys.* **76**, 1037–1069 (2005).

[9] Vandersypen, L. M. K., Steffen, M., Breyta, G., Yannoni, C. S., Sherwood, M. H., and Chuang, I. L. *Nature* **414**, 883–887 (2001).

[10] Loss, D. and DiVincenzo, D. P. *Phys. Rev. A* **57**, 120–126 (1998).

[11] Elzerman, J., Hanson, R., van Beveren, L. H. W., Witkamp, B., Vandersypen, L. M. K., and Kouwenhoven, L. P. *Nature* **430**, 431 (2004).

[12] Field, M., Smith, C. G., Pepper, M., Ritchie, D. A., Frost, J. E. F., Jones, G. A. C., and Hasko, D. G. *Phys. Rev. Lett.* **70**, 1311 (1993).

[13] Reilly, D., Marcus, C., Hanson, M., and Gossard, A. *App. Phys. Lett.* **91**, 162101 (2007).

[14] Barthel, C., Reilly, D. J., Marcus, C. M., Hanson, M. P., and Gossard, A. C. *Phys. Rev. Lett.* **103**, 160503 (2009).

[15] Barthel, C., Kjærgaard, M., Medford, J., Stopa, M., Marcus, C. M., Hanson, M. P., and Gossard, A. C. *Phys. Rev. B* **81**, 161308 (2010).

[16] Koppens, F. H. L., Buizert, C., Tielrooij, K., Vink, I., Nowack, K., , Meunier, T., Kouwenhoven, L. P., and Vandersypen, L. M. K. *Nature* **442**, 766 (2006).

[17] Chekhovich, E. A., Makhonin, M. N., Tartakovskii, A. I., A.Yacoby, Bluhm, H., Nowack, K. C., and Vandersypen, L. M. K. (submitted to Nature Materials), (2012).

[18] Nowack, K. C., Koppens, F. H. L., Nazarov, Y. V., and Vandersypen, L. M. K. *Science* **318**, 1430 (2007).

[19] Pioro-Ladrire, M., Obata, T., Tokura, Y., Shin, Y.-S., Kubo, T., Yoshida, K., Taniyama, T., and Tarucha, S. *Nature Physics* **4**, 776–779 (2008).

[20] Obata, T., Pioro-Ladrière, M., Tokura, Y., Shin, Y.-S., Kubo, T., Yoshida, K., Taniyama, T., and Tarucha, S. *Phys. Rev. B* **81**, 085317 (2010).

[21] Khodjasteh, K., Bluhm, H., and Viola, L. *Phys. Rev. A* **86**, 042329 (2012).

[22] DiVincenzo, D. P., Bacon, D., Kempe, J., Burkard, G., and Whaley, K. B. *Nature* **408**, 339 (2000).

[23] Taylor, J. M., Marcus, C. M., and Lukin, M. D. *Phys. Rev. Lett.* **90**, 206803 (2003).

[24] Abragam, A. *The principles of Nuclear Magnetism*. Oxford University Press, London, (1961).

[25] Khaetskii, A. V., Loss, D., and Glazman, L. *Phys. Rev. Lett.* **88**, 186802 (2002).

[26] Merkulov, I. A., Efros, A. L., and Rosen, M. *Phys. Rev. B* **65**, 205309 (2002).

[27] Koppens, F. H. L., Nowack, K. C., and Vandersypen, L. M. K. *Phys. Rev. Lett.* **100**, 236802 (2008).

[28] Bluhm, H., Foletti, S., Neder, I., Rudner, M., Mahalu, D., Umansky, V., and Yacoby, A. *Nature Physics* **7**, 109–113 (2010).

[29] Witzel, W. M. and Das Sarma, S. *Phys. Rev. B* **76**, 241303 (2007).

[30] Yao, W., Lui, R.-B., and Sham, L. J. *PRL* **98**, 077602 (2007).

[31] Vink, I., Nowack, K., Koppens, F., Danon, J., Nazarov, Y., and Vandersypen, L. *Nature Physics* **5**, 764–768 (2009).

[32] Laird, E. A., Barthel, C., Rashba, E. I., Marcus, C. M., Hanson, M. P., and Gossard, A. C. *Phys. Rev. Lett.* **99**, 246601 (2007).

[33] Barthel, C., Reilly, D., Marcus, C., Hanson, M., and Gossard, A. *Phys. Rev. Lett.* **103**, 160503 (2009).

[34] Bluhm, H., Foletti, S., Mahalu, D., Umansky, V., and Yacoby, A. *Phys. Rev. Lett.* **105**, 216803 (2010).

[35] Petta, J. R., Taylor, J. M., Johnson, A. C., Yacoby, A., Lukin, M. D., Marcus, C. M., Hanson, M. P., and Gossard, A. C. *Phys. Rev. Lett.* **100**, 067601 (2008).

[36] Reilly, D. J., Taylor, J. M., Laird, E. A., Petta, J. R., Marcus, C. M., Hanson, M. P., and Gossard, A. C. *Phys. Rev. Lett.* **101**, 236803 (2008).

[37] Reilly, D., Taylor, J., Petta, J., Marcus, C., Hanson, M., and Gossard, A. *Physical review letters* **104**, 236802 (2010).

[38] Neder, I., Rudner, M., Bluhm, H., and Yacoby, A. (to be published).

[39] Hahn, E. L. *Phys. Rev.* **80**, 580 (1950).

[40] Witzel, W. M. and Das Sarma, S. *Phys. Rev. B.* **74**, 035322 (2006).

[41] Yao, W., Lui, R.-B., and Sham, L. J. *Phys. Rev. B* **74**, 195301 (2006).

[42] Cywiński, L., Witzel, W. M., and Das Sarma, S. *Phys. Rev. B* **79**, 245314 (2009).

[43] Cywiński, L., Witzel, W. M., and Das Sarma, S. *Phys. Rev. Lett.* **102**, 057601 (2009).

[44] Lai, C. W., Maletinsky, P., Badolato, A., and Imamoglu, A. *Phys. Rev. Lett.* **96**, 167403 (2006).

[45] Baugh, J., Kitamura, Y., Ono, K., and Tarucha, S. *Phys. Rev. Lett.* **99**, 096804 (2007).

[46] Foletti, S., Bluhm, H., Mahalu, D., Umansky, V., and Yacoby, A. *Nature Physics* **5**, 903 (2009).

[47] Laird, E. A., Barthel, C., Rashba, E. I., Marcus, C. M., Hanson, M. P., and Gossard, A. C. *Phys. Rev. Lett.* **99**, 246601 (2007).

[48] Ono, K. and Tarucha, S. *Phys. Rev. Lett.* **92**, 256803 (2004).

[49] Koppens, F. H. L., Folk, J. A., Elzerman, J. M., Hanson, R., van Beveren, L. H. W., Vink, I. T., Tranitz, H. P., Wegscheider, W., Kouwenhoven, L. P., and Vandersypen, L. M. K. *Science* **309**, 1346–1350 (2005).

[50] Tarucha, S., Kitamura, Y., Kodera, T., and Ono, K. *physica status solidi (b)* **243**, 3673–3677 (2006).

[51] Foletti, S., Bluhm, H., Mahalu, D., Umansky, V., and Yacoby, A. *Nature Physics* **5**, 903–908 (2009).

[52] Stopa, M., Krich, J. J., and Yacoby, A. *Phys. Rev. B* **81**, 041304 (2010).

[53] Gullans, M., Krich, J. J., Taylor, J. M., Bluhm, H., Halperin, B. I., Marcus, C. M., Stopa, M., Yacoby, A., and Lukin, M. D. *Phys. Rev. Lett.* **104**, 226807 (2010).

[54] Brunner, R., Shin, Y.-S., Obata, T., Pioro-Ladrière, M., Kubo, T., Yoshida, K., Taniyama, T., Tokura, Y., and Tarucha, S. *Phys. Rev. Lett.* **107**, 146801 (2011).

[55] Nowack, K. C., Koppens, F. H. L., Nazarov, Y. V., and Vandersypen, L. M. K. *Science* **318**, 1430 (2007).

[56] Levy, J. *Phys. Rev. Lett.* **89**, 147902 (2002).

[57] Klinovaja, J., Stepanenko, D., Halperin, B. I., and Loss, D. *Phys. Rev. B* **86**, 085423 (2012).

[58] Shulman, M. D., Dial, O. E., Harvey, S. P., Bluhm, H., Umansky, V., and Yacoby, A. *Science* **336**, 202–205 (2012).

[59] Reilly, D. J., Marcus, C. M., Hanson, M. P., and Gossard, A. C. *App. Phys. Lett.* **91**, 162101 (2007).

[60] Trifunovic, L., Dial, O., Trif, M., Wootton, J. R., Abebe, R., Yacoby, A., and Loss, D. *Phys. Rev. X* **2**, 011006 (2012).

[61] Motzoi, F., Gambetta, J. M., Rebentrost, P., and Wilhelm, F. K. *Phys. Rev. Lett.* **103**, 110501 (2009).

[62] Lucero, E., Kelly, J., Bialczak, R. C., Lenander, M., Mariantoni, M., Neeley, M., O'Connell, A. D., Sank, D., Wang, H., Weides, M., Wenner, J., Yamamoto, T., Cleland, A. N., and Martinis, J. M. *Phys. Rev. A* **82**, 042339 (2010).

[63] Chow, J. M., DiCarlo, L., Gambetta, J. M., Motzoi, F., Frunzio, L., Girvin, S. M., and Schoelkopf, R. J. *Phys. Rev. A* **82**, 040305 (2010).

[64] Hanson, R. and Burkard, G. *Phys. Rev. Lett.* **98**, 050502 (2007).

[65] Fedorov, A., Macha, P., Feofanov, A. K., Harmans, C. J. P. M., and Mooij, J. E. *Phys. Rev. Lett.* **106**, 170404 (2011).

[66] Green, T., Uys, H., and Biercuk, M. J. *Phys. Rev. Lett.* **109**, 020501 (2012).

[67] Khodjasteh, K. and Viola, L. *Phys. Rev. Lett.* **102**, 080501 (2009).

B 1 Quantum computing based on donor spins in silicon[1]

Lloyd C.L. Hollenberg
Centre for Quantum Computation and
Communication Technology
School of Physics, University of Melbourne,
Parkville 3010, Australia

Contents

1 Introduction **2**

2 Background theory of shallow dopants in silicon **3**

3 Qubit gates **6**
3.1 Single qubit operations: nuclear magnetic resonance 6
3.2 Controlling the contact-hyperfine interaction 8
3.3 Coupling donor qubits 9
3.4 Voltage control of the exchange coupling 12
3.5 CNOT gate in the Kane scheme 13

4 Qubit readout **15**

5 Decoherence **15**

6 Issues for scale-up of donor based architectures **15**

7 Conclusions and outlook **18**

[1]Lecture Notes of the 44^{th} IFF Spring School "Quantum Information Processing" (Forschungszentrum Jülich, 2013). All rights reserved. Some material in these notes is based (with permission) from "Computational Modeling of Donor-Based Quantum Computer Architectures in Silicon", L. Hollenberg, C. Wellard and A. Greentree, Handbook of Theoretical and Computational Nanotechnology Edited by Michael Rieth and Wolfram Schommers, ASP 2006

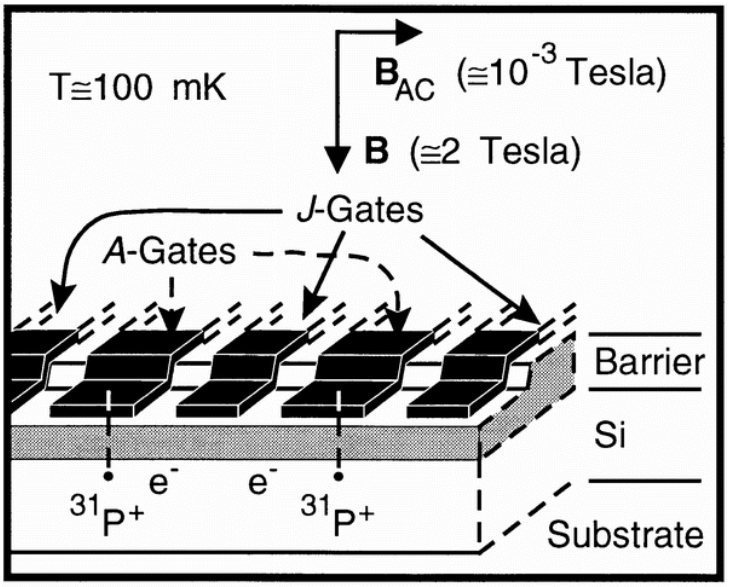

Fig. 1: *Schematic of the Kane proposal for a phosphorus in silicon based quantum computer [Reproduced from [1]]. Phosphorus donor are placed in a silicon lattice approx 20 nm apart and the single donor electron wave function is manipulated by bias applied to surface A and J gates, which in turn allows addressing, control and interaction of the ^{31}P nuclear spin qubits. The donor electrons are spin polarised by the background magnetic field, and the spin manipulations are effected by an RF field.*

1 Introduction

In 1998 Kane proposed a nuclear spin quantum computer based on phosphorus donors in silicon[1]. Given the long-lived quantum coherence of donor nuclear spins in the silicon crystal and the strong link to the silicon nanoelectronics industry this proposal has received significant attention. However, as a proposal for qubits based on spins in the solid-state, the Kane proposal was quite challenging in terms of the required theoretical and technological development. A schematic of the Kane proposal is shown in Figure 1.

We will first overview the basic physics of the Kane qubit system and then go into more details on the various components in the quantum computing context. The scheme requires the placement of individual donors in the silicon matrix of order 20 nm apart and in proximity to surface A and J gates which control the individual donor electron wave function and their interactions. The qubit information is encoded on the phosphorus nuclear spin and because the Si(28) atoms in the crystal have zero nuclear spin, the coherence time of the nuclear spin qubits can be very long. The system is at low temperature to minimise phonon induced decoherence. Decoherence is then due primarily to Si(29) impurities and background (non-qubit) phosphorus dopants. A large magnetic field of 2T is required to polarise the electron spins. To address the qubits the idea is to Stark shift the hyperfine interaction between the nucleus and the electron spin using the specific A gate above the qubit. The hyperfine interaction is governed by the value of the donor electron wave function at the nucleus and can be reduced by an applied electric field, in this case from a bias applied to the nearby A gate. Changing the hyperfine frequency in this way can bring that particular nuclear spin (or a set thereof if several A-gates are activated) in resonance with a global RF field in order to perform single qubit rotations, whilst all other qubits

under un-biased A gates are detuned. Interactions between neighboring nuclear spin qubits take place through the exchange interaction of the donor electrons. The exchange interaction is highly sensitive to the overlap of the donor electron wave functions, and in principle can be tuned by applying a bias to the surface J gate between the donors. A CNOT gate between neighboring nuclear spin qubits would be carried out through a particular sequence of A and J gate control together with a suitably tuned RF field. Readout of the qubit spin is effected by transferring the information to the donor electron spin and using spin-charge conversion – i.e. spin dependent tunneling of the electron to a dedicated readout-donor – to detect the electron spin state via a single electron transistor device which is sensitive to the resulting change in charge configuration. Variations on the basic Kane theme based on donors in silicon include electron spins qubits [2, 4, 5, 6], P-P^+ charge qubits[3], dipolar coupled qubits[4], and hybrid donor-surface qubits [7] to name a few.

Generally speaking, the key to proposals for donor based qubits is the control over the donor electron wave function via the nanoelectronic A and J gates. Since the original Kane proposal was published there has been a large amount of theoretical work on quantifying the level of control which might be achieved and the fidelity, specifically in the context of quantum computing. On the experimental front there has been steady progress, particularly in the enormous challenge of placing individual donors with high precision in the silicon matrix and registered to nanoelectronic gates. It is only relatively recently that the readout and quantum control of a single donor electron spin has been achieved, however, one would expect that progress towards multiple qubit systems will accelerate from this point now that these technological hurdles have been overcome.

In terms of scale-up to a quantum computer the critical feature of the Kane proposal is the closely spaced qubits which forces a stringent gate separation of about 5 nm (assuming gate widths of 5nm). Such a high density may be seen as positive from the perspective of the overall size of a full scale quantum computer requiring many millions of qubits, however, it also raises several immediate issues quite apart from the obvious challenges of placing gates and SETs in such a high density array and inevitable cross-talk in control. A challenge for scale-up is the fact that the qubit array is constrained dimensionally ($\sim$ 1D) and with only nearest neighbor interactions. Implementing quantum error correction on a 1D array carries significant SWAP gate overheads and reduces the fault-tolerant threshold. Attempts to alleviate these problems by introducing short range qubit transport and allowing the nanoelectronics to be more spread out in a bi-linear arrangement improves the situation, however, the threshold is still quite low – calculations based on the Steane code, and assuming fault-tolerant transport, put the asymptotic threshold at about 10^{-7} for a bi-linear array. With rapid progress on the experimental front in controlling single electron and nuclear spins in silicon a major challenge for scale-up is to find ways of engaging with the relatively high surface code thresholds of $\sim 10^{-2}$ – this requires a genuine 2D qubit array architecture.

2 Background theory of shallow dopants in silicon

Shallow donors in silicon can in a first approximation be thought of as hydrogenic type systems existing in a uniform dielectric substrate. At this level one simply ignores the silicon lattice potential altogether. In this approximation the Hamiltonian of the excess valence electron is that of a Coulombic hydrogen atom in a dielectric medium with the dielectric constant of the silicon substrate $\kappa \sim 12$ and an effective electron mass in silicon $m^* = 0.2m_e$. The hydrogenic

orbitals are simply scaled by κ and m^* to give an effective Bohr radius and binding energy

$$a^* = \frac{\kappa}{m^*} a_B = 3.4 \text{ nm}, \quad E_n^* = \frac{m^*}{\kappa^2} E_n = 18 \text{ meV}.$$

Although this model underestimates the binding energy of the electron, which has been measured at 45.5 meV [8], it is an often useful starting point to describe donor physics. However, particularly in the context of nanoelectronics, it is often necessary to go beyond this simple model and include the interaction of the electron with the silicon lattice. One usually begins by considering the electronic structure of the undoped silicon lattice. Because this is an essentially untractable problem from first principles, and we are primarily interested in the non-core electrons, a mean-field description in the Born-Oppenheimer approximation is used to reduce the problem to that of a single (valence) electron with a Hamiltonian

$$H_0 = -\nabla^2 + V_{\text{Si}}(\mathbf{r}), \tag{1}$$

where $V_{Si}(\vec{r})$ is the effective silicon crystal potential and possess the symmetries of the face-centred cubic crystal lattice. The periodic nature of the crystal potential, $V_{Si}(\mathbf{r}) = V_{Si}(\mathbf{r} + \mathbf{R})$, where $\mathbf{R}$ is any lattice vector, allows one to use Bloch's theorem and write the eigenstates of the Hamiltonian Eq. 1 in the form

$$\phi_{\mathbf{k}}(\mathbf{r}) = u_{\mathbf{k}}(\mathbf{r}) \mathrm{e}^{i\mathbf{k}.\mathbf{r}}, \tag{2}$$

where the Bloch states $\phi_{\mathbf{k}}(\mathbf{r})$ have the symmetry of the lattice via $u_{\mathbf{k}}(\mathbf{r}) = u_{\mathbf{k}}(\mathbf{r} + \mathbf{R})$. The periodic part of the Bloch function $u_{\mathbf{k}}(\mathbf{r})$ can be expanded in plane waves with wavevectors given by the reciprocal vectors, G, of the crystal lattice:

$$u_{\mathbf{k}}(\mathbf{r}) = \sum_{\mathbf{G}} A_{\mathbf{k}}(\mathbf{G}) \mathrm{e}^{i\mathbf{G}.\mathbf{r}}. \tag{3}$$

By using the lattice symmetry in this way, the problem of calculating the eigenfunctions of Eq. 1 reduces to the determination of the coefficients $A_{\mathbf{k}}(\mathbf{G})$. In momentum space the Schrödinger equation in terms of the coefficients $A_{\mathbf{k}}(\mathbf{G})$ becomes

$$(\mathbf{k} + \mathbf{G}')^2 A_{\mathbf{k}}(\mathbf{G}') + \sum_{\mathbf{G}} A_{\mathbf{k}}(\mathbf{G}) V_{\text{Si}}(\mathbf{G} - \mathbf{G}') = E_{\mathbf{k}} A_{\mathbf{k}}(\mathbf{G}'), \tag{4}$$

where $E_{\mathbf{k}}$ are the single particle energies and $V_{\text{Si}}(\mathbf{G})$ is the momentum space representation of the crystal potential. Given a representation for the crystal potential (e.g. in the pseudopotential approach), the $A_{\mathbf{k}}(\mathbf{G})$ can be computed and the bandstructure of the undoped crystal determined.

We can now review the treatment of a donor electron beyond the simple hydrogenic approximation, including physics of the silicon bandstructure, first developed by Kohn and Luttinger [9]. With a single impurity potential added to the problem we wish to solve the Schrödinger equation for a single donor electron

$$(H_0 + U(\mathbf{r}))\psi(\mathbf{r}) = E\psi(\mathbf{r}), \tag{5}$$

where H_0 is the Hamiltonian for the silicon lattice (given above) and $U(\mathbf{r})$ is the impurity potential. For simplicity of notation we consider the ground state of the system with energy E. The donor electron wave function $\psi(\mathbf{r})$ can be expanded in terms of the Bloch states $\phi_{\mathbf{k}}(\mathbf{r})$ as,

$$\psi(\mathbf{r}) = \int F(\mathbf{k}) \phi_{\mathbf{k}}(\mathbf{r}) d\mathbf{k}, \tag{6}$$

In momentum space the $F(\mathbf{k})$ obey a Schrödinger equation in terms of the energies and Bloch states of the pure silicon crystal problem:

$$EF(\mathbf{k}') = E_{\mathbf{k}'}F(\mathbf{k}') + \int \phi^*_{\mathbf{k}'}(\mathbf{r})U(\mathbf{r})\phi_{\mathbf{k}}(\mathbf{r})F(\mathbf{k})d\mathbf{k}d\mathbf{r}. \tag{7}$$

Expanding the Bloch functions according to Eq. 3 in Eq 7 yields

$$\begin{aligned} EF(\mathbf{k}') &= E_{\mathbf{k}'}F(\mathbf{k}') \\ &+ \int \sum_{\mathbf{G},\mathbf{G}'} A^*_{\mathbf{k}',\mathbf{G}'}A_{\mathbf{k},\mathbf{G}}\tilde{U}(\mathbf{k}-\mathbf{k}'+\mathbf{G}-\mathbf{G}')F(\mathbf{k})d\mathbf{k} \end{aligned} \tag{8}$$

where $\tilde{U}(\mathbf{k}) = \int \mathrm{e}^{i\mathbf{k}.\mathbf{r}}U(\mathbf{r})d\mathbf{r}$ is the Fourier transform of the impurity potential. This is the starting point for the band minima basis approach where the system is diagonalised in a large basis of states around each conduction band minima [16]. However, the effective mass theory relies of three approximations from this point. First, the band energies $E_{\mathbf{k}'}$ are expanded to second order in $\mathbf{k}-\mathbf{k}_\mu$, around the six degenerate conduction band minima (labelled by μ) located at:

$$\left\{\mathbf{k}^{(\min)}_\mu\right\}_{\mu=1..6} = \{(\pm k_0,0,0),(0,\pm k_0,0),(0,0,\pm k_0)\}, \tag{9}$$

where $k_0 = (2\pi/a_0)0.85$ and $a_0 = 5.43$Å is the lattice constant of silicon. Critically, we can therefore write

$$E_{\mathbf{k}} \approx \sum_\mu \hbar^2(k^2_\parallel/(2m^*_\parallel) + \mathbf{k}^2_\perp/(2m^*_\perp)), \tag{10}$$

where $k_\parallel$ ($\mathbf{k}_\perp$) is the component of $\mathbf{k}-\mathbf{k}_\mu$ parallel (perpendicular) to the position of the conduction band minimum μ. The non-isotropic $m^*_\perp \neq m^*_\parallel$ are the effective electron masses, reflecting the non-isotropic conduction band minima. The second approximation is to assume that terms which behave as $\mathrm{e}^{i(\mathbf{G}-\mathbf{G}').\mathbf{r}}$ are sufficiently rapidly oscillating over the scale in which $U(\mathbf{r})$ varies to average the integrand to zero over the range of the integral and decouples the functions $F_\mu(\mathbf{k})$ around different conduction band minima. The third approximation amounts to setting $A^*_{\mathbf{k}',\mathbf{G}} \approx A_{\mathbf{k},\mathbf{G}'}$ and using the completeness identity $\sum_{\mathbf{G}}|A_{\mathbf{k},\mathbf{G}}|^2 = 1$. We then obtain an effective Schrödinger equation for each minima:

$$EF_\mu(\mathbf{k}') = \hbar^2(k^2_\parallel/(2m^*_\parallel) + \mathbf{k}^2_\perp/(2m^*_\perp))F_\mu(\mathbf{k}') + \int \tilde{U}(\mathbf{k}-\mathbf{k}')F_\mu(\mathbf{k})d\mathbf{k}, \tag{11}$$

Kohn and Luttinger obtained variations solutions of the form

$$F_{\pm z}(\mathbf{r}) = \frac{\exp\left[-\sqrt{(x^2+y^2)/a_\perp + z^2/a_\parallel}\,\right]}{\sqrt{6\pi a^2_\perp a_\parallel}}, \tag{12}$$

where $F_\mu(\mathbf{r}) = \int \mathrm{e}^{i(\mathbf{k}-\mathbf{k}_\mu).\mathbf{r}}F_\mu(\mathbf{k}-\mathbf{k}_\mu)d\mathbf{r}$, and $a_\perp, a_\parallel$ are the effective Bohr radii in the transverse and parallel directions respectively. At this level of approximation we have six degenerate states localised around each conduction band minimum;

$$\psi_\mu(\mathbf{r}) = F_\mu(\mathbf{r})\phi_{\mathbf{k}_\mu}(\mathbf{r}), \tag{13}$$

This effective mass description of a six-fold degenerate donor ground state is only part of the story - experimentally the 6-fold degeneracy is lifted by interactions between contributions from

different conduction band minima (valleys). Various approaches have been taken to introduce such interactions into the theory by including corrections to the impurity potential that couple the different valley states [10, 16], or by derivation of a multi-valley effective mass equation[11]. The effective mass wave function for the lowest six eigenstates are of the form:

$$\psi(\mathbf{r}) = \sum_{\mu} \alpha_{\mu} F_{\mu}(\mathbf{r}) \phi_{\mathbf{k}_{\mu}}(\mathbf{r}), \tag{14}$$

where the coefficients α_{μ} reflect the point group symmetry of the Hamiltonian, and give a non-degenerate A_1 ground, state, plus triply degenerate T and doubly degenerate E excited states. The coefficients are given by:

$$\alpha = \begin{cases} \frac{1}{\sqrt{6}}(1,1,1,1,1,1) & A_1 \\ \left.\begin{array}{l} \frac{1}{\sqrt{12}}(-1,-1,-1,-1,2,2) \\ \frac{1}{2}(1,1,-1,-1,0,0) \end{array}\right\} & E \\ \left.\begin{array}{l} \frac{1}{\sqrt{2}}(1,-1,0,0,0,0) \\ \frac{1}{\sqrt{2}}(0,0,1,-1,0,0) \\ \frac{1}{\sqrt{2}}(0,0,0,0,1,-1) \end{array}\right\} & T \end{cases} \tag{15}$$

This wave function is the cornerstone of the effective mass formalism (see Figure 2). The parameters $a_{\perp}$ and $a_{\parallel}$ can be determined variationally, using the effective mass formalism with a Coulombic potential. A minimum of $E = -30$meV is found with $a_{\perp} = 25.09$Å, $a_{\parallel} = 14.43$Å[13]. This is significantly higher than the experimentally observed value of $E = -45.5$meV; however, including the inter-valley coupling for these parameters reduces the ground-state energy to $E = 40$meV [12], in reasonable agreement with experiment. The simplicity of the effective mass approach makes it ideal as a starting point for understanding donor physics in a variety of devices. However, for more quantitative comparisons with experiment more complex treatments summing over many Bloch states [14, 15, 16] or tight-binding approaches [17, 18] are required. Of all of these approaches the highly optimised tight-binding codes have become the method of choice given that realistic device volumes over tens of millions of atoms can now be simulated with arbitrary external electric and magnetic fields [18].

3 Qubit gates

3.1 Single qubit operations: nuclear magnetic resonance

Starting with single qubit gates the Hamiltonian of the isolated donor nucleus-electron system is written as

$$H_0 = \mu_B B_z \sigma_e^z - g_n \mu_n B_z \sigma_n^z + A \vec{\sigma}_n \cdot \vec{\sigma}_e. \tag{16}$$

In this expression μ_B is the Bohr magneton, g_n the Lande factor for ^{31}P, and μ_n is the nuclear magneton. The hyperfine interaction constant (in response to a gate bias V_A) is given by

$$A(V_A) = \frac{8\pi}{3} |\psi(0, V_A)|^2 \mu_B g_n \mu_n, \tag{17}$$

where $\psi(0, V_A)$ is the donor electron wave function evaluated at the position of the nucleus ($\vec{r} \sim 0$) under the electric field produced by a gate bias V_A. The application of a potential bias

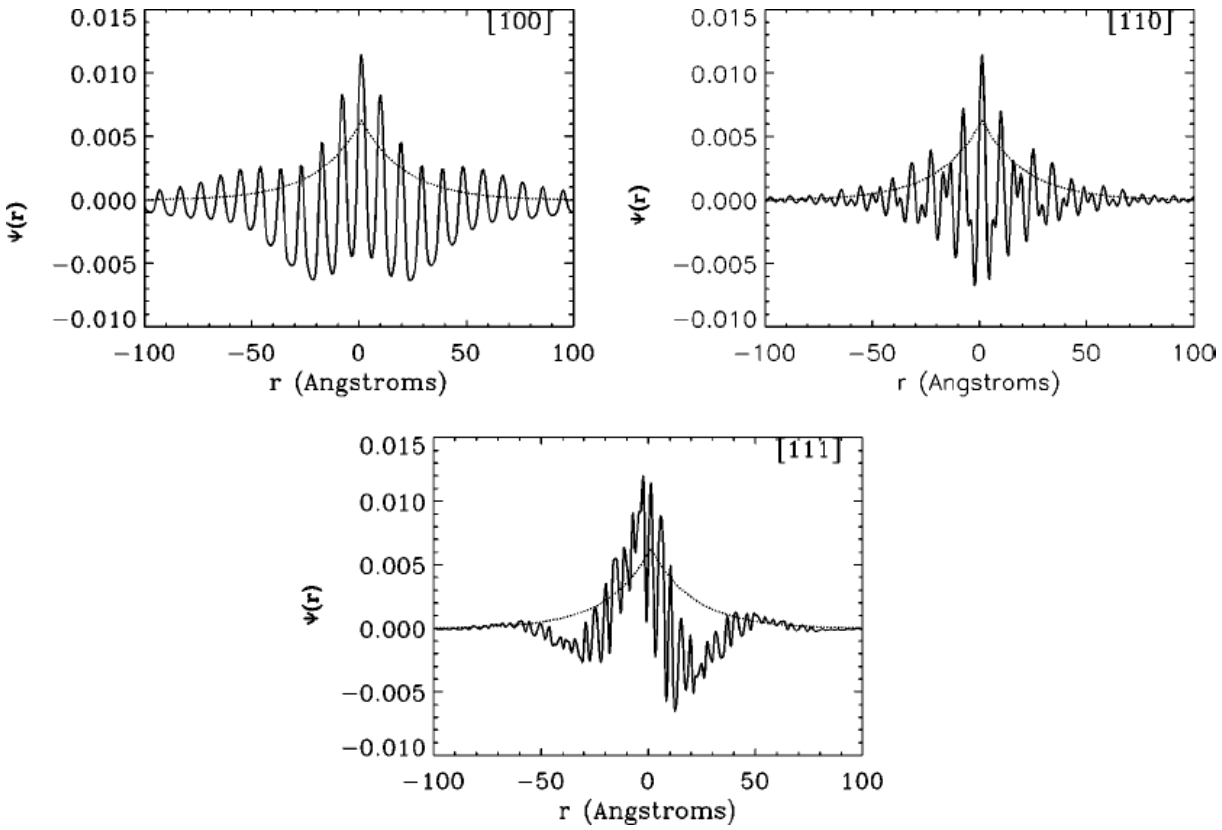

Fig. 2: *The Kohn-Luttinger wave function (solid line) for a phosphorus donor electron in silicon, plotted along directions of high symmetry within the crystal. The dotted line shows an isotropic 1s hydrogenic wave function, with a Bohr radius of* ~ 2 *nm. (reproduced from [19]).*

V_A to an A-gate electrode located above the qubit distorts the electron wave function allowing the hyperfine interaction strength to be tuned. The nuclear spin is controlled through NMR, and so we first need to understand how the tuning of the hyperfine parameter A affects the energy levels of the system. We write our basis spins states as computational basis states in nuclear spin, i.e. $\{|en\rangle\} = \{|\downarrow\downarrow\rangle, |\downarrow\uparrow\rangle, |\uparrow\downarrow\rangle, |\uparrow\uparrow\rangle\} \rightarrow \{|\downarrow 1\rangle, |\downarrow 0\rangle, |\uparrow 1\rangle, |\uparrow 0\rangle\}$. One can diagonalise the Hamiltonian exactly, but it is more instructive to write down the energy levels in perturbation theory to second order in A (and using $\mu_B B >> g_n \mu_B B$):

$$
\begin{aligned}
E_{\uparrow 0} &= \mu_B B - g_n \mu_n B + A \\
E_{\uparrow 1} &= \mu_B B + g_n \mu_n B - A + \frac{2A^2}{\mu_B B} \\
E_{\downarrow 0} &= -\mu_B B - g_n \mu_n B - A - \frac{2A^2}{\mu_B B} \\
E_{\downarrow 1} &= -\mu_B B + g_n \mu_n B + A.
\end{aligned}
\tag{18}
$$

Hence, in the sub-space with the electron spin polarised down the resonant frequency ω_{01} between the nuclear computational spin states is:

$$
\omega_{01} = \frac{1}{h}\left(2 g_n \mu_u B + 2A + 2A^2/\mu_B B\right) \tag{19}
$$

Through the A-gate control of A the system can be brought in and out of resonance with an external oscillating RF magnetic field B_{RF} to perform the required single qubit gates. For

example, a RF field applied in the x-y plane resonant with ω_{01} will produce Rabi oscillations $|\downarrow 0\rangle \leftrightarrow |\downarrow 1\rangle$ with Rabi frequency $g_n\mu_n B_{\rm AC}/2\hbar$. For typical operating conditions with mT RF fields this gives a π rotation time of about 50 μs.

3.2 Controlling the contact-hyperfine interaction

Clearly, the key to the addressability and control of the donor nuclear spin qubit is the ability to tune the hyperfine interaction. In most proposals this would be done by a proximate A-gate as described above, although it should be noted that in the so-called "digital" Kane architecture, the hyperfine coupling is controlled through complete ionisation of the donor[20]. The change in the strength of the contact-hyperfine coupling due to the application of gate biases has been studied theoretically by a number of authors in various approximations from hydrogenic and effective mass to more sophisticated tight-binding treatments (see [21] for a comprehensive review). Essentially, one needs to describe how the donor electron wave function at the nuclear position changes as a result of the applied gate field. Because it is non-trivial to describe the fine details of the wave function at the nucleus [22] for device level physics the relative change is usually calculated:

$$\frac{A(V_A)}{A(0)} = \frac{|\psi(V_A,0)|^2}{|\psi(0,0)|^2} \equiv \eta_1 \vec{E}_A + \eta_2 \vec{E}_A^2, \tag{20}$$

where $A(0)$ is the non-gated value of the hyperfine coupling determined experimentally[23]. In terms of the corresponding electric field $\vec{E}_A$ at the donor position, the linear and quadratic Stark shift coefficients of the hyperfine interaction are η_1 and η_2 respectively. Whilst there were many theoretical calculations of the Stark shift of the hyperfine interaction, it was not until 2006 that this effect was first determined experimentally for donors in silicon [24]. In Ref. [25] the results of two theoretical approaches using distinct momentum and real-space methodology were used to describe the quantity $\frac{A(V_A)}{A(0)}$ as a function of depth and in comparison with the experimental measurement of the hyperfine Stark shift for As donors in low fields. In the band minima basis method [16] the direct diagonalisation in momentum space was carried out over all six valleys allowing the potential due to an A-gate to be included at the Hamiltonian level. The momentum space diagonalisation approach, is computationally expensive, but it provided an important check against large scale tight-binding calculations, which in turn match well against the experimental determination of the Stark shift. The overall picture is that the theoretical description of has converged to a reasonable level in terms of internal consistency and compares well with experiment (see Figure 3.2).

Since this theoretical development on the Stark shift of donors in bulk silicon, the attention has turned towards more realistic situations with proximate interfaces [7, 26, 27, 28, 29] as key experimental measurements became available. An important check of the overall description of donor wave function control under nanoelectronic gate fields came with the measurement of donor orbital states through transport in FinFET devices [30], which showed significant deviation from the expected bulk spectrum. Large-scale tight-binding and band minima calculations were used to explore the space of electric field and donor depth on the quantum confinement conditions of the donor-associated electron, providing an excellent description of the low lying donor states observed and even allowing a determination of the donor species [30].

An important theoretical prediction is that with such closely spaced gates the level of spill-over field from neighboring A-gates to neighboring qubits will be a significant source of cross-talk in control for which complex compensation schemes may be required [26]. The "digital" Kane

approach may be an elegant solution to this particular issue. In moving to an electron spin donor qubit it was also recognized that even the maximum level of control of the A-gate is not sufficient to switch off non-addressed qubits. In Ref. [5] a donor electron spin architecture was proposed with a synchronous control scheme designed to mitigate the cross-talk problem. With the theoretical description of the gate control of donor electron states well under control, the wider context of the Kane donor spin qubit has spurred further refinements of existing treatments of donor states, including the site-specific contact and non-isotropic hyperfine interaction terms for wave function mapping under electric fields, interaction with magnetic fields and gate control of the g-factor, dynamics of molecular donor-based systems, coherent single electron transport through chains of ionised donor chains, and spin-to-charge readout mechanisms (a comprehensive list and references can be found in [21]).

3.3 Coupling donor qubits

In donor spin-based quantum computing, with qubits encoded on either the electron or nuclear spins, the quantum gates between the qubits are generally mediated by the interactions between the donor electrons (having the larger magnetic moment), and these are either based on exchange or dipole interactions. The exchange energy is based on the wave function overlap between the donors and is stronger for smaller separations, and for hydrogenic orbitals it decays asymptotically as [31]

$$J(r) \sim (R/a^*)^{5/2}\exp(-2R/a^*), \tag{21}$$

where R is the donor separation and a^* is the effective Bohr radius of the electron wave function (around 2 nm). The strength of the dipole coupling is much weaker and the exchange coupling dominates for donors that are separated by less than $\sim$ 30 nm.

In the original Kane proposal, and the synchronous donor electron spin qubit version [5], qubit coupling is based on the exchange interaction. In general, for two spin-1/2 particles a and b, the exchange interaction can be written in the form

$$H_{ex} = J\vec{\sigma}_a.\vec{\sigma}_b = J(\sigma_a^x\sigma_b^x + \sigma_a^y\sigma_b^y + \sigma_a^z\sigma_b^z), \tag{22}$$

where the σ_i^α represent the Pauli spin operators acting on particle i. The origin of this spin interaction lies in the anti-symmetry of the electron wave function. Consider a system composed of two donor atoms separated by a vector $\mathbf{R}$, where R is greater than the effective Bohr radius of the single donor wave functions. In this case, to a good approximation the two electron wave function can be written as an anti-symmetrised products of the single donor wave functions. We denote the singe donor spatial wave functions localised around donor a or b as $\psi_a(\mathbf{r}), \psi_b(\mathbf{r})$ respectively, and the two possible spin states of the electron as α, β. There are thus four different possible single donor wave functions from which we can choose to construct our two donor function $\psi_a(\mathbf{r})\alpha, \psi_a(\mathbf{r})\beta, \psi_b(\mathbf{r})\alpha$ and $\psi_b(\mathbf{r})\beta$. There are therefore six possible ways that we can construct our two-electron wave function (remember each two particle wave function is a anti-symmetric combination of a product of two of these single particle states). Two of these possibilities however involve both electrons localised around the same donor, a possibility that we ignore in the limit $R >> a^*$, as these state will be much higher in energy than when each electron is localised around a separate donor. The spin part of the wave function for the remaining four possibilities can be written as either a spin singlet or a spin triplet state. Because the spin singlet is anti-symmetric in exchange of particles, the corresponding spatial

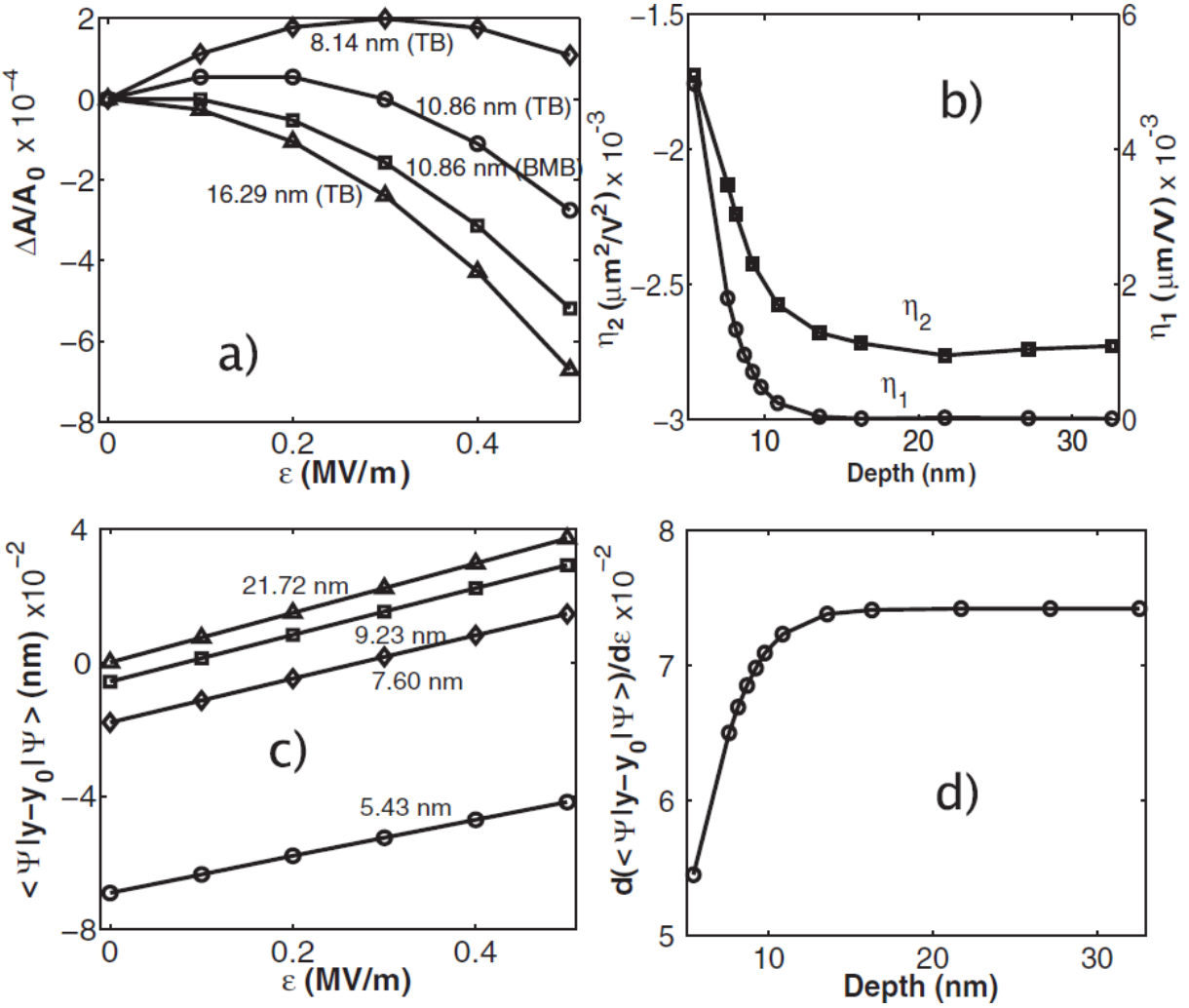

Fig. 3: *Calculations of the Stark shift of the P donor hyperfine interaction at low fields (reproduced from [25]). (a) Real space tight-binding (TB) and momentum space band minima basis (BMB) calculations of the electric field response of the hyperfine coupling at various donor depths are directly compared. (b) Tight-binding calculations of the quadratic and linear Stark coefficients (left-hand and right-hand axes respectively) as a function of donor depth. (c) Tight-binding calculation of the shift of the ground state electron dipole moment as a function of the electric field. (d) Tight-binding calculation of the electric field gradient of the dipole moments as a function of donor depth.*

wave function must be symmetric, and vice-versa for the spin-triplet state. These two-particle states can be written, unnormalised, as;

$$\{\Psi(\mathbf{r}_1,\mathbf{r}_2)\} = \begin{cases} (\psi_a(\mathbf{r}_1)\psi_b(\mathbf{r}_2) - \psi_a(\mathbf{r}_2)\psi_b(\mathbf{r}_1))\alpha(1)\alpha(2) \\ (\psi_a(\mathbf{r}_1)\psi_b(\mathbf{r}_2) - \psi_a(\mathbf{r}_2)\psi_b(\mathbf{r}_1))\beta(1)\beta(2) \\ (\psi_a(\mathbf{r}_1)\psi_b(\mathbf{r}_2) - \psi_a(\mathbf{r}_2)\psi_b(\mathbf{r}_1))(\alpha(1)\beta(2) + \alpha(2)\beta(1)) \\ (\psi_a(\mathbf{r}_1)\psi_b(\mathbf{r}_2) + \psi_a(\mathbf{r}_2)\psi_b(\mathbf{r}_1))(\alpha(1)\beta(2) - \alpha(2)\beta(1)) \end{cases} \tag{23}$$

In this way, a purely electronic two-donor Hamiltonian, can lead to a spin-dependent exchange coupling. The energy difference between the spin-triplet and the spin-singlet state is due to the different spatial probability distributions associated with the two states. In particular, the

spin-symmetric triplet state is associated with an anti-symmetric spatial wave function, which has a node midway between the two donors, in a region of relatively low potential. The symmetric spatial wave function has a higher average probability density in this region, this is of course compensated by a lower probability density elsewhere. However, it is this region of low potential between the two donors that is responsible for the exchange splitting, the spatially symmetric, singlet state has a higher probability density in this region and therefore has a lower overall energy than does the spin-triplet state.
The two electron Hamiltonian for a system of two donors separated by a vector $\mathbf{R}$ is:

$$\begin{aligned} H &= -\frac{\hbar}{2m}\nabla_1^2 - \frac{\hbar}{2m}\nabla_2^2 - \frac{e^2}{4\pi\epsilon\mathbf{r}_1} - \frac{e^2}{4\pi\epsilon|\mathbf{R}-\mathbf{r}_1|} \\ &- \frac{e^2}{4\pi\epsilon\mathbf{r}_2} - \frac{e^2}{4\pi\epsilon|\mathbf{R}-\mathbf{r}_2|} + \frac{e^2}{4\pi\epsilon|\mathbf{r}_1-\mathbf{r}_2|} \\ &+ \frac{e^2}{4\pi\epsilon\mathbf{R}} + V_{\mathrm{Si}}(\mathbf{r}_1,\mathbf{r}_2). \end{aligned} \tag{24}$$

In the standard Heitler-London approximation the strength of the exchange coupling J, which is proportional to the energy difference between spin-singlet and the spin-triplet states, is determined by calculating the energy difference between the even and odd superpositions of spatial wave functions due to the above Hamiltonian. The correctly normalised two-electron spatial wave functions corresponding to the even and odd superpositions of single donor wave functions for donors separated by the vector R are given by

$$\Psi_{\pm}(\mathbf{r}_1,\mathbf{r}_2) = \frac{1}{\sqrt{2(1\pm S^2)}}\left(\psi(\mathbf{r}_1-\mathbf{R}/2)\psi(\mathbf{r}_2+\mathbf{R}/2) \pm \psi(\mathbf{r}_1+\mathbf{R}/2)\psi(\mathbf{r}_2-\mathbf{R}/2)\right), \tag{25}$$

where the two donors are located at positions $\pm\mathbf{R}/2$. The normalisation factor is given by

$$S(\mathbf{R}) = \int d^3\mathbf{r}\,\Psi^*(\mathbf{r}+\mathbf{R}/2)\Psi(\mathbf{r}-\mathbf{R}/2). \tag{26}$$

In the Heitler-London formalism the exchange coupling can be expressed in terms of matrix elements of the two-donor Hamiltonian, one can rewrite this as:

$$J(\mathbf{R}) = \frac{1}{2}S(\mathbf{R})^2(I_1(\mathbf{R}) - I_2(\mathbf{R}))/(1-S(\mathbf{R})^4), \tag{27}$$

where the overlap integrals are given explicitly by:

$$\begin{aligned} I_1(\mathbf{R}) &= \int d^3\mathbf{r}_1\, d^3\mathbf{r}_2\, \Psi^*(\mathbf{r}_1+\mathbf{R}/2)\Psi^*(\mathbf{r}_2-\mathbf{R}/2)H\,\Psi(\mathbf{r}_1+\mathbf{R}/2)\Psi(\mathbf{r}_2-\mathbf{R}/2), \\ I_2(\mathbf{R}) &= \int d^3\mathbf{r}_1\, d^3\mathbf{r}_2\, \Psi^*(\mathbf{r}_1+\mathbf{R}/2)\Psi^*(\mathbf{r}_2-\mathbf{R}/2)H\,\Psi(\mathbf{r}_2+\mathbf{R}/2)\Psi(\mathbf{r}_1-\mathbf{R}/2). \end{aligned} \tag{28}$$

Computation of these expressions using the Kohn-Luttinger wave function without approximation is rather tedious because of the large number reciprocal lattice vectors it is necessary to sum over to evaluate the periodic part of the Bloch functions. In Figure 3.3 we plot the exchange energy as a function of donor separation in each of the major lattice directions, as calculated in [32]. In order to make the calculation more tractable, in [32] the (excellent) approximation was made to ignore the contribution of the periodic part of the Bloch functions $u_\mu(\mathbf{r}) = 1$. In [19]

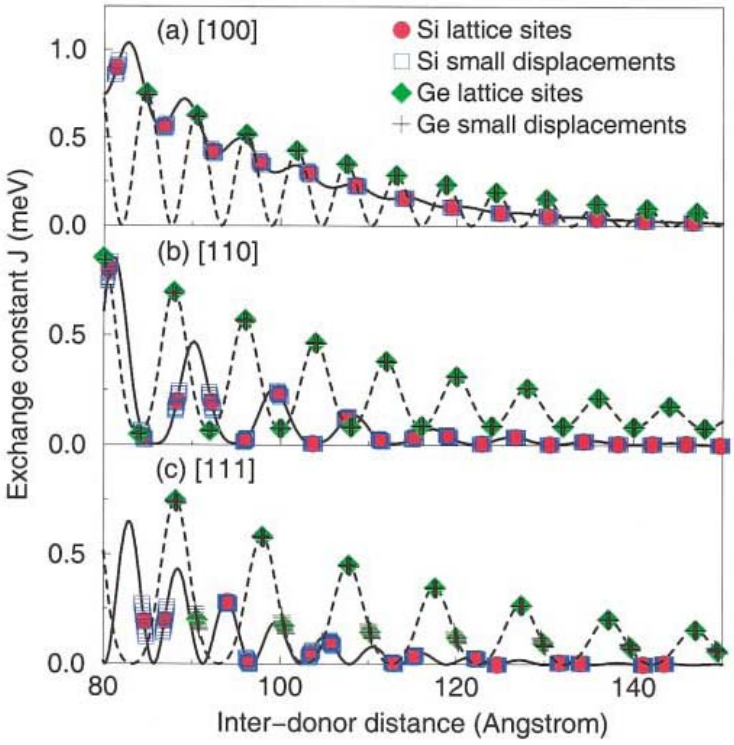

Fig. 4: *Calculated exchange interaction J (Heitler-London) as a function of donor separation ("exchange oscillations") (reproduced from [32]) between two phosphorus donors in Si (solid lines) and Ge (dashed lines) along various crystal directions in the effective mass formalism: (a) [100], (b) [110] and (c) [111]. Values corresponding to impurities at substitutional sites are given by the circles (Si) and diamonds (Ge). Perturbed values due to off-lattice displacements by 10% indicated by the squares (Si) and crosses (Ge).*

the full Bloch wave function was integrated over and gave good agreement. The ability to ignore the periodic part of the Bloch structure in the computation of the Heitler-London integrals significantly reduces the complexity of the calculation by eliminating the sums over reciprocal lattice vectors. The most striking aspect of these calculation is that the valley physics of the silicon complicates the simple picture of the exchange coupling somewhat – because the exchange coupling is dependent on the overlap of the donor electron wave functions whose Bloch components oscillate on the order of the lattice constant the value of J (non-biased) is sensitive to even lattice-site level variations in the donor separation.

3.4 Voltage control of the exchange coupling

The exchange coupling between neighbouring phosphorus donor electrons can, in principle, be controlled via the use of J-gate control electrodes placed above and between the donor qubits. Application of a voltage bias to such a gate produces an electrostatic potential inside the device, which will perturb the orbits of the donor electrons, thus altering the exchange coupling. Of course, calculating the magnitude of this effect is more complicated. Several authors have, to various levels of approximation, studied the change in the exchange coupling under the influ-

ence of an applied electro-static field [33, 34, 35]. Fang *et. al.* [33] calculated the exchange coupling in a simplified electrostatic potential, using an unrestricted Hartree-Fock (HF) approach over a hydrogenic basis. In principle, the HF approach should give a better estimate for the exchange coupling than the Heitler-London technique, for an equivalent set of trial states, due to the fact the Hartree-Fock technique self-consistently optimises the wave function, however, in practice the more computationally expensive Hartree-Fock technique may be impractical to implement for realistic device potentials and a basis set describing Bloch and valley physics.
In [35] a basis of envelope functions was used to expand the donor wave function in the presence of a field, using the full 6-valley, effective mass description. In this case the single electron donor wave functions were given by

$$\psi_(\mathbf{r} \pm \mathbf{R}/2) = \sum_{n,l,m} c_{n,l,m} \sum_{\mu} \chi^{\mu}_{n,l,m}(\mathbf{r} \pm \mathbf{R}/2) \mathrm{e}^{i\mathbf{k}_{\mu}.(\mathbf{r}\pm\mathbf{R}/2)} u_{\mu}(\mathbf{r}). \tag{29}$$

Here the envelope functions $\chi^{\mu}_{n.l.m}$ are the non-isotropic scaled hydrogenic orbitals associated with the conduction band minimum labelled by μ. The coefficients $c_{n,l,m}$ where determined by numerical diagonalisation of the Hamiltonian. These calculations showed that the strength of the exchange coupling can be significantly increased by the application of a J-gate bias, however the strength of the interaction remains strongly dependent on both the magnitude and orientation of the donor separation. In principle, this is not an issue as long as the gate bias can tune the value of J sufficiently, however, in practice it means that every qubit pair must be characterised in order to mitigate the variability in J. Schemes to do this at the Hamiltonian level using only the in-situ resources of the qubit array have been developed [36], which, together with robust pulse control which specifically caters for some level of unknown variation in the exchange coupling [37], may provide the solution to this issue.

3.5 CNOT gate in the Kane scheme

The effective spin Hamiltonian of the two donor system is:

$$H_{2q} = \mu_B B_z \sigma^z_{e1} - g_n \mu_n B_z \sigma^z_{n1} + A_1 \vec{\sigma}_{n1} \cdot \vec{\sigma}_{e1} + \mu_B B_z \sigma^z_{e2} - g_n \mu_n B_z \sigma^z_{n2} + A_2 \vec{\sigma}_{n2} \cdot \vec{\sigma}_{e2} + J \vec{\sigma}_{e1} \cdot \vec{\sigma}_{e2}, \tag{30}$$

where we assume there is individual control over the hyperfine coefficients ($A_1(t)$ and $A_2(t)$) and the exchange coupling $J(t)$ through appropriate time-dependent gate biases, as discussed above. Because we are dealing with a four-spin system, the actual details of the control required and state evolution for a CNOT gate is rather complicated. In Figure 5 we show the control paths and the state evolution as a function of time for the adiabatic case described in Ref [38] (NB. A faster CNOT gate was developed in [39]).
The steps proceeds as follows (assuming the system is one of the four 2-qubit computational states):
Step 1: Break the qubit degeneracy to distinguish the control (qubit 1) and target (qubit 2) by increasing A_1.
Step 2: The value of J is increased adiabatically.
Step 3: The value of A_1 is reduced (adiabatically) to the initial value so that the anti-crossing behaviour produces transitions of the computational states $|10\rangle$ and $|01\rangle$ to symmetric and anti-symmetric combinations, i.e. $|10\rangle \rightarrow |\mathrm{symm}\rangle$ and $|01\rangle \rightarrow |\mathrm{anti-symm}\rangle$.
Step 4: An RF field resonant with the transition $|\mathrm{symm}\rangle|11\rangle \rightarrow$ is applied.
Step 5-7: Reversal of the steps 1-3.

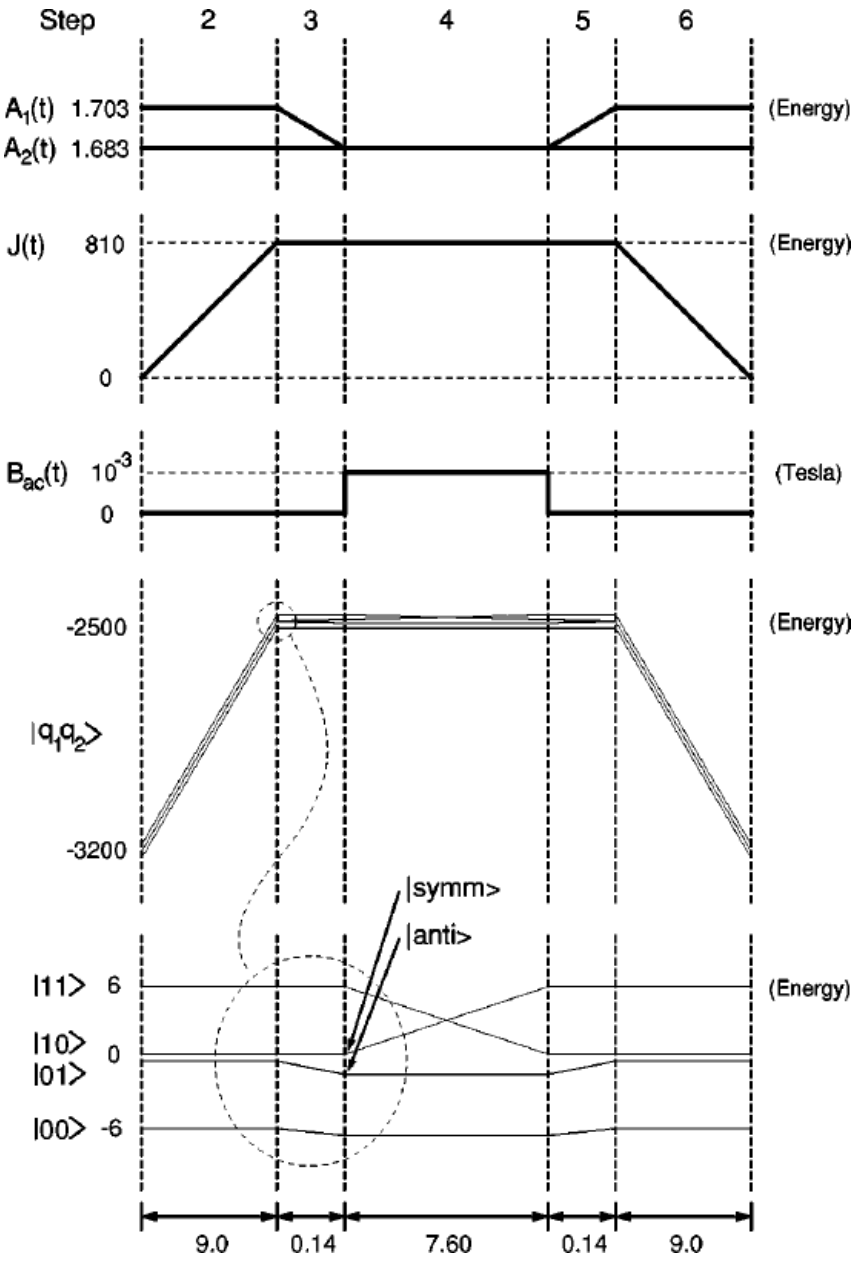

Fig. 5: *Control profiles of the A and J parameters (units of $g_n\mu_n B_z = 7.1 \times 10^{-5}$ meV) in the two-qubit effective electron-nuclear spin Hamiltonian required to carry out an adiabatic CNOT gate in the Kane quantum computer (reproduced from [38]). Timing shown along the horizontal axes is in μs.*

Since Step 1 is assumed to be relatively fast, the total time for the CNOT gate ($\sim$ 26 μs in this case) is governed by the adiabatic steps and the duration of the RF field. With sufficiently long dephasing times and accurate gate bias control the fidelity of the CNOT gate can be made reasonably precise.

4 Qubit readout

The difficulties inherent in direct, single-nuclear spin readout for the Si:P system requires an indirect mechanism for measuring the qubit state following computation. Kane's solution involved converting the the nuclear spin information into electron spin information, which was then mapped onto a change in overall charge distribution through spin-dependent tunneling of the electron to an ancilla read-out donor, facilitating measurement with a highly sensitive electrometer, such as a single electron transistor (SET). As two electrons can only occupy the same site if they have opposite spins the tunneling process to the ancilla donor selects one of the spin states. A doubly occupied donor site is termed a D^- state, and the resulting two-donor system is the D^+D^- system. This system has been observed in bulk optical experiments of Si doped with P (for example Ref. [40]). The D^- system has a binding energy of 1.7 meV as compared with the binding energy of a neutral donor which is 45 meV. In order to get tunneling, the two-electron system must therefore have been in a spin singlet state, and a potential gradient applied across the donors. This bias might be achieved by differentially biasing the A gates. In practice, however, single spin electron read-out has recently been achieved by a spin-charge transduction process where instead of an ancilla donor the electron tunnels directly into the island of the SET formed by a two-dimensional electron gas (2DEG) under the interface [41]. In terms of overall scale-up, it remains to be seen whether spin-charge transduction mediated by a 2DEG dot is a better option than an ancilla qubit, but the fact remains that the former is the only case that has been demonstrated experimentally so far.

5 Decoherence

To maintain the fragile and tenuous multi-qubit entanglement long enough to perform useful quantum computing, it is axiomatic that the decoherence time of the qubit system must be long compared with the operation time. Although the Kane qubits are nuclear spins, the role of electron spins in the gate operations means that the overall gate fidelities are controlled by the electron spin coherence time in all these manifestations of spin qubits in silicon (i.e. electron or nuclear spin qubits). The quest to understand and quantify relaxation rates for donors in silicon has a long history, extending to well before the impetus of quantum computing was conceived. Very early results from Gordon and Bowers [42] showed that the T_1 time for P donors could be of order 100 seconds, and that the T_2 time was of order 100μs, at 1.4K. Interestingly, an application suggested even in those days was for memory, one of their conclusions was "On the basis of these measurements, one may envisage a memory device in which each element can store more than 10^4 bits of information" [42]. The early experiments included important measurements of spin relaxation rates as a function of P concentration, temperature and optical illumination. The recent work of Tyryshkin *et al.* [43] has measured the coherence times for electron spins in isotopically purified silicon and found very long T_2 times in the second regime, which bodes well for quantum computing in silicon.

6 Issues for scale-up of donor based architectures

The dopant based quantum computer architectures so far proposed share a common feature – the array of qubits is inherently low dimensional, i.e. in simplest terms a linear array of qubits where controlled interactions are between nearest-neighbors only. On the face of it, the linear

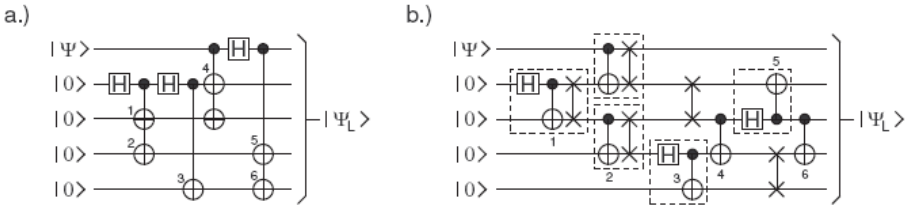

Fig. 6: *Five qubit encode step (reproduced from [44]). a) General qubit array with two-qubit gates between non-nearest neighbor qubits. b) Linear nearest-neighbor (LNN) qubit array with required swap gates shown.*

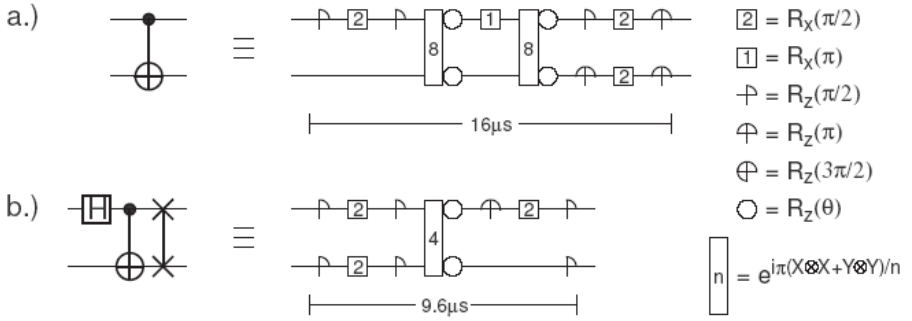

Fig. 7: *Combining gates through canonical decomposition in native gates available in the Kane system (reproduced from [39]).*

nearest-neighbor (LNN) array may face severe constraints since general quantum algorithm circuits require interactions between arbitrary qubits, and the LNN architecture would then require a large overhead in SWAP gates. It is important to understand potential information bottlenecks and seek solutions as the LNN constraint is fundamental to the Kane design.

As an example of the effect of the LNN constraint we consider the swap gates required in the simple 5-qubit quantum error correction encoding circuit [44]. In Figure 6 the encode step is contrasted for the general connected array LNN array where five SWAP gates are required to implement the same circuit. One immediately suspects the threshold for the LNN circuit will be considerably higher since the bare gate count has more than doubled. However, it turns out that in the actual implementation of the required gates in terms of the "native" gates available in the physical system (interacting donors in the Kane case) one can combine gates quite effectively (i.e. the gates in the dashed boxes)[39]. For instance, in Figure 7 the first sequence of Hadamard-CNOT-swap is combined to form a gate sequence that is actually considerably faster than implementing a CNOT on its own. Another example of how swap gate bottlenecks can be avoided in LNN arrays was shown for the quantum Fourier transform (QFT) circuit[45]. The QFT is central to the implementation of Shor's factoring algorithm, which is inherently so complex that it was first assumed that LNN quantum computers would suffer from severe information flow bottlenecks due to the preponderance of SWAP gates.

There are a number of ways to implement Shor's algorithm on a quantum computer. Circuits can be constructed which minimize the number qubits, or total number of gates. Beauregard[46] has presented a circuit for a general connected array which uses the so-called "one qubit trick"

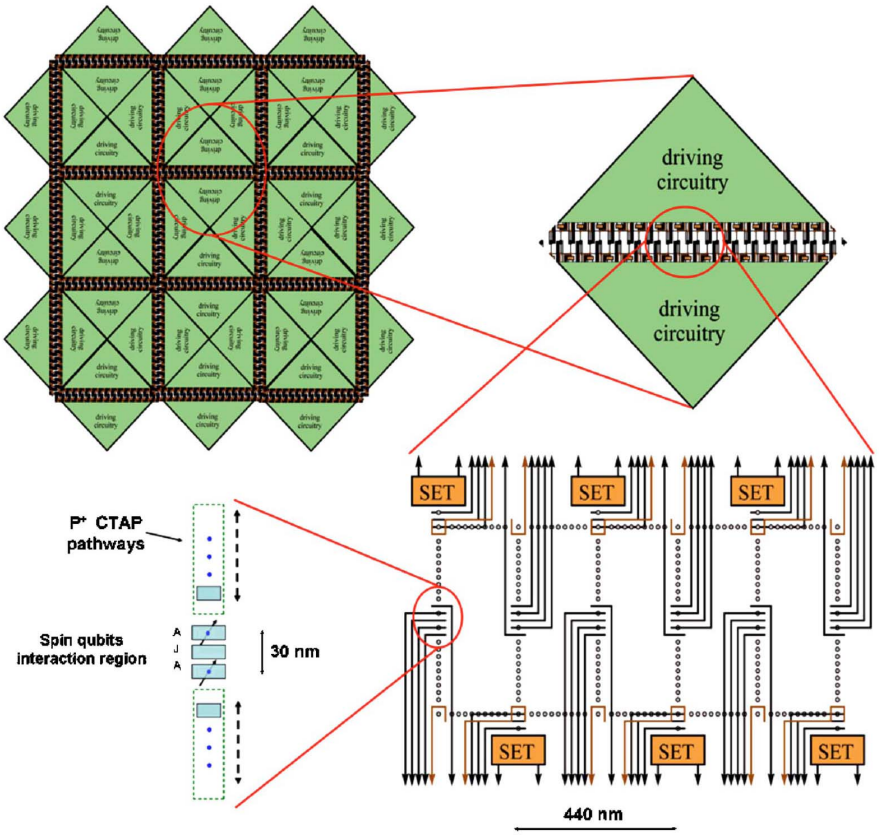

Fig. 8: *A bi-linear donor qubit array incorporating adiabatic electron spin transport (reproduced from [6]).*

which outputs the final integer j (to be used to determine the period of the function) in a bit-wise fashion. This circuit minimizes the number of qubits required: for a number to be factorized of bit-length L, the number of qubits is $2L + 3$, with depth (number of time steps, each with multiple gates) growing as $32L^3$ and total number of gates $8L^4$. Fowler et al[47] have constructed a LNN circuit, based on the one-qubit trick, which includes all required SWAP operations efficiently – the final circuit required just one extra qubit (i.e $2L + 4$) and to first order the same depth and gate count as the general array with arbitrary interactions.

Important issues for scale-up of the Kane-type architectures are the effects of misplacement of dopants at the 1-2 atom level leading to large oscillations in the intrinsic exchange coupling as previously mentioned, and the engineering level challenges in wiring and controlling so many nanoelectronic gates which are only of order 5 nm apart. In terms of the first problem, although the dopant qubits exist in probably the most uniform of confinement potentials, such variations in intrinsic qubit couplings would mean a high level characterization [36] of gates and/or the system Hamiltonian is required (as will be the case for all architectures) to below the fault-tolerant threshold. In response to these a bi-linear array including electron spin transport was proposed [6] (Figure 8).

The previous discussion gives some indication that the LNN constraint for the Kane type QC might not be as severe as first thought. However, one must bear in mind that in reality a quantum computer cannot operate without some form of fault-tolerant error correction. There have been numerous estimates for the resources required for quantum factoring of interesting prob-

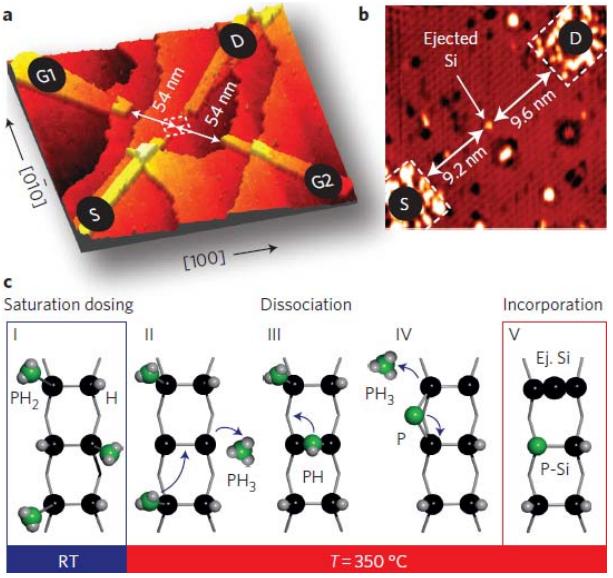

Fig. 9: *A single P atom transistor device fabricated using a Scanning Tunneling Microscope (STM). Conduction measured through the device displays the quantised energy levels associated with donor levels and agrees well with calculations based on a multi-million atom tight-binding framework (reproduced from [52]).*

lem sizes, running up to the millions of qubits level. Recently, the LNN Shor circuit has been simulated directly with environmental errors (discrete and continuous models) for small problem sizes to gain some idea of the task ahead[48]. It was found that the maximum number of errors tolerable in the circuit scaled approximately linearly with the bit-length L. For a modest size problem $L = 128$ this translates to a maximum error rate of order 10^{-10}: assuming a fault-tolerant threshold of 10^{-4} this result implies that concatenation of quantum error correction is required for even this modest problem. While the LNN circuit can match the general connected circuits in terms of inter-qubit connectedness, concatenation requires level of QEC encoding and a high level of intra-qubit information flow. For the seven-qubit Steane code error threshold has been computed for the bi-linear qubit array (with SWAP gate transport) to be about 10^{-6} depending on the physical assumptions made [49]. This is at least an order of magnitude lower than the threshold for the Steane code on a nearest-neighbor coupled 2D array[50] and indicates that an incredible level of precision in control and materials engineering would be required to keep the errors well below the threshold value.

7 Conclusions and outlook

While these notes have focussed on the background physics of the Kane quantum computer from a theoretical viewpoint, including solid-state theory and simulations of donor electron wave function control, there has been in recent years a number of significant breakthroughs on the experimental side. The key challenge of precision placement of donors to $\pm \sim 1$ lattice site has been met using Scanning Tunneling Microscopy fabrication technology producing gated single atom transistor devices (see Figure 9) and nanowires just a few atoms in width [51, 52]. In terms of qubit physics a key breakthrough was the demonstration of single electron spin detection using a MOS based single electron transistor (SET) device fabricated by ion-implantation

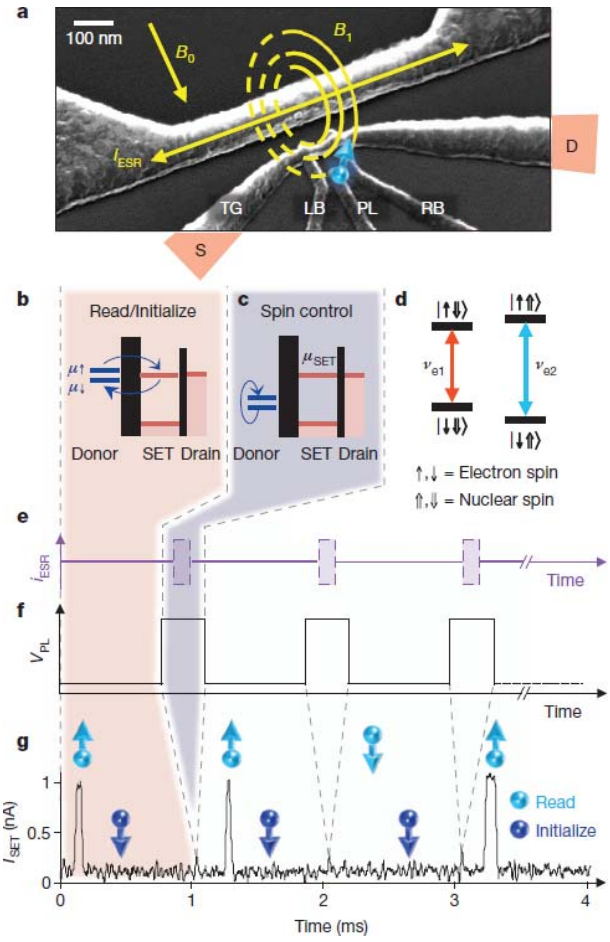

Fig. 10: *Experimental realisation of a P donor electron spin qubit. (reproduced from [53]).*

[41]. In this device the 2DEG island of the SET formed the reservoir for the electron to tunnel into in the spin-charge transduction step. Finally, control of an electron spin donor qubit has been achieved this year in a MOS based device (see Figure 10)[53]. Rabi and spin-echo measurements showed that the decoherence times for the single electron spin in this device are consistent with the existing bulk measurements.

With such focussed efforts on the fabrication and measurement of donor based silicon spin qubit devices the outlook is very good for qubit physics in the short term. A more pointed question is, given the rather stringent thresholds for quantum computing over low dimensional arrays (<2D), what are the prospects for large scale quantum computing using donors in silicon? The answer may lie in the ability to go to a genuinely two-dimensional qubit array. For although the Steane code threshold in 2D is only a factor 10 improvement, the implementation of the surface code[54, 55] on a 2D nearest-neighbour array gives a surprisingly high threshold of around 10^{-2}[56]. Thus, the key challenge is to find a way to engineer a donor qubit array in two-dimensions. Because of the closeness of the A and J gates required this is a highly non-trivial engineering task and may require new creative hybrid ideas (possibly including optical interconnects) which take advantage of the long memory times of nuclear spins in silicon, but do not require a high density of nanoelectronic gates.

References

[1] B. Kane, *Nature* **393**, 133 (1998).

[2] R. Vrijen et al, *Phys. Rev. A* **62**, 012306 (2000).

[3] L.C.L. Hollenberg, A.D. Dzurak, C.J. Wellard, A. Hamilton, D.J. Reilly, G.J. Milburn, and R. Clark, *Phys. Rev. B* **69**, 113301 (2004).

[4] R. de Sousa, J. D. Delgado and S. Das Sarma, *Phys. Rev. A* **70**, 052304 (2004).

[5] C. D. Hill, L. C. L. Hollenberg, A. G. Fowler, C. J. Wellard, A. D. Greentree, and H.-S. Goan, *Phys. Rev. B* **72**, 045350 (2005).

[6] L.C.L. Hollenberg, A.D. Greentree, A.G. Fowler, C.J. Wellard, *Phys. Rev. B* **74** 045311 (2006).

[7] M.J. Calderon, B. Koiler, X. Hu, S. Das Sarma, *Phys. Rev. Lett.* **96** 096802 (2006).

[8] R. L. Aggarwal and A. K. Ramdas, *Phys. Rev.* **140** A1246 (1965).

[9] J. M. Luttinger and W. Kohn, *Phys. Rev.* **97** 869 (1955).

[10] S. T. Pantelides and C. T. Sah, *Phys. Rev. B* **10** 621 (1974).

[11] H. Fritzsche, *Phys. Rev.* **125** 1560 (1962)

[12] B. Koiller and X. Hu and S. Das Sarma, *Phys. Rev. B* **66** 115201 (2002).

[13] R.A. Faulkner, *Phys. Rev.* **184** 713 (1969).

[14] J.L. Ivey and R.L. Mieher, *Phys. Rev. B* **11** 849 (1976).

[15] L.J. Sham, *Phys. Rev.* **150** 720 (1966).

[16] C.J. Wellard and L.C.L. Hollenberg, *Phys. Rev. B* **72** 085202 (2005).

[17] A. S. Martins and R. B. Capaz and B. Koiller, *Phys. Rev. B* **69** 85320 (2004).

[18] G. Klimeck, F. Oyafuso, T.B. Boykin, R.C. Bowen and P. von Allmen, *Computer Modeling in Engineering and Science* **3** 601 (2002).

[19] C. J. Wellard, L. C. L. Hollenberg, F. Parisoli, L. M. Kettle, H.-S. Goan, J. A. L. McIntosh, and D. N. Jamieson, *Phys. Rev. B* **68**, 195209 (2003).

[20] A.J. Skinner, M.E. Davenport, and B.E. Kane, *Phys. Rev. Lett.* **90**, 087901 (2003).

[21] Floris A. Zwanenburg, Andrew S. Dzurak, Andrea Morello, Michelle Y. Simmons, Lloyd C. L. Hollenberg, Gerhard Klimeck, Sven Rogge, Susan N. Coppersmith, Mark A. Eriksson, *arXiv:1206.5276*.

[22] Harald Overhof and Uwe Gerstmann, *Phys. Rev. Lett.* **92** 087602 (2004).

[23] R. C. Fletcher and W. A. Yager and G. L. Pearsona and F. R. Merritt, *Phys. Rev.* **95** 844 (1954).

[24] F. R. Bradbury et al., *Phys. Rev. Lett.* **97** 176404 (2006).

[25] R. Rahman et al, *Phys. Rev. Lett.* **99** 036403 (2007).

[26] G. Kandasamy, C. J. Wellard and L.C.L. Hollenberg, *Nanotechnology* **17** 4572 (2006).

[27] M.J. Calderon, B. Koiller and S. Das Sarma, *Phys. Rev. B* **77** 155302 (2008).

[28] R. Rahman et al, *Phys. Rev. B* **80** 165314 (2009).

[29] Y.L. Hao et al, *Phys. Rev. B* **80** 035329 (2009).

[30] G. Lansbergen et al, *Nature Physics* **4** 656 (2008).

[31] C. Herring and M. Flicker, *Phys. Rev.* **134** A362 (1064).

[32] B. Koiller, X. Hu and S. Das Sarma, *Phys. Rev. Lett.* **99**, 027903 (2002).

[33] A. Fang, Y. C. Chang and J.R. Tucker, *Phys. Rev. B* **66** 155331 (2002).

[34] L.M. Kettle et al, *J. Phys. Cond. Mat.* **16** 1011 (2004).

[35] C.J. Wellard et al, *J. Phys. Cond. Mat.* **16** 5697 (2004).

[36] J.H. Cole, S.J. Devitt, L.C.L. Hollenberg, *J. Phys. Math. Gen.* **39** 14649 (2006).

[37] C.D. Hill, *Phys. Rev. Lett.* **98** 180501 (2007).

[38] A. Fowler, C.J. Wellard and L.C.L. Hollenberg, *Phys. Rev. A* **67** 012301 (2003).

[39] C.D. Hill and H-S Goan, *Phys. Rev. A* **68** 012321 (2003).

[40] M. Capizzi, G. A. Thomas, F. DeRosa and R. N. Bhatt, *Solid State Comm.* **31** 611 (1979).

[41] A. Morello et al, *Nature* **467** 687 (2010).

[42] J.P. Gordon and K.D. Bowers, *Phys. Rev. Lett.* **10** 368 (1958).

[43] A. M. Tyryshkin et al, *Nature Mater.* **11** 143 (2012).

[44] A.G. Fowler, C.D. Hill and L.C.L. Hollenberg, *Phys. Rev. A* **69** 042314 (2004).

[45] A.G. Fowler, C.D. Hill and L.C.L. Hollenberg, *Phys. Rev. A* **70** 032329 (2004).

[46] S. Beauregard, *Quant. Inf. and Comp.* **3** 175 (2003).

[47] A.G. Fowler, S.J. Devitt and L.C.L. Hollenberg, *Quant. Inf. and Comp.* **4** 237 (2004).

[48] S.J. Devitt, A.G. Fowler and L.C.L. Hollenberg, *Quant. Inf. and Comp.* **6** 616 (2006).

[49] A.M. Stephens, A.G. Fowler and L.C.L. Hollenberg, *Quant. Inf. and Comp.* **8** 330 (2008).

[50] K. Svore, D. DiVincenzo, and B. Terhal. *Quant. Inf. Comp.* **7**, 297 (2007).

[51] B. Weber et al, *Science* **335** 64 (2012).

[52] M. Fuechsle et al, *Nature Nanotech.***7** 242 (2012).

[53] J. Pla et al, *Nature* **489** 541 (2012).

[54] A. Yu. Kitaev. quant-ph/9707021, 1997.

[55] R. Raussendorf and J. Harrington,. *Phys. Rev. Lett.* **98** 190504 (2007).

[56] D.S. Wang, A.G. Fowler and L.C.L. Hollenberg, *Phys. Rev. A* **83** 020302 (2011).

B 2 Majorana Qubits[1]

Fabian Hassler
Institute for Quantum Information
RWTH Aachen University

Contents

1 Introduction **2**

2 Majorana fermions **2**
2.1 Bogoliubov-de Gennes equation 3
2.2 Spinless *p*-wave superconducting nanowire 5
2.3 Topological charge 7

3 Quantum computation with Majorana fermions **8**
3.1 Fermionic quantum computation 8
3.2 Parity-protected quantum computation 9
3.3 Anyons 10
3.4 Majorana fermions as non-Abelian particles 12

4 Implementations **13**
4.1 Semiconducting nanowires 13
4.2 Hybrid structures 15

5 Conclusion **18**

[1]Lecture Notes of the 44^{th} IFF Spring School "Quantum Information Processing" (Forschungszentrum Jülich, 2013). All rights reserved.

1 Introduction

Ideas of topology a branch of mathematics which studies whether two objects can be transformed into each other under continuous deformations have proven to provide very fruitful concepts also in physics. Examples in classical physics involve vortices in fluid dynamics, electrical charges in electrodynamics, and the classification of defects in crystals [1]. In quantum mechanics the prime example of a topological effect is the Aharonov-Bohm effect [2]. Soon after the discovery of the quantum Hall effect [3], it was realized that the new phase is not characterized by a broken symmetry but that the topology of the Bloch wavefunction in the Brillouin zone described by the Chern number changes when entering the quantum Hall regime [4]. For some time the quantum Hall effect was considered the only example of a topological phase in a noninteracting system, nowadays called topological insulator. More recently, a second example was devised theoretically [5, 6, 7] in the form of the quantum spin Hall effect and confirmed experimentally in HgTe quantum wells [8]. This sparked further research in this area and culminated in the classification of all topological insulators and superconductors [9, 10]. The subject of this lecture are states, called Majorana fermions, which appear at defects in topological superconductors with broken time-reversal and spin-rotation symmetry in one or two dimensions.
The outline of the lecture is as follows. We will first introduce the notion of Majorana fermions. We will then show how these states appear as zero energy solutions of the Bogoliubov-de Gennes equation describing a spinless *p*-wave superconductor in one dimension. We will describe their usefulness in term of quantum information applications as they encode quantum information in a protected fashion before we will finish off discussing a possible experimental implementation. There are by now several reviews on this subject, see Refs. [11, 12, 13], where further information on this subject can be found.

2 Majorana fermions

Majorana fermions are fermionic particles which are their own antiparticles. Why the corresponding context is quite natural for bosons—most bosons (phonon, photons, magnons, plasmons, ...) are their own antiparticles—this is a rather uncommon property for fermions. In fact so far no elementary fermionic particle has been experimentally confirmed to be its own antiparticle. In more mathematical terms, a Majorana operator γ_1 (an operator which creates a Majorana particle) is a Hermitian operator $\gamma_1 = \gamma_1^\dagger$ which anticommutes with other Majorana operators γ_2 and squares to one $\gamma_1^2 = 1$; summarizing, the Majorana operators form a Clifford algebra defined by the anticommutation relation

$$\{\gamma_k, \gamma_l\} = 2\delta_{kl}. \tag{1}$$

Given the fact that these particles do not exist as elementary particles, we would like to know how to construct them from conventional Dirac fermions created by the operator $c_k^\dagger$. In fact, it is an easy exercise in algebra to show that given a set of N Dirac fermions defined by $c_k^\dagger$, $k = 1, \ldots, N$, with the canonical anticommutation relations $\{c_k, c_l^\dagger\} = \delta_{kl}$ and $\{c_k, c_l\} = 0$, we can construct $2N$ Majorana operators γ_k via

$$\gamma_{2k-1} = c_k + c_k^\dagger, \qquad \gamma_{2k} = i(c_k^\dagger - c_k). \tag{2}$$

Inverting the defining Eq. (2), we find an expression of the Dirac fermions in terms of the Majorana operators

$$c_k = \frac{1}{2}(\gamma_{2k-1} + i\gamma_{2k}), \qquad c_k^\dagger = \frac{1}{2}(\gamma_{2k-1} - i\gamma_{2k}). \tag{3}$$

The Hilbert space of a single fermionic mode is two-dimensional: the mode is either filled or empty distinguished by the eigenvalue of the number operators $n_k = c_k^\dagger c_k$ which has eigenvalues 0 or 1.[2] An operator which will turn out to be important in the following discussion is the fermion parity operator $\mathcal{P}_k = 1 - 2n_k = (-1)^{n_k}$ which has the eigenvalue $+1$ if the number of fermions is even and -1 if the number of fermions is odd. In terms of the Majorana operators, the parity operator assumes the simple form

$$\mathcal{P}_k = -i\gamma_{2k-1}\gamma_{2k}. \tag{4}$$

So far, the introduction of Majorana fermions was an algebraic trick to go from one set of complex operators c_k to an equivalent description in terms of the Hermitian operators γ_k. Naturally, the question arises if these operators are 'physical' in the sense that they describe the excitations of a physical system/Hamiltonian. The answer to this question is (maybe surprisingly) yes: over a decade ago, Kitaev constructed a model which leads to Majorana fermions [14].

To appreciate the difficulty in constructing such a model as well as to understand the resolution, we dwell a bit on the requirement/hurdles to construct such a model. Starting from Dirac fermions, we see from (2) that the Majorana operators are superposition of electron and hole operators. We know that ordinary (many-body) quantum mechanics is invariant under global $U(1)$ transformations $c_k \mapsto U_\varphi^\dagger c_k U_\varphi = e^{i\varphi} c_k$ with φ an arbitrary phase. The reason for this is the conservation of the total particle number (or charge for that matter). However, it is easy to check that under the same transformation Majorana operators corresponding to the same fermionic mode mix with each other

$$\gamma_{2k-1} \mapsto U_\varphi^\dagger \gamma_{2k-1} U_\varphi = \cos(\varphi)\,\gamma_{2k-1} - \sin(\varphi)\,\gamma_{2k}. \tag{5}$$

Thus, if we were to construct a Hamiltonian which has γ_{2k-1} (or γ_{2k} for that matter) as an elementary, localized excitation, we will have to break the global $U(1)$ invariance as it mixes the two different physical modes γ_{2k-1} and γ_{2k}. In fact, the $U(1)$ symmetry (given by the phase φ) is broken down to a $\mathbb{Z}_2$ symmetry (corresponding to $\varphi = 0, \pi$). This is exactly what happens in superconducting systems, so we should look a bit more closely into the theory of superconductivity.

2.1 Bogoliubov-de Gennes equation

Superconductivity is an ordering phenomena which happens in interacting system at low temperatures. Experimentally, the state is characterized by a vanishing of the resistance and, more importantly, by a perfect diamagnetic response called Meißner-Ochsenfeld effect [15, 16].

[2] Note that n_k is idempotent as $n_k^2 = c_k^\dagger c_k c_k^\dagger c_k = c_k^\dagger(1 - c_k^\dagger c_k)c_k = n_k$ which proves the fact that the eigenvalues of n_k are 0 or 1.

Starting from a model of interacting spinless electrons[3]

$$H = \int d^3r \left[\frac{\hbar^2}{2m}|\nabla\psi(\boldsymbol{r})|^2 - \mu|\psi(\boldsymbol{r})|^2\right] - \frac{1}{2}\int d^3r\, d^3r'\, \psi^\dagger(\boldsymbol{r})\psi^\dagger(\boldsymbol{r}')V(\boldsymbol{r}-\boldsymbol{r}')\psi(\boldsymbol{r}')\psi(\boldsymbol{r}), \quad (6)$$

we employ the mean-field decoupling with the superconducting pair-potential $\Delta(\boldsymbol{r}-\boldsymbol{r}') = V(\boldsymbol{r}-\boldsymbol{r}')\langle\psi(\boldsymbol{r}')\psi(\boldsymbol{r})\rangle$ [17] and arrive at the effective BCS mean-field Hamiltonian

$$H_{\text{MF}} = \int d^3r \left[\frac{\hbar^2}{2m}|\nabla\psi(\boldsymbol{r})|^2 - \mu|\psi(\boldsymbol{r})|^2\right] - \frac{1}{2}\int d^3r\, d^3r'\, \psi^\dagger(\boldsymbol{r})\psi^\dagger(\boldsymbol{r}')\Delta(\boldsymbol{r}-\boldsymbol{r}') - \frac{1}{2}\int d^3r\, d^3r'\, \Delta^*(\boldsymbol{r}-\boldsymbol{r}')\psi(\boldsymbol{r}')\psi(\boldsymbol{r}) + \frac{1}{2}\int d^3r\, d^3r'\, \frac{\Delta(\boldsymbol{r}-\boldsymbol{r}')}{V(\boldsymbol{r}-\boldsymbol{r}')}. \quad (7)$$

In the resulting Hamiltonian, the $U(1)$ degree of freedom $\psi \mapsto e^{i\varphi}\psi$ for fixed 'external field' Δ is broken down to a $\mathbb{Z}_2$ degree of freedom just as we wished.
Apart from an unimportant constant, the resulting Hamiltonian can be written as a quadratic form

$$H_{\text{MF}} = \frac{1}{2}\int d^3r\, d^3r'\, \Psi^\dagger(\boldsymbol{r})h_{\text{BdG}}(\boldsymbol{r}-\boldsymbol{r}')\Psi(\boldsymbol{r}') + \text{const.} \quad (8)$$

in Nambu space $\Psi^\dagger = \begin{pmatrix}\psi^\dagger & \psi\end{pmatrix}$ with the Bogoliubov-de Gennes Hamiltonian

$$h_{\text{BdG}}(\boldsymbol{r}-\boldsymbol{r}') = \begin{pmatrix}\xi(\boldsymbol{p})\delta(\boldsymbol{r}-\boldsymbol{r}') & -\Delta(\boldsymbol{r}-\boldsymbol{r}') \\ \Delta^*(\boldsymbol{r}-\boldsymbol{r}') & -\xi(\boldsymbol{p})\delta(\boldsymbol{r}-\boldsymbol{r}')\end{pmatrix}, \quad (9)$$

where $\xi(\boldsymbol{p}) = \frac{p^2}{2m} - \mu = -\frac{\hbar^2}{2m}\nabla^2 - \mu$; note that h_{BdG} is Hermitian due to the fact that $\Delta(-\boldsymbol{r}) = -\Delta(\boldsymbol{r})$. The Hamiltonian is 'diagonalized' by a Bogoliubov transformation, i.e., by introducing new fermionic operators β_{E_n} which fulfill the canonical anticommutation relation and in terms of which the mean-field Hamiltonian assumes the form [15, 16]

$$H_{\text{MF}} = \frac{1}{2}\sum_{E_n} E_n\beta^\dagger_{E_n}\beta_{E_n} + \text{const.}; \quad (10)$$

here, E_n are the eigenvalues of h_{BdG} and $\beta_{E_n} = \int d^3r\, v^\dagger_{E_n}(\boldsymbol{r})\Psi(\boldsymbol{r})$ where $v_{E_n}(\boldsymbol{r})$ are the associated eigenvectors.
Note that in getting to Eq. (9), we have apparently doubled the degrees of freedom. However, the resulting Bogoliubov-de Gennes Hamiltonian h_{BdG} enjoys an additional symmetry: in fact, the particle-hole symmetry operator $\mathcal{C} = \tau^x K$ with K the complex conjugation and τ^x acting on the Nambu index anticommutes with the Hamiltonian $\{h_{\text{BdG}}, \mathcal{C}\} = 0$. This symmetry guarantees that for every eigenvector v_{E_n} of h_{BdG} to eigenvalue $E_n \geq 0$ there is an additional eigenvector $v_{-E_n} = \mathcal{C}v_{E_n}$ to eigenvalues $-E_n$. Expressing this fact in terms of the second quantized Bogoliubov operators, we have

$$\beta^\dagger_{-E_n} = \int d^3r\, \Psi^\dagger(\boldsymbol{r})\underbrace{v_{-E_n}(\boldsymbol{r})}_{\mathcal{C}v_{E_n}} = \int d^3r\, \underbrace{\Psi^\dagger(\boldsymbol{r})\tau^x}_{\Psi^T(\boldsymbol{r})} v^*_{E_n}(\boldsymbol{r}) = \beta_{E_n}. \quad (11)$$

[3] As we want to end up with single unpaired Majorana fermions, we have to get rid of all possible degeneracies in particular the spin degeneracy.

In the end, combining the terms with E_n and $-E_n$, we have $E_n(\beta^\dagger_{E_n}\beta_{E_n} - \beta^\dagger_{-E_n}\beta_{-E_n}) = 2E_n(\beta^\dagger_{E_n}\beta_{E_n} - 1)$ such that we only need to include the eigenvectors to positive eigenvalues in (10) on the expense of the factor $\frac{1}{2}$ in front of the sum.
Now, we are very close to our goal of realizing Majorana fermions starting from conventional Dirac fermions. Looking at Eq. (11), we see that if an eigenstate $n = 0$ of the Bogoliubov-de Gennes Hamiltonian has a vanishing eigenvalue, $E_0 = 0$, it is in fact a Majorana fermion with $\gamma_1 = \beta_0$.[4] Given this insight, we try to construct a physical situation where (9) incorporates such a zero mode. Here, I want to point out that there is a principle difference between the more general term Majorana fermion and the Majorana zero mode. Whereas Majorana fermion simply denotes a 'real' fermion, Majorana zero mode denotes Majorana fermions bound to zero energy at a topological defect in a superconductor/superfluid.[5] While the statistics of the former is simply fermionic, the latter shows non-Abelian exchange statistics, see below.

2.2 Spinless *p*-wave superconducting nanowire

Following Kitaev [14], we would like to construct a simple model which shows Majorana zero modes. Thus, we consider a one-dimensional situation with $\boldsymbol{r} = z$. The simplest choice of paring, *s*-wave pairing, with $\Delta(z) = \Delta\,\delta(z)$ is not allowed for spinless electrons as $\Delta(-z) \neq -\Delta(z)$. Thus, we take the next term in the gradient expansion into account, *p*-wave pairing, with $\Delta(z) = -i\Delta\,\lambda_F\,\delta'(z)$; here, we have introduced the (reduced) Fermi wavelength $\lambda_F = \hbar/\sqrt{2m\mu}$ such that Δ has the dimension of energy. Going over to momentum space, the Bogoliubov-de Gennes Hamiltonian can be written as

$$h_{\text{BdG}} = \xi(p)\tau^z - \Delta\frac{p}{p_F}\,\tau^x, \tag{12}$$

where we have assumed that $\Delta > 0$ for convenience.[6] It turns out that the model of the spinless *p*-wave superconducting wire (12) is closely related to the so-called Su, Schrieffer, Heeger model studied some time ago as a model for polyacetylene [19, 20]. We will not go into a detailed discussion of the similarities and difference of the two model, we just want to point out that Su *et al.* have found that their model in polyacetylene generates zero energy state of certain topological criteria are satisfied.
Being interested in solutions of (12) with vanishing eigenvalue, we note first that the spectrum of the system $E_p = \sqrt{\xi(p)^2 + \Delta^2(p/p_F)^2}$ is fully gapped in the translationally invariant case with $\mu \neq 0$, see Fig. 1(a). In order to find a zero mode, we have to look at interfaces between different materials such that the parameters μ, Δ, m become spatially dependent. In the simplest case, we look at an interface between vacuum for $z < 0$ (modeled by $\mu \to -\infty$) and a *p*-wave superconductor for $z > 0$, see Fig. 1(b). To simplify the discussion, we assume that only the states close to the Fermi surface are important[7] and that the wire is long enough such that the second interface does not influence our discussion. Thus, we can write $\psi(z) = e^{ik_F z}\psi_L(z) +$

[4] Here, it is important that there is only a single zero mode present. Having two modes β_1 and β_2 at zero energy, we can only conclude that $\beta_1 = \beta_2^\dagger$.

[5] However in the recent literature, the general term 'Majorana fermion' is often used to denote the more special term 'Majorana zero mode'.

[6] The phase of Δ is in fact an unobservable quantity as only phase-differences are observable, e.g., via the Josephson effect [15, 16, 18].

[7] Physically this assumption means that the interface is not too abrupt in order not to scatter states with vastly different momentum into each other.

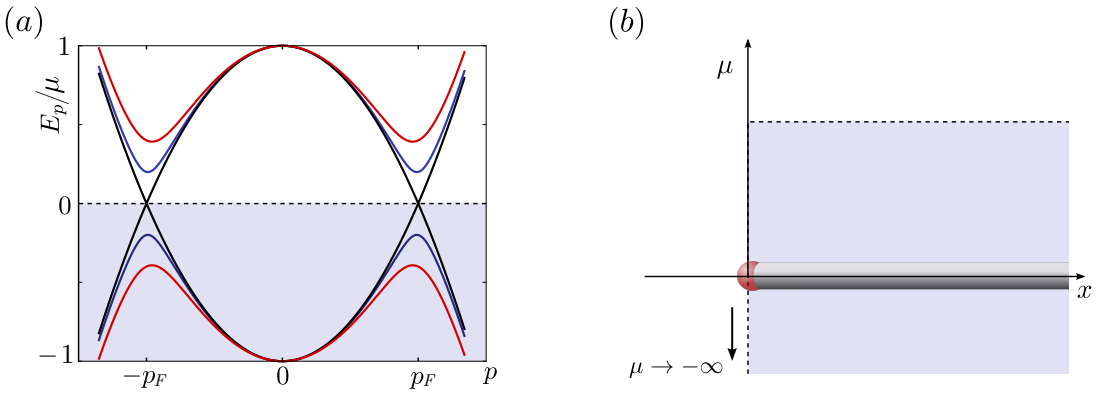

Fig. 1: *(a) Plot of the energy-momentum relation of a p-wave superconducting nanowire. All energies are measured with respect to the chemical potential $\mu > 0$ which is indicated by the dashed line. Above the chemical the spectrum corresponds to an excitation spectrum; below the chemical potential it should be understood as an absorption spectrum. Due to the presence of the superconductivity the two spectra are equivalent when mirrored at the dashed line. The black line shows two parabolas which is the spectrum without superconductivity, i.e., $\Delta = 0$. The blue and red lines correspond to a superconducting pair-potential $\Delta = 0.2\mu$ and $\Delta = 0.4\mu$, respectively. The presence of the superconductor opens a gap of size 2Δ at the chemical potential. Note that for any finite superconducting pairing $\Delta \neq 0$ the system is completely gapped. At $p = 0$ and $E_{p=0} = \pm\mu$ the bottom of the band is visible. Decreasing μ brings the two vertices of the black parabolas closer together until they cross for $\mu = 0$ which is the point of the topological phase transition. (b) Interface of a p-wave superconducting nanowire (gray cylinder) with vacuum. The interface is located at $x = 0$. To the right there is the nanowire with $\mu > 0$ the vacuum is modeled by $\mu \to -\infty$, i.e., a vanishing electron density. Due to the fact that the topological charge changes at the interface a single zero mode emerges which is a Majorana fermion depicted by the red sphere.*

$e^{-ik_F z}\psi_R(z)$ where we assume ψ_L and ψ_R to be slowly varying on the scale λ_F. This ansatz effectively linearize the spectrum $\xi(p)$ around the Fermi points and leads to the Hamiltonian

$$h_{\text{BdG}} = v_F p\, \eta^z + \Delta\, \tau^y \eta^y \tag{13}$$

with $v_F = p_F/m$ and where η^z acts on the left/right-moving basis. As the Hamiltonian commutes with $\tau^z\eta^z$, we can block diagonalize it in each of the eigenspaces $\tau^z\eta^z = \pm 1$ with the result of having two decoupled problems. A state v_0 at zero energy thus satisfies the differential equation $h_{\text{BdG}}\, v_0 = 0$ with $p = -i\hbar\partial_z$. The solutions are given by

$$(v_0^{\pm})_{\tau^z,\eta^z} = e^{-z/\xi - i\pi\tau^z/4}\, \delta_{\tau^z,\pm\eta^z} \tag{14}$$

with the superconducting coherence length $\xi = \hbar v_F/\Delta$; note that we have retained only those solutions which are exponentially decaying away from the interface such that the wavefunction remain normalizable. Additionally, we have chosen the overall phase of the wavefunctions such that $\mathcal{C} v_0^{\pm} = v_0^{\mp}$.

The system is terminated with vacuum for $z < 0$. In our description in terms of linearized spectrum, the boundary condition with vacuum is implemented by demanding a vanishing quasiparticle density at $z = 0$. The quasiparticle density operator is given by $\rho = \frac{1}{2}(1 + \eta^x)\delta(z)$. Thus,

we seek a solution of the form $v_0(z) = \alpha v_0^+(z) + \beta v_0^-(z)$ with the requirement $0 \stackrel{!}{=} \langle v_0|\rho|v_0\rangle \propto |\alpha+\beta|^2$. The condition is satisfied for $\alpha = -\beta$ yielding a single bound state of the form

$$v_0(z) = \alpha e^{-z/\xi} \begin{pmatrix} e^{-i\pi/4} \\ -e^{i\pi/4} \end{pmatrix}_\tau \otimes \begin{pmatrix} 1 \\ -1 \end{pmatrix}_\eta \tag{15}$$

at zero energy located at the interface between the *p*-wave superconductor and vacuum. In order that the Bogoliubov operator $\gamma_1 = \beta_0$ associated to v_0 is a Majorana operator with $\beta_0^\dagger = \beta_0$, we need to have $\mathcal{C}v_0 = v_0$ which demands that $\alpha = \pm i\mathbb{R}$.[8] The proper normalization of the Majorana operator to $\gamma_1^2 = 1$ is realized with $\alpha = i/\sqrt{2\xi}$ and the Majorana operator assumes the form

$$\begin{aligned}\gamma_1 &= \int_{z\geq 0} dz\, v_0(z)^\dagger \Psi(z) = (2\xi)^{-1/2} \int_{z\geq 0} dz\, e^{-z/\xi} \left\{ e^{i\pi/4}[\Psi_L(z) - \Psi_R(z)] + \text{H.c.} \right\} \\ &= \sqrt{\frac{2}{\xi}} \int_{z\geq 0} dz\, \sin(k_F z) e^{-z/\xi} \left[e^{-i\pi/4}\Psi(z) + e^{i\pi/4}\Psi^\dagger(z) \right]. \end{aligned} \tag{16}$$

The analysis can be generalized to include the second interface of the *p*-wave superconducting nanowire with vacuum which yields a second Majorana operator γ_2. In fact, it is a physical constraint that on each connected piece of superconductor there is an even number of Majorana fermions. Two Majorana fermions together can host a conventional fermionic quasiparticle. Note that due to the superconducting condensate the fermion number is not conserved.[9] However, the fermion parity is still conserved. Thus in the situation as in Fig. 1(b), the parity $\mathcal{P} = -i\gamma_1\gamma_2$ encodes the parity of the total number of electrons in the combined system of the superconducting island and the nanowire.

2.3 Topological charge

The appearance of the single zero mode which lead to the Majorana operator in the last section was not an accident. In fact, its presence follows from the general classification of topological insulators/superconductors that at interfaces between superconductors with different topological charge there will be a certain number of topological states which are protected and do not depend on microscopic details. In the classification of topological matter, one considers the question whether two Hamiltonians can be smoothly deformed into each other without closing the gap. In the classification of topological superconductors, one does not allow for arbitrary single-particle Hamiltonians but restricts the class of Hamiltonians in such a way that one only allows for Hermitian matrices which have a particle-hole symmetry and thus represent a Bogoliubov-de Gennes Hamiltonian of a mean-field problem of the form Eq. (8) [9, 10]. A topological charge is an integer which is the same for all Hamiltonians which can be deformed into each other and which differs for two Hamiltonian for which this cannot be achieved. The classification tells us that in the case of a one-dimensional superconductor with particle-hole symmetry $\mathcal{P}$ and $\mathcal{P}^2 = 1$ (as in our case), there are two distinct topological classes. We have found that at an interface between vacuum (read conventional insulator) with $\mu \to -\infty$ and a *p*-wave superconductor there is always a bound state [21, 22, 23]. This indicates that the two

[8] We do not allow for $\alpha \in \mathbb{C}$ as the corresponding operator β_0 would not be Hermitian in this case. What is left is the possibility to choose the sign of α which exactly corresponds to the $\mathbb{Z}_2$ symmetry described above.

[9] Two electrons can be taken out of superconducting condensate by breaking up a Cooper-pair.

parts are in different topological classes; we denote the topological charge $\mathcal{Q}$ of the trivial insulator by 0 and the one of the *p*-wave superconductor by 1. As the topological charge can only change when the gap closes and the gap of (12) only closes for $\mu = 0$, we find that

$$\mathcal{Q}(h_{\text{BdG}}) = \begin{cases} 1, & \mu > 0, \\ 0, & \mu < 0. \end{cases} \tag{17}$$

Due to this reasoning, the Majorana mode is always present in the model as long as μ changes sign across the interface. For a more complete discussion of this fact in the simpler model of polyacetylene see Ref. [24].

3 Quantum computation with Majorana fermions

If we think about an implementation for a quantum computer, we are used to the example of a spin-$\frac{1}{2}$ particle which is a drosophila for a generic two-level system [25]. However, we can ask ourself the question whether we can also use the many-body Fock space for quantum computation purposes. We know that the occupation states $|n_1, n_2, \ldots, n_N\rangle$ with $n_j \in \{0, 1\}$ form a basis for the N-mode fermionic Fock space generated by the creation operators $c_j^\dagger$, $j \in \{1, \ldots, N\}$, starting from the vacuum state denoted by $|0\rangle$. The Fock space has dimension 2^N (each mode can be either occupied or empty). Thus counting the degrees of freedom, we are tempted to conclude that a fermionic system with N-modes emulates N-qubits. In the next section, we will see that this naïve counting argument is not completely correct as it violates the so-called superselection rule. We will argue that quantum computation with noninteracting fermions is not complete and will show what is needed to make the setup complete. Then, we will show that Majorana fermions are in fact non-Abelian particles such that some gates can be performed in a parity-protected way.

3.1 Fermionic quantum computation

Expressing a Hamiltonian H or in fact any physical observable A which are bosonic operators in terms of fermionic creation and annihilation operators, we are bound to only include terms where an even number of fermion operators appear.[10] The result is that the total fermion parity $\mathcal{P} = \prod_k \mathcal{P}_k = (-1)^{\sum_k n_k}$ is strictly conserved in a closed system; the reason for this is the fact that

$$\mathcal{P} A \mathcal{P} = A \tag{18}$$

which follows from $\mathcal{P} c_j \mathcal{P} = -c_j$ and the fact that each term in A involves an even number of fermionic operators. Note that the superconducting Hamiltonian (7) conserves the total fermion parity even so the number of fermions is not conserved. Due to this constraint, we have the following superselection rule: given two states in a fermionic Fock space $|\psi_+\rangle$ and $|\psi_-\rangle$ with different fermion parity, $\mathcal{P}|\psi_\pm\rangle = \pm|\psi_\pm\rangle$ we have

$$\langle\psi_-|A|\psi_+\rangle = \langle\psi_-|\mathcal{P}A\mathcal{P}|\psi_+\rangle = -\langle\psi_-|A|\psi_+\rangle = 0 \tag{19}$$

[10] From the correspondence principle, we know that for large quantum numbers the expectation values of operators for physical observables should behave like (real) numbers. Due to the anticommutation relation of fermionic operators, the correspondence principle for a potential fermionic observable would instead lead to anticommuting Graßmann numbers.

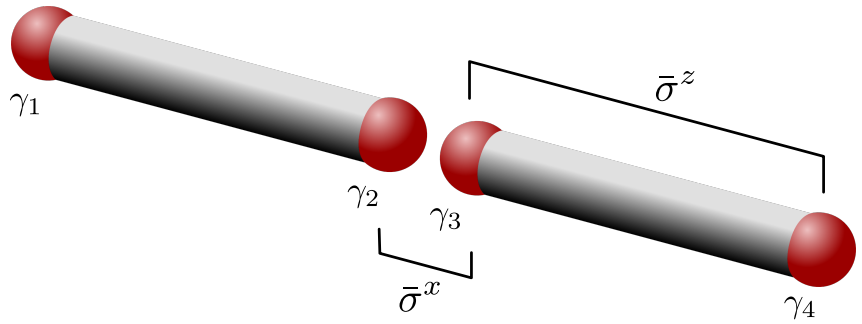

Fig. 2: *Sketch of the parity Majorana qubit. Two Majorana fermions together form a single Dirac fermionic mode whose Hilbert space is two-dimensional as the mode can either be empty or filled, both states at the same energy. Four Majorana fermions thus form a four-dimensional Hilbert space of which due to the conservation of the total fermion parity only a two-dimensional subspace can be accessed. This degenerate two-dimensional subspace is the Majorana qubit. Gates on the qubit can be either performed by braiding or by coupling two Majorana fermions. As indicated in the figure, coupling γ_3 to γ_4 implements a $\bar{\sigma}^z$-operation whereas coupling γ_2 to γ_3 leads to a $\bar{\sigma}^x$-operation. Given the fact that the Majorana fermions are sufficiently far apart from each other and that the environment only acts locally on the system, these operations are not performed 'accidentally' by the environment and the Majorana qubit is protected from both sign flip and bit flip errors. As these protection originates from the conservation of the total fermion parity, the qubit is called parity-protected.*

for all observables A. Thus, there is no point in making superpositions between states of different parity as there will be no effect on any observable. We can thus restrict ourselves to one superselection sector and keep the fermion parity fixed with either $\mathcal{P} = +1$ or $\mathcal{P} = -1$. The conclusion of this argument is that out of the 2^N states in a fermionic Fock space, only 2^{N-1} can be effectively used for quantum computation purposes.
A further restriction to quantum computation using fermions arises from the fact that noninteracting fermions subject to beam splitters, phase-shifters (delay lines), measurements of the state of a single electron (so-called fermionic linear optics) does in fact not lead to any entanglement [26]. In order to generate entanglement, we need to add parity measurement of two electrons which effectively involves interactions between different electrons [27].

3.2 Parity-protected quantum computation

We have seen in the last section that due to the parity-conservation, we need to have two fermionic modes to encode a single qubit. For concreteness, we will work in the even parity superselection sector and have the single logical qubit encodes as $|\bar{0}\rangle = |00\rangle$ and $|\bar{1}\rangle = |11\rangle$. Thinking about a possible implementation in terms of Majorana fermions, we encode each fermionic mode in a pair of Majorana fermions which are localized states sufficiently far separated from each other. As we have seen before, two segments of p-wave superconducting nanowires exactly implement this situation, see Fig. 2. We denote the Majorana fermions in the left segment as γ_1 and γ_2 and the one on the right segment as γ_3 and γ_4 correspondingly. The Majorana fermions are at zero energy thus the two states $|\bar{0}\rangle$ and $|\bar{1}\rangle$ are degenerate in energy. The parity of the number of electrons on the superconducting segments are given by $\mathcal{P}_L = -i\gamma_1\gamma_2$ and $\mathcal{P}_R = -i\gamma_3\gamma_4$. Due to the parity constraint, we have $\mathcal{P}_L = \mathcal{P}_R$ and the action

of both operators on the logical qubit emulates the σ^z Pauli-operator,

$$\bar{\sigma}^z = -i\gamma_1\gamma_2 = -i\gamma_3\gamma_4 \tag{20}$$

In order to have a complete qubit, we are left with the task to find a logical $\bar{\sigma}^x$, an operator which anticommutes with $\bar{\sigma}^z$. It is easy to see that

$$\bar{\sigma}^x = -i\gamma_2\gamma_3 = -i\gamma_1\gamma_4 \tag{21}$$

anticommutes with $\bar{\sigma}^z$ due to the fact that the single Majorana fermions shared by both operators anticommute with each other. In the situation where all the Majorana fermions are sufficiently far separated from each other, either gate on the logical qubit is a nonlocal operator. Due to this nonlocality, it is highly unlikely that uncontrolled, random fluctuations in the environment will execute a gate thus acts as an error on the logical qubit. This protection of the Majorana qubit is called symmetry-protected topological order [28, 29] or simply parity-protection [30]. The decisive difference to full topological order, as it is for example present in Kitaev's toric code [31], is the fact that logical Pauli operators are only required to be nonlocal as long as the parity symmetry is conserved. Having a reservoir tunneling single electrons on the superconducting island is a local process which violates the parity-conservation and immediately brings the Majorana qubit out of its computational subspace.
The requirement for operating the Majorana qubit successfully in a protected manner is that the environment does not provide single unpaired electrons. This sounds on the first sight very stringent. However, the physical implementation of the system does only involve superconductors where most of the electrons are paired up into Cooper pairs and where at temperature T only a exponentially small fraction proportional to the Boltzmann factor $e^{-\Delta/T}$ remains unpaired. The storage time of quantum information in a Majorana qubit thus will increase exponentially when lowering the electron temperature.

3.3 Anyons

In $3+1$ dimensions, we are use to the dichotomy of bosons and fermions. In fact the spin-statistic theorem can be proven in the context of relativistic field theory which states that particles with integer spin are bosons whereas particles with half-integer spin are fermions. The origin of this distinction lies in the fact that the Hamiltonian of identical particles commutes with an arbitrary element of the symmetric group $\mathcal{S}_N$ which exchanges the N identical particles. Thus, it is possible to classify the eigenstates of the Hamiltonian in terms of irreducible representations of the permutation group. Any representation whose dimension is larger than one leads to a degeneracy, which is called exchange degeneracy as it originates simply from the fact that particles are indistinguishable. Now it is an experimental fact that exchange degeneracies do not exist; the absence of exchange degeneracy was first noted in the context of statistical mechanics where it manifests itself in an entropy which is not extensive and where it has been dubbed Gibbs paradox.[11]

[11] The statistics of identical particles which transforms according to higher dimension representations of the permutation groups is called parastatistics. However, even if particles with parastatistics where to exist they would offer nothing new as a set of Klein transformations could be used to map particles with parastatistics as bosons or fermions with a set of internal quantum numbers (like spin, ...). Later, we will see that such a mapping is not possible in $2+1$ dimension and that higher dimensional representations of the braid group are truly different from the one-dimensional representations.

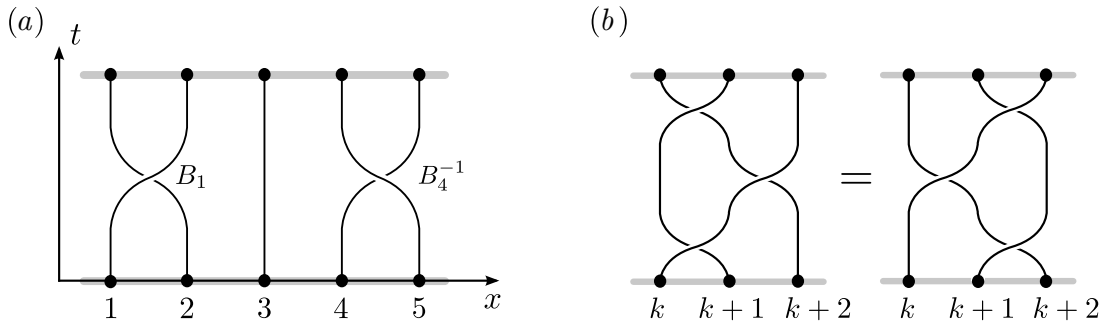

Fig. 3: *(a) Elementary operation of the braid group. The geometric representation of the braid group is in space-time; the horizontal axis is the spacial axis whereas the vertical one is temporal. Every element (called braid) of the braid group $\mathcal{B}_N$ consists of N strands. In our example, we have $N = 5$ strands which are numbered from 1 to 5. The generators of the group B_k denote the braiding two strands counterclockwise (in the figure, B_1 braids strand 1 and 2 counterclockwise). The inverse operation braids the strand clockwise (in the figure, B_4^{-1} braids strand 4 and 5 clockwise). Two elements of the group are equivalent if the corresponding braids can be smoothly deformed into each other without moving the endpoints denoted by the black dots. The Yang-Baxter equation $B_kB_{k+1}B_k = B_{k+1}B_kB_{k+1}$ provides an important relation between the generators B_k and B_{k+1} and is shown pictorially in (b). That the two braids are topological equivalent can be seen as follows: in both braids strand $k + 2$ can be considered to lie in the very back and to end up at the initial position of strand k. Similarly strand k lies in front and ends up at the initial position of strand $k + 2$. The middle strand starts at $k + 1$ and ends at the same place. The braids are equivalent as they can be deformed into each other by sliding the middle strand $k + 1$ in between the two other strands from the left to the right.*

In $2 + 1$ dimension, the relevant group is the braid group $\mathcal{B}_N$ of N strands as trajectory in space-time for exchanging two particles clock or counterclockwise are topological distinct.[12] We denote with B_j the counter-clockwise exchange of strand j and $j + 1$ ($1 \leq j \leq N - 1$). Note that different from the symmetric group $B_j \neq B_j^{-1}$. The braid group fulfills the following relations

$$B_kB_l = B_lB_k, \quad |k - l| \geq 2 \qquad \text{and} \qquad B_kB_{k+1}B_k = B_{k+1}B_kB_{k+1}, \tag{22}$$

the latter is called Yang-Baxter equation. Different from the symmetric group $\mathcal{S}_N$ the group order is infinity which makes the classification of all irreducible representation difficult.
The one-dimensional (unitary) representations of the braid group are simple to construct; representing the action of B_j onto a wavefunction by $e^{i\theta_j}$ with $\theta_j \in [0, 2\pi)$, we immediately get from the Yang-Baxter equation that all the angles are equal, i.e., $\theta_j \equiv \theta$. Note that for $\theta = 0$, we get the customary result for bosons that interchanging two particles does nothing to the wavefunction whereas for $\theta = \pi$ interchanging introduces a minus sign which is the result for fermions. In $2 + 1$ dimension, all angles in between 0 and π are allowed and particles with $\theta \neq 0$ or π are called (Abelian) anyons. As an example, we note that quasiparticles in the fractional quantum Hall effect at filling fraction $\nu = \frac{1}{n}$ with n an odd integer are anyons with $\theta = \nu\pi$.
Particles whose wavefunctions transform according to higher dimensional irreducible representations of the braid group are called non-Abelian anyons. A necessary ingredient is a ground

[12] In $3 + 1$ dimension clock and counterclockwise depends on the observer (coordinate system) and thus the two exchanges are topologically equivalent.

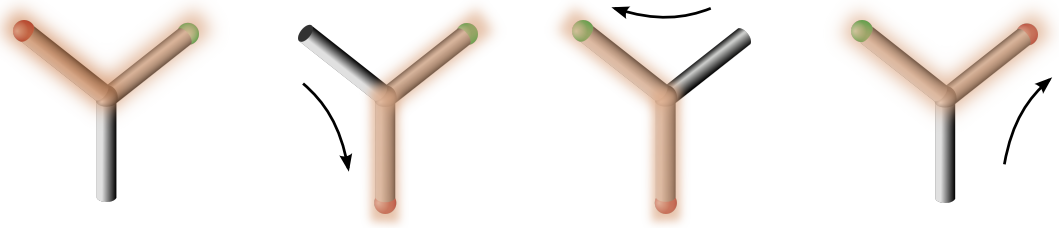

Fig. 4: *Sketch of a Y-junction where three superconducting nanowires meet. Having a Y-junction is an essential ingredient to be able to braid the Majorana fermions as exchanging two particles is not possible in a strictly one-dimensional setting. The two Majorana fermions symbolized by red and green spheres are situated at the ends of the segment of the wire in the topological phase with $\mathcal{Q}=1$ indicated by the brown shading. The gray part of the nanowire is depleted such that it is topological trivial with $\mathcal{Q}=0$. Exchanging the red and green Majorana fermion is done in four steps indicated in the figure. In each step, one of the Majorana fermion is moved to another end of the Y-junction by swapping the corresponding segments of the wire between topological and trivial.*

state degeneracy (which grows exponentially with the number of particles). The effect of B_j, the counterclockwise exchange two particles j and $j+1$, is then represented by a unitary matrix U_j on the ground state manifold. As different unitary matrices do not commute, the representation is non-Abelian and thus the particles are called non-Abelian anyons. The usefulness of non-Abelian anyons for topological quantum computation relies on the fact that the degeneracy of the ground state manifold is protected and the gates implemented by the exchange of particles are exact (up to an unimportant global phase) [32]. If for a specific species of non-Abelian anyons for any given gate a braid can be found which approximates the gate with arbitrary accuracy, the non-Abelian anyons are called universal for quantum computation.

3.4 Majorana fermions as non-Abelian particles

We restrict ourself to the discussion of two Majorana fermions. Braiding is local, so it should only affect those particles which are being braided. We will see that the braid statistics can be simply deduced from the fact that the parity remains conserved [33].[13] First, we have to see that moving a Majorana fermions: braiding of the Majorana fermions the system has to stay in the ground state manifold. Thus everything has to be adiabatic. We change parameters in the Hamiltonian slowly in such a way that everything is slow with respect to the gap. The system then evolves according to the unitary evolution $U(t)=\mathcal{T}\exp[-i\int_0^t dt'\,H(t')]$ where $\mathcal{T}$ is the time ordering operator. The operators transform like

$$\gamma_k(t)=U^\dagger(t)\gamma_k U(t). \tag{23}$$

In a first step, we want to show that we can in fact move a single Majorana fermion without changing its state. Having two adjacent Majorana fermions γ_k and γ_{k+1} moving the former a bit in the time T results in new Majorana fermions $\gamma'_k=\gamma_k(T)$ and $\gamma'_{k+1}=\gamma_{k+1}(T)$. As fermion parity is conserved, we have

$$\mathcal{P}=-i\gamma_k\gamma_{k+1}=-i\gamma'_k\gamma'_{k+1} \tag{24}$$

[13] In two dimensions, Majorana fermions exist as bound state in the vortex of chiral p-wave superconductors. To determine the braid statistics in this case is a bit more involved [34, 35].

Since nothing has happened to γ_{k+1} (the evolution did not affect the right Majorana fermion), we have $\gamma'_{k+1} = \gamma_{k+1}$. Plugging this into Eq. (24), we have $\gamma'_k = \gamma_k$, i.e., we can move the Majorana fermion without perturbing it.
In order to obtain the braid group, we need to find the effect of B_k, i.e., exchanging the two Majorana fermions in the clockwise direction. This cannot be done in strictly one dimension but involves Y-junctions, see Fig. 4 and Refs. [36, 37, 38]. As above, we will again denote the operators after time T, that is after the braiding operators with a prime. As the positions of the Majorana fermions is switched after the time T, we have $\gamma'_k = \alpha_{k+1}\gamma_{k+1}$ and $\gamma'_{k+1} = \alpha_k\gamma_k$. Due to the fact that the operators have to remain Majorana fermions, we need to require that $\alpha_k, \alpha_{k+1} \in \{\pm 1\}$. The conservation of the parity leads to the relation

$$\mathcal{P} = -i\gamma_k\gamma_{k+1} = -i\gamma'_k\gamma'_{k+1} = -i\alpha_k\alpha_{k+1}\gamma_{k+1}\gamma_k \tag{25}$$

thus, we need that $\alpha_k\alpha_{k+1} = -1$: one of the Majorana fermions picks up a minus sign and one does not. Which of the Majorana fermions picks up a minus sign is a gauge choice and there are no physical effect; so we choose $\alpha_k = -1$ and $\alpha_{k+1} = 1$. Note that braiding the Majorana fermions in the counter-clockwise direction is the inverse operation and thus reverses the sign of both α_k and α_{k+1}. It is easy to see that the operator

$$U(T) \equiv U_k = \exp\left(\frac{\pi}{4}\gamma_k\gamma_{k+1}\right) = \frac{1}{\sqrt{2}}(1 + \gamma_k\gamma_{k+1}), \tag{26}$$

implements this unitary operation, where ‘ $\equiv'$ denotes the fact that the time-evolution $U(T)$ and U_k are equivalent up to an unimportant overall phase. Furthermore, one can check explicitly that the U_ks obey the relations in Eqs. (22) and thus they are a representation of the braid group. We would like to explicitly find the gates generated by braiding the Majorana zero mode for the example of a single Majorana qubit, cf. Fig. 2. Straightforward calculation shows

$$U_1 = U_3 = e^{\pi\gamma_1\gamma_2/4} = e^{i\pi\bar{\sigma}^z/4}, \qquad U_2 = e^{\pi\gamma_2\gamma_3/4} = e^{i\pi\bar{\sigma}^x/4}, \tag{27}$$

which are elements of the Clifford group. In fact, it can be shown that in general only Clifford gates can be implemented via braiding. So neither the single qubit rotations are universal nor there is an entangling gate.[14] However in order to make the setup universal, we need to subjoin only a two qubit parity measurement (to generate entanglement) and a $\frac{\pi}{8}$-phase gate [39, 32].[15] We will show a way to implement such a unprotected gate in Sec. 4.2.

4 Implementations

4.1 Semiconducting nanowires

Last year at TU Delft evidence of Majorana fermions has been found in semiconducting InSb nanowires coupled to a NbTiN superconductor in the presence of a magnetic field of around 100 mT [40]. The experiment realized an idea of Refs. [41, 42] which extended earlier ideas for quantum wells to nanowires [43, 44]. In this chapter, we provide a brief introduction into

[14] Majorana fermions are in essence noninteracting particles described by the quadratic Hamiltonian Eq. (8) and thus the restrictions of Sec. 3.1 apply.

[15] In fact, it is enough if the $\frac{\pi}{8}$-phase gate is implemented with a fidelity $\gtrsim 90\%$ as a distillation protocol using the exact Clifford gates called the Magic state distillation can be employed to purify the state [39].

the physics of semiconducting nanowires and motivate the connection to Majorana fermions in spinless p-wave nanowires. The simplest model for conduction electrons a semiconducting nanowire in a magnetic field B pointed along the nanowire direction is given by

$$H_{\rm NW}=\int dz\,\left[\frac{\hbar^2}{2m}|\Psi'(z)|^2-\mu|\Psi(z)|^2+\frac{\alpha_{\rm so}}{\hbar}\Psi^\dagger(z)\sigma^y p\Psi(z)-\frac{g\mu_B B}{2}\Psi^\dagger(z)\sigma^z\Psi(z)\right] \tag{28}$$

with the field operator $\Psi^T=\begin{pmatrix}\psi_\uparrow & \psi_\downarrow\end{pmatrix}$. Here, we have assumed that the spin-orbit characterized by $\alpha_{\rm so}$ is of Rashba-type due to electric fields perpendicular to the substrate as Dresselhaus terms are absent for experimentally-relevant zincblende nanowires grown along the 111 crystal direction. For InSb nanowires the parameters are given by $m\simeq 0.015m_e$, $g\simeq 50$, and $\alpha\simeq 0.2\,\mathrm{eV\AA}$. In writing down the Hamiltonian (28), we have silently assumed that only a single mode is relevant in the nanowire whereas in the experiment there are most likely of the order of 5 modes contributing. This difference, even though important for a detailed description of the experimental findings, is not relevant for the generic discussion we intend to provide. In the same spirit, we have neglected any orbital effects of the magnetic field on the nanowire.
The proximity to an s-wave superconductor introduces pair-correlations in the nanowire. This can be expressed with an additional term in the Hamiltonian of the form

$$H_{\rm SC}=\Delta\int dz\,\left[\psi_\downarrow^\dagger(z)\psi_\uparrow^\dagger(z)+\psi_\uparrow(z)\psi_\downarrow(z)\right] \tag{29}$$

where $\Delta/\hbar>0$ is the rate at which Cooper pairs are injected into the nanowire. For reasonable strong superconductors and clean interfaces between the superconductor and the nanowire we may expect $\Delta\simeq 1\,\mathrm{K}$.
Following Ref. [44], we want to show that for strong magnetic fields such that the Zeeman energy $E_Z=\frac{1}{2}g\mu_B B$ is larger than Δ and $m\alpha_{\rm so}^2/\hbar^2$ the system is equivalent to the spinless nanowire discussed in Sec. 2.2. For such large magnetic fields basically only electrons with spin-up are present. We thus write $\psi(z)=\psi_\uparrow(z)$. As the spin-orbit term in (28) does not commute with the Zeeman term, it admixes the spin-down component. In lowest order perturbation theory, we thus have

$$\psi_\downarrow(z)=\frac{\alpha_{\rm so}\sigma^y p}{2\hbar E_Z}\psi(z)=\frac{\alpha_{\rm so}}{2\hbar E_Z}\psi'(z) \tag{30}$$

Plugging this expression into the full Hamiltonian $H_{\rm NW}+H_{\rm SC}$, we obtain to lowest order the effective Hamiltonian

$$H_{\rm eff}=\int dz\,\left[\frac{\hbar^2}{2m}|\psi'(z)|^2-\mu_{\rm eff}|\psi(z)|^2-\Delta_{\rm eff}[\psi^\dagger(z)\psi^{\dagger\prime}(z)-\psi(z)\psi'(z)]\right] \tag{31}$$

with $\mu_{\rm eff}=\mu+E_Z$ and $\Delta_{\rm eff}=\Delta\alpha_{\rm so}/2\hbar E_Z$. The expression (31) coincides with the BCS mean-field Hamiltonian $H_{\rm MF}$ for spinless electrons Eq. (7) with an effective p-wave pairing $\Delta(z)=\Delta_{\rm eff}\delta'(z)$. We have seen in Sec. 2.3 that this system hosts Majorana fermions at its ends provided that $\mu_{\rm eff}>0$.
We know however that the topological phase is stable and can only be removed by closing the bulk gap of the nanowire. The condition for the closing of the gap of $H_{\rm NW}+H_{\rm SC}$ is a zero eigenvalue of the Bogoliubov-de Gennes Hamiltonian

$$h_{\rm BdG}(p)=\xi(p)\tau^z+\frac{\alpha_{\rm so}p}{\hbar}\sigma^y\tau^z-E_Z\sigma^z+\Delta\tau^x \tag{32}$$

subject to periodic boundary conditions. Due to the presence of the spin-orbit term proportional to $\alpha_{\rm so}$ the gap can only be closed for $p = 0$. At $p = 0$, the energy eigenvalues of $h_{\rm BdG}$ are given by

$$E_{p=0} = \pm \left| \sqrt{\mu^2 + \Delta^2} - E_Z \right| . \tag{33}$$

We have seen before that for large magnetic field with $E_Z \gg \Delta, |\mu|$ the system essentially implement a spinless *p*-wave nanowire in the topological phase with Majorana fermions at the end. This phase extends in the full model up to the point where $E_{p=0} = 0$, i.e., the gap closes. As a consequence, we obtain an expression for the topological charge

$$\mathcal{Q}(h_{\rm BdG}) = \begin{cases} 1, & |\mu| < \mu_c, \\ 0, & |\mu| > \mu_c, \end{cases} \qquad \text{with} \qquad \mu_c = \begin{cases} \sqrt{E_Z^2 - \Delta^2}, & E_Z > \Delta, \\ 0, & E_Z < \Delta. \end{cases} \tag{34}$$

In order for the experiments to be in the regime where there are Majorana fermions (indicated by $\mathcal{Q} = 1$), we thus need $E_Z > \Delta$. This is only possible due to the large g-factor of the InSb nanowire with respect to the superconductor with $g_{\rm SC} \simeq 2$ as the superconducting state is destroyed latest at a magnetic field such that $\frac{1}{2} g_{\rm SC} \mu_B B = (g_{\rm SC}/g) E_Z \lesssim \Delta$ which is the so-called Pauli limit.

4.2 Hybrid structures

As discussed in details above, the parity protection of the Majorana qubit is potentially useful as it allows quantum computation where the qubit as well as the gates are topological protected. However, we have also seen that the braiding operation do not allow for universal quantum computation. In particular, a $\frac{\pi}{8}$-phase gate and a parity measurement of two qubits are missing. In this section, we want to show how hybrid structures involving superconducting qubits besides the Majorana qubits offer a way to make the Majorana qubits universal for quantum computation.

It is important to note that in order to be able to measure the state of the Majorana qubit its parity-protection has to be removed. This can in principle be achieve by fusing two Majorana fermions, i.e., make their wavefunctions overlapping, and measuring the resulting ground state energy of the system. However, as we need additionally a measurement of the parity of two qubits (without determining the state of each of the qubits) interactions, terms which couple four Majorana fermions, are indispensable [32].

The most natural choice for an interaction is the Coulomb interaction due to the charge of the electrons which form the basis for the Majorana fermions [45, 30]. Starting with a Majorana qubit involving four Majorana fermions on a superconducting island, cf. Fig. 2 the protection of the qubit can be lifted by 'cutting' the superconducting islands into two pieces each of them having two Majorana fermions present. The state of the Majorana qubit is then encoded in the fact whether there is an even or odd number of electrons on each of the parts, see Fig. 5. The 'cutting' is of course not meant literally. In fact having from the beginning two separate superconducting islands coupled with a Josephson coupling with strength E_J (originating from Cooper pairs tunneling between the two superconductors) and a capacitive coupling with strength E_C (originating from the charging energy between the two superconducting islands). In the regime $E_J \gg E_C$, the two superconducting islands behave essentially as if they where a single piece of superconductor and the qubit is protected. Lowering the ratio E_J/E_C increases the charge sensitivity (the difference in energy between the islands having even and

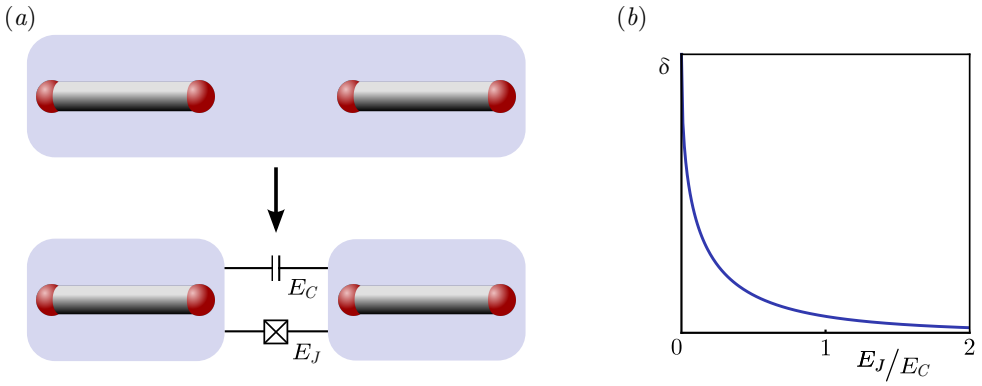

Fig. 5: *(a) In order to measure and/or manipulate the Majorana qubit the topological protection has to be removed. This can be achieved by 'cutting' the superconducting island into two parts, a process which is implemented in reality by having from the beginning two superconducting islands which are coupled by a capacitance with energy E_C and a Josephson junction with energy E_J (bottom). In the regime where $E_J \gg E_C$, superconducting correlations between the two islands are strong and tnus the two islands essentially behave like a single superconducting islands with a Majorana qubit consisting of four Majorana fermions. (b) Lowering the ratio E_J/E_C the charge sensitivity δ which describes the energy difference between the two logical states of the Majorana qubit increases exponentially and readout and manipulation becomes possible.*

odd number of electrons) and thereby lifts the parity-protection. In fact, the difference in energy of the two states of the Majorana qubit is exponentially depending on the ratio E_J/E_C as $\delta \propto \exp\left(-\sqrt{8E_J/E_C}\right)$, see Ref. [46]. The protected qubit discussed so far is given for large E_J/E_C where δ essentially vanishes.

In the concrete implementation proposed in [30], the read-out of the Majorana qubit is achieved by distribution the four Majorana fermions which form the logical qubits on the two plates of the capacitor in a Cooper pair box, see Fig. 6. By varying the flux Φ through a split Josephson junction, the Josephson energy $E_J \propto \cos(e\Phi/\hbar)$ becomes tunable. As the charge sensitivity depends exponentially on the ratio E_J/E_C, a variation of the charge sensitivity (the degree of protection of the qubit) over two orders of magnitude has been achieved in the transmon qubit design of the Yale group [47].[16] Due to this exponential dependence it becomes possible to turn the protection of the qubit on and off at will. The fact that there is a tunable energy difference δ of the two states of the Majorana qubit directly leads to the possibility of implementing an arbitrary phase gate. Starting and ending with a qubit in the protected state with $\delta = 0$, we can make δ finite for some time τ such that $\delta\,\tau/\hbar = 2\phi$ which implement the phase gate $\exp(i\phi\bar{\sigma}_z)$. Especially for $\phi = \frac{\pi}{8}$, we obtain the missing $\frac{\pi}{8}$ phase gate.

Similarly, for the readout of the Majorana qubit we use the fact that due to the same interaction the energy difference $\Delta\varepsilon_{\bar{\sigma}_z} = \Delta\varepsilon + \delta\,\bar{\sigma}_z$ between the ground state and the first excited state of the transmon qubit depends on the state of the Majorana qubit $\bar{\sigma}_z = \pm 1$. The state of the transmon qubit can be read out by sending a microwave probe beam through the transmission

[16] The transmon is simply a Cooper pair box with $E_J \gtrsim E_C$ which is placed in a transmission line resonator for read-out, hence the name.

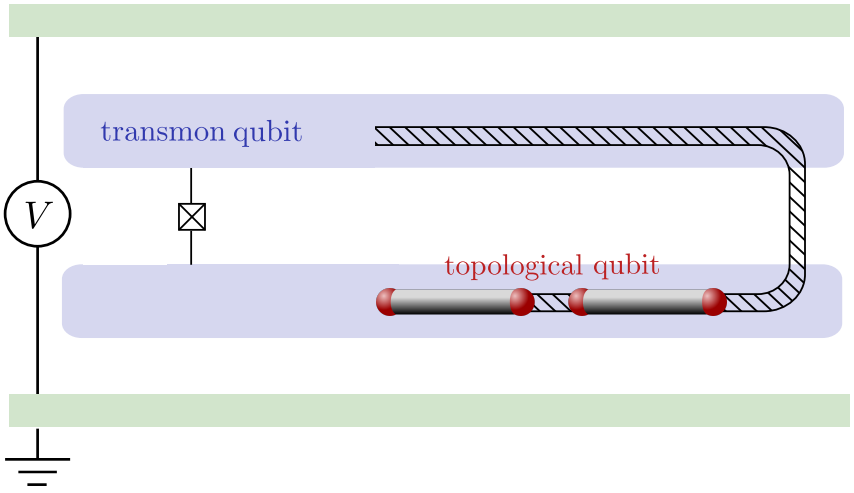

Fig. 6: *Read out of a parity qubit in a Cooper pair box. Two superconducting islands (blue), connected by a split Josephson junction (crosses) form the Cooper pair box. The topological Majorana qubit is formed by four Majorana fermions (red spheres), at the end points of two undepleted segments of a semiconductor nanowire (striped ribbon indicates the depleted region). A magnetic flux Φ enclosed by the Josephson junction controls the charge sensitivity of the Cooper pair box. To read out the topological qubit, two of the four Majorana fermions that encode the logical qubit are moved from one island to the other. Depending on the quasiparticle parity, the resonance frequency in a superconducting transmission line enclosing the Cooper pair box (green) is shifted upwards or downwards by the amount which is exponentially small in E_J/E_C.*

line resonator [48, 49, 47]. The resonance frequency $\omega_{\rm res}$ of the cavity is given by

$$\omega_{\rm res} = \omega_0 - \frac{g^2}{\omega_0 - \Delta\varepsilon_{\bar\sigma_z}/\hbar} \tag{35}$$

provided the fact that the qubit is initially in its ground state and the cavity frequency ω_0 is far detuned from $\Delta\varepsilon/\hbar$; here, ω_0 is the bare resonance frequency of the cavity and g is the Jaynes-Cummings coupling between the cavity mode and the transmon qubit. The small shift of the cavity frequency due to the dependence of $\omega_{\rm res}$ on the state $\bar\sigma_z$ of the Majorana qubit can be measured sensitively as a phase shift of the transmitted microwaves.

In the case where there are more than two Majorana fermions per superconducting island, the transmon qubit couples directly to parity of the number of electrons on each of the island. Thus, a joint parity measurement on two Majorana qubits can likewise be performed by moving four out of the eight Majorana fermions to the other island.

Summarizing, the hybrid design of a coupled transmon and Majorana qubit retains the full topological protection with exponential accuracy in the off-state ($E_J/E_C \gg 1$). This hybrid device can be used to implement a phase gate on the Majorana qubit as well as to jointly read out sets of Majorana qubits. Together with braiding and single qubit readout, these are the operations required for a universal quantum computer.

5 Conclusion

We have shown that Majorana fermions can be perceived as 'half' and ordinary Dirac fermion. Interestingly, these particles emerge as end states at zero energy in superconducting p-wave nanowires independent of any microscopic details, a fact which can be traced back to the change of the topological charge from the nanowire to the surrounding vacuum. Four Majorana fermions encode a single qubit. Keeping the fermion parity in the system conserved, gates on the qubit can only be performed by operators which involve two Majorana fermions. As the Majorana fermions are spatially separated, random (local) noise due to environmental fluctuations will not couple to the Majorana qubit and thus will not lead to decoherence of the Majorana qubit. Most importantly, we have seen that Majorana fermions are non-Abelian particles which implies that one can perform protected gates just by braiding the particles around each other. Alas, the operations generated by braiding the particles are not enough to make the system a universal quantum computer. For that reason, we have shown how the coupling of a Majorana qubit to a superconducting transmon qubit can be used both for performing measurments of the Majorana qubit and implementing the missing gates. Finally, we have discussed the essential ingredients (semiconducting nanowire with strong spin-orbit interaction and large g-factor coupled to an s-wave superconductor) for implementing these ideas in a laboratory without the need for the elusive p-wave superconductor.

References

[1] N.D. Mermin, *The topological theory of defects in ordered media*, Rev. Mod. Phys. **51**, 591 (1979).

[2] Y. Aharonov and D. Bohm, *Significance of electromagnetic potentials in the quantum theory*, Phys. Rev. **115**, 485 (1959).

[3] K. von Klitzing, G. Dorda, and M. Pepper, *New method for high-accuracy determination of the fine-structure constant based on quantized Hall resistance*, Phys. Rev. Lett. **45**, 494 (1980).

[4] D.J. Thouless, M. Kohmoto, M.P. Nightingale, and M. den Nijs, *Quantized Hall conductance in a two-dimensional periodic potential*, Phys. Rev. Lett. **49**, 405 (1982).

[5] F.D.M. Haldane, *Model for a quantum Hall effect without Landau levels: Condensed-matter realization of the "parity anomaly"*, Phys. Rev. Lett. **61**, 2015 (1988).

[6] C.L. Kane and E.J. Mele, $\mathbb{Z}_2$ *topological order and the quantum spin Hall effect*, Phys. Rev. Lett. **95**, 146802 (2005).

[7] B.A. Bernevig, T.L. Hughes, and S.-C. Zhang, *Quantum spin Hall effect and topological phase transition in HgTe quantum wells*, Science **314**, 1757 (2006).

[8] M. König, S. Wiedmann, C. Brüne, A. Roth, H. Buhmann, L.W. Molenkamp, X.-L. Qi, and S.-C. Zhang, *Quantum spin Hall insulator state in HgTe quantum wells*, Science **318**, 766 (2007).

[9] A.P. Schnyder, S. Ryu, A. Furusaki, and A.W.W. Ludwig, *Classification of topological insulators and superconductors in three spatial dimensions*, Phys. Rev. B **78**, 195125 (2008).

[10] A. Kitaev, *Periodic table for topological insulators and superconductors*, in ADVANCES IN THEORETICAL PHYSICS*: Landau Memorial Conference*, edited by V.V. Lebedev and M.V. Feigel'man, AIP Conf. Proc. **1134**, 22 (2009).

[11] C.W.J. Beenakker, *Search for Majorana fermions in superconductors*, arXiv:1112.1950 (2011).

[12] J. Alicea, *New directions in the pursuit of Majorana fermions in solid state systems*, Rep. Prog. Phys. **75**, 076501 (2012).

[13] M. Leijnse and K. Flensberg, *Introduction to topological superconductivity and Majorana fermions*, arXiv:1206.1736 (2012).

[14] A.Yu. Kitaev, *Unpaired Majorana fermions in quantum wires*, Phys.-Usp. **44**, 131 (2001), cond-mat/0010440.

[15] P.G. de Gennes, *Superconductivity of Metals and Alloys* (Addison-Wesley, Redwood City, 1989).

[16] M. Tinkham, *Introduction to Superconductivity*, 2nd edition (McGraw-Hill, New York, 1996).

[17] J.W. Negele and H. Orland, *Quantum many-particle systems* (Westview Press, Boulder, 1988).

[18] K.K. Likharev, *Superconducting weak links*, Rev. Mod. Phys. **51**, 101 (1979).

[19] W.-P. Su, J.R. Schrieffer, and A.J. Heeger, *Solitons in polyacetylene*, Phys. Rev. Lett. **42**, 1698 (1979).

[20] A.J. Heeger, S. Kivelson, J.R. Schrieffer, and W.-P. Su, *Solitons in conducting polymers*, Rev. Mod. Phys. **60**, 781 (1988).

[21] J.C.Y. Teo and C.L. Kane, *Topological defects and gapless modes in insulators and superconductors*, Phys. Rev. B **82**, 115120 (2010).

[22] M.A. Silaev and G.E. Volovik, *Topological superfluid ^{3}He-B: fermion zero modes on interfaces and in the vortex core*, J. Low Temp. Phys. **161**, 460 (2010).

[23] T. Fukui and T. Fujiwara, *$\mathbb{Z}_2$ index theorem for Majorana zero modes in a class D topological superconductor*, Phys. Rev. B **82**, 184536 (2010).

[24] R. Jackiw and J.R. Schrieffer, *Solitons with fermion number 1/2 in condensed matter and relativistic field theories*, Nucl. Phys. B **190**, 253 (1981).

[25] R.P. Feynman, R.B. Leighton, and M. Sands, *Feynman lectures on physics: Quantum mechanics*, vol. 3 (Addison-Wesley, Reading, 1965).

[26] B.M. Terhal and D.P. DiVincenzo, *Classical simulation of noninteracting-fermion quantum circuits*, Phys. Rev. A **65**, 032325 (2002).

[27] C.W.J. Beenakker, D.P. DiVincenzo, C. Emary, and M. Kindermann, *Charge detection enables free-electron quantum computation*, Phys. Rev. Lett. **93**, 020501 (2004).

[28] Z.-C. Gu and X.-G. Wen, *Tensor-entanglement-filtering renormalization approach and symmetry protected topological order*, Phys. Rev. B **80**, 155131 (2009).

[29] F. Pollmann, E. Berg, A.M. Turner, and M. Oshikawa, *Symmetry protection of topological order in one-dimensional quantum spin systems*, Phys. Rev. B **85**, 075125 (2012).

[30] F. Hassler, A.R. Akhmerov, and C.W.J. Beenakker, *Top-transmon: Hybrid superconducting qubit for parity-protected quantum computation*, New J. Phys. **13**, 095004 (2011).

[31] A. Kitaev, *Anyons in an exactly solved model and beyond*, Ann. Phys. (NY) **321**, 2 (2006).

[32] C. Nayak, S.H. Simon, A. Stern, M. Freedman, and S. Das Sarma, *Non-Abelian anyons and topological quantum computation*, Rev. Mod. Phys. **80**, 1083 (2008).

[33] B.I. Halperin, Y. Oreg, A. Stern, G. Refael, J. Alicea, and F. von Oppen, *Adiabatic manipulations of Majorana fermions in a three-dimensional network of quantum wires*, Phys. Rev. B **85**, 144501 (2012).

[34] N. Read and D. Green, *Paired states of fermions in two dimensions with breaking of parity and time-reversal symmetries and the fractional quantum Hall effect*, Phys. Rev. B **61**, 10267 (2000).

[35] D.A. Ivanov, *Non-Abelian statistics of half-quantum vortices in p-wave superconductors*, Phys. Rev. Lett. **86**, 268 (2001).

[36] J. Alicea, Y. Oreg, G. Refael, F. von Oppen, and M.P.A. Fisher, *Non-Abelian statistics and topological quantum computation in 1D wire networks*, Nature Phys. **7**, 412 (2011).

[37] D.J. Clarke, J.D. Sau, and S. Tewari, *Majorana fermion exchange in quasi-one-dimensional networks*, Phys. Rev. B **84**, 035120 (2011).

[38] B. van Heck, A.R. Akhmerov, F. Hassler, M. Burrello, and C.W.J. Beenakker, *Coulomb-assisted braiding of Majorana fermions in a Josephson junction array*, New J. Phys. **14**, 035019 (2012).

[39] S. Bravyi and A.Yu. Kitaev, *Universal quantum computation with ideal Clifford gates and noisy ancillas*, Phys. Rev. A **71**, 022316 (2005).

[40] V. Mourik, K. Zuo, S.M. Frolov, S.R. Plissard, E.P. A.M. Bakkers, and L.P. Kouwenhoven, *Signatures of Majorana fermions in hybrid superconductor-semiconductor nanowire devices*, Science **336**, 1003 (2012).

[41] R.M. Lutchyn, J.D. Sau, and S. Das Sarma, *Majorana fermions and a topological phase transition in semiconductor-superconductor heterostructures*, Phys. Rev. Lett. **105**, 077001 (2010).

[42] Y. Oreg, G. Refael, and F. von Oppen, *Helical liquids and Majorana bound states in quantum wires*, Phys. Rev. Lett. **105**, 177002 (2010).

[43] J.D. Sau, R.M. Lutchyn, S. Tewari, and S. Das Sarma, *A generic new platform for topological quantum computation using semiconductor heterostructures*, Phys. Rev. Lett. **104**, 040502 (2010).

[44] J. Alicea, *Majorana fermions in a tunable semiconductor device*, Phys. Rev. B **81**, 125318 (2010).

[45] F. Hassler, A.R. Akhmerov, C.-Y. Hou, and C.W.J. Beenakker, *Anyonic interferometry without anyons: How a flux qubit can read out a topological qubit*, New J. Phys. **12**, 125002 (2010).

[46] J. Koch, T.M. Yu, J. Gambetta, A.A. Houck, D.I. Schuster, J. Majer, A. Blais, M.H. Devoret, S.M. Girvin, and R.J. Schoelkopf, *Charge insensitive qubit design derived from the Cooper pair box*, Phys. Rev. A **76**, 042319 (2007).

[47] J.A. Schreier, A.A. Houck, J. Koch, D.I. Schuster, B.R. Johnson, J.M. Chow, J.M. Gambetta, J. Majer, L. Frunzio, M.H. Devoret, S.M. Girvin, and R.J. Schoelkopf, *Suppressing charge noise decoherence in superconducting charge qubits*, Phys. Rev. B **77**, 180502(R) (2008).

[48] A. Wallraff, D.I. Schuster, A. Blais, L. Frunzio, R.-S. Huang, J. Majer, S. Kumar, S.M. Girvin, and R.J. Schoelkopf, *Strong coupling of a single photon to a superconducting qubit using circuit quantum electrodynamics*, Nature **431**, 162 (2004).

[49] D.I. Schuster, A. Wallraff, A. Blais, L. Frunzio, R.-S. Huang, J. Majer, S.M. Girvin, and R.J. Schoelkopf, *AC-Stark shift and dephasing of a superconducting qubit strongly coupled to a cavity field*, Phys. Rev. Lett. **94**, 123602 (2005).

B 3 New Developments in Spin Qubits[1]

L. R. Schreiber
II. Physics Institute
RWTH Aachen, University

Contents

1 Introduction **2**

2 Micro-magnets and Spin Qubits **2**
2.1 Coherent manipulation of a single electron spin by ESR 2
2.2 Gradient magnetic field generated by a micro-magnet 5
2.3 Electric dipole resonance using a micro-magnet 8
2.4 Single spin read-out using a micro-magnet 9
2.5 Two-spin read-out and manipulation using a micro-magnet 11
2.6 Micro-magnets and what else? 15

3 Alternative Material: Silicon-Germanium **15**
3.1 The quantization to start with 16
3.2 Si/SiGe heterostructures for quantum computation 16
3.3 Valley physics in Si/SiGe 18
3.4 Spin relaxation, decoherence and reduced hyperfine effects 19
3.5 Latest experimental progress in Si/SiGe 21

4 Summary **26**

[1]Lecture Notes of the 44^{th} IFF Spring School "Quantum Information Processing" (Forschungszentrum Jülich, 2013). All rights reserved.

1 Introduction

There is a zoo of solid-state spin quantum bit (qubit) systems and within this Springschool we have heard and will hear about many of them. The use of electron spins to define qubits has some common advantages, which are more or less pronounced in the individual spin qubit systems[1, 2]: (i) Electron spins are a natural two-level system, which couples only weakly to the solid state host (their environment). (ii) Due to its charge the electron can be localized in a quantum dot. (iii) The energy splitting of the two qubit states, e.g. the Zeeman energy, is much larger than the experimentally available electron temperature. This allows qubit initialization by energy relaxation into the ground state. (iv) Electrons are mobile in contrast to nuclei. This allows converting a spin state into a charge polarization or tuning the exchange interaction of two tunnel-coupled spins. Both are crucial to detect or couple spin qubit states.
For scaling up the number of qubits, a solid-state approach is promising. Charge fluctuations in the solid state do not couple directly to a localized electron spin, but a large number of nuclear spins (up to millions some systems) couple via the hyperfine contact interaction. The fluctuating nuclear spin bath is found to be the dominant source of electron spin decoherence, which is the loss of the qubit information.
Although there is progress in controlling the nuclear spin bath [3, 4] (see for example spin qubits in GaAs, chapter A6), there is large interest in solids with potentially a few or even zero nuclear spins. To achieve this, the solid has to consist of chemical elements with at least one isotope having zero nuclear spin. Most promising approaches are based on the group IV elements carbon C, silicon Si and germanium Ge. Examples for carbon-based systems are spin qubits in graphene, carbon-nanotubes (chapter D3) or color centers in diamond (chapter D2). Electron spin qubits can be localized at single dopants in silicon. Here we will focus on electron spins, which are trapped in electrostatically defined quantum dots in a Si/SiGe heterostructure. This is the nuclear spin-free analog to the successful GaAs/AlGaAs system discussed in chapter A6.

2 Micro-magnets and Spin Qubits

Next to increasing the available coherence time, it can be equally helpful to achieve faster qubit operations. After all, in order to judge the potential of a system for quantum computation, the decoherence time has to be compared with the time scale of qubit initialization, manipulation and detection. One way to speed up manipulation and enable new detection and manipulation schemes is to engineer a micro-magnet, which generates a static inhomogeneous magnetic field across the quantum dots. Before introducing these new schemes involving a micro-magnet, we briefly review the first experimental demonstration of coherent single electron spin manipulation in GaAs (cmp. chapter A6)

2.1 Coherent manipulation of a single electron spin by ESR

In their influential paper Ref. [5], Daniel Loss and David DiVincenzo propose to use electron spins localized in a linear array of semiconductor quantum dots as qubits. Each electron defines one qubit. The array can be realized in a two-dimensional electron gas (2DEG) with a metallic depletion gate-pattern as depicted in Fig. 1. The tunnel coupling between two adjacent dots that are occupied by one electron each leads to an exchange interaction between the electron

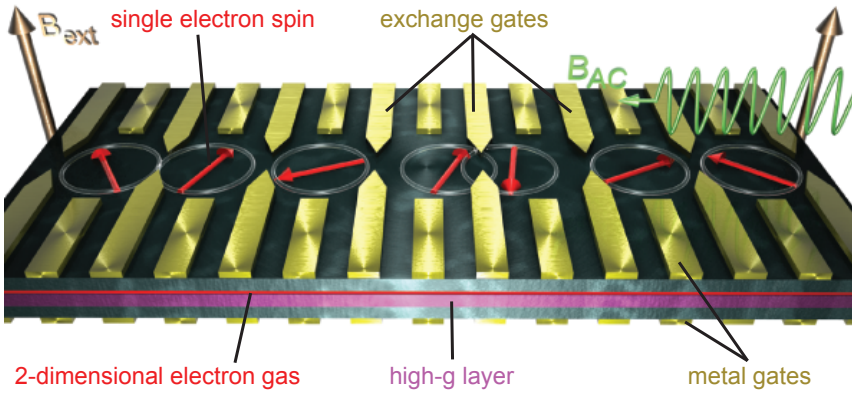

Fig. 1: *A scalable (solid-state) electron spin quantum computer according to Ref. [5]. The electron spins (red arrows) in a 2DEG (red layer) are localized in a lateral quantum dot array defined by metallic gates (gold). Ramping up the voltage on the exchange gates, reduces the interdot tunnel barrier and switches on the exchange interaction between adjacent spins. Electron spin resonance is used to manipulate single electron spins by means of an alternating magnetic field B_{AC}. Ramping up the voltage on individual backgates pulls the electron wave function into a layer (violett) with different electron g-factor. This local change of the ESR frequency allows addressing of individual spins. (Adopted from [2])*

spins. This interaction is controlled by the so-called exchange gates and is the bases for two-qubit gates. Bursts of alternating magnetic fields applied to certain dots reorient individual spins via electron spin resonance (ESR), thereby achieving single-qubit gates. Thus, together with a suitable spin detection scheme, arbitrary quantum algorithms can be executed.
For the demonstration of single qubit operations[6], two tunnel-coupled dots (a double dot) were formed in the GaAs 2DEG by the gate pattern shown in Fig. 2a. On top of the metallic gates isolated by a dielectric layer a relatively massive radio-frequency (RF) gold antenna was placed (Fig. 2b). In the experiment a bias was applied between the left and right electron reservoirs surrounding the double dot and the current I_{dot} across the double dot was measured (Fig. 2a). Applying an RF current I_{CPS} to the antenna, a sudden increase in I_{dot} is detected, if the ESR condition is fulfilled, i.e. if the RF frequency ω_{RF} matches the Zeeman energy E_Z of the dots given by an applied homogeneous magnetic field B_0:

$$\hbar\omega_{RF} = E_Z = g\mu_B B_0, \tag{1}$$

where g and μ_B are the effective electron g-factor of the dots and the Bohr magneton, respectively. Fulfillment of Eq. 1 can be clearly seen from the V-shape of the detected signal in Fig. 2c.
I_{dot} is sensitive to the ESR, since the double dot is tuned into Pauli blockade [7] (cmp. chapter A6). The right dot is occupied by an electron spin in the ground state. If the electron, which tunnels from the left reservoir onto the left dot is parallel to the first spin and thus forms a triplet state $T^+ = |\uparrow\uparrow\rangle$, it cannot tunnel further to the right dot, since the triplet state T_{02} is energetically unavailable and the singlet S_{02} is blocked due to spin conservation during tunneling (Fig. 3a). Only spin relaxation can slowly lift the Pauli blockade and thus I_{dot} is low. ESR lifts quickly the blockade (Fig. 3b) and I_{dot} is increased to ≈ 400 fA in Fig. 2c. (The peak at $B_0 = 0$ mT is the lifting of the Pauli blockade due to the nuclear spin bath [8]. It is independent from ESR.)
In a second experiment, RF-bursts are applied to the antenna on spin resonance, when both

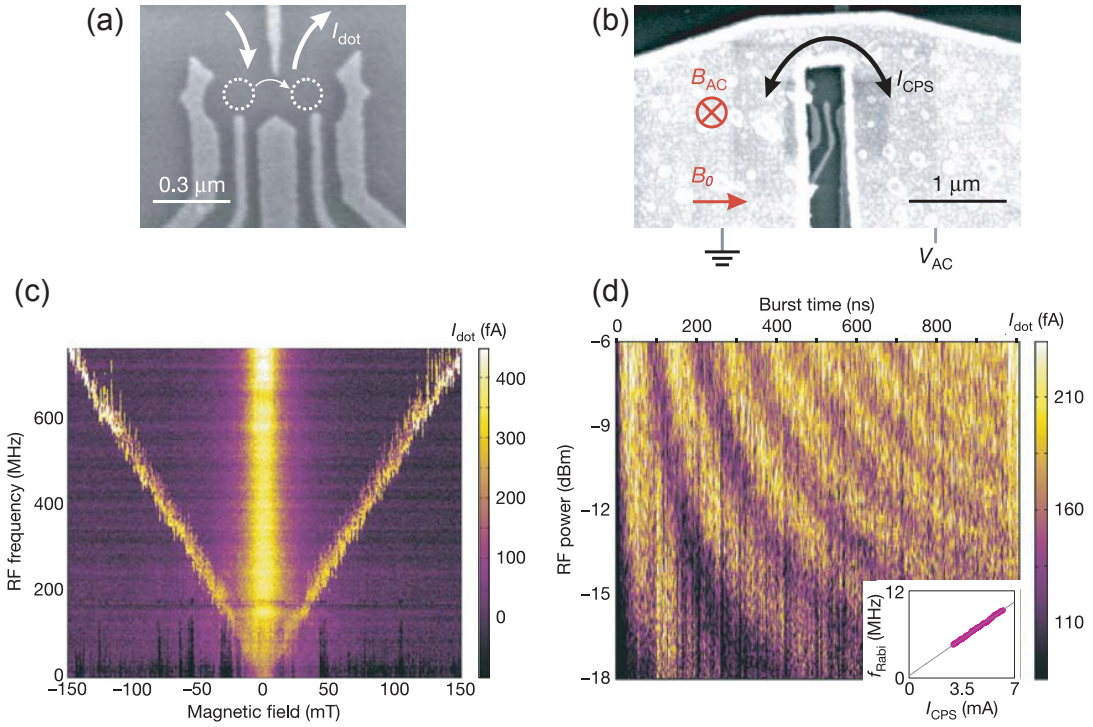

Fig. 2: *Coherent manipulation of a single electron spin by ESR. (a) Scanning-electron micrograph of the gate pattern defining a double quantum dot. (b) On top of the depletion gates, a massive antenna is fabricated generating the alternating magnetic field B_{AC}. (c) Current across the double dot as a function of magnetic field and RF frequency continuously applied to the antenna. (d) Current as a function of burst time and frequency. Inset: The dependency of the Rabi-frequency on the RF-current. (From [6])*

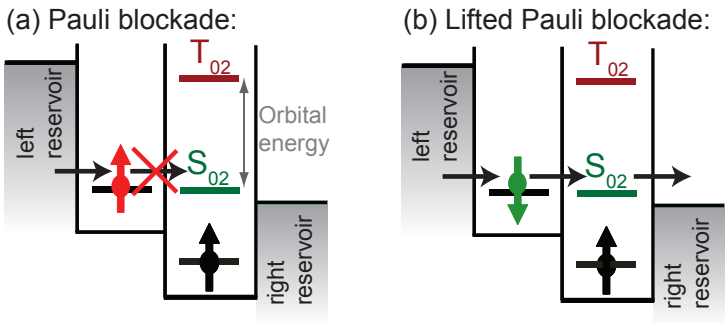

Fig. 3: *Spin-to-charge conversion by Pauli blockade. (a) The chemical potential of the left and right dot is tuned such that the $|\uparrow\rangle$ electron on the left dot cannot enter the right dot, because Pauli principle demands that it occupies an excited orbital (T_{02}), which is energetically forbidden. Thus, the current flow is blocked. (b) The left electron can pass the right dot via the (S_{02}). The Pauli blockade is lifted.*

electrons cannot escape the double dot irrespective of their spin state (Coulomb blockade). The pulsed alternating magnetic field B_{AC} coherently rotates one spin between the $|\uparrow\rangle$ and $|\downarrow\rangle$ state. Finally, after the B_{AC} burst, checking for Pauli blockade allows to read-out the spin state by means of I_{dot}. Indeed, the so-called Rabi oscillations were observed as a function of the burst length (Fig. 2d). As expected the Rabi frequency f_{Rabi} is proportional to the driving strength B_{AC} given by the current I_{CPS} applied to the antenna. Changing the relative phase of B_{AC} from one RF-burst to the next, allows to change the rotation axis. Therefore universal control of the electron spin is achieved.

Which electron spin is actually manipulated, the one in the left or the one in the right dot? To answer this question one should keep in mind that the lateral distance of the electrons is roughly 100 nm to obtain sufficient tunnel coupling. The bulky antenna, however, is placed approximately 200 nm above the 2DEG. Thus, it is impossible to address only one spin.

Why is it then possible to observe Rabi oscillations of a single electron spin? This is possible because of the fluctuating magnetic background originating from the nuclear spins in GaAs. These fluctuations are $\approx$ 3 mT and larger than the driving amplitude $B_{AC} \approx 1$ mT. They generate an unequal Zeeman splitting in the two dots so that only one of the two spins is on resonance. Since the fluctuations in the nuclear spin bath are much slower compared to the electron Rabi frequency, this one electron stays on resonance during the whole RF-burst. Since we cannot control the nuclear spin bath completely, we cannot exactly determine, which spin is addressed. This is unsatisfactory for quantum computing. The need for the antenna has more disadvantages: The antenna is difficult to fabricate, difficult to upscale and generates heat due to ohmic losses. In the next subsections a different approach is explained which is based on a micro-magnet.

2.2 Gradient magnetic field generated by a micro-magnet

In order to coherently manipulate and address single electron spins, which define a qubit each, a magnet with micrometer dimensions (a micro-magnet) can be fabricated on top of the sample. The local micro-magnet generates an inhomogeneous magnetic field

$$\mathbf{\Delta B} = \left(\Delta B_x^{\perp}, \Delta B_y^{\perp}, \Delta B_z^{\parallel}\right) \tag{2}$$

across the dot. The basic idea is to alternatingly displace the electron within this inhomogeneous magnetic field by an oscillating electric field so that in the electron's rest frame a B_{AC} appears driving coherent Rabi rotations. This technique was pioneered by the authors of Ref. [9, 10]. Let us assume an external magnetic field B_0 points in the z-direction, the component $\Delta B_z^{\parallel}$ sets the difference in Zeeman energy of the dots and thus the addressability for ESR. The perpendicular components $\Delta B_x^{\perp}$ and $\Delta B_y^{\perp}$ set the magnitude of B_{AC} and thus the manipulation speed. Before we go into the details of coherent manipulation of the electron spin with a micro-magnet, we have a look into some practical details.

It is important to engineer the micro-magnet such that $\mathbf{\Delta B}$ is optimized. In general a large $\mathbf{\Delta B}$ is desired. Thus ferromagnetic materials with large saturation magnetization $\mu_0 M_s$ are chosen. Although the samples are operated in a dilution refrigerator at ≈ 10 mK, materials with high Curie temperature T_C are preferred to avoid thermal fluctuations of the magnetization. Thermal fluctuations are a source of spin decoherence. To keep the evaporation of the micro-magnet simple, scientists focused on elementary or simple ferromagnets. Some of these materials are shown in the table:

Material	T_C ($^\circ C$)	$\mu_0 M_s$ (T)
Fe	768	2.19
Co	1121	1.82
Ni	360	0.64
$Fe_{0.2}Ni_{0.8}$ (Permalloy)	596	1.70
Dy (Dysprosium)	-188	3.7

Fe despite its high $\mu_0 M_s$, is less preferred since it oxidizes through the bulk, which is especially critical for microscale magnets. The micro-magnet (thickness ≈ 200 nm) and the metallic gates (thickness ≈ 30 nm) are both fabricated by electron beam lithography, but in two separated steps. Thus, the micro-magnet can only be positioned with a precision of ≈ 10 nm with respect to the metallic gate pattern. Additionally, the position of the electron wave function in the dot is influenced by unknown potential fluctuations in the 2DEG. The engineered $\mathbf{\Delta B}$ has to be robust against these alignment errors.

Fig. 4a displays a scanning electron micrograph of a GaAs sample with a double dot gate structure and two Co micro-magnets (yellow) on the top. An external magnetic field $B_0 \approx 1$ T is applied along the z-direction. This field is sufficient to nearly saturate the magnetization $\mathbf{M}_{\mathrm{Co}}$ of the Co in the same (in-plane) direction. By a spin resonance experiment, which will be explained in detail in the next section, the difference in the Zeeman splitting of the two dots was measured to be $\Delta B_z^{\parallel} = 15$ mT (Fig. 4b). The resonance peaks of the electron spin in the left (red) and in the right dot (blue) are clearly separated from each other. Thus, in contrast to the ESR experiment using only an antenna, the electrons in the left and the right dot can be addressed individually.

Fig. 4c-d display simulations of two components of $\mathbf{\Delta B}$. Compared to the geometry in Fig. 4a, the micro-magnet geometry (left insert in Fig. 4c) is further optimized by adding a third square to the left, which mainly generates the $\Delta B_z^{\parallel}$ component. The insert of Fig. 4d shows line-cuts of $\Delta B_z^{\parallel}$ along the y-direction, along which the two electrons in the double dot are positioned. Assuming a lateral electron separation of 100 nm, $\Delta B_z^{\parallel} = 10$ mT (blue dots) and $\Delta B_z^{\parallel} = 20$ mT (red dots) are found, if the distance between the 2DEG and the micro-magnet is 130 nm and 30 nm, respectively. In addition, the micro-magnet's stray field is composed of a slanted out-of-plane component $\Delta B_x^{\perp}$ mainly due to the opposing bar magnets. $\Delta B_x^{\perp}/\Delta z$ is

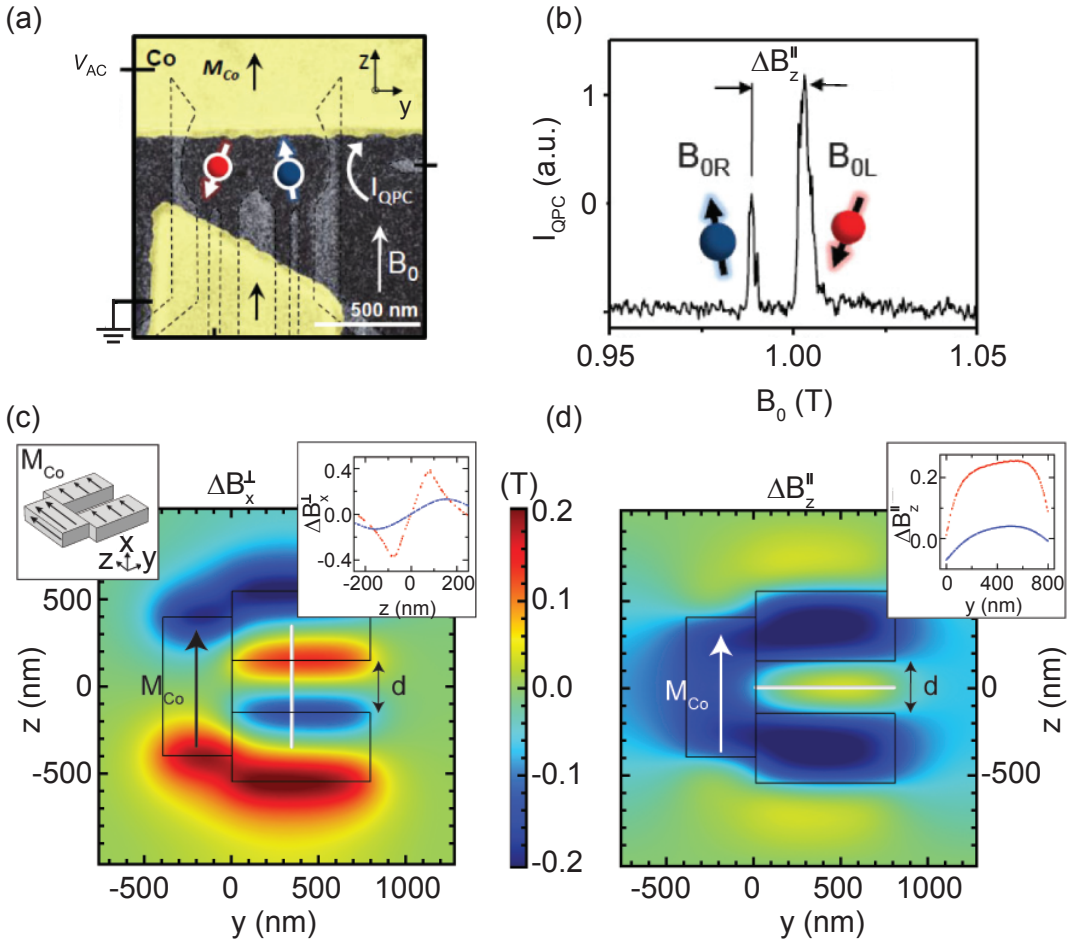

Fig. 4: *Stray magnetic field of a micro-magnet. (a) Scanning-electron micrograph of two Co micro-magnets on top of metallic gates (dashed lines). (b) Splitting of the resonances for the left and right dot due to the gradient magnetic field. (from [11]) (c) and (d) COMSOL simulations of the stray-magnetic field of the micro-magnet shown in the insert. The transverse (a) and longitudinal (b) gradient is plotted in the yz-plane of the 2DEG. Inserts are line-cuts along the white lines for a micro-magnet to 2DEG distance of 130 nm (blue) and 30 nm (red),respectively. (From [12])*

as large as 1.2 mT/1 nm (blue lines) or even 6.0 mT/1 nm (red dots) over a fairly large lateral distance.
Recently, nano-magnets were fabricated directly on top of one of the metallic gates. These single domain magnets are smaller, but can be fabricated closer to the electrons. However, their shape is set by the shape of the gate forming the dot thus letting less freedom of engineering the inhomogeneous magnetic field.

2.3 Electric dipole resonance using a micro-magnet

¿From the previous section, we know how to generate an inhomogeneous magnetic field across the gate-defined dots. In contrast to the ESR experiment in Fig. 2, it is sufficient to apply an alternating voltage V_{AC} to one of the micro-magnets (see Fig. 4a) to alternatingly displace the electron wave function in the z-direction. The slanting stray field component $\Delta B_x^{\perp}$ then creates the B_{AC} in the rest frame of the electron spin. Since B_{AC} is perpendicular to the external magnetic field B_0, the electron spin can be coherently rotated between $|\uparrow\rangle$ and $|\downarrow\rangle$, if the resonance condition (Eq. 1) is fulfilled. In contrast to the usual ESR experiment, this is called electric dipole spin resonance (EDSR) to point out that an electric driving field is required. The advantage of using an electric field is obvious: (i) It can be readily generated by the metallic gates or micro-magnets on the sample and (ii) it is localized.
Let us go into the details of qubit manipulation using EDSR: In analogy to the experiment shown in Fig. 2d, the double dot is first prepared with two electrons being in Pauli blockade (Fig. 3a). Thus each electron occupies one dot and the spins are parallel. Then the energy levels of the double dot are changed to Coulomb blockade so that none of the electrons can tunnel irrespective of their spin state. Next a V_{AC} burst is applied to shake the electron wave function in the z-direction. Finally, a quantum point contact (QPC) charge meter [13] (cmp. chapter A6) is used to check whether the Pauli blockade is lifted i.e. whether the two spins are anti-parallel. The measurement outcome is shown in Fig. 5a for two different magnetic fields.
It is important to note that in contrast to the ESR experiment in Fig. 2d, we know exactly which one of the spins is manipulated. Due to the $\Delta B_z^{\parallel}$ component of the micro-magnet' stray field exactly one spin is on resonance as confirmed by the two resonance peaks in the incoherent ESDR experiment (Fig. 4b). In the analog ESR experiment only one spin resonance is observed (Fig. 2c). The Rabi frequency of the spin in the right dot (lower graph in Fig. 5a) is smaller (at the same V_{AC}), because $\Delta B_x^{\perp}$ is smaller in the right dot due to the tappered form of the lower micro-magnet in Fig. 4a. This disadvantage is fixed by the micro-magnet geometry shown in the insert of Fig. 4c.
Due to the parabolic confinement of the quantum well, the voltage V_{AC} is proportional to the lateral electron displacement and thus proportional to the B_{AC} and to the Rabi frequency f_{Rabi}. Accordingly, a linear dependence of f_{Rabi} is found as a function of the square root of the microwave power applied to the micro-magnet (Fig. 5b).
A maximum Rabi frequency of 15 MHz in GaAs was reached [10]. More sophisticated micro-magnet geometries and larger V_{AC} can push the Rabi frequency to ≈ 100 MHz. In materials with larger g-factor (e.g. Si has a five times larger absolute g-factor than GaAs) the Rabi frequency increases then proportionally. For comparison: By ESR a maximum Rabi frequency of 10 MHz was achieved in GaAs[6].
The micro-magnet approach is scalable to a larger number of qubits as suggested in Fig. 6. The quantum dot array approach is motivated by the proposal shown in Fig. 1. It was estimated that up to eight electron spins can be addressed individually in GaAs. This estimation is based

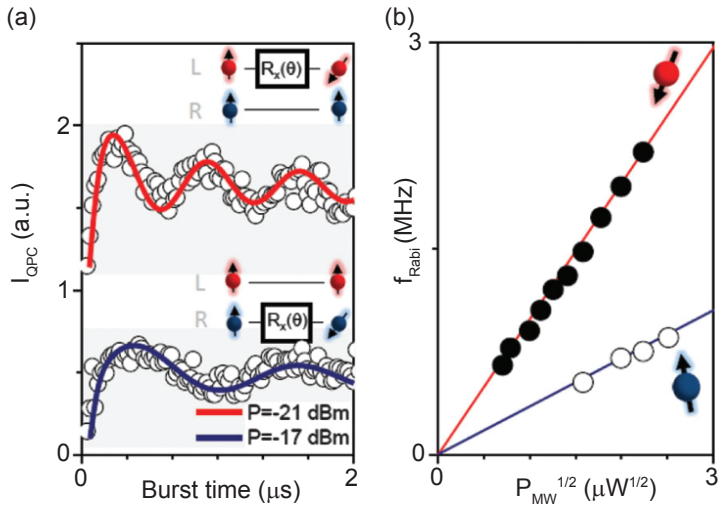

Fig. 5: *Coherent and dot-selective spin manipualtion by EDSR. (a) Rabi oscillations of the spin in the left (upper) and the right (lower) graph. The frequency was chosen according to the resonances shown in Fig. 4b. (b) Rabi frequency as a function of applied AC electric field for the left dot (filled dots) and the right dot (open dots). (From [11])*

on the width of the resonance, which is limited by fluctuating magnetic fields from the nuclear spin bath. Therefore it is expected that this number can be further increased in a nuclear spin free material (e.g. Si/SiGe). Another way to increase the number of qubits, is to increase the number of dot array blocks each equipped with their own micro-magnet.

2.4 Single spin read-out using a micro-magnet

Despite the coherent spin manipulation using EDSR, a micro-magnet can also be used to read out a single electron spin. Using Pauli blockade (Fig. 3) only the relative orientation (parallel spins vs. anti-parallel) of the two spins can be distinguished. In this section we will learn that it is possible to read out a single spin non-destructively making use of the inhomogeneous magnetic field component $\Delta B_z^{\parallel}$ of Eq. 2 [14, 15]. We have learned in chapter A6 that an electrostatically defined double dot can be detuned from a symmetric potential configuration to an asymmetric one by tuning the voltages of the top-gates. In this way the number of electrons (n, m) occupying the left (n) and the right (m) dot can be altered. Changing the detuning with microwave frequency ν ($h\nu$ has to be larger than the tunnel coupling of the dots), photon-assisted tunneling (PAT) is observed [1]. The electron tunnels between the dots by absorbing (or emitting) a microwave photon, which is resonant with the energy difference of the occupied state in the first quantum dot and the final, empty state in the second quantum dot.

In the presence of $\Delta B_z^{\parallel} \neq 0$, the Zeeman splittings E_{Zi} of quantum dot i are different by $g\mu_B \Delta B_z^{\parallel} = |E_{Z2} - E_{Z1}|$ (Fig. 7). Consequently, the PAT transition becomes spin selective: Applying only one frequency, only e.g. spin state $|\uparrow\rangle$ can tunnel. The PAT transition is detected by means of a QPC charge detector. Remarkably, this spin read-out scheme is non-destructive [14, 15] (i.e. the electron spin does not get lost). Fig. 7 shows a measurement performed at two different magnetic fields B_0. At $B_0 = 5$ T (down-pointing triangles), the spin is dominantly in its ground state $|\uparrow\rangle$ (due to spin relaxation), while it is in a mixed state of $|\uparrow\rangle$ and $|\downarrow\rangle$ at the lower magnetic field (up-pointing triangles). In the former case one and in the latter case two

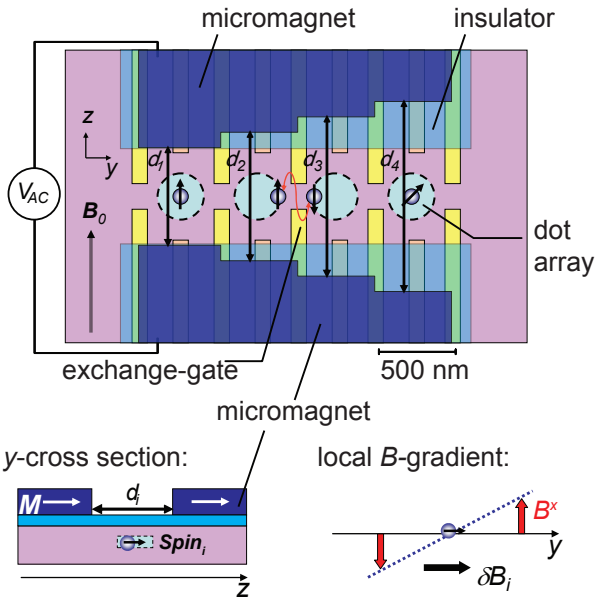

Fig. 6: *Quantum dot array design using micro-magnets. Isolated from the top-gates, two tapered micro-magnets on top of the dot array. The stray-field of the homogeneously magnetized micro-magnets create an inhomogeneous at the position of the dot enabling individual addressing by EDSR. (From the supplements in [9])*

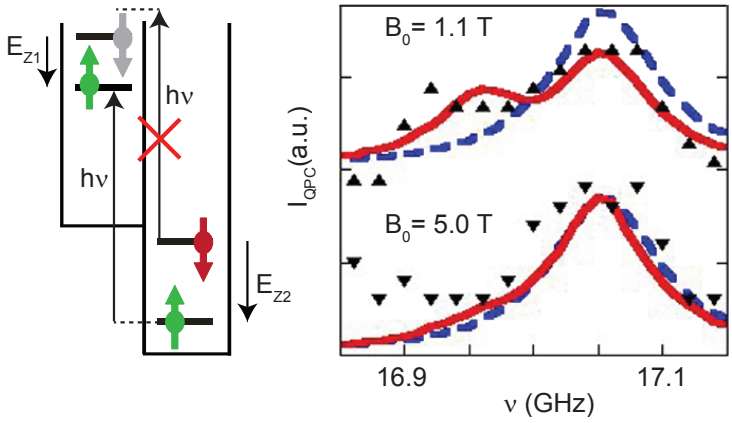

Fig. 7: *Single spin read out by PAT. The schematic on the left shown a double dot with differenz Zeeman-energies E_zi. At a fixed microwave frequency ν only one PAT transition is resonant. The current through a QPC charge detector is measured. (From [15])*

PAT peaks are observed demonstrating the working principle. The contrast between the two PAT peaks is poor, since a nickel micro-magnet with improvable geometry was used on the sample.

2.5 Two-spin read-out and manipulation using a micro-magnet

In the previous sections we discussed how a micro-magnet facilitates single spin coherent manipulation and non-destructive spin read-out. In this section, we expand the concept to two spins. They will be not addressed individually, but their two-spin state will be detected and manipulated. In this section we will have a closer look into the two-spin states of a double dot. Let us consider a doubled dot occupied with two electrons, which either occupy both the right dot or one dot each. In the former case the charge state is called $(0,2)$ and in the latter $(1,1)$. We choose a bases consisting of the following five spin/charge states

$$|\uparrow\uparrow\rangle\,(1,1);\ |\uparrow\downarrow\rangle\,(1,1);\ |\downarrow\uparrow\rangle\,(1,1);\ |\downarrow\downarrow\rangle\,(1,1);\ S(0,2),$$

where

$$S(0,2) \equiv \frac{1}{\sqrt{2}}\left(|\uparrow\downarrow\rangle - |\downarrow\uparrow\rangle\right)(0,2).$$

The $T(0,2)$ states are higher in energy due to Pauli exclusion principle and will not play a role here (cmp. Fig. 3).
In this bases the two electron Hamiltonian, which includes $\mathbf{\Delta B}$ from Eq. 2 and the singlet tunnel coupling t_s between $S(1,1)$ and $S(0,2)$, has the form [16]

$$\begin{pmatrix}
g\mu_B B_z & -g\mu_B\frac{\Delta B_x^\perp + i\Delta B_y^\perp}{2} & g\mu_B\frac{\Delta B_x^\perp + i\Delta B_y^\perp}{2} & 0 & 0 \\
-g\mu_B\frac{\Delta B_x^\perp - i\Delta B_y^\perp}{2} & -g\mu_B\Delta B_z^\parallel & 0 & g\mu_B\frac{\Delta B_x^\perp + i\Delta B_y^\perp}{2} & -t_s/\sqrt{2} \\
g\mu_B\frac{\Delta B_x^\perp - i\Delta B_y^\perp}{2} & 0 & g\mu_B\Delta B_z^\parallel & -g\mu_B\frac{\Delta B_x^\perp + i\Delta B_y^\perp}{2} & t_s/\sqrt{2} \\
0 & g\mu_B\frac{\Delta B_x^\perp - i\Delta B_y^\perp}{2} & -g\mu_B\frac{\Delta B_x^\perp - i\Delta B_y^\perp}{2} & 0 & \\
0 & -t_s/\sqrt{2} & t_s/\sqrt{2} & 0 & -\varepsilon
\end{pmatrix} \tag{3}$$

where, e.g., the Larmor precession frequency of an electron spin in the left dot is $g\mu_B(B_z - \Delta B^\parallel)$. Note that this Hamiltonian ignores spin-orbit and nuclear spin effects present in some semiconductors like GaAs. The double dot detuning energy ϵ is chosen, such that $\epsilon = 0$ at the singlet charge transition between $S(1,1)$ and $S(0,2)$.
To illustrate the meaning of this Hamiltonian the eigenstates and eigenenergies of the spin/charge states are plottet in Fig. 8a-c for an external magnetic field $B_0 = B_z = 400$ mT and $g = 2$. For a moderate $\Delta B_z^\parallel = 20$ mT, the eigenstates of the $(1,1)$ charge state are $S \equiv \frac{1}{\sqrt{2}}\left(|\uparrow\downarrow\rangle - |\downarrow\uparrow\rangle\right)$ (green) and the triplets $T^+ \equiv |\uparrow\uparrow\rangle$,$T^- \equiv |\downarrow\downarrow\rangle$ and $T^0 = \frac{1}{\sqrt{2}}\left(|\uparrow\downarrow\rangle + |\downarrow\uparrow\rangle\right)$ (red). These eigenstates are governed by the exchange interaction, which is a result of the tunnel coupling t_s. The triplet states are independent from ϵ around $\epsilon = 0$, since only the $S(1,1)$ state is tunnel-coupled to the $S(0,2)$ state as can be seen from the large anti-crossing. (Note that the energy scale is defined such that the (1,1) charge state is independent from ϵ.) The colorshading indicates that the eigenstates just at the anti-crossing are superpositions of $S(1,1)$ and $S(0,2)$. If $\Delta B_{x,y}^\perp \neq 0$, also the states $T^+(1,1)$ and $T^-(1,1)$ couple with singlet $S(1,1) + S(0,2)$, as can be seen from the two anti-crossings appearing in Fig. 8b. If $\Delta B_z^\parallel$ is large compared to the exchange interaction, the eigenstates are dominantly $|\uparrow\downarrow\rangle$ and $|\downarrow\uparrow\rangle$, which both anti-cross with the singlet state (Fig. 8c).

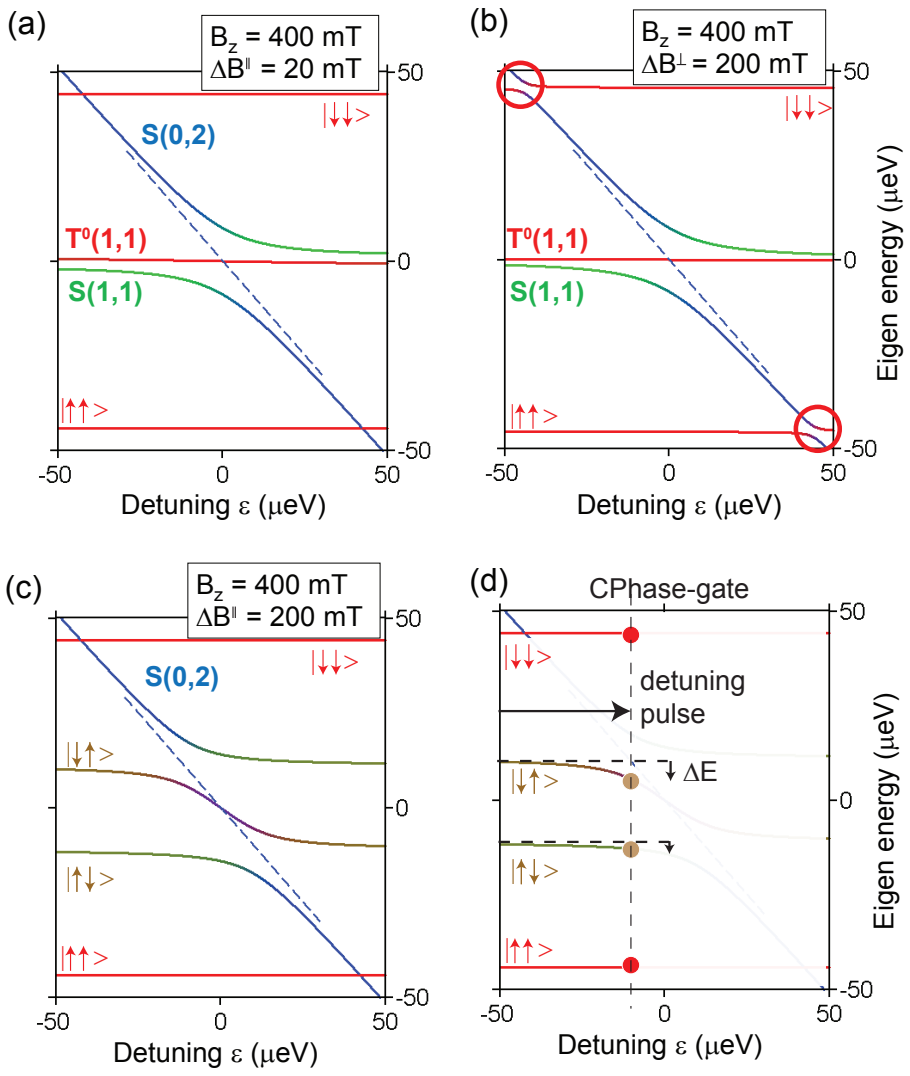

Fig. 8: *Eigenenergies of a double dot occupied with two electrons including spin. The eigenstate is color-coded according to contributions from $S(1,1)$ (green), $T(1,1)$ (red) and $S(0,2)$ (blue). Eigenstates and eigenenergies are calculated from Hamiltonian Eq. 3 using $g = 2$. The dashed lines indicate the $S(0,2)$ eigenenergy for zero tunnel-coupling. (d) is a copy of (c) with only the relevant states of the operations of the $CPhase$-gate shown.*

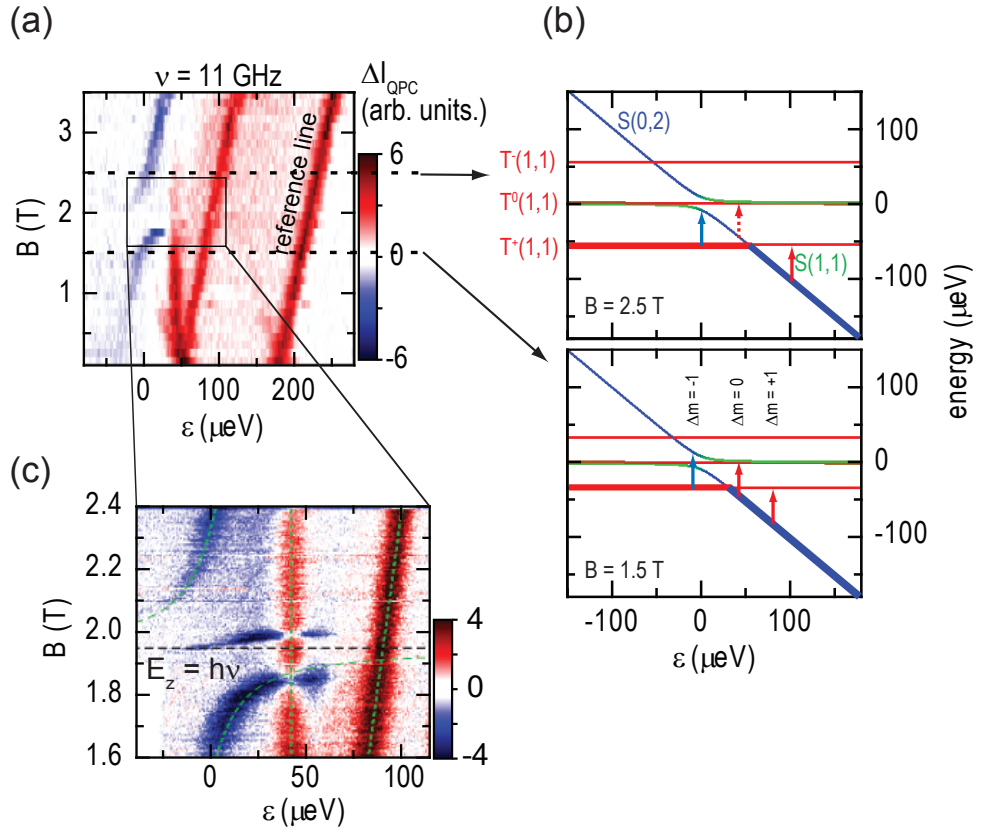

Fig. 9: *Spectrum of photon-assisted tunneling as a function of detuning ϵ and external magnetic field B. Transitions from charge ground state (0,2) to excited state (1,1) (red) and vice versa (blue) are observed. (b) Energetically allowed transitions are indicated by vertical arrows connecting eigenenergies of the two-spin states for two magnetic fields. The thick line indicates the ground state. (c) Zoom-in of the rectangular region in (a) showing a PAT transition, which deviates from the expectation (dashed-line) due to an inhomogeneous magnetic field component. (From [16])*

Similar to the single spin read-out discussed in the previous section, it is possible to read out the two-spin states by photo-assisted tunneling. The experiment was performed in a electrostatically defined double quantum dot in GaAs with a cobalt micro-magnet and a QPC charge meter [16]. Modulating the detuning with a fixed microwave frequency ν, a complex spectrum of transitions between the $(0,2)$ and the $(1,1)$ charge state was observed as a function of the detuning ϵ and the external, homogeneous magnetic field B (Fig. 9a). The photon energy $h\nu$ matches the energy difference of the initial and final electron state. Thus, the electron absorbs or emits exactly one photon. Remarkably however, the spin state is not conserved during the tunneling process. Transitions e.g. from $S(0,2)$ to $T^+(1,1)$ (the magnetic quantum number m changes by +1) could be identified by their slope as a function of B and ϵ (Fig. 9a-b).

As a consequence the eigenergies of the two-electron states as displayed in Fig. 8a, can be imaged easily and important properties such as the tunnel coupling t_s and the electron g-factor g from Eq. 3 can be fitted directly from the PAT spectrum. Even $B^{\|}$ is determined from a PAT resonance involving the $T^0(1,1)$ state. The $T^0(1,1)$ becomes mixed with $S(1,1)$ by $B^{\|}$ and thus obtains a small dependence on ϵ observed in Fig. 9c. PAT transitions become visible, if the resonance condition of PAT (energy conservation) is fulfilled and if the initial state is occupied.

The latter condition allows to detect all four two-electron spin states, provided that ν and ϵ are chosen appropriately in order energetically resolve the corresponding PAT transitions.
Resonant microwave radiation also enables the coherent manipulation of states in the $(1,1)$ charge manifold, which constitutes two-qubit gates. In the GaAs sample spin-orbit coupling was found to dominate the breaking of spin conservation during PAT. However, in materials with low spin-orbit coupling, a micro-magnet can be used to provide the required coupling within the $(1,1)$ spin manifold.
Another proposal [17] uses the inhomogeneous magnetic field of a micro-magnet to implement an efficient controlled phase ($CPhase$) gate in a double dot. This gate multiplies a phase factor $\exp(i\phi)$ to the state of the second qubit, if and only if the first qubit is in state $|1\rangle$. We have already heard that another two-qubit gate, the $\sqrt{SWAP}$ gate, can be implemented in a double dot by exchange interaction (Fig. 1 and cmp. chapter A6). Although the $\sqrt{SWAP}$ gate together with single gate operations forms a universal set of gates, the $\sqrt{SWAP}$ is barely employed for quantum algorithms. The $CPhase$ gate and especially one of its subtypes the $CNOT$ gate (the CPhase gate with $\phi = \pi$), are very often required directly in quantum algorithms. It is thus significant to realize the $CPhase$ as efficient as possible. We need for example two $\sqrt{SWAP}$ and three single qubit operations to compose a $CNOT$-gate.
For the efficient $CPhase$ a large and stable $\Delta B_z^{\|}$-component of the inhomogeneous magnetic field is required, so that we obtain two-electron spin eigenergies as plotted in Fig. 8c. Let us assume the double dot is detuned to negative ϵ deep into the $(1,1)$ charge region, where the spin eigenstates are (exchange energy J is negligible small)

$$|\uparrow\uparrow\rangle\,;\ |\uparrow\downarrow\rangle\,;\ |\downarrow\uparrow\rangle\,;\ |\downarrow\downarrow\rangle \tag{4}$$

If we pulse adiabatically towards positive ϵ and back as sketched in 8d, only the anti-parallel spin states $|\uparrow\downarrow\rangle\,;\ |\downarrow\uparrow\rangle$ are lowered in energy by $\Delta E(\epsilon)$ (compared to the parallel spin states) and thus accumulate a phase factor $\exp(i\Delta E(\epsilon)\tau/\hbar)$, where τ is the time the system is positively detuned. (To be precise, we have to integrate the phase over the whole pulse including the ramps.) Thus the pulse is described by the following unitary transformation in the bases of Eq. 4

$$\begin{pmatrix} 1 & 0 & 0 & 0 \\ 0 & \exp(-i\phi_1) & 0 & 0 \\ 0 & 0 & \exp(-i\phi_2) & 0 \\ 0 & 0 & 0 & 1 \end{pmatrix} \tag{5}$$

Up to the single z-rotations

$$\begin{pmatrix} 1 & 0 \\ 0 & 1 \end{pmatrix} \otimes \begin{pmatrix} 1 & 0 \\ 0 & \exp(i\phi_1) \end{pmatrix} \text{and} \begin{pmatrix} 1 & 0 \\ 0 & \exp(i\phi_2) \end{pmatrix} \otimes \begin{pmatrix} 1 & 0 \\ 0 & 1 \end{pmatrix}$$

this is equal to

$$\begin{pmatrix} 1 & 0 & 0 & 0 \\ 0 & 1 & 0 & 0 \\ 0 & 0 & 1 & 0 \\ 0 & 0 & 0 & \exp(i\phi_1+\phi_2) \end{pmatrix} \tag{6}$$

In this system, z-rotations can be absorbed into the phase of subsequent single-spin $x-$ or y-rotations. Thus, $CNOT$ is practically realized in one step with $\phi_1 + \phi_2 = \pi$.

2.6 Micro-magnets and what else?

The inhomogeneous magnetic field of micro-magnets can be used to coherently manipulate spins by electric fields (ESDR) and to address single spins. Single-spin and two-spin state read-out as well as more sophisticated two-spin manipulation schemes e.g. an efficient $CPhase$-gate are facilitated.
In some material systems other coupling mechanisms can replace the functionality of the micro-magnet. In GaAs [18] and especially in InAs [19], spin-orbit interaction can be used to drive EDSR. In InAs the g-factor can be tuned by the dot-size, such that a relevant effective $\Delta B_z^{\|}$ can be created in an unequally sized double dot in an homogeneous magnetic field. Incoherent EDSR due to the fluctuating nuclear spin was observed as well [20, 21]. An effective inhomogeneous magnetic field can also be created by polarizing and stabilizing the nuclear spin bath [3]. However, complex and time-inefficient pulse schemes are required for this procedure. Additionally, quantum processing and control of the nuclear spin bath cannot be executed simultaneously. Thus, the nuclear spin bath fluctuates and depolarizes during quantum operations generating errors.
For some spin qubit experiments nuclear spins are even required. Let us assume there is no hyperfine interaction in the ESR experiment we discussed in the very beginning of the chapter (Fig. 2). Then either both or none of the two electrons in the double dot are on resonance. Since the electrons are very close compared to the antenna, the antenna drives both spins with nearly the same Rabi frequency. The Pauli blockade initializes the spins in a triplet state. However, driving both spins with equal Rabi frequency preserves the spin triplet subspace and Pauli blockade is never lifted by the driving. Thus, the spin-to-charge conversion malfunctions. So the nuclear spins and the hyperfine interaction is required to make the experiment work. A micro-magnet does provide the required addressability of the spins. Therefore, combining a nuclear spin-free material with a suitable micro-magnet renders an ESR experiment with Pauli blockade possible.
There is large interest in materials with low intrinsic coupling of the spin to the environment, e.g. due to hyperfine or spin-orbit interaction. Spins exhibit long spin relaxation and coherence times in these materials. (We have a closer look at one of these materials in the next section.) However, in order to manipulate the qubit, coupling with the environment is required. Micro-magnets render it possible to engineer the type and strength of this coupling.

3 Alternative Material: Silicon-Germanium

Silicon has become a highly interesting chemical element for electron spin based quantum computation [22, 23]. The spin relaxation and dephasing times are both long in silicon, since the spin-orbit interaction and the hyperfine coupling is small in this material. The latter can be further reduced by isotopical purification to achieve even longer coherence times. Silicon like all elements of group IV (e.g. carbon and germanium) has at least one isotope with zero nuclear spin. In bulk silicon with a ^{29}Si fraction of less than 50 ppm, a donor electron spin coherence time of 2 s was observed. In contrast III-V semiconductors (e.g. GaAs) have no isotope with zero nuclear spin and electron spin decoherence due to the randomly fluctuating nuclear spin bath is one of the dominant sources for spin decoherence.
In addition, silicon is highly compatible with standard silicon-based electronics, which will be required for embedded circuits controlling the quantum computing part. Since it is implemented in a solid, a scalable architecture is possible to integrate several hundred of qubits on a chip.

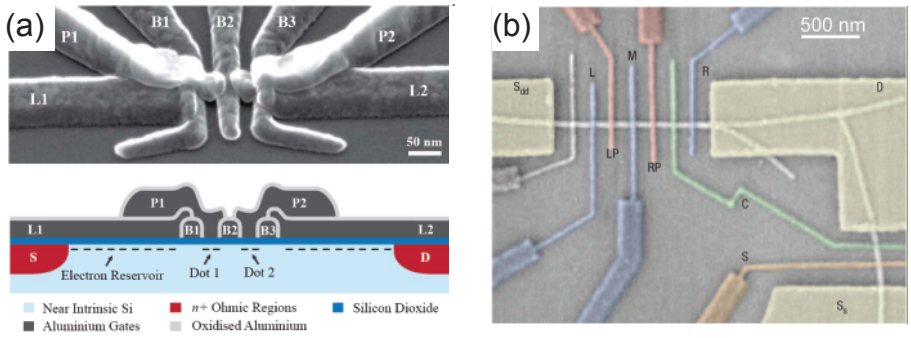

Fig. 10: *Scanning-electron micrographs of SiGe dot systems. (a) MOS structure with complex metallic gate pattern to induce electrons and form dots. (From [24]) (b) Ge/Si core/shell wire (white) with gates to confine hole spins. (From [25])*

3.1 The quantization to start with

There are different approaches to localize spins in a SiGe heterostructure: Self-assembled Ge nanocrystals (with diameter down to 10 nm) are grown on a Si substrate. Their confinement potential traps holes in Ge in all space directions (0D confinement), but it is difficult to tune post growth. Single phosphor dopants in Si provide strong 0D electron confinement and successfully combine electron and single nuclear spins (cmp. B1). In Si/Ge quantum wires, charges are trapped in a 1D confinement. Thus an array of metallic gates is required to localize the charges to 0D. The metallic gates on the other hand provide the required tunability of the confinement. Such a germanium core/silicon shell wire is displayed in Fig. 10b. It traps hole spins exhibiting no hyperfine interaction, but a large spin-orbit coupling. The latter can be useful for EDSR [26] (see the previous section). Finally, one can start with a quantum well and use a 2D top-gate pattern to electrostatically form the quantum dots. This approach requires many gates, but offers the highest flexibility in tuning and allows arranging the quantum dots in a 2D plane.

As established by standard CMOS technology, a 2DEG is formed in the inversion layer of the silicon/silicon-oxid interface. This 2DEG can also be employed to form quantum dots [24, 23] as shown in Fig. 10a. The metallic gate structure is complex and delicate to fabricate. It consists of negatively biased depletion gates B forming barriers. The other gates are positively biased to induce charges at the silicon/silicon-oxid interface. In such a double dot Pauli blockade could be observed, but so far it was not possible to trap exactly two electrons in a double dot.

A quantum well is also formed by growing a heterostructure of Si and SiGe layers. In such a heterostructure (Fig. 11b), electron quantum dots are electrostatically defined in analogy to the GaAs/(Al,Ga)As samples (Fig. 11a) we heard about in chapter A6. In the following we are going to learn more about these samples, challenges and progress towards silicon quantum computing.

3.2 Si/SiGe heterostructures for quantum computation

Si/SiGe heterostructure can be grown with high quality by molecular beam epitaxy or chemical vapor deposition. Si and Ge both crystallize in the diamond lattice with a lattice mismatch of 4% [27]. To grow them epitaxially without interface defects, we first grow a stoichiometric mixture of strain-relaxed $Si_{1-x}Ge_x$ with slowly increasing Ge content up to $x = 0.3$ on a silicon wafer. The following ≈ 10 nm thick Si layer sandwiched between $Si_{0.7}Ge_{0.3}$ layers is tensile

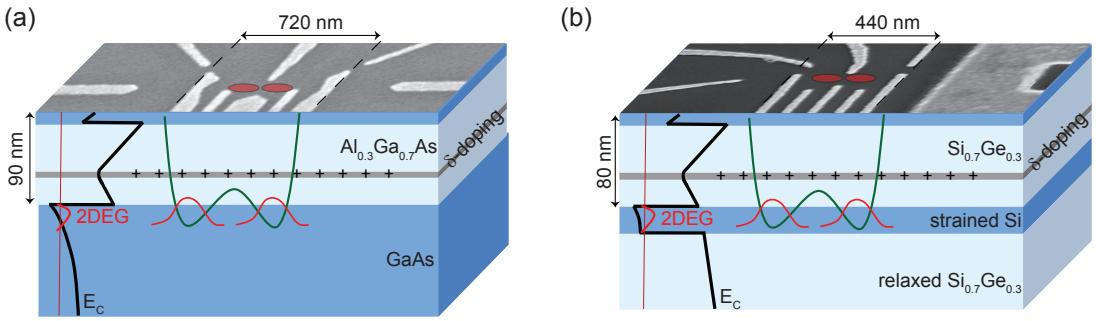

Fig. 11: *Comparison of electrostatically defined quantum dots in GaAs and Si. The layer structure of a doped GaAs/(Al,Ga)As (a) and Si/SiGe (b) heterostructure with corresponding conduction band E_c forming a 2DEG. On top: Scanning electron micrographs of gate patterns used to define double dots in the 2DEG.*

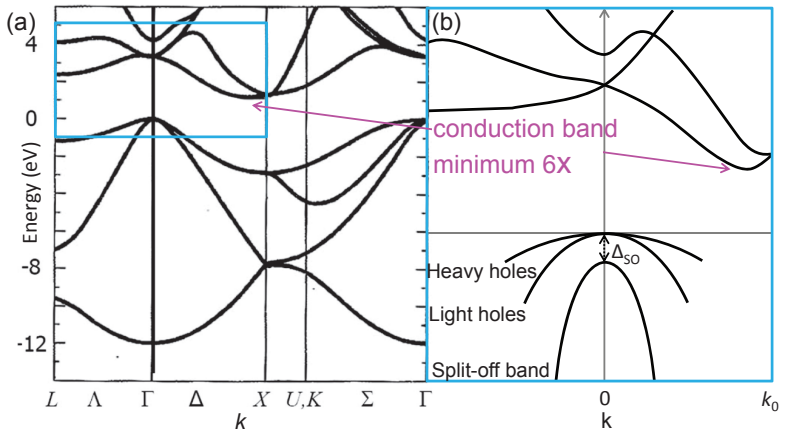

Fig. 12: *(a) Band structure of bulk silicon. (b) Zoom-in of the transport relevant bands.*

strained. The electrons are confined in this strained Si layer with $Si_{0.7}Ge_{0.3}$ barriers forming the quantum well (see the conduction band E_c in Fig. 11b). (Note that Si has a larger bandgap than Ge, but forms a so-called type II interface with Ge having a negative electron band offset. Thus, Si/Ge heterostructures confine electrons in Si and holes in Ge.)

Crystalline silicon (in contrast to GaAs) has an indirect band gap and the conduction band minimum (valley) is six times degenerate (Fig. 12). Due to the biaxial tensile strain in the $Si/Si_{0.7}Ge_{0.3}$ heterostructure this degeneracy is partly lifted and split by $\Delta E_c \approx 200$ meV (Fig. 13a and b). The two valleys with $\mathbf{k}$ in z-direction (the growth direction of the heterostructure) remain lowest in energy. The remaining valley degeneracy greatly complicates experiments, since it can lift the Pauli blockade (see Fig. 3): There is a $T(0,2)$ state with both electrons occupy the same orbital but different valleys. Therefore, the $S(0,2)$ and $T(0,2)$ states have about the same energy. Fortunately, there exists a mechanism that can lift the valley degeneracy completely (as we will see in the section).

Another challenge is the relatively large (transverse) electron mass of the z-valleys, which is 0.19 times the free electron mass. This is three times larger than the GaAs effective electron mass. A large electron mass, and thus a short de Broglie wavelength requires smaller gate patterns to localize a single electron. Shrinking the gate patterns is limited by the resolution of the ebeam lithography. Fig. 11 gives an impression of realistic gate patterns for both systems.

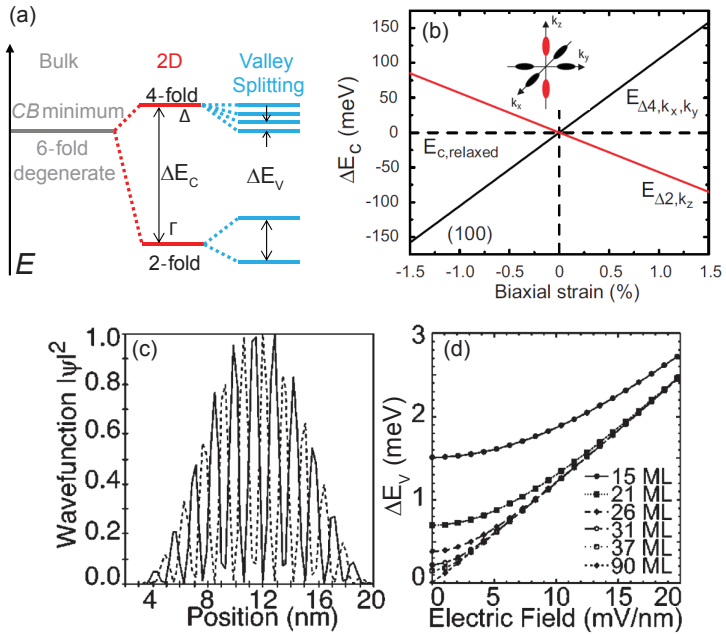

Fig. 13: *Lifting of the valley degeneracy in Si/SiGe. (a) Schematic of the liftung of the 6 fold valley degeneracy from bulk Si due to strain ΔE_c and confinement ΔE_v. (b) Valley energies under biaxial strain. (c) Symmetric and antisymmetric wave function in a quantum well in z-direction. (d) ΔE_v as a function of quantum well width and and applied electric field. (c-d From [28])*

Metallic gates on Si are made of palladium (not gold as used for GaAs), in order obtain a Schottky contact without leakage to the 2DEG at cryogenic temperature.
The advantages of Si/SiGe are (i) the small hyperfine coupling and the chance to remove the nuclear spin bath complectly, (ii) the low spin-orbit interaction and (iii) the large g-factor of $g = 2$ ($g = -0.44$ in GaAs). The large g-factor is a result of the small spin orbit splitting $\Delta_{SO} \approx 40$ meV (Si is a small atom) and the relatively large band gap $E_g = 1.12$ eV (see Fig. 12). The large g-factor speeds up the manipulation of the spin by means of a homogeneous magnetic field from a micro-magnet. Small coupling with the environment due to (i) and (ii) lead to long spin relaxation and coherence times (as will be discussed below).

3.3 Valley physics in Si/SiGe

The valley splitting in the Si/SiGe heterostructure can be understood from tight-binding calculations and theories that use an effective mass formalism [23]. Using the former approach, the symmetric and anti-symmetric electron wave function is calculated along the quantization z-direction of the quantum well [28] as plotted in Fig. 13c. The wave function results from the mixing of the two z-direction valleys at the two Si/SiGe interfaces. The interfaces break the translational symmetry in the z-direction. The overlap of the wave functions with the potential of the quantum well barrier differs and therefore the wave function splits by the energy ΔE_v. This effect is more pronounced in narrow quantum wells (Fig. 13d). Due to the large k_z involved, the wave function oscillates at the atomic scale. This makes the valley splitting ΔE_v sensitive to alloy disorder in the SiGe barrier and interface disorder on an atomistic length scale. In addition, the valley splitting ΔE_v increases by applying an electric field perpendicular

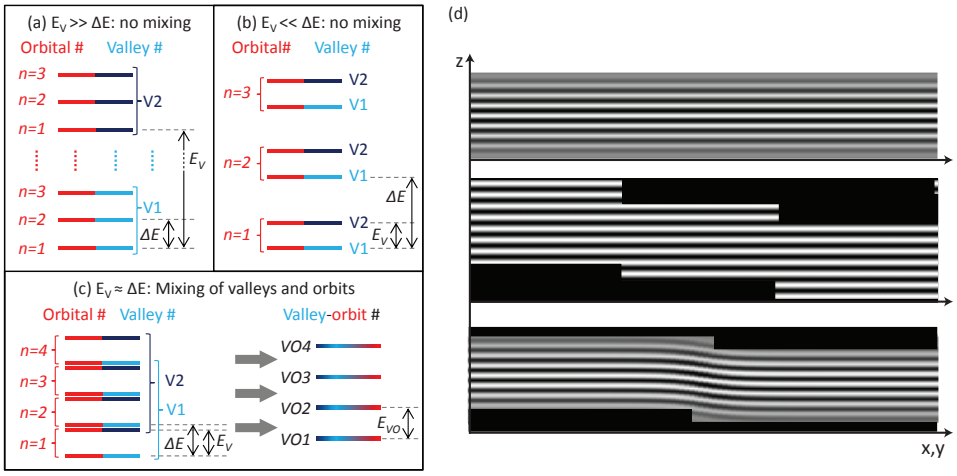

Fig. 14: *Valley-orbit mixing in Si/SiGe. (a-b) The value of the valley splitting $E_V = \Delta E_V$ and orbital splitting ΔE sets the energetic order of higher orbital and valley states. (c) For similar values mixed valley and orbit states are formed. (d) Sketch of the valley wave function (grey-scale) in three quantum wells (with z confinement) with different step density at the barrier (black) interface. (From [23])*

to the quantum well (Fig. 13d).
The good news is, the valley degeneracy can be lifted entirely as displayed in Fig. 13a. The bad news is that it is difficult to control the magnitude of ΔE_v, since it depends on atomistic details at the interface like atomistic steps. If ΔE_v has the same magnitude as the orbital splitting ΔE, valleys also mix with orbital states to valley-orbit states as displayed in Fig. 14a. The interplay of valley splitting and valley-orbit mixing visualized in Fig. 14b: If the quantum well has laterally flat barriers (top panel), the fast oscillating valley-wave function is translational symmetric along the quantum well plane. A high density of atomic steps at the barrier interface (middle panel), randomizes the phase of the valley wave function with respect to the barrier long the quantum well plane and ΔE_v is reduced. If the step density is low (bottom panel), the phase of the valley wave function aligns with the barrier, but becomes dependent on x and y coordinates. Thus, valley and orbital degrees of freedom become coupled.
It was reported that in a set of equally grown and fabricated Si/SiGe double dots, only some exhibit Pauli blockade [29, 30]. The likely reason is the irreproducibility of ΔE_v. If the dot is formed in a region of many atomistic steps $\Delta E_v \approx 0$. If Pauli-blockade worked, a singlet-triplet splitting of 0.1 meV to 0.2 meV was observed, which is the lower bound of ΔE_v and sufficiently higher than the electron temperature in a dilution refrigerator. Note that the dependence of ΔE_v on the local interface disorder, renders it possible to tune ΔE_v by shifting the electrostatically defined dot between a step-region and a flat barrier-region [31].

3.4 Spin relaxation, decoherence and reduced hyperfine effects

The relaxation time T_1 and the decoherence time T_2 are two important parameters describing the preservation of quantum information. The former T_1 describes the timescale, on which a qubit (or a qubit system) relaxes to its ground state. The latter T_2 describes the timescale on which the phase between quantum states is preserved (or follows the evolution given by the system Hamiltonian).

Relaxtion of a single electron spin in a silicon quantum dot involves photons to exchange energy with the solid. As a covalently bonded crystal, Si lacks piezoelectric effect, which is often the dominant relaxation process in III-V semiconductors (e.g. GaAs). The only type of phonons present in Si are deformation potential phonons. The alternating electric field generated by phonons cannot couple directly to the spin. It requires an additional coupling mechanism e.g. spin-orbit interaction. Spin-orbit interaction is small in Si, because Si has a relatively small atomic number and exhibits no bulk inversion asymmetry, so only Rashba type spin-orbit interaction is present. The corresponding relaxation time T_1 is proportional to B^{-7}, where B is the external magnetic field [1, 32].

There is a second spin relaxation mechanism in Si quantum dots: The deformation potential phonons induce strain, which modulates slightly ΔE_c (defined in Fig. 13) and the anisotropy of the electron g-factor. This can couple to the spin and yields a relaxation time $T_1 \propto B^{-5}$.

For both mechanisms spin relaxation is drastically enhanced by applying a large magnetic field. Experimentally, a $T_1 \propto B^{-7}$ was observed [33]. In a Si quantum dot $T_1 = 2.8$ s was observed at $B = 1.75$ T [34]. To get the same Zeeman energy in GaAs, a magnetic field of $B = 8$ T is required yielding only $T_1 = 0.85$ ms [35].

The main source of decoherence of electron spins in solid state is the coupling to the bath of nuclear spins in the host material. In an electrostatically defined Si/SiGe quantum dot of typical size, the electron couples to roughly $N_T = 10^5$ nuclei. In silicon with natural abundance of isotopes, $N_S = 4.7\% N_T$ nuclei carry a spin. ^{29}Si ($I = 1/2$) is the only stable Si-isotope with non-zero nuclear spin. The hyperfine coupling of the electron spin with the nuclear spin bath, can be expressed as an effective magnetic field, the Overhauser field with corresponding Zeeman-Energy AI, where I is the nuclear spin and A a measure of the hyperfine strength. Although the nuclear magnetic field is unpolarized on average, it fluctuates statistically. This yields a Gaussian distribution of Overhauser fields with a of width of $\delta AI = AI/\sqrt{N_S}$ [36, 37]. δA causes spin decoherence with timescale T_2^* due to spectral diffusion. (To measure T_2^* the electron spin dynamics has to be repeated on a timescale longer than the nuclear spin dynamics, which is typically the case.) The following table compares these parameters for Si/SiGe and GaAs electrostatically defined dots [37]:

Host	N_T	N_S	$A/(g\mu_B)$	δA	T_2^*
GaAs	10^6	10^6	3.6 T	92 neV	7.2 ns
natural Si	10^5	5000	1.85 mT	3.0 neV	0.22 μs
100% ^{29}Si	10^5	10^5	37 mT	13,6 neV	49 ns
0.01% ^{29}Si	10^5	10	3.7 μT	0.136 neV	4.9 μs

T_2^* is orders of magnitudes longer in Si than in GaAs. Note that $N_T = N_S$ is larger in GaAs, since the quantum dots are wider and all isotopes carry nuclear spin (most of them $I = 3/2$). A $T_2^* = 360 \pm 30$ ns was measured in electrostatically defined Si/SiGe double quantum dot [38]. Potentially much longer coherence times can be achieved by using echo techniques.

Remarkably, the number of nuclear spins in Si can be further reduced by isotopical purification. Very isotopically pure ^{28}Si was produced for the Avogadro project with only 0.005% of remaining ^{29}Si isotopes. In these quantum wells the electron is only coupled to about 10 nuclear spins. One also has to bear in mind that about 1% of the electron wave function overlaps with the $Si_{0.7}Ge_{0.3}$ barrier. Thus, there is an overlap with a small number of Ge nuclei as well. However, only 7.7% of these nuclear isotopes carry a spin in natural abundance. Isotopic purification of

Ge can lower this small fraction further to practically zero. A gate-defined double quantum dot in isotopically purified Si was already fabricated [39, 40].
The question arises: What limits the electron spin coherence, if the hyperfine coupling is reduced further and further. Another phenomenon that must be taken into account is the dipole-dipole coupling among electron spins. In a highly isotopically purified bulk silicon samples with phosphor donors, dipole-dipole coupling had to be taken into account to explain the measured spin decoherence time of the P-bound electron spins [41]. The dipole-dipole interaction yields flip/flops between two electron spins. This effect could be energetically suppressed by applying a gradient magnetic field. In this way a record T_2 value of $T_2 = 10$ s was found in silicon. [41].
So far we considered spin coherence, if no intentional manipulation is performed on the electron spin. During a quantum algorithm we also want to manipulate the spin. This is done by electrical means. It is thus unavoidable that the electron spin becomes sensitive to electronic noise from the metallic gates or from charge fluctuations in the sample, e.g. if we switch on the exchange interaction $J(\epsilon)$ for a two-qubit gate operation, where ϵ is the double dot detuning (see [42]). During exchange the spin phase is very sensitive to charge fluctuations randomizing ϵ. It will be seen in the future whether charge fluctuations become the dominant decoherence in silicon.
Nuclear spins are promising candidates for long-lived quantum memory, since they exhibit very long coherence times exceeding tens of seconds[43, 44]. If the electron spin is hyperfine coupled to only a small number of nuclear spins, the electron spin can swap preferably with only one initialized nuclear spin. This only makes sense with the time requires for the swap is shorter than the electron spin coherence time. Such quantum memories were already realized in NV centers in diamond and P:Si (see chapter D5), where the electron wavelength is very localized at the position of the nitrogen and the phosphor nuclear spin. It needs to be tested whether also in electrostatically defined Si/SiGe quantum dots the electron spin qubit information can be transferred on a few ^{29}Si nuclear spins.

3.5 Latest experimental progress in Si/SiGe

In this section the latest experimental progress on spin qubits in gate-defined Si/SiGe quantum dots is presented. One milestone experiment in the analog GaAs system was the single-shot read-out and initialization of one electron spin [35]. Later this measurement scheme was expanded to two-qubit single shot-read-out in a GaAs double dot [45] facilitating correlation measurements. The same single spin detection scheme was demonstrated for donor bound electron spins in P:Si [46] and briefly afterwards in a gate-defined Si/SiGe quantum dot [34].
The measurement scheme of the last experiment is plotted in Fig. 15. It is based on energy-dependent spin-to-charge conversion with the electron reservoir, a technique which is explained in details in chapter A6 for GaAs[35]. Therefore, we only mention here the Si specific features. First of all, the single-shot experiment can be done on a much longer time-scale than in GaAs due to the longer spin relaxation time in Si ($T_1 \approx 3$ s for the applied external magnetic field $B = 1.75$ T). In the dot a spin-split ground and the first spin-splitted orbital excitation is considered. The orbital exited state is not required for the spin read-out, but can be used to speed up the initialization: Loading only by tunneling into the spin-split ground (Fig. 15 a) is relatively slow. By lowering the chemical potential further during the loading state, the electron can also tunnel via the excited states and then relax fast to the ground orbital states (Fig. 15 b,c). This enhances the speed of the spin initialization procedure by one order of magnitude [34]. In

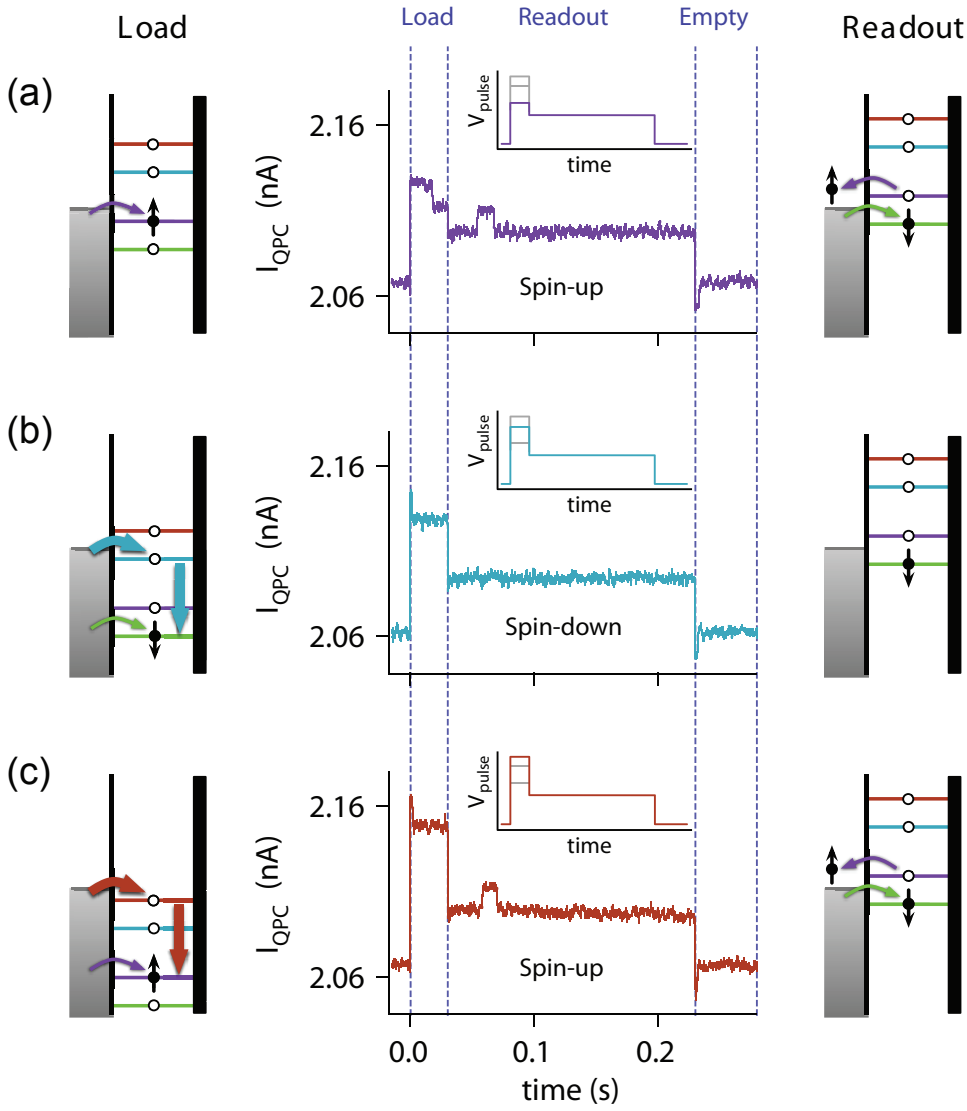

Fig. 15: *Spin loading and single-shot spin read-out in Si/SiGe. The position of the dot's chemical potential is plotted during the load and read-out stage. QPC current traces during one measurement cycle. The current bump during read-out is the signature of a spin-up electron. From (a-c) the loading scheme is altered. (From [34])*

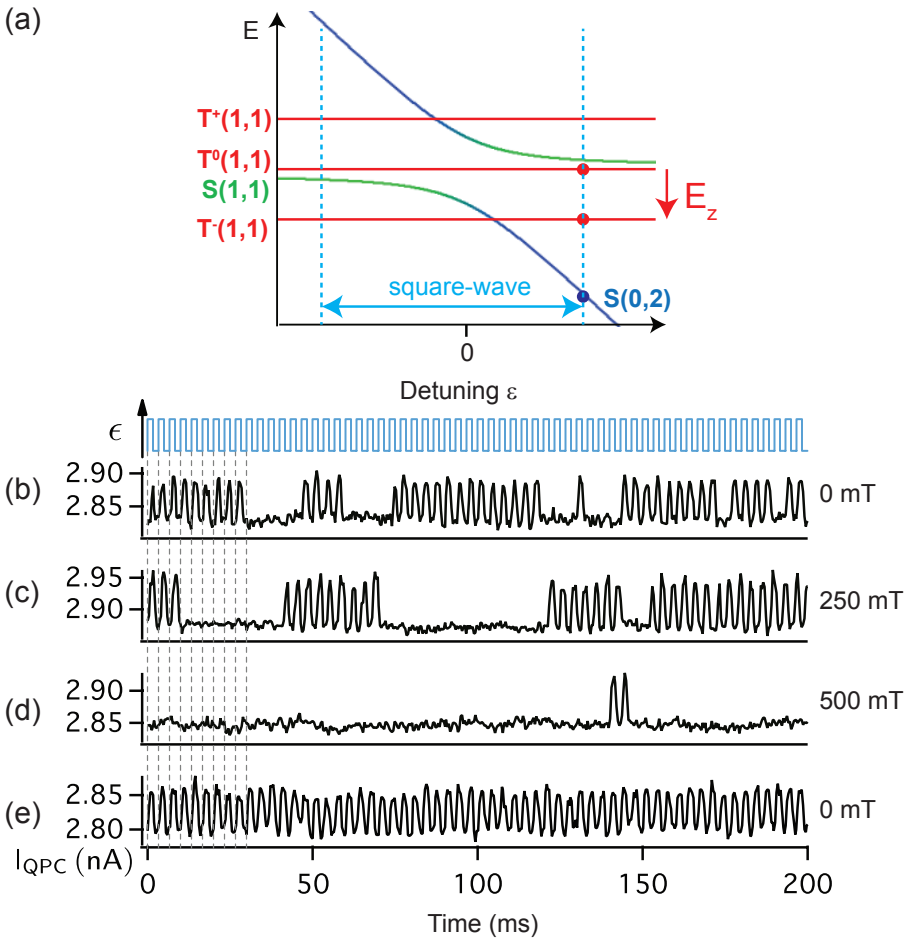

Fig. 16: *Real-time traces of electron tunneling demonstrating singlet-triplet relaxation in a Si/SiGe double quantum dot. (a) Relevant eigenenergies of the two-qubit states (cmp. Fig. 8). The double dot is repetitively detuned between the* $(1,1)$ *and* $(0,2)$ *charge state (dashed lines). (b-d) Real time traces of the QPC current during detuning pulses measured at different external magnetic fields. (e) like (b) but detuning pulses include the* $T(0,2)$ *state. (b-e from [47])*

addition, the electron spin is preferentially prepared into the $|\downarrow\rangle$ (spin ground state), by adjusting the chemical potential such that only the excited $|\downarrow\rangle$ orbital can be occupied (Fig. 15 b). Note that in Si the electron g-factor is $g > 0$, whereas it is $g < 0$ in GaAs. The spin ground state in Si (GaAs) is thus $|\downarrow\rangle$ ($|\uparrow\rangle$).

Next we have a look at two experiments done in gate-defined Si/SiGe double quantum dots. Both experiments are especially interesting in the context of ST^0 qubits (cmp. chapter A6). The ST^0 qubits states are defined by the two-spin singlet $S(1,1)$ and triplet $T^0(1,1)$ state. $(1,1)$ means that two electrons are involved which occupy one dot each. The energy difference of both states is set by the exchange energy in the double dot.

In Si/SiGe it is challenging to reach the exact two electron charge regime in a double dot. Due to both the relatively high electron mass and potential disorder, one dot tends to break up unintentionally in two dots as more and more electrons are repelled [48]. Another problem is that the tunnel barriers to the surrounding electron reservoirs become more opaque with lower dot occupation until the electrons become basically stuck on the dot [49, 50].

In the experiment described in Ref. [47] only two electrons occupy the double dot and by

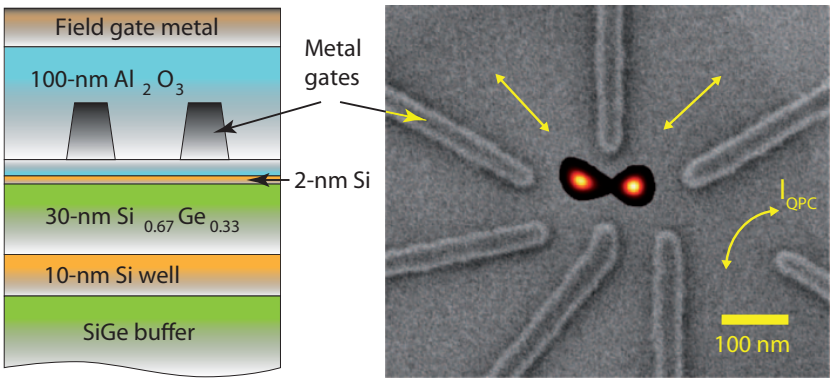

Fig. 17: *Si/SiGe sample used to demonstrate coherent sinlget-triplet manipulation. (a) Layer structure of the undoped sample with top accumulation gate. (b) scanning electron micrograph of the depletion gate pattern defining a double dot. A QPC charge meter is formed on the right hand-side. (From [38])*

detuning the double dot potential via the voltages on the top gates, the electrons can be either separated $(1,1)$ or occupy the same dot $(0,2)$. Pulsing the detuning ϵ back and forth using a 300 Hz square wave (Fig. 16), one electron tunnels between the dots. If the detuning range is appropriately chosen such that the double dot remains in the Pauli blockade regime (Fig. 16a, cmp. Fig. 3), the electron can only tunnel if the two spins form a singlet state. The triplet $T(0,2)$ state is energetically unavailable. The tunneling events are observed in real-time by means of a QPC charge detector [51]. (Here on the left hand-side of the double dot.) Therefore, it is possible to detect in a single shot, whether the spin state is singlet or triplet.

Real-time QPC current traces are plotted in Fig. 16b-e for different homogeneous, external magnetic fields. For some period of time, one can follow the electron tunneling triggered by the square wave. Some period of time the double dot is stuck in the $(1,1)$ charge state due to Pauli blockade. So the state switches (relaxes) between singlet and triplet state. Statistically, the time spend in the Pauli blocked regime increases with the increase of the external magnetic field (Fig. 16b-d). In the reference trace Fig. 16e, the pulsed detuning range is chosen such that the triplet $T(0,2)$ state becomes energetically available for positive detuning. Therefore, Pauli blockade is never observed and the electron tunneling always follows the square wave.

Statistically analyzing the periods of blocked and unblocked tunneling, a relaxation time of 10 ms for all triplets was found at $B = 0$ mT [47], which is two orders of magnitude larger than in GaAs [42, 52] due to the lower hyperfine coupling. At higher magnetic fields, electrons are dominantly blockaded in the $T^-(1,1)$ state, for which a life time of $T_1 \approx 3$ s at $B = 1$ T was calculated [47].

Just recently, first coherent control of singlet and triplet states was demonstrated in silicon [38]. The experiment was performed in an undoped gate-defined Si/SiGe double quantum dot. Its layer structure is depicted in Fig. 17a. Removing the doping layer reduces charge noise and potential disorder in the 2DEG (discussed in [53]) and allows to bring the 2DEG closer to the sample surface. Consequently, a smaller depletion gate pattern (Fig. 17b) is reasonable, which makes the double dot even less sensitive to long-range potential disorder. Since there is no doping layer, electrons are induced by a top accumulation gate (like in the MOS structure based qubits shown in Fig. 10a).

The experiment is analog to the coherent ST^0 manipulation experiment in Ref. [42] performed

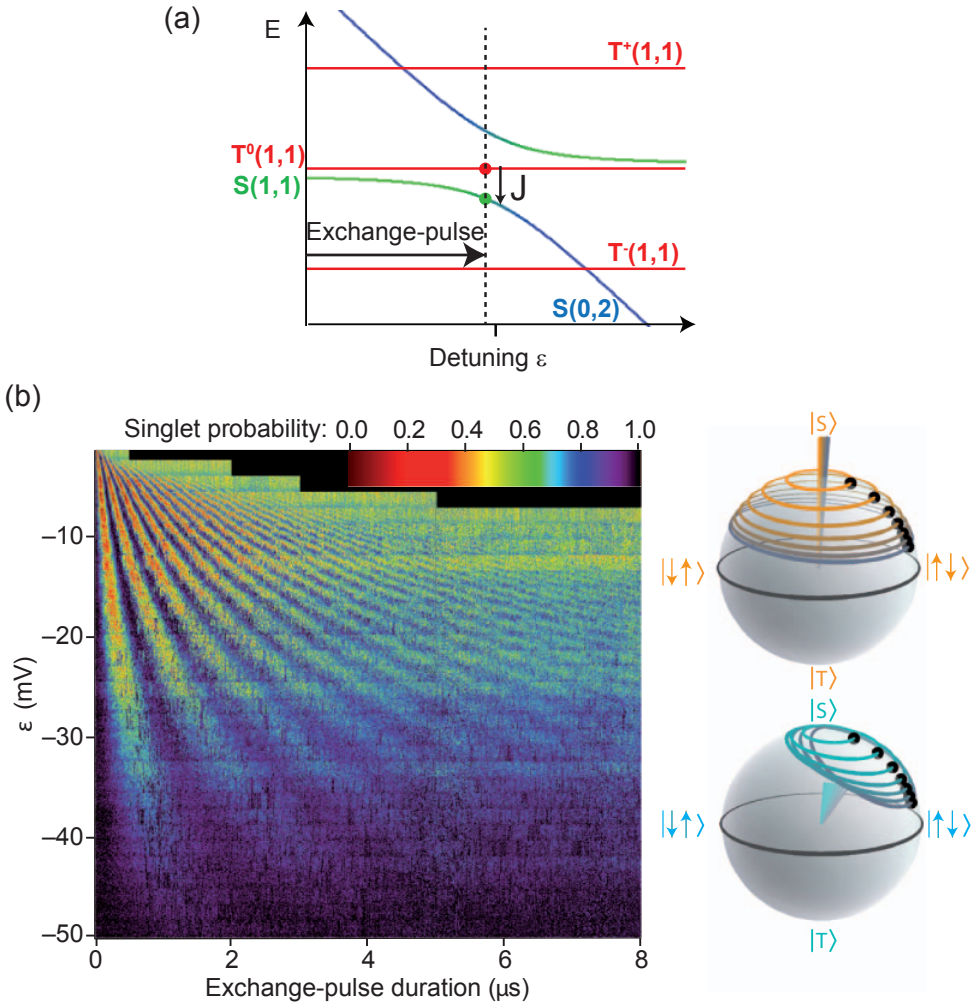

Fig. 18: *Coherent two-spin manipualtion in Si/SiGe. (a) Eigenenergies of the two-qubit states plotted as a function of the double dot detuning ϵ. After initialization at negative ϵ, coherent oscillations are triggered by a non-adiabatic, positive detuning pulse switching on the exchange energy J (cmp. Fig. 8). (b) Singlet return probability plotted as a function of exchange-pulse duration and detuning during exchange. Right: Spin trajectories on the ST^0 Bloch sphere for different initial hyperfine fields (dots) and large (top) and small J (bottom). (b from [38])*

in GaAs. Since the latter is discussed extensively in chapter A6, we focus here on the specific features of silicon. The ST^0 qubit implementation in GaAs makes use of a gradient hyperfine field between the dots to initialize a $|\uparrow\downarrow\rangle$ or $|\downarrow\uparrow\rangle$ state by an adiabatic passage. Furthermore, the effective gradient magnetic field gives rise to a second, orthogonal rotation axis, which is required to gain universal control over the qubit [54]. Due to the weak hyperfine interaction in Si, the gradient hyperfine field is much smaller and the initialization into $|\uparrow\downarrow\rangle$ or $|\downarrow\uparrow\rangle$ (the superpositions of S and T^0) is incomplete. Therefore, the Bloch vector on the ST^0 Bloch sphere can only slightly be tilted towards the equatorial plane during initialization. Also Hahn echo experiments like in Ref. [42] are challenging.
After initialization deep in the $(1,1)$ charge regime (negative detuning ϵ) in Fig. 18a, the exchange interaction $J(\epsilon)$ is switched on by a positive detuning pulse. The coherent oscillations measured by the $S(0,2)$ return probability are plotted in Fig. 18b. Remarkably, the oscillations survive over micro-seconds and their frequency can be tuned over a wide range of $J(\epsilon)$. In the two Bloch spheres, the two-spin state trajectories for different inital values of the hyperfine fields are simulated for large J (top) and small J (bottom) compared to the width of the hyperfine fluctuations. The measured dephasing time T_2^* represents an improvement by nearly two orders of magnitude over the value observed in GaAs dots. This result follows the expectations in silicon and the coherence can be further boosted by isotopical purifications (as discussed in the previous section. To gain universal control over the ST^0 qubit, a local micro-magnet might be implemented. Tt will generate a stable gradient magnetic field required for $|\uparrow\downarrow\rangle$, $|\downarrow\uparrow\rangle$ initialization and provides a second rotation axis orthogonal to J (cmp. chapter A6).

4 Summary

Micro-magnets can be used to engineer the coupling of electron spins to each other and to their environment. We presented new schemes for faster single and two-qubit manipulation and detection all based on micro-magnets. Micro-magnets become especially important for electron spin systems with intrinsically low coupling to the environment like Si/SiGe. Highly flexible gate-defined quantum dots can be formed in a Si/SiGe 2DEG. As expected from the small spin coupling to the environment, long relaxation and coherence times were observed in Si/SiGe. The spin coherence time can be improved further by isotopical purification. Some basic building blocks of quantum computation (e.g. spin initialization and single-shot spin detection as well as coherent singlet-triplet manipulation) were demonstrated in Si/SiGe. Universal control of a single electron spin qubit and a ST^0 qubit is still lacking. The use of micro-magnets might be the key technology to realize these milestone experiments.

References

[1] R. Hanson, L. P. Kouwenhoven, J. R. Petta, S. Tarucha, and L. M. K. Vandersypen, Rev. Mod. Phys. **79**, 1217 (2007).

[2] D. DiVincenzo, J. Lisenfeld, A. V. Ustinov, L. R. Schreiber, and L. M. K. Vandersypen, *Quantum Computing- Fundamentals and Solid-State Realizations*, Nanoelectronics and Information Technology (Wiley-VCH, 2012), 3rd ed., ISBN 978-3-527-40927-3.

[3] H. Bluhm, S. Foletti, D. Mahalu, V. Umansky, and A. Yacoby, Phys. Rev. Lett **105**, 216803 (2010).

[4] H. Bluhm, S. Foletti, I. Neder, M. Rudner, D. Mahalu, V. Umansky, and A. Yacoby, Nature Physics **7**, 109 (2011).

[5] D. Loss and D. P. DiVincenzo, Phys. Rev. A **57**, 120 (1998).

[6] F. H. L. Koppens, C. Buizert, K. J. Tielrooij, I. T. Vink, K. C. Nowack, T. Meunier, L. P. Kouwenhoven, and L. M. K. Vandersypen, Nature **442**, 766 (2006).

[7] K. Ono, D. G. Austing, Y. Tokura, and S. Tarucha, Science **297**, 1313 (2002).

[8] F. H. L. Koppens, J. A. Folk, J. M. Elzerman, R. Hanson, L. H. W. van Beveren, I. T. Vink, H. P. Tranitz, W. Wegscheider, L. P. Kouwenhoven, and L. M. K. Vandersypen, Science **309**, 1346 (2005).

[9] M. Pioro-Ladriere, T. Obata, Y. Tokura, Y.-S. Shin, T. Kubo, K. Yoshida, T. Taniyama, and S. Tarucha, Nat. Phys. **4**, 776 (2008).

[10] T. Obata, M. Pioro-Ladrière, Y. Tokura, Y.-S. Shin, T. Kubo, K. Yoshida, T. Taniyama, and S. Tarucha, Phys. Rev. B **81**, 085317 (2010).

[11] R. Brunner, Y.-S. Shin, T. Obata, M. Pioro-Ladrière, T. Kubo, K. Yoshida, T. Taniyama, Y. Tokura, and S. Tarucha, Phys. Rev. Lett. **107**, 146801 (2011).

[12] R. Neumann, BSc thesis, RWTH Aachen, University, 2012.

[13] M. Field, C. G. Smith, M. Pepper, D. A. Ritchie, J. E. F. Frost, G. A. C. Jones, and D. G. Hasko, Phys. Rev. Lett. **70**, 1311 (1993).

[14] Y.-S. Shin, T. Obata, M. Pioro-Ladriere, Y. Tokura, R. Brunner, T. Kubo, K. Yoshida, and S. Tarucha, Physica E **42**, 825 (2010).

[15] Y.-S. Shin, T. Obata, Y. Tokura, M. Pioro-Ladrière, R. Brunner, T. Kubo, K. Yoshida, and S. Tarucha, Phys. Rev. Lett. **104**, 046802 (2010).

[16] L. R. Schreiber, F. R. Braakman, T. Meunier, V. Calado, J. Danon, J. M. Taylor, W. Wegscheider, and L. M. K. Vandersypen, Nat Commun **2**, 556 (2011).

[17] T. Meunier, V. E. Calado, and L. M. K. Vandersypen, Phys. Rev. B **83**, 121403 (2011).

[18] K. C. Nowack, F. H. L. Koppens, Y. V. Nazarov, and L. M. K. Vandersypen, Science **318**, 1430 (2007).

[19] S. Nadj-Perge, S. M. Frolov, E. P. A. M. Bakkers, and L. P. Kouwenhoven, Nature **468**, 1084 (2010), ISSN 0028-0836.

[20] E. A. Laird, C. Barthel, E. I. Rashba, C. M. Marcus, M. P. Hanson, and A. C. Gossard, Phys. Rev. Lett. **99**, 246601 (2007).

[21] M. Shafiei, K. C. Nowack, C. Reichl, W. Wegscheider, and L. M. K. Vandersypen, ArXiv e-prints (2012), 1207.3331.

[22] J. J. L. Morton, D. R. McCamey, M. A. Eriksson, and S. A. Lyon, Nature **479**, 345 (2011).

[23] F. A. Zwanenburg, A. S. Dzurak, A. Morello, M. Y. Simmons, L. C. L. Hollenberg, G. Klimeck, S. Rogge, S. N. Coppersmith, and M. A. Eriksson, ArXiv e-prints (2012), 1206.5202.

[24] N. S. Lai, W. H. Lim, C. H. Yang, F. A. Zwanenburg, W. A. Coish, F. Qassemi, A. Morello, and A. S. Dzurak, Sci. Rep. **1** (2011).

[25] Y. Hu, H. O. H. Churchill, D. J. Reilly, J. Xiang, C. M. Lieber, and C. M. Marcus, Nature Nanotechnology **2**, 622 (2007).

[26] C. Kloeffel, M. Trif, and D. Loss, Phys. Rev. B **84**, 195314 (2011).

[27] F. Schäffler, Semicond. Sci. Technol. **12**, 1515 (1997).

[28] T. B. Boykin, G. Klimeck, M. A. Eriksson, M. Friesen, S. N. Coppersmith, P. von Allmen, F. Oyafuso, and S. Lee, Applied Physics Letters **84** (2004).

[29] M. G. Borselli, R. S. Ross, A. A. Kiselev, E. T. Croke, K. S. Holabird, P. W. Deelman, L. D. Warren, I. Alvarado-Rodriguez, I. Milosavljevic, F. C. Ku, et al., Applied Physics Letters **98**, 123118 (2011).

[30] M. G. Borselli, K. Eng, E. T. Croke, B. M. Maune, B. Huang, R. S. Ross, A. A. Kiselev, P. W. Deelman, I. Alvarado-Rodriguez, A. E. Schmitz, et al., Applied Physics Letters **99**, 063109 (2011).

[31] S. Goswami, K. A. Slinker, M. Friesen, L. M. McGuire, J. L. Truitt, C. Tahan, L. J. Klein, J. O. Chu, P. M. Mooney, D. W. van der Weide, et al., Nat Phys **3** (2007).

[32] C. Tahan, ArXiv e-prints (2007), 0710.4263.

[33] R. R. Hayes, A. A. Kiselev, M. G. Borselli, S. S. Bui, E. T. Croke, III, P. W. Deelman, B. M. Maune, I. Milosavljevic, J.-S. Moon, R. S. Ross, et al., ArXiv e-prints (2009), 0908.0173.

[34] C. B. Simmons, J. R. Prance, B. J. Van Bael, T. S. Koh, Z. Shi, D. E. Savage, M. G. Lagally, R. Joynt, M. Friesen, S. N. Coppersmith, et al., Phys. Rev. Lett. **106**, 156804 (2011).

[35] J. M. Elzerman, R. Hanson, L. H. W. van Beveren, B. Witkamp, L. M. K. Vandersypen, and L. P. Kouwenhoven, Nature **430**, 431 (2004).

[36] J. M. Taylor, W. Dür, P. Zoller, A. Yacoby, C. M. Marcus, and M. D. Lukin, Phys. Rev. Lett. **94**, 236803 (2005).

[37] L. V. C. Assali, H. M. Petrilli, R. B. Capaz, B. Koiller, X. Hu, and S. Das Sarma, Phys. Rev. B **83**, 165301 (2011).

[38] B. M. Maune, M. G. Borselli, B. Huang, T. D. Ladd, P. W. Deelman, K. S. Holabird, A. A. Kiselev, I. Alvarado-Rodriguez, R. S. Ross, A. E. Schmitz, et al., Nature **481**, 344 (2012).

[39] J. Sailer, V. Lang, G. Abstreiter, G. Tsuchiya, K. M. Itoh, J. W. Ager, E. E. Haller, D. Kupidura, D. Harbusch, S. Ludwig, et al., physica status solidi (RRL) Rapid Research Letters **3** (2009).

[40] A. Wild, J. Kierig, J. Sailer, J. W. Ager, III, E. E. Haller, G. Abstreiter, S. Ludwig, and D. Bougeard, Applied Physics Letters **100**, 143110 (2012).

[41] A. M. Tyryshkin, S. Tojo, J. J. L. Morton, H. Riemann, N. V. Abrosimov, P. Becker, H.-J. Pohl, T. Schenkel, M. L. W. Thewalt, K. M. Itoh, et al., Nat Mater **11**, 143 (2012).

[42] J. R. Petta, A. C. Johnson, J. M. Taylor, E. A. Laird, A. Yacoby, M. D. Lukin, C. M. Marcus, M. P. Hanson, and A. C. Gossard, Science **309**, 2180 (2005).

[43] B. E. Kane, Nature **393**, 133 (1998).

[44] W. M. Witzel and S. Das Sarma, Phys. Rev. B **76**, 045218 (2007).

[45] K. C. Nowack, M. Shafiei, M. Laforest, G. E. D. K. Prawiroatmodjo, L. R. Schreiber, C. Reichl, W. Wegscheider, and L. M. K. Vandersypen, Science **333**, 1269 (2011).

[46] A. Morello, J. J. Pla, F. A. Zwanenburg, K. W. Chan, K. Y. Tan, H. Huebl, M. Mottonen, C. D. Nugroho, C. Yang, J. A. van Donkelaar, et al., Nature **467**, 687 (2010).

[47] J. R. Prance, Z. Shi, C. B. Simmons, D. E. Savage, M. G. Lagally, L. R. Schreiber, L. M. K. Vandersypen, M. Friesen, R. Joynt, S. N. Coppersmith, et al., Phys. Rev. Lett. **108**, 046808 (2012).

[48] N. Shaji, C. B. Simmons, M. Thalakulam, L. J. Klein, H. Qin, H. Luo, D. E. Savage, M. G. Lagally, A. J. Rimberg, R. Joynt, et al., Nat Phys **4** (2008).

[49] M. Thalakulam, C. B. Simmons, B. M. Rosemeyer, D. E. Savage, M. G. Lagally, M. Friesen, S. N. Coppersmith, and M. A. Eriksson, Applied Physics Letters **96**, 183104 (2010).

[50] M. Thalakulam, C. B. Simmons, B. J. Van Bael, B. M. Rosemeyer, D. E. Savage, M. G. Lagally, M. Friesen, S. N. Coppersmith, and M. A. Eriksson, Phys. Rev. B **84**, 045307 (2011).

[51] C. B. Simmons, M. Thalakulam, B. M. Rosemeyer, B. J. Van Bael, E. K. Sackmann, D. E. Savage, M. G. Lagally, R. Joynt, M. Friesen, S. N. Coppersmith, et al., Nano Letters **9**, 3234 (2009).

[52] A. C. Johnson, J. R. Petta, J. M. Taylor, A. Yacoby, M. D. Lukin, C. M. Marcus, M. P. Hanson, and A. C. Gossard, Nature **435**, 925 (2005).

[53] A. Wild, J. Sailer, J. Nützel, G. Abstreiter, S. Ludwig, and D. Bougeard, New Journal of Physics **12**, 113019 (2010).

[54] S. Foletti, H. Bluhm, D. Mahalu, V. Umansky, and A. Yacoby, Nature Physics **5**, 903 (2009).

B 4 Control of Superconducting Qubits [1]

Jay M. Gambetta
IBM T.J. Watson Research Center
Yorktown Heights, New York 10598, USA

Contents

1 The Transmon **3**
1.1 The model . . . 3
1.2 The charge dispersion of the transmon . . . 5
1.3 Large E_J/E_C effective Hamiltonian . . . 8
1.4 Control of ω by external flux . . . 9
1.5 External driving by capacitively coupled transmission lines . . . 10
1.6 Rotating frame and single qubit gates . . . 11

2 Circuit quantum electrodynamics **12**
2.1 Dispersive regime . . . 13
2.2 Quantum non-demolition measurement . . . 14
2.3 Two-qubit exchange interaction . . . 17
2.4 The 3D cavity architecture . . . 18
2.5 Implementation of the iSwap gate by virtual qubit-qubit interactions . . . 19
2.6 Implementation of the cPhase gate by higher level interactions . . . 20
2.7 Implementation of the $ZX_{\pi/2}$ gate by the cross resonance effect . . . 21
2.8 Implementation of the bSwap gate by higher level induced transitions . . . 25
2.9 Summary of two-qubit gates . . . 26

3 Optimal single qubit gates **28**
3.1 Leakage errors in single qubit gates . . . 28
3.2 Correcting for leakage with DRAG shaping . . . 30
3.2.1 Zero order solution . . . 31
3.2.2 First order solution . . . 31

4 Benchmarking quantum processes **33**
4.1 Quantum process tomography 33
4.2 Randomized benchmarking 36

A Effective Hamiltonians: Outline of the Schrieffer-Wolff transformation **38**
A.1 Diagonalizing the system 40
A.2 Eliminating coupling across subspaces 40

B General leakage removal **41**

C State and gate fidelities **43**
C.1 Representations of a quantum state 43
C.2 Representations of a map 44

[1]Lecture Notes of the 44^{th} IFF Spring School "Quantum Information Processing" (Forschungszentrum Jülich, 2013). All rights reserved.

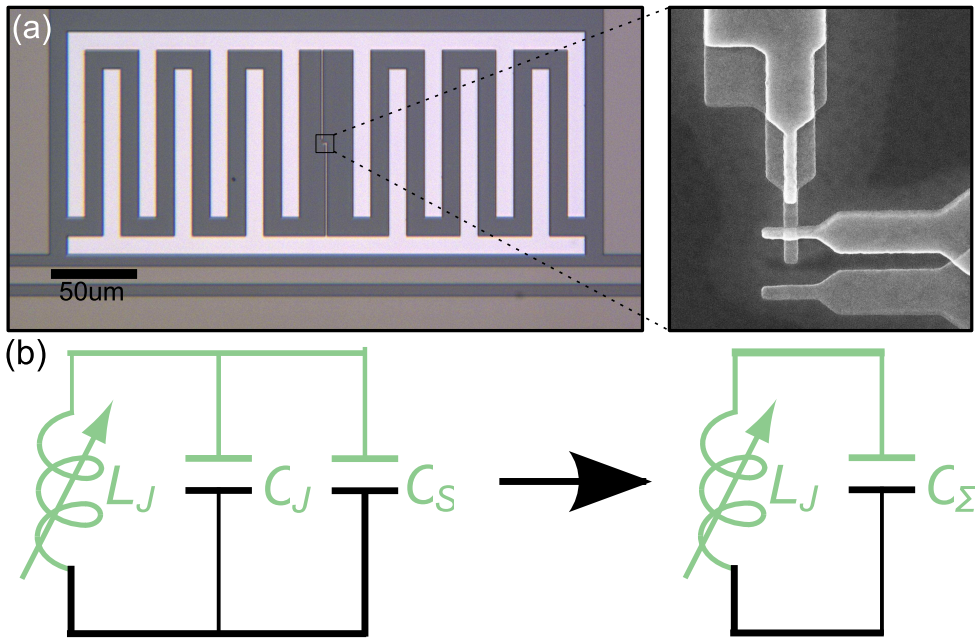

Fig. 1: *Single-junction transmon and effective circuit diagrams. (a) Optical micrograph of the single-junction transmon device used in Ref. [5] showing the interdigitated capacitors shunting the Al/AlOx Josephson junction. Inset is a scanning-electron micrograph of Josephson junction, with critical current I_0 = 30 nA ($L_J = 11$ nH). (b) A schematic of the effective circuit diagram of the transmon with C_S representing the shunting capacitor, C_J the junction capacitance and L_J the junction inductance. All the parallel capacitors can be grouped into an effective capacitor $C_\Sigma = C_J + C_S$ which for this device is ≈ 85 fF giving a E_J/E_C ratio of 65.*

1 The Transmon

Until recently achieving long coherence times has been the main challenge for realizing a quantum information processor with superconducting qubits. The transmon initially developed by the group lead by Professor Schoelkopf at Yale [1, 2] and now routinely used in many labs around the world has achieved T_1 and T_2^* times as large as 70 μs and 92 μs when placed in a 3D waveguide cavity [3, 4] and as large as 9.7 μs and 10.3 μs when embedded in a 2D co-planner waveguide resonator [5].

1.1 The model

The transmon is a superconducting qubit consisting of usually a Al/AlOx Josephson junction shunted by large capacitor. A typical device is shown in figure 1a where the large shunting capacitance is clearly observed (interdigitated fingers) and the inset shows a zoomed in scanning-electron micrograph of the Josephson junction. The resonance frequency of these devices are typically in the range of $4 - 6$ GHz giving a wavelength in the mm range. This wavelength is much larger than the dimensions (μm) of the transmon and as such, like most superconducting qubits, it is well approximated by a lumped circuit model. The effective circuit model is shown in figure 1b and is a parallel LC oscillator with the inductor L_J being nonlinear and the capacitor C_Σ being linear. The meaning of linear and nonlinear will become clearer below.
In general a lumped electrical circuit can be formally described as a network whose branches

consist of two-terminal electrical elements. Each branch can be described by the voltage across it, V, and the current flowing into it, I. For the capacitor the voltage is related to the charge on it q though the standard linear relation $V(q) = q/C_\Sigma$ and for the Josephson junction the current is related to the flux though it ϕ by the nonlinear relation $I(\phi) = I_0 \sin(\phi/\varphi_0)$ where $\varphi_0 = \hbar/2e$ is the reduced flux quantum and I_0 is the critical current. This is the standard Josephson effect [6] and for a nice derivation of this result see Feynman's phenomenological model in his lecture series [7]. In general the branch fluxes and charges do not take into account the topology of the circuit (Kirchhoff's laws) and a more formal technique is needed to find the Hamiltonian of the circuit [8, 9]. Here since the circuit is simple and only has one degree of freedom the Hamiltonian can be found by summing the energy stored in the capacitor and junction.
The energy stored in the capacitor is given by

$$E_{\rm cap}(Q) = \int_0^Q V(q)dq = \frac{Q^2}{2C_\Sigma}, \tag{1}$$

while the energy stored in the junction is given by

$$E_{\rm ind}(\Phi) = \int_0^\Phi I(\phi)d\phi = E_J[1 - \cos(\Phi/\varphi_0)]. \tag{2}$$

Here $E_J = I_0\varphi_0$ is the Josephson energy. It is convenient to define the Josephson inductance by $L_J = \varphi_0^2/E_J$ which is the linear inductance that approximates the junction in the small Φ limit. The above results in a transmon Hamiltonian of the form

$$\hat{H}_{\rm tr} = \frac{\hat{Q}^2}{2C_\Sigma} - E_J \cos(\hat{\Phi}/\varphi_0). \tag{3}$$

Here we have introduced the notation of a hat to signify a quantum operator.
In many cases the transmon is not isolated from the environment and any voltage source V_i can be capacitively coupled. In this case the charge on the capacitor becomes $\hat{Q} \rightarrow \hat{Q} - \sum_i C_i V_i$ where C_i represents the capacitor coupling the $i^{\rm th}$ voltage source to the transmon. This results in the Hamiltonian becoming

$$\hat{H}_{\rm tr} = \frac{(\hat{Q} - \sum_i C_i V_i)^2}{2\bar{C}_\Sigma} - E_J \cos(\hat{\Phi}/\varphi_0), \tag{4}$$

where $\bar{C}_\Sigma = C_S + C_J + \sum_i C_i$. This voltage term is important as it will be this term that represents the coupling of the transmon to the resonator (see section 2), external control lines, and the fact that it is experimentally hard to make the environment clean of fluctuating voltages (charge noise) this term will also lead to decoherence.
While equation (4) is a complete description of the system it is convenient to replace the conjugate variables $\hat{Q}$ and $\hat{\Phi}$ with dimensionless conjugate variables $\hat{\gamma} = \hat{\Phi}/\varphi_0$ and $\hat{n} = \hat{Q}/2e$. These represent the superconducting phase difference and the number of cooper pairs respectively. In terms of these variables the standard form of the transmon Hamiltonian is

$$\hat{H}_{\rm tr} = 4E_C(\hat{n} - n_g)^2 - E_J \cos(\hat{\gamma}), \tag{5}$$

where $E_C = e^2/2C_\Sigma$ is the single-electron charging energy and $n_g = \sum_i C_i V_i/2e$ is the effective offset charge. The astute reader will of noticed that this is exactly the same Hamiltonian as the cooper-pair box (CPB) [10, 11]. This is because the transmon is essentially a charge qubit. The difference between the CPB and the transmon is that the CPB operates in the limit $E_C \gg E_J$ whereas the transmon has $E_C \ll E_J$. This difference in parameter space is achieved by the shunting capacitor and as we will see in the next section it is this difference that makes the transmon exponentially less sensitive to charge noise than the CPB.

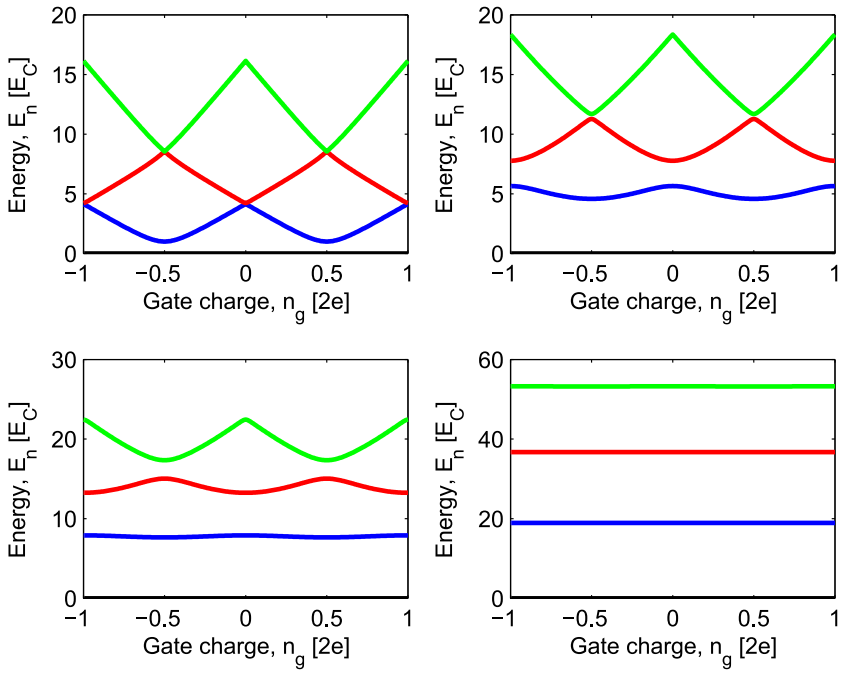

Fig. 2: *Eigenenergies $E_{m0} = E_m - E_0$ for the first threes levels (blue $m = 1$, red $m = 2$, and greed $m = 3$) of the transmon Hamiltonian* (5) *as a function of the effective offset charge n_g for $E_J/E_C = 1, 5, 10$, and 50 respectively. Energies are given in units of the single-electron charging energy E_C.*

1.2 The charge dispersion of the transmon

To find the energy eigenvalues of equation (5) we first note that $\hat{\gamma}$, the superconducting phase, is only defined over $[0, 2\pi]$ which means the wave functions must satisfy the periodic boundary condition $\psi(\gamma) = \psi(\gamma + 2\pi)$. For any periodic function we can decompose it into a Fourier series $\psi(\gamma) = \sum_n \psi_n e^{in\gamma}$. Furthermore, the potential is also periodic over 2π and can be written as $V(\gamma) = -E_J \cos(\gamma) = -E_J(e^{i\gamma} + e^{-i\gamma})/2$ and finally since n and γ are conjugate variables then $\langle\gamma|\hat{n}|\psi\rangle = -i\partial_\gamma\psi(\gamma) = \sum_n n\psi_n e^{in\gamma}$. Using the above we can write the time-independent Schrödinger equation as

$$\sum_n 4E_C(n - n_g)^2\psi_n e^{in\gamma} - \sum_n \frac{E_J}{2}(\psi_{n-1} + \psi_{n+1})e^{in\gamma} = \sum_n E\psi_n e^{in\gamma}, \tag{6}$$

where E is the eigenenergy. Solving for ψ_n and E amounts to finding the eigenvalues and eigenvectors of the matrix $\hat{H}_{\text{tr}} = \sum_n 4E_C(n - n_g)^2|n\rangle\langle n| - E_J(|n+1\rangle\langle n| + |n\rangle\langle n+1|)/2$. This is called the charge representation of the transmon and here we see that due to the superconducting phase only being define over $[0, 2\pi]$ the number of Cooper pairs on the island come in discrete values. This is an alternative way of seeing that charge on a superconductor is quantized.

This Hamiltonian is simple to diagonalize numerically by truncating the summation at some large value of $n_{\max}$. Plots for the lowest three energy levels E_{10}, E_{20}, and E_{30} (with the ground state subtracted), as a function of the effective offset charge n_g, are shown in figure 2 for several values of E_J/E_C. One clearly observes that the anharmonicity depends on E_J/E_C, and that the

total charge dispersion decreases very rapidly with E_J/E_C. Both factors influence the operation of the system as a qubit. The charge dispersion immediately translates into the sensitivity of the system with respect to n_g. A sufficiently large anharmonicity is required for selective control of the transitions, and the effective separation of the Hilbert space into the relevant qubit part and the rest, $\hat{H}_{\rm tr} = \hat{H}_{\rm qb} \oplus \hat{H}_{\rm rest}$.

To get an understanding of the scaling of charge dispersion in figure 3a we have plotted the peak to peak value for the charge dispersion

$$\epsilon_m = E_{m0}(n_g = 1/2) - E_{m0}(n_g = 0) \tag{7}$$

as a function of the ratio E_J/E_C as solid lines. Here it is clearly visible that the charge dispersion decreases exponentially with this ratio. In the large E_J/E_C it is possible to perform a semi-classical analysis using the WKB (Wentzel-Kramers-Brillouin) approximation. One can think of the WKB approximation as a expansion of eigenfunctions in orders of $\hbar$. The application of WKB to a periodical potential is non-trivial and for a nice review of this method see Ref. [12]. Here we will just quote the results from Ref. [1] which predicts that when $E_J/E_C \gg 1$ the energy levels are well approximated by

$$E_{m0}(n_g) \simeq E_{m0}(n_g = 1/4) - \frac{\epsilon_m}{2}\cos(2\pi n_g), \tag{8}$$

where

$$\epsilon_m \simeq (-1)^m E_C \frac{2^{4m+5}}{m!}\sqrt{\frac{2}{\pi}}\left(\frac{E_J}{2E_C}\right)^{\frac{m}{2}+\frac{3}{4}} e^{-\sqrt{8E_J/E_C}}. \tag{9}$$

This prediction is also plotted in figure 3a as a dashed line where we observed that in the large E_J/E_C limit it correctly predicts the numerical calculation.

It is simple to see how having a smaller charge dispersion results in a larger T_ϕ (dephasing time). To do this we start by deriving a general expression for the dephasing in terms of the noise power spectrum S_f for a given noisy signal $f(t)$. S_f is defined as the mean-squared amplitude of the noise f at frequency ω per 1 Hz bandwidth. For typical experiments this has a $1/f$ dependence ($S(\omega) = 2\pi A^2/|\omega|$) where the parameter A determines the overall amplitude of the fluctuations. For a superposition of the ground and excited state the ρ_{10} component of the state will evolve according to

$$\rho_{10}(t) = \exp\left[-i\int_0^t E_{10}(f(t'))dt'/\hbar\right]\rho_{10}(0). \tag{10}$$

Performing a Taylor expansion of E_{10} for small variations in f this can be rewritten as

$$\rho_{10}(t) = \exp\left[-i\omega t - i\Delta\phi(t)\right]\rho_{10}(0). \tag{11}$$

where ω is the resonance frequency of the lowest two levels and $\Delta\phi(t) = (\partial_f E_{10})\int_0^t \Delta f(t')dt'/\hbar$ is a is random and uncertain phase that will change with time and experimental run. If this random phase is Gaussian distributed then due to the cumulant expandsion the ensemble average $\langle\exp(i\Delta\phi(t))\rangle = \exp(-\langle\Delta\phi^2(t)\rangle/2)$. Defining the dephasing rate by $\gamma_\phi(t) = \langle\Delta\phi^2(t)\rangle/2t$ gives

$$\gamma_\phi(t) = \frac{(\partial_f E_{10})^2}{2\hbar^2 t}\int_0^t\int_0^t \langle f(t')f(t'')\rangle dt'dt'' = \frac{(\partial_f E_{10})^2}{2\hbar^2 t}\int_{-\infty}^{\infty} S_f(\omega)\frac{\sin(\omega t/2)}{(\omega t/2)}\frac{d\omega}{2\pi}, \tag{12}$$

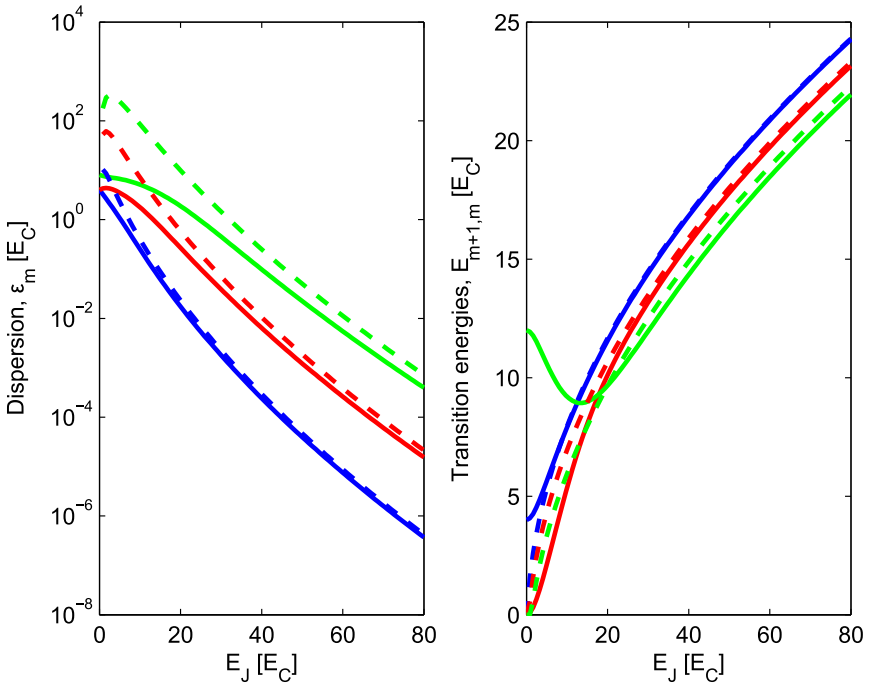

Fig. 3: *Comparison of numerically and asymptotic expressions for the charge dispersion and transition energies. a) Charge dispersion* $|\epsilon_m|$ *as a function of the ratio* E_J/E_C *for the lowest four levels. The solid curves depict the numerical results and the dashed curves represent the asymptotic expansion, equation* (9)*. b) Transition energies* $E_{m+1,m} = E_{m+1} - E_m$ *at* $n_g = 0$ *as a function of the* E_J/E_C *ratio. Solid curves show the numerical results; dashed lines are based on the Duffing oscillator approximation, equation* (20)*.*

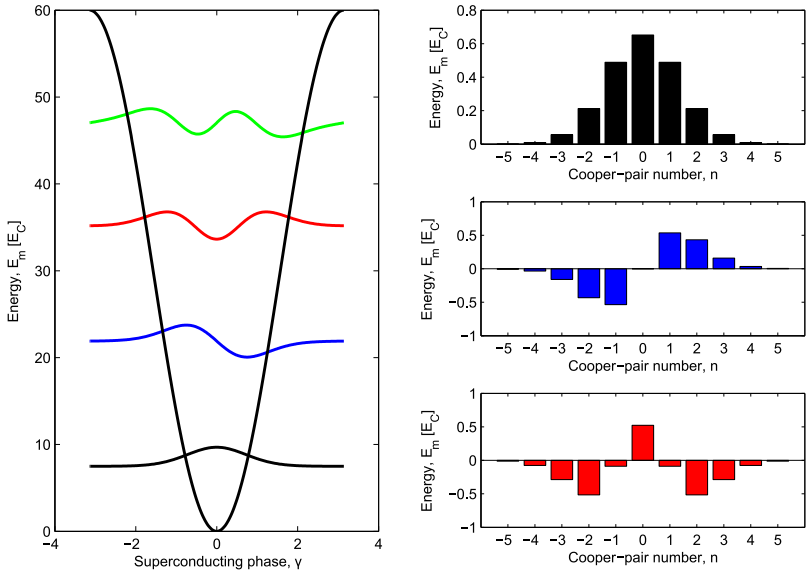

Fig. 4: *The eigenfunctions for the transmon for $E_J/E_C = 30$ in the superconducting phase basis (a) and Cooper-pair number basis (b).*

and for $1/f$ noise the integral can be performed provided there is a low (ω_i) and high (ω_c) frequency cutoff. Doing this results in

$$\gamma_\phi(t) = \frac{(\partial_f E_{10})^2}{\hbar^2} A^2 t |\ln(\omega_i t)| \tag{13}$$

and for a rough estimate of dephasing time T_ϕ we take the time t for $\gamma_\phi = 1/t$. This gives

$$T_\phi = \frac{\hbar}{|\partial_f E_{10}| A}. \tag{14}$$

For charge noise $f(t) = Q_{\text{off}}(t) = 2en_g(t)$ and this expression predicts

$$T_\phi = \frac{2e\hbar}{|\epsilon_1|\pi A \sin(2\pi n_g)}. \tag{15}$$

Here it is clear that T_ϕ is inversely related to the charge dispersion and as such the dephasing time wil increase exponentially with the ratio E_J/E_C. For typical experiments [13, 14] it has been shown that $A = 10^{-4} - 10^{-3}e$ and for the parameters fo the device shown in figure 1 the estimated charge noise dephasing time is $T_\phi \approx 730$ ms.

1.3 Large E_J/E_C effective Hamiltonian

From the above it is clear that we want to be in the large E_J/E_C regime. In this limit there are many levels confined to the cosine and neither $\hat{n}$ or $\hat{\gamma}$ are good quantum numbers. Instead the eigenfunctions are reminiscent of a harmonic oscillator (see figure 4). For this reason it is a good approximation to treat the system in the harmonic oscillator basis. To do this we start by expanding the cosine in equation (4) to 4^{th} order in Φ,

$$\hat{H}_{\text{tr}} \approx \frac{\hat{Q}^2}{2\bar{C}_\Sigma} + \frac{\hat{\Phi}^2}{2L_J} - \frac{E_C \hat{\Phi}^4}{3Z_{\text{tr}}^2 \hbar^2} + \mathcal{O}(\hat{\Phi}^6) \tag{16}$$

where $Z_{\rm tr} = \sqrt{L_J/\bar{C}_\Sigma} = (\hbar/e^2)\sqrt{E_C/2E_J}$ is the characteristic impedance of the LC oscillator representing the transmon. The typically values for this give $Z_{\rm tr} = 300 - 400\ \Omega$. This Hamiltonian is the standard Duffing oscillator and for convenience I find it simpler to work with the dimensionless conjugate variables $\hat{x} = \sqrt{1/\hbar Z_{\rm tr}}\hat{\Phi}$ and $\hat{y} = \sqrt{Z_{\rm tr}/\hbar}\hat{Q}$. Using these variables the Hamiltonian becomes

$$\hat{H}_{\rm tr} = \frac{\hbar\omega_0}{2}(\hat{y}^2 + \hat{x}^2) - \frac{E_C\hat{x}^4}{3} \tag{17}$$

where $\omega_0 = 1/\sqrt{\bar{C}_\Sigma L_J} = \sqrt{8E_C E_J}/\hbar$ is the standard expression for the resonance frequency of a linear LC circuit (harmonic oscillator) approximation of the transmon. Finally by introducing the ladder operators $\hat{b}$ and $\hat{b}^\dagger$ where

$$\hat{b} = \frac{i}{\sqrt{2}}(\hat{x} + i\hat{y}) \tag{18}$$

and by expanding the nonlinearity we find

$$\hat{H}_{\rm tr} \;=\; \hbar\left[\omega\hat{b}^\dagger\hat{b} + \frac{1}{2}\delta\hat{b}^\dagger\hat{b}(\hat{b}^\dagger\hat{b} - 1)\right] + \frac{\hbar\delta}{12}(\hat{b}^{\dagger 4} - 6\hat{b}^{\dagger 2} - 4\hat{b}^\dagger(\hat{b}^2 + \hat{b}^{\dagger 2})\hat{b} - 6\hat{b}^2 + \hat{b}^4), \tag{19}$$

where $\omega = \omega_0 + \delta$, and $\delta = -E_C$. For the transmon $|\omega| \gg |\delta|$ and due to the rotating wave approximation it is fine to drop the last term and simply write the effective Hamiltonian as

$$\hat{H}_{\rm tr} \;=\; \hbar\left[\omega\hat{b}^\dagger\hat{b} + \frac{1}{2}\delta\hat{b}^\dagger\hat{b}(\hat{b}^\dagger\hat{b} - 1)\right]. \tag{20}$$

Denoting the transition frequencies as $\omega_{i,j} = (E_i - E_j)/\hbar$, it simply to show that $\omega_{n+1,n} = \omega + \delta n$ and we see that ω is the resonance frequency of the qubit transition and δ is the anharmonicity. In figure 3 the transition frequency $\omega_{n+1,n}$ are plotted for the first three levels for both numerical simulation (solid) and the using equation (20) (dashed lines). Here we see that the system is well described by this simple Hamiltonian and we will use this for the rest of the lecture notes.

1.4 Control of ω by external flux

In making the transmon insensitivity to the gate charge the qubit frequency ω remains fixed. For long coherence times this is a good thing and is the method the IBM group is pursuing, however in some situations it advantageous to restore tuneability. This can be done by splitting the Josephson junction into two junctions with Josephson energies $E_J(1-d)/2$ and $E_J(1+d)/2$ respectively. Here d is represents the asymmetry and has domain $d \in [0, 1]$. These two junctions form a dc-SQUID which can be biased by a magnetic flux $\Phi_x = \gamma_x\varphi_0$ in order to impose a superconducting phase γ_x accross the two junctions. To describe this situation the cosine term in Hamiltonian (5) is replaced by

$$E_{\rm ind}(\gamma_x) = -E_J(1-d)\cos(\hat{\gamma}_1)/2 - E_J(1+d)\cos(\hat{\gamma}_2)/2 \tag{21}$$

where $\hat{\gamma}_1$ and $\hat{\gamma}_2$ are the individual superconducitng phase differences across the junctions. In the case where the inductance of the loop is negligible when compared to the junctions inductance

L_J then flux quantization gives $\hat{\gamma}_1 - \hat{\gamma}_2 = \gamma_x$. This allows us to eliminate one degree of freedom and by defining $\hat{\gamma} = (\hat{\gamma}_1 + \hat{\gamma}_2)/2$ the above becomes

$$\begin{aligned} E_{\rm ind}(\gamma_x) &= -E_J(1-d)\cos(\hat{\gamma}+\gamma_x/2)/2 - E_J(1+d)\cos(\hat{\gamma}-\gamma_x/2)/2 \\ &= -E_J^{\rm eff}\cos(\hat{\gamma}-\gamma_0) \end{aligned} \tag{22}$$

where $\gamma_0 = \arctan(d\tan(\gamma_x/2))$ is the minimum of the potential and the effective Josephson energy is given by $E_J^{\rm eff} = E_J\cos(\gamma_x/2)\sqrt{1+d^2\tan^2(\gamma_x/2))}$. Since the resonance frequency is proportional to $\sqrt{E_J^{\rm eff}}$ it can be tuned by changing the external flux.
The addition of flux loop comes at a cost of adding an extra port for decoherence. This port will provide a mechanism for both relaxation and dephasing. Using equation (14) T_ϕ can be estimated by

$$T_\phi = \left| \frac{4\phi_0 \left(\cos(\gamma_x/2)\sqrt{1+d^2\tan^2(\gamma_x/2)}\right)^{3/2}}{A\sin(\gamma_x)(1-d^2)\pi\omega_0} \right|. \tag{23}$$

Experiments [15] have shown $A = 10^{-6}\phi_0$ which at ($\gamma_x = \pi/2$) for typical parameters gives $T_\phi = 24\mu$s. However, at the *sweet spot* position ($\gamma_x = 0$) this gives ∞ this is because the first order expression for the dephasing time is incomplete and we should include the second order terms. It is not trivial to derive this higher order contributions as the square of the noise does not obey Gaussian statistics, but essentially it will be proportional to the inverse of the second derivative of the energy with respect to flux.

1.5 External driving by capacitively coupled transmission lines

For full single qubit control it is necessary to drive transitions between the eigenstates. For the transmons this is achieved by external microwave driving though a capacitively coupled transmission line (figure 5 clearly shows that each qubit has an external drive line). To model this effect we include the voltages sources back into equation (16). This results in the additional control Hamiltonian

$$\hat{H}_{\rm dr} = -\frac{C_i V_i \hat{Q}}{C_\Sigma} = -\beta_i\sqrt{\frac{\hbar}{2Z_{\rm tr}}}(\hat{b}+\hat{b}^\dagger)V_i = -\frac{2e\beta_i}{\sqrt{2}}\left(\frac{E_J}{8E_C}\right)^{1/4}(\hat{b}+\hat{b}^\dagger)V_i \tag{24}$$

where $\beta_i = C_i/C_\Sigma$ is the ratio of capacitive coupling to total qubit capacitance. Assuming the voltage is a microwave field of frequency ω_d then the above can be written as

$$\hat{H}_{\rm dr} = \hbar\Omega(t)(\hat{b}+\hat{b}^\dagger), \tag{25}$$

where

$$\Omega(t) = \Omega_x(t)\cos(\omega_d t) + \Omega_y(t)\sin(\omega_d t) = \frac{e^{-i\omega_d t}}{2}[\Omega_x(t) + i\Omega_y(t)] + \text{c.c.} \tag{26}$$

Here it is interesting to see that while the transmon is very insensitive to low frequency voltage fluctuations as little as $100\mu V$ for typical parameters ($\beta = 1/2500$) gives $\mathcal{E}/2\pi = 20$ MHz. Keeping β small is required as if this is two large vacuum flucations in the bias lines will have an adverse effect on the T_1 time. To estimate the effect on T_1 we can use the relation

$$T_1 = C_\Sigma/{\rm Re}[Y] \tag{27}$$

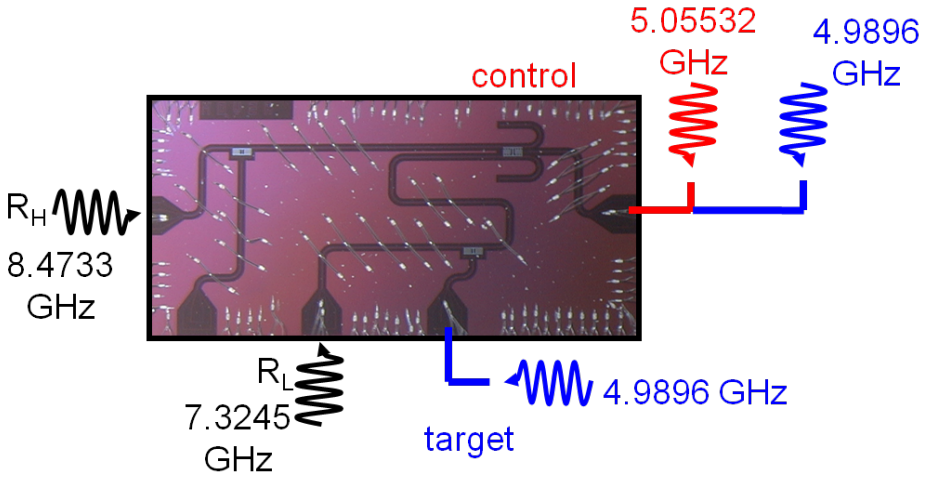

Fig. 5: *The device used in Ref. [5] showing two resonators R_L and R_H, three qubits, and three individual capacitively coupled transmission lines.*

where Y is the admittance of the rest of the circuit seen by the qubit. This is a simple extension of the RC time of a lossy capacitor. For a 50 Ω environment ($Z_{\rm en}$) this gives $T_1 = Z_{\rm tr}/\beta^2\omega_{01}Z_{\rm en}$ which unless $\beta \ll 1/2000$ limits T_1 to about a ms. For this reason it is very important to insure that the system is very well isolated from the external world.

1.6 Rotating frame and single qubit gates

In these systems it is typical to work in the rotating frame. Moving to this frame is achieved by the rotation

$$\hat{R} = \exp(-i\omega_d t\hat{b}^\dagger\hat{b}) = \sum_n \exp(-i\omega_d tn)|n\rangle\langle n|. \tag{28}$$

and the effective Hamiltonian can be found by the transformation

$$\hat{H}^R = \hat{R}^\dagger\hat{H}\hat{R} - i\hbar\hat{R}^\dagger\dot{\hat{R}}. \tag{29}$$

Applying this transformation gives

$$\begin{aligned}\hat{H}^R_{\rm tr} &= \hbar[-\Delta\hat{b}^\dagger\hat{b} + \frac{1}{2}\delta\hat{b}^\dagger\hat{b}(\hat{b}^\dagger\hat{b}-1)]\\ \hat{H}^R_{\rm dr} &= \hbar\Omega(t)(\exp(-i\omega_d t)b + b^\dagger\exp(i\omega_d t))\end{aligned} \tag{30}$$

where $\Delta = \omega_d - \omega$. Making the rotating wave approximation (dropping terms rotating at $2\omega_d$) gives

$$\hat{H}^R_{\rm tr+dr} = \hbar[-\Delta\hat{b}^\dagger\hat{b} + \frac{1}{2}\delta\hat{b}^\dagger\hat{b}(\hat{b}^\dagger\hat{b}-1)] + \frac{\hbar\Omega_x(t)}{2}(\hat{b}+\hat{b}^\dagger) + \frac{\hbar\Omega_y(t)}{2}(-i\hat{b}+i\hat{b}^\dagger). \tag{31}$$

Taking the two lowest levels of the system as the qubit with the lowest energy level being state $|0\rangle$ and the next level being state $|1\rangle$ gives

$$\hat{H}^R_{\rm tr+dr} = \frac{\hbar\Delta(t)}{2}\hat{Z} + \frac{\hbar\Omega_x(t)}{2}\hat{X} + \frac{\hbar\Omega_y(t)}{2}\hat{Y}, \tag{32}$$

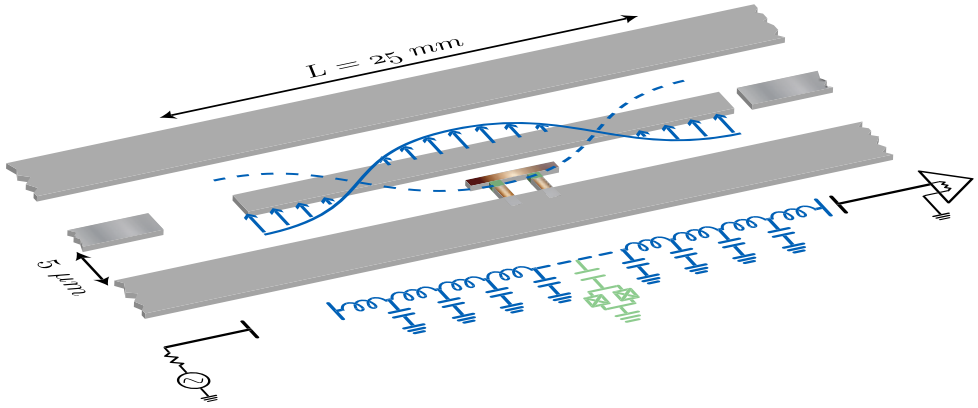

Fig. 6: *Schematic layout and lumped element version of the circuit QED architecture. A superconducting charge transmon is fabricated inside a superconducting co-planner waveguide resonator.*

where $\hat{X}$, $\hat{Y}$ and $\hat{Z}$ are the standard Pauli operators

$$\hat{X} = \begin{pmatrix} 0 & 1 \\ 1 & 0 \end{pmatrix} \quad \hat{Y} = \begin{pmatrix} 0 & -i \\ i & 0 \end{pmatrix} \quad \hat{Z} = \begin{pmatrix} 1 & 0 \\ 0 & -1 \end{pmatrix}. \tag{33}$$

Since all the variables $\Delta(t)$, $\Omega_x(t)$, and $\Omega_y(t)$ can be independently controlled it is possible to realize arbitrary single qubit gates in this system. For example, rotations around the Pauli operators are achieved by

$$\begin{aligned} \mathsf{X}_\theta &= \exp[-i\hat{X}\theta/2] = \cos(\theta/2) - i\sin(\theta/2)\hat{X} \\ \mathsf{Y}_\theta &= \exp[-i\hat{Y}\theta/2] = \cos(\theta/2) - i\sin(\theta/2)\hat{Y} \\ \mathsf{Z}_\theta &= \exp[-i\hat{Z}\theta/2] = \cos(\theta/2) - i\sin(\theta/2)\hat{Z} \end{aligned} \tag{34}$$

where $\theta = \{\Omega_x t, \Omega_y t, \Delta t\}$ for each equation in (34). By choosing $\theta = \pi$ Pauli gates are implement and by setting $\theta = \pi/2$ the generators of the single qubit Clifford group are implemented ($\pi/2$ gates). Note in general the Z_θ gate is not needed as arbitrary rotations around $\hat{Z}$ can be done by a combination of X_θ and Y_θ. This is more motivation for having fixed frequency transmons.

2 Circuit quantum electrodynamics

In this section we briefly review the circuit quantum electrodynamics (QED) architecture first introduced in Ref. [16] and first experimentally studied in Refs. [17]. As shown in figure 6, the system consists of a superconducting qubit, typically a transmon (but flux qubits can also be used [18, 19]), strongly coupled to a transmission line resonator. Near its resonance frequency ω_r, the transmission line resonator can be modeled as a simple harmonic oscillator composed of the parallel combination of an inductor L and a capacitor C. Introducing the annihilation and creation operators $\hat{a}$ and $\hat{a}^\dagger$, the resonator can be described by the Hamiltonian

$$\hat{H}_\mathrm{r} = \hbar\omega_r \hat{a}^\dagger \hat{a}, \tag{35}$$

with $\omega_r = 1/\sqrt{LC}$. Using this simple model, one finds that the voltage across the LC circuit (or, equivalently, on the center conductor of the resonator) is $\hat{V}_r = V^0_\mathrm{rms}(\hat{a} + \hat{a}^\dagger)$, where $V^0_\mathrm{rms} =$

$\sqrt{\hbar\omega_r^2 Z_r/2}$ is the rms value of the voltage in the ground state. An important advantage of this architecture is the extremely small separation $b \sim 5$ μm between the center conductor of the resonator and its ground planes. This leads to a large rms value of the electric field $E^0_{\rm rms} = V^0_{\rm rms}/b \sim 1.0$ V/m for typical realizations. As illustrated in figure 6, by placing the qubit at an antinode of the voltage, it will strongly interact with the resonator through the large electric field $E^0_{\rm rms}$.
Due to capacitive coupling (C_g) with the center conductor the gate voltage has an extra term $\hat{V}_{\rm r}$ and the resonator-transmon Hamilton is

$$\hat{H}_{\rm int} = -\frac{C_g \hat{V}_r \hat{Q}}{C_\Sigma} = \hbar g(\hat{a} + \hat{a}^\dagger)(\hat{b} + \hat{b}^\dagger), \tag{36}$$

where

$$g = -\beta\omega_r \sqrt{\frac{Z_r}{4Z_{\rm tr}}} = -\beta\omega_r e \sqrt{\frac{Z_r}{\hbar}} \left(\frac{E_J}{8E_C}\right)^{1/4}. \tag{37}$$

This Hamiltonian is the multilevel version of the Rabi Hamiltonian and under the rotating wave approximation it can be reduced to the multilevel version of the Jaynes-Cummings Hamiltonian

$$\hat{H}_{\rm int} = \hbar g(\hat{a}\hat{b}^\dagger + \hat{a}^\dagger \hat{b}). \tag{38}$$

As we will see the qubit can be measured by applying microwaves around the frequency ω_r to the input port of the resonator. This can be described by the additional Hamiltonian

$$\hat{H}_{\rm meas} = \hbar\mathcal{E}(t)\left(\hat{a} + \hat{a}^\dagger\right), \tag{39}$$

where $\mathcal{E}(t) = \mathcal{E}_x(t)\cos(\omega_m t) + \mathcal{E}_y(t)\sin(\omega_m t)$.

2.1 Dispersive regime

In the situation where the qubit is strongly detuned from the cavity, $|\omega_r - \omega| \gg |g|$, the total Hamiltonian $\hat{H}_{\rm tot} = \hat{H}_{\rm tr} + \hat{H}_{\rm int} + \hat{H}_{\rm r}$ can be approximately diagonalized to second order in $g/(\omega_{i+1,i} - \omega_r)$ by finding a unitary transformation $\hat{D}$ such that the effective Hamiltonian

$$\hat{H}^D_{\rm tot} = \hat{D}^\dagger \hat{H}_{\rm tot} \hat{D}. \tag{40}$$

is diagonal. A perturbative method is outlined in Appendix A which consists of finding an iteratively operator $\hat{S}$ which gives $\hat{D} = \exp(-i\hat{S})$ that diagonalizes the system to the desired order. Doing this to second gives the following quantized version of the dynamical Stark shift Hamiltonian

$$\hat{H}^D_{\rm tot} = \hbar\tilde{\omega}_r \hat{a}^\dagger\hat{a} + \hbar\sum_j \chi_j \hat{a}^\dagger\hat{a}|j\rangle\langle j| + \hbar\sum_{j\neq 0}\tilde{\omega}_j|j\rangle\langle j|, \tag{41}$$

where D represents the diagonal frame (or dressed frame) and

$$\begin{aligned} \chi_j &= \frac{g^2(\delta - \omega + \omega_r)}{(\omega + j\delta - \omega_r)(\omega + (j-1)\delta - \omega_r)}, \\ \tilde{\omega}_j &= j\omega + \frac{\delta}{2}(j-1)j + \frac{jg^2}{\omega + (j-1)\delta - \omega_r}. \end{aligned} \tag{42}$$

Here χ_j represents the shift on the cavity frequency depending on the transmon state and $\tilde{\omega}_j$ represents the Lamb shifted energy levels of the transmon. The cavity drive in this dressed frame becomes

$$\hat{H}^D_{\rm meas} = \hbar\mathcal{E}(t)\left[\hat{a}+\hat{a}^\dagger+\sum_j \frac{\sqrt{j}g}{\omega-\omega_r+\delta j}\left(|j+1\rangle\langle j|+|j\rangle\langle j+1|\right)\right] \tag{43}$$

and we see that it can be used to either drive the resonator or qubit by setting the drive frequency to be close to either ω_r or ω respectively.

2.2 Quantum non-demolition measurement

One of the main reasons for the addition of the resonator is the term proportional to $\hat{a}^\dagger\hat{a}|j\rangle\langle j|$ in equation (41) can be interpreted as a pull on the resonator frequency by the transmon. Without going into the full details (for a more complete treatment see Refs [20, 21]) the resonator will have many frequencies depending on the state of the transmon and if we can measure this frequency we have a good quantum measurement. Furthermore, since the coupling commutes with the transmons free Hamiltonian it is possible for the measurement to be quantum non-demolition.

Assuming the transmon is initially in either the 0 or 1 state and since equation (41) is linear in the photon number the state of the resonator if started in a coherent state (the ground state is a coherent state) will remain in one. As such this system can be described by two complex numbers α_0 and α_1 which represent the expectation value of $\hat{a}$ condition on the qubit state. These have the following equations of motion

$$\begin{aligned}\dot{\alpha}_0 &= -i\mathcal{E}(t) - i(\omega_r+\chi_0)\alpha_0 - \kappa\alpha_0/2\\ \dot{\alpha}_1 &= -i\mathcal{E}(t) - i(\omega_r+\chi_1)\alpha_1 - \kappa\alpha_1/2\end{aligned} \tag{44}$$

where $\mathcal{E}(t)$ is defined below equation (39), and κ is the rate at which photons leave the resonator. The resonator will have two times scales one evolving at the drive frequency and a slow one representing the response of the oscillator in the rotating frame. In the rotating frame the resonator is better represented by the complex number $\tilde{\alpha}_i = \alpha_i e^{i\omega_m t}$ and some typical trajectories are shown in figure 7a. Heere we see that over time the pointer states separate by an amount $\beta(t) = \tilde{\alpha}_0 - \tilde{\alpha}_1$. It is this difference that determines the measurement rate but before we can derive this we need to review how the measurement is performed. In a typical circuit QED experiment the voltage leaving the cavity is usually amplified by a phase preserving amplifier. This amplifier has the relation

$$\hat{a}_{\rm out}(t) = \sqrt{G}\hat{a}_{\rm in}(t) + \hat{F}(t) \tag{45}$$

where G is the power gain, $\hat{F}(t)$ is the added noise that must obey $[\hat{F}(t), \hat{F}^\dagger(t')] = (1-G)\delta(t-t')$, and $\hat{a}_{\rm out}(t)$ and $\hat{a}_{\rm in}(t)$ are the input and output operators representing the field before and after the amplifier. Here we have made an assumption the bandwidth of the amplifier is constant and larger the then the bandwidth of the signal being measured. The fluctuations in the amplified field is determined by

$$\begin{aligned}|\Delta a_{\rm out}|^2 &= \frac{1}{2}\langle\hat{a}^\dagger_{\rm out}\hat{a}_{\rm out}\rangle + \frac{1}{2}\langle\hat{a}_{\rm out}\hat{a}^\dagger_{\rm out}\rangle - \langle\hat{a}_{\rm out}\rangle\langle\hat{a}^\dagger_{\rm out}\rangle\\ &= G(|\Delta a_{\rm in}|^2 + A\delta(t-t')) = G(1/2+A)\delta(t-t')\end{aligned} \tag{46}$$

where $A \geq |1-G|/2G$ is the added noise and we have used the fact that for a coherent field $|\Delta a_{\rm in}|^2 = \delta(t-t')/2$. The output signal will be proportional to $\mathrm{Re}(\hat{a}_{\rm out}e^{-i(\omega_m t+\phi)}) = I_\phi \cos(\omega_m t) + Q_\phi \sin(\omega_m t)$ where $2I_{\rm out} = \hat{a}_{\rm out}e^{-i\phi} + \hat{a}^\dagger_{\rm out}e^{i\phi}$ and $2Q_{\rm out} = -i\hat{a}_{\rm out}e^{-i\phi} + i\hat{a}^\dagger_{\rm out}e^{i\phi}$ are the standard quadratures of the field with the phase ϕ being a user set phase defined with respect to the phase of the original drive. These quadratures can be measured by mixing this voltage with a local oscillator of frequency ω_m. The fluctuations in the quadratures will be given by $|\Delta I_{\rm out}|^2 = |\Delta Q_{\rm out}|^2 = G(1/4 + A/2)\delta(t-t')$ and by defining the integrated signal for measurement time t_m by

$$S(t_m) = \frac{1}{t_m}\int_0^{t_m} \langle \hat{I}_{\rm in}\rangle(t)dt \tag{47}$$

the SNR (signal-noise-ratio) is

$$\mathrm{SNR} = \frac{\left(\frac{1}{t_m}\int_0^{t_m}\langle \hat{I}_{\rm in}(t)\rangle dt\right)^2}{\frac{1}{t_m}\int_0^{t_m}|\Delta I_{\rm out}|^2 dt} = \eta\frac{\left(\int_0^{t_m}\langle \hat{I}_{\rm in}(t)\rangle dt\right)^2}{t_m}, \tag{48}$$

where $\eta = 1/(1+2A)$ is the efficiency. Here we see that for a linear phase preserving amplifier this can never be larger then $1/2$ and to get equal to 1 we would need to used a phase sensitive amplifier. In term of the qubit $\langle \hat{I}_{\rm in}\rangle = \sqrt{\kappa}\langle\hat{\sigma}_z\rangle|\beta|\cos(\theta_\beta - \phi)/2 + \sqrt{\kappa}|\mu|\cos(\theta_\mu - \phi)/2$ where $\theta_\beta = \arg(\beta)$, $\mu = \tilde{\alpha}_0 + \tilde{\alpha}_1$ and $\theta_\mu = \arg(\mu)$. Here we see that by setting $\phi = \theta_\beta$ we perform a quantum measurement of the qubit state. To get estimate of the SNR in terms of the system parameters we can assume that the dynamics of $\tilde{\alpha}_{0(1)}$ can be ignored ($t \gg 1/\kappa$), here the SNR is given by

$$\mathrm{SNR} = \eta\Gamma_m t_m, \tag{49}$$

where we refer to $\Gamma_m = \kappa|\beta|^2$ as the measurement rate [21]. Since Γ_m scales with the measurement amplitude, and thus with the number of photons populating the resonator, this expression indicates that arbitrarily large SNRs can be reached in principle by simply increasing this amplitude. However, at large photon numbers the dispersive Hamiltonian, equation (41), breaks down and the results obtained here are simply no longer valid.

As a result, we must maximize the SNR at a fixed number of photons which is assumed to be small enough for the dispersive approximation to be valid. The number of photons inside the resonator depends on the drive amplitude $\mathcal{E}_x$, on resonator damping κ, resonator-drive detuning $\Delta_r = \omega_r + (\chi_0 + \chi_1)/2 - \omega_m$, and on the dispersive transmon-resonator coupling $\chi_{1(0)}$. When optimizing the SNR we assume a fixed $\bar{n}$ well below the dispersive breakdown. Under this constraint, and assuming that the resonator has reached steady state, we find that the optimal SNR, for arbitrary $\chi_{1(0)}$ and κ, occurs at $\Delta_r = 0$ and is given by (see [21])

$$\mathrm{SNR} = \frac{4\bar{n}\eta\kappa(\chi_1-\chi_0)^2 t_m}{\kappa^2 + (\chi_1-\chi_0)^2} \tag{50}$$

which is optimized at $\kappa = |\chi_1 - \chi_0|$ to give $\mathrm{SNR} = 2\bar{n}\eta|\chi_1 - \chi_0|t_m$. As shown in Ref. [23] this can be related to the measurement fidelity F_m by

$$F_m = \mathrm{erf}\left(\sqrt{\frac{\mathrm{SNR}}{2}}\right). \tag{51}$$

which means for a $F_m = 0.99$ we require a $\mathrm{SNR} = 6.64$. With current experiments we can arrange them such that $\mathrm{SNR} \sim 100\eta$ and until recently [24, 25] amplifies have not existed that

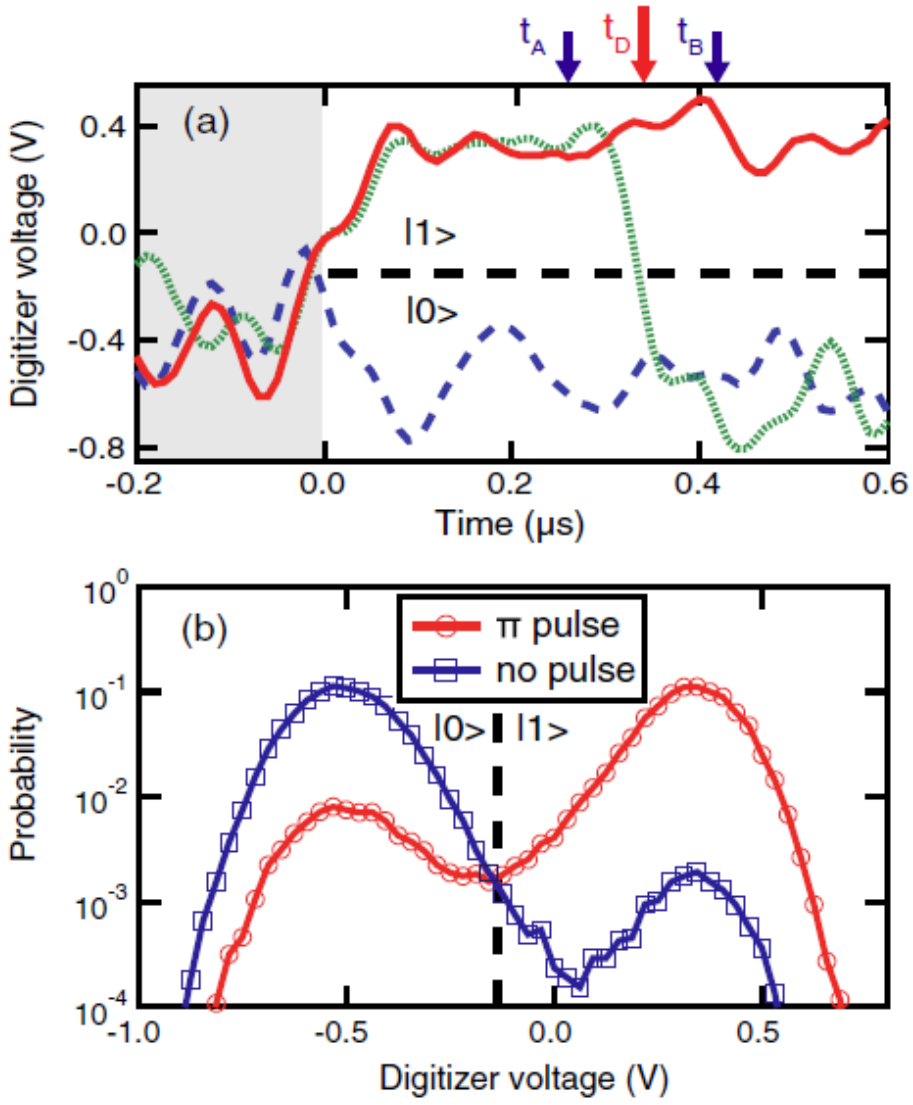

Fig. 7: *Qubit readout at $\bar{n} = 14.6$ photons. (a) Three individual qubit readouts starting at $t = 0$: $|1\rangle$ (solid red line), $|0\rangle$ (long blue dashed line), abrupt quantum jump from the excited to ground state (short green dashed line). (b) Log-linear distributions of many $|0\rangle$ and $|1\rangle$ state preparations. Figure and caption reproduced from Ref. [22].*

have η large enough to allow single shot readout. Current state of the art [22, 26] have shown single shot readout $> 90\%$ with the main limitation being initial heating. Shown in figure 7b is a histogram of many $|0\rangle$ and $|1\rangle$ state preparations showing clearly that the initial states can be distinguished.

2.3 Two-qubit exchange interaction

Another application of a resonator is as a quantum bus [27, 28]. Here two or more transmons (or other superconducting qubits) are coupled to one or more resonators to allow the formation of a lattice. This lattice could be the building blocks for a large scale quantum information processor and since 2009 at IBM we have been investigating how the surface code could be realized on such a lattice.
To understand the physics we consider only two transmons and one resonator. In this case the Hamiltonian in the bare frame will be given by

$$\hat{H}_{\rm tot} = \hat{H}_{\rm r} + \hat{H}_{\rm tr_1} + \hat{H}_{\rm tr_2} + \hbar g_1(\hat{a}\hat{b}^\dagger + \hat{a}^\dagger\hat{b}) + \hbar g_2(\hat{a}\hat{c}^\dagger + \hat{a}^\dagger\hat{c}) \tag{52}$$

where $\hat{c}$ represents the second transmon and we have used ω_i to label the resonance frequency of transmon i and not the state dependence as used above. When we need to label both the state dependence and transmon number we will use a subscript $i:j$. In the limit that the cavity frequency is very detunned from either of the two transmons, such that $|\omega_r - \omega_i| >> |g_i|$ we can used the second case in Appendix A to eliminated the single photon transitions between the resonator and either transmon. In this case the effective Hamiltonian becomes

$$\begin{aligned}\hat{H}^D_{\rm tot} =& \hbar\tilde{\omega}_r\hat{a}^\dagger\hat{a} + \hbar\sum_j \chi_{1:j}\hat{a}^\dagger\hat{a}|j\rangle\langle j| + \hbar\sum_{j\neq 0}\tilde{\omega}^{(1)}_j|j\rangle\langle j| + \hbar\sum_k \chi_{2:k}\hat{a}^\dagger\hat{a}|k\rangle\langle k| + \hbar\sum_{k\neq 0}\tilde{\omega}_{2:k}|k\rangle\langle k| \\ &+ \hbar\sum_{j,k}\sqrt{(j+1)(k+1)}J_{j,k}(|j,k+1\rangle\langle j+1,k| + |j+1,k\rangle\langle j,k+1|)\end{aligned} \tag{53}$$

where we will again use D to refer to dressed frame and the two-photon virtual coupling rate $J_{j,k}$ is given by

$$J_{j,k} = \frac{g_1 g_2(\omega_1 + \omega_2 + j\delta_1 + k\delta_2 - 2\omega_r)}{2(\omega_1 + j\delta_1 - \omega_r)(\omega_2 + k\delta_2 - \omega_r)}. \tag{54}$$

Here we see that while the transmons can exchange excitations the interaction of the transmons with the resonator is purely dispersive. Each transmon has a χ shift on the cavity frequency which allows a joint measurement of the two-transmon state [29, 30].
The interaction between the transmons is of a simple form, it exchanges one excitation between the transmons. This can be interpreted as two virtual photons mediate an exchange between the two transmon by the resonator. In the limit that $|\omega_i - \omega_r| \gg \delta_i$ and we have zero photons in the cavity the above is well approximated by

$$\hat{H}^D_{\rm sys} = \hbar\left[\tilde{\omega}_1\hat{b}^\dagger\hat{b} + \frac{1}{2}\delta_1\hat{b}^\dagger\hat{b}(\hat{b}^\dagger\hat{b} - 1)\right] + \hbar\left[\tilde{\omega}_2\hat{c}^\dagger\hat{c} + \frac{1}{2}\delta_2\hat{c}^\dagger\hat{c}(\hat{c}^\dagger\hat{c} - 1)\right] + \hbar J(\hat{b}\hat{c}^\dagger + \hat{b}^\dagger\hat{c}) \tag{55}$$

where $J = J_{0,0}$. In the following sections we will use this Hamiltonian as our starting point. It looks quite simple but as we will see it contains allot of interesting physics which can be used to implement a number of different two-qubit gates.
It is also worth noting here all the approximations that we have made to derive this equations:

1. We assumed that the trasmon can be approximated by a duffing oscillator. This is valid in the very large E_J/E_C limit, however, for the experimental regime $E_J/E_C = 30 - 60$ the matrix elements do not quite obey the $\sqrt{n+1}$ rule and the anharmonicity is not quited δ.

2. We made the rotating wave approximation and ignored terms like $\hat{a}\hat{b}$. While these have an energy cost of $\omega_r + \omega_i$ which is larger than $\omega_r - \omega_i$ (cost from terms like $\hat{a}\hat{b}^\dagger$) in current experiments where $\omega_r \gg \omega_i$ we have started to see frequency shifts similar in nature to the Bloch-Siegert shift and these terms must be included [4]. Including these terms is non-trivial as they don't conserved total excitation number so diagonalizing the cavity-resonator Hamiltonian becomes more complicated.

3. We have assumed that we only need to go to second order in $g_i/(\omega_r - \omega_i)$ when going to the dressed frame. This is not enough to explain some of the experiments and higher order effects must be included. For the interested reader see Ref. [31, 32] where we show how to include higher order terms in the dressed frame.

4. We assumed that $|(\omega_r - \omega_i)| \gg |\delta_i|$ this allowed us to removed the j dependences from equation (54). I have not really looked into the effects this assumptions has on the dynamics but I suspect in does not have much effect in the two-qubit subspace.

5. We assumed that the transmons where so far apart that the coupling between them was induced completely from the resonator. In reality these are quite large devices and will have a capacitive coupling $J_{\rm cap}$ of their own. To first order it will either add or subtract to the above J (depending on the locations and frequencies of the transmons) but unlike the cavity induced coupling it will have non-rotating terms which we will induce Bloch-Siegert like frequency shift of the order $J_{\rm cap}^2/(\omega_1 + \omega_2)$ which we may need to include.

2.4 The 3D cavity architecture

Recently Professor Schoelkopf at Yale has shown that we can also use a 3 dimensional cavity for a quantum circuit QED architecture [3], termed 3D. In the 3D cQED framework, transmons are manufactured with standard lithographic processes while the cavities, simple macroscopic resonant enclosures, are made independently with very different techniques, such as precision machining. They can be made out of either copper or aluminum. The cavity usually have an interior volume of $(15.5 \times 18.6 \times 4.2)\ \mathrm{mm}^3$ giving it a resonance frequency in the 10-12 GHz range. An example of a copper enclosure consisting of two cavities (and three transmons) is shown in figure 8. The interaction of the 3D cavity and the transmon can be described by the above Hamiltonians so there are many similarities to the standard 2D framework. In fact the device shown in figure 8 is the 3D analog to the device shown in figure 5.
One of the advantages of the 3D architecture is the modularity of the design. It is possible to build up a multi-qubit system from individual discrete components, each of which is independently designed, tested, characterized, and selected, for optimal parameters to realize the desired effect. It is possible to build up a library of transmons. Another advantage (the most important in my opinion) is I believe the current limit to coherence times is surface loss and to some extent dielectric loss. This is just crap in the substrate or the interface between the substrate and the aluminum having a loss tangent. The 3D architecture allows us to make the devices bigger thereby reducing the participation of the electric field in these high loss sections. Furthermore since the cavity is simply a box it is possible to ensure the higher or unwanted

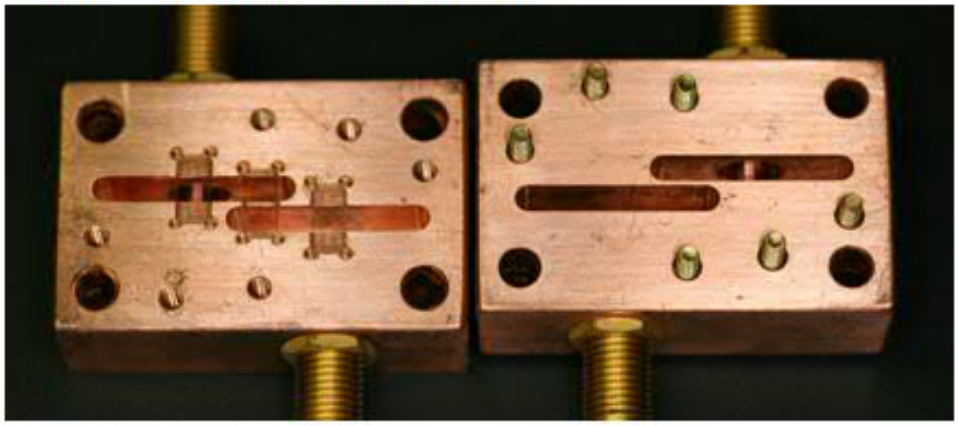

Fig. 8: *A copper enclosure consisting of two cavities (and three transmons). The transmons are fabricated on individual sapphire or silicon chips and are independently pre-characterization and chosen for there desired application.*

modes are very far away from the transmon resonance frequency. That is, it is possible to design the system such that the standard single-mode cavity approximation is more robust. For this reason the 3D architecture offers us a method to test the physics in a cleaner environment. It has already being very successful at this goal as by showing that it is not the junction that limits the coherence time in 2D to 10-20 μs. They can be as long as 90 μs.
In my opinion it is not clear that there is really a difference between these architectures and both offer a promising avenue for developing a large scale quantum information processor.

2.5 Implementation of the iSwap gate by virtual qubit-qubit interactions

One of the most simple ways to implement a two-qubit gate is to used flux to tune the two transmons into resonance (see Sec. 1.4). In this case we start with the qubit very far apart and provided $|J| \ll |\Delta_{12}|$ where $\Delta_{12} = \omega_1 - \omega_2$, then the interaction can be consider *off*. In this case the eigenstates of the transmon will be close to the uncoupled $J = 0$ eigenstates. If now we can tune ω_1 into resonance with ω_2 (or vice versa) the uncoupled transmons will now swap between the states $|01\rangle$ and $|10\rangle$ with a swap time $t_g = 2\pi/4J$. That is, if we restrict equation (55) to the qubit subspace the unitary representing the two-qubit gate will be given by

$$\hat{U}_{\mathsf{iSwap}}(\theta) = \exp(-i\theta(\hat{X}\hat{X} + \hat{Y}\hat{Y})/2) = \begin{pmatrix} 1 & 0 & 0 & 0 \\ 0 & \cos(\theta) & -i\sin(\theta) & 0 \\ 0 & -i\sin(\theta) & \cos(\theta) & 0 \\ 0 & 0 & 0 & 1 \end{pmatrix} \tag{56}$$

where $\theta = Jt$. Choosing $\theta = \pi/4$ gives the $\sqrt{\mathsf{iSwap}}$ gate and $\theta = \pi/2$ gives the iSwap gate. Both of these are known to be universal for quantum computing [33] but personally I prefer the iSwap as it is a Clifford operation. This was demonstrated experimentally in Ref. [34] for two capacitively coupled phase qubits, and for two transmons coupled by a resonator in Ref. [28]. Recently the Saclay group lead by Professor Esteve have shown that this gate can be implemented with high fidelity in two capacitively coupled transmons by generating Bell states with state fidelity $F_s = 0.91$ and gate fidelity $F_g = 0.92$ [35] (see appendix C for my definitions of gate and state fidelity). Figure 9a shows the data from reference [35] where it is clear that the

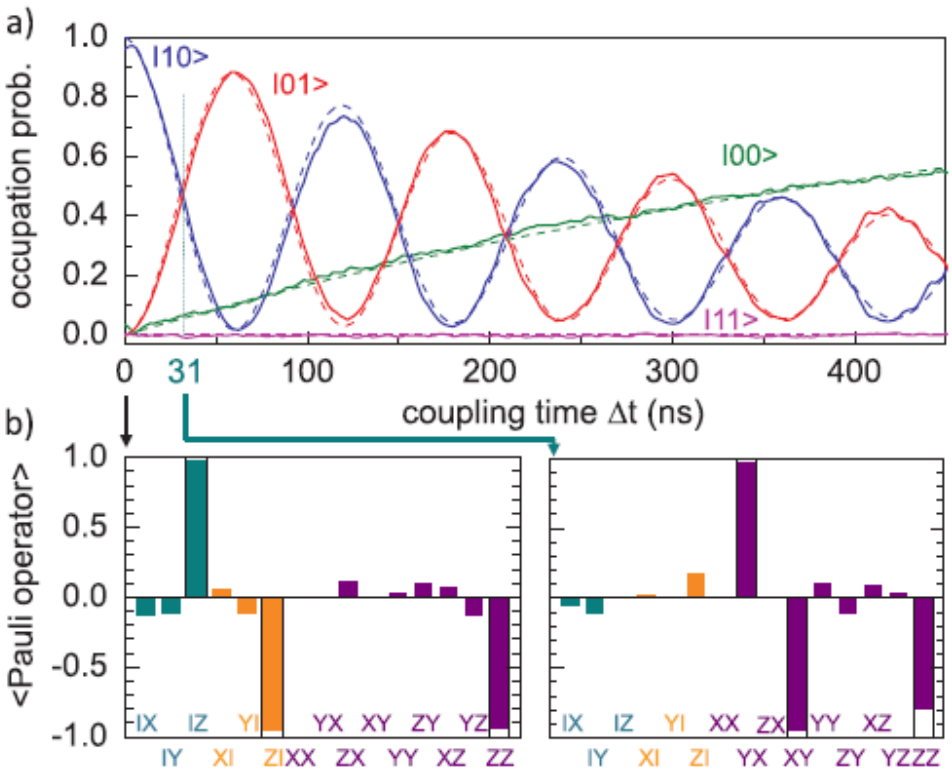

Fig. 9: *Coherent swapping of a single excitation between the qubits. (a) Experimental (solid lines) and fitted (dashed lines) occupation probabilities of the four computational states* $|00\rangle$, $|01\rangle$, $|10\rangle$, $|1\rangle$ *as a function of the coupling duration. State tomography in the Pauli state vector representation of the initial state (b) and of the state produced by the* $\sqrt{\text{iSwap}}$ *gate (c). Ideal is shown as an empty bar and experiment by colors. Figure reproduced from Ref. [35].*

states $|01\rangle$ and $|10\rangle$ are swapping while the states $|00\rangle$ and $|11\rangle$ remain unaffected by the gate. The slow decay of the $|00\rangle$ state is due to T_1 (they are using a differently labeling for the 0 and 1 state). In figure 9b they show the initial state in the Pauli state vector representation (see Ref. [29] or appendix C) where it is clear that at the beginning the expectation of the two-qubit Pauli operators is just the product of the one-qubit Pauli operators while after the gate has interacted for the time of 31 ns ($\sqrt{\text{iSwap}}$ time) all the correlations are in the two-qubit Pauli operators indicating that they have created an entangled state.

2.6 Implementation of the cPhase gate by higher level interactions

Another gate which can be activated by tuning the frequency of the transmon is the cPhase gate used in Ref. [36, 29, 37] and originally proposed in Ref. [38]. This gate works by exploiting resonances in the higher levels. If we start with the Hamiltonian [equation (55)] and in the limit that $|\Delta_{12}| \gg J$ we can used Appendix A to removed the exchange coupling and find a diagonal Hamiltonian. Doing this we find that this system in the two-qubit subspace is described by the Hamiltonian

$$\hat{H}^{D_2}_{\text{sys}} = -\frac{\omega_1 + J^2/\Delta_{12} + \zeta/2}{2}\hat{Z}\hat{I} - \frac{\omega_2 - J^2/\Delta_{12} + \zeta/2}{2}\hat{I}\hat{Z} + \frac{\zeta}{4}\hat{Z}\hat{Z} \tag{57}$$

where D_2 means that we have diagonalized the exchange coupling. The difference between the trasmons resonance frequency conditioned on the state of the other transmon is given by

$$\zeta = (E_{11} - E_{10} - E_{01})/\hbar = -\frac{2J^2(\delta_1 + \delta_2)}{(\Delta_{12} + \delta_1)(\delta_2 - \Delta_{12})}. \tag{58}$$

Here we see that the higher levels have result in a ZZ interaction between the two transmons. The strength of the interaction is given by ζ and is largest when either $\delta_1 = -\Delta_{12}$ or $\delta_2 = \Delta_{12}$. This gate can be implemented by stating with the transmons well separated ($\zeta = 0$) and then by adiabatically tunning the $0 - 1$ transition close to the $1 - 2$ of the other transmon results in each basis state acquiring both one- and two-qubit phases. After adjusting the rising and falling edges of the flux pulse used to tune the qubits into the coupling position the two-qubit gate implement is

$$\hat{U}_{\mathsf{cPhase}}(\theta) = \exp[-i\theta(\hat{Z}\hat{Z} - \hat{I}\hat{Z} - \hat{Z}\hat{I})/4] = \begin{pmatrix} 1 & 0 & 0 & 0 \\ 0 & 1 & 0 & 0 \\ 0 & 0 & 1 & 0 \\ 0 & 0 & 0 & e^{-i\theta} \end{pmatrix} \tag{59}$$

where $\theta = \zeta t$ and we have ignored global phases. Now by choosing $\theta = \pi$ implements a cPhase which is universal for quantum computation. This gate was used in Refs. [36] and [29] to generate highly entangled Bell states (state fidelity $F_s = 0.95$) and the first implementation of a quantum two-qubit algorithm with superconducting qubits. In figure 10a both experimental measurements from Ref. [36] of ζ and theoretical prediction are shown. Here we can see that the above model represents the system quite well and the rate ζ can be large. In figure 10b the Pauli state vector of Bell states $|\Psi_+\rangle = (|00\rangle + |11\rangle)/\sqrt{2}$ and $(|00\rangle + |01\rangle - |10\rangle + |11\rangle)/2$ are shown. These have state fidelity $F_s = 0.90 \pm 0.006$, and $F_s = 0.925 \pm 0.007$ and again both show that very little weight is left in the separable space indicating that a large amount of entanglement is present.

Note the higher level does not have to be used in an adiabatic way, instead we could suddenly tune the qubits into the point $\delta_1 = -\Delta_{12}$ (or $\delta_2 = \Delta_{12}$). At this point the $|11\rangle$ will swap with either the $|20\rangle$ or $|02\rangle$ at a rate $\sqrt{2}J$. This is very similar to the iSwap interaction just in a higher level subspace. In this subspace when the $|11\rangle$ state returns back (after a time $t = \pi/\sqrt{2}J$) it will have an additional phase -1 giving the state $-|11\rangle$ whereas the rest of the two-qubit basis states remain unchanged. That is, we can implement a cPhase gate with a minimum time $t = \pi/\sqrt{2}J$. This version of the gate was used in [37] on a three qubit sample to general both high fidelity Bell states ($F_s = 0.94$) and GHZ states ($F_s = 0.88$).

2.7 Implementation of the $\mathsf{ZX}_{\pi/2}$ gate by the cross resonance effect

In the above two gates the two-qubit interaction was turned on by tunning the transmons resonance frequency. The biggest problem with these procedures is the transmon when it has left its *sweet* spot the dephasing time can be substantially reduced (see section 1.4) and for this reason it is desirable to have a gate that can be turned *on* with microwaves. This way we can use single junction transmon (fixed frequency) and microwave only control to implement both the single and two-qubit gates. This removes the flux bias lines which lowers the input/output requirements for a large scale device. This is important when thinking about how to scale this system up to many qubits. The cross resonance effect is a simple approach that allows us to

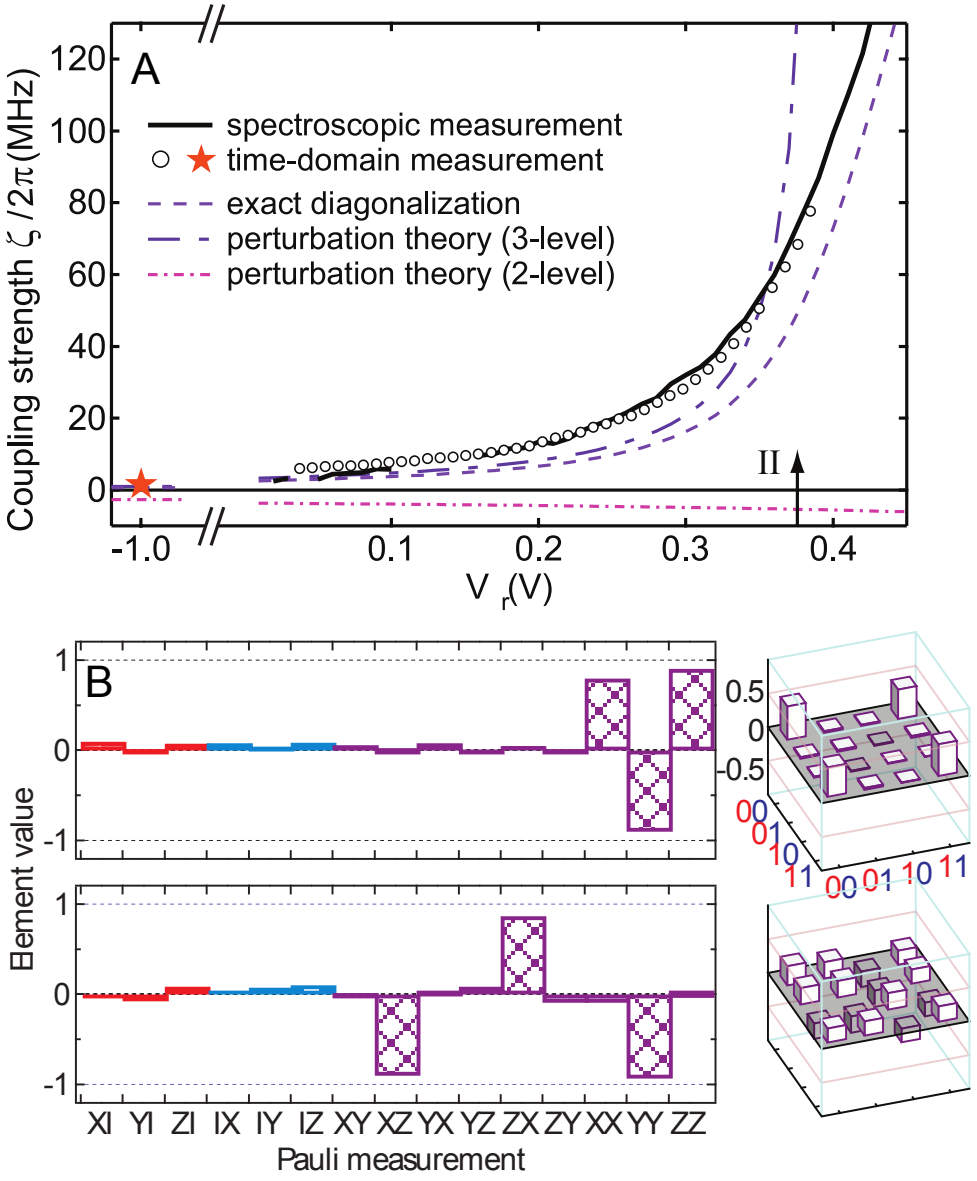

Fig. 10: *Characterization of the controlled-phase gate. (a) The coupling strength ζ of the effective ZZ interaction, obtained both from spectroscopy (solid curve) and theory. The Numerical diagonalization and perturbation theory for three-level transmons agree reasonably with the data. Perturbation theory for two-level qubits gives the wrong magnitude and sign for ζ, and demonstrates that the higher transmon excitations are necessary for the interaction. b) Experimental Pauli state vector of the two entangled states $|\Psi_+\rangle = (|00\rangle + |11\rangle)/\sqrt{2}$ and $(|00\rangle + |01\rangle - |10\rangle + |11\rangle)/2$ with state fidelity $F_s = 0.90 \pm 0.006$, and $F_s = 0.925 \pm 0.007$ respectively. Figure reproduced from Refs. [36] and [29].*

realize this goal. It was first proposed in Ref. [39] and later independently rediscovered in Ref. [40, 41]. It has now been experimentally implement by IBM group in Ref. [42, 5, 43] where high fidelity operations have been realized.

The essential idea of the cross resonance effect is that if we define the qubits in the dressed basis then individual capacitive drive lines will now drive both single and two-qubit gates. To see this we note that in the *off* state the qubits are chosen to have resonance frequencies such that $|\Delta_{12}| \gg J$ and the free Hamiltonian of the system is given by equation (57). Provided the qubits are far apart we can engineer ζ to be small and even it is not small we can use a echo pulse to decouple its effect (see below). In deriving this Hamiltonian we had to move to a frame defined by the unitary operator $\hat{D}_2 = \exp(-i\hat{S})$ where $\hat{S}$ was found using the methods in Appendix A. This transformation must also be applied to the external individual drives, giving

$$\begin{aligned}\hat{H}^{D_2}_{\mathrm{dr}_1} =& \hbar\Omega_1(t)\hat{D}_2^\dagger\hat{X}\hat{D}_2\hat{I} = \hbar\Omega_1(t)[\hat{X}\hat{I} - \nu_1\hat{I}\hat{X} - \mu_1\hat{Z}\hat{X}] \\ \hat{H}^{D_2}_{\mathrm{dr}_2} =& \hbar\Omega_2(t)\hat{I}\hat{D}_2^\dagger\hat{X}\hat{D}_2 = \hbar\Omega_2(t)[\hat{I}\hat{X} + \nu_2\hat{X}\hat{I} + \mu_2\hat{X}\hat{Z}]\end{aligned} \tag{60}$$

where

$$\begin{aligned}\mu_1 =& \frac{J}{\Delta_{12}}\frac{\delta_1}{(\delta_1+\Delta_{12})} \\ \mu_2 =& \frac{J}{\Delta_{12}}\frac{\delta_2}{(\delta_2-\Delta_{12})} \\ \nu_1 =& \frac{J}{\Delta_{12}}\frac{\Delta_{12}}{(\delta_1+\Delta_{12})} \\ \nu_2 =& \frac{J}{\Delta_{12}}\frac{(-\Delta_{12})}{(\delta_2-\Delta_{12})}\end{aligned} \tag{61}$$

Here we see that the external drive line for transmon 1 can now be used to drive either transmon 1 by setting the drive frequency to ω_1 and transmon 2 by setting the drive frequency to ω_2. The drive at frequency ω_2 does a combination of a conditional rotation of the second transmon $\hat{Z}\hat{X}$ or a unconditional $\hat{I}\hat{X}$ depending on the δ_1 of transmon 1. In the limit that δ_1 is zero it is all an unconditional rotation (we can not make entanglement with harmonic oscillators) and when $|\delta_i| \to \infty$ it is all conditional rotation and can be used to make a universal two-qubit gate.

In figure 11a the response of driving the second transmon is shown for different initial states of transmon 1. It is clear that the two responses rotate at a different rate and we have implemented a $\hat{Z}\hat{X}$ rotation (along with a single qubit $\hat{I}\hat{X}$ rotation). That is, the two qubit gate will be of the form ZX_θ where

$$\mathsf{ZX}_\theta = \exp[-i\theta(\hat{Z}\hat{X})/2] = \begin{pmatrix} \cos(\theta/2) & -i\sin(\theta/2) & 0 & 0 \\ -i\sin(\theta/2) & \cos(\theta/2) & 0 & 0 \\ 0 & 0 & \cos(\theta/2) & i\sin(\theta/2) \\ 0 & 0 & i\sin(\theta/2) & \cos(\theta/2) \end{pmatrix} \tag{62}$$

where $\theta = -\Omega_x\mu_1 t$. Setting $\theta = -\pi/2$ does a universal quantum gate and can be related to the CNOT by $\mathsf{CNOT} = \mathsf{ZX}_{-\pi/2}\mathsf{IX}_{\pi/2}\mathsf{ZI}_{\pi/2}$. The error terms will be of the form $\hat{I}\hat{X}$ (due to the left over unconditional rotation) and $\hat{Z}\hat{I}$ (ac-stark induced phase gate on transmon 1 from driving off resonance). We can either design the errors such that they implement a $\pi/2$ rotation thereby implementing the CNOT gate or we can get try to get rid of them. To get rid of these errors in

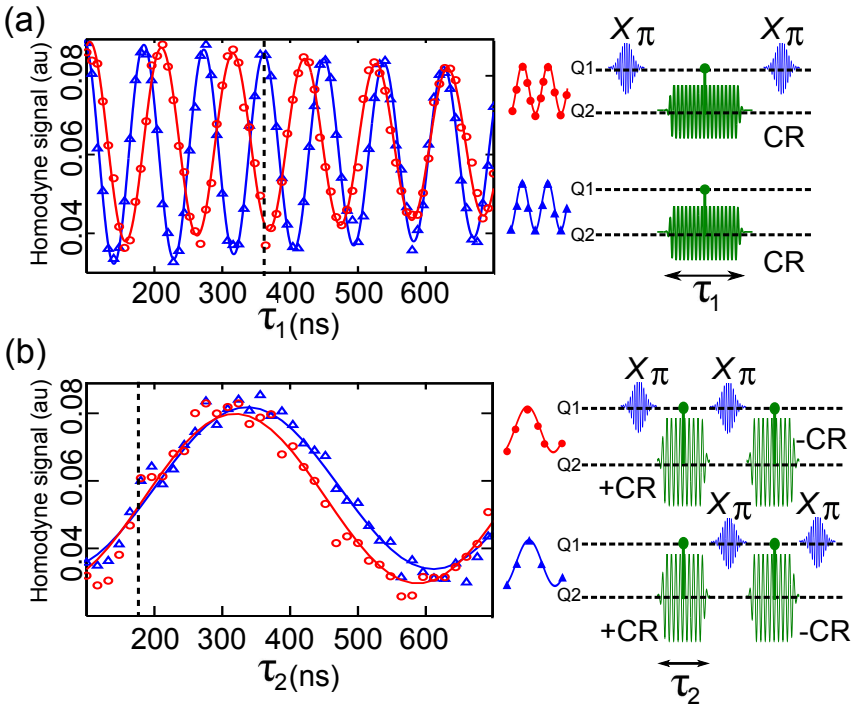

Fig. 11: *Homodyne signal as a function of the cross-resonance tone length and pulse sequences for the standard cross-resonance gate (a) and for the refocused* $\mathrm{ZX}_{-\pi/2}$ *(b). All tones are applied to the control qubit driving line, with the* π *pulses and cross-resonance tones applied at the control and target qubit frequencies, respectively. The* π *pulse between the two cross-resonance tones in the* $\mathrm{ZX}_{-\pi/2}$ *gate, along with the opposite sign of the second cross-resonance pulse, echo away the fast* $\hat{I}\hat{X}$ *component of the driving Hamiltonian seen in (a) and leave only the* $\hat{Z}\hat{X}$ *interaction. Figures reproduced from Ref. [43]*

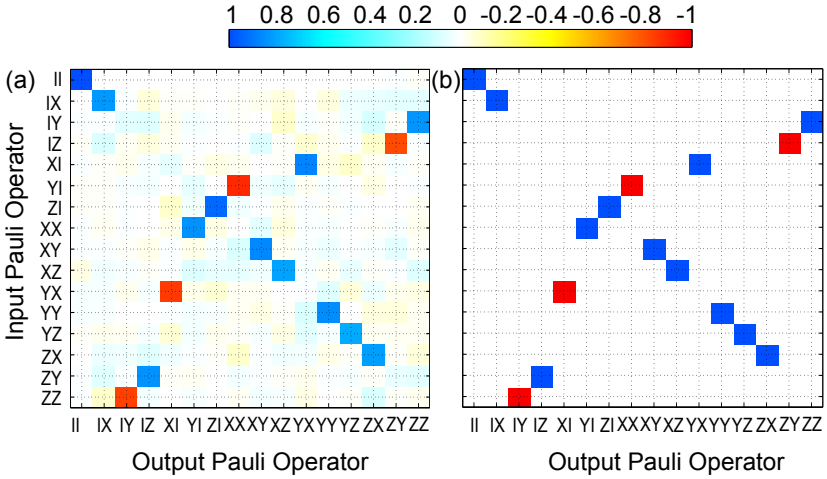

Fig. 12: *(a) Experimentally extracted Pauli transfer matrix of the* $\mathrm{ZX}_{-\pi/2}$ *gate with* $t_2 = 178ns$. *The gate fidelity is* $F_g = 0.88$. *(b) Ideal Pauli transfer matrix representation of the* $\mathrm{ZX}_{-\pi/2}$ *gate. Figures reproduced from Ref. [43]*

Ref. [43] we used an echo scheme consisting of a four pulses: positive CR pulse, π pulse on the control transmon, negative CR pulse, π pulse on the control transmon. Then net result of all these removes the $\hat{I}\hat{X}$ and $\hat{Z}\hat{I}$ component. This is shown in figure 12b. The reason why this works is that for the first CR pulse the $\hat{I}\hat{X}$ and $\hat{Z}\hat{X}$ evolve with a rate proportional to Ω_x, after the π pulse $\hat{Z}\hat{I}$ goes to $-\hat{Z}\hat{I}$ and then the follow negative CR pulse undoes the $\hat{I}\hat{X}$ contribution from the first CR pulse while doubling the $\hat{Z}\hat{X}$ contribution. The final π pulse simply returns $-\hat{Z}\hat{I}$ to $\hat{Z}\hat{I}$. The $\hat{Z}\hat{I}$ error will grow at a rate proportional to Ω_x^2 which does not depend on the sign of Ω_x and as such will be undone by the middle π pulse. It is also worth pointing out that this scheme will also echo away the $\hat{Z}\hat{Z}$ contribution provided it accumulates slower than the cross resonance rate $\Omega_x\mu_1$. In figure 12 the experimentally extracted Pauli transfer matrix is shown for the $\mathsf{ZX}_{-\pi/2}$ gate with $t_2 = 178ns$. This had a gate fidelity is $F_g = 0.88$ which as we will see is limited by errors is quantum process tomography and in other samples we have measured gate fidelities as high as $F_g = 0.95$ for the non-echoed scheme [5].

2.8 Implementation of the bSwap gate by higher level induced transitions

Another all microwave gate is the bSwap introduced in Ref. [44]. This gate is only possible because the higher levels of the transmon make possible the two-photon direct driving of the $|00\rangle \rightarrow |11\rangle$ transition. This transition is impossible in harmonic systems and is a small third order interaction in coupled qubit systems. However, as we will see, it can be made bright in coupled multilevel systems when the qubit-qubit detuning approaches the anharmonicity. A microwave pulse tuned to this two-photon transition induces an effective Hamiltonian which implements a rotation in the $\{|00\rangle,\ |11\rangle\}$ subspace whose angle is set by the action of the pulse, allowing the direct generation of entanglement from the ground state. The gate is similar to that proposed by Mølmer and Sorenson [45] which is a bi-chromatic two-photon excitation and has become commonplace in trapped ion quantum computing [46, 47].

To derive the effective Hamiltonian for the two-photon transition $|00\rangle \rightarrow |11\rangle$ we perform the following procedure. First we use the same transformation as used in section 2.7 to go to a frame which diagonalizes the system Hamiltonian $\hat{H}_{\rm sys}^{D_2}$ to second order in J/Δ_{12} and changes the controls by $\hat{D}_2^\dagger \hat{H}_{\mathrm{dr}_{1(2)}} \hat{D}_2$. The next step is to move to a frame at the drive frequency which is close to $\omega_d = (\omega_1 + \omega_2)/2 - \delta$ and then finally we separate the levels into high and low energy manifolds. In the case when Δ_{12} is approximately equal to δ_2 the low subspace is spanned by the states $|00\rangle$, $|11\rangle$, and $|02\rangle$ (it would switch to $|20\rangle$ if Δ_{12} approaches $-\delta_1$). Here we can use another Schrieffer-Wolff transformation to eliminate the coupling between theses manifolds. This is done using (107). This whole procedure is performed using *Mathematica*® and returns a second order effective Hamiltonian in the two-qubit subspace of the form

$$\begin{aligned}\hat{H}_{\rm sys}^{D_2R} =& \frac{\alpha_{IZ}}{2}\hat{I}\hat{Z} + \frac{\alpha_{ZI}}{2}\hat{Z}\hat{I} + \frac{\alpha_{ZZ}}{4}\hat{Z}\hat{Z} + \frac{\Omega_{BR}}{2}(\hat{X}\hat{X} - \hat{Y}\hat{Y}) + \frac{\Omega_{BI}}{2}(\hat{X}\hat{Y} + \hat{Y}\hat{X}) \\ &+ \frac{\Omega_S}{2}(\hat{X}\hat{X} + \hat{Y}\hat{Y}),\end{aligned} \tag{63}$$

and are given by

$$\begin{aligned}\Omega_{BR} =& \cos(2\phi)\Omega_B, \\ \Omega_{BI} =& \sin(2\phi)\Omega_B, \\ \Omega_S =& \frac{-2J\delta\left(J\Omega_1\Omega_2(\delta_1 - \delta_2) + \Omega_2^2\delta_2(\delta_1 + \Delta_{12}) + \Omega_1^2\delta_1(-\delta_2 + \Delta_{12})\right)}{\Delta_{12}(\delta_2 - \Delta)(\delta_1 + \Delta_{12})\left(-4\delta^2 + \Delta_{12}^2\right)},\end{aligned} \tag{64}$$

with

$$\Omega_B = \frac{-J\left(-J\Omega_1\Omega_2(\delta_1+\delta_2)+\Omega_2^2\delta_2(\delta_1+\Delta_{12})+\Omega_1^2\delta_1(\delta_2-\Delta_{12})\right)}{(\delta_2-\Delta_{12})(\delta_1+\Delta_{12})\left(-4\delta^2+\Delta_{12}^2\right)}. \tag{65}$$

Here I have defined Ω_B to be a factor of two different to Ref. [44] and ϕ is the phase difference between the drive used for the $|00\rangle \rightarrow |11\rangle$ transition and the single qubit drives. We find rather long expressions for α_{IZ}, α_{ZI} and α_{ZZ} and for the interested reader see Ref. [44]. We note that the three operators $(XX-YY)/2$, $(XY+YX)/2$ and $(ZI+IZ)/2$ form a SU(2) algebra and that both ZZ and $IZ-ZI$ commute with all three of these operators. Also, Ω_S is smaller than Ω_B by a factor of δ/Δ_{12} which leaves only the term described by $\alpha_{IZ}+\alpha_{ZI}$ in equation (63) as a non-trivial error. Therefore, we choose δ such that $\alpha_{IZ}+\alpha_{ZI}=0$ which corresponds, for a given power, to the drive frequency that shows the largest amplitude oscillations in two-photon spectroscopy. This leads to the unitary operator

$$U = U_{\mathsf{bSwap}}(\theta,\varphi)U_{ZZ}U_{IZ-ZI} \tag{66}$$

where

$$U_{\mathsf{bSwap}}(\theta,\varphi) = \begin{pmatrix} \cos(\theta) & 0 & 0 & e^{-i\varphi}\sin(\theta) \\ 0 & 1 & 0 & 0 \\ 0 & 0 & 1 & 0 \\ e^{i\varphi}\sin(\theta) & 0 & 0 & \cos(\theta) \end{pmatrix} \tag{67}$$

with $\theta = \Omega_{\mathrm{B}}t$, $\varphi = 2\phi + \pi/2$ and $U_{ZZ} = \exp(-i\alpha_{ZZ}\hat{Z}\hat{Z}t/4)$ and $U_{IZ-ZI} = \exp(-i(\alpha_{IZ} - \alpha_{ZI})(\hat{I}\hat{Z}-\hat{Z}\hat{I})t/4)$.

Considering only $U_{\mathsf{bSwap}}(\theta,\varphi)$ a gate that is locally equivalent to iSwap is implemented by choosing $\theta=\pi/2$ and $\varphi=0$. We refer to this gate as the bSwap. This Clifford gate, along with single qubit unitaries, forms a universal set of gates for fault-tolerant computation. With $\theta=\pi/4$ it implements the $\sqrt{\mathsf{bSwap}}$ gate, which when applied to the ground state produces the Bell state $\frac{1}{\sqrt{2}}(|00\rangle + e^{i\varphi}|11\rangle)$. This gate, accordingly, is locally equivalent to $\sqrt{\mathsf{iSwap}}$.

The magnitude of Ω_B has some interesting limits. In the limit of $\delta_i \ll \Delta_{12}$ (the harmonic oscillator limit) $\Omega_B \rightarrow 0$ as expected, while for $\delta_i \gg \Delta_{12}$ (pure qubit limit) it reduces to $\Omega_B = -2J\Omega^2/\Delta^2$ and for typical values of Ω, J, and Δ_{12} it is extremely small, explaining why this effect has not previously been exploited. The relevant case for this work is the limit in which Δ_{12} approaches either $-\delta_1$ or δ_2 since the rate passes through a resonance and becomes large. Such condition is met when the $|0\rangle \rightarrow |1\rangle$ transition of one transmon approaches the $|1\rangle \rightarrow |2\rangle$ transition of the other. As a consequence the energy level $|11\rangle$ is close to $|02\rangle$ and the leakages from the computational subspace are increased. It is essentially this leakage rate that determines the maximum Ω_B with which the gate can be operated.

In reference [44] δ_2 is close to Δ_{12} which results in an enhancement of Ω_B by a multiplicative factor of $\delta_2/2(\delta_2-\Delta_{12})$ relative to the pure qubit limit. This allowed the observation of the Two-photon coherent oscillation between the states $|00\rangle$ and $|11\rangle$ (see figure 13a). At the bSwap point quantum process tomography was performed and a gate fidelity of $F_g = 0.873$ (raw) and 0.80 (MLE) was measured (see figure 13c).

2.9 Summary of two-qubit gates

From the above it is clear the two-qubit gates are starting to be implemented with high fidelity in these systems. I like to separate them into three categories: 1) tunable ω, 2) all microwave and 3) real resonator photons. I have not talked about case three but essentially they use a

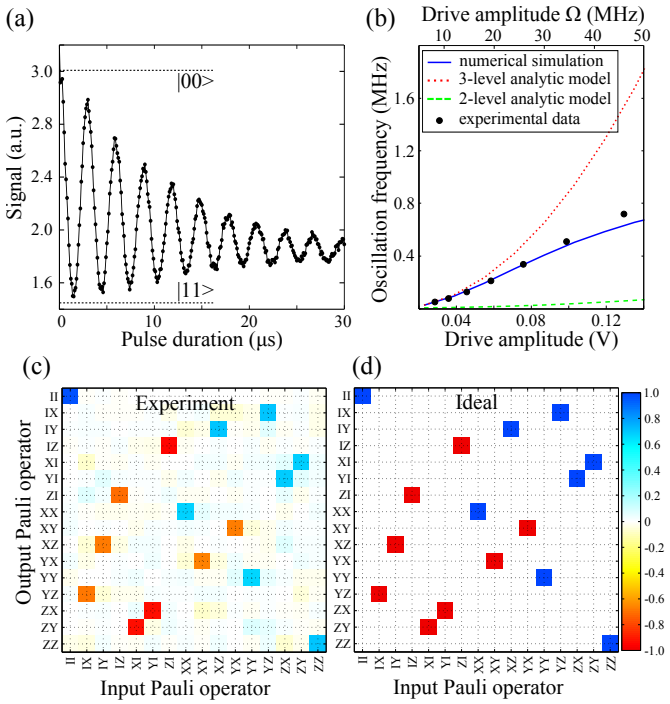

Fig. 13: *(a) Two-photon coherent oscillation between the states* $|00\rangle$ *and* $|11\rangle$*. The oscillation saturates at approximately* $1/4$ *of its visibility because in the steady state all four states* $|00\rangle$ *through* $|11\rangle$ *are equally populated. (b) Oscillation frequency versus driving amplitude. Black dots are experimental data; solid blue line is a multilevel numerical simulation; dotted red line is derived from perturbation theory of coupled multilevel systems; and dashed green line is from perturbation theory applied to coupled two-level systems. We ascribe the discrepancy observed at large amplitudes to the higher levels of the system, an effect that is captured by the numerical simulation. (c) Experimental and ideal (d) Pauli transfer matrices for the* bSWAP *gate. The measured gate fidelity is* $F_g = 0.873$ *(raw) and* 0.80 *(MLE). Figures taken from reference [44].*

excitation in the quantum bus to allow a two-qubit gate (for example the sideband transitions used in Ref. [48]). The tunable ω have the advantage that we can tune to special points where we can have the largest two-qubit interaction whereas in the all microwave case we never get the full two-qubit interaction rate. However, with the all microwave approach we do not need to have tunable resonance frequencies and dephasing from flux noise is not a problem. Below is table that summaries the above gates for transmons and phase qubits.

Gate	Reference	F_s (Bell)	Process tomography F_g	Benchmarking F_g
iSwap	[35]	0.91	0.92	-
iSwap (phase)	[49]	-	0.70	-
cPhase	[36, 29]	0.94	-	-
cPhase (phase)	[50]	-	0.76	-
ZX_{90}	[5]	0.983	0.968 (raw) 0.95 (mle)	-
ZX_{90} echo	[43]	-	0.883 (mle) 0.880 (mle)	0.935
bSwap	[44]	> 0.99	0.873 (raw) and 0.80 (mle)	-
sideband	[48]	0.58	-	-

3 Optimal single qubit gates

To derive the effective single and two-qubit gates we have made many approximations. These approximations will give rise to small but important errors when trying to understand their limitations. The most important approximation is how to treat the higher levels of the transmon.

3.1 Leakage errors in single qubit gates

Having a weakly anharmonic qubit poses a challenge in the implementation of quantum gates. It is known that the time evolution operator of a linearly driven harmonic oscillator is a combination of a coherent displacement operator tracking the classical trajectory of the driven oscillator and a global phase factor. This evolution encompasses all energy levels and cannot be reduced to a single-qubit rotation. In a harmonic oscillator, all energy splittings are the same, so driving one transition drives all others at the same time. A system starting initially in an energy eigenstate will quickly be driven into a superposition over many energy eigenstates. By this token, it is crucial that a qubit is nonlinear, that is that the transition frequency of the qubit levels is different by an amount δ from the transition frequencies to the non-qubit levels. Spectroscopically, we would expect that whenever the bandwidth of the pulse comes close to δ, i.e., when its duration becomes short on the scale of $1/\delta$, we expect significant leakage to higher states. Thus, it is a challenge to implement fast single-qubit gates in weakly anharmonic systems. The implementation of faster gates is important as it allows more gates to be executed in a given coherence time, an important step toward high-fidelity quantum logic.

Our goal is to implement gates contained within the qubit subspace. That is, we want to shape $\Omega_x(t)$, $\Omega_y(t)$ and $\Delta(t)$ in equation (31) so that

$$\hat{U}_{\rm ideal} = \mathcal{T}\exp\left[-i\int_0^{t_g}\hat{H}^R_{\rm tr+dr}(t)dt\right] = e^{i\phi}\hat{U}_{\rm qb}\oplus\hat{U}_{\rm rest}, \tag{68}$$

where t_g is the gate time, $\mathcal{T}$ is the time ordering operator, $\hat{U}_{\rm qb}$ is a unitary that acts only in the qubit subspace, $\hat{U}_{\rm rest}$ acts only outside of the qubit space, and ϕ describes a relative phase. Therefore, $\hat{U}_{\rm rest}$ as well as the phase ϕ are completely irrelevant for operations in the Hilbert space formed by the qubit.

To demonstrate the typical set of errors we choose $\hat{U}_{\rm qb} = \hat{X}$, the NOT gate. For a leakage-free qubit this would be implemented by simply setting $\Delta(t) = 0$, $\Omega_x(t) = \Omega_G(t)$, and $\Omega_y(t) = 0$, with the only requirement that that $\int_0^{t_g}\Omega_G(t)dt = \pi$. To reduce the leakage to the third level a good guess would be to use a Gaussian modulation of the envelope [51, 52]. In this case $\Omega_G(t)$ takes the form

$$\Omega_G(t) = A\frac{\exp\left[-\frac{(t-t_g/2)^2}{2\sigma^2}\right] - \exp\left[-\frac{t_g^2}{8\sigma^2}\right]}{\sqrt{2\pi\sigma^2}\mathrm{erf}[t_g/\sqrt{8}\sigma] - t_g\exp[-t_g^2/8\sigma^2]}, \tag{69}$$

where $t \in [0, t_g]$, σ is the standard deviation and A is chosen such that the correct amount of rotation is implemented (e.g. $A = \pi$ for a NOT). This functional form is chosen to enforce that the pulse start and end at zero. In the limit that $t_g \to \infty$ we recover the standard Gaussian function. The motivation for Gaussian shaping is that the small and strictly limited frequency bandwidth $(1/\sigma)$ ensures little excitation at the leakage transition frequency. For short pulses however, there is still significant spectral weight at δ. This is shown in figure 14 (a, c, e) where the Fourier transforms of $\Omega_G(t)$ are plotted for $\sigma = \{1/3, 2/3, 3/2\}2\pi/\delta$ and $t_g = 4\sigma$ respectively.

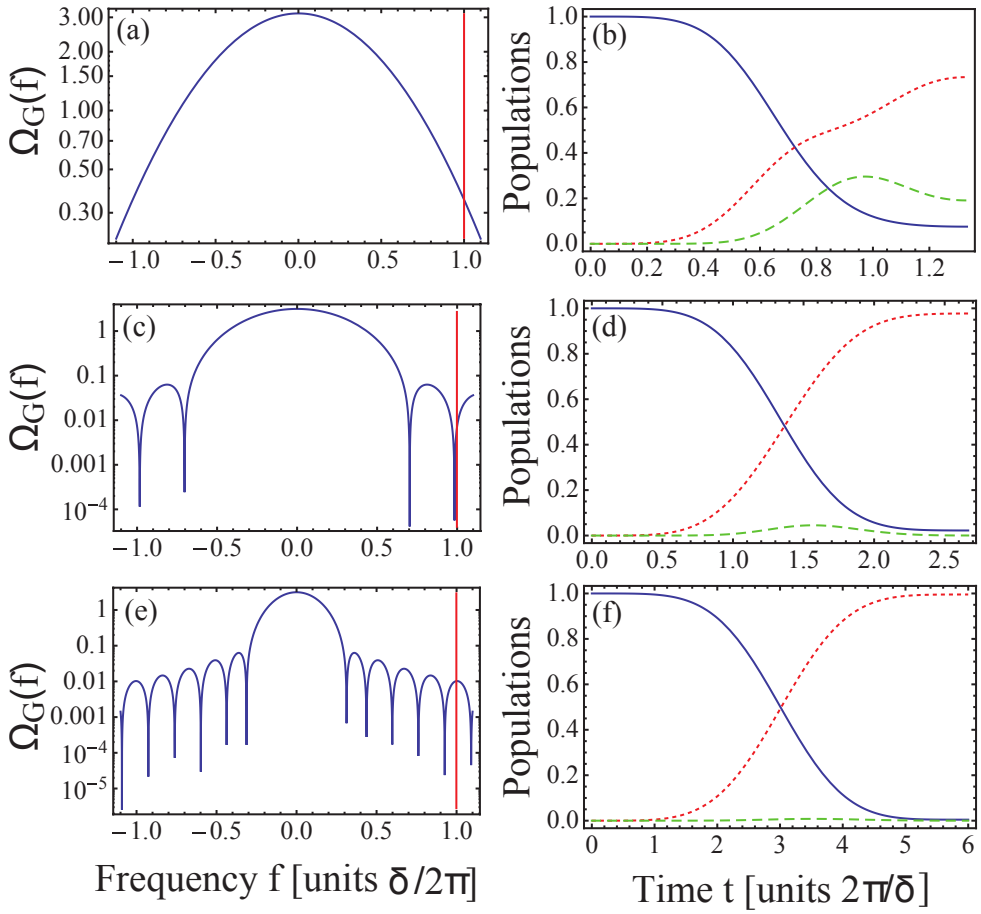

Fig. 14: *(color online) Fourier transforms of the control fields (a, c, e) and populations (b, d, f) of the ground (blue solid), first (red dotted), and second excited (green dash) in a simulation of a NOT gate with a Gaussian amplitude pulse for a Duffing oscillator (with 5 levels). In (a, b)* $\sigma = 2\pi/3\delta$*, (c, d)* $\sigma = 4\pi/3\delta$*, and (e, f)* $\sigma = 3\pi/\delta$ *and the gate time is taken to be* 4σ*.*

To quantify this error, we use the gate fidelity [equation (129)] averaged over all input states existing in the qubit subspace. To demonstrate the errors arising from Gaussian shaping we numerically solve the evolution given by equation (31) truncated at 5 levels and calculate the gate error $(1 - F_g)$ for $\sigma = \{1/3, 2/3, 3/2\}2\pi/\delta$ and $t_g = 4\sigma$. Doing this we find gate errors of 0.198, 0.0160, and 0.0030 respectively.
To understand these error values we plot the populations of the first three levels in Fig. 14 (b, d, f). The ground state populations are given by the blue solid line; the red dotted line shows the first excited state; the green dashed line is the second excited state. We observe that for the shortest gate, $\sigma = 2\pi/3\delta$, the error after the pulse is mostly residual population of the third and higher level. This is what we refer to as the leakage error. For longer gates, e.g. $\sigma = 4\pi/3\delta$, the residual population does not account for the calculated error. This error is mostly a phase error resulting from the finite population of the third level *during* the pulse. Even though the final state is restricted to the computational levels, the admixture of the third level leads to a phase shift on the second level, resulting in a net phase error at the end of the pulse. At the longest time when the population of the third level is nearly negligible there is still a large gate error. From these results we conclude that Gaussian shaping is of limited performance even if the pulse bandwidth is somewhat smaller than δ. Thus a more advanced pulse is needed. In Ref. [53, 54], we provided a simple scheme which we called Derivative Removal by Adiabatic Gate (DRAG).

3.2 Correcting for leakage with DRAG shaping

To go beyond the Gaussian control methods presented above, we introduce the DRAG technique. In this technique we want to find a time-dependent unitary transformation $\hat{A}(t)$ such that the effective Hamiltonian

$$\hat{H}^{RA}_{\rm tr+dr} = \hat{A}^\dagger(t)\hat{H}^{R}_{\rm tr+dr}(t)\hat{A}(t) + i\dot{\hat{A}}^\dagger(t)\hat{A}(t). \tag{70}$$

has the form $h_x(t)\hat{X} \oplus \hat{H}_{\rm rest}(t)/2$ where $h_x(t)\hat{X}/2$ is a Hamiltonian in the effective qubit subspace and $\hat{H}_{\rm rest}(t)$ generates evolution in the rest of the system. The direct sum form implies that if the state of the system starts in the qubit subspace, then it remains there during and after the pulse. We impose the additional requirement that $\hat{A}(0) = \hat{A}(t_g) = \hat{I}$, i.e. the frame transformation vanishes at the boundaries. Both conditions together imply that we have decoupled the qubit subspace from the leakage subspace since the qubit subspace is mapped back onto itself by the end of the pulse.
In appendix B the general procedure is given and in this section we will just outline the important steps. We start by defining $\lambda = \max|\Omega_x|/\delta$ to be a small parameter. That is, we will never consider controls which require amplitudes greater than the anharmonicity. In terms of this small parameter there is an iterative procedure for finding a transformation $\hat{A}(t) = \exp[-iS(t)]$ where $\hat{S}(t) = \sum_{m=1} \lambda^m \hat{S}_m(t)$ that to order λ makes sure the implemented Hamiltonian has the form $h_x(t)\hat{X} \oplus \hat{H}_{\rm rest}(t)/2$. It is very similar to the Schrieffer-Wolff transformations we used in the previous sections except we include the time dependence and count the orders slightly different. As shown in appendix B the desired qubit Hamiltonian for order n is implemented by setting

$$\Omega_x^{(n)}(t) = h_x^{(n)}(t) - {\rm Tr}[H_{\rm x}^{(n)}(t)\hat{X}], \tag{71}$$
$$\Omega_y^{(n)}(t) = -{\rm Tr}[H_{\rm x}^{(n)}(t)\hat{Y}], \tag{72}$$
$$\Delta^{(n)}(t) = -{\rm Tr}[H_{\rm x}^{(n)}(t)\hat{Z}], \tag{73}$$

where $H_{\rm x}^{(n)}(t)$ contains terms generated by the lower orders of the transformation and the controls. It is a rather complicated expression which can be derived following the procedure in appendix B and the first few orders are listed in this appendix. For the removal of leakage we also derive in appendix B the following constraints on the frame transformation:

$$\begin{aligned} S_{0,k}^{(n+1)}(t) =& i\frac{1}{\lambda\delta_k}\langle 0|H_{\rm x}^{(n)}(t)|k\rangle, \\ S_{1,k}^{(n+1)}(t) =& i\frac{1}{\lambda\delta_k}\langle 1|H_{\rm x}^{(n)}(t)|k\rangle + \frac{\sqrt{2}\delta_{2,k}}{\lambda\delta}\frac{i\Omega_x^{(n)} - \Omega_y^{(n)}}{2}. \end{aligned} \tag{74}$$

That is

$$\hat{S}^{(n+1)} = S_X^{(n+1)}\hat{X} + S_y^{(n+1)}\hat{Y} + S_z^{(n+1)}\hat{Z} + \sum_{k=2}\left[S_{1,k}^{(n+1)}|1\rangle\langle k| + (S_{1,k}^{(n+1)})^*|k\rangle\langle 1|\right] \tag{75}$$

where $S_X^{(n+1)}$, $S_Y^{(n+1)}$ and $S_Z^{(n+1)}$ are free parameters in our theory. Choosing a different functional form for them result in different DRAG solutions. In the next section we will give some practical examples for this choice.

3.2.1 Zero order solution

For the zeroth order $H_{\rm x}^{(0)}(t) = 0$ and from the above we find

$$\Omega_x(t) = \Omega_G(t), \quad \Omega_y(t) = 0, \quad \delta(t) = 0. \tag{76}$$

These are the controls used in figure 14 and here we will use them as a benchmark for the higher order solutions. In figure 15a, we plot the error, $1 - F_g$ (blue dashed line), between a NOT gate an a unitary from the control field given by equation (69) with $A = \pi$ and $t_g = 4\sigma$. In this figure it is clearly seen that the error associated with these controls is quite large; for fast gate times this error is unacceptable for quantum information processing, and long gate times will have additional error arising from decoherence.

3.2.2 First order solution

To determine the first order solutions we need $H_{\rm x}^{(1)}(t)$, which requires $S^{(1)}(t)$. From the constraints (74) the frame needs to have

$$S_{0,k}^{(1)}(t) = 0, \; S_{1,k}^{(1)}(t) = \frac{\sqrt{2}\delta_{2,k}}{\lambda\delta}\frac{i\Omega_G}{2}. \tag{77}$$

Using these and the above we find the first order corrections to the control fields are

$$\begin{aligned} \Omega_x^{(1)}(t) =& 2\dot{S}_X^{(1)}(t), \\ \Omega_y^{(1)}(t) =& 2\dot{S}_Y^{(1)}(t) + 2\Omega_G S_Z^{(1)}, \\ \Delta^{(1)}(t) =& 2\dot{S}_Z^{(1)} - 2\Omega_G S_Y^{(1)} - \frac{\Omega_G^2(t)}{2\lambda\delta}. \end{aligned} \tag{78}$$

Here we see that there is a continuous family of DRAG pulses; however, in this section we will consider three particular solutions. In all of these solutions we take $S_x^{(1)}(t) = 0$ as it has no influence on our choice for $\Omega_y^{(1)}(t)$ and $\Delta^{(1)}(t)$.

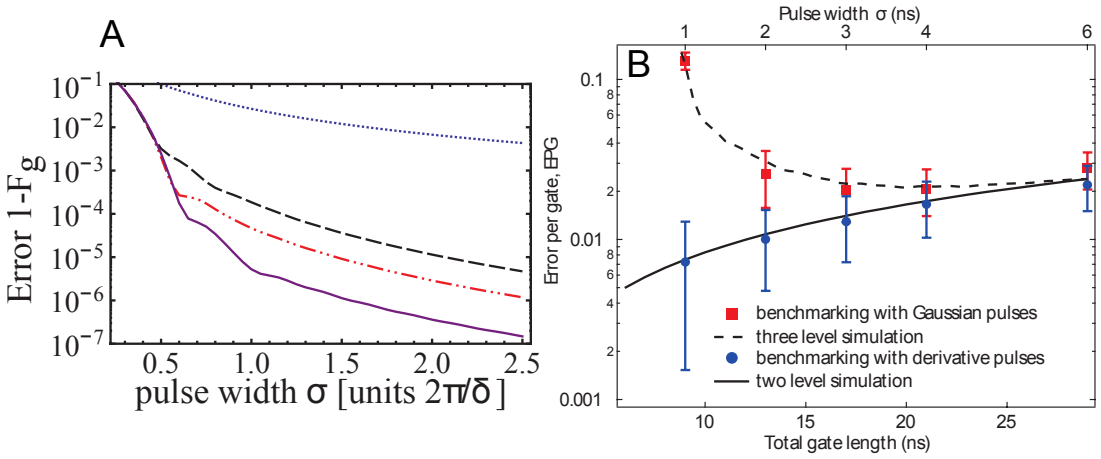

Fig. 15: *a) Gate error for the implementation of a NOT gate as a function of σ, with $t_g = 4\sigma$, and a Gaussian shaped pulse. The blue dotted line is the zeroth order solution. The black dash line is the first order Z-only correction. The red dash-dot-dot line is the first order Y-only correction. The purple solid line is for the optimal first order correction. b) Error per gate extracted from a randomized benchmarking experiment for different gate lengths using both Gaussian pulses (red squares) and first-order DRAG pulses (blue squares). This was reproduced from [55].*

The first solution we consider is one where the control field $\Omega_y(t) = 0$. This is achieved by setting $S_Y^{(1)} = S_Z^{(1)} = 0$, resulting in

$$\Omega_x(t) = \Omega_G, \quad \Omega_y(t) = 0, \quad \Delta(t) = -\frac{\Omega_G^2(t)}{2\delta}. \tag{79}$$

In figure 15a, the error for this control set is plotted as the black dashed line. It clearly has a much lower error then the standard Gaussian amplitude modulation control, and we will refer to this as the Z-only correction.

The second control solution we consider is when the control field $\Delta(t) = 0$. This is achieved by setting $S_Z^{(1)} = 0$ and $S_Y^{(1)} = -\Omega_G(t)/4\lambda\delta$, which results in

$$\Omega_x(t) = \Omega_G(t), \quad \Omega_y(t) = -\frac{\dot{\Omega}_G(t)}{2\delta}, \quad \delta(t) = 0, \tag{80}$$

and the error for this control set is plotted in figure 15a as the red dash-dot-dot line. Its error rate is lower then both the standard Gaussian controls and the Z-only correction. Here we will refer to this as simply Y-only correction.

The third control solution we consider is what we refer to as the optimal first order solution. This is achieved by minimizing the elements in $H_{\mathrm{x}}^{(2)}(t)$ such that the second order corrections to the control fields are zero. From Ref. [54] this is achieved by setting

$$\Omega_x(t) = \Omega_G(t), \quad \Omega_y(t) = -\frac{\dot{\Omega}_G(t)}{\sqrt{2}\delta}, \quad \Delta(t) = \frac{\Omega_G^2(t)}{2\delta}[\sqrt{2} - 1]. \tag{81}$$

This optimal first order solution is plotted in figure 15a) as the solid purple line. This error is substantially lower than the other first order correction methods.

The DRAG scheme has been experimentally used in Ref. [55] and Ref. [56], where it was shown to substantially lower the gate errors. In figure 15b we have reproduced the results from

Ref. [55] where the error per gate for a transmon was extracted from randomized benchmarking experiments for different gate lengths using both Gaussian pulses (red squares) and first-order Y-only DRAG pulses (blue squares). Excellent overlap with theory for gate error including qubit decoherence (black curve) suggests that the DRAG pulses successfully eliminate the errors due to the presence of higher levels.

4 Benchmarking quantum processes

As I have eluded to in the previous sections measuring how good a quantum gate was implemented is not a simple task. I hope that by the end of this section I have convinced you that is the case.

4.1 Quantum process tomography

In quantum process tomography (QPT) the goal is to determine the experimental map Λ. I prefer to use the Pauli transfer matrix $\mathcal{R}$ (see Appendix C) which is just a real matrix of dimensions $d^2 \times d^2$ which represents the action of the map on the Pauli state vector. The essential idea of tomography is that by preparing different input states and measuring different observables we try to match $\mathcal{R}$ to the observed measurements.

Let start by defining an experiment by the triple $\{\rho_j, \hat{M}_j, m_j\}$ which describes preparing the system in state ρ_j measuring the operator $\hat{M}_j$ and obtaining an expectation value m_j according to

$$m_j = \text{Tr}\left(\hat{M}_j \Lambda(\rho_j)\right). \tag{82}$$

In the Pauli representation it is simple to show that

$$m_j = \mathbf{M}_j^T \cdot \mathcal{R} \cdot \mathbf{p}_j \tag{83}$$

where we have used $M_j = \mathbf{M}_j \cdot \mathbf{P}$. Using column major vectorization we can write this as

$$m_j = \mathbf{s}_j^T \cdot \mathbf{R} \tag{84}$$

where $\mathbf{R}$ is the vectorized $\mathcal{R}$ and $\mathbf{s}_j = \mathbf{p}_j \otimes \mathbf{M}_j$ (dimensions d^4). We can now express the entire set of experiments as

$$\mathbf{m} = S^T \mathbf{R}, \tag{85}$$

where the columns of the rectangular matrix S are the vectors $\mathbf{s}_j$. That is S is a $d^4 \times T$ matrix where T is the number of different experiments.

The first estimate for our quantum process, $\mathbf{R}_{\text{bare}}$, arises from linear inversion. While S is typically not square we can invert SS^T or, in the case of an incomplete set of measurements, find its pseudo inverse. This leads to the bare estimate

$$\mathbf{R}_{\text{bare}} = (SS^T)^{-1} S\mathbf{m}. \tag{86}$$

At no point have we enforced that our estimate $\mathbf{R}_{\text{bare}}$ correspond to a physical map, and we will find that for many error models it does not.

For example it is possible that statistical error due to finite measurement statistics may give unphysical estimates [57, 58, 59, 60]. Instead of direct access to m_j we measure

$$m_j = \mathbf{s}_j^T \mathbf{R} + \sqrt{N_j} W_j, \tag{87}$$

where W_j is a Gaussian random variable with mean zero and unit variance and N_j is the noise power. Due to the central limit theorem we can always approximate the error model as Gaussian if we repeat the measurement sufficiently many times in which case N_j scales as $1/(\#$ of repetitions of experiment $j)$. The transformation $m'_j = m_j/\sqrt{N_j}$ and $\mathbf{s}'_j = \mathbf{s}_j/\sqrt{N_j}$ simplifies the Gaussian likelihood function to

$$\mathcal{L}(\mathbf{m}'|\mathbf{R}) = \exp\left(-\frac{1}{2}\sum_j |m'_j - \mathbf{s}'^T_j \mathbf{R}|^2\right). \tag{88}$$

For this error model the most rigorous estimate of the gate would be to perform a Bayesian estimation where $\mathbf{R}_{\text{Bayes}} = \int \mathbf{R}\mathcal{L}(\mathbf{m}'|\mathbf{R})\mathrm{d}\mathbf{R}/\int \mathcal{L}(\mathbf{m}'|\mathbf{R})\mathrm{d}\mathbf{R}$ but these integrals are often extremely hard to calculate, especially since there is no uniquely good measure over quantum channels $\mathrm{d}\mathbf{R}$. A much simpler technique is to report the maximum of the likelihood function. If the global maximum lies inside the space of physical maps then it is simply the $\mathbf{R}_{\text{bare}}$ from Eq. (86), and if most of the support of $\mathcal{L}(\mathbf{m}'|\mathbf{R})$ is also physical then the Bayesian estimate and the maximum likelihood estimate will be be approximately the same. In the case where the bare estimate is unphysical maximizing $\mathcal{L}(\mathbf{m}'|\mathbf{R})$ over the space of physical $\mathbf{R}$ is a semidefinte program and can be solved for small instances easily with optimizers such as SeDuMi. This is because the likelihood function is of the form of a 2-norm distance between vectors $\mathbf{m}'$ and $S'^T\mathbf{R}$ and the constraints are that the Choi matrix is positive semidefinite. For the interested reader the approach we use is outlined in the supplement of Ref. [5].

While there are issues regarding maximum likelihood estimation (MLE) for QPT [59], there is a deeper problem that affects any reconstruction method that utilizes the likelihood function. To calculate the likelihood function we require $\mathbf{s}_j$ which in turn implies we have a complete characterization of ρ_j and $\hat{M}_j$. In any experimental implementation of tomography there will be (state preparation and measurement) SPAM errors and in many situations the magnitude of the SPAM errors is the same order as the size of the gate errors we are trying to estimate. If the SPAM errors are stochastic, then the situation is reducible to the previous case by effectively treating the SPAM errors as additional sampling noise on the measurement. When the errors are systematic we may write $\mathbf{p}_j \to \mathcal{R}_{\mathcal{E}_j} \cdot \mathbf{p}_j$, $\mathbf{M}_j \to \mathcal{R}^T_{\mathcal{F}_j} \cdot \mathbf{M}_j$ and therefore $\mathbf{s}_j \to \mathcal{R}_{\mathcal{E}_j} \otimes \mathcal{R}^T_{\mathcal{F}_j}\mathbf{s}_j$. Here we see that if the error maps are completely unknown our prediction for the S matrix is wrong and thus both the inversion and the MLE will give the wrong answer. We are using the wrong likelihood function.

In most experiments we dont have access to preparing many different states and measurement operators, instead there is one fixed initial state (usually the ground state) and a fixed measurement operator (which in circuit QED is diagonal in the computational basis) and we make the different preparations and measurements by the application of unitary operators. If these are not done perfectly then we will have systematic errors. To demonstrate this we have plotted in figure 16a the effects of both systematic and stochastic measurement noise in the case where the measured gate is a perfect identity gate. In this figure the systematic SPAM error comes from a depolarizing channel of varying strengths. We do not impose the reconstructed $\mathbf{R}$ to be physical and therefore we measure the difference between the reconstructed gate and the identity by a diamond norm distance [61]. We observe that for large noise powers the error in the estimate decreases exponentially with respect to decreasing noise power (and thus increasing repetitions) until it hits a floor determined by the systematic error in the interrogating gates.

In figure 16b we look at the error in reconstructing the identity, in the absence of stochastic measurement errors, for different models of the systematic errors. We find the closest physical

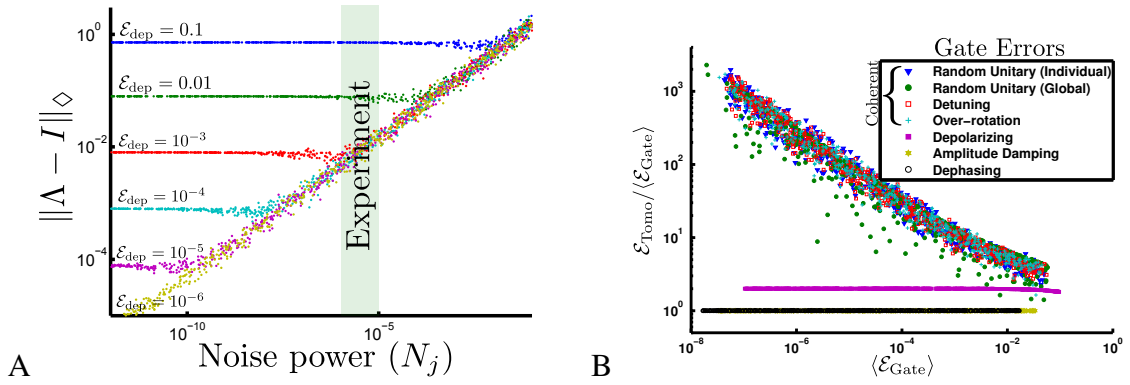

Fig. 16: *a) Reconstructing a perfect identity gate with imperfect tomography due to depolarizing errors on the SPAM gates as well as Gaussian random noise on the measurement outcomes. We plot the diamond norm distance between the bare estimate Eq.* (86) *and the identity versus the noise power. We vary the strength of the depolarizing error for a fixed gate-set with four elements corresponding to mapping the ground state to the four corners of a tetrahedron. The experimental noise power is obtained from [5]. b) The ratio of the error in reconstructing the identity to the average gate error plotted versus the average gate error for a single qubit using a tetrahedral gate-set and no stochastic measurement noise. The estimated operation is the 'closest' physical map to the bare reconstruction. Seven different error models are compared, four coherent errors (different random unitary maps applied to each gate, a single random unitary map applied to each gate, a detuning error and over-rotation) as well three incoherent processes (amplitude damping, dephasing and depolarizing errors)*

state to the estimate. Since the two gates under comparison are physical we can compare them with the gate error, $1 - F_g$. There is a stark difference between coherent errors (over-rotation, detuning errors etc.) and incoherent error models (T_1 or T_2 processes for example). In the incoherent case the error in estimating the identity is proportional to the error on the individual gates while for the coherent model the ratio of the errors grows exponentially poorly as the gate error decreases.

In summary QPT can be used to give us a complete estimated of the quantum map but it has two significant problem:

1. It scales exponentially with the dimensions of the system.

2. It does not take into account SPAM errors.

Recently we have developed self-consistent QPT [62] which is an extension to QPT to account for SPAM. The essential idea of self-consistent QPT is we estimate a complete gate set rather then an individual gate. This allows us to define a new likelihood function that takes into account SPAM errors. It has two draw backs the first is likelihood function can not be cast into a semidefinite program and secondly the size of the space grows to d^6. If the errors are small the problem can be linearized and made into a semidefinite program (but the dimensions are still d^6). Using this we have shown experimentally that for one qubit that estimated gate errors can be significantly improved using this method. However due to the poor scaling we have not been able to get this to work for more then one qubit.

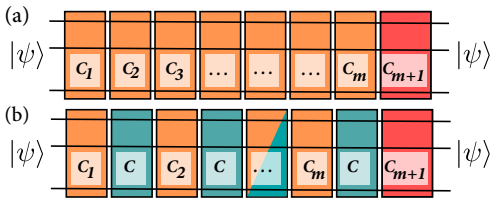

Fig. 17: *Randomized benchmarking protocols. (a) Schemes for the standard benchmarking protocol. Random gates $\hat{C}_i$ (orange) chosen from $\mathcal{C}$ are applied for different lengths m. A final gate $\hat{C}_{m+1}$ (red) is performed to make the total sequence equal to the identity operation. (b) Scheme for the interleaved benchmarking protocols. It is the same as above except a target gate, $\hat{C}$ (green) is interleaved between the random gates $\hat{C}_i$ (orange).*

4.2 Randomized benchmarking

An alternative to QPT is randomized benchmarking (RB) [63, 64, 65, 66, 67, 68], which has been used to characterize single qubit gates in liquid-state NMR [69], trapped atomic ions [63, 70, 71, 72, 67], and superconducting qubits [73, 55, 3, 65, 68, 43]. RB is specifically tailored to compensate for SPAM errors by considering only the exponential decay of sequences of random gates. This comes at the cost of only obtaining information about the average gate error over the group of random gates, although some alternative approaches have been recently devised for extending RB to estimate the error of a individual gate [65, 67] and addressability errors [68].

We start by defining a general RB protocol (see figure 17a). We choose a sequence of $m+1$ unitary gates where the first m gates are chosen uniformly at random from a group $\mathcal{G} = \{\hat{U}_i\}$ and the $(m+1)^{\text{th}}$ gate is chosen to be the inverse of the composition of the first m random gates. Provided $\mathcal{G}$ is at most the Clifford group, this undo gate can be found efficiently by the Gottesman-Knill theorem [74]. Assuming each gate $\hat{U}_i$ has some associated error, represented by $\mathcal{R}_i^{\Lambda}$, the sequence of gates is modeled by

$$\mathcal{R}_{\mathcal{S}_{\mathbf{i_m}}} = \mathcal{R}_{\Lambda_{i_{m+1}}} \mathcal{R}_{U_{i_{m+1}}} \left(\prod_{j=1}^{m} \left[\mathcal{R}_{\Lambda_{i_j}} \mathcal{R}_{U_{i_j}} \right] \right), \tag{89}$$

where $\mathbf{i_m}$ is the m-tuple $(i_1, ..., i_m)$ describing the sequence, and the recovery gate $\hat{U}_{i_{m+1}}$ is uniquely determined by $\mathbf{i_m}$. Since $\{\hat{U}_i\}$ forms a group, the sequence can be rewritten as

$$\mathcal{R}_{S_{\mathbf{i_m}}} = \mathcal{R}_{\Lambda_{i_{m+1}}} \left(\prod_{j=1}^{m} \left[\mathcal{R}_{U_{\tilde{i}_j}^{\dagger}} \mathcal{R}_{\Lambda_{i_j}} \mathcal{R}_{U_{\tilde{i}_j}} \right] \right), \tag{90}$$

where $\hat{U}_{\tilde{i}_j}$ is another element of $\mathcal{G}$.

For each sequence the overlap between $\hat{E} = \mathbf{e} \cdot \mathbf{P}$, an operator representing the measurement (with errors), and $\mathcal{R}_{S_{\mathbf{i_m}}} \cdot \mathbf{p}$, the final state, is measured. Averaging this overlap over K independent sequences of length m gives an estimate of the average sequence fidelity $F_{\text{seq}}(m, E, \rho) = \mathbf{e}^T \cdot \mathcal{R}_{S_m} \cdot \mathbf{p}$ where $\mathcal{R}_{S_m}$ is the average sequence superoperator given by $\mathcal{R}_{S_m} = \sum_{\mathbf{i_m}} \mathcal{R}_{S_{\mathbf{i_m}}}/K$. Now by defining $\bar{\Lambda}$ to be the average over Λ_{i_j} and by assuming that $\delta\Lambda_{i_j} = \Lambda_{i_j} - \bar{\Lambda}$ is small [64, 65], the average sequence superoperator can be written as

$$\mathcal{R}_{S_m} = \mathcal{R}_{\bar{\Lambda}} [\mathcal{W}_{\mathcal{G}}(\mathcal{R}_{\bar{\Lambda}})]^m + \mathcal{O}(\delta\Lambda), \tag{91}$$

where $\mathcal{W}$ represents the twirl over the group $\mathcal{G}$ and is given by

$$\mathcal{W}_{\mathcal{G}}(\mathcal{R}_{\bar{\Lambda}}) = \frac{1}{|\mathcal{G}|}\sum_{\mathcal{U}\in\mathcal{G}} \mathcal{R}_{\mathcal{U}}^{\dagger}\mathcal{R}_{\bar{\Lambda}}\mathcal{R}_{\mathcal{U}}. \tag{92}$$

Depending on the group $\mathcal{G}$, this map can have a simple structure with a small number of parameters. The group average over the conjugation action of a group is well known in the representation theory of finite groups and, as a corollary of Shur's lemma, would be proportional to the identity if the $\mathcal{R}$ matrices were irreducible (i.e. there is no basis in which each $\mathcal{R}_{\mathcal{U}}$ is block-diagonal) [75].
In the case of the full Clifford group, $\mathcal{G} = \mathcal{C}$ ($\hat{U} = \hat{C}$) there are two irreducible subspaces corresponding to two stabilized operators: the projector onto Π_0 (the identity operator) and a projector (Π) onto the remainder of the Pauli group. This is easy to see as for any two Pauli matrices P_i and P_j ($i, j \neq 0$) there exists an element of the Clifford group, $\mathcal{C}$, such that $\hat{C}\hat{P}_i\hat{C} = \hat{P}_j$. Therefore no subspace of the Pauli's is stabilized except for the entire group (minus the identity). Because of this we find for the full Clifford group

$$\mathcal{W}_{\mathcal{C}}(\mathcal{R}_{\bar{\Lambda}}) = \begin{pmatrix} 1 & 0 \\ 0 & \alpha\Pi \end{pmatrix}, \tag{93}$$

which is a depolarizing channel with $\alpha = \mathrm{Tr}(\Pi\mathcal{R}_{\bar{\Lambda}})/\mathrm{Tr}(\Pi)$. With this the sequence fidelity becomes

$$F_{\mathrm{seq}}(m, E, \rho) = A\alpha^m + \tilde{e}_0, \tag{94}$$

where $A = \sum_{j\neq 0} \tilde{e}_j p_j$. As shown previously [64], the average gate error averaged over the Clifford group is related to α by

$$r = (d-1)(1-\alpha)/d. \tag{95}$$

Here we see the beauty of randomly selecting from the Clifford group as in this case not matter what initial state is prepared and measurement operator measured, provided that $\tilde{e}_j p_j$ is non-zero (we have an initial state with some polarization in the same direction as our measurement), the parameter α can be extracted by fitting the sequence fidelity to a decaying exponential. Furthermore as shown in Ref. [65] it is possible to efficiently (polynomial in the number of qubits) randomly select and implement a Clifford operator form a given generating set. Thus this scheme scales efficiently with the number of qubits. In summary it solves two of the problems of QPT but it only gives the average gate error averaged over the Clifford group. It is possible to get different information by using different groups such as the Pauli and single qubit Clifford group, however these smaller groups dont completely depolarize the noise and there is a trade off with gaining more information about the average map $\mathcal{R}_{\bar{\Lambda}}$ and incurring more SPAM errors. If you are interested see Ref. [68] for more information.
To get an estimate of the error on an individual gate Ref. [66, 67] proposed interleaved RB. In this protocol a deterministic gate is interleaved between random gates chosen from the same group $\mathcal{G}$ (see figure 17b). That is, the sequence is given by

$$\mathcal{R}_{\mathcal{V}_{\mathbf{i_m}}} = \mathcal{R}_{\Lambda_{i_{m+1}}}\mathcal{R}_{U_{i_{m+1}}}\left(\prod_{j=1}^{m}\left[\mathcal{R}_U\mathcal{R}_{\Lambda_U}\mathcal{R}_{\Lambda_{i_j}}\mathcal{R}_{U_{i_j}}\right]\right), \tag{96}$$

where we have simply written the error for the deterministic gate to happen before the actual gate. Because $\hat{U}$ is an element of $\mathcal{G}$ we can follow the same procedure as above with the

only change being that $\mathcal{R}_{\Lambda_{i_j}} \rightarrow \mathcal{R}_{\Lambda_U}\mathcal{R}_{\Lambda_{i_j}}$. That is, the decay of this sequence will follow the exponential

$$F_{\text{seq}}(m, E, \rho) = A\alpha_U^m + \tilde{e}_0, \tag{97}$$

where $\alpha_U = \text{Tr}(\Pi\mathcal{R}_{\Lambda_U}\mathcal{R}_{\bar{\Lambda}})/\text{Tr}(\Pi)$. Now if we assume that we can replace $\mathcal{R}_{\bar{\Lambda}}$ with a depolarizing channel of strength α then we can define the estimated error per interleave gate $\hat{U}$ to be

$$r_U = (d-1)(1-\alpha_U/\alpha)/d. \tag{98}$$

This is a huge approximation and we should be scared of it and we are currently investigating when it can be made. As shown in Ref. [66] we can bound this by using a diamond norm. Doing this we find that the error in the gate must be in the range $r_U \pm E$ where

$$E = \frac{2(d^2-1)(1-\alpha)}{\alpha d^2} + \frac{4\sqrt{1-\alpha}\sqrt{d^2-1}}{\alpha}. \tag{99}$$

Here we see that the bound scales with the dimensions so it is not very useful. However, numerical simulations show that this approximations is much better then the above bound provided the error $\mathcal{R}_{\bar{\Lambda}}$ is not a unitary that undoes $\mathcal{R}_U$. Since $\mathcal{R}_{\bar{\Lambda}}$ is the average error for all the gates used it is very unlikely that this will be unitary let alone equal to the inverse of $\mathcal{R}_U$. In fact the averaging effect will tend to have a depolarizing effect which makes our assumption more justified.

In anycase, blindly trusting this result we can perform interleave RB protocol. This has been done in ions [67] and superconducting qubit [66, 43]. In both the superconducting qubit experiments it was shown that standard RB and interleave RB always give a lower estimate for the gate error. We believe this is due to the systematic errors studied above, which is also consistent with the self-consistent QPT in Ref. [62] as this gave a result which is closer to RB than QPT. The results of Ref. [43] are reproduced in figure 18. This shows the average sequence fidelity over random sequences of Clifford gates with lengths ranging from 1 to 20 for both the standard (circles) and the interleaved (triangles) RB protocols. Each data point was averaged over 40 different random sequences. Both sets of RB data are well described by an exponential model, with reduced χ^2 values of 0.589 and 0.386 for the standard and interleaved RB protocols, respectively. In the case of the standard RB experiment, we obtain $\alpha = 0.8752 \pm 0.0078$, which results in an average error per Clifford operation of $r = 0.0936 \pm 0.0058$. For the interleaved experiment, $\alpha_{\mathcal{C}} = 0.7990 \pm 0.0058$, from which $r_{\mathsf{ZX}_{-\pi/2}} = 0.0653 \pm 0.0014$, which compares favorably with the 0.12 estimated by QPT (see figure 12) . All errors here represent a 1σ confidence interval obtained from the fitting model [68]. The average error per Clifford operation for the single-qubit Clifford group for each qubit was also measured and observed to be $r_1 = 0.0041 \pm 0.0001$ for qubit 1 and $r_2 = 0.0048 \pm 0.0002$ for qubit 2.

Appendices

A Effective Hamiltonians: Outline of the Schrieffer-Wolff transformation

In this section we outline the Schrieffer-Wolff transformation used to derive the effective Hamiltonian. We start by making the assumption that the general Hamiltonian is of the form $\hat{H} =$

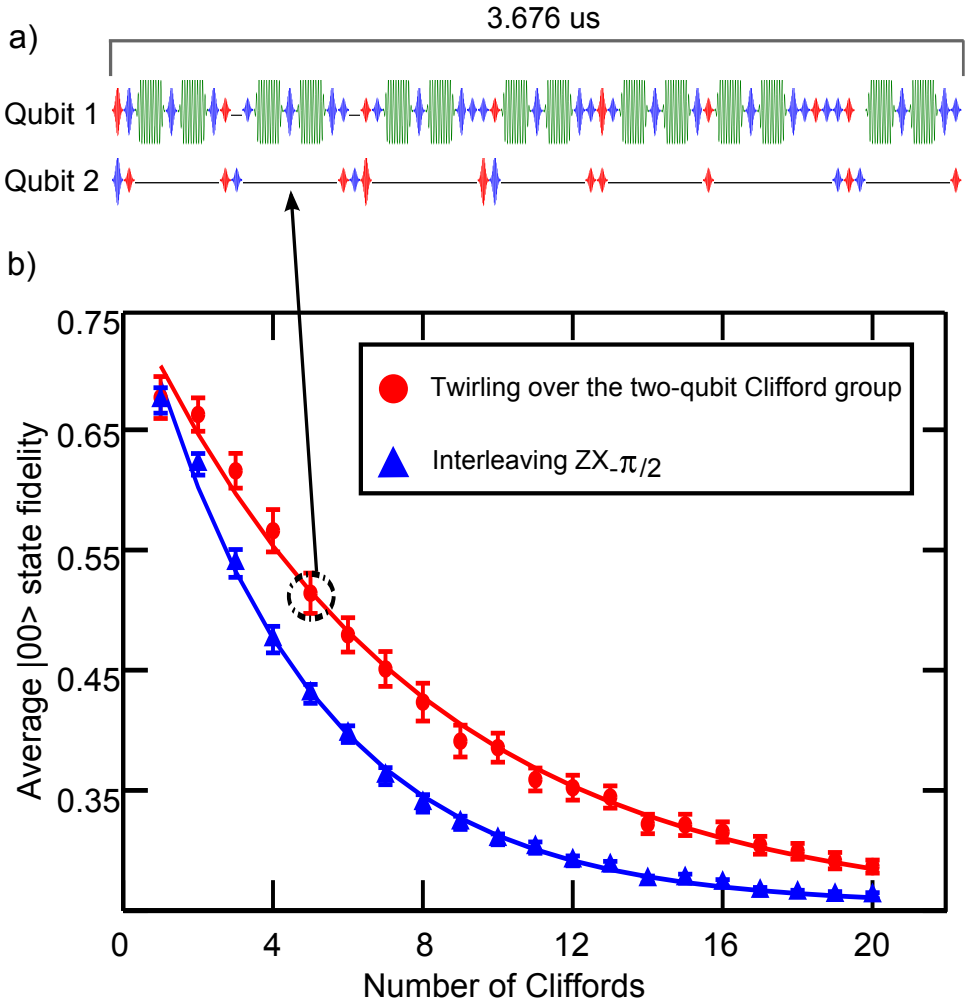

Fig. 18: *RB experiments on a two-qubit system. (a) Two-qubit pulse sequence for 5 Clifford gates randomly selected from the 11520 elements of the two-qubit Clifford group. Tall Gaussians represent π rotations, whereas short ones represent $\pi/2$ rotations. A final Clifford gate is added to make the sequence self-inverting. (b) Fidelity decay for the $|00\rangle$ in the standard RB protocol where the twirling is performed over the two-qubit Clifford group (circles) and in the interleaved protocol (triangles), in which each Clifford gate has an additional $ZX_{-\pi/2}$ gate appended at the end. The decays are fitted to an exponential model to extract an average error per Clifford operation of $r = 0.0936 \pm 0.0058$ (standard protocol) and a $ZX_{-\pi/2}$ error of $r_{\mathrm{ZX}_{-\pi/2}} = 0.0653 \pm 0.0014$. The arrow shows the truncation that would correspond to the pulse sequence shown in (a) and which has an average $|00\rangle$ state fidelity of over 50%.*

$\hat{H}_0 + \lambda\hat{V}$ where λ is a small parameter and $\hat{H}_0$ is some free Hamiltonian. An effective Hamiltonian for the system in this frame is $\hat{H}^A = \hat{A}^\dagger \hat{H} \hat{A}$ where $\hat{A} = \exp(-i\hat{S})$. Assuming a power series expansion of $\hat{S}$ (which we restrict to be at least first order in λ)

$$\hat{S} = \sum_{n=1}^{\infty} \hat{S}^{(n)} \lambda^n, \tag{100}$$

we derive $\hat{H}^A$ from the Baker-Campbell-Hausdorff formula as

$$\begin{aligned}\hat{H}^A =& \sum_{j=0}^{\infty} \mathrm{ad}[i\sum_{n=1}^{\infty}\hat{S}^{(n)}\lambda^n]^j \frac{\hat{H}_0+\lambda\hat{V}}{j!},\\ =& \sum_{m=0}^{\infty}\lambda^m\hat{H}^{(m)},\end{aligned} \tag{101}$$

where $\hat{H}^{(0)}=\hat{H}_0$ and for $m>0$

$$\hat{H}^{(m)} = i[\hat{S}^{(m)},\hat{H}_0]+\hat{H}_{\mathrm{x}}^{(m)}, \tag{102}$$

with

$$\begin{aligned}\hat{H}_{\mathrm{x}}^{(1)} =& \hat{V},\\ \hat{H}_{\mathrm{x}}^{(2)} =& -[\hat{S}^{(1)},[\hat{S}^{(1)},\hat{H}_0]]/2 + i[\hat{S}^{(1)},\hat{V}],\\ \hat{H}_{\mathrm{x}}^{(3)} =& -[\hat{S}^{(1)},[\hat{S}^{(2)},\hat{H}_0]]/2 - [\hat{S}^{(2)},[\hat{S}^{(1)},\hat{H}_0]]/2 - i[\hat{S}^{(1)},[\hat{S}^{(1)},[\hat{S}^{(1)},\hat{H}_0]]]/3!\\ &+ i[\hat{S}^{(2)},\hat{V}] - [\hat{S}^{(1)},[\hat{S}^{(1)},V]]/2.\end{aligned} \tag{103}$$

Since m^{th} order of $\hat{H}_{\mathrm{x}}$ depends on strictly lower orders of the frame transformation we can solve for the frame $\hat{S}^{(m)}$ at each order by enforcing that the effective Hamiltonian $\hat{H}^{(m)}$ describes our desired dynamics.

A.1 Diagonalizing the system

For example if we are interested in diagonalizing the system ($\hat{H}^{(m)}$ to be diagonal in the basis of $\hat{H}_0$) then we find

$$\sum_p E_p^{(m)}|p\rangle\langle p| = i\sum_p E_p^{(0)}(S^{(m)}|p\rangle\langle p| - |p\rangle\langle p|\hat{S}^{(m)}) + \hat{H}_{\mathrm{x}}^{(m)}, \tag{104}$$

which gives

$$\begin{aligned}E_p^{(m)} =& \langle p|\hat{H}_{\mathrm{x}}^{(m)}|p\rangle,\\ \langle p|\hat{S}^{(m)}|q\rangle =& \frac{-i\langle p|\hat{H}_{\mathrm{x}}^{(m)}|q\rangle}{E_p^{(0)}-E_q^{(0)}},\end{aligned} \tag{105}$$

for $p\neq q$ and $\langle p|\hat{S}^{(m)}|p\rangle = 0$

A.2 Eliminating coupling across subspaces

Another example of interest is when we want to find an effective Hamiltonian after we have eliminated coupling between subspaces which are separated by a large energy. For example we have a free Hamiltonian of the form $\hat{H}_0 = \hat{H}_{0_1}\oplus\ldots\hat{H}_{0_j}\oplus\ldots\hat{H}_{0_k}$ where j labels each subspace and k is the total number of subspaces and we want to find the m^{th} approximated Hamiltonian

$\hat{H}^{(m)} = \hat{H}_1^{(m)} \oplus \ldots \hat{H}_j^{(m)} \oplus \ldots \hat{H}_k^{(m)}$ when there is a small coupling between these subspaces. In this case equation (102) becomes

$$\begin{aligned} \hat{H}_j^{(m)} =& \hat{H}_{\mathrm{x_{jj}}}^{(m)}, \\ \hat{H}_{0_j}\hat{S}_{jk}^{(m)} - \hat{S}_{jk}^{(m)}\hat{H}_{0_k} =& -i\hat{H}_{\mathrm{x}_{jk}}^{(m)} \end{aligned} \tag{106}$$

where without loss of generality we have taken $\hat{S}_{jj}^{(m)} = 0$. If H_0 is diagonal then this reduces to

$$\langle p|\hat{S}_{jk}^{(m)}|q\rangle = \frac{-i\langle p|\hat{H}_{\mathrm{x}_{jk}}^{(m)}|q\rangle}{\langle p|\hat{H}_{0_j}|p\rangle - \langle q|H_{0_k}|q\rangle}. \tag{107}$$

B General leakage removal

In this appendix, we give the general theory for finding adiabatic pulses for controlling subsystems of a larger system. The systems that will obey this theory are those in which transitions out of the subspace occur an energy cost δ. Furthermore, we assume this cost is the largest rate in the problem so that we can form a perturbation expansion around $\lambda = \Omega/\delta$ where Ω is the max of the control fields Ω_m. To be more specific, imagine a Hilbert space that can be partitioned into two subspaces, $\hat{H} = \hat{H}_{\mathrm{control}} \oplus \hat{H}_{\mathrm{leakage}}$, where we wish to perform some quantum gate solely in the control subspace, but with control Hamiltonians $\Omega_m\hat{K}_m$ that act on the complete Hilbert space. That is, the general Hamiltonian for this system is

$$\hat{H}(t) = \frac{1}{\lambda}\hat{H}_0 + \sum_m \Omega_m(t)\hat{K}_m, \tag{108}$$

where we require that H_0 takes the form

$$\hat{H}_0 = 0 \oplus \lambda \sum_k \delta_k |k\rangle\langle k|. \tag{109}$$

Here we note that $\hat{H}_0$ only has support on the leakage subspace. Since, δ is assumed to be large then $\hat{H}_0$ is the dominant term in the Hamiltonian, and the leakage subspace is off-resonant. It is less clear what constraints must be placed on the control Hamiltonians, $\Omega_m\hat{K}_m$. Certainly, if we wish to perform a general gate on the control subspace, then they must be controllable on that subspace, however, in order to completely eliminate leakage errors there are additional constraints, which we now determine.

The general protocol to determine these extra constraints arising from leakage is to first determine the Hamiltonian in the control subspace that implements the desired gate. That is, find the functions $h_l(t)$ of the Hamiltonian $\hat{H}_{\mathrm{sp}}$

$$\hat{H}_{\mathrm{sp}} = \sum_{l=1}^{d_c^2-1} \frac{h_l(t)}{d_c}\hat{B}_l \tag{110}$$

where $\hat{B}_l$ is some orthogonal basis for operators in the control subspace of dimension d_c, that implement the desired gate. Next we define an effective Hamiltonian in the complete space by

$$\hat{H}^A = \hat{A}^\dagger(t)\hat{H}(t)\hat{A}(t) + i\dot{\hat{A}}^\dagger(t)\hat{A}(t). \tag{111}$$

with the only requirement on $\hat{A}$ being that $\hat{A}(0) = \hat{A}(t_g) = \hat{I}$ so that the frame transformation vanishes at the boundaries. Note the additional term $i\dot{\hat{A}}^\dagger(t)\hat{A}(t)$ when compared to the previous appendix. The constraints on this effective Hamiltonian to be satisfied are

$$\mathrm{Tr}[\hat{H}^A(t)\hat{B}_l] = h_l(t), \tag{112}$$
$$\langle j|\hat{H}^A(t)|k\rangle = 0 \text{ for } 0 \leq j < d_c \text{ and } d_c \leq k < d, \tag{113}$$

Here equation (112) constrains the $H^A(t)$ to be equivalent to equation (110) and equation (113) cancels the coupling between the control subspace and the leakage subspace. If theses constraints can be satisfied we have found a control set $\{\Omega_m(t)\}$ that implements the desired gate with out leakage. In practice, this will not be possible but using the following procedure we can develop a perturbative approach.

The adiabatic transformation $\hat{A}$ can be written as $\hat{A}(t) = e^{-i\hat{S}(t)}$ and we can write both $\hat{H}(t)$ and the frame transformation $\hat{S}(t)$ as power series in the small parameter λ, as

$$\hat{H}(t) = \frac{1}{\lambda}\hat{H}_0 + \sum_{n=0,m}^{\infty} \lambda^n \Omega_m^{(n)}(t)\hat{K}_m. \tag{114}$$

and

$$\hat{S}(t) = \sum_{n=1}^{\infty} \hat{S}^{(n)}(t)\lambda^l. \tag{115}$$

This is very similar to appendix A and using a Baker-Campbell-Hausdorff (BCH) and Taylor expansion we find $\hat{H}^A = \sum_n \lambda^n \hat{H}^{(n)}(t)$ where

$$\hat{H}^{(n)}(t) = \hat{H}_{\mathrm{x}}^{(n)}(t) + \sum_m \Omega_m^{(n)}(t)\hat{K}_m + i[\hat{S}^{(n+1)}(t), \hat{H}_0] \tag{116}$$

for $n \geq 0$. Here $H_{\mathrm{x}}^{(n)}(t)$ is a rather complicated expression which for the first few orders is

$$\begin{aligned}
\hat{H}_{\mathrm{x}}^{(0)}(t) =& 0 \\
\hat{H}_{\mathrm{x}}^{(1)}(t) =& i[\hat{S}^{(1)}(t), \sum_m \Omega_m^{(0)}(t)\hat{K}_m] - [\hat{S}^{(1)}(t), [\hat{S}^{(1)}(t), \hat{H}_0]]/2 - \dot{\hat{S}}^{(1)}(t). \\
\hat{H}_{\mathrm{x}}^{(2)}(t) =& i[\hat{S}^{(2)}(t), \sum_m \Omega_m^{(0)}(t)\hat{K}_m] + i[\hat{S}^{(1)}(t), \sum_m \Omega_m^{(1)}(t)\hat{K}_m] \\
& - [\hat{S}^{(1)}(t), [\hat{S}^{(1)}(t), \sum_m \Omega_m^{(0)}(t)\hat{K}_m]]/2 - [\hat{S}^{(1)}(t), [\hat{S}^{(2)}(t), \hat{H}_0]]/2 \\
& - [\hat{S}^{(2)}(t), [\hat{S}^{(1)}(t), \hat{H}_0]]/2 - i[\hat{S}^{(1)}(t), [\hat{S}^{(1)}(t), [\hat{S}^{(1)}(t), \hat{H}_0]]]/6 \\
& + i[\dot{\hat{S}}^{(1)}(t), \hat{S}^{(1)}(t)]/2 - \dot{\hat{S}}^{(2)}(t).
\end{aligned} \tag{117}$$

This expansion bears some formal similarity to the Schrieffer-Wolf expansion used in appendix A which means that a compact closed expression to any order is unlikely to exist. This expression for $\hat{H}^{(n)}(t)$ is useful as it allows us to separate the free variables $\Omega_m^{(n)}(t)$ and $\hat{S}^{(n+1)}(t)$ for the order n expression from those that are used to satisfy the conditions in equations (112) and (113) for order $n-1$, which only occur in the expression for $H_{\mathrm{x}}^{(n)}(t)$. To see this more clearly we can used the above to rewrite equation (112) for each order n as

$$\sum_m \Omega_m^{(n)} \mathrm{Tr}[\hat{K}_m\hat{B}_l] = h_l^{(n)} - \mathrm{Tr}[\hat{H}_{\mathrm{x}}^{(n)}(t)\hat{B}_l]. \tag{118}$$

for $0 < l < d_c^2$ where $h_l^{(n)}$ is the n^{th} order expression for h_l. Furthermore equation (113) for each order n becomes

$$S_{j,k}^{(n+1)} = i\frac{1}{\lambda\delta_k}\langle j| \left[\hat{H}_{\text{x}}^{(n)}(t) + \sum_m \Omega_m^{(n)}\hat{K}_m\right] |k\rangle \tag{119}$$

for $0 \leq j \leq d_c$ and $d_c \leq k < d$. Here we have used that H_0 has no weight in the control subspace. Since $H_{\text{x}}^{(n)}$ only depends on $S_{j,k}^{(n)}$, H_0, and $u_m^{(n-1)}$ then equations (118) and (119) are well formed. The components of $S^{(n+1)}(t)$ that haven't yet been defined are free parameters in our theory. Choosing a different functional form for the remaining matrix elements gives us the different forms of a DRAG solution. It is necessary that the frame transformation vanish at $t = 0$ and $t = t_g$, which may restrict some of the freedoms we have in assigning value to the otherwise unconstrained elements of $S^{(n+1)}(t)$. At each order of approximation, specifying the values of $\Omega_m^{(n)}(t)$ and $\hat{S}^{(n+1)}(t)$ fully determines $\hat{H}_{\text{x}}^{(n+1)}(t)$ and so we can iterate this procedure indefinitely, though at some point the derivatives of $\hat{S}$ that appear in $\hat{H}_{\text{x}}(t)$ will likely become large, causing the adiabatic expansion to break down.

C State and gate fidelities

C.1 Representations of a quantum state

Defining $\mathcal{H}_d$ as a Hilbert space of dimensions d, a quantum state is described by the state matrix ρ. ρ is simply a member of $\mathcal{L}(\mathcal{H}_d)$ (the set of linear operators on the Hilbert space) with the following constraints

- Normalized, $\text{Tr}[\rho] = 1$.
- Hermitian, $\rho^\dagger = \rho$.
- positive semi-definite $\rho \geq 0$

Any linear operator can be written as $\hat{A} = \sum_p a_p \hat{B}_p$ where $\{B_p\}$ is a basis for $\mathcal{L}(\mathcal{H}_d)$. For n qubits a convenient choice for this basis is the Pauli operator basis $\mathbf{P} = \{\hat{I}, \hat{X}, \hat{Y}, \hat{Z}\}^{\otimes n}$ which from the first two constraints allows us to write the quantum state matrix as

$$\rho = \frac{1}{d}\mathbf{p}\cdot\mathbf{P} \tag{120}$$

where $\mathbf{p}$ is the Pauli state vector which consists of only real elements (with the first element set to one).
The state fidelity of ρ with some ideal pure state, $|\psi_{\text{ideal}}\rangle$ is given by

$$F_s = \langle\psi_{\text{ideal}}|\rho|\psi_{\text{ideal}}\rangle, \tag{121}$$

which in the Pauli representation is

$$F_s = \frac{1}{d}\mathbf{p}_{\text{ideal}}\cdot\mathbf{p}. \tag{122}$$

C.2 Representations of a map

A general quantum process on a finite d-dimensional Hilbert space $\mathcal{H}_d$ ($d = 2^n$ for qubit systems) is a completely positive trace-preserving (CPTP) map (Λ) that maps one state to a new state and from the Choi-Jamiolkowski isomorphism any map $\Lambda : \mathcal{L}(\mathcal{H}_d) \rightarrow \mathcal{L}(\mathcal{H}_d)$ can be represented by the Choi matrix

$$\rho_\Lambda = \frac{1}{d}\sum_{i,j} E_{ij} \otimes \Lambda(E_{ij}). \tag{123}$$

Here $\rho_\Lambda \in \mathcal{L}(\mathcal{H}_d^{(A)} \otimes \mathcal{H}_d^{(B)})$ and E_{ij} is the matrix with 1 in the ij^{th} entry and 0's elsewhere. In Ref. [76], Choi proved that Λ is completely positive if and only if ρ_Λ is positive semidefinite. The Choi matrix allows us to test if the map is trace preserving from the partial trace over the second subsystem $\mathrm{Tr_B}[\rho_\Lambda] = I/d$ and if the map is unital by $\mathrm{Tr_A}[\rho_\Lambda] = I/d$. Furthermore, the action of the map on any state $\rho \in \mathcal{L}(\mathcal{H}_d)$ is given by

$$\Lambda(\rho) = d\mathrm{Tr_A}[(\rho^T \otimes I)\rho_\Lambda]. \tag{124}$$

An alternative representation of a map is the Pauli transfer matrix, $\mathcal{R}$, defined by

$$\mathcal{R}_{ij} = \frac{1}{d}\mathrm{Tr}[P_i \Lambda(P_j)]. \tag{125}$$

This representation is simply the Choi matrix expanded in the Pauli operator basis, since it can be shown that

$$\mathcal{R}_{ij} = \mathrm{Tr}[\rho_\Lambda P_j^T \otimes P_i], \tag{126}$$

and therefore

$$\rho_\Lambda = \frac{1}{d^2}\sum_{i,j} \mathcal{R}_{ij} P_j^T \otimes P_i. \tag{127}$$

This is a useful representation since the action of the map on a state ρ in the Pauli representation is a simple matrix transformation of the Pauli state-vector $\mathbf{p}$ given by

$$\mathbf{p}' = \mathcal{R}\mathbf{p}, \tag{128}$$

which is obvious from our definition of $\mathcal{R}$. Therefore, the Pauli transfer matrix is also related to the Liouville or superoperator representation by a basis transformation (the transformation from E_{ij} to P_k) and composition of maps is described simply by matrix multiplication.
The $\mathcal{R}$ matrix has a few useful properties when compared to the standard chi-matrix [77] for determining whether a map is physical. Firstly, $\mathcal{R}$ consists of only real numbers and so contains exactly the same number of parameters as the gate, with no redundancy due to Hermiticity. Secondly, the operators that are mapped to and from the identity are revealed by looking at the first row and column respectively (assuming $P_0 = I$). If only the identity is mapped back onto itself, then the map is trace-preserving, and if the identity remains the identity, the map is unitial. This corresponds to a final row or column of all zeros and a single one. Lastly, the elements of $\mathcal{R}$ are bounded by ± 1, and for any Clifford operations there is exactly one non-zero element in each row and column with magnitude one, as Clifford operators simply map Pauli operators to other Pauli operators.

The average gate fidelity between an ideal unitary gate $U_{\rm ideal}$ and the experimentally reconstructed map Λ is defined as

$$F_g = \int \langle\psi|U_{\rm ideal}^\dagger \Lambda\left(|\psi\rangle\langle\psi|\right) U_{\rm ideal}|\psi\rangle \mathrm{d}|\psi\rangle. \tag{129}$$

The corresponding expressions in terms of the Choi or PTM representation can be found using the techniques from [78] as

$$F_g = \frac{d\mathrm{Tr}[\rho_{\rm ideal}\rho]+1}{d+1} = \frac{\mathrm{Tr}[\mathcal{R}_{\rm ideal}^T\mathcal{R}]/d+1}{d+1} \tag{130}$$

where we have made the implicit assumption that the ideal map is a unitary map.

References

[1] J. Koch, T. M. Yu, J. Gambetta, A. A. Houck, D. I. Schuster, J. Majer, A. Blais, M. H. Devoret, S. M. Girvin, and R. J. Schoelkopf, Phys. Rev. A **76**, 042319 (2007).

[2] J. A. Schreier, A. A. Houck, J. Koch, D. I. Schuster, B. R. Johnson, J. M. Chow, J. M. Gambetta, J. Majer, L. Frunzio, M. H. Devoret, S. M. Girvin, and R. J. Schoelkopf, Phys. Rev. B **77**, 180502 (2008).

[3] H. Paik, D. I. Schuster, L. S. Bishop, G. Kirchmair, G. Catelani, A. P. Sears, B. R. Johnson, M. J. Reagor, L. Frunzio, L. I. Glazman, S. M. Girvin, M. H. Devoret, and R. J. Schoelkopf, Phys. Rev. Lett. **107**, 240501 (2011).

[4] C. Rigetti, J. M. Gambetta, S. Poletto, B. L. T. Plourde, J. M. Chow, A. D. Córcoles, J. A. Smolin, S. T. Merkel, J. R. Rozen, G. A. Keefe, M. B. Rothwell, M. B. Ketchen, and M. Steffen, Phys. Rev. B **86**, 100506 (2012).

[5] J. M. Chow, J. M. Gambetta, A. D. Córcoles, S. T. Merkel, J. A. Smolin, C. Rigetti, S. Poletto, G. A. Keefe, M. B. Rothwell, J. R. Rozen, M. B. Ketchen, and M. Steffen, Phys. Rev. Lett. **109**, 060501 (2012).

[6] B. Josephson, Physics Letters **1**, 251 (1962).

[7] R. P. Feynman, *Feynman Lectures On Physics* (Addison Wesley Longman, New York, 1970).

[8] M. H. Devoret, in *Quantum fluctuations*, edited by S. Reynaud, E. Giacobino, and J. Zinn-Justin (Elsevier, 1997).

[9] G. Burkard, R. H. Koch, and D. P. DiVincenzo, Phys. Rev. B **69**, 064503 (2004).

[10] A. Shnirman, G. Schön, and Z. Hermon, Phys. Rev. Lett. **79**, 2371 (1997).

[11] Y. Nakamura, Y. A. Pashkin, and J. S. Tsai, Nature (London) **398**, 786 (1999).

[12] J. N. L. Connor, T. Uzer, R. A. Marcus, and A. D. Smith, The Journal of Chemical Physics **80**, 5095 (1984).

[13] Y. Nakamura, Y. A. Pashkin, T. Yamamoto, and J. S. Tsai, Phys. Rev. Lett. **88**, 047901 (2002).

[14] A. B. Zorin, F.-J. Ahlers, J. Niemeyer, T. Weimann, H. Wolf, V. A. Krupenin, and S. V. Lotkhov, Phys. Rev. B **53**, 13682 (1996).

[15] F. Yoshihara, K. Harrabi, A. O. Niskanen, Y. Nakamura, and J. S. Tsai, Phys. Rev. Lett. **97**, 167001 (2006).

[16] A. Blais, R.-S. Huang, A. Wallraff, S. M. Girvin, and R. J. Schoelkopfb, Phys. Rev. A **69**, 062320 (2004).

[17] A. Wallraff, D. I. Schuster, A. Blais, L. Frunzio, R.-S. Huang, J. Majer, S. Kumar, S. M. Girvin, and R. J. Schoelkopf, Nature (London) **431**, 162 (2004).

[18] J. Bourassa, J. M. Gambetta, A. A. Abdumalikov, O. Astafiev, Y. Nakamura, and A. Blais, Phys. Rev. A **80**, 032109 (2009).

[19] T. Niemczyk, F. Deppe, H. Huebl, E. P. Menzel, F. Hocke, M. J. Schwarz, J. J. Garcia-Ripoll, D. Zueco, T. Hummer, E. Solano, A. Marx, and R. Gross, Nat Phys **6**, 772 (2010).

[20] J. Gambetta, A. Blais, D. I. Schuster, A. Wallraff, L. Frunzio, J. Majer, M. H. Devoret, S. M. Girvin, and R. J. Schoelkopf, Phys. Rev. A **74**, 042318 (2006).

[21] J. Gambetta, A. Blais, M. Boissonneault, A. A. Houck, D. I. Schuster, and S. M. Girvin, Phys. Rev. A **77**, 012112 (2008).

[22] J. E. Johnson, C. Macklin, D. H. Slichter, R. Vijay, E. B. Weingarten, J. Clarke, and I. Siddiqi, Phys. Rev. Lett. **109**, 050506 (2012).

[23] J. Gambetta, W. A. Braff, A. Wallraff, S. M. Girvin, and R. J. Schoelkopf, Phys. Rev. A **76**, 012325 (2007).

[24] M. Hatridge, R. Vijay, D. H. Slichter, J. Clarke, and I. Siddiqi, Phys. Rev. B **83**, 134501 (2011).

[25] M. A. Castellanos-Beltran, K. D. Irwin, G. C. Hilton, L. R. Vale, and K. W. Lehnert, Nat Phys **4**, 929 (2008).

[26] D. Ristè, J. G. van Leeuwen, H.-S. Ku, K. W. Lehnert, and L. DiCarlo, Phys. Rev. Lett. **109**, 050507 (2012).

[27] A. Blais, J. Gambetta, A. Wallraff, D. I. Schuster, S. M. Girvin, M. H. Devoret, and R. J. Schoelkopf, Phys. Rev. A **75**, 032329 (2007).

[28] J. Majer, J. M. Chow, J. M. Gambetta, J. Koch, B. R. Johnson, J. A. Schreier, L. Frunzio, D. I. Schuster, A. A. Houck, A. Wallraff, A. Blais, M. H. Devoret, S. M. Girvin, and R. J. Schoelkopf, Nature (London) **449**, 443 (2007).

[29] J. M. Chow, L. DiCarlo, J. M. Gambetta, A. Nunnenkamp, L. S. Bishop, L. Frunzio, M. H. Devoret, S. M. Girvin, and R. J. Schoelkopf, Phys. Rev. A **81**, 062325 (2010).

[30] S. Filipp, P. Maurer, P. J. Leek, M. Baur, R. Bianchetti, J. M. Fink, M. Göppl, L. Steffen, J. M. Gambetta, A. Blais, and A. Wallraff, Phys. Rev. Lett. **102**, 200402 (2009).

[31] M. Boissonneault, J. M. Gambetta, and A. Blais, Phys. Rev. A **79**, 013819 (2009).

[32] M. Boissonneault, J. M. Gambetta, and A. Blais, Phys. Rev. Lett. **105**, 100504 (2010).

[33] N. Schuch and J. Siewert, Phys. Rev. A **67**, 032301 (2003).

[34] M. Steffen, M. Ansmann, R. McDermott, N. Katz, R. C. Bialczak, E. Lucero, M. Neeley, E. M. Weig, A. N. Cleland, and J. M. Martinis, Phys. Rev. Lett. **97**, 050502 (2006).

[35] A. Dewes, F. R. Ong, V. Schmitt, R. Lauro, N. Boulant, P. Bertet, D. Vion, and D. Esteve, Phys. Rev. Lett. **108**, 057002 (2012).

[36] L. DiCarlo, J. M. Chow, J. M. Gambetta, L. S. Bishop, B. R. Johnson, D. I. Schuster, J. Majer, A. Blais, L. Frunzio, S. M. Girvin, and R. J. Schoelkopf, Nature **460**, 240 (2009).

[37] L. DiCarlo, M. D. Reed, L. Sun, B. R. Johnson, J. M. Chow, J. M. Gambetta, L. Frunzio, S. M. Girvin, M. H. Devoret, and R. J. Schoelkopf, Nature **467**, 574 (2010).

[38] F. W. Strauch, P. R. Johnson, A. J. Dragt, C. J. Lobb, J. R. Anderson, and F. C. Wellstood, Phys. Rev. Lett. **91**, 167005 (2003).

[39] G. S. Paraoanu, Phys. Rev. B **74**, 140504 (2006).

[40] C. Rigetti and M. Devoret, Phys. Rev. B **81**, 134507 (2010).

[41] P. C. de Groot, J. Lisenfeld, R. N. Schouten, S. Ashhab, A. Lupascu, C. J. P. M. Harmans, and J. E. Mooij, Nat Phys **6**, 763 (2010).

[42] J. M. Chow, A. D. Córcoles, J. M. Gambetta, C. Rigetti, B. R. Johnson, J. A. Smolin, J. R. Rozen, G. A. Keefe, M. B. Rothwell, M. B. Ketchen, and M. Steffen, Phys. Rev. Lett. **107**, 080502 (2011).

[43] A. D. Córcoles, J. M. Gambetta, J. M. Chow, J. A. Smolin, M. Ware, J. D. Strand, B. L. T. Plourde, and M. Steffen, ArXiv e-prints (2012).

[44] S. Poletto, J. M. Gambetta, S. T. Merkel, J. A. Smolin, J. M. Chow, A. D. Córcoles, G. A. Keefe, M. B. Rothwell, J. R. Rozen, D. W. Abraham, C. Rigetti, and M. Steffen, Phys. Rev. Lett. **109**, 240505 (2012).

[45] A. Sørensen and K. Mølmer, Phys. Rev. A **62**, 022311 (2000).

[46] J. Benhelm, G. Kirchmair, C. F. Roos, and R. Blatt, Nat Phys **4**, 463 (2008).

[47] T. Monz, P. Schindler, J. T. Barreiro, M. Chwalla, D. Nigg, W. A. Coish, M. Harlander, W. Hänsel, M. Hennrich, and R. Blatt, Phys. Rev. Lett. **106**, 130506 (2011).

[48] P. J. Leek, S. Filipp, P. Maurer, M. Baur, R. Bianchetti, J. M. Fink, M. Göppl, L. Steffen, and A. Wallraff, Phys. Rev. B **79**, 180511 (2009).

[49] R. C. Bialczak, M. Ansmann, M. Hofheinz, E. Lucero, M. Neeley, A. D. O/'Connell, D. Sank, H. Wang, J. Wenner, M. Steffen, A. N. Cleland, and J. M. Martinis, Nat Phys **6**, 409 (2010).

[50] T. Yamamoto, M. Neeley, E. Lucero, R. C. Bialczak, J. Kelly, M. Lenander, M. Mariantoni, A. D. O'Connell, D. Sank, H. Wang, M. Weides, J. Wenner, Y. Yin, A. N. Cleland, and J. M. Martinis, Phys. Rev. B **82**, 184515 (2010).

[51] C. Bauer, R. Freeman, T. Frenkiel, J. Keeler, and A. J. Shaka, J. Magn. Reson. **58**, 442 (1984).

[52] M. Steffen, J. M. Martinis, and I. L. Chuang, Phys. Rev. B **68**, 224518 (2003).

[53] F. Motzoi, J. M. Gambetta, P. Rebentrost, and F. K. Wilhelm, Phys. Rev. Lett. **103**, 110501 (2009).

[54] J. M. Gambetta, F. Motzoi, S. T. Merkel, and F. K. Wilhelm, Phys. Rev. A **83**, 012308 (2011).

[55] J. M. Chow, L. DiCarlo, J. M. Gambetta, F. Motzoi, L. Frunzio, S. M. Girvin, and R. J. Schoelkopf, Phys. Rev. A **82**, 040305 (2010).

[56] E. Lucero, J. Kelly, R. C. Bialczak, M. Lenander, M. Mariantoni, M. Neeley, A. D. O'Connell, D. Sank, H. Wang, M. Weides, J. Wenner, T. Yamamoto, A. N. Cleland, and J. M. Martinis, Phys. Rev. A **82**, 042339 (2010).

[57] D. F. V. James, P. G. Kwiat, W. J. Munro, and A. G. White, Phys. Rev. A **64**, 052312 (2001).

[58] J. Fiurasek and Z. Hradil, Phys. Rev. A **63**, 020101 (2001).

[59] R. Blume-Kohout, New Journal of Physics **12**, 043034 (2010).

[60] A. I. Lvovsky, Journal of Optics B: Quantum and Semiclassical Optics **6**, S556 (2004).

[61] J. Watrous, Quantum Inf. Comput. **5**, 058 (2005).

[62] S. T. Merkel, J. M. Gambetta, J. A. Smolin, S. Poletto, A. D. Córcoles, B. R. Johnson, C. A. Ryan, and M. Steffen, ArXiv e-prints (2012).

[63] E. Knill, D. Leibfried, R. Reichle, J. Britton, R. B. Blakestad, J. D. Jost, C. Langer, R. Ozeri, S. Seidelin, and D. J. Wineland, Phys. Rev. A **77**, 012307 (2008).

[64] E. Magesan, J. M. Gambetta, and J. Emerson, Phys. Rev. Lett. **106**, 180504 (2011).

[65] E. Magesan, J. M. Gambetta, and J. Emerson, Phys. Rev. A **85**, 042311 (2012).

[66] E. Magesan, J. M. Gambetta, B. R. Johnson, C. A. Ryan, J. M. Chow, S. T. Merkel, M. P. da Silva, G. A. Keefe, M. B. Rothwell, T. A. Ohki, M. B. Ketchen, and M. Steffen, Phys. Rev. Lett. **109**, 080505 (2012).

[67] J. P. Gaebler, A. M. Meier, T. R. Tan, R. Bowler, Y. Lin, D. Hanneke, J. D. Jost, J. P. Home, E. Knill, D. Leibfried, and D. J. Wineland, Phys. Rev. Lett. **108**, 260503 (2012).

[68] J. M. Gambetta, A. D. Córcoles, S. T. Merkel, B. R. Johnson, J. A. Smolin, J. M. Chow, C. A. Ryan, C. Rigetti, S. Poletto, T. A. Ohki, M. B. Ketchen, and M. Steffen, Phys. Rev. Lett. **109**, 240504 (2012).

[69] C. A. Ryan, M. Laforest, and R. Laflamme, New J. Phys. **11**, 013034 (2009).

[70] M. J. Biercuk, H. Uys, A. P. VanDevender, N. Shiga, W. M. Itano, and J. J. Bollinger, Quantum Inf. Comput. **9**, 0920 (2009).

[71] K. R. Brown, A. C. Wilson, Y. Colombe, C. Ospelkaus, A. M. Meier, E. Knill, D. Leibfried, and D. J. Wineland, Phys. Rev. A **84**, 030303 (2011).

[72] S. Olmschenk, R. Chicireanu, K. D. Nelson, and J. V. Porto, New Journal of Physics **12**, 113007 (2010).

[73] J. M. Chow, J. M. Gambetta, L. Tornberg, J. Koch, L. S. Bishop, A. A. Houck, B. R. Johnson, L. Frunzio, S. M. Girvin, and R. J. Schoelkopf, Phys. Rev. Lett. **102**, 090502 (2009).

[74] S. Aaronson and D. Gottesman, Phys. Rev. A **70**, 052328 (2004).

[75] M. Tinkham, *Group theory and qauntum mechanics* (Dover, Cambridge, 1964).

[76] M.-D. Choi, Linear Algebra and its Applications **10**, 285 (1975).

[77] I. L. Chuang and M. A. Nielsen, J. Mod. Opt. **44**, 2455 (1997).

[78] M. A. Nielsen, Phys. Lett. A **303**, 249 (2002).

C 1 Quantum Error Correction for Quantum Memories [1]

Barbara M. Terhal
Institute for Quantum Information
RWTH Aachen, 52056 Aachen, Germany

Contents

1 Introduction **2**
1.1 Shor's Code and The Stabilizer Formalism 2
1.1.1 Stabilizer (Subsystem) Codes 5
1.1.2 Stabilizer Code Examples and The CSS Construction 7
1.2 QEC Conditions and Other Small Codes of Physical Interest 8
1.3 Error Correction and Fault Tolerance 12
1.4 Universality 14

2 2D (Topological) Error Correction **17**
2.1 Surface Code 17
2.1.1 Multiple Qubits and Operations by Lattice Surgery 21
2.1.2 Topological Qubits and CNOT via Braiding 23
2.2 Bacon-Shor Code 25
2.3 Subsystem Surface Code 28

3 Discussion **29**

[1] Lecture Notes of the 44^{th} IFF Spring School "Quantum Information Processing" (Forschungszentrum Jülich, 2013). All rights reserved.

1 Introduction

When the idea of a quantum computer took hold in the '90s it was immediately realized that its implementation would require some form of robustness and error correction. Alexei Kitaev proposed a scheme in which the physical representation of quantum information and realization of logical gates would be naturally robust due to the topological nature of the 2D physical system [1]. Around the same time Peter Shor formulated a first quantum error-correcting code and proved that a quantum computer could be made fault-tolerant [2]. Several authors then established the fault-tolerant threshold theorem (Theorem 1) which shows that in principle one can realize almost noise-free quantum computation using noisy components at the cost of moderate overhead.

In these lectures we will discuss the basic ideas behind error correction: we will focus on quantum error correction using stabilizer codes for the purpose of making a quantum memory. Experimental efforts have not advanced very much into the domain of quantum error correction. Several experiments exist realizing the 3-qubit repetition code in NMR, ion-trap, optical and superconducting qubits. Four qubit stabilizer pumping has been realized in ion-trap qubits [3]. Some topological quantum error correction has been implemented with eight-photon cluster states in [4]. As current experiments, in particular in ion-trap and superconducting qubits, are getting closer to a noise error rate of $O(10^{-4})$ (below the threshold for the surface code discussed in Section 2), one may expect to see more scalable realizations of quantum error correction which are fine-tuned to experimental capabilities and constraints.

1.1 Shor's Code and The Stabilizer Formalism

The smallest classical code which can correct a single bit-flip error (represented by Pauli X [2]) is the 3-(qu)bit repetition code where we encode $\left|\overline{0}\right\rangle = |000\rangle$ and $\left|\overline{1}\right\rangle = |111\rangle$. A single error can be corrected by taking the majority of the three bit values and flipping the bit which is different from the majority. In quantum error correction we don't want to measure the 3 qubits to take a majority vote, as we would immediately loose the quantum information represented in the phase and amplitude of an encoded state $\left|\overline{\psi}\right\rangle = \alpha \left|\overline{0}\right\rangle + \beta \left|\overline{1}\right\rangle$.

But we can imagine measuring the parity checks Z_1Z_2 and Z_2Z_3 *without learning the state of each individual qubit*. Fig. 1(a) shows the quantum circuit which measures a parity check represented by a Pauli operator P using an ancilla qubit. Other than giving us parity information, the ideal parity measurement also provides a discretization of errors which is not naturally present in elementary quantum systems. Through interaction with classical or quantum systems the amplitude and phase of a qubit will fluctuate over time: bare quantum information encoded in atomic, photonic, spin or other single quantum systems is barely information as it is constantly at drift. An ideal parity measurement discretizes this continuum of errors into a discrete set of a Pauli errors (X, Y, Z or I on each qubit) which are amenable to correction. If the parity checks Z_1Z_2 and Z_2Z_3 have eigenvalues +1, one concludes no error. An outcome, say, of $Z_1Z_2 = -1$ and $Z_2Z_3 = 1$ is consistent with the erred state $X_1 \left|\overline{\psi}\right\rangle$ where $\left|\overline{\psi}\right\rangle$ is any encoded state.

Let us informally introduce some of the notions used in describing a quantum (stabilizer) code. For a code C encoding k qubits, one defines k pairs of logical Pauli operators $(\overline{X}_i, \overline{Z}_i)$, $i = 1, \ldots k$, such that $\overline{X}_i\overline{Z}_i = -\overline{X}_i\overline{Z}_i$ while logical Pauli operators with labels i and i' mutually

[2] Pauli $X = \begin{pmatrix} 0 & 1 \\ 1 & 0 \end{pmatrix}$, $Z = \begin{pmatrix} 1 & 0 \\ 0 & -1 \end{pmatrix}$ and $Y = \begin{pmatrix} 0 & -i \\ i & 0 \end{pmatrix} = iXZ$.

commute (realizing the algebra of Pauli operators acting on k logical qubits). For the 3-qubit code we have $\overline{X} = X_1X_2X_3$ and $\overline{Z} = Z_1$.

The *code space* of a code C encoding k qubits is spanned by the codewords $|\overline{x}\rangle$ where x is a k-bitstring. All states in the codespace obey the parity checks, meaning that the parity check operators have eigenvalue $+1$ for all states in the code space. In other words, the parity checks act trivially on the codespace. The logical operators of a quantum error-correcting code are non-unique as we can multiply them by the trivially-acting parity check operators to obtain equivalent operators. For example, $\overline{Z}$ for the 3-qubit code is either Z_1 or Z_2, or Z_3 or $Z_1Z_2Z_3$.

The 3-qubit repetition code does not protect or detect Z (dephasing) errors as the parity checks only measure information in the Z-basis (M_Z). Shor's 9-qubit code was the first quantum error-correcting code which encodes a single qubit and corrects any single qubit Pauli error. Shor's code is obtained from the 3-qubit repetition code by *concatenation*. Code concatenation is a procedure in which we take the elementary qubits of the codewords of a code C and replace them by encoded qubits of a new code C'. In Shor's construction we choose the first code C as the repetition code in the Hadamard-rotated basis ($H : X \leftrightarrow Z$) with codewords $|\overline{+}\rangle = |+++\rangle$ and $|\overline{-}\rangle = |---\rangle$. The parity checks of C are X_1X_2 and X_2X_3 and the logical operators are $\overline{Z}_C = Z_1Z_2Z_3$ and $\overline{X}_C = X_1$. As the second code C' we choose the normal 3-qubit repetition code, i.e. we replace $|+\rangle$ by $|\overline{+}\rangle = \frac{1}{\sqrt{2}}(|000\rangle + |111\rangle)$ etc.

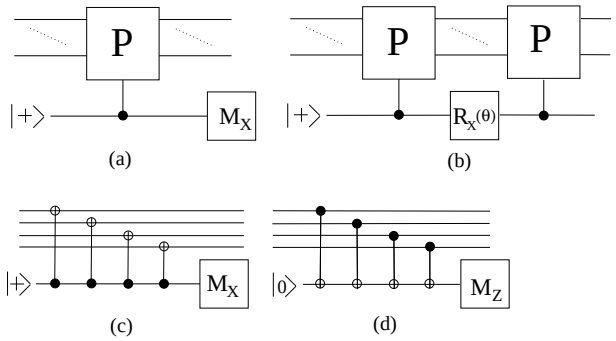

Fig. 1: *Measuring parity checks the quantum circuit-way. (a) Circuit to measure the* ± 1 *eigenvalues of a unitary multi-qubit Pauli operator* P*. The gate is the controlled-*P *gate which applies* P *when the control qubit is 1 and* I *if the control qubit is 0. One measures the qubit in the* $|\pm\rangle$ *basis denoted as* M_X*. (b) Realizing the evolution* $\exp(-i\theta P/2)$ *itself (with* $R_x(\theta) = \exp(-i\theta X/2)$*). (c) Realization of circuit (a) using CNOTS when* $P = X_1X_2X_3X_4$*. (d) Realization of circuit (a) using CNOTs when* $P = Z_1Z_2Z_2Z_4$*.*

We get all the parity checks for the concatenated 9-qubit code by taking all the parity checks of the codes C' and taking the C'-encoded parity checks of C. For Shor's code this will give: the Z-checks Z_1Z_2, Z_2Z_3, Z_4Z_5, Z_5Z_6, Z_7Z_8 and Z_8Z_9 (from three uses of the code C') and the X-checks $X_1X_2X_3X_4X_5X_6$, $X_4X_5X_6X_7X_8X_9$ (from the parity checks $\overline{X}_1\overline{X}_2$ and $\overline{X}_2\overline{X}_3$ where $\overline{X}$ is the logical operator of the code C'). The non-unique logical operators of the encoded qubit are $\overline{Z} = Z_1Z_4Z_7$ are $\overline{X} = X_1X_2X_3$.

This code can clearly correct any X error as it consists of three qubits each of which is encoded in the repetition code which can correct an X error. What happens if a single Z error occurs on any of the qubits? A single Z error will anti-commute with one of the parity X-checks or with both. For example, the error Z_1 anti-commutes with $X_1X_2X_3X_4X_5X_6$ so that the state $Z_1|\overline{\psi}\rangle$ has eigenvalue -1 with respect to this parity check. The eigenvalues of the parity check

operators are called the *error syndrome*. Aside from detecting errors (finding -1 syndrome values) the error syndrome should allow one to infer which error occurred.

One feature of quantum error correcting codes which is different from classical error correcting codes, is that this inference step does not necessarily has to point to a unique error. For example: for the 9-qubit code, the error Z_1 and the error Z_2 have an equivalent effect on the codespace as Z_1Z_2 is a parity check which acts trivially on the code space. The syndromes for errors which are related by parity checks are always identical. The classical algorithm which processes the syndrome to infer an error, —this procedure is called *decoding*—, does not need to choose between such equivalent errors. But there is further ambiguity in the error syndrome. For Shor's code the error Z_1 and the error Z_4Z_7 have an identical syndrome as $Z_1Z_4Z_7$ is the $\overline{Z}$ operator which commutes with all parity checks. If we get a single non-trivial (-1) syndrome for the parity check $X_1X_2X_3X_4X_5X_6$ we could decide that the error is Z_1 or Z_4Z_7. But if we make a mistake in this decision and correct with Z_4Z_7 while Z_1 happened then we have effectively performed a $\overline{Z}$ without knowing it! This means that the decoding procedure should decide between errors, —all consistent with the error syndrome—, which are mutually related by logical operators.

How is this decision made? We could assign a probability to each possible error: this assignment is captured by the *error model*. Then our decoding procedure can simply choose an error (or class of equivalent errors), consistent with the syndrome, which has highest probability. We will discuss the procedure of decoding more formally in Section 1.1.1 after we introduce the stabilizer formalism. For Shor's code we decode the syndrome by picking a single qubit error which is consistent with the syndrome. If a two-qubit error occurred we may thus have made a mistake. However, for Shor's code there are no two single-qubit errors E_1 and E_2 with the same syndrome whose product E_1E_2 is a logical operator. This implies that Shor's code can correct any single qubit error. It is a $[[n, k, d]] = [[9, 1, 3]]$ code, encoding $k = 1$ qubit into $n = 9$ (n is called the *block size* of the code) and having *distance* $d = 3$. The distance d of the code is defined as the minimum weight of any logical operator (see the formal definition in Eq. (1)). The weight of a Pauli operator is the number of qubits on which it acts non-trivially. We take the minimum weight as there are several logical operators and the weight of each one of them can be varied by multiplication with parity checks. It is simple to understand why a code with distance $d = 2t + 1$ can correct t errors: errors of weight at most t have the property that their products have weight at most $2t < d$ and therefore the product can never be a logical operator as those have weight d or more. Thus our decoding procedure which picks an error of weight at most t can never lead to a logical error.

Clearly the usefulness of (quantum) error correction is directly related to the error model; it hinges on the assumption that low-weight errors are more likely than high-weight errors. Error-correcting a code which can perfectly correct errors with weight at most t, will lead to failure with probability roughly equal to the total probability of errors of weight larger than t. This probability for failure of error correction is called the *logical error rate*. The goal of quantum error correction is to use redundancy and correction to realize logical qubits with logical error rates below the error rate of the elementary constituent qubits.

It seems rather simplistic to use error models which assign X, Z and Y errors probabilistically to qubits as in real quantum information amplitudes and phases are drifting rather than undergoing discretized errors. Ideal parity measurement can induce such discrete error model stated in terms of probabilities, but as parity measurements themselves will be inaccurate in a continuous fashion, such fully digitized picture is an oversimplification. The theory of quantum fault-tolerance, see Section 1.3, has developed a framework which allows one to establish

the results of quantum error correction and fault-tolerance for very general quantum dynamics obeying physical locality assumptions (see the comprehensive results in [5]). However, for numerical studies of code performance it is impossible to simulate such more general open system dynamics and several simple error models are used to capture the expected performance of the codes.
Three important remarks can be made with this general framework in mind. The simplest message is that a code which can correct t Pauli errors can in fact correct any possible error on a subset of t qubits (described for example by some noisy superoperator or master equation for the qubits). This point can be readily understood in the case of ideal parity check measurements where the measurement projects the set of possible errors onto the set of Pauli errors. Secondly, errors can be correlated in space and time arising from non-Markovian dynamics, but as long as (1) we use the proper estimate of the strength of the noise (which may involve using amplitudes and norms rather than probabilities) and (2) the noise is sufficiently short-ranged (meaning that noisy interactions between distant uncoupled qubits are sufficiently weak [6]), fault-tolerance threshold results can be established. The third simple remark is that qubit coding does not deal with leakage errors. As many elementary qubits are realized as two-level subspaces of higher-dimensional systems to which they can leak, other protective mechanisms such as cooling (or teleporting to a fresh qubit) will need to be employed in order for qubits to remain in their two-dimensional homespace.

Let us come back to Shor's code and imagine that the nine qubits are laid out in a 3×3 square array as in Fig. 12. It looks relatively simple to measure the parity Z-checks locally, while the weight-6 X-checks would require a larger circuit. But why should there be such asymmetry between the X- and Z-checks? Imagine that instead of measuring $\mathbf{X}_{=,1} \equiv X_1X_2X_3X_4X_5X_6$, we measure (in parallel or sequentially) the eigenvalues of X_1X_4, X_2X_5 and X_3X_6 and take the product of these eigenvalues to obtain the eigenvalue of $\mathbf{X}_{=,1}$. The important property of these weight-2 operators is that all individually commute with the logical operators $\overline{X}$ and $\overline{Z}$ of the Shor code, hence measuring them does not change the expectation values of $\overline{X}$ and $\overline{Z}$. These weight-2 X-checks do not commute with the weight-2 Z-checks however. If we first measure all the weight-2 X-checks and then measure the Z-checks, then with the second step the eigenvalues of individual X-checks are randomized but correlated. Namely, their product $X_1X_2X_3X_4X_5X_6$ remains fixed as $X_1X_2X_3X_4X_5X_6$ commutes with the weight-2 Z-checks. By symmetry the weight-2 X-checks commute with $\mathbf{Z}_{||,1} = Z_1Z_2Z_4Z_5Z_7Z_8$ and $\mathbf{Z}_{||,2} = Z_2Z_3Z_5Z_6Z_8Z_9$. Viewing the Shor code this way we can imagine doing error correction and decoding using the stable commuting parity checks $\mathbf{X}_{=,1}, \mathbf{X}_{=,2}, \mathbf{Z}_{||,1}, \mathbf{Z}_{||,2}$ while we deduce their eigenvalues from measuring 12 weight-2 parity checks. Shor's code in this form is the smallest member in the family of Bacon-Shor codes $[[n^2, 1, n]]$ whose qubits can be laid out in a $n \times n$ array as in Fig. 12, see Section 2.2. The Bacon-Shor code family in which non-commuting (low-weight) parity checks are measured in order to deduce the eigenvalues of commuting parity checks is an example of a (stabilizer) subsystem code.

1.1.1 Stabilizer (Subsystem) Codes[3]

Shor's code and many existing codes defined on qubits are examples of *stabilizer* codes [7]. Stabilizer codes are attractive as (i) they are the straightforward quantum generalization of classical binary linear codes, (ii) their logical operators and distance are easily determined, (iii)

[3]Readers less interested in this general framework can skip this section without major inconveniences.

understanding of how to construct universal sets of logical gates and (iv) the numerical analysis of code performance are relatively simple. The main idea of stabilizer codes is to encode k logical qubits into n physical qubits using a subspace, the codespace, $\mathcal{L} \subseteq (\mathbb{C}^2)^{\otimes n}$ spanned by states $|\psi\rangle$ that are invariant under the action of a *stabilizer group* $\mathcal{S}$,

$$\mathcal{L} = \{|\psi\rangle \in (\mathbb{C}^2)^{\otimes n} \,:\, P\,|\psi\rangle = |\psi\rangle \quad \forall P \in \mathcal{S}\}.$$

Here $\mathcal{S}$ is an Abelian subgroup of the Pauli group $\mathcal{P}_n = \langle iI, X_1, Z_1, \ldots, X_n, Z_n\rangle$ such $-I \notin \mathcal{S}$. For any stabilizer group $\mathcal{S}$ one can always choose a set of generators $\mathcal{S} = \langle S_1, \ldots, S_m\rangle$ such that $S_a \in \mathcal{P}_n$ are hermitian Pauli operators. The mutually commuting parity check which we considered before are the generators of the stabilizer group. In general they will be composed of products of Pauli X, Y, Z. If there are $n-k$ linearly independent generators (parity checks) then the codespace $\mathcal{L}$ is 2^k-dimensional, or encodes k qubits. The *weight* $|P|$ of a Pauli operator $P = P_1 \ldots P_n \in \mathcal{P}_n$ is the number of non-identity single-qubit Pauli operators P_i. If the code encodes k logical qubits it is possible to find k pairs of logical operators $(\overline{X}_j, \overline{Z}_j)_{j=1,\ldots,k}$. These logical operators commute with all the parity checks, i.e. they commute with all elements in $\mathcal{S}$ as they preserve the codespace. However they should not be generated by the parity checks themselves otherwise their action on the code space is trivial. The centralizer $\mathcal{C}(\mathcal{S})$ of $\mathcal{S}$ in $\mathcal{P}_n$ is defined as $\mathcal{C}(\mathcal{S}) = \{P \in \mathcal{P}_n | \forall s \in \mathcal{S},\ Ps = sP\}$, i.e. all operators in $\mathcal{P}_n$ which commute with $\mathcal{S}$. We thus have $\mathcal{C}(\mathcal{S}) = \langle \mathcal{S}, \overline{X}_1, \overline{Z}_1, \ldots, \overline{X}_k, \overline{Z}_k\rangle$, i.e. the logical operators of the code are elements of $\mathcal{C}(\mathcal{S}) \setminus \mathcal{S}$ as they are in $\mathcal{C}(\mathcal{S})$ but not in $\mathcal{S}$. The distance d of a stabilizer code can then be defined as

$$d = \min_{P \in \mathcal{C}(\mathcal{S}) \setminus \mathcal{S}} |P|. \tag{1}$$

Error correction proceeds by measuring the error syndrome $\mathbf{s}$ which are the ± 1 eigenvalues of the generators of $\mathcal{S}$. As we mentioned in Section 1.1 this syndrome will not point to a unique Pauli error but an *equivalent class of errors*. This class is a coset $E\mathcal{S}$ of the group $\mathcal{S}$ in $\mathcal{P}_n$, where $E = E(\mathbf{s})$ is an error which is consistent with the syndrome $\mathbf{s}$. We can denote the coset as $[E] = E\mathcal{S}$ with coset representative E [4] and associate a total probability $\mathrm{Prob}([E]) = \sum_{s \in S} \mathrm{Prob}(Es)$ with the coset depending on some error model which assigns a probability $\mathrm{Prob}(P)$ to every Pauli operator $P \in \mathcal{P}_n$. If the syndrome is consistent with $[E]$ it is also consistent with $[E\overline{P}]$ where $\overline{P}$ is any logical operator (as the logical operators commute with $\mathcal{S}$).

Maximum likelihood decoding is the procedure by which, given a syndrome $\mathbf{s}$ and a coset representative $E(\mathbf{s})$, one finds the logical operator $\overline{P}$ (which could be I) which has the maximum value for $\mathrm{Prob}([E\overline{P}])$. It is important to consider how efficiently (in the number n of elementary qubits) this task can be done as $\mathrm{Prob}([E\overline{P}])$, —essentially a partition function—, is a sum over the number of elements in $\mathcal{S}$ which is exponential in n. For a simple depolarizing error model where each qubit undergoes a X, Y or Z error with probability $p/3$ and no error with probability $1-p$, we have $\mathrm{Prob}([E\overline{P}]) = (1-p)^n \sum_{s \in \mathcal{S}} \exp(-\beta |E\overline{P}s|)$ with inverse 'temperature' $\beta = \ln(3(1-p)/p)$. For small error rates $p \ll 1$ corresponding to low temperatures $\beta \to \infty$ the value of the partition function is dominated by the contribution of the lowest-weight error(s). Thus, instead of maximum likelihood decoding which compares the relative values of $\mathrm{Prob}([E\overline{P}])$, one can also opt for *minimum-weight* decoding. In minimum-weight decoding one simply picks an error $E(\mathbf{s})$, consistent with the syndrome $\mathbf{s}$, which has minimum weight $|E|$. We will discuss this decoding method for the surface code in Section 2.

[4] Note that left and right cosets are the same modulo trivial errors proportional to I.

Subsystem codes can be viewed as stabilizer codes in which some logical qubits, called gauge qubits, are not used to encode information. The state of these qubits is irrelevant and can be fixed (gauge-fixing) or left variable. The presence of the gauge qubits sometimes lets one simplify the measurement of the stabilizer parity checks as the state of the gauge qubits is allowed to freely change under these measurements. One takes a stabilizer code $\mathcal{S}$ and splits its logical operators $(\overline{X}_i, \overline{Z}_i)$ into two groups: the gauge qubit logical operators $(\overline{X}_i, \overline{Z}_i)$, $i = 1 \dots m$ and the remaining logical operators $(\overline{X}_i, \overline{Z}_i)$ with $i = m+1, \dots k$. We define a new subgroup $\mathcal{G} = \langle \mathcal{S}, \overline{X}_1, \overline{Z}_1, \dots \overline{X}_m, \overline{Z}_m \rangle$ which is non-Abelian and contains $\mathcal{S}$. As $\mathcal{G}$ is non-Abelian we can consider its center, i.e. $\mathcal{G} \cap \mathcal{C}(\mathcal{G}) = \{P \in \mathcal{G} |\ \forall g \in \mathcal{G}, Pg = gP\} = \mathcal{S}$ (modulo trivial elements).

If we measure the generators of the group $\mathcal{G}$ we can deduce the eigenvalues of $\mathcal{S}$. Since the $k-m$ logical operators $(\overline{X}_i, \overline{Z}_i)$, $i = m+1, \dots, k$ commute with $\mathcal{G}$, these logical operators are unaffected by the measurement. A priori there is no reason why measuring the generators of $\mathcal{G}$ would be simpler than measuring the generators of the stabilizer $\mathcal{S}$. In the interesting constructions such as the Bacon-Shor code and the subsystem surface code discussed in Section 2, we gain as we measure very low-weight parity checks in $\mathcal{G}$ (while we lose by allowing more qubit-overhead or declining noise threshold).

The distance of a subsystem code is not the same as that of a stabilizer code, Eq. (1), as we should only consider the minimum weight of the $k-m$ logical operators. These logical operators are not unique as they can be multiplied by elements in $\mathcal{S}$ *but also* by the logical operators of the irrelevant gauge qubits. This motivates the definition of the distance as $d = \min_{P \in \mathcal{C}(\mathcal{S}) \setminus \mathcal{G}} |P|$. As errors on the gauge qubits are harmless it means that equivalent classes of errors are those related to each other by elements in $\mathcal{G}$. Given the eigenvalues of the stabilizer generators, the syndrome s, the decoding algorithm considers cosets $E(\mathrm{s})\mathcal{G} \in \mathcal{P}_n$, denoted as $[E] = E\mathcal{G}$. Maximum likelihood decoding proceeds by determining the coset $[E\overline{P}]$ which has a maximum value for $\mathrm{Prob}([E\overline{P}]) = \sum_{g \in \mathcal{G}} \mathrm{Prob}(E\overline{P}g)$ where $\overline{P}$ varies over the possible logical operators.

1.1.2 Stabilizer Code Examples and The CSS Construction

We discuss a few small examples of stabilizer codes to illustrate the formalism. The smallest non-trivial quantum code is the $[[4, 2, 2]]$ error-detecting code. Its linearly independent parity checks are $X_1X_2X_3X_4$ and $Z_1Z_2Z_3Z_4$: the code encodes $4 - 2 = 2$ qubits. You can verify that you can choose $\overline{X}_1 = X_1X_2, \overline{Z}_1 = Z_1Z_3$ and $\overline{X}_2 = X_2X_4$, $\overline{Z}_2 = Z_3Z_4$ as the logical operators which commute with the parity checks. The code distance is 2 which means that the code cannot correct a single qubit error. The code can however still *detect* any single qubit error as any single qubit error anti-commutes with at least one of the parity checks which leads to a nontrivial -1 syndrome. Alternatively, we can view this code as a subsystem code which has one logical qubit, say, qubit 1, and one gauge qubit, qubit 2. In that case $\mathcal{G} = \langle X_1X_2X_3X_4, Z_1Z_2Z_3Z_4, Z_3Z_4, X_2X_4 \rangle = \langle Z_1Z_2, Z_3Z_4, X_1X_3, X_2X_4 \rangle$, showing that measuring weight-2 checks would suffice to detect single qubit errors on the encoded qubit 1.

Exercise: Consider the stabilizer code C_6 (defined in [8]) with parity checks $X_1X_4X_5X_6$, $X_1X_2X_3X_6$, $Z_1Z_4Z_5Z_6$ and $Z_1Z_2Z_3Z_6$ acting on 6 qubits. How many qubits does it encode, what are its logical operators and distance? One can concatenate the code C_6 with the code $[[4, 2, 2]]$ (called C_4 in [8]) by replacing the three pairs of qubits in C_6 by three pairs of C_4-encoded qubits, to obtain a new code. What are the parameters d, k, n of this concatenated code?

The smallest stabilizer code which encodes 1 qubit and corrects 1 error is the $[[5,1,3]]$ code; you can find its parity checks in [9]. Another well-known code is Steane's 7-qubit code, $[[7,1,3]]$ which is constructed from two classical codes using the Calderbank-Shor-Steane (CSS) construction. Classical binary linear codes are fully characterized by their parity check matrix H. The parity check matrix H_1 of a code C_1 encoding k_1 bits is a $(n-k_1)\times n$ matrix with 0,1 entries where linearly independent rows represent the parity checks. The binary vectors $c \in \{0,1\}^n$ which obey the parity checks, i.e. $Hc = 0$ (where addition is modulo 2), are the codewords. The distance $d = 2t+1$ of such classical code is the minimum (Hamming) weight of any codeword and the code can correct t errors.
We can represent a row r of H_1 of a code C_1 by a parity check operator $s(Z)$ such that for the bit $r_i = 1$ we take $s(Z)_i = Z$ and for bit $r_i = 0$ we set $s(Z)_i = I$. These parity checks generate some stabilizer group $\mathcal{S}_1(Z)$. In order to make this into a quantum code with distance larger than one, one needs to add X-type parity checks. These could simply be obtained from the $(n-k_2)\times n$ parity check matrix H_2 of another classical code C_2. We obtain the stabilizer parity checks $\mathcal{S}_2(X)$ by replacing the 1s in each row of this matrix by Pauli X and I otherwise. But in order for $\mathcal{S} = \langle \mathcal{S}_1(Z), \mathcal{S}_2(X)\rangle$ to be an Abelian group the checks all have to commute. This implies that every parity X-check should overlap on an even number of qubits with every parity Z-check. In coding words it means that the rows of H_2 have to be orthogonal to the rows of H_1. This in turn can be expressed as $C_2^\perp \subseteq C_1$ where $C_2^\perp$ is the code dual to C_2 (codewords of $C_2^\perp$ are all the binary vectors orthogonal to all codewords $c \in C_2$).
In total $\mathcal{S} = \langle \mathcal{S}_1(Z), \mathcal{S}_2(X)\rangle$ will be generated by $2n - k_1 - k_2$ independent parity checks so that the quantum code encodes $k_1 + k_2 - n$ qubits. The distance of the quantum code is the minimum of the distance $d(C_1)$ and $d(C_2)$ as one code is used to correct Z errors and the other code is used to correct X errors.

Exercise: Steane's code is constructed using a classical binary code C which encodes 4 bits into 7 bits and has distance 3. Its parity check matrix is

$$H = \begin{pmatrix} 0 & 0 & 0 & 1 & 1 & 1 & 1 \\ 0 & 1 & 1 & 0 & 0 & 1 & 1 \\ 1 & 0 & 1 & 0 & 1 & 0 & 1 \end{pmatrix}. \tag{2}$$

Show that $C^\perp \subseteq C$. Steane's $[[7,1,3]]$ code is obtained using the CSS construction with $C_1 = C$ and $C_2 = C$. What are the parity checks for Steane's code?

Exercise: Show that the two-qubit code $|\overline{0}\rangle = \frac{1}{\sqrt{2}}(|00\rangle + |11\rangle)$ and $|\overline{1}\rangle = \frac{1}{\sqrt{2}}(|01\rangle + |10\rangle)$ is a code which can detect a single Z error.

1.2 QEC Conditions and Other Small Codes of Physical Interest

One may ask what properties a general quantum code, —defined as some subspace C of a physical state space—, should obey in order for a certain set of errors to be correctable. These properties are expressed as the quantum error-correcting conditions which can hold exactly or only approximately. We encode some k qubits into a codespace C so that $|\overline{i}\rangle$ are the codewords encoding the k-bit strings i. Assume there is a set of errors $\mathcal{E} = \{E_l\}$ against which we wish to correct. For example we can describe the short-term decoherence effects on the qubits by a

superoperator $\mathcal{S}(\rho) = \sum_l E_l \rho E_l^\dagger$ which has the Kraus error operators E_l. The quantum error-correcting conditions say that there exists an error-correcting operation, a reversal of the error, if and only if the following conditions are obeyed for all errors $E_k, E_l \in \mathcal{E}$

$$(1)\ \forall i,j\ , \left\langle \bar{i} \right| E_k^\dagger E_l \left| \bar{j} \right\rangle = c_{kl}\delta_{ij}. \tag{3}$$

Here c_{kl} is a constant *independent* of the codeword $\left|\bar{i}\right\rangle$. The condition for $i = j$ says that the codewords are not distinguished by the error observables. The condition for $i \neq j$ indicates that the orthogonal codewords need to remain orthogonal after the action of the errors (otherwise we could not undo the effect of the noise). Note that if a code can correct the error set $\{E_i\}$ it can also correct an error set $\{F_j\}$ where each F_j is any linear combination of the elements E_i as the set $\{F_j\}$ will also obey the quantum error-correcting conditions of Eq. (3).

Quite commonly one describes an open system dynamics by a Markovian master equation of Lindblad form

$$\frac{d\rho}{dt} = -i[H,\rho] + \mathcal{L}(\rho) \equiv \mathcal{L}_{\rm tot}(\rho), \tag{4}$$

where $\mathcal{L}(\rho) = \sum_j L_j \rho L_j^\dagger - \frac{1}{2}\{L_j^\dagger L_j, \rho\}$ with quantum-jump or Lindblad operators L_j while H is a harmless or desired driving Hamiltonian. For short times τ we have $\rho(\tau) = \mathcal{S}_\tau(\rho(0)) = E_0 \rho E_0^\dagger + \sum_i E_i \rho E_i^\dagger$ with $E_0 \approx I - i\tau H - \frac{1}{2}\tau \sum_i L_i^\dagger L_i = I - O(\tau)$ and $E_i \approx \sqrt{\tau} L_i$. Thus the error set is approximately given by the quantum jump operators L_i.
Let us consider two simple codes which approximately obey the conditions in Eq. (3) for the physically relevant decoherence due to (amplitude) damping for qubits and bosonic modes. Even though the $[[5,1,3]]$ code is the smallest code which can correct against any single qubit error one can use 4 qubits to approximately correct any *amplitude-damping* error which can model energy loss [10]. The noise process for amplitude damping on a single qubit is given by the superoperator $\mathcal{S}(\rho) = \sum_i A_i \rho A_i^\dagger$ with $A_0 = \frac{1}{2}((1+\sqrt{1-\gamma})I + (1-\sqrt{1-\gamma})Z) \approx I - O(\gamma)$ and $A_1 = \sqrt{\gamma}\sigma_-$. The codewords for the 4-qubit amplitude damping code are $\left|\bar{0}\right\rangle = \frac{1}{\sqrt{2}}(|0000\rangle + |1111\rangle)$ and $\left|\bar{1}\right\rangle = \frac{1}{\sqrt{2}}(|0011\rangle + |1100\rangle)$. Each qubit in this code is subjected to amplitude-damping noise. We wish to approximately correct against the error set $E_0 = A_0^{\otimes 4}$, $E_1 = A_1 \otimes A_0^{\otimes 3}$, $E_2 = A_0 \otimes A_1 \otimes A_0^{\otimes 2}$, $E_3 = A_0^{\otimes 2} \otimes A_1 \otimes A_0$ and $E_4 = A_0^{\otimes 3} \otimes A_1$ which correspond to no damping and single qubit damping on any of the four qubits respectively. The authors in [10] show that this code obeys the QEC conditions approximately with $O(\gamma^2)$ corrections which is a quadratic improvement over the basic error rate γ.

Another interesting example is that of a single bosonic mode (with creation and annihilation operators $a^\dagger, a$) which is used to encode a qubit in two orthogonal states which are approximately protected against photon loss [11]. The damping process can be modeled with the Lindblad equation, Eq. (4), with $L = \sqrt{\kappa}a$ while $H = (\omega + \frac{1}{2})a^\dagger a$ (which we can transform away by going to the rotating frame at frequency ω). One can choose two Schrödinger cat states as encoded states

$$\left|\bar{0}_+\right\rangle = \frac{1}{\sqrt{N_+}}(|\alpha\rangle + |\text{-}\alpha\rangle), \quad \left|\bar{1}_+\right\rangle = \frac{1}{\sqrt{N_+}}(|i\alpha\rangle + |\text{-}i\alpha\rangle).$$

Here $|\alpha\rangle$ is a coherent state $|\alpha\rangle = \exp(-|\alpha|^2/2)\sum_n \frac{\alpha^n}{\sqrt{n!}}|n\rangle$ and $N_\pm = 2(1 \pm \exp(-2|\alpha|^2)) \approx 2$. For sufficiently large photon number $\langle n\rangle = |\alpha|^2$, the states $|\pm\alpha\rangle, |\pm i\alpha\rangle$ (and thus $\left|\bar{0}_+\right\rangle$ and $\left|\bar{1}_+\right\rangle$) are approximately orthogonal. The creation and manipulation of such cat states has

been actively explored for cavity modes in micro-wave cavities, see e.g. [12]. The code states are chosen such that loss of a photon from the cavity maps the states onto (approximately) orthogonal states. As $a\,|\alpha\rangle = \alpha\,|\alpha\rangle$, we have

$$a\left|\overline{0}_+\right\rangle = \alpha\sqrt{N_+/N_-}\left|\overline{0}_-\right\rangle,\ a\left|\overline{1}_+\right\rangle = i\alpha\sqrt{N_+/N_-}\left|\overline{1}_-\right\rangle\ , \tag{5}$$

with $\left|\overline{0}_-\right\rangle = \frac{1}{\sqrt{N_-}}(|\alpha\rangle - |\text{-}\alpha\rangle)$ and $\left|\overline{1}_-\right\rangle = \frac{1}{\sqrt{N_-}}(|i\alpha\rangle - |\text{-}i\alpha\rangle)$. As we know the preservation of orthogonality is a prerequisite for these code states to be correctable. One can verify that in the limit of $|\alpha| \to \infty$ we obey the QEC conditions[5], Eq. (3), for $E_0 = \sqrt{\kappa}a$ and $E_1 = I - \frac{\kappa}{2}a^\dagger a$. The cat states will gradually loose their intensity and thus their approximate protection under these processes as the vacuum state $|0\rangle$ is the only stationary state of the Lindblad equation. Counter-intuitively they do this by the process with Kraus operator E_1, i.e. by not observing the photon emission, while the Kraus operator E_0 maps the state $\left|\overline{0}_+\right\rangle$ onto $\left|\overline{0}_-\right\rangle$ and vice-versa [12]. The codespace (spanned by $\left|\overline{0}_+\right\rangle, \left|\overline{1}_+\right\rangle$) is distinguished from the orthogonal erred space (spanned by $\left|\overline{0}_-\right\rangle$ and $\left|\overline{1}_-\right\rangle$) by the parity operator $\exp(i\pi a^\dagger a) = \sum_n (-1)^n\,|n\rangle\,\langle n| = P_{even} - P_{odd}$. This parity operator has $+1$ eigenvalue for the states $\left|\overline{0}_+\right\rangle, \left|\overline{1}_+\right\rangle$ and -1 eigenvalue for the states $\left|\overline{0}_-\right\rangle, \left|\overline{1}_-\right\rangle$. By continuously monitoring the value of the parity operator $\exp(i\pi a^\dagger a)$ one could track the occurrence of errors. Better even would be the realization of a restoring operation which puts back an erred state with decayed amplitude $\alpha e^{-\kappa t/2}$ into the code space while restoring the amplitude back to α as proposed in [11] [6]. In [11] the interaction with superconducting qubits coupled to the cavity is proposed to be used for encoding, correction and decoding of the cat states.

One can generalize the stabilizer formalism to continuous-variable systems characterized by an infinite-dimensional Hilbert space. Of particular interest are codes which encode a discrete amount of information, a qubit say, in a harmonic oscillator [13]. Given are two conjugate variables $\hat{p}$ and $\hat{q}$ which represent generalized momentum and position, obeying $[\hat{q}, \hat{p}] = i$. The idea is to encode the information such that *small* shifts in position or momentum correspond to correctable errors while logical operators are represented as large shifts. For a harmonic oscillator space, the Pauli group P_n can be generalized to the Weyl-Heisenberg group generated by the operators $\exp(it\hat{p})$ and $\exp(is\hat{q})$ for real s and t. In order to define a qubit in this infinite-dimensional space we select a set of commuting check generators whose $+1$ eigenvalue space is two-dimensional.
We will consider three examples. In our first example the 'code' encodes a single state and essentially represents a quantum rotor. We choose $S_q = e^{2i\hat{q}}$ and $S_p = e^{-i\pi\hat{p}}$ as commuting check operators [7]. When $S_p = 1$ and $S_q = 1$ the eigenvalues of $\hat{p}$ are even integers while $\hat{q}$ should have eigenvalues $0 \mod \pi$. Defining $\hat{n} = \hat{p}/2$ and $\hat{\phi} = 2\hat{q}$, we obtain a quantum rotor with conjugate variables $\hat{n} = 0, \pm 1, \ldots$ and 2π-periodic phase $\hat{\phi}$. A realization of the quantum rotor is the quantization of a superconducting circuit where ϕ is the superconducting phase (across a junction) and $\hat{n}$ represents the number of Cooper pairs. As there is a unique state with

[5] If we were to use two coherent states as code states, say, $\left|\overline{0}\right\rangle = |\alpha\rangle$ and $\left|\overline{1}\right\rangle = |\text{-}\alpha\rangle$, the QEC conditions would not be obeyed, as $\langle\alpha|\,E_1^\dagger E_0\,|\alpha\rangle \neq \langle\text{-}\alpha|\,E_1^\dagger E_0\,|\text{-}\alpha\rangle$ for any α.

[6] Such restorative process is physically impossible for all states in the code space as it would increase the distinguishability of states.

[7] As $\hat{q}$ and $\hat{p}$ are dimensionfull quantities one should take $S_q = e^{2i\hat{q}/q_0}$ and $S_p = e^{-i\pi\hat{p}/p_0}$ where q_0 and p_0 set the scale so that $\hat{q}/q_0$ etc. are dimensionless. In what follows we tacitly assume the existence of such a scale so that if, say, the codespace corresponds to integer $\hat{p}$ it is an integer in units of p_0.

fixed (say $+1$) eigenvalues for S_q and S_p, superconducting qubits such as the transmon qubit (see e.g. Lectures by Jay Gambetta) use superpositions of states with different eigenvalues for $S_q = e^{i\phi}$ in order to encode information.
A different choice of S_q and S_p leads to a real code which encodes a single qubit and has built-in protection. We choose as checks the operators $S_q = e^{2i\hat{q}}$ and $S_p = e^{-2i\pi\hat{p}}$. Fixing the eigenvalues of these operators to be $+1$ leads to the discretization $\hat{p} = 0, \pm 1, \pm 2 \ldots$ and again $\hat{q}$ should have eigenvalues which are multiples of π. Now there are two operators which commute with S_q and S_p but which mutually anti-commute: these are $\overline{Z} = e^{i\hat{q}}$ and $\overline{X} = e^{-i\pi\hat{p}}$.

Exercise: Verify the proper commutation relations of S_q, S_p, $\overline{X}$ and $\overline{Z}$ using $e^A e^B = e^{[A,B]} e^B e^A$ where A, B are any linear combinations of $\hat{q}$ and $\hat{p}$.

The state $\left|\overline{0}\right\rangle$ (defined by $\overline{Z}\left|\overline{0}\right\rangle = \left|\overline{0}\right\rangle$ and $S_p\left|\overline{0}\right\rangle = \left|\overline{0}\right\rangle$) is a uniform superposition of states with $\hat{q} = 0, \pm 2\pi, \ldots$. Similarly, $\left|\overline{1}\right\rangle$ corresponds to a uniform superposition of $\hat{q} = \pm\pi, \pm 3\pi, \ldots$, see Fig. 2 with $\alpha = \pi$. Consider the effect of shifts of the form $e^{-i\delta\hat{p}}$ where $|\delta| < \pi/2$, which are correctable. Such shifts map the codewords outside of the codespace as they do not commute with the stabilizer operator S_q. Error correction thus takes place by measuring $q \mod \pi$ and applying the smallest shift which resets $q = 0 \mod \pi$. Similarly, the $|\overline{+}\rangle$ is a uniform superposition of states with $\hat{p} = 0, \pm 2, \pm 4, \ldots$ while $|\overline{-}\rangle$ is a uniform superposition of states with $\hat{p} = \pm 1, \pm 3, \ldots$, see Fig. 2. The qubit is protected against shifts $e^{i\epsilon\hat{q}}$ with $|\epsilon| < 1/2$. This code is realized as a Majorana fermion qubit (see Lectures by F. Hassler) where $\hat{p} = \hat{n}$ counts the total number of electrons while $\hat{q} = \hat{\phi}$ is the π-periodic conjugate phase variable. The $|\overline{+}\rangle$ eigenstate of $\overline{X}$ with an even number of electrons correspond to the Majorana mode unoccupied while $|\overline{-}\rangle$ is the state with an odd number of electrons as the Majorana mode is occupied. The protection of the Majorana fermion qubit can thus also be understood from this coding perspective although the formalism does of course not shed light on how to realize this qubit. Another realization of this code, which does not use Majorana fermion qubits, but superconducting circuits is the 0-π qubit (see e.g. [14]) which is designed such that the superconducting phase difference between terminals has degenerate energy minima at 0 and π corresponding to the approximate codewords $\left|\overline{0}\right\rangle$ and $\left|\overline{1}\right\rangle$.

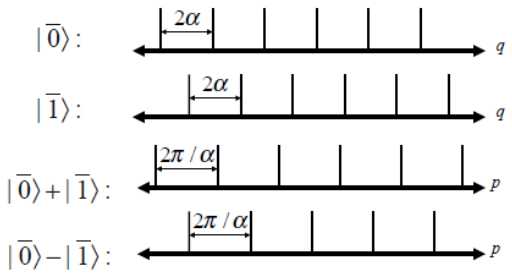

Fig. 2: *Picture from [13]: Amplitude of codewords for the stabilizer code with commuting checks $S_q(\alpha) = e^{2i\pi\hat{q}/\alpha}$ and $S_p(\alpha) = e^{-2i\hat{p}\alpha}$ which encodes a qubit in an oscillator.*

More generally, we can parametrize this code by a real number α by taking the stabilizer checks as $S_q = e^{2i\pi\hat{q}/\alpha}$ and $S_p = e^{-2i\hat{p}\alpha}$ (above we took $\alpha = \pi$). The logical operators are $\overline{Z} = e^{\pi i\hat{q}/\alpha}$ and $\overline{X} = e^{-i\hat{p}\alpha}$ [13], see the codewords in Fig. 2. The code can correct against shifts $e^{i\epsilon\hat{q}}$ with

$|\epsilon| < \frac{\pi}{2\alpha}$ and $e^{-i\delta\hat{p}}$ where $|\delta| < \frac{\alpha}{2}$. One can use this code for encoding a qubit in a bosonic mode where $\hat{q}$ and $\hat{p}$ arise as quadrature variables, i.e. $\hat{q} = \frac{1}{\sqrt{2}}(a^\dagger + a)$ and $\hat{p} = \frac{i}{\sqrt{2}}(a^\dagger - a)$.
The free Hamiltonian $H_0 = \omega(a^\dagger a + \frac{1}{2})$ will periodically transform $\hat{q}$ into $\hat{p}$ and vice versa so it is natural to let S_q be of the same form as S_p and choose $\alpha = \sqrt{\pi}$. The codewords of this code in Fig. 2 are not physically achievable as it requires an infinite amount of squeezing to prepare (superpositions of) of a quadrature eigenstates such as $|q\rangle$ or $|p\rangle$. Ref. [13] proposed to use approximate codewords. For example the approximate codeword $|\tilde{0}\rangle$ is a superposition of Gaussian peaks in q-space, —each one centered at integer multiples of $2\sqrt{\pi}$ with width Δ—, in a total Gaussian envelope of width $1/\kappa$. Viewed as a superposition of p-eigenstates, such state is a superposition of peaks with width κ and total envelope of width Δ^{-1}. An error analyis of this approximate encoding was done in [15].

There are of course many codes which are not captured by the qubit (or qudit) stabilizer formalism. Here I would like to briefly mention the class of 2D topological qubit codes where the stabilizer checks are still commuting, but they are no longer simple Pauli operators. As Hamiltonians these correspond to the so-called 2D Levin-Wen models [16], as codes they are called Turaev-Viro codes [17]. The advantage of these codes which generalize the 2D surface code in Section 2, is that universal quantum computation can achieved by purely topological means. The disadvantage from the coding perspective is that (1) the stabilizer checks are more complicated as operators, e.g. for the so-called Fibonacci code on a hexagonal lattice, the stabilizer checks act on 3 and 12 qubits and (2) no one has established a scheme for error correction or a noise-threshold for these codes.

1.3 Error Correction and Fault Tolerance

We have understood from the previous sections that the crucial element of quantum error correction for stabilizer codes is the realization of the (parity) check measurement as in Fig. 1. The immediate problem is that the parity check measurement suffers from the same imperfections and noise as any other gate or measurement that one may wish to do. The parity check measurement should be a non-demolition single-shot measurement which has both the effect of projecting the state in either the code space or a discrete set of error spaces while giving at the same time accurate information about which event occurred. In practice a parity check measurement may arise as a continuous weak measurement leaving a classical stochastic data record which hovers around the value $+1$ (pointing to the state being in the code space) while occasionally *jumping* to a value centered around -1. One can imagine that this continuously acquired record is immediately fed back to unitarily steer the qubits to the code space [18]. Advantages of such immediate feed-back or 'closed-loop' form of error correction are that it eliminates the need for a fast and accurate quantum measurement in which weak quantum signals are amplified to our classical macroscopic world. A disadvantage which we will discuss at the end of Section 2.1 is that the correction mechanism is purely *local* in time and space.
We could set up such local error correction mechanism by explicitly engineering a dissipative dynamics which drives/corrects the qubits towards the code space as proposed in [3, 19]. We assume that the open-system dynamics of code qubits and environment is described by a Lindblad equation as in Eq. (4). For simplicity we consider the case in which we would like to *pump* or drive four qubits into a state with even parity so that the 4-qubit parity Z-check, $Z_1Z_2Z_3Z_4$ has eigenvalue $+1$. Imagine that we can engineer the dissipation (in the interaction picture) such that there is a single quantum jump operator $L = \sqrt{\gamma}X_1P_{odd}$ with $P_{odd} = \frac{1}{2}(I - Z_1Z_2Z_3Z_4)$, the

projector onto the odd parity space, and $H \propto Z_1Z_2Z_3Z_4$. Integration of the Lindblad equation gives rise to the time-dynamics $\rho(t) = \exp(t\mathcal{L}_{tot})(\rho(t=0))$ with stationary states ρ determined by $\mathcal{L}_{tot}(\rho) = 0$. States supported on the even-parity subspace are dark states with $\mathcal{L}(\rho) = 0$ and $[H, \rho] = 0$. The odd-parity subspace is not stationary as the quantum jump operator L flips the first qubit so that an odd parity state becomes an even parity state pumping the system towards the stationary dark subspace.

In [19] one considers the following stroboscopic evolution using an ancillary dissipative qubit or mode which approximately gives rise to such Lindblad equation. The idea is to alternate (or *trotterize*) the coherent evolution with H and the dissipative evolution with $\mathcal{L}$ for short periods of time τ so that $\exp(\tau\mathcal{L}_{tot}) \approx \exp(-i\tau[H, .]) \exp(\tau\mathcal{L})$. The dynamics of H can be obtained by a small modification of the parity check measurement circuits in Fig. 1: for the evolution $\exp(-i\theta P)$ where P is a multi-qubit Pauli operator we can use the circuit in Fig. 1(b).

The dissipative evolution $\mathcal{L}$ could be implemented for short times $\tau \ll 1$ using a circuit consisting of a dissipative ancilla coupled to the four qubits as in Fig. 1(d). Instead of immediately measuring the ancilla qubit, we apply a CNOT with the ancilla qubit as control and qubit 1 as target (to change the parity of the odd states to even), followed by decay (σ_-) of the ancilla qubit from $|1\rangle$ to $|0\rangle$. These ideas of stabilizer pumping were experimentally tested on two and four ion-trap qubits in Ref. [3].

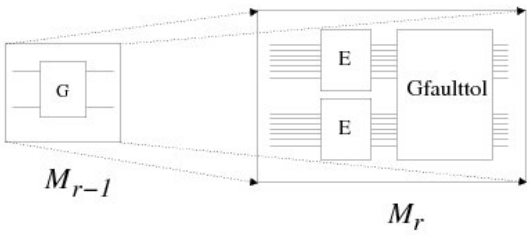

Fig. 3: *Concatenation: a gate G in the circuit M_{r-1} is replaced by a rectangle consisting of error-correcting steps (E) followed by a fault-tolerant encoded realization of the gate. The process can be repeated for every elementary gate in the new circuit M_r.*

As any realization, closed or open-loop, of quantum error correction will suffer from inaccuracies there is no guarantee that one will improve coherence times by encoding a qubit in a code as it may introduce more errors that it takes away. This has been the reason for the construction of a theory of quantum fault tolerance which addresses this problem using recursively applied code concatenation. For simplicity we assume that every such elementary gate, idling step or measurement, —these are called *locations*—, can fail independently with some error probability p (independent stochastic noise). In a concatenation scheme every qubit and operation in a quantum circuit is replaced by an encoded qubit resp. encoded operation and the process is recursively repeated. The encoded operation consists of an error correction step and a fault-tolerant realization of the operation, see Fig. 3, which together constitute a *rectangle*. For a code such as Steane's $[[7, 1, 3]]$ code which can correct a single error, the fault-tolerance of the rectangle should be such that a single error in any of the locations of the rectangle cannot lead to two (incorrectable) errors in one code block. Then, if the elementary error rate scales as p, it follows that the encoded error rate scales as Cp^2 as two elementary errors are required for a logical error. Here C is a constant which roughly counts the number of pairs of locations in the rectangle where failure can lead to a logical error. If $Cp^2 < p$ the concatenation step helps and r steps of concatenation will drive down the error rate to $\sim p^{2^r}$ while the overhead in terms of

qubits and gates increase only exponentially in r. The equality $Cp^2 = p$ sets the *noise threshold* p_c.
This idea of repeated code concatenation was used in the early days of quantum error correction to prove the *Threshold Theorem* which says that fault-tolerant computation is possible with arbitrary small error rate if one is willing to tolerate an overhead which scales polylogarithmically with the *size* N of the computation to be performed. The size of a quantum circuit is the number of elementary gates, measurements and idle steps in it, that is, all places which can fail.

Theorem 1 ([5, 20, 21, 22]) *An ideal circuit of size N can be simulated with arbitrary small error δ by a noisy quantum circuit subjected to independent stochastic noise of strength less than $p < p_c$ where the noisy quantum circuit is of size $O(N(\log N)^c)$ with some constant c.*

The important question is of course what is the noise threshold p_c and how large is the constant c? The best performing concatenated coding scheme to date is the C_4/C_6 scheme of Knill [8] for which he estimated a noise threshold as high as $p_c \approx 3\%$ but at the cost of huge overheads. In general, the overhead that one incurs by code concatenation tends to be worse than the overhead (or mere complexity) that is incurred using the idea of topological error correction (Section 2). One reason is that in topological quantum error correction parity check measurements are simply made robust by repeating the measurement needing no additional qubits. The constant c in the Theorem equals $c = \log_2 S$ where S is the number of locations in a rectangle. For example, in a 2D realization of the concatenated Steane $[[7, 1, 3]]$ code, the fault-tolerant CNOT has $S = O(10^3)$ [23] so that $c \approx 10$ demonstrating the potential inefficiency of code concatenation.

1.4 Universality

An important feature of error correction with stabilizer (subsystem) codes is the fact that one never physically has to do the correcting Pauli operation *as long as the qubits only undergo Clifford group operations*. The decoding procedure gives a Pauli error which is interpreted as a frame, the so-called Pauli frame [8] which we can efficiently track during the computation using the Knill-Gottesman theorem. The Clifford group $\mathcal{C}_n$ is a finite subgroup of the group of unitary transformations $\mathcal{U}(2^n)$ on n qubits. It is defined as the normalizer of the Pauli group: $\mathcal{C}_n = \{U \in \mathcal{U}(2^n) | \forall P \in \mathcal{P}_n, \exists P',\ UPU^\dagger = P'\}$. The generators of the Clifford group are the 2-qubit CNOT gate, the Hadamard H gate, the phase gate S [8] and the Pauli's X, Z. The Knill-Gottesman theorem [24] proves that one can efficiently classically simulate any quantum circuit with Clifford group gates. One does this by tracking the stabilizer group, more precisely its generators, which has the input state of the quantum circuit as its unique $+1$ state. Every Clifford gate and measurement maps the stabilizer generators onto new stabilizer generators providing an efficient representation of the action of the quantum circuit. The presence of additional Pauli errors can thus be represented as additional updates of the stabilizer generators.

For universal quantum computation one needs additional gates such as the T gate ($\pi/8$ rotation). Examples of universal gate sets are $\{H, T, \text{CNOT}\}$, $\{H, \text{Toffoli}\}$ and $\{H, \Lambda(S)\}$ where $\Lambda(S)$ is the two-qubit controlled-S gate [9]. Even though Clifford group gates have no quantum

[8] $H = \frac{1}{\sqrt{2}} \begin{pmatrix} 1 & 1 \\ 1 & -1 \end{pmatrix}, S = \begin{pmatrix} 1 & 0 \\ 0 & i \end{pmatrix}, T = \begin{pmatrix} 1 & 0 \\ 0 & e^{i\pi/4} \end{pmatrix}$.
[9] $\Lambda(S) |b_1, b_2\rangle = |b_1\rangle S^{b_1} |b_2\rangle$ for $b_1, b_2 = 0, 1$.

computational power they can be used to develop a *quantum substrate* on which to build universal computation using stabilizer codes. This comes about by combining the following sets of ideas. First of all, note that stabilizer error correction by itself only uses CNOT gates, preparations of $|+\rangle, |-\rangle, |0\rangle, |1\rangle$ and measurements in the Z- and X-basis as is clear from Fig. 1. The T, $\Lambda(S)$ and the Toffoli gate, each of which can be used with Clifford gates to get universality, are special unitary gates as they map Pauli errors onto elements of the Clifford group. One can define a Clifford hierarchy [25] $\mathcal{C}(j) = \{U \in \mathcal{U}(2^n) | U\mathcal{P}_n U^\dagger \subseteq C(j-1)\}$ such that $\mathcal{C}(1) = \mathcal{P}_n$, $\mathcal{C}(2) = \mathcal{C}_n$. The $T, \Lambda(S)$ and Toffoli are thus members of $\mathcal{C}(3)$. Such gates in $\mathcal{C}(3)$ (and similarly gates in $C(j)$ for $j > 3$) can be realized with ancillas and Clifford group gates using quantum teleportation ideas [25, 26]. The idea is illustrated in Fig. 5 for the T gate. One teleports the qubit on which the T gate has to act, prior to applying the gate, using the bottom one-bit teleportation circuit in Fig. 4. Inserting $TT^\dagger$ prior to the corrective Pauli X and using that $TXT^\dagger = e^{-i\pi/4}SX$ which is an element of the Clifford group, we obtain the circuit in Fig. 5.

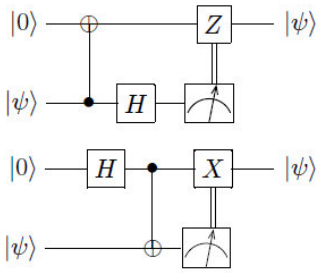

Fig. 4: *Picture from [26]: so-called one-bit teleportation circuits. The measurement denoted by the meter is a measurement in the Z-basis and determines whether to do a Pauli on the output qubit.*

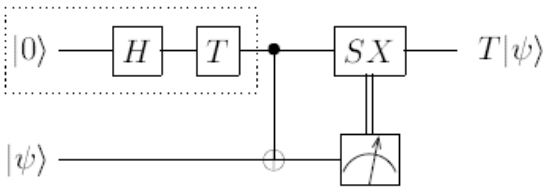

Fig. 5: *Picture from [26]: using the ancilla $T|+\rangle$ in the dashed box, one can realize the T gate by doing a corrective operation SX.*

Exercise: Show how to do the same trick for the S gate, i.e. reducing the S gate to the preparation of a $|+i\rangle = \frac{1}{\sqrt{2}}(|0\rangle + i|1\rangle)$ ancilla, a CNOT gate and a corrective Pauli Y.

How do we realize a universal set of logical fault-tolerant gates for a code? In principle, fault-tolerant gate constructions can be made for any stabilizer code [7]. The question is how to do computation with resource requirements and overheads similar as those needed for a quantum memory. Ideally, the computation threshold, i.e. the performance of the code when used for computation is close to the memory noise threshold, the performance of the code as a pure quantum memory. An example of a gate which does not require new resources is a *transversal* CNOT between two code blocks in which every qubit in the block is paired with a qubit in

the other block in a CNOT gate. Such transversal CNOT represents a valid logical CNOT for stabilizer codes $\mathcal{S} = \langle \mathcal{S}(X), \mathcal{S}(Z) \rangle$, i.e. the parity X-checks are the same as parity Z-checks. Examples are Steane's $[[7, 1, 3]]$ code or any other CSS code constructed from a classical code C with $C^{\perp} \subseteq C$.

In [27] it was shown for any 2D stabilizer code that the logical gates which can be performed by constant-depth circuits employing only local gates, are members of the Clifford group. The reason to focus on constant-depth local circuits is that such circuits are small and are naturally fault-tolerant. Namely, any number of errors which occurs in the circuit will only affect a patch of $O(1)$ qubits on the 2D lattice, and such $O(1)$ error patches are correctable. Hence we expect that their implementation does not negatively impact the noise threshold or the overhead.

As we will discuss in Section 2 one can implement the logical H and CNOT by topological means in the 2D surface code, but one cannot do the logical S gate in this manner. For the surface code one can do the logical S in the same fashion as the logical T, see below (for a different logical S trick, see [28]). Other stabilizer codes, 2D color codes, have been found which allow for a topological realization of the full Clifford group [29]. Interestingly, Ref. [27] shows that for D-dimensional stabilizer codes [10] all logical encoded gates which are *composed* from constant-depth logical gates are contained in the Clifford hierarchy $\mathcal{C}(D)$. This is a subtle result as we can realize a fault-tolerant set of universal gates for any stabilizer code, but apparently we cannot do this by composing a sequence of constant-depth encoded gates.

For gates such as the T gate the method of magic-state-distillation has been developed [30] showing how to realize these gates fault-tolerantly assuming the availability of noiseless Clifford group operations. Thus, once we have built a low-noise Clifford computation substrate universal quantum computation can be bootstrapped from it. The strength of the distillation scheme is that the noise threshold for it to work is high, approximately 15%. The downside is that the qubit/gate overhead per logical T gate is orders of magnitude larger that of a'topological' CNOT (see e.g. Fig. 11 in [31]). In a nutshell, the ideas are as follows. We implement the T gate at the logical level using Fig. 5 which requires the preparation of low-noise logical ancillas $\overline{T}\,|\overline{+}\rangle$. We can obtain such an ancilla in non-fault-tolerant noisy manner by, for example, *injecting* several noisy unencoded ancillas into the code [8]. From many of these noisy encoded ancillas we distill using logical H, CNOTs and measurements, a single low-error encoded ancilla.

Note that prior to the action of logical non-Clifford gates one *does* need to physically implement the inferred *logical* Pauli errors obtained from decoding as gates such as the T gate do not map Pauli errors onto Pauli errors but onto Clifford errors. What one never needs to physically do is a correction which maps one back to the $+1$ eigenspace of the stabilizer $\mathcal{S}$: any syndrome eigenspace of $\mathcal{S}$ is a good code.

The upshot of these considerations is that 2D and 3D stabilizer codes will be most suitable for building a quantum memory and performing Clifford group operations. The goal of universal quantum computation within the same platform can be reached using methods such as injection-and-distillation but the additional overhead and complexity of distillation (and demands for fast decoding) are considerable. Several recent papers have been devoted to reducing this overhead, see e.g. [32] and references therein.

[10] A D-dimensional stabilizer code is a stabilizer code for which the parity checks are local on some D-dimensional lattice.

2 2D (Topological) Error Correction

In this section we discuss three stabilizer/subsystem codes in which the parity checks act locally on qubits laid out on a 2D lattice. Two of these codes are topological codes: if the code was defined on a 2D lattice with periodic boundary conditions,—a torus—, then the logical operators would relate to the non-trivial loops around the torus.

Most experimental qubit quality is assessed by the twin parameters T_2 and T_1 which capture the decay of off-diagonal matrix elements resp. the relaxation to steady state of the diagonal matrix elements in the qubit density matrix. A simple estimate for an error rate can be made by taking τ/T_1 to be the probability for an X error where τ is a time-scale which captures the time needed for error-correction through single and two-qubit gates. Similarly τ/T_2 can provide an estimate for the Z error rate. In numerical or analytical studies of code performance, one uses simple error models such the independent *depolarizing noise model*. Independent depolarizing noise assumes that every qubit *independently* undergoes a X, Y or Z error with equal probabilities $p/3$ and no error with probability $1-p$. A related noise model is that of independent X and Z errors in which a qubit can undergo independently an X error with probability p and a Z error with probability p in each time-step. In all three codes the parity checks are either X or Z-like, detecting either Z or X errors. In addition, the parity Z- and X-checks have the same form so error correction proceeds identically (but simultaneously) for both types of errors.

We will consider codes which encode a single qubit in a block of n qubits with $n = O(L^2)$ with L the linear size of the 2D array. Important parameters of the code performance are the pseudo-threshold $p_c(L)$ which is the error probability at which the elementary error rate p equals the logical error rate for a given size L, the asymptotic threshold $p_c = \lim_{n\to\infty} p_c(L)$ and the logical error rate $\overline{p}(p, L)$ which is a function of the block size and the elementary error rate p. For the Bacon-Shor code in Section 2.2, the asymptotic threshold $p_c = 0$, hence it is of interest to consider what is the optimal block size for this code. Another interesting class of 2D topological stabilizer codes are the color codes [29]. The color codes offer little practical advantage over the surface code if the goal is to build a quantum memory as some of the parity checks involve more than 4 qubits and the noise thresholds are similar as for the surface code, see e. g. [33].

2.1 Surface Code

The surface code is a version of Kitaev's toric code [1] in which the closed periodic boundaries of the torus have been replaced by open boundaries. Many of its properties and ideas for its use as a quantum memory were first analyzed in the seminal paper [34]. The topological 2D realization of the CNOT gate was first proposed in [35, 36].

A simple sheet, depicted in Fig. 6, can encode one logical qubit. The linearly-independent parity checks are weight-4 plaquette Z-checks B_p and star X-checks A_s which mutually commute and are modified at the boundary to act on 3 qubits, see Fig. 6. Note that the star operators are just plaquette operators on the dual lattice when interchanging $X \leftrightarrow Z$. The smallest surface code encoding 1 logical qubit which can correct 1 error is the code $[[13, 1, 3]]$ [11]. $\overline{Z}$ is any Z-string which connects the north and south *rough* boundaries, we can deform this string by multiplication by the trivially-acting plaquette operators. $\overline{X}$ is any X string (on the dual lattice) connecting the *smooth* east and west boundary. As these strings have to connect boundaries in

[11] One can minimize the qubit overhead while keeping the distance equal to 3 by rotating the lattice and chopping off some qubits to get a total of 9 qubits, see e.g. [37].

order to commute with the check operators, their minimum weight is L. Thus for general L the code parameters are $[[L^2 + (L-1)^2, 1, L]]$.
Using 13 qubits to correct 1 error does not seem very efficient, but the strength of the surface code is not fully expressed in its distance which only scales as the square root of the number of qubits in the block [12].

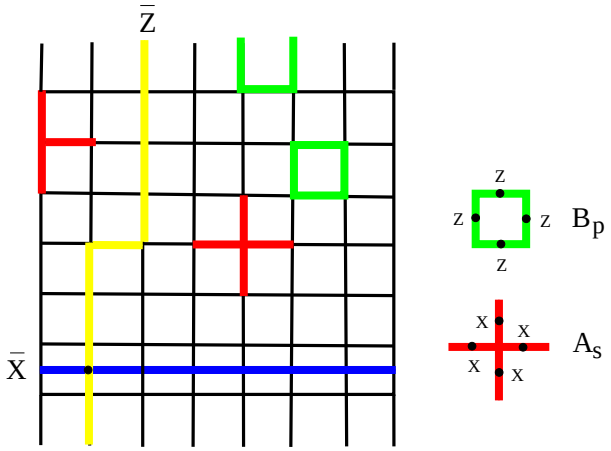

Fig. 6: *Surface Code on a $L \times L$ lattice. On every edge of the black lattice there is a qubit, in total $L^2 + (L-1)^2$ qubits (depicted is $L = 8$). Two types of local parity checks, A_s and B_p, each act on four qubits (except at the boundary). The subspace of states which satisfy the parity checks is two-dimensional and hence represents a qubit. $\overline{Z}$ (yellow) is any Z-string connecting the north to the south boundary while $\overline{X}$ (blue) is any X-string connecting the east to west boundary of the lattice.*

Let us consider how quantum error correction can take place first assuming that the parity check measurements are noise-free. If a single X error occurs on an edge in the bulk of the system, then the two plaquette operators next to it will have eigenvalue -1. The places where these plaquette eigenvalues are -1 are called defects. A string of X errors will thus produce two defects at its boundary. If the X error rate p is sufficiently small, one obtains a low *density* of close-by defects. Such errors are correctable as defects can be locally paired without much ambiguity. As we know, inferring an error E' which differs from the real error E by only stabilizer operators, plaquettes operators in this case, is harmless. Here it means that we decode correctly as long as $E'E$ does not represent $\overline{X}$, an X-string which goes from one boundary to the other. From this picture it is clear that there should be a finite asymptotic threshold p_c for noise-free error correction.
For the bulk system the error syndrome thus gives us the location of the defects. A minimum-weight decoding algorithm then corresponds to finding a minimum-weight error string $E(X)$ which has these defects as end-points. This decoding algorithm can be implemented using Edmond's minimum-weight matching (Blossom) algorithm [40]. Ideal decoding is not minimum weight decoding, but maximum-likelihood decoding as described in Section 1.1.1. One can estimate the threshold p_c assuming optimal maximum likelihood-decoding by mapping the

[12] One can prove that the distance of any 2D stabilizer code is at most $O(L)$ [38]. However, one can also show [39] that any block of size $R \times R$ where R is less than some constant times the distance, is correctable, i.e. *all* errors in such $R \times R$ patch can be corrected. These arguments show that there are no other 2D stabilizer codes with better distance scaling and that this scaling allows one to correct failed blocks of size beyond the distance.

problem onto a phase transition in a 2D random-bond Ising model [41]. The value for p_c assuming noise-free parity checks, ideal decoding and independent X errors is $p_c \approx 11\%$ [34].
This picture gets modified when the parity checks are inaccurate. A simple way to model noisy parity checks is to assign a probability q for the parity check outcome to be inaccurate while in between the parity checks qubits undergo X and Z errors with probability p as before. In practice, one would expect the parity check measurements to induce some correlated errors between the qubits of which we take the parity. For example, for the parity Z-check one may expect to cause additional qubit dephasing when more information than merely the parity is read out.
As the parity check measurements are no longer reliable one needs to change their use as an error record. For example, a single isolated defect which appears for a few time-steps and then disappears for a long time is more likely due to a faulty parity measurement outcome than due to a string of X errors (which terminates at the isolated defect) that suddenly pops up and disappears without trace after a few time-steps. The strength of topological codes for sufficiently large L (as compared to using small codes and code concatenation) is that noisy parity checks can be dealt with by repeating their measurement as the additional noise which the parity checks produce on the code qubits is local and, at sufficiently low rate, correctable.
Both minimum weight decoding and maximum likelihood decoding can be generalized to this setting. We extend the lattice into the third (time) dimension [34], see Fig. 7. Vertical links, corresponding to parity check measurements, fail with probability q while horizontal links fail with probability p. In minimum weight decoding the goal is now to find a minimum weight error E which has vertical defect links, where the parity check is -1, as boundary, see Fig. 7.
If the parity check measurements are ongoing one needs to decide how long a record to keep before starting to infer the possible errors which depends on the failure probability q. In the simple case when $q = p$ the record length is taken as L [41]. An analytical lower bound on the noise threshold for $q < p$ is derived in [34] with the value $p_c \geq 1.1\%$. Numerical studies in [41] (using minimum weight-decoding) show a threshold of $p_c \approx 2.9\%$ for $p = q$. Below the noise threshold the logical error rate $\overline{p}(p, L) \sim \exp(-\kappa(p)L)$ where $\kappa(p) \approx 0.8 - 0.9$ at $p = p_c/3$ [41, 31]. All these results have been obtained for toric codes, assuming periodic boundary conditions: one may expect results to be somewhat worse for surface codes [42].
The practical relevant question is how much overhead L is needed before one is in the scaling regime where the pseudo-threshold is close to the asymptotic threshold $p_c(L) \approx p_c$? The pseudo-threshold for a small code such as $[[13, 1, 3]]$ is very tiny, *certainly* no higher than 0.1% [13]. Even though small codes have worse performance than large codes they could still be used as testbeds for individual components and error scaling behavior [44].
Minimum-weight decoding with Edmonds' matching algorithm is a good method for decoding if our goal is to realize a quantum memory (with or without encoded Clifford group operations). As one never needs to physically do any correction (see the notion of Pauli frame discussed in Section 1.4), the measurement record can be stored. This data record can then be processed at leisure and used to interpret a final $M_{\overline{X}}$ or $M_{\overline{Z}}$ measurement on the qubits. The realization of such quantum memory will require that the record of parity check measurements is obtained at sufficiently high rate compared the error rate, since a low rate stroboscopic picture of the defects (even if they are obtained perfectly) could potentially miss the occurrence of a logical error.
If our goal is to implement universal quantum computation, then the decoding algorithm will have to keep up with the logical error rate of the quantum computer as every time a non-Clifford

[13] Fig. 11 in [43] estimates a pseudo-threshold of 6.8×10^{-5} for the $[[41, 1, 5]]$ surface code for an encoded transversal CNOT gate. This may be worse by a factor 2 from the pseudo-threshold for a single encoded qubit.

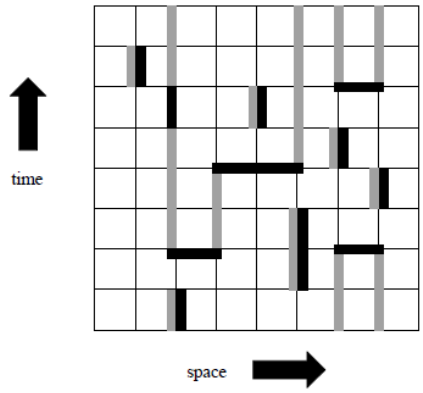

Fig. 7: *Picture from [34]: 1D cross-section of the lattice in space, and time. Grey links correspond to non-trivial -1 syndromes. Errors which could have caused such a syndrome are represented by black links. Horizontal black links are qubit errors while vertical black links are parity check measurement errors. Note that a possible error E has the same boundary as the grey defect links: a likely error E (in the bulk) can be found by looking for a minimum-weighted matching of the end-points of the grey links.*

gate is realized in the quantum circuit, one needs to know whether to do an additional logical Pauli. Researchers have developed faster renormalization-group decoders [45, 46] which process the defects using parallel processing over the 2D or 3D lattice in time $O(\log L)$. The idea of the simple decoder in [46] which works for any D-dimensional stabilizer codes is to recursively match defects locally. For a 2D surface code with perfect parity check measurements one starts by dividing up the defect record into local clusters of O(1) size. In each cluster the algorithm tries to find a local error which removes the defect. If a cluster contains a single defect for example, then no such local error can be found. Thus the next step is to enlarge the linear size of the cluster by a factor of 2 and reapply the same procedure on the leftover defect record. The decoder stops when no more defects are present or when one has a reached a certain maximum number of iterations r scaling as $r = O(\log L)$. For the toric code with perfect parity checks, Ref. [46] has obtained a noise threshold of $p_c = 6.7\%$ using this RG decoder while the RG decoder in [45] achieves 9% (minimum-weight decoding via matching gives 10.3%).

One can ask whether quantum error correction for the surface or other topological codes in $D = 2$ or higher is possible by purely local means. Is there a non-zero noise threshold p_c when error correction has to be performed by a 2D noisy automaton which locally interacts with the surface code qubits [34]. The dissipative correction procedure described in Section 1.3 is an example of a purely local error correction mechanism. Such local dissipative mechanisms will not be able to efficiently remove error strings in the surface code beyond the shortest length as an error string is only heralded by its two end-point defects. The local observation of one defect gives no information where the position of another matching defect is, except if one searches the entire neighborhood around the defect. One should contrast this with the 4D toric code [34] where an error cluster is surrounded by defect surfaces such that the cluster can be removed by locally shrinking the defect surface. This weakness of the surface code is a generic property of 2D stabilizer codes and ties in with the discussion of self-correcting quantum memories which are unlikely to exist in 2D.

The classical non-local minimum-weight matching decoder can be viewed as a way of jump-starting our quantum memory with the power of reliably non-local classical computation. Note that the RG decoder is non-local (even allowing for parallel processing of clusters on the lattice by local automata) as the maximum number of recursions r scales as $O(\log L)$ leading to a maximum cluster size proportional to the linear size of the lattice. The lowest levels of the RG decoder are of course local and will provide some measure of protection by local means. In [47] the author devises an intricate scheme for doing purely local quantum error correction for the surface code by a 2D noisy cellular automaton assuming independent local errors; the mere existence of such a scheme is nontrivial.
The idea of realizing the surface code in superconducting systems using ancilla qubits for measurement was considered in [48]. The pseudo-threshold for the surface code for small block sizes, say $[[13, 1, 3]]$, is considerably worse than 1% which implies that small realizations of this code may not allow one to see the benefits of quantum error correction. Ref. [44] consider experimental benchmarks for parity check measurements in a circuit QED setting. In order to reduce qubit overhead and possibly make better and more direct use of the cavity mode-transmon interaction, Ref. [49] considers a direct 3-qubit parity check measurement. In this scheme 3 transmon qubits are dispersively coupled to two transmission-line resonators such that the phase-shift picked up by an incoming microwave-pulse is ideally (a) the same for qubit states with the same parity but differs by π for qubit states with different parities. A simpler scheme for a two-qubit parity measurement in the cavity QED setting was proposed in Ref. [50]. In [51] the dispersive coupling of a set of transmon qubits to the cavity mode was proposed for the measurement of a multi-qubit parity check.

2.1.1 Multiple Qubits and Operations by Lattice Surgery

How do we prepare the surface code memory in the states $\left|\overline{0}\right\rangle, \left|\overline{1}\right\rangle$ or $|\overline{\pm}\rangle$? And how do we read out information, that is, realize $M_{\overline{X}}$ and $M_{\overline{Z}}$? We prepare all elementary qubits in Fig. 6 in the state $|0\rangle$ and start measuring the parity checks with the goal of preparing the state $\left|\overline{0}\right\rangle$. The state $|00\ldots0\rangle$ has $B_p = +1$ and $\overline{Z} = +1$ while the star operators A_s have random eigenvalues ±1 corresponding to the presence of many Z errors. Thus we choose some correction E for these Z errors (we pick a Pauli frame): the choice will not matter as E commutes with $\overline{Z}$. If the preparation of $|0\rangle$ and the parity check measurements are noisy, one need to measure the parity checks for a while before deciding on a Pauli frame for both X and Z errors. The preparation of $\left|\overline{1}\right\rangle$ and $|\overline{\pm}\rangle$ can be performed analogously using the ability to prepare the elementary qubits in $|1\rangle$ and $|\pm\rangle$ respectively. A projective measurement in, say, the $\left|\overline{0}\right\rangle, \left|\overline{1}\right\rangle$-basis ($M_{\overline{Z}}$) proceeds essentially in reverse order. One measures all qubits in the Z-basis. Using the past record of parity Z-check measurements and this last measurement, one infers what X errors have taken place and corrects the outcome of $\overline{Z} = \pm1$ accordingly.
There are various ways in which we can encode multiple qubits in the surface code and do a logical Hadamard and CNOT gate. The simplest and most efficient method in terms of qubit overhead is to encode multiple qubits in multiple separate sheets (as in Fig. 6) laid out next to each other in a 2D array as in Fig. 10. Using operations on a single sheet one can do a logical Hadamard gate [34]. A CNOT between qubits in separate sheets can be realized using the idea of lattice surgery in which sheets are merged and split as proposed in [37]. One can also encode a qubit in an arbitrary state into the code, see [34, 37].
We first consider the Hadamard gate for which $\overline{HX}\overline{H^\dagger} = \overline{Z}$ and $\overline{HZ}\overline{H^\dagger} = \overline{X}$. Consider doing a Hadamard rotation on every elementary qubit on a sheet. The resulting state is a $+1$ eigenstate

of the Hadamard-transformed parity checks $HA_sH^\dagger$ and $HB_pH^\dagger$ which are the plaquette Z-check resp. the star X-check of the code $\mathcal{S}_{dual}$ defined on the dual lattice. The Hadamard gates map $\overline{Z}$ onto $\overline{X}_{dual}$ and $\overline{X}$ onto $\overline{Z}_{dual}$. In the dual code $\mathcal{S}_{dual}$ the rough and smooth boundaries are interchanged so that the lattice is effectively rotated by 90°. In order to complete the Hadamard gate and return back to the original code one can modify the parity checks at boundaries such that rough becomes smooth and smooth becomes rough again, see the details in [34, 37].

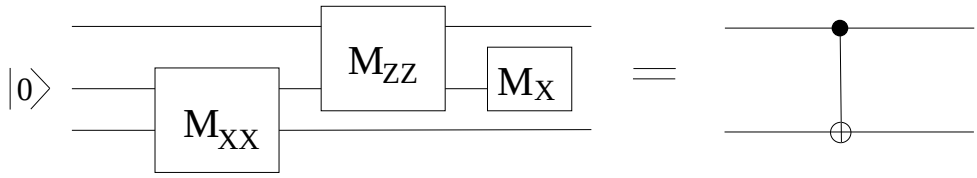

Fig. 8: *CNOT via 2-qubit quantum measurements. Here M_{XX} measures the operator $X \otimes X$ etc. The ancilla qubit in the middle is discarded after the last measurement M_X disentangles it from the other two input qubits. Each measurement has equal probability for outcome ± 1 and Pauli corrections (not shown) depending on these measurement outcomes are done on the two output qubits.*

The construction for the CNOT is based on the circuit in Fig. 8 which implements the CNOT gate through 2-qubit parity measurements, originally described in Ref. [52].

Exercise: Verify the identity in Fig. 8 by considering the input states as a stabilizer subspace with stabilizer Z_2 and logical operators $\overline{X}_1, \overline{Z_1}, \overline{X}_3, \overline{Z}_3$. Follow how the stabilizer and these logical operators transform through the measurements using the Knill-Gottesman simulation technique, see Section 7 in [24], so that a CNOT is realized. What are the Pauli corrections on the output qubits?

This circuit identity implies that we can realize a logical CNOT gate if we have the capability of projectively measuring the operators $\overline{X} \otimes \overline{X}$ and $\overline{Z} \otimes \overline{Z}$ of two qubits encoded in different sheets. The capability to prepare a sheet in $|\overline{0}\rangle$ and the measurement $M_{\overline{X}}$ was discussed before. The realization of such joint measurement, say, $\overline{X} \otimes \overline{X}$ is possible by temporarily merging the two sheets, realizing the measurement and then splitting the sheets as follows. Consider two sheets laid out as in Fig. 9 where a row of ancillary qubits is prepared in $|0\rangle$ between the sheets. We realize a *rough* merge between the sheets by including the parity checks, plaquette and star operators, at this boundary. If the parity check measurements are perfect, the new weight-4 plaquette Z-checks have $+1$ eigenvalue as the ancilla qubits are prepared in $|0\rangle$. The 4 new star boundary checks have random ± 1 eigenvalues subject to the constraint that the product of these boundary checks equals the product of $\overline{X}$s of the two sheets. Hence a perfect measurement would let us do a $\overline{X} \otimes \overline{X}$ measurement. As the parity check measurements are imperfect, one needs to repeat the procedure in the usual way to reliably infer the sign of $\overline{X} \otimes \overline{X}$. We are however not yet done as we wish to realize a projective $\overline{X} \otimes \overline{X}$ measurement on the qubits encoded in two *separate* sheets. This means that we should split the two sheets again: we can do this by reversing the merge operation and measure the ancillary qubits in the Z-basis and stop measuring the 4 boundary X-checks. Again, if the parity check measurements are perfect the plaquette Z-checks at the boundary of both sheets will be randomized, but both correlated with the outcome of the Z-measurement of the ancillary qubits. Hence the individual $\overline{X}$ eigenvalues of the separate sheets may be randomized, but they are correlated so that $\overline{X} \otimes \overline{X}$ remains fixed.

Similarly, a smooth merging and splitting (as between qubits C and INT in Fig. 10) with the ancillary qubits prepared and measured in the X-basis accomplishes a $\overline{Z} \otimes \overline{Z}$ measurement. The procedure for a CNOT in Fig. 10 then consists of: first a preparation of the INT qubit in $|\overline{0}\rangle$, then a rough merge and split of qubits T and INT followed by a smooth merge and split between qubits INT and C followed by a final $M_{\overline{X}}$ measurement of qubit INT. The information of all three measurement outcomes is used as a Pauli frame to be recorded.

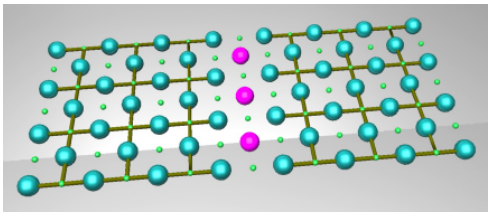

Fig. 9: *Picture from [37]: two sheets are merged at their rough boundary by placing a row of ancilla qubits in the $|0\rangle$ state at their boundary and measuring the parity checks of the entire sheet. For a similar smooth merge, the ancillary qubits in between the two sheets are prepared in the $|+\rangle$ state, see the INT and C sheets in Fig. 10.*

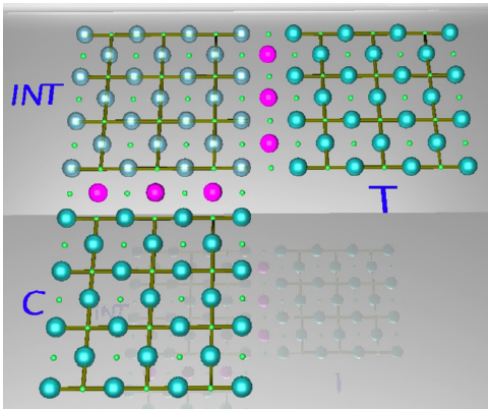

Fig. 10: *Picture from [37]: using an ancilla (INT) qubit sheet we can do a CNOT between the control (C) and target sheet (T) by a sequence of mergings and splittings between the sheets.*

2.1.2 Topological Qubits and CNOT via Braiding

A different way of encoding multiple qubits and realizing a CNOT gate was first proposed in [31, 35]. This disadvantage of this method is that it has an additional qubit overhead. A distance-3 smooth hole qubit (see the description below) costs many more than 13 physical qubits but such overhead or redundancy could also lead to greater robustness.
In order to see how to encode multiple qubits we start with a simple square sheet with all smooth boundaries which encodes no qubits, Fig. 11(a). For a sheet with all smooth boundaries, the star operators are linearly-dependent while the plaquette operators are linearly independent so that no qubit is encoded. To encode qubits one makes a *hole* in the lattice, that is, one removes some checks from the stabilizer $\mathcal{S}$. This is a change in topology which affects the code space dimension. In stabilizer terms: when we remove one plaquette, say, B_{p_*} for some p_* from the stabilizer $\mathcal{S}$, then B_{p_*} is no longer an element in $\mathcal{S}$ but still commutes with $\mathcal{S}$, therefore B_{p_*}

is a logical operator. The matching logical operator which anti-commutes with it starts at the hole and goes to the boundary. This encoded qubit has poor distance namely $d = 4$ as B_{p*} is of weight 4. We can modify this procedure in two ways such that logical qubits have a large distance and its logical operators do not relate to the boundary. The particular choice of logical qubits will allow one to do a CNOT by moving holes.

To get a logical qubit with large distance we simply make a bigger hole. We remove all, say, k^2 plaquette operators in a block (and all $(k-1)^2$ star operators acting in the interior of this block) and modify the star operators at the boundary to be weight-3, no longer acting on the qubits in the interior, see Fig.11(a). The qubits in the interior of the block are now decoupled from the code qubits. The procedure creates one qubit with $\overline{Z}$ equal to any Z-loop around the hole. The $\overline{X}$ operator is a X-string which starts at the boundary and ends at the hole. Clearly, the distance is the minimum of the perimeter of the hole and the distance to the boundary. We call this a *smooth* hole as the hole boundary is smooth. Of course, we could do an identical procedure to the star operators, removing a cluster of stars and smaller subset of plaquette operators and adapting the plaquette operators at the boundary. Such qubit will be called a *rough* hole and its $\overline{X}$ operator is a X-string around the hole (a string on the dual lattice) and $\overline{Z}$ is a Z-string to the boundary.

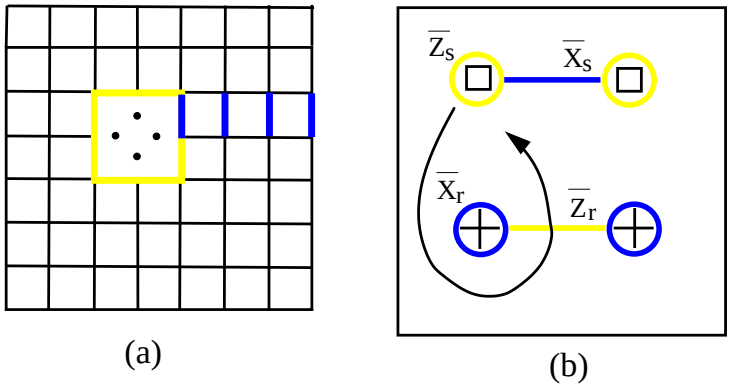

Fig. 11: *(a) A smooth hole is created by removing a block of plaquette operators and the star operators acting on qubits in the interior of the block. The Z-loop around the hole is $\overline{Z}$ while $\overline{X}$ is an X-string to the boundary. The qubits inside the hole (4 in the picture) are decoupled from the lattice. (b) Two smooth holes can make one smooth qubit and two rough holes can make one rough qubit so that moving a smooth hole around a rough hole realizes a CNOT gate.*

In order to be independent of the boundary we use two smooth holes to define one *smooth or primal qubit* and use two rough holes to define one *rough or dual qubit* as follows. Consider two smooth holes $1, 2$ and define a new smooth qubit as $|\overline{0}\rangle_s = |\overline{0},\overline{0}\rangle_{1,2}$ and $|\overline{1}\rangle_s = |\overline{1},\overline{1}\rangle_{1,2}$. For this smooth qubit s we have $\overline{Z}_s = \overline{Z}_i, i = 1, 2$ (we can deform $\overline{Z}_1$ into $\overline{Z}_2$ by plaquette operators) and $\overline{X}_s = \overline{X}_1\overline{X}_2$ which we can deform to an X-string which connects the two holes, see Fig. (11)(b). The distance of this smooth qubit is the minimum of the distance between the holes and the perimeter of one of the holes (assuming the boundary is sufficiently far). Similarly, we can create a *rough* qubit by taking two rough holes and defining

$$|\overline{0}\rangle_r = \frac{1}{\sqrt{2}}\left(|\overline{0},\overline{0}\rangle_{3,4} + |\overline{1},\overline{1}\rangle_{3,4}\right), \; |\overline{1}\rangle_r = \frac{1}{\sqrt{2}}\left(|\overline{0},\overline{1}\rangle_{3,4} + |\overline{1},\overline{0}\rangle_{3,4}\right).$$

With this choice $\overline{X}_r$ is the loop $\overline{X}_3$ (or equivalently $\overline{X}_4$) while $\overline{Z}_r = \overline{Z}_1\overline{Z}_2$ is equivalent to the Z-string connecting the holes.

Imagine moving smooth hole 1 around rough hole 3 as in Fig. 11. After the move, the X-string connecting the smooth holes will additionally go around the rough hole enacting the transformation $\overline{X}_s \to \overline{X}_r \otimes \overline{X}_s$. Similarly, the Z-string $\overline{Z}_r$ connecting the rough holes will wind around the smooth hole, leading to the transformation $\overline{Z}_r \to \overline{Z}_s \otimes \overline{Z}_r$. The loops $\overline{Z}_s$ and $\overline{X}_r$ are not changed by the move. This action precisely corresponds to the action of a CNOT with smooth qubit as control and rough qubit as target.

Exercise: Verify that a CNOT with smooth qubit as control and rough qubit as target transforms $X_s \otimes I_r \to X_s \otimes X_r$, $I_s \otimes X_r \to I_s \otimes X_r$, $Z_s \otimes I_r \to Z_s \otimes I_r$ and $I_s \otimes Z_r \to Z_s \otimes Z_r$.

The ability to do a CNOT with smooth qubit as control and rough qubit as target seems limited as all such gates commute. However one can use the one-bit teleportation circuits in Fig. 4 to convert a smooth qubit into a rough qubit and a rough qubit into a smooth qubit, using *only* CNOTs with smooth qubits as controls. We have already shown how to realize the other components in the one-bit teleportation circuit such as $M_{\overline{X}}$ and $M_{\overline{Z}}$. Thus by composing these circuits we can do a CNOT between smooth qubits alone (or rough qubits alone).
How is the braiding done in practice? The advantage of realizing topological gates in stabilizer codes (as opposed to braiding of Majorana fermions or non-Abelian anyons in quantum Hall systems) is that braiding can be realized by changing where we measure the parity checks, or *deforming the code*. For example, one can enlarge the hole in Fig. 11 to include, say, 2 more plaquettes and 3 more qubits in the interior. We stop measuring those two plaquette checks and the star checks in the interior, modify the star boundary measurements and measure the qubits in the interior in the X-basis. The modified weight-3 boundary checks will have random ± 1 eigenvalues as their previous eigenstates were perfectly entangled with the qubits in the interior. This corresponds to a high Z-error rate around the modified boundary. By repeating the measurement and solidifying the results one can correct these Z-errors, but of course we may partially complete a $\overline{Z}$-loop this way. The protection against a full $\overline{Z}$-loop around the hole is thus provided by *the part of the hole boundary which remains fixed*.
This implies that the hole can safely be moved and braided in the following *caterpillar* manner. One first enlarges the hole (while keeping its 'back-end' fixed providing the protection) so that it reaches its new position. In terms of parity check measurements it means that from one time-step to the next one, one switches from measuring the small hole to the large hole parity checks. Due this extension errors will occur along the path over which the hole is moved and if error correction is noisy we should not act immediately to infer the new Pauli frame, but repeat the new check measurements to make this new frame more robust. Then as a last step, we shrink the hole to its new position and corroborate the new measurement record by repetition. Alternatively, one can move the hole by a sequence of small translations, so that the hole never becomes large. The speed at which the hole can then be safely moved is determined by the time it takes to establish a new Pauli frame (eliminate errors) after a small move. Details of hole moving schemes are discussed in e.g. [53].

2.2 Bacon-Shor Code

An interesting family of subsystem codes are the Bacon-Shor codes [54] which are competitive with the surface code for small numbers of qubits. For the $[[n^2, 1, n]]$ Bacon-Shor code the qubits are laid out in a 2D $n \times n$ square array, see Fig. 12. The stabilizer parity checks are the double Z-column operators $\mathbf{Z}_{||,i}$ for columns $i = 1, \ldots n-1$ and double X-row operators $\mathbf{X}_{=,j}$

for rows $j = 1, \ldots n-1$. It is also possible to work with asymmetric Bacon-Shor codes with qubits in a $n \times m$ array. Asymmetric codes can have better performance when, say, Z-errors are more likely than X-errors (when $T_2 \ll T_1$), see [55]. The gauge group $\mathcal{G}$ (see Section 1.1.1) is generated by weight-2 vertical XX links and horizontal ZZ links and contains the parity checks. The logical operators (which commute with $\mathcal{G}$ but are not in $\mathcal{S}$) are the single Z-column $\overline{Z}$ and a single X-row $\overline{X}$.

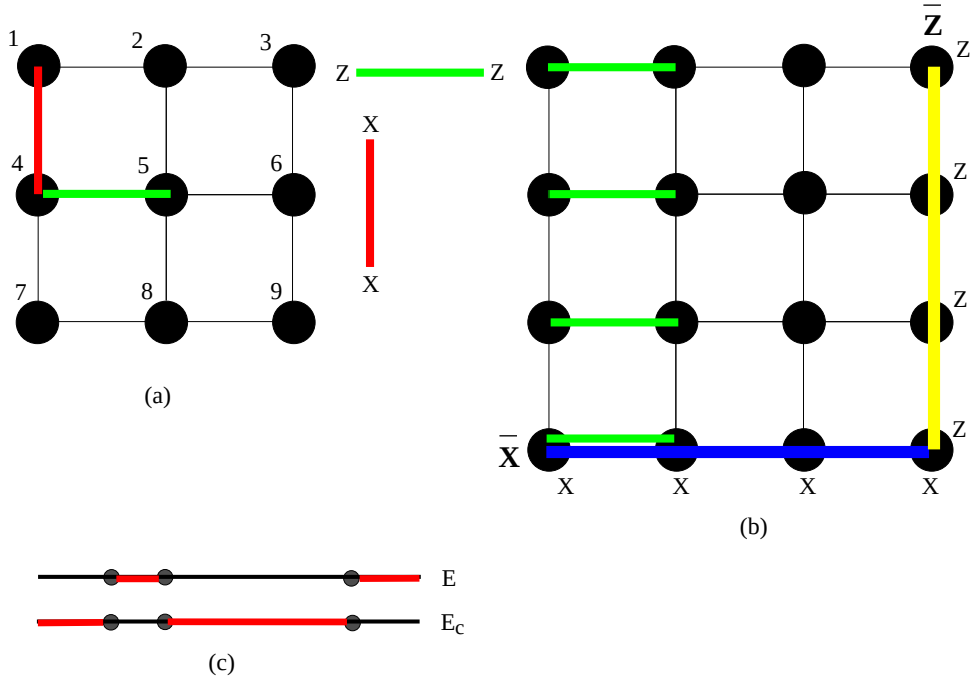

Fig. 12: *(a) 9-qubit $[[9,1,3]]$ (Bacon) Shor code with black qubits on the vertices. Depicted are the 2-qubit XX and ZZ gauge operators. (b) $[[25,1,5]]$ Bacon-Shor code with $\overline{X}$, a row of Xs (blue), and $\overline{Z}$, a column of Zs (yellow). The stabilizer generators are double columns of Zs, $\mathbf{Z}_{||,i}$ (one is depicted) and double rows of Xs, $\mathbf{X}_{=,j}$.(c) Decoding for X errors (or Z errors in the other direction). Black dots denote the places where the double column parity checks $\mathbf{Z}_{||,i}$ have eigenvalue -1 (defects). The X error string E has X errors in the red region and no errors elsewhere and E_c is its complement. Clearly the string E has lower weight than E_c and is chosen as the likely error.*

Consider the correction of X errors sprinkled on the lattice, assuming for the moment that the parity check measurements of $\mathbf{Z}_{||,i}$ is noise-free. For each column we note that an even number of X errors is a product of the vertical XX gauge operators and therefore does not affect the state of the logical qubit. This means that per column only the parity of the number of X errors is relevant. The double column operator $\mathbf{Z}_{||,i}$ determines whether this parity flips from column i to column $i+1$. The interpretation of the eigenvalues of $\mathbf{Z}_{||,i}$ is then the same as for a 1D repetition code (or 1D Ising model) with parity checks Z_iZ_{i+1}. Double columns where $\mathbf{Z}_{||,i} \equiv Z_iZ_{i+1} = -1$ are *defects* marking the end-points of X-strings (domain walls in the 1D Ising model). Minimum-weight decoding is very simple as it corresponds to choosing the minimum weight one between two possible X-error strings: E or the complement string E_c which both have the faulty double columns defects as end-points, see Fig. 12(c). The code can thus correct all errors of weight at most $\lfloor \frac{n}{2} \rfloor$ for odd n. Higher-weight errors can also be corrected as long they induce a low density of defects on the boundary. Note however that

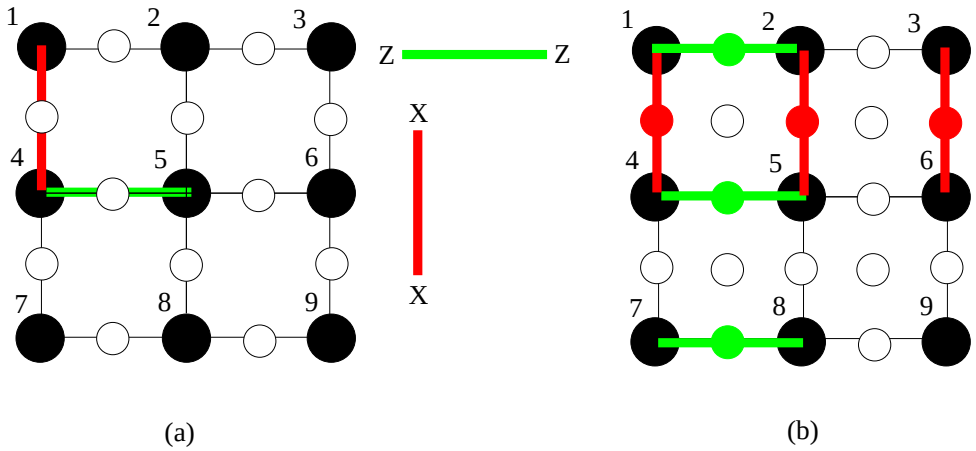

(a) (b)

Fig. 13: *(a) In order to measure the XX and ZZ operators one can place ancilla qubits (open dots) in between the data qubits. For example, for the ZZ measurement the ancilla qubit is placed in the $|0\rangle$ basis and 2 CNOTS on its adjacent data qubits are performed to collect the syndrome and the qubits is measured in the $|0\rangle, |1\rangle$ basis. (b) Alternatively, to measure $\mathbf{Z}_{||,i}$ one can prepare a 3-qubit entangled cat state $\frac{1}{\sqrt{2}}(|000\rangle + |111\rangle)$ (green dots) which interacts locally with the adjacent system qubits. $\mathbf{X}_{=,1}$ could be measured by preparing a cat state for the ancilla qubits at, say, the red dots. The ancilla qubits at the open dots can be used to prepare the cat states.*

the number of syndrome bits scales as n whereas the number of errors scales with n^2. This means that in the limit $n \to \infty$ the noise-free pseudo-threshold $p_c(n) \to 0$ as the fraction of incorrectable errors will grow with n. So, how do we choose n in order to minimize the logical error rate $\overline{p}(p, n)$: in [56] the authors find that the optimally-sized Bacon-Shor code for equal X and Z error rate p is given by $n = \frac{\ln 2}{4p}$ and for that optimal choice they can bound $\overline{p}(p, n) \lesssim \exp(-0.06/p)$.

How do we obtain the non-local parity check values? One can either measure the XX and ZZ gauge operators and use this information to get the eigenvalues of $\mathbf{X}_{=,i}$ and $\mathbf{Z}_{||,j}$, or one measures the parity checks directly. The first method has the advantage of being fully local: the ancilla qubits for measuring XX and ZZ can be placed in between the data qubits, see Fig.13(a). In the second method we can prepare an n-qubit cat state, see e.g. [55]. We could measure $\mathbf{ZZ}_{||,1}$ using the circuit in Fig. 1(a) with a single ancilla in the $|+\rangle$ state and controlled-phase gates (CZ) gates. However, a single X error on the ancilla qubit can feed back to the code qubits and cause multiple Z errors making the procedure non fault-tolerant. In addition the interaction between the ancilla qubit and the code qubits is non-local. Instead, we encode the ancilla qubit $|+\rangle$ using the repetition code, i.e. we prepare the n-qubit cat state $\frac{1}{\sqrt{2}}(|00\ldots0\rangle + |11\ldots1\rangle)$ such that a CZ-gate acts between one cat qubit and one code qubit. The n-qubit cat state, which is stabilized by Z_iZ_{i+1} and $X_1\ldots X_n$, can be made by preparing $|+\rangle^{\otimes n}$ and measuring Z_iZ_{i+1} using local ancilla qubits. The Z_iZ_{i+1} eigenvalues are recorded to provide the Pauli frame. In [55] further details of this scheme are given, including estimates of the noise threshold for asymmetric Bacon-Shor codes.

Consider what happens when the local XX and ZZ checks are measured inaccurately. The good news is this only causes *local* errors on the system qubits. The bad news is that if the measurement outcome has some probability of error q, then the error probability for the nonlocal stabilizer checks outcomes will be approximately qn. This is a disadvantage of the Bacon-Shor

code. Previous work [57, 55] has sought to improve the fault-tolerance of the parity check measurements by replacing the preparation of simple single qubit ancillas by fault-tolerant ones (methods by Steane and Knill). In [57] a best noise-threshold of $p_c \approx 0.02\%$ was numerically obtained for the (concatenated) $[[25, 1, 5]]$ code. Recently, [56] considered an alternative way of making the syndrome more robust, namely by simple repetition of the XX and ZZ measurements and a collective processing of the information (as is done for the surface code). We can view the effect of repetition as extending the 1D line of defects to a 2D lattice of defects, as in Fig. 7, so that minimum weight decoding corresponds to finding a minimum weight matching of defect end-points. The error rate for vertical (black) links representing the parity check errors scales with n while the error rate for horizontal links (when one column has an even and the other column has an odd number of errors) scales, for low p, also with n. In [56] the authors estimate that the optimal size for the Bacon-Shor code is then $n \approx 0.014/p$ and that for this choice, the failure probability $\overline{p}(p) \lesssim \exp(-0.0068/p)$. Hence for an error rate of $p = 5 \times 10^{-4}$ we can choose $n = 28$ giving a logical error rate of $\overline{p} \approx 1.25 \times 10^{-6}$.

2.3 Subsystem Surface Code

One can ask whether it is possible to reduce the requirement to measure 4-qubit parities by using subsystem codes [14]. The Bacon-Shor code exemplifies this, but the Bacon-Shor code is not a topological subsystem codes as the stabilizer checks are nonlocal on the 2D lattice. Several topological subsystem codes have been proposed in which weight-2 parity checks are measured [59], but the asymptotic noise threshold for such codes is typically quite a bit lower than for the surface code, see e.g. [60].

In [61] a topological subsystem code was proposed,—a subsystem surface code—, in which the non-commuting parity checks are of weight-3 and the stabilizer generators are of weight 6, see Fig. 14. More precisely, the gauge group $\mathcal{G}$ is generated by the triangle operators XXX and ZZZ, including cut-off weight-2 operators at the boundary. The stabilizer group $\mathcal{S} = \mathcal{G} \cap \mathcal{C}(\mathcal{G})$ is generated by weight-6 plaquette operators (at the boundary $\rightarrow$ weight-2 operators). By measuring, say, the Z-triangles we can deduce the eigenvalues of the Z-plaquettes which are used to do error correction.

For a $L \times L$ lattice one has a total of $3L^2 + 4L + 1$ qubits and $2L^2 + 4L$ independent stabilizer generators which gives $L^2 + 1$ qubits. One of these qubits is the logical qubit whose $\overline{Z}$ and $\overline{X}$ commute with all Z and X-triangles. Similar as in the surface code, a vertical Z-line through $2L$ qubits can realize $\overline{Z}$ while a horizontal X-line realizes $\overline{X}$. The logical operators for the L^2 gauge qubits, one for each plaquette, are pairs of triangle operators on a plaquette generating the group $\mathcal{G}$. One can multiply, say, the vertical Z-line by Z-triangles to become a $\overline{Z}$ which acts only on L qubits: in [61] it is indeed proved that the distance of the code is L. Note that such weight-L $\overline{Z}$ acts on the logical qubit and the irrelevant gauge qubits.

For a code with distance $L = 3$ one thus needs 41 elementary qubits, substantially more than for the surface code. Multiple qubits can be encoded in this subsystem code by making holes as for the surface code. One can expect that braiding and lattice surgery methods for this code can be established in the same way as for the surface code. The interesting feature of this code are its relatively-high noise threshold obtained by reduced-weight parity checks (at the price of a bit more overhead). Decoding of stabilizer syndrome information is done by interpreting the syndrome as defects on a virtual lattice which can processed, similar as for the surface code, by

[14] One can prove that 2D qubit codes defined as eigenspaces of 3-local mutually commuting terms are trivial as quantum codes [58].

minimum weight matching of defects or by RG decoding. For noise-free perfect error correction and independent X, Z noise the authors report a maximum threshold of $p_c \approx 7\%$ (compare with 11% for the surface code). For noisy error correction the threshold depends on how single errors with probability p in the parity check circuit affect the error rate on the virtual lattice. Modeling this effective noise-rate on the virtual lattice, the authors find a noise threshold of $p_c \approx 0.6\%$.
It is not surprising that decoding for the subsystem surface codes can be done using the decoding method for the surface code. It was proved in [62] that any 2D topological subsystem or stabilizer code can be locally mapped onto copies of the toric code. The upshot is that for any such code one can find, after removing some local errors by local correction, a virtual lattice with toric code parity checks and an underlying effective error model. An example of another 2D topological subsystem code which may be analyzed this way is a concatenation of the $[[4, 2, 2]]$ code with the surface code. If we use the $[[4, 2, 2]]$ code as subsystem code then the concatenated code has weight-2 and weight-8 check operators. The scheme may be of interest if the weight-2 checks can be measured fast and with high accuracy.
A possible lay-out of the elementary qubits for this code with superconducting transmon qubits coupled through resonators (including ancilla transmon qubits for measurement) was considered in [63]. The idea of a direct 3-qubit parity measurement [49] via a parity-dependent shift of the cavity mode in the circuit QED setting could be useful in reducing the need for ancillas, in addition to being making better use of the given physical interactions. The authors of [61] report a threshold at least 0.97% by modeling such direct parity measurement.

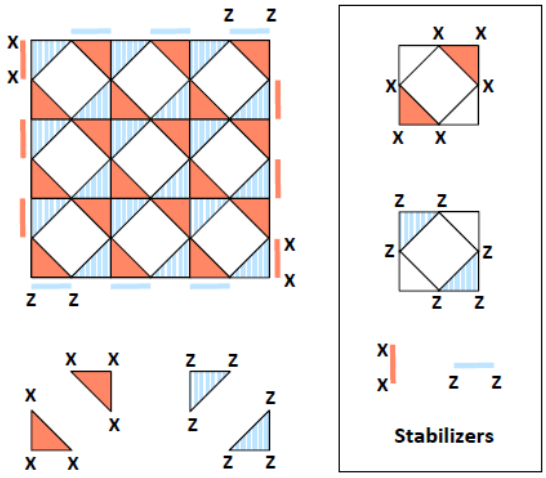

Fig. 14: *Picture from [61]: subsystem surface code on a lattice of size $L \times L$ with L^2 square plaquettes (depicted is $L = 3$). The qubits live on the edges and vertices of the plaquettes and are acted upon by weight-3 X and Z-triangle operators (which are modified to become weight-2 operators at the boundary). The stabilizer checks are weight 6 except at the boundary.*

3 Discussion

The current qubit realizations seem in many ways not well suited to constitute the elementary qubits of an error-correcting code. Most elementary qubits are realized as nondegenerate eigenlevels (in a higher-dimensional space), approximately described by some $H_0 = \frac{\omega}{2}Z$. The

presence of H_0 immediately gives a handle on this qubit, i.e. processes which exchange energy with this qubit will drive it from $|1\rangle$ to $|0\rangle$ and vice versa (Rabi oscillations), while a different coupling of $|0\rangle$ and $|1\rangle$ to other quantum degrees of freedom can be used for qubit read-out. Passive (non-time dependent) interactions with other quantum systems are relatively weak and can only lead to two-qubit interactions if we rotate away the single qubit precession and supply energy in the form of time-dependent AC fields. This also means that energy is necessary to drive and keep multiple qubits in the code space where they are highly entangled. One can strive to engineer the dissipation of such coupled qubits such that they couple jointly to the environment instead of each qubit dissipating and decohering by itself. However, the realization of parity checks involving Z and X operators has to be realized sequentially as the X-check circuits require going to the Hadamard transformed basis. Using elementary qubits with protected degenerate eigenlevels, such as Majorana fermion qubits, may have the advantage that interqubit coupling is strong (as there is no other coupling) and treats X and Z symmetrically. However, one needs to set this up such that there are effective 4-body parity-check interactions between the qubits while the 2-body interactions are trivial or suppressed. The desired 4-body interactions will always be relatively weak as they come about perturbatively. One can, for example, realize the parity checks in the surface code quite naturally as interacting terms in 2D arrays of Majorana fermion qubits [64].

References

[1] A. Kitaev. Fault-tolerant quantum computation by anyons. *Ann. Phys.*, 303:2–30, 2003. http://arxiv.org/abs/quant-ph/9707021.

[2] P. W. Shor. Fault-tolerant quantum computation. In *Proceedings of 37th FOCS*, pages 56–65, 1996.

[3] J. T. Barreiro, M. Müller, P. Schindler, D. Nigg, T. Monz, M. Chwalla, M. Hennrich, C. F. Roos, P. Zoller, and R. Blatt. An open-system quantum simulator with trapped ions. *Nature*, 470:486–491, February 2011.

[4] X.-C. Yao, T.-X. Wang, H.-Z. Chen, W.-B. Gao, A. G. Fowler, R. Raussendorf, Z.-B. Chen, N.-L. Liu, C.-Y. Lu, Y.-J. Deng, Y.-A. Chen, and J.-W. Pan. Experimental demonstration of topological error correction. *Nature*, 482:489–494, February 2012.

[5] Panos Aliferis, Daniel Gottesman, and John Preskill. Quantum accuracy threshold for concatenated distance-3 codes. *Quantum Information and Computation*, 6:97–165, 2006.

[6] D. Aharonov, A. Kitaev, and J. Preskill. Fault-Tolerant Quantum Computation with Long-Range Correlated Noise. *Physical Review Letters*, 96(5):050504, February 2006.

[7] D. Gottesman. *Stabilizer Codes and Quantum Error Correction*. PhD thesis, CalTech, 1997. http://arxiv.org/abs/quant-ph/9705052.

[8] E. Knill. Quantum computing with realistically noisy devices. *Nature*, 434:39–44, 2005.

[9] M. A. Nielsen and I. L. Chuang. *Quantum computation and quantum information*. Cambridge University Press, Cambridge, U.K., 2000.

[10] D. W. Leung, M. A. Nielsen, I. L. Chuang, and Y. Yamamoto. Approximate quantum error correction can lead to better codes. *Phys. Rev. A*, 56:2567–2573, October 1997.

[11] Z. Leghtas, G. Kirchmair, B. Vlastakis, R. Schoelkopf, M. Devoret, and M. Mirrahimi. Hardware-efficient autonomous quantum error correction. July 2012. `http://arxiv.org/abs/1207.0679`.

[12] Serge Haroche and Jean Michel Raimond. *Exploring the Quantum: Atoms, Cavities, and Photons*. Oxford Univ. Press, Oxford, 2006.

[13] D. Gottesman, A.Yu. Kitaev, and J. Preskill. Encoding a qubit in an oscillator. *Phys. Rev. A*, 64:012310, 2001.

[14] A. Kitaev. Protected qubit based on a superconducting current mirror. 2006. `http://arxiv.org/abs/cond-mat/0609441`.

[15] S. Glancy and E. Knill. Error analysis for encoding a qubit in an oscillator. *Phys. Rev. A*, 73(1):012325, 2006.

[16] M. A. Levin and X.-G. Wen. String-net condensation: A physical mechanism for topological phases. *Phys. Rev. B*, 71(4):045110, January 2005.

[17] R. Koenig, G. Kuperberg, and B. W. Reichardt. Quantum computation with Turaev-Viro codes. *Annals of Physics*, 325:2707–2749, 2010.

[18] C. Ahn, A. C. Doherty, and A. J. Landahl. Continuous quantum error correction via quantum feedback control. *Phys. Rev. A*, 65(4):042301, April 2002.

[19] M. Müller, K. Hammerer, Y. L. Zhou, C. F. Roos, and P. Zoller. Simulating open quantum systems: from many-body interactions to stabilizer pumping. *New Journal of Physics*, 13(8):085007, August 2011.

[20] D. Aharonov and M. Ben-Or. Fault-tolerant quantum computation with constant error. In *Proceedings of 29th STOC*, pages 176–188, 1997.

[21] E. Knill, R. Laflamme, and W. Zurek. Resilient quantum computation: Error models and thresholds. *Proc. R. Soc. Lond. A*, 454:365–384, 1997.

[22] A.Yu. Kitaev. Quantum computations: algorithms and error correction. *Russian Math. Surveys*, 52:1191–1249, 1997.

[23] K.M. Svore, D.P. DiVincenzo, and B.M. Terhal. Noise threshold for a fault-tolerant two-dimensional lattice architecture. *Quantum Information and Computation*, 7:297–318, 2007.

[24] Daniel Gottesman. The Heisenberg Representation of Quantum Computers. In *Group22: Proceedings of the XXII International Colloquium on Group Theoretical Methods in Physics*, pages 32–43, 1999. `http://arxiv.org/abs/quant-ph/9807006`.

[25] D. Gottesman and I. L. Chuang. Demonstrating the viability of universal quantum computation using teleportation and single-qubit operations. *Nature*, 402:390–393, November 1999.

[26] X. Zhou, D. W. Leung, and I. L. Chuang. Methodology for quantum logic gate construction. *Phys. Rev. A*, 62(5):052316, November 2000.

[27] S. Bravyi and R. Koenig. Classification of topologically protected gates for local stabilizer codes. 2012. http://arxiv.org/abs/1206.1609.

[28] P. Aliferis. *Level Reduction and the Quantum Threshold Theorem*. PhD thesis, CalTech, 2007. http://arxiv.org/abs/quant-ph/0703230.

[29] H. Bombin and M. A. Martin-Delgado. Topological Quantum Distillation. *Physical Review Letters*, 97(18):180501, November 2006.

[30] S. Bravyi and A. Kitaev. Universal quantum computation with ideal Clifford gates and noisy ancillas. *Phys. Rev. A*, 71:022316, 2005.

[31] R. Raussendorf, J. Harrington, and K. Goyal. Topological fault-tolerance in cluster state quantum computation. *New J. Phys.*, 9:199–219, June 2007.

[32] C. Jones. Multilevel distillation of magic states for quantum computing. October 2012. http://arxiv.org/abs/1210.3388.

[33] A. J. Landahl, J. T. Anderson, and P. R. Rice. Fault-tolerant quantum computing with color codes. August 2011.

[34] E. Dennis, A. Kitaev, A. Landahl, and J. Preskill. Topological quantum memory. *J. Math. Phys.*, 43:4452–4505, 2002.

[35] H. Bombin and M. A. Martin-Delgado. Quantum measurements and gates by code deformation. *Journal of Physics A Mathematical General*, 42(9):095302–+, March 2009.

[36] R. Raussendorf and J. Harrington. Fault-Tolerant Quantum Computation with High Threshold in Two Dimensions. *Phys. Rev. Lett.*, 98(19):190504, May 2007.

[37] C. Horsman, A. G. Fowler, S. Devitt, and R. Van Meter. Surface code quantum computing by lattice surgery. November 2011. http://arxiv.org/abs/1111.4022.

[38] Sergey Bravyi and Barbara Terhal. A no-go theorem for a two-dimensional self-correcting quantum memory based on stabilizer codes. *New Journal of Physics*, 11:043029, 2009.

[39] S. Bravyi, D. Poulin, and B. Terhal. Tradeoffs for Reliable Quantum Information Storage in 2D Systems. *Physical Review Letters*, 104(5):050503, February 2010.

[40] Jack Edmonds. Paths, trees, and flowers. *Canad. J. Math.*, 17:449–467, 1965.

[41] C. Wang, J. Harrington, and J. Preskill. Confinement-Higgs transition in a disordered gauge theory and the accuracy threshold for quantum memory. *Annals of Physics*, 303:31–58, January 2003.

[42] A. G. Fowler. Accurate simulations of planar topological codes cannot use cyclic boundaries. September 2012. http://arxiv.org/abs/1209.3539.

[43] Andrew W. Cross, David P. DiVincenzo, and Barbara M. Terhal. A comparative code study for quantum fault tolerance. *Quantum Info. Comput.*, 9(7):541–572, July 2009.

[44] G. Denhez, A. Blais, and D. Poulin. Quantum-error-correction benchmarks for continuous weak-parity measurements. *Phys. Rev. A*, 86(3):032318, 2012.

[45] G. Duclos-Cianci and D. Poulin. A renormalization group decoding algorithm for topological quantum codes. *Information Theory Workshop (ITW), 2010 IEEE*.

[46] S. Bravyi and J. Haah. Analytic and numerical demonstration of quantum self-correction in the 3D Cubic Code. December 2011. http://arxiv.org/abs/1112.3252.

[47] J. Harrington. *Analysis of quantum error-correcting codes: symplectic lattice codes and toric codes*. PhD thesis, CalTech, 2004. http://thesis.library.caltech.edu/1747/.

[48] D. P. DiVincenzo. Fault-tolerant architectures for superconducting qubits. *Physica Scripta Volume T*, 137(1):014020, December 2009.

[49] D. P. DiVincenzo and F. Solgun. Multi-qubit parity measurement in circuit quantum electrodynamics. May 2012. http://arxiv.org/abs/1205.1910.

[50] K. Lalumière, J. M. Gambetta, and A. Blais. Tunable joint measurements in the dispersive regime of cavity QED. *Phys. Rev. A*, 81(4):040301, April 2010.

[51] S. E. Nigg and S. M. Girvin. Stabilizer quantum error correction toolbox for superconducting qubits. December 2012. http://arxiv.org/abs/1212.4000.

[52] Daniel Gottesman. Fault-Tolerant Quantum Computation with Higher-Dimensional Systems. *Chaos Solitons and Fractals*, 10:1749–1758, 1999.

[53] A. G. Fowler, A. M. Stephens, and P. Groszkowski. High-threshold universal quantum computation on the surface code. *Phys. Rev. A*, 80(5):052312–+, November 2009.

[54] Dave Bacon. Operator quantum error correcting subsystems for self-correcting quantum memories. *Physical Review A*, 73:012340, 2006.

[55] P. Brooks and J. Preskill. Fault-tolerant quantum computation with asymmetric Bacon-Shor codes. 2012. http://arxiv.org/abs/1211.1400.

[56] J. Napp and J. Preskill. Optimal Bacon-Shor codes. September 2012. http://arxiv.org/abs/1209.0794.

[57] P. Aliferis and A. Cross. Subsystem fault-tolerance with the Bacon-Shor code. *Phys. Rev. Lett.*, 98:220502, 2007.

[58] D. Aharonov and L. Eldar. On the complexity of Commuting Local Hamiltonians, and tight conditions for Topological Order in such systems. February 2011. http://arxiv.org/abs/1102.0770.

[59] H. Bombin. Topological subsystem codes. *Phys. Rev. A*, 81(3):032301, March 2010.

[60] M. Suchara, S. Bravyi, and B. Terhal. Constructions and noise threshold of topological subsystem codes. *Journal of Physics A Mathematical General*, 44(15):155301, 2011.

[61] S. Bravyi, G. Duclos-Cianci, D. Poulin, and M. Suchara. Subsystem surface codes with three-qubit check operators. http://arxiv.org/abs/1207.1443.

[62] H. Bombin, G. Duclos-Cianci, and D. Poulin. Universal topological phase of two-dimensional stabilizer codes. *New Journal of Physics*, 14(7):073048, July 2012.

[63] D. Huben. Bachelor Thesis, RWTH Aachen (Supervision of D. P. DiVincenzo). http://www.physik.rwth-aachen.de/en/institutes/institute-for-quantum-information/student-projects/past-theses/.

[64] B. M. Terhal, F. Hassler, and D. P. DiVincenzo. From Majorana fermions to topological order. *Physical Review Letters*, 108(26):260504, June 2012.

C 2 Ion Traps and Quantum Simulations [1]

E. Solano

Departamento de Química Física,
Universidad del País Vasco UPV/EHU,
Apartado 644, 48080 Bilbao, Spain

IKERBASQUE, Basque Foundation for Science,
Alameda Urquijo 36, 48011 Bilbao, Spain

Contents

1 Quantum simulations **2**

2 Trapped-ion technologies **3**

3 Dirac equation simulation in trapped ions **5**

4 Klein paradox simulation in trapped ions **8**

5 Quantum simulation of quantum fields in trapped ions **14**

6 Acknowledgments **18**

A Comoving modes formalism **18**

[1] Lecture Notes of the 44^{th} IFF Spring School "Quantum Information Processing" (Forschungszentrum Jülich, 2013). All rights reserved.

1 Quantum simulations

Quantum simulation is one of the most intriguing and exciting fields in the quantum information science. Feynman stated in 1982 [1] that a controllable quantum simulator could emulate the dynamics of another quantum system exponentially faster than classical computers. Since then, this hypothesis has been formalized [2], and relevant theoretical and experimental work has followed [3, 4, 5]. Quantum simulators do not have as a unique goal to outperform classical computers. They also represent communicating vessels between previously unconnected fields, while enhancing our scientific and artistic imagination as a stage for our quantum theater.

Among other topics, quantum simulators of quantum relativistic systems and quantum field theories are attracting the interest of wide interdisciplinary communities. Initial efforts include proposals for simulating analog black holes in Bose-Einstein condensates [6], or the expanding universe and particle creation [7, 8]. A milestone was achieved by the experimental implementation of the quantum simulation of the Dirac equation in a single trapped ion [9, 10], where a relativistic quantum dynamics was reproduced in a nonrelativistic system. This was the first experimental observation of a phenomenon analog to the *Zitterbewegung*, the fast quivering motion of a free Dirac particle, predicted by Erwin Schrödinger in the early days of quantum mechanics [11]. A key next step in this research line produced the theoretical proposal [12] and experimental realization [13] of the simulation of Klein paradox [14], and a proposal for simulating the complex Majorana equation and unphysical operations like time reversal or charge conjugation with trapped ions [15].

Many other theoretical proposals and some experiments for implementations in a wide variety of systems have been put forward as well, as the simulation of *Zitterbewegung* in semiconductor quantum wells [16], *Zitterbewegung* and Klein paradox in graphene [17, 18, 19], Dirac oscillator in trapped ions [20], *Zitterbewegung* and Dirac physics with ultracold atoms [21, 22, 23, 24, 25, 26, 27], Klein paradox with atomic ensembles [28], optical *Zitterbewegung* in metamaterials [29, 30], delocalization of relativistic Dirac particles in cold atoms [31], photon wave function and *Zitterbewegung* [32], similarity of electron *Zitterbewegung* to the Adler-Bell-Jackiw anomaly in QED and its manifestation in graphene [33], photonic analog of *Zitterbewegung* in binary waveguide arrays [34], *Zitterbewegung* theory in multiband Hamiltonians [35], classical *Zitterbewegung* in reduced plasma dynamics [36], *Zitterbewegung* analogs in nonlinear frequency conversion [37], experimental realization of an optical analog for relativistic quantum mechanics in an optical superlattice [38], relation between parity and *Zitterbewegung* and trapped-ion proposal [39], *Zitterbewegung* in a magnetic field proposal [40], Wilson fermions and axion electrodynamics in optical lattices [41], the Schwinger effect for a possible implementation with atoms in optical lattices [42], Dirac equation for cold atoms in artificial curved spacetimes [43], a theoretical analysis of cold atom simulation of interacting relativistic quantum field theories [44], an analysis of the photonic simulation of the quark model [45], quantum field theories [46], fermionic lattice models [47], and the Holstein model simulated with ions [48]. Further recent results involve the relativistic effects of spin splitting of neutral particles, or the quantum simulations of relativistic quantum physics in circuit QED. For a review of *Zitterbewegung* of electrons in semiconductors, see Ref. [51].

2 Trapped-ion technologies

Trapped-ion systems are among the most promising technologies for implementing quantum information protocols. Ions are charged particles that can be confined either in Penning traps or radio-frequency Paul traps (rf Paul traps) [52]. The former uses electrostatic and magnetic fields, whereas the latter requires time-dependent fields to confine the ions in an effective harmonic potential. In these lecture notes, we will focus on the case of rf Paul traps, see Fig $1a$. Two different kind of qubits are currently being used, optical qubits and radio-frecuency qubits (rf qubits). In the first case, see Fig. $1b$, two internal electronic levels corresponding to an optical transition are used to encode the logical qubit. In the second case, see Fig. $1c$, a third level is used to mediate a two-photon process between the electronic levels conforming the qubit. Through sideband cooling, the ionic motional degrees of freedom can reach the ground state of the quantum harmonic oscillator, which can be used as a quantum bus to perform gates between any two ions in a string. Finally, using resonance fluorescence with a cyclic transition, quantum nondemolition measurements of the qubit can be performed. Fidelities of state preparation, single-qubit gates, two-qubit gates, and qubit detection, can reach now values above 99% [52]. The fundamental Hamiltonian describing the interaction of a two-level trapped ion, cooled down to the motional quantum regime, with a laser beam is given by

$$\mathcal{H} = \hbar\frac{\omega_0}{2}\hat{\sigma}_z + \hbar\nu\hat{a}^\dagger\hat{a} + \hbar\Omega(\hat{\sigma}^+ + \hat{\sigma}^-)\big(\exp[i(kz - \omega_l t + \phi)] + \exp[-i(kz - \omega_l t + \phi)]\big), \quad (1)$$

where $\hat{\sigma}^\pm$ and $\hat{\sigma}_z$ are Pauli operators associated to the two internal levels of the ion, $\hat{a}(\hat{a}^\dagger)$ is the annihilation(creation) operator of the considered motional mode, ω_0 is the frequency of the internal electronic transition, ν is the trap frequency, ω_l is the frequency of the driving laser field, k is the laser wave vector, ϕ is the laser phase, and Ω is the Rabi frequency associated with the atom-laser coupling strength.

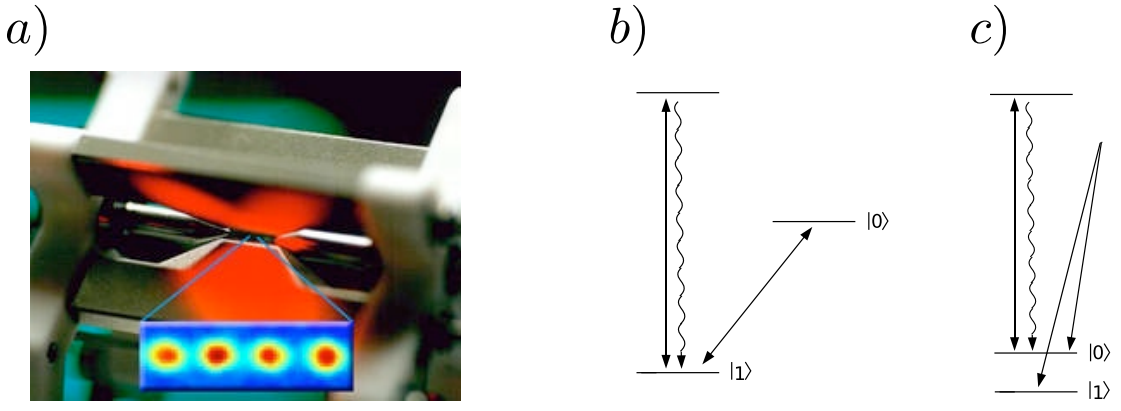

Fig. 1: *a) Picture of a rf Paul trap used in Innsbruck laboratories. Energy-level scheme for optical qubits (b), and rf qubits (c). In addition to the qubit levels* $|0\rangle$ *and* $|1\rangle$*, a third level is used for qubit readout.*

In an interaction picture with respect to the free-energy term $\hbar\frac{\omega_0}{2}\hat{\sigma}_z + \hbar\nu\hat{a}^\dagger\hat{a}$, and after applying the optical rotating-wave approximation, we obtain

$$\mathcal{H}^I = \hbar\Omega\hat{\sigma}^+ e^{-i(\Delta t-\phi)} \exp(i\eta[\hat{a}e^{-i\nu t} + \hat{a}^\dagger e^{i\nu t}]) + \text{H.c.}, \tag{2}$$

where Δ is the laser frequency detuning with respect to the internal ion transition, $\eta = kz_0$ is the Lamb-Dicke parameter, where $z_0 = \sqrt{\hbar/2m\nu}$ is the ground state width of the considered motional mode.
In the Lamb-Dicke regime, where $\eta\sqrt{\langle(\hat{a}+\hat{a}^\dagger)^2\rangle} \ll 1$, Eq. (4) can be rewritten as

$$\mathcal{H}^I = \hbar\Omega[\hat{\sigma}^+ e^{-i(\Delta t-\phi)} + i\eta\hat{\sigma}^+ e^{-i(\Delta t-\phi)}(\hat{a}e^{-i\nu t} + \hat{a}^\dagger e^{i\nu t}) + \text{H.c.}]. \tag{3}$$

$$\mathcal{H}^I = \hbar\Omega\hat{\sigma}^+ e^{-i(\Delta t-\phi)} \exp(i\eta[\hat{a}e^{-i\nu t} + \hat{a}^\dagger e^{i\nu t}]) + \text{H.c.}, \tag{4}$$

where Δ is the laser frequency detuning with respect to the internal ion transition, $\eta = kz_0$ is the Lamb-Dicke parameter, where $z_0 = \sqrt{\hbar/2m\nu}$ is the ground state width of the considered motional mode.

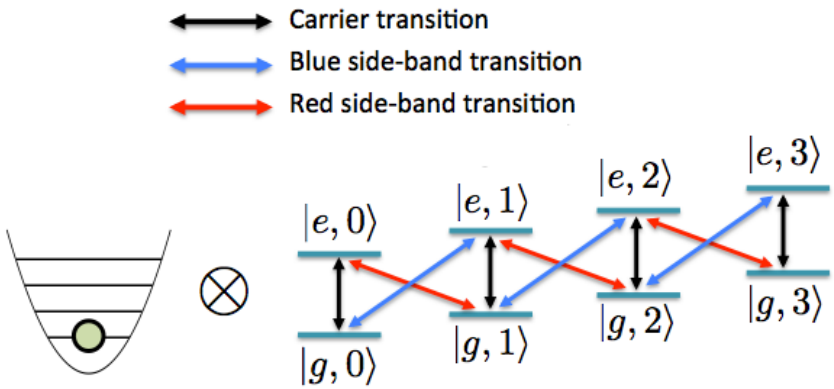

Fig. 2: *An ion confined in an effective harmonic potential with level transitions generated by the three basic interactions in Eqs. (5), (6), and (7).*

By selecting appropriate internal vibronic transitions with the variation of the laser frequency detuning, Δ, one can recover the three basic interactions in trapped-ion physics, see Fig. 2. These involve the carrier interaction ($\Delta = 0$),

$$\mathcal{H}_c^I = \hbar\Omega(\hat{\sigma}^+ e^{i\phi} + \hat{\sigma}^- e^{-i\phi}), \tag{5}$$

the red-sideband interaction ($\Delta = -\nu$),

$$\mathcal{H}_r^I = i\hbar\eta\Omega(\hat{\sigma}^+\hat{a}e^{i\phi} - \hat{\sigma}^-\hat{a}^\dagger e^{-i\phi}), \tag{6}$$

and the blue-sideband interaction ($\Delta = +\nu$),

$$\mathcal{H}_b^I = i\hbar\eta\Omega(\hat{\sigma}^+\hat{a}^\dagger e^{i\phi} - \hat{\sigma}^-\hat{a}e^{-i\phi}). \tag{7}$$

We can also consider several lasers interacting on different ions in a string. In that case, we can write the basic interactions as

$$\begin{aligned}
\mathcal{H}_{c,j}^I &= \hbar\Omega(\hat{\sigma}_j^+ e^{i\phi} + \hat{\sigma}_j^- e^{-i\phi}), \\
\mathcal{H}_{r,j,k}^I &= i\hbar\eta\Omega(\hat{\sigma}_j^+\hat{a}_k e^{i\phi} - \hat{\sigma}_j^-\hat{a}_k^\dagger e^{-i\phi}), \\
\mathcal{H}_{b,j,k}^I &= i\hbar\eta\Omega(\hat{\sigma}_j^+\hat{a}_k^\dagger e^{i\phi} - \hat{\sigma}_j^-\hat{a}_k e^{-i\phi}),
\end{aligned} \tag{8}$$

where $\hat{\sigma}_j^\pm$ and $\hat{a}_k^\dagger(\hat{a}_k)$ are the raising-lowering operators of the j-th ion and the creation(annihilation) bosonic operators of the k-th vibronic mode, respectively.
Appropriate combinations of the interactions appearing in Eq. (8) give rise to the generation of single and two-qubit gates necessary for standard quantum computing tasks. Paradigmatic examples of two-qubit gates that can be implemented in trapped ions are: the Cirac-Zoller gate, which is essentially a controlled-NOT (C-NOT) gate, and the Mølmer-Sørensen gate, that can be used to generate spin-spin interactions.

3 Dirac equation simulation in trapped ions

The Dirac equation is one of the cornerstones in the history of physics [54]. It represented a significant step forward in the task of unifying quantum mechanics and special relativity, describing accurately the hydrogen atom spectrum with relativistic corrections. It acquires full significance in the context of quantum fields and second quantization, where the number of quanta is not fixed. On the other hand, at the level of relativistic quantum mechanics, the single-particle solutions to this equation already contain intriguing and counterintuitive properties. Among them, perhaps the best known ones are the *Zitterbewegung* [11] and Klein paradox [14]. The 3+1 Dirac equation can be written as

$$i\hbar\frac{\partial\psi}{\partial t} = \mathcal{H}_{\rm D}^{3+1}\psi = (c\vec{\alpha}\cdot\vec{p} + \beta mc^2)\psi, \tag{9}$$

where $\vec{\alpha}$ and β are the Dirac matrices obeying the Clifford algebra structure, $\{\alpha_i, \alpha_j\} = 2\delta_{ij}$, $\{\alpha_i, \beta\} = 0$, $\beta^2 = I_4$, that appears when linearizing the expression for the relativistic energy, $E = \sqrt{p^2c^2 + m^2c^4}$.
The Hamiltonian operator in Eq. (9) expressed in its "supersymmetric" representation [54], takes the form

$$\mathcal{H}_{\rm D}^{3+1} = \begin{pmatrix} 0 & c(\vec{\sigma}\cdot\vec{p}) - imc^2 \\ c(\vec{\sigma}\cdot\vec{p}) + imc^2 & 0 \end{pmatrix}, \tag{10}$$

where $\vec{\alpha} := (\alpha_x, \alpha_y, \alpha_z) =$ off-diag$(\vec{\sigma}, \vec{\sigma})$ is the velocity operator, $\vec{\sigma} := (\sigma_x, \sigma_y, \sigma_z)$ are the Pauli matrices, $\beta :=$ off-diag$(-iI_2, iI_2)$, c is the speed of light and mc^2 the electron rest energy. A quantum simulation of the Dirac equation is a useful playground for analyzing different regimes and to verify in a table-top experiment paradigmatic phenomena like *Zitterbewegung* [9, 10] or Klein paradox [12, 13]. To perform just the Dirac equation and *Zitterbewegung*, one considers a single trapped ion of mass M inside a Paul trap, with motional-mode frequencies

ν_x, ν_y, and ν_z [9]. In the 3+1 case, the four-component Dirac bispinor is encoded in four internal levels of the trapped ion, $|a\rangle, |b\rangle, |c\rangle$, and $|d\rangle$. For any spacetime dimensions, one should realize that the Dirac equation contains basically couplings $\sigma_i p_i$ (spin-orbit), and $mc^2\sigma_j$ (mass term). In general, one may implement the first kind of couplings, $\sigma_i p_i$, by a combination of Jaynes-Cummings (JC, also named red-sideband) and anti-Jaynes-Cummings (AJC, also named blue-sideband) interactions. The JC interaction will excite one quantum of vibration while deexciting the internal state of the ion. The AJC interaction, in turn, excites one quantum of vibration while at the same time exciting the internal state of the ion. These interactions may be obtained by properly chosen lasers, either in Raman or quadrupole-transition configurations, depending on the chosen ion.
The resonant JC Hamiltonian can be written as

$$H_{\rm r} = \hbar\eta\tilde{\Omega}(\sigma^+ a e^{i\phi_{\rm r}} + \sigma^- a^\dagger e^{-i\phi_{\rm r}}), \tag{11}$$

where $\tilde{\Omega}$ is the coupling strength, σ^+ and σ^- are the raising and lowering spin-$1/2$ operators, and a and $a^\dagger$ are the annihilation and creation operators associated with the corresponding motional degree of freedom, either x, y, or z. $\eta = k\sqrt{\hbar/2M\nu}$ is the Lamb-Dicke parameter [52], where k is the wave number of the driving field. The AJC Hamiltonian reads

$$H_{\rm b} = \hbar\eta\tilde{\Omega}(\sigma^+ a^\dagger e^{i\phi_{\rm b}} + \sigma^- a e^{-i\phi_{\rm b}}). \tag{12}$$

Properly adjusting laser phases and frequencies, one may combine JC and AJC interactions to obtain the couplings aimed for, namely

$$H_{\sigma_x}^{p_x} = i\hbar\eta_x\tilde{\Omega}_x\sigma_x(a_x^\dagger - a_x) = 2\eta_x\Delta_x\tilde{\Omega}_x\sigma_x p_x, \tag{13}$$

with $i(a_x^\dagger - a_x)/2 = \Delta_x\, p_x/\hbar$, where $\Delta_x := \sqrt{\hbar/2M\nu_x}$ is the spread in position along the x-axis of the ground state harmonic-oscillator wavefunction and p_x the corresponding dimensioned momentum operator. These interactions may be addressed to different internal levels and motional modes, in order to get the terms in Eq. (10) that are linear in the momenta.
For implementing the second kind of couplings, $mc^2\sigma_j$, one may consider the carrier interaction between two internal levels of the ion. This consists of a coherent excitation of the internal level, while leaving the motion unaffected. The carrier Hamiltonian is

$$H_\sigma = \hbar\Omega(\sigma^+ e^{i\phi} + \sigma^- e^{-i\phi}), \tag{14}$$

that, for appropriately chosen phases, gives rise to the term $\hbar\Omega\sigma_y$, needed for the mass terms for 3+1 dimensions.
For the 3+1 dimension simulation [9], notice that the Hamiltonian

$$\begin{aligned} H_{\rm D}^{3+1} = \quad & 2\eta\Delta\tilde{\Omega}(\sigma_x^{ad} + \sigma_x^{bc})p_x + 2\eta\Delta\tilde{\Omega}(\sigma_y^{ad} - \sigma_y^{bc})p_y \\ & + 2\eta\Delta\tilde{\Omega}(\sigma_x^{ac} - \sigma_x^{bd})p_z + \hbar\Omega(\sigma_y^{ac} + \sigma_y^{bd}). \end{aligned} \tag{15}$$

is composed of basic JC, AJC and carrier units as exposed above. When this is expressed in matrix form, in the basis $|a\rangle, |b\rangle, |c\rangle$, and $|d\rangle$,

$$H_{\rm D}^{3+1} = \begin{pmatrix} 0 & 2\eta\Delta\tilde{\Omega}(\vec{\sigma}\cdot\vec{p}) - i\hbar\Omega \\ 2\eta\Delta\tilde{\Omega}(\vec{\sigma}\cdot\vec{p}) + i\hbar\Omega & 0 \end{pmatrix}, \tag{16}$$

it coincides with the Dirac equation Hamiltonian in 3+1 dimensions, Eq. (10), with the equivalences for the speed of light and rest energy,

$$c := 2\eta\Delta\tilde{\Omega} \ , \quad mc^2 := \hbar\Omega. \tag{17}$$

One big appeal of this simulation with trapped ions is that the values of the speed of light and rest energy in Eqs. (17) may be controlled at will just by changing the laser intensities, $\tilde{\Omega}$ and Ω. Thus, one may explore the transition from massless to massive Dirac fermions, or, equivalently, the transition from ultra-relativistic to non-relativistic physics.

One of the most astonishing predictions of the single-particle solutions of Dirac equation is the fast quivering motion so called *Zitterbewegung*. It is unexpected given that it is an oscillatory motion of a freely propagating electron. Thus, Galileo's inertia law is not fully verified for a free electron, that will quiver around an average, classical trajectory. The reason for this is the non-commutativity of the components of the velocity operator, which is given by $c\vec{\alpha}$. Thus, the marriage between quantum mechanics and special relativity seems to contradict the inertia law, at least to some extent. The real electron's *Zitterbewegung* has not been observed so far, given that the predicted frequency$\sim 10^{21}\mathrm{s}^{-1}$ is very fast and the amplitude$\sim 10^{-13}$m is exceedingly small, and its existence is sometimes questioned.

The expression for the Dirac electron position operator $\vec{r} = (x, y, z)$ in the Heisenberg picture, derived from $d\vec{r}/dt = [\vec{r}, H_{\mathrm{D}}]/i\hbar$, for 3+1 dimensions, reads [54]

$$\vec{r}(t) = \vec{r}(0) + \frac{c^2\vec{p}}{\mathcal{H}_{\mathrm{D}}^{3+1}}\, t + \frac{ic\hbar}{2}\left(\vec{\alpha} - \frac{c\vec{p}}{\mathcal{H}_{\mathrm{D}}^{3+1}}\right)\mathcal{H}_{\mathrm{D}}^{3+1-1}\left(e^{2i\mathcal{H}_{\mathrm{D}}^{3+1}t/\hbar} - 1\right), \tag{18}$$

where the first term on the r.h.s. is the initial position, the second is just the inertia law term, and the third one is the term associated to the *Zitterbewegung*.

In the trapped ion simulation, the position of the ion mimics the position of the simulated Dirac particle. The ionic position operator evolution under the Dirac dynamics in Eq. (16), in 3+1 dimensions, is

$$\vec{r}(t) \ = \ \vec{r}(0) + \frac{4\eta^2\Delta^2\tilde{\Omega}^2\vec{p}}{H_{\mathrm{D}}^{3+1}}\, t + \left(\vec{\alpha} - \frac{2\eta\Delta\tilde{\Omega}\vec{p}}{H_{\mathrm{D}}^{3+1}}\right)\frac{i\hbar\eta\Delta\tilde{\Omega}}{H_{\mathrm{D}}^{3+1}}\left(e^{2iH_{\mathrm{D}}^{3+1}t/\hbar} - 1\right), \tag{19}$$

the *Zitterbewegung* frequency can be estimated in the simulation as

$$\omega_{\mathrm{ZB}} \approx 2|\bar{E}_{\mathrm{D}}|/\hbar \equiv 2\sqrt{4\eta^2\Delta^2\tilde{\Omega}^2 p_0^2/\hbar^2 + \Omega^2} \approx 2\sqrt{N\eta^2\tilde{\Omega}^2 + \Omega^2}, \tag{20}$$

where $\bar{E}_{\mathrm{D}} \equiv \langle H_{\mathrm{D}}\rangle$ is the average energy, p_0 is the average momentum for a peaked distribution, and $N \equiv \langle a^\dagger a\rangle$ is the phonon number, respectively. Additionally, one can estimate the *Zitterbewegung* amplitude to be

$$R_{\mathrm{ZB}} = \frac{\hbar}{2mc}\left(\frac{mc^2}{E}\right)^2 = \frac{\eta\hbar^2\tilde{\Omega}\Omega\Delta}{4\eta^2\tilde{\Omega}^2\Delta^2 p_0^2 + \hbar^2\Omega^2}, \tag{21}$$

and $R_{\mathrm{ZB}} \approx \Delta$, if $\eta\tilde{\Omega} \sim \Omega$, which can be measurable in an experiment, as was shown in the 1+1 case in Ref. [10].

4 Klein paradox simulation in trapped ions

The Klein paradox is another counterintuitive feature of the relativistic quantum mechanics solutions of Dirac equation. A Dirac fermion that propagates freely until it encounters a potential barrier, may tunnel through the barrier unimpeded regardless of the fact that the potential may be extended until arbitrarily long distances. The reason for this is that the positive energy electron may become, upon collision with the barrier, a negative energy electron and as such propagate freely throughout the barrier, wherever the potential barrier is $V \geq 2mc^2$. The standard explanation in Quantum Field Theory is that there is enough energy in the system to produce a particle/antiparticle pair.
The theoretical proposal [12] and experimental realization [13] of the simulation of Klein paradox in 1+1 dimensions, was based on the Hamiltonian

$$\mathcal{H}_{\mathrm{D}}^{Kl,1+1} = c\sigma_x p_x + mc^2\sigma_z + \alpha x, \tag{22}$$

where α is the potential gradient constant.
The Klein paradox has been simulated in 1+1 dimensions by using two trapped ions. The center of mass mode together with the internal degrees of freedom of one of them simulates the positive and negative energy spinors, while the second one implements the external potential that produces the Klein paradox [12, 13].
In order to measure the motional state of the ions in the previous simulations, the standard approach is to couple the motion to the internal states of one ion, and then apply fluorescence detection to measure the internal state, as is customary in trapped ion technology. For details see [55, 9, 10]
The Dirac equation with a covariant potential [54] can be written as

$$\left[-i\hbar\partial\!\!\!/ - mc - \frac{1}{c}V_{cov}\right]\psi = 0, \tag{23}$$

where we used Feynman's notation, $A\!\!\!/ = \gamma^\mu A_\mu$, being γ^μ the Dirac matrices and A_μ a four-vector. The external potential V_{cov} can take many forms that transform differently under Lorentz rotations and boosts. In particular, V_{cov} includes scalar potentials that add to the relativistic mass term, as well as pseudoscalar, electric and magnetic potentials, among other cases. Multiplying Eq. (23) by $\gamma^0 := \beta$, and introducing the vector of matrices $\vec{\alpha} = \gamma^0\vec{\gamma}$, the momentum operator $\vec{p} = -i\hbar\nabla$, and the time $t = x_0/c$, we obtain

$$i\hbar\partial_t\psi = \left[c\vec{\alpha}.\vec{p} + mc^2\beta + \beta V_{cov}\right]\psi. \tag{24}$$

Up to unitary transformations, there are different sets of matrices, α and β, determining different Dirac representations. In the case of $1+1$ dimensions, in particular, α and β can be chosen as any two different Pauli matrices. For simplicity, we will use a real representation,

$$\gamma^0 = \beta = \sigma_z,\ \gamma^1 = i\sigma_y,\ \alpha = \sigma_x. \tag{25}$$

There are six ways to introduce a potential in the Dirac equation [54], depending on its behavior under Lorentz transformations. Using the pseudoscalar operator $\gamma^5 := i\prod_\mu \gamma^\mu$ and the tensor $\sigma^{\mu\nu} := i\gamma^\mu\gamma^\nu$, these are

$$\begin{aligned} V_{cov} &= V + qA\!\!\!/ + B_{\mu\nu}\sigma^{\mu\nu} + q\gamma^5\tilde{V} + \\ &+ q\gamma^5\tilde{A\!\!\!/} + \tilde{B}_{\mu\nu}\gamma^5\sigma^{\mu\nu}. \end{aligned} \tag{26}$$

The potential V transforms as a scalar and mimics an induced mass term. The field A transforms as a four-vector and corresponds to the electromagnetic potential acting on a charge q, with the electric potential $A_0 = \phi$ and a three-vector component $\vec{A}$. The remaining four potentials $B, \tilde{A}, \tilde{V}$ and $\tilde{B}$, transform as matrices, pseudoscalars, pseudovectors, and pseudotensors, respectively, and behave as anomalous field moments [54].
In $1+1$ dimensions the landscape simplifies considerably and we can choose a parametrization such that

$$\begin{aligned} i\hbar\partial_t\psi &= \left[c\sigma_x\left(p - \frac{q}{c}A\right) + q\phi + (mc^2 + V)\sigma_z - q\tilde{V}\sigma_y\right]\psi \\ &= H(q)\psi, \end{aligned} \tag{27}$$

where only A, ϕ, V, and $\tilde{V}$ are nonzero. We will first focus on potentials that are linear in the particle position

$$V = \upsilon_{sc}x,\ \phi = \upsilon_{el}x/e,\ A = \upsilon_{mag}x/e,\ \text{and}\ \tilde{V} = \upsilon_{ps}x/e, \tag{28}$$

where e is the unit charge, and we will assume $q = \pm e$.
All the preceding potentials can be simulated with trapped ions. Let us consider a string of two trapped ions, 1 and 2, which could be $^{40}Ca^{+}$ ions with long-lived internal states $|S_{1/2}, m = 1/2\rangle$ and $|D_{5/2}, m = 3/2\rangle$. The first ion will encode a Dirac spinor in those internal states, while the second ion will be used as an ancilla to implement potentials. Assuming the validity of the Lamb-Dicke approximation, addressed laser beams can be used to implement interactions of the forms $H_c = \hbar\tilde{\Omega}(\sigma_j^+ e^{i\phi} + \sigma_j^- e^{-i\phi})$ (carrier), $H_r = \hbar\eta\tilde{\Omega}_r(a\sigma_j^+ e^{i\phi_r} + a^\dagger\sigma_j^- e^{-i\phi_r})$ (red sideband) and $H_b = \hbar\eta\tilde{\Omega}_b(a^\dagger\sigma_j^+ e^{i\phi_b} + a\sigma_j^- e^{-i\phi_b})$ (blue sideband) on each ion $j = 1, 2$. Here, $\tilde{\Omega}_{(b,r)}$ and $\phi_{(b,r)}$ are the Rabi frequency and phase of each light field, $\eta \ll 1$ is the Lamb-Dicke parameter and σ_j^+ (σ_j^-) and $a^\dagger$ (a) are raising (lowering) operators for the ion's internal states and for a collective motional mode. For the one-dimensional case, we could use, for instance, the center-of-mass mode.
As shown in [9, 10], the Dirac Hamiltonian for a free particle, $H_D^{\text{free}} = c\sigma_x\hat{p} + mc^2\sigma_z$, can be engineered using a simultaneous blue and red sideband interaction of equal strength with the appropriate relative phase, amplitude and detuning $\hbar\Omega := mc^2$. Here, $\hat{p} = i\hbar\frac{a^\dagger - a}{2\Delta}$, $\Delta = \sqrt{\hbar/4\tilde{m}\omega}$ is the size of the ground state wave packet, $\tilde{m}$ is the mass of a single ion and ω is the trap frequency. We consider the laser coupled only to the internal state of ion 1 (see Fig. 1) and show how to extend this model to include each of the potentials V, $\tilde{V}$, A, and ϕ.
The potentials A and $\tilde{V}$ can be created simultaneously by changing the phase and the intensity of the sidebands. Note that the total Hamiltonian $(c\sigma_x\hat{p} - e\sigma_x\upsilon_{mag}\hat{x} - e\upsilon_{ps}\hat{x}\sigma_y)$, with $\hat{x} = (a^\dagger + a)\Delta$, can be decomposed in terms of $a^\dagger\sigma^\pm$, and $a\sigma^\pm$. For the implementation of the scalar potential, we can use two additional light fields acting on ion 1 with Rabi frequency $\tilde{\Omega}_{sc}$, one blue detuned by $\omega/2$ from the spinor transition, the other red detuned by the same amount to create a Hamiltonian term $4\hbar\eta\Omega_{sc}^2\hat{x}\sigma_1^z/\omega\Delta$ [56]. Alternatively, we can choose another representation in which the mass term acquires the Pauli matrix σ_y. In this case, the term mc^2 is created by a carrier excitation, whereas the scalar potential can be engineered from blue and red sidebands in the same way as A and $\tilde{V}$. Finally, the electrostatic field can be implemented by driving a blue and red sideband simultaneously on the auxiliary ion. With appropriate phases the resulting Hamiltonian term becomes $\propto \sigma_2^x\hat{x}$. Preparing the auxiliary ion in an eigenstate of σ_2^x, this operator can be replaced by its eigenvalue and the interaction reduces to the desired form. A general Hamiltonian for this system that can be compared to Eq. (27), in the rotating

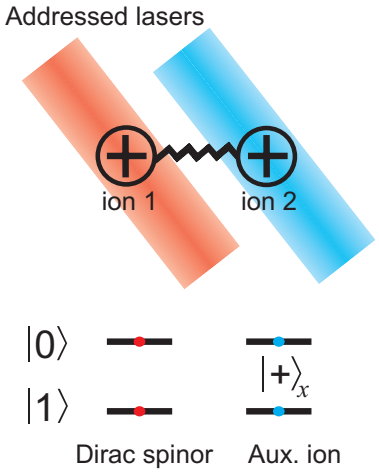

Fig. 3: *Setup for simulating a Dirac particle in an external potential. A string of two trapped ions is manipulated with addressed laser beams, coupling to each ion's internal state and the collective motion. The Hamiltonian for a free Dirac particle and the potentials A, V and $\tilde{V}$ can be implemented directly by the laser light impinging on ion 1. The electrostatic potential ϕ is implemented by red and blue sidebands applied to the auxiliary ion to create an interaction $\propto \sigma_2^x \hat{x}$, with the auxiliary ion prepared in an eigenstate of σ_2^x.*

frame and after rotating-wave approximation, reads

$$\begin{aligned} H = \quad & \hbar\eta \left(\tilde{\Omega}_b e^{i\phi_b} a^\dagger \sigma_1^+ + \tilde{\Omega}_r e^{i\phi_r} a \sigma_1^+ + \text{H.c.} \right) \\ & + \hbar\eta \tilde{\Omega}_2 \sigma_2^x \hat{x}/\Delta + \hbar(\Omega + 4\eta\Omega_{sc}^2 \hat{x}/\omega\Delta)\sigma_1^z. \end{aligned} \tag{29}$$

Here, the first two terms with their Hermitian conjugates describe blue and red motional sidebands, the term involving the second ion describe a conditional displacement, and the last term involves constant and position-dependent Stark shifts. The relations between the Dirac model in Eq. (27) and the ion system in Eq. (29) are

$$\hbar\Omega = mc^2, \quad \hbar\eta\tilde{\Omega}_2/\Delta = \upsilon_{el}, \quad 4\hbar\eta\Omega_{sc}^2/\omega\Delta = \upsilon_{sc}, \tag{30}$$

while the relative weights of c, υ_{mag}, and υ_{ps}, can be set by changing phases $\phi_{b,r}$ and amplitudes $\Omega_{r,b}$.

The creation of an electrostatic potential via a detuned laser acting on ion 2 yields the interesting case of interaction terms $\hbar\eta\tilde{\Omega}_2\hat{x}\sigma_2^x/\Delta + \hbar\Omega_2\sigma_2^z$. For a large detuning $\Omega_2 \gg \eta\tilde{\Omega}_2$ this interaction becomes effectively $\propto \hat{x}^2\sigma_2^z$, allowing the simulation of quadratic potentials [57].

Electric potential and Klein tunneling.- Not all potentials can actually confine a Dirac particle. To prove this let us introduce an antiunitary operation known as charge conjugation $\psi_c = K\psi = C\psi^\star$, combining complex conjugation and a unitary matrix $C\gamma^{\mu\star}C^{-1} = -\gamma^\mu$. The charge conjugate spinor satisfies a Dirac equation with opposite charge $i\hbar\partial_t\psi_c = H(-q)\psi_c$, in which certain terms of the covariant potential which are proportional to the charge "q" have

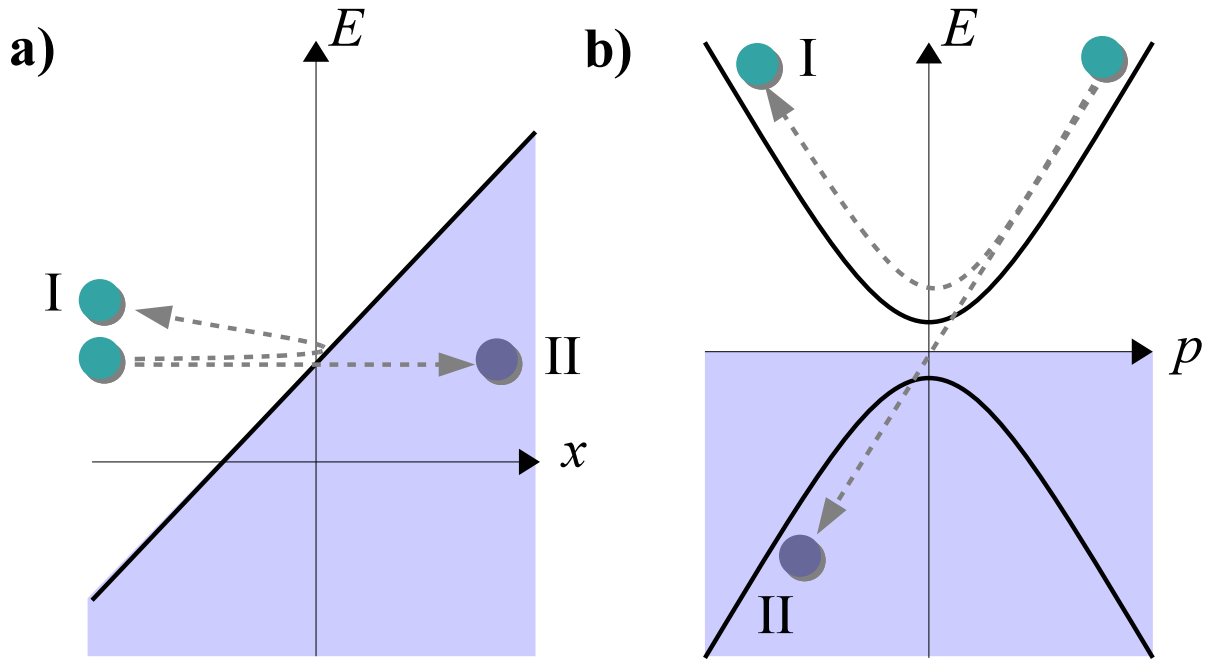

Fig. 4: *Klein tunneling in a repulsive potential, $\phi_{el}(x) = v_{el}x$. (a) In position space, the particle may bounce back (I) or enter the forbidden region by reducing its kinetic energy (II). (b) In momentum space, (I) and (II) correspond to the particle having positive energy or turning into an antiparticle.*

changed sign. We can also show that the negative energy branch of a Dirac equation can be antiunitarily related to the positive energy branch with opposite charge $KH(q)K^{-1} = -H(-q)$. In other words, the negative energy branch of the Dirac spectrum are indistinguishable from particles with opposite charge. Moreover, these antiparticles will see certain components of the covariant potential, $A, \tilde{V}, \tilde{A}$, with opposite sign as for their positive energy counterparts.

The fact that positive and negative energy states see different effective potentials, and that both components are coupled, allows the apparition of the so-called Klein paradox [54]. The electric potential in Eq. (28) is repulsive for positive-energy charged particles in a large region, $(q/e)v_{el}x > 0$, but it will allow the antiparticle or negative energy states tunnel into a region that would be forbidden in the (Schrödinger) nonrelativistic regime (see Fig. 4). The situation is even more interesting, for if we send a massive charged positive-energy particle against an electrostatic potential barrier and the particle has enough energy, it will split into a positive and negative wavepackets, the former bouncing back and the latter penetrating into the energy barrier (see Fig. 5).

We explain now how Klein tunneling can be interpreted in terms of a quantum optical concept: the Landau-Zener tunneling [58]. Working in momentum space, where $x = (+i\hbar\partial_p)$, and with charge $q = e$, the electric potential $v_{el}x$ is equivalent to a deceleration or a decrease in the particle momentum, which can be compensated using the change of variables $\psi(p,t) = \xi(p + v_{el}t)$,

$$i\hbar\partial_t\xi = [c\sigma_x(p - v_{el}t) + mc^2\sigma_z]\xi. \tag{31}$$

This equation corresponds exactly to a Landau-Zener process in which an effective magnetic field along the x direction is increased linearly in time.

The dynamics is summarized in Fig. 4. If the particle initially moves against the slope, that is

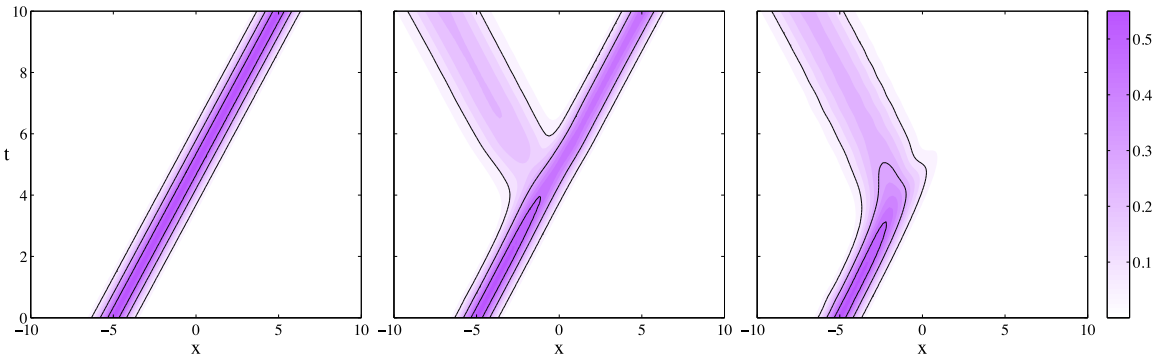

Fig. 5: *Scattering events for three effective masses,* $m = 0, 0.5$ *and* 1 *(left to right). We plot the total probability density as a function of space* x *and time* t*. We have used natural units* $c = \hbar = 1$*, and a fixed potential slope* $cv_{el} = 1$*.*

$p > 0$, the potential will decelerate the particle which may (I) bounce back or (II) tunel inside the potential barrier. The first case corresponds to adiabatic transition in the Landau-Zener picture, it happens when the change of the momentum is small, $\hbar c|v_{el}| \ll m^2c^4$, and is the typical behavior of nonrelativistic particles. However, for large enough slope or in the relativistic limit, it becomes possible for the particle to switch branch, acquiring negative kinetic energy and entering the originally forbidden region. More precisely, the probability of transition can be computed with the Landau-Zener formula as follows

$$P_{II} = \exp\left(-2\pi \frac{m^2c^4}{2\hbar c v_{el}}\right). \tag{32}$$

Note that once the particle has switched to negative energy states, it has an opposite charge and the potential ϕ_{el} accelerates the particle indefinitely in the opposite direction. This makes such a potential effectively a filter that separates particles from antiparticles.
Using Eq. (31), it is easy to perform numerically accurate simulations of the Klein scattering for arbitrary initial conditions and different ratios of the potential slope, $m^2c^4/\hbar c v_{el}$. In Fig. 5, we see that for very small masses the particle is either not confined, or it splits into a negative charge and a positive charge components [Fig. 5b]. In the nonrelativistic limit, $m^2c^4 \gg \hbar c v_{el}$, though, the particle mostly bounces back from the barrier. The first plot corresponds only to situation II, the second plot combines I and II, and finally the third situation is just I.

Scalar potential.- As we discussed above, the Klein paradox only applies to potentials which are not invariant under charge conjugation. A scalar potential [59] such as V in Eq. (26), acting similarly on both particle and antiparticle states, can still confine and reproduce the physics we are used to in the nonrelativistic limit. In particular for our choice of linearly growing potential $V = v_{sc}x$, with $v_{el}, v_{mag}, v_{ps} = 0$, it is possible to show the existence of bound orbits. This is best analyzed by squaring the effective Hamiltonian,

$$H^2 = cp^2 + (v_{sc}x + mc^2)^2 + c\hbar v_{sc}\sigma_y. \tag{33}$$

The first implication is that the scalar potential eigenenergies correspond to those of a harmonic oscillator

$$E^2 = 2\hbar c v_{sc}\left(n + \frac{1}{2} \pm 1\right). \tag{34}$$

The second implication is that the conserved quantity H^2 is defining elliptical orbits in the phase space of position and momentum $\{x, p\}$, once more as a harmonic oscillator but these orbits are now centered around the point $x = mc^2/\upsilon_{sc}$. These closed and bound orbits exist both for the Dirac particles and antiparticles, implying that both are confined around the same trajectories.

Pseudoscalar potential and Dirac oscillator.- The last analyzed case is the pseudo-scalar term $\upsilon_{ps} x \sigma_y$ with $\upsilon_{ps} = m\omega c$. There is a similarity between

$$H = c(\sigma_x p + \sigma_y m\omega x) + mc^2\sigma_z \tag{35}$$

and the Hamiltonian of a $1+1$ Dirac oscillator [20],

$$i\hbar\partial_t\psi = \left[c\vec{\alpha}(\vec{p} + im\omega\beta\vec{x}) + mc^2\beta\right]\psi, \tag{36}$$

but this coincidence only happens because of our restricted dimensionality, $\gamma^5 = \alpha\beta$. With the oscillator length scale, $a_{osc} = \sqrt{\hbar/m\omega}$, and the Rabi frequency $\hbar\Omega = \sqrt{\hbar\omega mc^2}$, the pseudoscalar potential can be reformulated as a detuned Jaynes-Cummings model

$$i\hbar\partial_t\psi = \left[\hbar\Omega(i\sigma_- a^\dagger - i\sigma_+ a) + mc^2\sigma_z\right]\psi, \tag{37}$$

which should be easy to simulate. A similar calculation as before produces again closed phase space orbits

$$\frac{1}{m\omega}p^2 + x^2 m\omega + \hbar\sigma_z = E^2, \tag{38}$$

which are a consequence of the JC discrete spectrum

$$E_n = \pm mc^2\sqrt{n\frac{\hbar\omega}{mc^2} + 1} \sim mc^2 + \frac{1}{2}n\omega\hbar. \tag{39}$$

Note also that a replacement of $\omega \to -\omega$ is still a Dirac oscillator, but then it turns into an anti-JC Hamiltonian.

Discussion.- We have considered the quantum simulation of the Dirac equation without and with potentials in trapped ions, bringing together the physics of relativistic quantum mechanics to a controllable tabletop experiment in quantum optics. Our simulation protocols can be combined with tools for monitoring and preparing the quantum state of the ions. In particular, newly developed techniques [55, 10] make it possible to obtain the position, momentum and probability distribution $|\psi(x)|^2$ of the particle in an efficient way, allowing the "frame-by-frame" reconstruction of the scattering event. Besides this, the initial state of the Dirac particle can be accurately engineered in position, momentum and even energy branch [10]. This is important for the electrostatic potential because, by preparing a particle with positive energy, we could see a full reflection for shallow slopes and full transmission for steeper slopes, making the Klein paradox visible. As an example, similar to Ref. [13], one could prepare a positive energy wave packet with average momentum $\hat{p} = 4\hbar/\Delta$ and choose experimentally accessible parameters $\tilde{\Omega}_b = \tilde{\Omega}_r = 2\pi\times$ 20 kHz, $\Omega_1 = 2\pi\times$ 1 kHz, $\eta = 0.05$ and $\tilde{\Omega}_2 = 2\pi\times$ 50 kHz. This permits to obtain a tunneling probability of 0.5 which could be observed in the lab. Numerical simulations show that the whole tunneling dynamics with these parameters takes place within 1 ms, which is well within the motional and internal state coherence time. To study the Klein tunneling, see the case of electric potential and Fig. 5, the slope strength of the mass of the simulated particle can be varied by changing laser intensities and frequencies.

5 Quantum simulation of quantum fields in trapped ions

Quantum field theories (QFTs) are among the most successful descriptions of the physical reality, giving rise to the Standard Model of elementary particles. There are different approaches to analize QFTs, of which one of the most prominent is the Dyson series expansion in perturbation theory obtaining the well-known Feynman diagrams formalism [53]. However, certain theories and parameter regimes cannot be analyzed in perturbation theory, like the strong coupling regime in which the coupling parameter is so large that perturbative methods fail. Quantum chromodynamics, for example, cannot be studied in this way for low energies or long distances. New techniques have been developed for overcoming these difficulties, as lattice gauge theory computations.

Here, we study a scalable quantum simulation of interacting bosonic and fermionic quantum field modes in trapped ions [46]. We consider first the case of a fermion and an antifermion field modes interacting via a bosonic field mode. This simplified model includes already some of the particular features of QFTs: particle creation and annihilation, self interactions and dressed states, and the possibility to study nonperturbative regimes. One of the main advantages of this proposal is that our quantum simulation is an unitary processes, thus, we are taking into account the effect of all Feynman diagrams in the simulated processes.

We will study a model under the following assumptions: i) 1+1 dimensions; ii) scalar fermions and bosons; iii) one fermionic, one antifermionic, and one bosonic field modes. These considerations purport to make a realistic proposal with current trapped-ion experiments. Using conditions i) and ii), we begin by considering a multimode bosonic and fermionic coupled system, with Hamiltonian ($\hbar = c = 1$)

$$\mathcal{H} = \int dp\, \omega(\hat{b}_p^\dagger \hat{b}_p + \hat{d}_p^\dagger \hat{d}_p) + \int dk\, \omega_k\, \hat{a}_k^\dagger \hat{a}_k + g \int dx\, \hat{\psi}^\dagger(0,x)\hat{\psi}(0,x)\hat{A}(0,x), \quad (40)$$

where the fermionic and bosonic fields are, in interaction picture with respect to $\int dp\, \omega(\hat{b}_p^\dagger \hat{b}_p + \hat{d}_p^\dagger \hat{d}_p) + \int dk\, \omega_k\, \hat{a}_k^\dagger \hat{a}_k$,

$$\hat{\psi}(t,x) = \frac{1}{\sqrt{2\pi}} \int dp \left(\hat{b}_p e^{-i\omega t} e^{ipx} + \hat{d}_p^\dagger e^{i\omega t} e^{-ipx} \right), \quad (41)$$

$$\hat{A}(t,x) = \frac{1}{\sqrt{2\pi}} \int dk \left(\hat{a}_k e^{-i\omega_k t} e^{ikx} + \hat{a}_k^\dagger e^{i\omega_k t} e^{-ikx} \right), \quad (42)$$

and a_k are the bosonic annihilation operators that follow the commutation rules $[\hat{a}_k, \hat{a}_{k'}^\dagger] = \delta(k - k')$ while $\hat{b}_p(\hat{d}_p)$ are fermionic(antifermionic) annihilation operators that obey the anticommutation rules $\{\hat{b}_p, \hat{b}_{p'}^\dagger\} = \delta(p - p')$ and $\{\hat{d}_p, \hat{d}_{p'}^\dagger\} = \delta(p - p')$. Including spinors and polarization amounts to incorporating additional modes and couplings, to be addressed with a many mode extension.

In the interaction picture of Eqs. (41) and (42), the Hamiltonian reads,

$$\mathcal{H} = g \int dx\, \hat{\psi}^\dagger(t,x)\hat{\psi}(t,x)\hat{A}(t,x). \quad (43)$$

This is a simplified version of the QED Hamiltonian, allowing also the description of Yukawa interactions and the coupling of fermions to the Higgs field.

Assumption iii) amounts to introducing two *comoving* fermionic and antifermionic modes, see Appendix. A. They will create single-excitation incoming wave packets when applied to the vacuum, at every time t in the Schrödinger picture,

$$\hat{b}^{\dagger,\mathrm{Sch.}}_{\mathrm{in}} = \int dp\, \mathcal{G}_f(p_f,p)\hat{b}^\dagger_p e^{-i\omega t}, \tag{44}$$

$$\hat{d}^{\dagger,\mathrm{Sch.}}_{\mathrm{in}} = \int dp\, \mathcal{G}_{\bar{f}}(p_{\bar{f}},p)\hat{d}^\dagger_p e^{-i\omega t}. \tag{45}$$

Here, $\mathcal{G}_{f,\bar{f}}(p_{f,\bar{f}},p)$ are the fermionic (f) and antifermionic ($\bar{f}$) envelopes of the incoming wave packets, that we consider as Gaussians centered in the average momenta, $p_{f,\bar{f}}$, with distant average initial positions. However, the shape of this functions admit any other form, depending on the initial state that we want to describe. We introduce these propagating modes instead of the standard momentum eigenstates, given that the latter are delocalized over all space and are less realistic than the normalizable wave packets for describing physical particles. Although we deal with localized fermions, we consider a delocalized bosonic mode. In this way, we will have pair creation/annihilation processes and self interactions by considering just one bosonic field mode for the ease of experimental realization, see Fig. 6. Expanding the fermion field (41)

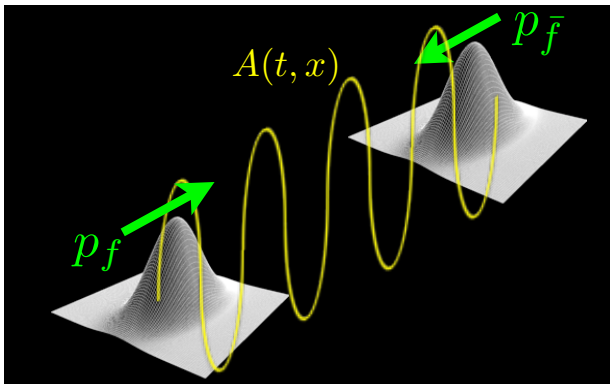

Fig. 6: *Scheme of the ingredients of our model. We consider two fermionic wavepackets, with certain average momenta p_f and $p_{\bar{f}}$, and a delocalized bosonic mode mediating the interaction between fermions and antifermions.*

in terms of these modes, and dropping the remaining anticommuting modes that complete the basis (not populated at lowest order) see Appedix. A, we get, in the interaction picture,

$$\hat{\psi}(t,x) \;=\; \tilde{\mathcal{G}}_f(p_f,x,t)\hat{b}_{\mathrm{in}}e^{i(p_f x-\omega_f t)} + \tilde{\mathcal{G}}_{\bar{f}}(p_{\bar{f}},x,t)\hat{d}^\dagger_{\mathrm{in}}e^{-i(p_{\bar{f}}x-\omega_{\bar{f}}t)}, \tag{46}$$

where the modes $\hat{b}^\dagger_{\mathrm{in}} = \int dp\, \mathcal{G}_f(p_f,p)\hat{b}^\dagger_p$ and $\hat{d}^\dagger_{\mathrm{in}} = \int dp\, \mathcal{G}_{\bar{f}}(p_{\bar{f}},p)\hat{d}^\dagger_p$ do not depend on time. Here,

$$\tilde{\mathcal{G}}_f(p_f,x,t) = \frac{1}{\sqrt{2\pi}}\int dp\, \mathcal{G}_f(p_f,p)e^{i[(p-p_f)x-(\omega-\omega_f)t]}, \tag{47}$$

$$\tilde{\mathcal{G}}_{\bar{f}}(p_{\bar{f}},x,t) = \frac{1}{\sqrt{2\pi}}\int dp\, \mathcal{G}^*_{\bar{f}}(p_{\bar{f}},p)e^{-i[(p-p_{\bar{f}})x-(\omega-\omega_{\bar{f}})t]}, \tag{48}$$

are Fourier transforms, where we consider the ultrarelativistic limit, for simplicity, in which $\omega_{f,\bar{f}} = |p_{f,\bar{f}}|$. With this simplification, all time and space dependence in Eq. (43) will be encoded in $\tilde{\mathcal{G}}_f(p_f,x,t)$, $\tilde{\mathcal{G}}_{\bar{f}}(p_{\bar{f}},x,t)$, representing Gaussian wave packets that propagate in space-time, and in the time- and space-dependent phases that are associated to energy and momentum conservation.

The bosonic field will, in addition, be written as

$$\hat{A}(t,x) = \hat{a}_0 e^{-i\omega_0 t} e^{ik_0 x} + \hat{a}_0^\dagger e^{i\omega_0 t} e^{-ik_0 x}. \tag{49}$$

Consequently, the resulting interaction Hamiltonian is

$$\mathcal{H} = g \sum_{i,j=f,\bar{f}} \mathcal{F}^{i,j}(p_i, p_j, k_0, t)\, \hat{\theta}_{p_i}^{i\dagger} \hat{\theta}_{p_j}^{j}\, \hat{a}_0 + \text{H.c.}, \tag{50}$$

where $\{\hat{\theta}_{p_i}^{i}\}_{i=f,\bar{f}} = \hat{b}_{\text{in}}, \hat{d}_{\text{in}}^\dagger$, and

$$\begin{aligned}
\mathcal{F}^{f,f}(p_f, p_f, k_0, t) &= \left(\int dx |\tilde{\mathcal{G}}_f(p_f, x, t)|^2 e^{ik_0 x} \right) e^{-i\omega_0 t}, \\
\mathcal{F}^{\bar{f},\bar{f}}(p_{\bar{f}}, p_{\bar{f}}, k_0, t) &= \left(\int dx |\tilde{\mathcal{G}}_{\bar{f}}(p_{\bar{f}}, x, t)|^2 e^{ik_0 x} \right) e^{-i\omega_0 t}, \\
\mathcal{F}^{f,\bar{f}}(p_f, p_{\bar{f}}, k_0, t) &= \Bigg(\int dx \tilde{\mathcal{G}}_f(p_f, x, t)^* \tilde{\mathcal{G}}_{\bar{f}}(p_{\bar{f}}, x, t) \\
&\times e^{-i(p_f + p_{\bar{f}} - k_0)x} \Bigg) e^{i(\omega_f + \omega_{\bar{f}} - \omega_0)t}.
\end{aligned} \tag{51}$$

For practical purposes, we consider $|k_0| \ll \omega_0$, i.e., a slow massive boson. We may then approximate $\mathcal{F}^{f,f}(p_f, p_f, k_0, t) = \mathcal{F}^{\bar{f},\bar{f}}(p_{\bar{f}}, p_{\bar{f}}, k_0, t) = g_1 \exp(-i\omega_0 t)$, and $\mathcal{F}^{f,\bar{f}}(p_f, p_{\bar{f}}, k_0, t) = g_2 \exp[-(t - T/2)^2/(2\sigma_t^2) + i\delta t]$, where g_2/g_1 gives the relative strength of the pair creation with respect to the self-interaction, $\delta = \omega_f + \omega_{\bar{f}} - \omega_0$ and T is the total time of the process, being σ_t the temporal interval of the interaction region. Thus, the self-interactions are always on, while the pair creation and annihilation take place only when the fermion and antifermion wavepackets overlap, as they should. Accordingly, the Hamiltonian we aim to simulate is

$$\mathcal{H} = g_1 e^{-i\omega_0 t} \left(\hat{b}_{\text{in}}^\dagger \hat{b}_{\text{in}} \hat{a}_0 + \hat{d}_{\text{in}} \hat{d}_{\text{in}}^\dagger \hat{a}_0 \right) + g_2 e^{-\frac{(t-T/2)^2}{2\sigma_t^2}} \left[e^{i\delta t} \hat{b}_{\text{in}}^\dagger \hat{d}_{\text{in}}^\dagger \hat{a}_0 + e^{-i(2\omega_0 + \delta)t} \hat{d}_{\text{in}} \hat{b}_{\text{in}} \hat{a}_0 \right] + \text{H.c.} \tag{52}$$

We propose to implement this Hamiltonian dynamics in a system of two trapped ions, see Fig. 7a. The bosonic mode will be encoded in the center-of-mass (COM) vibronic mode of the two-ion system. We envision to map the 4-dimensional Hilbert space associated to the fermionic/antifermionic operators onto 4 internal levels of the first ion. For this, we consider a Jordan-Wigner mapping, $\hat{b}_{\text{in}}^\dagger = \hat{I} \otimes \hat{\sigma}^+$, $\hat{b}_{\text{in}} = \hat{I} \otimes \hat{\sigma}^-$, $d_{\text{in}}^\dagger = \hat{\sigma}^+ \otimes \hat{\sigma}_z$, $\hat{d}_{\text{in}} = \hat{\sigma}^- \otimes \hat{\sigma}_z$, and encode it in four internal levels of the first ion, $|1\rangle$, $|2\rangle$, $|3\rangle$, $|4\rangle$, e.g., $b_{\text{in}}^\dagger = |4\rangle\langle 3| + |2\rangle\langle 1|$, $\hat{d}_{\text{in}}^\dagger = |4\rangle\langle 2| - |3\rangle\langle 1|$, the vacuum state is state $|1\rangle$, and $|f\rangle = |2\rangle$, $|\bar{f}\rangle = -|3\rangle$, $|f, \bar{f}\rangle = -|4\rangle$. Accordingly, Hamiltonian (52) results in

$$\begin{aligned}
\mathcal{H} \;=\; & -g(t) \Big(|4\rangle\langle 1|\, \hat{a}_0 e^{i\delta t} + |1\rangle\langle 4|\, \hat{a}_0^\dagger e^{-i\delta t} \Big) \\
& -g(t) \Big(|1\rangle\langle 4|\, \hat{a}_0 e^{-i(2\omega_0 + \delta)t} + |4\rangle\langle 1|\, \hat{a}_0^\dagger e^{i(2\omega_0 + \delta)t} \Big) \\
& -g_1 \Big(|3\rangle\langle 3| - |2\rangle\langle 2| \Big) \Big(\hat{a}_0 e^{-i\omega_0 t} + \hat{a}_0^\dagger e^{i\omega_0 t} \Big) \\
& +g_1\, \hat{I} \left(\hat{a}_0 e^{-i\omega_0 t} + \hat{a}_0^\dagger e^{i\omega_0 t} \right).
\end{aligned} \tag{53}$$

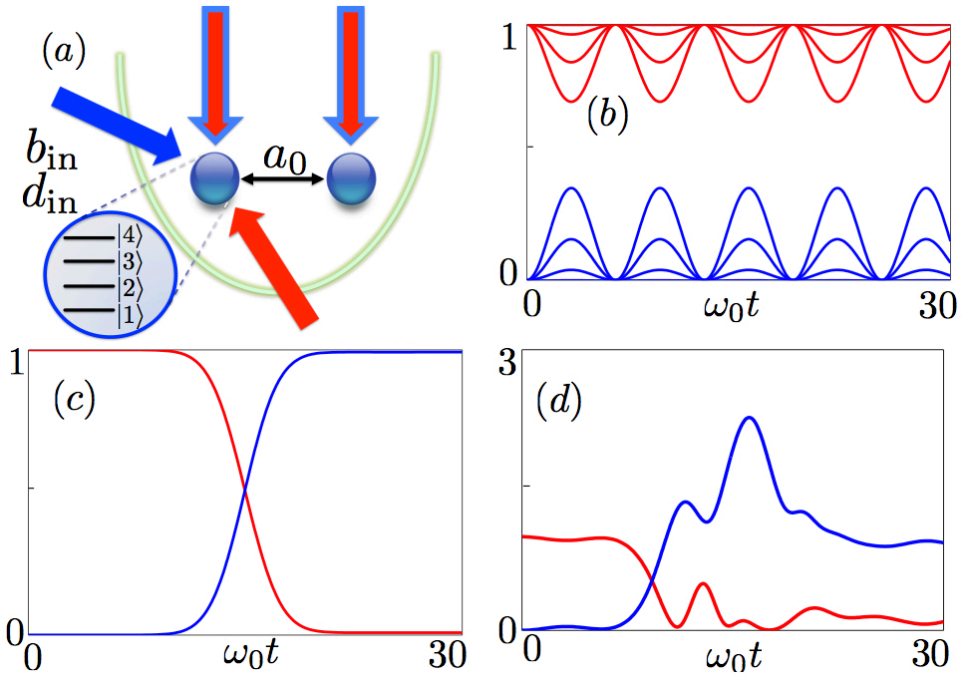

Fig. 7: *(a) Setup for the trapped-ion simulation. (b)* $|\langle f,0,0|\psi(t)_1\rangle|^2$ *as a function of* t *in units of* ω_0 *(red/upper curves), where* $|\psi(t)_1\rangle$ *is the evolved state from* $|\psi(0)_1\rangle = |f,0,0\rangle$*, and average number of virtual bosons (blue/lower curves),* $\langle a_0^\dagger a_0\rangle$*, for* $g_1 = 0.15\omega_0, 0.1\omega_0, 0.05\omega_0, 0.01\omega_0$*,* $g_2 = 0$*. The largest amplitudes correspond to the largest couplings. (c)* $|\langle f,\bar{f},0|\psi(t)_2\rangle|^2$ *as a function of* t *in units of* ω_0 *(red/upper left curve), where* $|\psi(t)_2\rangle$ *is the evolved state from* $|\psi(0)_2\rangle = |f,\bar{f},0\rangle$*, and average number of virtual bosons (blue/lower left curve),* $\langle a_0^\dagger a_0\rangle$*, for* $g_1 = 0.01\omega_0$*,* $g_2 = 0.21\omega_0$*,* $\sigma_t = 3/\omega_0$*,* $T = 30/\omega_0$*,* $\delta = 0$*. (d) The same as (c) for* $g_1 = 0.1\omega_0$*,* $g_2 = \omega_0$*,* $\sigma_t = 4/\omega_0$*,* $T = 30/\omega_0$*,* $\delta = 0$*.*

Here, the first line corresponds to a detuned red sideband interaction between $|4\rangle$ and $|1\rangle$ with time-dependent Rabi frequency $g(t) = g_2 \exp[-(t-T/2)^2/2\sigma_t^2]$. The second line is a detuned blue sideband interaction, between the same levels and with the same Rabi frequency. The third line can be developed applying detuned red and blue sideband interactions to $|3\rangle$ and $|2\rangle$ to produce $(|3\rangle\langle 2| - |2\rangle\langle 3|)[\hat{a}_0 \exp(-i\omega_0 t) + \hat{a}_0^\dagger \exp(i\omega_0 t)]/i$, and a rotation of $|3\rangle$ and $|2\rangle$ with a classical field to produce the change $(|3\rangle\langle 2| - |2\rangle\langle 3|)/i \longrightarrow (|3\rangle\langle 3| - |2\rangle\langle 2|)$. These operations are equivalent to a rotation from $\hat{\sigma}_y$ to $\hat{\sigma}_z$ in the subspace of $|3\rangle$ and $|2\rangle$ and, therefore, not affecting the other Hamiltonian terms. To implement the last line we could just periodically drive the trap, but this method is only applicable to the COM mode. The alternative scalable approach that we propose, applicable to any mode, consists of applying to the second ion detuned red and blue sidebands to generate the term $g_1\ \hat{\sigma}_x[\hat{a}_0 \exp(-i\omega_0 t) + \hat{a}_0^\dagger \exp(i\omega_0 t)]$ where the matrix $\hat{\sigma}_x$ corresponds to the second ion internal levels. Preparing this ion into an eigenstate of $\hat{\sigma}_x$, i.e $\hat{\sigma}_x|\psi\rangle = \pm|\psi\rangle$, we produce the desired interaction $\hat{a}_0 \exp(-i\omega_0 t) + \hat{a}_0^\dagger \exp(i\omega_0 t)$. Note that in the limit of large $|t|$ in Eq. (53), we could also study the spectrum properties in a straightforward manner.

We have numerically analyzed some of the features that could be simulated in the experiment: *i) Fermion self-interaction–*. In Fig. 7b, we show the self-energy processes of a single fermion, which emits and reabsorbs bosons as it evolves. The average number of emitted bosons grows with the coupling. Accordingly, what is observed is emission and reabsorption of the bosons at a period which goes as $2\pi/\omega_0$, where ω_0 is in our case the simulated boson frequency. *ii) Pair creation/annihilation–*. In Fig. 7c, we show how a fermion/antifermion pair is annihilated, giving rise to a boson. *iii) Nonperturbative regime–*. For large g_2 values, $g_2 \geq \omega_0$, we enter into the nonperturbative regime, in which Feynman-diagram techniques are of little help. Here, we obtain that the number of created bosons is much larger due to the nonresonant terms (see Fig. 7d). The dynamics becomes more complex and dependent on the specific coupling values.

6 Acknowledgments

I would want to thank valuable discussions from Jorge Casanova, Antonio Mezzacapo, and Lucas Lamata. I acknowledge funding from MINECO FIS2012-36673-C03-02, Basque Government IT472-10, and UPV/EHU UFI 11/55 grants; and also from SOLID, CCQED, PROMISCE, and SCALEQIT European projects.

Appendices

A Comoving modes formalism

We begin by defining the input comoving mode for the electronic field in the Schrödinger picture. In this case, the operator that depends on time is defined such that, at every t, it creates the state at time t when acting upon the vacuum. We consider a scalar theory of fermions, discarding for the moment the spinors, where things get more elaborate, given that one would have to consider double number of modes and 2×2 matrices for the Rabi frequencies. This incoming electronic field reads

$$\hat{b}_{\rm in}^{\dagger} = \sum_{p} \Omega(p_{0k}, p)\hat{b}_{p}^{\dagger}e^{-i\omega t}, \tag{54}$$

and the corresponding incoming positronic field

$$\hat{d}_{\rm in}^{\dagger} = \sum_{p} \Omega(p_{0k}, p)\hat{d}_{p}^{\dagger}e^{-i\omega t}. \tag{55}$$

Note that we are using $\sum$ instead of $\int$, this is just for the sake of clarity and of course you can replace the sum by the integral at any moment.
Now, we expand the field $\hat{\psi}(x)$ in terms of these incoming modes and commuting modes. The latter will not be populated initially and, although they could populate virtual levels, we will neglect them in the two-mode approximation. When including additional fermionic modes, the theory will approach more to usual QED.
In order to expand the field in these modes, we compute the corresponding anticommutators (notice that we are working in the Schrödinger picture, and the field does not evolve in time),

$$\hat{\psi}(x) = \sum_{p} (e^{ipx}\hat{b}_{p} + e^{-ipx}\hat{d}_{p}^{\dagger}), \tag{56}$$

$$\{\hat{\psi}(x), \hat{b}^{\dagger}_{\rm in}\} = \sum_p \Omega(p_{0k}, p) e^{i(px-\omega t)}, \tag{57}$$

$$\{\hat{\psi}(x), \hat{d}_{\rm in}\} = \sum_p \Omega(p_{0k}, p) e^{-i(px-\omega t)}. \tag{58}$$

Then, if we expand the field $\hat{\psi}(x)$ in terms of $\hat{b}_{\rm in}$, $\hat{d}^{\dagger}_{\rm in}$, and additional anticommuting modes that will not be populated to lowest order, we have

$$\hat{\psi}(x) = c_b \hat{b}_{\rm in} + \hat{c}_d d^{\dagger}_{\rm in} + \text{anticommuting modes}. \tag{59}$$

Consequently, $c_b = \{\hat{\psi}(x), \hat{b}^{\dagger}_{\rm in}\}$, and $c_d = \{\hat{\psi}(x), \hat{d}_{\rm in}\}$, given in Eqs. (57) and (58). Accordingly, $\hat{\psi}(x)$ will be, in the Schrödinger picture,

$$\hat{\psi}(x) = \Omega^{e^-}(p_{0k}, x, t)\hat{b}_{\rm in}(t) + \Omega^{e^+}(p_{0k}, x, t)\hat{d}^{\dagger}_{\rm in}(t), \tag{60}$$

where

$$\Omega^{e^-}(p_{0k}, x, t) = \sum_p \Omega(p_{0k}, p) e^{i(px-\omega t)}, \tag{61}$$

$$\Omega^{e^+}(p_{0k}, x, t) = \sum_p \Omega(p_{0k}, p) e^{-i(px-\omega t)}, \tag{62}$$

and, changing into the interaction picture, we will have

$$\hat{b}_{\rm in}(t) \to \hat{U}\hat{b}_{\rm in}(t)\hat{U}^{\dagger} = \hat{b}_{\rm in}(0), \tag{63}$$

$$\hat{d}_{\rm in}(t) \to \hat{U}\hat{d}_{\rm in}(t)\hat{U}^{\dagger} = \hat{d}_{\rm in}(0). \tag{64}$$

Thus, both phases cancel out when changing to the interaction picture.
Dropping the "(0)' in the operators notation from now on, we obatin the field in the interaction picture, expressed in terms of the incoming (comoving) modes,

$$\hat{\psi}(x,t) = \Omega^{e^-}(p_{0k}, x, t)\hat{b}_{\rm in} + \Omega^{e^+}(p_{0k}, x, t)\hat{d}^{\dagger}_{\rm in}, \tag{65}$$

where now all the spatial and time dependence is codified in the coefficients.
Given that the mode envelopes $\Omega(p_{0k}, p)$ are assumed to be peaked around p_{0k}, we extract the phases oscillating with p_{0k} and ω_{0k} as in the previous Section, by multiplying and dividing by them.
We redefine the operators

$$\tilde{\Omega}^{e^-}(p_{0k}, x, t) = \sum_p \Omega(p_{0k}, p) e^{i[(p-p_{0k})x-(\omega-\omega_{0k})t]} \tag{66}$$

and

$$\tilde{\Omega}^{e^+}(p_{0k}, x, t) = \sum_p \Omega(p_{0k}, p) e^{-i[(p-p_{0k})x-(\omega-\omega_{0k})t]}. \tag{67}$$

This acquires full justification in the case of Gaussian wave packets, in which

$$\Omega^{e^-}(p_{0k},x,t) = \int_p dp e^{-(p-p_0)^2/\sigma_p^2} e^{i[px-\omega t]} = \int_p' dp' e^{-(p'/\sigma_p)^2} e^{i(p'+p_0)x-(\omega'+\omega_0)t} \propto e^{-[(x-t)/\sigma_x]^2} e^{i(p_0x-\omega_0 t)}, \quad (68)$$

where the approximation of only positive momenta was made (right mover), and the ultrarelativistic limit in which $\omega = |p|$ was considered. Thus, these phases emerge naturally in this case. The approximation of the scalar particle wave packet as a Gaussian is a valid one, and slight variations of this kind of wave packet will introduce in principle small modifications. In this way, we may consider the extraction of these phases in general, although for very different wave packets one should compute the Fourier transform, and extract the x-dependent complex phase appearing in the result. And, accordingly, the final expression for the field reads

$$\hat{\psi}(x,t) = \tilde{\Omega}^{e^-}(p_{0k},x,t)\hat{b}_{\rm in}e^{i(p_{0k}x-\omega_{0k}t)} + \tilde{\Omega}^{e^+}(p_{0k},x,t)\hat{d}_{\rm in}^\dagger e^{-i(p_{0k}x-\omega_{0k}t)}. \quad (69)$$

Note that the same could be done with more modes which anticommute among themselves.

References

[1] R. P. Feynman, Int. J. Theor. Phys. **21**, 467 (1982).

[2] S. Lloyd, Science **273**, 1073 (1996).

[3] I. Buluta and F. Nori, Science **362**, 108 (2009).

[4] M. Johanning, A. F. Varón, and C. Wunderlich, J. Phys. B **42**, 154009 (2009).

[5] C. Schneider, D. Porras, and T. Schaetz, Rep. Prog. Phys. **75**, 024401 (2012).

[6] L. J. Garay, J. R. Anglin, J. I. Cirac, and P. Zoller, Phys. Rev. Lett. **85**, 4643 (2000).

[7] P. M. Alsing, J. P. Dowling, and G. J. Milburn, Phys. Rev. Lett. **94**, 220401 (2005).

[8] R. Schützhold, M. Uhlmann, L. Petersen, H. Schmitz, A. Friedenauer, and T. Schätz, Phys. Rev. Lett. **99**, 201301 (2007).

[9] L. Lamata, J. León, T. Schätz, and E. Solano, Phys. Rev. Lett. **98**, 253005 (2007).

[10] R. Gerritsma, G. Kirchmair, F. Zähringer, E. Solano, R. Blatt, and C. F. Roos, Nature **463**, 68 (2010).

[11] E. Schrödinger, Sitz. Preuss. Akad. Wiss. Phys.-Math. Kl. **24**, 418 (1930).

[12] J. Casanova, J. J. García-Ripoll, R. Gerritsma, C. F. Roos, and E. Solano, Phys. Rev. A **82**, 020101 (2010).

[13] R. Gerritsma, B. P. Lanyon, G. Kirchmair, F. Zähringer, C. Hempel, J. Casanova, J. J. García-Ripoll, E. Solano, R. Blatt and C. F. Roos, Phys. Rev. Lett. **106**, 060503 (2011).

[14] O. Klein, Z. Phys. **53**, 157 (1929).

[15] J. Casanova, C. Sabín, J. León, I. L. Egusquiza, R. Gerritsma, C. F. Roos, J. J. García-Ripoll, and E. Solano, Phys. Rev. X **1**, 021018 (2011).

[16] J. Schliemann, D. Loss, and R. M. Westervelt, Phys. Rev. Lett. **94**, 206801 (2005).

[17] M. I. Katsnelson, K. S. Novoselov, and A. K. Geim, Nature Phys. **2**, 620 (2006).

[18] J. Cserti and G. Dávid, Phys. Rev. B **74**, 172305 (2006).

[19] T. M. Rusin and W. Zawadzki, Phys. Rev. B **80**, 045416 (2009).

[20] A. Bermudez, M. A. Martin-Delgado, and E. Solano, Phys. Rev. A **76** 041801 (2007).

[21] J. Y. Vaishnav and C. W. Clark, Phys. Rev. Lett. **100**, 153002 (2008).

[22] M. Merkl, F. E. Zimmer, G. Juzeliunas, and P. Öhberg, Europhys. Lett. **83**, 54002 (2008).

[23] N. Goldman, A. Kubasiak, A. Bermudez, P. Gaspard, M. Lewenstein, and M. A. Martin-Delgado, Phys. Rev. Lett. **103**, 035301 (2009).

[24] Q. Zhang, J. Gong, and C. H. Oh, Phys. Rev. A **81**, 023608 (2010).

[25] L. Lepori, G. Mussardo, and A. Trombettoni, Europhys. Lett. **92**, 50003 (2010).

[26] D. Witthaut, T. Salger, S. Kling, C. Grossert and M. Weitz, Phys. Rev. A **84**, 033601 (2011).

[27] T. Salger, C. Grossert, S. Kling, M. Weitz, Phys. Rev. Lett. **107**, 240401 (2011).

[28] J. Otterbach, R. G. Unanyan, and M. Fleischhauer, Phys. Rev. Lett. **102**, 063602 (2009).

[29] L.-G. Wang, Z.-G. Wang, and S.-Y. Zhu, Europhys. Lett. **86**, 47008 (2009).

[30] X. Ling, Z. Tang, H. Luo, H. Dong, Z. Luo, S. Wen, and D. Fan, eprint arXiv:1010.4602

[31] S.-L. Zhu, D.-W. Zhang, and Z. D. Wang, Phys. Rev. Lett. **102**, 210403 (2009).

[32] Z.-Y. Wang, C.-D. Xiong, and Q. Qiu, Phys. Rev. A **80**, 032118 (2009).

[33] S. Arunagiri, eprint arXiv:0911.0975

[34] S. Longhi, Opt Lett. **35**, 235 (2010).

[35] G. Dávid and J. Cserti, Phys. Rev. B **81**, 121417 (2010).

[36] A. J. Brizard, eprint arXiv:1010.5710

[37] S. Longhi, J. Phys. B **43**, 205402 (2010).

[38] F. Dreisow, M. Heinrich, R. Keil, A. Tünnermann, S. Nolte, S. Longhi, and A. Szameit, Phys. Rev. Lett **105**, 143902 (2010).

[39] K. Wang, T. Liu, M. Feng, W. Yang, and K. Wang, Phys. Rev. A **82**, 064501 (2010).

[40] T. M. Rusin and W. Zawadzki, Phys. Rev. D **82**, 125031 (2010).

[41] A. Bermudez, L. Mazza, M. Rizzi, N. Goldman, M. Lewenstein, and M. A. Martin-Delgado, Phys. Rev. Lett. **105**, 190404 (2010).

[42] N. Szpak and R. Schützhold, Phys. Rev. A **84**, 050101(R) (2011).

[43] O. Boada, A. Celi, J. I. Latorre, and M. Lewenstein, New J. Phys. **13**, 035002 (2011).

[44] J. I. Cirac, P. Maraner, and J. Pachos, Phys. Rev. Lett. **105**, 190403 (2010).

[45] F. L. Semiao and M. Paternostro, Quant. Inf. Process., to appear.

[46] J. Casanova, L. Lamata, I. L. Egusquiza, R. Gerritsma, C. F. Roos, J. J. García-Ripoll, and E. Solano, Phys. Rev. Lett. **107**, 260501 (2011).

[47] J. Casanova, A. Mezzacapo, L. Lamata, and E. Solano, Phys. Rev. Lett. **108**, 190502 (2012).

[48] A. Mezzacapo, J. Casanova, L. Lamata, and E. Solano, Phys. Rev. Lett. **109**, 200501 (2012).

[49] T. G. Tenev and N. V. Vitanov, Phys. Rev. A **86**, 052114 (2012).

[50] J. S. Pedernales, R. Di Candia, D. Ballester, E. Solano, eprint arXiv:1211.3953

[51] W. Zawadzki and T. M. Rusin, J. Phys. Condens. Matter **23**, 143201 (2011).

[52] D. Leibfried, R. Blatt, C. Monroe, and D. Wineland, Rev. Mod. Phys. **75**, 281 (2003).

[53] M. E. Peskin and D. V. Schroeder, *Quantum Field Theory* (Westview Press, 1995).

[54] B. Thaller, *The Dirac Equation* (Springer-Verlag, Berlin, 1992).

[55] P. Lougovski, H. Walther, and E. Solano, Eur. Phys. J. D **38**, 423 (2006).

[56] K. Kim, C.F. Roos, L. Aolita, H. Häffner, V. Nebendahl and R. Blatt, Phys. Rev. A **77**, 050303(R) (2008).

[57] R. Giachetti and V. Grecchi, Phys. Rev. A **80**, 032107 (2009).

[58] F. Sauter, Z. Phys. **69**, 742 (1931).

[59] J. B. Hiller, Am. J. of Phys. **70**, 522 (2002).

C 3 Entanglement and Exchange in Correlated Electron Systems [1]

Erik Koch
Computational Materials Science
German Research School for Simulation Sciences
52425 Jülich

Contents

1 Introduction **2**

2 Coulomb exchange **4**

3 Kinetic exchange **6**
3.1 A toy model 6
3.2 Direct exchange 7
3.3 Second quantization 9
3.4 Mean-field treatment 11
3.5 Superexchange 12
3.6 Ferromagnetic superexchange 15

4 Orbital-ordering **17**

5 Conclusion **19**

A Down-folding **20**

B Pauli matrices **21**

[1] Lecture Notes of the 44^{th} IFF Spring School "Quantum Information Processing" (Forschungszentrum Jülich, 2013). All rights reserved.

1 Introduction

One of the early suggestions of the power of quantum computers was made by Richard Feynman at the 1st conference on the Physics of Computation held at MIT in 1981. Addressing the problem of efficiently *Simulating Physics with Computers*, he concluded [1]

> Nature isn't classical, dammit, and if you want to make a simulation of Nature, you'd better make it quantum mechanical, and by golly it's a wonderful problem, because it doesn't look so easy.

The fundamental problem making simulations of quantum many-body problems on classical computers so hard is the exponential size of the associated Hilbert space combined with the possibility of forming entangled states [2]. These complications are the very reason why chemistry and condensed-matter physics are still fields of intense research: Already shortly after the formulation of quantum mechanics, Dirac [3] observed that

> The underlying laws necessary for the mathematical theory of a large part of physics and the whole of chemistry are thus completely known, and the difficulty is only that exact applications of these laws lead to equations which are too complicated to be soluble.

To understand why, consider the example of a single atom of iron. Having 26 electrons, its wave function $\Psi(\mathbf{r}_1, \mathbf{r}_2, \ldots, \mathbf{r}_{26})$ is a function of 78 coordinates. What does it take to store such a wave function? If we record Ψ on a grid with merely ten values per coordinate, we would have to store 10^{78} values. There is not enough matter in the visible universe for storing even such a ridiculously crude representation of the wave function of a single atom of iron. Hence straightforward classical simulations are not just *too complicated*, they are a practical impossibility in the known universe.

We are, of course not really interested in the full complexity of the many-body wave function for it's own sake. It evidently contains more information than we could ever digest. We use it, however, as a computational tool for (classically) calculating the properties of actual atoms, molecules, or solids. This suggests one way a quantum computer could simulate quantum many-body systems efficiently: it could build an internal representation of the wave function, but need only output the small number of observables that actually are of interest to us.

A similar technique is the basis of a very successful approach used in materials simulations: density-functional theory (DFT) [4]. It reduces the complexity from dealing with the many-body wave function of $3N$ variables to working with the electron density $n(\mathbf{r})$, a function of only 3 variables. With such an approach efficient classical simulations can be done. The complication of the many-body physics is, of course, largely hidden in the density-functional. In practice only approximate density-functionals are known. The most successful route to constructing approximate density-functionals is via a mapping of the interacting system onto a non-interacting reference system. In this Kohn-Sham framework, already very simple approaches like the local-density approximation (LDA) result in functionals of surprising accuracy for wide classes of materials. The basis of their success is the Aufbauprinzip, which is firmly built into the functional via the filling of the single-electron levels of the reference system.

Such methods fail, however, to capture, even qualitatively, the essential physics of systems with strong correlations. For these the Coulomb repulsion becomes so important that electrons do their utmost to avoid each other in real space. This means that they can no longer be described as

moving independently in an average potential created by the other electrons. Instead, the behavior of one electron depends in a crucial way on the actual position of all the other electrons. In such a situation where the electrons become entangled, the picture of individual electrons, that forms the basis of the Kohn-Sham picture of density-functional theory breaks down completely.

Strong correlations are seen in materials where the Coulomb interaction is of the same order of, or larger than the kinetic energy. Examples are the open d- and f-shells of transition metal oxides. Since these orbitals are very localized, the Coulomb repulsion between the electrons in the same orbital is significant. Another important class of correlated materials are organic crystals. They are built from weakly interacting molecules. Accordingly their bands are so narrow that even though the Coulomb interaction in the relatively extended molecular orbitals is not particularly large, it is of the same order of the small kinetic energy.

Understanding the physics of strongly correlated systems is one of the grand challenges of modern condensed-matter physics. Modern simulations of correlated materials are based on the LDA+DMFT approach [5, 6]. The technique proceeds in two steps. First, density-functional calculations are performed to obtain an effective single-electron model of the correlated material under consideration. In the second step this model, augmented with the crucial Coulomb terms between the correlated electrons, is solved using non-perturbative many-body methods. For being realistic, such many-body simulations necessarily have to take advantage of the largest available (so far classical) supercomputers.

In the present lecture we will focus, however, not on the features that distinguish different correlated materials. Instead we will discuss general mechanisms that show the essence of strong correlations, namely how electrons behave in the presence of strong Coulomb repulsion. Surprisingly, together with the Pauli principle, the spin-independent Coulomb interaction and electron hopping can lead to strong magnetic coupling between correlated electrons and hence to the entanglement of electron spins.

Compared to the complexity of the many-body problem, the basic mechanisms of this exchange coupling are rather simple: Since many-body wave functions must change sign under the permutation of Fermions, electrons of the same spin cannot be at the same position. Electrons of like spin thus tend to avoid each other, i.e., the probability of finding them close to each other tends to be lower than for electrons of opposite spin (exchange hole). In that sense the Coulomb energy between two electrons depends on their relative spins. By this argument, aligning electron spins tends be energetically favorable. This *Coulomb exchange*, discussed in Sec. 2, is the basis of Hund's first rule. When more than one atom is involved, electrons can hop from one site to its neighbor. This kinetic term is, again, modified by the Pauli principle, as the hopping from an orbital to the neighboring orbital will only be possible, if there is not already an electron of the same spin occupying that orbital, and, of course, by the Coulomb repulsion among the electrons. This is the idea of *kinetic exchange*, which we explore in Sec. 3. While conceptually simple, this direct exchange mechanism is rarely found in real materials. There the hopping between correlated orbitals is not direct but via an intermediate weakly correlated orbital. In such a situation the *superexchange* mechanism is active. The derivation is very similar to that of kinetic exchange. However, the number of states involved, makes explicit book-keeping tedious. To simplify our work, we introduce second quantization as a simple notation of many-electron states. Finally we show that exchange is not restricted to coupling spins, but can also produce interactions between orbital occupations (Sec. 4).

2 Coulomb exchange

The Coulomb repulsion between electrons,

$$H_U = \sum_{i<j} \frac{1}{|\vec{r}_i - \vec{r}_j|}\,, \tag{1}$$

is manifestly spin-independent. Nevertheless, because of the antisymmetry of the many-electron wave function, the eigen-energies of H_U depend on the spin. This is the basis of the multiplet structure in atoms and of Hund's first two rules.
To understand the mechanism of this Coulomb exchange we consider a simple two-electron model. In the spirit of the tight-binding approach [7], we assume that we have solved the two-electron Hamiltonian H_0, replacing the interaction term H_U, e.g. as a self-consistent potential $\sum_i U(\vec{r}_i)$, obtaining an orthonormal set of one-electron eigen-states $\varphi_\alpha(\vec{r})$ with eigen-values ε_α. We now ask for the effect of re-introducing the interaction $H_U - \sum_i U(\vec{r}_i)$. The largest changes we will find for states that are degenerate.
Let us consider two orbitals $\alpha = a,\, b$. Then the two-electron Slater determinants with spins σ and σ'

$$\begin{aligned}\Psi_{a,\sigma;\,b\sigma'}(\vec{r}_1,s_1;\,\vec{r}_2,s_2) &= \frac{1}{\sqrt{2}}\begin{vmatrix}\varphi_a(\vec{r}_1)\,\sigma(s_1) & \varphi_a(\vec{r}_2)\,\sigma(s_2)\\ \varphi_b(\vec{r}_1)\,\sigma'(s_1) & \varphi_b(\vec{r}_2)\,\sigma'(s_2)\end{vmatrix}\\ &= \frac{1}{\sqrt{2}}\Big(\varphi_a(\vec{r}_1)\,\varphi_b(\vec{r}_2)\;\sigma(s_1)\,\sigma'(s_2) - \varphi_b(\vec{r}_1)\,\varphi_a(\vec{r}_2)\;\sigma'(s_1)\,\sigma(s_2)\Big)\end{aligned} \tag{2}$$

are degenerate eigen-states of H_0 with eigen-value $\varepsilon_a + \varepsilon_b$, independent of the spin orientations. To see how this degeneracy is lifted, we calculate the matrix elements of H_U in the basis of the Slater determinants $\Psi_{a,\sigma;\,b\sigma'}$.
When both electrons have the same spin ($\sigma = \sigma'$), we can factor out the spin functions

$$\Psi_{a,\sigma;\,b\sigma} = \frac{1}{\sqrt{2}}\Big(\varphi_a(\vec{r}_1)\varphi_b(\vec{r}_2) - \varphi_b(\vec{r}_1)\varphi_a(\vec{r}_2)\Big)\;\sigma(s_1)\sigma(s_2) \tag{3}$$

and obtain

$$\left\langle \Psi_{a,\sigma;\,b,\sigma}\left|\frac{1}{|\vec{r}_1-\vec{r}_2|}\right|\Psi_{a,\sigma;\,b,\sigma}\right\rangle = \frac{1}{2}\,(U_{ab} - J_{ab} - J_{ba} + U_{ba}) = U_{ab} - J_{ab} \tag{4}$$

where the direct terms are the Coulomb integral

$$U_{ab} = \int d^3r_1 \int d^3r_2\, \frac{|\varphi_a(\vec{r}_1)|^2\;|\varphi_b(\vec{r}_2)|^2}{|\vec{r}_1-\vec{r}_2|} \tag{5}$$

while the cross terms give the exchange integral

$$J_{ab} = \int d^3r_1 \int d^3r_2\, \frac{\overline{\varphi_a(\vec{r}_1)}\,\varphi_b(\vec{r}_1)\;\overline{\varphi_b(\vec{r}_2)}\,\varphi_a(\vec{r}_2)}{|\vec{r}_1-\vec{r}_2|}\,. \tag{6}$$

For the states where the electrons have opposite spin ($\sigma' = -\sigma$)

$$\left\langle \Psi_{a,\sigma;\,b,-\sigma}\left|\frac{1}{|\vec{r}_1-\vec{r}_2|}\right|\Psi_{a,\sigma;\,b,-\sigma}\right\rangle = U_{ab} \tag{7}$$

the diagonal matrix element has no exchange contribution, as the overlap of the spin functions for the cross terms vanish. There are however off-diagonal matrix elements coupling the two states

$$\left\langle \Psi_{a\uparrow;\,b\downarrow} \left| \frac{1}{|\vec{r}_1 - \vec{r}_2|} \right| \Psi_{a\downarrow;\,b\uparrow} \right\rangle = -J_{ab} \ . \tag{8}$$

Since H_U does not change the spins, these are the only non-zero matrix elements. In the basis of the states $\Psi_{\uparrow\uparrow}$, $\Psi_{\uparrow\downarrow}$, $\Psi_{\downarrow\uparrow}$ and $\Psi_{\downarrow\downarrow}$ the Coulomb term is thus given by

$$H_U = \begin{pmatrix} U_{ab} - J_{ab} & 0 & 0 & 0 \\ 0 & U_{ab} & -J_{ab} & 0 \\ 0 & -J_{ab} & U_{ab} & 0 \\ 0 & 0 & 0 & U_{ab} - J_{ab} \end{pmatrix} . \tag{9}$$

The triplet states $\Psi_{\uparrow\uparrow}$ and $\Psi_{\downarrow\downarrow}$ are obviously eigen-states of H_U with eigen-energy

$$\Delta\varepsilon_{\text{triplet}} = U_{ab} - J_{ab} \ . \tag{10}$$

Diagonalizing the 2×2 submatrix, we obtain the third triplet state $(\Psi_{\uparrow\downarrow} + \Psi_{\downarrow\uparrow})/\sqrt{2}$ and the singlet state $(\Psi_{\uparrow\downarrow} - \Psi_{\downarrow\uparrow})/\sqrt{2}$

$$\frac{1}{\sqrt{2}}\left(\Psi_{\uparrow\downarrow} - \Psi_{\downarrow\uparrow}\right) = \frac{1}{\sqrt{2}}\Big(\varphi_a(\vec{r}_1)\varphi_b(\vec{r}_2) + \varphi_b(\vec{r}_1)\varphi_a(\vec{r}_2)\Big)\ \frac{1}{\sqrt{2}}\Big(|\downarrow\uparrow\rangle - |\uparrow\downarrow\rangle\Big) \tag{11}$$

with energy

$$\Delta\varepsilon_{\text{singlet}} = U_{ab} + J_{ab} \ . \tag{12}$$

Thus the exchange interaction in the sector with $S_z = 0$ produces maximally entangled eigen-states.

To see whether the triplet or the singlet is lower in energy, we need to know the sign of the exchange matrix element. While the Coulomb integral U_{ab}, having a positive integrand, is obviously positive, it is less obvious that also $J_{ab} > 0$. Introducing $\Phi(\vec{r}) = \overline{\varphi_a(\vec{r})}\varphi_b(\vec{r})$ and rewriting the integral using the convolution theorem as well as the Fourier transform of $1/r$, we obtain [8, 9]:

$$J_{ab} = \int d^3r_1\, \overline{\Phi(\vec{r}_1)} \underbrace{\int d^3r_2\, \frac{1}{|\vec{r}_1 - \vec{r}_2|}\, \Phi(\vec{r}_2)}_{=\int dk\, e^{ikr_1}\, 4\pi/k^2 \Phi(k)\,/(2\pi)^3} \tag{13}$$

$$= \frac{1}{(2\pi)^3} \int d^3k \underbrace{\int d^3r_1\, e^{i\vec{k}\cdot\vec{r}_1} \overline{\Phi(\vec{r}_1)}}_{=\overline{\Phi(-k)}}\, \Phi(\vec{k}\,)\, \frac{4\pi}{k^2} \tag{14}$$

$$= \frac{1}{(2\pi)^3} \int d^3k\, |\Phi(\vec{k}\,)|^2\, \frac{4\pi}{k^2} > 0 \tag{15}$$

Thus the triplet states are below the singlet state by an energy $2J_{ab}$. If the φ_α are degenerate atomic orbitals, this is an example of Hund's first rule: For an atomic shell, the lowest state will have maximum spin.

3 Kinetic exchange

When electron-hopping plays the main role in the exchange mechanism, we speak of kinetic exchange. In contrast to Coulomb exchange the resulting interactions are usually antiferromagnetic, i.e., they prefer antiparallel spins. The physical principle of kinetic exchange can be understood in a simple two-site system. We discuss this problem in some detail and introduce two key concept along the way: down-folding and second quantization. More realistic exchange mechanisms are then natural generalizations of this simple mechanism [10, 11, 12].

3.1 A toy model

As a toy model, we consider the minimal model of an H_2 molecule. We restrict ourselves to two (orthogonal) orbitals, φ_1 and φ_2, separated by some distance. If we add an electron to the system, that electron will be able to move between the two orbitals, with a matrix element $-t$. Because we allow the electron to only occupy two s-orbitals, the Hamiltonian is a 2×2 matrix

$$H = \begin{pmatrix} 0 & -t \\ -t & 0 \end{pmatrix} . \tag{16}$$

This tight-binding Hamiltonian is easily diagonalized giving the linear combinations

$$\varphi_\pm = \frac{1}{\sqrt{2}} \Big(\varphi_1 \pm \varphi_2 \Big) \tag{17}$$

as eigen-states with eigen-energies $\varepsilon_\pm = \mp t$. We have written the hopping matrix element as $-t$, so that for $t > 0$ the state without a node, φ_+, is the ground state.
Pictorially we can write the basis states by specifying which orbital the electron occupies. For a spin-up electron we then write

$$\varphi_1 = |\uparrow , \cdot \rangle \qquad \text{and} \qquad \varphi_2 = | \cdot , \uparrow \rangle \tag{18}$$

where we now represent the basis states by where the electron is located.
If there are two electrons in the system, i.e., one electron per orbital, we can again use basis states which just specify, which orbitals the electrons occupy. For two electrons of opposite spin we then find two states where the electrons are in different orbitals (covalent states)

$$|\uparrow , \downarrow\rangle \qquad |\downarrow , \uparrow\rangle$$

and two states where the electrons are in the same orbital (ionic states)

$$|\updownarrow , \cdot \rangle \qquad | \cdot , \updownarrow\rangle \, .$$

In this basis the Hamiltonian matrix for our simple model of the H_2 molecule has the form

$$H = \begin{pmatrix} 0 & 0 & -t & -t \\ 0 & 0 & +t & +t \\ -t & +t & U & 0 \\ -t & +t & 0 & U \end{pmatrix} \qquad \begin{matrix} |\uparrow , \downarrow\rangle \\ |\downarrow , \uparrow\rangle \\ |\updownarrow , \cdot \rangle \\ | \cdot , \updownarrow\rangle \end{matrix} \tag{19}$$

As before, moving an electron to a neighboring orbital gives a matrix element $-t$, with an additional sign when the order of the electrons is changed (Fermi statistics!). For the ionic states,

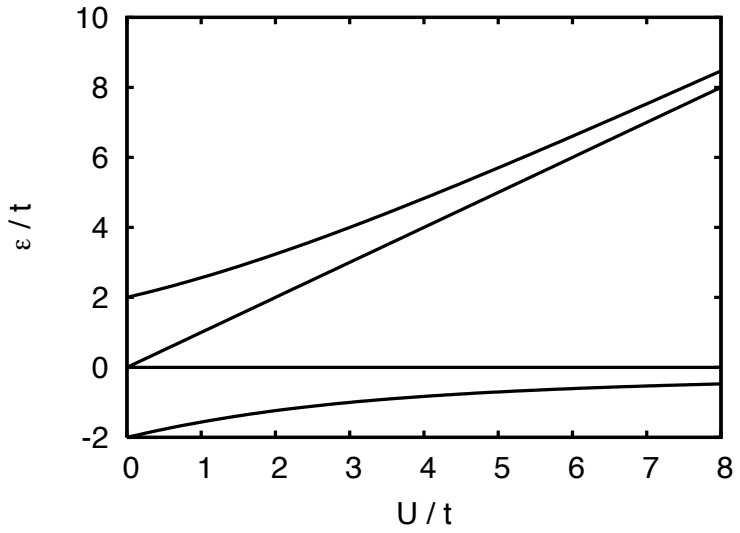

Fig. 1: *Spectrum of the two-site Hubbard model as a function of U. For large U there are two levels with energy close to zero. Their energy difference corresponds to the exchange energy. The remaining two states with ionic character have an energy roughly proportional to U.*

where both electrons are in the same orbital, we have the Coulomb matrix element U. Coulomb matrix elements involving electrons on different sites are, for reasonably large distance between the sites, negligible. So there is no Coulomb exchange, just the local Coulomb repulsion in our model. Diagonalizing H we find the energy spectrum (shown in figure 1) and the corresponding eigen-states:

$$\varepsilon_\pm = \frac{U}{2} \pm \frac{\sqrt{U^2 + 16\,t^2}}{2} \quad , \qquad \Psi_\pm = \frac{\Big(|\uparrow,\downarrow\rangle - |\downarrow,\uparrow\rangle - \frac{\varepsilon_\pm}{2t}\big[\,|\!\updownarrow,\,\cdot\,\rangle + |\,\cdot\,,\!\updownarrow\rangle\,\big]\Big)}{\sqrt{2 + \varepsilon_\pm^2/(2t^2)}}$$

$$\varepsilon_{\rm cov} = 0 \quad , \qquad \Psi_{\rm cov} = \frac{1}{\sqrt{2}}\Big(|\uparrow,\downarrow\rangle + |\downarrow,\uparrow\rangle\Big)$$

$$\varepsilon_{\rm ion} = U \quad , \qquad \Psi_{\rm ion} = \frac{1}{\sqrt{2}}\Big(|\!\updownarrow,\,\cdot\,\rangle - |\,\cdot\,,\!\updownarrow\rangle\Big)$$

As the Hamiltonian commutes with the total spin, its eigen-states are also eigen-states of $S^2_{\rm tot}$. This is most easily seen by realizing that the ionic states $|\!\updownarrow,\,\cdot\,\rangle$ and $|\,\cdot\,,\!\updownarrow\rangle$ are singlets, as is the covalent state $(|\uparrow,\downarrow\rangle - |\downarrow,\uparrow\rangle)/\sqrt{2}$, while $\Psi_{\rm cov} = (|\uparrow,\downarrow\rangle + |\downarrow,\uparrow\rangle)/\sqrt{2}$ together with the states $|\uparrow,\uparrow\rangle$ and $|\downarrow,\downarrow\rangle$ forms a spin triplet. The triplet states are degenerate.

3.2 Direct exchange

Again we have found that the energy of two-electron states depends on the relative spin of the electrons. To see this more clearly we analyze the limit when U is much larger than t. From Fig. 1 we see that there are two states with energies that increase with U. They are the states $\Psi_{\rm ion}$ and Ψ_+ that have considerable contributions of the ionic states. Then there are two states whose energy is close to zero. They are the states that have mainly covalent character. To find the energy and the character of these levels in the limit $U \to \infty$ we can just expand $\varepsilon_- \to -4t^2/U$ and $\varepsilon_+ \to U + 4t^2/U$. We thus see that while the purely covalent state, the spin-triplet state $\Psi_{\rm cov}$, is independent of U, Ψ_- has a slightly lower energy due to some small

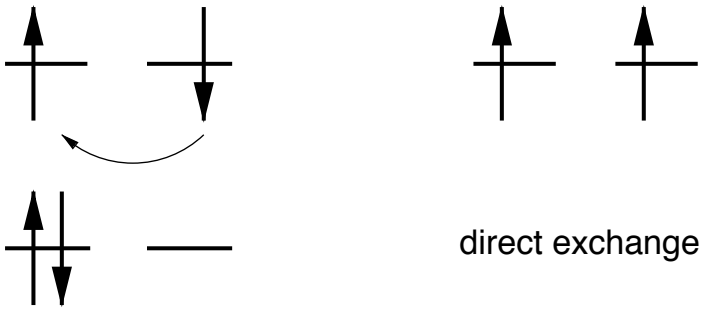

Fig. 2: *Simple picture of direct exchange: The antiparallel alignment of the spins (left) is favored, since it allows the electrons to hop to the neighboring site. For parallel spins (right) hopping is suppressed by the Pauli principle.*

admixture of the ionic states. In the limit $U \to \infty$ it becomes the maximally entangled state $(|\uparrow,\downarrow\rangle - |\downarrow,\uparrow\rangle)/\sqrt{2}$. We see that for large U, Ψ_- cannot be expressed, even approximately, as a Slater determinant. This failure of the mean-field approximation is further discussed in Sec. 3.4. It is the reason why strongly correlated systems are so difficult to describe.
A more instructive method to analyze the large-U limit, which is readily generalized to more complex situations, where we can no longer diagonalize the full Hamiltonian, is the down-folding technique. The mathematical background is explained in the appendix. The idea of down-folding is to partition the Hilbert space into parts that are of interest, here the low-energy convalent-type states, and states that should be projected out, in the present case the high-energy ionic states. With this partitioning we can view the Hamitonian matrix (19) as built of 2×2 submatrices. Calculating the inverse on the space of covalent states (see Eqn. (54) in the appendix) we find an *effective Hamiltonian* which now operates on the covalent states only:

$$H_{\text{eff}}(\varepsilon) = \begin{pmatrix} -t & -t \\ +t & +t \end{pmatrix} \begin{pmatrix} \varepsilon - U & 0 \\ 0 & \varepsilon - U \end{pmatrix}^{-1} \begin{pmatrix} -t & +t \\ -t & +t \end{pmatrix} \approx -\frac{2t^2}{U} \begin{pmatrix} 1 & -1 \\ -1 & 1 \end{pmatrix}. \qquad (20)$$

In the last step we have made an approximation by setting ε to zero, which is roughly the energy of the states with covalent character.
The process of eliminating the ionic states thus gives rise to an effective interaction between the covalent states, which was not present in the original Hamiltonian (19). Diagonalizing the effective Hamiltonian, we find

$$\varepsilon_s = -\frac{4t^2}{U} \quad , \qquad \Psi_s = \frac{1}{\sqrt{2}}\Big(|\uparrow,\downarrow\rangle - |\downarrow,\uparrow\rangle\Big)$$
$$\varepsilon_t = 0 \qquad , \qquad \Psi_t = \frac{1}{\sqrt{2}}\Big(|\uparrow,\downarrow\rangle + |\downarrow,\uparrow\rangle\Big)$$

These states correspond to the singlet and triplet states in the hydrogen molecule. Here the singlet-triplett splitting is $4t^2/U$. The other states in the triplet are those with two electrons of parallel spin: $|\uparrow,\uparrow\rangle$ and $|\downarrow,\downarrow\rangle$. They, of course, also have energy zero, as hopping is impossible due to the Pauli principle.
To understand the nature of the effective interaction in the low-energy Hamiltonian we observe that the off-diagonal matrix elements in (20) correspond to flipping the spin of both electrons

("exchange"). Remembering that

$$\vec{S}_1 \cdot \vec{S}_2 = S_1^z S_2^z + \frac{1}{2}\left(S_1^+ S_2^- + S_1^- S_2^+ \right) \tag{21}$$

we see that the effective interaction will contain a spin-spin coupling term.

3.3 Second quantization

A more systematic way for obtaining the form of the effective interaction is by using second quantization, which will also help us simplify our notation. In second quantization we use operators to specify in which orbital an electron is located. As an example, $c_{1,\uparrow}^\dagger$ puts a spin-up electron in orbital φ_1. Such an opperator is appropriately called a creation operator. Denoting the system with no electrons by $|0\rangle$, the (orthonormal) basis states that we have considered so far are written as

$$\begin{aligned} |\uparrow, \cdot\rangle &= c_{1\uparrow}^\dagger |0\rangle \\ |\cdot, \uparrow\rangle &= c_{2\uparrow}^\dagger |0\rangle \end{aligned}$$

for the single-electron states, and

$$\begin{aligned} |\uparrow, \downarrow\rangle &= c_{2\downarrow}^\dagger c_{1\uparrow}^\dagger |0\rangle \\ |\downarrow, \uparrow\rangle &= c_{2\uparrow}^\dagger c_{1\downarrow}^\dagger |0\rangle \\ |\updownarrow, \cdot\rangle &= c_{1\downarrow}^\dagger c_{1\uparrow}^\dagger |0\rangle \\ |\cdot, \updownarrow\rangle &= c_{2\downarrow}^\dagger c_{2\uparrow}^\dagger |0\rangle \end{aligned} \tag{22}$$

for the two-electron states.

As the wave functions describing indistinguishable electrons are antisymmetric under the exchange of two electrons, changing the order of the creation operators must result in a change of sign: $c_{i\sigma}^\dagger c_{j\sigma'}^\dagger = -c_{j\sigma'}^\dagger c_{i\sigma}^\dagger$. Using the notation $\{a, b\} = ab + ba$ this anticommutation relation is written as $\{c_{i\sigma}^\dagger, c_{j\sigma'}^\dagger\} = 0$. It immediately follows that $c_{i\sigma}^\dagger c_{i\sigma}^\dagger = 0$, i.e., that no two electrons can be in the same state, an expression of the Pauli principle.

Similar relations must hold for the adjoints of the creation operators. To see what the adjoint $c_{i\sigma}$ of the creation operator $c_{i\sigma}^\dagger$ does, we consider the norm of $c_{i\sigma}^\dagger|0\rangle$, i.e., the inner product with its adjoint $(c_{i\sigma}^\dagger|0\rangle)^\dagger = \langle 0|c_{i\sigma}$. Since the state is normalized, we get

$$\langle 0|c_{i\sigma} c_{i\sigma}^\dagger|0\rangle = 1 = \langle 0|0\rangle \,. \tag{23}$$

As the creation operator $c_{i\sigma}^\dagger$ puts an electron of spin σ in orbital φ_i, its adjoint must be removing this electron again. Thus $c_{i\sigma}$ is called an annihilation operator. In particular, we have $c_{i\sigma}|0\rangle = 0$. More generally, trying to put an electron into a state that is already occupied or trying to remove one from an unoccupied state will result in zero.

Obviously it makes a difference whether we first create an electron in a certain state and then take it out of the system again or whether we perform the operations in the reverse order. In particular, the operator $n_{i\sigma} = c_{i\sigma}^\dagger c_{i\sigma}$ will result in zero when operating on a basis state that does not have an electron of spin σ in orbital φ_i, while it returns the basis state unchanged if it has the orbital φ_i occupied with an electron of spin σ. Thus $n_{i\sigma}$ is called the occupation

number operator. On the other hand, applying $c_{i\sigma}c^\dagger_{i\sigma}$, obtained by reversing the order of the creation and annihilation operator, to a basis state will return that state unchanged if it does *not* have an electron of spin σ in orbital φ_i, while it returns zero otherwise. Hence the sum of the two operators is the identity: $c^\dagger_{i\sigma}c_{i\sigma} + c_{i\sigma}c^\dagger_{i\sigma} = 1$. When the states involved in the operation are orthogonal, i.e., $(i\sigma)$ and $(j\sigma')$ with either $\langle\varphi_j|\varphi_i\rangle = 0$ or $\sigma' \neq \sigma$, we obtain $c^\dagger_{i\sigma}c_{j\sigma'}+c_{j\sigma'}c^\dagger_{i\sigma} = 0$. To see this, consider how the annihilation operator $c_{j\sigma'}$ acts on a basis state $|b\rangle = \prod c^\dagger_{k\sigma_k}|0\rangle$. When state $(j\sigma')$ is not occupied in $|b\rangle$, we obtain $c_{j\sigma'}|b\rangle = 0$, when it is occupied, we can anticommute the corresponding creation operator to the left to obtain

$$c_{j\sigma'}\prod_k c^\dagger_{k\sigma_k}|0\rangle = (-1)^{P_j}c_{j\sigma'}c^\dagger_{j\sigma'}\prod_{k\neq j} c^\dagger_{k\sigma_k}|0\rangle = (-1)^{P_j}\prod_{i\neq j} c^\dagger_{k\sigma_k}|0\rangle\,,$$

where P_j is the number of anticommutations. Thus operating with $c_{j\sigma'}c^\dagger_{i\sigma}$ on $|b\rangle$ we obtain the same state as $c^\dagger_{i\sigma}c_{j\sigma'}|b\rangle$, but with an extra sign from the commutation with the additional creation operator on the right. The complete set of anticommutation relations for the electron creation and annihilation operators is thus

$$\Big\{c_{i\sigma},\, c_{j\sigma'}\Big\} = 0 \qquad \Big\{c^\dagger_{i\sigma},\, c^\dagger_{j\sigma'}\Big\} = 0 \qquad \Big\{c_{i\sigma},\, c^\dagger_{j\sigma'}\Big\} = \delta_{i,j}\delta_{\sigma,\sigma'}\,. \tag{24}$$

Using these operators it is straightforward to describe the hopping of an electron from one orbital to another: We take it out of the original orbital and put it into the new orbital; i.e., the hopping of an up electron from φ_1 to φ_2 is described by the operator $c^\dagger_{2\uparrow}c_{1\uparrow}$. The Hamiltonian for a spin-up electron hopping between two orbitals can thus be written as

$$H = -t\Big(c^\dagger_{1\uparrow}c_{2\uparrow} + c^\dagger_{2\uparrow}c_{1\uparrow}\Big)\,. \tag{25}$$

Calculating the matrix elements with the single-electron basis states, we recover the matrix (16), calculating them with the two-electron basis states (22), we obtain (19), where the signs of the hopping matrix elements reflect the anticommutation relations (24).
To model the Coulomb repulsion between two electrons in the same orbital we use the occupation number operators $n_{i\sigma}$: The Coulomb repulsion in orbital φ_1 is described by the operator $Un_{1\uparrow}n_{1\downarrow}$, which is non-zero only when there is a spin-up *and* a spin-down electron in φ_1. The Hamiltonian for our two-orbital model, where both up- and down-spin electrons can hop, and including the Coulomb repulsion for two electrons in the same orbital, is thus given by

$$\begin{aligned} H &= -t\left(c^\dagger_{1\uparrow}c_{2\uparrow} + c^\dagger_{2\uparrow}c_{1\uparrow} + c^\dagger_{1\downarrow}c_{2\downarrow} + c^\dagger_{2\downarrow}c_{1\downarrow}\right) + U\Big(n_{1\uparrow}n_{1\downarrow} + n_{2\uparrow}n_{2\downarrow}\Big) \\ &= -t\sum_{i,j,\sigma} c^\dagger_{j\sigma}c_{i\sigma} + U\sum_i n_{i\uparrow}n_{i\downarrow}\,. \end{aligned} \tag{26}$$

You should convince yourself that when you calculate the matrix elements for the two-electron states, you recover the matrix (19). The great advantage of writing the Hamiltonian in second-quantized form is that it is valid for any number of electrons, while the matrix form is restricted to a particular number of electrons.
Coming back to the effective Hamiltonian (20), we can rewrite H_{eff} in second quantized form:

$$\begin{aligned} H_{\text{eff}} &= -\frac{2t^2}{U}\left(c^\dagger_{2\uparrow}c^\dagger_{1\downarrow}c_{1\downarrow}c_{2\uparrow} - c^\dagger_{2\downarrow}c^\dagger_{1\uparrow}c_{1\downarrow}c_{2\uparrow} - c^\dagger_{2\uparrow}c^\dagger_{1\downarrow}c_{1\uparrow}c_{2\downarrow} + c^\dagger_{2\downarrow}c^\dagger_{1\uparrow}c_{1\uparrow}c_{2\downarrow}\right) \\ &= -\frac{2t^2}{U}\left(c^\dagger_{1\downarrow}c_{1\downarrow}c^\dagger_{2\uparrow}c_{2\uparrow} - c^\dagger_{1\uparrow}c_{1\downarrow}c^\dagger_{2\downarrow}c_{2\uparrow} - c^\dagger_{1\downarrow}c_{1\uparrow}c^\dagger_{2\uparrow}c_{2\downarrow} + c^\dagger_{1\uparrow}c_{1\uparrow}c^\dagger_{2\downarrow}c_{2\downarrow}\right) \end{aligned} \tag{27}$$

Looking at equation (59) in the appendix we see that the spin operators are given in second quantization by

$$S_i^x = \frac{1}{2}\Big(c_{i\uparrow}^\dagger c_{i\downarrow} + c_{i\downarrow}^\dagger c_{i\uparrow}\Big) \qquad S_i^y = -\frac{i}{2}\Big(c_{i\uparrow}^\dagger c_{i\downarrow} - c_{i\downarrow}^\dagger c_{i\uparrow}\Big) \qquad S_i^z = \frac{1}{2}\Big(n_{i\uparrow} - n_{i\downarrow}\Big). \tag{28}$$

or, in short, $\vec{S}_i = \frac{1}{2}\sum_{s,s'} c_{i,s}^\dagger \vec{\sigma}_{s,s'} c_{i,s'}$. From this we find (after some calculation) that the effective Hamiltonian can be written in terms of the spin operators

$$H_{\text{eff}} = \frac{4t^2}{U}\left(\vec{S}_1 \cdot \vec{S}_2 - \frac{n_1\, n_2}{4}\right). \tag{29}$$

To conclude, we see that the spin-independent Hamiltonian (26), in the limit of large U, gives rise to a spin-spin interaction which entangles the electrons. Since the exchange coupling $J = 4t^2/U$ is positive, states with antiparallel spins have lower energy. Thus direct exchange leads to *antiferromagnetism*.
It is important to realize that the singlet-triplet splitting for the effective Hamiltonian really arises from the admixture of ionic states into the singlet. By down-folding we eliminate the high-energy ionic states, i.e., charge fluctuations, from our Hilbert space. The eliminated states then give rise to an effective spin-spin interaction on the new reduced low-energy Hilbert space. We must therefore keep in mind that, when working with the effective Hamiltonian (29), we are considering slightly different states than when working with the original Hamiltonian (26).

3.4 Mean-field treatment

To conclude our discussion of the simplest kinetic exchange mechanism, it is instructive to consider the results of a mean-field treatment. For the two-electron Hamiltonian (19) it is straightforward to find the Hartree-Fock solution by directly minimizing the energy expectation value for a two-electron Slater determinant. The most general ansatz is a Slater determinant constructed from an orbital $\varphi(\theta_\uparrow) = \sin(\theta_\uparrow)\,\varphi_1 + \cos(\theta_\uparrow)\,\varphi_2$ for the spin-up, and $\varphi(\theta_\downarrow) = \sin(\theta_\downarrow)\,\varphi_1 + \cos(\theta_\downarrow)\,\varphi_2$ for the spin-down electron:

$$|\Psi(\theta_\uparrow,\theta_\downarrow)\rangle = \Big(\sin(\theta_\downarrow)\,c_{1\downarrow}^\dagger + \cos(\theta_\downarrow)\,c_{2\downarrow}^\dagger\Big)\ \Big(\sin(\theta_\uparrow)\,c_{1\uparrow}^\dagger + \cos(\theta_\uparrow)\,c_{2\uparrow}^\dagger\Big)\ |0\rangle\ . \tag{30}$$

Translating the second-quantized states via (22) into the basis used for writing the Hamiltonian matrix (19), we find the expectation value

$$\begin{aligned}\langle\Psi(\theta_\uparrow,\theta_\downarrow)|H|\Psi(\theta_\uparrow,\theta_\downarrow)\rangle = {} & -2t\,(\sin\theta_\uparrow\sin\theta_\downarrow + \cos\theta_\uparrow\cos\theta_\downarrow)\,(\cos\theta_\uparrow\sin\theta_\downarrow + \sin\theta_\uparrow\cos\theta_\downarrow)\\ & +U\left(\sin^2\theta_\uparrow\sin^2\theta_\downarrow + \cos^2\theta_\uparrow\cos^2\theta_\downarrow\right)\ .\end{aligned} \tag{31}$$

If the Slater determinant respects the symmetry of the molecule under the exchange of sites (mirror symmetry of the H_2 molecule), it follows that the Hartree-Fock orbitals for both spins are the bonding state φ_+ ($\theta = \pi/4$). This is the *restricted Hartree-Fock* solution. The corresponding energy is $E(\pi/4,\pi/4) = -2t + U/2$. The excited states are obtained by replacing occupied orbitals φ_+ with φ_-. Alltogether we obtain the restricted Hartree-Fock spectrum

$$\begin{aligned} E(\ \ \pi/4,\ \ \pi/4) &= -2t + U/2\\ E(\ \ \pi/4,-\pi/4) &= \qquad U/2\\ E(-\pi/4,\ \ \pi/4) &= \qquad U/2\\ E(-\pi/4,-\pi/4) &= \ \ \ 2t + U/2 \end{aligned} \tag{32}$$

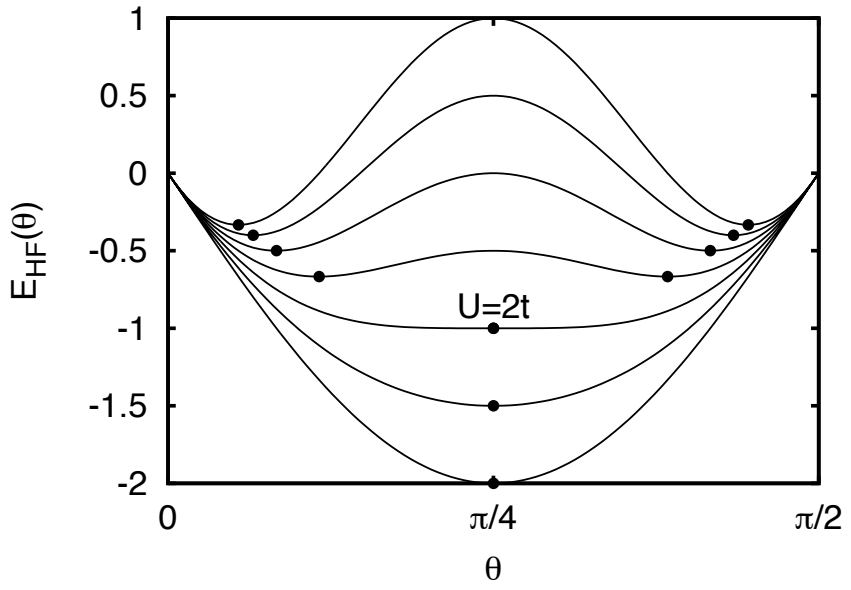

Fig. 3: *Energy expectation value for a Slater determinant $\Psi(\theta, \pi/2-\theta)$ for $U=0,\ t,\ 2t,\ \ldots,\ 6t$. When $U \leq 2t$ the minimum is at $\theta = \pi/4$. This is the Hartree-Fock solution with the bonding orbitals φ_+ occupied. For $U \geq 2t$, $\theta = \pi/4$ is still an extremal point (restricted Hartree-Fock solution), but an energy minimum is only attained when the symmetry is broken (unrestricted Hartree-Fock solution).*

Comparing to the energy for a state with both electrons of the same spin ($E = 0$), we see that there is no spin-triplet, i.e., Hartree-Fock breaks the spin symmetry. The states (32) are *spin-contaminated* [13]. Even worse, the Hartree-Fock ground state, and consequently all the states, are independent of U. The weight of the ionic states is always $1/2$, leading to an increase of the energy with $U/2$.
To avoid this, we can allow the Hartree-Fock solution to break the symmetry of the molecule (*unrestricted Hartree-Fock*), putting, e.g., more of the up-spin electron in the orbital on site 1 and more of the down-spin electron in orbital 2. For $U < 2t$ this does not lead to a state of lower energy. For larger U there is a symmetry-broken ground state

$$\Psi_{UHF} = \Psi(\theta, \pi/2 - \theta) \quad \text{with} \quad \theta(U) = \frac{\pi}{4} \pm \frac{1}{2} \arccos\left(\frac{2t}{U}\right) . \tag{33}$$

Its energy is $E_{UHF} = -2t^2/U$. This looks similar to the singlet energy ε_s, however, with a different prefactor. Still there is no triplet state (spin contamination) and, for $U \to \infty$, the overlap with the true singlet ground state goes to $|\langle \Psi_{UHF} | \Psi_- \rangle|^2 = 1/2$. In an extended system the breaking of the symmetry implies long-range order.

3.5 Superexchange

For the direct exchange mechanism discussed above, it is crucial that there is hopping between the orbitals. These orbitals are typically localized d-orbitals of transition-metals. However, direct exchange cannot explain the antiferromagnetism of most transition-metal compounds: Since the d-orbitals are so localized, hopping can only occur between orbitals on different atoms that are very close to each other. But most antiferromagnetic insulators are transition-metal

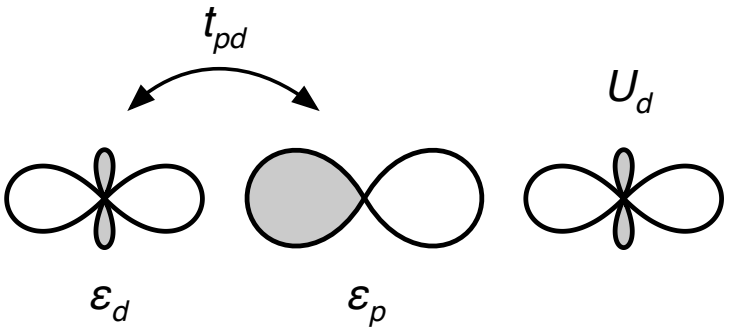

Fig. 4: *In superexchange an oxygen p-orbital mediates the exchange interaction between two transition-metal d-orbitals.*

oxides, where the transition-metal cations are separated by large oxygen anions. In such a situation, shown in figure 4, direct hopping between the d-orbitals is very unlikely. The concept of direct exchange can, however, be extended to these cases by taking into account hopping via the intermediate p-orbital. This mechanism is called superexchange.
To understand superexchange, we consider two d-orbitals with an oxygen p-orbital in-between. We introduce the operator $c^\dagger_{i\sigma}$, which creates a spin-σ electron in the d-orbital at site i, where $i = 1$ denotes the d-orbital on the left and $i = 2$ the one on the right (see figure 4). Likewise $c^\dagger_{p\sigma}$ creates an electron in the p-orbital. The energy of an electron in a d- or p-orbital is ε_d and ε_p, respectively. The Coulomb repulsion between two electrons in a d-orbital is U_d, while for the moment we neglect the repulsion between electrons in the p-orbital. Finally, $-t_{pd}$ is the hopping between p and d orbitals. The Hamiltonian for the system of figure 4 is then given by

$$H = \sum_\sigma \left(\varepsilon_d \sum_i n_{i\sigma} + \varepsilon_p \, n_{p\sigma} - t_{pd} \sum_i \left(c^\dagger_{i\sigma} c_{p\sigma} + c^\dagger_{p\sigma} c_{i\sigma} \right) \right) + U_d \sum_i n_{i\uparrow} n_{i\downarrow} \, . \tag{34}$$

In the absence of hopping, the ground state will have singly occupied d-orbitals, corresponding to a positively charged transition-metal ion, and a doubly occupied p-orbital, corresponding to an O^{2-} ion. To study a possible coupling between the spins on the d-orbitals, we first look at the case where both d-spins point upwards (see the far right of Fig. 5). The Hamiltonian matrix in the corresponding Hilbert space is then given by

$$H = \left(\begin{array}{c|cc} 0 & t_{pd} & t_{pd} \\ \hline t_{pd} & U_d + \Delta_{pd} & 0 \\ t_{pd} & 0 & U_d + \Delta_{pd} \end{array} \right) \begin{array}{l} c^\dagger_{2\uparrow} c^\dagger_{p\downarrow} c^\dagger_{p\uparrow} c^\dagger_{1\uparrow} |0\rangle \\ c^\dagger_{2\uparrow} c^\dagger_{p\uparrow} c^\dagger_{1\downarrow} c^\dagger_{1\uparrow} |0\rangle \\ c^\dagger_{2\downarrow} c^\dagger_{2\uparrow} c^\dagger_{p\uparrow} c^\dagger_{1\uparrow} |0\rangle \end{array} \tag{35}$$

where we have chosen $2(\varepsilon_p + \varepsilon_d)$ as the zero of our energy scale and defined $\Delta_{pd} = \varepsilon_d - \varepsilon_p$. The basis states of the Hilbert space are given on the right and the lines indicate the partitioning of the Hilbert space for down-folding. The effective Hamiltonian for parallel spins on d-orbitals is then

$$H_{\text{eff}} = (t_{pd}, t_{pd}) \begin{pmatrix} \varepsilon - (U_d + \Delta_{pd}) & 0 \\ 0 & \varepsilon - (U_d + \Delta_{pd}) \end{pmatrix} \begin{pmatrix} t_{pd} \\ t_{pd} \end{pmatrix} \approx - \frac{2 t_{pd}^2}{U_d + \Delta_{pd}} \tag{36}$$

where in the last step we have set ε to zero.
For antiparallel spins the Hilbert space is nine-dimensional. We sort the basis states into groups that are connected by the hopping of one electron. Starting from the two states with singly

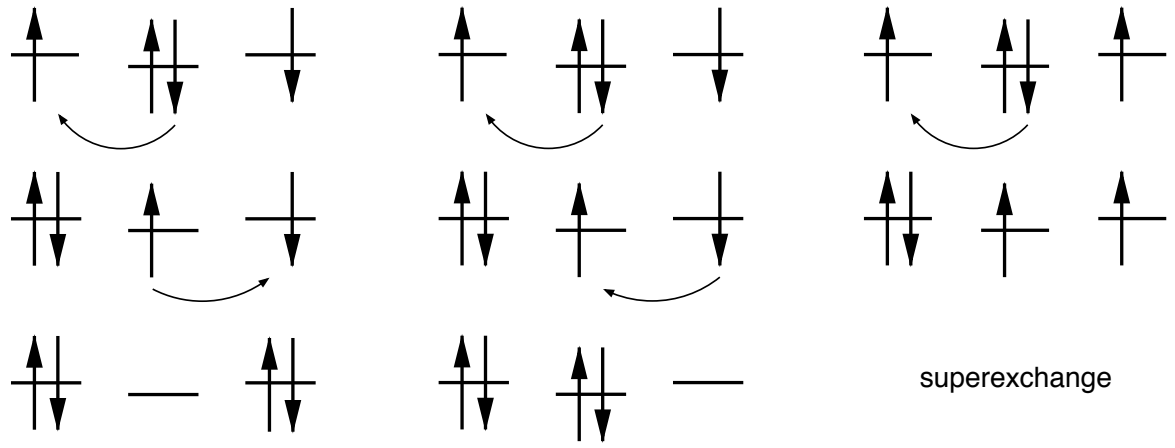

Fig. 5: *Simple picture of superexchange. Here the orbital on the central site is different from the orbitals on the sides. Typically, in the center there is a oxygen p-orbital coupling two d-orbitals. This situation is illustrated in Fig. 4. For antiparallel spins on the d-orbitals there are two ways that two consecutive hopping processes are possible. For parallel spins the Pauli principle suppresses the second hopping process.*

occupied d-orbitals, the second group has one of the p-electrons transfered to a d-orbital, leading to one doubly occupied d, while the last group has a second electron hopped, leading to either an empty p- or an empty d-orbital. The corresponding Hamiltonian matrix is

$$\left(\begin{array}{cc|cccc|ccc|l}
0 & 0 & +t_{pd} & +t_{pd} & 0 & 0 & 0 & 0 & 0 & c^\dagger_{2\downarrow}c^\dagger_{p\downarrow}c^\dagger_{p\uparrow}c^\dagger_{1\uparrow}|0\rangle \\
0 & 0 & 0 & 0 & +t_{pd} & +t_{pd} & 0 & 0 & 0 & c^\dagger_{2\uparrow}c^\dagger_{p\downarrow}c^\dagger_{p\uparrow}c^\dagger_{1\downarrow}|0\rangle \\
\hline
+t_{pd} & 0 & U_d+\Delta_{pd} & 0 & 0 & 0 & -t_{pd} & 0 & -t_{pd} & c^\dagger_{2\downarrow}c^\dagger_{p\uparrow}c^\dagger_{1\downarrow}c^\dagger_{1\uparrow}|0\rangle \\
+t_{pd} & 0 & 0 & U_d+\Delta_{pd} & 0 & 0 & 0 & -t_{pd} & -t_{pd} & c^\dagger_{2\downarrow}c^\dagger_{2\uparrow}c^\dagger_{p\downarrow}c^\dagger_{1\uparrow}|0\rangle \\
0 & +t_{pd} & 0 & 0 & U_d+\Delta_{pd} & 0 & +t_{pd} & 0 & +t_{pd} & c^\dagger_{2\uparrow}c^\dagger_{p\downarrow}c^\dagger_{1\downarrow}c^\dagger_{1\uparrow}|0\rangle \\
0 & +t_{pd} & 0 & 0 & 0 & U_d+\Delta_{pd} & 0 & +t_{pd} & +t_{pd} & c^\dagger_{2\downarrow}c^\dagger_{2\uparrow}c^\dagger_{p\uparrow}c^\dagger_{1\downarrow}|0\rangle \\
\hline
0 & 0 & -t_{pd} & 0 & +t_{pd} & 0 & U_d & 0 & 0 & c^\dagger_{p\downarrow}c^\dagger_{p\uparrow}c^\dagger_{1\downarrow}c^\dagger_{1\uparrow}|0\rangle \\
0 & 0 & 0 & -t_{pd} & 0 & +t_{pd} & 0 & U_d & 0 & c^\dagger_{2\downarrow}c^\dagger_{2\uparrow}c^\dagger_{p\downarrow}c^\dagger_{p\uparrow}|0\rangle \\
0 & 0 & -t_{pd} & -t_{pd} & +t_{pd} & +t_{pd} & 0 & 0 & 2(U_d+\Delta_{pd}) & c^\dagger_{2\downarrow}c^\dagger_{2\uparrow}c^\dagger_{1\downarrow}c^\dagger_{1\uparrow}|0\rangle
\end{array}\right)$$

Down-folding the high energy states with at least one doubly occupied d-orbital, setting $\varepsilon = 0$ and expanding in $1/U_d$ (remembering $(A+\Delta)^{-1} \approx A^{-1}(1-\Delta A^{-1})$), which is equivalent to second-order perturbation theory, leads to

$$\begin{aligned}
H_{\text{eff}} &= H_{00} + T_{01}\left(\varepsilon - \left(H_{11} + T_{12}\left(\varepsilon - H_{22}\right)^{-1} T_{21}\right)\right)^{-1} T_{10} \\
&\approx H_{00} - T_{01}H_{11}^{-1}T_{10} - T_{01}H_{11}^{-1}T_{12}H_{22}^{-1}T_{21}H_{11}^{-1}T_{10} \qquad (37) \\
&= -\frac{2t_{pd}^2}{U_d+\Delta_{pd}}\begin{pmatrix}1&0\\0&1\end{pmatrix} - \frac{2t_{pd}^4}{(U_d+\Delta_{pd})^2}\left(\frac{1}{U_d}+\frac{1}{U_d+\Delta_{pd}}\right)\begin{pmatrix}1&-1\\-1&1\end{pmatrix}. \qquad (38)
\end{aligned}$$

The first term is the same as for parallel spins (36). The additional term is of the same type as that found for the direct exchange mechanism. Again, it can be written in terms of spin operators. In the present case they are the spin operators for the d-orbitals, while the p-orbital

does no longer appear in the spin Hamiltonian. The spin coupling is now given by

$$J = \frac{4t_{pd}^4}{(U_d + \Delta_{pd})^2} \left(\frac{1}{U_d} + \frac{1}{U_d + \Delta_{pd}} \right), \tag{39}$$

which reflects that the superexchange mechanism involves four hopping processes (see Fig. 5), while direct exchange only involves two hoppings (see Fig. 2). The hopping process involving only a single doubly occupied d-orbital (middle of Fig. 5) is a generalization of the simple direct exchange with an effective hopping $t_{\rm eff} = t_{pd}^2/(U_d + \Delta_{pd})$ between the d-orbitals and gives the first term, $4t_{\rm eff}^2/U_d$, in (39), while the hopping process involving two occupied d-orbitals (left in Fig. 5) gives the second term $4t_{pd}^4/(U_d + \Delta_{pd})^3$.

3.6 Ferromagnetic superexchange

In the discussion of superexchange we have, so far, assumed that the oxygen ion lies between the two d-orbitals. This 180^o geometry is shown again on the left of Fig. 6. The situation is quite different, when the oxygen forms a 90^o bridge between the two d-orbitals, see the right of Fig. 6. By symmetry, there is only hopping between the d- and the p-orbitals that point towards each other. As there is also no hopping between the p-orbitals on the same site, the Hamiltonian for the system separates into two parts, one involving only the d orbital on site 1 and the p_x orbital and the other only involving d on site 2 and p_y, e.g.:

$$H_1 = \begin{pmatrix} 0 & +t_{pd} \\ +t_{pd} & U_d + \Delta_{pd} \end{pmatrix} \quad \begin{matrix} c_{x\downarrow}^\dagger c_{x\uparrow}^\dagger c_{1\downarrow}^\dagger |0\rangle \\ c_{x\downarrow}^\dagger c_{1\downarrow}^\dagger c_{1\uparrow}^\dagger |0\rangle \end{matrix} \tag{40}$$

Since it is not possible for an electron on site 1 to reach site 2, none of the superexchange processes discussed above are operational. Nevertheless, the energy for the system depends on the relative orientation of the electron spins in the two d-orbitals. To see this, we have to remember that Coulomb exchange prefers a triplet for two electrons in different orbitals on the same site (Hund's first rule). Including J_{xy} on the oxygen (but still neglecting U_p for simplicity), we get, for the triplet state with two up-electrons, the Hamiltonian

$$\left(\begin{array}{c|cc|c} 0 & t_{pd} & t_{pd} & 0 \\ \hline t_{pd} & U_d + \Delta_{pd} & 0 & t_{pd} \\ t_{pd} & 0 & U_d + \Delta_{pd} & t_{pd} \\ \hline 0 & t_{pd} & t_{pd} & 2(U_d + \Delta_{pd}) - J_{xy} \end{array} \right) \quad \begin{matrix} c_{1\uparrow}^\dagger c_{x\downarrow}^\dagger c_{x\uparrow}^\dagger c_{y\downarrow}^\dagger c_{y\uparrow}^\dagger c_{2\uparrow}^\dagger |0\rangle \\ c_{1\downarrow}^\dagger c_{1\uparrow}^\dagger c_{x\uparrow}^\dagger c_{y\downarrow}^\dagger c_{y\uparrow}^\dagger c_{2\uparrow}^\dagger |0\rangle \\ c_{1\uparrow}^\dagger c_{x\downarrow}^\dagger c_{x\uparrow}^\dagger c_{y\uparrow}^\dagger c_{2\downarrow}^\dagger c_{2\uparrow}^\dagger |0\rangle \\ c_{1\downarrow}^\dagger c_{1\uparrow}^\dagger c_{x\uparrow}^\dagger c_{y\uparrow}^\dagger c_{2\downarrow}^\dagger c_{2\downarrow}^\dagger |0\rangle \end{matrix} . \tag{41}$$

The first state has the two up-electrons on the d-orbitals. The second group of states has one d-orbital doubly occupied, while the last state has both d doubly occupied, i.e., two electrons on the two p-orbitals – the situation discussed in Sec. 2. Calculating the effective Hamiltonian as in (37) gives the energy of the triplet state

$$H_{\rm eff} = -\frac{2t_{pd}^2}{U_d + \Delta_{pd}} - \frac{4t_{pd}^4}{(U_d + \Delta_{pd})^2} \frac{1}{2(U_d + \Delta_{pd}) - J_{xy}} . \tag{42}$$

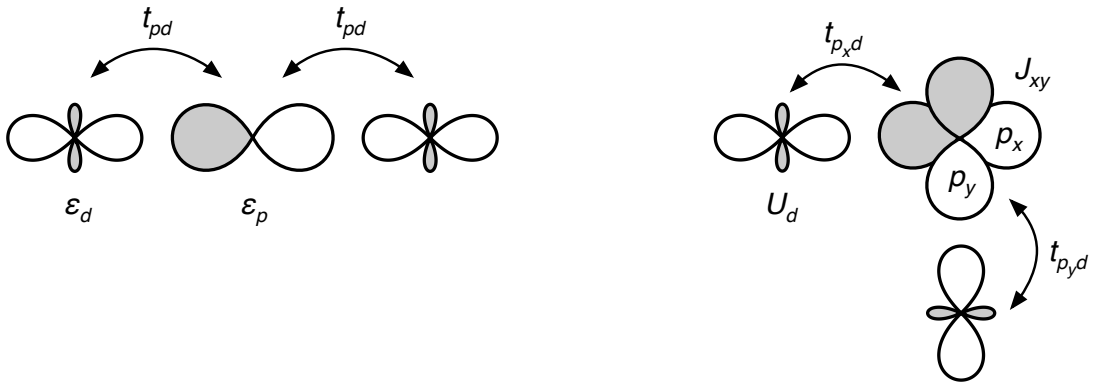

Fig. 6: *Dependence of superexchange on geometry: When the d-orbitals interact via an oxygen in-between (the 180^o geometry shown on the left), both d-orbitals couple to the same p-orbital, while the hopping to the two other p-orbitals vanishes by symmetry. The result is antiferromagnetic superexchange. When the angle of the M-O-M group is 90^o (right), the d-orbitals couple to orthogonal p-orbitals, making it impossible for an electron on one d-orbital to reach the d-orbital on the other site. In this case, superexchange is mediated via the Coulomb exchange on the connecting oxygen.*

Starting from singly occupied d-orbitals with opposite spin, we obtain

$$\left(\begin{array}{cc|cccc|cc}
0 & 0 & t_{pd} & 0 & t_{pd} & 0 & 0 & 0 \\
0 & 0 & 0 & t_{pd} & 0 & t_{pd} & 0 & 0 \\
\hline
t_{pd} & 0 & U_d+\Delta_{pd} & 0 & 0 & 0 & t_{pd} & 0 \\
0 & t_{pd} & 0 & U_d+\Delta_{pd} & 0 & 0 & 0 & t_{pd} \\
t_{pd} & 0 & 0 & 0 & U_d+\Delta_{pd} & 0 & t_{pd} & 0 \\
0 & t_{pd} & 0 & 0 & 0 & U_d+\Delta_{pd} & 0 & t_{pd} \\
\hline
0 & 0 & t_{pd} & 0 & t_{pd} & 0 & 2(U_d+\Delta_{pd}) & -J_{xy} \\
0 & 0 & 0 & t_{pd} & 0 & t_{pd} & -J_{xy} & 2(U_d+\Delta_{pd})
\end{array}\right)
\begin{array}{l}
c^\dagger_{1\uparrow}c^\dagger_{x\downarrow}c^\dagger_{x\uparrow}c^\dagger_{y\downarrow}c^\dagger_{y\uparrow}c^\dagger_{2\downarrow}|0\rangle \\
c^\dagger_{1\downarrow}c^\dagger_{x\downarrow}c^\dagger_{x\uparrow}c^\dagger_{y\downarrow}c^\dagger_{y\uparrow}c^\dagger_{2\uparrow}|0\rangle \\
c^\dagger_{1\downarrow}c^\dagger_{1\uparrow}c^\dagger_{x\uparrow}c^\dagger_{y\downarrow}c^\dagger_{y\uparrow}c^\dagger_{2\downarrow}|0\rangle \\
c^\dagger_{1\downarrow}c^\dagger_{1\uparrow}c^\dagger_{x\downarrow}c^\dagger_{y\downarrow}c^\dagger_{y\uparrow}c^\dagger_{2\uparrow}|0\rangle \\
c^\dagger_{1\uparrow}c^\dagger_{x\downarrow}c^\dagger_{x\uparrow}c^\dagger_{y\downarrow}c^\dagger_{2\downarrow}c^\dagger_{2\uparrow}|0\rangle \\
c^\dagger_{1\downarrow}c^\dagger_{x\downarrow}c^\dagger_{x\uparrow}c^\dagger_{y\uparrow}c^\dagger_{2\downarrow}c^\dagger_{2\uparrow}|0\rangle \\
c^\dagger_{1\downarrow}c^\dagger_{1\uparrow}c^\dagger_{x\uparrow}c^\dagger_{y\downarrow}c^\dagger_{2\downarrow}c^\dagger_{2\uparrow}|0\rangle \\
c^\dagger_{1\downarrow}c^\dagger_{1\uparrow}c^\dagger_{x\downarrow}c^\dagger_{y\uparrow}c^\dagger_{2\downarrow}c^\dagger_{2\uparrow}|0\rangle
\end{array}$$

giving the effective Hamiltonian

$$H_{\text{eff}} = -\frac{2t_{pd}^2}{U_d+\Delta_{pd}}\begin{pmatrix}1&0\\0&1\end{pmatrix} - \frac{4t_{pd}^4}{(U_d+\Delta_{pd})^2}\frac{1}{4(U_d+\Delta_{pd})^2-J_{xy}^2}\begin{pmatrix}2(U_d+\Delta_{pd}) & +J_{xy}\\ +J_{xy} & 2(U_d+\Delta_{pd})\end{pmatrix}.$$

Rearranging the matrices, we can bring this to the canonical form

$$\begin{aligned} H_{\text{eff}} = &-\left(\frac{2t_{pd}^2}{U_d+\Delta_{pd}} + \frac{4t_{pd}^4}{(U_d+\Delta_{pd})^2}\,\frac{1}{2(U_d+\Delta_{pd})-J_{xy}}\right) \\ &+ \frac{4t_{pd}^4}{(U_d+\Delta_{pd})^2}\,\frac{J_{xy}}{4(U_d+\Delta_{pd})^2-J_{xy}^2}\begin{pmatrix}1&-1\\-1&1\end{pmatrix}. \end{aligned} \tag{43}$$

The first term is just the energy of the triplet state (42). The second gives the difference in energy to the singlet. Despite the fact that the electrons cannot be transferred from one d-orbital to the other, we thus get a singlet-triplet splitting. This coupling of the spins originates from the states with both d-orbitals doubly occupied: the two remaining electrons, one each on the p_x- and p_y-orbital, respectively, form a triplet of energy $2J_{xy}$ lower than that of the singlet (see Eqn. (10)). When the electrons hop back from the d-orbital, the entanglement of the spins is

transferred to the remaining electron on the d. Originating from the Coulomb exchange on the oxygen, the exchange coupling is ferromagnetic

$$J = -\frac{4t_{pd}^4}{(U_d + \Delta_{pd})^2} \frac{2J_{xy}}{4(U_d + \Delta_{pd})^2 - J_{xy}^2} \,. \tag{44}$$

It tends to be significantly weaker than the antiferromagnetic 180^o superexchange coupling (39). When the angle of the M-O-M group is larger than 90^o, hopping to both p-orbitals becomes possible according to the Slater-Koster rules and the antiferromagnetic superexchange processes of Fig. 5 start to compete with the ferromagnetic superexchange mediated by the Coulomb exchange on the oxygen.

4 Orbital-ordering

Exchange mechanisms are not restricted to the coupling of spins. As pointed out by Kugel and Khomskii [14], also orbital occupations can interact. Such a coupling leads, besides an ordering of the spins, to an ordering of the orbitals.

To understand the mechanism of orbital-ordering, we consider an e_g-molecule, i.e., two sites with two orbitals a and b, as discussed in Sec. 2. The Hamiltonian on the sites is thus given by (9). In addition, the two sites are coupled by hopping matrix elements t_{aa} and t_{bb}, i.e., hopping does not change the type, a or b, of the occupied orbital. We now consider the case of one electron in orbital a and the other in orbital b.

First, we consider the situation when both electrons have the same spin, e.g., spin-up. The basis states are shown in Fig. 7. Setting up the Hamiltonian is analogous to setting up (19)

$$H = \left(\begin{array}{cc|cc} 0 & 0 & -t_{bb} & -t_{aa} \\ 0 & 0 & +t_{aa} & +t_{bb} \\ \hline -t_{bb} & +t_{aa} & U_{ab} - J_{ab} & 0 \\ -t_{aa} & +t_{bb} & 0 & U_{ab} - J_{ab} \end{array}\right) . \tag{45}$$

Down-folding to the states without doubly occupied sites, we obtain

$$H_{\text{eff}} \approx -\frac{1}{U_{ab} - J_{ab}} \begin{pmatrix} t_{aa}^2 + t_{bb}^2 & -2t_{aa}t_{bb} \\ -2t_{aa}t_{bb} & t_{aa}^2 + t_{bb}^2 \end{pmatrix} = -\frac{(t_{aa} - t_{bb})^2}{U_{ab} - J_{ab}} - \frac{2t_{aa}t_{bb}}{U_{ab} - J_{ab}} \begin{pmatrix} 1 & -1 \\ -1 & 1 \end{pmatrix} . \tag{46}$$

Thus we find that there is an interaction between the states with exchanged orbital-occupation, i.e., an orbital-exchange. For the present case of ferromagnetically aligned spins, the exchange

Fig. 7: *Basis states for an up-electron in orbital a and another up-electron in orbital b. Note that the states are ordered as in Eqn. (19).*

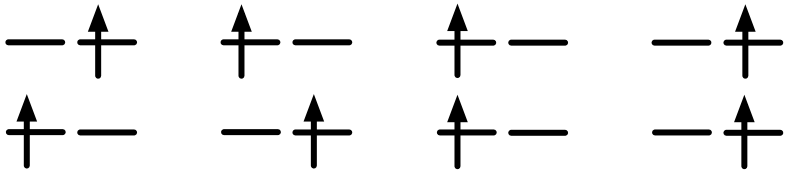

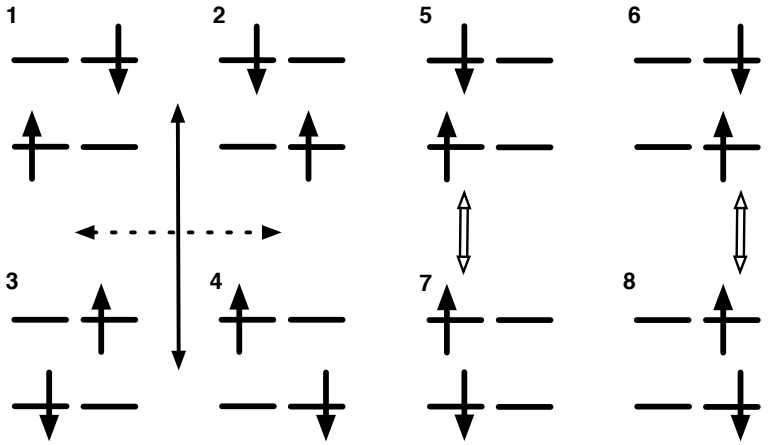

Fig. 8: *Basis states for electrons of opposite spin. The numbering used for the matrix (49) is indicated. Spin exchange is indicated by the full, orbital exchange by the dotted arrow. The states with both electrons on the same site are coupled via Coulomb exchange (double arrows).*

coupling favors the orbital singlet, when the hopping matrix elements are of the same sign. In analogy with the situation in kinetic exchange, this is called antiferro orbital exchange. To make the relation with kinetic exchange even more explicit, we can introduce, in analogy to (28), pseudo-spin operators $\vec{T}_{i\sigma}$

$$T^x_{i\sigma} = \frac{1}{2}\left(c^\dagger_{ai\sigma}c_{bi\sigma} + c^\dagger_{bi\sigma}c_{ai\sigma}\right),\ T^y_{i\sigma} = -\frac{i}{2}\left(c^\dagger_{ai\sigma}c_{bi\sigma} - c^\dagger_{bi\sigma}c_{ai\sigma}\right),\ T^z_{i\sigma} = \frac{1}{2}\left(n_{ai\sigma} - n_{bi\sigma}\right) \quad (47)$$

so that we can write

$$H_{\text{eff}} = -\frac{(t_{aa}-t_{bb})^2}{U_{ab}-J_{ab}} + \frac{4t_{aa}t_{bb}}{U_{ab}-J_{ab}}\left(\vec{T}_{1\uparrow}\cdot\vec{T}_{2\uparrow} - \frac{1}{4}\right). \quad (48)$$

When the two electrons have opposite spin, we can study the interplay of spin- and orbital-exchange. The basis states shown in Fig. 8. We expect orbital exchange to operate between the first two states in each row and spin exchange between the states between the rows. The Hamiltonian is

$$H = \left(\begin{array}{cccc|cccc}
0 & 0 & 0 & 0 & -t_{bb} & -t_{aa} & 0 & 0 \\
0 & 0 & 0 & 0 & +t_{aa} & +t_{bb} & 0 & 0 \\
0 & 0 & 0 & 0 & 0 & 0 & -t_{bb} & -t_{aa} \\
0 & 0 & 0 & 0 & 0 & 0 & +t_{aa} & +t_{bb} \\
\hline
-t_{bb} & +t_{aa} & 0 & 0 & U_{ab} & 0 & -J_{ab} & 0 \\
-t_{aa} & +t_{bb} & 0 & 0 & 0 & U_{ab} & 0 & -J_{ab} \\
0 & 0 & -t_{bb} & +t_{aa} & -J_{ab} & 0 & U_{ab} & 0 \\
0 & 0 & -t_{aa} & +t_{bb} & 0 & -J_{ab} & 0 & U_{ab}
\end{array}\right) \quad (49)$$

from which we obtain

$$
\begin{aligned}
H_{\text{eff}} &\approx -\frac{1}{U_{ab}^2 - J_{ab}^2} \begin{pmatrix} (t_{aa}^2 + t_{bb}^2)U_{ab} & -2t_{aa}t_{bb}\, U_{ab} & (t_{aa}^2 + t_{bb}^2)J_{ab} & -2t_{aa}t_{bb}\, J_{ab} \\ -2t_{aa}t_{bb}\, U_{ab} & (t_{aa}^2 + t_{bb}^2)U_{ab} & -2t_{aa}t_{bb}\, J_{ab} & (t_{aa}^2 + t_{bb}^2)J_{ab} \\ (t_{aa}^2 + t_{bb}^2)J_{ab} & -2t_{aa}t_{bb}\, J_{ab} & (t_{aa}^2 + t_{bb}^2)U_{ab} & -2t_{aa}t_{bb}\, U_{ab} \\ -2t_{aa}t_{bb}\, J_{ab} & (t_{aa}^2 + t_{bb}^2)J_{ab} & -2t_{aa}t_{bb}\, U_{ab} & (t_{aa}^2 + t_{bb}^2)J_{ab} \end{pmatrix} \\
&= -\frac{1}{U_{ab}^2 - J_{ab}^2} \begin{pmatrix} U_{ab} & J_{ab} \\ J_{ab} & U_{ab} \end{pmatrix} \otimes \begin{pmatrix} t_{aa}^2 + t_{bb}^2 & -2t_{aa}t_{bb} \\ -2t_{aa}t_{bb} & t_{aa}^2 + t_{bb}^2 \end{pmatrix} \qquad (50) \\
&= -\frac{1}{U_{ab}^2 - J_{ab}^2} \left[U_{ab} + J_{ab} - J_{ab} \begin{pmatrix} 1 & -1 \\ -1 & 1 \end{pmatrix} \right] \otimes \left[(t_{aa} - t_{bb})^2 + 2t_{aa}t_{bb} \begin{pmatrix} 1 & -1 \\ -1 & 1 \end{pmatrix} \right].
\end{aligned}
$$

I.e., we get a simultaneous coupling of the spin- and orbital degrees of freedom. The first term describes the coupling of the spins, which is antiferromagnetic, while the coupling of the orbitals is, for hopping matrix elements of the same sign, ferro, i.e., orbital triplet. In terms of the spin and pseudo-spin operators we can write, with $\vec{T}_i = \sum_\sigma \vec{T}_{i\sigma}$ and $\vec{S}_i = \sum_{\alpha\in\{a,b\}} \vec{S}_{\alpha,i}$

$$
H_{\text{eff}} = -\frac{1}{U_{ab}^2 - J_{ab}^2} \left[(U_{ab} + J_{ab}) + 2J_{ab} \left(\vec{S}_1 \cdot \vec{S}_2 - \frac{1}{4} \right) \right] \left[(t_{aa} - t_{bb})^2 - 4t_{aa}t_{bb} \left(\vec{T}_1 \cdot \vec{T}_2 - \frac{1}{4} \right) \right].
$$

5 Conclusion

We have seen in how in a number of simplified situations strong correlations give rise to magnetic interactions and the corresponding entangling of electronic spins. The exchange mechanisms responsible for this entanglement can be quite different. They can result from the direct interaction of the electrons on a correlated site (Coulomb exchange) or from the hopping between neighboring atoms (direct kinetic exchange). In more realistic settings the entanglement is mediated via intermediate sites (superexchange) or even transferred by the hopping electrons to neighboring sites (ferromagnetic superexchange). Since entanglement of the electron spins gives rise to magnetism, exchange mechanisms are often considered to be restricted to coupling only the spin degrees of freedom. They are, however, also active in coupling orbitals. The resulting physics of orbital degrees of freedom is an exciting topic in itself.
Exchange mechanisms are idealizations of characteristic situations found in real materials. As such they are merely approximations, but they afford a simplification of the complicated realistic description, which provides a good basis for thinking about the relevant effects in a real material.

Acknowledgment

Support of the Deutsche Forschungsgemeinschaft through FOR1346 is gratefully acknowledged.

Appendices

A Down-folding

To integrate-out high-energy degrees of freedom, we partition the Hilbert space of the full system into states of interest (low-energy states) and 'other' states, which will be integrated out. The Hamiltonian is then written in block form

$$H = \begin{pmatrix} H_{00} & T_{01} \\ T_{10} & H_{11} \end{pmatrix} , \tag{51}$$

where H_{00} is the Hamiltonian restricted to the states of interest (reduced Hilbert space), H_{11} the Hamiltonian for the 'other' states, and the T matrices describe transitions between the two subspaces. The resolvent is partitioned likewise

$$G(\varepsilon) = (\varepsilon - H)^{-1} = \begin{pmatrix} \varepsilon - H_{00} & T_{01} \\ T_{10} & \varepsilon - H_{11} \end{pmatrix}^{-1} . \tag{52}$$

The right-hand side is a 2 matrix whose entries are matrices themselves. It is easily inverted, the only complication being that we must take into account that the sub-matrices do not commute. Considering a general 2×2 block-matrix M and its inverse we have to solve the system of equations

$$M\,M^{-1} = \begin{pmatrix} A & B \\ C & D \end{pmatrix} \begin{pmatrix} \tilde{A} & \tilde{B} \\ \tilde{C} & \tilde{D} \end{pmatrix} = \begin{pmatrix} 1 & 0 \\ 0 & 1 \end{pmatrix} . \tag{53}$$

To obtain $\tilde{A}$ we first solve $C\tilde{A}+D\tilde{C} = 0$ for $\tilde{C} = -D^{-1}C\tilde{A}$ which we insert into $A\tilde{A}+B\tilde{C} = 1$ from which we obtain $\tilde{A} = (A - BD^{-1}C)^{-1}$. Thus, for the resolvent (52) we find

$$G_{00}(\varepsilon) = \Bigg(\varepsilon - [H_{00} + \underbrace{T_{01}(\varepsilon - H_{11})^{-1}\,T_{10}}_{=H_{\text{eff}}}] \Bigg)^{-1} . \tag{54}$$

This expression looks just like the resolvent for a Hamiltonian

$$\begin{aligned} H_{\text{eff}} &= H_{00} + T_{01}(\varepsilon\ - H_{11})^{-1}\,T_{10} && (55) \\ &\approx H_{00} + T_{01}(\varepsilon_0 - H_{11})^{-1}\,T_{10} && (56) \end{aligned}$$

on the reduced Hilbert space. This effective Hamiltonian describes the physics of the full system, but operates only on the small reduced Hilbert space. Of course, this drastic simplification comes at a price: the effective Hamiltonian is energy dependent. If the hopping matrix elements in T_{01} are small, and/or if the states in the part of the Hilbert space that has been integrated out are energetically well-separated from the states that are explicitly considered, this energy dependence can, to a good approximation, be neglected. We can then replace ε by a typical energy ε_0 for the states in the reduced Hilbert space to obtain an energy-independent Hamiltonian $H_{\text{eff}}(\varepsilon_0)$ that gives a good description of the electrons in the reduced Hilbert space, i.e., the states with an energy close to ε_0.

B Pauli matrices

Here we collect the most important properties of the Pauli matrices. They are defined as

$$\sigma_x = \begin{pmatrix} 0 & 1 \\ 1 & 0 \end{pmatrix} \quad \sigma_y = \begin{pmatrix} 0 & -i \\ i & 0 \end{pmatrix} \quad \sigma_z = \begin{pmatrix} 1 & 0 \\ 0 & -1 \end{pmatrix} \tag{57}$$

They are hermitean, i.e. $\sigma_i^\dagger = \sigma_i$, and $\sigma_i^2 = 1$. Therefore their eigen-values are ± 1. The eigenvectors of σ_z are $|m_z\rangle$, $m_z = \pm 1$:

$$|+1\rangle = \begin{pmatrix} 1 \\ 0 \end{pmatrix} \quad \text{and} \quad |-1\rangle = \begin{pmatrix} 0 \\ 1 \end{pmatrix} . \tag{58}$$

For these vectors we find

$$\sigma_x|\, m_z\rangle = |\, -m_z\rangle \quad \sigma_y|\, m_z\rangle = i m_z|\, -m_z\rangle \quad \sigma_z|\, m_z\rangle = m_z|\, m_z\rangle \tag{59}$$

The products of the Pauli matrices are $\sigma_x\, \sigma_y = i\sigma_z$, where the indices can be permuted cyclically. From this follows for the commutator

$$[\sigma_x, \sigma_y] = 2i\sigma_z \tag{60}$$

while the anticommutator vanishes:

$$\{\sigma_x, \sigma_y\} = 0 \tag{61}$$

Finally a rotation by an angle φ about the axis $\hat{n}$ changes the spin matrices

$$R_{\hat{n}}(\varphi) = e^{-i\hat{n}\cdot\vec{\sigma}\,\varphi/2} = cos(\varphi/2) - i\sin(\varphi/2)\,\hat{n}\cdot\vec{\sigma} . \tag{62}$$

References

[1] R.P. Feynman, International Journal of Theoretical Physics **21**, 467 (1982)

[2] E. Koch: *Correlated Electrons* in:
S. Blügel, G. Gompper, E. Koch, H.Müller-Krumbhaar, R. Spatschek, and R.G. Winkler:
Computational Condensed Matter Physics
Reihe Matter and Materials, Vol. 32 (Forschungszentrum Jülich, 2006)

[3] P.M.A. Dirac, Proc. Roy. Soc. **A 123**, 714 (1929)

[4] W. Kohn, Rev. Mod. Phys. **71**, 1253 (1999)

[5] E. Pavarini, E. Koch, D. Vollhardt, and A.I. Lichtenstein:
The LDA+DMFT approach to strongly correlated materials
Reihe Modeling and Simulation, Vol. 1 (Forschungszentrum Jülich, 2011)
`http://www.cond-mat.de/events/correl11`

[6] E. Pavarini, E. Koch, F. Anders, and M. Jarrell:
Correlated Electrons: From Models to Materials
Reihe Modeling and Simulation, Vol. 2 (Forschugszentrum Jülich, 2012)
`http://www.cond-mat.de/events/correl12`

[7] E. Pavarini: *Crystal-Field Theory, Tight-Binding Method, and Jahn-Teller Effect*, in [6]

[8] Patrik Fazekas: *Lecture Notes on Electron Correlation and Magnetism*
(World Scientific, Singapore, 1999)

[9] A. Auerbach: *Interacting Electrons and Quantum Magnetism*
(Springer, Heidelberg, 1994)

[10] P.W. Anderson: *Theory of Magnetic Exchange Interactions*,
in F. Seitz and D. Turnbull (eds.): *Solid State Physics* **14**, 99 (1963)

[11] D.C. Mattis: *The Theory of Magnetism Made Simple* (World Scientific, Singapore, 2006)

[12] S. Blundell: *Magnetism in Condensed Matter* (Oxford University Press, 2001)

[13] A. Szabo and N.S. Ostlund: *Modern Quantum Chemistry* (Dover Publications, 1996)

[14] K.I. Kugel and D.I. Khomskii, Zh. Eksp. Teor. Fiz. **64**, 1429 (1973)
[Sov. Phys. JETP **37**, 725 (1973)]

C 4 Condensed Matter Applications of Entanglement Theory[1]

Norbert Schuch
Institute for Quantum Information
RWTH Aachen, 52056 Aachen, Germany

Contents

1 Introduction **2**
1.1 Entanglement structure of ground states: The area law 2

2 One-dimensional systems: Matrix Product States **3**
2.1 Matrix Product States 3
2.2 Variational calculation with MPS: The DMRG method 6
2.3 MPS as a framework for solvable models 9

3 Tensor network states beyond one dimension and ground state problems **13**
3.1 PEPS: Tensor networks in two dimensions 13
3.2 Simulating time evolution and thermal states 18
3.3 Other tensor network ansatzes 19
3.4 Simulation of fermionic sytems 21

4 Quantum Complexity: Understanding the limitations to our understanding **22**
4.1 A crash course in complexity classes 22
4.2 The complexity of problems in many-body physics 23

5 Summary **25**

[1]Lecture Notes of the 44^{th} IFF Spring School "Quantum Information Processing" (Forschungszentrum Jülich, 2013). All rights reserved.

1 Introduction

The aim of this lecture is to show how the tools of quantum information theory and in particular entanglement theory can help us to understand the physics of condensed matter systems and other correlated quantum many-body systems. In a certain sense, many-body systems are all around in quantum information: The defining feature of these systems is that they consist of many subsystems of the same dimension, equipped with a natural tensor product structure[2] $(\mathbb{C}^d)^{\otimes N}$, and such structures appear in quantum information as quantum registers in quantum computers, as parties in multipartite protocols, and so on.

Most condensed matter systems exhibit only weak quantum correlations (this is, entanglement) between the individual subsystems. These systems are well described by a mean field ansatz (i.e., a product state), and their behavior can be understood using Landau theory. However, some of the most exciting phenomena discovered in condensed matter physics in the last decades, such as the fraction quantum Hall effect or high-temperature superconductivity, are based on systems with strong interactions in which entanglement plays an essential role. Given the refined understanding of entanglement which has been developed in the field of quantum information theory, it is thus natural to apply quantum information concepts, and in particular the theory of entanglement, towards an improved understanding of quantum many-body systems. Indeed, an active field of research has grown during the last decade at the interface of quantum information theory and quantum many-body physics, and the aim of this lecture is to give an introduction to this area.

In this lecture, we will highlight two complementary topics at the interface between condensed matter and quantum information: In the first part (Sec. 2, 3), we will show how we can use insights on the entanglement structure of condensed matter systems to develop powerful methods to both numerically simulate and analytically characterize correlated many-body systems; and in the second part (Sec. 4) we will show how the field of quantum complexity theory allows us to better understand the limitations to our (numerical) understanding of those systems.

1.1 Entanglement structure of ground states: The area law

For clarity of the presentation, we will in the following restrict our attention to quantum spin systems on a lattice (such as a line or a square lattice in 2D), with a corresponding Hilbert space $(\mathbb{C}^d)^{\otimes N}$ (where each spin has d levels, and the lattice has N sites); generalizations to fermionic systems and beyond lattices will be discussed later. Also, we will for the moment focus on ground state problems, i.e., given some Hamiltonian H acting or our spin system, we will ask about properties of its ground state $|\Psi\rangle$. The approach we pursue will be variational – we will try to obtain a family of states which gives a good approximation of the ground state, for which quantities of interest can be evaluated efficiently, and where the best approximation to the ground state can be found efficiently. For instance, mean-field theory is a variational theory based on the class of product states (for spin systems) or Slater determinants (for electronic systems).

So which states should we use for our variational description of quantum spin systems? Of course, one could simply try to parametrize the ground state as

$$|\Psi\rangle = \sum_{i_1,\ldots,i_N} c_{i_1\ldots i_N} |i_1,\ldots,i_N\rangle \,, \tag{1}$$

[2] We ignore fermionic systems for the moment, but as it turns out, many of the results described in this lecture also hold for fermionic systems, see Sec. 3.4.

Fig. 1: *Area law: The entropy of the reduced states of a block A scales like the length of its boundary ∂A; in one dimension, this implies that the entropy is bounded by a constant.*

and use the $c_{i_1 \ldots i_N}$ as variational parameters. Unfortunately, the number of parameters $c_{i_1 \ldots i_N}$ grows exponentially with N, making it impossible to have an efficient description of $|\Psi\rangle$ for growing system sizes. On the other hand, we know that efficient descriptions exist for physical Hamiltonians: Since $H = \sum_i h_i$ is a sum of few-body terms (even if we don't restrict to lattice systems), a polynomial number N^k of parameters (with k the bodiness of the interaction) allows to specify H, and thus its ground state. This is, while a general N-body quantum state can occupy an exponentially large Hilbert space, all physical states live in a very small "corner" of this space. The difficulty, of course, is to find an efficient parametrization which captures the states in this corner of Hilbert space, while at the same time allowing for efficient simulation methods.

In order to have a guideline for constructing an ansatz class, we choose to look at the entanglement properties of ground states of interacting quantum systems. To this end, we consider a ground state $|\Psi\rangle$ on a lattice and cut a contiguous region of length L (in one dimension) or an area A (in two dimensions), cf. Fig. 1. It is a well-known result from entanglement theory [1] that the von Neumann entropy of the reduced density matrix ρ_A of region A,

$$S(\rho_A) = -\rho_A \log \rho_A \, ,$$

quantifies the entanglement between region A and the rest of the system. For a random quantum state, we expect this entanglement to be almost maximal, i.e., on the order of $|A| \log d$ (where $|A|$ is the number of spins in region A). Yet, if we study the behavior of $S(\rho_A)$ for ground states of local Hamiltonians, it is found that $S(\rho_A)$ essentially scales like the *boundary* of region A, $S(\rho_A) \propto |\partial A|$, with possible corrections for gapless Hamiltonians which are at most logarithmic in the volume, $S(\rho_A) \propto |\partial A| \log |A|$. This behavior is known as the *area law* for the entanglement entropy and has been observed throughout for ground states of local Hamiltonians (see, e.g., Ref. [2] for a review); for gapped Hamiltonians in one dimension, this result has been recently proven rigorously [3].

2 One-dimensional systems: Matrix Product States

2.1 Matrix Product States

2.1.1 Construction and Matrix Product notation

Since the entropy $S(\rho_A)$ quantifies the entanglement between region A and its complement, the fact that $S(\rho_A)$ scales like the *boundary* of ρ_A suggests that the entanglement between region A and the rest of the system is essentially located around the boundary between the two regions, as illustrated in Fig. 2. We will now construct an ansatz for many-body quantum systems, starting from the insight that the entanglement is concentrated around the boundary of regions;

Fig. 2: *The area law suggests that the entanglement between two regions is located around the boundary.*

for the moment, we will focus on one-dimensional systems. Clearly, since we want to have this property for any partitioning of the lattice, we cannot just place entangled pairs as in Fig. 2, but we have to choose a more subtle strategy. To this end, we consider the system at each site as being composed of two "virtual" subsystems of dimension D each, as illustrated in Fig. 3a. Then, each of the two subsystems is placed in a maximally entangled state

$$|\omega_D\rangle = \sum_{i=1}^{D} |i,i\rangle$$

with the corresponding subsystems of the adjacent sites, as shown in Fig. 3b. The maximally entangled states are called "bonds", with D the "bond dimension". This construction already satisfies the area law: For any region we cut, there are exactly two maximally entangled states crossing the cuts, bounding the entanglement by $2\log D$. Finally, we apply linear maps $\mathcal{P}_s : \mathbb{C}^D \otimes \mathbb{C}^D \to \mathbb{C}^d$ at each site s, which creates a description of a state on a chain of d-level systems, cf. Fig. 3c. (Note that the rank of the reduced density operator of any region cannot be increased by applying the linear maps $\mathcal{P}_s$.) The construction can be carried out either with periodic boundary conditions, or with open boundary conditions by omitting the outermost virtual subsystems at the end of the chain. The total state of the chain can be written as

$$|\Psi\rangle = (\mathcal{P}_1 \otimes \cdots \otimes \mathcal{P}_N)|\omega_D\rangle^{\otimes N} , \tag{2}$$

where the maps $\mathcal{P}_s$ act on the maximally entangled states as illustrated in Fig. 3c.
This class of states can be rewritten as follows: For each site s, define a three-index tensor $A^{[s]}_{i,\alpha\beta}$, $i = 1,\ldots,d$, $\alpha,\beta = 1,\ldots,D$, where the $A^{[s]}_i$ can be interpreted as $D \times D$ matrices, such that

$$\mathcal{P}_s = \sum_{i,\alpha,\beta} A^{[s]}_{i,\alpha\beta} |i\rangle\langle\alpha,\beta| . \tag{3}$$

Then, the state (2) can be rewritten as

$$|\Psi\rangle = \sum_{i_1,\ldots,i_N} \mathrm{tr}\left[A^{[1]}_{i_1} A^{[2]}_{i_2} \cdots A^{[N]}_{i_N}\right] |i_1,\ldots,i_N\rangle , \tag{4}$$

i.e., the coefficient $c_{i_1\ldots i_N}$ in (1) can be expressed as a product of matrices.[3] For this reason, these states are called *Matrix Product States* (MPS). For systems with open boundary conditions, the matrices $A^{[1]}_{i_1}$ and $A^{[N]}_{i_N}$ are $1 \times D$ and $D \times 1$ matrices, respectively, so that the trace can be omitted. More generally, D can be chosen differently across each link.

[3]The equivalence of (2) and (4) can be proven straightforwardly by noting that for two maps $\mathcal{P}_1$ and $\mathcal{P}_2$, and the bond $|\omega_D\rangle$ between them, it holds that

$$\mathcal{P}_1 \otimes \mathcal{P}_2 |\omega_D\rangle = \sum_{i_1,i_2,\alpha,\beta} (A^{[1]}_{i_1} A^{[2]}_{i_2})_{\alpha\beta} |i_1,i_2\rangle\langle\alpha,\beta| ,$$

and iterating this argument through the chain.

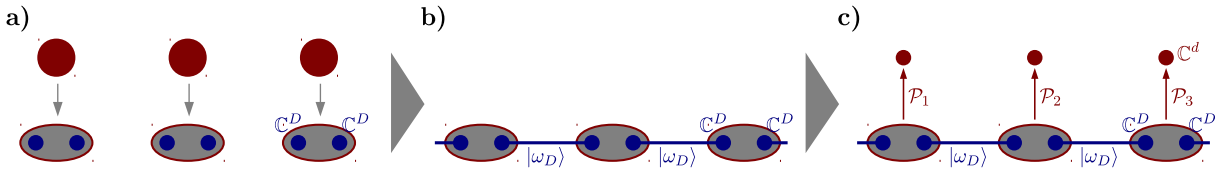

Fig. 3: *Construction of MPS:* ***a)*** *Each site is composed of two virtual subsystems.* ***b)*** *The virtual subsystems are placed in maximally entangled states.* ***c)*** *Linear maps $\mathcal{P}_s$ are applied which map the two virtual systems to the physical system.*

2.1.2 Tensor network notation

The defining equation (4) for Matrix Product States is a special case of a so-called *tensor network*. Generally, tensor networks are given by a number of tensors $A_{i_1,i_2,\ldots,i_K}$, $B_{i_1,i_2,\ldots,i_K}$, etc., where each tensor usually only depends on a few of the indices. Then, one takes the product of the tensors and sums over a subset of the indices,

$$c_{i_1\ldots i_k} = \sum_{i_{k+1},\ldots,i_K} A_{i_1,i_2,\ldots,i_K} B_{i_1,i_2,\ldots,i_K} \cdots .$$

For instance, in (4) the tensors are the $A^{[s]} \equiv A^{[s]}_{i,\alpha\beta}$, and we sum over the virtual indices $\alpha, \beta, \ldots$, yielding

$$c_{i_1\ldots i_N} = \sum_{\alpha,\beta,\gamma,\ldots,\zeta} A^{[1]}_{i_1,\alpha\beta} A^{[2]}_{i_2,\beta\gamma} \cdots A^{[N]}_{i_N,\zeta\alpha} = \mathrm{tr}\left[A^{[1]}_{i_1} A^{[2]}_{i_2} \cdots A^{[N]}_{i_N}\right] .$$

Tensor networks are most conveniently expressed in a graphical language. Each tensor is denoted by a box with "legs" attached to it, where each leg corresponds to an index – a three-index tensor $A^{[s]} \equiv A^{[s]}_{i,\alpha\beta}$ is then depicted as

$$A^{[s]}_{i,\alpha\beta} \equiv \alpha \; \boxed{A^{[s]}} \; \beta \quad , \qquad (i)$$

Summing over a joint index is denoted by connecting the corresponding legs, e.g.,

$$\sum_\beta A_{i,\alpha\beta} B_{j,\beta\gamma} \equiv \alpha \; \boxed{A} \; \beta \; \boxed{B} \; \gamma \quad . \qquad (i, j)$$

In this language, the expansion coefficient $c_{i_1\ldots i_N}$ [Eq. (1)] of an MPS (which we will further on use interchangably with the state itself) is written

$$|\Psi\rangle \equiv \boxed{c_{i_1,\ldots,i_N}} \; (i_1\; i_2\; i_3\; \cdots\; i_N) = \boxed{A^{[1]}} \; \alpha \; \boxed{A^{[2]}} \; \beta \; \boxed{A^{[3]}} \cdots \boxed{A^{[N]}} \quad . \qquad (5)$$

We will make heavy use of this graphical language for tensor networks in the following.

2.1.3 Approximating states as Matrix Product States

As it turns out, MPS are very well suited to describe ground states of one-dimensional quantum systems. On the one hand, we have seen that by construction, these states all satisfy the area law. On the other hand, it can be shown that all states which satisfies an area law, such as ground states of gapped Hamiltonians [3], as well as states for which the entanglement of a block grows slowly (such as for critical 1D systems), can be well approximated by an MPS [3, 4]: Given a state $|\Phi\rangle$ on a chain of length N for which the entropy of any block of length L is bounded by $S_{\max}$, $S(\rho_L) \leq S_{\max}$, there exists an MPS $|\Psi_D\rangle$ which approximates $|\Phi\rangle$ up to error[4]

$$||\Phi\rangle - |\Psi_D\rangle| =: \epsilon \leq \text{const} \times \frac{N e^{cS_{\max}}}{D^c} \,. \tag{6}$$

Note that even if $S_{\max}$ grows logarithmically with N, the numerator is still a polynomial in N. This is, in order to achieve a given accuracy ϵ, we need to choose a bond dimension D which scales polynomially in N and $1/\epsilon$, and thus, the total number of parameters (and, as we will see later, also the computation time) scales polynomially as long as the desired accuracy is at most $1/\text{poly}(N)$.

2.1.4 States with exact Matrix Product form

Beyond the fact that ground states of gapped Hamiltonians can be efficiently approximated by MPS, there is a large class of states which can be expressed exactly as MPS with a small bond dimension D. First of all, any product state is trivially an MPS with $D = 1$. The GHZ state

$$|\text{GHZ}\rangle = |0\cdots0\rangle + |1\cdots1\rangle$$

is an MPS with $D = 2$, with a translational invariant MPS representation $A^{[s]} \equiv A \; \forall \, s$, with $A_0 = |0\rangle\langle 0| \equiv \left(\begin{smallmatrix} 1 & 0 \\ 0 & 0 \end{smallmatrix}\right)$, and $A_1 = |1\rangle\langle 1| \equiv \left(\begin{smallmatrix} 0 & 0 \\ 0 & 1 \end{smallmatrix}\right)$. The W state

$$|\text{W}\rangle = |100\cdots00\rangle + |010\cdots00\rangle + \cdots + |000\cdots01\rangle$$

is an MPS with $D = 2$, and $A^{[s]} = A$ for $2 \leq s \leq N-1$, $A^{[1]} = \langle 0|A$, and $A^{[N]} = A|1\rangle$, where $A_0 = \mathbb{1}$ and $A_1 = |0\rangle\langle 1|$. Other states which have an MPS representation with small D are the cluster state used in measurement-based computation [6, 7] (with $D = 2$) or the 1D resonating valence bond state which appears as the ground state of the so-called Majumdar-Ghosh model [8, 9] (with $D = 3$), and the AKLT state which we will get to know in Section 2.3.1.

2.2 Variational calculation with MPS: The DMRG method

As we have discussed at the end of Section 2.1.3, MPS approximate ground states of local Hamiltonians efficiently, as the effort needed for a good approximation scales only polynomially in the length of the chain and the desired accuracy. Thus, it seems appealing to use the

[4] Stricly speaking, this bound only follows from an area law for the *Rényi entropy*

$$S_\alpha = \frac{\log \text{tr}[\rho^\alpha]}{1-\alpha}$$

for $\alpha < 1$, with c in (6) depending on α [4], which also holds for gapped Hamiltonians [3]. The proof uses the fact that a bound on the area law implies a fast decay of the Schmidt coefficients (i.e., the eigenvalues of the reduced density operator), and thus, one can construct an MPS by sequentially doing Schmidt decompositions of the state and discarding all but the largest D Schmidt coefficients [4, 5].

class of MPS as a variational ansatz to simulate the properties of quantum many-body systems. However, to this end it is not sufficient to have an efficient description of relevant states – after all, the Hamiltonian itself forms an efficient description of its ground state, but it is hard to extract information from it! Rather, a good variational class also requires that we can efficiently extract quantities of interest such as energies, correlation functions, and the like, and that there is an efficient way to *find* the ground state (i.e., minimize the energy within the variational class of states) in the first place.

2.2.1 Evaluating expectation values for MPS

Let us start by discussing how to compute the expectation value of a local operator h (such as a term in the Hamiltonian) for an MPS. To this end, note that

$$\langle\Psi|h|\Psi\rangle = \sum_{\substack{i_1,\ldots,i_N \\ j_1,\ldots,j_N}} c_{i_1\ldots i_N} c^*_{j_1\ldots j_N} \delta_{i_1,j_1}\cdots\delta_{i_{k-1},j_{k-1}} h^{j_k j_{k+1}}_{i_k i_{k+1}} \delta_{i_{k+2},j_{k+2}}\cdots\delta_{i_N,j_N}$$

where

$$h = \sum_{\substack{i_k,i_{k+1} \\ j_k,j_{k+1}}} h^{j_k j_{k+1}}_{i_k i_{k+1}} |i_k, i_{k+1}\rangle\langle j_k, j_{k+1}|$$

acts on sites k and $k+1$. Using the graphical tensor network notation, this can be written as

$\langle\Psi|h|\Psi\rangle =$ 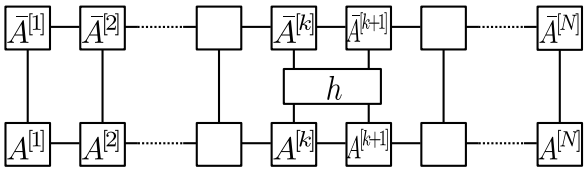

. (7)

In order to evaluate this quantity, we have to contract the whole diagram (7). In principle, contracting arbitrary tensor networks can become an extremely hard problem (strictly speaking, PP-hard [10]), as in some cases it essentially requires to determine exponentially big tensors (e.g., we might first have to compute $c_{i_1\ldots i_N}$ from the tensor network and from it determine the expectation value). Fortunately, it turns out that the tensor network of Eq. (7) can be contracted efficiently, i.e., with an effort polynomial in D and N. To this end, let us start from the very left of the tensor network in Eq. (7) and block the leftmost column (tensors $A^{[1]}$ and $\bar{A}^{[1]}$). Contracting the internal index, this gives a two-index tensor

$$\mathbb{L}^{\alpha\alpha'} = \sum_i A^{[1]}_{i\alpha} \bar{A}^{[1]}_{i\alpha'} ,$$

which we interpret as a (bra) *vector* with a "double index" $\alpha\alpha'$ of dimension D^2. Graphically, this can be denoted as

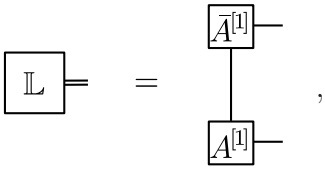

,

where we use a doubled line to denote the "doubled" index of dimension D^2. We can now continue this way, and define operators (called *transfer operators*)

$$(\mathbb{E}^{[s]})^{\beta\beta'}_{\alpha\alpha'} = \sum_i A^{[s]}_{i,\alpha\beta} \bar{A}^{[s]}_{i,\alpha'\beta'}$$

which we interpret as mapping the double index $\alpha\alpha'$ to $\beta\beta'$, and graphically write as

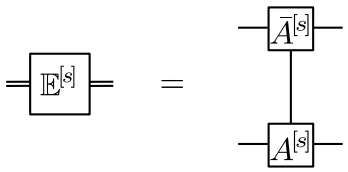

(8)

Similarly, we define operators

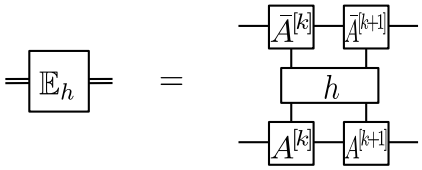

(9)

and

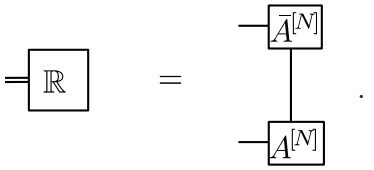

All of these operators can be computed efficiently (in the parameters D and N), as they are vectors/matrices of fixed dimension D^2, and can be obtained by contracting a constant number of indices.
Using the newly defined objects $\mathbb{L}$, $\mathbb{E}$, $\mathbb{E}_h$, and $\mathbb{R}$, the expectation value $\langle\Psi|h|\Psi\rangle$, Eq. (7), can be rewritten as

$$\langle\Psi|h|\Psi\rangle = \mathbb{L}\mathbb{E}^{[2]}\cdots\mathbb{E}^{[k-1]}\mathbb{E}_h\mathbb{E}^{[k+2]}\cdots\mathbb{R}$$

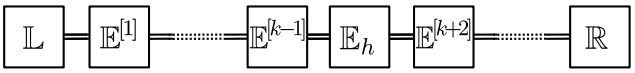

This is, $\langle\Psi|h|\Psi\rangle$ can be computed by multiplying a D^2-dimensional vector $O(N)$ times with $D^2 \times D^2$ matrices. Each of these multiplication takes $O(D^4)$ operations, and thus, $\langle\Psi|h|\Psi\rangle$ can be evaluated in $O(ND^4)$ operations. There are $O(N)$ terms in the Hamiltonian, and thus, the energy $\langle\Psi|\sum_i h_i|\Psi\rangle/\langle\Psi|\Psi\rangle$ can be evaluated in time $O(N^2D^4)$, and thus efficiently; in fact, this method can be easily improved to scale as $O(ND^3)$.[5] Similarly, one can see that e.g. correlation functions $\langle\Psi|P_i \otimes Q_j|\Psi\rangle$ or string order parameters $\langle\Psi|X \otimes X \otimes \cdots \otimes X|\Psi\rangle$ can be reduced to matrix multiplications and thus evaluated in $O(ND^3)$. Exactly the same way, evaluating expectation values for MPS with periodic boundary conditions can be reduced to computing the trace of a product of matrices $\mathbb{E}$ of size $D^2 \times D^2$. Each multiplication scales like $O(D^6)$, and using the same tricks as before, one can show that for systems with periodic boundary conditions, expectation values can be evaluated in time $O(ND^5)$.
In summary, we find that energies, correlations functions, etc. can be efficiently evaluated for MPS, with computation times scaling as $O(ND^3)$ and $O(ND^5)$ for open and periodic boundary conditions, respectively.

[5] Firstly, one uses that the products $\mathbb{L}\cdots\mathbb{E}^{[s]}$ and $\mathbb{E}^{[s]}\cdots\mathbb{R}$ need to be computed only once (this can be simplified even further by choosing the appropriate gauge [11, 12]), reducing the scaling in N to $O(N)$. Secondly, one slightly changes the contraction order: Starting from the left, one contracts $A^{[1]}$, $\bar{A}^{[1]}$, $A^{[2]}$, $\bar{A}^{[2]}$, $A^{[3]}$, etc.: This involves multiplications of $D \times D$ matrices with $D \times dD$ matrices, and $D \times Dd$ matrices with $Dd \times D$ matrices, yielding a $O(dD^3)$ scaling.

2.2.2 Variational optimization of MPS

As we have seen, we can efficiently compute the energy of an MPS with respect to a given local Hamiltonian $H = \sum_i h_i$. In order to use MPS for numerical simulations, we still need to figure out an efficient way to find the MPS which minimizes the energy for a given D. To this end, let us first pick a site k, and try to minimize the energy as a function of $A^{[k]}$, while keeping all other MPS tensors $A^{[s]}$, $s \neq k$, fixed. Now, since $|\Psi\rangle$ is a linear function of $A^{[k]}$, we have that

$$\frac{\langle\Psi|H|\Psi\rangle}{\langle\Psi|\Psi\rangle} = \frac{\vec{A}^{[k]\dagger} X \vec{A}^{[k]}}{\vec{A}^{[k]\dagger} Y \vec{A}^{[k]}}$$

is the ratio of two quadratic forms in $A^{[k]}$. Here, $\vec{A}^{[k]}$ denotes the vectorized version of $A^{[k]}_{i,\alpha\beta}$, where (i, α, β) is interpreted as a single index. The matrices X and Y can be obtained by contracting the full tensor network (7) except for the tensors $A^{[k]}$ and $\bar{A}^{[k]}$, which can be done efficiently. The $\vec{A}^{[k]}$ which minimizes this energy can be found by solving the generalized eigenvalue equation

$$X\vec{A}^{[k]} = E\, Y \vec{A}^{[k]}$$

where E is the energy; again, this can be done efficiently in D. For MPS with open boundary conditions, we can choose a gauge[6] for the tensors such that $Y = \mathbb{1}$ [11, 12] – this reduces the problem to a usual eigenvalue problem, and avoids problems due to ill-conditioned Y.
This shows that we can efficiently minimize the energy as a function of the tensor $A^{[k]}$ at an individual site k. In order to minimize the overall energy, we start from a randomly chosen MPS, and then sweep through the sites, sequentially optimizing the tensor at each site. Iterating this a few times over the system (usually sweeping back and forth) quickly converges to a state with low energy. Although in principle, such an optimization can get stuck [14, 15], in practice it works extremely well and generally converges to the optimal MPS (though some care might have to be put into choosing the initial conditions).
In summary, we find that we can use MPS to efficiently simulate ground state properties of one-dimensional quantum systems with both open and periodic boundary conditions. This simulation method can be understood as a reformulation of the Density Matrix Renormalization Group (DMRG) algorithm [16, 17], which is a renormalization algorithms based on keeping the states which are most relevant for the entanglement of the system, and which since its invention has been highly successful in simulating the physics of one-dimensional quantum systems (see Refs. [11, 18, 19] for a review of the DMRG algorithm and its relation to MPS, and a more detailed discussion of MPS algorithms).

2.3 MPS as a framework for solvable models

Up to now, we have seen that MPS form a powerful framework for the simulation of one-dimensional systems, due to their ability to efficiently approximate ground states of local Hamil-

[6] MPS have a natural gauge degree of freedom, since for any X_s with a right inverse X_s^{-1}, we can always replace

$$A_i^{[s]} \leftrightarrow A_i^{[s]} X_s$$
$$A_i^{[s+1]} \leftrightarrow X_s^{-1} A_i^{[s+1]}$$

without changing the state; this gauge degree of freedom can be used to obtain standard forms for MPS with particularly nice properties [12, 13].

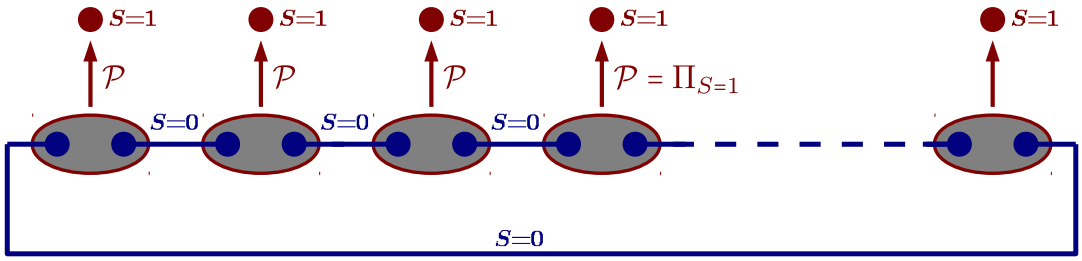

Fig. 4: *The AKLT model is built from spin-$\frac{1}{2}$ singlets ($S = 0$) between adjacent sites, which are projected onto the spin one subspace ($\mathcal{P} = \Pi_{S=1}$) as indicated.*

tonians, and due to the fact that the necessary variational minimization can be carried out efficiently. As we will see in the following, MPS can also be used as a framework to construct solvable models whose properties can be understood analytically, which makes them a powerful tool for resolving various analytical problems regarding quantum many-body systems.

2.3.1 The AKLT model and parent Hamiltonians

The paradigmatic analytical MPS model is the so-called AKLT state, named after Affleck, Kennedy, Lieb, and Tasaki [20, 21]. The construction of the translational invariant AKLT state is illustrated in Fig. 4: The auxiliary systems are spin-$\frac{1}{2}$ particles, which are put into a singlet (i.e., spin $S = 0$) state[7] $|\omega\rangle = |01\rangle - |10\rangle$. The two virtual spin-$\frac{1}{2}$'s at each site have jointly spin $\frac{1}{2} \otimes \frac{1}{2} = 0 \oplus 1$, and the map $\mathcal{P}$ projects onto the spin-1 subspace, thereby describing a translationally invariant chain of spin-1 particles.
Let us now see what we can say about the reduced density operator ρ_2 of two consecutive sites in the AKLT model. The following argument is illustrated in Fig. 5: On the virtual level, we start from two "open" bonds, each of which has spin $\frac{1}{2}$ (while we might have more information about their joint state, we are free to neglect it), as well as one "interior" bond which has spin 0; thus, the virtual state we start from has spin

$$\tfrac{1}{2} \otimes 0 \otimes \tfrac{1}{2} = 0 \oplus 1 \, .$$

The projections $\mathcal{P}$ onto the spin 1 subspace, on the other hand, do not change the total spin (they only affect the weight of different subspaces), which implies that ρ_2 has spin 0 or 1 as well. On the other hand, ρ_2 is a state of two physical sites, each of which has spin 1; this is, it could have spin $1 \otimes 1 = 0 \oplus 1 \oplus 2$. We therefore find that there is a non-trivial constraint on ρ_2 arising from the AKLT construction: ρ_2 cannot have spin 2.
We can now use this to construct a non-trivial Hamiltonian which has the AKLT state as its ground state. Namely, let $h_{i,i+1} = \Pi_{S=2}$ be a local Hamiltonian acting on sites i and $i+1$, projecting onto the spin $S = 2$ subspace of the two sites. Then, by the preceding argument, $h_{i,i+1}|\Psi_{\mathrm{AKLT}}\rangle = 0$ with $|\Psi_{\mathrm{AKLT}}\rangle$ the AKLT state, and thus, with

$$H = \sum_i h_{i,i+1} \, ,$$

we have that

$$H|\Psi_{\mathrm{AKLT}}\rangle = 0 \, .$$

[7] This bond can be easily replaced by a normal bond $|00\rangle + |11\rangle$ by applying the transformation $\left(\begin{smallmatrix} 0 & 1 \\ -1 & 0 \end{smallmatrix}\right)$ on one side, which can subsequently be absorbed in the map $\mathcal{P}$.

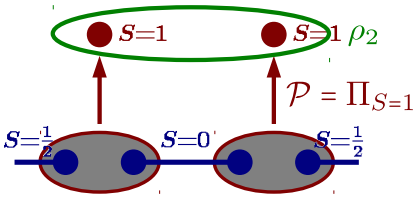

Fig. 5: *Construction of the parent Hamiltonian for the AKLT model.*

On the other hand, $H \geq 0$, and thus, the AKLT state is a ground state of the AKLT Hamiltonian H.

While the argument we have given right now seems specific to the AKLT model, it turns out that the very same way, we can construct a so-called "parent Hamiltonian" for any MPS. To this end, note that the reduced density operator ρ_k for k consecutive sites lives in a d^k dimensional space, yet it can have rank at most D^2 (since the only free parameters we have are the outermost "open" bonds). Thus, as soon as $d^k > D^2$, ρ_k does not have full rank, and we can build a local Hamiltonian h acting on k consecutive sites as $h = \mathbb{1} - \Pi_{\mathrm{supp}(\rho_k)}$ which has the given MPS as its ground state.

Of course, it is not sufficient to have a non-trivial Hamiltonian with the AKLT state (or any other MPS) as its ground state, but we want that the AKLT state is the unique ground state of this Hamiltonian. Indeed, it turns out that there is a simple condition which is satisfied for almost any MPS (and in particular for the AKLT state) which allows to prove that it is a unique ground state of a suitable chosen parent Hamiltonian; for the case of the AKLT model, it turns out that this Hamiltonian is the two-body Hamitonian which we defined originally.[8] Secondly, it can be shown that the parent Hamiltonian of MPS is always gapped, this is, there is a finite gap above the ground space which does not close even as $N \to \infty$.

Together, this proves that the AKLT state is the unique ground state of a gapped local Hamiltonian. It is an easy exercise to show that the AKLT Hamiltonian equals

$$h_{i,i+1} = \tfrac{1}{2}\boldsymbol{S}_i \cdot \boldsymbol{S}_{i+1} + \tfrac{1}{6}(\boldsymbol{S}_i \cdot \boldsymbol{S}_{i+1})^2 + \tfrac{1}{3}\,,$$

and is thus close to the spin-1 Heisenberg model. Indeed, proving that the spin-1 Heisenberg model is gapped, as conjectured by Haldane, was one motivation for the construction of the AKLT model, showing that MPS allow for the construction of models of interest for which certain properties can be rigorously proven.

The fact that MPS naturally appear as ground states of local Hamiltonians makes them a very powerful tool in studying the properties of one-dimensional gapped systems. In particular, one can use them to classify phases of one-dimensional systems: On the one hand, we know that the ground state of any gapped one-dimensional Hamiltonian is well approximated by an MPS. This allows us to replace the original Hamiltonian by the parent Hamiltonian of the MPS while keeping a gap (i.e., without crossing a phase transition). Given two MPS characterized by tensors $\mathcal{P}_1$ and $\mathcal{P}_2$, we can now build a smooth interpolation between the two models (i.e., Hamiltonians) by appropriately interpolating between $\mathcal{P}_1$ and $\mathcal{P}_2$: due to the very way the parent Hamiltonian

[8] This condition is known as "injectivity" and states there is a k such that after blocking k sites, the map $X \mapsto \sum \mathrm{tr}[A_{i_1} \cdots A_{i_k} X]|i_1, \ldots, i_k\rangle$ from the "open bonds" to the physical system is injective, or, differently speaking, that we can infer the state of the bonds by looking at the physical system; the AKLT state acquires injectivity for $k = 2$. It can then be shown that the parent Hamiltonian defined on $k+1$ sites has a unique ground state; in the case of the AKLT model, one can additionally show that the ground space of this three-body parent Hamiltonian and the original two-body one are identical [12, 13, 21–23].

is constructed, this will give rise to a smooth path of parent Hamiltonians as well [24]. This is particularly interesting if one imposes symmetries on the Hamiltonian, which (for a system with a unique MPS ground state $|\Psi\rangle$) implies that $U_g^{\otimes N}|\Psi\rangle = |\Psi\rangle$. For an MPS with such a symmetry, it can be shown [25,26] that the symmetry is reflected in a *local* symmetry of the MPS map $\mathcal{P}$, $U_g\mathcal{P} = \mathcal{P}(V_g \otimes \bar{V}_g)$, and classifying the possible inequivalent types of V_g allows to classify the different phases in one-dimensional systems in the presence of symmetries [24, 27, 28].

2.3.2 Correlation length and the transfer operator

As we have discussed in the preceding section, MPS form a powerful tool for the construction of solvable models. Let us now have a closer look at what we can say about the behavior of physical quantities. While we have discussed how to extract physically relevant quantities such as energies and correlation functions numerically in Sec. 2.2.1, the purpose of this section is different: Here, we focus on a translationally invariant exact MPS ansatz, and we are asking for simple (and ideally closed) expressions for quantities such as the correlation length.
In Sec. 2.2.1, the central object was the transfer operator,

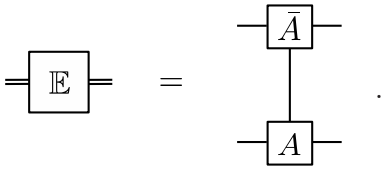

As compared to Eq. (8), we have omitted the site-dependency index $[s]$. It is easy to see that – up to local unitaries – the MPS is completely determined by the transfer operator $\mathbb{E}$: If A and B give rise to the same transfer operator, $\sum A_i \otimes \bar{A}_i = \sum B_i \otimes \bar{B}_i$, then we must have $A_i = \sum_j v_{ij} B_j$, with $V = (v_{ij})$ an isometry.[9] In the following, we would like to see how specific properties can be extracted from the transfer operator.
One property which is of particular interest are two-point correlations. To obtain those, let us first define

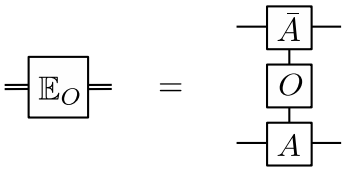

$$= \sum_{ij} \langle j|O|i\rangle A_i \otimes \bar{A}_j \; .$$

Then, the correlation between operator A at site 1 and B at site $j+2$ on a chain of length $N \to \infty$ is

$$\langle A_1 B_{j+2}\rangle = \frac{\mathrm{tr}[\mathbb{E}_A \mathbb{E}^j \mathbb{E}_B \mathbb{E}^{N-j-2}]}{\mathrm{tr}[\mathbb{E}^N]} \; . \tag{10}$$

If we now assume that $\mathbb{E}$ has a unique maximal eigenvalue λ_1, which we normalize to $\lambda_1 = 1$, with eigenvectors $|r\rangle$ and $\langle l|$, then for large N, $\mathbb{E}^N \to |r\rangle\langle l|$, and thus Eq. (10) converges to $\langle l|\mathbb{E}_A \mathbb{E}^j \mathbb{E}_B|r\rangle$. If we now expand

$$E^j = |r\rangle\langle l| + \sum_{k\geq 2} \lambda_k^j |r_k\rangle\langle l_k|$$

[9] This is nothing but the statement that two purifications of a mixed state are identical up to an isometry on the purifying system (this can be easily proven using the Schmidt decomposition, cf. Sec. 2.5 of Ref. [29]), where the index i corresponds to the purifying system.

(where $|\lambda_k| < 1$ for $k \geq 2$), we find that

$$\langle A_1 B_{j+2} \rangle = \langle l|\mathbb{E}_A|r\rangle\langle l|\mathbb{E}_B|l\rangle + \sum_{k\geq 2} \lambda_k^j \langle l|\mathbb{E}_A|r_k\rangle\langle l_k|\mathbb{E}_B|l\rangle \ ,$$

and thus decays exponentially with j; in particular, the correlation length ξ is given by the ratio of the second largest to the largest eigenvalue of $\mathbb{E}$,

$$\xi = -\frac{1}{\ln|\frac{\lambda_2}{\lambda_1}|} \ ,$$

i.e., it is determined solely by simple spectral properties of the transfer operator. Let us note that the same quantity, i.e. the ratio between the two largest eigenvalues, also bounds the gap of the parent Hamiltonian [13, 30].

The proof above that correlations in MPS decay exponentially is not restricted to the case of a unique maximal eigenvalue of the transfer operator: In case it is degenerate, this implies that the correlation function has a long-ranged part (i.e., one which is not decaying), such as in the GHZ state, while any other contribution still decays exponentially. In particular, MPS cannot exhibit algebraically decaying correlations, and in case MPS are used to simulate critical systems, one has to take into account that a critical decay of correlations in MPS simulations is always achieved by approximating it by a sum of exponentials.

3 Tensor network states beyond one dimension and ground state problems

3.1 PEPS: Tensor networks in two dimensions

As we have seen, MPS are very well suited for simulating ground state properties of one-dimensional systems. But what if we want to go beyond one-dimensional systems, and, e.g., study interacting spin systems in two dimensions? Two-dimensional systems can exhibit a rich variety of phenomena, such as topologically ordered states [31, 32] which are states distinct from those in the trivial phase, yet which do not break any (local) symmetry. Moreover, two-dimensional spin systems can be highly frustrated due to the presence of large loops in the interaction graph, and even classical two-dimensional spin glasses can be hard to solve [33]. In the following, we will focus on the square lattice without loss of generality.

A first idea to simulate two-dimensional systems would be to simply use an MPS, by choosing a one-dimensional ordering of the spins in the two-dimensional lattice. While this approach has been applied successfully (see, e.g., Ref. [34]), it cannot reproduce the entanglement features of typical ground states in two dimensions as one increases the system size: As we have discussed in Section 1.1, two-dimensional systems also satisfy an area law, i.e., in the ground state we expect the entanglement of a region A with its complement to scale like its boundary, $S(\rho_A) \sim |\partial A|$. To obtain an ansatz with such an entanglement scaling, we follow the same route as in the construction of MPS: We consider each site as being composed of *four* D-dimensional virtual subsystems, place each of them in a maximally entangled state $|\omega_D\rangle$ with the corresponding subsystem of each of the adjacent sites, and finally apply a linear map

$$\mathcal{P}_s : \mathbb{C}^D \otimes \mathbb{C}^D \otimes \mathbb{C}^D \otimes \mathbb{C}^D \to \mathbb{C}^d$$

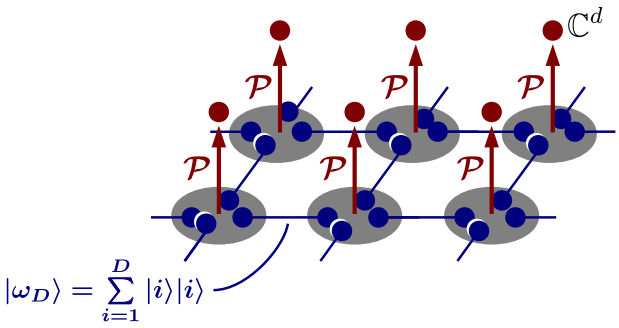

Fig. 6: *PEPS construction for a 2D square lattice, where we have omitted the site-dependence $\mathcal{P} \equiv \mathcal{P}_s$ of the maps $\mathcal{P}_s$.*

at each site s to obtain a description of the physical state on a 2D lattice of d-level sytems. The construction is illustrated in Fig. 6. Due to the way they are constructed, these states are called *Projected Entangled Pair States* (PEPS). Again, we can define five-index tensors $A^{[s]} = A^{[s]}_{i,\alpha\beta\gamma\delta}$, where now

$$\mathcal{P}_s = \sum_{i\alpha\beta\gamma\delta} A^{[s]}_{i,\alpha\beta\gamma\delta} |i\rangle\langle\alpha,\beta,\gamma,\delta| \ ,$$

and express the PEPS in Fig. 6 graphically as a tensor network

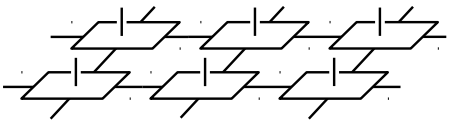

(where we have omitted the tensor labels). Similar to the result in one dimension, one can show that PEPS approximate ground states of local Hamiltonians well as long as the density of states grows at most polynomially with the energy [35, 36], and thereby provide a good variational ansatz for two-dimensional systems. (Note, however, that it is not known whether all 2D states which obey an area law are approximated well by PEPS.)

3.1.1 Contraction of PEPS

Let us next consider what happens if we try to compute expectation values of local observables for PEPS. For simplicity, we first discuss the evaluation of the normalization $\langle\Psi|\Psi\rangle$, which is obtained by sandwiching the ket and bra tensor network of $|\Psi\rangle$,

$\langle\Psi|\Psi\rangle \quad =$ 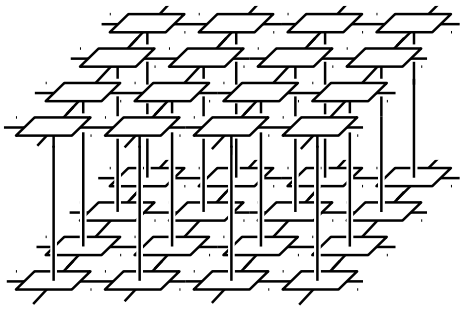 . (11)

This can again be expressed using transfer operators

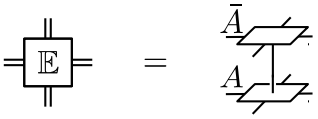

(the $\mathbb{E}$ should be thought of as being "viewed from the top"), leaving us with the task of contracting the network

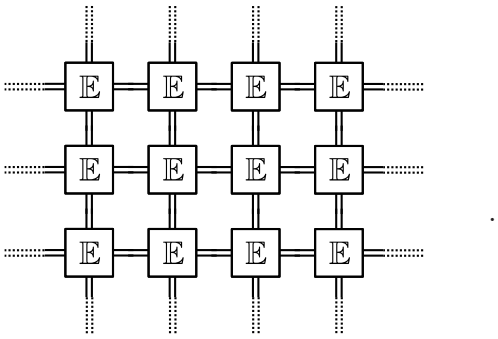

.

[This easily generalizes to the computation of expectation values, where some of the $\mathbb{E}$ have to be modified similar to Eq. (9)]. Different from the case of MPS, there is no one-dimensional structure which we can use to reduce this problem to matrix multiplication. In fact, it is easy to see that independent of the contraction order we choose, the cluster of tensors we get (such as a rectangle) will at some point have a boundary of a length comparable to the linear system size. This is, we need to store an object with a number of indices proportional to $\sqrt{N}$ – and thus an *exponential* number of parameters – at some point during the contraction, making it impossible to contract such a network efficiently. (Indeed, it can be proven that such a contraction is a computationally hard problem [10].)

This means that if we want to use PEPS for variational calculations in two dimensions, we have to make use of some approximate contraction scheme, which of course should have a small and ideally controlled error. To this end, we proceed as follows [37]: Consider the contraction of a two-dimensional PEPS with open boundary conditions,

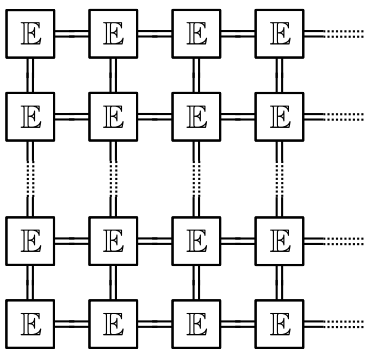

. (12)

Now consider the first two columns, and block the two tensors in each column into a new tensor

$\mathbb{F}$ (with vertical bond dimension D^4):

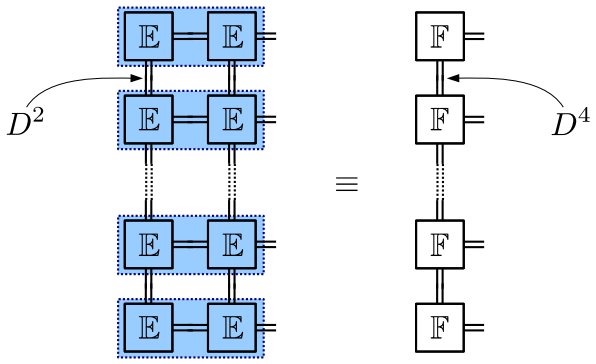

(13)

This way, we have reduced the number of columns in (12) by one. Of course, this came at the cost of squaring the bond dimension of the first column, so this doesn't help us yet. However, what we do now is to approximate the right hand side of (13) by an MPS with a (fixed) bond dimension αD^2 for some α. We can then iterate this procedure column by column, thereby contracting the whole MPS, and at any point, the size of our tensors stays bounded. It remains to be shown that the elementary step of approximating an MPS $|\Phi\rangle$ [such as the r.h.s. of (13)] by an MPS $|\Psi\rangle$ with smaller bond dimension can be done efficiently: To this end, it is sufficient to note that the overlap $\langle\Phi|\Psi\rangle$ is linear in each tensor $A^{[s]}$ of $|\Psi\rangle$, and thus, maximizing the overlap

$$\frac{\big|\langle\Phi|\Psi\rangle\big|^2}{\langle\Psi|\Psi\rangle}$$

can again be reduced to solving a generalized eigenvalue problem, just as the energy minimization for MPS in the one-dimensional variational method. Differently speaking, the approximate contraction scheme succeeds by reducing the two-dimensional contraction problem to a sequence of one-dimensional contractions, i.e., it is based on a dimensional reduction of the problem.

This shows that PEPS can be contracted approximately in an efficient way. The scaling in D is naturally much less favorable than in one dimension, and for the most simple approach one finds a scaling of D^{12} for open boundaries, which using several tricks can be improved down to D^8. Yet, the method is limited to much smaller D as compared to the MPS ansatz. It should be noted that the approximate contraction method we just described has a controlled error, as we know the error made in in each approximation step. Indeed, the approximation is very accurate as long as the system is short-range correlated, and the accuracy of the method is rather limited by the D needed to obtain a good enough approximation of the ground state. Just as in one dimension, we can use this approximate contraction method to build a variational method for two-dimensional systems by successively optimizing over individual tensors [37].

3.1.2 Alternative methods for PEPS calculations

The PEPS construction is not limited to square lattices, but can be adapted to other lattices, higher dimensions, and even arbitrary interaction graphs. Clearly, the approximate contraction scheme we just presented works for any two-dimensional lattice, and in fact for any planar graph. In order to approximately contract systems in more than two dimensions, note that the approximate contraction scheme is essentially a scheme for reducing the dimension of the problem by one; thus, in order to contract e.g. three-dimensional systems we can nest two layers

of the scheme. In cases with a highly connected PEPS graph (e.g., when considering systems with highly connected interaction graphs such as orbitals in a molecule), one can of course still try to find a sequential contraction scheme, though other contraction methods might be more promising.

The contraction method described in Section 3.1.1 is not the only contraction scheme for PEPS. One alternative method is based on renormalization ideas [38–40]: There, one takes blocks of e.g. 2×2 tensors and tries to approximate them by a tensor with lower bond dimension by appropriate truncation,

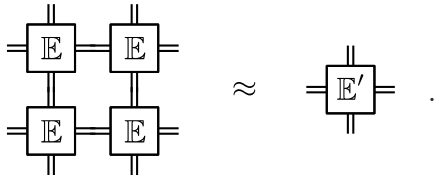

Finding the best truncation scheme requires exact knowledge of the environment, i.e., the contraction of the remaining tensor network. Since this is as hard as the original problem, heuristic methods to approximate the environment (such as to only contract a small number of surrounding tensors exactly, and imposing some boundary condition beyond that) have been introduced. While these approximations are in principle less accurate and the error is less controlled, their more favorable scaling allows for larger D and thus potentially better approximations of the ground state.

Another approach to speed up PEPS contraction is using Monte Carlo sampling [41–43]: We can always write

$$\frac{\langle\Psi|O|\Psi\rangle}{\langle\Psi|\Psi\rangle} = \sum_i p(i) \frac{\langle i|O|\Psi\rangle}{\langle i|\Psi\rangle} \,, \tag{14}$$

where the sum runs over an orthonormal basis $|i\rangle$, and $p(i) = |\langle i|\Psi\rangle|^2/\langle\Psi|\Psi\rangle$; in particular, we want to consider the local spin basis $i = (i_1, \ldots, i_N)$. If we can compute $\langle i|\Psi\rangle$ and $\langle i|O|\Psi\rangle$ (where the latter reduces to the former if O is a local operator), then we can use Monte Carlo sampling to approximate the expectation value $\langle\Psi|O|\Psi\rangle$. In particular, for PEPS $\langle i|\Psi\rangle$ can again be evaluated by contracting a two-dimension tensor network; however, this network now has bond dimension D rather than D^2. Thus, we can apply any of the approximate contraction schemes described before, but we can go to much larger D with the same computational resources; it should be noted, however, that the number of operations needs to be multiplied with the number M of sample points taken, and that the accuracy of Monte Carlo sampling improves as $1/\sqrt{M}$.

3.1.3 PEPS and exactly solvable models

Just as MPS, PEPS are also very well suited for the construction of solvable models. First of all, many relevant states have exact PEPS representations: For instance, the 2D cluster state underlying measurement based computation [6] is a PEPS with $D = 2$ [7], as well as various topological models such as Kitaev's toric code state [9, 22, 32] or Levin and Wen's string-net models [44–46]. A particularly interesting class of exact PEPS ansatzes is obtained by considering classical spin models $H(s_1, \ldots, s_N)$, such as the 2D Ising model $H = -\sum_{<i,j>} s_i s_j$, and defining a quantum state

$$|\psi\rangle = \sum_{s_1,\ldots,s_N} e^{-\beta/2\, H(s_1,\ldots,s_N)} |s_1, \ldots, s_N\rangle \,.$$

It is easy to see that this state has the same correlation functions in the z basis as the classical Gibbs state at inverse temperature β. On the other hand, this state has a PEPS representation (called the "Ising PEPS") with $\mathcal{P} = |0\rangle\langle a,a,a,a| + |1\rangle\langle b,b,b,b|$, where $\langle a|a\rangle = \langle b|b\rangle = 1$ and $\langle a|b\rangle = \langle b|a\rangle = e^{-\beta}$ [9]. This implies that in two dimensions, PEPS (e.g., the Ising PEPS at the critical β) can exhibit algebraically decaying correlations which implies that any corresponding Hamiltonian must be gapless.[10] This should be contrasted with the one-dimensional case, where we have seen that any MPS has exponentially decaying correlations and is the ground state of a gapped parent Hamiltonians.

Clearly, parent Hamiltonians can be defined for PEPS just the same way as for MPS: The reduced density operator $\rho_{k\times\ell}$ of a region of size $k\times\ell$ lives on a $d^{k\ell}$-dimensional system, yet can have rank at most $D^{2k+2\ell}$. Thus, by growing both k and ℓ we eventually reach the point where $\rho_{k\times\ell}$ becomes rank deficient, giving rise to a non-trivial parent Hamiltonian H with local terms H projecting onto the kernel of $\rho_{k\times\ell}$. Again, just as in one dimension it is possible to devise conditions under which the ground state of H is unique [49], as well as modified conditions under which the ground space of H has a topological structure [22], which turns out to be related to "hidden" (i.e., virtual) symmetries of the PEPS tensors. Unlike in one dimension, these parent Hamiltonians are not always gapped (such as for the critical Ising PEPS discussed above); however, techniques similar to the ones used in one dimension can be used to prove a gap for PEPS parent Hamiltonians under certain conditions [24].

3.2 Simulating time evolution and thermal states

Up to now, our discussion has been focused on ground states of many-body systems. However, the techniques described here can also be adapted to simulate thermal states as well as time evolution of systems governed by local Hamiltonians. In the following, we will discuss the implementation for one-dimensional systems; the generalization to to 2D and beyond is straightforward.

Let us start by discussing how to simulate time evolution. (This will also form the basis for the simulation of thermal states.) We want to study how an initial MPS $|\Psi\rangle$ changes under the evolution with e^{iHt}; w.l.o.g., we consider H to be nearest neighbor. To this end, we perform a Trotter decomposition

$$e^{iHt} \approx \left(e^{iH_{\text{even}}t/M} e^{iH_{\text{odd}}t/M}\right)^M$$

where we split $H = H_{\text{even}} + H_{\text{odd}}$ into even and odd terms (acting between sites 12, 34, …, and 23, 45, …, respectively), such that both H_{even} and H_{odd} are sums of non-overlapping terms. For large M, the Trotter expansion becomes exact, with the error scaling like $O(1/M)$. We can now write

$$e^{iH_{\text{even}}\tau} = \bigotimes_{i=1,3,5,\ldots} e^{ih_{i,i+1}\tau} = \boxed{e^{ih_{12}\tau}}\ \boxed{e^{ih_{34}\tau}}\ \cdots$$

(with $\tau = t/M$), and similarly for $e^{iH_{\text{odd}}\tau}$. Thus, after one time step τ the initial MPS is

[10] This follows from the so-called "exponential clustering theorem" [47, 48] which states that ground states of gapped Hamiltonians have exponentially decaying correlation functions.

transformed into

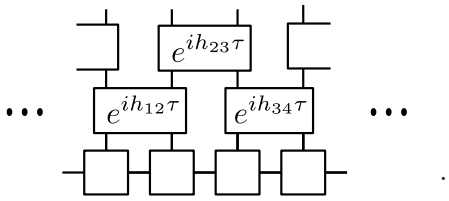

Here, the lowest line is the initial MPS, and the next two lines the evolution by H_{even} and H_{odd} for a time τ, respectively. We can proceed this way and find that the state after a time t is described as the boundary of a two-dimensional tensor network. We can then use the same procedure as for the approximate contraction of PEPS (proceeding row by row) to obtain an MPS description of the state at time t [5]. A caveat of this method is that this only works well as long as the state has low entanglement at all times, since only then, a good MPS approximation of the state exists [4, 50]. While this holds for low-lying excited states with a small number of quasiparticles, this is not true after a quench, i.e., a sudden change of the overall Hamiltonian of the system [51, 52]. However, this does not necessarily rule out the possibility to simulate time evolution using tensor networks, since in order to compute an expectation value $\langle\Psi|e^{-iHt}Oe^{iHt}|\Psi\rangle$, one only needs to contract a two-dimensional tensor network with no boundary, which can not only be done along the time direction (row-wise) but also along the space direction (column-wise), where such bounds on the correlations do not necessarily hold; indeed, much longer simulations times have be obtained this way [53].
In the same way as real time evolution, we can also implement imaginary time evolution; and since $e^{-\beta H}$ acting on a random initial state approximates the ground state for $\beta \to \infty$, this can be used as an alternative algorithm for obtaining MPS approximations of ground states.
In order to simulate thermal states, we use Matrix Product Density Operators (MPDOs) [54]

$$\rho = \sum_{\substack{i_1,\ldots,i_N \\ j_1,\ldots,j_N}} \mathrm{tr}[A^{[1]}_{i1,j1}\cdots A^{[N]}_{i_N,j_N}]|i_1,\ldots,i_N\rangle\langle j_1,\ldots,j_N|$$

$=$

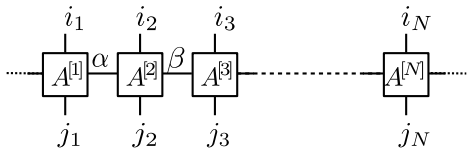

,

where each tensor $A^{[s]}$ now has two physical indices, one for the ket and one for the bra layer. We can then write the thermal state as

$$e^{-\beta H} = e^{-\beta H/2}\,\mathbb{1}\,e^{-\beta H/2}$$

and use imaginary time evolution (starting from the maximally mixed state $\mathbb{1}$ which has a trivial tensor network description) and the Trotter decomposition to obtain a tensor network for $e^{-\beta H}$, which can again be transformed into an MPDO with bounded bond dimension using approximate contraction [54].

3.3 Other tensor network ansatzes

There is a number of other entanglement based ansatzes beyond MPS and PEPS for interacting quantum systems, some of which we will briefly sketch in the following.
Firstly, there is the Multiscale Entanglement Renormalization Ansatz (MERA) [55], which is an ansatz for scale invariant systems (these are systems at a critical point where the Hamiltonian

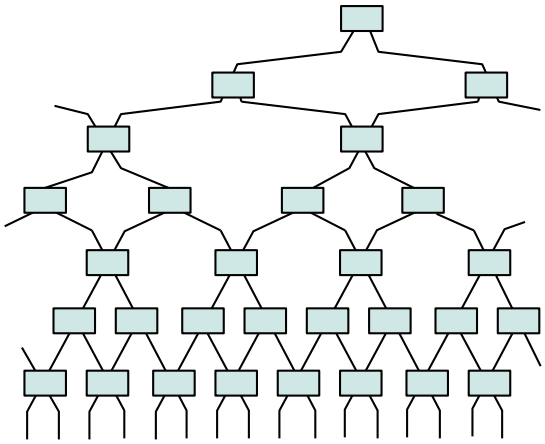

Fig. 7: *The Multi-Scale Entanglement Renormalization Ansatz (MERA) in 1D. (The left and right boundary are connected.)*

is gapless, and which have algebraically decaying correlation functions), and which incorporates the scale-invariance in the ansatz. A first step towards a scale-invariant ansatz would be to choose a tree-like tensor network. However, such an ansatz will not have sufficient entanglement between different blocks. Thus, one adds additional *disentanglers* which serve to remove the entanglement between different blocks, which gives rise to the tensor network shown in Fig. 7. In order to obtain an efficiently contractible tensor network, one chooses the tensors to be unitaries/isometries in vertical direction, such that each tensor cancels with its adjoint. It is easy to see that this way for any local O, in the tensor network for $\langle\Psi|O|\Psi\rangle$ most tensors cancel, and one only has to evaluate a tensor network of the size of the *depth* of the MERA, which is logarithmic in its length [55]. The MERA ansatz is not restricted to one dimension and can also be used to simulate critical system in 2D and beyond [56].

A different variational class is obtained by studying states for which expectation values can be computed efficiently using Monte Carlo sampling. Following Eq. (14), this requires (for local quantities O) that we can compute $\langle i|\Psi\rangle$ efficiently for all $i = (i_1, \ldots, i_N)$. One class of states for which this holds is formed by MPS, which implies that we can evaluate expectation values for MPS using Monte Carlo sampling [41, 42] (note that the scaling in D is more favorable since $\langle i|\Psi\rangle$ can be computed in time $\propto ND^2$). This can be extended to the case where $\langle i|\Psi\rangle$ is a product of efficiently computable objects, such as products of MPS coefficients defined on subsets of spins: We can arrange overlapping one-dimensional strings in a 2D geometry and associate to each of them an MPS, yielding a class known as string-bond states [41, 57], which combines a flexible geometry with the favorable scaling of MPS-based methods. We can also consider $\langle i|\Psi\rangle$ to be a product of coefficients each of which only depends on the spins i_k supported on a small plaquette, and where the lattice is covered with overlapping plaquettes, yielding a family of states known as Entangled Plaquette States (EPS) [58] or Correlator Product States (CPS) [59], which again yields an efficient algorithm with flexible geometries. In all of these ansatzes, the energy is minimized by using a gradient method, which is considerably facilitated by the fact that the gradient can be sampled directly without the need to first compute the energy landscape.

In order to simulate infinite lattices, it is possible to extend MPS and PEPS to work for infinite systems: iMPS and iPEPS. The underlying idea is to describe the system by an infinite MPS and PEPS with a periodic pattern of tensors such as ABABAB... (which allows the system to break

translational symmetry and makes the optimization more well-behaved). Then, one fixes all tensors except for one and minimizes the energy as a function of that tensor until convergence is reached. For the optimization, one needs to determine the dependence of the energy on the selected tensor, which can be accomplished in various ways, such as using the fixed point of the transfer operator, renormalization methods (cf. Section 3.1.2), or the corner transfer matrix approach. For more information, see, e.g., [60–62].

3.4 Simulation of fermionic sytems

Up to now, we have considered the simulation of spin systems using tensor networks. On the other hand, in many cases of interest, such as for the Hubbard model or the simulation of molecules, the underlying systems are fermionic in nature. In the following, we will discuss how tensor network methods such as MPS, PEPS, or MERA can be extended to the simulation of fermionic systems.

In order to obtain a natural description of fermionic systems, the idea is to replace each object (i.e., tensor) in the construction of PEPS or MERA by fermionic operators [63–65]. This is, in the construction of MPS and PEPS, Fig. 3 and Fig. 6, both the maximally entangled bonds and the $\mathcal{P}_s$ are now built from fermionic operators and need to preserve parity; equally, in the MERA construction, Fig. 7, all unitaries and isometries are fermionic in nature. The resulting states are called fermionic PEPS (fPEPS) and fermionic MERA (fMERA).

Let us now have a closer look at a fermionic tensor network, and discuss how to compute expectation values for those states. E.g., the fPEPS construction yields a state

$$(\mathcal{P}_1 \otimes \mathcal{P}_2 \otimes \cdots)(\omega_1 \otimes \omega_2 \otimes \cdots)|\Omega\rangle \ ,$$

where $|\Omega\rangle$ is the vacuum state, the ω_i create entangled fermionic states between the corresponding auxiliary modes, and the $\mathcal{P}_s$ map the auxiliary fermionic modes to the physical fermionic modes at site s (leaving the auxiliary modes in the vacuum). While the product of the ω_i contains only auxiliary mode operators in a given order, the product of the $\mathcal{P}_s$ contains the physical and auxiliary operators for each site grouped together. To compute expectation values, on the other hand, we need to move all the physical operators to the left and the virtual operators to the right in the product of the $\mathcal{P}_s$; additionally, the virtual operators have to be arranged such that they cancel with the ones arising from the product of the ω_i. Due to the fermionic anti-commutation relations, this reordering of fermionic operators results in an additional complication which was not present for spin systems. Fortunately, it turns out that there are various ways how to take care of the ordering of fermionic operators at no extra computational cost: One can use a Jordan-Wigner transformation to transform the fermionic system to a spin system [63, 65]; one can map the fPEPS to a normal PEPS with one additional bond which takes care of the fermionic anticommutation relations [64]; or one can replace the fermionic tensor network by a planar spin tensor network with parity preserving tensors, where each crossing of lines [note that a planar embedding of a network such as the 2D expectation value in Eq. (11) gives rise to crossings of lines, which corresponds to the reordering of fermionic operators] is replaced by a tensor which takes care of the anticommutation rules [66, 67].

4 Quantum Complexity: Understanding the limitations to our understanding

In the preceding sections, we have learned about different methods to simulate the physics of many-body systems governed by local interactions, using their specific entanglement structure. While these algorithms work very well in practice, the convergence of these methods can almost never be rigorously proven. But does this mean that we just haven't found the right proof yet, or is there a fundamental obstacle to proving that these methods work – and if yes, why do they work after all?

4.1 A crash course in complexity classes

These questions can be answered using the tools of complexity theory, which deals with classifying the difficulty of problems. Difficulty is typically classified by the resources needed to solve the problem on a computer (such as computation time or memory) as a function of the *problem size*, this is, the length of the problem description n.
Let us start by introducing some relevant complexity classes.[11] To simplify the comparison of problems, complexity theorists usually focus on "decision problems", i.e., problems with a yes/no answer. While this seems overly restrictive, being able to answer the right yes/no question typically enables one to also find an actual solution to the problem. (E.g., one can ask whether the solution is in a certain interval, and divide this interval by two in every step.) So let us get started with the complexity classes:

- P ("polynomial time"): The class of problems which can be solved in a time which scales at most as some polynomial $\mathrm{poly}(n)$ in the size of the problem. For instance, multiplying two numbers is in P – the number of elementary operators scales like the product of the number of digits of the two numbers to be multiplied. Generally, we consider the problems in P those which are efficiently solvable.

- NP ("non-deterministic polynomial time"): The class of all decision problems where for "yes" instances, there exists a "proof" (i.e., the solution to the problem) whose correctness can be *verified* in a time which is $\mathrm{poly}(n)$, while for "no" instances, no such proof exists. Typical problems are decomposing a number into its prime factors (given the prime factors, their product can easily be verified), or checking whether a given graph can be colored with a certain number of colors without coloring two adjacent vertices in the same color (for a given coloring, it can be efficiently checked whether all adjacent vertices have different colors).

- BQP (bounded-error quantum polynomial time), the quantum version of P: The class of problems which can be (probabilistically) solved by a quantum computer in time $\mathrm{poly}(n)$; a famous example of a problem in BQP which is not known to be in P is Shor's algorithm for factoring [70].

- QMA (quantum Merlin Arthur), one quantum version of NP: The class of decision problems where for a "yes" instance, there exists a quantum proof (i.e., a quantum state) which can be efficiently verified by a quantum computer, and no such proof exists for a "no" instance. For example, determining whether the ground state energy of a local Hamiltonian

[11] This is going to be a very brief introduction. If you want to learn more, consult e.g. Refs. [68, 69].

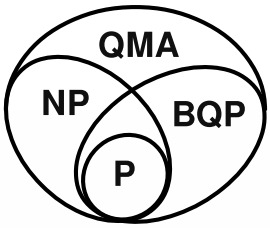

Fig. 8: *Relevant complexity classes and their relation.*

H is below some threshold E (up to a certain accuracy) is in QMA – in a "yes" case, the proof would be any state $|\psi\rangle$ with energy below the threshold, and the energy $\langle\psi|H|\psi\rangle$ can be efficiently estimated by a quantum computer, using e.g. phase estimation [71].

The relation of the classes to each other is illustrated in Fig. 8. All of the inclusions shown are generally believed to be strict, but none of them has up to now been rigorously proven. In particular, whether NP≠P is probably the most famous open problem in theoretical computer science.

An important concept it that of complete problems: A problem is complete for a class if it is as hard as any problem in the class. Completeness is established by showing that any problem in the class can be *reduced* to the complete problem, this is, it can be reformulated as an instance of the complete problem in $\mathrm{poly}(n)$ time. The relevance of complete problems lies in the fact that they are the hardest problems in a class: This is, if a problem is e.g. NP-complete, and we believe that NP≠P, then this problem cannot be solved in polynomial time; and on similar grounds, QMA-complete problems cannot be solved in polynomial time by either a classical or a quantum computer. We will discuss physically relevant complete problems relating to quantum many-body systems in the next section.

4.2 The complexity of problems in many-body physics

In the following, we will discuss the computational complexity of quantum many-body problems. The main problem we will consider is determining whether the ground state energy of a Hamiltonian H which is a sum of few-body terms is below a certain threshold (up to a certain accuracy). As we have argued above, this problem is inside the class QMA. In the following, we will argue that the problem is in fact QMA-complete, which implies that it is hard not only for classical, but even for quantum computers; the following construction is due to Kitaev [71, 72]. To this end, we need to consider an arbitrary problem in QMA and show that we can rephrase it as computing the ground state energy of a certain Hamiltonian. A problem in QMA is described by specifying the quantum circuit which verifies the proof, and asking whether it has an input which will be accepted with a certain probability. The verifying circuit is illustrated in Fig. 9. Now let us assume that there is a valid proof $|\phi_0\rangle$, and run the verifier with $|\phi_0\rangle$ (plus ancillas $|0\rangle$) as an input. At each time step t, the state of the register the verifier acts on is denoted by $|\psi_t\rangle$, and the proof is accepted if the first qubit of the state $|\psi_T\rangle$ at time T is in state $|1\rangle$.

Our aim will now be to build a Hamiltonian which has the "time history state"

$$|\Psi\rangle = \sum_t |\psi_t\rangle_R |t\rangle_T \tag{15}$$

as a ground state. To this end, we will use three types of terms: One term, H_{init}, will ensure that the ancillas are in the state $|0\rangle$ at time $t = 0$, by increasing the energy of non-zero ancillas

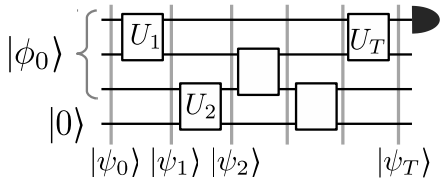

Fig. 9: *QMA verifier: The proof $|\phi_0\rangle$, together with some ancillas $|0\rangle$, is processed by the verifying circuit $U_T \cdots U_1$; the intermediate state at step t is denoted by $|\psi_t\rangle$. At $t = T$, the first qubit is measured in the computational basis to determine whether the proof is accepted.*

if $t = 0$. A second term, H_{prop}, will ensure correct propagation from time t to $t + 1$, i.e., $|\psi_t\rangle = U_t|\psi_{t-1}\rangle$. Finally, a last term H_{final} will increase the energy if the proof is not accepted, i.e., the first bit of $|\psi_T\rangle$ is not $|1\rangle$. Together,

$$H = H_{\text{init}} + H_{\text{prop}} + H_{\text{final}} \tag{16}$$

has a ground state with minimal energy if there exists a valid proof [which in that case is exactly the time history state $|\Psi\rangle$ of Eq. (15)]. On the other hand, in a "no" instance in which no valid proof exists, any ground state – which is still of the form (15) – must either start with incorrectly initialized ancillas, or propagate the states incorrectly (violating $|\psi_t\rangle = U_t|\psi_{t-1}\rangle$), or be rejected by H_{final}, thereby increasing the energy sufficiently to reliably distinguish "yes" from "no" instances. Together, this demonstrates that finding the ground state energy of the Hamiltonian (16) is a QMA-complete problem, showing that it is impossible to solve this problem even for a quantum computer [71, 72]).

While the Hamiltonian (16) is not spatially local, there has been a number of works sequentially proving QMA-hardness for more and more simple Hamiltonians. In particular, nearest-neighbor Hamiltonians on a 2D square lattice of qubits are QMA-complete [73], and, most notably, nearest neighbor Hamiltonians on one-dimensional chains [74], thus substantiating the difficulties encountered in searching for convergence proofs for simulation methods even in 1D.

Let us note that there is also a classical version of the above construction, showing NP-completeness of *classical* ground state problems: In that case, we can use a "history state"

$$|\psi_0\rangle \otimes |\psi_1\rangle \otimes \cdots \otimes |\psi_T\rangle$$

with no coherence between different times, where we think of the states as being arranged in columns. The Hamiltonian is similar to the one before, Eq. (16), just that the individual terms are no more conditioned on the value of a "time" register, but simply act on the columns of the history state corresponding to the right time t. (Sloppily speaking, the reason that we can do so is that all terms in the Hamiltonian act in a classical basis, and classical information can be cloned.) The resulting Hamiltonian is at most four-local, acting across 2×2 plaquettes of adjacent spins. Again, it has been shown using differerent techniques that even classical two-dimensional models with Ising-type couplings and local fields are still NP-complete [33].

Given all these hardness results for determining ground state properties of classical and quantum spin systems, one might wonder why in practice, simulation methods often work very well. First, let us note that these hardness result tell us why in many cases, we cannot *prove* that numerical methods work: This would require to identify the necessary conditions such as to exclude all hard instances, while still keeping the relevant problems, and to find a proof relying exactly on these conditions. Indeed, there are many properties which separate practical

problems from the hard instances we discussed: For instance, in practice one usually considers translationally invariant (or nearly translationally invariant) systems (though there exist hardness results for translationally invariant systems even in one dimension [75]), and the systems considered will have various symmetries. Even more importantly, all the QMA-complete models known have a spectral gap of at most $1/\mathrm{poly}(n)$, as opposed to the typically constant gap in many problems of interest. On the other hand, the NP-complete Hamiltonian outlined above is completely classical and thus has gap 1, while still being NP-complete. Overall, while there is no doubt that numerical methods are extremely successful in practice, computational complexity tells us that we have to carefully assess their applicability in every new scenario. It should also be pointed out that the the fact that a family of problems (such as ground state problems) is complete for a certain complexity class addresses only the worst-case complexity, and in many cases, typical instances of the same problem can be solved much more efficiently.

5 Summary

In this lecture, we have given an overview over condensed matter applications of quantum information methods, and in particular of entanglement theory. The main focus was on entanglement-based ansatzes for the description and simulation of quantum many-body systems. We started by discussing the area law for the entanglement entropy which is obeyed by ground states of local interactions, and used this to derive the Matrix Product State (MPS) ansatz which is well suited to describe the physics of such systems. We showed that the one-dimensional structure of MPS allows for the efficient evaluation of expectation values, and that this can be used to build a variational algorithm for the simulation of one-dimensional systems. We have also shown how MPS appear as ground state of local "parent Hamiltonians" which makes them suitable to construct solvable models, and thus for the study of specific models as well as the general structure of quantum phases.

We have then discussed Projected Entangled Pair States (PEPS), which naturally generalize MPS and are well suited for the description of two-dimensional systems, and we have shown how approximation methods can be used to implement efficient PEPS based simulations. Again, PEPS can also be used to construct solvable models very much the same way as for MPS. We have subsequently demonstrated that MPS and PEPS can be used to simulate the time evolution and thermal states of systems governed by local Hamiltonians. Moreover, we have discussed other tensor network based approaches, such as MERA for scale-invariant systems or iMPS and iPEPS for infinite sytems, and concluded with a discussion on how to apply tensor network methods to fermionic systems.

Finally, we have introduced another field in which quantum information tools are useful to understand condensed matter systems, namely the field of computational complexity. Complexity tools allow us to understand which problems we can or cannot solve. In particular, we have discussed the class QMA which contains the problems which are hard even for quantum computers, and we have argued that many ground state problems, including 2D lattices of qubits and 1D chains, are complete for this class. While this does not invalidate the applicability of simulation methods to these problems, it tells us that special care has to be taken, and points out to us why we cannot hope for convergence proofs without imposing further conditions.

References

[1] C. H. Bennett, H. J. Bernstein, S. Popescu, and B. Schumacher, Phys. Rev. A **53**, 2046 (1996), quant-ph/9511030.

[2] J. Eisert, M. Cramer, and M. Plenio, Rev. Mod. Phys. **82**, 277 (2010), arXiv:0808.3773.

[3] M. Hastings, J. Stat. Mech. P08024 (2007), arXiv:0705.2024.

[4] F. Verstraete and J. I. Cirac, Phys. Rev. B **73**, 094423 (2006), cond-mat/0505140.

[5] G. Vidal, Phys. Rev. Lett. **93**, 040502 (2004), quant-ph/0310089.

[6] R. Raussendorf and H. J. Briegel, Phys. Rev. Lett. **86**, 5188 (2001), quant-ph/0010033.

[7] F. Verstraete and J. I. Cirac, Phys. Rev. A **70**, 060302 (2004), quant-ph/0311130.

[8] C. K. Majumdar and D. Ghosh, J. Math. Phys. **10**, 1388 (1969).

[9] F. Verstraete, M. M. Wolf, D. Perez-Garcia, and J. I. Cirac, Phys. Rev. Lett. **96**, 220601 (2006), quant-ph/0601075.

[10] N. Schuch, M. M. Wolf, F. Verstraete, and J. I. Cirac, Phys. Rev. Lett. **98**, 140506 (2007), quant-ph/0611050.

[11] U. Schollwöck, Rev. Mod. Phys. **77**, 259 (2005), cond-mat/0409292.

[12] D. Perez-Garcia, F. Verstraete, M. M. Wolf, and J. I. Cirac, Quant. Inf. Comput. **7**, 401 (2007), quant-ph/0608197.

[13] M. Fannes, B. Nachtergaele, and R. F. Werner, Commun. Math. Phys. **144**, 443 (1992).

[14] J. Eisert, Phys. Rev. Lett. **97**, 260501 (2006), quant-ph/0609051.

[15] N. Schuch, I. Cirac, and F. Verstraete, Phys. Rev. Lett. **100**, 250501 (2008), arXiv:0802.3351.

[16] S. R. White, Phys. Rev. Lett. **69**, 2863 (1992).

[17] F. Verstraete, D. Porras, and J. I. Cirac, Phys. Rev. Lett. **93**, 227205 (2004), cond-mat/0404706.

[18] U. Schollwöck, Ann. Phys. **326**, 96 (2011), arXiv:1008.3477.

[19] F. Verstraete, V. Murg, and J. I. Cirac, Advances in Physics **57**, 143 (2008).

[20] I. Affleck, T. Kennedy, E. H. Lieb, and H. Tasaki, Phys. Rev. Lett. **59**, 799 (1987).

[21] A. Affleck, T. Kennedy, E. H. Lieb, and H. Tasaki, Commun. Math. Phys. **115**, 477 (1988).

[22] N. Schuch, I. Cirac, and D. Pérez-García, Ann. Phys. **325**, 2153 (2010), arXiv:1001.3807.

[23] N. Schuch, D. Poilblanc, J. I. Cirac, and D. Pérez-García, Phys. Rev. B **86**, 115108 (2012), arXiv:1203.4816.

[24] N. Schuch, D. Perez-Garcia, and I. Cirac, Phys. Rev. B **84**, 165139 (2011), arXiv:1010.3732.

[25] D. Perez-Garcia, M. Wolf, M. Sanz, F. Verstraete, and J. Cirac, Phys. Rev. Lett. **100**, 167202 (2008), arXiv:0802.0447.

[26] M. Sanz, M. M. Wolf, D. Perez-Garcia, and J. I. Cirac, Phys. Rev. A **79**, 042308 (2009), arXiv:0901.2223.

[27] F. Pollmann, A. M. Turner, E. Berg, and M. Oshikawa, Phys. Rev. B **81**, 064439 (2010), arXiv:0910.1811.

[28] X. Chen, Z. Gu, and X. Wen, Phys. Rev. B **83**, 035107 (2011), arXiv:1008.3745.

[29] M. A. Nielsen and I. A. Chuang, *Quantum Computation and Quantum Information* (Cambridge University Press, 2000).

[30] B. Nachtergaele, Commun. Math. Phys. **175**, 565 (1996).

[31] X.-G. Wen, *Quantum Field Theory of Many Body Systems* (Oxford University Press, 2004).

[32] A. Kitaev, Ann. Phys. **303**, 2 (2003), quant-ph/9707021.

[33] F. Barahona, J. Phys. A **15**, 3241 (1982).

[34] S. Yan, D. A. Huse, and S. R. White, Science **332**, 1173 (2011), arXiv:1011.6114.

[35] M. B. Hastings, Phys. Rev. B **73**, 085115 (2006), cond-mat/0508554.

[36] M. B. Hastings, Phys. Rev. B **76**, 035114 (2007), cond-mat/0701055.

[37] F. Verstraete and J. I. Cirac, (2004), cond-mat/0407066.

[38] H. C. Jiang, Z. Y. Weng, and T. Xiang, Phys. Rev. Lett. **101**, 090603 (2008), arXiv:0806.3719.

[39] Z.-C. Gu, M. Levin, and X.-G. Wen, Phys. Rev. B **78**, 205116 (2008), arXiv:0806.3509.

[40] Z. Y. Xie, H. C. Jiang, Q. N. Chen, Z. Y. Weng, and T. Xiang, Phys. Rev. Lett. **103**, 160601 (2009), arXiv:0809.0182.

[41] N. Schuch, M. M. Wolf, F. Verstraete, and J. I. Cirac, Phys. Rev. Lett. **100**, 40501 (2008), arXiv:0708.1567.

[42] A. W. Sandvik and G. Vidal, Phys. Rev. Lett. **99**, 220602 (2007), arXiv:0708.2232.

[43] L. Wang, I. Pizorn, and F. Verstraete, Phys. Rev. B **83**, 134421 (2011), arXiv:1010.5450.

[44] M. A. Levin and X.-G. Wen, Phys. Rev. B **71**, 045110 (2005), cond-mat/0404617.

[45] O. Buerschaper, M. Aguado, and G. Vidal, Phys. Rev. B **79**, 085119 (2009), arXiv:0809.2393.

[46] Z.-C. Gu, M. Levin, B. Swingle, and X.-G. Wen, Phys. Rev. B **79**, 085118 (2009), arXiv:0809.2821.

[47] M. B. Hastings and T. Koma, Commun. Math. Phys. **265**, 781 (2006), math-ph/0507008.

[48] B. Nachtergaele and R. Sims, Commun. Math. Phys. **265**, 119 (2006), math-ph/0506030.

[49] D. Perez-Garcia, F. Verstraete, J. I. Cirac, and M. M. Wolf, Quantum Inf. Comput. **8**, 0650 (2008), arXiv:0707.2260.

[50] N. Schuch, M. M. Wolf, F. Verstraete, and J. I. Cirac, Phys. Rev. Lett. **100**, 30504 (2008), arXiv:0705.0292.

[51] P. Calabrese and J. Cardy, J. Stat. Mech. P04010 (2005), cond-mat/0503393.

[52] N. Schuch, M. M. Wolf, K. G. H. Vollbrecht, and J. I. Cirac, New J. Phys. **10**, 33032 (2008), arXiv:0801.2078.

[53] M. C. Bañuls, M. B. Hastings, F. Verstraete, and J. I. Cirac, Phys. Rev. Lett. **102**, 240603 (2009), arXiv:0904.1926.

[54] F. Verstraete, J. J. Garcia-Ripoll, and J. I. Cirac, Phys. Rev. Lett. **93**, 207204 (2004), cond-mat/0406426.

[55] G. Vidal, Phys. Rev. Lett. **101**, 110501 (2008), quant-ph/0610099.

[56] G. Evenbly and G. Vidal, Phys. Rev. Lett. **102**, 180406 (2009), arXiv:0811.0879.

[57] A. Sfondrini, J. Cerrillo, N. Schuch, and J. I. Cirac, Phys. Rev. B **81**, 214426 (2010), arXiv:0908.4036.

[58] F. Mezzacapo, N. Schuch, M. Boninsegni, and J. I. Cirac, New J. Phys. **11**, 083026 (2009), arXiv:0905.3898.

[59] H. J. Changlani, J. M. Kinder, C. J. Umrigar, and G. K.-L. Chan, arXiv:0907.4646.

[60] G. Vidal, Phys. Rev. Lett. **98**, 070201 (2007), cond-mat/0605597.

[61] J. Jordan, R. Orus, G. Vidal, F. Verstraete, and J. I. Cirac, Phys. Rev. Lett. **101**, 250602 (2008), cond-mat/0703788.

[62] R. Orus and G. Vidal, Phys. Rev. B **80**, 094403 (2009), arXiv:0905.3225.

[63] P. Corboz, G. Evenbly, F. Verstraete, and G. Vidal, Phys. Rev. A **81**, 010303(R) (2010), arXiv:0904.4151.

[64] C. V. Kraus, N. Schuch, F. Verstraete, and J. I. Cirac, Phys. Rev. A **81**, 052338 (2010), arXiv:0904.4667.

[65] C. Pineda, T. Barthel, and J. Eisert, Phys. Rev. A **81**, 050303(R) (2010), arXiv:0905.0669.

[66] P. Corboz and G. Vidal, Phys. Rev. B **80**, 165129 (2009), arXiv:0907.3184.

[67] P. Corboz, R. Orus, B. Bauer, and G. Vidal, Phys. Rev. B **81**, 165104 (2010), arXiv:0912.0646.

[68] C. M. Papadimitriou, *Computational complexity* (Addison-Wesley, Reading, MA, 1994).

[69] M. Sipser, *Introduction To The Theory Of Computation* (Brooks Cole, 2006).

[70] P. W. Shor, SIAM J. Comput. **26**, 1484 (1997), quant-ph/9508027.

[71] A. Y. Kitaev, A. H. Shen, and M. N. Vyalyi, *Classical and quantum computation* (American Mathematical Society, Providence, Rhode Island, 2002).

[72] D. Aharonov and T. Naveh, (2002), quant-ph/0210077.

[73] R. Oliveira and B. M. Terhal, Quant. Inf. Comput. **8**, 900 (2009), quant-ph/0504050.

[74] D. Aharonov, D. Gottesman, S. Irani, and J. Kempe, Commun. Math. Phys. **287**, 41 (2009), arXiv:0705.4077.

[75] D. Gottesman and S. Irani, *Proc. 50th Annual Symp. on Foundations of Computer Science*, 95 (2009), arXiv:0905.2419.

D 1 Fluxonium qubit [1]

V. E. Manucharyan
Society of Fellows of Harvard University
78 Mt. Auburn st., Cambridge, MA, 02138 USA

Contents

1 Introduction **2**

2 Superinductance **3**
2.1 Fundamental asymmetry between charge and flux 3
2.2 Kinetic inductance of superconductors 6
2.3 Superinductance with a Josephson tunnel junction array 7
2.4 Limitation due to quantum phase-slip 9

3 Fluxonium as a Cooper-pair box shunted by a superinductance **10**
3.1 Spectrum: fluxons and plasmons 10
3.2 Matrix elements 13
3.3 Parameter regimes 15

4 Circuit quantum electrodynamics with fluxonium **17**
4.1 Dispersive shifts by an arbitrary atom 18
4.2 Dispersive shifts by fluxonium 20

5 Common decoherence mechanisms **25**
5.1 Two models of spontaneous emission 25
5.2 Purcell effect 26
5.3 Effects of flux and critical current noise 27

[1] Lecture Notes of the 44^{th} IFF Spring School "Quantum Information Processing" (Forschungszentrum Jülich, 2013). All rights reserved.

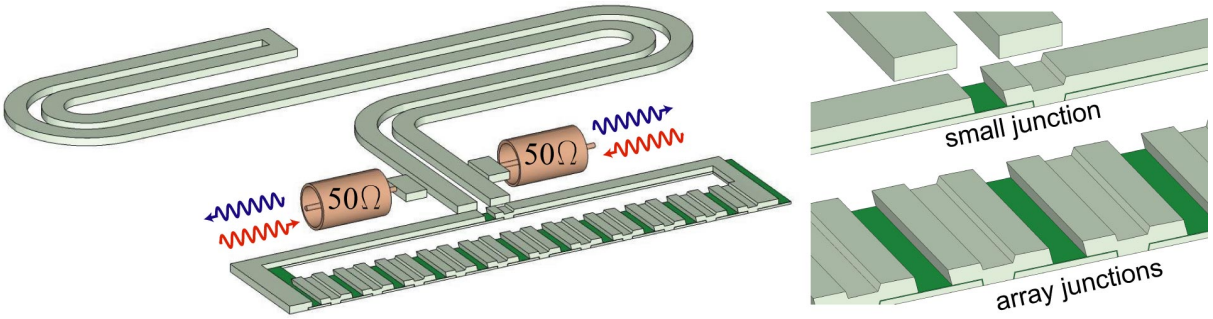

Fig. 1: *Sketch of fluxonium qubit and its readout. Josephson array is turned into a loop by shunting the small area "black-sheep" junction. Gray indicates superconducting aluminum electrodes, green indicates tunneling oxide. Black-sheep junction electrodes are coupled capacitively to the coplanar strips transmission line resonator with a short-circuit termination at the far end. The device is connected to the readout and control electronics by a pair of transmission lines (indicated with brown colored coaxials).*

1 Introduction

We introduce a novel quantum electrical circuits element, "superinductance", and describe a recently implemented superconducting fluxonium qubit, which is based on superinductance [2] [1, 2, 3]. These lecture notes aim at: (i) describing fundamental obstacles in engineering superinductances and explaining how these obstacles have been successfully bypassed using a Josephson tunnel junction array and (ii) providing a theoretical description of the basic properties of fluxonium qubit (Fig. 1).

Superinductance is defined by its two key properties. First, it must superconduct direct current (DC). Second, it must present to an alternating current (AC) the impedance of a frequency-independent inductance L with sufficiently small stray capacitance C_s, such that $\sqrt{L/C_s} > R_Q$, where $R_Q = h/(2e)^2 \simeq 6.5\ \mathrm{k\Omega}$ is the superconducting impedance quantum. The amount of dissipation to the alternating current determines the quality of the superinductance, the weaker the dissipation the better the quality. On the technical side, since quantum circuits operate in the microwave frequency range, the maximum operating frequency of the superinductance, which is for instance limited by the self resonance frequency $1/\sqrt{LC_s}$, should exceed at least $2\pi \times 10\ \mathrm{GHz}$. This latter condition translates into the following numerical estimate for the required magnitude of an inductance operating in the microwave range: $L > 6.5\ \mathrm{k\Omega}/2\pi \times 10\ \mathrm{GHz} \simeq 100\ \mathrm{nH}$.

Superinductance might find applications in establishing the quantum standard of electrical current [4, 5, 6, 7] and in intrinsically fault-tolerant schemes of quantum information processing [8]. Another interesting application of superinductance is circuit quantum electrodynamics (cQED) with hybrid systems, i.e. coupling Rydberg atoms, semiconducting quantum dots, or electrons on a helium surface to on-chip superconducting microwave resonators. Because the electromagnetic field in a superinductance-based resonator is governed by an affective fine structure constant exceeding a unity, the light-matter interaction is greatly enhanced.

One way to understand fluxonium qubit is to think that it is a superconducting loop interrupted by $N+1$ Josephson tunnel junctions, with one of the junction singled out (black-sheep junction) to be weaker than the rest (Fig. 2-left). The qubit states correspond to the number of flux

[2] Term introduced in an unpublished work by A. Kitaev

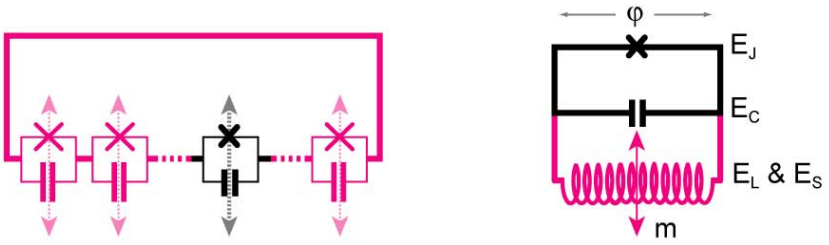

Fig. 2: *Two models of fluxonium circuit. (A). Array of $N+1$ junction, in which one of them, the black-sheep, is weaker than other. This model contains only one degree of freedom, the total number of phase-slips in the fluxonium loop (B). Junction shunted by a "slippery" inductance of the array of N junctions. This model contains two variables, phase φ across the black-sheep junction and m, the total number of phase-slips in the array.*

quanta (we call them fluxons) trapped in the loop. Fluxons can leave the loop by a quantum phase-slip across one of the junctions. The total quantum phase-slip amplitude is given by $E_S^{\Sigma} = E_{SB} + E_S$, where E_{SB} is the quantum phase-slip amplitude in the black-sheep junction, while E_S is that in the array. The inductive energy E_L is slightly renormalized to the value $E_L^{\Sigma} = (E_L^{-1} + E_J^{-1})^{-1} \simeq E_L$. Essentially, we have separated the roles of the array junctions and the black-sheep junction. The array junctions stores the inductive energy associated with the phase-slip in the fluxonium loop, the cost of charging the loop with a flux quanta, or fluxon. The black-sheep provides the quantum-mechanical amplitude for this event, i.e. it allows the fluxon number to change coherently by a unity.
Alternatively, fluxonium may be viewed as a Cooper-pair box type junction in the charge regime which is shunted by a superconducting wire comprised of N junctions in the phase regime (Fig. 2-right). This wire is a circuit element, which is characterized not only by its N-junction linear inductance L, but also by the quantum phase-slip energy amplitude E_S, where both quantities L and E_S are independent on the details of the embedding circuit, which is fair in the limit of large N. In practice we can always suppress the quantum phase-slips across the larger junctions of the array and therefore treat it as a purely linear inductance.
It turns out that when parameters E_J, E_L, and E_C are properly chosen, fluxonium qubit has a remarkably rich spectrum, which covers several octaves of frequency, flux-tunable selection rules, reduced sensitivity to conventional decoherences sources, and strong coupling to microwave resonators. The organization of these lecture notes is as follows. The second and third section describe the recipe to build superinductance and fluxonium, respectively. The fourth section provides an introduction to cQED with fluxonium qubit, emphasizing useful effects of its multi-level spectrum. Finally, the fifth section discusses how fluxonium deals with the decoherence mechanisms common to superconducting qubits.

2 Superinductance

2.1 Fundamental asymmetry between charge and flux

Let us examine quantum fluctuations in a dissipationless LC circuit described by the generalized flux Φ inside the inductor coil and the displacement charge Q at the capacitor plates (Fig. 3). A fluctuation of charge δQ contributes to the total energy of the circuit with capacitive contribution $\delta Q^2/2C$, while the fluctuations of flux $\delta\Phi$ contribute the inductive energy $\delta\Phi^2/2L$. The

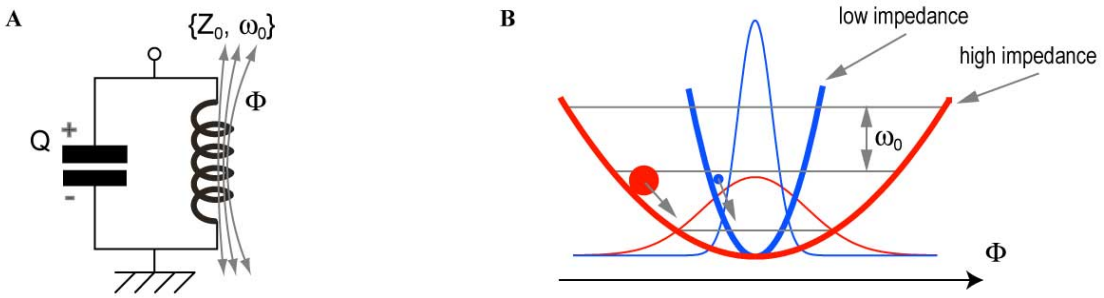

Fig. 3: *Quantum fluctuations in an LC-circuit. (A) Capacitance C in parallel with an inductance L. Alternatively such circuit may be described by the frequency $\omega_0 = 1/\sqrt{LC}$ and impedance $Z_0 = \sqrt{L/C}$. The flux in the inductance is Φ and the displacement charge on the capacitance is Q. (B) Flux representation of two LC oscillators with the same frequency but different impedance. Thick lines (blue - lower impedance, red - high impedance) represent parabolic inductive energies. Thin lines (same color scheme) represent ground-state wavefunctions. The higher the impedance, the larger the quantum fluctuations of flux, irrespective of frequency.*

two energies are equal by virtue of the virial theorem and also equal to the half a photon of zero-point motion energy $\frac{1}{2}\hbar\omega_0$. Therefore, we get $\delta Q^2 = \frac{1}{2}\hbar/Z_0$ and $\delta\Phi^2 = \frac{1}{2}\hbar Z_0$, where we introduced characteristic impedance of the resonator $Z_0 = \sqrt{L/C}$ and the resonant frequency $\omega_0 = 1/\sqrt{LC}$. Thus, irrespective of the resonance frequency, high impedance oscillators have large flux fluctuations and small charge fluctuations and vice versa for low impedance oscillators, verifying at all times Heisenberg's uncertainty relation. Let us introduce the superconducting flux quantum $\Phi_0 = h/2e \simeq 2.0 \times 10^{-15}$ Wb, the superconducting resistance quantum $R_Q = h/(2e)^2 \simeq 6.5$ kΩ, and express flux and charge fluctuations in terms of the charge and flux quanta, namely

$$\begin{aligned} \delta Q/2e &= \sqrt{\frac{1}{4\pi} R_Q/Z_0} \\ \delta\Phi/\Phi_0 &= \sqrt{\frac{1}{4\pi} Z_0/R_Q} \end{aligned} \tag{1}$$

In other words, 6.5 kΩ is a characteristic impedance scale for Z_0 which decides whether charge or flux fluctuate by an amount less or more than their respective fundamental units. We will therefore refer to impedances $Z_0 < R_Q$ as low and $Z_0 > R_Q$ as high. Low impedance oscillators keep flux in the inductance localized on the scale of flux quantum while high impedance oscillators localize charge on the capacitance plates below the single Cooper pair level. Now it is clear that the sub-Cooper pair fluctuations of charge are only possible with the superinductance. In typical radio-frequency electrical circuits, inductances and capacitances come, respectively, from magnetic and electric fields stored in the vacuum space between the circuit parts. It turns out that electromagnetic parameters of vacuum, namely the vacuum permeability ε_0 and the vacuum permittivity μ_0 in that case restrict the impedance Z_0 of such circuits to "low" values. Let us illustrate this point with two readily calculable physical implementations of an LC–circuit (Fig. 4). As a first example, consider two cylindrical parallel wires of radius r separated by a distance d small compared to the wavelength, shorted-circuited at one end and left

open at the other end (Fig. 4-A). The resulting transmission line can be modelled as a chain of inductance-capacitance cells where the specific inductance of the wires is calculated to be $l = \mu_0 \log(d/r)/\pi$ and the specific capacitance between the wires is $c = \varepsilon_0 \pi / \log(d/r)$ [9]. The frequency-dependent input impedance of the transmission line can be derived from the telegrapher's equation [9]:

$$Z(\omega) = Z_\infty \frac{e^{i\pi\omega/\omega_0} - 1}{e^{i\pi\omega/\omega_0} + 1} \tag{2}$$

where we have introduced the wave impedance $Z_\infty = \sqrt{l/c}$ and the quarter-wavelength resonance frequency $\omega_0 = \frac{\pi}{2}/(\sqrt{lc} \times \text{“length”})$. At low frequencies, the impedance $Z(\omega \to 0) \to i\frac{\pi}{2}\frac{Z_\infty}{\omega_0}\omega$ behaves inductively with the effective inductance value of $\frac{\pi}{2} Z_\infty/\omega_0$. Close to the resonance $\omega \to \omega_0$, the input impedance $Z(\omega)$ coincides with that of a parallel LC oscillator with the resonance frequency ω_0 and characteristic impedance $Z_0 = \frac{4}{\pi} Z_\infty$. Note that the transverse dimensions of our two-wire transmission line contribute very little[3] to its wave impedance. Namely, the wave impedance is given by $Z_\infty = Z_{\text{vac}} \log(d/r)/\pi$, where we introduce vacuum impedance Z_{vac}, given by $Z_{\text{vac}} = \sqrt{\mu_0/\varepsilon_0} = 377.0\ \Omega \ll R_Q$, resulting in $Z_0 \ll R_Q$. Essentially, as one increases the inductance by increasing the length of the wire, its self-capacitance increases proportionally, thus resulting in the characteristic impedance of order Z_{vac}.

As a second example, let us attempt to reduce the self-capacitance of an inductor by spreading the two wires from the previous example as far apart from each other as possible (Fig. 4-B). Here the catch is that as soon as the separation between the wires reaches the wavelength, the circuit starts to lose energy by radiating into the free space. The effect of radiation boils down to shunting the two terminals of the circuit with an effective radiation resistance $R_{\text{rad}} = \text{Re}[Z(\omega)]$ given by the standard theory of electric dipole radiation [10],

$$R_{\text{rad}} \approx Z_{\text{vac}} (\omega_0/\omega)^4 \tag{3}$$

While the radiation effect is drastically suppressed at low frequencies, at frequencies $\omega \to \omega_0$ the radiation matches to the free space and the wire is effectively shunted by the vacuum again, even though its total zero-frequency self-capacitance is somewhat reduced. A wide loop behaves just as an infinitely long transmission line with $Z_\infty = Z_{\text{vac}}$, a situation analogous to the previous example.

Although the intelligently chosen geometry of commercially available miniature on-chip inductors does reduce, to some extent, the effects of radiation and stray capacitance, low impedance parasitic resonances are unavoidable[4]. The situation is further worsened by the fact that microwave circuits have to be fabricated on substrates with the dielectric constant of about $5 - 10$ (corundum, silicon, etc.) which further reduces the wave impedance of the medium. In fact, electrical engineers chose the design wave impedance to be $50\ \Omega$ and not $377\ \Omega$ for this reason. We therefore conclude that Nature favors small quantum fluctuations of flux and large quantum fluctuations of charge when compared to their quantum units. In other words, Nature hates superinductors. To emphasize the fundamentallity of this asymmetry between charge and flux, we note the following relation:

[3]The phase velocity of the electromagnetic waves in this structure does not depend at all on the transverse dimensions and coincides with the speed of light in vacuum.

[4]It might appear that the inductance of a transmission line at frequencies $\omega = \omega_0 - \delta\omega$ effectively (Eq. 2) diverges at small $\delta\omega$ with a value of $-i\frac{dZ}{d\omega} \approx Z_\infty/\delta\omega$. Nevertheless, such resonant increase of inductance does not play any role in quantum fluctuations. What counts is the strength of the pole in the impedance function, which is our vacuum-limited characteristic impedance Z_0.

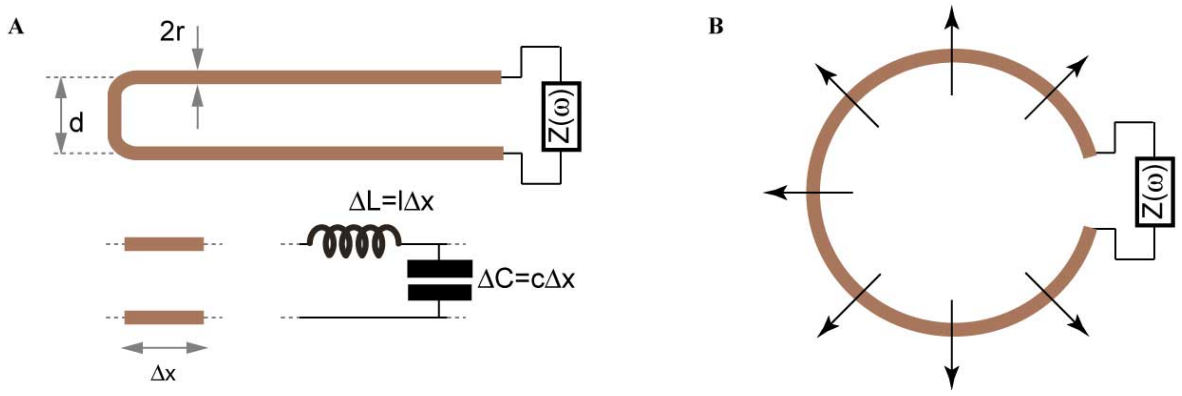

Fig. 4: *Low impedance resonant structures. (A) Parallel-wires transmission line, wire radius is a and the separation is d. The wires are short-circuited at the left end, the impedance measured at the right end is $Z(\omega)$. Inset below shows the electrical ladder model of a section of this transmission line of length Δx. (B). A loop with the circumference identical to the length of the transmission line from (A). Arrows indicate radiation into free space, once the size of the loop approaches the wavelength.*

$$\frac{\delta\Phi/\Phi_0}{\delta Q/2e} \lesssim \frac{Z_{\rm vac}}{R_Q} = 8\alpha \tag{4}$$

where $\alpha \simeq 1/137.0$ is the fine structure constant

2.2 Kinetic inductance of superconductors

Clearly, to beat the vacuum impedance and to offset the asymmetry between charge and flux one must abandon geometric inductances. One well-known non-geometric contribution to the inductance originates from the inertia of the charge carriers, the so-called kinetic inductance. This effect is particularly pronounced in superconducting films and wires, because there the inertia of the charge carriers is not suppressed by dissipation. Let us provide here an interpretation of kinetic inductance of a superconductor in terms of the Meissner effect. Namely, an electrical current in a superconducting wire generates a twist in the superconducting phase across the wire. This twist in phase, or the gradient $\nabla\varphi$, costs energy $\int dV \rho_s (\nabla\varphi)^2$, where ρ_s is the density of the superconducting condensate. The quantity $1/\rho_s$ is then analogous to the specific kinetic inductance of the wire. Increasing kinetic inductance reduces the energy cost of a phase-twist, therefore reducing the phase-rigidity of the superconductor.
It is possible to enhance kinetic inductance of a superconductor by introducing strong disorder. Then, the Cooper pair density ρ_s can be suppressed because of partial localization of charge carriers. However, increasing kinetic inductance indefinitely requires $\rho_s \to 0$, which cannot be great for the superconducting state. For instance, reduced density eventually increases the Coulomb interaction and therefore destroys the superconducting pairing [11]. Unfortunately, both theory and controlled fabrication of disordered superconductors are challenging [12]. On the contrary, a clean and comfortably thick superconducting wire interrupted by a large number of Josephson tunnel junctions represents one particular case of a "disordered" wire which is excellently suited for both transparent theoretical analysis and controlled experiments (Fig. 5). In a tunnel junction, the Cooper pair density is only suppressed inside a nm-thick insulating oxide. This bottleneck dominates the total kinetic inductance. The current I and superconduct-

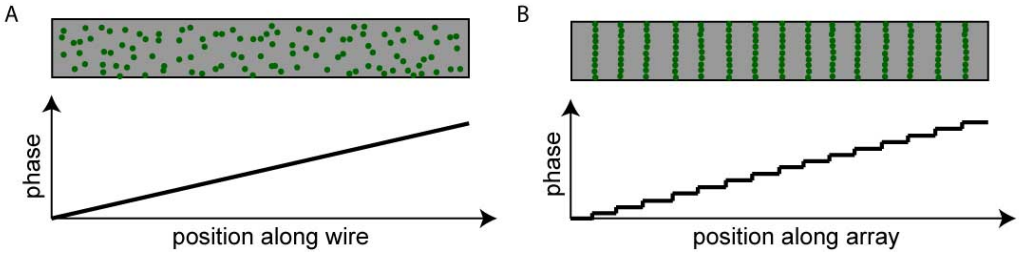

Fig. 5: *Uniform disordered superconductor vs. Josephson tunnel junction array. (A) Usual disordered wire with randomly distributed scatterers. Superconducting phase is a continuous function of the coordinate across the wire. (B) A particular implementation of disordered wire, in which all the scatterers are combined into a set of discrete tunneling barriers, tunneling junctions, between clean superconducting islands. In this case the superconducting phase is fixed within an given island and changes step-like across the junctions.*

ing phase difference θ across the junction obey to the Josephson relation $I = I_0 \sin\theta$, where I_0 the maximum possible supercurrent of the junction[5]. For small currents, Josephson relation implies that the junction is just a linear inductance with magnitude $L_J = \frac{1}{2\pi}\Phi_0/I_0$. Due to the Ambegaokar-Baratoff relation [13], the Josephson inductance L_J is linked to the junction normal resistance R_N and superconducting energy gap Δ as $L_J = \frac{\pi}{4}R_N/\Delta[\mathrm{Hz}]$. Therefore, the stronger the tunneling barrier, the larger the inductance. A similar relation between inductance per square and resistance per square holds for highly disordered but structurally continuous films.

Clearly, the value of kinetic inductance L_J has nothing to do with vacuum permeability μ_0 and may well beat its value with proper choice of junction parameters. For instance a choice of $Al/AlOx/Al$ tunnel junction with a comfortably achievable combination of size of $1\ \mu\mathrm{m}$ and critical current of $1\ \mu\mathrm{A}$ possesses specific inductance as large as $300\mu_0$, corresponding to the geometric inductance of a wire approximately $300\ \mu\mathrm{m}$ long.

2.3 Superinductance with a Josephson tunnel junction array

For frequencies approaching zero, the inductance of the array is obviously given by $L = N \times L_J$. However, for the inductance to operate at a finite frequency, the physical length of the array, or equivalently the number of junction N, also has to be finite. This is a familiar effect that both inductance and its stray capacitance of a piece of metallic wire grow with its size [14] and therefore the longer the wire, the lower its parasitic resonance. In fact, simple analysis of Eq. (2) show that above the self-resonance frequency, an inductance turns into a capacitance. Therefore, let us begin by figuring out the optimum length of the junction array which maximizes both its total inductance and operating frequency.

Junctions are fabricated on an insulating silicon substrate as a series of overlapping films separated by the layer of aluminum oxide (Fig. 6). Each superconducting island is thus connected to its neighbor island by a parallel-plate type capacitance C_J and Josephson inductance L_J. The frequency $\omega_p = 1/\sqrt{L_J C_J}$ is called junction plasma frequency. Given that $C_J \sim A$, with

[5]The phase θ is defined by $\theta(t) = \frac{2e}{\hbar}\int_{-\infty}^{t} \mathrm{d}t' V(t')$, where $V(t)$ is the voltage between the junction electrodes defined as $V(t) = \int \mathrm{d}\,\vec{l}\cdot\vec{E}$, where E is the electric field and the integration path goes through the junction oxide.

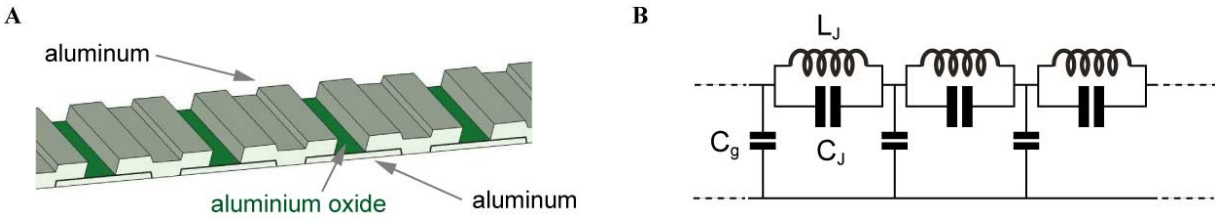

Fig. 6: *Array of Josephson tunnel junctions. (A) Sketch of the physical implementation. Gray regions indicate superconducting islands (aluminium), green layer indicates the tunneling barriers oxide (aluminium oxide). (B) Linear electrical circuit model. L_J stands for Josephson inductance, C_J for the oxide capacitance and C_g is the capacitance of the islands to the nearest metallic object, inevitably present in any experimental realization.*

A being junction area, and $L_J \sim R_N \sim 1/A$, the plasma frequency does not depend on the junction dimensions and is mainly determined by the transparency of the barrier or equivalently by the critical current density. For Al/AlOx/Al junctions $\omega_p \approx 10 - 40$ GHz, which is a few times lower than the Cooper pair breaking frequency $2\Delta \approx 80$ GHz. Every island also possesses a certain capacitance "to ground" C_g. Even when the chip carrying the circuit is mounted far away from metallic objects, some capacitance C_g still comes from capacitive coupling of the islands to the neighboring on-chip metallic structure. Roughly, this non-parallel plate type capacitance scales linearly with island dimensions (note the analogy with the transmission line specific capacitance) and is essentially impossible to get rid of. A fair evaluation would be to $C_g \approx \varepsilon_0 \varepsilon \sqrt{A} \approx 10 - 100\ \mathrm{aF}/\mu\mathrm{m}$.
The propagation of the electromagnetic waves in the Josephson array can be modelled by a dispersive transmission line (Fig. 6) with the following relation between the wave-vector k and the frequency ω [15]:

$$k(\omega) = \omega \frac{\sqrt{L_J C_g}}{\Delta x} \frac{1}{\sqrt{1 - \omega^2/\omega_p^2}} \tag{5}$$

where Δx is the physical length of the unit cell. For frequencies $\omega \lesssim \omega_p/2$ the dispersion relation is nearly linear, which can be interpreted as neglecting the AC current path via the capacitances C_J. Boundary conditions determine the frequencies of the standing wave modes. Figure 7 shows an example solution for the open-short boundary condition, which translates into $N\Delta x = \frac{\pi}{k(\omega_n)}(n + 1/2)$, where n takes integer values starting from zero. Qualitatively, other boundary conditions are equivalent for our purpose. For frequencies below the first standing wave resonance, $\omega < \omega_{n=0}$, the response of the array is purely inductive, with inductance $L = L_J N$. Clearly, the highest operation frequency for this inductance will be achieved if we push $\omega_{n=0}$ all the way towards the plasma frequency ω_p. Note that all other modes of the array bunch up slightly below the plasma frequency of the junctions. By setting $\omega_{n=0} = \omega_p$ we get the following estimate for the maximum number of junctions:

$$N \lesssim \sqrt{C_J/C_g} \tag{6}$$

Equation (6) in practice severely limits the number of junctions N. Even if the stray capacitance C_g is factor of 10^3 smaller than C_J, the number of junction N is limited to a number of about

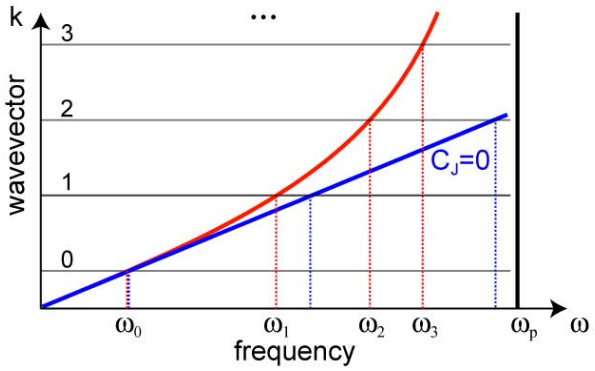

Fig. 7: *Linear modes of the Josephson array. Blue line – nondispersive linear $k(\omega)$ relation for $\omega_p = 1/\sqrt{L_J C_J} \to \infty$. Red line – dispersive $k(\omega)$ for finite ω_p. The indexed set of horizontal lines correspond to the condition of having quantized number of quarter wave-length matching the length of the transmission line. Corresponding solutions are found geometrically and marked on the x-axes with ω_n, $n = 0, 1, 2, ...$*

only 30! The larger the inductance gets, the less stray capacitance it needs to undesirably resonate at a given frequency; vacuum shunts kinetic inductances as well as the geometric ones. With N severely limited, the next question is in order: how large can we make the inductance per junction L_J, before something unwanted happens? In other words, how strongly can we make the "disorder" in a superconductor without destroying the superconducting behavior? Given that $N < \sqrt{C_J/C_g}$ and $\omega < \omega_p$, we can continue our analysis ignoring C_g. Then, the quantum fluctuations of the Josephson phase will be determined again by formulas (1). As we increase L_J, say by reducing the junction area A, the junction effective impedance $Z_J = \sqrt{L_J/C_J} \sim A$ also grows proportionally and causes the phase to fluctuate by an amount $\delta\theta = \sqrt{\pi Z_J/R_Q} \sim \sqrt{A}$. Clearly when the impedance Z_J approaches R_Q, the phase fluctuation $\delta\theta$ approaches π and the junction can no longer be treated as a linear circuit. Since the phase fluctuations cause current fluctuations, the condition $\delta\theta \sim \pi$ is equivalent to the condition $\delta I \sim I_0$, which clearly marks the end to a simple linear kinetic inductance behavior of a Josephson tunnel junction. Another way to put this is that a Josephson junction behaves as an inductance only if it is shunted by a sufficiently large capacitance. We can now explicitly write down the absolute upper limit estimate for the kinetic inductance L of a Josephson array:

$$\omega L|_{\max} \lesssim R_Q \sqrt{C_J/C_g} \tag{7}$$

Thus, according to purely linear analysis, superinductance appears possible for frequencies below ω_p provided one minimizes the ground capacitance C_g by tightly packing $N = \sqrt{C_J/C_g}$ Josephson tunnel junctions with impedance of order R_Q.

2.4 Limitation due to quantum phase-slip

Precisely how large can one make the impedance Z_J of an individual junction in the array? After all, why cannot one use $Z_J = R_Q$ and $N = 1$? Well, already linear analysis of the previous section indicated that something unwanted happens for junctions with $Z_J > R_Q$, i.e. as quantum fluctuations of the Josephson phase approach π. More specifically, another type of quantum fluctuation – the quantum phase-slip (QPS) – proliferates when Z_J approaches R_Q.

QPS corresponds to a 2π-slip in the phase across one of the array junctions, resulting in the phase-twist by 2π along the entire array. In other words, as we charge the superinductance with a flux approaching to Φ_0, it has an option to tunnel out in units of the flux quantum, introducing clear deviations from the linear inductive behavior. The frequency E_S/h associated with the quantum phase-slip process introduces a new scale to the superinductance problem. It is given by the following expression [16]:

$$E_S = \hbar\omega_p \times \frac{4}{\sqrt{\pi}}\sqrt{\frac{R_Q/2\pi}{Z_J}}\exp -\left(8\frac{R_Q/2\pi}{Z_J}\right) \tag{8}$$

To make sure that quantum phase-slip does not affect the inductive behavior of the supeinductance we must make sure that E_S/h is much smaller than the lowest frequency in the quantum electrical circuit involving this superinductance. In practice, because of the exponential dependence of E_S on Z_J/R_Q, and only linear dependence of L on Z_J, it should be possible to suppress E_S by many orders of magnitude at the expense of reducing L by a factor of two. For instance, at $Z_J = R_Q/10 \approx 650\Omega$ yields $E_S/\omega_p < 10^{-5}$, and $Z_J = R_Q/15$ lowers this quantity further to 10^{-8}. The precise effect of quantum phase-slips on an electrical circuit is discussed in references [17, 3]. We thus should correct the optimistic estimate of Eq. (7) by replacing Z_J with $Z_J/10 - Z_J/20$. This still allows reaching the superinductance regime, provided that N is chosen between 10 and 100.

3 Fluxonium as a Cooper-pair box shunted by a superinductance

Here we shall stick to the model of fluxonium as that of a Cooper pair box shunted by an inductance of the Josephson array (Fig. 2-right). Ingoring phase-slip in the array, the hamiltonian of the device is written as:

$$H_{\text{fluxonium}} = 4E_C n^2 - E_J\cos\varphi + \frac{1}{2}E_L(\varphi - \varphi_{\text{ext}})^2 \tag{9}$$

3.1 Spectrum: fluxons and plasmons

We remind the reader that $n = -i\frac{\mathrm{d}}{\mathrm{d}\varphi}$ is the conjugate momentum to the generalized coordinate φ with the resulting commutation relation $[n, \varphi] = i$. This way the first term in the hamiltonian (9) is analogous to mechanical kinetic energy, so that the larger E_C the lighter the equivalent mechanical particle is. The last two terms of (9) then depend only on the generalized coordinate φ and therefore play the role of the mechanical potential energy[6]. Note that in vast contrast to the Cooper pair box, here the number operator n has a continuous spectrum, while the phase φ is defined on the entire real axis, rather than being 2π-cyclic [1]. The latter fact is particularly obvious, given that $H_{\text{fluxonium}}(\varphi + 2\pi) \neq H_{\text{fluxonium}}(\varphi)$. The continuity of n follows directly from the extended nature of φ as a property of the Fourier transform, and also carries a simple

[6]The hamiltonian (9) is formally identical to the hamiltonian for the RF-SQUID [18, 19]. However, there is a vast difference in parameter regime. The RF-SQUID always operates in the regime of $E_L \sim E_J$ and $E_J/E_C \gg 1$. Fluxonium, on the contrary, operates in the regime $E_L \ll E_J$ and $E_J \sim E_C$.

physical interpretation: the charge at the electrodes of the black-sheep junction originates from the displacement of the Cooper-pair condensate with respect to the ions of the crystal lattice of the superconductor; since this displacement can be arbitrarily small, n does not have to be quantized. After all, by shunting the Cooper pair box junction with a piece of superconductor, the circuit loses its islands, therefore forgetting about the discreetness of charge and associated offset-charge sensitivity. Of course, here we neglect the effect of quantum phase-slip in the inductance, which will bring back some charge sensitivity.

The most straightforward way to understand the spectrum of the hamiltonian (9) is numerics [1]. To develop the fluxonium intuition, we plot the transition spectrum obtained numerically for several sets of circuit parameters. Let us fix the value of inductive energy at $E_L = h \times 0.5$ GHz, (a value very close to the actually implemented array inductance) and vary E_J, E_C and, and $\varphi_{\rm ext}$. Results of numerical diagonalizations are summarized in the Fig. (8).

The first pair of parameters is $E_J = 100$ and $E_C = 4$, or, equivalently, $E_J/E_C = 25$ and the plasma frequency $\omega_p = \sqrt{8E_J E_C} = 2\pi \times 56$ GHz. Although this example corresponds to an unlikely high plasma frequency for an aluminum junction, it is a useful example, as it justifies numerically the quantum phase-slip language. In this parameter regime the junction can be though of as a single phase-slip center of the fluxonium loop. The quantum phase-slip amplitude here calculates to $E_{SB} \ll 1$ MHz and therefore cannot be resolved in the plots.

Further insight comes from superimposing the energy levels with the potential energy of the hamiltonian (9) at $\varphi_{\rm ext} = 0$ (Fig. 8-C). It is clear that the first 5 energy levels correspond to a zero-point motion of a particle in the 5 Josephson wells – the fluxon states. Such states are very weakly coupled by tunneling, which is extremely weak for the choice of parameters. Each of the 5 fluxon states could be excited into a vibrational motion within one Josephson well at the frequency of approximately the plasma frequency ω_p (Fig. 8-C). The approximation of low energies, employed to develop the quantum phase-slip language precisely means that such vibrational states take place at sufficiently high frequencies.

Next, let us couple the fluxon states a bit more strongly by choosing $E_J = 20$ and $E_C = 2.5$, so that $E_J/E_C = 8$ and $\omega_p = 2\pi \times 20$ GHz. Now both the quantum phase-slip exponent and the plasma frequencies are substantially lowered, so that $E_{SB} \sim 10$ MHz and some mixing between fluxons and plasmons takes place (8-D, E, F). The plasma state indeed shows up at around 18 GHz, slightly smaller than our estimate due to finite value of $\beta_L = E_J/E_L = 40$. Although the splitting between fluxon states is still too small to be resolved on this figure, the splitting between vibrationally-excited fluxon states is clearly visible. This is expected, because the tunneling between vibrationally-excited fluxon states effectively undergoes a smaller potential barrier.

Pushing further toward coupled fluxon states, we turn to parameters $E_J = 10$ and $E_C = 2.5$, or $E_J/E_C = 4$ and $\omega_p = 2\pi \times 14$ GHz, (Fig. 8-G, H, I) we observe a rather strong splitting between the fluxon transition (ground-to-second excited) and the plasma state at about $10 - 11$ GHz. The phase-slip type spectrum is now almost completely destroyed with the exception of the lowest transition, which retained the correct zigzag shape. At higher energies the spectrum is dominated by a strongly coupled fluxon-plasmon motion. Turning to (Fig. 8-I), now only the lowest, central fluxon well contains both fluxon and plasmon levels. The other 4 lowest wells contain only a single semi-localized level each. In addition, a large number of vibrational states are present, which cannot be associated with a particular fluxon state.

Finally, let us fully destroy the phase-slip spectrum by further decreasing the inertia of the coordinate φ, by choosing $E_J = 10$, $E_C = 20$, so that $E_J/E_C = 1/2$ and $\omega_p = 40$ GHz (again somewhat at the higher end for aluminum devices). The resulting spectrum consists of tran-

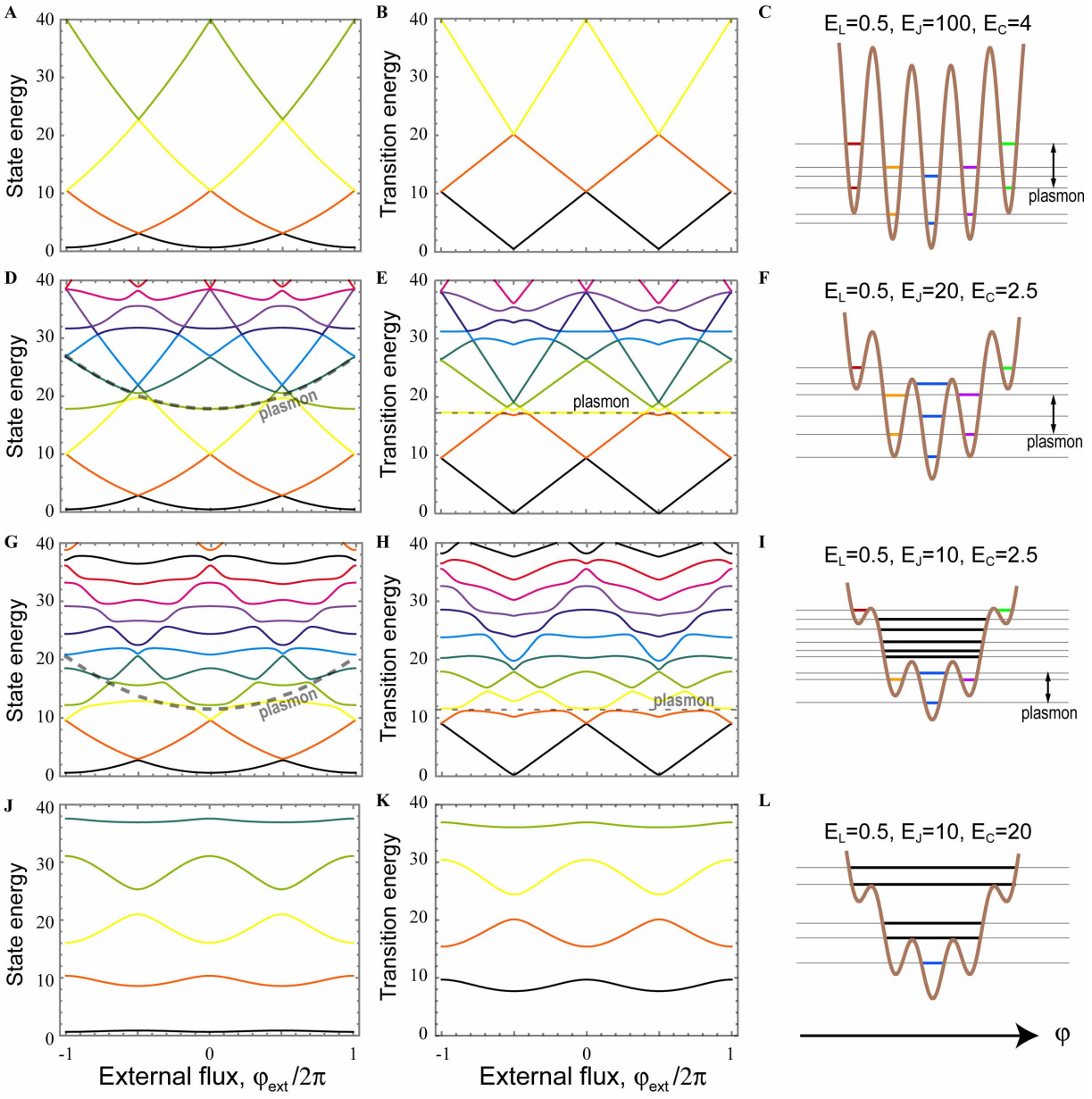

Fig. 8: *Fluxonium spectrum at a glance. Numerically computed spectrum (A, D, G, J), transitions from ground state (B, E, H, K) and the particle-in-a-box interpretation of the energy spectrum (C, F, I, L) for a set of parameters indicated on the figure. All energy units are in $h\times GHz$.*

sitions with much weaker flux dependence (Fig. 8-J,K,L). Not a single level could be interpreted as either a fluxon state or a plasmon state. On the contrary, now the spectrum could be interpreted as vibrational modes of the LC oscillator defined by the inductance L and the black-sheep junction capacitance C, with a small perturbation due to Josephson potential. Indeed, the average spacing between the levels is not given by ω_p but by a much smaller quantity, $\sqrt{8E_L E_C} \approx h \times 10$ GHz. In fact, at sufficiently high number of quanta, the non-linearity due to the black-sheep junction weakens and every fluxonium circuit responds as an LC oscillator.

3.2 Matrix elements

To understand the dynamics of an artificial atom one has to know the matrix elements of its generalized position and momentum. In our case, matrix elements of the reduced charge n and phase φ determine the coupling of fluxonium to both external signals, circuits, and internal degrees of freedom. The results of the numerics performed for the parameters from Fig. (8) are presented on Fig. 9, for the external flux range $\{-0.5,\ 0\}$. Most of the features can be explained with simple analytical analysis, involving the picture of weakly coupled fluxon and plasmon states. In the regime of parameters where the quantum phase-slip language is appropriate, we can estimate the phase matrix element φ_{ge} between the ground $|g\rangle$ and the first excited $|e\rangle$ fluxon states using the two-level approximation. Clearly, in the vicinity of $\varphi_{\rm ext} = \pi$, the states $|e\rangle$ and $|g\rangle$ could be very well approximated by linear combinations of states $|0\rangle$ and $|1\rangle$, which correspond to zero and one fluxon in the loop, respectively (or zero and one phase-slip through the black-sheep junction). The effective two-level hamiltonian reads

$$H_{ge} = \frac{1}{2}E_\varphi(\varphi_{\rm ext})(|0\rangle\langle 0| - |1\rangle\langle 1|) + \frac{1}{2}E_{SB}(|0\rangle\langle 1| + |0\rangle\langle 1|) \tag{10}$$

where we have introduced the zigzag-shaped fluxon inductive energy $E_\varphi = 4\pi^2 E_L^\Sigma |\varphi_{\rm ext}/2\pi - 1/2|$. Because of the finite E_{SB} we obtain the expected rounding of the $g \leftrightarrow e$ zigzag at $\varphi_{\rm ext} = \pi$, which is given by the hyperbolic expression for the eigenenergies $E_{g,e} = \pm\frac{1}{2}\sqrt{E_\varphi^2 + {E_{SB}}^2}$. The transition energy is given by

$$E_{ge} = \sqrt{E_\varphi^2 + {E_{SB}}^2} \tag{11}$$

The eigenvectors at $\varphi_{\rm ext} \simeq \pi$ ($E_\varphi \ll E_{SB}$) are given by symmetric and antisymmetric combinations of $|0\rangle$ and $|1\rangle$:

$$\begin{aligned} |g\rangle_{E_\varphi \ll E_{SB}} &= \frac{1}{\sqrt{2}}|0\rangle + \frac{1}{\sqrt{2}}|1\rangle \\ |e\rangle_{E_\varphi \ll E_{SB}} &= \frac{1}{\sqrt{2}}|0\rangle - \frac{1}{\sqrt{2}}|1\rangle \end{aligned} \tag{12}$$

and away from that spot, ($E_\varphi \gg E_{SB}$) by the weak mixing combinations of $|0\rangle$ and $|1\rangle$ (normalization is correct to first order in E_{SB}/E_φ!):

$$\begin{aligned} |g\rangle_{E_\varphi \gg E_{SB}} &= \frac{E_{SB}}{2E_\varphi}|0\rangle + |1\rangle \\ |e\rangle_{E_\varphi \gg E_{SB}} &= |0\rangle - \frac{E_{SB}}{2E_\varphi}|1\rangle \end{aligned} \tag{13}$$

Now we are ready to evaluate the matrix element φ_{eg} by recalling (see Fig. (8-C,F)) that in the φ-coordinate representation, the wavefunction $\psi_0(\varphi) = \langle\varphi|0\rangle$ is sharply peaked at $\varphi = 0$ and $\psi_1(\varphi) = \langle\varphi|1\rangle$ is sharply peaked at $\varphi = 2\pi$. This immediately provides us with the estimate of $\varphi_{eg} = \int_{-\infty}^{\infty} \mathrm{d}\varphi\psi_0(\varphi)\psi_1(\varphi)\varphi$:

$$\begin{aligned} \varphi_{eg}(\varphi_{\rm ext}) &= \pi,\ E_\varphi \ll E_{SB} \\ \varphi_{eg}(\varphi_{\rm ext}) &= \pi\frac{E_{SB}}{E_\varphi(\varphi_{\rm ext})},\ E_\varphi \gg E_{SB} \end{aligned} \tag{14}$$

We have thus arrived at the following property of the phase matrix element φ_{eg} in the phase-slip regime. It is sharply peaked at $\varphi_{\rm ext} = \pi$ reaching the value of π and away from that point reduces approximately as the inverse transition frequency $\nu_{eg} = E_{ge}/h$. The peak width can be evaluated as $\delta\varphi_{\rm ext} = E_{SB}/2\pi E_L^\Sigma$, so that the larger the splitting E_{SB}, the wider the peak. Overall, this behavior of $\varphi_{eg}(\varphi_{\rm ext})$ makes sense, because away from $\varphi_{\rm ext} = 0$, the number of fluxon states are no longer mixed, the total number of flux quanta in the loop is a conserved quantum number, so the dynamics freezes. Numerically, we confirm these conclusions in Fig. 9-A. The solid and dashed line both correspond to the deep phase-slip regime and fully concurs with expression (14). The dotted line agrees qualitatively, but instead of vanishing at $\varphi_{\rm ext} = 0$ actually shows a small rise – this is the effect of small mixing with the plasma states. Finally, the dash-dot-dash line bears no resemblance to expression (14), because the fluxon picture is lost and the ground to first excited transition is much closer to that of an oscillator made from inductance L and capacitance C, hence the weak flux dependence of φ_{eg} for that parameter choice.

As for the matrix element n_{eg}, it can be directly calculated from φ_{eg} and the transition frequency ν_{eg} using the following universal relation[7]:

$$|n_{\alpha\beta}| = |\varphi_{\alpha\beta}|\nu_{\alpha\beta}R_Q C_J \tag{15}$$

Combining the relations (15, 14, and 11), we conclude that the number matrix element would be flux-independent in the phase-slip regime, and is given by (we are only interested in the absolute values of matrix elements here)

$$|n_{eg}(\varphi_{\rm ext})| = \frac{\pi}{8}\frac{E_{SB}}{E_C} \tag{16}$$

The numerics fully respects (Fig. 9-A, bottom graph) the expressions (15, 16).

Next, we step forward and consider the third fluxonium state $|f\rangle$. In the case when $|f\rangle$ is still a fluxon state (plasma mode is higher up), the flux-dependence of the matrix element φ_{ef} counted from $\varphi_{\rm ext} = 0$ is very similar to that of the matrix element φ_{ge} counted from $\varphi_{\rm ext} = \pi$. There are two quantitative distinctions though. First, the peak value of φ_{ef} at $\varphi_{\rm ext} = 0$ is given by $\varphi_{ef} = 2\pi$, not π, because the transition $e \leftrightarrow f$ mixes the fluxon states differing by two flux quanta. Second, since the mixing of the states $|0\rangle$ and $|2\rangle$ occurs via the state $|1\rangle$ as a second order process in E_{SB} (which one could interpret as a double phase-slip in the black-sheep junction), the splitting between the states $|e\rangle$ and $|f\rangle$ would be $E_{SB}^2/2E_\varphi(\varphi_{\rm ext} = 0)$; the

[7]This expression is valid for arbitrary non-linear oscillator defined by a linear capacitance C and a non-linear inductance. For derivation, see the discussion around Eq.(31) and Eq.(34).

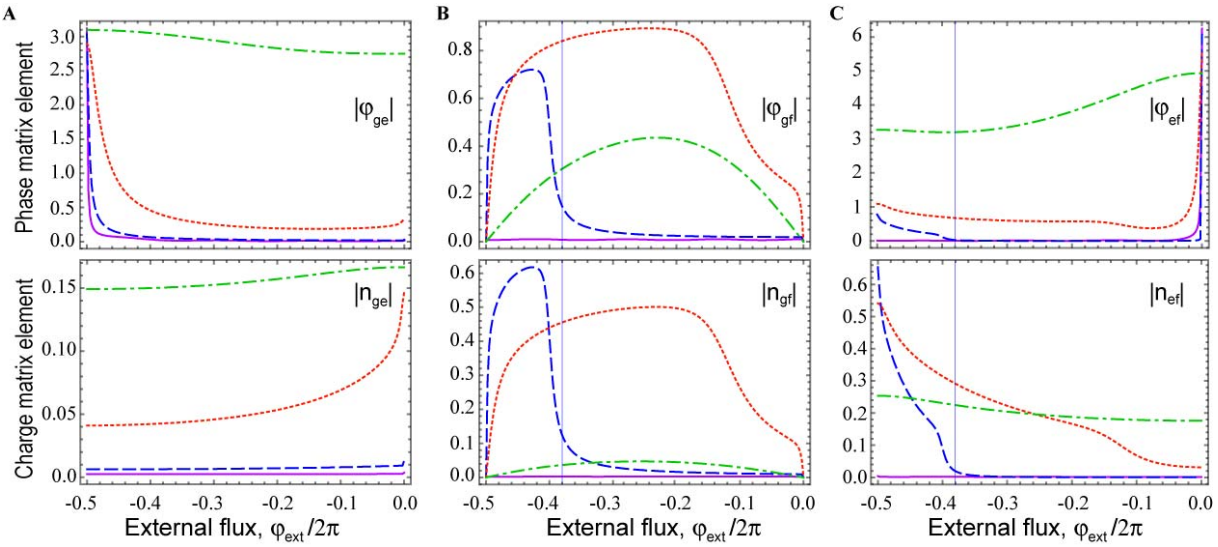

Fig. 9: *Matrix elements of n and φ for the fluxonium transitions as a function of external flux $\varphi_{\rm ext}$: (A) $g \leftrightarrow e$, (B) $g \leftrightarrow f$, and (C) $e \leftrightarrow f$. Parameter choice coincides with that of Fig. (8): solid lines ($E_J = 100,\ E_C = 4$), dashed lines ($E_J = 20,\ E_C = 2.5$), dotted line ($E_J = 10,\ E_C = 2.5$) and dash-dot-dash line ($E_J = 10,\ E_C = 20$). Thin vertical line in (B) and (C) schematically separates the region in flux $\varphi_{\rm ext}$ where the f state changes from fluxon-like (to the right of the line) to the plasmon-like (to the left of the line), for the dashed line case ($E_J = 20,\ E_C = 2.5$).*

same quantity determines the width of the peak in φ_{ef} around $\varphi_{\rm ext} = 0$. The situation gets more complicated when the $|f\rangle$ state mixes strongly with the plasma vibration states. Fig. (9-C) illustrates the discussion of this paragraph.

The direct $g \leftrightarrow f$ transition and its matrix elements (Fig. 9-B) display an additional feature. Since at the symmetry spots $\varphi_{\rm ext} = 0$ and $\varphi_{\rm ext} = \pi$ the fluxonium wavefunctions respect coordinate inversion symmetry, $\varphi_{gf}(\varphi_{\rm ext} = 0,\ \pi) = 0$. Away from the symmetry spots, φ_{gf} is also strongly suppressed as it involves connecting the states involving zero and two flux quanta. In the case that the $|f\rangle$ state is a plasmon state, the matrix element would be similar to that in an harmonic oscillator of inductance L_J and capacitance C, and will show weak dependence on flux.

3.3 Parameter regimes

Which parameter set defines the fluxonium qubit? Let us go over the possible qualitatively-different regimes of our circuit.

First of all, let us again emphasize that we at all times work in the regime $E_L \ll E_J$, or using the RF-SQUID language, $\beta_L \gg 1$. In this regime the effective potential energy has well-defined fluxon wells, with the depth approaching E_J and separation approaching 2π. This is an inevitable requirement from having large number of junctions in the array. Depending on the E_J/E_C ratio, each fluxon well hosts a number of semi-stable plasmon states with approximate energy separation $\sqrt{8E_JE_C}$. For very large inertia, corresponding to the case $E_J/E_C \ll 1$, each fluxon well will host a forest of nearly harmonic states, corresponding to vibrating fluxons within each well. In the case of $\sqrt{8E_JE_C} \ll 2\pi^2 E_L^\Sigma$ these harmonic states will dominate the

low-energy spectrum. It being somewhat trivial, we did not present this case in our numerical analysis.

The next regime corresponds to a smaller inertia of the phase coordinate, such, that $\sqrt{8E_JE_C} > 2\pi^2 E_L^{\Sigma}$, and $\exp(-\sqrt{8E_J/E_C}) \ll 1$. Then, the fluxon states dominate the low-energy spectrum (Fig. 8-A,D) and the inter-well tunneling is weak (or the quantum phase-slip amplitude via the black-sheep junction is small), and so the phase-slip language efficiently describes the lowest transitions.

The extreme limit of very large E_C (vanishing inertia) corresponds again to a harmonic low-energy spectrum, but this time with the transition energy is $\sqrt{8E_LE_C}$. The equivalent particle is so light that it does not feel the potential barriers of the fluxon wells and eventually undergoes bound motion due to the parabolic part of the potential given by the array inductance L. This regime starts when the parameter $\sqrt{E_J/E_C} < 1$ (Fig. 8-J). Although this qubit regime presents an attractive energy spectrum, easily tunable over several GHz frequency range, but essentially insensitive to practical levels of flux noise, it suffers from one serious disadvantage. The vibrations in the LC oscillator involve the flux motion of order Φ_0 (superinductance!), which results in a strong coupling of the $g \leftrightarrow e$ transition to the outside world (dissipation!).

The fluxonium qubit regime corresponds to a special choice of parameters, similar to that used for the Fig. 8-J. In this regime, the lowest energy $g \leftrightarrow e$ transition still retains its fluxon character. On the contrary, the next transition $g \leftrightarrow f$ corresponds to a strong hybridization between plasmons and fluxons. This requires the approximate balance $\sqrt{8E_JE_C} \simeq 2\pi^2 E_L^{\Sigma}$ and a certain range of the quantum phase-slip energies E_{SB} , such that $E_{SB}/8E_JE_C \approx \exp(-\sqrt{8E_J/E_C}) \in [10^{-3},\ 10^{-1}]$. The key interests of this regime to our experiments are: (i) the multi-octave frequency range of the fluxon-like $g \leftrightarrow e$ from nearly zero (actually E_{SB}/h) to the value of approximately $2\pi^2 E_L^{\Sigma}/h$; (ii) the suppressed transition matrix elements (Fig. 9-A, dotted red lines) leading to weaker energy relaxation and longer life-times; (iii) options to read the weakly coupled $g \leftrightarrow e$ transitions using strong coupled (due to the plasmon nature of the f level) $g \leftrightarrow f$ and/or $e \leftrightarrow f$ transitions.

What about the absolute value of E_L and the practical frequency range? Well, an inductance satisfying $L\omega_p \gtrsim R_Q$ calculates to $L \gtrsim 100$ nH or $E_L = (\Phi_0/2\pi)^2/L < 1$ GHz. Then, the maximum $g \leftrightarrow e$ transition frequency (at $\varphi_{\rm ext} = 0$) is $2\pi^2 \times 1$ GHz $= 20$ GHz. Therefore, the absolute value of L just entering the superinductance regime naturally lands inside the range of parameters necessary to reach the fluxonium qubit regime.

Although fluxonium circuit reminds that of a flux qubit, its typical parameters make it considerably different. Indeed, the three junction flux qubit [20], corresponds to parameter regime $\beta_L \gtrsim 1$ and $E_J/E_C \gtrsim 10$. Qualitatively, the fluxonium qubit regime may be defined approximately as such that the particle has only one (may be two at most) bound state per Josephson well. We call such bound states "fluxons", because in each state the loop is charged with approximately an integer times the flux quantum Φ_0, provided that $\beta_L \gg 1$. Hence the choice of name for our qubit – "fluxon-ium". On the contrary, typical flux qubit parameters are such that the bound states exist only for $\varphi_{\rm ext}$ very close to π. Perhaps it is fair to say that from the point of view of a theorist, flux qubit and fluxonium close to $\varphi_{\rm ext} = \pi$ and at low energies are essentially indistinguishable. However, the number of important practical differences, for instance the rich spectrum around $\varphi_{\rm ext} = 0$, certainly call for a separate name.

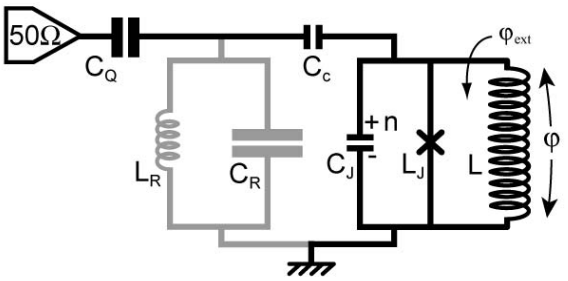

Fig. 10: *Circuit model of the fluxonium-readout resonator interaction. The physical readout resonator (Fig. 1) appears to the fluxonium circuit as an L_RC_R-circuit (marked in grey) which is decoupled from the 50Ω line by the capacitance C_Q, resulting in the resonator loaded quality factor Q. The fluxonium circuit, represented by the Josephson inductance L_J, capacitance C_J and the array inductance L, is coupled via the charge operator n, by means of the capacitance $C_c \ll C_J$.*

4 Circuit quantum electrodynamics with fluxonium

The interaction between a fluxonium circuit and a microwave cavity can be represented by an equivalent electrical circuit (Fig. 10). To the qubit circuit, the resonator appears as a *parallel* effective LCR circuit. The parameters of the parallel circuit are the inductance L_R and the capacitance C_R, or, more relevant to our discussion, the resonance frequency $\nu_0 = \omega_0/2\pi$, $\omega_0 = 1/\sqrt{L_RC_R}$ and the impedance $Z_0 = \sqrt{L_R/C_R}$. The coupling capacitance C_Q sets the quality factor Q of the resonator due to dissipation in the measurement leads. The voltage U across the capacitance C_R could be written in terms of creation and annihilation operators, $U = U_0(a+a^\dagger)$, where U_0 has the physical meaning of the vacuum RMS voltage. The coupling of the qubit to the resonator is given, according to the circuit theory, by the product $-2en\frac{C_c}{C_c+C_J} \times U$, where $2en\frac{C_c}{C_c+C_J}$ is the operator of the displacement charge on the coupling capacitance C_c. Estimating U_0 using Eq. (1) we introduce the coupling constant g:

$$g = \frac{C_c}{C_c + C_J}\sqrt{\pi\frac{Z_0}{R_Q}}h\nu_0 \tag{17}$$

and the hamiltonian describing the coupled fluxonium and readout:

$$H_{\mathrm{F+R}} = 4E_Cn^2 - E_J\cos\varphi + \frac{1}{2}E_L(\varphi-\varphi_{\mathrm{ext}})^2 + h\nu_0a^\dagger a - gn(a+a^\dagger) + H_{\mathrm{bath}}[a,\ a^\dagger] \tag{18}$$

Here the term $H_{\mathrm{bath}}[a,\ a^\dagger]$ describes the coupling of the readout degree of freedom to the dissipation, which eventually is responsible for the finite quality factor of the resonator. However, since in practice $Q \gg 1$ we can always treat the dissipation perturbatively. It is interesting to note that the fine structure constant essentially determines g, just as it does in the case of real-atom QED [21]. However in the case of circuits, other coupling schemes exist where the effect of the fine structure constant can even by inverted [22].

The type of coupling $gn(a + a^\dagger)$ between an atomic momentum n and the resonator mode coordinate $a+a^\dagger$ is usually treated in terms of effective Jaynes-Cummings hamiltonian [23, 24]. The atom is usually replaced with an effective spin with the transition frequency ν_{ge} detuned

from the readout resonator frequency ν_0 by an amount Δ. The main result of this treatment is that the resonator frequency acquires dispersive shifts χ_g and χ_e when the qubit is prepared in the ground or first excited states. The difference $\Delta\nu_0 = (\chi_e - \chi_g)$ defines the sensitivity of the readout resonator to the qubit state change, and can be used for both qubit state monitoring, and qubit-qubit coupling via the cavity. At the same time, since the resonator has a finite quality factor, even a purely dissipationless artificial atom will acquire certain finite lifetime, or linewidth κ, due to the energy emission via the resonator, the so-called Purcell effect [25, 26]. For a two-level-like atoms, κ and $\Delta\nu_0$ are very strongly linked, so that the larger the signal the smaller the lifetime. In practice, this link limits the range of qubit frequencies in which the readout works with a reasonable fidelity.
Quite on the contrary, the coupled fluxon-plasmon spectrum of the fluxonium qubit allows to break this unwanted link between κ and $\Delta\nu_0$. In this section, we will treat the coupling of the fluxonium to its readout (Eq. 18), entirely within second-order perturbation theory, in a somewhat more transparent way compared to the conventional Jaynes-Cummings approach.

4.1 Dispersive shifts by an arbitrary atom

Here we will derive the generic formula for the dispersive shifts of the resonator frequency by an arbitrary multi-level artificial atom. We ignore the term $H_{\rm bath}[a,\ a^\dagger]$ and treat the coupling $V = -gn(a+a^\dagger)$ perturbatively in the coupling constant g. Let us label the unperturbed states of the qubit-resonator system as $|\alpha, i\rangle$ or $|\beta, j\rangle$ where $\alpha,\ \beta = g,\ e,\ f,\ ...$ denote the number of quanta in the atom and $i,\ j = 0,\ 1,\ 2,\ ...$, denote the number of photons in the resonator. The states can be conveniently arranged into the following groups (or ladders) $\{|g,0\rangle,\ |e,0\rangle,\ |f,0\rangle,\ ...\}$, $\{\ |g,1\rangle,\ |e,1\rangle,\ |f,1\rangle,\ ...\}$, $\{|g,2\rangle,\ |e,2\rangle,\ |f,2\rangle, ...\}$, etc., so that each group corresponds to a fixed number of quanta in the resonator. The energy of the state $|\alpha, i\rangle$ is given by $E_{\alpha,i} = E_\alpha + ih\nu_0$. Turning on the interaction causes shifts to every energy level $E_{\alpha,i}$ by $\delta E_{\alpha,i}$. According to second order perturbation theory, the shifts $\delta E_{\alpha i}$ are given by the expression

$$\delta E_{\alpha,i} = g^2 \sum_{\beta\neq\alpha,\ j\neq i} \frac{|\langle j|a+a^\dagger|i\rangle|^2 ||n_{\alpha\beta}|^2}{E_{\alpha,i} - E_{\beta,j}} \tag{19}$$

Each term in the sum (19) contributes a shift to the level $|\alpha, i\rangle$ due to its repulsion from the level $|\beta, j\rangle$. Since $a^\dagger|i\rangle = \sqrt{i+1}|i+1\rangle$ and $a|i\rangle = \sqrt{i}|i-1\rangle$, only the levels from the nearest neighbor ladders actually repel each other. The closer the two repelling levels, the stronger the repulsion, due to the energy denominators in (19). The expression (19) thus drastically simplifies to the following:

$$\delta E_{\alpha,i} = g^2 \sum_{\beta\neq\alpha} \frac{i|n_{\alpha\beta}|^2}{(E_\alpha - E_\beta + h\nu_0)} + g^2 \sum_{\beta\neq\alpha} \frac{(i+1)|n_{\alpha\beta}|^2}{(E_\alpha - E_\beta - h\nu_0)} \tag{20}$$

The expression (19) has an intuitive interpretation in terms of level repulsion (Fig. 11-A). For fixed i, each term in the sum (19) comes from the repulsion of level $\{\alpha, i\}$ from level $\{\beta \neq \alpha, i\pm 1\}$. The transitions $\{\alpha, i\} \leftrightarrow \{\beta \neq \alpha, i\pm 1\}$ are called side-bands [27, 28] to the qubit transition $\alpha \leftrightarrow \beta$. The side-band transition frequency could take two types of values: $||\nu_{\alpha\beta}| - \nu_0|$ and $||\nu_{\alpha\beta}| + \nu_0|$; the former is called the "red" side-band, the latter is called the "blue" side-band, respecting the link between frequency and color. Within the framework of the rotating-wave approximation [24] (RWA), the terms involving blue side-bands are called "counter-rotating" terms and are often neglected when calculating the dispersive shifts. The dispersive shift of the

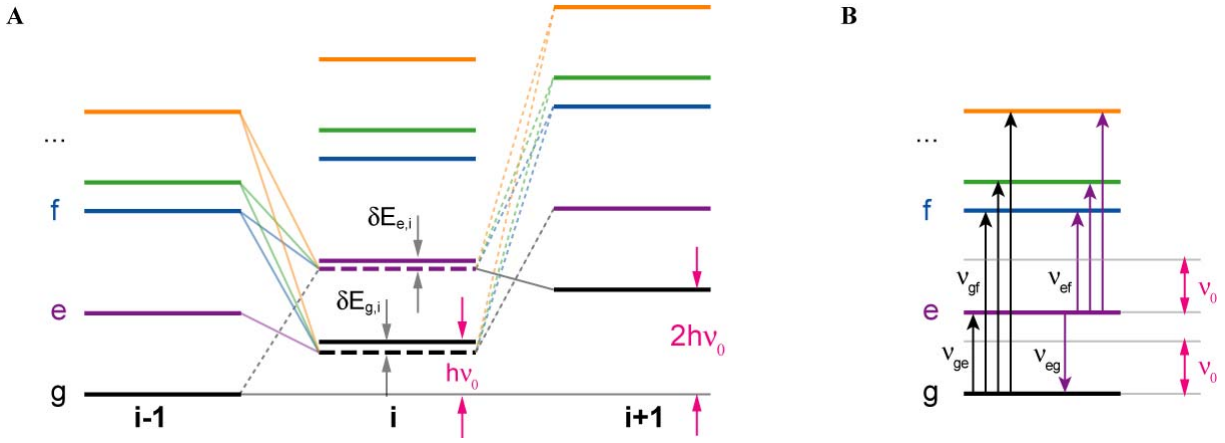

Fig. 11: *Dispersive shifts of the cavity by an atom with an arbitrary spectrum. (A) Interpretation of formula (20) using the combined atom-cavity spectrum, arranged into a set of ladders. The three ladders correspond to a fixed number i of quanta in the resonator. Atomic states within each ladder are labeled as g, e, f, ... etc. Only levels from the neighboring ladders can repel each other due to harmonic oscillator selection rules. Repulsion "forces" exerted by the neighbors at the pair of levels (g, i) and (e, i) are indicated with colored lines. Each line corresponds to a term in the sum (20). Dashed lines correspond to the weaker terms ("blue" side-bands, or the "counter-rotating" terms) in the expression (20).. They correspond to the addition of the transition frequency and the resonator frequency in the denominators. (B) Diagrammatic representation of the formula (20) for the dispersive shift. Each transition connecting the given atomic state to any other atomic state contributes to the dispersive shift, with the appropriate sign. The contribution is stronger for nearly resonant transitions.*

cavity frequency defined as $\chi_\alpha = (E_{\alpha,i+1} - E_{\alpha,i})/h$, does not depend on the occupation of the cavity i to the second order in g. The dispersive shift of the cavity frequency is given only in terms of the charge matrix elements $n_{\alpha\beta}$ and the transition frequencies $\nu_{\alpha\beta} = (E_\alpha - E_\beta)/h$ (the sign is crucial here!):

$$\chi_\alpha = g^2 \sum_{\beta\neq\alpha} |n_{\alpha\beta}|^2 \frac{2\nu_{\alpha\beta}}{\nu_{\alpha\beta}^2 - \nu_0^2} \tag{21}$$

This is the most general expression for the dispersive shift of the readout resonator frequency coupled to an arbitrary artificial atom. Every term in the sum (21) could be represented as a virtual transition in the atomic spectrum (Fig. 11-B). The expression is valid as long as $\chi_\alpha/g \ll 1$. The perturbation theory breaks down whenever expression (21) happens to have a pole, $|\nu_{\alpha\beta}| = \nu_0$. This situation corresponds to the vacuum Rabi resonance between the atomic transition $\alpha \leftrightarrow \beta$ and the readout resonator frequency ν_0. The degeneracy between the two transitions is then lifted by the vacuum Rabi frequency, given by the typical secular perturbation theory expression

$$\Omega_{\alpha\beta} = 2g|n_{\alpha\beta}| \tag{22}$$

Experimentally we usually measure the differential dispersive shift $\chi_{\alpha\beta} = \chi_\alpha - \chi_\beta$, which is given by:

$$\chi_{\alpha\beta} = g^2 \sum_{\gamma\neq\alpha} |n_{\alpha\beta}|^2 \frac{2\nu_{\alpha\gamma}}{\nu_{\alpha\gamma}^2 - \nu_0^2} - g^2 \sum_{\gamma\neq\beta} |n_{\alpha\gamma}|^2 \frac{2\nu_{\beta\gamma}}{\nu_{\beta\gamma}^2 - \nu_0^2} \tag{23}$$

4.2 Dispersive shifts by fluxonium

In order to investigate the dispersive shifts of a fluxonium circuit it is more convenient to change the labeling of the atomic states from letters to numbers, $\{e, g, f, ...\} \to \{0, 1, 2, ...\}$. This is because far more than two states contribute to the shift. We examine the dispersive shifts by the fluxonium qubit for the two sets of parameters, $\{E_L = 0.5, E_J = 20, E_C = 2.5\}$ (see Fig. 8-D,E,F), characteristic of the phase-slip regime, and $\{E_L = 0.5, E_J = 10, E_C = 2.5\}$ (see Fig. 8-G,H,I), characteristic of the fluxonium qubit regime, as well as several values of the readout frequency ν_0.

Deep in the phase-slip regime the origin of the dispersive shifts may be understood from the following qualitative picture. For $E_L \ll E_J$ (our usual condition) and $\exp(-\sqrt{8E_J/E_C}) \ll 1$, the plasmon and fluxon levels are clearly separated in the spectrum (Fig. 8-D,E,F; Fig. 12). The plasmon frequency is given by the curvature of the fluxon well. This curvature is approximately given by L_J, but has some weak dependence on the fluxon well number. By employing standard differential analysis, one can calculate that the curvature of the second minimum of the potential in the hamiltonian (9) differs from L_J by a fraction of order $\beta_L^{-1} = L_J/L$ [18]. Therefore, while the plasma vibration in the zero fluxon state takes place at the frequency $\nu_{p,0} \simeq \sqrt{8E_J E_C}$, the vibration in the excited fluxon state takes place at a slightly smaller frequency $\nu_{p,1} < \nu_{p,0}$, given by

$$\nu_{p,1} \simeq \nu_{p,0}(1 - \frac{L_J}{L}) \simeq \nu_{p,0} - E_L\sqrt{8E_C/E_J} \tag{24}$$

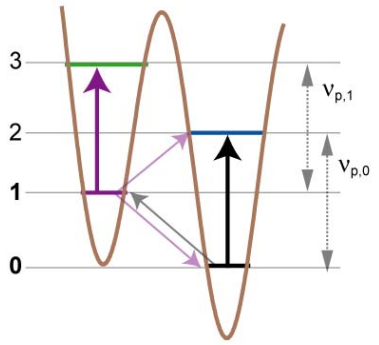

Fig. 12: *Origin of dispersive shift by the fluxonium circuit, phase-slip regime. The two neighboring fluxon wells (Fig. 8-F) each host a ladder of plasmon states (only two states in each ladder in this case). The ground state of the right ladder is the ground state of the entire circuit, corresponding to zero fluxons in the loop. The ground state of the left ladder is the second excited state of the entire circuit. Interwell transitions ($0 \leftrightarrow 1$ and $1 \leftrightarrow 2$, faint arrows) contribute negligibly to the the dispersive shift (23), while the plasmon transitions ($0 \leftrightarrow 2$ and $1 \leftrightarrow 3$, thick arrows) contribute dominantly. The frequency of the plasmon vibrations in the left well $\nu_{p,1}$ is slightly lower than that, $\nu_{p,0}$, in the right well, due to finite value of E_L/E_J. This difference in the plasma frequencies in the two fluxon wells eventually yields a finite dispersive shift χ_{01} for the qubit transition (see Eq. 25), provided that the readout frequency is chosen to be close to the plasmon frequency (see Eq. (27) and Eq. (26)). Importantly, in contrast to the case of either spin or transmon qubits, this mechanism of dispersive shift makes the latter to be independent of the properties of the qubit transition.*

Given the weakness of the inter-well transition matrix elements, as well as the harmonic oscillator selection rules, only two terms contribute to the dispersive shift χ_{eg} (even if each fluxon well contains a large number of plasma states):

$$\chi_{01} = 2g^2 \left(\frac{\nu_{p,0}|n_{02}|^2}{\nu_{p,0}^2 - \nu_0^2} - \frac{\nu_{p,1}|n_{13}|^2}{\nu_{p,0}^2 - \nu_0^2} \right) \tag{25}$$

Now, taking into account the relation (24), and also the fact that $|n_{02}|^2 \simeq |n_{13}|^2 \simeq (E_J/8E_C)^{1/2}$ (harmonic oscillator approximation [29]), we get two simple expressions for the dispersive shift, depending on the choice of the readout frequency ν_0. The largest shift takes place when $\nu_{p,1} < \nu_0 < \nu_{p,0}$, so that the transitions $0 \to 2$ and $1 \to 3$ contribute to the dispersive shift with equal signs (straddling regime again!), and we get

$$\chi_{01} = \frac{1}{4} \frac{g^2}{E_C} E_J/E_L \tag{26}$$

We remind the reader again that this formula is only valid when $\chi_{01} \ll g$. In the case of some detuning of the readout frequency from the plasmon frequency, $|\nu_0 - \nu_{p,0}| > E_L\sqrt{8E_C/E_J}$, we get a transmon-like [29] expression

$$\chi_{01} = \frac{g^2}{\nu_{p,0} - \nu_0} \times \sqrt{\frac{8E_C}{E_J}} \frac{1}{\beta_L} \tag{27}$$

in which the quantity $\sqrt{\frac{8E_C}{E_J}} \frac{1}{\beta_L}$ plays the role of the transmon anharmonicity. Note, however, that unlike the transmon case, here the dispersive shift χ_{01} essentially depends on neither the

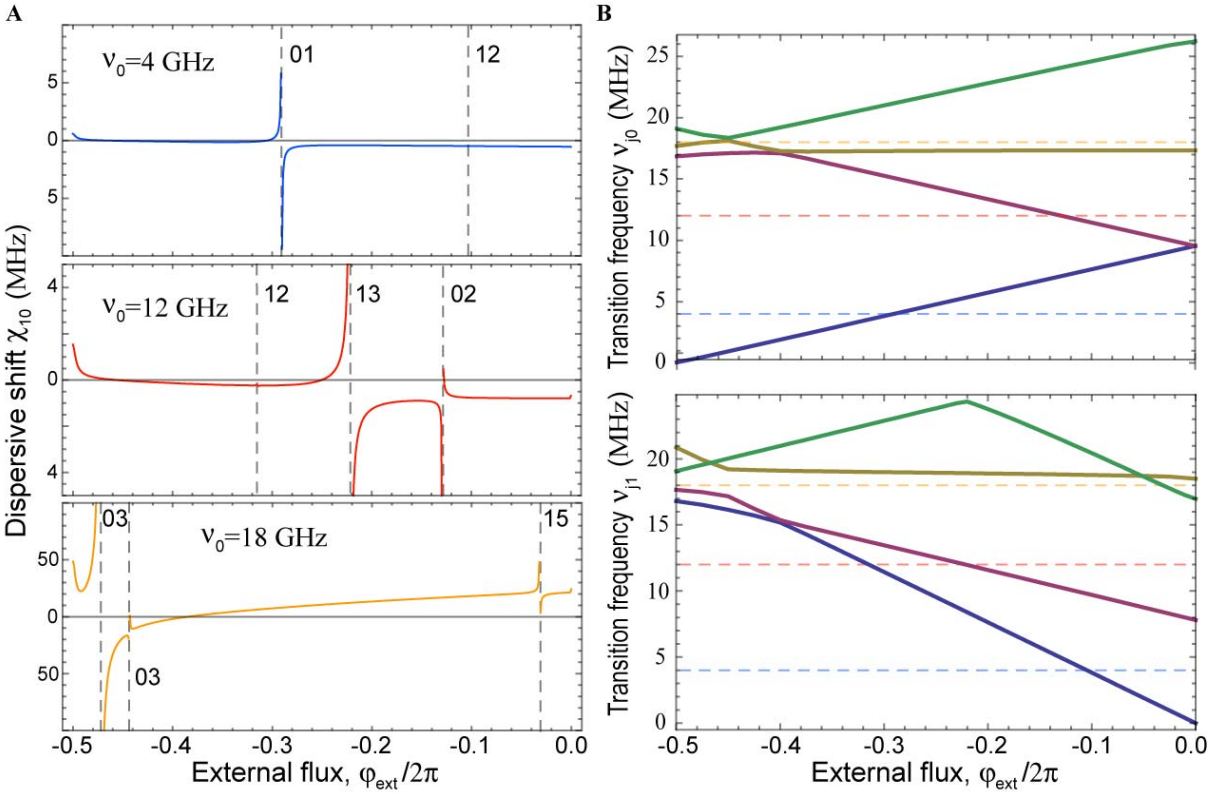

Fig. 13: *Numerically computed dispersive shifts, phase-slip regime. The choice of parameters is the same as in Fig. (8-D,E,F). (A) Dispersive shifts for the three values of the readout frequency, top to bottom* $\nu_0 = 4$, 12, *and* 18. *Vacuum Rabi resonances indicated with vertical dashed lines. (B) Transition spectrum from ground state (top graph) and from the first excited state (bottom graph). Location of the vacuum Rabi resonances in the qubit dispersive shifts correspond to the crossing of the transitions connecting either qubit states with the readout frequency (blue, red and orange faint dashed lines). Note how* $\nu_0 = 12$ GHz *lies between the* $0 \leftrightarrow 3$ *and* $1 \leftrightarrow 4$, *satisfying the straddling condition (see Eq. 27).*

flux or the qubit transition frequency ν_{01}. A proper choice of cavity frequency ν_0 would guarantee the visibility of the $g \to e$ transition in the entire multi-octave frequency range. Note also that the estimates (27 and 26) fail near the sweet-spots $\varphi_{\rm ext} = 0$, π, where the fluxon transitions become degenerate and the selection rules for the matrix elements apply. For instance, the increase in χ_{01} towards $\varphi_{\rm ext} = \pi$, happens because $n_{02}(\pi) = 0$ there due to the parity conservation and $n_{12}(\pi)$ sharply takes the maximum value.

Turning to numerical analysis, we compute the dispersive shifts $\chi_{eg}(\varphi_{\rm ext})$ using the transition spectrum (Fig. 8), the matrix elements (Fig. 9) and our general expression (23). We choose three readout frequencies, $\nu_0 = 4$, 12, and 18 GHz. The results of the numerics for χ_{01} in the case of the deep phase-slip regime, $\{E_L = 0.5, E_J = 20, E_C = 2.5\}$ are summarized in Fig. (13). Each time either the transition frequency ν_{j0} or ν_{j1} ($j = 0, 1, 2, ...$) crosses ν_0, we get a corresponding vacuum Rabi resonance in the dispersive shift. The stronger the corresponding matrix element $|n_{0j}|$ or $|n_{1j}|$, the broader the resonance. Quantitative values of the dispersive shifts cannot be trusted if they are not much smaller than the coupling constant g.

The readout frequency $\nu_0 = 4$ GHz corresponds to two resonances, the $0 \leftrightarrow 1$ and $1 \leftrightarrow 2$. The resonance $1 \leftrightarrow 2$ is so narrow, that it cannot even be resolved, because of the extremely small

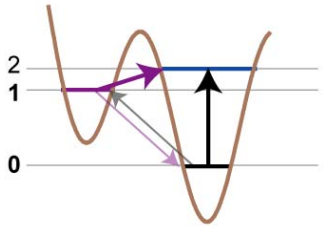

Fig. 14: *Origin of dispersive shift by the fluxonium circuit, fluxonium qubit regime. The lowest transition from the ground state corresponds to the excitation of a fluxon, which is still fairly well localized in its respective fluxn well, while the second transition from the ground state corresponds to a plasmon, which is fairly well spread between the two wells. Therefore, the direct* $0 \leftrightarrow 1$ *transition is still negligible (faint lines), so the dispersive shift is determined by the competition between the intense transitions* $1 \leftrightarrow 2$ *and* $0 \leftrightarrow 2$ *(Eq. 28).*

matrix element $|n_{12}|$. Due to the large (compared to g) detuning between the plasmon frequency and the readout frequency, the dispersive shift is tiny away from the vacuum Rabi resonances. The readout frequency $\nu_0 = 8$ GHz crosses transitions $1 \leftrightarrow 3$ and $0 \leftrightarrow 2$ with stronger matrix elements, so the corresponding vacuum Rabi resonances are wider. Since $\nu_0 = 8$ GHz is closer to the plasmon frequency, the dispersive shift in between the resonances is larger than in the case $\nu_0 = 4$ GHz and is indeed weakly dependent on the external flux, just as the qualitative formula (27) predicts. The choice of readout frequency $\nu_0 = 12$ GHz satisfies the "straddling" condition $\nu_{p,1} < \nu_0 < \nu_{p,0}$, and leads to very large dispersive shift of order $g/10$. Note, how the competition between different transitions can lead to strictly zero dispersive shifts for certain values of external flux.

In this regime of circuit parameters $\{E_L = 0.5, E_J = 10, E_C = 2.5\}$ (Fig. 8-G,H,I) the best way to intuitively understand the dispersive shift, is to approximate the spectrum with a three-level system, in which the ground and first excited states are fluxon-like while the third state is plasmon-like state (Fig. 14). In this model, only one plasmon transition is present, which provides the dominant contribution to the dispersive shift. An approximate expression for the dispersive shift then will be

$$\chi_{01} \sim -\frac{g^2}{\nu_{02} - \nu_0}|n_{02}|^2 + \frac{g^2}{\nu_{12} - \nu_0}|n_{12}|^2 \tag{28}$$

which clearly can be quite large with the proper choice of ν_0 even when $\nu_{01} \ll \nu_0$. The behavior of the matrix elements could be seen from the Fig. (9, red dotted lines) and the discussion in the corresponding section.

Numerically, we try the set of three frequencies $\nu_0 = 4$, 8, and 12 GHz. The vacuum Rabi resonances here are stronger than in the phase-slip regime, due to larger charge matrix elements. For low readout frequency, $\nu_0 = 4$ GHz, the vacuum Rabi resonances $1 \leftrightarrow 2$ and $1 \leftrightarrow 3$ contribute as much as the conventional $0 \leftrightarrow 1$ resonance. Moving the frequency closer toward the plasmon frequency, by setting $\nu_0 = 8$ GHz, changes the vacuum Rabi resonance pattern, but in general produces a larger shift, in accord with our estimate (28). Finally, the case of $\nu_0 = 12$ GHz shows even stronger resonances and larger shifts, with the level number as high as 5 contributing. These analyses confirm that choosing the readout close to the plasmon frequency guarantees large dispersive shift for the $0 \leftrightarrow 1$ fluxon transition in the fluxonium qubit regime. Just as in the case of the phase-slip regime, the interference between different vacuum

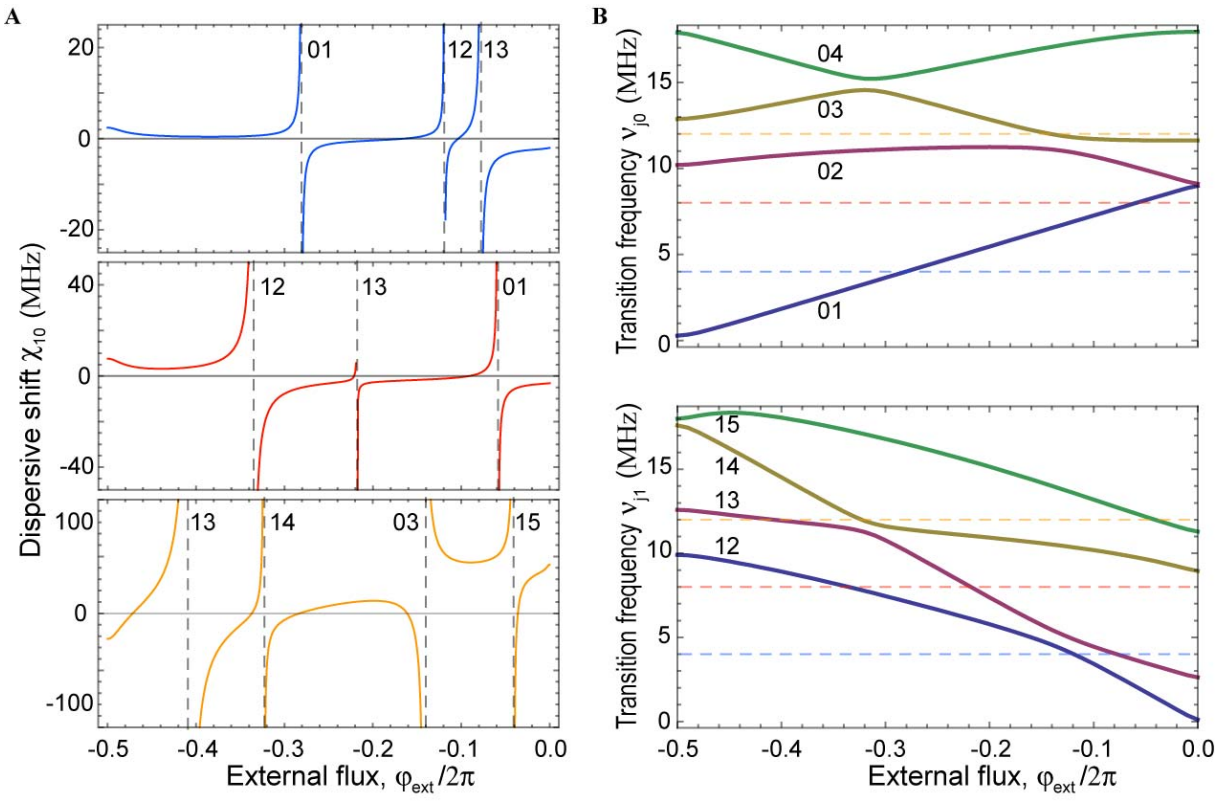

Fig. 15: *Numerically computed dispersive shifts, the fluxonium qubit regime. The choice of parameters is the same as in Fig. (8-G,H,I). (A) Dispersive shifts for the three values of the readout frequency, top to bottom $\nu_0 = 4$, 8, and 12. Vacuum Rabi resonances indicated with vertical dashed lines. (B) Transition spectrum from ground state (top graph) and from the first excited state (bottom graph). Location of the vacuum Rabi resonances in the qubit dispersive shifts correspond to the crossing of the transitions connecting either qubit states with the readout frequency (blue, red and orange faint dashed lines).*

Rabi resonances results in a large number of nulls in the dispersive shift as a function of flux. Nevertheless, the qubit transition is, on average, equally well visible in the entire frequency range from nearly zero frequency to as high as $2\pi^2 E_L/h$.

5 Common decoherence mechanisms

In a spectroscopy experiment, every qubit resonance has a finite width in frequency. This width appears either from the finite lifetime of the qubit excited state, a process called spontaneous emission (or energy relaxation), or because the circuit parameters defining the transition frequency fluctuate in time, on the time scale faster than the time of the experiment, a process called dephasing.

5.1 Two models of spontaneous emission

The energy relaxation of the fluxonium circuit comes from the coupling of either its charge n or phase φ operator to a bath capable of dissipating an electromagnetic wave at the frequency of the qubit transition. Irrespective of the microscopic origin of the bath, its effect on the qubit can be modelled as a frequency-dependent resistance. The coupling to the the charge n is represented by replacing the readout resonator in Fig. (10) with a resistance R. The perturbation to the circuit hamiltonian due to the coupling to this resistance is given by $V = -4E_C n C_c U_R = \frac{C_c}{C_J+C_c} 2enU_R$, where U_R is the voltage operator across the resistance. The rate of energy loss resulting in the qubit transition $\alpha \to \beta$ is given by the generic Fermi's Golden Rule expression [30]

$$\Gamma_{\alpha\beta} = \frac{1}{(\Phi_0/2\pi)^2} \left(\frac{C_c}{C_J+C_c}\right)^2 |\langle\alpha|n|\beta\rangle|^2 \, S_{U_R}(\omega_{\alpha\beta}) \tag{29}$$

in which the spectral density of the voltage quantum noise $S_{U_R}(\omega)$, defined as $S_{U_R}(\omega) = \int dt \, \langle U_R(t) U_R(0)\rangle \exp(i\omega t)$ (the average $\langle..\rangle$ is taken over the ground state of the resistor R) is given by

$$S_{U_R}(\omega) = R\hbar\omega \left(1 + \coth\left(\frac{\hbar\omega}{2k_B T}\right)\right) \tag{30}$$

resulting in the final expression for the energy relaxation rate

$$\Gamma_{\alpha\beta}(\nu_{\alpha\beta}) = (2\pi)^2 \left(\frac{C_c}{C_J+C_c}\right)^2 \frac{R}{R_Q} |n_{\alpha\beta}|^2 \, \nu_{\alpha\beta} \left(1 + \coth\left(\frac{h\nu_{\alpha\beta}}{2k_B T}\right)\right) \tag{31}$$

This expression is valid as long as $\Gamma_{\alpha\beta} \ll \nu_{\alpha\beta} \equiv \omega_{\alpha\beta}/2\pi$, which is easily satisfied if $C_c \ll C_J$, or $R \ll R_Q$, or if the transition is naturally weak, i.e. $|n_{\alpha\beta}| \ll 1$.
It is interesting to look at the alternative way of coupling of the fluxonium to the resistor R, by treating the series combination of R and the coupling capacitance C as an admittance $Y(\nu) = (R + (i2\pi\nu C_c)^{-1})^{-1}$, directly shunting the black-sheep junction. Then the coupling hamiltonian is given by $\tilde{V} = -(\Phi_0/2\pi)\varphi I_Y$, where I_Y is the operator of the current noise generated in the admittance Y. The Fermi's golden rule expression for the relaxation rate is now:

$$\Gamma_{\alpha\beta} = \frac{1}{(2e)^2} |\varphi_{\alpha\beta}|^2 S_{I_Y}(\omega_{\alpha\beta}) \tag{32}$$

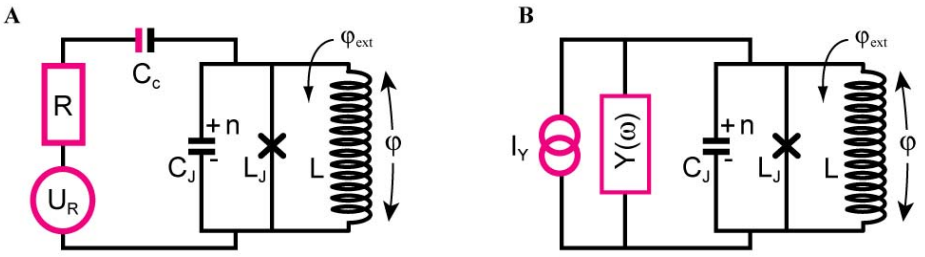

Fig. 16: *Two models of spontaneous emission. (A) The fluxonium charge operator n couples to the fluctuating voltage U_R across a resistance R via a series capacitance C_c. (B) The fluxonium phase operator φ couples to the fluctuating current I_Y in an admittance $Y(\omega)$ directly shunting the junction.*

The spectral density $S_{I_Y}(\nu)$ of the current noise in the admittance Y is given by

$$S_{I_Y}(\omega) = 2\mathrm{Re}[Y(\omega)]\hbar\omega \coth\left(\frac{\hbar\omega}{2k_BT}\right) \tag{33}$$

Taking into account that $\mathrm{Re}[Y(\omega)] = \frac{1}{R}\frac{(\omega RC_c)^2}{1+(\omega RC_c)^2} \simeq (\omega RC_c)^2/R$ for sufficiently small R or C_c, we get the following final expression for the relaxation rate:

$$\Gamma_{\alpha\beta} = (2\pi)^2(\nu_{\alpha\beta}R_QC_c)^2\frac{R_Q}{R}\left|\varphi_{\alpha\beta}\right|^2\nu_{\alpha\beta}\left(1+\coth\left(\frac{h\nu_{\alpha\beta}}{2k_BT}\right)\right) \tag{34}$$

Now an important remark is in order. The two expressions (31) and (34) must give identical relaxation rates, which could only be satisfied if $|n_{\alpha\beta}|^2 = |\varphi_{\alpha\beta}|^2(\nu_{\alpha\beta}R_QC_J)^2$ (assuming $C_c \ll C_J$). The reasoning above is a proof by the circuit theory of the formula (15), which links the matrix elements of the phase φ and its conjugate reduced charge n of an arbitrary non-linear oscillator circuit. Note, that formula (15) is nothing else than a manifestation of the fact that the phase φ and the reduced charge n are conjugate variables, like position x and momentum p of a particle with a mass m described by a hamiltonian $H(x,p)$. Indeed, since $p = m\dot{x}$ we have $p_{\alpha\beta} = m\left\langle\alpha\right|\frac{i}{\hbar}[H,x]\left|\beta\right\rangle = im2\pi\nu_{\alpha\beta}\times x_{\alpha\beta}$, where $\nu_{\alpha\beta} = (H_{\alpha\alpha}-H_{\beta\beta})/h$ is the transition frequency between the eigenstates α and β. Similarly, given that $n = (C_JR_Q/2\pi)\times\dot{\varphi}$ (capacitance plays the role of mass) we arrive at formula (15).

In analyzing the relaxation of the fluxonium qubit, we prefer to use the admittance representation and the resulting formula (32). Any linear dissipation source which is coupled to the fluxonium device could be represented as an admittance shunting the junction. More generally, the linear dissipation sources coupled to the junctions of the fluxonium could be represented as admittances shunting the junctions.

5.2 Purcell effect

Here we calculate the relaxation rate due to the coupling of the fluxonium to the $50\,\Omega$ dissipation via the readout resonator. The classical version of our analysis was performed in the past in Ref. [26] for the case of the transmon qubit. This source of dissipation corresponds to shunting the black-sheep junction with the admittance

$$Y_{\rm Purcell}(\omega) = \left(\left(\left(iZ_\infty \tan \frac{\pi}{2} \frac{\omega}{\omega_0^{\rm geom}} \right)^{-1} + (R + (i\omega C_Q)^{-1})^{-1} \right)^{-1} + (i\omega C_c)^{-1} \right)^{-1} \tag{35}$$

where the $R \sim 50\ \Omega$ is the effective resistance experienced by a microwave photon escaping from the cavity into a matched transmission line and $\omega_0^{\rm geom}$ is the resonance frequency associated with the geometry of the resonator. The resonator contribution (the Z_∞-term) comes directly from the formula (2). The function (35) has a pole at the frequency of the fundamental resonance $\omega_0 = \omega_0^{\rm geom}(1 - \frac{2}{\pi} Z_\infty (C_Q + C_c)\omega_0^{\rm geom}) \approx \omega_0^{\rm geom}$, with the quality factor Q given by

$$Q = \frac{4}{\pi} / Z_\infty R (\omega_0 C_Q)^2 \tag{36}$$

Assuming that $Q \gg 1$, we can find the simplified expression for $\mathrm{Re}[Y(\omega)]$:

$$R^{-1}_{\rm Purcell}(\omega) \equiv \mathrm{Re}[Y(\omega)] = Z_\infty^{-1} \frac{(\omega Z_\infty C_c)^2}{Q} \times \frac{\pi}{4} \left(\omega/\omega_0\right)^2 \tan^2(\frac{\pi}{2}\omega/\omega_0) \tag{37}$$

The life-time $T_1^{eg}$of the ground to first excited state transition $g \leftrightarrow e$ can then be calculated using the formula (34) by substituting R with $R^{-1}_{\rm Purcell}$. For a fixed Q and ω, one can increase T_1^{eg} by making the matrix element $|\varphi_{eg}|$ small. Unfortunately, for transmons and two-level qubits, this is not an option because the same matrix elements n_{eg} and φ_{eg} determine the magnitude of the dispersive shift. On the contrary, the dispersive shifts of fluxonium are determined by the transitions other than $g \leftrightarrow e$ so choosing the parameters such that $|\varphi_{eg}| \to 0$ is quite possible.

5.3 Effects of flux and critical current noise

Flux noise. There is one remarkable fact about the sensitivity of the fluxonium to the flux bias. External flux $\varphi_{\rm ext}$ through the fluxonium loop tunes the transition frequencies, so any fluctuations in $\varphi_{\rm ext}$ would dephase the spectrum. The fluctuations of $\varphi_{\rm ext}$ could come from improper shielding or from the dynamics of microscopic flux-generating degrees of freedom located directly "inside" the qubit: on the surface of the superconducting films, to give an example. The resulting dephasing time is given by

$$1/T_\phi^{\varphi_{\rm ext}}(\alpha \leftrightarrow \beta) \approx \delta\varphi_{\rm ext} \times \frac{{\rm d}\nu_{\alpha\beta}}{{\rm d}\varphi_{\rm ext}} \tag{38}$$

Qualitatively, the sensitivity ${\rm d}\nu_{\alpha\beta}/{\rm d}\varphi_{\rm ext}$ is easy to evaluate. For the fluxon-like transitions the sensitivity ${\rm d}\nu_{\alpha\beta}/{\rm d}\varphi_{\rm ext} \simeq E_L/\hbar$, for the plasmon transitions ${\rm d}\nu_{\alpha\beta}/{\rm d}\varphi_{\rm ext} \sim 0$, flux-bias-independent for either. At the sweet-spots, even the fluxon transitions become insensitive to first order to the fluctuations in flux. The magnitude of the flux noise $\delta\varphi_{\rm ext}$ depends on the spectral density of flux noise. Its presently accepted value is in the range $\delta\varphi_{\rm ext} \sim 10^{-5} - 10^{-6}$. Note that the sensitivity of the fluxon transitions to the flux noise is almost a factor of $100-1000$ lower than that of the flux qubit [31] away from the sweet-spots, due to the small value of E_L, or equivalently, due to the large value of the array inductance L.

Critical current noise. There are two remarkable facts about the sensitivity to of the fluxonium transitions to the critical current noise in its junctions. Fluctuations in the critical current [32] of the array junctions cause E_L to fluctuate, contributing to the dephasing time:

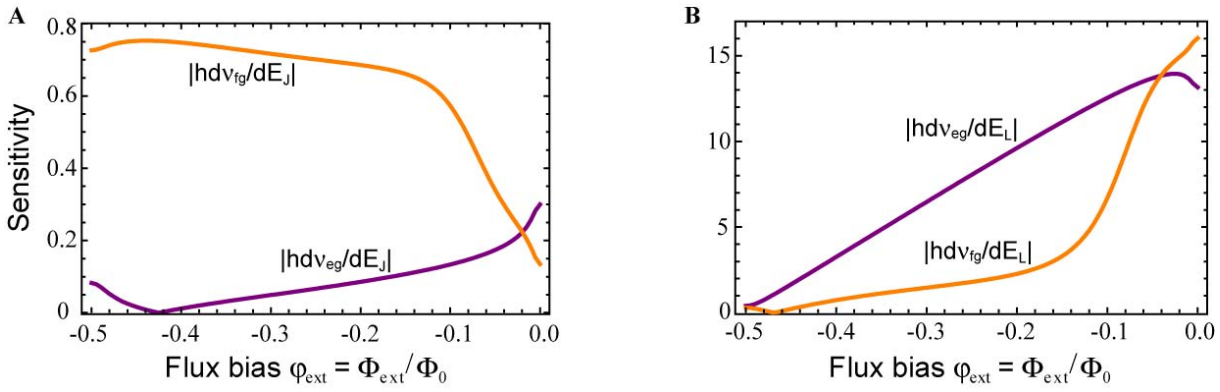

Fig. 17: *Sensitivity of fluxonium transitions to critical current noise. (A) Sensitivity to fluctuations in E_J. (B) Sensitivity to fluctuations in E_L.*

$$1/T_\phi^L(\alpha \leftrightarrow \beta) \approx \delta E_L \times \frac{\mathrm{d}\nu_{\alpha\beta}}{\mathrm{d}E_L} \tag{39}$$

The sensitivity $\mathrm{d}\nu_{\alpha\beta}/\mathrm{d}E_L$ of the plasmon-like transitions is again approximately zero. Away from the sweet-spots, the sensitivity of the fluxon transitions grows linearly from nearly zero at $|\varphi_{\text{ext}}| = \pi$ to the maximum value of $h\mathrm{d}\nu_{\text{fluxon}}/\mathrm{d}E_L|_{\max} = 2\pi^2$. At the $|\varphi_{\text{ext}}| = \pi$ the sensitivity to E_L of the $g \leftrightarrow e$ transition is still minimal as it is approximately given by an E_L-independent quantity E_{SB}.

Turning to the magnitude of the noise δE_L, a statistical argument would imply that it should be $\sqrt{N}$ times smaller than that of an individual junction. Indeed, the quantity $E_L^{-1} = \sum_{j=1}^{N} E_{J_j}^{-1}$, where the sum is taken over all the array junctions. Fluctuations in E_{J_j}presumably come from the dynamics of the tunneling channels in the oxide, so the noise in different junctions should be uncorrelated. This immediately implies that $\delta E_L/E_L \simeq (\delta E_{J_j}/E_{J_j})/\sqrt{N} = (\delta I_0/I_0)/\sqrt{N}$, where I_0 is approximate value of the critical current of the array junctions. The presently accepted estimate of δI_0 is such that $\delta I_0/I_0 < 10^{-6}$, which gives $\delta E_{J_j}/E_{J_j} < 10^{-6}$ and $\delta E_L/E_L < 10^{-7}$.

Thus, in the event that critical current noise would end up dominating superconducting qubit coherence, one may expect a $1/\sqrt{N}$ suppression of this effect using an N junction array. For instance, fluxonium $g \leftrightarrow e$ transition away from flux sweet-spots and in the limit $E_{SB} \ll 2\pi^2 E_L$ is entirely fixed by E_L and φ_{ext}, hence the quality factor due to critical current noise estimates simply as $(\delta I_0/I_0)/\sqrt{N}$, winning the $1/\sqrt{N}$ factor compared to a transmon qubit of similar frequency [29]. This is remarkable fact number one.

Fluctuations in the critical current of the black-sheep junction lead to fluctuating E_J and the dephasing time contribution

$$1/T_\phi^{E_J}(\alpha \leftrightarrow \beta) \approx \delta E_J \times \frac{\mathrm{d}\nu_{\alpha\beta}}{\mathrm{d}E_J} \tag{40}$$

Qualitatively, the sensitivity of the fluxonium spectrum to E_J can be understood as follows: plasmon-like states have sensitivity to E_J exactly the same as the transmon qubits, $h\mathrm{d}\nu_p/\mathrm{d}E_J = \sqrt{2E_C/E_J} \sim 1$. As for the fluxon transitions, the sensitivity to E_J away from flux sweet spots comes from the small contribution of the black sheep inductance to the total inductance of the ring. Interestingly, one can argue that there must exist a value of φ_{ext} at which the sensitivity to

E_J of the fluxon transitions in the spectrum (Fig. 8-G,H,I) turns to zero. Indeed, for $E_J \to 0$, the fluxon transitions are entirely determined by E_L. The finite E_J, apart from the contribution to the total inductance of the ring discussed above, rounds the sharp corners of the zigzag. Around zero flux, this rounding clearly reduces the transition frequency from its $E_J = 0$ value, while around half flux quantum bias point the rounding increases the transition frequency. Therefore, somewhere in the middle between $|\varphi_{\rm ext}| = \pi$ and $|\varphi_{\rm ext}| = 0$, the sensitivity to E_J of the fluxon transition passes through zero. This is the remarkable fact number two.

References

[1] J. Koch, V. E. Manucharyan, M. H. Devoret, L. I. Glazman, *Physical Review Letters* **103**, 217004 (2009).

[2] V. E. Manucharyan, J. Koch, L. I. Glazman, M. H. Devoret, *Science* **326**, 113 (2009).

[3] V. E. Manucharyan, *et al.*, *Phys. Rev. B* **85**, 024521 (2012).

[4] D. V. Averin, A. B. Zorin, K. K. Likharev, *Zh. Exp. Teor. Phys.* **88**, 692 (1985).

[5] L. S. Kuzmin, D. B. Haviland, *Physical Review Letters* **67**, 2890 (1991).

[6] M. Watanabe, D. B. Haviland, *Physical Review Letters* **86**, 5120 (2001).

[7] F. Nguyen, *et al.*, *Physical Review Letters* **99**, 187005 (2007).

[8] S. Gladchenko, *et al.*, *Nature Physics* **5**, 48 (2008).

[9] D. M. Pozar, *Microwave engineering* (Wiley-India, 2009).

[10] J. D. Jackson, *Wiley & Sons Inc., New York* (1962).

[11] A. M. Finkel'Stein, *Physica B: Condensed Matter* **197**, 636 (1994).

[12] A. J. Annunziata, *et al.*, *Applied Superconductivity, IEEE Transactions on* **19**, 327 (2009).

[13] V. V. Shmidt, P. Muller, A. V. Ustinov, *The physics of superconductors: introduction to fundamentals and applications* (Springer Verlag, 1997).

[14] R. P. Feynman, R. B. Leighton, M. Sands, *The Feynman Lectures on Physics including Feynmans Tips on Physics: The Definitive and Extended Edition* (Addison Wesley, Reading, 2005).

[15] C. Hutter, K. Stannigel, E. A. Tholén, J. Lidmar, D. Haviland, *Arxiv preprint arXiv:0804.2099* (2008).

[16] K. A. Matveev, A. I. Larkin, L. I. Glazman, *Physical Review Letters* **89**, 96802 (2002).

[17] A. Hriscu, Y. Nazarov, *Physical Review Letters* **106**, 77004 (2011).

[18] A. Barone, G. Paterno, *Physics and Applications of the Josephson Effect.* (John Wiley & Sons inc., New York, 1982).

[19] J. R. Friedman, V. Patel, W. Chen, S. K. Tolpygo, J. E. Lukens, *Nature* **406**, 43 (2000).

[20] I. Chiorescu, Y. Nakamura, C. Harmans, J. E. Mooij, *Science* **299**, 1869 (2003).

[21] J. M. Raimond, M. Brune, S. Haroche, *Reviews of Modern Physics* **73**, 565 (2001).

[22] M. H. Devoret, S. M. Girvin, R. J. Schoelkopf, *Annalen der Physik* **16**, 767 (2007).

[23] A. Blais, R. S. Huang, A. Wallraff, S. M. Girvin, R. J. Schoelkopf, *Physical Review A* **69**, 062320 (2004).

[24] L. S. Bishop, Circuit quantum electrodynamics 2, Ph.D. thesis, Yale University (2010).

[25] E. M. Purcell, *Physical Review* **69**, 681 (1946).

[26] A. A. Houck, *et al.*, *Physical Review Letters* **101**, 80502 (2008).

[27] I. Chiorescu, *et al.*, *Nature* **431**, 159 (2004).

[28] A. Wallraff, *et al.*, *Physical Review Letters* **99**, 50501 (2007).

[29] J. Koch, *et al.*, *Physical Review A* **76**, 042319 (2007).

[30] A. A. Clerk, M. H. Devoret, S. M. Girvin, F. Marquardt, R. J. Schoelkopf, *Reviews of Modern Physics* **82**, 1155 (2010).

[31] F. Yoshihara, K. Harrabi, A. O. Niskanen, Y. Nakamura, J. S. Tsai, *Physical Review Letters* **97**, 167001 (2006).

[32] D. J. Van Harlingen, *et al.*, *Physical Review B* **70**, 064517 (2004).

D 2 Coherent control of single spins in diamond[1]

Fedor Jelezko
Institute of Quantum Optics
Ulm University

Contents

1 Introduction 2
1.1 Defects in Diamond 2
1.2 Optical Porperties of NV Defects 4
1.3 Spin Properties and Spin Readout 6
1.4 Diamond Quantum Registers 8
1.5 Applications of Single-Color Centers for Novel Imaging Techniques 9
1.6 Magnetometry with Single Diamond Spins 10

2 In conclusion 12

3 References 13

[1] Lecture Notes of the 44th IFF Spring School "Quantum Information Processing" (Forschungszentrum Jülich, 2013). All rights reserved.

1 Introduction

Coherent control and readout of single spins in solids is attracting considerable attention, owing to potential application of atomic-scale technologies in novel information processing protocols and sensing at the nanoscale[1]. Spins are particularly interesting candidates for achieving such control, owing to the long coherence time. This isolation from the environment makes the readout of individual spins quite challenging. It was shown that the magnetic moment associated with single quantum systems can be detected in transport measurements with single quantum dots[2] and defects in silicon[3]. Magnetic resonance force microscopy was also able to reach the ultimate sensitivity regime[4]. Recently developed optical readout techniques explore new avenue in single-spin detection by combining high-sensitivity optical microscopy techniques and conventional magnetic resonance control methods. Following detection of single molecular spin[5], quantum states associated with single defects in diamond were explored[6]. Experiments with single defects in diamond are particularly interesting owing to the long coherence time associated with spins of color centers. This lecture shows the basics of single-spin detection and highlights the importance of coherent control of spins in solids for novel quantum technologies.

1.1 Defects in Diamond

Diamond is an exceptional material for technological applications, including novel technologies that use quantum properties of matter. Apart from its extreme hardness and high thermal conductivity, a diamond lattice hosts a large number of optically active defects (color centers). Owing to their importance in jeweler applications, many of these defects were studied using optical spectroscopy and magnetic resonance techniques for decades[7]. Several color centers show strong optical transitions, allowing us to detect them at the single-site level using optical microscopy techniques[6]. One of the most studied defects in this context is the nitrogen-vacancy (NV) defect. The NV defect consists of a nitrogen atom at the lattice site (see Fig. 1) and a vacancy at the neighbor lattice position.

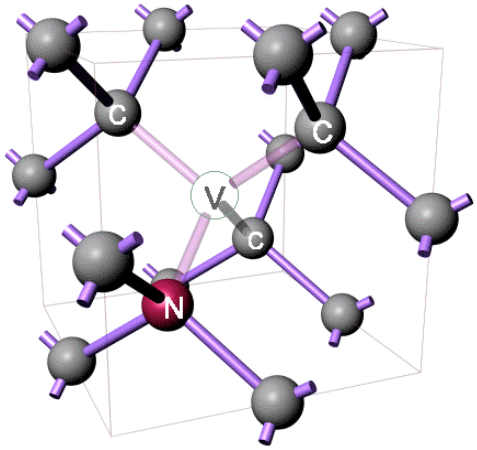

Fig. 1: *Structure of the NV center in diamond.*

NV defects can be found in natural nitrogen-containing diamond and in synthetic diamonds grown by chemical vapor deposition (CVD) and high-pressure, high-temperature (HPHT) techniques. It was also shown that single defects can be created artificially in synthetic diamonds using electron irradiation[8] and nitrogen implantation (Fig. 2) [9-11]. The first approach relies on existence of substitutional nitrogen in the diamond lattice and diffusion of vacancies created by electron irradiation during annealing. Therefore the position of the implanted NV defect cannot be controlled with high precision. However, this technique allows generation of a dense ensemble of NV defects[12]. Implantation of single ions into nitrogen-free crystals allows us to reach positioning accuracy solely limited by straggling of nitrogen ions during implantation. Straggling can be controlled by an appropriate choice of energy. Low energy is preferable for achieving high accuracy of implantation, but the yield of creation of NV defects is lower in this case, owing to a low number of created vacancies[13]. It was also shown that postirradiation of diamond with carbon ions allows us to improve the creation yield of NV centers[14].

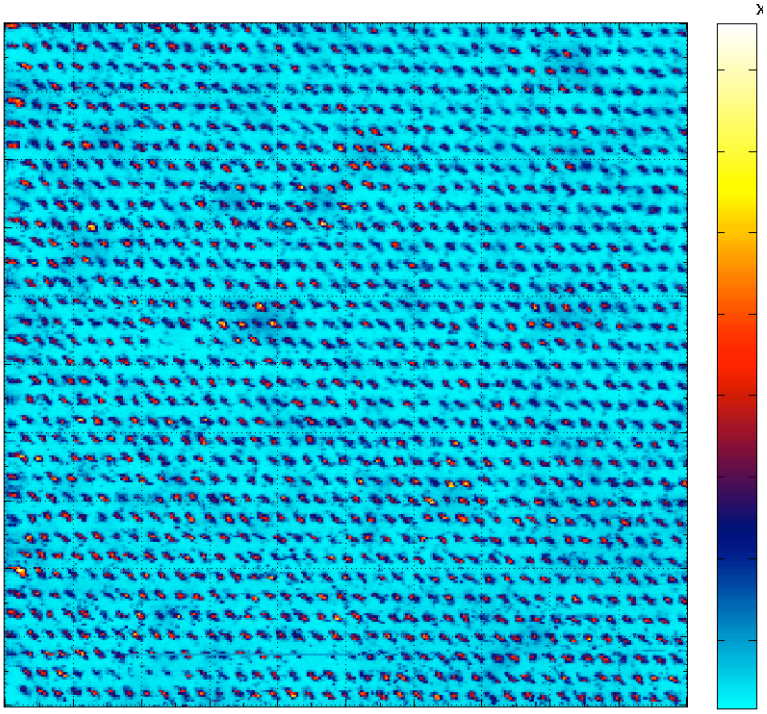

Fig. 2: *Pattern of implanted NV centers visualized by confocal microscopy.*

The structure of the defects shows C_{3v} symmetry with a symmetry axe connecting the nitrogen atom and the vacancy. The electronic structure of NV centers is governed by dangling bond electrons belonging to the vacancy and electrons of the nitrogen atom. The neutral charge state of the NV center possesses five electrons (four forming the dangling bonds and one additional electron from nitrogen). When electron donors are present in the lattice, the NV center can exist in a negatively charged state having six electrons[15]. The negatively charged state possesses electronic spin one, whereas the neutral state is the S = 1/2 system. The electronic states of a negatively charged NV defect can be modeled using six electrons or two hole models[16]. The spin density of the ground state of the NV defect shows

that spin density is mostly concentrated at three carbon atoms surrounding the vacancy[17]. In the excited state there is a significant shift of the electron spin density toward nitrogen atoms, resulting in a stronger hyperfine coupling to the N^{14} nucleus.

1.2 Optical Properties of NV Defects

The excited state of the NV center is located 1.945 eV above the ground state and is also spin triplet. In addition to the triplet ground and excited states, a negatively charged NV center has two metastable singlet states playing a crucial role for optical spin polarization[18, 19]. The metastable singlet states can be detected in fluorescence as infrared emission[20]. The strongest optical transition for an NV defect is related to the transition between ground- and excited-state triplets. The fluorescence lifetime of the excited triplet state is 12 ns, and the fluorescence quantum yield is close to unity[21]. This allows detection of single-color centers by conventional confocal microscopy techniques[6]. Optical transition of the NV center is coupling to phonons, resulting in the strong emission into phonon sidebands (intensity of the zero phonon line is only 4%).

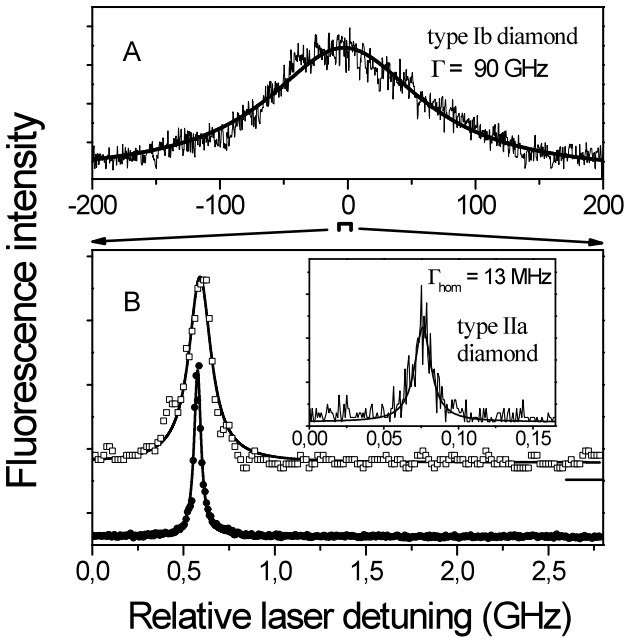

Fig. 3: *Low-temperature fluorescence excitation spectra of single NV defects. (A) Spectrum of a single NV center in a diamond nanorystal (type 1b diamond) averaged over 5 min. (B) Spectra averaged during a few seconds. The upper graph shows a spectrum of the V center in type 1b diamond. The lower graph shows a spectrum of the NV defect in ultrapure type IIa diamond. The inset shows a single-scan spectrum obtained with low excitation power. The line width of the NV spectrum approaches a transform-limited value (12 MHz).*

Early ensemble studies show the strong inhomogeneous broadening of optical transition (the line width of the zero phonon line of 1,000 GHz)[22]. Single-center experiments show that the line of individual color centers is narrow[23]. The line width of the transition of single centers strongly depends on the sample quality. In nitrogen-rich diamonds (type 1b) the line width is typically a few hundreds of MHz. The main source of spectral diffusion is most probably an ionization process related to nitrogen donors (ionization energy 1.8 eV)[23]. For the case of ultrapure diamonds with a concentration of nitrogen impurities on the order of parts per billion, the line width approaches the limit imposed solely by the lifetime of the excited state[24] (10 MHz; see Fig. 3).

The line width of the optical transition is significantly narrower than the splitting between spin-state sublevels of the NV center. This opens the door toward manipulation and readout of the spin states using optical spectroscopy techniques. Spin orbit coupling leads to the mixing of the spin state in the excited states. As a result one of the sublevels of the excited state forms a lambda scheme with two ground-state spin sublevels. The existence of this λ-type transition allows for observation of the electromagnetically induced transparency[25], nondestructive readout of the spin state[26], and demonstration of entanglement between the photon and the spin states[27]. Intrinsic coupling between spins and photons are crucial for application of NV centers in the area of quantum communication.

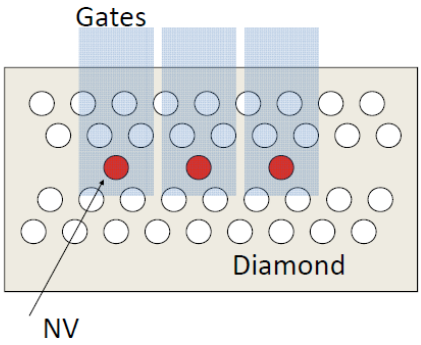

Fig. 4: *Schematics of NV color centers coupled to a photonic crystal cavity.*

Single defects placed in a photonic structure can provide basic blocks for quantum repeaters and scalable quantum registers (Fig. 4). It is important to mention that intrinsic inhomogeneity present in a diamond lattice might appear to be a serious obstacle for the above-mentioned protocols. Important progress has been made toward control of optical transition using electric fields. The possibility of tuning was demonstrated experimentally within a spectral range covering the entire inhomogeneous bandwidth (see Fig. 5)[24, 28]. Another important element of the diamond nanophotonics platform is the ability to collect the photons efficiently. This can be achieved by building optical elements around single defects. Integrated diamond optics, including solid immersion lenses and optical resonators, is undergoing a fast development period. It was shown that by using solid immersion lenses it is possible to increase the collection efficiency of the detection system by an order of magnitude[29-31]. Furthermore, efficient extraction of photons made it possible to show the effect of photon interference for two individual color centers[32] (crucial blocks for quantum

information processing protocols) and achieve a single-shot readout of single-electron spins[33].

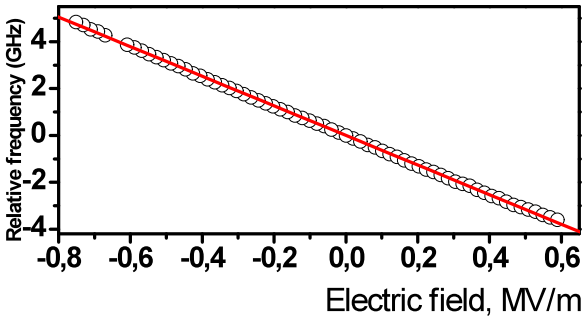

Fig. 5: *Stark shift control of the NV center spectral lines*.

1.3 Spin Properties and Spin Readout

Remarkable photophysical properties of NV defects offer the possibility for readout and manipulating of spin[34]. When combined with the ultrasensitive optical detection technique, this provides the basis for single-spin control[6]. Notably, the optically assisted spin readout technique allows for efficient spin detection at room temperature. Optical transitions between the ground ^{3}A and excited ^{3}E states (see Fig. 6), under ambient conditions, are strongly broadened, and spectral selection of individual spin sublevels is not possible. However, owing to spin orbit coupling, spin sublevels with the magnetic quantum number m_s = +/–1 have higher probabilities to undergo intersystem crossing to metastable singlet states (^{1}E and ^{1}A in Fig.6)[35, 36]. As a result fluorescence emission of an NV center is higher for an $m_s = 0$ spin sublevel. In addition, intersystem crossing allows for efficient spin polarization, owing to spin-selective decay of the metastable singlet state to the $m_s = 0$ sublevel of the ground-state triplet.

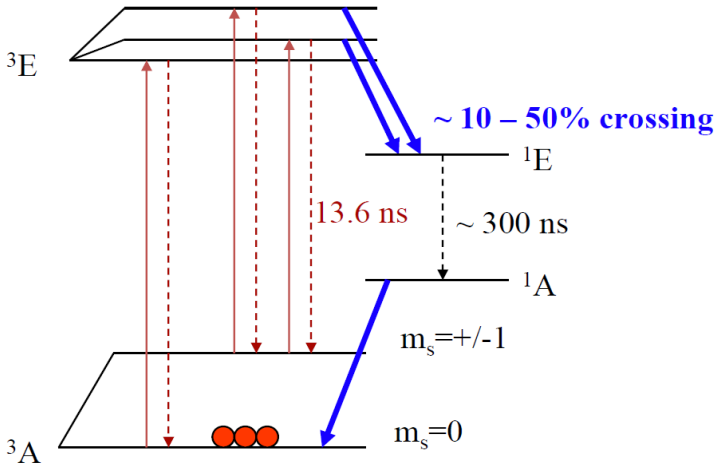

Fig. 6: *Energy-level scheme of an NV center, illustrating room-temperature single-spin readout.*

First experiments show that a combination of optical readout and conventional magnetic resonance techniques allows for reliable state control of individual spins[37]. Owing to a spin-free diamond lattice (the most abundant carbon isotope is nuclear spin free), long coherence times were detected in diamond with low concentration of paramagnetic impurities. It was also shown that rare ^{13}C nuclear spins can be explored as the resource for quantum information protocols. Hyperfine interaction between electron spins and nuclear spins located in the so-called "frozen core" make possible the realization of two and three quantum bit (qubit) gates[38, 39]. Nuclear spins located outside the frozen core are a source of decoherence. It was shown that growth of isotopically pure C^{12} diamond allows us to extend the coherence time of single-electron spins associated with NV centers to values close to the spin lattice relaxation time (2 ms)[40].

The optical readout of the single-electron spin state leads to repolarization of the electron spin. Owing to the fast time scale of this process, the so-called "single shot" readout regime remains challenging under ambient conditions for the case of the electron spin. However, nuclear spins can provide an important resource for achieving a high-fidelity readout regime. It was shown that the state of the nuclear spins can be efficiently controlled by manipulation via the electron spin of NV centers. The state of the electron spin can be efficiently mapped to nuclear spins and the readout repetitively[41]. During each readout cycle the electron spin is repolarized, but the nuclear spin state remains unchanged. Application of this readout cycle allows for projective readout of nitrogen nuclear spins of the NV center (Fig. 7)[42].

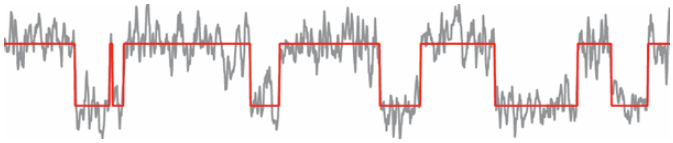

Fig. 7: *Fluorescence time trace showing quantum jumps of a single nitrogen nuclear spin.*

1.4 Diamond Quantum Registers

A long coherence time and possibly single defects generated by ion implantation are crucial elements for building quantum logic based on individual impurity atoms. Two types of interactions can be employed for building scalable quantum registers. The first is the optical coupling between qubits. The second type of coupling, which can be explored, is magnetic dipole–dipole coupling between qubits (see Fig. 8).

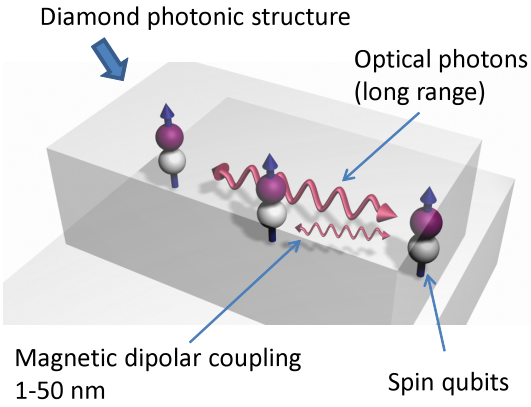

Fig. 8: *Concept of the spin-diamond quantum register. Single, optically active spins are embedded into a photonic structure, allowing the use of long-range coupling via optical photons. In addition, short-range magnetic dipolar coupling between spins can be explored. The range at which such coupling prevails over decoherence depends on the coherence time of the electron spin.*

The first proof-of-principle experiments toward implementation of scalable quantum register architectures were demonstrated recently. These experiments showing the potential of diamond spins for quantum information were based on coupling of a single-electron spin to the nuclear spin associated with C^{13} nuclear spins[43, 44]. Although the electron spin surrounded by a few nuclei might serve as a model system for spin-based quantum registers[45, 46], its scalability is limited, owing to the limited number of nuclear spins in the so-called “frozen core.” Therefore longer-range dipolar interactions between electron spins are more promising for use in quantum information processing protocols. Dipolar coupling between two implanted NV centers was employed for realization of a quantum gate[47].

Recently schemes for probabilistic entanglement between color centers using optical channels were proposed[48] and important steps toward their realization using color centers in diamond were demonstrated. Two-photon interference from distant NV defects was observed[32]. Further progress is critically dependent on the experimental ability to generate an array of NV centers with high fidelity (for magnetic coupling) and the ability to couple NV defects to optical cavities (for long-range optical coupling). Several approaches were explored on the way to create an integrated diamond photonics platform. First, NV centers in diamond were adjusted and coupled to high Q resonators made from GaP[49]. Integrated diamond cavities were designed and fabricated[50, 51]. Coupling of color centers to photons is crucial for building elements of quantum communications, such as quantum repeaters[52], and may improve readout fidelity for single-spin measurements[53].

Besides conventional approaches for quantum computing (based on quantum gates), there are other implementations called “one-way quantum computing” or measurement-based quantum computing. These techniques allow us to create entangled states of large systems by measurement of qubits. Typically, the measurement is not performed on the qubits themselves, but state information is transferred from the qubits to photons, which interact in an interferometric scheme to erase the which-path information. As there is no need for direct interaction of qubits, and as photons can be transferred over large distances, measurement-based entanglement creation allows for entangling remote qubits in a distributed quantum computer. Technically, the requirements for realization of such entangling schemes are similar to the ones for spin detection - due to the combination of long spin coherence times and strong optical transitions, NV centers are promising candidates[54]; high-purity diamond reduces possible sources of dephasing, and coupling to optical cavities enhances emission into desired modes. Cavity coupling may be employed in two different regimes; in the weak coupling regime (coherent emission rate into the cavity is faster than spontaneous decay of the dipole moment), one relies on the spontaneous emission enhancement by the Purcell effect[55] or dispersive shifts of the cavity resonance detected in reflection from the cavity [56]. Ultimate control over the emission process is gained in the strong coupling regime where the coherent coupling rate is larger than the incoherent decay channels; here stimulated Raman-type transitions allow for coherent emission into the cavity mode and for emission of transform-limited photons. To allow for two-photon interference, as required for many entanglement schemes, the emitted photons have to be identical to a high degree. The technical preconditions are long, pure dephasing times of the excited state (need for ultrapure diamond), suppression of emission into phonon sidebands by enhancement of the zero phonon line (strong Purcell effect, i.e., cavities with a small modal volume and high quality factor), and the ability to precisely tune the cavity mode to the emitter’s optical resonance.

1.5 Applications of Single-Color Centers for Novel Imaging Techniques

There is much interest toward extending the principle of fluorescence microscopy down to the level of single molecules[57]. While fluorescent signals from single molecules can be detected using a confocal microscope and fluorescence microscopy, the resolution is not high enough to image the location of individual molecules. Conventionally, multicolor dyes (or

quantum dots) have been used to allow selective detection and localization of multiple dye molecules within the focal volume. However, the number of colors that can be cleanly resolved is limited to less than 10 because of the broad optical spectrum of fluorescence emitters at room temperature.

Recently much effort has been put into nonlinear resolution enhancement techniques, for example, stimulated-emission depletion (STED)[58], which works by saturation of the fluorescence emitter, and photoactivated localization microscopy (PALM)[59], which works by activating only a portion of the dye molecules for each image and then postprocessing. While these techniques have achieved just over an order of magnitude improvement over the optical wavelength (≈tens of nanometers), there is a barrier to reaching molecular-scale resolution. This is because the intensity near optical field nodes (STED) and antinodes (PALM) varies quadratically with the position so that the extra factor of 10 needed to reach single-molecule (or submacromolecule) resolution (≈a few nanometers) would be 100 times more difficult to achieve. Unique photostability of diamond defects can potentially allow us to achieve this goal[60].

At the same time, nuclear magnetic resonance (NMR) imaging routinely produces images whose resolution is far below the wavelength of the microwave excitation. The apparatus and highly complex microwave pulse sequencing that are needed have already be engineered to the level where clinical application is routine. Therefore, to extend the resolution limit of fluorescence microscopy down to the single-molecule scale, a miniature version of a magnetic resonance imaging (MRI) system can be used, where the dye molecule has an electron spin resonance (ESR) transition. The NV color center in diamond is a promising candidate for new MRI because even single defects have a detectable ESR signal at room temperature, and its spin line width (which determines resolution) is very narrow[61]. The nanodiamond ESR tags are consumables, and large quantities would eventually be needed. The key diamond technologies to be developed include functionalization and growth of ultrapure diamonds with high NV yield. For functionalization, the surface of either crushed or CVD-grown nanodiamonds must be modified by attaching an intermediate linker, for example, silanes, that in turn can be used to attach functional groups, such as biotin, that can later be used to attach biologically specific tags. For growth all spins except the NV must be eliminated from the lattice.

Bioimaging applications can profit from biocompatibility of nanodiamonds. Recent studies show that dimoand nanoparticles are not toxic[62]. The wavefunction of color centers is localized within a few Angstroms, allowing us to produce fluorescent, small diamond nanoparticles without affecting the stable, strong fluorescence associated with NV centers. Fluorescence of nanodianonds with a typical size below 10 nm was reported[63, 64].

1.6 Magnetometry with Single Diamond Spins

One of the most promising applications of single-color centers is related to development of diamond-based electric and magnetic field sensors that are able to detect minute fields associated with single-electron and nuclear spins and that can be positioned to achieve atomic-scale spatial resolution. Atomic-scale spin sensors based on highly localized color

centers in diamonds can be placed in close vicinity to external spins, thus allowing distances to be reached at which their associated magnetic fields are sufficiently large to be measured.

The ultrasensitive detection of magnetic and electric fields with high sensitivity and nanometer spatial resolution is an outstanding challenge with a strong impact on modern science and technology that cannot be underestimated. As a result, numerous attempts for sensitive detection of, for example, magnetic fields are known. Prominent examples are SQUIDS, atom vapor magnetometers, magnetic resonance force microscopy, and Hall sensors. However, either the systems do not allow for miniaturization or they require special working conditions, such as ultrahigh vacuum or low temperature. This is why alternative magnetic field–sensing devices based on diamond defects have gained considerable attention. Here, magnetic fields are sensed by localized electron spins, which are then read out optically. The energy separation of spin states depends on an external magnetic field, and the frequency is measured with optically detected magnetic resonance, which allows for detecting of external fields. When used as a magnetic field measurement device, the sensitivity of the sensor is defined by the smallest shift in resonance frequency shift one can measure, which is limited by the coherence time of the spin transition. In addition, the NV sensor has the unique ability to switch between electric or magnetic field detection modes, making it a universal detector system for biology[65]. Although single-diamond spins are known to have the longest coherence times among all solid-state systems (reaching milliseconds for isotopically purified nuclear spin–free ^{12}C diamond), coherence properties for defects close to the surface are less spectacular. Therefore recent demonstration of active decoupling techniques can be important for magnetometry applications[66-68].

Quantum properties for single spins can be used to enhance sensitivity of diamond field sensors. It was shown that the sensitivity and dynamic range of diamond magnetometers can be improved up to the limit solely imposed by Heisenberg uncertainty relations when a quantum nondemolition technique is used for readout[69]. Entanglement between spins in diamond quantum registers can also improve sensitivity, allowing Heisenberg scaling[70].

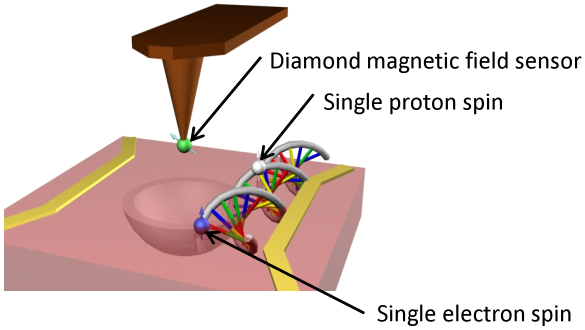

Fig. 9: *Scanning probe single-spin magnetometer.*

When combined with nanopositioning instrumentation the single-spin NV defect can be used as an atomic-size scanning probe vector magnetometer. The MRI with single-spin

sensitivity will provide new information about the dynamics of a broad range of biological processes at the nanometer scale, for example, unravel signal cascades responsible for deceases or accessing structure of single proteins under physiological conditions. Furthermore, it will potentially allow the resolution of the structure of single biomolecules under physiological conditions (using similar techniques developed for liquid-state NMR)[71]. First proof of principle demonstrations were realized recently[72, 73].

2 In conclusion

Quantum technology based on coherent control of diamond spins is rapidly developing for the past two decades. A combination of ultrasensitive optical detection techniques, super-resolution imaging, and robust coherent control using NMR techniques is a key ingredient of building the first quantum devices based on diamond. The ability to engineer defects with high accuracy and their long coherence time open new possibilities for so-called hybrid quantum processors where NV centers are connected to different types of qubits. Interesting examples of such hybrid quantum processors are based on coupling of diamond spins to nanomechanical systems[74] and superconducting qubits[75]. Strong coupling between an ensemble of spins in diamond and superconducting resonators[76, 77] and qubits[78] was demonstrated recently opening new avenues for solid-state quantum information processing. There is no doubt that this field will develop rapidly in the nearest future, resulting in developments of novel types of quantum technologies. Applications related to magnetometry and imaging techniques are expected to be developed, further resulting in diamond-based devices on the market in the next few years.

Most of the experimental demonstrations were achieved using NV defects. It is worth to mention that diamond hosts more than 500 documented color centers[79]. Recently nickel[80-82], chromium[83], and silicon-vacancy[84, 85] defects were identified as promising candidates for quantum technologies in diamond. The energy-level structure for these systems is less studied, and the technology of engineering is less developed compared to NV defects. However, attractive optical properties (strong zero photon line) are important for the integration of diamond quantum devices in photonics platform and imaging applications.

3 References

[1] Ladd, T.D., et al., Quantum computers. Nature, 2010. **464**(7285): p. 45-53.

[2] Elzerman, J.M., et al., Single-shot read-out of an individual electron spin in a quantum dot. Nature, 2004. **430**(6998): p. 431-435.

[3] Xiao, M., et al., Electrical detection of the spin resonance of a single electron in a silicon field-effect transistor. Nature, 2004. **430**(6998): p. 435-439.

[4] Rugar, D., et al., Single spin detection by magnetic resonance force microscopy. Nature, 2004. **430**(6997): p. 329-332.

[5] Wrachtrup, J., et al., Optical-Detection of Magnetic-Resonance in a Single Molecule. Nature, 1993. **363**(6426): p. 244-245.

[6] Gruber, A., et al., Scanning confocal optical microscopy and magnetic resonance on single defect centers. Science, 1997. **276**(5321): p. 2012-2014.

[7] Collins, A.T., The detection of colour-enhanced and synthetic gem diamonds by optical spectroscopy. Diamond and Related Materials, 2003. **12**(10-11): p. 1976-1983.

[8] Martin, J., et al., Generation and detection of fluorescent color centers in diamond with submicron resolution. Applied Physics Letters, 1999. **75**(20): p. 3096-3098.

[9] Rabeau, J.R., et al., Fabrication of single nickel-nitrogen defects in diamond by chemical vapor deposition. Applied Physics Letters, 2005. **86**(13).

[10] Pezzagna, S., et al., Creation of colour centres in diamond by collimated ion-implantation through nano-channels in mica. Physica Status Solidi a-Applications and Materials Science, 2011. **208**(9): p. 2017-2022.

[11] Meijer, J., et al., Generation of single color centers by focused nitrogen implantation. Applied Physics Letters, 2005. **87**(26).

[12] Boudou, J.P., et al., High yield fabrication of fluorescent nanodiamonds (vol 20, 235602, 2009). Nanotechnology, 2009. **20**(35).

[13] Rabeau, J.R., et al., Implantation of labelled single nitrogen vacancy centers in diamond using N-15. Applied Physics Letters, 2006. **88**(2).

[14] Naydenov, B., et al., Enhanced generation of single optically active spins in diamond by ion implantation. Applied Physics Letters, 2010. **96**(16).

[15] Goss, J.P., et al., Comment on "Electronic structure of the N-V center in diamond: Theory". Physical Review B, 1997. **56**(24): p. 16031-16032.

[16] Maze, J.R., et al., Properties of nitrogen-vacancy centers in diamond: the group theoretic approach. New Journal of Physics, 2011. **13**.

[17] Gali, A., M. Fyta, and E. Kaxiras, Ab initio supercell calculations on nitrogen-vacancy center in diamond: Electronic structure and hyperfine tensors. Physical Review B, 2008. **77**(15).

[18] Nizovtsev, A.P., et al., NV centers in diamond: spin-selective photokinetics, optical ground-state spin alignment and hole burning. Physica B-Condensed Matter, 2003. **340**: p. 106-110.

[19] Nizovtsev, A.P., et al., Spin-selective low temperature spectroscopy on single molecules with a triplet-triplet optical transition: Application to the NV defect center in diamond. Optics and Spectroscopy, 2003. **94**(6): p. 848-858.

[20] Rogers, L.J., et al., Infrared emission of the NV centre in diamond: Zeeman and uniaxial stress studies. New Journal of Physics, 2008. **10**.

[21] Jelezko, F. and J. Wrachtrup, Single defect centres in diamond: A review. Physica Status Solidi a-Applications and Materials Science, 2006. **203**(13): p. 3207-3225.

[22] Redman, D., S. Brown, and S.C. Rand, Origin of Persistent Hole Burning of N-V Centers in Diamond. Journal of the Optical Society of America B-Optical Physics, 1992. **9**(5): p. 768-774.

[23] Jelezko, F., et al., Single spin states in a defect center resolved by optical spectroscopy. Applied Physics Letters, 2002. **81**(12): p. 2160-2162.

[24] Tamarat, P., et al., Stark shift control of single optical centers in diamond. Physical Review Letters, 2006. **97**(8).

[25] Santori, C., et al., Coherent population trapping of single spins in diamond under optical excitation. Physical Review Letters, 2006. **97**(24).

[26] Buckley, B.B., et al., Spin-Light Coherence for Single-Spin Measurement and Control in Diamond. Science, 2010. **330**(6008): p. 1212-1215.

[27] Togan, E., et al., Quantum entanglement between an optical photon and a solid-state spin qubit. Nature, 2010. **466**(7307): p. 730-U4.

[28] Bassett, L.C., et al., Electrical Tuning of Single Nitrogen-Vacancy Center Optical Transitions Enhanced by Photoinduced Fields. Physical Review Letters, 2011. **107**(26).

[29] Marseglia, L., et al., Nanofabricated solid immersion lenses registered to single emitters in diamond (vol 98, 133107, 2011). Applied Physics Letters, 2011. **98**(18).

[30] Castelletto, S., et al., Diamond-based structures to collect and guide light. New Journal of Physics, 2011. **13**.

[31] Siyushev, P., et al., Monolithic diamond optics for single photon detection. Applied Physics Letters, 2010. **97**(24).

[32] Bernien, H., et al., Two-Photon Quantum Interference from Separate Nitrogen Vacancy Centers in Diamond. Physical Review Letters, 2012. **108**(4).

[33] Robledo, L., et al., High-fidelity projective read-out of a solid-state spin quantum register. Nature, 2011. **477**(7366): p. 574-578.

[34] Vanoort, E., N.B. Manson, and M. Glasbeek, Optically Detected Spin Coherence of the Diamond N-V Center in Its Triplet Ground-State. Journal of Physics C-Solid State Physics, 1988. **21**(23): p. 4385-4391.

[35] Doherty, M.W., et al., The negatively charged nitrogen-vacancy centre in diamond: the electronic solution. New Journal of Physics, 2011. **13**.

[36] Harrison, J., M.J. Sellars, and N.B. Manson, Optical spin polarisation of the N-V centre in diamond. Journal of Luminescence, 2004. **107**(1-4): p. 245-248.

[37] Jelezko, F., et al., Observation of coherent oscillations in a single electron spin. Physical Review Letters, 2004. **92**(7).

[38] Neumann, P., et al., Multipartite entanglement among single spins in diamond. Science, 2008. **320**(5881): p. 1326-1329.

[39] Jelezko, F., et al., Observation of coherent oscillation of a single nuclear spin and realization of a two-qubit conditional quantum gate. Physical Review Letters, 2004. **93**(13).

[40] Balasubramanian, G., et al., Ultralong spin coherence time in isotopically engineered diamond. Nature Materials, 2009. **8**(5): p. 383-387.

[41] Jiang, L., et al., Repetitive Readout of a Single Electronic Spin via Quantum Logic with Nuclear Spin Ancillae. Science, 2009. **326**(5950): p. 267-272.

[42] Neumann, P., et al., Single-Shot Readout of a Single Nuclear Spin. Science, 2010. **329**(5991): p. 542-544.

[43] Dutt, M.V.G., et al., Quantum register based on individual electronic and nuclear spin qubits in diamond. Science, 2007. **316**(5829): p. 1312-1316.

[44] Childress, L., et al., Coherent dynamics of coupled electron and nuclear spin qubits in diamond. Science, 2006. **314**(5797): p. 281-285.

[45] Nizovtsev, A.P., et al., A quantum computer based on NV centers in diamond: Optically detected nutations of single electron and nuclear spins. Optics and Spectroscopy, 2005. **99**(2): p. 233-244.

[46] Wrachtrup, J., S.Y. Kilin, and A.P. Nizovtsev, Quantum computation using the C-13 nuclear spins near the single NV defect center in diamond. Optics and Spectroscopy, 2001. **91**(3): p. 429-437.

[47] Neumann, P., et al., Quantum register based on coupled electron spins in a room-temperature solid. Nature Physics, 2010. **6**(4): p. 249-253.

[48] Cabrillo, C., et al., Creation of entangled states of distant atoms by interference. Physical Review A, 1999. **59**(2): p. 1025-1033.

[49] Barclay, P.E., et al., Hybrid photonic crystal cavity and waveguide for coupling to diamond NV-centers. Optics Express, 2009. **17**(12): p. 9588-9601.

[50] Bayn, I., et al., Triangular nanobeam photonic cavities in single-crystal diamond. New Journal of Physics, 2011. **13**.

[51] Bayn, I., et al., Processing of photonic crystal nanocavity for quantum information in diamond. Diamond and Related Materials, 2011. **20**(7): p. 937-943.

[52] Childress, L., et al., Fault-tolerant quantum repeaters with minimal physical resources and implementations based on single-photon emitters. Physical Review A, 2005. **72**(5).

[53] Young, A., et al., Cavity enhanced spin measurement of the ground state spin of an NV center in diamond. New Journal of Physics, 2009. **11**.

[54] Benjamin, S.C., B.W. Lovett, and J.M. Smith, Prospects for measurement-based quantum computing with solid state spins,. Las. Phot. Rev: p. DOI: 10.1002/lpor.20081005.

[55] Su, C.H., A.D. Greentree, and L.C.L. Hollenberg, Towards a picosecond transform-limited nitrogen-vacancy based single photon source. Optics Express, 2008. **16**(9): p. 6240-6250.

[56] Young, A., et al., Cavity enhanced spin measurement of the ground state spin of an NV center in diamond. New Journal of Physics, 2009. **11**: p. 013007.

[57] Moerner, W.E. and M. Orrit, Illuminating single molecules in condensed matter. Science, 1999. **283**(5408): p. 1670-+.

[58] Willig, K.I., et al., STED microscopy reveals that synaptotagmin remains clustered after synaptic vesicle exocytosis. Nature, 2006. **440**(7086): p. 935-939.

[59] Brown, T.A., et al., Approaches toward super-resolution fluorescence imaging of mitochondrial proteins using PALM. Methods, 2010. **51**(4): p. 458-463.

[60] Rittweger, E., et al., STED microscopy reveals crystal colour centres with nanometric resolution. Nature Photonics, 2009. **3**(3): p. 144-147.

[61] Shin, C., et al., Sub-optical resolution of single spins using magnetic resonance imaging at room temperature in diamond. Journal of Luminescence, 2010. **130**(9): p. 1635-1645.

[62] Liu, K.K., et al., Biocompatible and detectable carboxylated nanodiamond on human cell. Nanotechnology, 2007. **18**(32).

[63] Tisler, J., et al., Fluorescence and Spin Properties of Defects in Single Digit Nanodiamonds. Acs Nano, 2009. **3**(7): p. 1959-1965.

[64] Bradac, C., et al., Observation and control of blinking nitrogen-vacancy centres in discrete nanodiamonds. Nature Nanotechnology, 2010. **5**(5): p. 345-349.

[65] Dolde, F., et al., Electric-field sensing using single diamond spins. Nature Physics, 2011. **7**(6): p. 459-463.

[66] Laraoui, A. and C.A. Meriles, Rotating frame spin dynamics of a nitrogen-vacancy center in a diamond nanocrystal. Physical Review B, 2011. **84**(16).

[67] Hall, L.T., et al., Ultrasensitive diamond magnetometry using optimal dynamic decoupling. Physical Review B, 2010. **82**(4).

[68] de Lange, G., et al., Universal Dynamical Decoupling of a Single Solid-State Spin from a Spin Bath. Science, 2010. **330**(6000): p. 60-63.

[69] Waldherr, G., et al., High-dynamic-range magnetometry with a single nuclear spin in diamond. Nature Nanotechnology, 2012. **7**(2): p. 105-108.

[70] Cappellaro, P. and M.D. Lukin, Quantum correlation in disordered spin systems: Applications to magnetic sensing. Physical Review A, 2009. **80**(3).

[71] Degen, C.L., Scanning magnetic field microscope with a diamond single-spin sensor. Applied Physics Letters, 2008. **92**(24).

[72] Balasubramanian, G., et al., Nanoscale imaging magnetometry with diamond spins under ambient conditions. Nature, 2008. **455**(7213): p. 648-U46.

[73] McGuinness, L.P., et al., Quantum measurement and orientation tracking of fluorescent nanodiamonds inside living cells. Nature Nanotechnology, 2011. **6**(6): p. 358-363.

[74] Rabl, P., et al., Strong magnetic coupling between an electronic spin qubit and a mechanical resonator. Physical Review B, 2009. **79**(4).

[75] Twamley, J. and S.D. Barrett, Superconducting cavity bus for single nitrogen-vacancy defect centers in diamond. Physical Review B, 2010. **81**(24).

[76] Kubo, Y., et al., Strong Coupling of a Spin Ensemble to a Superconducting Resonator. Physical Review Letters, 2010. **105**(14).

[77] Amsuss, R., et al., Cavity QED with Magnetically Coupled Collective Spin States. Physical Review Letters, 2011. **107**(6).

[78] Zhu, X.B., et al., Coherent coupling of a superconducting flux qubit to an electron spin ensemble in diamond. Nature, 2011. **478**(7368): p. 221-224.

[79] Zaitsev, A.M., Optical properties of diamond : a data handbook. 2001, Berlin ; New York: Springer. xvii, 502 p.

[80] Orwa, J.O., et al., Nickel related optical centres in diamond created by ion implantation. Journal of Applied Physics, 2010. **107**(9).

[81] Siyushev, P., et al., Low-temperature optical characterization of a near-infrared single-photon emitter in nanodiamonds. New Journal of Physics, 2009. **11**.

[82] Gaebel, T., et al., Stable single-photon source in the near infrared. New Journal of Physics, 2004. **6**.

[83] Muller, T., et al., Wide-range electrical tunability of single-photon emission from chromium-based colour centres in diamond. New Journal of Physics, 2011. **13**.

[84] Wang, C.L., et al., Single photon emission from SiV centres in diamond produced by ion implantation. Journal of Physics B-Atomic Molecular and Optical Physics, 2006. **39**(1): p. 37-41.

[85] Neu, E., et al., Narrowband fluorescent nanodiamonds produced from chemical vapor deposition films. Applied Physics Letters, 2011. **98**(24).

D 3 Qubits and the New Semiconductors [1]

Guido Burkard
Department of Physics
Universität Konstanz

Contents

1 Spin qubits in conventional semiconductors **2**

2 The hyperfine coupling to nuclear spins **2**

3 Carbon as a material for spin qubits **4**

4 The basics of graphene **6**

5 Quantum dots in graphene I **8**

6 Spin and valley **9**

7 Quantum dots in graphene II **12**
7.1 Quantum dots in a graphene nanoribbon 12
7.2 Quantum dots in gapped graphene 13

8 Spin coherence in graphene **14**
8.1 Hyperfine interaction in graphene 14
8.2 Nuclear-spin induced spin decoherence 15
8.3 Spin-orbit induced spin relaxation 16

[1] Lecture Notes of the 44^{th} IFF Spring School "Quantum Information Processing" (Forschungszentrum Jülich, 2013). All rights reserved.

1 Spin qubits in conventional semiconductors

Semiconductor quantum dots have provided a nearly ideal arena for demonstrating and studying a wide spectrum of quantum coherent effects involving one or few electron spins only [1, 2, 3]. These demonstrations have further corroborated the potential of the electron spin degree of freedom in solid-state nanostructures as a quantum bit (qubit) for quantum information processing [4]. In a spin-based quantum processor, a series of quantum dots, each occupied by single (or an odd number of) electrons would represent a quantum register (Fig. 1), with the Heisenberg exchange coupling between them acting as the generating interaction for the necessary two-qubit gates. The implementations of single spin preparation, manipulation, and read-out in semiconductor quantum dots have been done almost exclusively with materials belonging to a particular family of semiconductors, namely binary compounds of elements from groups III and V of the periodic table, thus called the III/V semiconductors, e.g., gallium arsenide (GaAs) or indium arsenide (InAs). Some optical experiments were also done on II/VI materials, such as cadmium selenide (CdSe).
An idealized Hamiltonian for the spin qubit register (Fig. 1) is

$$H = \sum_{<i,j>} J_{ij} \mathbf{S}_i \cdot \mathbf{S}_j + \sum_i \mathbf{b}_i \cdot \mathbf{S}_i, \tag{1}$$

where the first sum runs over nearest-neighbor spin sites i and j, and where the parameters J_{ij} and $\mathbf{b}_i$ are controllable. One can envision that the exchange coupling strengths J_{ij} are controlled using the gate potentials of electrodes between dots and $\mathbf{b}_i$ is some sort of localized magnetic field at the site i only. For the actual physical implementation of such controllable interactions, which is a bit more involved, we refer to [2, 3, 1]. What is important is that the Hamiltonian (1) with controllable parameters J_{ij} and $\mathbf{b}_i$ is sufficiently powerful to generate a universal gate repertoire for quantum computation [4]. Spin-based quantum computation architectures with two- [5, 2] and three-spin [6] qubits exist, but will not be discussed here.

2 The hyperfine coupling to nuclear spins

It has been predicted early on that nuclear spins might limit electron spin qubit coherence [7]. Indeed, experiments found a strikingly short (averaged) spin coherence time $T_2^* \approx 10\,\mathrm{ns}$ in

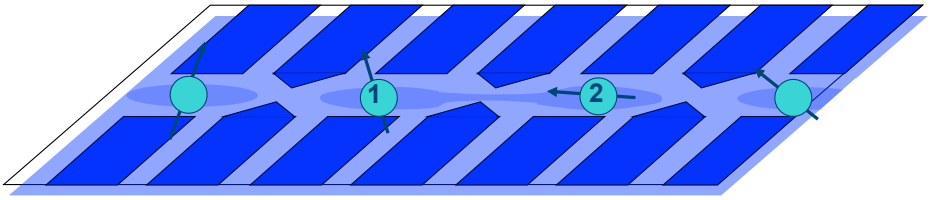

Fig. 1: *Schematic of a quantum dot array formed in a two-dimensional electron gas (light blue) when the electrostatic potential on the top gate electrodes (dark blue) is adjusted to be negative. Quantum dots are represented as round blue shapes. The electron number can be controlled by the gate potentials, and ideally, every quantum dot hosts only one single electron (green dot). The spin 1/2 of these electrons (black arrows) is then used as a qubit. Adjacent electron spins (e.g., those labeled 1 and 2 here) can interact via the exchange coupling.*

GaAs quantum dots [8]. This number is related to the fact that in GaAs (as in all common III/V semiconductors), every atomic nucleus has a nonzero spin. In other words, even if the quantum dots are emptied down to a single electron, there are as many other spins present as there are atoms in the quantum dot, typically about 10^5 to 10^6 (Fig. 2). The nuclear spins have only a small magnetic moment, and thus interact with the electron spin via the relatively weak hyperfine coupling. (Therefore, more precisely, the number of relevant nuclear spins is given by those who are within the volume where the electron wavefunction is sizeable.) The hyperfine coupling to the nuclear spins gives rise to an additional term in the Hamiltonian,

$$H_{\rm hf} = \sum_{ik} \mathbf{S}_i A_{ik} \mathbf{I}_k = \sum_i \mathbf{S}_i \cdot \mathbf{b}_i^{\rm n}, \tag{2}$$

where $\mathbf{I}_k$ denotes the operator of the k-th nuclear spin and A_{ik} is the hyperfine tensor describing the coupling of the spin of electron i to the spin of the atomic nucleus k (in GaAs, $A \approx 90\,\mu$eV). In the case of contact hyperfine interaction the hyperfine tensor is isotropic and $A_{ik} = a_k |\psi_i(\mathbf{r}_k)|^2 \mathbb{1}$, where a_k is a hyperfine coupling constant characteristic for the nuclear species of atom k and $\psi_i(\mathbf{r}_k)$ is the wavefunction of the i-th electron at the site of the k-th atomic nucleus. We neglect the nuclear Zeeman splitting since it is much smaller than both the electronic Zeeman splitting and the hyperfine interaction. We can describe the effect of the nuclear spin on the electron spin $\mathbf{S}_i$ as an effective magnetic field, called the Overhauser field, $\mathbf{b}_i^{\rm n} = \sum_k A_{ik} \mathbf{I}_k$. The Hamiltonian for a single spin $\mathbf{S}$ can thus be written as

$$H = S_z \left(b + \hat{b}_z^{\rm n} \right), \tag{3}$$

where we have chosen the magnetic field to lie along the z direction and where we have used that since $b \gg b^{\rm n}$ the spin flip processes described by S_x and S_y are suppressed. What is important here is that while b is a number, $\hat{b}_z^{\rm n}$ is an operator. The value assigned to a quantum operator is fluctuating if the system is not in one of its eigenstates. Such (quantum and thermal) flucutuations lead to the dephasing of the electron spin.

Let us start at some time $t = 0$ with an electron spin 1/2 in a quantum superposition of spin up and down, i.e., a spin prepared perpendicular to the external field, $|\psi(0)\rangle = \frac{1}{\sqrt{2}}(|\uparrow\rangle + |\downarrow\rangle) \otimes |\psi^{\rm n}\rangle$, where $|\psi^{\rm n}\rangle$ denotes the state of the nuclear spins. As a first simple case, let us further assume that the nuclear spins are in an eigenstate of the operator $\hat{b}_z^{\rm n}$ with eigenvalue $b_z^{\rm n}$, i.e., $\hat{b}_z^{\rm n} |\psi^{\rm n}\rangle = b_z^{\rm n} |\psi^{\rm n}\rangle$. In this case, the state after a time t has the form,

$$|\psi(t)\rangle = e^{-itH} |\psi(0)\rangle = |\psi^{\rm e}(t)\rangle \otimes |\psi^{\rm n}\rangle, \tag{4}$$

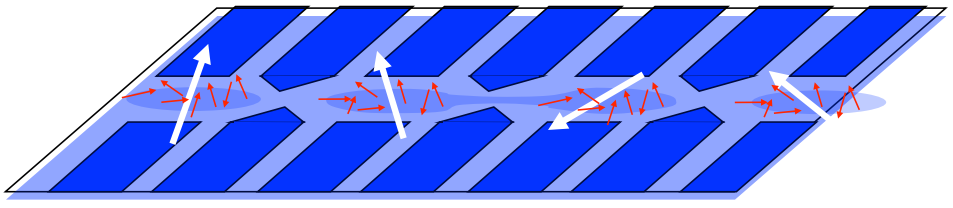

Fig. 2: *Even if only one electron is present in each quantum dot, there may be a large number of spins from the nuclei of the atoms forming the solid.*

with the pure electron spin state

$$|\psi^{\mathrm{e}}(t)\rangle = \frac{1}{\sqrt{2}}\left\{\exp\left(-\frac{it}{2\hbar}\left(b+b_z^{\mathrm{n}}\right)\right)|\uparrow\rangle + \exp\left(\frac{it}{2\hbar}\left(b+b_z^{\mathrm{n}}\right)\right)|\downarrow\rangle\right\}, \tag{5}$$

or expressed as in terms of the (pure-state) electron spin density matrix,

$$\rho(t) = |\psi^{\mathrm{e}}(t)\rangle\langle\psi^{\mathrm{e}}(t)| = \frac{1}{2}\begin{pmatrix} 1 & \exp(-it(b+b_z^{\mathrm{n}})/\hbar) \\ \exp(it(b+b_z^{\mathrm{n}})/\hbar) & 1 \end{pmatrix}. \tag{6}$$

In a real quantum dot, the nuclear spins typically won't be in an eigenstate of $\hat{b}_z^{\mathrm{n}}$, but in a thermal equilibrium state. Since the temperature is typically much larger than the nuclear Zeeman energy, we can assume that the nuclear spins are in a fully mixed state, $\rho^{\mathrm{n}} \propto \mathbb{1}$. We can now average over the probability distribution for the nuclear spins which in the limit of many nuclear spins and isotropic hyperfine coupling approaches a Gaussian for $N \gg 1$,

$$p(b_z^{\mathrm{n}}) = \mathrm{Tr}\left[\delta(\hat{b}_z^{\mathrm{n}} - b_z^{\mathrm{n}})\rho^{\mathrm{n}}\right] \approx (2\pi\sigma^2)^{-1/2}\exp(-(b_z^{\mathrm{n}})^2/2\sigma^2), \tag{7}$$

where the width of the distribution given as $\sigma \approx A/\sqrt{N}$ with N the number of nuclear spins. Averaging Eq. (6) over this probability distribution for the Overhauser field, we obtain the electron spin density matrix after time t in contact with an unpolarized nuclear spin system as

$$\rho(t) = \frac{1}{2}\begin{pmatrix} 1 & \exp\left(-itb/\hbar - \frac{1}{2\hbar^2}\sigma^2 t^2\right) \\ \exp\left(itb/\hbar - \frac{1}{2\hbar^2}\sigma^2 t^2\right) & 1 \end{pmatrix}. \tag{8}$$

The spin coherence is decaying, as can be seen from the transverse spin components, e.g.,

$$\langle S_x\rangle = \mathrm{Tr}\left[S_x\rho(t)\right] = \cos(bt)e^{-(t/\tau)^2/2}, \tag{9}$$

with the coherence time $\tau = \hbar/\sigma \approx \hbar\sqrt{N}/A$. For GaAs and $N \approx 10^6$, we recover $\tau \approx 10\,\mathrm{ns}$. Typical gate operation times for two-qubit gates are roughly $200\,\mathrm{ps}$ [8], but single qubit gates have typically required much longer times, about $100\,\mathrm{ns}$ [9] for single-spin qubits, and down to about $10\,\mathrm{ns}$ for two-spin singlet-triplet qubits [10].

3 Carbon as a material for spin qubits

Various strategies towards extending the spin coherence time have been investigated, including nuclear-spin preparation with electric control [10, 11, 12, 13], or optically [14, 15]. The goal of those strategies is to reach the first case discussed above, where the nuclear spins are in an eigenstate of $\hat{b}_z^{\mathrm{n}}$ which would make the electron spin decoherence-free. A more radical measure would be to replace GaAs with a nuclear-spin free material, or at least one with a low concentration of nuclear spins. Such materials can be found in the fourth (IV) group of the periodic table: carbon, silicon, and germanium. These elements all occur naturally in an isotope mixture, but with the dominant isotope being nuclear-spin free. In the case of carbon, the natural isotope mixture is approximately 99% of ^{12}C with nuclear spin $I = 0$ and 1% of ^{13}C with nuclear spin $I = 1/2$. In addition, the elements mentioned above (and in particular carbon) are all much lighter than Ga and As, and thus we can also expect spin-orbit effects to be weaker. This appears to be the case for carbon, however, the strength of the spin-orbit effects

depends strongly on the form of the material, e.g. carbon nanotubes give rise much stronger spin-orbit coupling than flat graphene.
To distinguish them from the semiconductor materials conventionally used for spin qubit experiments (GaAs, InAs, etc.), we refer to these group IV elemental materials as the "new" semiconductors. This nomenclature certainly requires some explanation because some of these materials are not particularly new, while others aren't even semiconductors! Therefore, we note the following:

- Si, Ge are of course well-known semiconductors, and Si is the basis of most of today's microelectronics industry. These materials are new only in the sense of their use for certain nanostructures, in particular few-electron quantum dots, and for single-spin experiments. Si and Ge are discussed in [3].

- Elemental carbon occurs in two different allotropes: diamond, with its characteristic sp^3 bonds, and graphite, with sp^2 bonds. Diamond with its 5.5 eV band gap is essentially an insulator, but can be viewed as a large-gap semiconductor. Some defects in diamond (most notably the nitrogen-vacancy center) posess a spin with a long and very robust coherence and are interesting as qubits for quantum information processing, see [16]. Graphite is a semimetal, and consists of atomically thin layers of carbon stacked on top of each other (Fig. 3). These layers are in fact two-dimensional carbon crystals known as graphene, and they are the topic of the following sections of this lecture. Graphene itself is not a semiconductor, because it lacks an energy gap (somethimes graphene is called a gapless semiconductor, sometimes it is also referred to as a semimetal). For the formation of quantum dots in which electrons can be localized, we are going to require a band gap, and therefore some of the following discussion will be about ways to create a bandgap in a gapless material such as graphene. Carbon nanotubes are essentially rolled up graphene, and can be either metallic or semiconducting.

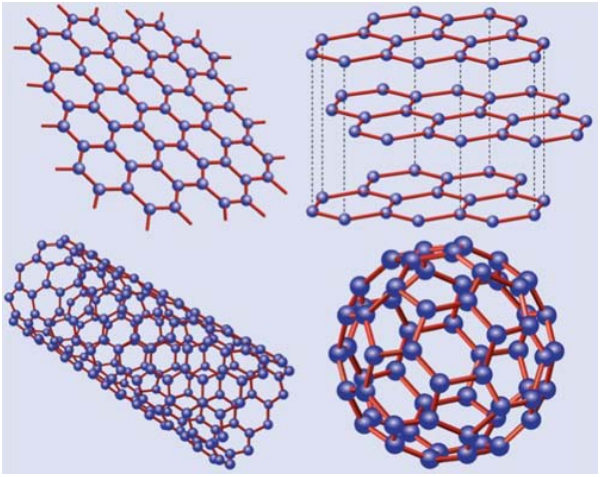

Fig. 3: *Carbon structures formed with the sp^2 bond. The 3D material graphite (upper right corner) is built up from layers of 2D graphene (upper left). When rolled up into a cylinder, graphene can form a 1D carbon nanotube (lower left). Another graphitic form are buckminster fullerenes (buckey balls, lower right). Reproduced from Ref. [17] with permission from the Authors.*

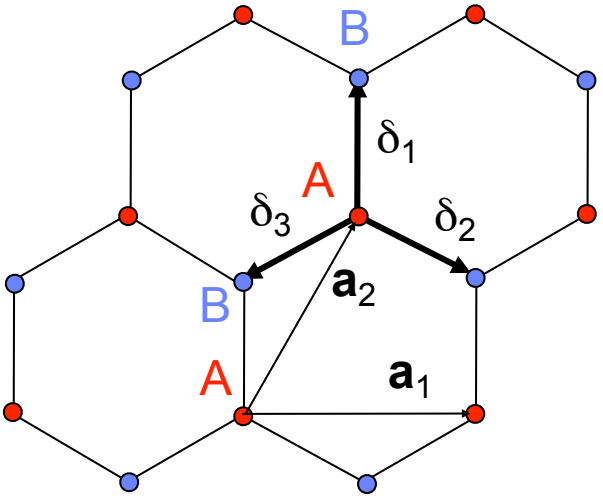

Fig. 4: *Two-dimensional crystal lattice of graphene. The blue and red dots indicate carbon atoms and form a hexagonal (honeycomb) lattice structure. The lattice is invariant under discrete translations by the primitive lattice vectors* $\mathbf{a}_1$ *und* $\mathbf{a}_2$ *(and multiples thereof). The unit cell of the lattice consists of two neighboring atomic sites, denoted A and B. The atom A (B) together with atoms obtained from it by translation with primitive lattice vectors, is called the A (B) sublattice. Starting from any atomic site, the three nearest neighbors are located at relative positions* $\boldsymbol{\delta}_i$ *on the other sublattice.*

4 The basics of graphene

Before entering the discussion about how to use graphene to make qubits, let us first review the basic properties of this remarkable material. For more details, see e.g. [17, 18].
Graphene is a two-dimensional crystal in which carbon atoms are arranged in a hexagonal or honeycomb lattice structure (Fig. 4). The lattice is composed of two equivalent sublattices A and B. We now consider the problem of a single electron moving in this periodic structure – a typical solid-state problem. We denote the orthogonalized set of states in which the electron is localized at a given atomic lattice site $\mathbf{R} = n_1\mathbf{a}_1 + n_2\mathbf{a}_2$ on the A sublattice or $\mathbf{R} + \boldsymbol{\delta}_1$ on the B sublattice as $|\mathbf{R}\rangle$ or $|\mathbf{R} + \boldsymbol{\delta}_1\rangle$ where $\mathbf{a}_i$ are the primitive lattice vectors and n_i are integers (these states are the so-called Wannier orbitals). The Hamiltonian of a single electron moving in this lattice can be written as a sum over the lattice sites $\mathbf{R}$ and nearest neighbors j,

$$H_0 = t \sum_{\mathbf{R}} \sum_{j=1}^{3} \Big(|\mathbf{R}\rangle\langle \mathbf{R}+\boldsymbol{\delta}_j| + |\mathbf{R}+\boldsymbol{\delta}_j\rangle\langle \mathbf{R}| \Big), \tag{10}$$

where t is the hopping matrix elements between nearest neighbor sites. In graphene, $t \approx 2.8\,\mathrm{eV}$. Here, we neglect next-to-nearest neighbor hopping because its matrix element is significantly smaller, $t' \approx 0.1\,\mathrm{eV}$ (however, see also Ref. [17]). Since the atomic sites in both sublattices are occupied by the same atomic species, there is no sublattice potential in pristine graphene. If a sublattice potential can be induced by some means, it would be of the form

$$H_\Delta = \Delta \sum_{\mathbf{R}} \Big(|\mathbf{R}\rangle\langle \mathbf{R}| - |\mathbf{R}+\boldsymbol{\delta}_1\rangle\langle \mathbf{R}+\boldsymbol{\delta}_1| \Big). \tag{11}$$

We repeat, however, that in pristine graphene, we have $\Delta = 0$.

To solve the single-particle Schrödinger equation $H|\psi\rangle = E|\psi\rangle$ for this lattice periodic problem, we use Bloch's theorem and write the solutions as

$$|\psi_{\mathbf{k}}\rangle = \sum_{\mathbf{R}} e^{i\mathbf{k}\cdot\mathbf{R}} \left(\alpha_{\mathbf{k}}|\mathbf{R}\rangle + \beta_{\mathbf{k}}|\mathbf{R}+\boldsymbol{\delta}_1\rangle\right) =: |\mathbf{k}\rangle \otimes \begin{pmatrix} \alpha_{\mathbf{k}} \\ \beta_{\mathbf{k}} \end{pmatrix}, \tag{12}$$

with the Bloch state on the A sublattice,

$$|\mathbf{k}\rangle \otimes \begin{pmatrix} 1 \\ 0 \end{pmatrix} = \sum_{\mathbf{R}} e^{i\mathbf{k}\cdot\mathbf{R}}|\mathbf{R}\rangle, \tag{13}$$

and on the B sublattice,

$$|\mathbf{k}\rangle \otimes \begin{pmatrix} 0 \\ 1 \end{pmatrix} = \sum_{\mathbf{R}} e^{i\mathbf{k}\cdot(\mathbf{R}+\boldsymbol{\delta}_1)}|\mathbf{R}+\boldsymbol{\delta}_1\rangle, \tag{14}$$

Substituting the inverse relations

$$|\mathbf{R}\rangle = \sum_{\mathbf{k}} e^{-i\mathbf{k}\cdot\mathbf{R}}|\mathbf{k}\rangle \otimes \begin{pmatrix} 1 \\ 0 \end{pmatrix}, \tag{15}$$

and ($j = 1, 2, 3$)

$$|\mathbf{R}+\boldsymbol{\delta}_{\mathbf{j}}\rangle = \sum_{\mathbf{k}} e^{-i\mathbf{k}\cdot(\mathbf{R}+\boldsymbol{\delta}_j)}|\mathbf{k}\rangle \otimes \begin{pmatrix} 0 \\ 1 \end{pmatrix}, \tag{16}$$

into the Hamiltonian (10) and using the relation $\sum_{\mathbf{R}} e^{i(\mathbf{k}-\mathbf{k}')\cdot\mathbf{R}} = \delta_{\mathbf{k},\mathbf{k}'}$, we find

$$H_0 = t\sum_{\mathbf{k}} |\mathbf{k}\rangle\langle\mathbf{k}| \otimes \begin{pmatrix} 0 & \gamma_{\mathbf{k}} \\ \gamma_{\mathbf{k}}^* & 0 \end{pmatrix}, \tag{17}$$

with $\gamma_{\mathbf{k}} = \sum_{j=1}^{3} e^{i\mathbf{k}\cdot\boldsymbol{\delta}_j} = 2e^{-ik_y a/2}\cos(\sqrt{3}k_x a/2) + e^{ik_y a}$ where $a = |\boldsymbol{\delta}_i| = |\mathbf{a}_i|/\sqrt{3}$ denotes the nearest-neighbor distance in the graphene lattice. Diagonalizing the 2x2 matrix we find the eigenvalues

$$E_{\mathbf{k}} = \pm t|\gamma_{\mathbf{k}}|. \tag{18}$$

This is essentially the band structure of graphene, which is plotted in Fig. 5 (also including nearest-neighbor hopping). Writing $\gamma_{\mathbf{k}}$ in polar form, $\gamma_{\mathbf{k}} = |\gamma_{\mathbf{k}}|e^{\phi_{\mathbf{k}}}$, we find the eigenvectors

$$\frac{1}{\sqrt{2}} \begin{pmatrix} e^{\pm\phi_{\mathbf{k}}} \\ 1 \end{pmatrix}. \tag{19}$$

There is a band crossing at $\mathbf{K} = \left(\frac{4\pi}{3\sqrt{3}a}, 0\right)$ and at $\mathbf{K}' = -\mathbf{K}$, because $\gamma_{\mathbf{K}} = \gamma_{\mathbf{K}'} = 0$. Expanding $\gamma_{\mathbf{k}}$ around $\mathbf{k} = \mathbf{K}$, we obtain $\gamma_{\mathbf{K}+\mathbf{k}} = \frac{3a}{2}(-k_x + ik_y) + O(k^2)$, and $\gamma_{\mathbf{K}'+\mathbf{k}} = \frac{3a}{2}(k_x + ik_y) + O(k^2)$, and thus, for low electron energies,

$$H_0 \simeq v_F \sum_{\mathbf{k},\tau=\pm1} |\tau\mathbf{K}+\mathbf{k}\rangle\langle\tau\mathbf{K}+\mathbf{k}| \otimes (\tau k_x\sigma_x + k_y\sigma_y), \tag{20}$$

with the Fermi velocity $v_F = 3a|t|/2$ (here, the sign in front of H_0 is not important). One finds $v_F \approx 10^6\,\mathrm{m/s}$. Only including momenta $k \ll K$ in the vicinity of $\mathbf{K}$ and transforming back

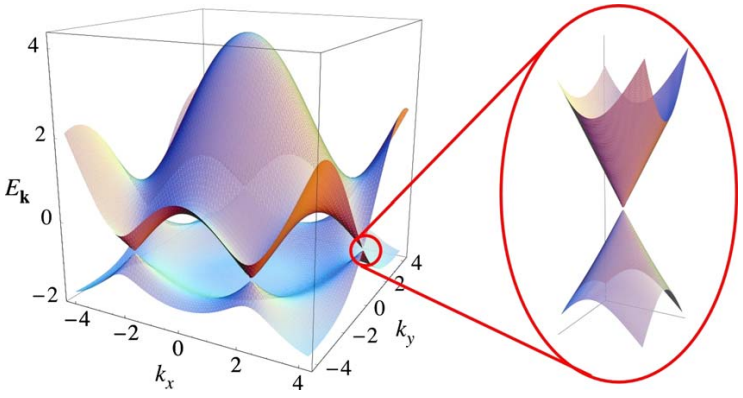

Fig. 5: *Band structure of graphene. Reproduced from Ref. [17] with permission from the Authors.*

to a position representation with $|\mathbf{K}+\mathbf{k}\rangle = \int e^{i\mathbf{k}\cdot\mathbf{r}}|\mathbf{r}\rangle \mathrm{d}\mathbf{r}$, we find the Hamiltonian in position representation,

$$H_0 \simeq v_F\left(-i\partial_x\sigma_x - i\partial_y\sigma_y\right) = v_F\mathbf{p}\cdot\boldsymbol{\sigma}, \tag{21}$$

with the momentum operator $\mathbf{p} = (p_x, p_y) = -i\boldsymbol{\nabla}$. The Schrödinger equation $i\partial_t\psi = H_0\psi$ for low-energy band electrons around the $\mathbf{K}$ point therefore has the form of the Dirac equation for massless relativistic particles [19]. Remember, the two-component vector structure and corresponding operator $\boldsymbol{\sigma}$ refers to the two sublattices of the graphene. However, due to the similarity of (21) with the Dirac Hamiltonian, one refers to $\boldsymbol{\sigma}$ as the "pseudo-spin". Similar considerations hold for the $\mathbf{K}'$ point. These two points in k-space where low-energy electrons can exist are known as "valleys" in solid-state physics. The fact that they give rise to two a priori identical states for each $\mathbf{k}$ is known as valley degeneracy. A sublattice potential (11)–if it could be induced e.g. by the substrate–leads to an additional "mass" term,

$$H_\Delta \simeq \Delta\sigma_z, \tag{22}$$

which opens a band gap Δ. An externally applied electrostatic potential $V(\mathbf{r})$, e.g., from patterned electrodes on top of the graphene layer, can also be included in the Hamiltonian. This term has no sublattice (pseudo-spin) structure. The question is now whether $V(\mathbf{r})$ can be used to make a quantum dot, similarly as in GaAs systems.

5 Quantum dots in graphene I

Unfortunately, localizing electrons in a quantum dot in graphene is not straight-forward, because the absence of a band gap ($\Delta = 0$) does not allow the formation of an energetically "forbidden" region, thus forming a potential barrier for electrons (Fig. 6).
This is one aspect of the famous Klein paradox for relativistic particles which states that such particles can penetrate through arbitrarily high potential barriers [20]. However, there are several ways around this:

1. Graphene can be etched or "cut" to form small connected pieces in which quantum-dot-like behavior in the electrical conduction have already been demonstrated [21, 22].

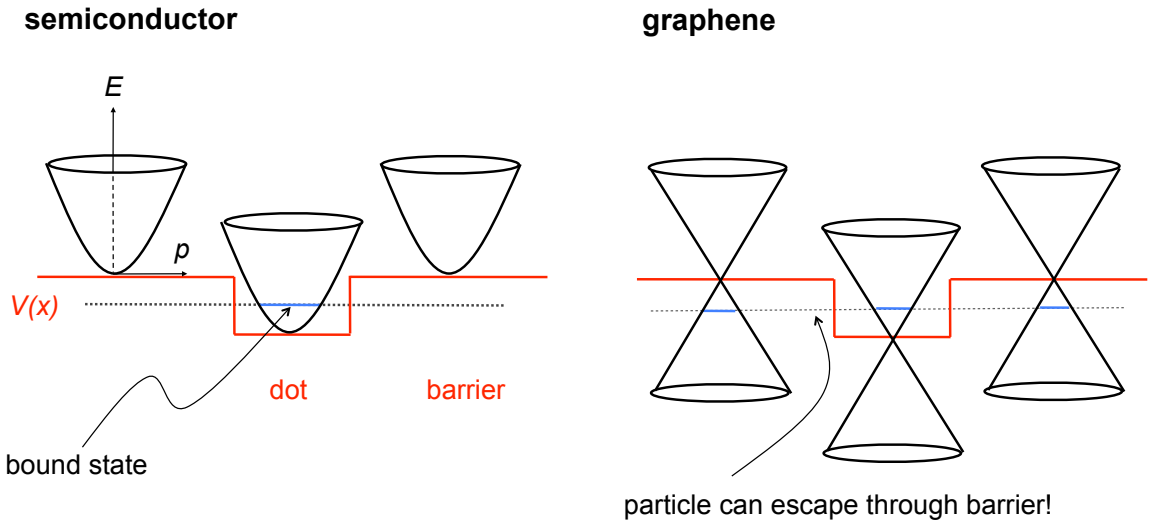

Fig. 6: *Particles in gapless graphene cannot be confined to a quantum dot. Left: An electrostatic potential can spatially bias the position of the lower edge of the conduction band in normal semiconductors, thus leading to bound states at energies within the band gap in the barriers. Right: The absence of a band gap in graphene leads to an overlap of the conduction and valence bands when a potential is applied and therefore to Klein tunneling into the barrier.*

2. In graphene nanoribbons, the edges can lead to the opening of a band gap. The remaining structure is a (quasi-) one-dimensional semiconductor [23] in which quantum dots can be formed electrostatically (Fig. 7).

3. In mono-layer graphene placed on a substrate, the substrate material can induce a small band gap $\Delta \neq 0$. In this case, quantum dots can be formed with an electrostatic potential $V(\mathbf{r})$ [24].

4. In bilayer graphene (two stacked layers of graphene), a perpendicular electric field leads to the opening of a band gap. Also in this case, quantum dots can be formed with an electrostatic potential $V(\mathbf{r})$ [24].

We will have a closer look at the options 2 and 3, but before this, we need to discuss the valley degree of freedom in the graphene bandstructure.

6 Spin and valley

It turns out that in addition to the lack of a band gap, there is another obstacle on the way to graphene-based spin qubits: We have seen above that there are two identical points $\mathbf{K}$ and $\mathbf{K}'$ in k-space where electrons can exist at relatively low energies. Typically, these two points are fairly well decoupled from each other because the corresponding electronic Bloch states have very different crystal momenta. In first approximation, we can therefore assume that all states, e.g. those in a quantum dot, come in two copies, one formed from electronic states in $\mathbf{K}$ and another from those in $\mathbf{K}'$. This is the valley degeneracy which we have alluded to already before.

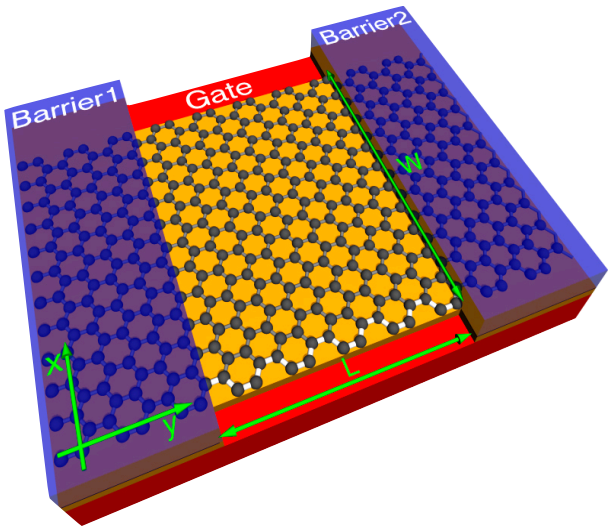

Fig. 7: *Schematic rendering of a quantum dot formed in a semiconducting armchair graphene nanoribbon by electrical gating [23].*

Formally, we can describe the valley degree of freedom by starting from (20) and writing

$$|\mathbf{K}+\mathbf{k}\rangle = \int e^{i\mathbf{k}\cdot\mathbf{r}}|\mathbf{r}\rangle \mathrm{d}\mathbf{r} \otimes \begin{pmatrix} 1 \\ 0 \end{pmatrix}, \tag{23}$$

$$|\mathbf{K}'+\mathbf{k}\rangle = \int e^{i\mathbf{k}\cdot\mathbf{r}}|\mathbf{r}\rangle \mathrm{d}\mathbf{r} \otimes \begin{pmatrix} 0 \\ 1 \end{pmatrix}, \tag{24}$$

where the vectors $\begin{pmatrix} 1 \\ 0 \end{pmatrix}$ and $\begin{pmatrix} 0 \\ 1 \end{pmatrix}$ describe the two valleys $\mathbf{K}$ and $\mathbf{K}'$ and are not to be confused with those describing the pseudo-spin. The tensor product of the vectors related to the two-valued pseudo-spin and valley degrees of freedom can also be represented as a four-spinor

$$\Psi(\mathbf{r}) = \begin{pmatrix} \Psi_A(\mathbf{r}) \\ \Psi_B(\mathbf{r}) \\ \Psi'_A(\mathbf{r}) \\ \Psi'_B(\mathbf{r}) \end{pmatrix}, \tag{25}$$

where $\mathbf{r}$ is the (coarse-grained) real-space position, Ψ_A (Ψ'_A) denotes the probability amplitude (density) for the electron to be on sublattice A and around the $\mathbf{K}$ ($\mathbf{K}'$) point in k-space, etc.[2] [3] Operators acting on the internal space of pseudo-spin and valley are linear combinations of the tensor products

$$\sigma_i \otimes \tau_j, \tag{26}$$

[2]The four components occurring here are not the same as in the Dirac theory of relativistic quantum mechanics. Relativistic electrons in free space do not have any valley degeneracy, but for them, the spin occurs in the free Hamiltonian. The graphene Hamiltonian we have discussed so far is independent of the real physical spin (not the pseudo spin).

[3]Other orderings and sign conventions for the amplitudes in the four spinor are used.

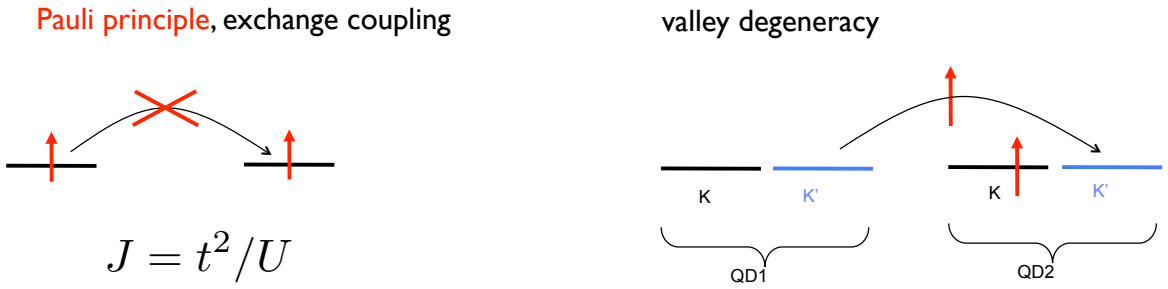

Fig. 8: *The exchange coupling between spins is modified in the presence of an additional orbital degeneracy, in this case the valley degeneracy arising from the existence of two inequivalent touching points* $\mathbf{K}$ *and* $\mathbf{K}'$ *in the band structure of graphene. Left: Virtual hopping processes between non-degenerate sites are possible for the spin singlet, while being forbidden by the Pauli exclusion principle for the spin triplet. As a consequence, the energy of the singlet is reduced by the energy* $J = t^2/4U$ *while that of the triplet is unchanged. This singlet-triplet splitting manifests itself in the Heisenberg exchange Hamiltonian* $H = J\mathbf{S}_1 \cdot \mathbf{S}_2$*. Right: In graphene, the valley degeneracy allows for hopping even in the spin triplet in some cases, and leads to an effective spin-valley coupling.*

with $i, j = 0, 1, 2, 3$, $\sigma_0 = \tau_0 = \mathbb{1}$, and the Pauli matrices $\sigma_1 = \tau_1 = \begin{pmatrix} 0 & 1 \\ 1 & 0 \end{pmatrix}$, $\sigma_2 = \tau_2 = \begin{pmatrix} 0 & -i \\ i & 0 \end{pmatrix}$, and $\sigma_3 = \tau_3 = \begin{pmatrix} 1 & 0 \\ 0 & -1 \end{pmatrix}$. Using this notation, the Hamiltonian (20) becomes

$$H_0 = v_F \begin{pmatrix} \mathbf{p} \cdot \boldsymbol{\sigma} & 0 \\ 0 & \mathbf{p} \cdot \boldsymbol{\sigma}^* \end{pmatrix}, \tag{27}$$

with $\boldsymbol{\sigma} = (\sigma_x, \sigma_y)$ and $\boldsymbol{\sigma}^* = (\sigma_x, -\sigma_y)$.
The existence of the valley degeneracy invalidates one of the assumptions that goes into the derivation of the spin exchange coupling J in (1), namely that the orbital states in each quantum dot are non-degenerate and thus double occupation with the same spin is forbidden (see Fig. 8).

This problem can be avoided if the valley degeneracy is lifted by a term $\mathbf{h} \cdot \boldsymbol{\tau}$ in the Hamiltonian. In some of the graphene quantum dot schemes enumerated above, the valley degeneracy is in some cases already lifted (1 and 2), while in others it can be lifted in a magnetic field perpendicular to the graphene sheet (3 and 4).
Despite the fact the valley-degeneracy problem can be circumvented, it is interesting to think about ways to perform universal quantum computation with spin qubits in the presence of the valley degeneracy. For this purpose, one can first derive the exchange Hamiltonian in the presence of valley degeracy [25],

$$H = -JP_{\text{as}} = \frac{J}{8}\Big[(\mathbf{S}_1 \cdot \mathbf{S}_2)(\boldsymbol{\tau}_1 \cdot \boldsymbol{\tau}_2) + \mathbf{S}_1 \cdot \mathbf{S}_2 + \boldsymbol{\tau}_1 \cdot \boldsymbol{\tau}_2 - 3\Big], \tag{28}$$

where P_{as} denotes the projection operator on the subspace of the six completely antisymmetric spin-valley states. To generate a CNOT gate from this coupling, we define the time-evolution operator

$$U(\phi) = e^{-i\int_0^{t_e} dt'\, H(t')} = \mathbb{1} + \left(e^{i\phi} - 1\right) P_{\text{as}}, \tag{29}$$

where $\phi = \int_0^{t_e} dt'\, J(t')$ is the time-integrated exchange coupling and H is the exchange Hamiltonian defined in Eq. (28). One can use this interaction to generate a spin-only entangling gate, the square-root-swap [25],

$$\sqrt{\mathrm{SWAP}}_{\mathrm{spin}} \equiv \sqrt{\mathrm{SWAP}} \otimes \mathbb{1} = e^{i\frac{3\pi}{4}} \left(U(\pi/4)\tau_{1x}U(\pi/4)\tau_{1z}\right)^2, \tag{30}$$

from which CNOT can be constructed [4]. Upon interchanging the role of spin and valley in (30), i.e. $\tau \leftrightarrow S$, one could in principle also implement valley-only quantum computation. It is also possible to use both spin and valley degrees of freedom at the same time, thereby doubling the capacity of the quantum register [25]. However, currently little is known about valley coherence in graphene.

7 Quantum dots in graphene II

Let us now have a closer look at the options 2 and 3 for implementing graphene quantum dots.

7.1 Quantum dots in a graphene nanoribbon

To study the 1D states in a graphene nanoribbon, we study the Dirac equation (28) for a ribbon of width W i.e. $0 \le x \le W$, and in a potential $V(y)$ with steps transverse to the ribbon direction[23],

$$-iv_F \begin{pmatrix} \sigma_x\partial_x + \sigma_y\partial_y & 0 \\ 0 & -\sigma_x\partial_x + \sigma_y\partial_y \end{pmatrix} \Psi + eV(y)\Psi = \varepsilon\Psi, \tag{31}$$

with a piecewise constant electric gate potential, $V(y) = V_{\mathrm{gate}}$ in the dot region ($0 \le y \le L$), and $V(y) = V_{\mathrm{barrier}}$ in the barrier region (where $y < 0$ or $y > L$). See Fig. 7. The semiconducting armchair boundary conditions can be written as ($\alpha = A, B$)

$$\Psi_\alpha|_{x=0} = \Psi'_\alpha|_{x=0}, \quad \Psi_\alpha|_{x=W} = e^{\pm 2\pi/3}\Psi'_\alpha|_{x=W}, \tag{32}$$

implying quantization conditions for the wave vector $k_x \equiv q_n$ in x-direction

$$q_n = (n \pm 1/3)\pi/W, \quad n \in \mathbb{Z}. \tag{33}$$

From this, we can read off an energy gap $E_g = \frac{4\pi v_F}{3W}$. For $W = 30\,\mathrm{nm}$, this amounts to about $E_g \approx 60\,\mathrm{meV}$.

It is convenient that due to the coupling between the two valleys at the boundary, the valley degeneracy is broken in the lowest one-dimensional subband. Picking out the lowest-energy one-dimensional mode, we can solve the one-dimensional textbook problem of a particle in a rectangular well $V(y)$, with the Schrödinger equation replaced by the Dirac equation [23]. This yields a finite number of bound states, as shown in Fig. 9. It can be envisioned that these qantum dots are placed next to each other, separated by a controllable electrostatic barrier, such that the electron spins can be exchange coupled. In turns out that the nearby (in energy) to the valence band can potentially be used to mediate non-nearest neighbor exchange in a quantum dot array [32].

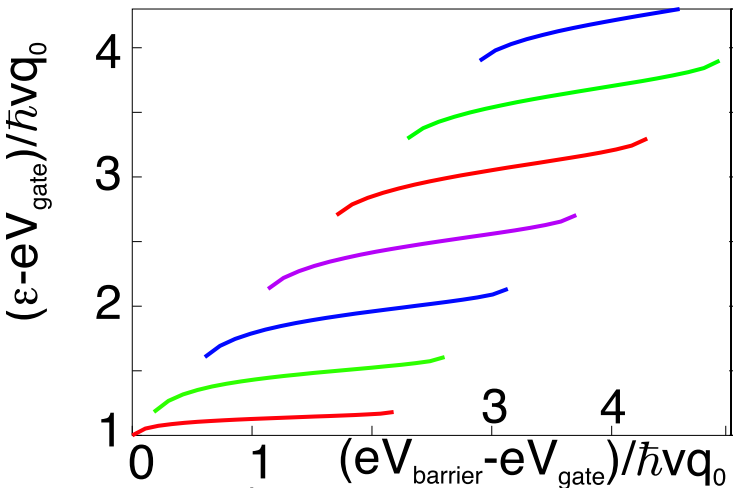

Fig. 9: *Energy levels in a quantum dot formed by electrical gating in an armchair graphene nanoribbon, as a function of the barrier potential height [23]. Note that due to the smallness of the band gap, The bound states disappear due to Klein tunneling if the barrier is too large.*

7.2 Quantum dots in gapped graphene

To describe localized states in a circular quantum dot in gapped graphene, we can treat the two (uncoupled) valleys separately, and for each write the Hamiltonian [24][4]

$$H_\tau = v_F(\boldsymbol{p} + e\boldsymbol{A}) \cdot \boldsymbol{\sigma} + \tau\Delta\sigma_z + U(\mathbf{r}), \tag{34}$$

where a magnetic field $\boldsymbol{B} = \nabla \times \boldsymbol{A} = (0, 0, B)$ has been introduced. Due to the circular symmetry, this problem is best solved in polar coordinates, and leads to wavefunctions described by confluent hypergeometric functions U and M (Bessel functions in the case $B = 0$), of the form

$$\chi^\tau_\sigma(r) = 2^{(1+n_\sigma)/2} e^{-br^2/2} r^{n_\sigma} \times \begin{cases} \alpha_\sigma U(q_\sigma, 1+n_\sigma, br^2) & , r > R\,, \\ \beta_\sigma M(q_\sigma, 1+n_\sigma, br^2) & , r < R\,, \end{cases} , \tag{35}$$

where

$$\Psi^\tau(r,\varphi) = e^{i(j-1/2)\varphi} \begin{pmatrix} \chi^\tau_A(r) \\ \chi^\tau_B(r) e^{i\varphi} \end{pmatrix}, \tag{36}$$

$$\Psi^\tau(r,\varphi) = e^{i(j-1/2)\varphi} \begin{pmatrix} \chi^\tau_A(r) \\ \chi^\tau_B(r) e^{i\varphi} \end{pmatrix}, \tag{37}$$

and where $b = eB/2$, $a_\sigma = 2b(j+\sigma/2) - (\epsilon^2 - \Delta^2)/v^2$, j is the eigenvalue of the total angular momentum $J_z = -i\partial_\varphi + \sigma_z/2$, $n_\sigma = |j - \sigma/2|$, and $q_\sigma \equiv \frac{1}{4}[\frac{a_\sigma}{b} + 2(1+n_\sigma)]$.c The coefficients α_σ and β_σ can be obtained form the continuity condition for the wavefunction at the circumference of the quantum dot. Interestingly, the valley degeneracy can by lifted with the magnetic field (Fig. 10), an effect that also occurs when an axial magnetic field is applied in a carbon nanotube. At large fields, different levels with the same j converge to form a Landau level.

[4]Here, the valley-isotropic form of the Dirac spinors is used.

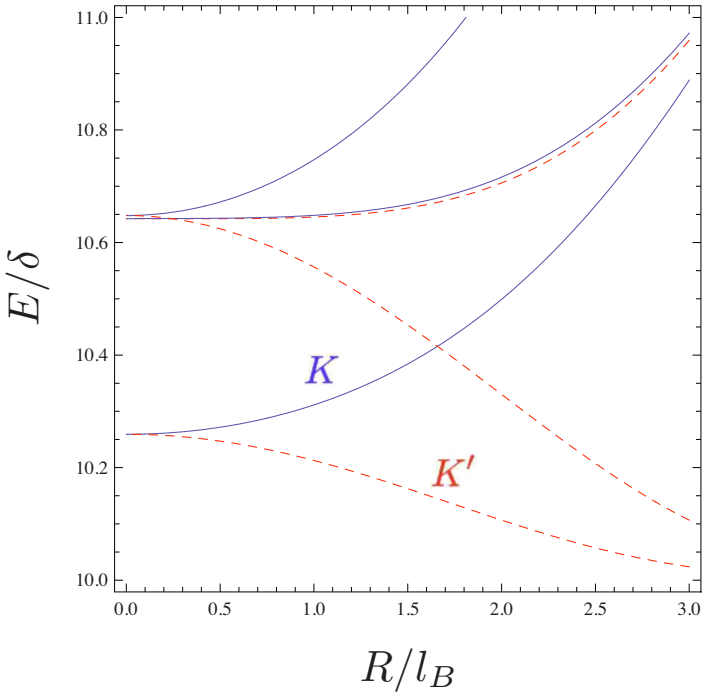

Fig. 10: *Energy levels in a circular quantum dot of radius R obtained by electrical gating of extended gapped graphene as a function of the applied magnetic field B, where $l_B = \sqrt{\hbar/eB}$ perpendicular to the graphene sheet [24]. The valley degeneracy is lifted at finite field. Energies are plotted in units of $\delta = \hbar v_F/R$.*

8 Spin coherence in graphene

Much less is known from experiments about spin coherence in graphene quantum dots than in semiconductor quantum dots (not to mention valley coherence, see above). Nevertheless, we can calculate the expected spin decoherence and relaxation rates due to certain processes.

8.1 Hyperfine interaction in graphene

When using naturally occurring carbon, about every one in a hundred carbon atoms in the graphene host material is a ^{13}C carbon atom with nuclear spin I=1/2 while the remaining atoms are ^{12}C with spin $I = 0$. Starting from the hopping model (10), we add the hyperfine interaction term

$$H_{\rm hf} = \sum_{\mathbf{R}} \mathbf{S} A \mathbf{I}_{\mathbf{R}} \otimes |\mathbf{R}\rangle\langle\mathbf{R}|, \tag{38}$$

where $\mathbf{I}_{\mathbf{R}}$ is the nuclear spin of the atom on the lattice site $\mathbf{R}$ and A is the hyperfine tensor [5]. After some calculation [26], one arrives at the low-energy Dirac Hamiltonian

$$H_{\rm hf} \simeq \mathbf{S} \cdot \left(\mathbf{h}^{(0)} \tau_0 + \sum_{i=x,y,z} \mathbf{h}^{(i)} \tau_i \right), \tag{39}$$

[5] Here we neglect the dipolar coupling to nuclear spins at distant atomic sites, as well as the orbital hyperfine coupling.

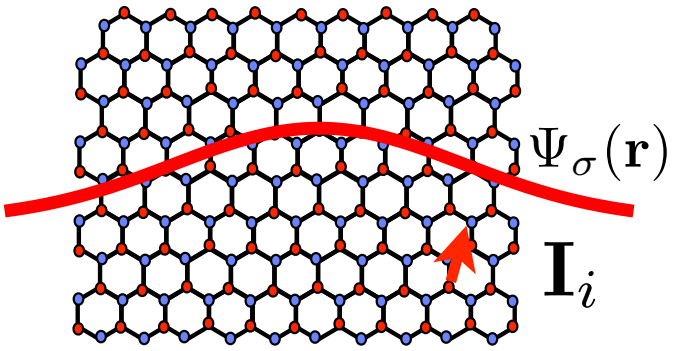

Fig. 11: *A ^{13}C atom acts as a weak but strongly localized scatterer, thus allowing for large momentum scattering from one valley to the other.*

with the ordinary hyperfine field (as in GaAs, see above)

$$\mathbf{h}^{(0)} = \frac{\Omega_{\text{cell}}}{2} A \sum_{\mathbf{R},\tau=\pm 1} \left(\mathbf{I}_{\mathbf{R}} |\Psi_A^{(\tau)}(\mathbf{R})|^2 + \mathbf{I}_{\mathbf{R}+\boldsymbol{\delta}_1} |\Psi_B^{(\tau)}(\mathbf{R}+\boldsymbol{\delta}_1)|^2 \right), \tag{40}$$

where $\Psi_i^{(+1)} = \Psi_i$ and $\Psi_i^{(-1)} = \Psi_i'$, the area of the unit cell Ω_{cell}, and the valley-flip field

$$\mathbf{h}^{(x)} = \Omega_{\text{cell}} A \text{Re} \sum_{\mathbf{R}} e^{-2i\mathbf{K}\cdot\mathbf{R}} \left(\mathbf{I}_{\mathbf{R}} \Psi_A(\mathbf{R})^* \Psi_A'(\mathbf{R}) + e^{-2i\mathbf{K}\cdot\boldsymbol{\delta}_1} \mathbf{I}_{\mathbf{R}+\boldsymbol{\delta}_1} \Psi_B(\mathbf{R}+\boldsymbol{\delta}_1)^* \Psi_B'(\mathbf{R}+\boldsymbol{\delta}_1) \right). \tag{41}$$

The valley-flip field $\mathbf{h}^{(y)}$ can be obtained from (41) by taking the imaginary part instead of the real part. Finally, the valley bias field $\mathbf{h}^{(z)}$ is obtained from (40) by changing the sign of the $\tau = -1$ term.

The most important observation about the hyperfine coupling (39) is that the ^{13}C atoms give rise to a weak but very strongly localized impurity potential which is able to scatter electrons from one $\mathbf{K}$ to $\mathbf{K}'$ (Fig. 10). This is the origin of the $\mathbf{h}^{(x)}$ and $\mathbf{h}^{(y)}$ terms.

8.2 Nuclear-spin induced spin decoherence

The electron spin decoherence in a graphene or carbon nanotube (CNT, see below) quantum dot with lifted valley degeneracy can be calculated in a similar way as in Sec. 2 above [27]. Besides the small abundance of nuclear-spin carrying atoms in natural carbon, the main difference to GaAs lies in the hyperfine tensor. The hyperfine tensor in graphene and carbon nanotubes differs from that of GaAs in two important ways:

- The hyperfine interaction in grahene (CNTs) is more than two orders of magnitude smaller than in III-V semiconductors, below $1\,\mu$eV.

- Since the atomic orbitals that constitute the mobile electrons in graphene are p rather than s orbitals, the contact hyperfine interaction $\propto |\psi_p(\mathbf{R})|^2$ vanishes, and is replaced by the

somewhat smaller and anisotropic coupling[6],

$$A = A_0 \begin{pmatrix} -1 & 0 & 0 \\ 0 & -1 & 0 \\ 0 & 0 & 2 \end{pmatrix}, \tag{42}$$

with $A_0 = 0.3\,\mu\mathrm{eV}$ [27]. In CNTs, the curvature of the graphene sheet leads to a small admixture of the s to the p orbital, which adds a small $\approx 0.1\,\mu\mathrm{eV}$ isotropic component to the traceless tensor (42).

8.3 Spin-orbit induced spin relaxation

While spin decoherence as described e.g. in equation (8) destroys the phase relation between the $|\uparrow\rangle$ and $|\downarrow\rangle$ components relative to an externally applied magnetic field, the probabilites for the spin to be up or down are unaffected. Such decoherence processes takes place without any energy exchange with the environment. In contrast, spin relaxation is a process where the probabilities for $|\uparrow\rangle$ and $|\downarrow\rangle$ decay to their thermal equilibrium values (at temperatures much smaller than the Zeeman splitting, to the lower energy state, say, $|\downarrow\rangle$.) Spin relaxation requires energy exchange with the environment.
The dominant spin relaxation mechanism in GaAs quantum dots involves two ingredients [28, 29]:

1. the spin-orbit coupling, allowing for a flip of the spin component along the magnetic field (taking care of angular momentum conservation), and

2. the electron-photon coupling, allowing for energy exchange with the environment, in this case the lattice vibrations in the solid (acoustic phonons, because the Zeeman energy is typically much smaller than the Debye energy). This takes care of energy conservation.

Again considering only one electron in a quantum dot with orbital eigenstates $|n\rangle$ and energies ϵ_n, we can write the relevant Hamiltonian as

$$H = \sum_n \epsilon_n |n\rangle\langle n| + bS_z + H_{\mathrm{SO}} + H_{\mathrm{ep}} + H_{\mathrm{phonons}}, \tag{43}$$

where the relevant spin-orbit interaction takes the form

$$H_{\mathrm{SO}} = \sum_{n \neq n'} \left(\lambda_{n',n} |n' \downarrow\rangle\langle n \uparrow| + h.c.\right). \tag{44}$$

The last two terms in (43) describe the (spin-independent) electron-phonon coupling and phonon Hamiltonian. The spin relaxation in, say, the ground state $n = 0$ at low temperatures is a process where $|0\uparrow\rangle$ decays into $|0\downarrow\rangle$ by spontaneously emitting a phonon with energy $b = g\mu_B B_z$. We can treat $H' = H_{\mathrm{SO}} + H_{\mathrm{ep}}$ as a small perturbation and use perturbation theory[7]. Since

[6] We are using a coordinate system different from that in [27]. We define the z axis as the normal to the graphene plane.

[7] We use time dependent perturbation theory although H is not explicitly time-dependent. Loading an electron with a given spin projection along B amounts to switching on the perturbation abruptly.

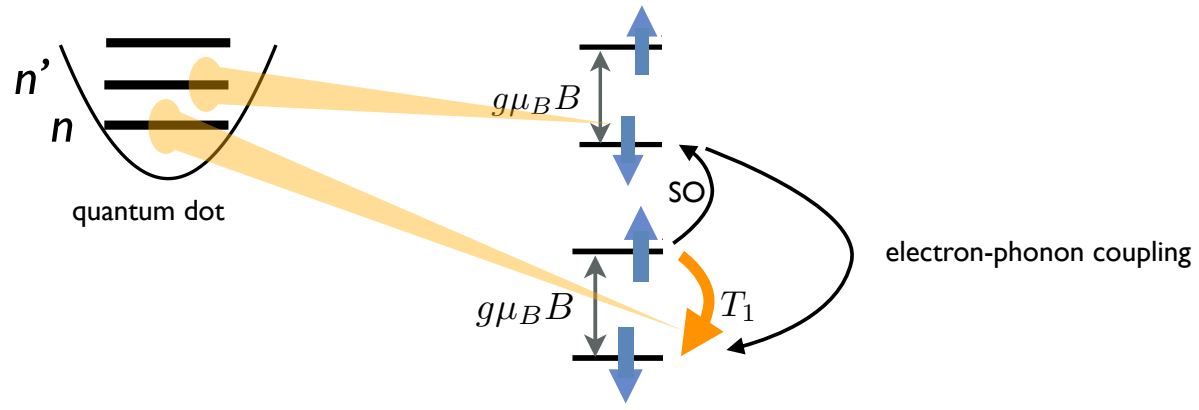

Fig. 12: *Spin relaxation (T_1) process. The spin-orbit coupling (SO) takes the system from $|n\uparrow\rangle$ into a virtual state with flipped spin and ecxited orbital $|n'\rangle$, followed by a phonon emission which carries away the Zeeman energy required to end up in a state $|n\downarrow\rangle$ with opposite spin.*

$\langle 0\downarrow|H|0\uparrow\rangle = 0$, this process must be of at least second order in H'. Indeed, in second order, we find the spin relaxation rate using Fermi's Golden Rule (for a general orbital state n),

$$\frac{1}{T_1} = \frac{2\pi}{\hbar}\left|\sum_{n'\neq n}\frac{\langle n\downarrow|H_{\rm SO}|n'\uparrow\rangle\langle n'\uparrow|H_{\rm ep}|n\uparrow\rangle}{\epsilon_{n'}-\epsilon_n-b}+\frac{\langle n\downarrow|H_{\rm ep}|n'\downarrow\rangle\langle n'\downarrow|H_{\rm SO}|n\uparrow\rangle}{\epsilon_n-\epsilon_{n'}+b}\right|^2\rho(b), \tag{45}$$

with the phonon density of states at the Zeeman energy, $\rho(b)$. The second term in (45) is illustrated in Fig. 12. An important feature of the rate (45) is the so-called van Vleck cancellation: For zero field $b = 0$, the rate vanishes, $1/T_1 = 0$. This is because at $b = 0$, due to time-reversal symmetry of each term in H, the matrix elements are invariant under complex conjugation and simultaneous spin reversal. In particular, the degenerate qubits states $|0\uparrow\rangle$ and $|0\downarrow\rangle$ result from each other under time reversal (they form a Kramers pair). At low fields $b \ll |\epsilon_n - \epsilon_{n'}|$, the denominators can be expanded and the lowest order in b cancels, leaving a factor b^2 in the rate. Together with more factors of b from $H_{\rm ep}$ and $\rho(b)$, one finds $q/T_1 \propto B^5$ which leads to long spin relaxation times at low fields in GaAs dots, exceeding one second [30].
The situation is graphene is quite different:

1. The qubit states obtained from two opposite spin states and the same orbital state in a given valley $\mathbf{K}$ are not a Kramers pair because time reversal maps $\mathbf{K}$ to $\mathbf{K}'$ and vice versa. As a conseqence, the van Vleck cancellation does not apply.

2. Due to the linear dispersion, the electron velocity is a constant v_F rather than proportional to the momentum p/m. Thus, the spin orbit coupling does not depend on momentum in graphene.

3. GaAs is piezoelectric while graphene is not. The dominant electron phonon coupling mechanism in GaAs is piezoelectric while in grpahene the deformation potential dominates.

4. Graphene is two-dimensional. This means that the acoustic phonon density of states is linear rather than quadratic (as in 3D) in the phonon frequency (energy).

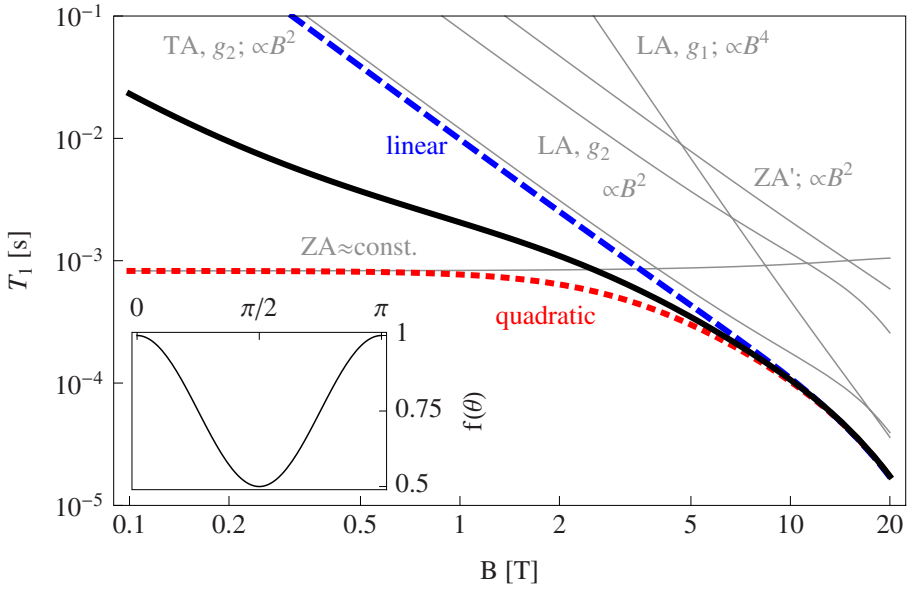

Fig. 13: *Calculated Spin relaxation time T_1 in a circular graphene quantum dot, as a function of the applied perpendicular magnetic field [31]. Inset: Dependence on the direction of the magnetic field.*

5. In a perfectly flat and infinite 2D crystal, there are out-of plane lattice vibrations with a quadratic dispersion and diverging density of states at zero energy. Such flexural phonons destabilize the graphene sheet, but in practice this can be counter-acted by the support on a substrate, the finite size of the sample, tension from the support, the presence of frozen ripples, etc.

Going through a similar calculation as previously done in GaAs for graphene, and assuming a perfectly flat and infinite graphene sample, we have predicted [31] that for a certain type of dots (the third kind in the list presented above) the relaxation rate becomes independent of the magnetic field at low field, saturating approximately in the millisecond range. At some field value, perhaps roughly around $1\,\mathrm{T}$, the behavior of the relaxation rate should become smaller again, and finally cross over to quadratic, i.e., $\propto B^2$ (Fig. 13).

References

[1] R. Hanson, L. P. Kouwenhoven, J. R. Petta, S. Tarucha, L. M. K. Vandersypen, Spins in few-electron quantum dots, Rev. Mod. Phys. 79, 1217 (2007).

[2] H. Bluhm, lecture A6 of this spring school.

[3] L. Schreiber, lecture B3 of this spring school.

[4] D. Loss, D. P. DiVincenzo, Quantum computation with quantum dots, Phys. Rev. A 57, 120126 (1998).

[5] J. Levy, Universal quantum computation with spin-1/2 pairs and Heisenberg exchange, Phys. Rev. Lett 89, 147902 (2002).

[6] D. P. DiVincenzo, D. Bacon, J. Kempe, G. Burkard, K. B. Whaley, Universal quantum computation with the exchange interaction, Nature 408, 339-342 (2000).

[7] G. Burkard, D. Loss, D. P. DiVincenzo, Coupled quantum dots as quantum gates, Phys. Rev. B 59, 2070-2078 (1999).

[8] J. R. Petta *et al.*, Coherent manipulation of coupled electron spins in semiconductor quantum dots, Science 309, 2180-2184 (2005).

[9] F. H. L. Koppens *et al.*, Driven coherent oscillations of a single electron spin in a quantum dot, Nature 442, 766-771 (2006).

[10] S. Foletti, H. Bluhm, D. Mahalu, V. Umansky, A. Yacoby, Universal quantum control of two-electron spin quantum bits using dynamic nuclear polarization, Nature Phys. 5, 903-908 (2009).

[11] D. Stepanenko, G. Burkard, G. Giedke, A. Imamoglu, Enhancement of electron spin coherence by optical preparation of nuclear spins, Phys. Rev. Lett 96, 136401 (2006).

[12] D. Klauser, W. A. Coish, D. Loss, Nuclear spin state narrowing via gate-controlled Rabi oscillations in a double quantum dot, Phys. Rev. B 73, 205302 (2006).

[13] H. Ribeiro, G. Burkard, Nuclear state preparation via Landau-Zener-Stückelberg transitions in double quantum dots, Phys. Rev. Lett. 102, 216802 (2009).

[14] C. Latta *et al.*, Confluence of resonant laser excitation and bidirectional quantum-dot nuclear-spin polarization, Nature Phys. 5, 758-763 (2009).

[15] M. N. Makhonin *et al.*, Fast control of nuclear spin polarization in an optically pumped single quantum dot, Nature Mater. 10, 844-848 (2011).

[16] F. Jelezko, lecture D2 of this spring school.

[17] A. H. Castro Neto, F. Guinea, N. M. R. Peres, K. S. Novoselov, A. K. Geim, The electronic properties of graphene, Rev. Mod. Phys. 81, 109-162 (2009).

[18] M. I. Katsnelson, Graphene (Cambridge University Press, 2012).

[19] D. P. DiVincenzo, E. J. Mele, Self-consistent effective-mass theory for intralayer screening in graphite intercalation compounds, Phys. Rev. B 29, 16851694 (1984).

[20] J. J. Sakurai, Advanced Quantum Mechanics (Addison-Wesley, 1967).

[21] L. A. Ponomarenko *et al.*, Chaotic Dirac Billiard in Graphene Quantum Dots, Science 320, 356358 (2008).

[22] C. Stampfer *et al.*, Tunable Coulomb blockade in nanostructured graphene, Appl Phys Lett 92, 012102 (2008).

[23] B. Trauzettel, D. V. Bulaev, D. Loss, G. Burkard, Spin qubits in graphene quantum dots, Nature Phys. 3, 192-196 (2007).

[24] P. Recher, J. Nilsson, G. Burkard, B. Trauzettel, Bound states and magnetic field induced valley splitting in gate-tunable graphene quantum dots, Phys. Rev. B 79, 085407 (2009).

[25] N. Rohling, G. Burkard, Universal quantum computing with spin and valley states, New J. Phys. 14, 083008 (2012).

[26] A. Pályi, G. Burkard, Hyperfine-induced valley mixing and the spin-valley blockade in carbon-based quantum dots, Phys. Rev. B 80, 201404(R) (2009).

[27] J. Fischer, B. Trauzettel, D. Loss, Hyperfine interaction and electron-spin decoherence in graphene and carbon nanotube quantum dots, Phys. Rev. B 80, 155401 (2009).

[28] J. Van Vleck, Paramagnetic Relaxation Times for Titanium and Chrome Alum, Phys. Rev. 57, 426 (1940).

[29] A. V. Khaetskii, Y. V. Nazarov, Spin-flip transitions between Zeeman sublevels in semiconductor quantum dots, Phys. Rev. B 64, 125316 (2001).

[30] S. Amasha *et al.*, Electrical Control of Spin Relaxation in a Quantum Dot, Phys. Rev. Lett 100, 046803 (2008).

[31] P. R. Struck, G. Burkard, Effective time-reversal symmetry breaking in the spin relaxation in a graphene quantum dot, Phys. Rev. B 82, 125401 (2010).

[32] M. Braun, P. R. Struck, G. Burkard, Spin exchange interaction with tunable range between graphene quantum dots, Phys. Rev. B 84, 115445 (2011).

D 4 Optical Quantum Dot Qubits [1]

Thaddeus D. Ladd
HRL Laboratories, LLC
3011 Malibu Canyon Rd., Malibu, CA, 90265

Contents

1 Introduction **2**

2 Quantum Dot Self-Assembly and Isolation **2**

3 Quantum Dot Quantum Optics **8**

4 Single Photon and Entangled Photon Sources **16**

5 Spin Preparation, Measurement, and Control **22**

6 Nuclear Spins **28**

7 Entangling Multiple Quantum Dots **39**

8 Prospects **45**

[1] Lecture Notes of the 44^{th} IFF Spring School "Quantum Information Processing" (Forschungszentrum Jülich, 2013).

1 Introduction

Nearly every device technology under consideration as a solid-state qubit has been referred to at one time or another as an "artifical atom." Solid-state qubits are necessarily atom-like, requiring the discrete energy levels resulting from the confinement of charge. In the case of electrically controlled quantum dots (QDs) or Josephson-junction-based qubits, however, qubit initialization and read-out are generally achieved through charge transport processes that resemble electrical circuitry far more than any processes in atomic and molecular optics (AMO). In contrast, optically controlled QDs are closer to AMO systems such as trapped ions; they are often (but not always) initialized through optical pumping, controlled with optical pulses, and measured via spontaneous emission and photon counting. The optical control of QDs makes enormous engineering differences in contrast to electrically controlled qubit technologies; easy differences to point to are the required operating temperatures and wiring requirements. In comparison to AMO qubits, optically controlled QDs share many of the control aspects of trapped atoms, without the speed-limiting requirements of controlling atom motion. Of course, the corresponding disadvantage with respect to AMO, as with electrically controlled dots, is the additional decoherence sources arising from the semiconductor host.

These notes introduce optically controlled QDs, without attempting a thorough review of research in the area. For a useful and reasonably recent glimpse into many facets of research into optically controlled QDs, see Ref. [1]. Many of the topics in these notes are covered by Ref. [2]; other reviews will be cited in each section. Section 2 begins by describing what optically controlled QDs are, and in particular how they are grown, characterized, and isolated. The quantum optics needed to describe their operation as qubits is introduced in Sec. 3, with a brief discussion of their incorporation into optical cavities. Their use as sources of optical photons in useful quantum states (Fock states or entangled states) is then summarized in Sec. 4. Means for quantum initialization, measurement, and coherent control are described in Sec. 5. Section 6 addresses perhaps the most scientifically interesting difference between QDs and isolated individual atoms: the presence of many nuclear spins. At the present time, the largest outstanding challenge in optical QDs is entangling them in an effective and flexible manner. The progress in both spin-photon entanglement and optically controlled spin-spin couplings will be discussed in Sec. 7. Finally, Sec. 8 will summarize the prospects for putting the various demonstrations together to engineer a viable qubit technology.

2 Quantum Dot Self-Assembly and Isolation

In the field of semiconductor heterostructure engineering, the term "quantum well" refers to a structure in which material interfaces confine charge carriers in a single dimension; if a second dimension of confinement is introduced, we have a "quantum wire," and a third and final dimension of confinement produces a "quantum dot." Two aspects of this terminology must be clarified to avoid confusion. First, a colloquial well — i.e. one that traps water — typically has three dimensional confinement, two provided by its walls and a third provided by gravity; it is therefore more like a "quantum dot" than a "quantum well." Second, in these terms the word "quantum" refers to quantized energy levels arising from confinement; these allow many applications which would be considered "classical" in the context of "quantum information." Examples of "classical" applications for optically active QDs include solar cells and bio-imaging; none of these are addressed in these notes.

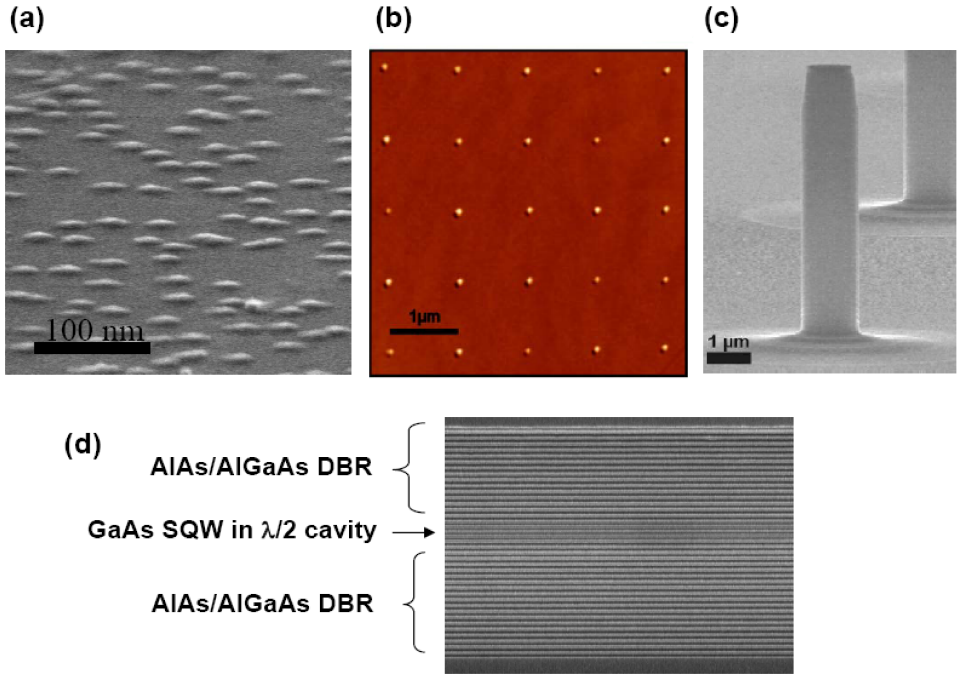

Fig. 1: *(a) Scanning electron micrograph (SEM) of uncapped self-assembled (SK-grown) InGaAs QDs prior to nanostructure fabrication. (b) Two-dimensional array of position controlled QDs [3] (c) Micropost microcavities with top and bottom DBRs serve to isolate and direct the emission from single QDs. (d) Monolithic planar microcavity showing top and bottom DBRs. The middle layer is a single quantum well (SQW). These device micrographs are from the research group Technische Physik, University of Würzburg.*

In the quantum information context, optically controlled QDs are most commonly based on heterostructures in III-V semiconductor materials. The most prominent examples are InGaAs QDs grown in GaAs via the Stranski-Krastanov (SK) method and GaAs/AlGaAs quantum well fluctuations, as we detail separately below. A dot may also be considered to be defined by a single-atom impurity in the semiconductor; such systems are rarely referred to as QDs in semiconductor device physics, we will refer to them as dots here as the relevant physics is very similar.

Stranski-Krastanov (SK) growth is a molecular beam epitaxy (MBE) method in which a thin layer of material (e.g. InAs) is grown on a non-lattice-matched substrate (GaAs); the non-lattice matched growth material nucleates into small islands which become the QDs [4]. The resulting dots are said to be "self-assembled," and are found in random locations as visible in Fig. 1(a). This method can be modified to allow site-control of the QDs, essentially by fabricating the nucleation sites, often using e-beam lithography, prior to self-assembly [3]. Figure 1(b) shows an example of such site-controlled QDs. The control of the location and size of QDs at the growth level remains an active area of research, and it is complicated by the observation that the optical qualities of dots are often adversely affected by added steps in the fabrication procedure. However, site control will be important for integrating large arrays of functioning qubits.

An important feature of SK dots is that the strain-based growth technique leaves behind a large amount of in-grown strain in the final devices. This impacts spin physics as we will discuss in later sections, in particular splittings between hole states and quadrupole effects for nuclear

spins. Other QD techniques for growth, such as droplet-epitaxy [5], can allow dots with lower strain.

A similar kind of QD arises from fluctuations on the edge of barriers of quantum wells [6]. These dots are often larger than SK dots, and the in-grown strain is substantially smaller. However, excitons bound to QDs are more likely to have strong spectral overlap with free exciton states in the quantum well, a property detrimental to integration of cavities as we discuss below.

For these dot growth methods, the self-assembled dots may be found to be charge-neutral, or they may contain one or more trapped electrons or holes. Trapped charges are our key interest for quantum information, as their spins provide matter qubits. The probability of finding a randomly charged dot may be enhanced by growing the QD layer in close vicinity to a layer of dopants; electrons from the dopant layer yield their extra electron to the deeper potentials of the QDs in equilibrium. Even more control is obtained by growing the QD layer inside a diode-like structure, in which electrically contacted back-gates and top-gates allow control of the voltage bias across the dots, allowing the tuning of the appropriate potential structure. One may use optical spectroscopy to find the bias at which the dots contain the desired amount of charge at equilibrium.

A small self-assembled dot may be thought of as an impurity complex, with fewer than a million atoms defining the structure. One may then ask how small a QD may be formed and still bind charge carriers. Long before self-assembled QDs such as those above were studied, dot-like complexes created by a single atom impurity in a semiconductor host were characterized [7, 8, 9]. For example, a donor impurity such as a single silicon atom in GaAs, or a single phoshphorous atom in silicon, can bind one or more electrons as well as additional excitons, similar to InAs QDs. The existence of these bound-exciton states is evident in the optical spectroscopy of semiconductors, where they arise as sharp resonances beneath the broad emission from free-exciton states. However, they are more difficult to isolate. In GaAs, where the effective mass is small, shallow donors provide a very weak potential which is easily disturbed by edge effects in nanostructures intended to isolate them. To date, a single isolated GaAs donor-bound exciton system has not been observed. In silicon, the donor-bound exciton potential is substantially deeper, but the weak optical emission from the donor-bound exciton is far more difficult to observe due to the material's indirect bandgap. Single donor bound excitons are observable from nanostructures in systems with a direct and wider bandgap, such as the II-VI material ZnSe [10].

Far more QD systems other than those discussed above have been studied in many other contexts. For the remainder of these notes, "quantum dots" will refer to self-assembled, SK-grown InGaAs QDs in GaAs, unless explicitly noted otherwise.

Quantum dot growth techniques generally result in a large ensemble of QDs, rather than just a single dot. To use QDs as qubits, however, a single dot must be isolated. Isolation occurs via two methods: spectroscopy, and nanostructure engineering.

Spectroscopy

Optical spectroscopy is critical for isolating and characterizing QDs. The basis for optical spectroscopy is that electron-hole pairs are created in the semiconductor, sometimes with electrical

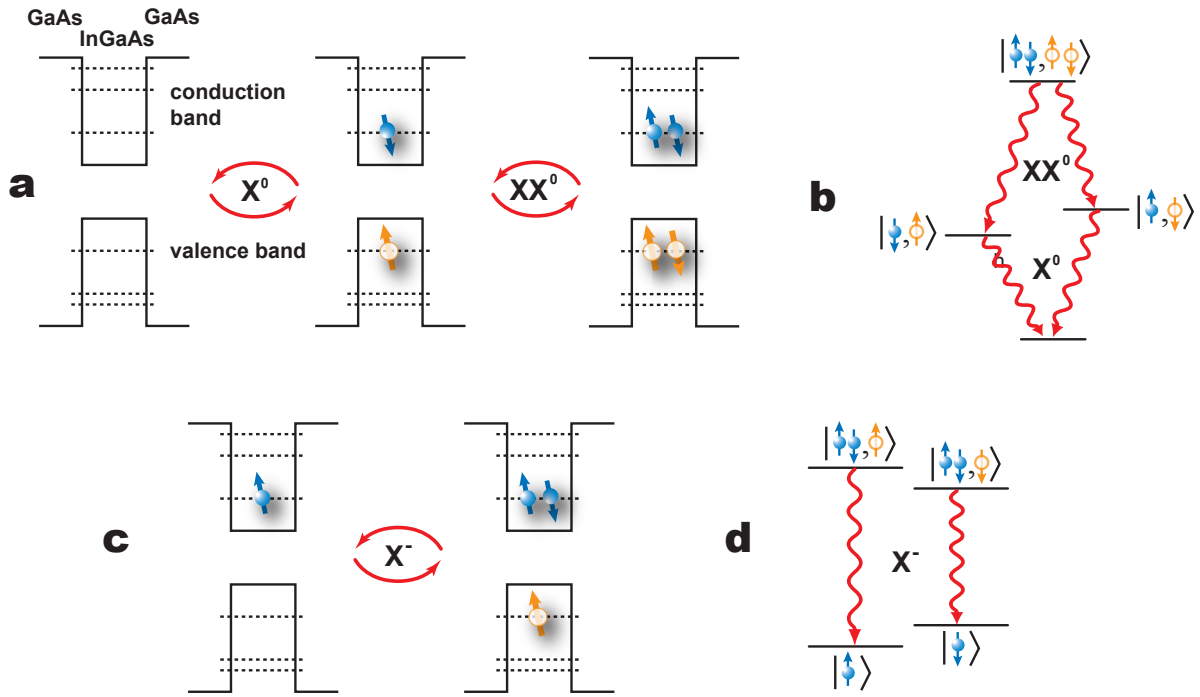

Fig. 2: *(a) Band energy diagram versus growth direction of single InGaAs QD, showing the conduction band and the valence band. The creation or annihilation of the first QD exciton (consisting of a blue electron in the conduction band and an orange heavy hole in the valence band) is labeled X^0, while the creation of a second exciton is labeled XX^0. (b) Energy levels of the neutral dot, with wavy lines showing biexciton (XX^0) and exciton (X^0) decay. Dark exciton states are not shown. The two exciton levels are usually nondegenerate even in zero magnetic field. (c) Band energy diagram for a dot charged with a single electron, showing trion transition (X^-) (d) Energy levels for charged dot. In Faraday geometry, the two spin trion channels decay as shown, with oppositely polarized photons. In Voigt geometry (not shown here; see Fig. 4), each trion state may decay into either of the two spin ground states.*

pumping but more often with optical pumping. Excitons may be resonantly pumped using a tunable laser, or excitation well above the bandgap may create electron-hole pairs which quickly relax into the exciton states of interest. Either way, once localized in QDs, excitons quickly recombine; typical spontaneous decay times are on the order of a nanosecond. Upon decay, QD excitons emit a photon whose wavelength depends on the bandgap of the QD material, the exciton binding energy, and the binding energy of the QD. The latter is a strong function of the QD size. Since QDs are generally grown by a random self-assembly process, they each have a random size and therefore a random wavelength. As a result, QD ensembles have an extremely large inhomogeneous linewidth. This can be a strong feature in some applications; in particular, it substantially eases the difficulty of isolating a single QD. One may grow dots with a sufficiently low spatial density that the focal spot of a microscope (typically many μm in size at the near-infrared wavelengths typical of dots) contains only a few tens of dots. As the wavelengths of these dots are each extremely different, the final stage of single-dot isolation occurs via a monochromator, limiting the view to a small portion of optical bandwidth that only excites or measures photons from a single dot.

Spectroscopy reveals more than just the existence of a dot. Spectroscopy is ultimately used to identify the charge state of a dot (in contrast to electrically controlled dots, where charges are directly sensed via transconductance measurements). Several spectroscopic lines are typical of a QD spectrum. In a neutral QD, the fundamental exciton transition is labeled X^0, as shown in Fig. 2. For a dot charged with a single electron, the transition to the state with that single electron plus an exciton (the "trion"), is labeled X^-. It is possible for a single dot to exhibit spectral lines for both of these transitions under repeated excitation, indicating that the charge state of the QD ground state is fluctuating through the experiment. (Post-selection of one such spectral line is sometimes used in a repeated experiment to isolate trials in which the dot begins in a particular desired charge state.) One usually also finds biexciton lines, labeled XX^0 for neutral dots. The biexciton line (corresponding to a transition from two excitons to a single exciton in the dot) does not have the same energy as the single exciton line due to Coulomb and spin effects inside the dot. However, these effects depend on the size and shape of the dot and therefore the biexciton transition has been found with both higher and lower energies than exciton transitions in different samples. The biexciton is distinguishable from the exciton line by its dependence on pump power; since it generally requires a double excitation to create, its intensity generally scales quadratically with pump power while the single exciton intensity scales linearly. Even more lines result from excited orbital states within these dots; these are sometimes useful for resonant pumping, but we will address these lines no further in these notes. For example spectra from a single InGaAs dot, see Ref. [11].

Basic Spin Physics

To elaborate on the use of spectroscopy, we must divert slightly into the basic spin physics of QDs; we will return to this topic multiple times in subsequent sections. When performing single dot spectroscopy, exciton and biexciton lines by themselves reveal little about the charge state of the dot unless either the electrical bias of the QD is tuned, or a magnetic field is changed. Strong characterization of a biased dot will generally employ both, as magnetic field splittings are critical to identify charge configurations. Neutral dots and charged dots behave very differently in the presence of a magnetic field. While the spin physics can be quite complicated, for our purposes here we can present a very simple picture. In the semiconductors relevant for optical QD qubits, conduction band electrons are s-like, meaning that the Bloch functions have no orbital angular momentum and so their total angular momentum J comes entirely from spin; hence $J = 1/2$. Valence band holes, in contrast, are p-like and hence provide an additional quantum of orbital angular momentum in addition to spin. There are therefore two angular momentum manifolds, the $J = 1/2$ manifold and the $J = 3/2$ manifold. These manifolds are split in energy by spin-orbit coupling; the $J = 1/2$ split-off band is further from the band edge by 0.34 eV in GaAs and is therefore so energetically removed that we may safely ignore it. The $J = 3/2$ manifold is then further split by strain in the device into "heavy holes" with spin projection 3/2, which have a larger effective mass, and "light holes" with spin projection 1/2, which have smaller effective mass. As the light holes are typically split from the band edge by 10s of meV, they are often ignored as well.

The dismissal of the light holes on energetic grounds is not always appropriate. Their role depends on the strain of the QD, as well as the relative directions of the applied magnetic field and the strain direction. To clarify these directions, we assume (as is almost always the case) that optical excitation is applied in the growth direction of the QD, and also any luminescence is collected from this direction. Hence we assume the strain direction and the photon

absorption/emission axis are the same. If also the direction of the applied magnetic field is along this axis, then the experiment is said to be in "Faraday geometry." In this case the magnetic field does not mix the heavy and light holes. However, for most quantum control experiments, we will suppose that the magnetic field is orthogonal to the growth/excitation/collection axis. Such an experiment is said to be in "Voigt geometry." In this case we will label the growth/excitation/collection axis the x-direction. This convention is contrary to that typically used when describing heterostructure growth, where z is traditional. However, we reserve z for the direction of the orthogonally applied magnetic field, to connect more readily to conventions in magnetic resonance. In this case, the hole-spin quantum number defined by strain and that defined by magnetic field are incompatible, and so the eigenstates are mixed between light-hole and heavy-hole states. For highly strained dots (typical of InAs SK dots) and typical magnetic fields (no more than a few Tesla), this mixing is often negligible, as strain dominates. However, a reduction of strain or the application of a very large field can make light-holes important, so they should not be forgotten entirely.

For now, however, we will limit our discussion only to the heavy-holes. In this case, a neutral exciton (combination of Coulomb-coupled electron and hole) has four possible spin projections, $m = \pm 2$ and $m = \pm 1$. The photons which create and result from the annihilation of excitons themselves have $m = \pm 1$, and therefore selection rules favor optical transitions to and from the $m = \pm 1$ states. These states are therefore known as "bright excitons." The $m = +1$ and $m = -1$ transitions are split in a magnetic field by an amount depending on the effective g-factors of both the constituent electron and hole; in a high magnetic field or a very symmetric dot, each transition emits the corresponding circular polarization of light. In low field, strain asymmetries in the QD result in linear polarization. The $m = \pm 2$ "dark exciton" states can be obtained, for example, by optical excitation of a bright exciton followed by a single electron spin-flip. These states are longer-lived due to the angular momentum selection rules prohibiting direct spontaneous emission, and hence can form a bottleneck in some processes.

The distinction of bright and dark excitons does not exist for trions. For example, if a QD contains a single electron, then the introduction of an exciton results in two electrons, whose ground state is a spin-singlet. The total trion spin state is therefore determined entirely by the heavy-hole. In Faraday geometry, the $\pm 3/2$ heavy-hole trions decay directly to $\pm 1/2$ electron-spin ground ground states, as in the neutral dot case; this is shown in Fig. 2(d). In Voigt geometry, a single trion state can decay into either of the Zeeman-split single electron ground states. In general, therefore, there are four split transitions observable in magnetic field, with more complicated selection rules. For the moment, we will suffice to conclude that charged QDs and neutral QDs have easily distinguished spectra in magnetospectroscopy; more detailed discussion of selection rules will be addressed when we detail quantum control methods in Sec. 5. All of the geometric considerations and resulting transition rules are well tabulated and experimentally confirmed in Ref. [12].

As a final sidenote, I have above introduced exciton/biexciton transitions in the context of spectroscopy. These optical transitions are imagined to be used in these notes as tools for either created photons as flying qubits, or as means for manipulating spin-based qubits in the QD ground state. Another point of view is to treat the excitons as qubits themselves, and demonstrations of quantum information concepts such as quantum gates in excitons have certainly been explored; see, for example, Ref. [13]. But these excitonic states are very shortlived, and

therefore unlikely to be a sufficient resource for quantum computing beyond a single qubit or two; hence this line of thinking will be considered no further in these notes.

Nanostructures

So far, we have only indicated spectroscopic techniques as a means to isolate and characterize a single QD. However, more control over dot growth and isolation results from the use of lithographically defined nanostructures such as holes in a metal mask, mesas, and posts. Examples of posts each containing only a few QDs are shown in Fig. 1(c). These allow spatial isolation of a sample region much smaller than the focal spot of a microscope; a structure may be smaller than a μm in width and hence may contain only one, or perhaps just a few, QDs; again these are spectroscopically isolated. This allows the growth of dots with higher density and reduces the demands on microscopy (which is very helpful when, as usual, dots are kept cold in a cryostat, and especially when maintained in the bore of a large superconducting magnet). Unfortunately, one all too frequently encounters the possibility that the behavior of a QD is altered by the surfaces of the nanostructure, usually in a detrimental way.

Nanostructures provide another critical benefit of optically controlled QDs: the possibility of using the effects of cavity quantum electrodynamics (CQED). We detail this topic in the next section.

3 Quantum Dot Quantum Optics

In this section, we detail the basic quantum optics theory needed to understand the experiments and proposals discussed in latter sections. We begin with a general description of the Hamiltonian describing the optical system, and the rotating wave approximation. This Hamiltonian is then used to analyze the effects of optical cavities, as well as the spin-controlled phase shifts which will be the basis for spin measurement, control, and perhaps entanglement.

Optical Hamiltonian

We begin with a Hamiltonian composed in terms of QD ground-state energy levels $|\phi_j\rangle$ and excited-state energy levels $|\xi_k\rangle$. For a charged QD, the ground states $|\phi_j\rangle$ include the spin states of the charged ground state and the optically excitable trion states. In the "laboratory frame," such a Hamiltonian is written

$$\mathcal{H}_{\text{lab}} = \sum_j \delta_j \left|\phi_j\right\rangle\!\left\langle\phi_j\right| + \sum_k (\omega_0 + \Delta_k) \left|\xi_k\right\rangle\!\left\langle\xi_k\right| + \sum_m (\omega_0 + \omega_m) a_m^\dagger a_m + \sum_{jkm} g_m [\left|\phi_j\right\rangle\!\left\langle\xi_k\right| + \left|\xi_k\right\rangle\!\left\langle\phi_j\right|][u_{jkm} a_m^\dagger + u_{jkm}^* a_m]. \quad (1)$$

Throughout these notes, we write Hamiltonians in units of angular frequency; a Hamiltonian in units of energy would be $\hbar\mathcal{H}$. A Hamiltonian of the form Eq. (1) results from the fundamental expansion of the electromagnetic field into harmonic oscillations annihilated by a_m; the specific coupling constants $g_m u_{jkm}$ are generally assumed to follow from the electric dipole approximation as

$$g_m u_{jkm} = -ie\sqrt{\frac{\omega_0 + \omega_m}{2\epsilon\hbar V_m}}\mathbf{p}_m \cdot \left\langle\xi_k\right| \mathbf{r} \left|\phi_j\right\rangle, \quad (2)$$

where $\mathbf{r}$ is a position operator, $\mathbf{p}_m$ is the polarization and V_m the volume of mode m, ϵ is the permittivity of the semiconductor, and e is the electron charge. We briefly note that for dots with spatial scales approaching or exceeding the wavelength of light they emit, which certainly exist, the electric dipole approximation may not apply. However, one may usually still employ Eq. (1) just with a different definition for g_m and u_{jkm}; the detailed fundamental constants will not be very important for the discussions that follow, as we will whenever possible rely on empirically measured parameters rather than equations like Eq. (2). In the general case, we assume by convention that g_m is real, and for each optical mode m we introduce complex unitary coupling matrices u_{jkm} between ground states and excitable states that depend on the selection rules of the QD and the polarization $\mathbf{p}_m$. The introduction of a mode volume V_m in Eq. (1) is a reminder that theoretical quantum optics is *always* in a cavity; when describing free-space modes, the cavity volume is allowed to become infinite, but if done right this volume cancels (usually from a volume term in the optical density of states). When we address CQED below, V_m will represent the finite mode volume of a real cavity.

Let us first take a moment to consider the dipole moment $e\langle\xi_k|\mathbf{r}|\phi_j\rangle$. In general, this involves the wave-function overlap of the electrons and holes in the QD. The evaluation of this integral becomes complicated in general, as there are three spatial scales of importance which are sufficiently close to render low-order approximations inaccurate. The smallest is usually the exciton Bohr radius in the semiconductor, a_{B}^*, which is on the order of 10 nanometers, depending on the material. The next largest scale is the radius of the QD structure, a, which is typically 100s of nm. As the QD becomes larger, the overlap integral between electrons and holes becomes larger as well, and the dipole moment increases as $(a/a_{\mathrm{B}}^*)^{3/2}$. This effect is known as mesoscopic enhancement and is most strongly observed in the larger QDs resulting from fluctuations of quantum well interfaces. It cannot make optical dipoles arbitrarily large, however; the effect saturates once a becomes comparable to the wavelength of the emitted light (typically order 1 μm), and the dipole approximation breaks down.

The first step for simplifying Eq. (1) is to enter the "rotating reference frame" using the Hamiltonian term

$$\mathcal{H}_{\omega_0} = \omega_0\left[\sum_k |\xi_k\rangle\langle\xi_k| + \sum_m a_m^\dagger a_m\right]. \tag{3}$$

The rotating reference frame is then defined by

$$\begin{aligned}\mathcal{H}_{\mathrm{rot}} =& e^{i\mathcal{H}_{\omega_0}t}[\mathcal{H}_{\mathrm{lab}} - \mathcal{H}_{\omega_0}]e^{-i\mathcal{H}_{\omega_0}t} \\ =& \sum_j \delta_j |\phi_j\rangle\langle\phi_j| + \sum_k \Delta_k |\xi_k\rangle\langle\xi_k| + \sum_m \omega_m a_m^\dagger a_m \\ &+ \sum_{jkm} g_m[|\phi_j\rangle\langle\xi_k| e^{-i\omega_0 t} + |\xi_k\rangle\langle\phi_j| e^{i\omega_0 t}u_{jk}^*][u_{jkm}a_m^\dagger e^{i\omega_0 t} + u_{jkm}^* a_m e^{-i\omega_0 t}].\end{aligned} \tag{4}$$

We emphasize that the frequencies Δ_k and ω_m are *detunings* from the rotation frequency ω_0. Now, we note that the factors of $e^{\pm i\omega_0 t}$ only partially cancel in the driving term. In the rotating frame, there are time-independent "rotating wave" terms, and "counter-rotating" terms which vary as $\exp(\pm 2i\omega_0 t)$. The rotating wave approximation (RWA) is to assume that the harmonic motion at frequency $2\omega_0$ is so much faster than any of the other dynamics governed by the Hamiltonian that these terms effectively average to zero. This is valid if $\omega_0 \gg \{\Delta_k, \delta_j, \omega_m, g_m\}$.

In the case of QDs, ω_0 is an optical frequency with typical value 300 THz, while g_m and detunings Δ_k are typically less than 1 THz. Ground state splittings δ_j are much smaller, on the order of 100s of GHz in large magnetic fields. Therefore, the RWA for optical transitions is strongly valid.

The RWA is also typically used in magnetic resonance, where RF or microwave magnetic fields drive transitions near the resonance of spins precessing in a fixed DC magnetic field (Larmor precession). We will describe in Sec. 5 a scheme where again we have spins precessing in a fixed DC magnetic field, and an ultrafast optical pulse provides the same effect as a rapidly modulated AC magnetic field. Unlike in magnetic resonance, however, the AC magnetic field modulation in ultrafast optical control is so much faster than the Larmor precession frequency that the RWA would be a very poor description of the spin control. Hence, in what follows, we always use rotating wave approximation for the optical transitions, and we never use the rotating wave approximation for the spin transitions.

Under the RWA, then, our Hamiltonian becomes

$$\mathcal{H}_{\text{rot}} = \sum_j \delta_j \left|\phi_j\right\rangle\!\left\langle\phi_j\right| + \sum_k \Delta_k \left|\xi_k\right\rangle\!\left\langle\xi_k\right| + \sum_m \omega_m a_m^\dagger a_m + \sum_{jkm} g_m [u_{jkm} \left|\phi_j\right\rangle\!\left\langle\xi_k\right| a_m^\dagger + u_{jkm}^* \left|\xi_k\right\rangle\!\left\langle\phi_j\right| a_m]. \quad (5)$$

Cavity QED

In short, the role of a cavity is to alter the photonic density of states. Without a cavity, the coupling of an atomic transition to a large continuum of optical modes results in spontaneous emission; this is the Wigner-Weisskopf model. A cavity, however, makes the atomic coupling to a discrete, small set of cavity modes far stronger than the coupling to other modes by assuring constructive interference of those cavity modes at the atom or dot. For this discussion, let us consider only one ground state $|\phi\rangle$ (with energy chosen as $\hbar\delta = 0$), one excited state $|\xi\rangle$, and a single cavity mode of frequency $\omega_0 + \omega_c$ annihilated by a. Denote atomic transitions as $\sigma^+ = |\xi\rangle\langle\phi|$. Then for that single mode, Eq. (5) becomes the Jaynes-Cummings Hamiltonian

$$\mathcal{H}_{\text{JC}} = \Delta\sigma^+\sigma^- + \omega_c a^\dagger a + g(a^\dagger\sigma^- + a\sigma^+). \quad (6)$$

The coupling to the continuum of non-cavity modes still allows spontaneous emission, but as these photons are lost we treat this as an incoherent process through a linear process on the density operator of Lindblad form,

$$\mathcal{L}_\gamma[\rho] = -\frac{\gamma}{2}[\{\sigma^+\sigma^-, \rho\} - 2\sigma^-\rho\sigma^+], \quad (7)$$

with spontaneous emission rate γ. The sum from the Wigner-Weisskopf and dipole approximations using the density of states for free-space photons would give

$$\gamma = \sum_m \frac{g_m^2}{s + i(\omega_m - \Delta)} = \frac{n\omega_0^3 e^2}{3\pi\epsilon\hbar c^3} |\langle\xi| \mathbf{r} |\phi\rangle|^2. \quad (8)$$

In the summation, s is a small real number (resulting from a Laplace transform of the Schrödinger equation); the essence of Wigner-Weisskopf approximation is to convert the summation into an

integral using the optical density of states and to take the limiting principle value as $s \to 0$ [14]. Technically, the ω_0^3 in this expression should correspond to the atomic energy $\omega_0 + \Delta$ in our notation, but we will use ω_0 for brevity and recalling the assumption $\Delta \ll \omega_0$ already employed in the RWA. We have also introduced $n = \sqrt{\epsilon\mu}/c$, the index of refraction of the material, where c is the speed of light in vacuum.

The coherent coupling g between the cavity photon and the optical transition in the dot and the related spontaneous emission rate γ are sometimes characterized by the unitless oscillator strength f, found from the ratio of the radiative decay rate γ normalized by that of a classical electron dipole emitter of frequency ω_0 and wavelength λ:

$$f = \frac{3}{(4\pi k)^2}\left(\frac{\lambda}{n}\right)^3 \omega_0 \gamma. \tag{9}$$

Here the constant k is $e/\sqrt{4\epsilon m_{\mathrm{e}}}$ where m_{e} is the electron mass. The coupling g is then given by $k\sqrt{f/V}$. For strong CQED effects, one wants a high value of g, which requires both a high f and a small mode volume V. Nanofabrication techniques in semiconductors allow V to be made as small as $(\lambda/n)^3/2$. The oscillator strength of a large QD can also be very high due to the mesoscopic enhancement effect discussed above, which gives $f \propto (a/a_{\mathrm{B}}^*)^3$.

One more process is important for CQED. The cavity mode is assumed to be able to leak from the cavity, a process which may be modeled as a beamsplitter-like coupling to an infinite continuum of free-space modes. Wigner-Weisskopf-like arguments can lead to a similar Lindblad term

$$\mathcal{L}_\kappa[\rho] = -\frac{\kappa}{2}[\{a^\dagger a, \rho\} - 2a\rho a^\dagger]. \tag{10}$$

The quality factor of the cavity, Q, is defined as the cavity resonant frequency divided by κ.

We can now describe the basic problem of CQED as the master equation

$$\frac{d\rho}{dt} = -i[\mathcal{H}_{\mathrm{JC}}, \rho] + \mathcal{L}_\gamma[\rho] + \mathcal{L}_\kappa[\rho], \tag{11}$$

which even in simple cases contains rich physics. In order to elaborate the basic figures of merit of CQED, we here consider the simple case of only a single transition, a single mode, and a single excitation in the CQED system. In this case the master equation can be cast in terms of three real variables,

$$\begin{aligned} p(t) &= \langle \xi, 0 | \, \rho(t) \, | \xi, 0 \rangle + \langle \phi, 1 | \, \rho(t) \, | \phi, 1 \rangle \, , \\ z(t) &= \langle \xi, 0 | \, \rho(t) \, | \xi, 0 \rangle - \langle \phi, 1 | \, \rho(t) \, | \phi, 1 \rangle \, , \text{ and} \\ c(t) &= i \, \langle \xi, 0 | \, \rho(t) \, | \phi, 1 \rangle \, , \end{aligned}$$

where the number in each state label is the photon number in the cavity mode. Eventually, any excitation will leak into the final ground state population $\langle \phi, 0 | \, \rho \, | \phi, 0 \rangle$, but this plays little role in the master equation in this subspace since this population is constrained by normalization to be $1 - p(t)$. In terms of these variables, our master equation gives

$$\frac{d}{dt}\begin{bmatrix} p(t) \\ z(t) \\ c(t) \end{bmatrix} = -\frac{\gamma + \kappa}{2}\begin{bmatrix} p(t) \\ z(t) \\ c(t) \end{bmatrix} + \begin{bmatrix} 0 & (\gamma - \kappa)/2 & 0 \\ (\kappa - \gamma)/2 & 0 & 4g \\ 0 & g & i(\omega - \Delta) \end{bmatrix}\begin{bmatrix} p(t) \\ z(t) \\ c(t) \end{bmatrix}. \tag{12}$$

The characteristic equation of the matrix in the second term is

$$\lambda\left[\lambda^2 + \frac{(\gamma-\kappa)^2}{4} - 4g^2\right] = i(\omega-\Delta)\left[\lambda^2 + \frac{(\gamma-\kappa)^2}{4}\right] \tag{13}$$

In the case where the cavity is resonant with the QD transition ($\omega = \Delta$), we see that the complex decay rates of the master equation involving the coherent coupling g are

$$\Gamma_\pm = \frac{\gamma+\kappa}{2} \pm \sqrt{\frac{(\gamma-\kappa)^2}{4} - 4g^2}. \tag{14}$$

The real part of these eigenvalues correspond to optical lifetimes (and therefore limiting spectral widths), while the imaginary part corresponds to frequency shifts. From this simple equation, we can identify three regimes of importance for CQED. The *weak-coupling* regime is for $g \ll \gamma \ll \kappa$, in which case we can expand the square root to lowest order in g to find the perturbative result

$$\gamma \to \gamma + \frac{4g^2}{\kappa}, \tag{15}$$

indicating slightly enhanced emission from the QD due to the cavity. This effect is known as the Purcell effect. From this equation we introduce another important figure of merit, known as the cooperativity,

$$C = \frac{4g^2}{\kappa\gamma}, \tag{16}$$

which is the ratio of the cavity-enhanced emission $4g^2/\kappa$ to the non-cavity spontaneous emission rate γ. When this factor is large but still $g \ll \kappa$, we say the system is in the *intermediate coupling* or *Purcell regime*. C may be quickly estimated as $C = 3/4\pi^2 \times (\lambda/n)^3 \times Q/V$. The oscillator strength has cancelled out; up to polarization/alignment factors, this is a property of the cavity alone. Semiconductor microcavity systems show a key advantage in achieving high values of C in comparison to larger cavities that might be used with trapped atoms or ions, since they may be made very small. (Of course, much higher cooperativity is typical of circuit CQED systems, in which case two dimensions of the superconducting-resonator-based cavity are much smaller than the wavelength of microwave photons, and the Q factors in superconductors are very high.)

The *strong coupling regime* occurs when $g > |\kappa - \gamma|/4$, in which case the system shows a frequency splitting into two eigenmodes separated by a frequency called the vacuum Rabi splitting, given by $2g$ as $g \to \infty$. This means that the coherent coupling between the dot and the cavity is faster than incoherent relaxation processes. Strong coupling is not needed for coherent technologies using QDs, but it makes some schemes simpler.

The strong coupling regime has now been achieved for optically controlled QDs in a number of different kinds of semiconductor microcavities. For a review and description of a number of real microcavities, see Ref. [15]. Here, I will only briefly outline the core concepts of microcavity physics. In principle, a cavity is any device that, as the first sentence of this section indicates, alters the local density of states of photons. In practice, there are two general methods for doing so. The simplest is to assure as much internal reflection as possible from a surface of reflecting materials. The canonical picture is two metal mirrors, bouncing light between them; for very small cavities, the mirrors are usually the interface between the semiconductor dielectric and

vacuum. One form of high-Q that relies on a single surface is a microring or microtoroid resonator, in which light is totally internally reflected along the inner surface of a round ring. These modes are known as "whispering gallery modes." A second flavor of cavity is to make a "photonic crystal" out of periodic structures of dielectric interfaces. Light waves traversing through such a crystal will constructively interfere for some directions and wavelengths, and destructively interfere for others; in general, a periodic structure will feature a photonic band structure, following the same physics as the electronic band structure of semiconductors. To make a good cavity, a defect is introduced in that periodic structure which assures constructive interference of photons which are otherwise in the bandgap of the photonic crystal. Figure 1(d) shows a one-dimensional photonic crystal, in which the periodic structure in the vertical direction are alternating layers of GaAs and AlGaAs, which have differing indices of refraction n. Such a structure is called a distributed Bragg reflector (DBR). These layers are separated by a thickness of $\lambda/4n$ for the target wavelength λ. The center of the cavity contains the "defect," a region of size $\lambda/2n$, the center of which features the strong constructive interference for the cavity modes; it is here that a quantum well or QD would be placed during growth.

While the periodicity of a large, planar DBR is strictly in one dimension, there is some confinement in transverse dimensions as well. A photon at resonant wavelength λ cannot traverse the cavity in the vertical direction, nor can it at a small angle from the vertical direction; in general, a critical angle will exist at which transverse transmission is possible. This angle depends on the refractive index change between the two materials, and it sets the effective mode volume for a large planar DBR. As the refractive indices of GaAs and AlGaAs are similar, a planar DBR has a mode volume much larger than a cubit wavelength. To reach high values of Q/V, an additional method for transverse confinement is needed. This may be provided by smooth sidewalls of a vertical post or pillar, as in the microcavity structures of Fig. 1(c). These structures can have Q values approaching 10^6 for large pillars; smaller pillars have smaller Q values as one becomes limited by losses at the sidewalls.

Higher values of Q/V are available from two-dimensional photonic crystals, usually formed by etching circular holes in slabs of semiconductor. Using the confinement of a defect in a 2D photonic cavity gives smaller mode volumes V than micropillars, while the reduced sidewall loss (in this case the two straight walls of the semiconductor slab) can give comparable values of Q.

The variety of cavities which have successfully reached the intermediate and strong coupling regimes of CQED suggests flexibility in QD CQED engineering, but I would emphasize that obtaining strong coupling still requires a substantial amount of luck in obtaining a high-quality QD located at the right location and the right wavelength of a high-Q cavity. While research efforts continue to improve the yield on good CQED devices, theoretical proposals for multi-dot schemes relying on many CQED systems in the strong coupling regime must at this time be considered highly speculative, and dependent on engineering advances in both QD and cavity fabrication.

Adiabatic Elimination

The other critical concept from quantum optics we will use repeatedly in these notes is the adiabatic elimination of exciton states. Adiabatic elimination is the basic principle by which we use short-lived, high energy optical states (the excitons) to measure or coherently control

the metastable spin ground states of a charged QD. Although there is a simple recipe for adiabatic elimination (which we describe below), the more fundamental assumptions underlying this recipe are very important to understand, since it is a common error to apply the recipe inappropriately. At its core, adiabatic elimination is an application of the adiabatic theorem of quantum mechanics.

To approach adiabatic elimination, we will consider the RWA Hamiltonian Eq. (5), but make a semiclassical approximation where quantization of the optical field plays no role. This is appropriate when controlling with a strong laser source. Hence in this section, we will use the interaction-picture Hamiltonian $e^{i\mathcal{H}_{\text{O}}t}[\mathcal{H}_{\text{rot}} - \mathcal{H}_{\text{O}}]e^{-i\mathcal{H}_{\text{O}}t}$ with $\mathcal{H}_{\text{O}} = \sum_m \omega_m a_m^\dagger a_m$ and then the substitution

$$\sum_m g_m a_m^\dagger e^{i\omega_m t} \to \frac{1}{2}\Omega(t), \tag{17}$$

where $\Omega(t)$ is treated as a classical driving field. (One may still consider adiabatic elimination with a quantized field. Doing so is important for the analysis of dispersive effects in CQED. We do not pursue this here as the approximations one must employ require more care.)

Consider a Hamiltonian with a single excited state $|\xi\rangle$, with unperturbed eigenenergy $\hbar\Delta$. (We refer to this as an energy although in our target application it is in fact a detuning in the rotating frame.) The procedure we will now describe must be slightly generalized if there are multiple excited states, but for simplicity in this section let us consider only one. At lower energy, we will still consider a set of ground states $|\phi_j\rangle$; we assume the Hamiltonian in this subspace, $\mathcal{H}_{\text{G}}$, is time-independent, traceless, and has eigenvalues much smaller than the energy of excited state $|\xi\rangle$. The assumption of being traceless means that the average unperturbed energy of the ground states is zero ($\sum_j \delta_j = 0$). This is only for notational convenience, and a total energy offset may always be introduced to assure it. The time-dependent Hamiltonian term connecting the ground states $|\phi_j\rangle$ to $|\xi\rangle$ now has the form

$$\mathcal{H}_{\text{G}\xi} = \frac{\Omega(t)}{2}\sum_j u_{j\xi}\,|\phi_j\rangle\langle\xi| + \text{H.C.}, \tag{18}$$

where H.C. is hermitian conjugate and by definition $\sum_j |u_{j\xi}|^2 = 1$.

In the case of a single QD, $\mathcal{H}_{\text{G}}$ describes the Zeeman splitting of a single spin for a magnetic field in the z direction, $\mathcal{H}_{\text{G}} = g_{\text{e}}\mu_{\text{B}}B_0 S^z$, for ground states $|\phi_j\rangle$ being the spin-up and spin-down states of the charged dot. The excited state $|\xi\rangle$ would be the lowest trion state, and the factors $u_{j\xi}$ are related to selection rules and the polarization of the driving optical pulse.

We are now ready to apply the quantum adiabatic theorem. We first find the eigenstates and eigenvalues of the instantaneous Hamiltonian at each instant of time t. In quantum optics these are sometimes referred to as "dressed states." Under the adiabatic assumption that the rate of change of these states is smaller than the lowest energy splitting, the evolution of state j is very simple; if its dressed eigenvalue is $\omega_j(t)$, it accrues a phase factor $\exp(-i\int_0^t \omega_j(\tau)d\tau)$. For the purposes of this exposition, we will make a simplifying assumption that the eigenvalues of $\mathcal{H}_{\text{G}}$ are much smaller than the pulse amplitude $|\Omega(t)|$ as well as the inverse duration of the pulse; this is not a critical part of adiabatic elimination in general, but it simplifies analytic diagonalization

and is certainly an appropriate assumption for QDs under ultrafast control. Therefore, for the moment we ignore $\mathcal{H}_{\rm G}$ and diagonalize the simple Hamiltonian

$$\mathcal{H}^{(0)} = \Delta\,|\xi\rangle\langle\xi| + \frac{\Omega(t)}{2}\sum_j u_{j\xi}\,|\phi_j\rangle\langle\xi| + \frac{\Omega^*(t)}{2}\sum_j u^*_{j\xi}\,|\xi\rangle\langle\phi_j|\,. \tag{19}$$

This Hamiltonian term has no effect outside the subspace of the two states $|\xi\rangle$ and $|Y\rangle = \sum_j u_{j\xi}\,|\phi_j\rangle$. These are dressed as

$$|Y\rangle \to \cos\frac{\Theta(t)}{2}\,|Y\rangle + e^{-i\Phi(t)}\sin\frac{\Theta}{2}\,|\xi\rangle\,, \qquad \omega_Y(t) = \frac{\Delta}{2}\left[1-\sqrt{1+\frac{\Omega^2(t)}{\Delta^2}}\right], \tag{20}$$

$$|\xi\rangle \to \cos\frac{\Theta(t)}{2}\,|X\rangle - e^{i\Phi(t)}\sin\frac{\Theta}{2}\,|Y\rangle\,, \qquad \omega_X(t) = \frac{\Delta}{2}\left[1+\sqrt{1+\frac{\Omega^2(t)}{\Delta^2}}\right], \tag{21}$$

where $\Omega(t) = |\Omega(t)|\exp[i\Phi(t)]$ and $\tan\Theta(t) = |\Omega(t)|/\Delta$. The adiabatic condition is that the overlap of the time derivative of one of these states with the other has magnitude much less than their energy difference; this explicitly requires

$$\frac{\dot\Theta^2}{4} + \sin^2\frac{\Theta}{2}\dot\Phi^2 \ll \Delta^2. \tag{22}$$

If we consider the case of simple pulses with no chirp, $\Omega(t)$ is real and $\Phi(t) = 0$, in which case this condition simplifies to

$$\left|\frac{d\Omega}{dt}\right| \ll 2[\Delta^2 + \Omega^2(t)]; \tag{23}$$

from this we obtain the result that the pulse width should be substantially longer than $\Omega/(\Omega^2 + \Delta^2)$.

Now, we will do no further manipulations of the excited state, and assert (incorrectly) that the $|Y\rangle$ state does not mix with $|\xi\rangle$ through the pulse; we track only its phase. The excited state has been "adiabatically eliminated." This procedure has two interpretations which one will find in the literature describing the protocols to be discussed in Sec. 5. One is the "AC-Stark shift", in which the presence of the optical field is considered to "shift the energy" of $|Y\rangle$. Another interpretation is that of "stimulated Raman transitions," in which transitions occur between states $|\phi_j\rangle$ due to "virtual" excitation of state $|\xi\rangle$. In either case we must not forget that during the pulse the dressed state which starts and ends as $|Y\rangle$ certainly includes the excited state. During the pulse, the population in this excited state goes instantaneously as $\sin^2\Theta(t)/2 = \Omega^2(t)/[\Delta^2 + \Omega^2(t)]$. This is critical for analyzing error. For considering the action of the gate itself, the important result from the time-integrated phase shift is that after the pulse,

$$|Y(t)\rangle = \exp\left\{-i\frac{\Delta}{2}\int_0^t d\tau\left[1-\sqrt{1+\frac{\Omega^2(\tau)}{\Delta^2}}\right]\right\}|Y(0)\rangle\,. \tag{24}$$

Under our simplifying assumption, we consider this phase shift to happen simultaneously with the much slower dynamics of $\mathcal{H}_{\rm G}$, so after "adiabatically eliminating" the mixing to the excited states, we obtain effective subspace Hamiltonian

$$\mathcal{H}_{\rm eff} = \frac{\Delta}{2}\left[1-\sqrt{1+\frac{\Omega^2(t)}{\Delta^2}}\right]|Y\rangle\langle Y| + \mathcal{H}_{\rm G}. \tag{25}$$

We now address a common "shortcut" to this result, which is very useful in many contexts but far less rigorous. The shortcut to adiabatic elimination is to begin with the Schrödinger equation, for which the $|\xi\rangle$ term is

$$\frac{d}{dt}\langle\xi|\psi(t)\rangle = -i\Delta\langle\xi|\psi(t)\rangle - i\frac{\Omega^*(t)}{2}\langle Y|\psi(t)\rangle . \tag{26}$$

From our dressed state considerations, we know that the left-hand-side of this equation has magnitude $\dot{\Theta}(t)$, while the dominant term of the right-hand-side goes as Δ. From our adiabatic condition Eq. (22), then, the magnitude of the left-hand-side is always much smaller, and therefore the two terms on the right-hand-side must nearly cancel. Therefore, our shortcut is to just assume that they do cancel, so that

$$\frac{d}{dt}\langle\xi|\psi(t)\rangle \approx 0, \qquad \Rightarrow \qquad \langle\xi|\psi(t)\rangle \approx -\frac{\Omega^*(t)}{2\Delta}\langle Y|\psi(t)\rangle . \tag{27}$$

Then, the $|Y\rangle$ component of the Schrödinger equation reads

$$\frac{d}{dt}\langle Y|\psi(t)\rangle = -i\frac{\Omega(t)}{2}\langle\xi|\psi(t)\rangle - i\langle Y|\,\mathcal{H}_{\rm G}\,|\psi(t)\rangle , \tag{28}$$

to which we include our assertion to find

$$\frac{d}{dt}\langle Y|\psi(t)\rangle \approx i\frac{\Omega^2(t)}{4\Delta}\langle Y|\psi(t)\rangle - i\langle Y|\,\mathcal{H}_{\rm G}\,|\psi(t)\rangle . \tag{29}$$

From this we may assume an effective Hamiltonian

$$\mathcal{H}_{\rm eff} \approx -\frac{\Omega^2(t)}{4\Delta}|Y\rangle\langle Y| + \mathcal{H}_{\rm G}. \tag{30}$$

As a result of this trick we have nearly ended up with Eq. (25), except we have in a subtle way introduced the assumption $\Omega(t) \ll \Delta$, and arrived at the lowest order approximation to the first term in Eq. (25). While this trick is simple to apply, it has eliminated higher order terms in $\Omega(t)/\Delta$ which may be (and, as we will see, are) physically present. We emphasize that $\Omega(t) \ll \Delta$ is *not* the adiabatic condition of Eq. (22); a strong but slow pulse may still be adiabatic while allowing $\Omega(t)$ to be on the same order as Δ.

The basic analyses of CQED and adiabatic elimination we have covered in this section are sufficient to understand most quantum information applications of optically controlled QDs. We begin with one of the simplest but most promising quantum information applications of QDs: that of sources of photons with quantum characteristics.

4 Single Photon and Entangled Photon Sources

In the previous section, I indicated that the "quantum" in "quantum dot" refers to a discretization of energy levels, and as such is not used in the same sense as "quantum information." However, discrete quantum states and the ability to isolate just one QD and collect photons from it lead to an immediate use for quantum information: the generation of single photons.

One touted application for single photons is for quantum key distribution (QKD), in which quantum information encoded on single photons allows the distribution of random numbers between two trusted parties. An intermediate eavesdropper who attempts to measure or capture those single photons will inevitably disturb them, and a well arranged protocol can therefore detect that eavesdropper and reject those random bits that may have been leaked. The resulting private shared randomness is then a valuable resource for information security. From a practical viewpoint, it is unclear whether true single photon sources make sense for QKD, since one may alternatively use attenuated classical sources (such as lasers) and achieve comparable security [16] at the gain of a much easier system to engineer. From a more fundamental viewpoint, it is notable that in simple protocols such as BB84 [17], secure shared randomness is achievable *without* using entangled photons. This hints at the notion that single photons are as powerful as entangled photons, at least in some contexts.

The following simple example shows that single photons are highly "quantum" objects, in the information sense [18]. What happens when a single photon encounters a simple 50/50 beamsplitter? If given a single photon Fock state in one input to the beamsplitter and vacuum in the other, the output is

$$|\psi\rangle = \frac{1}{\sqrt{2}}[|0\rangle|1\rangle + |1\rangle|0\rangle], \tag{31}$$

where the two kets refer to the photon number in the two output modes. This is a pure state, and if we trace over every possible photon number in one of the modes, the resulting density matrix shows a full bit of entropy in the other. Therefore, this very simple set-up has all the hallmarks of multimode entanglement, without any notion of postselection.

From where did the entanglement come from? Certainly, if a coherent state $|\alpha\rangle\,|0\rangle$ (as output from a laser) were input into the beamsplitter, the resulting output $|\alpha/2\rangle\,|\alpha/2\rangle$ would contain no entanglement at all, indicating that the beamsplitter is a kind of classical device. The single photon Fock state contains the quantumness, and a whole suite of measures (such as negativity of the Wigner function) have emerged in quantum optics to better quantify this notion. A careful consideration of optical states shows that coherent states $|\alpha\rangle$ have balanced quantum uncertainties in suitably defined conjugate quantum variables; reducing one such uncertainty substantially is known as squeezing. One pair of conjugate variables is photon number and optical phase; a Fock state is infinitely squeezed to have zero photon number uncertainty and infinite phase uncertainty. This is a very quantum object indeed.

One cannot do much with the entanglement resulting from a single photon and a beamsplitter beyond QKD, but if multiple modes of multiple indistinguishable single photons are available, one ought to be able to exploit that entanglement for quantum information applications, such as computing. This notion forms the basis of linear optics quantum computing, pioneered by Ref. [19]. This scheme may not be practical in the number of sources and single photon detectors it requires to achieve a high probability of success for reasonably large problem sizes, but it underscores the "quantumness" of single photons, and the impact practical sources of many indistinguishable single photons could have. Another evocative theoretical result exemplifying this point of view is a mathematical proof that an array of single photon states input into a linear network results in a probability distribution of output photon numbers which becomes computationally intractable for larger and larger networks; this is surprising, since laser sources of many photons input into that same network result in an easily calculable result [20].

From all this, we conclude that indistinguishable single photon sources are very valuable for quantum information, and with their solid-state platfrom, QDs seem like they might provide very practical implementations of such sources.

Generation of single photons and quantum interference

We begin with a discussion of what a real "single-photon sources" really are. There are three important aspects: first, the ratio of probabilities of numbers of photons from pulse to pulse (i.e. Poissonian vs. sub-Poissoinan); second, the probability that a single photon emerges when desired, rather than the vacuum (i.e. the efficiency); and third, whether multiple single photons from the same device or different devices are indistinguishable.

The defining characteristic of a single-photon source is that its output is sub-Poissonian. To clarify what this means, let us first consider classical sources of light, such as a light-bulb or a laser. A light-bulb emits thermal light, meaning that in a given pulse, the photon number is described by the probability distribution

$$\langle n|\,\rho_{\text{thermal}}\,|n\rangle = \frac{\langle n\rangle^n}{[1+\langle n\rangle]^{1+n}}. \tag{32}$$

A laser emits coherent light, which has photon number distribution

$$\langle n|\,\rho_{\text{coherent}}\,|n\rangle = \frac{1}{n!}e^{-\langle n\rangle}\langle n\rangle^n. \tag{33}$$

In either case, you can reduce the *average* photon number $\langle n\rangle$ to one or fewer photons simply via attenuation, but suppose you want the probability of one photon divided by the probability of no photons, the efficiency, to be reasonably large. For both coherent and thermal light, the unfortunate consequence is that the probability of two photons divided by the probability of one photon will be just as large, i.e.

$$\frac{\langle 2|\,\rho\,|2\rangle}{\langle 1|\,\rho\,|1\rangle} \propto \frac{\langle 1|\,\rho\,|1\rangle}{\langle 0|\,\rho\,|0\rangle}, \tag{34}$$

where the constant of proportionality is unity for thermal states and 2 for coherent states. Classical light shows Poisson statistics, meaning that photons are just as likely to arrive "clumped" as not "clumped."

Generally, the way to quantify the statistics of an optical source sending photons into a mode annihilated by $a_m(t)$ is via coherence functions. The simplest of these is the first-order coherence function

$$g_m^{(1)}(t,\tau) = \frac{\langle a_m^\dagger(t+\tau)a_m(t)\rangle}{\langle a_m^\dagger(t+\tau)a_m(t)\rangle}. \tag{35}$$

This function[2] is an amplitude autocorrelation; it is the result of interfering an optical beam with itself after some delay τ and looking at the resulting interference fringes. These generally

[2]Unfortunately, the letter g is overused by tradition in this research field and these notes, referring to atom-light coupling, a factor in a spin's magnetic moment, and coherence functions; applying the proper meaning requires context!

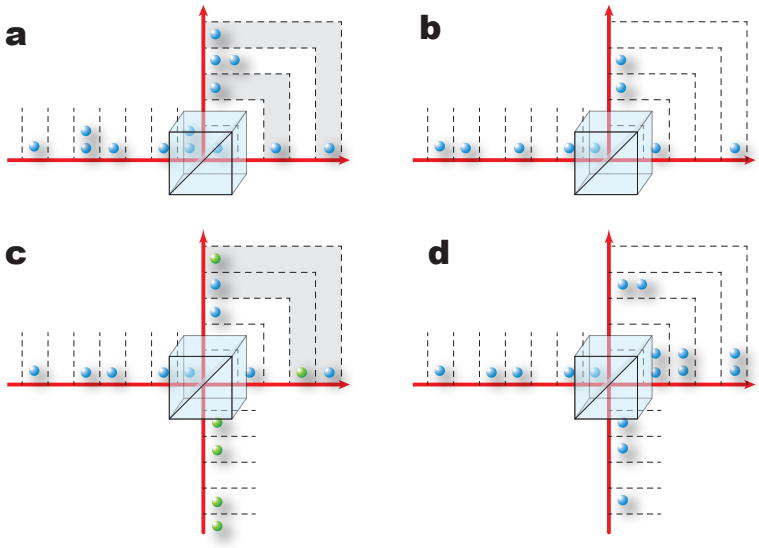

Fig. 3: *Measuring second order coherence. Dots represent photon numbers as deduced after photon counting at the output ports of the beamsplitters; coincidence counts are colored in grey. (a) Hanbury Brown-Twiss (HBT) experiment for classical (coherent) light; multiphoton pulses allow coincidences. (b) HBT for single-photon source; photons emerge randomly in the two output modes, but never simultaneously. (c) Hong-Ou-Mandel (HOM) experiment for distinguishable (blue and green) single photons; coincidences of the distinguishable photons sometimes occur. (d) HOM experiment for indistinguishable single photons; photons bunch into pairs which emerge in random modes, without detection coincidences.*

decay with some coherence time or length. Single photon sources are primarily characterized by the second order coherence function

$$g^{(2)}_{mr}(t;\tau) = \frac{\langle a^\dagger_m(t) a^\dagger_r(t+\tau) a_r(t+\tau) a_m(t)\rangle}{\langle a^\dagger_m(t) a_m(t)\rangle \langle a^\dagger_r(t+\tau) a_r(t+\tau)\rangle}, \tag{36}$$

which is an intensity-intensity correlation. Single photon sources are primarily characterized by intensity-intensity autocorrelations in a single mode, say mode 1. One approaches $g^{(0)}_{11}(t,\tau)$ by putting mode 1 into a 50-50 beamsplitter, as shown in Fig. 3(a) and (b). Label the beamsplitter output modes 3 and 4. One then integrates for a time T the photon counts from modes 3 and 4 and counts how many coincidences at time delay τ occur. After normalizing for the input flux, this technically gives the correlation $\int_0^T g^{(2)}_{34}(t,\tau)dt$, but under reasonable assumptions this may be taken to be the autocorrelation $g^{(0)}_{11}(t,\tau)$. This is known as the Hanbury Brown-Twiss experiment (HBT). Of particular relevance is this measured quantity at zero-delay ($\tau = 0$); we abbreviate this fairly detailed description by $g^{(2)}(0)$. Under certain assumptions of stationarity,

$$g^{(2)}(0) = \frac{\langle n(n-1)\rangle}{\langle n\rangle^2}, \tag{37}$$

which may easily be seen to be equal to 2 for thermal light and 1 for coherent light. (Coherent light gives $g^{(2)}(\tau) = 1$ at all τ, whereas thermal light decays from $g^{(2)}(0) = 2$ to $g^{(2)}(\tau) = 1$ for τ larger than a correlation time). A sub-Poissonian source has $g^{(2)}(0) < 1$ and a perfect single-photon source has $g^{(2)}(0) = 0$.

Another important second-order coherence function is the one measured when putting a single photon into each of two inputs in a beamsplitter, as shown in Fig. 3(c) and (d). The outputs for a balanced beamsplitter are $a_3 = (a_1 + a_2)/\sqrt{2}$, $a_4 = (a_2 - a_1)/\sqrt{2}$. The resulting second-order coherence function is

$$g^{(2)}_{34}(t;\tau) = \frac{1}{4}[2 - 2I(t;\tau) + g^{(2)}_{11}(t;\tau) + g^{(2)}_{22}(t;\tau)], \tag{38}$$

where $I(t;\tau)$ is an indistinguishability function, involving both the wave-function overlap of the two photons on the beamsplitter and products of their first-order coherence functions $g^{(1)}_1(t;\tau)$ and $g^{(1)}_2(t;\tau)$. In the case of perfect single photon sources [$g^{(2)}_{mm} = 0$] and perfect indistinguishability [$I(0) = 1$], this function also vanishes at $\tau = 0$. However, due to the finite coherence between the two photons, it does not vanish at $\tau \neq 0$; in practice it shows a dip as a function of τ called the Hong-Ou-Mandel (HOM) dip.

An excellent recent summary on the progress of single photon sources appears in Ref. [21], which cites the history of measurements of single-photon sources using HBT to quantify $g^{(2)}(t;0)$ dating back to the 1970s. Solid-state sources of single photons began with isolated single molecules in the early 90s, and generation of single photons from a patterned quantum well was demonstrated in 1999 [22]. Self-assembled QDs began seeing use as single photon sources in 2000 [23, 24, 25].

These early results, however, did not test indistinguishability, which is critical for quantum information applications. A good source of indistinguishable single photons should be spectrally stable and exhibit low dephasing, meaning that the temporal characteristics of each emitted photon should be limited by the underlying process of spontaneous emission rather than additional dephasing mechanisms. Such photons are called Fourier-transform-limited, since their pulse width is given by the Fourier transform of their spectral width. A bare QD, or other solid-state sources such as single molecules or nitrogen-vacancy centers in diamond, are rarely transform-limited, because noise processes in the solid-state host cause fluctuations in the phase during the excitation/emission process. Slow spectral diffusion problems are a major challenge for indistinguishability, limiting the utility of high temperature sources. Dipole dephasing can also present a problem, even at low temperature; dipole dephasing is caused by any process which couples to the optical dipole, including thermal phonon processes and charge fluctuations. The noise sources can be outraced, however, by finding sources with fast spontaneous emission rates. In general, $I(0)$ is reduced by the factor $\Gamma/(\Gamma + T_2^{-1})$, where Γ is the spontaneous emission rate and T_2^{-1} is a dipole dephasing rate. The simplest way to overcome dipole dephasing is to shorten the spontaneous emission time Γ^{-1}, and as indicated in Sec. 3 one way to do this is to integrate the QD into a microcavity with a high value of Q/V. Then the Purcell-enhanced emission can overcome dipole dephasing and result in Fourier-limited pulses. The cavity has a second benefit of improving the directionality of the emitted photons, improving collection efficiency. Measured indistinguishability can also be reduced by timing jitter, which generally results from the random pumping processes of the QDs and is improved by resonant pumping techniques. Indistinguishability is also reduced by mode mismatch; this can almost always be reduced by spatial filtering at the cost of efficiency.

A single photon source based on an InGaAs QD embedded in a post-microcavity was demonstrated in 2002 [26]. In this system, the spontaneous emission lifetime was Purcell-enhanced to values on the order of 100s of ps, which is short compared to the dipole dephasing time of

$\sim$1 ns. The second-order coherence function $g^{(2)}(0)$ was less than 0.1 in these early devices, confirming a single QD emitter existed inside the cavity. The indistinguishability was measured by the HOM experiment, showing indistinguishability values $I(0)$ on the order of 70%. Many similar demonstrations have occurred since.

The HOM experiment can be easily converted into an experiment generating and testing polarization entanglement. The basic principle is simple: the HOM dip occurs because two identical photons will bunch at a beamsplitter and go to a single detector. If the two modes are of opposing polarization, sometimes they will bunch and sometimes they will not. If a coincidence detection is recorded, then we have post selected the impossibility of the same polarization. If we notate polarization by $|V\rangle$ and $|H\rangle$ for vertical and horizontal, we can easily create the unentangled two-photon state $(|VV\rangle + |VH\rangle + |HV\rangle + |HH\rangle)/4$ using linear optics. Sending this state into the two arms of the HOM set-up and post-selecting coincidences tells us only that the final state was *not* $|VV\rangle$ or $|HH\rangle$; the measurement will therefore project out the entangled state $(|VH\rangle + |HV\rangle)/\sqrt{2}$ with probability 1/2. Variations on this concept allow the detection of violation of Bell inequalities [27], quantum teleportation [28], and basic photonic quantum logic gates [29].

The problem with the experiments described above, however, is that they use a single QD to generate all of the photons, and the efficiency of the source is limited primarily by the collection efficiency of the cryogenic optical microscope. Reasonably sized networks for quantum computing would scale poorly using a single source; multiple indistinguishable sources are ultimately necessary. This is extremely challenging for QDs because of their high inhomogeneity. With a little bit of luck in finding spectrally similar dots, one may then remove any remaining spectral and spatial mismatch using tuning techniques such as DC or AC Stark shifts, magnetic field, or temperature, and some degree of spatial filtering. This was recently accomplished for both self-assembled QDs [30, 31] and impurity complexes in ZnSe [32]. Another possibility to compensate for inhomogeneity is to use nonlinear optics to tune photons into resonance after they have been emitted from different dots; the ability to demonstrate indistinguishability in HOM experiments this way was recently demonstrated in Ref. [33].

Entangled photon sources

The biexciton decay of a QD seems in principle to be able to generate entangled photons [34]. The two upper XX^0 decay channels shown in Fig. 2 have opposite polarizations; for an asymmetric QD in zero magnetic field these are vertical (V) and horizontal (H) with respect to some strain or shape asymmetry axis. The two lower X^0 decay channels are then also V and H. As indicated in the figure, however, these are not exactly degenerate. Suppose they are split by fine structure splitting $\hbar\omega_{\rm fss}$. If one analyzes the state of two output photons, using the Wigner-Weisskopf rules to collapse integrals over coupling constants, and integrates over the frequencies of all output photons (corresponding to using detectors that are insensitive to small changes in photon frequency), one obtains a polarization density matrix of the form

$$\rho = \frac{1}{2}[|HH\rangle\langle HH| + |VV\rangle\langle VV| + \frac{1}{1+i\omega_{\rm fss}/\Gamma_X}\,|HH\rangle\langle VV| + \frac{1}{1-i\omega_{\rm fss}/\Gamma_X}\,|VV\rangle\langle HH|\,, \quad (39)$$

where Γ_X is the single exciton decay rate. If $\omega_{\rm fss} = 0$, this is a fully polarization entangled Bell state in two photons, the first of which has frequency corresponding to the XX^0 transition

and the second corresponding to the X^0 transition. The slightly different frequencies of these photons allows one to spectrally separate them for tomography to verify entanglement.

Unfortunately, most QDs have $\omega_{\text{fss}} > \Gamma_X$, which results in a mixed state showing only classical correlation between the H and V polarizations. In order to assure entanglement, one must somehow tune away the fine structure splitting.

Active removal of the fine structure splitting may be done in several ways. One may introduce strain [35] to counter the built-in strain, or one may compete against the strain using magnetic Zeeman splitting [36]. One may also compete against built in strain using DC [37] or AC [38] Stark shifts. Unfortunately, the built-in dot asymmetry is in a random direction for typical self-assembled dots, and the engineering of these tuning methods to compensate for both a particular value and a particular direction of strain still requires a bit of luck. Recently, efforts have been made to combine tuning methods in multiple directions [39], in this case using a combination of piezoelectric strain tuning and electric field tuning.

To conclude this section, single QDs have performed admirably as sources of single and entangled photons, and if they can be engineered to form large arrays of efficient and homogeneous sources, they can be combined with linear optics and photon counters to enable truly useful quantum information applications. However, large and efficient arrays have not yet been engineered; only single or few-dot demonstrations have been performed, and the difference is significant since QDs are randomly grown. As fabrication technologies improve, linear optical quantum information technologies may be enabled by QDs. In the remainder of these notes, however, we will consider schemes in which the dots are themselves qubits, and will consider their use as sources not of independent photons, but of photons entangled to the quantum states of the constituent spin qubits for purposes of measurement or dot-to-dot entanglement.

5 Spin Preparation, Measurement, and Control

As discussed in Sec. 2, QDs may be grown to include a single charge, whose spin states provide the qubit. To use this spin as a qubit, we should be able to initialize it, coherently control it, and measure it. Self-assembled QDs enable all of these processes to be done optically.

Initialization and Photon Counting Measurement

Preparation can be performed via optical pumping. Figure 4(a) shows the photoluminescence spectrum of a single InGaAs dot. The outer two peaks are vertically polarized, while the middle two peaks, overlapping in this figure, are horizontally polarized. Optical pumping is performed using a narrowband laser tuned at the lowest energy transition. In Voigt geometry, the lowest energy trion state decays at total rate Γ equally into both spin ground states, but pumping depopulates $|\downarrow\rangle$ resulting in a high net population of $|\uparrow\rangle$. The trion states are shown featuring an orange hole pointing sideways, as the heavy-holes are primarily quantized along a strain direction, while the electron spins are quantized along the magnetic field direction, and these are orthogonal in the Voigt geometry.

Optical pumping is best described via a rate equation, as transitions of populations are dominated ultimately by incoherent spontaneous emission processes. The resulting equation in the

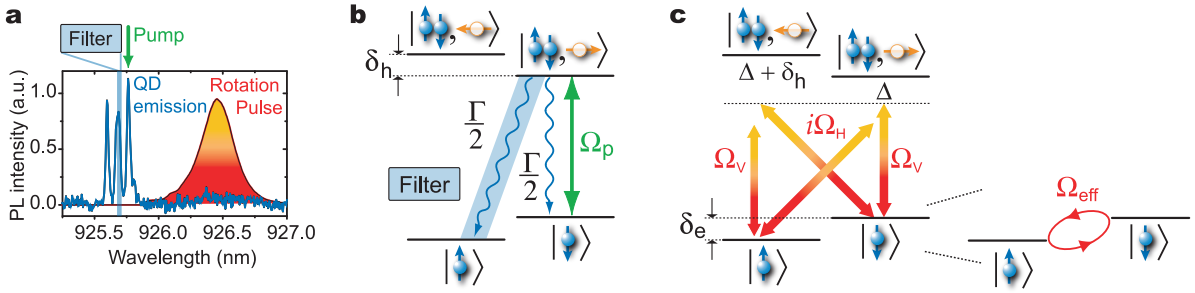

Fig. 4: *Optical control of a single spin. (a) Photoluminescence spectrum of single QD in 4T magnetic field in Voigt geometry, showing the four X^- peaks of a single QD. Coherent rotations are performed using ultrafast pulses, whose approximate spectra are shown as the red and yellow curve. (b) Energy level diagram showing spin preparation and measurement in Voigt geometry. The green arrow shows the lowest energy transition, upon which optical pumping is performed. (c) Energy level diagram showing ultrafast control.*

qubit subspace follows a standard Bloch equation for the spin operator **S** of the spin-qubit,

$$\frac{d}{dt}\langle S^z\rangle = -\beta(\lambda)[\langle S^z\rangle - S^z_{\rm p}], \tag{40}$$

where $S^z_{\rm p}$ is a final equilibrium population. In this equation $\beta(\lambda)$ is a pumping rate which depends on the pumping wavelength λ. On resonance, this rate has been measured to be on the order of ns^{-1} for a typical InGaAs dot and reasonable focused laser power [40].

The process of optical pumping may be performed in other geometries [41], and its ultimate performance is limited by either nuclear spin effects (to be discussed in Sec. 6), hole mixing phenomena, or power broadening effects [42]. Because it is a resonant technique, one cannot pump too quickly, as fast processes have reduced spectral selectivity. Nonetheless, initialization fidelities in excess of 99.9% with pumping times on the order of 10 ns are possible using this technique.

This preparation method also provides a means for measurement. Measurement may be performed using photon counting on the middle peaks. Referring to Fig. 4, if the electron begins in state $|\uparrow\rangle$, and the optical field (of narrow bandwidth and finite power) $\Omega_{\rm p}$ is introduced, no populations will change and no spontaneously emitted photons will result. In contrast, if the electron spin begins in state $|\downarrow\rangle$, the introduction of the optical pumping field $\Omega_{\rm p}$ will eventually result in a photon resulting from decay into the $|\uparrow\rangle$ state. Although this photon may not be collected and detected due to the finite collection and detection efficiencies of a real experiment, in a large ensemble of experiments the average photon count from this transition will reveal the probability of having begun in state $|\downarrow\rangle$, and most of the results presented in what follows will use this form of time-ensemble measurement.

This form of measurement is not sufficient for quantum computing, however. The fact that its ultimate efficiency in a single shot is small ($<$1%) means that its result would not be reliable for quantum error correction (QEC). Further, it is a destructive measurement; after a single shot, the spin has certainly (up to the initialization fidelity) been placed in state $|\uparrow\rangle$ regardless of where it started. This means one may not immediately measure the state a second time to

improve the result; one must instead repeat the state preparation prior to another trial, an acceptable procedure for single qubit experiments but an untenable procedure for sizeable quantum algorithms. More promising measurement techniques are non-destructive; these are termed quantum non-demolition (QND) measurements. A single measurement may not fully resolve the spin population (a measurement that does so is called "single-shot"), but it at least preserves it. Of course it does not preserve the quantum state; a measurement will inevitably decohere superpositions. At the end of this section, after further discussing spin-dependent phase shifts, we will return to means for optical QND measurements in single QDs, and then extend them to schemes for entanglement in Sec. 7.

Coherent Control

As mentioned in Sec. 3, optical control of a spin in a QD is achieved by optically controlling the trion states, and relying on selection rules and adiabatic elimination. One method to do this is traditional stimulated adiabatic rapid passage (STIRAP) using multiple narrow-band lasers on the trion transitions. This is very similar to the use of such transitions in trapped ion experiments, although consideration of the particular selection rules in QDs must be made. A thorough analysis appears in Ref. [43]. A possibility also under exploration in trapped ions but with particular convenience for QDs, which we will focus on here, is the use of single ultrafast (typically few psec) pulses to achieve effectively the same results as STIRAP tenchiques.

The understanding of ultrafast optical spin control relies on the adiabatic elimination procedure detailed in Sec. 3. The particular level structure of importance is shown in Fig. 4(c), where the trion states in Voigt geometry are optically connected to the ground states with both horizontal and vertical polarizations. Circularly polarized, broadband, detuned optical pulses, whose typical spectra are shown relative to the trion resonances in Fig. 4(a), in principle cause all four trion transitions with nearly equal amplitude, but upon adiabatic elimination the net effect is a rotation of the spin ground states at angular frequency Ω_{eff}. In particular, following the notation of Sec. 3, circularly polarized optical pulses dress a ground state close to the equal superposition

$$|Y\rangle = \frac{1}{\sqrt{2}}[|\uparrow\rangle + |\downarrow\rangle], \tag{41}$$

and the ground state spins simultaneously precess in a magnetic field B in the z-direction. The resulting effective Hamiltonian after adiabatic elimination and ignoring identity components then follows from Eq. (25) as

$$\mathcal{H}_{\text{eff}} = \frac{\Delta}{2}\left[1 - \sqrt{1 + \frac{\Omega^2(t)}{\Delta^2}}\right] S^x - g_{\text{e}}\mu_{\text{B}} B S^z. \tag{42}$$

This simple Hamiltonian results in the Bloch sphere trajectories shown in Ref. [40].

It is remarkable that a picosecond or even femtosecond pulse can result in an adiabatic process. As derived in Sec. 3, the adiabatic condition is that the pulse width must be longer than $\Omega/(\Omega^2 + \Delta^2)$, where Δ is the detuning and Ω is trion Rabi frequency. This can be quite short for $\Delta \gg \Omega$. The only real limit to how large Δ can be comes from the RWA, which required $\hbar\Delta$ to be much smaller than the optical energy of order about one eV. (Of course, one would also encounter difficulties if the pulse overlapped other resonances.) In practice, the qubit rotation frequency is roughly Ω^2/Δ. Therefore, if a π pulse is desired and the pulse width is τ, then roughly

$\Delta = \Omega^2\tau/\pi$, and hence our adiabatic condition is roughly $(\Omega\tau)^2 \gg 1$. Unless we encounter some limit in Δ, we can operate adiabatically and still operate quickly as long as we can have large enough values of Ω. Here QDs show two advantages over AMO systems, each relating to the two factors which contribute to Ω. First, QD wavelengths are typically in the middle range of a tunable Ti:Sapphire solid-state modelocked laser, from which substantial optical power is available from routine commercial systems. Second, the mesoscopic enhancement described in Sec. 3 results in a high oscillator strength. In QDs, Ω can easily exceed THz, and there is no problem for adiabatic operation with a τ of a few picoseconds. This regime is possible but more challenging in AMO systems, typically requiring much stronger laser power.

The adiabatic elimination procedure which allows spin control are usually described using one of two equivalent points of view. One point of view, described in Refs. [44, 40] and elsewhere, is that the pulses work via stimulated Raman transitions. Physically, a train of pulses from a modelocked laser may be considered to have a comb of frequencies; two peaks of such a comb can provide the two excitations of a Raman transition. The train of pulses (in the time domain) which leads to the frequency comb (in the frequency domain) will, if their timing is tuned to the Larmor period of the single electron spin, always rotate the electron spin with the same phase, constructively achieving a rotation. If the pulse power or oscillator strength is high enough, substantial rotations can occur with just a single pulse, and the relative timing between just a pair of pulses can achieve complete qubit control.

Another point of view for ultrafast coherent control is that it results from an AC-stark shift, indicated in Ref. [45] and elsewhere. For this picture, we note that the pulse length is much shorter than the Larmor precession period. On this timescale, the electron ground state is effectively degenerate, and as a result there exists an optically dark ground state (for example, $|\uparrow\rangle - |\downarrow\rangle$, neglecting normalization), and an orthogonal optically bright state (for example, $|\uparrow\rangle + |\downarrow\rangle$). The details of these states will depend on the selection rules of the dot, which in turn depends on details of the dot's symmetry. In this point of view, the arrival of the pulse "slowly" mixes the bright state and the excited state to which it is optically connected. This mixing shifts the eigenvalues, providing the AC-stark shift of the bright state. A spin beginning in a superposition of bright and dark states will therefore see its bright state component shifted relative to the dark state, thereby accomplishing a spin rotation.

In either picture, multiple-pulse control requires pulses to arrive timed to the spin precession frequency of the spin qubit. In general, quantum control of a non-degenerate qubit requires some clock which tracks phase evolution of the two qubit states. In the case of controlling single spins in the QD, the relevant clock synchronization occurs between the spin Larmor precession, set by the spin's g-factor and the size of the applied magnetic field, and the pulse generation rate of a modelocked laser, set by the laser's effective cavity length. Beautiful demonstrations of these synchronization effects are visible when shining ultrafast pulse trains on large ensembles of QDs, which have very inhomogeneous g-factors. A subensemble of those dots will become spin-locked to the pulse arrival rate of the modelocked laser, and spin coherences from this spectral selection may be observed [46, 47, 48].

Ultrafast optical control of single QD spins was demonstrated in 2007 [40, 45]. In these experiments, circularly-polarized pulses with durations ranging from 4 to 40 ps and detuned by ~ 150 GHz below the exciton transitions were used. Example Rabi oscillations from these first experiments are shown in Fig. 5; later experiments had much improved Rabi oscillations, as

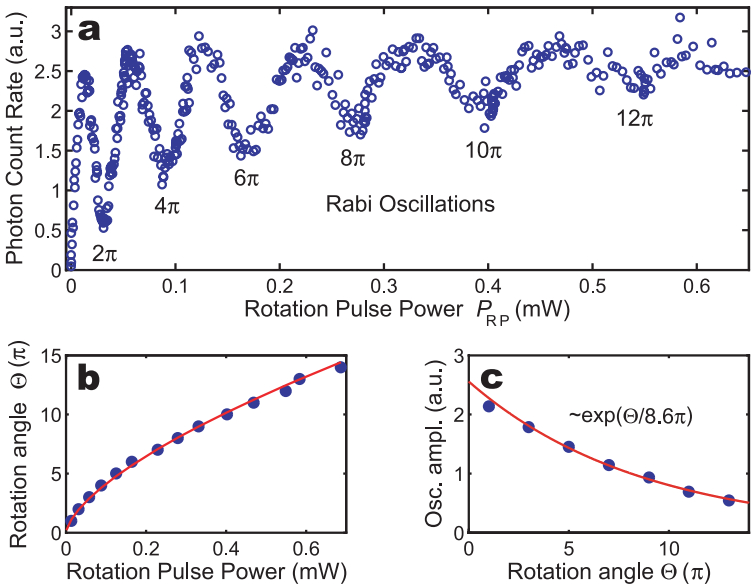

Fig. 5: *Rabi oscillations in a single QD, as reported in Ref. [40]. (a) As optical power, which is proportional to* $\int dt\Omega(t)^2$*, is increased, more oscillations occur in a pulse interval of finite duration, following Eq. (42). (b) The dependence of oscillation frequency on power follows the non-perturbative formula of Eq. (25), rather than the approximation of Eq. (30). (c) The decay rate of the Rabi oscillation is proportional to the angle* Θ*, indicating it is related to trion dephasing.*

seen for example in Ref. [49]. Although not stated in Ref. [40], the nonlinear dependence of the Rabi rotation angle θ with pulse power is well described by the time-integral of Eq. (24), as seen in Fig. 5(b). Similar behavior is observed in other ultrafast QD spin control experiments as well [50], all indicating that the adiabatic elimination picture well supports the underlying physics of the process.

One aspect of these ultrafast control results remains unclear, however. As the optical power $P = \int dt\Omega^2(t)$ is increased, the Rabi oscillations between states $|\uparrow\rangle$ and $|\downarrow\rangle$ predicted by Eq. (42) are damped in a way which Eq. (42) is certainly insufficient to explain. As seen in Fig. 5(c) the rate of damping is not constant, but is rather proportional to P, almost certainly because damping occurs proportional to the real trion population which we have omitted from Eq. (42) during adiabatic elimination. Indeed, a full consideration of the theory indicates that trion relaxation due to spontaneous emission or dipole dephasing must eventually damp Rabi oscillations. However, the magnitude of Rabi oscillation damping observed in real experiments is much larger than the predicted result from independently measured spontaneous emission or dipole dephasing rates. Another process drives this damping, with some evidence pointing to thermal effects. This source should be better understood, as it limits single-qubit rotation infidelities to a few percent in most experiments, which is insufficient for fault tolerant quantum computing.

Optical pulse sequences more sophisticated than the single or double pulses used in [40, 45] are available using electro-optic modulators (EOMs) to time-control the optical initialization pulses and the ultrafast pulses. Figure 6 shows three sample sequences which have been employed to study single QDs. Obviously, quantum algorithms might some day employ pulse sequences far

more complicated than these. The examples of Fig. 6 are primarily to explore decoherence, whose primary source is nuclei. As nuclear spin dynamics can be quite complicated, we defer this discussion to Sec. 6 where a phenomenological model for nuclear polarization is introduced.

QND Measurement

The ultrafast control described above used a strong laser pulse, modeled with semiclassical amplitude $\Omega(t)$, to induce a phase shift on the qubit. It is natural to ask whether the qubit also imparts a phase shift on the classical field. If we return to a fully quantized view of the laser field, treat it as a single mode annihilated by a, use the $\Omega(t) \ll \Delta$ approximation, and ignore $\mathcal{H}_{\rm G}$, we can rewrite Eq. (30) as

$$\mathcal{H}_{\rm eff} \approx -\frac{g^2}{\Delta} a^\dagger a \left|Y\right\rangle\!\left\langle Y\right| . \tag{43}$$

Let us suppose our spin is in a superposition of state $|Y\rangle$ and some orthogonal state, say $|X\rangle$, and our single mode is populated by a coherent state $|\alpha\rangle$. Then the action of this Hamiltonian after duration τ is actually to entangle the spin to the phase of the coherent state:

$$\left[c_Y \left|Y\right\rangle + c_X \left|X\right\rangle\right] \otimes \left|\alpha\right\rangle \rightarrow c_Y \left|Y\right\rangle \otimes \left|\alpha e^{-ig^2\tau/\Delta}\right\rangle + c_X \left|X\right\rangle \otimes \left|\alpha\right\rangle . \tag{44}$$

In the semiclassical picture, state $|Y\rangle$ has received the phase shift $|\alpha|^2 g^2\tau/\Delta$ which is very large for high average photon number $|\alpha|^2 = \langle a^\dagger a\rangle$ and as we saw above, can lead to phase shifts of many π. But Eq. (44) suggests that the optical field has also received a spin-dependent phase shift of magnitude $g^2\tau/\Delta$, which is much smaller by assumption. The amount of entanglement can be quantified by tracing over the optical field and seeing by what factor coherences of the single spin are damped. Doing so shows that they are damped by the factor

$$\left|\left\langle \alpha e^{-ig^2\tau/\Delta} \middle| \alpha \right\rangle\right| = e^{-|\alpha|^2 |1-\exp(-ig^2\tau/\Delta)|/2} = e^{-2|\alpha|^2 \sin^2(g^2\tau/2\Delta)} \approx e^{-|\alpha|^2 g^4 \tau^2/2\Delta^2} . \tag{45}$$

This factor is very nearly unity in the ultrafast control experiments indicating small phase information (and subsequent decoherence) carried away by the photons. If we want to use this entanglement to measure the spin in a non-destructive way, we would like this factor to be very small. This means using smaller detunings and maximizing τ.

One may increase the effective interaction time by using a high-Q cavity, in which case the light may be regarded to traverse the cavity Q times before leaking out, and the interaction time is essentially κ^{-1}. The detuning Δ should be made small to maximize g^2/Δ, but not so small that spontaneous emission becomes important, so Δ should detune by at least the lifetime broadened width of the QD resonance given by the spontaneous decay rate γ. If Δ is set to γ and τ is set to κ^{-1}, we see that the available spin-dependent phase shift scales as $g^2/(\gamma\kappa)$. We encountered this ratio before in Sec. 3; it is the cooperativity factor of the cavity, which scales as Q/V. Evidently, this is the figure of merit for dispersive phase shifts; more rigorous analyses than this simple one confirm this notion.

Practically speaking, the simplest means for measuring this spin-dependent phase shift in the Voigt geometry is to measure relative phase shifts between horizontally and vertically polarized light. If a cavity is to be employed, it should then support both horizontal and vertical polarizations; the DBR cavities such as those shown in Fig. 1 do support linear polarization. Then,

if the optical field is nearly resonant with the horizontally polarized, lowest energy trion transition shown in Fig. 4, then a spin down electron will lag the horizontal component of the light more than the vertical. A polarization rotation will be observed of approximate angle $g^2\tau/\Delta$. The basic principle of the measurement in single QDs was demonstrated without a cavity in Refs. [51, 52], and the phase shift of a cavity field induced by a single neutral QD was measured for a 2D photonic crystal in Ref. [53] and for DBR micropillars in Ref. [54]. Very recently a charged QD containing a spin qubit under coherent control has been coupled to a high Q/V 2D photonic crystal cavity [55], but full, cavity-enhanced single-shot QND measurement of a single QD still has not yet been fully demonstrated.

A nondestructive measurement of a QD state is also possible via "shelving transitions," as performed with trapped ions, if the energy level structure is more complicated than that of a single electron and trion. This has been demonstrated in multiple exchange-coupled QDs [56] and in magnetic impurities trapped in QDs [57].

6 Nuclear Spins

Most of the basic, quantum-information-related concepts of the previous three sections originated with atoms rather than QDs. A defining characteristic of an atom, however, is that it contains one and only one nucleus, and by extension one and only one nuclear spin. In contrast, a typical QD contains about 10^5 nuclei, and if the QD is made using III-V semiconductors, each nucleus has non-zero spin, all of which couple in some way to the electronic or excitonic states. An immediate manifestation of this nuclear spin ensemble is dephasing and decoherence of electron spin qubits. The random nuclear configuration leads to random phase shifts which dephase ensemble experiments with characteristic timescale T_2^* of a few nanoseconds. While such randomness can be compensated for by various techniques, the total nuclear spin also diffuses on a slow timescale, resulting in decoherence times of a few microseconds.

The need to compensate for the drift of random nuclear fields can therefore be viewed as an obstacle. However, recent experimental discoveries suggest that the nuclei instead can be used as another tuning knob for a nuclei. This suggestion is supported by nuclear feedback phenomena observed in electrically controlled double QDs, discussed elsewhere in these lecture notes [58, 59, 60]. In single QDs under microwave control, nuclear effects dynamically tune the electron spin resonance to the applied microwave frequency [61]. Tuning effects are also observed in two-color continuous-wave (CW) laser experiments in self-assembled QDs, in which the appearance of coherent electronic effects such as population trapping are modified by nonlinear feedback processes with nuclear spins [62, 63]. Nuclear spins have been shown to dynamically bring ensembles of inhomogeneous QDs into spin-resonance with a train of ultrafast pulses [47, 48], and similar nuclear feedback phenomena have also been observed for a single self-assembled QD under pulsed ultrafast control[64].

In single quantum dots, nuclear feedback occurs when the Larmor frequency of the electron spin in a QD is dynamically altered by the hyperfine interaction with QD nuclei, and the nuclear polarization is in turn altered by the measurement results of pulsed experiments. This phenomenon is one of a large number of nuclear effects which have been observed in the optical manipulation of QDs, but we focus on a mathematical description of this feedback process as it provides an excellent opportunity for intuitive modeling of nuclear dynamics in general.

Physical Processes Driving Nuclear Polarization

We begin by describing the physical interactions between the nuclei and the electron and hole spins in the QD. The largest magnitude hyperfine interaction in a QD is the Fermi contact hyperfine interaction,

$$\mathcal{H}_{\text{chf}} = \sum_n A_n \mathbf{S} \cdot \mathbf{I}_n, \tag{46}$$

where $\mathbf{S}$ is the spin operator for the electron ($S = 1/2$) and $\mathbf{I}$ is the spin operator for the nth nucleus ($I = 3/2$ for all isotopes in GaAs, and $I = 9/2$ for the two isotopes of In.) Here the coupling constant A_n varies across the dot and by isotope; the sum $A = \sum_n A_n$ is on the order of 100 μeV. The portion of this Hamiltonian proportional to S^z is the dominant source of hyperfine shifts in a QD. We denote this shift for some particular nuclear configuration as $\Omega = \sum_n A_n I_n^z/\hbar$, and refer to it as the Overhauser shift.[3]
The Overhauser shift is the only important hyperfine interaction with the ground state electron, as all other terms are suppressed by symmetry or by an energy barrier. The terms of Eq. (46) proportional to S^x and S^y are suppressed in a large magnetic field by the electron Zeeman energy $g_{\text{e}}\mu_{\text{B}}B$. One may estimate the probability of a contact-hyperfine-induced spin flip during a trion emission as $|A_n/g_{\text{e}}\mu_{\text{B}}|^2$, with the electron Zeeman energy compensated for in a slight shift of the energy of the emitted photon. The Zeeman energy is on the order of 30 GHz $\times\, h$, putting this probability at roughly 10^{-8} to 10^{-9} per nucleus, or with a timescale of about 100 ms to 1 sec.

The QD ground state also features the electron-nuclear dipole-dipole interaction,

$$\mathcal{H}_{\text{e-n}} = \sum_n \frac{\mu_0}{4\pi}\hbar\gamma_n g_{\text{e}}\mu_{\text{B}} \left\langle \frac{3(\mathbf{r}_n \cdot \mathbf{S})(\mathbf{r}_n \cdot \mathbf{I}_n) - r_n^2(\mathbf{S} \cdot \mathbf{I}_n)}{r_n^5} \right\rangle, \tag{47}$$

where $\mathbf{r}_n = \mathbf{r} - \mathbf{R}_n$ for (assumed fixed) nth nuclear position $\mathbf{R}_n$ and the brackets $\langle\cdot\rangle$ now refer to an average over the electron wavefunction. This varies from the contact hyperfine term due to terms like the $S^z I^x$ term, for example, which allow nuclear spin flips with a smaller energy barrier. However, this term involves an integral of the form

$$\left\langle \frac{\sin 2\theta \cos\phi}{r^3} \right\rangle, \tag{48}$$

which vanishes for a pure hydrogenic s-shell wavefunction and nearly vanishes for a GaAs conduction electron.

Nuclear spin-flips due to the dipole-dipole interaction are more important for the heavy hole of a trion. The strain-split p-like configuration of the valence holes allows averages like Eq. (48) to survive. The average of $1/r^3$, where r is the distance from a nucleus to a hole, is a nontrivial number to calculate from first principles, especially in the presence of strain. For a back-of-the-envelope estimate, $\langle 1/r^3 \rangle$ should be estimated as the size of a Wannier function on a single atomic site for the extended hole wavefunction. More detailed calculations, such as that in Ref. [65], put the strength of the heavy-hole nuclear dipole coupling in a GaAs quantum well or QD, summed over all nuclei, in the vicinity of 10 μeV. The average effective field of a heavy hole at an arsenic nucleus, for example, is therefore on the order of this number divided by

[3] This is a redefinition of the symbol Ω, as until now I have always used it as some sort of Rabi frequency.

$N\hbar\gamma_n$, where $N \sim 10^6$ is the number of nuclei and for Arsenic $\gamma_n \approx 5 \times 10^7 (\text{T sec})^{-1}$. Using these numbers, the local magnetic field seen by a nucleus due to the dipole moment of the hole is on the order of 10 G. We denote this field $B_n^{(\text{h})}$. As previously indicated, in the Voigt geometry for self-assembled dots, the dominant spin direction for heavy-hole eigenstates the ground state is at some angle between the strain (x) and magnetic field (z) directions, closer to the x-direction. Suppose this direction is labeled $\hat{r}_0$; then the dipolar coupling between the hole and nucleus n contains the non-vanishing hole-Zeeman-energy-conserving term $(\mathbf{J} \cdot \hat{r}_0) I^x$. This term is nearly energy-conserving, with an energy denominator on the order of the nuclear Zeeman energy of order MHz instead of the electron Zeeman energy of order GHz. Fermi's golden rule in second order allows an estimate of the rate Γ_n at which a trion hole nearly polarized along the sample growth axis (orthogonal to the magnetic field) randomly flips the nth nuclear spin during spontaneous emission, with the nuclear Zeeman energy compensated by the broad width of the emitted photon and the photonic density of states negligibly changed by the Zeeman energy of the nucleus. The result is $\Gamma_n \approx (B_n^{(\text{h})}/B_0)^2 \gamma \approx 1/(10\,\text{ms})$. This is the rough timescale on which trion-induced nuclear polarization occurs.

Trion emission is not the only process affecting nuclear polarization. Nuclear spin diffusion in the semiconductor allows nuclear polarization in a single dot to randomly change. Technically speaking, diffusion in the most classical sense is not a complete description of the loss of nuclear polarization in a QD. The reason is that the hyperfine field of the electron introduces a magnetic field gradient, which makes dipole-dipole induced changes in the nuclear field energy-nonconserving. Polarization may still move and change, however, due to the finite dipolar width in the large three-dimensional bath of spins and due to fluctuations of the gradient. In general, the magnitude of the nuclear dipole-dipole coupling sets a spin-diffusion timescale on the order of milliseconds. However, the more complex processes occurring in the presence of the hyperfine field gradient allow for a hierarchy of timescales. The fastest, millisecond timescales would describe nuclei approaching a quasi-equilibrium dipolar configuration, which may depend on the history of magnetic interactions inside the dot. We will denote[4] the timescale to reach this quasi-equilibrium κ^{-1}. Eventually, diffusion should cause nuclear polarization to "leak out" of the QD and reach thermal equilibrium. This timescale may be far longer, however, on the order the nuclear T_1 rate, which is observed to be on the order of 20 minutes in typical QDs.

We have discussed five very distinct timescales in a QD control experiment. The fastest timescale is the dynamics during picosecond pulses, which play no role for the nuclei; hence in nuclear analyses we can safely consider electron rotations to be instantaneous. The next slower timescale is that of the pulse sequence and resulting electron-spin dynamics, repeated continuously with a repetition period limited by measurement to be on the order of hundreds of nanoseconds. This is still much faster than the third timescale, that of the millisecond-speed nuclear dynamics. Next, the averaging timescale of the measurement is much longer still, on the order of several seconds, allowing the nuclei substantial time to reach quasi-equilibrium. The longest timescale, that of nuclear T_1, is far longer still, and can usually be neglected.

We now discuss nuclear processes as observed when performing the three sequences shown in Fig. 6. The detailed experimental means of achieving these pulse sequences, using optical interferometers and EOMs, are treated in more detail in Ref. [64]. After reporting the observations, I will present a common mathematical model to explain them all.

[4]This is another symbol re-use, as elsewhere in these notes κ represents the unrelated process of cavity decay.

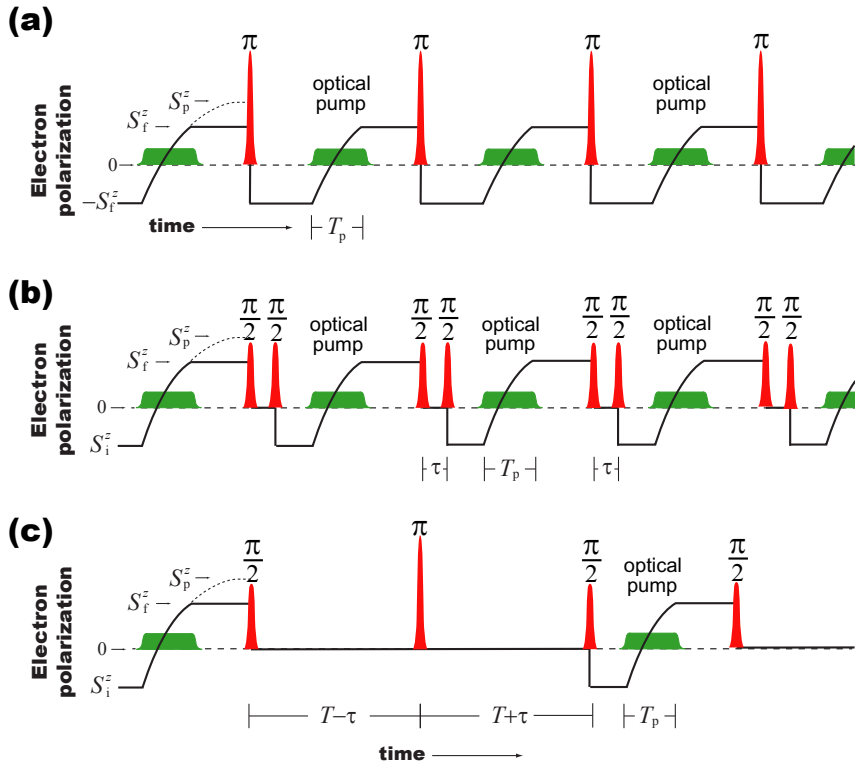

Fig. 6: *Pulse sequences for optical control. (a) One-pulse, optical pumping sequence. After the optical pump (green pulse) polarizes the spin to final polarization S_f^z, as shown by the black line, an ultrafast π pulse (red) inverts the polarization, and the sequence is repeated. (b) Two-pulse, FID or Ramsey interference sequence. The optical pump (green pulse) polarizes the spin from S_i^z to a final polarization S_f^z, after which it is rotated to the Bloch-sphere equator by an ultrafast $\pi/2$ pulse (red). A second $\pi/2$ pulse a time τ later rotates the spin to a location on the Bloch sphere with z-projection S_i^z that depends on τ, and the sequence is repeated. During optical pumping, $S_f^z - S_i^z$ is measured. (c) Three-pulse, spin echo sequence. The sequence is the same as (b), except an optical π-pulse is inserted approximately halfway between the $\pi/2$ pulses, refocusing nuclear Overhauser shifts in the electron spin's precession. The z-projection of the spin after the last pulse, S_i^z, depends on the offset τ of the π pulse from the center of the $\pi/2$ pulses.*

One-pulse Sequence: Optical Pumping

In a one-pulse or "optical pumping" sequence, illustrated in Fig. 6(a), a single ultrafast π pulse is applied. This sequence is designed to give maximal signal during optical pumping, allowing measurements such as the spectral absorption while scanning the pumping laser across the resonance. The absorption spectrum results from the dependence of the steady-state polarization S_f^z on the optical wavelength λ of the pumping laser.

If observing the count rate as the wavelength of the optical pumping laser is scanned, one expects, in the absence of nuclear effects, a symmetric absorption lineshape. This is not observed, however; instead, an asymmetric lineshape is observed. Most notably, this lineshape shows hysteretic behavior, changing its shape depending on the direction of the scan and the history of the experiment. This behavior is shown in Fig. 7. Such effects were also observed in experiments

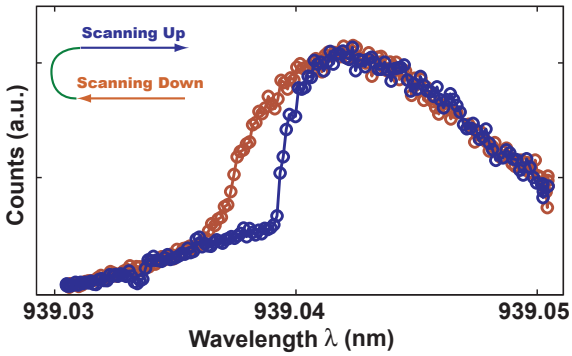

Fig. 7: *Hysteretic absorption trace observed in a single-pulse experiment, while scanning the wavelength λ of the pumping laser down and then up.*

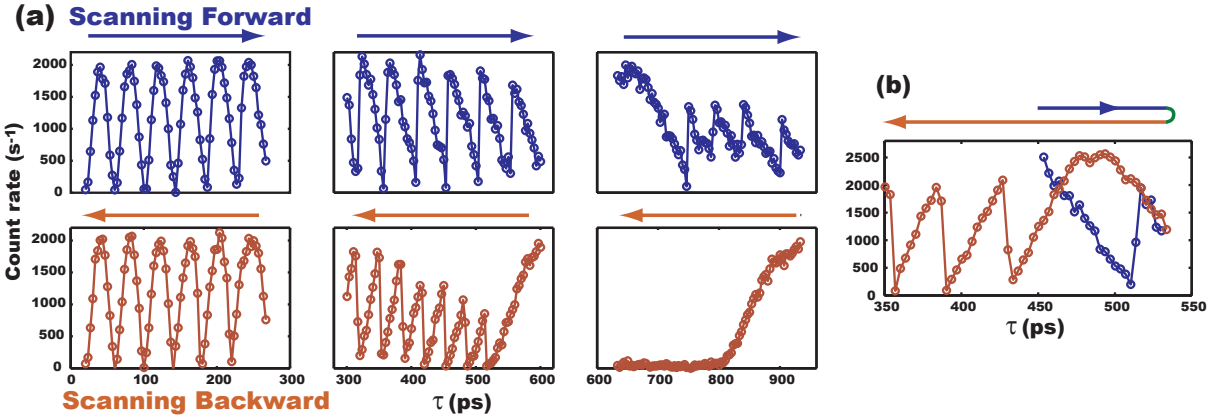

Fig. 8: *(a) Experimental FID count-rate as a function of two-pulse time delay τ. (b) Experimental FID fringe count-rate as τ is continuously scanned longer and then shorter, showing clear hysteresis.*

in which the repumping was achieved with a second CW-laser [62, 63], rather than an ultrafast pulse. Either way, a nuclear origin to the hysteresis is evident from the long timescale at which the hysteretic features survive.

Two-pulse Sequence: Ramsey interferometry/Free Induction Decay

In a two pulse sequence, illustrated in Fig. 6(b), the spin is first initialized into $|\uparrow\rangle$. After the first $\pi/2$ rotation, the electron spin freely precesses around the equator of the Bloch sphere at its Larmor precession frequency, including any Overhauser shifts. A second $\pi/2$ rotation introduces a projection onto the z-axis which varies sinusoidally with τ; that projection is measured during the subsequent initialization step as the entire sequence is repeated. After averaging, the resulting trion count rate is expected to show sinusoidal fringes as a function of τ. In AMO physics this would be referred to as Ramsey interferometry, whereas in magnetic resonance it would be referred to as the free induction decay (FID).

For the two-pulse experiment in the absence of any electron-nuclear spin feedback mechanisms, the nuclear spins would be expected to fluctuate randomly on a timescale slow compared to the

Larmor precession, leading to random Overhauser shifts of the electron's Larmor frequency due to the contact-hyperfine interaction. Repeated measurements of the same spin with different Larmor frequencies would lead to the sinusoidal FID fringes decaying with a Gaussian shape on a timescale T_2^*, known to be on the order of nanoseconds from theoretical calculations. However, such a Gaussian decay was not observed. Figure 8 shows the result of the FID experiment. The top three traces show the fringes seen as the delay τ is increased, and the bottom three correspond to decreasing τ. The oscillatory fringes, rather than decaying, evolve into a sawtooth pattern at high values of τ. Similar data were observed elsewhere as well: see the top trace of Fig. 3b of Ref. [66]. This pattern also shows hysteresis depending on the direction in which τ is scanned.

Three-pulse Sequence: spin echo

In the spin echo experiment, illustrated in Fig. 6(c), the three separate pulses from the mode-locked laser are each gated by multiple EOMs on two split optical paths. The two paths have different optical attenuations, assuring a $\pi/2 - \pi - \pi/2$ Hahn echo sequence. We denote the time between the first $\pi/2$ rotation and the π rotation $T-\tau$, while the π-to-$\pi/2$-pulse separation is $T + \tau$. Fringes are therefore observed as a function of τ at twice the Larmor frequency.

The principal goal of the spin echo measurement is to observe fringe visibility reduction as T is increased, allowing a measurement of T_2. Such results are reported in Ref. [67]. Not reported there are notable effects observed in the shape of the echo fringes as a function of τ, which we qualitatively explain in the following sections. Examples are shown in Fig. 9(a,b). The two principal effects are non-sinusoidal "spikiness" of the echo fringes as a function of τ [Fig. 9(a)], and a decay of the fringe count rate to a constant value substantially higher than the average count-rate [Fig. 9(b)].

Mathematical Model of Nuclear Feedback

The first element of our model is the assumption that trion transitions drive an unbiased random walk in nuclear polarization, with a *rate* proportional to the probability that a trion is created by the pulse sequence. We will therefore derive a trion-driven diffusion equation. We describe the nuclear hyperfine shift as a random variable Ω with time-dependent probability density function (PDF) $f(\Omega, t)$. Time-dependent averages of general functions of Ω over this PDF are given by $\langle F(\Omega)\rangle = \int d\Omega F(\Omega) f(\Omega, t)$, and in particular we write $\omega(t) = \langle\Omega\rangle$.

The trion creation probability will be the crucial term in our diffusion equation. We derive this function as follows. Let us suppose that, for any pulse sequence, the average value of the electron spin for each cycle before optical pumping is $\langle S(\Omega)\rangle_{\text{before}}$, and the average spin afterwards is $\langle S(\Omega)\rangle_{\text{after}}$. Note that coherences are not important for the dynamics studied here, so S refers only to S^z, and the z is dropped. After optical pumping for a time T_p, Eq. (40) gives

$$\langle S(\Omega)\rangle_{\text{after}} = S^z_\text{p}(1 - e^{-\beta(\Omega,\lambda)T_\text{p}}) + \langle S(\Omega)\rangle_{\text{before}} e^{-\beta(\Omega,\lambda)T_\text{p}}. \tag{49}$$

This relation may then be combined with a second relation between $\langle S(\Omega)\rangle_{\text{after}}$ and $\langle S(\Omega)\rangle_{\text{before}}$ that depends on the pulse sequence. In the single-pulse case, the π pulse assures $\langle S(\Omega)\rangle_{\text{after}} = -\langle S(\Omega)\rangle_{\text{before}}$, and therefore the one-pulse trion count rate is

$$C_1(\Omega) = \langle S(\Omega)\rangle_{\text{after}} - \langle S(\Omega)\rangle_{\text{before}} = 2S^z_\text{p} \tanh[\beta(\Omega,\lambda)T_\text{p}/2]. \tag{50}$$

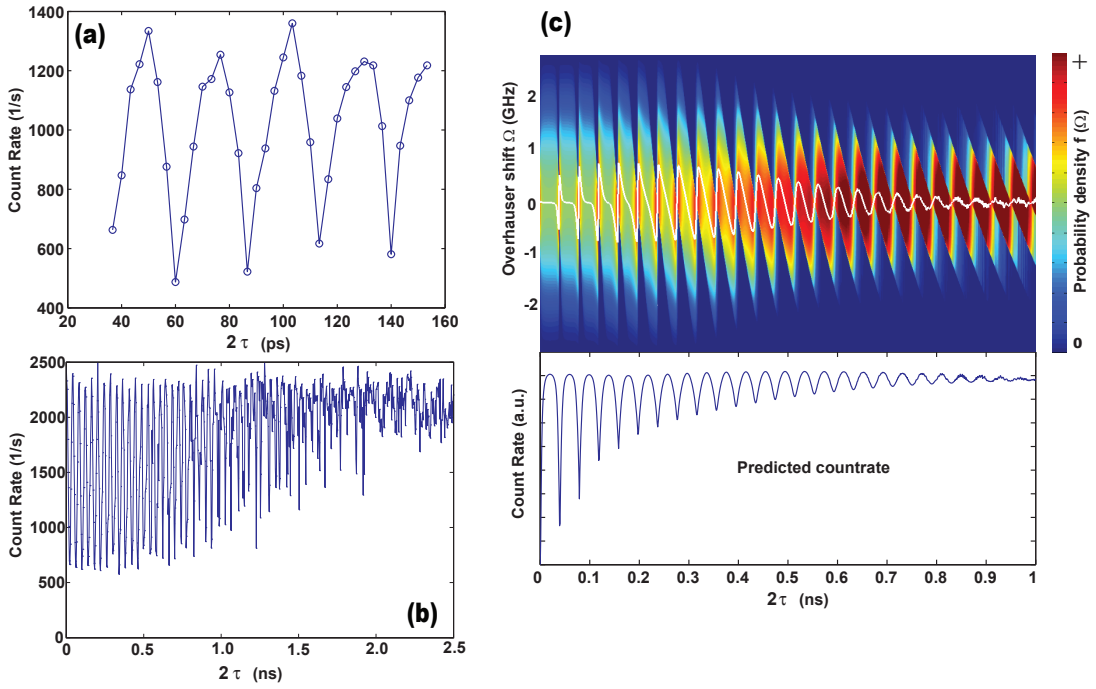

Fig. 9: *Experimental results for spin echo fringes and theoretical model. (a) At low times τ, "spiky" fringes are observed. These have clear deviation from sinusoidal behavior, with smoother curvature on the top of the oscillations and sharp cusps on the bottom. This particular data was taken at magnetic field $B = 3$ T with a π-pulse delay of $T = 78$ ns. (b) At longer times τ, the fringes are often observed to decay to a final count-rate which is not the expected "middle" of the oscillations, but rather the maximum count-rate. This particular data was taken at magnetic field $B = 4$ T with a π-pulse delay of $T = 13$ ns. (c) Mathematical model explaining both spikey data and decay to a high value. The top panel shows the $t \to \infty$ solution to Eq. (56), i.e. Eq. (57), in the colorscale. Superimposed in white is the average polarization $\langle\Omega\rangle$ for each τ. The resulting average countrate $\langle C_3(\Omega)\rangle$ is shown in the lower panel. The timescale and Larmor frequency have been chosen not to match the data, but rather to easily show spiky oscillations and a decay to a high count-rate in a single plot. This particular model uses $D/\kappa = 0.3$ ns^{-2}, $\delta_e/2\pi = 25.3$ GHz, $\zeta/\kappa = 10^3$ ns^{-2}, and $\beta(\omega, \lambda_0) = \beta_0 \exp(-\omega^2/2\sigma^2)$ with $\sigma/2\pi =$1.6 GHz and $\beta_0 = 0.1/T_p$.*

Note that $C_1(\Omega)$ depends on λ, but we shall not explicitly notate this dependence for brevity. For the two-pulse experiment, the pumping laser wavelength is held fixed at $\lambda = \lambda_0$, but the varying pulse separation of τ gives

$$\langle S(\Omega)\rangle_{\text{before}} = \cos[\phi_0 + (\delta_e + \Omega)\tau]\langle S(\Omega)\rangle_{\text{after}}. \tag{51}$$

The phase ϕ_0 depends on offsets in the zero of τ. Strictly speaking, at $\tau = 0$, the two pulses overlap and $\phi_0 = \pi$. In practice, there is a small offset in τ that plays little role in the important features of the dynamics. For a more direct comparison to Fig. 8, we set $\phi_0 = 0$. Hence in the two-pulse case the average number of trions created per cycle is now given by

$$C_2(\Omega) = \langle S(\Omega)\rangle_{\text{after}} - \langle S(\Omega)\rangle_{\text{before}} = S_{\text{p}}^z \frac{[1 - \exp(-\beta(\Omega, \lambda_0)T)][1 - \cos[(\delta_e + \Omega)\tau]]}{1 - \cos[(\delta_e + \Omega)\tau]\exp(-\beta(\Omega, \lambda_0)T)}. \tag{52}$$

Now $C_2(\Omega)$ depends on τ, although again we will not notate this explicitly. This trion creation

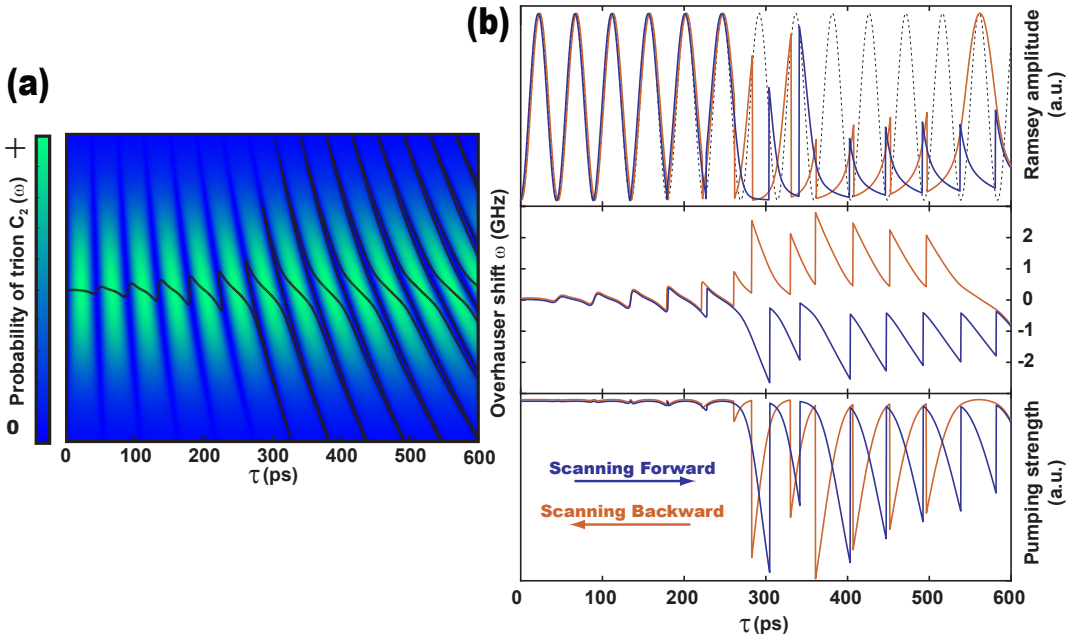

Fig. 10: *(a) The colorscale shows the count rate $C_2(\omega)$ as a function of average Overhauser shift ω (vertical axis, scale shown in GHz in second panel of subfigure 2), and two-pulse delay τ (horizontal axis). The green areas indicate where a higher count-rate is expected. Oscillations in the horizontal directions at frequency $\delta_e + \omega$ are due to Ramsey interference; the Gaussian envelope in the vertical direction is due to the reduction of optical pumping with detuning. The superimposed black line indicates stable points where $\partial\omega/\partial t = 0$ according to Eq. (60). (b) Results of the two-pulse model, to be compared against Fig. 8. The top panel shows the predicted shape of the Ramsey fringes. These result from an Overhauser shift shown on the second panel, which hysteretically follows stable regions of the black curve in (a). The third panel shows the pumping efficiency at each τ. This particular model uses $\kappa/\zeta = 10^4$ ps^2 and $\beta(\omega, \lambda_0) = \beta_0 \exp(-\omega^2/2\sigma^2)$ with $\sigma/2\pi$ =1.6 GHz and $\beta_0 = 3/T_p$.*

probability is plotted in the green and blue colorscale of Fig. 10(a) as a function of pulse delay τ and Overhauser shift Ω. This function oscillates sinusoidally with increasing τ due to the spin's Larmor precession, and would lead to FID oscillations for fixed Ω. The Overhauser shift Ω changes the frequency of Larmor precession. The trion creation probability drops to 0 for large values of $|\Omega|$ because the trion transition shifts away from resonance with the optical pumping laser, leading to reduced pumping efficiency ($\beta(\Omega, \lambda_0) \to 0$) and therefore reduced trion creation.

The three-pulse case, at fixed $\lambda = \lambda_0$ and fixed T, gives a very similar result. Indeed, the only difference is that the relative position of the π pulse drives the rotation angle, rather than the second $\pi/2$ pulse, hence effectively doubling τ:

$$C_3(\Omega, \tau) = C_2(\Omega, 2\tau). \tag{53}$$

The diffusive terms of our equation are generated by the following argument, supposing a nuclear flip causes a change $d\Omega$ in the Overhauser shift in time dt. The probability of finding an Overhauser shift between Ω and $\Omega + d\Omega$ at time $t + dt$ is, by definition, $f(\Omega, t + dt)dx$, and

is the sum of three possibilities. In time dt, Ω may increase by $d\Omega$ from $\Omega - d\Omega$, it may decrease by $d\Omega$ from $\Omega + d\Omega$, or it may stay the same at Ω. If Ω jumps up by $d\Omega$ with probability $[\delta + \epsilon C_j(x)]/2$, where δ is a trion-independent spin diffusion probability and ϵ quantifies the total trion-nuclear spin-flip probability, and if Ω jumps down with the same probability, then the probability density of seeing Ω at time $t + dt$ is

$$f(\Omega, t+dt) = \frac{1}{2}[\delta+\epsilon C_j(\Omega+d\Omega)]f(\Omega+d\Omega,t)+\frac{1}{2}[\delta+\epsilon C_j(\Omega-d\Omega)]f(\Omega-d\Omega,t)+[1-\delta-\epsilon C_j(\Omega)]f(\Omega,t). \tag{54}$$

In the limit that dt and $d\Omega$ become vanishingly small, and defining $\zeta = d\Omega^2\epsilon/2dt$ and $D = d\Omega^2\delta/2dt$, this expression becomes

$$\frac{\partial}{\partial t}f(x,t) = D\frac{\partial}{\partial \Omega^2}f(\Omega,t) + \zeta\frac{\partial}{\partial\Omega}\left[C_j(\Omega)\frac{\partial}{\partial\Omega}f(\Omega,t)\right]. \tag{55}$$

The parameter ζ may be estimated as $\sum_n \Gamma_n(A_n/\hbar)^2 \approx \delta_e^2/1$ sec.

An additional term is required to describe the phenomena by which nuclear spin diffusion reduces large shifts and results in a finite-width distribution (of nominal width of order $1/T_2^*$.) These effects may be phenomenologically captured by a term which drives the mean of $f(\Omega, t)$ to zero at a rate κ. The entire evolution for $f(x, t)$ might therefore considered to be

$$\frac{\partial}{\partial t}f(\Omega,t) = \kappa\frac{\partial}{\partial\Omega}[\Omega f(\Omega,t)] + \frac{\partial}{\partial\Omega}\left\{[D+\zeta C_j(\Omega)]\,\frac{\partial}{\partial\Omega}f(\Omega,t)\right\}. \tag{56}$$

Note that if $f(\Omega, t)$ is a proper PDF with unit integral, then this equation conserves that property.

We now examine Eq. (56) in three important regimes. The first regime is where trion-induced effects are unimportant. One way to achieve this is to set $\zeta \ll D$; in that case the steady-state solution is a Gaussian distribution with mean decaying to zero at rate κ and variance which exponentially approaches D/κ in time. In this respect, we might associate D/κ with $1/T_2^*$, so that this equation could describe a simple picture of the FID; that is, the fluctuation rate would be independent of the pulse-sequence and the fringes of $\langle C(\Omega, \tau)\rangle$ would undergo Gaussian decay with time-constant T_2^*. Another regime in which simple Gaussian decay is seen is if $f(\Omega, 0)$ is Gaussian, and the amount of time t the system is allowed to evolve is small. In this case, solutions remain Gaussian and ordinary dephasing processes are observed. This regime is accessed only in experiments employing a spin echo. Critically, in a spin echo experiment there is substantial time for the nuclei to diffuse unhindered by electron polarization, since for the majority of the pulse sequence, the electron spin is precessing in its Bloch sphere, which effectively decouples the electron from the nuclear dipole-dipole dynamics. The subsequent lack of z-oriented polarization results in a zero average hyperfine gradient on the nuclear spins, allowing maximal diffusion and therefore the $D \gg \zeta$ regime. If in addition relatively low averaging times are employed (resulting in decay dominated by observable noise), trion effects may be ignored, Gaussian decay may be observed, and T_2^* may be measured, as performed in Ref. [67].

A second regime is where $\zeta \sim D$, and a steady-state solution is reached ($t \to \infty$). This is believed to occur when diffusion is relatively unhindered, as in a spin echo experiment, but long

averaging times are employed. In this regime, this flux-conservative PDE is well-behaved, and predicts that $f(\Omega, t)$ eventually evolves, from any initial condition, into a steady-state solution. That steady-state solution may be written

$$f(\Omega, t \to \infty) = f(0, t \to \infty) \exp\left[-\kappa \int_0^{\Omega} \frac{u}{D + \zeta C_j(u)} du\right]. \tag{57}$$

The prefactor $f(0, t \to \infty)$ may be found via normalization. This solution describes a distribution with a mean that fluctuates around 0 as τ is increased, and whose variance varies periodically with τ. Such a solution is plotted in Fig. 9(c), upper panel. If this solution is used to find the average expected count rate in a spin echo experiment, $\langle C_3(\Omega)\rangle$ as a function of τ, the result shows qualitative features observed in spin echo experiments, as seen in Fig. 9(c), lower panel. Oscillations at short times show spiky, non-sinusoidal character, and when the oscillations damp at high values of τ, they do so to a value close to the maximum count-rate. The physical origin of these effects in this model is evidently that, at those places where the fringes look spiky, the nuclei have become polarized and their distribution is substantially narrowed. As τ is increased, this degree of narrowing decreases at the spiky (minimum count rate) locations, but there is little change in the distribution at the maximum count rate locations, accounting for the decay to near the the maximum count rate.

While this solution captures some of the puzzling features of spin echo fringes, it cannot be a complete model for the FID data shown in Fig. 8, or even the hysteresis in Fig. 7. Indeed, a linear PDE such as Eq. (56) under assumptions of full equilibrium cannot show hysteresis. However, only one more simple assumption is needed to arrive at a model which does match our data well. This final assumption is that the width of $f(\Omega, \tau)$ is constrained to be small; much smaller than the inverse Larmor period, despite the influence of trion-induced diffusion. This is possible if the nuclear system has neither the time nor the freedom to fully fill the distribution predicted by Eq. (56), possibly because nuclear spin diffusion is suppressed by hyperfine magnetic field gradients from polarized electron spins. Recall that in our FID experiment, the electron spends the bulk of its time with some polarization on the z-axis. This assumption is further motivated by the fact that, in FID experiments, the sawtooth-like fringes we observe persist for at least an order-of-magnitude longer than T_2^*, suggesting that the distribution $f(\Omega, t)$ is substantially narrowed.

Under this assumption of a narrow distribution due to suppressed diffusion, we model only the first moment of $f(\Omega, \tau)$, $\omega(t) = \langle \Omega(t) \rangle$, and assume the second moment is much smaller than $1/\tau$. Thereby, using integration by parts,

$$\frac{\partial \omega}{\partial t} = -\kappa\omega + \zeta \left\langle \frac{\partial^2}{\partial \Omega^2} [\Omega C_j(\Omega)] \right\rangle. \tag{58}$$

Unfortunately, Eq. (58) is not a closed system of equations, because it still requires knowledge of all moments of $f(\Omega, t)$ to complete the average. However, to approximately remove the average, we apply our assumption about the width of $f(\Omega, \tau)$ to write

$$C_j'[\Omega] \approx C_j'[\omega(t)] + [\Omega - \omega(t)] C_j''[\omega(t)] + \cdots, \tag{59}$$

leaving, to lowest order,

$$\frac{\partial \omega}{\partial t} = -\kappa\omega + \zeta C_j'(\omega). \tag{60}$$

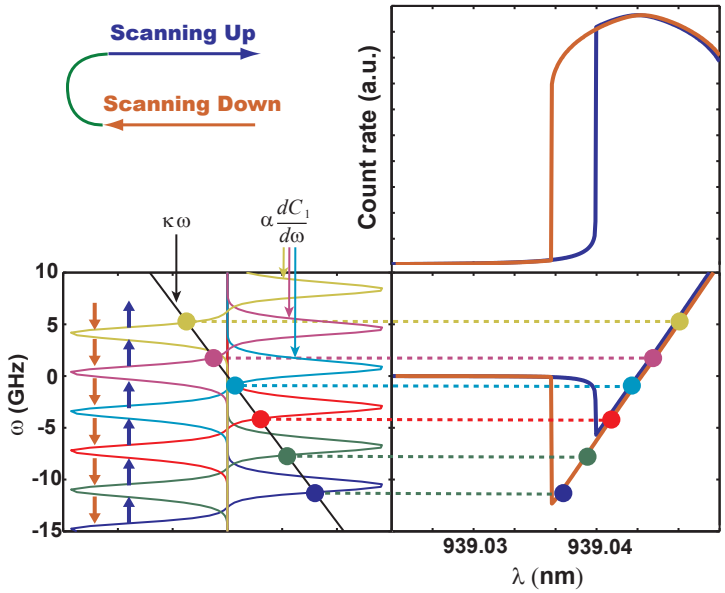

Fig. 11: *Elements of the model for the one-pulse experiment. The panel on the lower left shows $\kappa\omega$ (black line) and $\zeta dC_1(\omega)/d\omega$ for several values of λ, as λ is scanned downwards (indicated by the brown arrows) and then upwards (indicated by the blue arrows). The circles indicate locations where $\kappa\omega = \zeta dC_1(\omega)/d\omega$, i.e. the steady-state solutions of Eq. (60) for $j = 1$. As λ is scanned downward, the polarization ω "surfs" the same edge of the of the $\zeta dC_1(\omega)/d\omega$ curve, and ω steadily decreases, as shown in the lower-right panel. Eventually, at low enough λ, the peak of $\zeta dC_1(\omega)/d\omega$ is passed and the only remaining steady-state solution shifts to $\omega = 0$. This solution is maintained as λ is scanned upwards, until the peak of $\zeta dC_1(\omega)/d\omega$ reaches $\omega = 0$, at which point ω again surfs the $\zeta dC_1(\omega)/d\omega$. The resulting countrate, $C_1(\omega)$, is shown in the upper right panel, and is to be qualitatively compared to Fig. 7. This particular model uses $\kappa/\zeta = 3 \times 10^4$ ps^2,*

Invoking our separation of timescales, we presume $\omega(t)$ evolves from its initial value (set by the last chosen value of λ or τ) to a quasi-equilibrium final value ω_f. This final value determines the expected count rate $C_j(\omega_f)$ at this value of λ or τ. We solve by assuming $\omega(0) = 0$ at the first attempted value of λ or τ, and then we scan the parameter as in the experiment, finding the steady-state solution of Eq. (60) at each value.

The nonlinearity in this ordinary differential equation now allows hysteresis. The hysteresis is most easily understood in the one-pulse experiment, whose model is illustrated in Fig. 11. Scanning the parameter λ is easy to envision graphically, since for this sequence a change in scanning frequency $\delta\omega = \delta(2\pi c/\lambda)$ amounts to a linear shift in $C_1'(\omega)$, i.e. $C_1'(\omega) \to C_1'(\omega + \delta\omega)$. The steady-state solution is where $\zeta C_1'(\omega) = \kappa\omega$; several such solutions exist at particular values of λ. When one such solution lives on the edge of a peak of $C_1'(\omega)$, it "surfs" that edge until its crest. This picture explains bistability and hence hysteresis; see Fig. 11. With the exception of experimental differences, this model is similar to that used to explain hysteresis in CW experiments [62].

This basic model allows an analysis of the more complicated two-pulse experiment. The essence of our model is that the system quasi-equilibrates to a stable value of nuclear polarization that

lives on the edge of the fringes shown in Fig. 10(a); with our separation of timescales, the nuclear polarization then "surfs" along the edge of this function as τ is changed. As τ is increased, $|\omega|$ increases causing the observable photon count to decrease due to the reduced degree of optical pumping. When $|\omega|$ is so high that pumping is ineffective ($\beta(\omega) \to 0$) and the trion-induced walk stops, spin-diffusion causes the system to drift back to a new stable magnetization at a lower value of $|\omega|$, and the process continues.

Figure 10 shows the modeled $C_2(\omega_\mathrm{f})$ and $\omega_\mathrm{f}/2\pi$ as a function of τ. This particular model used $\kappa/\zeta = 10^4$ ps^2, which provides the estimate $\kappa^{-1} \sim 100$ ms, a relevant timescale for dipolar-induced nuclear spin diffusion. This choice of parameters reproduces the qualitative shape of the data quite well, and quantitatively reproduces the location where sinusoidal fringes evolve into sawtooth-like fringes. Detailed curve fitting is not reasonable for this process, since the quantitative behavior depends on a random initial conditions.

Despite the small differences, the success of our simple mathematical model in qualitatively reproducing the initially mysterious hysteretic and non-sinusoidal phenomena in one-, two-, and three-pulse experiments provides high confidence that the basic physics of nuclear feedback is understood in this system.

7 Entangling Multiple Quantum Dots

Multi-dot entanglement remains the most challenging direction in optically controlled QDs for quantum information. Certainly, spins in dots may be exchange coupled and then controlled using the ultrafast control techniques discussed in Sec. 5, but this has only been demonstrated for vertically stacked QDs [50], a geometry which cannot scale beyond a few dots. The two major strategies for optical entanglement of QDs are to either put them both in a single optical cavity, or to couple them remotely using intermediate photons. In this section, we discuss both possibilities.

We use the notation of Sec. 3, but our ground states are now the two logical states of two qubits, notated $\left|\phi_{[0,j]}\right\rangle = |0\rangle_j$ and $\left|\phi_{[1,j]}\right\rangle = |1\rangle_j$, where now j labels the qubits as A and B. In this section we consider only a single excited state for each qubit $\left|\xi_{[\mathrm{e},j]}\right\rangle = |\mathrm{e}\rangle_j$. We consider the case that for a particular optical mode, only state $|1\rangle_j$ is optically coupled to $|\mathrm{e}\rangle_j$. For example, we might use the selection rules of a Voigt geometry dot with a single trapped electron shown in Fig. 4(c), with bright logical state $|1\rangle_j$ being $|\downarrow\rangle_j$ and the excited state being the lowest optically connected trion with vertically polarized light, $|\mathrm{e}\rangle_j = |\uparrow\downarrow, \Rightarrow\rangle_j$. The following analysis then neglects the coupling of the other spin state to the other trion state with the same polarization, due to its larger detuning.

Local Gates

A two-qubit gate in a cavity is analyzed using the adiabatic elimination procedure of Sec. 3, except we now add an optical cavity mode and imagine two QDs in the cavity. As in Eq. (5), we consider optical cavity modes m, annihilated by a_m, each with detuning ω_m from optical frequency ω_0. The state of a cavity with no photons will be labeled $|\mathrm{vac}\rangle$. We abbreviate the Jaynes-Cummings coupling parameter for the $|1\rangle_j$ to $|e\rangle_j$ transition and cavity mode m as $g_{jm} = g_m u_{[1,j]\mathrm{e}m}$.

For the a two-qubit gate, we consider shining a bright laser pulse on the cavity, and we will treat the laser pulse classically, but still quantize the cavity modes. For this problem it is the laser which sets the optical frequency ω_0 of the rotating frame. An optical pulse will couple to each cavity mode m differently depending on the type of cavity. We suppose the laser has (semi-classical) envelope $F_m(t)$ and coupling rate χ_m to each mode m, so the Hamiltonian for the optical pulse and the empty cavity is written

$$\mathcal{H}_{\text{optical}}(t) = \sum_m \omega_m a_m^\dagger a_m + \chi_m F_m(t) a_m^\dagger + \chi_m^* F_m^*(t) a_m. \tag{61}$$

Adding optical loss from cavity mode m at rate κ_m as discussed in Sec. 3, we may solve the classical problem of a driven, lossy, initially empty cavity via master equation techniques and find that an empty cavity would evolve by this Hamiltonian with state $\prod_m D_m[\alpha_m(t)] \left|\text{vac}\right\rangle$, for displacement operator $D_m[\alpha_m(t)] = \exp[\alpha_m(t) a_m^\dagger - \alpha_m^*(t) a_m]$ and

$$\alpha_m(t) = -i \int_0^t F_m(\tau) \exp[(\tau - t)(i\omega_m + \kappa_m/2)] d\tau. \tag{62}$$

This equation describes time-domain filtering from optical pulse $F_m(t)$ to cavity mode amplitude $\alpha_m(t)$.

To analyze CQED effects for a driven cavity, we work in an interaction picture where these classical filtering dynamics are removed; i.e. we move from a density matrix $\rho(t)$ in the rotating reference frame to $\tilde{\rho}(t)$ in a new reference frame with the definition

$$\rho(t) = \prod_m D_m[\alpha_m(t)] \tilde{\rho}(t) \prod_\mu D_\mu^\dagger[\alpha_\mu(t)]. \tag{63}$$

This is a time-dependent basis change, and so it introduces new time-dependent terms in our Hamiltonian; in particular the CQED Hamiltonian becomes

$$\begin{aligned} \mathcal{H}_{\text{CQED}} &= \sum_{j=\text{A,B}} \sum_m g_{jm} \left|\text{e}\right\rangle\!\left\langle 1\right|_j a_m + \text{H.C.} \rightarrow \\ \tilde{\mathcal{H}}_{\text{CQED}}(t) &= \sum_{j=\text{A,B}} \sum_m g_{jm} \left|\text{e}\right\rangle\!\left\langle 1\right|_j [a_m + \alpha_m(t)] + \text{H.C.} \end{aligned} \tag{64}$$

If we now define $\Omega_j(t) = \sum_m g_{jm} \alpha_m(t)$, then in this reference frame we have a cavity QED system with an additional semiclassical driving term as already introduced in Sec. 5, so the full Hamiltonian is

$$\tilde{\mathcal{H}}(t) = \sum_m \omega_m a_m^\dagger a_m + \sum_{j=\text{A,B}} \mathcal{H}_j(t) + \mathcal{H}_{\text{CQED}}. \tag{65}$$

As in the single-QD case, if each $\Omega_j(t)$ evolves slowly enough, the action of the pulse is only to cause a phase shift on the adiabatically maintained bright states of the system. To fourth-order in perturbation theory, the energies of the four qubit states shift according to the Feynman-like diagrams of Fig. 12. A superposition of qubit states evolves via these energy shifts, as

$$\left|\psi(t)\right\rangle = \sum_{j,k=\{0,1\}} c_{jk}(0) \exp\left[-i \int_0^t \lambda_{jk}(\tau)\right] \left|\lambda_{jk}(t)\right\rangle, \tag{66}$$

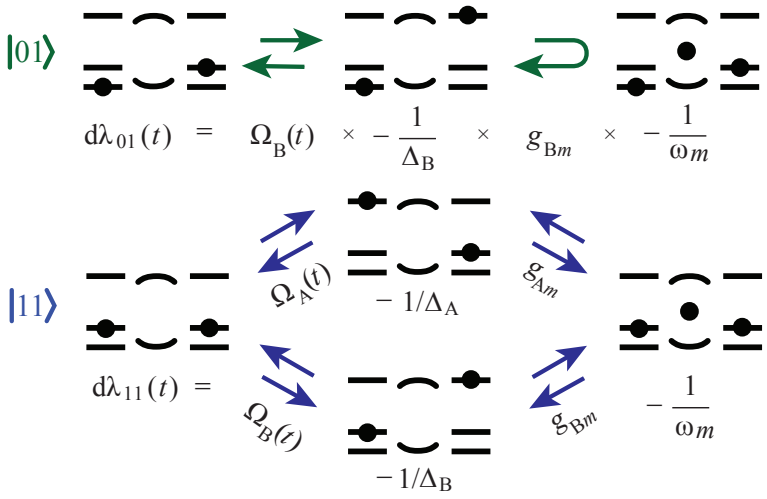

Fig. 12: *(Color online) Feynman-like diagrams for perturbative shifts of states* $|01\rangle$ *and* $|11\rangle$*. The stacks of three levels indicate the QD levels* $|0\rangle, |1\rangle,$ *and* $|e\rangle$ *from bottom to top, and a cavity photon is indicated by a dot in the curved mirrors between them. The arrows indicate vertex terms, and the equations below indicate propagators. A complete (fourth-order) term is a product of each vertex and propagator, summed over paths.*

where $|\lambda_{jk}(t)\rangle$ are the time-varying eigenstates of H which begin and end as separable qubit states, $|\lambda_{jk}(0)\rangle = |\lambda_{jk}(\infty)\rangle = |j\rangle_{\rm A} \otimes |k\rangle_{\rm B} \otimes |{\rm vac}\rangle$. An entangling gate results from the fact that the two-qubit bright-state, $|1\rangle_{\rm A} \otimes |1\rangle_{\rm B} \otimes |{\rm vac}\rangle$, accrues less than twice the phase shift of either of the single qubit bright states, such as $|1\rangle_{\rm A} \otimes |0\rangle_{\rm B} \otimes |{\rm vac}\rangle$. The unitary evolution due to the pulse in this adiabatic, coherent approximation is $U = \exp(i\theta_{\rm A}\sigma_{\rm A}^z)\exp(i\theta_{\rm B}\sigma_{\rm B}^z)\exp(i\theta_{\rm AB}\sigma_{\rm A}^z\sigma_{\rm B}^z)$, in terms of single qubit Pauli matrices σ_j^z. The first two (commuting) terms are single qubit phase shifts. These shifts may be large, as in the single-qubit rotations of Sec. 5. The entanglement results entirely from the smaller nonlinear phase $\theta_{\rm AB}$. As an example, a fully entangling controlled-Z gate (which can be converted to controlled-NOT via Hadamard gates on the target qubit) can be written $U_{\rm CZ} = \exp(-i\pi/4)\exp(i\sigma_{\rm A}^z\pi/4)\exp(i\sigma_{\rm B}^z\pi/4)\exp(-i\sigma_{\rm A}^z\sigma_{\rm B}^z\pi/4)$, so this may be accomplished if $\theta_{\rm AB} = \pi/4$ and appropriate single qubit phase shifts are provided. The CQED gate we have described has a nonlinear phase shift whose leading term at fourth-order is

$$\begin{aligned}\theta_{\rm AB} &= -\int [\lambda_{11}(t) + \lambda_{00}(t) - \lambda_{01}(t) - \lambda_{10}(t)]dt \\ &= 2{\rm Re}\sum_{\mu}\int dt \frac{\Omega_{\rm A}(t)\Omega_{\rm B}^*(t)g_{{\rm A}m}g_{{\rm B}m}^*}{\Delta_{\rm A}\Delta_{\rm B}\omega_m} + O(g^6).\end{aligned} \tag{67}$$

Note that there is no need for the QDs to be resonant with each other (i.e. it is okay that $\Delta_{\rm A} \neq \Delta_{\rm B}$) for this phase shift to occur, a critically important feature for inhomogeneous, self-assembled QDs.

Decoherence results from both cavity loss (at rate κ_m) and spontaneous emission from the QDs (at rate γ). We may roughly estimate these effects with the following argument, in which we drop qubit subscripts for brevity. The dressed states of the system due to the pulse have a trion component with probability $(\Omega/\Delta)^2$ in first order, and they have a cavity photon with

probability $(\Omega/\Delta)^2(g/\delta)^2$ in second order. Therefore, an off-diagonal term of the density matrix $\tilde{\rho}(t)$ decays at a combined exponent $\Gamma(t)$ of approximately

$$\Gamma(t) \approx x\gamma\frac{|\Omega|^2(t)}{\Delta^2} + y\sum_m \kappa_m \frac{\Omega^2(t)|g_m|^2}{\Delta^2\omega_m^2}. \tag{68}$$

The unknowns x and y are in place to remind us that there are other, order-unity constants in place depending on the particular coherence studied. Regardless, optimal gate operations *must* work as a trade-off between the two decoherence terms. In the limit of large cavity-pulse detuning δ, taken as much larger than the cavity bandwidth so that $\omega_m \approx \delta$, the rate of growth of the nonlinear phase divided by the rate of decoherence, $\Gamma^{-1}(t)\dot{\theta}_{\text{AB}}$, has a maximum with respect to δ at $\delta \propto \sqrt{\sum_m \kappa_m |g_m|^2/\gamma}$. If we tune the laser in order to set δ at this value, and assure that $\int \Omega^2(t)dt$ is large enough that $\theta_{\text{AB}} = \pi/4$, then off diagonal terms decay to roughly $\exp[-\int \Gamma(t)dt] \approx \exp[-(\pi/2)\sqrt{xy/C}]$, where where $C = 4\sum_m |g_m|^2/\gamma\kappa_m$ is once again the *cooperativity* of the QD/cavity system. The fidelity of the gate is then approximately $\sim [1/2][1 + \exp(-1/\sqrt{C})]$. Note that QD inhomogeneity is not critical for determining the gate fidelity. A high fidelity gate uses a laser detuned $\sqrt{C}$ cavity-bandwidths from the cavity resonance.

As $C \propto Q/V$ is the important figure of merit for this type of gate, one may suspect that it should work well for microwave circuit CQED with superconducting qubits, where the small size of microfabricated superconducting resonators relative to large microwave wavelengths enable values of C far larger than in optical microcavities. Indeed, with only slight variation, this form of gate has proven very successful with superconducting qubits, as discussed elsewhere in this volume.

In the above, I have considered a single optical pulse to achieve the CQED mediated gate. Other variations have also been considered. The very influential early proposal of Ref. [68] proposed a CQED-mediated gate based on adiabatic elimination using two lasers, as in traditional STIRAP. A related set of possibilities occur when the cavity mode is replaced by a quantum-well exciton mode, or a hybridization of quantum-well excitons and cavity photons known as exciton polaritons; in this case the gate resembles Ruderman-Kittel-Kasuya-Yosida (RKKY) interactions in metals [2].

Distant Gates

The above gate is reasonably local, since the two qubits must share a mode to which they have a strong coupling; e.g. the fundamental mode of a microcavity which has a scale of a few optical wavelengths. But one of the appealing features of optically controlled QD is the light-matter interaction, and the fact that photons can be transfered many kilometers without losing phase coherence. While deterministic coherent quantum gates at this distance are unlikely to be practical due to photon loss, there are many schemes for the heralded creation of entanglement between distant qubits. "Heralding" means that a photon detection event informs the system that entanglement has occurred without photon loss, and would presumedly trigger the use of that entanglement in a teleportation-based operation for the quantum information processing task at hand. In this section, we will discuss only two of the many heralded entanglement schemes that have been proposed for QDs, the first using many photons in a coherent state, and the second using single photons emitted from QDs.

In Sec. 5 we showed how phase shifts in coherent states allowed QND measurement. If instead of immediately measuring the photons, we allow that coherent state to interact with a second QD, we open the possibility of entanglement distribution. This basic scheme of entanglement distribution with a coherent state bus is detailed in Ref. [69]. Two qubits are independently prepared in linear superposition states, $(1/\sqrt{2})(|0\rangle_j + |1\rangle_j)$, perhaps using the single-pulse methods of Sec. 5. A clock must track the phase of these qubits, or they must be continually refocussed with clocked π-pulses; such an element allows us to neglect the time-dependent phase that accrues between the two logical states. A polarized coherent state pulse (in optical coherent state $|\alpha\rangle$) from a laser is incident upon qubit A, entangling the relevant optical mode into the state $(1/\sqrt{2})(|0\rangle_A |\alpha\rangle + |1\rangle_A |\alpha e^{-i\theta}\rangle)$, where $\theta \sim g^2/(\Delta\kappa)$ is the dispersive QND phase shift discussed in Sec. 5. If using polarization, this phase shift is for one polarization mode relative to another. One may also use the relative phase of two spatially separated modes in an interferometer, or two time-separated pulses. If we repeat the same process for qubit B, the combined state is

$$|\psi\rangle = \frac{1}{2}[|00\rangle |\alpha\rangle + (|01\rangle + |10\rangle)|\alpha e^{-i\theta}\rangle + |11\rangle |\alpha e^{-2i\theta}\rangle]. \quad (69)$$

If the average photon number $|\alpha|^2$ is very large, the phase θ can be easily resolved via homodyne detection or a polarization rotation measurement, and with probability $1/2$ the measured phase will be θ, heralding the entangled state $(1/\sqrt{2})(|01\rangle + |10\rangle)$.

However, there are at least two problems with this scheme; these are quantified in Ref. [69]. One is that we have assumed the phase shift θ is the same for the two qubits; which may be highly unlikely for inhomogeneous QDs. A scheme in Ref. [69] allows for compensation of inhomogeneity by modifying the optical beam in between the two QD interactions. A more severe difficulty is that there will be optical loss between the two interactions. As indicated in Eq. (45), photons carried away for measurement decohere a qubit's coherences by the approximate factor $e^{-|\alpha|^2\theta^2}$. If there were no loss, the photons lost to our detectors would only dephase the relative phases of the $|00\rangle$ and $|11\rangle$ states, which we intend to discard via post-selection anyway. Unfortunately, any optical loss in between the two qubits decoheres the desired entangled state, at a rate $e^{-L|\alpha\theta|^2}$, where L is the portion of photons lost. We cannot compensate by making $\alpha\theta$ smaller than order unity, since this is required for phase-based heralding. This means entanglement fidelity shrinks exponentially with loss. If one desires to engineer an extremely low loss optical system, however, the advantages of this scheme include a fast operation time, a high success probability, and robustness against optical path fluctuations.

Single-photon-based schemes are more robust to optical loss because, if given a guarantee that only a single photon was present in the system, a click from a single-photon detector effectively projects out a process in which that photon was not lost. One class of schemes employs the observation that, due to selection rules, single photons emitted from QDs containing spin-qubits in superposition states are entangled to those spins. In principle, the single pulse control experiments described in the previous two sections created many millions of entangled spin-photon pairs, as these were the basis of the measurements. However, verifying the presence of that entanglement is an experimental challenge that has only been performed very recently [70, 71]. One of these experiments [70] has further included the conversion of the emitted photon to telecom wavelength, offering strong promise for long-distance entanglement.

Entanglement of two spins requires two QDs capable of generating single indistinguishable photons as discussed in Sec. 4 (or a nonlinear optical wavelength conversion mechanism, as demon-

strated in for spin-photon entanglement in Ref. [70] and for indistinguishability in Ref. [33]). Two QDs are simultaneously excited to the trion states $|\mathrm{e}\rangle_j$. As indicated in the diagram of Fig. 4(c), the trion state can emit photons into two modes, of differing polarization and/or energy, and of course each dot emits into separate spatial modes. Notate these modes $m = [0, j]$ and $m = [1, j]$, so that the resulting spin-photon entangled state is

$$|\psi\rangle = \left\{ \prod_j \otimes \left[u_{[0,j][\mathrm{e},j][0,j]} \, |0\rangle_j \, a^\dagger_{[0,j]} + u_{[1,j][\mathrm{e},j][1,j]} \, |1\rangle_j \, a^\dagger_{[1,j]} \right] \right\} |\mathrm{vac}\rangle \tag{70}$$

We now use physics of indistinguishable photons as in the HOM experiment discussed in Sec. 4, in which the photons from the two dots are sent to a non-polarizing beamsplitter. We consider modes C and D, equally split from modes A and B coming from each QD. Indistinguishability assures that for the same logical state, photons bunch, e.g. $a^\dagger_{[0,A]} a^\dagger_{[0,B]} \to a^\dagger_{[0,C]} a^\dagger_{[0,C]} - a^\dagger_{[0,D]} a^\dagger_{[0,D]}$. In particular, if all selection amplitudes u_{jkm} were equal, we would obtain

$$\begin{aligned} |\psi\rangle = \frac{1}{2\sqrt{2}} |00\rangle \, [a^\dagger_{[0,C]} a^\dagger_{[0,C]} - a^\dagger_{[0,D]} a^\dagger_{[0,D]}] \, |\mathrm{vac}\rangle + \frac{1}{2\sqrt{2}} |11\rangle \, [a^\dagger_{[1,C]} a^\dagger_{[1,C]} - a^\dagger_{[1,D]} a^\dagger_{[1,D]}] \, |\mathrm{vac}\rangle \\ + \frac{1}{4} [|01\rangle + |10\rangle] [a^\dagger_{[0,C]} a^\dagger_{[1,C]} - a^\dagger_{[0,D]} a^\dagger_{[1,D]}] \, |\mathrm{vac}\rangle \\ + \frac{1}{4} [|01\rangle - |10\rangle] [a^\dagger_{0,D]} a^\dagger_{[1,C]} - a^\dagger_{[1,D]} a^\dagger_{[0,C]}] \, |\mathrm{vac}\rangle \, . \end{aligned} \tag{71}$$

In this highly symmetric case, any symmetric qubit state results in bunching, and therefore no detection coincidences for detectors on modes C and D. In contrast, photons corresponding to the antisymmetric Bell state do not bunch, and therefore a coincidence detection assures that the corresponding spins have opposite states. Hence a coincidence projects the spins into an entangled state of the form $|01\rangle - |10\rangle$. In fact, one may do even better by adding a beamsplitter which distinguishes modes $[0, j]$ and $[1, j]$, e.g. a polarizing beamsplitter, to each of modes C and D. One then has four output modes, which we might notate C0, C1, D0, and D1. A coincidence between any C mode and any D mode heralds $|01\rangle - |10\rangle$, while a coincidence between $C0$ and $C1$ or $D0$ and $D1$ heralds $|01\rangle + |10\rangle$.

This scheme follows the same principles of the HOM-based photon entanglement post-selection scheme discussed in Sec. 4. If one can post-select entangled photons, and those entangled photons are themselves entangled to spins, it follows that one has heralded entangled spins. While this has not yet been performed for QDs, entanglement between two trapped ions has been demonstrated in this way [72]. As already indicated, the primary advantage of this scheme is that the fidelity of the resulting entanglement in the presence of photon loss; it can also be highly robust to optical path (phase) fluctuations, as indicated in References [73, 74, 75]. The disadvantage is the low success probability, since a single photon can be easily lost due to scattering, absorption and reflection loss of optical circuits, and we require a coincidence count.

In summary, entangling two optically controlled QDs in a useful way remains a severe engineering challenge, since local or distant gates mediated by strong photon fields have fidelities strongly degraded by optical losses, and single-photon-based schemes using lossy optics are slow. However, entangling gates provide the primary direction in which quantum information with optically controlled dots is currently being advanced, and I expect long-distance multi-dot entanglement will be demonstrated relatively soon.

8 Prospects

Section 2 described how QDs may be relatively easily fabricated inside a semiconductor nanostructure; cooling a QD to sufficiently low temperature for operation is then as simple as putting that semiconductor in a refrigerator. This is in contrast to AMO systems, where the process of acquiring cold atoms is substantially more involved, especially if chip-scale systems are ultimately desired. While fabrication advancements in QD placement, homogeneity, and yield are still required, many routes lay open for such advancements. Section 4 introduced one way QDs may enable quantum technologies: by providing the single photon sources that, combined with linear optics and single photon detectors, enable photonic quantum information processing. But this ability presaged another ability for dots: the ability to provide an optical interface between their internal quantum degrees of freedom and photonic qubits. Section 5 showed how those internal degrees of freedom can be made into an optically controlled qubit, with initialization, rotation, and measurement occurring at perhaps the fastest timescales relative to any qubit currently under development. While nuclear spins can be considered a problem for QDs, Sec. 6 indicated some promise that polarized nuclei may in fact be a useful tool for QD tuning. And while Sec. 7 did not definitively identify a certain method for high-fidelity multiqubit gates, it did suggest a number of research routes.

So if these pieces are assembled into a complete, optically controlled quantum information processing device, what might it look like? Given the speculative nature of the multi-dot entanglement schemes introduced in Sec. 7, such a device is inevitably very, very speculative. One possibility is a collection of microcavities, each containing a small handful of dots; this most strongly resembles current experiments. These microcavities must have a highly efficient photonic coupling, which might be achieved by on-chip waveguides. These coupling efficiencies are not likely to be sufficient to enable fault tolerant quantum computing, however, and so some amount of entanglement purification is likely to be required to compensate. This picture is sketched in Ref. [76]. Another possibility is to have regular arrays of QDs in a single planar microcavity, relying on the spatial confinement offered by high-contrast, high-quality DBR stacks, and assuming QDs are coupled via overlapping detuned optical pulses. Such a picture is sketched in Ref. [77]. In both of these sketches, but more so the latter, rough resource counts are made based on means for QEC discussed in other notes in this volume.

I emphasize that schemes like this only exist as a very rough estimation of resources, in part because QD devices are likely to be drastically different than the current state of the art before any such device is ever constructed, and in part because the means for QEC and even the quantum algorithms will probably undergo substantial improvement as well. Nonetheless, for some proposed quantum technologies even very rough estimations can show untenable scaling in space or time. The small size and fast speeds of optically controlled QDs appear to be critical for enabling practical quantum information processing.

References

[1] F. Henneberger and O. Benson, eds., *Semiconductor Quantum Bits* (Pan Stanford Publishing, 2009).

[2] R.-B. Liu, W. Yao, and L. Sham, Adv. Phys. **59**, 703 (2010).

[3] C. Schneider *et al.*, Appl. Phys. Lett. **92**, 183101 (2008).

[4] D. Leonard *et al.*, Appl. Phys. Lett. **63**, 3203 (1993).

[5] N. Koguchi, K. Ishige, and S. Takahashi, J. Vac. Sci. Technol. B **11**, 787 (1993).

[6] A. Zrenner *et al.*, Phys. Rev. Lett. **72**, 3382 (1994).

[7] M. A. Lampert, Phys. Rev. Lett. **1** (1958).

[8] D. G. Thomas and J. J. Hopfield, Phys. Rev. Lett. **7**, 316 (1961).

[9] V. A. Karasyuk *et al.*, Phys. Rev. B **49**, 16381 (1994).

[10] K. Sanaka, *et al.*, Phys. Rev. Lett. **103**, 053601 (2009).

[11] K. Hinzer *et al.*, Phys. Rev. B **63**, 075314 (2001).

[12] M. Bayer *et al.*, Phys. Rev. B **65**, 195315 (2002).

[13] G. Chen *et al.*, Science **289**, 1906 (2000).

[14] Y. Yamamoto and A. Imamoglu, *Mesoscopic Quantum Optics* (John Wiley and Sons, Inc., 1999).

[15] G. Khitrova *et al.*, Nature Phys. **2**, 81 (2006).

[16] H.-K. Lo, X. Ma, and K. Chen, Phys. Rev. Lett. **94**, 230504 (2005).

[17] C. H. Bennett and G. Brassard, in *Proceedings of the IEEE International Conference on Computers, Systems, and Signal Processing* (1984), p. 175.

[18] S. J. van Enk, $|0\rangle|1\rangle + |1\rangle|0\rangle$ (2005), arXiv:quant-ph/0507189.

[19] E. Knill, R. Laflamme, and G. J. Milburn, Nature **409**, 46 (2001).

[20] S. Aaronson and A. Arkhipov, in *Proceedings of the 43rd annual ACM symposium on Theory of computing* (ACM, New York, NY, USA, 2011), STOC '11, p. 333.

[21] S. Buckley, K. Rivoire, and J. Vuckovic, Rep. Prog. Phys. **75**, 126503 (2012).

[22] J. Kim, O. Benson, H. Kan, and Y. Yamamoto, Nature **397**, 500 (1999).

[23] P. Michler *et al.*, Nature **290**, 2282 (2000).

[24] C. Santori *et al.*, Phys. Rev. Lett. **86**, 1502 (2001).

[25] Z. Yuan *et al.*, Science **295**, 102 (2002).

[26] C. Santori *et al.*, Nature **419**, 594 (2002).

[27] D. Fattal *et al.*, Phys. Rev. Lett. **92**, 037903 (2004).

[28] D. Fattal, E. Diamanti, K. Inoue, and Y. Yamamoto, Phys. Rev. Lett. **92**, 037904 (2004).

[29] P. Kok *et al.*, Rev. Mod. Phys. **79**, 135 (2007).

[30] R. B. Patel *et al.*, Nature Photon. **4**, 632 (2010).

[31] E. B. Flagg *et al.*, Phys. Rev. Lett. **104**, 137401 (2010).

[32] K. Sanaka *et al.*, Nanolett. **12**, 4611 (2012).

[33] S. Ates *et al.*, Phys. Rev. Lett. **109**, 147405 (2012).

[34] O. Benson, C. Santori, M. Pelton, and Y. Yamamoto, Phys. Rev. Lett. **84**, 2513 (2000).

[35] C. E. Kuklewicz, R. N. E. Malein, P. M. Petroff, and B. D. Gerardot, Nanolett. **12**, 3761 (2012).

[36] A. J. Hudson *et al.*, Phys. Rev. Lett. **99**, 266802 (2007).

[37] A. J. Bennett *et al.*, Nat. Phys. **6**, 947 (2010).

[38] A. Muller, W. Fang, J. Lawall, and G. S. Solomon, Phys. Rev. Lett. **103**, 217402 (2009).

[39] R. Trotta *et al.*, Phys. Rev. Lett. **109**, 147401 (2012).

[40] D. Press, T. D. Ladd, B. Y. Zhang, and Y. Yamamoto, Nature **456**, 218 (2008).

[41] M. Atatüre *et al.*, Science **312**, 551 (2006).

[42] C. Emary *et al.*, Phys. Rev. Lett. **98**, 047401 (2007).

[43] P. Chen *et al.*, Phys. Rev. B **69**, 075320 (2004).

[44] S. M. Clark, K. M. C. Fu, T. D. Ladd, and Y. Yamamoto, Phys. Rev. Lett. **99**, 40501 (2007).

[45] J. Berezovsky *et al.*, Science **320**, 349 (2008).

[46] A. Greilich *et al.*, Science **313**, 341 (2006).

[47] A. Greilich *et al.*, Science **317**, 1896 (2007).

[48] S. G. Carter *et al.*, Phys. Rev. Lett. **102**, 167403 (2009).

[49] K. De Greve *et al.*, Nat. Phys. **7**, 872 (2011).

[50] D. Kim *et al.*, Nat. Phys. **7**, 223 (2011).

[51] J. Berezovsky *et al.*, Science **314**, 1916 (2006).

[52] M. Atatüre, J. Dreiser, A. Badolato, and A. Imamoglu, Nat. Phys. **3**, 101 (2007).

[53] I. Fushman *et al.*, Science **320**, 769 (2008).

[54] A. B. Young *et al.*, Phys. Rev. A **84**, 011803 (2011).

[55] S. G. Carter *et al.*, *Quantum control of a spin qubit coupled to a photonic crystal cavity*, arXiv:12114540.

[56] D. Kim *et al.*, Phys. Rev. Lett. **101**, 236804 (2008).

[57] E. Baudin, E. Benjamin, A. Lemaître, and O. Krebs, Phys. Rev. Lett. **107**, 197402 (2011).

[58] F. H. L. Koppens *et al.*, Science **309**, 1346 (2005).

[59] D. J. Reilly *et al.*, Science **321**, 817 (2008).

[60] H. Bluhm *et al.*, Phys. Rev. Lett. **105**, 216803 (2010).

[61] I. T. Vink *et al.*, Nat. Phys. **5**, 764 (2009).

[62] X. Xu *et al.*, Nature **459**, 1105 (2009).

[63] C. Latta *et al.*, Nat. Phys. **5**, 758 (2009).

[64] T. D. Ladd *et al.*, Phys. Rev. Lett. **105**, 107401 (2010).

[65] J. Fischer, W. A. Coish, D. V. Bulaev, and D. Loss, Phys. Rev. B **78**, 155329 (2008).

[66] E. D. Kim *et al.*, Phys. Rev. Lett. **104**, 167401 (2010).

[67] D. Press *et al.*, Nature Photon. **4**, 367 (2010).

[68] A. Imamoglu *et al.*, Phys. Rev. Lett. **83**, 4204 (1999).

[69] T. D. Ladd *et al.*, New J. Phys. **8**, 184 (2006).

[70] K. De Greve *et al.*, Nature **491**, 421 (2012).

[71] W. B. Gao *et al.*, Nature **491**, 426 (2012).

[72] D. L. Moehring *et al.*, Nature **449**, 68 (2007).

[73] X. L. Feng *et al.*, Phys. Rev. Lett. **90**, 217902 (2003).

[74] L. M. Duan and H. J. Kimble, Phys. Rev. Lett. **90**, 253601 (2003).

[75] C. Simon and W. T. M. Irvine, Phys. Rev. Lett. p. 110405 (2003).

[76] R. Van Meter *et al.*, Int. J. Quantum Inform. **8**, 295 (2010).

[77] N. C. Jones *et al.*, Phys. Rev. X **2**, 031007 (2012).

D 5 Spintronics and Emergent Qubits [1]

Thomas Schäpers
Peter Grünberg Institut
Forschungszentrum Jülich GmbH

Contents

1 Introduction **2**

2 Low dimensional semiconductor systems **2**

3 Spin-orbit coupling in semiconductor structures **6**

4 Electron interference effects **13**

5 Rashba effect in quasi-one-dimensional structures **17**

6 Spin-orbit quantum-bits **22**

7 Andreev level qubits **29**

[1] Lecture Notes of the 44^{th} IFF Spring School "Quantum Information Processing" (Forschungszentrum Jülich, 2013). All rights reserved.

1 Introduction

In this lecture the basic concepts of spintronics will be introduced. The main focus lies on effects related to spin-orbit coupling in semiconductor heterostructures, i.e. the Rashba and Dresselhaus effect. Especially the former allows to control the spin orientation by electrical means. The Rashba effect is essential for the realization of the spin field-effect transistor [1]. By reducing the structure size to one dimension, the properties of spintronic devices can be improved. Here, we will particularly discuss cylindrical semiconductor nanowires, which are prepared by the so-called bottom up approach. By confining the electrons in a gate-defined quantum dot based on semiconductor nanowires, a spin qubits can be realized. It will be discussed, how spin-orbit coupling is employed to manipulate the spin orientation in these qubits. Semiconductor nanowires are also very interesting elements to realize Andreev level qubits. Here, the nanowire is used as a normal conducting link between two superconducting electrodes. Owing to phase-coherent Andreev reflection, a Josephson supercurrent can be observed.

2 Low dimensional semiconductor systems

InAs-based 2-dimensional electron gases

Semiconductor heterostructures based on InAs or its alloys are particularly suited for observing a strong spin-orbit coupling. A typical layer sequence is depicted in Fig. 1(a) [2]. Here, the 2-dimensional electron gas is located in a $Ga_{0.47}In_{0.53}As$ layer at the boundary to the InP spacer layer. The $Ga_{0.47}In_{0.53}As$ semiconductor has a smaller band gap compared to InP. At an indium content of 53% of the GaInAs layer the lattice constant fits to the lattice constant of InP. The electrons in the 2DEG are provided by the n-type doped InP layer which is separated from the 2DEG by a spacer layer (modulation doping). The whole structure is grown on an InP wafer. Heterostructures containing phosphorus are mostly grown by means of metal-organic vapor phase epitaxy (MOVPE). Here, the metal-organic precursors, e.g. trimethylindium (TMIn), trimethylgallium (TMGa), AsH_3, or PH_3, are added to the carrier gas, i.e. H_2 or N_2, which flows in a reactor over the surface of the wafer.
In Fig. 2 the temperature dependence of the mobility of a 2-dimensional electron gas in an InGaAs/InP heterostructure is shown. Down to temperatures of around 40 K the mobility is limited by phonon scattering. At temperatures below 40 K the mobility saturates, which can be attributed to alloy scattering. Mobilities above 100000 cm^2/Vs can be achieved [2]. In contrast to a 2-dimensional electron gas in a GaAs/AlGaAs heterostructures, the electron gas is located in a ternary material, where the In and Ga atoms are statistically distributed in the crystal. The corresponding disorder potential results in an additional scattering contribution, which limits the mobility at low temperatures.
A typical conduction band profile of a GaInAs/InP heterostructure with an additional strained $Ga_{0.23}In_{0.77}As$ layer is depicted in Fig. 3. The larger In content of 77% leads to a smaller band gap and a smaller effective electron mass compared to $Ga_{0.47}In_{0.53}As$. Furthermore, due to the smaller disorder potential the alloy scattering contribution is lowered. As can be seen in Fig. 3, the electron wave function ξ is mainly located in the strained $Ga_{0.23}In_{0.77}As$ layer. Owing to the different barrier materials and the doping at only one side of the $Ga_{0.23}In_{0.77}As$ well, the rectangular quantum well is tilted. The tilted potential profile results in an electric field in the quantum well. The presence of an electric field in the 2-dimensional electron gas is an important prerequisite for the Rashba effect introduced below.

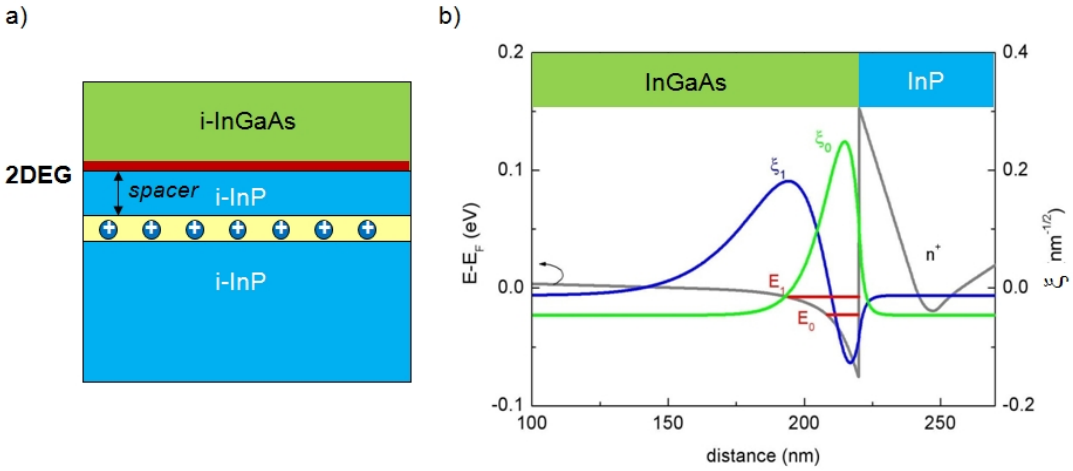

Fig. 1: *(a) Layer sequence of a GaInAs/InP heterostructure. The 2DEG is located in the GaInAs layer at the boundary to the InP spacer. (b) Conduction band profile and electron wave functions of the 2DEG at the boundary of the GaInAs/InP interface.*

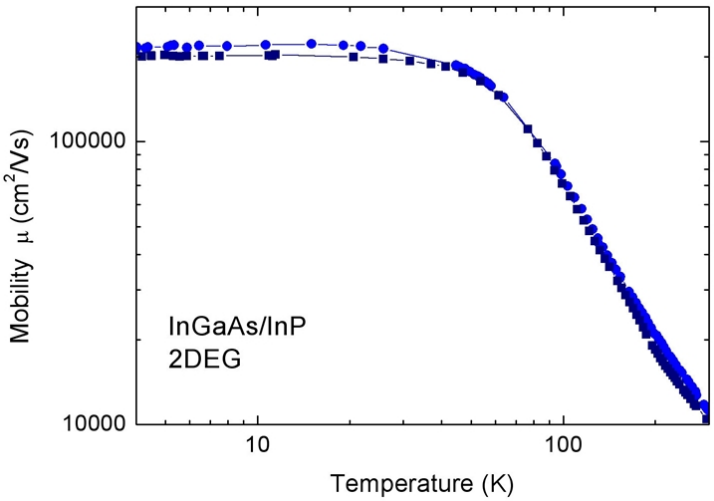

Fig. 2: *Temperature dependence of a 2-dimensional electron gas in a GaInAs/InP heterostructure. At low temperatures the mobility is limited by alloy scattering.*

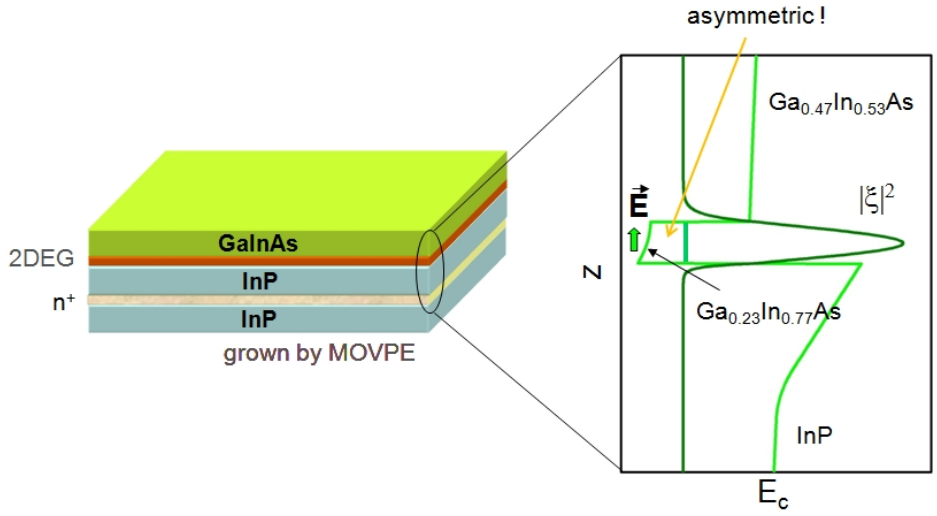

Fig. 3: *Conduction band profile and squared amplitude $|\xi|^2$ of the electron wave function in a GaInAs/InP heterstructures with an inserted strained $Ga_{0.23}In_{0.77}As$ layer.*

By employing etching methods the dimension of 2-dimensional electron gas can be reduced to a 1-dimensional wire structure. The etching process can either be performed by wet chemical etching or by dry etching methods. As described in the next section, a more elegant way is to prepare these wire structures directly by means of epitaxial growth.

Semiconductor nanowires

Nano-scaled wire structures can also be fabricated by self-organized growth without using elaborate lithographical means. One possible approach is to use the vapor-liquid-solid (VLS) growth mode [3]. Here, a nanometer-size gold particle is used as a seed particle for the nanowire growth. In many cases InAs is used as a semiconductor material. The underlying reason is that at the surface an electron accumulation layer is formed due to the Fermi level pinning within the conduction band [cf. Fig. 4(a)]. This property is only found in a few semiconductors, e.g. InAs, InN, or InSb. It ensures that even for low nanowire diameters the nanowires contain conductive electrons. For most other semiconductors a depletion layer is formed at the surface, e.g. for GaAs or Si, owing to the Fermi level pinning within the band gap [cf. Fig. 4(b)].

As an alternative to the VLS method, nanowires can also be fabricated by selective-area metal-organic vapor phase epitaxy (SA-MOVPE). Here, a pre-patterned substrate is used, where the nanowires are grown only at those positions where holes are present in a dielectric mask layer. By this method the location of the nanowires can be determined, which is advantageous for subsequent device processing [cf. Fig. 5(b)].

For transport measurements the as-grown nanowires are usually separated from the substrate and transferred to another substrate with alignment markers. By employing electron beam lithography these nanowire are contacted. A scanning electron micrograph of a typical contacted semiconductor nanowire is shown in Fig. 5(a).

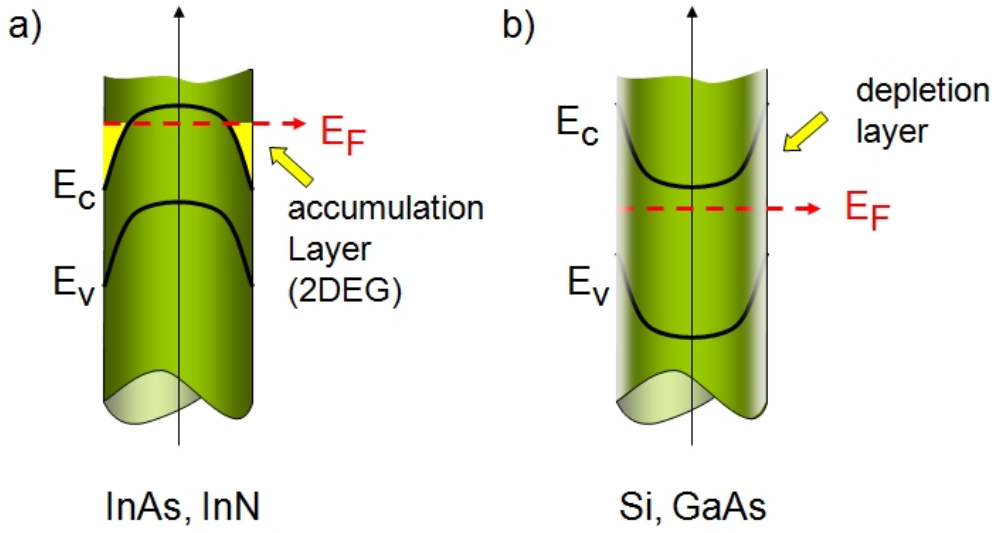

Fig. 4: *(a) Semiconductor nanowire with a surface accumulation layer. (b) Nanowire with a depletion layer at the surface.*

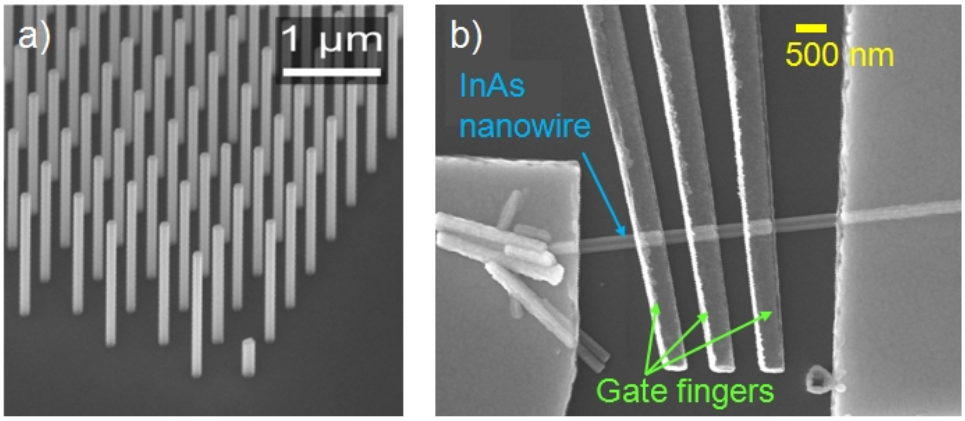

Fig. 5: *(a) Scanning electron beam micrograph of a field of InAs nanowires grown by selective-area MOVPE. (b) InAs nanowire contacted with ohmic contacts on both terminals. In addition, gate fingers are placed in the center, in order to control the electron concentration.*

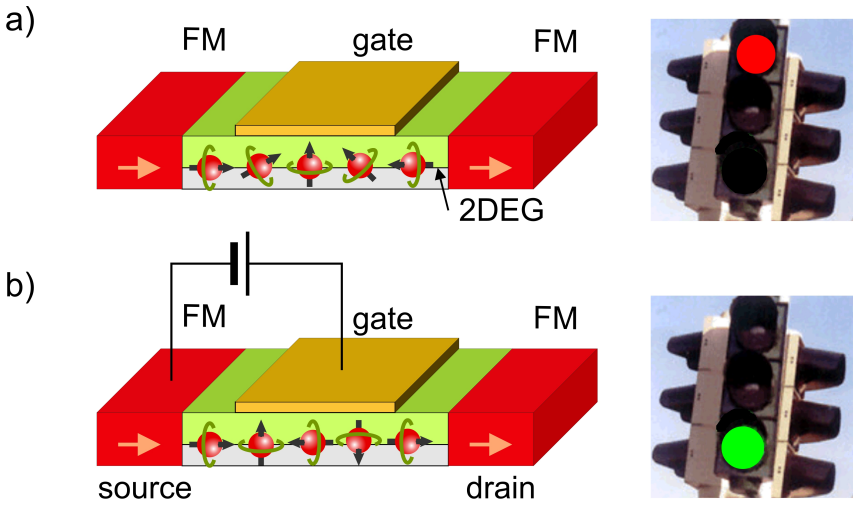

Fig. 6: *Schematics of a spin transistor: (a) No gate voltage is applied. The spin precession due to the presence of the Rashba effect leads to a spin orientation which is opposite to the magnetization of the drain electrode. No current can flow in this case, corresponding to a red traffic light. (b) A gate voltage is applied, which enhances the Rashba effect. Owing to stronger spin precession, the spin orientation of the electrons arriving at the drain electrode fits to its magnetization. A current can flow, corresponding to a green traffic light.*

3 Spin-orbit coupling in semiconductor structures

Spintronics: Basic concept

A well-known example of a spintronic device is the spin field-effect transistor. In Fig. 6 a schematics of the spin field-effect transistor is shown [1, 4]. The spin transistor consist of three components: a spin injector as the source electrode, a semiconducting area where the spin orientation is controlled, and a spin detector as the drain electrode. Here, we will focus on the properties of the semiconductor channel located in between the magnetic contacts. In Fig. 6(a) the spin precession in a spin transistor is shown, when no voltage is applied to the gate electrode on top of the semiconductor channel. In the channel the spin is precessing owing to the presence of the Rashba spin-orbit coupling [5]. For the sake of simplicity we assumed that the electron arrives at the drain contact with a spin orientation opposite to the spin orientation in the detector electrode. In this case the electrons cannot enter the detector, since there are no states available the incoming electrons can occupy. As a consequence, the current through the spin transistor is blocked. As will be explained below in detail, by applying a gate voltage the strength of the Rashba spin-orbit coupling can be enhanced. This leads to a stronger spin precession so that the spin orientation of the electrons arriving at the drain electrode fits to the magnetization of the detector electrodes. Now a current can flow in the structure, since the electrons can enter the drain electrode.

Below we will explain the physical background of spin-orbit coupling in a semiconductor heterostructure in detail. Furthermore, a method will be introduced to determine the strength of spin-orbit coupling by transport experiments. Finally, spin-orbit coupling in wire structures will be discussed.

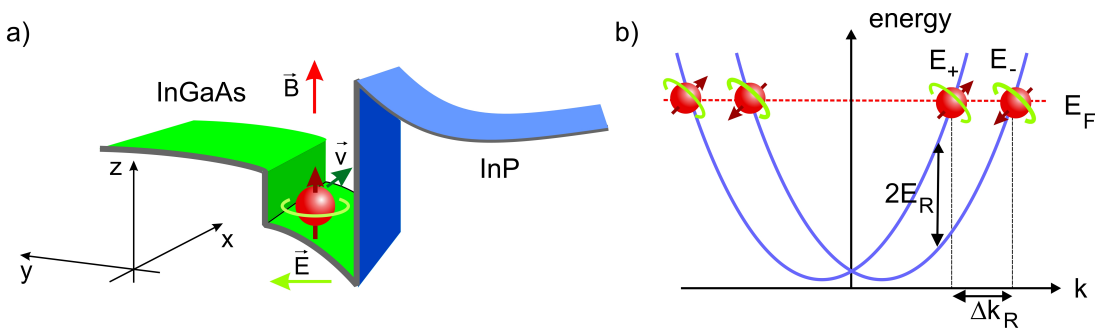

Fig. 7: *(a) Schematic illustration of the Rashba spin-orbit coupling in a 2-dimensional electron gas (b) Energy-momentum dispersion with an energy splitting due to the Rashba effect.*

The Rashba effect

We have seen above that owing to the different materials forming the barriers and owing to the doping from only one side, the potential profile of the quantum well of the 2-dimensional electron gas in a GaInAs/InP heterostructure is asymmetric. This tilted potential is connected to an electric field $\mathcal{E} = -\nabla V/e$, which is oriented perpendicularly to the plane of the 2-dimensional electron gas. In general, in their own frame of reference electrons propagating in an electric field experience an effective magnetic field B given by

$$\mathbf{B} = \frac{1}{c}\mathbf{v} \times \mathcal{E} \ . \tag{1}$$

with c the velocity of light. As illustrated in Fig. 7(a), this magnetic field is oriented perpendicularly to the direction of propagation and to the electric field $\mathcal{E}$. In the non-relativistic approximation the Hamiltonian responsible for the spin-orbit coupling of a free electron propagation in an electric field can be directly derived from the Dirac equation by a power expansion in $(v/c)^2$

$$H_{\rm so} = \frac{\hbar}{(2m_0c)^2}\nabla V \left(\sigma \times \mathbf{p}\right) \ , \tag{2}$$

with $\mathbf{p}$ the momentum and σ the Pauli spin matrices. The corresponding Rashba Hamiltonian for propagating electrons in a 2-dimensional electron gas which are exposed to an electric field is given by

$$H_{\rm R} = \alpha_{\rm R}\mathbf{e}_z(\sigma \times \mathbf{k}) \ , \tag{3}$$

with the wave vector of the electrons in the 2-dimensional electron gas given by $\mathbf{k} = \mathbf{p}/\hbar$ and $\mathbf{e}_z$ the unit vector in z-direction. We assumed that the electric field is oriented along the z-direction, perpendicular to the plane of the 2-dimensional electron gas. The parameter $\alpha_{\rm R}$ is the Rashba parameter which is a measure for the strength of the spin-orbit coupling. In that given frame of reference the Hamiltonian can also be written as

$$H_{\rm R} = \alpha_{\rm R}(\sigma_x k_y - \sigma_y k_x) \ . \tag{4}$$

More stringent calculations show, that the Rashba coefficient is considerably larger than naively expected for free electrons in the 2-dimensional electron gas propagating in the electric field $\mathcal{E}$ [6]. The reason is, that the electrons not only experience the electric field $\mathcal{E}$ due to the macroscopic potential in the quantum well, but also the potential gradients due to the electron

orbitals of the atoms forming the crystal. This is also the reason, why the Rashba effect is particularly strong for crystals containing atoms with a large atomic number, i.e. In or Sb, since here the potential modulations are strong. As shown in Fig. 7(b), the Rashba effect results in an energy splitting. For electrons with two spin orientations being perpendicular to the electric field and the direction of propagation, the energy splitting for a given value of $|\mathbf{k}|$ can be expressed as

$$E_R = \pm\alpha_{\mathrm{R}}|\mathbf{k}| \ . \tag{5}$$

For a given fixed energy, e.g. the Fermi energy E_{F}, the wave vector difference Δk_{R} can be evaluated analytically [cf. Fig. 7(b)]

$$\Delta k_{\mathrm{R}} = \frac{2m^*\alpha_{\mathrm{R}}}{\hbar^2} \ . \tag{6}$$

Here, a parabolic band relation with a constant effective mass m^* was assumed. The spin orientations of the corresponding eigenstates are oriented perpendicular to the direction of motion in the plane of the 2-dimensional electron gas. As for free electrons aligned parallel or anti-parallel to an external magnetic field, one can also define an effective magnetic field

$$\mathbf{B}_{\mathrm{eff}} = \kappa\langle\mathbf{s}\rangle_+\Delta k_{\mathrm{R}} \ , \tag{7}$$

with

$$\langle\mathbf{s}\rangle_+ = \langle\psi_+|\widehat{s}|\psi_+\rangle \tag{8}$$

the spin expectation value belonging to the upper of the two energy branches E_+ and E_- shown in Fig. 7(b). κ is a parameter quantifying the strength of B_{eff} [7]. The eigenfunctions for each branch are $\psi^{\mathrm{R}}_{\pm}$ and can be written as

$$|\psi^{\mathrm{R}}_{\pm}(\mathbf{k}_\parallel)\rangle = \frac{e^{i\mathbf{k}_\parallel\mathbf{r}_\parallel}}{2\pi}\xi_{\mathbf{k}_\parallel}(z)\frac{1}{\sqrt{2}}\left|\begin{array}{c}1\\ \mp ie^{i\varphi}\end{array}\right\rangle \ , \tag{9}$$

with $\mathbf{k}_\parallel = \mathbf{k}_\parallel(\cos\varphi, \sin\varphi)$ the in-plane k vector described in polar coordinates and $\mathbf{r}_\parallel = (x, y, 0)$. The in-plane component of the wave function is described by a plane wave $\exp(i\mathbf{k}_\parallel\mathbf{r}_\parallel)$, while the envelope function of the confined state of the quantum well is given by $\xi_{\mathbf{k}_\parallel}(z)$.
According to the definition in Eq. (7), the effective magnetic field has the same orientation as $\langle\mathbf{s}\rangle_+$. In Fig. 8(a) the energy-momentum paraboloids are shown for the two Rashba spin-split branches. As can be seen here, the effective magnetic field is always perpendicular to the direction of the k-vector. The spin eigenvalues of the upper and lower branches are aligned parallel and anti-parallel to B_{eff}, respectively. In contrast to the Zeeman effect, where an external magnetic field is applied, here the orientations of the spin eigenvalues are not fixed for all k-values.

In case that for a given k-vector the spin state is not an eigenstate the spin is precessing around the effective magnetic field. This is illustrated in Fig. 9(a). This precession is the same as for free electrons with a magnetic moment $\mathbf{m}$ in an external magnetic field $\mathbf{B}$, where the torque leading to the spin precession is given by $\tau = \mathbf{m} \times \mathbf{B}$. Generally, the spin precession from an initial state $|\psi\rangle$ to a final state $|\psi'\rangle$ after a certain propagation of the electron can be described by a 2×2 rotation matrix U_{r}

$$|\psi'\rangle = U_{\mathrm{r}}|\psi\rangle \ . \tag{10}$$

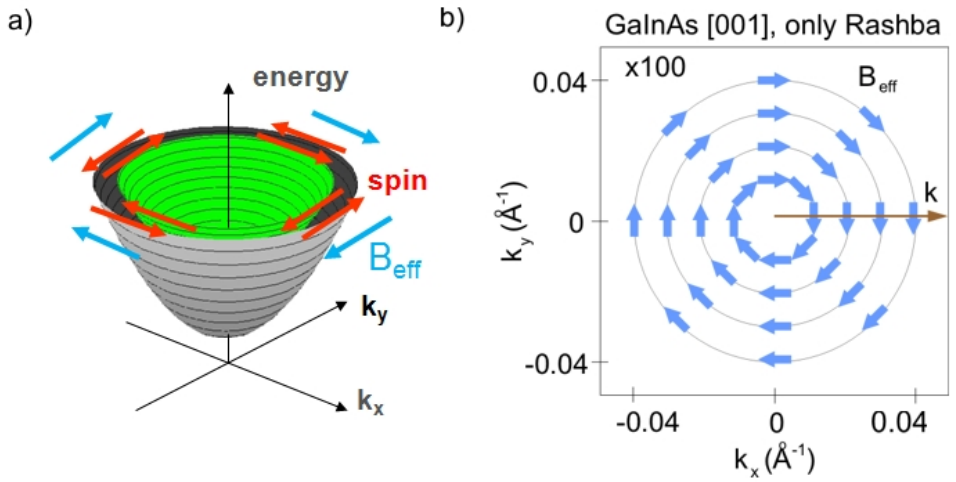

Fig. 8: *Energy-momentum dispersion for electrons in a 2-dimensional electron gas including the Rashba effect. The effective magnetic field is oriented perpendicularly to the corresponding k-vector. The spin eigenvalues are arranged clockwise and counter-clockwise around the energy axis. (b) Orientation of the effective magnetic field in k-space in the presence of the Rashba effect. (Figure adopted from Winkler [7]).*

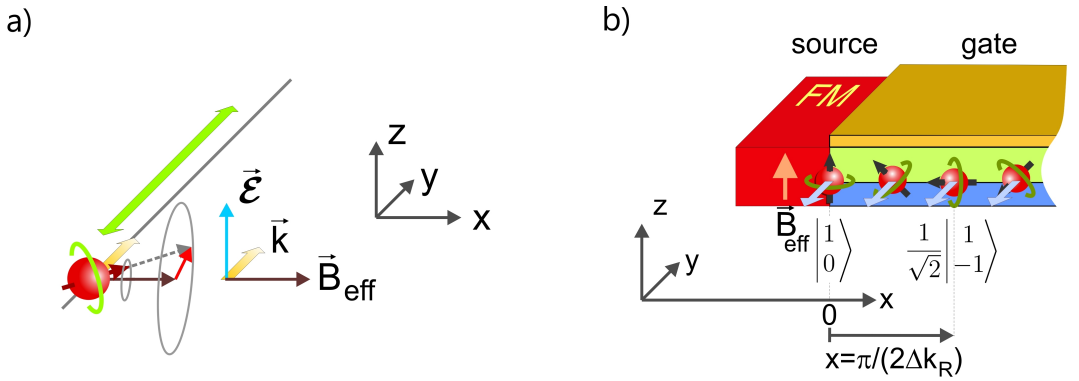

Fig. 9: *(a) Spin precession of the electron spin with the wave vector* $\mathbf{k}$ *around an effective magnetic field* $\mathbf{B}_{\text{eff}}$*. (b) Spin precession in a spin field-effect transistor. The magnetization of the source electrode is along the z-direction. The effective magnetic field* $\mathbf{B}_{\text{eff}}$ *is assumed to be along the $-y$-direction.*

To be more specific, let us consider the situation in a spin field-effect transistor. In Fig. 9(b) the area around the ferromagnetic source contact used as a spin injector is depicted. The electrons in the source contact are assumed to be polarized along the z-direction. Neglecting the contribution from the envelope function $\xi_{\mathbf{k}_\parallel}(z)$, the wave function at $x = 0$ is given by

$$|\psi_i(x=0)\rangle = \left| \begin{matrix} 1 \\ 0 \end{matrix} \right\rangle = \frac{1}{2}\left(\left| \begin{matrix} 1 \\ -i \end{matrix} \right\rangle + \left| \begin{matrix} 1 \\ i \end{matrix} \right\rangle \right) . \tag{11}$$

Here, the spin state along the z-direction is decomposed into the eigenstates for the electron propagation along the x-direction. These two basis states propagate the wave vectors are $k_x \mp \Delta k_{\mathrm{R}}/2$, respectively,

$$|\psi_i\rangle = \frac{1}{2}\left(\exp[i(k_x - \Delta k_{\mathrm{R}}/2)x] \left| \begin{matrix} 1 \\ -i \end{matrix} \right\rangle + \exp[i(k_x + \Delta k_{\mathrm{R}}/2)x] \left| \begin{matrix} 1 \\ +i \end{matrix} \right\rangle \right) \tag{12}$$

Owing to the different phase accumulations $(k_x \mp \Delta k_{\mathrm{R}}/2)x$, the spin vector after a distance x is given by

$$\langle \mathbf{s}(x) \rangle = \begin{pmatrix} \sin(-\Delta k_{\mathrm{R}} x) \\ 0 \\ \cos(\Delta k_{\mathrm{R}} x) \end{pmatrix} . \tag{13}$$

As can be seen in Fig. 9(b), the spin precesses around the effective magnetic field $\mathbf{B}_{\text{eff}} = (0, B_y, 0)$. After a distance $x = \pi/(2\Delta k_{\mathrm{R}})$ the spin is rotated by 90° about $\mathbf{B}_{\text{eff}}$.

Strength of the Rashba spin-orbit coupling

In order to calculate the strength of the Rashba coupling parameter in a 2-dimensional electron gas at a heterointerface, the band structure parameters of each semiconductor material (A,B), i.e. the band gap $E_{\mathrm{g}}^{\mathrm{A,B}}$ and the separation of the split-off band $\Delta_{\mathrm{so}}^{\mathrm{A,B}}$ need to be known [cf. Fig. 10(a)]. Furthermore, for the heterostructure formed by the low band gap material A and the large band gap material B the values of the conduction and valence band offsets ΔE_{c}, ΔE_{v}, and the offset between the split-off bands $\Delta_{\mathrm{so}}^{\mathrm{B}} - \Delta_{\mathrm{so}}^{\mathrm{A}}$ are required. In Fig. 10(b) the corresponding conduction and valence band profiles are depicted. By employing the so-called $k \cdot p$ theory the following formula for the Rashba-coupling parameter can be be derived [8]:

$$\begin{aligned} \alpha_{\mathrm{R}} \;=\; & \frac{\hbar^2 E_{\mathrm{p}}}{6m_0}\mathbf{e}_z \left\langle \xi \left| \left[\left(\frac{1}{(E_{\mathrm{g}}^{\mathrm{A}} + \Delta_{\mathrm{so}}^{\mathrm{A}})^2} - \frac{1}{(E_{\mathrm{g}}^{\mathrm{A}})^2} \right) (1 - \Theta_B(z))\varphi'(z) \right.\right. \right. \\ & \left.\left.\left. + \left(\frac{1}{(E_{\mathrm{g}}^{\mathrm{B}} - \Delta E_{\mathrm{c}} + \Delta_{\mathrm{so}}^{\mathrm{B}})^2} - \frac{1}{(E_{\mathrm{g}}^{\mathrm{B}} - \Delta E_{\mathrm{c}})^2} \right) \Theta_B(z)\varphi'(z) \right] \right| \xi \right\rangle \\ & + \frac{\hbar^2 E_{\mathrm{p}}}{6m_0}\mathbf{e}_z \sum_n \left(\frac{\Delta_{\mathrm{so}}^{\mathrm{B}} - \Delta_{\mathrm{so}}^{\mathrm{A}}}{2(E_{\mathrm{g}}^{\mathrm{B}} - \Delta E_{\mathrm{c}} + \Delta_{\mathrm{so}}^{\mathrm{B}})^2} + \frac{\Delta_{\mathrm{so}}^{B} - \Delta_{\mathrm{so}}^{A}}{2(E_{\mathrm{g}}^{\mathrm{A}} + \Delta_{so}^{\mathrm{A}})^2} \right. \\ & \left. - \frac{\Delta E_{\mathrm{c}}}{2(E_{\mathrm{g}}^{\mathrm{B}} - \Delta E_{\mathrm{c}})^2} - \frac{\Delta E_{\mathrm{c}}}{2(E_{\mathrm{g}}^{\mathrm{A}})^2} \right) |\xi(z_0)|^2 . \end{aligned} \tag{14}$$

Here, $E_{\mathrm{p}} = (\hbar/m_0)\langle S|p_x|X\rangle$ is the $k \cdot p$ interaction parameter, which describes the interaction between the conduction band $|S\rangle$ and the valence bands $|X\rangle$. The macroscopic electrical potential energy is given by $\varphi(z)$.

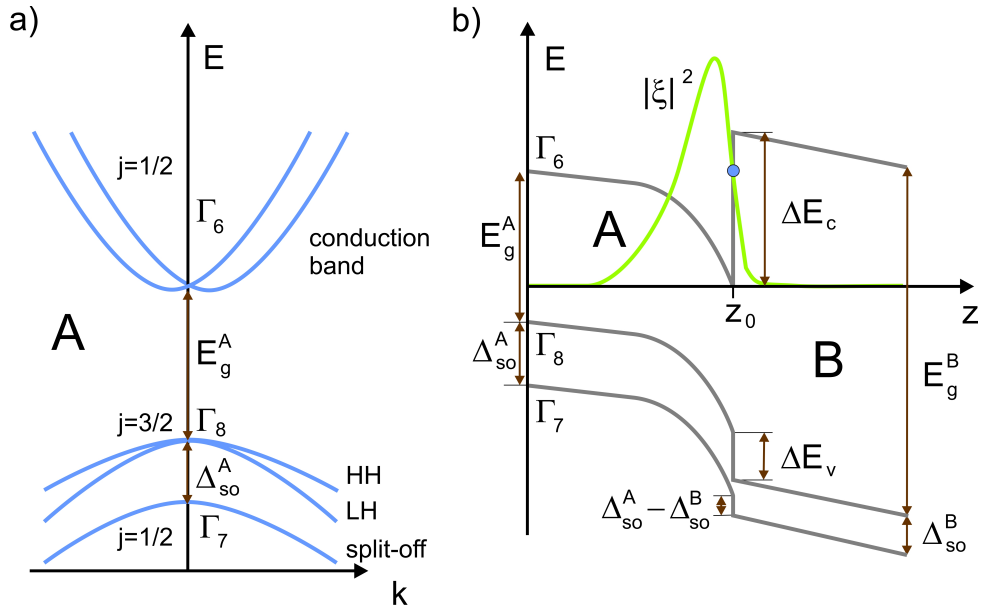

Fig. 10: *(a) Schematic band structure of a III-V semiconductor (material A), with an energy band gap $E_{\mathrm{g}}^{\mathrm{A}}$. The split-off band is separated by $\Delta_{\mathrm{so}}^{\mathrm{A}}$ from the light and heavy hole band. (b) Profile of the conduction and valence band at the interface of a semiconductor with a smaller (A) and and larger (B) band gap. $E_{\mathrm{g}}^{\mathrm{A}}$ and $E_{\mathrm{g}}^{\mathrm{B}}$ denote the band gaps of semiconductor A and B, respectively, while ΔE_{c} and ΔE_{v} denote the conduction and valence band offsets, respectively. Also shown is $|\psi|^2$ of the wave function in the quantum well.*

Although Eq. (14) looks rather complicate, some general requirements can be formulated to gain a large value of α_{R}. First of all, due to the inverse of the squared energies, a small band gap is advantageous. Furthermore, in order to prevent that the differences in Eq. (14) are not canceled out, $\Delta_{\mathrm{so}}^{\mathrm{A,B}}$ should be as large as possible. Thus, the Rashba spin-orbit coupling parameter is directly connected to the spin-orbit coupling in the valence band. This reflects, that the Rashba effect originates from the coupling of the upper valence band and the split-off valence band to the conduction band. The smaller the energy differences between the valence band and the conduction band, the larger is the coupling. The coupling itself is quantified by the interaction parameter E_{p}.
In a spin field-effect transistor the potential profile can be tilted by applying a gate voltage. According to Eq. (14) this leads to a modification of the Rashba coupling parameter α_{R}. Since the spin precession is determined by α_{R}, the orientation of the spins arriving at the drain current and thus the resistance between source and drain can be controlled.

Dresselhaus term

Beside the Rashba spin-orbit coupling there is another contribution, the so-called Dresselhaus term, which results in a spin-splitting of the conduction band. The origin of this effect lies in the symmetry of the crystal. Let us first consider a crystal structure with an inversion center. A typical lattice is the diamond lattice, as shown in Fig. 11(a). As indicated here, the crystal possesses an inversion center, thus the crystal is spatial inversion symmetric.
Owing to this spatial inversion symmetry of the lattice potential in the Hamiltonian the electron

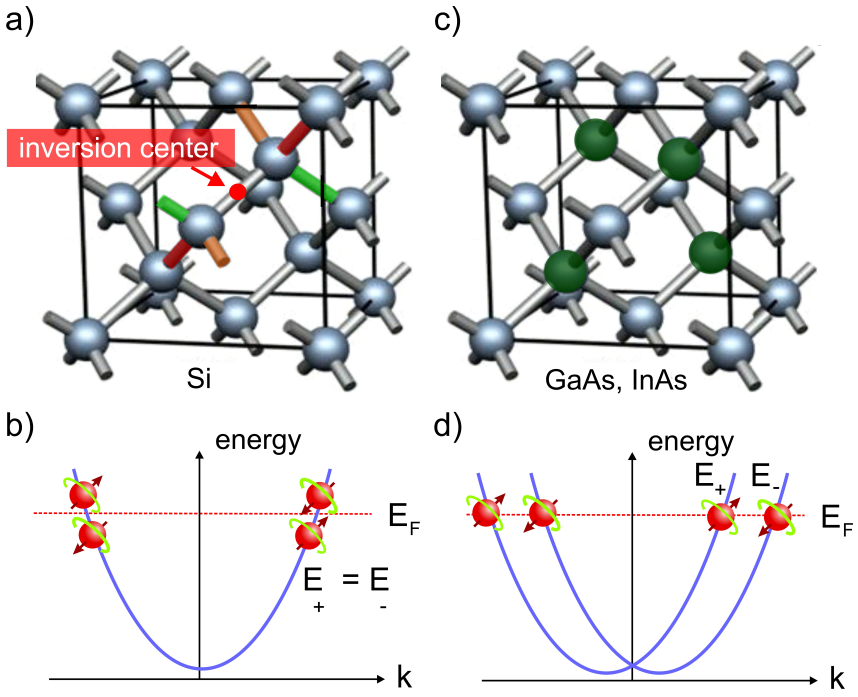

Fig. 11: *(a) Diamond lattice with an inversion center located in between two atoms in the lattice. The colored bars indicate the corresponding inversion symmetric bonds. A typical semiconductor with a diamond lattice is Si. (b) Energy-momentum relation in case of inversion symmetry, where the states are spin degenerate. (c) In the zincblende crystal no inversion center is found because every second site in the lattice contains a different atom. Typical semiconductors with a zincblende configuration are GaAs or InAs. (b) Energy-momentum relation in case of no inversion symmetry, where the spin degeneracy is lifted.*

energy must be the same under inversion of the k-vector

$$E_{\pm}(\mathbf{k}) = E_{\pm}(-\mathbf{k}) \ . \tag{15}$$

with $\pm$ indicating the spin-up and spin-down orientations, respectively. Furthermore, in the absence of a magnetic field time-inversion symmetry (Kramer's degeneracy) holds, which implies

$$E_{+}(\mathbf{k}) = E_{-}(-\mathbf{k}) \ . \tag{16}$$

Combining both symmetry relations results in

$$E_{+}(\mathbf{k}) = E_{-}(\mathbf{k}) \ . \tag{17}$$

Thus, the energies of the two spin orientation for any k-vector are degenerate. No spin-splitting of the energy levels can occur in principle due to symmetry reasons [cf. Fig. 11(b)].
In a crystal lattice which does not posses an spatial inversion center, e.g. a zincblende lattice as it found for most III-V semiconductor [cf. Fig. 11(b)], the energies for a particle under reversal of the k-vector are not equal any more

$$E_{\pm}(\mathbf{k}) \neq E_{\pm}(-\mathbf{k}) \ . \tag{18}$$

This together with the time inversion symmetry Eq. (16), which still holds, one finds that in general $E_{+}(\mathbf{k})$ is not the same as $E_{+}(\mathbf{k})$. Thus the spin degeneracy in the conduction band is lifted, as illustrated in Fig. 11(d). Only at $k = 0$ the states are degenerate.
Following from the general considerations given above, in a lattice which does not possess an inversion center another spin-splitting contribution is found in addition to the Rashba effect. This contribution is due to the internal electric field in the crystal, which is not canceled out due to the lack of inversion symmetry. This results in an additional spin-orbit coupling term. For zincblende crystals this contribution is called Dresselhaus term or bulk inversion asymmetry term [9]. For a 2-dimensional electron gas in the xy-plane the corresponding Hamiltonian is given by

$$H_{\mathrm{D}} = \eta \left[\sigma_x k_x \left(k_y^2 - \langle k_z^2 \rangle \right) + \sigma_y k_y \left(\langle k_z^2 \rangle - k_x^2 \right) \right] \ . \tag{19}$$

The Dresselhaus term contains k^3-contributions. That is the reason why it is also called cubic spin-orbit contribution. In case of a 2-dimensional electron gas the expectation value of $\langle k_z^2 \rangle$ has to be inserted for the confinement direction. In contrast to $\langle k_z \rangle$ this is non-zero. For strong confinement one can assume $\langle k_z^2 \rangle \gg k_x^2, k_y^2$. In that case Eq. (19) can be approximated by a linearized form

$$H_{\mathrm{D}} = \beta_{\mathrm{D}} \left(\sigma_y k_y - \sigma_x k_x \right) \ , \tag{20}$$

with $\beta_{\mathrm{D}} = \eta \langle k_z^2 \rangle$.

4 Electron interference effects

The strength of spin-orbit coupling in semiconductor structures can be analyzed by means of the weak-antilocalization effect, which is is an extension of the weak-localization effect by including spin precession. Weak-localization is an electron interference effect, where an increase of the sample resistance is observed due to electron localization. If spin-orbit coupling is present, the opposite behavior is found, i.e. a decrease of the resistance. Below, first the basics of the weak localization will be explained, while in the second part spin-orbit coupling will be included into the interference effects.

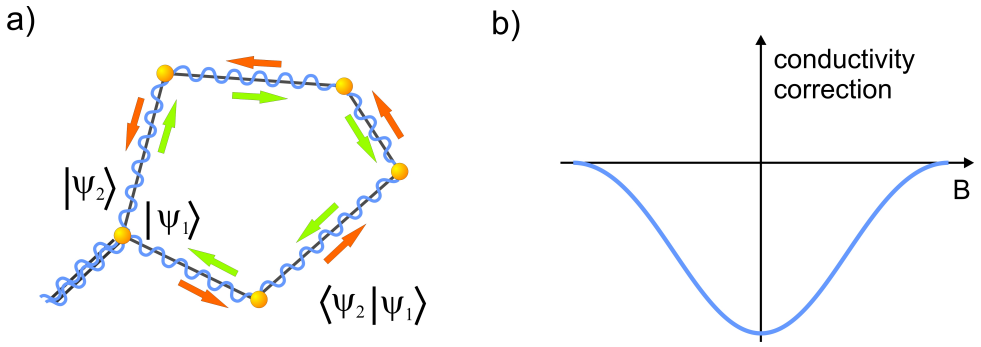

Fig. 12: *(a) Electron interference in closed loops leading to the weak localization effect. (b) Conductivity correction due to weak localization: The conductivity at zero magnetic field is reduced.*

Weak localization

Interference effects of electron waves can be observed in samples where the phase coherence length l_φ is much smaller than the dimensions of the sample. This effect is called weak localization. It is observed if the temperature is sufficiently low so that the phase coherence time τ_ϕ is larger than the elastic scattering time.
In a diffusive conductor with many scattering centers there are usually many possible electron trajectories from a starting at point A and to a second point Q. If we assumed that the elastic mean free path l_e is considerably smaller than the distance between these two points, an electron undergoes many elastic scattering events on its way. However, during elastic scattering the electron does not lose its phase memory. Since the phase coherence length l_φ is assumed to be much longer than the distance between A and Q we can assume that the phase information is not lost. After Feynman we can describe each path j by a complex amplitude given by

$$A_j = C_j e^{i\varphi_j} \ . \tag{21}$$

Here, φ_j is the phase shift the electron acquires on its way from A to Q due to propagating a certain distance. The total probability P_{AQ} for an electron to be transported from A to Q is determined by the square of the total amplitude

$$P_{AQ} = |\sum_j A_j|^2 = \left|\sum_j C_j e^{i\varphi_j}\right|^2 \ . \tag{22}$$

In systems with a large number of possible paths usually the phases φ_j are randomly distributed. Therefore, owing to averaging, the wave nature should have no effect on the electron transport. The fact, that nevertheless an increase of the resistance is observed compared to the classical transport, is a result of closed loops. A typical closed loop is shown in Fig. 12(a). Along these loops, an electron can propagate in two opposite orientations with the corresponding complex amplitudes $A_{1,2} = C_{1,2}\exp(i\varphi_{1,2})$. The current contribution of the current returning to the starting point of the loop (O) is given by

$$P_{OO} = |A_1 + A_2|^2 = |C_1|^2 + |C_2|^2 + 2\mathrm{Re}(C_1^* e^{-i\varphi_1} C_2 e^{i\varphi_2}) \ . \tag{23}$$

Since for time reversed pathes $C_1 = C_2$ and $\varphi_1 = \varphi_2$, we obtain

$$|A_1 + A_2|^2 = 4|C_1|^2 \ . \tag{24}$$

For classical non-phase coherent transport regime the probability would simply be $|C_1|^2+|C_2|^2$, which is a factor of two smaller than for the phase coherent transport. A larger probability to return to the origin implies that the current through the sample is reduced. The carriers are *localized* in the loop. The localization does not dependent on the size of the loop as long as its length is smaller than the phase coherence length. It is important to notice that constructive interference occurs for *all* possible closed loops in the conductor and it is thus not averaged out. As a result, the total resistance is increased compared to the classical case.
If the sample is penetrated by a magnetic field the phase accumulation is modified due to the additional contribution of the vector potential $\mathbf{A}$. The additional accumulated phase along a closed loop with area S is expressed by

$$C_1 \rightarrow C_1 \exp\left(\frac{ie}{\hbar}\oint \mathbf{A}d\mathbf{l}\right) = C_1 \exp\left(i\frac{2\pi\Phi}{\Phi_0}\right) \ , \tag{25}$$

where $\mathbf{A}$ is the vector potential, Φ is the magnetic flux penetrating the loop, and $\Phi = h/e$ is the magnetic flux quantum. For a propagation in the opposite direction one obtains

$$C_2 \rightarrow C_2 \exp\left(-i\frac{2\pi\Phi}{\Phi_0}\right) \ . \tag{26}$$

The phase difference between both trajectories is therefore

$$\Delta\varphi = 2\pi\frac{2\Phi}{\Phi_0} \ . \tag{27}$$

Thus by the presence of a vector potential the localization is partially lifted. In a diffusive conductor usually many loops of different sizes are found. For a particular magnetic field the localization is lifted to a different extent depending on the size of the loops. On average the degree of localization decreases with increasing magnetic field, which results in a continuous decrease of the resistance.

Weak antilocalization

So far spin effects were neglected, which means that the spin orientation was assumed to be preserved when the electron propagated along a closed loop. Here, we will discuss the case that the spin orientation is altered while the electron moves through the sample. One possible mechanism which leads to a change of the spin orientation is the Rashba spin-orbit coupling [5]. As discussed above, it leads to a precession of the spin during its propagation. Other possible effects leading to a change of the spin orientation are spin-orbit coupling due to crystal lattice asymmetry [9] or spin-orbit scattering at impurities [10]. In contrast to the weak localization effect, the presence of spin-orbit coupling can result in a decrease of the sample resistance around zero magnetic field.
Below, we will give a simple explanation of the weak antilocalization, following the approach by Bergmann [11]. When the spin orientation is altered while the electron is propagating in a closed loop, the interference is not necessarily constructive as for the spin-conserving weak localization case. For the latter the interference is always constructive at zero magnetic field, no matter which shape the closed loops have. If we take into account a change of the spin orientation, the total spin rotation after the propagation through a closed loop depends on the geometry of this particular loop and/or the spin-orbit scattering at impurities. Thus each particular loop

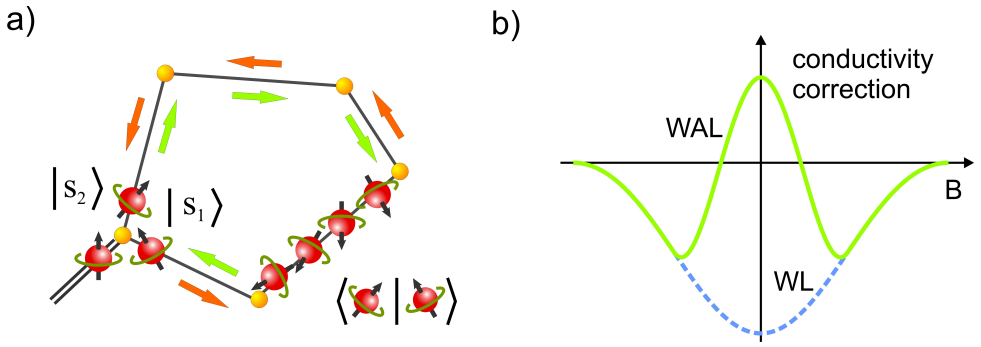

Fig. 13: *(a) Electron interference in closed loops leading to the weak antilocalization effect. Here spin precession due to spin-orbit coupling is included. (b) The weak antilocalization effect (WAL) leads to an enhanced conductivity at zero magnetic field, whereas the weak localization effect (WL) leads to a decrease of the conductivity.*

causes a different spin rotation of the electrons. In order to calculate the total interference amplitude the spin rotation has to be included. It will be shown below that due to averaging effects of different interference amplitudes destructive interference can dominate, which leads to an enhanced conductance.
Let us first analyze the interference effects in arbitrarily chosen closed loop if spin-orbit coupling is present. The spin-related effects can be summarized by assigning a total spin rotation after propagation along the loop. Most generally the rotation of a spin 1/2 particle can be represented by three characteristic rotation angles β, θ and α (Euler's angles), where the rotation is decomposed in three rotations about certain axes. The first and third rotation (β, α) are about the z-axis, while the second rotation (θ) is about the y-axis. The corresponding matrices which have to be applied to the spin state represented by the spinors are

$$U_r = R_z(\alpha)R_y(\theta)R_z(\beta) = \begin{pmatrix} e^{i\alpha/2} & 0 \\ 0 & e^{-i\alpha/2} \end{pmatrix} \begin{pmatrix} \cos\theta/2 & \sin\theta/2 \\ -\sin\theta/2 & \cos\theta/2 \end{pmatrix} \begin{pmatrix} e^{i\beta/2} & 0 \\ 0 & e^{-i\beta/2} \end{pmatrix} . \quad (28)$$

By multiplying the three matrices given above, the general rotation matrix can be written as

$$U_r = \begin{pmatrix} e^{i/2(\alpha+\beta)}\cos\theta/2 & e^{i/2(\alpha-\beta)}\sin\theta/2 \\ -e^{-i/2(\alpha-\beta)}\sin\theta/2 & e^{-i/2(\alpha+\beta)}\cos\theta/2 \end{pmatrix} . \quad (29)$$

Thus, we can express the final state $|s'\rangle$, resulting from the rotation of the initial spin state $|s\rangle$ after propagation along a closed loop by

$$|s'\rangle = U_r|s\rangle . \quad (30)$$

For the propagation in opposite direction, the spin rotation is reversed so that the final spin state is given by

$$|s''\rangle = U_r^{-1}|s\rangle . \quad (31)$$

Regarding the localization effects we are interested in the amplitude of the interference of the two states after propagation in opposite orientations along the loop

$$\langle s''|s'\rangle = \langle (U_r^{-1}s)|(U_r s)\rangle = \langle s|\left(U_r^{-1}\right)^\dagger U_r|s\rangle = \langle s|U_r^2|s\rangle . \quad (32)$$

Here, we made use of the property that U_r is a unitary transformation, so that $U_r^\dagger = U_r^{-1}$. The square of U_r is given by the matrix

$$U_r^2 = \begin{pmatrix} e^{i/2(\alpha+\beta)}\cos^2\frac{\theta}{2} - \sin^2\frac{\theta}{2} & \frac{1}{2}\left(e^{i\alpha}+e^{-i\beta}\right)\sin\theta \\ -\frac{1}{2}\left(e^{-i\alpha}+e^{i\beta}\right)\sin\theta & e^{i/2(\alpha+\beta)}\cos^2\frac{\theta}{2} - \sin^2\frac{\theta}{2} \end{pmatrix} . \tag{33}$$

If the original spin state has the form (a, b) one obtains for the expectation value of U_r^2

$$e^{i(\alpha+\beta)}\cos^2\frac{\theta}{2} - \sin^2\frac{\theta}{2} + \frac{1}{2}\sin\theta\left[a^*b\left(e^{i\alpha}+e^{-i\beta}\right) + \text{c.c.}\right] . \tag{34}$$

In order to understand, under which condition weak antilocalization occurs one has to analyze this expression. For strong spin-orbit coupling the orientation of the final spin states are distributed statistically. The only term, which does not vanish after averaging over all angle is $\sin^2(\theta/2)$, since it can be written as $(\cos\theta - 1)/2$, it yields a factor of $-1/2$. Thus the destructive interference dominates for the case of strong spin scattering. In contrast, if there is no spin rotation $\alpha,\ \beta,\ \theta = 0$, only the $\cos^2$-term in Eq. (34) remains. Thus in this case only constructive interference occurs, leading to the well-known weak localization effect. Please note, that the weak antilocalization effect is by a factor of $1/2$ smaller compared to the weak localization effect.
In Fig. 14(a) the weak antilocalization effect in a GaInAs/InP 2-dimensional electron gas is shown for different gate voltages. As can be seen here, for smaller electron concentrations at more negative gate voltages the weak antilocalization feature is more pronounced. This is due to the fact that here the mobility and thus the elastic mean free path is smaller. By fitting the experimental signature of the weak antilocalization to a theoretical model [12], the Rashba coupling coefficient can be extracted [cf. Fig. 14(b)] [13]. As can be seen here, by changing the gate voltage and thus changing the electron concentration the strength of the Rashba coupling parameter can be changed. This mechanism is the essential ingredient for the operation of the spin field-effect transistor.

5 Rashba effect in quasi-one-dimensional structures

So far, we only considered spin-orbit coupling in 2-dimensional electron systems. However it was already pointed out by Datta and Das [1] that a better signal modulation is expected if the transport is restricted to only one dimension. In addition, many concepts of spin electronic devices rely on 1-dimensional transport channels.

Rashba effect in planar quasi one-dimensional structures

One possible way to include spin-orbit coupling in a 1-dimensional structure is to assume a 2-dimensional electron gas which is additionally confined by a harmonic confinement potential

$$V(x) = \frac{1}{2}m^*\omega_0^2 x^2 , \tag{35}$$

where ω_0 is the characteristic oscillator frequency. The advantage of using a parabolic confinement potential is, that a magnetic field can be included relatively easily. The energy eigenvalues of the 1-dimensional system can be determined by numerical diagonalization of the Hamilton

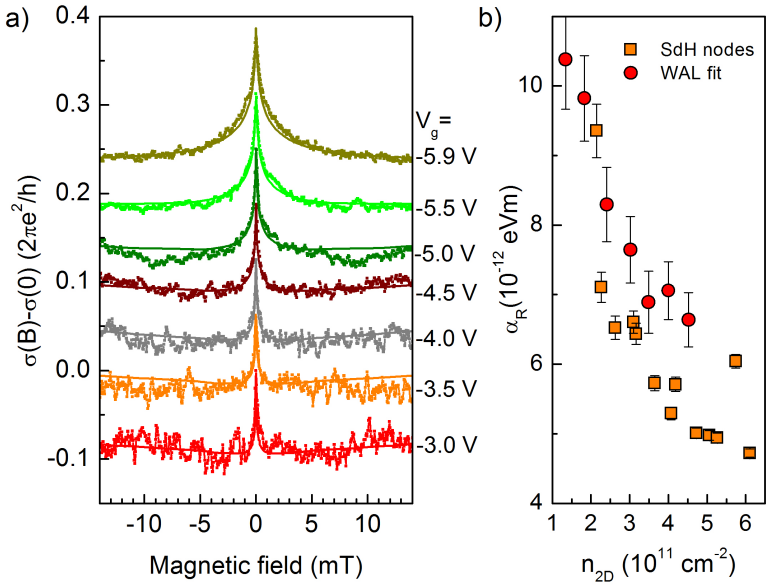

Fig. 14: *(a) Weak antilocalization in a GaInAs/InP 2-dimensional electron gas for various gate voltages (b) Rashba coefficient as a function of electron concentration determined from the beating pattern in the Shubnikov–de Haas oscillations and from weak antilocalization measurements.*

matrix, using the eigenfunctions of the harmonic oscillator. In order to compare the confinement effects with the effects due to the Rashba spin-orbit coupling the characteristic Rashba spin-orbit coupling energy

$$\Delta_{\mathrm{R}} = \frac{m^*}{2\hbar^2}\alpha_{\mathrm{R}}^2 \tag{36}$$

can be related to the confinement energy $\hbar\omega_0$. In Fig. 15 typical energy-momentum dispersions of 1-dimensional systems with a harmonic confinement potential are shown. In Fig. 15(a) the Rashba coupling energy is small compared to the confinement energy $\Delta_{\mathrm{R}}/\hbar\omega_0 = 0.01$. Here, one finds a Rashba splitting of each subband. No coupling between neighboring bands is observed. The situation differs for a stronger Rashba contribution $\Delta_{\mathrm{R}}/\hbar\omega_0 = 1$. In this case an anti-crossing of bands is observed. In this range a superposition the two anti-crossing spin states occurs. Thus, the spin orientations do not correspond to the usual spin orientations of the bands far away from the anti-crossing area.

Rashba effect in tubular structures

Very interesting alternative systems for employing the Rashba effect in quasi 1-dimensional systems are semiconductor nanowires. As depicted in Fig. 4(a) for semiconductors with a small band gap, i.e. InAs, InSb or InN, a surface accumulation layer is formed. The electrons are confined in a triangular quantum well. The strong potential gradient and the corresponding electric field lead to the presence of the Rasbha spin-orbit coupling. Usually the cross section of a semiconductor nanowire has a hexagonal shape due to the different crystal facets on the

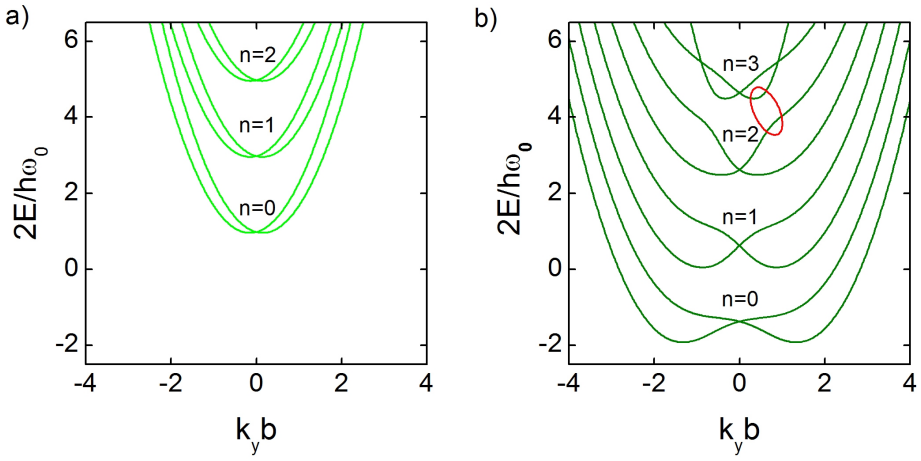

Fig. 15: *Energy-momentum dispersion relation for a one-dimensional conductor with a parabolic confinement potential along the x-direction. The k_z vector is normalized to the oscillator length $b = \sqrt{\hbar/m^*\omega_0}$, while the energy is normalized to $\hbar\omega_0/2$. (a) Weak coupling limit for $\Delta_{\rm R}/\hbar\omega_0 = 0.01$ (b) Strong coupling limit for $\Delta_{\rm R}/\hbar\omega_0 = 1$.*

side walls of the nanowire. However, for the sake of simplicity we will assume a cylindrical shape of the nanowires.
In a cylindrical coordinate system the wave function can be expressed as

$$\psi(\mathbf{r}) = \exp(ikz)\exp(il\phi)\, f(r) \ . \tag{37}$$

It is a product of exponential functions in z and ϕ, the coordinate along the axis, and the azimuthal angle around the axis respectively, and a radial distribution function $f(r)$. Furthermore, k is the wave vector for the free motion along the wire, while l is the angular momentum number.
Owing to the electric field $\mathcal{E} = -\nabla V/e$ across the surface of the cylinder the spin of the electron is coupled to its orbital motion. The corresponding contribution to the Hamiltonian can be written as [14]

$$\begin{aligned} H_{\rm R} &= \sigma \cdot [\mathbf{p} \times e\mathcal{E}]\, \frac{\gamma}{\hbar} \\ &= \gamma V' \left[\begin{pmatrix} 0 & i\, e^{-i\phi} \\ -i\, e^{i\phi} & 0 \end{pmatrix} \frac{\partial}{i\partial z} \right. \\ &\quad \left. + \begin{pmatrix} 1 & 0 \\ 0 & -1 \end{pmatrix} \frac{\partial}{ri\partial\phi} \right] . \end{aligned} \tag{38}$$

Owing to the radial symmetry one cannot assign a Rashba coupling parameter but rather use the electric field $\mathcal{E}(\mathbf{r})$ which is oriented along the radial coordinate and the coupling-strength γ is determined by the band structure of the cylinder material (1.17 nm^2 for InAs) [6].
The stationary states are eigenstates of the total angular momentum $\hat{j}_z = \hat{l}_z + \hat{s}_z$, with $\hat{s}_z = \hbar\sigma_z/2$ with eigenvalues $j = l \pm 1/2$. The spinor is of the form:

$$\left| \begin{matrix} \psi_\uparrow \\ \psi_\downarrow \end{matrix} \right\rangle = e^{ikz} e^{il\phi} \left| \begin{matrix} f(r) \\ ie^{i\phi} h(r) \end{matrix} \right\rangle \ . \tag{39}$$

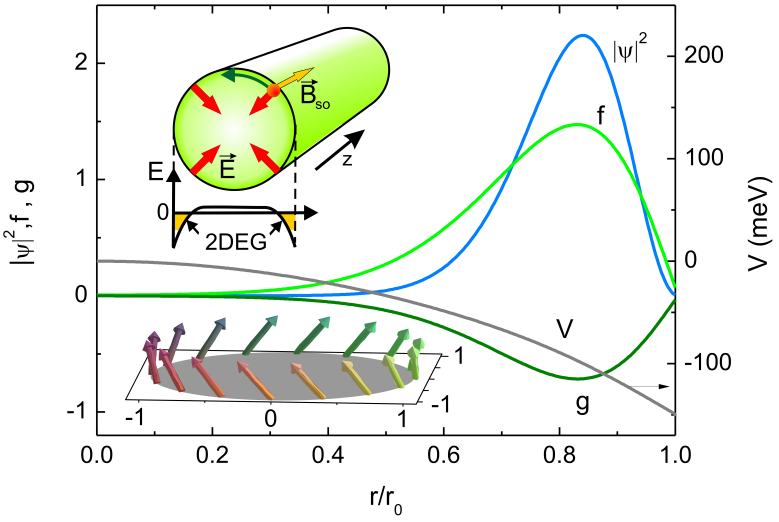

Fig. 16: *Squared amplitude of the wave function $|\psi|^2$ with the corresponding the spinor components f and h and the conduction band profile V as a function of the normalized radius r/r_0 for $j = 1/2$. The radius r_0 is assumed to be 50 nm. The upper inset depicts a schematic illustration of the nanowires, including the relevant electric and magnetic fields. The lower inset shows the spin orientation along the circumference for $j = 1/2$.*

Here, f and h are real functions and solve the differential equations

$$\begin{aligned} -\frac{\hbar^2}{2m^*}\left(f'' + \frac{1}{r}f'\right) + \left(\widetilde{V}_{l,+} - \widetilde{E}\right) f &= k\gamma V' h \,, \\ -\frac{\hbar^2}{2m^*}\left(h'' + \frac{1}{r}h'\right) + \left(\widetilde{V}_{l+1,-} - \widetilde{E}\right) h &= k\gamma V' f \,. \end{aligned} \tag{40}$$

The potential $\tilde{V}_{l,\pm} = (\hbar l)^2/(2m^* r^2) + V \pm \gamma V' l/r$ contains the contributions of the centrifugal force and the diagonal spin-orbit term while $\tilde{E} = E - (\hbar k)^2/(2m^*)$ is the energy without the axial kinetic energy. At the wire boundary we assumed a barrier of infinite height.[2]
In Fig. 16 the squared amplitude $|\psi|^2$ is shown for $j = 1/2$ at k_F. Also shown are the components f and h of the spinor given by Eq. (39). By knowing f and h, the spin expectation values in different orientations can be determined by integration over the corresponding spin densities. One finds that the spin density in radial direction is zero. The tangential component of the spin density is given by

$$s_T = \begin{pmatrix} \psi_\uparrow^* \\ \psi_\downarrow^* \end{pmatrix} \begin{pmatrix} 0 & -i\, e^{-i\phi} \\ i\, e^{i\phi} & 0 \end{pmatrix} \begin{pmatrix} \psi_\uparrow \\ \psi_\downarrow \end{pmatrix} = 2fh. \tag{41}$$

[2]By assuming an infinite barrier at the wire boundary the leakage of the wave function into the barrier is neglected. As has been shown above, the leakage of the wave function can contribute significantly to the Rashba effect [8, 6]. However, since the InAs interface to the environment, e.g. to vacuum, cannot be described with sufficient accuracy, it was decided to assume a barrier of infinite height nonetheless [15].

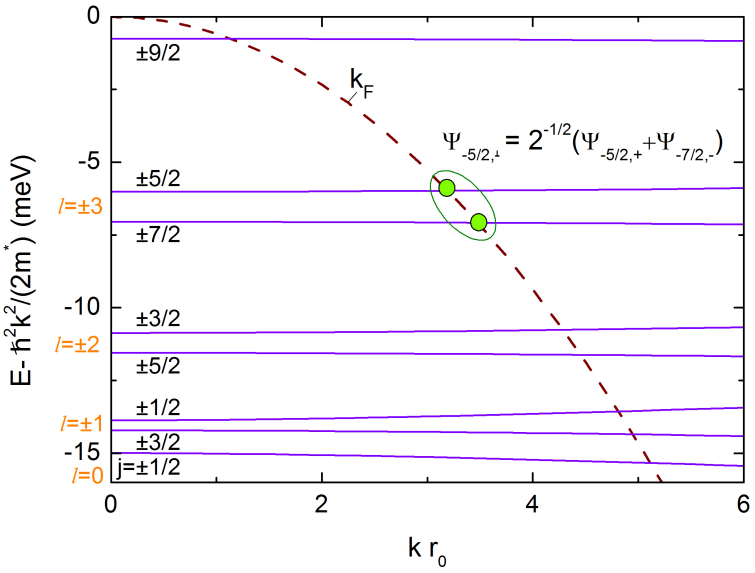

Fig. 17: *Energy vs. k dispersion. The dashed line indicates the axial kinetic energy left out, which crosses the bands at k_F. The pair of dots represent states forming the superpositions states $\psi_{-5/2,\perp} = \psi_{-5/2,+} + \psi_{-7/2,-}$ shown in Fig. 18.*

The component along the wire axis is

$$s_z = \begin{pmatrix} \psi_\uparrow^* \\ \psi_\downarrow^* \end{pmatrix} \begin{pmatrix} 1 & 0 \\ 0 & -1 \end{pmatrix} \begin{pmatrix} \psi_\uparrow \\ \psi_\downarrow \end{pmatrix} = f^2 - h^2. \tag{42}$$

In Fig. 16 the spin orientation along the circumference is shown for $j = 1/2$. It can be seen that the spin has a tangential and axial component only.
In Fig. 17 the energy $\tilde{E}$ versus k is shown for several j-values. The axial kinetic energy was left out in this plot. The corresponding Fermi wave vectors are indicated by the dashed line. At $k = 0$ the coupling between l and $l + 1$ vanishes [cf. Eq. (38)]. Therefore a classification with respect to l is possible. The splitting between the second and third band ($l = \pm 1$) is caused by the diagonal part of H_R and increases proportional to l for the higher states. All bands are twofold degenerate, since states with a reversed angular momentum and spin have the same energy.
Generally, the states defined by Eq. (39) are non-precessing eigenstates, thus the spin does not change its orientation while the electron propagates along the nanowire. However, by superposition of these states a spin precession can be achieved. This is shown in Fig. 18(a) where the spin orientation of the $\psi_{-5/2,\perp}$ state (being a superposition of the states $\psi_{-5/2,+}$ and $\psi_{-7/2,-}$) at the Fermi energy is shown. Here, $j = -5/2$ and $-7/2$ are the corresponding total angular momentums. The $(+)$ and $(-)$ state originates from $(\psi_l, 0)$ and $(0, \psi_{l+1})$, respectively. It was assumed that at $z = 0$ the spin is injected along the $-y$ direction, e.g. by means of a spin injector electrode. The spin is precessing counter-clockwise. However, owing to the twofold degeneracy of the states, a corresponding superposition state exists, with a clockwise spin precession. Since both states are present simultaneously both contributions are superimposed,

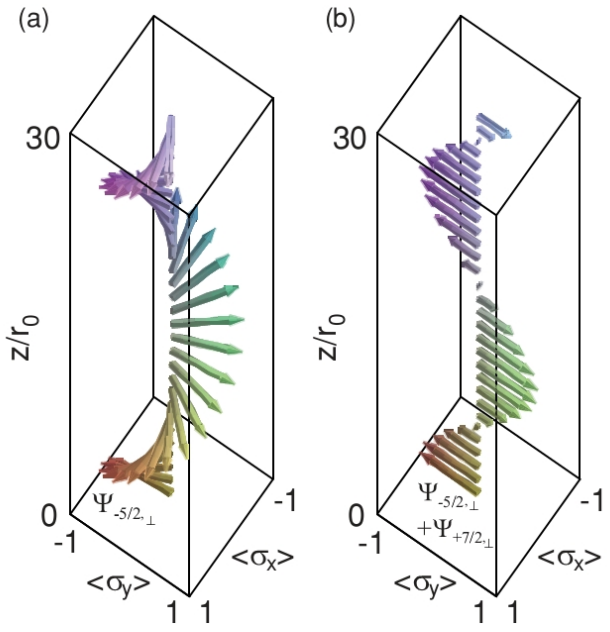

Fig. 18: *(a) Counter-clockwise spin precession of electrons in the superposition state* $\psi_{-5/2,\perp}$ *at the Fermi energy constituted of the states* $\psi_{-5/2,+}$ *and* $\psi_{-7/2,-}$ *for a propagation along the wire axis from* $z/r_0 = 0$ *to* 30*. (b) Spin orientation of the sum of the contribution shown in (a) and the corresponding clockwise contribution* $\psi_{+7/2,\perp}$ *being a superposition of* $\psi_{+7/2,+}$ *and* $\psi_{+5/2,-}$*.*

finally leading to the oscillating spin density shown in Fig. 18(b).

6 Spin-orbit quantum-bits

Spin-orbit coupling can also be employed to control the spin orientation in a quantum dot qubit by electrical means. This technique is called electric-dipole spin-resonance (EDSR). In contrast to electron spin resonance (ESR) where an oscillating magnetic field induces spin transitions, here an oscillating electric field $\mathcal{E}(t)$ is used. We will first describe the double quantum dot system and the spin blockade. Subsequently, the theoretical background of the EDSR mechanism in a quantum dot structure will be introduced. Finally, the corresponding measurements will be shown.

Spin-blockade in a double quantum dot

In Fig. 19 a schematics illustration of a double dot structure based on a 2-dimensional electron gas is shown [16]. By applying negative voltages to the gate electrodes the electron gas underneath is depleted forming a double dot structure. The two dots are tunnel-coupled by a barrier imposed by the center gate electrodes. The quantum dots can be filled and emptied by tunneling through the upper two split-gate openings. The properties of the double-dot systems is measured by the current flowing from the left to the right quantum dot. For the experiments described below an in-plane external magnetic field $\mathbf{B}$ is applied to induce a Zeeman energy splitting.

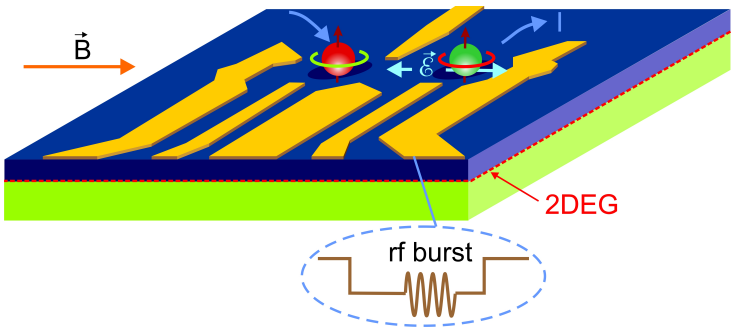

Fig. 19: *Schematic illustration of a double quantum dot realized in a 2-dimensional electron gas (2DEG). The external magnetic field is oriented in-plane. On the right-hand-side gate the a rf burst is applied to induce EDSR.*

For the EDSR experiments the double quantum dot has to be prepared in the spin-blockade state [16]. The underlying sequence is depicted in Fig. 20. Let us assume that the right-hand quantum dot is occupied with a spin-up electron. By applying an appropriate bias to the left reservoir the left-hand quantum dot is filled with an electron. The spin orientation can either be up or down. In case that the spin in the left-hand dot is in the up-state a triplet T_+ (1,1) state in the coupled double dot system is formed, with (1,1) denoting single electron occupation in the left- and right-hand dot, respectively. The transfer of this electron from the left to the right dot is blocked, since the dot occupied with two electrons would be in a triplet T_+ (0,2) state, which is energetically too high. Since the transfer of the electron from the left is blocked due to its spin orientation, this is called *spin blockade*. The same is true, if the electron in the right-hand dot is in a spin-down state and the second electron entering from the left is also in a spin-down state forming a double-dot triplet T_- (1,1) state. Once again, the transfer is blocked, since the energy of the double-occupied T_- (0,2) state is too high. If in the double-dot system is in a singlet state S (1,1) a transfer to the singlet S (0,2) state is possible. In case that the double dot is in the triplet state T_0 (1,1) a transfer is not possible directly. However, due to the interaction with the nuclear field B_{nucl} of the GaAs lattice a transfer into the S (1,1) can happen, so that a transfer to the S (0,2) state can be achieved. In general, only if the singlet state S (0,2) state is reached, the second electron can leave the double dot system on the right-hand side, so that a current flows. For the EDSR studies, the double-dot system has to be prepared in the spin blockade regime. Here, the electron in the left-hand dot is manipulated by an oscillatory electric field, which can lift the spin blockade. Thus only after a successful manipulation carrier transfer is enabled.

EDSR in a quantum dot: Theoretical background

In this section the theoretical background for the spin manipulation in a quantum dot occupied with a single electron is outlined. We closely follow the approach of Golovach *et al.* [17]. The system considered is illustrated in Fig. 21.

The Hamiltonian describing the quantum dot electron in an external alternating potential $V(\mathbf{r}, t)$ can be written as

$$H_0 = H_{\mathrm{d}} + H_{\mathrm{Z}} + H_{\mathrm{SO}} + V(\mathbf{r}, t) \; . \tag{43}$$

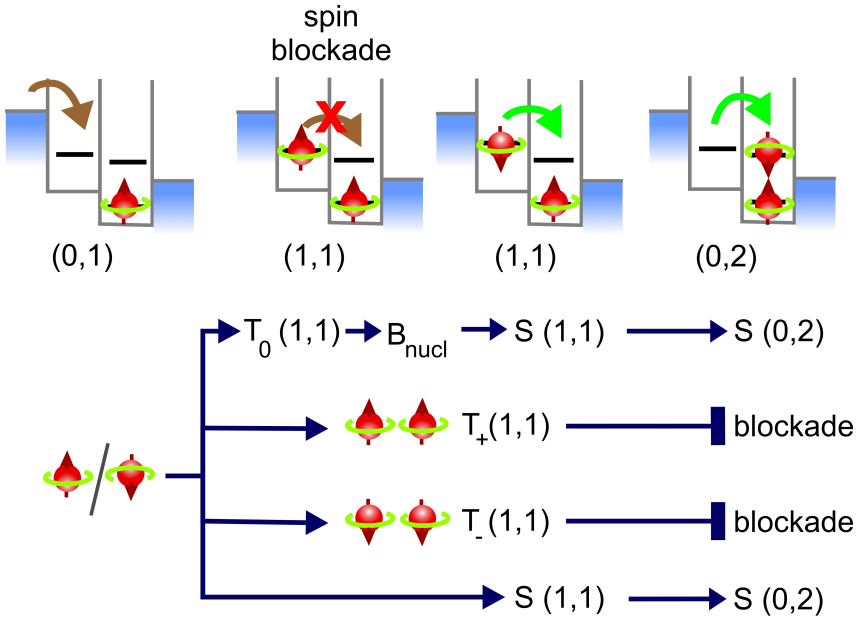

Fig. 20: *Spin-blockade in a double dot system. An electron is transferred to the left-hand dot. Depending on the spin orientation with respect to the right-hand dot a transfer to the right-hand dot is blocked (spin-blockade) or allowed. In the bottom scheme the four different transfer channels are shown.*

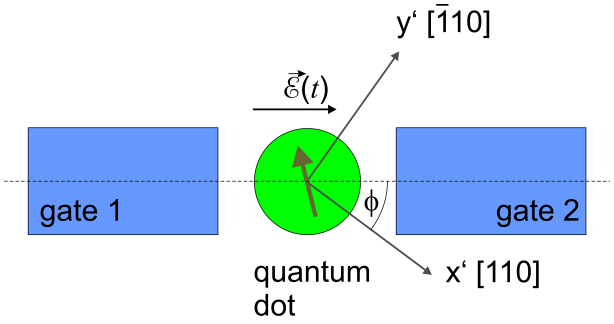

Fig. 21: *Schematic setup for electric field control by means of spin-orbit coupling. By using gate 1 and 2 an alternating electric field $\mathcal{E}(t)$ is generated. (After Golovach* et al. *[17]).*

Here, the Hamiltonian of the confined electron is

$$H_{\rm d} = \frac{p^2}{2m^*} + U(\mathbf{r}) \ , \tag{44}$$

with $U(\mathbf{r})$ the lateral confinement potential and $\mathbf{r} = (x, y)$. The electron momentum of the 2-dimensional system is $\mathbf{p} = i\hbar\nabla + e\mathbf{A}(\mathbf{r})$. For $U(\mathbf{r})$ we assume a harmonic potential

$$U(\mathbf{r}) = \frac{1}{2} m^* \omega_0^2 r^2 \, , \tag{45}$$

with ω_0 the characteristic frequency. The Zeeman Hamiltonian can be written as

$$H_{\rm Z} = \frac{1}{2} g \mu_{\rm B} \mathbf{B} \cdot \sigma \tag{46}$$

with $\mathbf{B}$ an external magnetic field, g the g-factor, and $\mu_{\rm B}$ the Bohr magneton. In the spin-orbit coupling Hamiltonian a Rashba as well as a Dresselhaus contribution are included

$$H_{\rm SO} = H_{\rm R} + H_{\rm D} = \alpha_{\rm R}(p_x\sigma_y - p_y\sigma_x) + \beta_{\rm D}(-p_x\sigma_x + p_y\sigma_y) \ . \tag{47}$$

By performing a Schrieffer–Wolff transformation [18, 19, 17]

$$\tilde{H}_0 \equiv e^S H_0 e^{-S} \tag{48}$$

with S the transformation matrix given by

$$[H_{\rm d} + H_{\rm Z}, S] = H_{\rm SO} \ , \tag{49}$$

the spin-orbit Hamiltonian can be removed in leading order

$$\begin{aligned}
\tilde{H}_0 &\equiv e^S H_0 e^{-S} \\
&= e^S (H_{\rm d} + H_{\rm Z} + H_{\rm SO}) e^{-S} \\
&\approx (1 + S)(H_{\rm d} + H_{\rm Z} + H_{\rm SO})(1 - S) \\
&\approx H_{\rm d} + H_{\rm Z} + H_{\rm SO} + S(H_{\rm d} + H_{\rm Z}) - (H_{\rm d} + H_{\rm Z})S \\
&= H_{\rm d} + H_{\rm Z} + H_{\rm SO} - [S, H_{\rm d} + H_{\rm Z}] \\
&= H_{\rm d} + H_{\rm Z} \ .
\end{aligned} \tag{50}$$

The transformation matrix S is given by [19]

$$S = \frac{1}{L_{\rm d} + L_{\rm Z}} = \frac{1}{L_{\rm d}} \sum_{m=0}^{\infty} \left(-L_{\rm Z} \frac{1}{L_{\rm d}} \right)^m H_{\rm SO} \tag{51}$$

and

$$H_{\rm SO} = i L_{\rm d} (\sigma \cdot \xi) \tag{52}$$

where $L_{\rm d}$ and $L_{\rm Z}$ are Liouville superoperators, i.e. $L_{\rm d} A = [H_{\rm d}, A]$ and $L_{\rm Z} A = [H_{\rm Z}, A]$, $\forall A$. Here, ξ is a vector in the plane of the 2-dimensional electron gas, which is given in the coordinate frame $x' = (x + y)/\sqrt{2}$, $y' = (y - x)/\sqrt{2}$, and $z' = z$ by

$$\xi = (y'/\lambda_-, x'/\lambda_+, 0) \ . \tag{53}$$

The corresponding spin-orbit lengths are

$$\lambda_{\pm} = \frac{\hbar}{m^*(\beta \pm \alpha)} \ . \tag{54}$$

For a harmonic confinement potential one gets [19]

$$\frac{1}{L_{\rm d}} x = \frac{-i}{\hbar m^* \omega_0^2} \left(p_x + eB_z y\right) \ , \tag{55}$$

$$\frac{1}{L_{\rm d}} y = \frac{-i}{\hbar m^* \omega_0^2} \left(p_y + eB_z x\right) \ , \tag{56}$$

$$\frac{1}{L_{\rm d}} p_j = \frac{im^*}{\hbar} r_j \quad (j = x, y) \ , \tag{57}$$

while for the Zeeman Liouvillian on gets

$$L_{\rm Z}^m(\sigma \cdot \xi) = \begin{cases} iE_{\rm Z}^m[\mathbf{n} \times \xi] \cdot \sigma, & \text{for odd} \quad m > 0 \\ -E_{\rm Z}^m[\mathbf{n} \times (\mathbf{n} \times \xi)] \cdot \sigma, & \text{for even} \quad m > 0 \end{cases} \ , \tag{58}$$

with $E_Z = g\mu_{\rm B}B$ the Zeeman splitting energy. By considering only terms linear in B one gets for the transformation matrix

$$S = i\xi \cdot \sigma - \frac{E_{\rm Z}}{m^*\omega_0^2}[\mathbf{n} \times \zeta] \cdot \sigma \ , \tag{59}$$

with $\zeta = (\lambda_-^{-1}\partial/\partial y', \lambda_+^{-1}\partial/\partial x', 0)$ and $\mathbf{n} = \mathbf{B}/B$.
The second term of Eq. (59) allows to express the coupling of the spin to the charge via the electric field

$$\mathcal{E}(t) = \frac{1}{e}\langle\psi_0|\nabla V(\mathbf{r}, z, t)|\psi_0\rangle \tag{60}$$

so that one obtains the effective Hamiltonian

$$H_{\rm eff} = \frac{1}{e} g\mu_{\rm B}\mathbf{B} \cdot \sigma + \frac{1}{2}\mathbf{h}(t) \cdot \sigma \tag{61}$$

with the field due to the oscillating electrical potential given by

$$\mathbf{h}(t) = 2g\mu_B \mathbf{B} \times \Omega(t) \ , \tag{62}$$

and

$$\Omega(t) = \frac{-e}{m^*\omega_0^2} \left[\lambda_-^{-1}\mathcal{E}_{y'}(t), \lambda_+^{-1}\mathcal{E}_{x'}(t), 0\right] \ . \tag{63}$$

For $\mathcal{E}_0 = \mathcal{E}_0(\cos\phi, \sin\phi, 0)$ with ϕ the angle of $\mathcal{E}_0$ with respect to the x' axis one explicitly obtains

$$\Omega(t) = \frac{-e\mathcal{E}_0}{m^*\omega_0^2} \left[\lambda_-^{-1}\sin\phi, \lambda_+^{-1}\cos\phi, 0\right] \ . \tag{64}$$

In summary, by applying an oscillating electric field $\mathcal{E}_0(t)$ an effective oscillating magnetic field $\mathbf{h}(t)$ is produced. Similarly to the conventional ESR experiments, this oscillating magnetic field can induce coherent transitions between two Zeeman split energy levels. The frequency $f_{\rm ac}$ of the magnetic field has match the resonance condition.

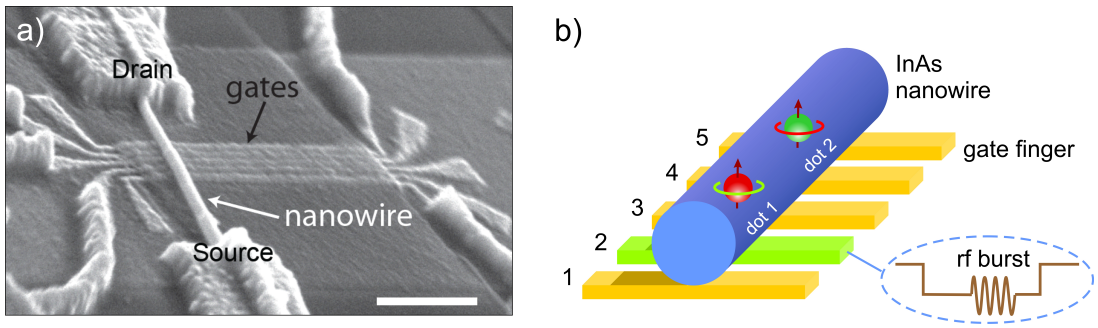

Fig. 22: *(a) Scanning electron micrograph of an InSb nanowire with bottom gate fingers. (b) Schematic illustration of a double quantum dot formed in an InAs nanowire. Gate 1, 3, and 5 are employed to define the barriers of the quantum dot. Gate 2 is used to apply the rf-burst for the EDSR transitions. (The scanning electron micrograph was kindly provided by S. Frolov, University of Pittsburgh and L. P. Kouwenhoven, TU Delft)*

EDSR in a quantum dot: Experiments

The electron-dipole spin-resonance was first demonstrated in a double quantum dot system formed in a 2-dimensional electron gas [16]. It is also possible to observe EDSR in a double-dot based on an InAs semiconductor nanowire [20]. The corresponding setup is shown in Fig. 22. The double quantum dot is formed by applying an appropriate voltage to the gate fingers underneath the nanowires. For the EDSR experiment each quantum dot is filled with a single electron. The quantum dot needs to be initiated in the spin blockade state described above.

The pulse sequence of the experiment is shown in Fig. 23. First, the potential of the left-hand quantum dot is lifted, so that an electron is transferred from the source to the left-hand quantum dot. For the EDSR experiment the state of the quantum dot has to be either in the T_+ (1,1) or in the $T_-(1,1)$ triplet state, so that a transfer of the electron in the left-hand quantum dot to the right-hand dot is inhibited. Next, the potential of the left-hand dot is lowered, in order to stabilize the state by making use of the Coulomb blockade. Here, charging effects prevent an electron transfer. By applying an rf-burst for a period $\tau_{\rm burst}$ with a frequency $f_{\rm ac}$ to gate 2 [cf. Fig. 22(b)] the spin-orientation of the electron in the left-hand quantum dot is rotated by means of EDSR. Here, an effective magnetic field is produced by means of an oscillatory voltage applied to the gate. Depending on the period $\tau_{\rm burst}$ the spin orientation of the electron is eventually reversed. Only then this electron can be transferred to the right-hand quantum dot, so that finally an electron can leave by tunneling to the drain contact. Thus, a net current flows through the double dot. Similar to electron spin resonance the excitation frequency $f_{\rm ac}$ has to match the resonance condition

$$hf_{\rm ac} = g\mu_{\rm B}|\mathbf{B}| \; . \tag{65}$$

i.e. $hf_{\rm ac}$ corresponds to the Zeeman energy splitting.

By increasing the burst time $\tau_{\rm burst}$ the electron spin in the left-hand quantum dot can be rotated systematically [20]. This is shown in Fig. 24, where the current through the double quantum dot oscillates. Each time the spin-blockade is lifted the current has a maximum. These current coherent oscillations are called Rabi oscillations. The Rabi frequency depends on the amplitude of the effective magnetic field. Owing to decoherence effects the oscillation amplitude is damped exponentially with increasing $\tau_{\rm burst}$.

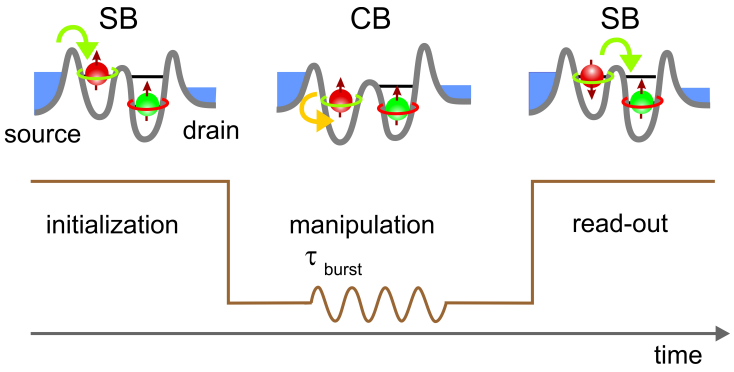

Fig. 23: *Sequence of the EDSR experiment. During initialization the left-hand quantum dot is filled with an up-spin electron. Since the right-hand quantum dot is also occupied with an up-spin electron, the double quantum dot is in the spin-blockade state. Lowering the potential of the double dot brings the system into the Coulomb blockade regime, where the electron transfer is inhibited due to charging effects. By applying an rf-burst the spin orientation of the electron is manipulated. Finally, the potential of the left-hand quantum dot is lifted, so that an electron transfer is allowed for the singlet state [20].*

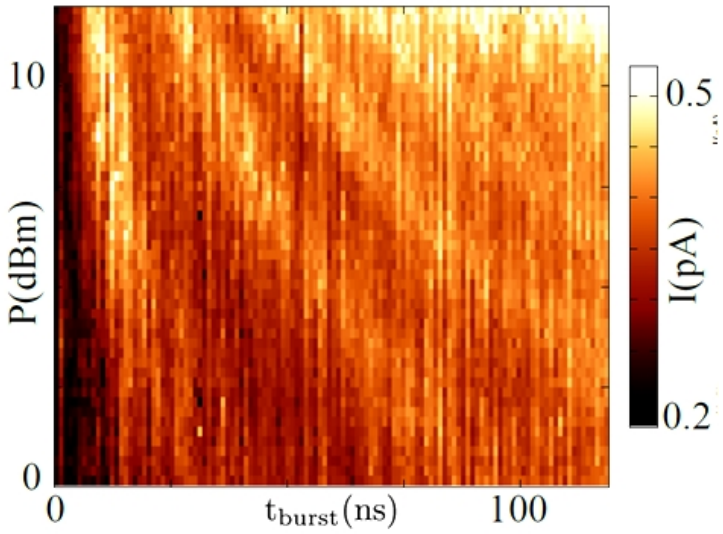

Fig. 24: *Rabi oscillations as a function of τ_{burst} for a range of microwave power. (The graph was kindly provided by S. Frolov, University of Pittsburgh and L. P. Kouwenhoven, TU Delft)*

7 Andreev level qubits

In this section the basic idea of an Andreev level qubit is outlined. This qubit is based on a special reflection process at a normal conductor/superconductor interface, i.e. the Andreev reflection. In a junction with two superconductors connected by a short normal conductive bridge supercurrent-carrying Andreev bound states are formed. A pair of these bound states is employed to define a quantum bit.

Andreev reflection

If a normal conductor is coupled to a superconductor a unique reflection process, namely Andreev reflection, can occur [21]. A schematics of the reflection mechanism is depicted in Fig. 25. An electron with an energy $E < \Delta_0$ slightly above the Fermi level μ moves towards the normal conductor/superconductor interface. Here, Δ_0 is the gap energy in superconductor. Because no quasiparticle states are provided in the superconductor, transmission through the interface is prohibited. Furthermore, no normal reflection is allowed, because there is no barrier present at the interface, which can absorb the momentum difference. However, a Cooper pair can be formed in the superconductor, with the consequence that an additional electron is taken from the completely filled Fermi sea of the normal conductor. In a degenerate electron gas this electron vacancy can be interpreted as a hole carrying a positive charge.

For the generation of a Cooper pair in the superconductor, the wave vector of the electron taken from the Fermi sea needs to have a direction opposite to the wave vector of the incident electron. Since in a completely filled Fermi sea the total wave vector is zero, the remaining wave vector of the system after one electron has been removed for the Cooper pair has the same direction as the incident electron. The wave vector of the system is identical to the wave vector of the hole. Thus, the incident electron and the created hole have a wave vector in the same direction. However the wave vector and the group velocity of a hole are in opposite directions. Therefore, the hole takes the same path as the incident electron in the reverse direction; therefore this process is called *retroreflection*. Due to the opposite charge and opposite group velocity of electrons and holes, this also implies that the conductance is twice as large as for an ideal normal transmission through the interface.

For an incident electron with $|E| > \Delta_0$, quasiparticles, electron- or hole-like, are excited in the superconductor. In this case not only Andreev reflection but also normal specular electron reflection take place with a certain probability. An Andreev reflection probability less than one is found even for $|E| < \Delta_0$ if a potential barrier is introduced at the superconductor/normal-conductor interface, because now normal reflection at the barrier is allowed.

Superconductor/normal-conductor/superconductor junction

In order to understand the basic transport mechanisms in a superconductor/normal-conductor /superconductor (SNS) junction, it is instructive to discuss a short one-dimensional junction. In contrast to a single SN interface considered in the previous section, now the phase difference ϕ of the pair potential between the two superconducting electrodes must be taken into account (cf. Fig. 26). A step-like superconducting pair potential $\Delta(x)$ is assumed, which is zero in the

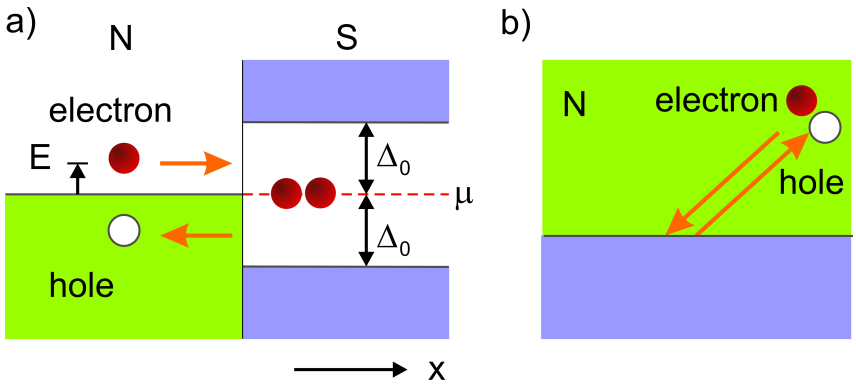

Fig. 25: *Energy diagram of the Andreev reflection process: an incident electron from the normal-conductor side is retroreflected as a hole, while a Cooper pair is formed in the superconductor. (b) In real space: in contrast to the normal reflection process, the retroreflected hole takes the same path as the incident electron in reverse direction.*

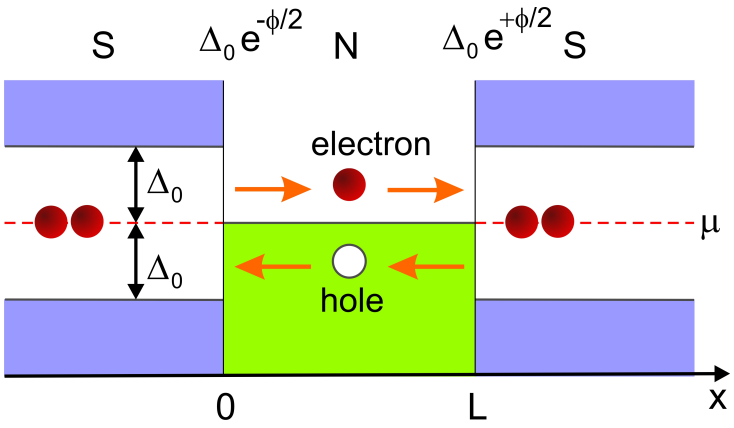

Fig. 26: *Schematic illustration of the transport based on Andreev reflection in an ideal 1-dimensional SNS junction. The arrows represent the group velocities of an electron and a hole. The wave vectors of the two particles have the same direction.*

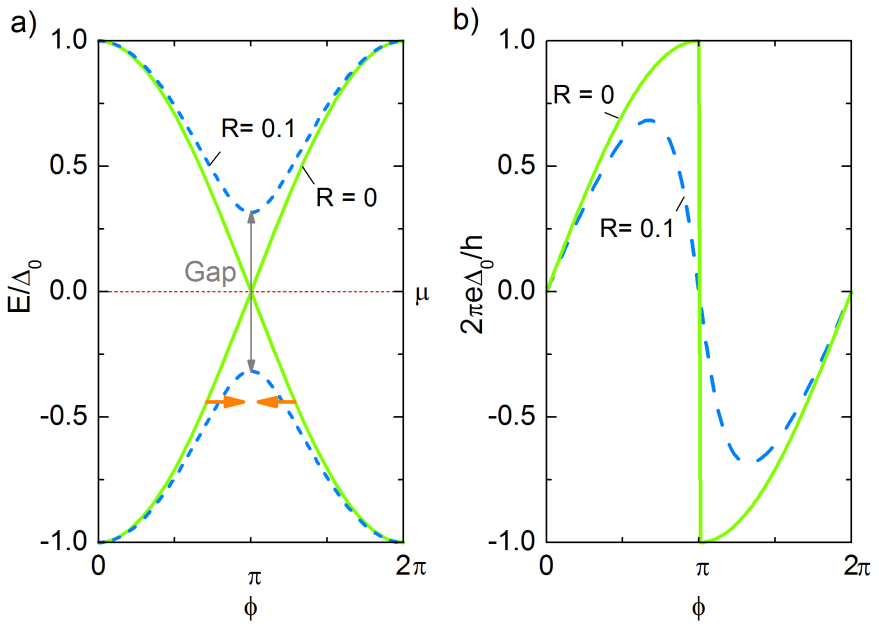

Fig. 27: *(a) Normalized Andreev levels and (b) Josephson current of a short junction as a function of the phase difference ϕ for $R = 0$ (solid lines), $R = 0.1$ (dashed lines). The direction of the electron motion for the corresponding Andreev levels is denoted by arrows.*

normal conductor:

$$\Delta(x) = \begin{cases} \Delta_0 e^{-i\phi/2} & , \quad x < 0 \\ 0 & , \quad 0 < x < L \\ \Delta_0 e^{+i\phi/2} & , \quad x > L \end{cases} . \tag{66}$$

In addition, a finite reflection probability R at the superconductor interface can also be included. Similar to a semiconductor quantum well in an SNS system bound states are formed, due to coherent normal and Andreev reflections at each SN interface. However, in contrast to an ordinary quantum well the bound state energy depends on the phase difference ϕ between the two superconductors. In Fig. 27(a) the energy spectrum is shown for a short SNS junction. The corresponding energy levels are given by [22, 23]

$$E_{\rm a} = \Delta_0 \sqrt{\cos^2(\phi/2) + R \sin^2(\phi/2)} \; . \tag{67}$$

For an ideal junction with $R = 0$ the energy levels are crossing at $\phi = \pi$. In case of a finite reflection probability a gap opens up. At zero temperature ($T = 0$) only the discrete level below the electro-chemical potential μ is occupied and contribute to the net supercurrent. The Josephson supercurrent $I_{\rm SNS}$ carried by this level, determined from Eq. (67), is obtained from

$$I_{\rm SNS} = \frac{2e}{\hbar} \frac{dE_{\rm a}}{d\phi} \; . \tag{68}$$

The resulting supercurrent as a function of the phase difference ϕ between the superconducting electrodes is plotted in Fig. 27(a). As can be seen here for a finite reflection probability the

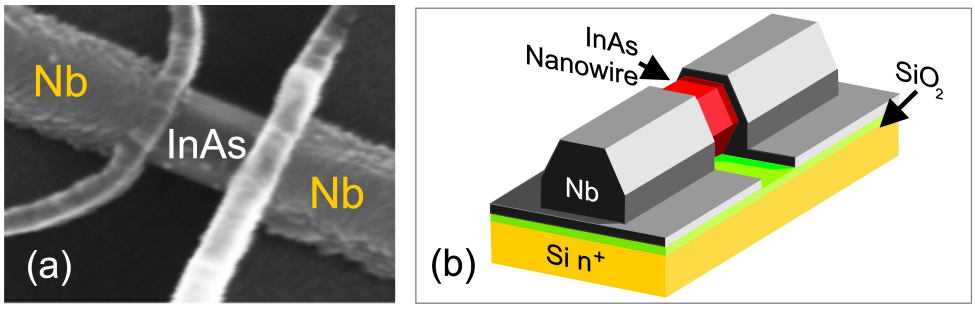

Fig. 28: *(a) scanning electron micrograph of a Nb/InAs nanowire/Nb junction. (b) Schematic illustration of the junction layout.*

maximum supercurrent I_c, i.e. the critical current, is reduced compared to the ideal junction. Furthermore, the current phase relation approaches the sinusoidal shape known from Josephson tunnel junctions.

SNS junctions based on semiconductor nanowires

Superconductor/normal conductor/superconductor Josephson junctions can be realized by using a semiconductor nanowire as a normal conducting link. A typical example is shown in Fig. 28, where an InAs nanowire serves as a link between two superconducting Nb electrodes [24]. The advantage of Nb is its high critical temperature ($T_c = 9.2$ K) compared to other superconductors like Al. In order to maintain a sufficiently good coupling between the superconducting electrodes, their distance has to be small, in the order of a few tenth of nanometers.
In Fig. 29 a typical current-voltage characteristic of a Nb/InAs-nanowire/Nb junction can be seen. At low temperatures of 0.4 K a clear supercurrent is observed. The critical current is about 100 nA. With increasing temperatures the critical current decreases, while at 4.8 K the current-voltage characteristics is almost linear.

Andreev level qubit

The Andreev level qubit is based on a superconducting quantum interference device (rf-SQUID) as sketched in Fig. 30 [25, 26]. The rf-SQUID contains an SNS junction, e.g. with a nanowire as a weak link. The cross section of the junction needs to be that small, that electronic modes in the junction are quantized [cf. Fig. 27(a)]. Thus the Josephson current is carried by a number of independent conducting electronic modes. As illustrated in Fig. 27(a), for a finite reflectivity $R \neq 0$, the backscattering induces a hybridization of the persistent current states in the closed SQUID loop. As shown there, an Andreev two-level system is established. The expectation value of the Josephson current carried by these two levels is determined by Eq. (68). Since the supercurrent is determined by the phase difference, its value can be manipulated by driving a magnetic flux through the SQUID loop.

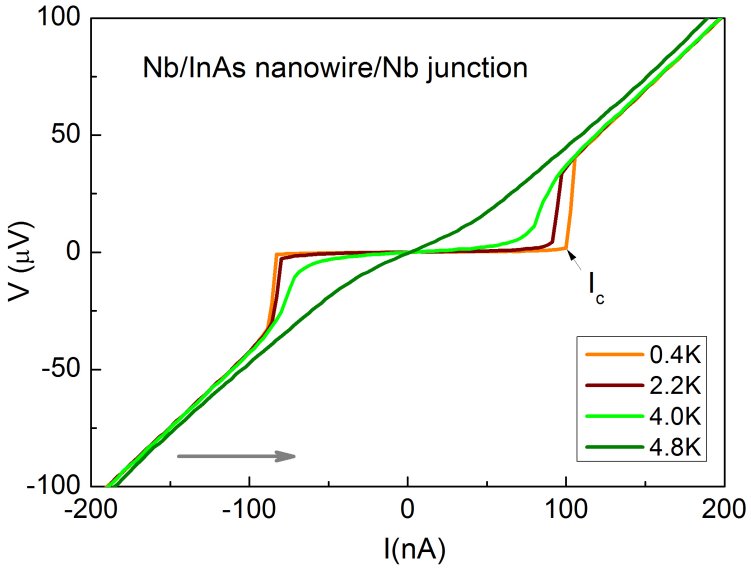

Fig. 29: *IV-characteristics of a Nb/InAs nanowire/Nb junction at various temperatures. The arrow indicates the sweep direction. I_c is the critical current.*

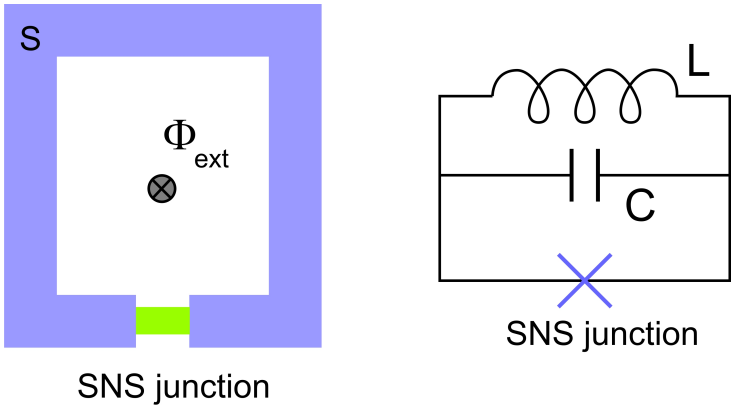

Fig. 30: *Schematics of an Andreev level qubit which is formed by a rf-SQUID with a non-hysteretic SNS junction. The equivalent circuit contains an SNS junction and an LC oscillator.*

References

[1] S. Datta and B. Das. Appl. Phys. Lett., **56**, 665 (1990).

[2] H. Hardtdegen, R. Meyer, H. Løken-Larsen, J. Appenzeller, Th. Schäpers, and H. Lüth. J. Crystal Growth , **116**, 521 (1992).

[3] C. Thelander, P. Agarwal, S. Brongersma, J. Eymery, L.F. Feiner, A. Forchel, M. Scheffler, W. Riess, B.J. Ohlsson, U. Gösele, and L. Samuelson. Materials Today , **9**, 28 (2006).

[4] S. Bandyopadhyay and M. Cahay. Appl. Phys. Lett. , **85** 1814 (2005).

[5] Yu.A. Bychkov and E. I. Rashba. Journal of Physics C (Solid State Physics) , **17**, 6039 (1984).

[6] R. Winkler. *Spin orbit coupling effects in two-dimensional electron and hole systems*. Springer–Verlag, Berlin, Heidelberg, New York, 2003.

[7] R. Winkler. Phys. Rev. B , **69**, 45317 (2004).

[8] Th. Schäpers, G. Engels, J. Lange, Th. Klocke, M. Hollfelder, and H. Lüth. J. Appl. Phys. , **83**, 4324 (1998).

[9] G. Dresselhaus. Phys. Rev. , **100**, 580 (1955).

[10] R. J. Elliot. Phys. Rev. , **96**, 266 (1964).

[11] G. Bergmann. Solid State Communications , **42**, 815 (1982).

[12] L. E. Golub. Weak antilocalization in high-mobility two-dimensional systems. Physical Review B, **71**, 235310 (2005).

[13] Vitaliy A. Guzenko, Thomas Schäpers, and Hilde Hardtdegen. Physical Review B , **76**, 165301 (2007).

[14] A. Bringer and Th. Schäpers. Phys. Rev. B , **83**, 115305 (2011).

[15] C. Schierholz, T. Matsuyama, U. Merkt, and G. Meier. Phys. Rev. B , **70**, 233311 (2004).

[16] K. C. Nowack, F. H. L. Koppens, Yu. V. Nazarov, and L. M. K. Vandersypen. Science , **318**, 1430 (2007).

[17] Vitaly N. Golovach, Massoud Borhani, and Daniel Loss. Phys. Rev. B , **74**, 165319 (2006).

[18] V. N. Golovach, A. Khaetskii, and D. Loss. Phys. Rev. Lett. , **93**, 016601 (2004).

[19] Massoud Borhani, Vitaly N. Golovach, and Daniel Loss. Phys. Rev. B , **73**, 155311 (2006).

[20] S. Nadj-Perge, S. M. Frolov, E. P. A. M. Bakkers, and L. P. Kouwenhoven. Nature , **468**, 1084 (2010).

[21] A. F. Andreev. Zh. Éksp. Teor. Fiz. [Sov. Phys. JETP **19**, 1228–1231 (1964)], **46** 1823 (1964).

[22] A. Furusaki, H. Takayanagi, and M. Tsukada. Phys. Rev. Lett., **67**, 132 (1991).

[23] C. W. J. Beenakker and H. van Houten. Phys. Rev. Lett., **66**, 3056 (1991).

[24] H. Y. Günel, I. E. Batov, H. Hardtdegen, K. Sladek, A. Winden, K. Weis, G. Panaitov, and D. Grützmacherand Th. Schäpers. Journal of Applied Physics, **112**, 034316 (2012).

[25] A. Zazunov, V. S., Shumeiko, E. N. Bratus, J. Lantz, and G. Wendin. Phys. Rev. Lett., **90**, 087003 (2003).

[26] G. Wendin and V. S. Shumeiko. Low Temperature Physics, **33**,9 (2007).

I'VE INVENTED A QUANTUM COMPUTER, CAPABLE OF INTERACTING WITH MATTER FROM OTHER UNIVERSES TO SOLVE COMPLEX EQUATIONS.
ACCORDING TO CHAOS THEORY, YOUR TINY CHANGE TO ANOTHER UNIVERSE WILL SHIFT ITS DESTINY, POSSIBLY KILLING EVERY INHABITANT.
SHIFT HAPPENS.
FIRE IT UP.
www.unitedmedia.com
3|22|97
© 1997 United Feature Syndicate, Inc.

Index

- A -	
AC Stark shift	D4.15, D4.21, D4.25
adiabatic condition	D4.15-16, D4.24
adiabatic elimination	D4.13-16, D4.24-26, D4.39-41
adiabatic theorem	D4.14
AKLT model	C4.10
Amplitude spectroscopy	A4.57
ancilla	A2.5
Andreev bound state	D5.31
Andreev level qubit	D5.32
Andreev reflection	D5.29
Anharmoncity	B4.9
anti-bunching	A3.11
area law	C4.2
artificial atom	D1.4
atom-cavity system	A3.9
atomic ensemble	A3.11
average fidelity	A3.13
- B -	
B92 protocol	A5.8
Bacon-Shor code	C1.25
BB84	A1.9
BB84 protocol	A5.7
BCS	B2.4
Bell inequalities	A1.6 , D4.21
Bell Rabi Transition	B4.25
Bell state	A2.11
Bernstein-Vazirani algorithm	A1.10
biexciton	D4.5f, D4.6, D4.21
bioimaging	D2.9
biseparability	A5.23
Bloch sphere	A2.10, A6.15
Bloch vector	A2.9
Bloch-Redfield equations	A4.34
Blue-sideband interaction	C2.5
Boolean function	A2.17
BQP (bounded-error quantum polynomial time)	C4.22
braid group	B2.12
- C -	
C-13 nuclear spins	D2.5
Calderbank-Shor-Steane (CSS) construction	C1.7
carbon	D3.4
carbon nanotubes	D3.5
Carrier interaction	C2.4
cavity	D1.17
Cavity pull	B4.14
cavity quantum electrodynamics (CQED)	D4.8-14, D4.16, D4.27-28, D4.40-42
charge detection	A6.9
Charge dispersion	B4.5
Charge noise	B4.8
charge qubit	A4.13
check operators	C1.3
chemical vapor deposition	D2.2
Cirac-Zoller gate	A3.5
circuit model	A2.17
Circuit QED	B4.12
Clifford gates	C1.14
cluster state	A2.22
CNOT gate	A2.20, A3.6, B1.14
code concatenation	C1.3
coherence function	D4.18-20
cohereren spin manipulation	B3.3, B3.8, B3.24
collective emission	A3.11
completely positive (CP) map	A2.24
composite pulses	A6.32
Conditional resonance frequency	B4.21
confocal microscopy	D2.3
controlled phase gate	A3.6
Cooper pair box	B2.16, A4.14
Cooperativity	D4.12, D4.27, D4.42
correlated materials	C3.3
Coulomb exchange	C3.4
Coulomb integral	C3.4
cphase gate, effective	B3.14
CPMG sequence	A6.21
Cross resonance effect	B4.21
- D -	
Dark exciton	D4.5f, D4.7
dark state	A3.15
DC SQUID	A4.9
decoherence	A2.24, D3.2, D3.15
dense coding	A5.5
density-functional theory	C3.2
dephasing (NV)	D2.8
depolarising channel	A2.24
Deutsch algorithm	A1.10, A5.16
Deutsch-Jozsa algorithm	A1.10
diamond defects	D2.1
diamond quantum registers	D2.7
dimond color centers	D2.12
Dipole dephasing	D4.20, D4.26
Dirac	D3.8
Dirac equation	C2.5
direct exchange	C3.7
dispersive	D1.18
dissipation	A2.24
Distributed Bragg Reflector (DBR)	D4.3, D4.13, D4.27, D4.28, D4.45

DLCZ scheme	A3.10
DMRG (Density Matrix Renormalization Group)	C4.6,C4.9
donor	B1.2
double quantum dot, spin states	B3.12
down-folding	C3.8
DRAG	B4.30
Dresselhaus term	D5.11
dynamic nuclear polarization	A6.21
dynamically corrected gates	A6.32
- E -	
E91 protocol	A5.9
Effective Hamiltonian	B4.38
effective magnetic field	D5.8
effective mass	B1.4
effective spin Hamiltonian	B1.11
Einstein-Podolsky-Rosen pair	A1.4.
electric dipole approximation	D4.8-10
electric dipole spin resonance	A6.12, B3.8, D5.22
electromagnetically induced transparency (EIT)	A3.14
electron interference	D5.14
electron spin qubit	B1.9
electron spin resonance	A6.11, B3.3
electrooptic modulator (EOM)	D4.26, D4.30, D4.33
encoded qubit	A6.13
energy diagram	A5.13
entangled photons	D4.21-22, D4.44
entanglement	A1.5, A2.10, C3.8
entanglement measure	A2.12
error syndrome	C1.4
error threshold	B1.18
exchange	D3.4, D3.11
exchange integral	C3.4
exchange interaction	A6.14, B1.11, B3.14
- F -	
Faraday geometry	D4.5f, D4.7
fault tolerant quantum computing	C1.12
fermion parity	B2.3
fermionic MERA	C4.21
fermionic PEPS	C4.21
fidelity	A2.15, A3.7
fine structure splitting	D4.21
Fluctuation Quantum Dot	D4.3-4, D4.9
fluorescence spectra (NV)	D2.4
Flux noise	B4.10
flux qubit	A4.19
fluxon	D1.10
fluxonium	A4.28, D1.3
Fourier-transform-limited pulses	D4.20
Free induction decay (FID)	D4.32-38
- G -	
Gate fidelity	B4.45
Gaussian pulse	B4.28
geometric phase gate	A3.7
germanium	B3.15
GHZ state	A2.22, A5.23
graphene	D3.5
graphene nanoribbon	D3.12
Grover algorithm	A5.17
- H -	
Hadamard gate	A2.19
Hahn echo	A6.19
Hanbury Brown-Twiss (HBT)	D4.19f, D4.19
Harmonic basis	B4.9
Hartree-Fock method	C3.11
heavy holes	D4.6-7
Heisenberg limited measurement	D2.10
herald	A3.10
heterostructure	A6.6, D5.2
heterostructure, SiGe	B3.17
Hong-Ou-Mandel (HOM)	D4.20-21, D4.44
Hubbard model	C3.17
hyperfine	D3.2, D3.15
hyperfine interaction	B1.8, A6.16, D4.28-39
hysteresis	D4.32-38
- I -	
imaging techniques (NV)	D2.9
iMPS	C4.20
Impurity complex	D4.3-4, D4.21
Indistinguishable single photons	D4.18-21, D4.42-44
Inhomogeneity (of quantum dots)	D4.5, D4.21, D4.25, D4.28, D4.41-43
injectivity	C4.11
Intermediate coupling regime	D4.12-13
ion	A3.2
iPEPS	C4.20
Ising PEPS	C4.18
isotopical purification	B3.20
- J -	
Jaynes Cummings model	A4.19
Josephson	D1.3
Josephson equations	A4.4
Josephson junction	A4.4
- K -	
Kane	B1.2
kinetic	D1.6

kinetic exchange	C3.6
Klein paradox	C2.8
Klein tunneling	C2.10
Kramer degeneracy	D5.13
Kraus operator	A2.25
- L -	
lambda level scheme	D2.5
Landau-Zener tunneling	A4.52
Landauer principle	A1.6
Larmor precession	D4.10, D4.25, D4.28, D4.32-37
lattice surgery	C1.21
LDA+DMFT	C3.3
Leakage	B4.28
Lie-Trotter formula	A5.20
light holes	D4.6-7
Lindblad master equation	C1.9
linear nearest neighbour (LNN)	B1.17
linear optics quantum computing	D4.17, D4.21
logic gate	A2.17
- M -	
Macroscopic quantum tunneling	A4.8
magnetometry (NV)	D2.10
magnon	A3.16
Majorana fermions	B2.2, B2.7, B2.13
Majorana fermions, universal quantum computation	B2.13, B2.17
Majorana qubit	B2.9, B2.10
Majorana qubit, measurement of	B2.17
Majorana qubit, parity-protection	B2.9
Majorana zero mode	B2.5
many-body problem	C3.2
Matrix Product Density Operator (MPDO)	C4.19
Matrix Product State (MPS)	C4.3
Measurement fidelity	B4.15
Measurement Rate	B4.15
mesoscopic enhancement	D4.9, D4.25
micro-magnet	B3.5
Microcavity	D4.3, D4.3f, D4.12-13, D4.20, D4.42, D4.45
microwave	D1.2
mixed state	A2.2
Mølmer-Sørensen gate	A3.7
Monte Carlo	C4.17,C4.20
Multiscale Entangle-ment Renormalization Ansatz (MERA)	C4.19
mutual information	A2.8
- N -	
nanophotonics	D2.4
nanopositioning	D2.11
nanostructures	D4.8
nanowires	D5.4
narrowed nuclear states	A6.24
NMR	B1.6
no-cloning theorem	A2.15
Nobel Prize	A1.11
noise threshold for fault tolerance	C1.14
non-Abelian anyon	B2.12, B2.13
NP (non-deterministic polynomial time)	C4.22
nuclear polarization	D4.32-38
nuclear spin diffusion	D4.30
nuclear spin qubit	B1.3
nuclear spin-free material	B3.15
NV center	D2.2
- O -	
one-qubit teleportation	C1.15
one-way Q. C.	A2.21, D2.8
optical pumping	D4.22-23
Optical spectroscopy	D4.4-6
optimal control	A6.33
orbital ordering	C3.17
oscillator strength	D4.11-12, D4.25, D4.33
Overhauser field	A6.16
Overhauser shift	D4.32-38
- P -	
P (polynomial time)	C4.22
p-wave pairing	B2.5
pair-correlation function	A3.10
parent Hamiltonian	C4.11
parity protection	B2.9, B2.10
partial trace	A2.12
partial transpose	A2.14
particle-hole symmetry	B2.4
Paul trap	C2.3
Pauli blockade	A6.12, B3.3, B3.23
Pauli matrices	C3.17
Pauli matrix	A2.9
Pauli state vector	B4.43
Pauli transfer matrix	B4.44
Peres-Horodecki-criterion	A2.14
phase qubit	A4.25
phase-damping channel	A2.24
phase-slip	D1.9
phonons	D3.16
Phosphorus	B1.2, D4.4
photoactivated localization microscopy (PALM)	D2.9
photon-assisted tunneling	B3.10, B3.13
Photonic crystal	D4.13, D4.28
Plasmon	D1.10

Poissonian light	D4.18-19
polariton	A3.16
POVM	A2.4
power spectral density (PSD)	A4.36
PPT criterion	A2.14
Projected Entangled Pair State (PEPS)	C4.13
projective readout (NV)	D2.6
pseudospin	D3.8
Purcell	D1.26
Purcell effect	D4.12, D4.20
Purcell regime	D4.12
pure state	A2.2
- Q -	
q. repeater	A5.21
q. computing	A5.13
QMA (quantum Merlin Arthur)	C4.22
QMA-complete	C4.23
Quantronium	A4.16
quantum channel	A2.24
quantum complexity	C4.22
quantum computer	A1.8
quantum cryptography	A1.9
quantum dot	D3.2, D3.8, D5.22,A6.7
quantum electrodynamics	D1.5
quantum error correcting codes	C1.2
quantum error correction (QEC)	D4.23, D4.45
Quantum field theories	C2.14
quantum gate	A2.17
quantum gates by braiding	C1.24
quantum information science	A1.2
quantum key distribution	A5.7
quantum key distribution (QKD)	D4.17
quantum measurement as photograph	A1.5
quantum memory	A3.13
quantum money	A1.7
quantum nondemolition measurement (QND)	D4.24, D4.27-28, D4.43
quantum simulation	A5.20, C2.2
quantum teleportation	D4.21, D4.42, A5.3, A2.16
Quantum well	D4.2, D4.3, D4.4, D4.3f, D4.9, D4.13, D4.20, D4.29, D4.42
Quantum wire	D4.2
qubit	A1.11, A2.8
qubit coupling	B1.11
qudit	A2.9
- R -	
Rabi frequency	B3.4, B3.8
Rabi oscillations	D4.25-26, D4.26f, D5.27
Ramsey interferometry	D4.32-38
Randomized benchmarking	B4.36
Rashba coupling parameter	D5.7
Rashba effect	D5.7
RCSJ model	A4.5
read-out, single spin	B3.10
Red-sideband interaction	C2.4
remote entanglement	A3.15
renormalization	C4.17
resonant readout, flux qubit	A4.24
reversible computation	A1.7
Rotating frame	B4.11
rotating wave approximation (RWA)	D4.9-11, D4.14, D4.24, D4.32
Rydberg states	A3.8
- S -	
S-T_0 qubit	A6.13
s-wave pairing	B2.5, B2.14
scale-up	B1.17
Schmidt decomposition	A2.11
Schrieffer-Wolff transformation	B4.38
Schrödinger cat	A1.5
second quantization	C3.9
selection rules	D4.7, D4.9, D4.14, D4.24, D4.25, D4.39, D4.43, D4.44
Self-assembled quantum dot	D4.2-D4.44
semiconducting nanowire	B2.13, B2.14
separable state	A2.11
Shannon entropy	A1.3, A2.6
Shor 9-qubit code	C1.2
Shor algorithm	A1.10, A5.18
shot-noise limited measurement	D2.10
Signal to noise ratio	B4.15
silicon	B1.2, B3.15, D4.4
Simon algorithm	A1.10, A5.17
single atom fabrication	B1.20
single photon sources	D4.17-22
single qubit operations	B1.6
single spin readout	A6.9
single-photon source	A3.9
singlet	C3.7
singlet-triplet qubit	B3.23
Site-controlled quantum dot	D4.3, D4.4.3f
slow light	A3.14
spin coherence, silicon	B3.19
spin echo	D4.33-38
spin field-effect transistor	D5.6

spin locking	A4.46
spin qubits	A6.3
spin read-out, single-shot	B3.22
spin readout	B1.16
spin readout (NV)	D2.5
spin relaxation	D3.16
spin relaxation, silicon	B3.19
spin states of two spins	B3.12
spin to charge conversion	A6.9
spin-blockade	D5.23
spin-off band	D4.6
spin-orbit coupling	D4.6
spin-orbit coupling	D3.16
spin-orbit coupling	D5.6
spin-orbit effect	B2.14
spin-orbit interaction	B3.14, B3.20
spin-orbit qubit	D5.22
spin-precession	D5.6
Spontaneous Emission/Decay	D4.2, D4.5, D4.7, D4.10, D4.20-23, D4.26-27, D4.30, D4.41
stabilizer formalism (quantum codes)	C1.2
State fidelity	B4.43
Stewart-McCumber model	A4.5
stimulated emission depletion (STED)	D2.9
stimulated Raman adiabatic passage (STIRAP)	A3.17
stimulated Raman transitions	D4.15, D4.25
stopped light	A3.16
Strain	D4.3, D4.4, D4.6, D4.7, D4.21-22, D4.29-30
Stranski-Krastanov (SK)	D4.3-4, D4.7
stray magnetic field, micro-magnet	B3.7
Strong coupling regime	D4.12-13
subPoissonian light	D4.18-19
subsystem codes	C1.5
subsystem surface code	C1.28
superconducting coherence length	B2.6
superconducting pair potential	B2.4
superconducting qubit	A4.13, D1.2
superexchange	C3.12
superinductance	D1.2
superselection rule	B2.8
surface code	B1.18, C1.17
symmetry-protected topological order	B2.10
Systematic errors	B4.34

- T -	
T gate	C1.16
Teleportation	A1.11
tensor network	C4.5
tensor product	A2.10
thermal light	D4.18
time evolution	C4.18
Toffoli gate	A1.7
Toffoli-gate	A2.21
topological charge	B2.8, B2.15
transfer operator	C4.7, C4.12
transmission matrix	D1.7
Transmon	A4.17, B4.3
transmon qubit	B2.16
Trapped ions	C2.3, D4.2, D4.12, D4.24,D4.28,D4.44
trion	D4.5f, D4.6-8, D4.14, D4.22, D4.24, D4.26, D4.28, D4.29, D4.30, D4.32, D4.35, D4.36, D4.37, D4.39, D4.41, D4.44
triplet	C3.7
tubular nanowire system	D5.16
Tunable resonance frequency	B4.9
two dimensional electron gas	A6.6
two-photon interference	D2.8
- U -	
U(1) symmetry	B2.3
ultrafast optical control	D4.24-27
unitary time evolution	A2.2
universal quantum gates	C1.14
universality	A2.21
- V -	
vacuum Rabi splitting	D4.12
valley	D3.9
valley-orbit mixing	B3.19
valleys, silicon of	B3.18
van Vleck	D3.17
Verschränkung	A1.5
Virtual two-qubit interaction	B4.17
Voigt geometry	D4.5f, D4.7, D4.22, D4.23f, D4.24, D4.27, D4.29, D4.39
von Neumann entropy	A2.12
von Neumann measurement	A2.4
- W -	
W state	A5.23
weak antilocalization	D5.15
weak coupling regime	D4.12
weak localization	D5.14
whispering gallery modes	D4.13

Wigner-Weisskopf model	D4.10-11, D4.21
- Y -	
Y-junction	B2.12
Yang-Baxter equation	B2.12
- Z -	
Z_2 symmetry	B2.3
Zitterbewegung	C2.7
ZnSe	D4.4, D4.21

0-pi qubit	C1.11
2-dimensional electron gas	D5.2
3D cavity	B4.18

The IFF Spring School & Quantum Information in Jülich

PGI-JCNS-TA
52425 Jülich
Phone: *++49 2461 61-1739*
Fax: *++49 2461 61-2410*
email: *springschool@fz-juelich.de*
web: *www.iff-springschool.de*

The IFF Spring Schools were first brought into being in 1970 by the Jülich "Institute of Solid State Research" (IFF). Since then, the schools have made it possible for students and young scientists to gain a two-week insight into a current topic related to condensed matter physics. In 2011, IFF was dissolved as part of a restructuring process within Forschungszentrum Jülich, and new institutes, namely the "Peter Grünberg Institute" (PGI), the "Jülich Centre for Neutron Science" (JCNS) and the "Institute of Complex Systems" (ICS) were established. Together with the "Institute for Advanced Simulation" (IAS), the three institutes continue to organize the IFF Spring Schools. The 44th Spring School 2013 was organized by PGI-2: Theoretical Nanoelectronics.

Under the umbrella of the Jülich-Aachen Research Alliance (JARA), extensive activity is underway at the forefront of quantum information science at Jülich. The "Institute for Quantum Information" (IQI) of the RWTH Aachen University in close cooperation with the PGI "Institute for Theoretical Nanoelectronics", focuses on the many and growing connections between quantum information and condensed matter physics. Experimental groups work on the realization of quantum bits in single-spin quantum dots in semiconducting systems (both gallium-arsenide and silicon-germanium based). In cooperation with other experimental groups, emphasis is placed on the design and realization of functioning quantum-computing modules using current developments in circuit quantum-electrodynamics and superconducting qubits. Concepts are also being developed for the next steps in the use of nanowire devices to realize arrays of Majorana qubits, within the context of a larger theoretical effort to define the possibilities and constraints involved in using Fermionic particles for quantum information processing. In simulation sciences, the group has led the way in developing new, entanglement-motivated representations of quantum states for the efficient simulation of properties in 2D spin systems.

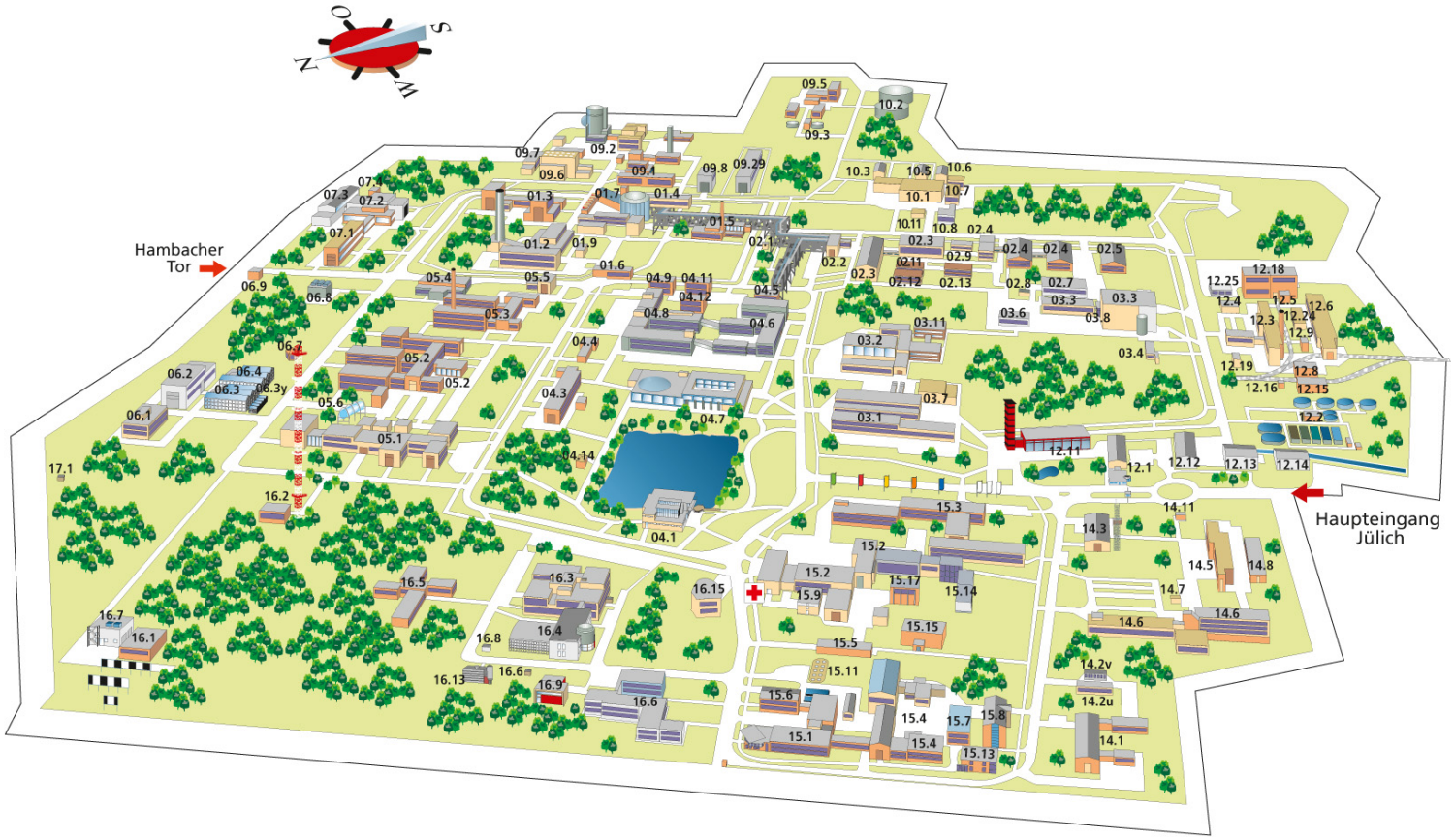
O
S
N
W
Hambacher Tor
Haupteingang Jülich

Schriften des Forschungszentrums Jülich
Reihe Schlüsseltechnologien / Key Technologies

1. **Soft Matter**
   From Synthetic to Biological Materials
   Lecture manuscripts of the 39th IFF Spring School March 3 – 14, 2008
   Jülich, Germany
   edited by J.K.G. Dhont, G. Gompper, G. Nägele, D. Richter, R.G. Winkler (2008),
   c. 1000 pages
   ISBN: 978-3-89336-517-3

2. **Structural analysis of diblock copolymer nanotemplates using grazing incidence scattering**
   by D. Korolkov (2008), III, 167 pages
   ISBN: 978-3-89336-522-7

3. **Thermal Nonequilibrium**
   Thermal forces in fluid mixtures
   Lecture Notes of the 8th International Meeting on Thermodiffusion,
   9 – 13 June 2008, Bonn, Germany
   edited by S. Wiegand, W. Köhler (2008), 300 pages
   ISBN: 978-3-89336-523-4

4. **Synthesis of CMR manganites and ordering phenomena in complex transition metal oxides**
   by H. Li (2008), IV, 176 pages
   ISBN: 978-3-89336-527-2

5. **Neutron Scattering**
   Lectures of the JCNS Laboratory Course held at the Forschungszentrum Jülich and the research reactor FRM II of TU Munich
   edited by R. Zorn, Th. Brückel, D. Richter (2008), ca. 500 pages
   ISBN: 978-3-89336-532-6

6. **Ultrafast Magnetization Dynamics**
   by S. Woodford (2008), 130 pages
   ISBN: 978-3-89336-536-4

7. **Role of Surface Roughness inTribology: from Atomic to Macroscopic Scale**
   by C. Yang (2008), VII, 166 pages
   ISBN: 978-3-89336-537-1

8. **Strahl- und Spindynamik von Hadronenstrahlen in Mittelenergie-Ringbeschleunigern**
   von A. Lehrach (2008), II, 171 Seiten
   ISBN: 978-3-89336-548-7

9. **Phase Behaviour of Proteins and Colloid-Polymer Mixtures**
   by C. Gögelein (2008), II, 147 pages
   ISBN: 978-3-89336-555-5

10. **Spintronics – From GMR to Quantum Information**
    Lecture Notes of the 40th IFF Spring School March 9 – 20, 2009
    Jülich, Germany
    edited by St. Blügel, D. Bürgler, M. Morgenstern, C. M. Schneider,
    R. Waser (2009), c. 1000 pages
    ISBN: 978-3-89336-559-3

11. **ANKE / PAX Workshop on SPIN Physics**
    JINR, Dubna, Russia / June 22. – 26, 2009
    Org. Committee: A. Kacharava, V. Komarov, A. Kulikov, P. Lenisa, R. Rathmann,
    H. Ströher (2009), CD-ROM
    ISBN: 978-3-89336-586-9

12. **Entwicklung einer Nanotechnologie-Plattform für die Herstellung Crossbar-basierter Speicherarchitekturen**
    von M. Meier (2009), 135 Seiten
    ISBN: 978-3-89336-598-2

13. **Electronic Oxides –**
    Correlation Phenomena, Exotic Phases and Novel Functionalities
    Lecture Notes of the 41st IFF Spring School March 8 – 19, 2010
    Jülich, Germany
    edited by St. Blügel, T. Brückel, R. Waser, C.M. Schneider (2010), ca. 1000 pages
    ISBN: 978-3-89336-609-5

14. **4th Georgian-German School and Workshop in Basic Science**
    Tbilisi, Georgia / May 3 – 7, 2010
    Org. Committee: E. Abrosimova, R. Botchorishvili, A. Kacharava, M. Nioradze,
    A. Prangishvili, H. Ströher (2010); CD-ROM
    ISBN: 978-3-89336-629-3

15. **Neutron Scattering**
    Lectures of the JCNS Laboratory Course held at Forschungszentrum Jülich and the research reactor FRM II of TU Munich
    edited by Th. Brückel, G. Heger, D. Richter, G. Roth and R. Zorn (2010),
    ca 350 pages
    ISBN: 978-3-89336-635-4

16. **Ab *initio* investigations of magnetic properties of ultrathin transition-metal films on *4d* substrates**
    by A. Al-Zubi (2010), II, 143 pages
    ISBN: 978-3-89336-641-5

17. **Investigation of a metal-organic interface realization and understanding of a molecular switch**
    by O. Neucheva (2010), 134 pages
    ISBN: 978-3-89336-650-7

18. **Reine Spinströme in lateralen Spinventilen, *in situ* Erzeugung und Nachweis**
von J. Mennig (2010), V, 95 Seiten
ISBN: 978-3-89336-684-2

19. **Nanoimprint Lithographie als Methode zur chemischen Oberflächen-strukturierung für Anwendungen in der Bioelektronik**
von S. Gilles (2010), II, 169 Seiten
ISBN: 978-3-89336-686-6

20. **Macromolecular Systems in Soft- and Living-Matter**
Lecture Notes of the 42nd IFF Spring School 2011 February 14 – 25, 2011 Jülich, Germany
edited by J. K.G. Dhont, G. Gompper, P. R.Lang, D. Richter, M. Ripoll, D. Willbold, R. Zorn (2011), ca. 1000 pages
ISBN: 978-3-89336-688-0

21. **The spin structure of magnetic nanoparticles and in magnetic nanostructures**
by S. Disch (2011), V, 342 pages
ISBN: 978-3-89336-704-7

22. **Element-selective and time-resolved magnetic investigations in the extreme ultraviolet range**
by P. Grychtol (2011), xii, 144 pages
ISBN: 978-3-89336-706-1

23. **Spin-Transfer Torque Induced Dynamics of Magnetic Vortices in Nanopillars**
by V. Sluka (2011), 121 pages
ISBN: 978-3-89336-717-7

24. **Adsorption von Phthalocyaninen auf Edelmetalloberflächen**
von I. Kröger (2011), vi, 206 Seiten
ISBN: 978-3-89336-720-7

25. **Time-Resolved Single Molecule FRET Studies on Folding/Unfolding Transitions and on Functional Conformational Changes of Phospho-glycerate Kinase**
by T. Rosenkranz (2011), III, 139 pages
ISBN: 978-3-89336-721-4

26. **NMR solution structures of the MloK1 cyclic nucleotide-gated ion channel binding domain**
by S. Schünke (2011), VI, (getr. pag.)
ISBN: 978-3-89336-722-1

27. **Neutron Scattering**
    Lectures of the JCNS Laboratory Course held at Forschungszentrum Jülich and the research reactor FRM II of TU Munich
    edited by Th. Brückel, G. Heger, D. Richter, G. Roth and R. Zorn (2011), ca 350 pages
    ISBN: 978-3-89336-725-2

28. **Neutron Scattering**
    Experiment Manuals of the JCNS Laborator Course held at Forschungszentrum Jülich and the research reactorFRM II of TU Munich
    edited by Th. Brückel, G. Heger, D. Richter, G. Roth and R. Zorn (2011), ca. 180 pages
    ISBN: 978-3-89336-726-9

29. **Silicon nanowire transistor arrays for biomolecular detection**
    by X.T.Vu (2011), vii, 174 pages
    ISBN: 978-3-89336-739-9

30. **Interactions between parallel carbon nanotube quantum dots**
    by K. Goß (2011), viii, 139 pages
    ISBN: 978-3-89336-740-5

31. **Effect of spin-orbit scattering on transport properties of low-dimensional dilute alloys**
    by S. Heers (2011), viii, 216 pages
    ISBN: 978-3-89336-747-4

32. **Charged colloids and proteins: Structure, diffusion, and rheology**
    by M. Heinen (2011), xii, 186 pages
    ISBN: 978-3-89336-751-1

33. **Scattering Methods for Condensed Matter Research: Towards Novel Applications at Future Sources**
    Lecture Notes of the 43rd IFF Spring School 2012
    March 5 – 16, 2012 Jülich, Germany
    edited by M. Angst, T. Brückel, D. Richter, R. Zorn ca. 1000 pages
    ISBN: 978-3-89336-759-7

34. **Single-Site Green Function of the Dirac Equation for Full-Potential Electron Scattering**
    by P. Kordt (2012), 138 pages
    ISBN: 978-3-89336-760-3

35. **Time Resolved Single Molecule Fluorescence Spectroscopy on Surface Tethered and Freely Diffusing Proteins**
    by D. Atta (2012), iv, 126 pages
    ISBN: 978-3-89336-763-4

36. **Fabrication and Utilization of Mechanically Controllable Break Junction for Bioelectronics**
by D. Xiang (2012), 129 pages
ISBN: 978-3-89336-769-6

37. **Contact Mechanics and Friction of Elastic Solids on Hard and Rough Substrates**
by B. Lorenz (2012), iv, 121 pages
ISBN: 978-3-89336-779-5

38. **Ab initio Calculations of Spin-Wave Excitation Spectra from Time-Dependent Density-Functional Theory**
by M. Niesert (2012), 146 pages
ISBN: 978-3-89336-786-3

39. **Neutron Scattering**
Lectures of the JCNS Laboratory Course held at Forschungszentrum Jülich and the research reactor FRM II of TU Munich
edited by Th. Brückel, G. Heger, D. Richter, G. Roth and R. Zorn (2012),
ca 350 pages
ISBN: 978-3-89336-789-4

40. **Neutron Scattering**
Experiment Manuals of the JCNS Laborator Course held at Forschungszentrum Jülich and the research reactorFRM II of TU Munich
edited by Th. Brückel, G. Heger, D. Richter, G. Roth and R. Zorn (2012),
ca. 175 pages
ISBN: 978-3-89336-790-0

41. **Influence of a shear flow on colloidal depletion interaction**
by C. July (2012), xviii, 105 pages
ISBN: 978-3-89336-791-7

42. **NMR studies on the isolated C39 peptidase-like domain of ABC transporter Haemolysin B from *E. coli*: Investigation of the solution structure and the binding interface with HlyA**
by J. Lecher (2012), 126 pages
ISBN: 978-3-89336-793-1

43. **Spin Correlations and Excitations in Spin-frustrated Molecular and Molecule-based Magnets**
by Z. Fu (2012), 208 pages
ISBN: 978-3-89336-797-9

44. **Crystal and spin structure and their relation to physical properties in some geometrical and spin spiral multiferroics**
by N. K. Chogondahalli Muniraju (2012), iii, 190 pages
ISBN: 978-3-89336-802-0

45. **Multiferroicity in oxide thin films and heterostructures**
by A. Glavic (2012), xi, 152 pages
ISBN: 978-3-89336-803-7

46. **German Neutron Scattering Conference 2012**
September 24 -26, 2012. Gustav-Stresemann-Institut, Bonn, Germany
edited by Th. Brückel (2012)
ISBN: 978-3-89336-807-5

47. **STM beyond vacuum tunnelling: Scanning Tunnelling Hydrogen Microscopy as a route to ultra-high resolution**
by C. Weiss (2012), II, 165 pages
ISBN: 978-3-89336-813-6

48. **High Temperature Radio-Frequency Superconducting Quantum Interference Device System for Detection of Magnetic Nanoparticles**
by A. Pretzell (2012), 122 pages
ISBN: 978-3-89336-814-3

49. **Study of Molecule-Metal Interfaces by Means of the Normal Incidence X-ray Standing Wave Technique**
by G. Mercurio (2012), XXII, 361 pages
ISBN: 978-3-89336-816-7

50. **5th Georgian-German School and Workshop in Basic Science**
Tbilisi, Georgia/August 6 – 10, 2012. Batumi, Georgia/August 13 – 17, 2012.
Org. Committee: E. Abrosimova, A. Bakuridze, A. Kacharava, A. Kvitashvili, A. Prangishvili, H. Ströher (2012); CD-ROM
ISBN: 978-3-89336-818-1

51. **Exploring the electronic properties of novel spintronic materials by photoelectron spectroscopy**
by A. Herdt (2012), ii, 126 pages
ISBN: 978-3-89336-831-0

52. **Quantum Information Processing**
Lecture Notes of the 44th IFF Spring School 2013
February 25 – March 8, 2013 Jülich, Germany
edited by D. DiVincenzo …. ca. 1000 pages
ISBN: 978-3-89336-833-4